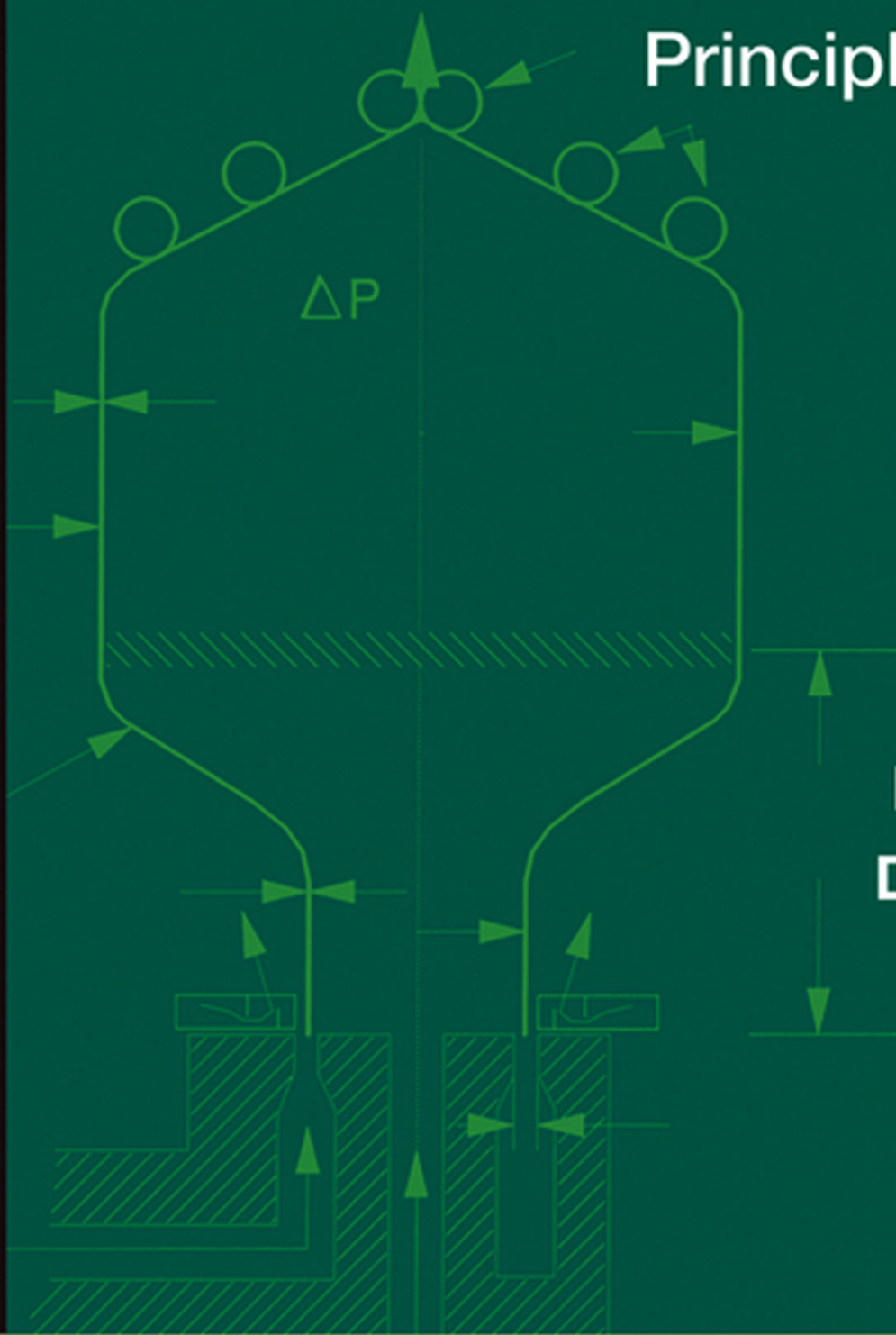


SECOND EDITION

Polymer Processing

Principles and Design



Donald G. Baird
Dimitris I. Collias

WILEY

POLYMER PROCESSING

POLYMER PROCESSING

Principles and Design

Second Edition

DONALD G. BAIRD

Department of Chemical Engineering
Virginia Polytechnic Institute and State University
Blacksburg, Virginia

DIMITRIS I. COLLIAS

Procter & Gamble Co.
Cincinnati, Ohio

WILEY

Copyright © 2014 by John Wiley & Sons, Inc. All rights reserved.

Published by John Wiley & Sons, Inc., Hoboken, New Jersey.
Published simultaneously in Canada.

No part of this publication may be reproduced, stored in a retrieval system, or transmitted in any form or by any means, electronic, mechanical, photocopying, recording, scanning, or otherwise, except as permitted under Section 107 or 108 of the 1976 United States Copyright Act, without either the prior written permission of the Publisher, or authorization through payment of the appropriate per-copy fee to the Copyright Clearance Center, Inc., 222 Rosewood Drive, Danvers, MA 01923, (978) 750-8400, fax (978) 750-4470, or on the web at www.copyright.com. Requests to the Publisher for permission should be addressed to the Permissions Department, John Wiley & Sons, Inc., 111 River Street, Hoboken, NJ 07030, (201) 748-6011, fax (201) 748-6008, or online at <http://www.wiley.com/go/permission>.

Limit of Liability/Disclaimer of Warranty: While the publisher and author have used their best efforts in preparing this book, they make no representations or warranties with respect to the accuracy or completeness of the contents of this book and specifically disclaim any implied warranties of merchantability or fitness for a particular purpose. No warranty may be created or extended by sales representatives or written sales materials. The advice and strategies contained herein may not be suitable for your situation. You should consult with a professional where appropriate. Neither the publisher nor author shall be liable for any loss of profit or any other commercial damages, including but not limited to special, incidental, consequential, or other damages.

For general information on our other products and services or for technical support, please contact our Customer Care Department within the United States at (800) 762-2974, outside the United States at (317) 572-3993 or fax (317) 572-4002.

Wiley also publishes its books in a variety of electronic formats and by print-on-demand. Not all content that is available in standard print versions of this book may appear or be packaged in all book formats. If you have purchased a version of this book that did not include media that is referenced by or accompanies a standard print version, you may request this media by visiting <http://booksupport.wiley.com>. For more information about Wiley products, visit us at www.wiley.com.

Library of Congress Cataloging-in-Publication Data:

Baird, Donald G.

Polymer processing : principles and design / by Donald G. Baird, Department of Chemical Engineering, Virginia Polytechnic Institute and State University, Blacksburg, VA, Dimitris I. Collias, Procter & Gamble Co., Cincinnati, OH. – Second edition.

pages cm

Includes index.

ISBN 978-0-470-93058-8 (cloth)

1. Thermoplastics. I. Collias, Dimitris I. II. Title.

TP1180.T5B26 2014

668.4'23–dc23

2013021897

Printed in the United States of America

10 9 8 7 6 5 4 3 2 1

CONTENTS

Preface	xi
Preface to the First Edition	xiii
Acknowledgments	xv
1 Importance of Process Design	1
1.1 Classification of Polymer Processes, 1	
1.2 Film Blowing: Case Study, 5	
1.3 Basics of Polymer Process Design, 7	
References, 8	
2 Isothermal Flow of Purely Viscous Non-Newtonian Fluids	9
Design Problem I Design of a Blow Molding Die, 9	
2.1 Viscous Behavior of Polymer Melts, 10	
2.2 One-Dimensional Isothermal Flows, 13	
2.2.1 Flow Through an Annular Die, 14	
2.2.2 Flow in a Wire Coating Die, 17	
2.3 Equations of Change for Isothermal Systems, 19	
2.4 Useful Approximations, 26	
2.5 Solution to Design Problem I, 27	
2.5.1 Lubrication Approximation Solution, 27	
2.5.2 Computer Solution, 29	
Problems, 30	
References, 34	
3 Viscoelastic Response of Polymeric Fluids and Fiber Suspensions	37
Design Problem II Design of a Parison Die for a Viscoelastic Fluid, 37	
3.1 Material Functions for Viscoelastic Fluids, 38	
3.1.1 Kinematics, 38	
3.1.2 Stress Tensor Components, 39	
3.1.3 Material Functions for Shear Flow, 40	
3.1.4 Shear-Free Flow Material Functions, 43	

3.2	Nonlinear Constitutive Equations, 44	
3.2.1	Description of Several Models, 44	
3.2.2	Fiber Suspensions, 52	
3.3	Rheometry, 55	
3.3.1	Shear Flow Measurements, 56	
3.3.2	Shear-Free Flow Measurements, 58	
3.4	Useful Relations for Material Functions, 60	
3.4.1	Effect of Molecular Weight, 60	
3.4.2	Relations Between Linear Viscoelastic Properties and Viscometric Functions, 61	
3.4.3	Branching, 61	
3.5	Rheological Measurements and Polymer Processability, 62	
3.6	Solution to Design Problem II, 64	
	Problems, 66	
	References, 70	
4	Diffusion and Mass Transfer	73
	Design Problem III Design of a Dry-Spinning System, 73	
4.1	Mass Transfer Fundamentals, 74	
4.1.1	Definitions of Concentrations and Velocities, 74	
4.1.2	Fluxes and Their Relationships, 76	
4.1.3	Fick's First Law of Diffusion, 76	
4.1.4	Microscopic Material Balance, 78	
4.1.5	Similarity with Heat Transfer: Simple Applications, 80	
4.2	Diffusivity, Solubility, and Permeability in Polymer Systems, 84	
4.2.1	Diffusivity and Solubility of Simple Gases, 84	
4.2.2	Permeability of Simple Gases and Permachor, 87	
4.2.3	Moisture Sorption and Diffusion, 90	
4.2.4	Permeation of Higher-Activity Permeants, 90	
4.2.5	Polymer-Polymer Diffusion, 93	
4.2.6	Measurement Techniques and Their Mathematics, 94	
4.3	Non-Fickian Transport, 95	
4.4	Mass Transfer Coefficients, 96	
4.4.1	Definitions, 96	
4.4.2	Analogies Between Heat and Mass Transfer, 97	
4.5	Solution to Design Problem III, 99	
	Problems, 101	
	References, 108	
5	Nonisothermal Aspects of Polymer Processing	111
	Design Problem IV Casting of Polypropylene Film, 111	
5.1	Temperature Effects on Rheological Properties, 111	
5.2	The Energy Equation, 113	
5.2.1	Shell Energy Balances, 113	
5.2.2	Equation of Thermal Energy, 117	
5.3	Thermal Transport Properties, 120	
5.3.1	Homogeneous Polymer Systems, 120	
5.3.2	Thermal Properties of Composite Systems, 123	
5.4	Heating and Cooling of Nondeforming Polymeric Materials, 124	
5.4.1	Transient Heat Conduction in Nondeforming Systems, 125	
5.4.2	Heat Transfer Coefficients, 130	
5.4.3	Radiation Heat Transfer, 132	

- 5.5 Crystallization, Morphology, and Orientation, 135
 - 5.5.1 Crystallization in the Quiescent State, 136
 - 5.5.2 Other Factors Affecting Crystallization, 142
 - 5.5.3 Polymer Molecular Orientation, 143
- 5.6 Solution to Design Problem IV, 145
 - Problems, 147
 - References, 150

6 Mixing 153

- Design Problem V Design of a Multilayered Extrusion Die, 153
- 6.1 Description of Mixing, 154
- 6.2 Characterization of the State of Mixture, 156
 - 6.2.1 Statistical Description of Mixing, 157
 - 6.2.2 Scale and Intensity of Segregation, 161
 - 6.2.3 Mixing Measurement Techniques, 163
- 6.3 Striation Thickness and Laminar Mixing, 164
 - 6.3.1 Striation Thickness Reduction from Geometrical Arguments, 164
 - 6.3.2 Striation Thickness Reduction from Kinematical Arguments, 169
 - 6.3.3 Laminar Mixing in Simple Geometries, 171
- 6.4 Residence Time and Strain Distributions, 174
 - 6.4.1 Residence Time Distribution, 174
 - 6.4.2 Strain Distribution, 177
- 6.5 Dispersive Mixing, 180
 - 6.5.1 Dispersion of Agglomerates, 180
 - 6.5.2 Liquid–Liquid Dispersion, 182
- 6.6 Thermodynamics of Mixing, 188
- 6.7 Chaotic Mixing, 189
- 6.8 Solution to Design Problem V, 191
 - Problems, 194
 - References, 198

7 Extrusion Dies 201

- Design Problem VI Coextrusion Blow Molding Die, 201
- 7.1 Extrudate Nonuniformities, 202
- 7.2 Viscoelastic Phenomena, 203
 - 7.2.1 Flow Behavior in Contractions, 203
 - 7.2.2 Extrusion Instabilities, 203
 - 7.2.3 Die Swell, 207
- 7.3 Sheet and Film Dies, 212
- 7.4 Annular Dies, 216
 - 7.4.1 Center-Fed Annular Dies, 216
 - 7.4.2 Side-Fed and Spiral Mandrel Dies, 217
 - 7.4.3 Wire Coating Dies, 217
- 7.5 Profile Extrusion Dies, 220
- 7.6 Multiple Layer Extrusion, 222
 - 7.6.1 General Considerations, 222
 - 7.6.2 Design Equations, 224
 - 7.6.3 Flow Instabilities in Multiple Layer Flow, 227
- 7.7 Solution to Design Problem VI, 228
 - Problems, 230
 - References, 234

8 Extruders	235
Design Problem VII Design of a Devolatilization Section for a Single-Screw Extruder, 235	
8.1 Description of Extruders, 235	
8.1.1 Single-Screw Extruders, 237	
8.1.2 Twin-Screw Extruders, 238	
8.2 Hopper Design, 239	
8.3 Plasticating Single-Screw Extruders, 242	
8.3.1 Solids Transport, 242	
8.3.2 Delay and Melting Zones, 246	
8.3.3 Metering Section, 250	
8.4 Twin-Screw Extruders, 253	
8.4.1 Self-wiping Corotating Twin-Screw Extruders, 253	
8.4.2 Intermeshing Counterrotating Extruders, 256	
8.5 Mixing, Devolatilization, and Reactions in Extruders, 258	
8.5.1 Mixing, 258	
8.5.2 Devolatilization in Extruders, 262	
8.5.3 Reactive Extrusion, 264	
8.6 Solution to Design Problem VII, 265	
8.6.1 Dimensional Analysis, 265	
8.6.2 Diffusion Theory, 267	
Problems, 268	
References, 272	
9 Postdie Processing	275
Design Problem VIII Design of a Film Blowing Process for Garbage Bags, 275	
9.1 Fiber Spinning, 276	
9.1.1 Isothermal Newtonian Model, 278	
9.1.2 Nonisothermal Newtonian Model, 281	
9.1.3 Isothermal Viscoelastic Model, 285	
9.1.4 High-Speed Spinning and Structure Formation, 287	
9.1.5 Instabilities in Fiber Spinning, 290	
9.2 Film Casting and Stretching, 293	
9.2.1 Film Casting, 293	
9.2.2 Stability of Film Casting, 296	
9.2.3 Film Stretching and Properties, 297	
9.3 Film Blowing, 297	
9.3.1 Isothermal Newtonian Model, 299	
9.3.2 Nonisothermal Newtonian Model, 302	
9.3.3 Nonisothermal Non-Newtonian Model, 303	
9.3.4 Biaxial Stretching and Mechanical Properties, 304	
9.3.5 Stability of Film Blowing, 304	
9.3.6 Scaleup, 305	
9.4 Solution to Design Problem VIII, 305	
Problems, 306	
References, 308	

10 Molding and Forming	311
Design Problem IX Design of a Compression Molding Process,	311
10.1 Injection Molding,	311
10.1.1 General Aspects of Injection Molding,	311
10.1.2 Simulation of Injection Molding,	315
10.1.3 Microinjection Molding,	318
10.2 Compression Molding,	319
10.2.1 General Aspects of Compression Molding,	319
10.2.2 Simulation of Compression Molding,	320
10.3 Thermoforming,	322
10.3.1 General Aspects of Thermoforming,	322
10.3.2 Modeling of Thermoforming,	324
10.4 Blow Molding,	328
10.4.1 Technological Aspects of Blow Molding,	328
10.4.2 Simulation of Blow Molding,	330
10.5 Solution to Design Problem IX,	332
Problems,	335
References,	340
11 Process Engineering for Recycled and Renewable Polymers	343
11.1 Life-Cycle Assessment,	343
11.2 Primary Recycling,	348
11.3 Mechanical or Secondary Recycling,	351
11.3.1 Rheology of Mixed Systems,	352
11.3.2 Filtration,	352
11.4 Tertiary or Feedstock Recycling,	354
11.5 Renewable Polymers and Their Processability,	357
11.5.1 Thermal Stability and Processing of Renewable Polymers,	358
Problems,	362
References,	363
Nomenclature	365
Appendix A Rheological Data for Several Polymer Melts	373
Appendix B Physical Properties and Friction Coefficients for Some Common Polymers in the Bulk State	379
Appendix C Thermal Properties of Materials	381
Appendix D Conversion Table	385
Index	387

PREFACE

Since the appearance of the first edition of this textbook in 1995 the main changes that have occurred in the field of polymer processing are the use of polymers from renewable resources and more interest in recycling and reprocessing of polymers (i.e., green engineering). Furthermore, processing technology for the most part has not changed significantly except for a technique referred to as “microinjection molding,” a process designed to deliver extremely small parts (~ 1.0 mg in mass). Hence, the coverage of material as outlined in the original preface can still be followed. We outline the major changes in the textbook below.

Because the field of polymer processing has not changed drastically since the appearance of the first edition of this book nearly 20 years ago, there are no major changes in the overall thrust and purpose of the book. The goal of the book remains unchanged and is to teach the basic principles needed in the design of polymer processing operations for thermoplastics. The main change in the field has been in the area of microinjection molding in which objects such as miniature gears and biomedical devices weighing only a fraction of a gram are produced. Although the general features of the process rely on injection molding, there are still some differences in the design considerations of the process because of the high shear rates and high temperatures required during processing. We have added discussion of the microinjection molding process in Chapter 10.

The major change in the field of polymer processing is the polymers that are processed, which is driven by the need to practice “green engineering.” There is a greater interest in the processing of polymers from renewable resources and reprocessing (i.e., recycling) of polymers that have already been subjected to a processing history. For this reason a new chapter, Chapter 11, has been added to the book, which is concerned with the recycling of thermoplastics and the

processing of renewable polymers. Because the decision to recycle a polymer or to use a polymer from renewable resources cannot be made without the appropriate analysis guided by the purpose to recycle, we introduce the concept of *life cycle assessment* (LCA), which provides a systematic method for determining whether recycling and which form of recycling is the proper environmental choice. Furthermore, we include background, which considers material and energy flows associated with various types of recycling streams as it is important that more energy not be used in recycling plastics than is required in the conversion of raw materials to virgin resin. Chapter 11 also includes discussion of the processing of new-to-world renewable polymers (i.e., polymers that come from renewable resources, e.g., carbohydrates, and are not identical to today’s petroleum-derived polymers). Examples of these polymers are poly(lactic acid) (PLA), thermoplastic starch (TPS), and polyhydroxyalkanoate (PHA). The other category of renewable polymers is that of identical renewable polymers (also called bioidentical polymers), but these polymers require no new knowledge for processing as these renewable polymers have identical structure, performance, and processing to petroleum-derived polymers, with examples being bio-HDPE, bio-PP, and biopoly(butylene succinate) (bio-PBS). The teaching of the subject matter in Chapter 11 can require five or six lectures to do it completely. However, the very basics such as those in Sections 11.1 and 11.2 coupled with an overview of the other sections can be done in two or three lectures. It is recommended that the students at least be exposed to the green engineering topics in Chapter 11.

The other additions to the book include discussion of the rheology of polymers containing fibers that serve to reinforce the solid polymer and the role of sparse long chain branching on the rheology of polymer melts. These topics are discussed

in Chapter 3, and additional problems using the theory are found there also. Fiber suspensions have always been of interest and are included in books on processing of fiber composites. However, because these materials are processed by means of equipment used for thermoplastics and because of their importance in the generation of lightweight parts, we have included the subject matter in this book. Furthermore, the significant changes in the rheology and processing of polymers containing sparse long chain branching, that is, chains with less than about 10 long branches per chain (greater than the critical entanglement molecular weight), justify the inclusion of a brief coverage of this topic in Chapter 3.

Finally, in the first edition of this book we included numerical subroutines (International Mathematics and Statistical Libraries, IMSL, from Visual Numerics). However, the use of these subroutines requires knowledge of a higher

level programming language, such as Fortran, which is typically not taught in the engineering curriculums any more. Hence, we have removed from the numerical examples the use of these specific subroutines and report only the numerical results that may have been obtained by means of either the IMSL subroutines or Excel or MATLAB. These solutions are available on the Wiley website (<http://booksupport.wiley.com>) and are listed via the example number and which numerical method is employed. Many engineering students have been exposed to MATLAB and certainly have access to Excel. The discussion of the use of the IMSL subroutines is also given on the website, but the subroutines are no longer included with the book.

DONALD G. BAIRD
DIMITRIS I. COLLIAS

November 2013

PREFACE TO THE FIRST EDITION

This book is intended to serve as an introduction to the design of processes for thermoplastics. It is intended to meet the needs of senior chemical, mechanical, and materials engineers who have been exposed to fluid mechanics, heat transfer, and mass transfer. With the supplementing of certain parts, the book can also be used by graduate students. In particular by supplementing the material in Chapters 2 and 3 with a more sophisticated coverage of nonlinear constitutive equations and the addition of topics in finite element methods, the book can be used in more advanced courses.

A large number of chemical and mechanical engineers are employed in the polymer industry. They are asked to improve existing processes or to design new ones with the intent of providing polymeric materials with a certain level of properties: for example, mechanical, optical, electrical, or barrier. Although there has been a belief that when a given polymer system does not meet the desired requirements that a new polymer must be used, it is becoming more apparent that the properties of the given polymer can be altered by the method of processing or the addition of other materials such as other polymers, fillers, glass fibers, or plasticizers. Certainly a large number of these activities are carried out by trial-and-error (Edisonian research) approaches. The time to carry out the experiments can be reduced considerably by quantitative design work aimed at estimating the processing conditions which will provide the desired properties. Yet, engineers receive little or no training in the design of polymer processes during their education. Part of the reason is they have an inappropriate background in transport phenomena, and the other is the lack of the mathematical tools required to solve the equations which arise in the design of polymer processes. One aim of this book is to strengthen the background of engineering students in transport phenomena as applied

to polymer processing and the other is to introduce them to numerical simulation.

As there are several books available concerned with the processing of polymers with an emphasis on thermoplastics, the question is: How does this book meet the needs as described in the above paragraph any differently or better than existing books? First of all we cannot revolutionize the area of teaching polymer processing as the principles do not change. What we have done, however, is make the material more accessible for solving polymer processing design problems. Many times there may be several theories available to use in the modeling of a process. Rather than discuss all the different approaches, we choose what we think is the best theory (but pointing out its limitations and shortcomings) and show how to use it in solving design problems. Another important feature is that we provide the mathematical tools for solving the equations. Other books leave the student with the equations and a description of how they were solved. This does not help someone who has a slightly different set of equations and needs an answer. In this book as much as possible we leave the student with several methods for getting a solution. Included with this book are a selection of the subroutines from the International Mathematics and Statistical Libraries (IMSL) (Visual Numerics Inc., Houston, TX) for the solution of various types of equations which arise in the design of polymer processes. The subroutines have been made relatively “user-friendly,” and by following the examples and the descriptions of each subroutine given in Appendix D solutions are readily available to a number of complex problems. The book is not totally dependent on the use of the computer, but there are certain problems which just can’t be solved without resorting to numerical techniques. Rather than dwell on the numerical techniques we choose to use them in somewhat of a “black box” form. However,

sufficient documentation is available in the references if it becomes necessary to understand the numerical technique. Although there are many who will criticize this approach, during the time of their objection the equations will be solved and an answer will be available. With practice the student will learn when the “black box” has spit out senseless results.

The book is organized in such a way that the first five chapters are concerned with the background needed to design polymer processes while the last five chapters are concerned with the specifics of various types of processes. Chapter 1 contains an overview of polymer processing techniques with the intent of facilitating examples and problems used throughout the next four chapters. Furthermore, a case study presented at the end of Chapter 1 shows how the properties of blown film strongly depend on the processing conditions. Each of the remaining chapters is started with a design problem which serves to motivate the material presented in the chapter. Chapters 2 and 3 present the basics of non-Newtonian fluid mechanics which are crucial to the design of polymer processes. In Chapter 4 we introduce the topic of mass transfer as applied to polymeric systems. Finally, in Chapter 5 the non-isothermal aspects of polymer processing are discussed. In Chapter 5 the interrelation between processing, structure, and properties is emphasized. These first five chapters contain all the background information including examples illustrating the use of the IMSL subroutines. Mixing is so important to the processing of polymers that we have devoted a full chapter, Chapter 6, to this topic. The remaining chapters are devoted to the factors associated with the design of various processing methods. We have tried to arrange the subject matter by similarities in the process. In each chapter we are careful to make it known what aspects of design the student should be able to execute based on their educational level. In many books on polymer processing it is not clear to the student just what part of the design he or she should be able to carry out.

All but the first chapter contain problem sets. The problems are grouped into four classes:

Class A: These problems can be solved using equations or graphs given in the chapter and usually involve arithmetic manipulations.

Class B: These problems require the development of equations and serve to reinforce the major subject matter in the chapter.

Class C: These problems require the use of the computer and are aimed at making direct use of the IMSL subroutines.

Class D: These problems are design problems and as such have a number of solutions. They require the use of all the previous subject matter but with an emphasis on the material presented in the given chapter.

We have attempted to integrate the problems with the subject matter in an effort to reinforce the material in the given chapter. Furthermore, most of the problems have been motivated by situations which might be encountered in industry.

The coverage of the material in this book requires from 45 to 60 lectures. The number of lectures depends on the background of the students and the depth to which one covers the last five chapters of the book. In most cases, it is recommended to teach the material in Chapter 5 first before teaching Chapter 4, as the heat transfer topics facilitate the teaching of mass transfer. If only 30 lectures are available for teaching the material, then it is recommended to eliminate Chapters 4 and 6. However, this depends on the specific preference of the instructor.

Finally, the book has evolved out of teaching a senior level course in polymer processing at Virginia Tech, the teaching of numerical methods to undergraduate chemical engineers, and consulting experiences. First, it was apparent that a reinforcement of transport phenomena was needed before one could begin to teach polymer processing. Second, it was recognized that B.S. engineers are required to deliver answers and don't have time to weigh out all the variations and perturbations in the various theories. Third, undergraduate engineers are becoming computer literate and have less fear of using computers than many professors. With these ideas in mind we tried to write a book on polymer processing which provides the necessary tools to do design calculations and at the same time informs the student exactly what he or she can be expected to do with the level of material at hand.

DONALD G. BAIRD
DIMITRIS I. COLLIAS

*Blacksburg, Virginia
February 1993*

ACKNOWLEDGMENTS

Without the contributions of a number of people our efforts in writing this book would have been fruitless.

One of us (D.G.B.) would specifically like to thank the Department of Chemical Engineering and the College of Engineering at Virginia Polytechnic Institute and State University for providing study leave during the Spring Semester of 1992 so that a full effort could be devoted to writing the book.

Diane Cannaday deserves our most sincere appreciation for typing of the manuscript and enduring the continuous changes and modifications. The help of Tina Kirk in preparing changes in the second edition is sincerely appreciated.

Sylvan Chardon and Jennifer Brooks produced the numerous figures and graphs.

A number of graduate students in the polymer processing group have contributed to the text in various ways. In particular, we would like to thank Will Hartt, Hugh O'Donnell, Paulo de Souza, Gerhard Guenther, Agnita Handlos, David Shelby, Ed Sabol, and Roger Davis. Kevin J. Meyer prepared many of the new figures associated with the second edition.

Finally, we would like to thank our families, especially our wives, Patricia and Eugenia, for their patience and consideration during times when it seemed that all that mattered was the writing of the book.

D. G. B.
D. I. C.

1

IMPORTANCE OF PROCESS DESIGN

The intention of this chapter is not merely to present the technology of polymer processing but to initiate the concepts required in the design of polymer processes. A knowledge of the types of polymers available today and the methods by which they are processed is certainly needed, but this is available in several sources such as *Modern Plastics Encyclopedia* (Green, 1992) and the *Plastics Engineering Handbook* (Frados, 1976). In this chapter we present primarily an overview of the major processes used in the processing of thermoplastics. In Section 1.1 we begin by classifying the various processes and point out where design is important. In Section 1.2 we present a case study concerned with film blowing to illustrate how the final physical properties are related all the way back to the melt flow of a polymer through the die. Finally, in Section 1.3 we summarize the principles on which polymer process design and analysis are based.

1.1 CLASSIFICATION OF POLYMER PROCESSES

The major processes for thermoplastics can be categorized as follows: extrusion, postdie processing, forming, and injection molding. We describe specific examples of some of the more common of these processes here.

The largest volume of thermoplastics is probably processed by means of extrusion. The extruder is the main device used to melt and pump thermoplastics through the shaping device called a die. There are basically two types of extruders: single and twin screws. The single-screw extruder is shown in Figure 1.1. The single-screw extruder basically consists of a screw (Fig. 1.2) that rotates within a metallic barrel. The

length to diameter ratio (L/D) usually falls in the range of 20 to 24 with diameters falling in the range of 1.25 to 50 cm. The primary design factors are the screw pitch (or helix angle, θ) and the channel depth profile. The main function of the plasticating extruder is to melt solid polymer and to deliver a homogeneous melt to the die at the end of the extruder. The extruder can also be used as a mixing device, a reactor, and a devolatilization tool (see Chapter 8).

There are an equal number of twin-screw extruders in use as single-screw extruders today. There are many different configurations available including corotating and counterrotating screws (see Fig. 1.3) and intermeshing and nonintermeshing screws. These extruders are primarily adapted to handling difficult to process materials and are used for compounding and mixing operations. The analysis and design of these devices is quite complicated and somewhat out of the range of the material level in this text. However, some of the basic design elements are discussed in Chapter 8.

The extruder feeds a shaping device called a die. The performance of the single-screw and corotating twin-screw extruders is affected by resistance to flow offered by the die. Hence, we cannot separate extruder design from the die design. Problems in die design include distributing the melt flow uniformly over the width of a die, obtaining a uniform thermal history, predicting the die dimensions that lead to the desired final shape, and the production of a smooth extrudate free of surface irregularities. Some of these design problems are accessible at this level of material while others are still research problems (see Chapter 6).

There are many types of extrusion die geometries including those for producing sheet and film, pipe and tubing, rods

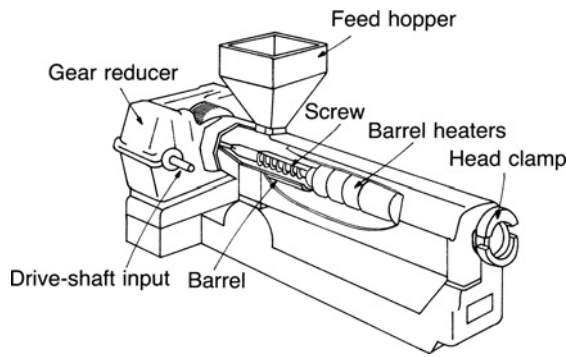


FIGURE 1.1 Typical single-screw extruder. (Reprinted by permission of the author from Middleman, 1977.)

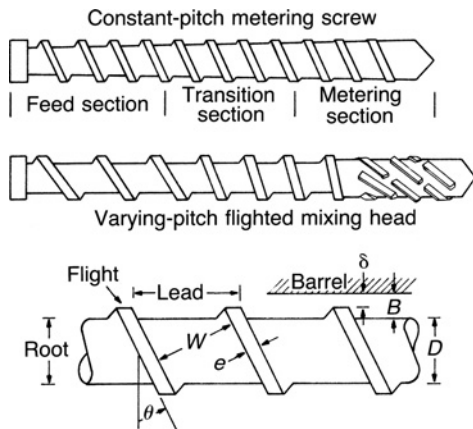


FIGURE 1.2 Two different extruder screw geometries along with the various geometric factors that describe the characteristics of the screw. (Reprinted by permission of the publisher from Middleman, 1977.)

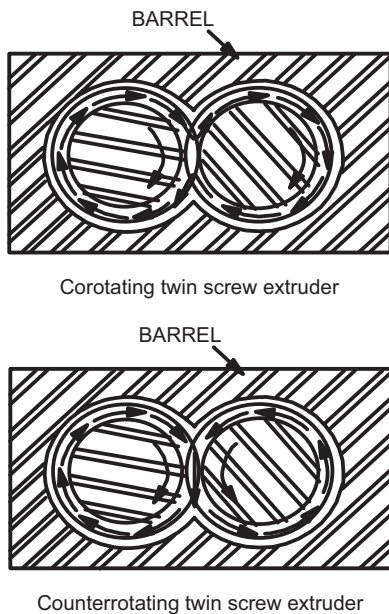


FIGURE 1.3 Cross-sectional view of corotating and counterrotating twin-screw extruders.

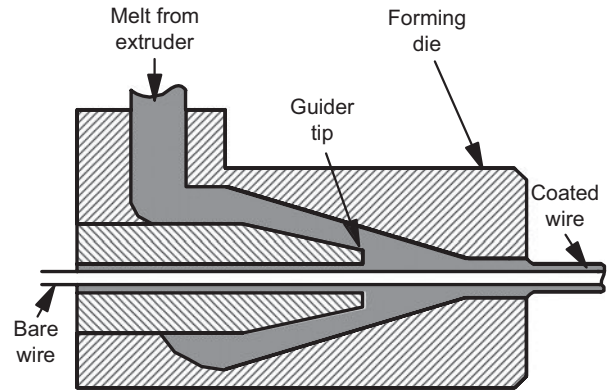


FIGURE 1.4 Cross-head wire coating die. (Reprinted by permission of the publisher from Tadmor and Gogos, 1979.)

and fiber, irregular cross sections (profiles), and coating wire. As an example, a wire coating die is shown in Figure 1.4. Here metal wire is pulled through the center of the die with melt being pumped through the opening to encapsulate the wire. The design problems encountered here are concerned with providing melt flowing under laminar flow conditions at the highest extrusion rate possible and to give a coating of polymer of specified thickness and uniformity. At some critical condition polymers undergo a low Reynolds number flow instability, which is called melt fracture and which leads to a nonuniform coating. Furthermore, the melt expands on leaving the die leading to a coating that can be several times thicker than the die gap itself. (This is associated with the phenomenon of die swell.) The problems are quite similar for other types of extrusion processes even though the die geometry is different. The details associated with die design are presented in Chapter 7.

We next turn to postdie processing operations. Examples of these processes include fiber spinning (Fig. 1.5), film blowing (Fig. 1.6), and sheet forming (Fig. 1.7). These processes have a number of similarities. In particular, they are free surface processes in which the shape and thickness or diameter of the extrudate are determined by the rheological (flow) properties of the melt, the die dimensions, cooling conditions, and take-up speed relative to the extrusion rate. The physical and, in the case of film blowing and sheet forming, the

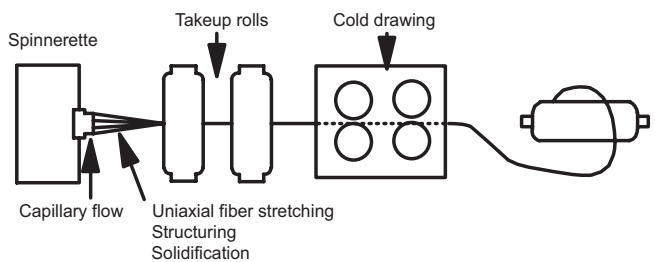


FIGURE 1.5 Fiber melt spinning process. (Reprinted by permission of the publisher from Tadmor and Gogos, 1979.)

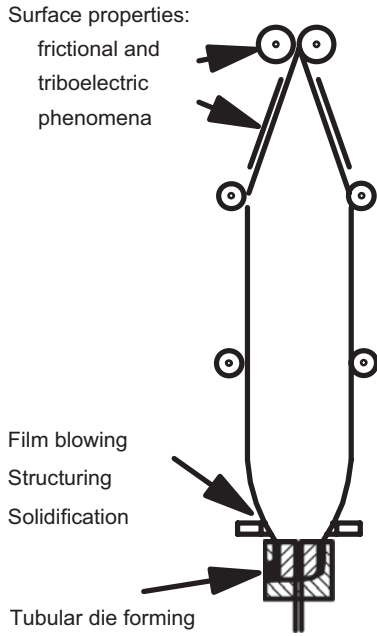


FIGURE 1.6 Film blowing process. (Reprinted by permission of the publisher from Richardson, 1974.)

optical properties are determined by both the conditions of flow in the die as well as cooling rates and stretching conditions of the melt during the cooling process. Furthermore, slight changes in the rheological properties of the melt can have a significant effect on the final film or fiber properties. Design considerations must include predictions of conditions which provide not only the desired dimensions but the optical and physical properties of the film, fiber, or sheet.

The third category of processing of thermoplastics is forming. Three examples of this type of process are blow molding (Fig. 1.8), thermoforming (Fig. 1.9), and compression molding (Fig. 1.10). Blow molding is primarily employed for making containers used to package a wide variety of

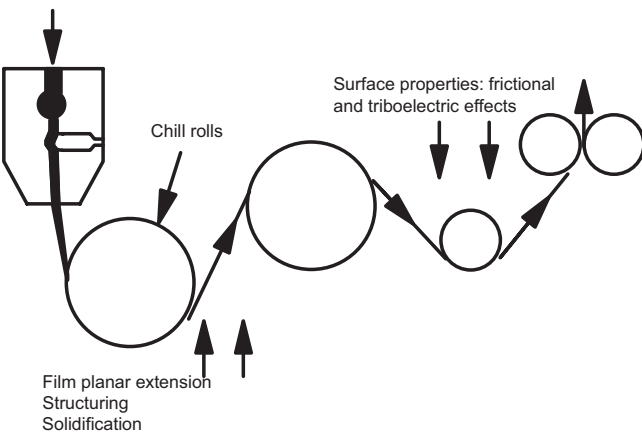


FIGURE 1.7 Flat film and sheet process. (Reprinted by permission of the publisher from Tadmor and Gogos, 1979.)

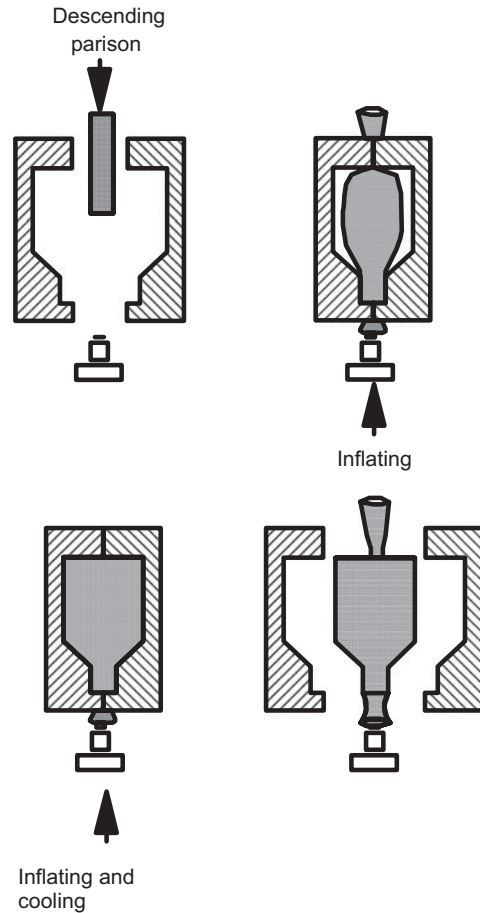


FIGURE 1.8 Blow molding process. (Reprinted by permission of the publisher from Holmes-Walker, 1975.)

fluids. Although polyolefins, such as high density polyethylene (HDPE), or polyethyleneterephthalate (PET), both of which can be considered as commodity resins, are commonly used, interest is growing in using this technique for the processing of higher performance engineering thermoplastics.

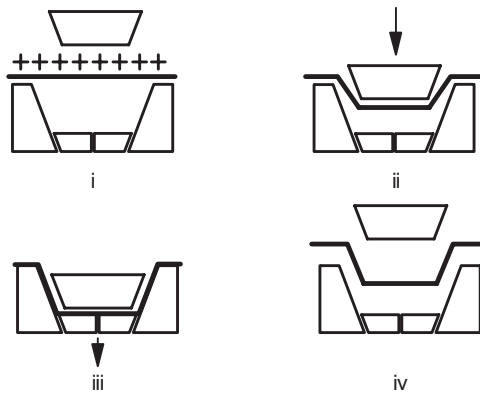


FIGURE 1.9 Plug-assisted vacuum thermoforming. (Reprinted by permission of the publisher from Greene, 1977.)

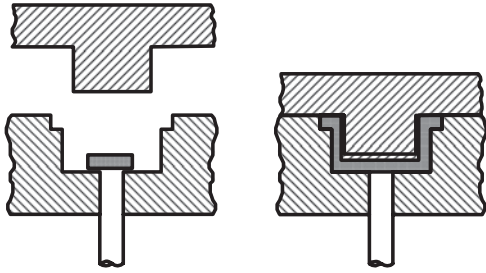


FIGURE 1.10 Compression molding process. (Reprinted by permission of the publisher from Tadmor and Gogos, 1979.)

Essentially a parison, which has been extruded or injection molded, is inflated by air until it fills the mold cavity. The inflated parison is held in contact with the cold mold walls until it is solidified. Considering the process of thermoforming, a sheet of polymer is heated by radiation (and sometimes cooled intermittently by forced convection) to a temperature above its glass transition temperature or in some cases above the crystalline melting temperature and then pressed into the bottom part of the mold (female part) either using mechanical force, pressure, or by pulling a vacuum. The key flow property is the extensional flow behavior of the melt, which controls the uniformity of the part thickness. Sometimes the deformation is applied at a temperature just below the onset of melting, in which case the process is referred to as solid phase forming. At other times the sheet is extruded directly to the forming unit and is formed before it cools down. (This is called scrapless or continuous thermoforming.) Some of the key design considerations are the time required to heat the sheet, the final thickness of the part especially around sharp corners, and the cooling rate which controls the amount and type of crystallinity. In compression molding a slug of polymer is heated and then pressure is applied to squeeze the material into the remaining part of the mold. Some aspects of forming are discussed in Chapter 10.

The last general category is that of injection molding, which is shown in Figure 1.11. Polymer is melted and pumped forward just as in a screw extruder. The screw is then advanced forward by a hydraulic system that pushes the melt into the mold. Because of the high deformation and cooling rates, a considerable degree of structuring and molecular orientation occurs during mold filling. The physical properties of injection molded parts can be affected significantly

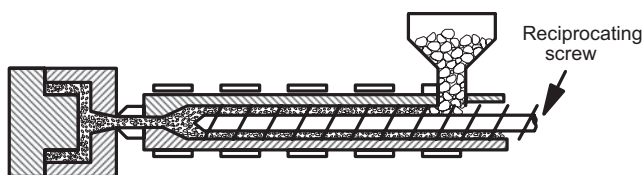


FIGURE 1.11 Typical injection molding unit. (Reprinted by permission of the publisher from Tadmor and Gogos, 1979.)

by processing conditions. Design considerations include the required injection pressure to fill the mold cavity, the location of weld lines (places where two melt fronts come together), cooling rates, length of hold time in the mold, and distribution of molecular orientation. In conventional injection molding, parts may vary from a few grams to many kilograms (e.g., a car hood or trunk).

In the last 10 to 15 years one of the major variations in the injection molding process has been *microinjection molding* (μ IM), which appears to be one of the most efficient processes for the large-scale production of thermoplastic polymer microparts (Giboz et al., 2007). These microparts can be as small as 0.6 mg and possess dimensions in the micron range along with dimensional tolerances in the range of microns. Examples of microparts are microelectromechanical systems, which is the name given to the combination of miniaturized mechanical and electronic structures in a system, and miniature gears and lenses. Biomedical parts for insertion into the body such as heart stents and sensors are also produced by this method. Micromolding is still very much in its infancy as a new branch of injection molding. As will be discussed in Chapter 10 (Section 10.1.3), it is not just about scaling everything down, but it is a specialized technique in its own right, with a different set of challenges. Some of these factors are out of the realm of the material that can be covered by this book, but those aspects that are accessible are presented in Chapter 10.

Although the majority of the material in this book is concerned with the processing of thermoplastics, the processing of thermosetting systems should also be mentioned for the sake of completeness. We describe three types of processes involving reactive processing: reaction injection molding (RIM), compression molding, and pultrusion. RIM is a process in which two liquid intermediates are metered separately to a mixing head where they are combined by high pressure impingement mixing and subsequently flow into a mold where they are polymerized to form a molded part (see Fig. 1.12). A typical process consists of the reaction of diisocyanate and a polyol to form polyurethane. The important design factors are the degree of mixing and the appropriate heat transfer conditions to ensure uniform curing conditions in the mold. This process is discussed in more detail elsewhere (Becker, 1979).

Thermosetting composites can be processed by means of compression molding of uncured resin. Usually fiber reinforcement is used to provide additional strength and stiffness. The application of pressure pushes the resin into the fiber reinforcement and heat crosslinks the resin to form a solid material. The critical factors are the flow of the uncured resin into and around the reinforcement and the uniform and complete cure of the resin throughout the part. This technique is used primarily in the aerospace and automobile industries.

Pultrusion is a process used for making continuous filament reinforced composite extruded profiles (see Fig. 1.13).

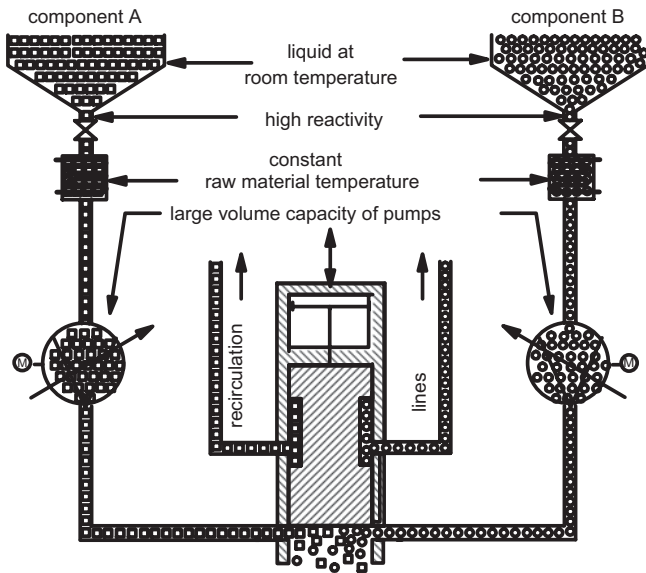


FIGURE 1.12 Reaction injection molding (RIM) process. (Reprinted by permission of the publisher from Becker, 1979.)

Reinforcing filaments, such as glass fiber roving, are saturated with catalyzed resin and then pulled through an orifice similar to an extrusion die. As the two materials pass through the die, polymerization of the resin occurs to continuously form a rigid cured profile corresponding to the die orifice shape. The materials are pulled through the die rather than being pumped. Although the primary resins used are of the thermosetting type such as polyester, vinyl ester, and epoxy, thermoplastic resins can be utilized in the same process. The major design considerations for thermosetting systems consist of dispersion of the resin in the reinforcement and the conditions for complete cure of the resin. The processing

of thermosetting systems is discussed elsewhere (Macosko, 1989).

The intention in Section 1.1 was more than just to review the technology of polymer processing, but to point out factors that must be considered in the design of polymer processes. However, since most students have little knowledge of the technology of processing of polymers, some general introduction is of value. Furthermore, a physical picture of the various processes is required to facilitate the discussion of the material presented in the next four chapters.

1.2 FILM BLOWING: CASE STUDY

The last section was merely concerned with describing the technology of polymer processing. This section is concerned with illustrating the role of processing in affecting the properties of polymeric systems. In particular, the properties of films of polybutylene (PB1) generated by means of film blowing are shown to be highly sensitive to processing conditions.

Most blown film is made from some form of polyethylene (PE), but polybutylene, PB1, has been considered because it is slightly cheaper to use in the production of film. However, it does not lead to the same physical properties without changing the processing conditions. Identification of the appropriate processing conditions is usually done either by a trial-and-error approach or through statistically designed experiments. If a model of film blowing was available, or if one could apply dimensional analysis concepts, then it might be possible to find the appropriate processing conditions without carrying out a lengthy set of costly experiments. The following example illustrates the many factors that affect the properties of blown PB1 film.

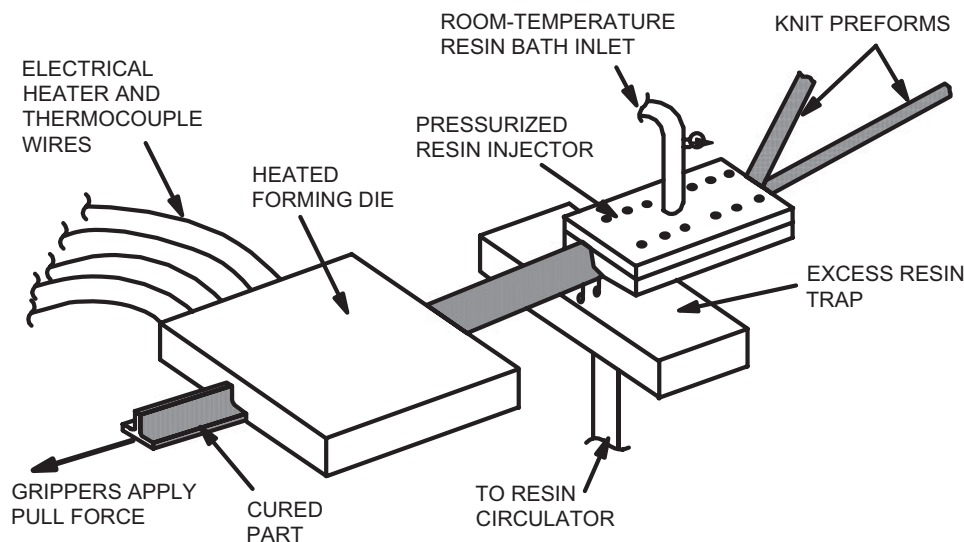


FIGURE 1.13 Pultrusion process.

The film blowing process was shown in Figure 1.6. Polymer pellets are fed to the extruder in which melting, homogenization, and pumping occur. The melt then passes through the die, which is designed such that as it leaves the die, the melt has been subjected to both a uniform deformation as well as thermal history. Air is blown through the center of the die to expand the molten bubble to impart orientation of the molecules in the hoop direction. At the same time the bubble is being stretched as a result of the take-up velocity being greater than the average velocity of the melt leaving the die. The stretching imparted in the two directions controls the degree to which the molecules orient and hence affects the physical properties. Cooling air is blown along the bubble by an air ring, which is placed around the outside of the die. This serves to cause the film to solidify or crystallize and lock in the orientation imparted by the biaxial stretching process. The film is then taken up on a roller and either slit to make flat film or sealed and cut to make bags.

We now look at some of the factors that affect the physical properties of the blown film. The recommendations for the annular die gap opening for a desired film thickness are given in Table 1.1. It is probably clear as to why the die gap is larger than the desired film thickness as the film is to be drawn down to create molecular orientation. What is not clear is why it is recommended that the die land (the annular portion of the die) be shortened as the die gap increases. The physical properties based on the tear strength of the film are found to be significantly affected by the length of the die land as shown in Figure 1.14. Here the tear strength is plotted versus the blow up ratio, BUR, which is the ratio of the final film diameter to the die diameter (outer diameter). It is observed that there is on the order of a threefold difference in the tear strength for a 2.0×10^{-3} in. thick film when the die land is decreased from 1.5 in. to 1.0 in. One reason for this result is that more “die swell” (the expansion of a polymer melt on leaving a die) occurs for the die with the 1.0 in. land length, and hence a higher stretch ratio is required to draw the film down to 2.0×10^{-3} in. This leads to higher orientation of the molecules along the draw direction than in the case of the die with a 1.5 in. land length. Finally, the effect of the die gap on the tear strength measured both along the film length

TABLE 1.1 Die Recommendations for the Blowing of PB1 with a Blow Up Ratio of 2.4–2.8 at a Melt Temperature of 370–390 °F

Film Thickness ($\times 10^3$ in.)	Die Gap (inches)	Land Length (inches)
0.5–1	0.015	$1\frac{1}{2}$ –2
1–2	0.018–0.023	$1\frac{1}{2}$
2–7	0.028–0.032	1
8–15	0.040–0.050	1
15–40	0.050–0.060	1

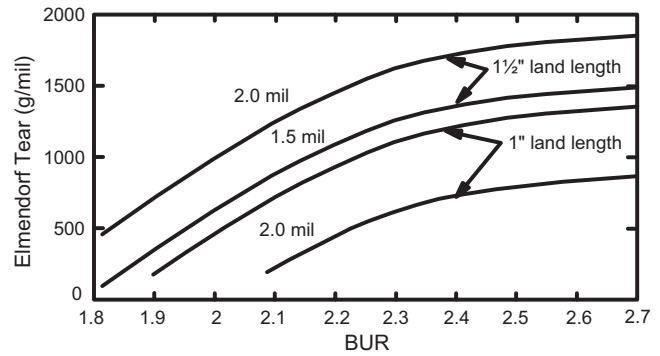


FIGURE 1.14 Effect of the annular die land length on the film tear strength of polybutylene extruded at the rate of 10 m/min for two different film thicknesses.

(this is called the machine direction, MD) and along the circumference of the film (this is called the transverse direction, TD) is shown in Figure 1.15. Here we see that the tear strength in the TD decreases significantly with an increase in die gap, while in the machine direction the effect is significant but nowhere near as large. Again it is not clear as to what would cause the loss of properties in both directions as the die gap increases other than the longer time available for molecular relaxation due to the increase in time required for cooling of the film. Factors other than orientation must be involved in controlling the properties. For example, the amount of crystallinity and the size of the spherulitic regions may play a significant role.

The melt extrusion temperature is also observed (Fig. 1.16) to have a significant effect on the physical properties as the tear strength in both directions increases with increasing melt temperature. This is probably due to lower levels of orientation as the result of lower stress levels in the melt and shorter relaxation times allowing a rapid relaxation of molecular orientation.

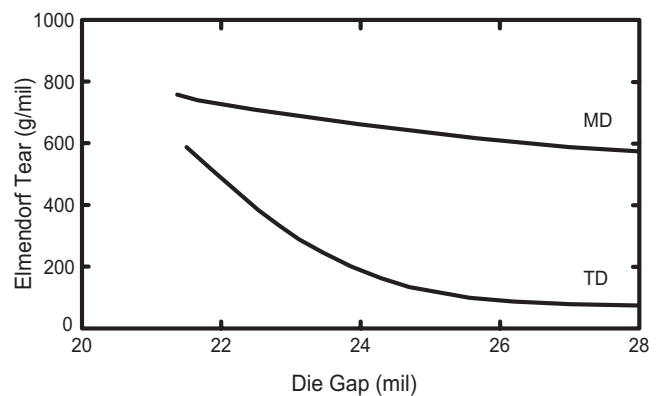


FIGURE 1.15 Effect of die gap on the film tear strength of polybutylene extruded at the rate of 10 m/min. The film thickness is 0.002 in. and the blow up ratio is 2.8.

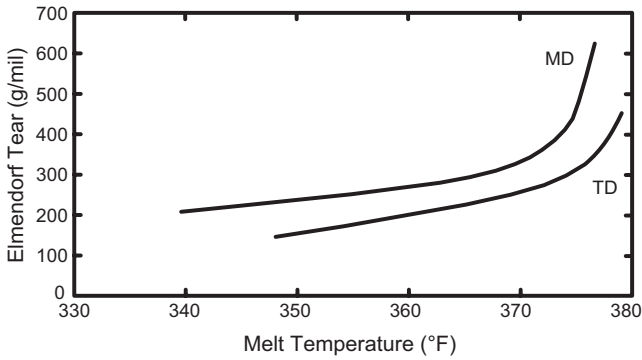


FIGURE 1.16 The effect of melt temperature on the film tear strength of polybutylene film extruded at the rate of 10 m/min. The film thickness is 0.002 in. and the blow up ratio is 2.8.

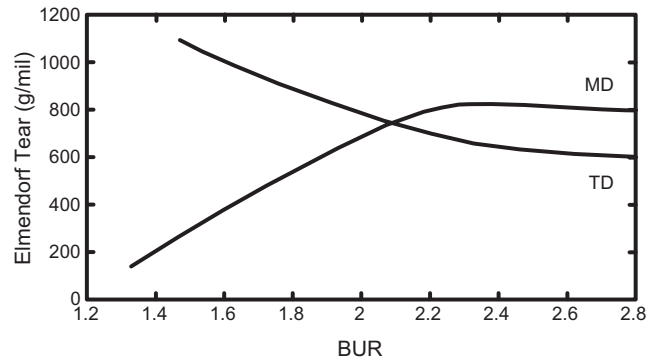


FIGURE 1.17 Effect of blow up ratio on the film tear strength measured along the machine direction (MD) and transverse direction (TD).

The line speed, given in feet per minute (fpm), as shown in Table 1.2, has a very significant effect on the properties. For example, as the line speed increases from 14 fpm, the breaking strength in the MD increases from 4800 g/mil to 6600 g/mil but decreases in the TD from 5000 g/mil to 2300 g/mil (mil here means 0.001 in.). This is mostly associated with the degree of molecular orientation. The more the molecules are oriented along the MD the stronger the films are, but the poorer the tear strength in this direction. The other properties given here can be explained by similar arguments.

The blow up ratio, BUR, can be used to obtain a better balance of properties as shown in Figure 1.17. As BUR increases the tear properties become more uniform in both directions. Biaxial orientation (i.e., orientation of molecules in two directions) is generated in the blowing process, which leads to more uniform properties.

As one can imagine the film blowing process is very difficult to model and, hence, very little quantitative design work has been done. Although the complete modeling of this process is beyond the level of the material in this book (or even an advanced book for that matter), the example serves to illustrate that the properties of a polymeric material are highly dependent on the processing conditions and some of the problems faced by the engineer. In designing a polymer process one must be concerned with not only how much

material per unit time can be produced but with the properties of the material. In the next section we look at the fundamental principles on which the design and analysis of polymer processes is based.

1.3 BASICS OF POLYMER PROCESS DESIGN

In order to design and analyze polymer processes there are common steps associated with nearly every process. Following Tadmor and Gogos (1979), these basic steps are given below:

1. Handling of particulate solids
2. Melting, cooling, and crystallization
3. Pumping and pressurization
4. Mixing
5. Devolatilization and stripping
6. Flow and molecular orientation

These basic steps are based on the following concepts:

1. Transport phenomena—fluid mechanics, heat transfer, and mass transfer
2. Polymer rheology
3. Solid mechanics and flow

TABLE 1.2 Line Speed Versus Properties for PB1

Line Speed (fpm)	Break Strength		Yield Strength		Ultimate Elongation			Tear Strength	
	MD (g/mil)	TD (g/mil)	MD (g/mil)	TD (g/mil)	MD (%)	TD (%)	Dart Drop (g/m ² ·s ²)	MD (g/mil)	TD (g/mil)
14	4800	5000	2000	2000	220	260	350	1700	550
20	4600	3700	2100	2000	160	230	280	1500	550
30	5500	2800	2500	1900	110	170	190	680	390
40	6600	2300	3000	1900	80	150	90	80	270

4. Principles of mixing
5. Chemical reactions

In the first five chapters of this book we deal with the fundamental principles required in the design of polymer processes. The last six chapters are concerned with the details of specific types of processes and the reprocessing of polymers and the processing of renewable polymers.

REFERENCES

- Becker, W. E., Ed. 1979. *Reaction Injection Molding* (Van Nostrand Reinhold Company, New York).
- Frados, J., Ed. 1976. *Plastics Engineering Handbook* (Van Nostrand Reinhold, New York).
- Green, E., Ed. 1992. *Modern Plastics Encyclopedia* (McGraw Hill, New York).
- Greene, R., Ed. 1977. *Modern Plastics Encyclopedia*, Vol. 53 (McGraw Hill, New York).
- Giboz, J., T. Copponnex, and P. Mélé. 2007. "Microinjection Molding of Thermoplastic Polymers: A Review," *J. Micromech. Microeng.*, **17**, R96–R109.
- Holmes-Walker, W. A. 1975. *Polymer Conversion* (Elsevier, London).
- Macosko, C. W. 1989. *RIM: Fundamentals of Reaction Injection Molding* (Hanser, New York).
- Middleman, S. 1977. *Fundamentals of Polymer Processing* (McGraw Hill, New York).
- Richardson, P. N. 1974. *Introduction to Extrusion* (Society of Plastics Engineers, Inc., Greenwich, CT).
- Tadmor, Z. and C. G. Gogos. 1979. *Principles of Polymer Processing* (Wiley, Hoboken, NJ).
- Tadmor, Z. and C. G. Gogos. 2007. *Principles of Polymer Processing*, 2nd edition (Wiley, Hoboken, NJ).

2

ISOTHERMAL FLOW OF PURELY VISCOUS NON-NEWTONIAN FLUIDS

DESIGN PROBLEM I DESIGN OF A BLOW MOLDING DIE

A typical blow molding die is shown in Figure 2.1. The region of particular interest is shown in Figure 2.2. The die exit is the region that controls the final dimensions of the parison, which is a cylindrically shaped tube of polymer. The parison consisting of HDPE is to have a weight of 90 g with an outside diameter of 0.127 m and a wall thickness of 3.81×10^{-4} m. Consider only the conical region in your calculations. The angles α and θ are taken as 0° and 30° , respectively. The distance z_1 should be 20 times the gap thickness. Determine the remaining dimensions of the die required to produce the desired extrudate. At this point neglect die swell (i.e., the increase in diameter and thickness due to elastic recovery) in your calculations. Determine the maximum extrusion rate (m^3/s) and pressure drop assuming the limiting factor is melt fracture. (This occurs when the wall shear stress, τ_w , reaches 1.4×10^5 Pa.) Use the rheological parameters given in Table 2.1. Determine the length of time required to extrude the parison.

- Use the lubrication approximation to determine a design equation (i.e., Q vs. ΔP) and then provide the required information.
- Carry out the design calculations by breaking up the flow region into a series of cones of length Δz . Use the annular flow equations presented in Section 2.2.1 and the computer to get a solution. At 180°C (453 K), $\rho = 965 \text{ kg/m}^3$.

The transport properties of polymeric materials which distinguish them most from other materials are their flow properties or rheological behavior. There are many differences between the flow properties of a polymeric fluid and typical low molecular weight fluids such as water, benzene, sulfuric acid, and other fluids, which we classify as Newtonian. Newtonian fluids can be characterized by a single flow property called viscosity (μ) and their density (ρ). Polymeric fluids, on the other hand, exhibit a viscosity function that depends on shear rate or shear stress, time-dependent rheological properties, viscoelastic behavior such as elastic recoil (memory), additional normal stresses in shear flow, and an extensional viscosity that is not simply related to the shear viscosity, to name a few differences.

Because of these vastly different rheological properties, polymeric fluids are known to exhibit flow behavior that cannot be accounted for merely through a single rheological parameter such as the viscosity. Some of the differences in flow behavior include a nonlinear relation between pressure drop and volumetric flow rate for flow through a tube, swelling of the extrudate on emerging from a tube, the onset of a low Reynolds number flow instability called melt fracture, gradual relaxation of stresses on cessation of flow, and the ability of the molecules to orient during flow. These phenomena are discussed in more detail elsewhere (Bird et al., 1987; Larson, 1999).

The emphasis in this chapter is on the viscous behavior of polymeric fluids and in particular their pseudoplastic behavior. The chapter is arranged in the following manner. First, in Section 2.1 we review the definition of a Newtonian fluid, and then we present empiricisms for describing the viscosity of polymeric fluids. In Section 2.2

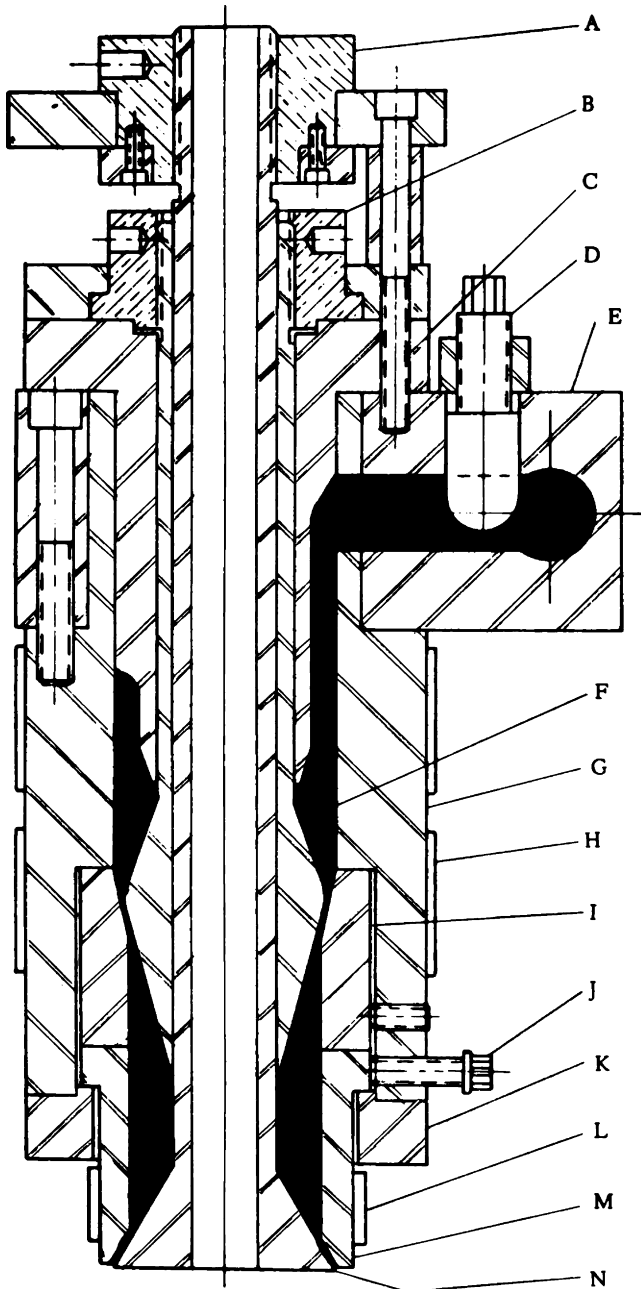


FIGURE 2.1 Typical blow molding die: A, choke adjusting nut; B, mandrel adjustment; C, feed throat; D, choke screw; E, die head; F, plastic melt; G, die barrel; H, heater band; I, choke ring; J, centering screw; K, clamp ring; L, die heater; M, die; N, mandrel. (Reprinted by permission of the publisher from Frankland, 1975.)

we use shell force or momentum balances to solve one-dimensional flow problems commonly found in polymer processing. In Section 2.3 we generalize the force or momentum balances to give the equations of motion, and we generalize the constitutive equation presented in Section 2.1. In Section 2.4 we present two useful approximations for solving

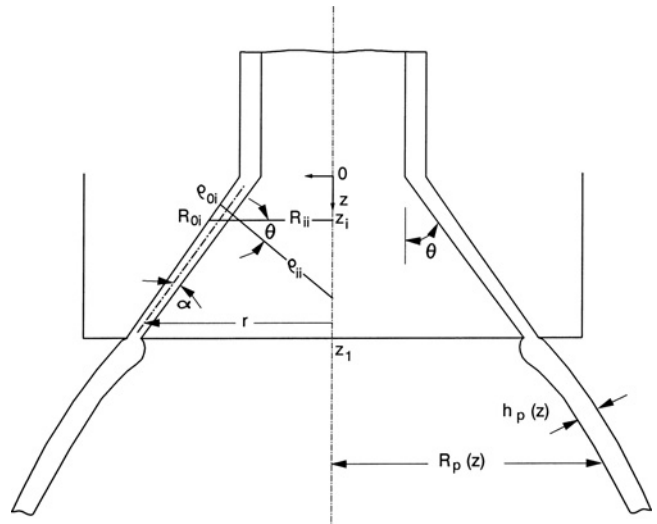


FIGURE 2.2 Detailed drawing of the conical region of the blow molding die.

TABLE 2.1 Parameters in Various Viscosity Models

Graphically Obtained		From Nonlinear Regression Analysis
Power law		
m (Pa·s ^{<i>n</i>})	2.374E+04	1.616E+04
n	0.424	0.520
Ellis		
η_0 (Pa·s)	1.33E+04	1.33E+04
$\tau_{1/2}$ (Pa)	3.325E+04	1.03E+05
$\alpha - 1$	1.54	2.24
Carreau		
η_0	1.33E+04	1.33E+04
n	2.0	1.747
λ (s)	5.0	0.14
Cross		
η_0	1.33E+04	1.18E+04
n	0.9	0.783
λ (s)	0.5	0.0976

polymeric flow problems. Finally, in Section 2.5 the topics discussed in the previous sections are used to solve Design Problem I.

2.1 VISCOUS BEHAVIOR OF POLYMER MELTS

When a Newtonian fluid is placed between the two plates as shown in Figure 2.3 in which the top plate is moved to the right with constant velocity, V , the relation between force, F , divided by the area of the plates, A , and the velocity divided by the separation distance, H , is given as follows:

$$F/A = \mu V/H \quad (2.1)$$

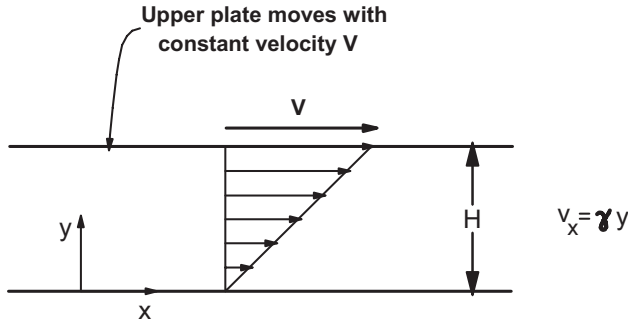


FIGURE 2.3 Steady simple shear flow with shear rate $= V/H$.

The constant of proportionality, μ , is called the viscosity of the fluid. The force, F , is the force required to keep the top plate moving with a constant velocity. The force per unit area acting in the x direction on a fluid surface at constant y by the fluid in the region of lesser y is the shear stress, τ_{yx} . Since the velocity of the fluid particles varies in a linear manner with respect to the y coordinate, it is clear that $V/H = dv_x/dy$ as shown below:

$$\lim_{\Delta y \rightarrow 0} \frac{\Delta v_x}{\Delta y} = \frac{dv_x}{dy} = \frac{V - 0}{H - 0} = \frac{V}{H} \quad (2.2)$$

Equation 2.1 can be rewritten as

$$\tau_{yx} = -\mu(dv_x/dy) \quad (2.3)$$

This states that the shear force per unit area is proportional to the negative of the local velocity gradient and is known as *Newton's law of viscosity*. The sign convention used here follows that of Bird et al. (2007).

τ_{yx} can also be interpreted in another fashion. τ_{yx} may be considered as the viscous flux of x momentum in the y direction. The idea here is that the plate located at $y = H$ transmits its x momentum to the layer below, which in turn transmits momentum to the next layer. The momentum flux, τ_{yx} , is negative in this case as the momentum is transferred in the negative y direction. The sign convention follows the ideas used for heat flux in that heat flows from hot to cold or in the direction of a negative temperature gradient. This also makes the law of viscosity fit with the ideas of diffusion in which matter flows in the direction of decreasing concentration.

Probably the most frequently used notation, however, is that found in mechanics in which material at greater y exerts force in the x direction on a layer of fluid at lesser y . The shear stress, τ_{xy}^* , is then related to that used above as follows:

$$\tau_{yx} = -\tau_{xy}^* \quad (2.4)$$

τ_{xy}^* is then defined as the force per unit area acting in the x direction by fluid at y on a surface of lesser y with a unit outward normal in the $+y$ direction.

Non-Newtonian Viscosity

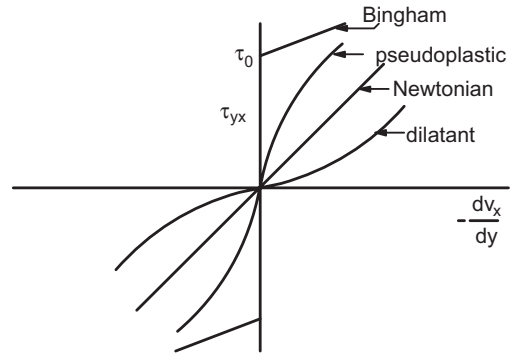


FIGURE 2.4 Viscous response of non-Newtonian fluids.

The flow behavior of most thermoplastics does not follow Newton's law of viscosity. To quantitatively describe the viscous behavior of polymeric fluids, Newton's law of viscosity is generalized as follows:

$$\tau_{yx} = -\eta dv_x/dy \quad (2.5)$$

where η can be expressed as a function of either dv_x/dy or τ_{yx} . Some typical responses of polymeric fluids are shown in Figure 2.4, where τ_{yx} is plotted versus the velocity gradient. For a pseudoplastic fluid the slope of the line decreases with increasing magnitude of dv_x/dy , or in essence the viscosity decreases. Some polymeric fluids (in some cases polymer blends and filled polymers) exhibit a yield stress, which is the stress that must be overcome before flow can occur. When flow occurs, if the slope of the line is constant, then the fluid is referred to as a *Bingham fluid*. In many cases the fluid is still pseudoplastic once flow begins. Finally, in some cases the viscosity of the material increases with increasing velocity gradient. The fluid is then referred to as *dilatant*.

Many empiricisms have been proposed to describe the steady-state relation between τ_{yx} and dv_x/dy , but we mention only a few that are most useful for polymeric fluids. The first is the *power law of Ostwald-de Waele*:

$$\eta = m \left| \frac{dv_x}{dy} \right|^{n-1} \quad (2.6)$$

This is a two-parameter model in which n describes the degree of deviation from Newtonian behavior. m , which has the units of $\text{Pa}\cdot\text{s}^n$, is called the *consistency*. For $n = 1$ and $m = \mu$, this model predicts Newtonian fluid behavior. For $n < 1$, the fluid is pseudoplastic while for $n > 1$ the fluid is dilatant. The *Ellis model* is a three-parameter model and is defined as

$$\frac{\eta_0}{\eta} = 1 + \left(\frac{\tau_{yx}}{\tau_{1/2}} \right)^{\alpha-1} \quad (2.7)$$

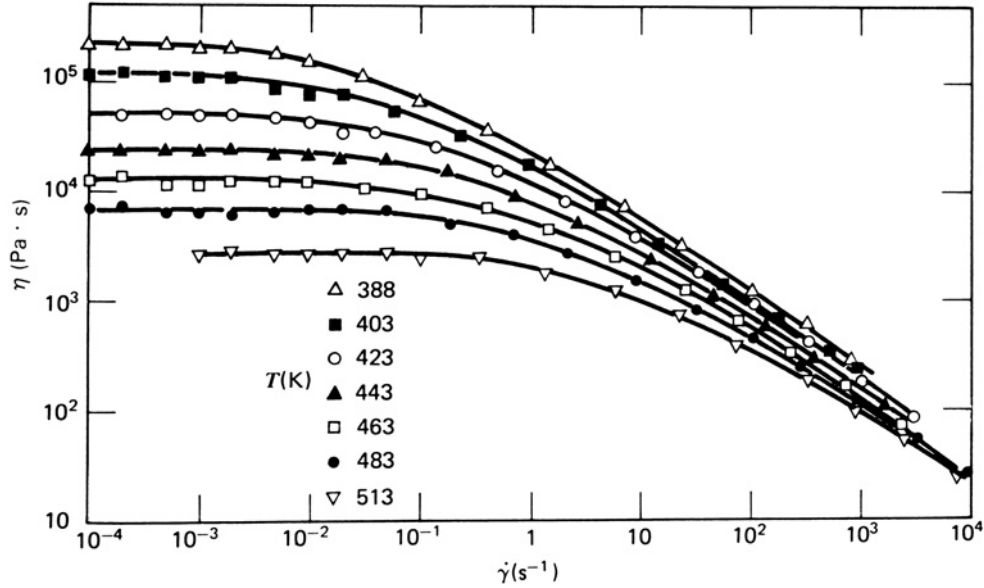


FIGURE 2.5 Non-Newtonian viscosity of a low density polyethylene (LDPE) melt at several different temperatures as shown in the figure. (Reprinted by permission of the publisher from Meissner, 1971.)

Here η_0 is the zero shear viscosity and $\tau_{1/2}$ is the value of τ_{yx} when $\eta = \frac{1}{2} \eta_0$. Actually most polymeric fluids exhibit a constant viscosity at low shear rates and then shear thin at higher shear rates (see Fig. 2.5). A model that is used often in numerical calculations, because it fits the full flow curve, is the *Bird–Carreau model*:

$$\frac{\eta - \eta_\infty}{\eta_0 - \eta_\infty} = [1 + (\lambda\dot{\gamma})^2]^{(n-1)/2} \quad (2.8)$$

When the 2's in the exponents in Eq. 2.8 are replaced by a 's, where a is a parameter that controls the width of the transition from constant viscosity into the shear-thinning region, then the model is referred to as the *Carreau–Yasuda model*. This Bird–Carreau model contains four parameters: η_0 , η_∞ , λ , and n . η_0 is the zero shear viscosity just as above. η_∞ is the viscosity as the shear rate ($\dot{\gamma}$) or $dv_x/dy \rightarrow \infty$, and for polymer melts this can be taken as zero. λ has units of seconds and approximately represents the reciprocal of the shear rate for the onset of shear thinning behavior. n represents the degree of shear thinning and is nearly the same as the value in the power-law model. As a number of polymeric fluids exhibit yield stresses, models that include these are the *Bingham* and *Herschel–Bulkley models*. The Bingham model is given as

$$\eta = \mu_0 + \frac{|\tau_0|}{dv_x/dy} \quad \text{if } |\tau_{yx}| \geq |\tau_0| \quad (2.9)$$

$$\eta = \infty \quad \text{if } |\tau_{yx}| < |\tau_0| \quad (2.10)$$

Here τ_0 is the yield stress and μ_0 is the slope of the line of $\tau_{yx} - \tau_0$ versus dv_x/dy . The Hershel–Bulkley model is given as

$$\eta = m' \left| \frac{dv_x}{dy} \right|^{n'-1} + \frac{|\tau_0|}{dv_x/dy} \quad \text{if } |\tau_{yx}| \geq \tau_0 \quad (2.11)$$

Here m' and n' are power-law parameters determined from $\tau_{yx} - \tau_0$ versus dv_x/dy . This model describes fluids that are pseudoplastic once flow starts.

Example 2.1. Power-Law and Ellis Model Parameters for LLDPE

Determine the power-law (Eq. 2.6) and Ellis (Eq. 2.7) model parameters for LLDPE (NTA 101) at 170 °C using the rheological data given in the Appendix Tables A.7–A.9.

Solution. To find the parameters m and n in Eq. 2.6 we first plot $\ln \eta$ versus $\ln \dot{\gamma}$ as shown in Figure 2.6. The slope of the line in the linear region is $n - 1$ and is estimated to be -0.576 . Hence, n is 0.424. m is found by taking the natural logarithm of both sides of Eq. 2.6:

$$\ln \eta = \ln m + (n - 1) \ln \dot{\gamma} \quad (2.12)$$

and then arbitrarily selecting values of η and $\dot{\gamma}$ in the linear region. For example, by substituting $\dot{\gamma} = 140 \text{ s}^{-1}$ and $\eta = 1.45 \times 10^3 \text{ Pa}\cdot\text{s}$ into Eq. 2.12, we find m to be $2.374 \times 10^4 \text{ Pa}\cdot\text{s}^n$.

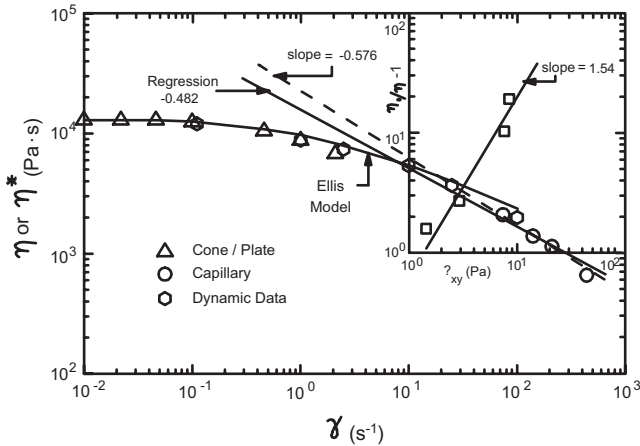


FIGURE 2.6 Viscosity versus shear rate (ln–ln plot) for LLDPE at 170 °C. The data were obtained by various types of rheometers as indicated in the figure. (---) Graphical fit of power law; (—) fit of power law using regression analysis. Insert shows plot of $(\eta/\eta_0) - 1$ versus shear stress used to obtain Ellis model parameters.

To find the Ellis model parameters we plot $\ln(\eta_0/\eta - 1.0)$ versus $\ln \tau_{yx}$ as shown in the upper right-hand corner of Figure 2.6. $\tau_{1/2}$ is the value of τ_{yx} when $\eta = \frac{1}{2} \eta_0$ and is estimated from the graph in Figure 2.6 to be 3.325×10^4 Pa. $\alpha - 1$ is estimated from the slope of the line to be 1.54. η_0 is read directly from the data and is 1.33×10^4 Pa·s. All the parameters for both models are summarized in Table 2.1. ■

Example 2.2. Power-Law, Carreau, Ellis, and Cross Model Parameters for LLDPE Using Nonlinear Regression Analysis

- Determine the power-law and Ellis model parameters for LLDPE using nonlinear regression analysis. In particular, use the IMSL (International Mathematics and Statistics Libraries) subroutine RNLIN described on the accompanying website to find m and n in the power-law model and η_0 , $\tau_{1/2}$, and α in the Ellis model for LLDPE at 170 °C. Also use Excel and the *Solve* function (Billo, 2007).
- The Cross model (Dealy and Wissbrun, 1999) defined in Eq. 2.13 below is another empiricism frequently used to model the viscosity of shear thinning or pseudoplastic fluids. Find the parameters in this model using nonlinear regression analysis and the *Solve* function in Excel.

$$\eta = \frac{\eta_0}{[1 + (\lambda\dot{\gamma})^n]} \quad (2.13)$$

λ here is again related to the reciprocal of the shear rate, $\dot{\gamma}$, for the onset of shear thinning behavior. We

also note that in the limit of high $\dot{\gamma}$ Eq. 2.13 reduces to approximately the power-law model as shown below:

$$\eta \cong \eta_0(\lambda\dot{\gamma})^n \quad (2.14)$$

Solution. The solution to this problem is given in the accompanying website in the folder under “Numerical Examples, Chapter 2.” The method of nonlinear regression analysis is used to find the parameters that minimize the sum of the residual errors between the predicted and experimental values of viscosity. Details of the procedure using Excel can be found in the book by Billo (2007). The main item to note is that the fitting is done based on the natural logarithm of the viscosity values. A summary of the parameter values is given in Table 2.1. Graphical estimates are usually used to make initial guesses of the parameters. The parameters that are obtained from nonlinear regression analysis will depend on the choices of the estimates for the parameters. It is advised to plot the predicted viscosity values along with the measured values on the same plot in order to observe the quality of the fit. This is done on sheet 2 in the Excel file “EX2-2-Excel.doc,” on the accompanying website.

A few comments should be made regarding the selection of data points used in the regression analysis. In the case of the power law, only the data in the linear region are used. Certainly the regression analysis could have been carried out on all the data, but the coefficients obtained would not lead to an accurate prediction of η at intermediate shear rates.

It is also observed that the power-law parameters obtained graphically differ from those obtained by nonlinear regression analysis. The function with the two different sets of parameters is plotted in Figure 2.6. Regression analysis basically removes the arbitrariness of finding n . It should also be noted that the Ellis model with the parameters even obtained graphically fits the data well over the full range. ■

Shear thinning or pseudoplastic behavior is an important property that must be taken into account in the design of polymer processes. However, it is not the only property, and in Chapter 3 models that describe the viscoelastic response of polymeric fluids will be discussed. However, first we would like to solve some basic one-dimensional isothermal flow problems using the shell momentum balance and the empiricisms for viscosity described in this section.

2.2 ONE-DIMENSIONAL ISOTHERMAL FLOWS

In this section we make use of a shell momentum or force balance plus the Newtonian fluid model and the generalized Newtonian fluid (GNF) model to solve some basic flow

TABLE 2.2 Parameters for High Density Polyethylene, Alathon, DuPont

Temperature (K)	Power Law Model			η_0 (Pa·s)	Carreau Model			Ellis Model	
	Range (s ⁻¹)	m (Pa·s ⁿ)	n		Range (s ⁻¹)	n	λ (s)	α	$\tau_{1/2}$ (Pa)
453	100–1000	6.19×10^3	0.56	2.1×10^3	100–1200	0.54	0.07	2.57	7.50×10^4
473	100–1000	4.68×10^3	0.59	1.52×10^3	100–1200	0.50	0.08	2.51	7.49×10^4
493	100–1000	3.73×10^3	0.61	1.17×10^3	186–1400	0.58	0.05	2.49	7.67×10^4

Source: Data from Tadmor and Gogos, 1979, Table A.1.

problems. Although some students have been exposed to transport phenomena, there are a number who have not. For this reason the subject matter is started by considering the use of shell momentum balances rather than the use of the equations of change, which are presented in Section 2.3. The material is arranged in such a way that a number of useful processing flows can be analyzed without the use of the three-dimensional equations of change.

2.2.1 Flow Through an Annular Die

The manufacture of pipe and the generation of parisons used in blow molding involve flow through an annular die. Our first goal is to design an annular die for extruding a pipe at 180 °C with an O.D. of 0.0762 m (3.0 in.) and an I.D. of 0.0635 m (2.5 in.) for high density polyethylene (HDPE) at the highest extrusion rate possible (m/min). Assume that the limiting factor is the onset of melt fracture, which occurs at a wall shear stress, τ_w , of 1.0×10^5 Pa (melt fracture is discussed in Section 7.1). The rheological data for this polymer (i.e., η vs. dv_z/dr) have been analyzed, and the parameters for the various models discussed in Section 2.1 are given in Table 2.2.

To solve this problem we must obtain relationships between the wall shear stress, τ_w , and the pressure drop, ΔP , as well as the volumetric flow rate, Q . This is done by carrying out a momentum or force balance on a differential element of fluid to obtain a differential equation for the stress distribution. A constitutive equation is then substituted into the stress equation to obtain a differential equation for the velocity field. This is then integrated, and the velocity field is found when the appropriate boundary conditions are specified. We make the following assumptions:

1. The flow is steady, laminar, and isothermal.
2. There are no entry or exit effects.
3. Inertia is insignificant (i.e., the Reynolds number is negligible).
4. The fluid is inelastic, and hence die swell is not considered.
5. The fluid does not slip on the die surfaces.

A cross section of the annular die required to produce the pipe is shown in Figure 2.7. The approximate velocity and stress profiles for this flow are sketched here also. A thin cylindrical shell is now chosen of length L and thickness Δr as shown in Figure 2.8. The shell is selected so that the surface is parallel to the flow direction. A force (or momentum) balance is now performed on the shell. Because the flow is under steady-state conditions, the forces in the z direction must sum to zero as shown below:

$$\tau_{rz}|_r 2\pi r L - \tau_{rz}|_{r+\Delta r} 2\pi(r + \Delta r)L - \rho g 2\pi r \Delta r L + (p_o - p_L) 2\pi r \Delta r = 0 \tag{2.15}$$

τ_{rz} is the force per unit area acting in the z direction on a surface at r by a layer of fluid at lesser r . It is customary to take the force per unit area acting at r to be positive while

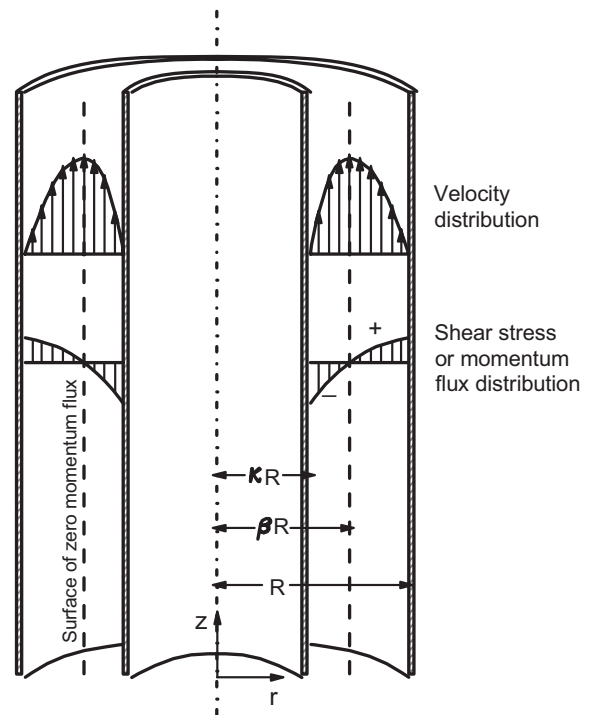


FIGURE 2.7 Flow through a cylindrical annulus.

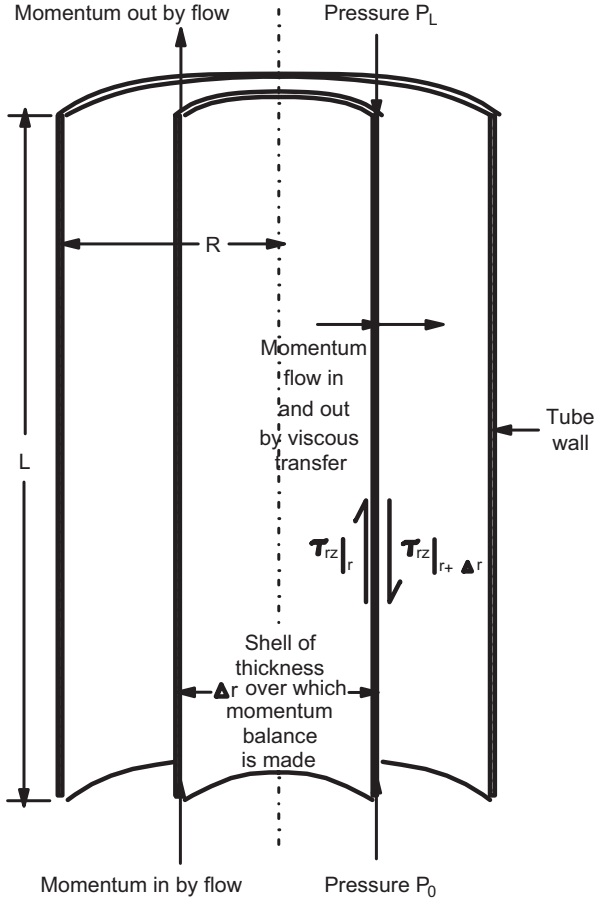


FIGURE 2.8 Cylindrical shell of fluid over which the momentum or force balance is performed.

that at $r + \Delta r$ to be negative. We now divide Eq. 2.15 by $2\pi \Delta r L$ and take the limit as $\Delta r \rightarrow 0$:

$$\lim_{\Delta r \rightarrow 0} \left(\frac{(r\tau_{rz})|_{r+\Delta r} - (r\tau_{rz})|_r}{\Delta r} \right) = \left(\frac{p_0 - p_L}{L} - \rho g \right) r \quad (2.16)$$

But this first term is just the derivative, and this gives the following differential equation:

$$\frac{d}{dr}(r\tau_{rz}) = + \left(\frac{P'_0 - P'_L}{L} \right) r \quad (2.17)$$

where $P = p_0$ and $P = p_L + \rho gL$.^{*} This gives a differential equation for which we can solve for τ_{rz} by integration to give

$$\tau_{rz} = \left(\frac{P'_0 - P'_L}{L} \right) \frac{r}{2} + \frac{C_1}{r} \quad (2.18)$$

^{*}The pressure P'_L represents the combined effect of dynamic pressure and the pressure due to gravity. In general, P' may be defined as $P' = p + \rho gh$, where h is the distance upward from any chosen plane.

At some distance, βR , the velocity field must pass through a maximum and τ_{rz} (which is proportional to dv_z/dr) must be zero. Utilizing this information C_1 is replaced by $-(P'_0 - P'_L)(\beta R)^2/2L$, which leads to the following equation in place of Eq. 2.18:

$$\tau_{rz} = \frac{(P'_0 - P'_L)R}{2L} \left[\frac{r}{R} - \beta^2 \left(\frac{R}{r} \right) \right] \quad (2.19)$$

Our next goal is to find the velocity field. To do this the type of fluid and an appropriate constitutive equation must be specified. In the first case the fluid is considered to be Newtonian. τ_{rz} is replaced with Newton's law of viscosity to obtain a differential equation for v_z :

$$\frac{dv_z}{dr} = - \frac{(P'_0 - P'_L)R}{2\mu L} \left[\left(\frac{r}{R} \right) - \beta^2 \left(\frac{R}{r} \right) \right] \quad (2.20)$$

The flow is considered to consist of two parts:

$$\kappa R \leq r < \beta R \quad v_z = v_{z<} \quad (2.21)$$

$$\beta R < r \leq R \quad v_z = v_{z>} \quad (2.22)$$

Furthermore, the no-slip boundary conditions are assumed at the walls:

$$\text{B.C.1: at } r = \kappa R, \quad v_z = 0 \quad (2.23)$$

$$\text{B.C.2: at } r = R, \quad v_z = 0 \quad (2.24)$$

Equation 2.20 is integrated using the boundary conditions to obtain

$$v_{z<} = R \left[\frac{(P'_0 - P'_L)R}{2\mu L} \right] \int_{\kappa}^{\xi} \left(\frac{\beta^2}{\xi'} - \xi' \right) d\xi', \quad \kappa \leq \xi \leq \beta \quad (2.25)$$

$$v_{z>} = R \left[\frac{(P'_0 - P'_L)R}{2\mu L} \right] \int_{\xi}^1 \left(\xi' - \frac{\beta^2}{\xi'} \right) d\xi', \quad \beta \leq \xi \leq 1 \quad (2.26)$$

where $\xi' = r/R$ is a dummy variable of integration. At $r = \beta R$, $v_{z<} = v_{z>}$ and one can equate Eqs. (2.25) and (2.26) to find β as follows:

$$\int_{\kappa}^{\beta} \left(\frac{\beta^2}{\xi} - \xi \right) d\xi = \int_{\beta}^1 \left(\xi - \frac{\beta^2}{\xi} \right) d\xi \quad (2.27)$$

For a Newtonian fluid these expressions can be integrated to give β :

$$2\beta^2 = (1 - \kappa^2) / \ln(1/\kappa) \quad (2.28)$$

For a Newtonian fluid it is observed that β is determined merely by geometric factors. For a Newtonian fluid one can then write down the solutions for τ_{rz} and v_z :

$$\tau_{rz} = \frac{(P'_0 - P'_L)R}{2L} \left[\frac{r}{R} - \frac{1 - \kappa^2}{2 \ln(1/\kappa)} \left(\frac{R}{r} \right) \right] \quad (2.29)$$

$$v_z = \frac{(P'_0 - P'_L)R^2}{4\mu L} \left[1 - \left(\frac{r}{R} \right)^2 + \frac{1 - \kappa^2}{\ln(1/\kappa)} \ln \left(\frac{r}{R} \right) \right] \quad (2.30)$$

We can now integrate Eq. 2.30 over the cross section of the annulus to find the volumetric flow rate, Q :

$$\begin{aligned} Q &= \pi R^2 (1 - \kappa^2) \langle v_z \rangle \\ &= \frac{\pi (P'_0 - P'_L) R^4}{8\mu L} \left((1 - \kappa^4) - \frac{(1 - \kappa^2)^2}{\ln(1/\kappa)} \right) \end{aligned} \quad (2.31)$$

One can now determine Q and the extrusion rate, which is the average velocity, $\langle v_z \rangle = Q/A$. With the assumption that the fluid leaves the die with the same dimensions as the die, then one can calculate that $\kappa R = 0.03175$ m and $R = 0.0381$ m. However, these values will not quite be correct as the melt will swell on leaving the die, but shrink as it cools because of the change in density. These factors will be considered in Section 7.2.1. Furthermore, we have not specified the die length, which must be long enough to eliminate any effects from the entry but not so long as to create excessive pressures. For the time being we will take L to be 10 times the die gap $[R(1 - \kappa)]$, which makes $L = 0.0635$ m. One now calculates $P'_0 - P'_L$, Q , and $\langle v_z \rangle$ assuming $\tau_w = 1 \times 10^5$ Pa:

$$\begin{aligned} P'_0 - P'_L &= 2.024 \times 10^6 \text{ Pa} \\ Q &= 7.24 \times 10^{-5} \text{ m}^3/\text{s} \\ \langle v_z \rangle &= 3.12 \text{ m/min} \end{aligned}$$

Next we consider the case in which the fluid is shear thinning, and the viscosity is described by the power-law model. The derivation leading to Eq. 2.19 is unchanged. Starting with this equation one now solves for the velocity field using the power-law model:

$$\tau_{rz} = -m |(dv_z/dr)|^{n-1} (dv_z/dr) \quad (2.32)$$

For $\kappa R < r < \beta R$, $dv_z/dr > 0$ and we express Eq. 2.32 as

$$\tau_{rz} = -m (dv/dr)^n \quad (2.33)$$

For $\beta R < r < R$, $dv_z/dr < 0$ and Eq. 2.32 becomes

$$\tau_{rz} = m (-dv/dr)^n \quad (2.34)$$

Two different expressions for τ_{rz} are required to ensure that a negative number is not raised to a fractional exponent, which will lead to an imaginary number. Analogous to Eqs. 2.25 and 2.26 we solve for $v_{z>}$ and $v_{z<}$:

$$-m \left(\frac{dv_{z<}}{dr} \right)^n = C \left[\frac{r}{R} - \beta^2 \frac{R}{r} \right] \quad (2.35)$$

$$m \left(\frac{-dv_{z>}}{dr} \right)^n = C \left[\frac{r}{R} - \beta^2 \frac{R}{r} \right] \quad (2.36)$$

where $C = (P'_0 - P'_L)R^2/2L$. We now integrate these equations after taking the $1/n$ power of both sides:

$$v_{z<} = R \left[\frac{(P'_0 - P'_L)R}{2mL} \right]^s \int_{\kappa}^{\xi} \left(\frac{\beta^2}{\xi'} - \xi' \right)^s d\xi', \quad \kappa \leq \xi \leq \beta \quad (2.37)$$

$$v_{z>} = R \left[\frac{(P'_0 - P'_L)R}{2mL} \right]^s \int_{\xi}^1 \left(\xi' - \frac{\beta^2}{\xi'} \right)^s d\xi', \quad \beta \leq \xi \leq 1 \quad (2.38)$$

When $1/n$ is a whole number (e.g., 1, 2, 3, etc.), then these integrals can be integrated to directly obtain expressions for $v_{z<}$ and $v_{z>}$. However, n is usually some decimal number such as 0.52; in which case we must evaluate the integrals numerically. First we employ the expression for finding β by equating $v_{z>}$ and $v_{z<}$:

$$\int_{\kappa}^{\beta} \left(\frac{\beta^2}{\xi} - \xi \right)^s d\xi = \int_{\beta}^1 \left(\xi - \frac{\beta^2}{\xi} \right)^s d\xi \quad (2.39)$$

Equation 2.39 gives β as a function of κ and s , but must be evaluated numerically unless $1/n$ is an integer. Q is found by integrating Eqs. 2.37 and 2.38 over the cross section of the die:

$$\begin{aligned} Q &= 2\pi \int_{\kappa R}^R v_z r dr \\ &= \pi R^3 \left[\frac{(P'_0 - P'_L)R}{2mL} \right]^s \int_{\kappa}^1 |\beta^2 - \xi^2|^{s+1} \xi^{-s} d\xi \end{aligned} \quad (2.40)$$

If we treat each term within the integral as a function of ξ' , that is, $F(\xi')$, then Eq. 2.40 can be integrated by parts (*Note:* Let $u = F(\xi')$ and $dv = \xi' d\xi'$) to obtain

$$\begin{aligned} Q &= \frac{\pi R^3}{(1/n) + 3} \left(\frac{P'_0 - P'_L}{2mL} \right)^{1/n} \\ &\quad \times \left[(1 - \beta^2)^{1+(1/n)} - \kappa^{1-(1/n)} (\beta^2 - \kappa^2)^{1+(1/n)} \right] \end{aligned} \quad (2.41)$$

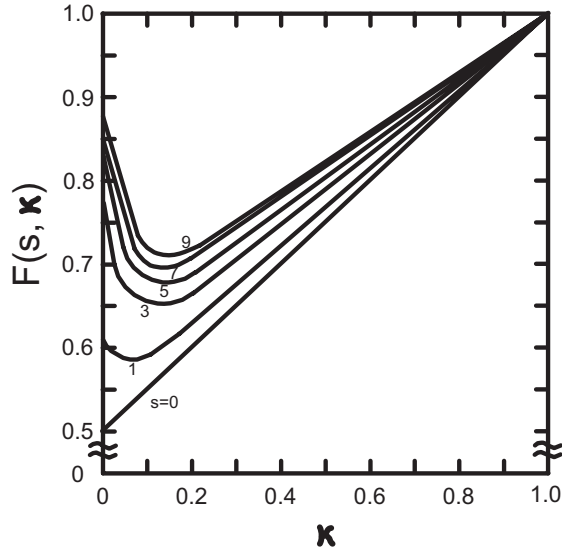


FIGURE 2.9 The function $F(s, \kappa)$ needed for obtaining the volume rate of flow through an annulus for a power-law fluid.

Once β is known from Eq. 2.29, then Eq. 2.41 can be evaluated. We express Eq. 2.41 as follows:

$$Q = \pi R^3 \left(\frac{(P'_0 - P'_L) R}{2mL} \right)^{1/n} \frac{(1 - \kappa)^{1/n+2}}{s + 2} F(s, \kappa) \quad (2.42)$$

where $F(1/n, \kappa)$ is given for several values of $1/n$ in Figure 2.9.

Now referring back to Eq. 2.19 we determine that melt fracture will occur at the outer wall first, since the shear stress is higher here than at the inner wall:

$$\tau_w(\kappa R) = \left(\frac{(P'_0 - P'_L) \kappa R}{2L} \right) \left[1 - \frac{\beta^2}{\kappa^2} \right] \quad (2.43a)$$

$$\tau_w(R) = \left(\frac{(P'_0 - P'_L) R}{2L} \right) (1 - \beta^2) \quad (2.43b)$$

This follows from the fact that $\kappa < 1$. From Eq. 2.39 and using $n = 0.56$, we find that β is about 0.91. We can now calculate $P'_0 - P'_L$, Q , and $\langle v_z \rangle$:

$$\begin{aligned} P'_0 - P'_L &= 1.91 \times 10^6 \text{ Pa} \\ Q &= 1.56 \times 10^{-4} \text{ m}^3/\text{s} \\ \langle v_z \rangle &= 6.72 \text{ m/min} \end{aligned}$$

We observe that although the pressure drop is only slightly lower than for the Newtonian case, the extrusion rate is more than twice as large.

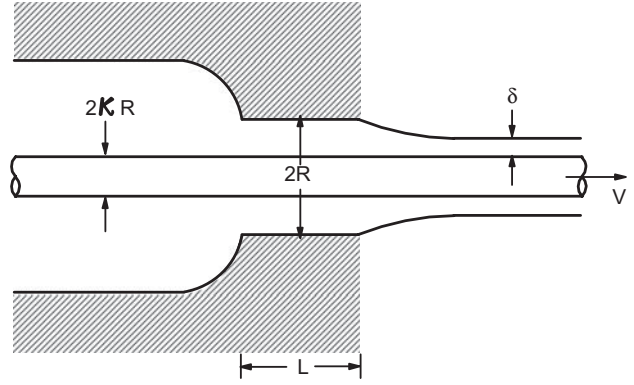


FIGURE 2.10 Simplified view of a wire coating die with no imposed pressure gradient.

2.2.2 Flow in a Wire Coating Die

To further illustrate the use of the force balance on a differential element of fluid to obtain an equation for the shear stress distribution, the design of a wire coating die is considered next. The problem is to design a wire coating die to coat a 0.655×10^{-2} m diameter wire with a 0.330×10^{-2} m thick layer of HDPE at 200°C at the highest extrusion rate possible. (Assume again that the extrusion rate limit is the onset of melt fracture at $\tau_w = 1.4 \times 10^5$ Pa.)

A typical wire coating die was shown in Figure 1.4. The design that is shown there is somewhat beyond our capabilities at this point. For this reason we consider only the annular flow region as shown in Figure 2.10. We make the following assumptions:

1. The flow is steady, incompressible and isothermal.
2. The rheological properties of the fluid are described by the power-law model and elastic effects (i.e., die swell) can be neglected.
3. The converging part of the die will be neglected.
4. There is no significant pressure drop (ΔP) across the die. However, in practice a small ΔP is used to control the thickness as shown in Figure 2.11.

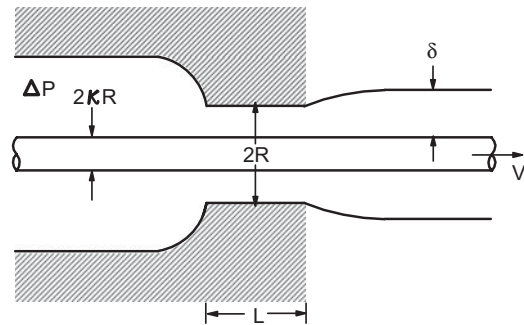


FIGURE 2.11 Wire coating die with an imposed pressure gradient.

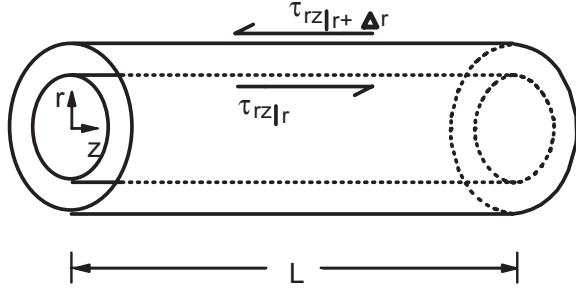


FIGURE 2.12 Cylindrical element of differential thickness, Δr , on which momentum balance is made.

The shell force or momentum balance is performed on an element of fluid as shown in Figure 2.12, which is similar to that shown in Figure 2.8. Here the only terms that have to be considered are due to the stresses exerted by one layer of fluid on another as there are no effects due to gravity or pressure. The force or momentum balance is

$$\tau_{rz}|_r 2\pi r - \tau_{rz}|_{r+\Delta r} 2\pi(r + \Delta r) = 0 \quad (2.44)$$

In the limit as $\Delta r \rightarrow 0$, Eq. 2.44 becomes

$$-\frac{d}{dr}(r\tau_{rz}) = 0 \quad (2.45)$$

This can now be integrated to find τ_{rz} :

$$\tau_{rz} = C_1/r \quad (2.46)$$

We use the power-law model to find $v_z(r)$:

$$m(-dv_z/dr)^n = C_1/r \quad (2.47)$$

Here we have used the fact that $dv_z/dr < 0$. This equation can be integrated to find v_z :

$$v_z \equiv (C_1/m)^{1/n} \frac{r^{-1/n+1}}{(1-n)/n} - C_2 \quad (2.48)$$

The following boundary conditions are used to find C_1 and C_2 :

$$\text{B.C.1: at } r = R, \quad v_z = 0 \quad (2.49)$$

$$\text{B.C.2: at } r = \kappa R, \quad v_z = V \quad (2.50)$$

Using the above conditions, the velocity profile becomes

$$\frac{v_z(r)}{V} = \frac{\xi^{1-s} - 1}{\kappa^{1-s} - 1} \quad (2.51)$$

where $\xi = r/R$ and $s = 1/n$. τ_{rz} becomes

$$\tau_{rz} = \frac{mV^n(s-1)^n}{R^n(\kappa^{1-s}-1)^n} \left(\frac{R}{r}\right) \quad (2.52)$$

At this point we cannot specify V or R , until we relate the thickness of the coating to these variables. To do this we perform a mass balance on the region starting at the exit of the die and ending where the fluid takes on the same velocity as the wire (the density, ρ , is assumed not to change, although the melt and solid would in reality have different densities):

$$2\pi \int_{\kappa R}^R v_z r dr = V\pi[(\kappa R + \delta)^2 - (\kappa R)^2] \quad (2.53)$$

where δ is the coating thickness. On substituting Eq. 2.51 into the integral in Eq. 2.53 we obtain the following equation for the coating thickness, δ :

$$\frac{2\pi VR^2}{\kappa^{1-s}-1} \left[\frac{1-\kappa^{3-s}}{3-s} - \frac{1-\kappa^2}{2} \right] = V\pi[(\kappa R + \delta)^2 - (\kappa R)^2] \quad (2.54)$$

Equations 2.52 and 2.54 represent two nonlinear equations for R and V . Actually V drops out of Eq. 2.54 allowing us to solve for R . Once R is found it can be substituted back into Eq. 2.52 to find V . This is done in Example 2.3, which follows.

Example 2.3. Die Radius and Wire Speed

Equations 2.52 and 2.54 represent two nonlinear algebraic equations for finding the wire velocity and radius. Find R and V for HDPE at 200 °C using the IMSL subroutine NEQNF, which is described in Appendix D.4 on the accompanying website. Also use Excel and the *Solve* function or *Goal Seek* to find the roots of these two equations.

Solution. Since Eq. 2.54 does not contain V , we can first find R and then substitute R into Eq. 2.52 to find V . According to the program description for subroutine NEQNF, we must write Eq. 2.54 in the following form:

$$\frac{2R^2(1-\kappa^{3-s})}{(\kappa^{1-s}-1)(3-s)} - \frac{R^2(1-\kappa^2)}{(\kappa^{1-s}-1)} - 2\kappa R\delta - \delta^2 = 0 \quad (2.55)$$

Using the following information given in the problem

$$s = 1.6949, \quad \kappa = 3.275 \times 10^{-3} R^{-1}, \quad \delta = 3.30 \times 10^{-3} \text{ m}$$

Eq. 2.55 becomes

$$1.032 R^2 - 2.608 \times 10^{-3} R^{s-1} + 4.323 \times 10^{-5} = 0 \quad (2.56)$$

Subroutine NEQNF solves a single nonlinear algebraic equation or a system of nonlinear algebraic equations for the roots. The calling program listing is given in the accompanying website in Chapter 2 of the Numerical solutions in the file called EX2-3-Fortran. To use the subroutine one must provide an initial guess for R . As there are more than one root, then obtaining a realistic value of R depends on the initial guess. If n is a value such as $\frac{1}{2}$, $\frac{1}{4}$, and so on, then s is an integer. Taking $n = 0.5$, and hence $s = 2$ in Eq. 2.42, a quadratic equation is formed for which the physically realistic solution is $R = 4.33 \times 10^{-3}$ m. Another approach is to start with the solution for the Newtonian case ($s = 1$), but this requires additional algebraic manipulations. Using the initial guess as 4.33×10^{-3} m, R is calculated to be 4.549×10^{-3} m. We can now substitute this value back into Eq. 2.52 to find V subject to the condition that melt fracture will be visible at the outer surface at $\tau_{rz}(R) = 1.4 \times 10^5$ Pa:

$$V = \left[\frac{\tau_{rz}(R) R^n (1 - \kappa^{s-1})}{m(s-1)^n} \right]^{1/n} = 0.141 \text{ m/s} \quad (2.57)$$

As discussed in Chapter 7 line speeds in actual processes can run in the range of 10 m/s to 40 m/s, which actually leads to conditions well beyond where melt fracture is initiated.

Excel and *Solve* or *Goal Seek* can also be used to find the real root of Eq. 2.56. The Excel solution is file EX2-3-Excel in the Chapter 2 of the numerical solutions. The initial guess is crucial to getting the proper solution. Because κR is $3.275\text{E}-03$ m, then the guess for R must be chosen slightly bigger than this value. The value for R obtained using Excel is $4.55\text{E}-3$ m.

Several points should be made concerning this solution. The program was written so that the initial guess, the accuracy of the solution, and the maximum number of iterations could be input through the terminal. This made it easy to change these variables without having to compile the program each time. Furthermore, the program could easily have been written in a more general form by starting with Eq. 2.55 and then reading in quantities such as s , δ , and κR .

Although we have made a number of simplifications to get a solution to this problem, it is seen that the situation is still complicated and that computational techniques must be used. The addition of a pressure drop (see Problem 2B.5) and the use of the converging geometry even present more difficulties. The addition of fluid elasticity (die swell) will be dealt with later in Section 7.2.

Finally, there are a number of flow geometries for which the shell balance approach can be used and which are

found frequently in polymer processing. We summarize these results in Tables 2.3 through 2.5 for future reference. Here solutions are given for flow between parallel plates, tube flow, and flow through an annulus. Solutions are given for Newtonian, power-law, and Ellis models. ■

The use of the shell balance cannot accommodate all the flows we find in polymer processing. In the next section we summarize the isothermal equations of change plus generalize the Newtonian and non-Newtonian constitutive equations to three dimensions.

2.3 EQUATIONS OF CHANGE FOR ISOTHERMAL SYSTEMS

As the process becomes more complex in terms of flow patterns, then the shell balance approach is inadequate. Therefore, we introduce the equations of conservation of mass and momentum, which are suited for handling multidimensional flows. We do not intend to rederive these equations, as they are discussed in detail elsewhere (Bird et al., 2007, Chap. 3). Suffice it to say that the principles of conservation of mass and momentum applied to a differential cubic element of fluid lead to the equations of continuity and motion, respectively. We give these without derivation with emphasis on their use.

The equation of continuity is presented in Table 2.6 for three coordinate systems. Basically this equation represents a constraint on the velocity field as a result of the fact that one cannot generate voids in the material during deformation. When ρ is constant, then we consider the flow to be incompressible and for rectangular coordinates the continuity equation becomes

$$\frac{\partial v_x}{\partial x} + \frac{\partial v_y}{\partial y} + \frac{\partial v_z}{\partial z} = 0 \quad (2.58)$$

The use of the continuity equation is illustrated in Example 2.4.

The equation of motion is obtained by generalizing the momentum or force balance for a three-dimensional element of fluid. The components of the equation of motion are given in Table 2.7. The terms on the left side of the equations are associated with the transport of momentum by bulk flow. For nearly all polymer processes these terms are negligible compared to the terms on the right side. This is equivalent to saying that the Reynolds number, Re , is negligible where $\text{Re} = \rho D \langle v \rangle / \eta$. In this expression D is a characteristic length and $\langle v \rangle$ is the average velocity.

In order to solve these equations one needs to relate the stresses to the velocity gradients through a relation called the constitutive equation. For a Newtonian fluid the components of the constitutive equation are given by multiplying the

TABLE 2.3 Parallel Plate Pressure Flow

$\tau_{yz} = -\mu \frac{dv_z}{dy}$	$\tau_{yz} = -m \left \frac{dv_z}{dy} \right ^{n-1} \frac{dv_z}{dy}$
$\tau_{yz}(y) = \left(\frac{\Delta P}{L} \right) y$	$\tau_{yz}(y) = \left(\frac{\Delta P}{L} \right) y$
$\tau_w = \tau_{yz} \left(\frac{H}{2} \right) = \frac{H \Delta P}{2L}$	$\tau_w = \tau_{yz} \left(\frac{H}{2} \right) = \frac{H \Delta P}{2L}$
$-\dot{\gamma}_{yz}(y) = \left(\frac{\Delta P}{\mu L} \right) y$	$-\dot{\gamma}_{yz}(y) = \left(\frac{\Delta P}{mL} y \right)^s \quad y \geq 0$
$\dot{\gamma}_w = -\dot{\gamma}_{yz} \left(\frac{H}{2} \right) = \frac{H \Delta P}{2\mu L}$	$\dot{\gamma}_w = -\dot{\gamma}_{yz} \left(\frac{H}{2} \right) = \left(\frac{H \Delta P}{2mL} \right)^s$
$v_z(y) = \left(\frac{H^2 \Delta P}{8\mu L} \right) \left[1 - \left(\frac{2y}{H} \right)^2 \right]$	$v_z(y) = \frac{H}{2(s+1)} \left(\frac{H \Delta P}{2mL} \right)^s \left[1 - \left(\frac{2y}{H} \right)^{s+1} \right] \quad y \geq 0$
$v_z(0) = v_{\max} = \frac{H^2 \Delta P}{8\mu L}$	$v_z(0) = v_{\max} = \frac{H}{2(s+1)} \left(\frac{H \Delta P}{2mL} \right)^s$
$Q = \frac{WH^3 \Delta P}{12\mu L}$	$Q = \frac{WH^2}{2(s+2)} \left(\frac{H \Delta P}{2mL} \right)^s$
$\tau_{yz} = -\eta(\tau) \frac{dv_z}{dy}, \quad \text{where } \eta(\tau) = \frac{\eta_0}{1 + (\tau/\tau_{1/2})^{\alpha-1}} \quad \tau = \tau_{yz} $	

$$\begin{aligned}
 \tau_{yz}(y) &= \left(\frac{\Delta P}{L} \right) y \\
 \tau_w &= \tau_{yz} \left(\frac{H}{2} \right) = \frac{H \Delta P}{2L} \\
 -\dot{\gamma}_{yz} &= \left(\frac{\Delta P}{\eta_0 L} \right) y \left[1 + \left(\frac{\Delta P y}{\tau_{1/2} L} \right)^{\alpha-1} \right] \\
 \dot{\gamma}_w &= -\dot{\gamma}_{yz} \left(\frac{H}{2} \right) = \frac{H \Delta P}{2\eta_0 L} \left[1 + \left(\frac{H \Delta P}{2\tau_{1/2} L} \right)^{\alpha-1} \right] \\
 v_z(y) &= \frac{H^2 \Delta P}{8\eta_0 L} \left\{ \left[1 - \left(\frac{2y}{H} \right)^2 \right] + \left(\frac{2}{1+\alpha} \right) \left(\frac{H \Delta P}{2L\tau_{1/2}} \right)^{\alpha-1} \left[1 - \left(\frac{2y}{H} \right)^{\alpha+1} \right] \right\} \\
 v_z(0) &= v_{\max} = \frac{H^2 \Delta P}{8\eta_0 L} \left[1 + \left(\frac{2}{1+\alpha} \right) \left(\frac{H \Delta P}{2L\tau_{1/2}} \right)^{\alpha-1} \right] \\
 Q &= \frac{WH^3 \Delta P}{12\eta_0 L} \left[1 + \left(\frac{3}{2+\alpha} \right) \left(\frac{H \Delta P}{2L\tau_{1/2}} \right)^{\alpha-1} \right]
 \end{aligned}$$

Source: Data from Tadmor and Gogos, 1979.

components of the rate of deformation tensor by the viscosity, μ . The components of the rate deformation are given in Table 2.8. In taking the constitutive equation as the product of the components of the rate of deformation tensor and μ , expressions are generated for fluids which are incompressible and in which the bulk viscosity has been neglected (Bird et al., 2007). In general tensor notation we write Newton's law of viscosity for an incompressible isotropic fluid as

$$\boldsymbol{\tau} = -\mu \dot{\boldsymbol{\gamma}} \quad (2.59)$$

This notation will not be explained in this text, but suffice it to say that it represents all the components given in Table 2.8 multiplied by μ . If we substitute the components of Eq. 2.59 into the equation of motion, the Navier–Stokes equations are obtained.

In order to deal with the viscous response of non-Newtonian fluids it is necessary to generalize Eq. 2.59 to include a viscosity function, η , which must depend on the magnitude of the rate of deformation or stress tensors. In actuality η is a scalar quantity which must be a scalar

TABLE 2.4 Circular Tube Pressure Flow

$\tau_{rz} = -\mu \frac{dv_z}{dr}$	$\tau_{rz} = -m \left \frac{dv_z}{dr} \right ^{n-1} \frac{dv_z}{dr}$
$\tau_{rz}(r) = \left(\frac{\Delta P}{2L} \right) r$	$\tau_{rz}(r) = \left(\frac{\Delta P}{2L} \right) r$
$\tau_w = \tau_{rz}(R) = \frac{R \Delta P}{2L}$	$\tau_w = \tau_{rz}(R) = \frac{R \Delta P}{2L}$
$-\dot{\gamma}_{rz}(r) = \left(\frac{\Delta P}{2\mu L} \right) r$	$-\dot{\gamma}_{rz}(r) = \left(\frac{\Delta P}{2mL} \right)^s$
$\dot{\gamma}_w = -\dot{\gamma}_{rz}(R) = \frac{R \Delta P}{2\mu L}$	$\dot{\gamma}_w = -\dot{\gamma}_{rz}(R) = \left(\frac{R \Delta P}{2mL} \right)^s$
$v_z(r) = \frac{R^2 \Delta P}{4\mu L} \left[1 - \left(\frac{r}{R} \right)^2 \right]$	$v_z(r) = \frac{R}{1+s} \left(\frac{R \Delta P}{2mL} \right)^s \left[1 - \left(\frac{r}{R} \right)^{s+1} \right]$
$v_z(0) = v_{\max} = \frac{R^2 \Delta P}{4\mu L}$	$v_z(0) = v_{\max} = \frac{R}{1+s} \left(\frac{R \Delta P}{2mL} \right)^s$
$Q = \frac{\pi R^4 \Delta P}{8\mu L}$	$Q = \left(\frac{\pi R^3}{s+3} \right) \left(\frac{R \Delta P}{2mL} \right)^s$
$\tau_{rz} = -\eta(\tau) \frac{dv_z}{dr}$, where $\eta(\tau) = \frac{\eta_0}{1 + (\tau/\tau_{1/2})^{\alpha-1}}$ $\tau = \tau_{rz} $	

$$\tau_{rz}(r) = \left(\frac{\Delta P}{2L} \right) r$$

$$\tau_w = \tau_{rz}(R) = \frac{R \Delta P}{2L}$$

$$-\dot{\gamma}_{rz}(r) = \left(\frac{\Delta P}{2\eta_0 L} \right) r \left[1 + \left(\frac{\Delta P r}{2L \tau_{1/2}} \right)^{\alpha-1} \right]$$

$$\dot{\gamma}_w = -\dot{\gamma}_{rz}(R) = \left(\frac{R \Delta P}{2\eta_0 L} \right) \left[1 + \left(\frac{R \Delta P}{2L \tau_{1/2}} \right)^{\alpha-1} \right]$$

$$v_z(r) = \frac{R^2 \Delta P}{4L \eta_0} \left\{ \left[1 - \left(\frac{r}{R} \right)^2 \right] + \left(\frac{2}{1+\alpha} \right) \left(\frac{R \Delta P}{2L \tau_{1/2}} \right)^{\alpha-1} \left[1 - \left(\frac{r}{R} \right)^{\alpha+1} \right] \right\}$$

$$v_z(0) = v_{\max} = \frac{R^2 \Delta P}{4L \eta_0} \left[1 + \left(\frac{2}{1+\alpha} \right) \left(\frac{R \Delta P}{2L \tau_{1/2}} \right)^{\alpha-1} \right]$$

$$Q = \frac{\pi R^4 \Delta P}{8\eta_0 L} \left[1 + \left(\frac{4}{3+\alpha} \right) \left(\frac{R \Delta P}{2L \tau_{1/2}} \right)^{\alpha-1} \right]$$

Source: Data from Tadmor and Gogos, 1979.

function of the rate of deformation tensor, $\dot{\gamma}$ or the stress tensor, τ . The scalar quantities associated with any tensorial quantity (i.e., with any second ranked tensor) are the invariants of the tensor which are given as (Bird et al., 1987, Chap. 4)

$$I_1 = \Sigma \dot{\gamma}_u = 2 \left[\frac{\partial v_x}{\partial x} + \frac{\partial v_y}{\partial y} + \frac{\partial v_z}{\partial z} \right] = 0 \quad (2.60)$$

$$I_2 = \Sigma_i \Sigma_j \dot{\gamma}_{ij} \dot{\gamma}_{ji} = \dot{\gamma}_{xx}^2 + \dot{\gamma}_{yy}^2 + \dot{\gamma}_{zz}^2 + \dot{\gamma}_{xy}^2 + \dot{\gamma}_{yx}^2 + \dot{\gamma}_{yz}^2 + \dot{\gamma}_{zy}^2 + \dot{\gamma}_{zx}^2 + \dot{\gamma}_{xz}^2 + \dot{\gamma}_{zy}^2 + \dot{\gamma}_{yz}^2 \quad (2.61)$$

and

$$I_3 = \det \dot{\gamma} \quad (2.62)$$

where $\det \dot{\gamma}$ is the determinant of the matrix consisting of the components of $\dot{\gamma}$. For incompressible flow $I_1 = 0$ and hence

$$\eta = \eta(I_2, I_3) \quad (2.63)$$

For flows dominated by shear flow rather than extensional flow (see Section 3.1), I_3 is not very significant and η is

TABLE 2.5 Concentric Annular Pressure Flows

$$\tau_{rz} = -\mu \frac{dv_z}{dr}$$

$$\tau_{rz}(r) = \frac{\Delta P R}{2L} \left[\left(\frac{r}{R} \right) - \left(\frac{1 - \kappa^2}{2 \ln(1/\kappa)} \right) \left(\frac{R}{r} \right) \right]$$

$$\tau_{w1} = \tau_{rz}(R) = \frac{\Delta P R}{2L} \left[1 - \left(\frac{1 - \kappa^2}{2 \ln(1/\kappa)} \right) \right]$$

$$\tau_{w2} = \tau_{rz}(\kappa R) = \frac{\Delta P R}{2L} \left[\kappa - \left(\frac{1 - \kappa^2}{2 \ln(1/\kappa)} \right) \left(\frac{1}{\kappa} \right) \right]$$

$$\dot{\gamma}_{w1} = -\dot{\gamma}_{rz}(R) = \frac{\Delta P R}{2\mu L} \left[1 - \left(\frac{1 - \kappa^2}{2 \ln(1/\kappa)} \right) \right]$$

$$\dot{\gamma}_{w2} = \dot{\gamma}_{rz}(\kappa R) = \frac{\Delta P R}{2\mu L} \left[\kappa - \left(\frac{1 - \kappa^2}{2 \ln(1/\kappa)} \right) \left(\frac{1}{\kappa} \right) \right]$$

$$v_z(r) = \frac{\Delta P R^2}{4\mu L} \left[1 - \left(\frac{r}{R} \right)^2 + \left(\frac{1 - \kappa^2}{\ln(1/\kappa)} \right) \ln \left(\frac{r}{R} \right) \right]$$

$$v_z(\lambda R) = v_{\max} = \frac{\Delta P R^2}{4\mu L} \left\{ 1 - \left(\frac{1 - \kappa^2}{2 \ln(1/\kappa)} \right) \left[1 - \ln \left(\frac{1 - \kappa^2}{2 \ln(1/\kappa)} \right) \right] \right\} \quad \lambda^2 = \frac{1 - \kappa^2}{2 \ln(1/\kappa)}$$

$$Q = \frac{\pi \Delta P R^4}{8\mu L} \left[(1 - \kappa^4) - \frac{(1 - \kappa^2)^2}{\ln(1/\kappa)} \right]$$

$$\tau_{rz} = - \left| \frac{dv_z}{dr} \right|^{n-1} \left(\frac{dv_z}{dr} \right) \quad \xi = \frac{r}{R} \quad s = \frac{1}{n} \tau_{rz}(\beta R) = 0$$

$$v_z^1(r) = R \left(\frac{\Delta P R}{2\mu L} \right)^s \int_{\kappa}^{\xi} \left(\frac{\beta^2}{\xi'} - \xi' \right)^s d\xi' \quad \kappa \leq \xi \leq \lambda$$

$$v_z^{11} = R \left(\frac{\Delta P R}{2\mu L} \right)^s \int_{\xi}^1 \left(\xi' - \frac{\beta^2}{\xi'} \right)^s d\xi' \quad \lambda \leq \xi \leq 1$$

λ is evaluated numerically for the equations above using the boundary condition

$$v_z^1(\beta R) = v_z^{11}(\beta R)$$

TABLE 2.6 Equation of Continuity in Several Coordinate Systems

Rectangular coordinates (x, y, z) :

$$\frac{\partial \rho}{\partial t} + \frac{\partial}{\partial x} (\rho v_x) + \frac{\partial}{\partial y} (\rho v_y) + \frac{\partial}{\partial z} (\rho v_z) = 0 \tag{A}$$

Cylindrical coordinates (r, θ, z) :

$$\frac{\partial \rho}{\partial t} + \frac{1}{r} \frac{\partial}{\partial r} (\rho r v_r) + \frac{1}{r} \frac{\partial}{\partial \theta} (\rho v_\theta) + \frac{\partial}{\partial z} (\rho v_z) = 0 \tag{B}$$

Spherical coordinates (r, θ, ϕ) :

$$\frac{\partial \rho}{\partial t} + \frac{1}{r^2} \frac{\partial}{\partial r} (\rho r^2 v_r) + \frac{1}{r \sin \theta} \frac{\partial}{\partial \theta} (\rho v_\theta \sin \theta) + \frac{1}{r \sin \theta} \frac{\partial}{\partial \phi} (\rho v_\phi) = 0 \tag{C}$$

Source: Data from Bird et al., 1960.

TABLE 2.7 Equation of Motion in Terms of τ Rectangular coordinates (x, y, z) :

$$\rho \left(\frac{\partial v_x}{\partial t} + v_x \frac{\partial}{\partial x} v_x + v_y \frac{\partial}{\partial y} v_x + v_z \frac{\partial}{\partial z} v_x \right) = - \left[\frac{\partial}{\partial x} \tau_{xx} + \frac{\partial}{\partial y} \tau_{yx} + \frac{\partial}{\partial z} \tau_{zx} \right] - \frac{\partial p}{\partial x} + \rho g_x \quad (\text{A})$$

$$\rho \left(\frac{\partial v_y}{\partial t} + v_x \frac{\partial}{\partial x} v_y + v_y \frac{\partial}{\partial y} v_y + v_z \frac{\partial}{\partial z} v_y \right) = - \left[\frac{\partial}{\partial x} \tau_{xy} + \frac{\partial}{\partial y} \tau_{yy} + \frac{\partial}{\partial z} \tau_{zy} \right] - \frac{\partial p}{\partial y} + \rho g_y \quad (\text{B})$$

$$\rho \left(\frac{\partial v_z}{\partial t} + v_x \frac{\partial}{\partial x} v_z + v_y \frac{\partial}{\partial y} v_z + v_z \frac{\partial}{\partial z} v_z \right) = - \left[\frac{\partial}{\partial x} \tau_{xz} + \frac{\partial}{\partial y} \tau_{yx} + \frac{\partial}{\partial z} \tau_{zz} \right] - \frac{\partial p}{\partial z} + \rho g_z \quad (\text{C})$$

Cylindrical coordinates (r, θ, z) :

$$\rho \left(\frac{\partial v_r}{\partial t} + v_r \frac{\partial v_r}{\partial r} + \frac{v_\theta}{r} \frac{\partial v_r}{\partial \theta} - \frac{v_\theta^2}{r} + v_z \frac{\partial v_r}{\partial z} \right) = - \left[\frac{1}{r} \frac{\partial}{\partial r} (r \tau_{rr}) + \frac{1}{r} \frac{\partial}{\partial \theta} \tau_{\theta r} + \frac{\partial}{\partial z} \tau_{zr} - \frac{\tau_{\theta\theta}}{r} \right] - \frac{\partial p}{\partial r} + \rho g_r \quad (\text{D})$$

$$\rho \left(\frac{\partial v_\theta}{\partial t} + v_r \frac{\partial v_\theta}{\partial r} + \frac{v_\theta}{r} \frac{\partial v_\theta}{\partial \theta} - \frac{v_r v_\theta}{r} + v_z \frac{\partial v_\theta}{\partial z} \right) = - \left[\frac{1}{r^2} \frac{\partial}{\partial r} (r^2 \tau_{r\theta}) + \frac{1}{r} \frac{\partial}{\partial \theta} \tau_{\theta\theta} + \frac{\partial}{\partial z} \tau_{z\theta} + \frac{\tau_{\theta r} - \tau_{r\theta}}{r} \right] - \frac{1}{r} \frac{\partial p}{\partial \theta} + \rho g_\theta \quad (\text{E})$$

$$\rho \left(\frac{\partial v_z}{\partial t} + v_r \frac{\partial v_z}{\partial r} + \frac{v_\theta}{r} \frac{\partial v_z}{\partial \theta} + v_z \frac{\partial v_z}{\partial z} \right) = - \left[\frac{1}{r} \frac{\partial}{\partial r} (r \tau_{rz}) + \frac{1}{r} \frac{\partial}{\partial \theta} \tau_{\theta z} + \frac{\partial}{\partial z} \tau_{zz} \right] - \frac{\partial p}{\partial z} + \rho g_z \quad (\text{F})$$

Spherical coordinates (r, θ, ϕ) :

$$\begin{aligned} \rho \left(\frac{\partial v_r}{\partial t} + v_r \frac{\partial v_r}{\partial r} + \frac{v_\theta}{r} \frac{\partial v_r}{\partial \theta} + \frac{v_\phi}{r \sin \theta} \frac{\partial v_r}{\partial \phi} - \frac{v_\theta^2 + v_\phi^2}{r} \right) \\ = - \left[\frac{1}{r^2} \frac{\partial}{\partial r} (r^2 \tau_{rr}) + \frac{1}{r \sin \theta} \frac{\partial}{\partial \theta} (\tau_{\theta r} \sin \theta) + \frac{1}{r \sin \theta} \frac{\partial}{\partial \phi} \tau_{\phi r} - \frac{\tau_{\theta\theta} + \tau_{\phi\phi}}{r} \right] - \frac{\partial p}{\partial r} + \rho g_r \end{aligned} \quad (\text{G})$$

$$\begin{aligned} \rho \left(\frac{\partial v_\theta}{\partial t} + v_r \frac{\partial v_\theta}{\partial r} + \frac{v_\theta}{r} \frac{\partial v_\theta}{\partial \theta} + \frac{v_\phi}{r \sin \theta} \frac{\partial v_\theta}{\partial \phi} - \frac{v_r v_\theta}{r} - \frac{v_\phi^2 \cot \theta}{r} \right) \\ = - \left[\frac{1}{r^3} \frac{\partial}{\partial r} (r^3 \tau_{r\theta}) + \frac{1}{r \sin \theta} \frac{\partial}{\partial \theta} (\tau_{\theta\theta} \sin \theta) + \frac{1}{r \sin \theta} \frac{\partial}{\partial \phi} \tau_{\phi\theta} + \frac{\tau_{\theta r} - \tau_{r\theta} - \tau_{\phi\phi} \cot \theta}{r} \right] - \frac{1}{r} \frac{\partial p}{\partial \theta} + \rho g_\theta \end{aligned} \quad (\text{H})$$

Source: Data from Bird et al., 1987.

TABLE 2.8 Rate-of-Strain TensorRectangular coordinates (x, y, z) :

$$\begin{aligned} \dot{\gamma}_{xx} &= 2 \frac{\partial v_x}{\partial x} & \dot{\gamma}_{xy} = \dot{\gamma}_{yx} &= \frac{\partial v_y}{\partial x} + \frac{\partial v_x}{\partial y} \\ \dot{\gamma}_{yy} &= 2 \frac{\partial v_y}{\partial y} & \dot{\gamma}_{yz} = \dot{\gamma}_{zy} &= \frac{\partial v_z}{\partial y} + \frac{\partial v_y}{\partial z} \\ \dot{\gamma}_{zz} &= 2 \frac{\partial v_z}{\partial z} & \dot{\gamma}_{zx} = \dot{\gamma}_{xz} &= \frac{\partial v_x}{\partial z} + \frac{\partial v_z}{\partial x} \end{aligned}$$

Cylindrical coordinates (r, θ, z) :

$$\begin{aligned} \dot{\gamma}_{rr} &= 2 \frac{\partial v_r}{\partial r} & \dot{\gamma}_{r\theta} = \dot{\gamma}_{\theta r} &= r \frac{\partial}{\partial r} \left(\frac{v_\theta}{r} \right) + \frac{1}{r} \frac{\partial v_r}{\partial \theta} \\ \dot{\gamma}_{\theta\theta} &= 2 \left(\frac{1}{r} \frac{\partial v_\theta}{\partial \theta} + \frac{v_r}{r} \right) & \dot{\gamma}_{\theta z} = \dot{\gamma}_{z\theta} &= \frac{1}{r} \frac{\partial v_z}{\partial \theta} + \frac{\partial v_\theta}{\partial z} \\ \dot{\gamma}_{zz} &= 2 \frac{\partial v_z}{\partial z} & \dot{\gamma}_{zr} = \dot{\gamma}_{rz} &= \frac{\partial v_r}{\partial z} + \frac{\partial v_z}{\partial r} \end{aligned}$$

Spherical coordinates (r, θ, ϕ) :

$$\begin{aligned} \dot{\gamma}_{rr} &= 2 \frac{\partial v_r}{\partial r} & \dot{\gamma}_{r\theta} = \dot{\gamma}_{\theta r} &= r \frac{\partial}{\partial r} \left(\frac{v_\theta}{r} \right) + \frac{1}{r} \frac{\partial v_r}{\partial \theta} \\ \dot{\gamma}_{\theta\theta} &= 2 \left(\frac{1}{r} \frac{\partial v_\theta}{\partial \theta} + \frac{v_r}{r} \right) & \dot{\gamma}_{\theta\phi} = \dot{\gamma}_{\phi\theta} &= \frac{\sin \theta}{r} \frac{\partial}{\partial \theta} \left(\frac{v_\phi}{\sin \theta} \right) + \frac{1}{r \sin \theta} \frac{\partial v_\theta}{\partial \phi} \\ \dot{\gamma}_{\phi\phi} &= 2 \left(\frac{1}{r \sin \theta} \frac{\partial v_\phi}{\partial \phi} + \frac{v_r}{r} + \frac{v_\theta \cot \theta}{r} \right) & \dot{\gamma}_{\phi r} = \dot{\gamma}_{r\phi} &= \frac{1}{r \sin \theta} \frac{\partial v_r}{\partial \phi} + r \frac{\partial}{\partial r} \left(\frac{v_\phi}{r} \right) \end{aligned}$$

Source: Data from Bird et al., 1987.

taken to be a function of I_2 only (Bird et al., 1987, p. 171). Actually we use $\sqrt{\frac{1}{2}I_2}$, which is called the shear rate, $\dot{\gamma}$. Likewise for models for which η depends on the invariants of $\boldsymbol{\tau}$, η is taken to be a function of $\Sigma_i \Sigma_j \tau_{ij} \tau_{ji}$, which can be found by replacing terms such as $\dot{\gamma}_{xy}$ by τ_{xy} in Eq. 2.61.

One can generalize the expression for $\boldsymbol{\tau}$ as follows:

$$\boldsymbol{\tau} = -\eta(\dot{\gamma})\dot{\boldsymbol{\gamma}} \tag{2.64}$$

Equation 2.64 is called the *generalized Newtonian fluid (GNF) model*. The empiricisms for $\eta(\dot{\gamma})$ analogous to those given in Eqs. 2.6 to 2.9 become, respectively,

$$\eta = m\dot{\gamma}^{n-1} \tag{2.65}$$

$$\frac{\eta_0}{\eta} = 1 + \left(\frac{\tau}{\tau_{1/2}}\right)^{\alpha-1} \tag{2.66}$$

$$\frac{\eta - \eta_\infty}{\eta_0 - \eta_\infty} = [1 + (\lambda\dot{\gamma})^2]^{(n-1)/2} \tag{2.67a}$$

$$\eta = \mu_0 + (\tau_0/\dot{\gamma}) \quad \tau \geq \tau_0 \tag{2.67b}$$

$$\eta = \infty \quad \tau < \tau_0 \tag{2.67c}$$

where $\tau = \sqrt{\frac{1}{2}(\boldsymbol{\tau} : \boldsymbol{\tau})}$ and $\dot{\gamma} = \sqrt{\frac{1}{2}I_2}$. In one-dimensional flows such as those considered in Section 2.2 these equations reduce to the same form with $\dot{\gamma}$ becoming dv_x/dy or τ becoming τ_{yx} .

Before considering two examples that illustrate the use of the equations of motion, it is necessary to discuss the equation of mechanical energy. For single particles the work done on a particle is given by taking the dot product of Newton’s second law of motion with the velocity; that is,

$$\mathbf{F} \cdot \mathbf{v} = m\mathbf{a} \cdot \mathbf{v} = 0.5m \left(\frac{dv^2}{dt}\right) = \frac{d}{dt} \left(\frac{1}{2}mv^2\right) \tag{2.68}$$

This equation tells us that the work done on the particle is just equal to the change in kinetic energy. For a continuum most mechanical and chemical engineers have solved the macroscopic mechanical energy balance, which is shown below for a fluid of constant ρ :

$$\frac{d}{dt}(K_{\text{tot}} + \phi_{\text{tot}}) = -\Delta \left[\left(\frac{1 \langle \bar{v}^3 \rangle}{2 \langle \bar{v} \rangle} + \hat{\phi} + \frac{p}{\rho} \right) w \right] - W - E_v \tag{2.69}$$

where K_{tot} and ϕ_{tot} are the total kinetic energy and potential energy, respectively, \bar{v} is the time averaged velocity, w is the mass flow rate, W is the work input to the system, E_v is the friction loss, $\hat{\phi}$ is the potential energy per unit mass, and Δ represents the change in the quantities (Bird et al., 2007). By

taking the “dot” or scalar product of the equation of motion with the velocity field one obtains the mechanical energy equation for a continuum:

$\frac{\partial}{\partial t} \left(\frac{1}{2} \rho v^2 \right)$ rate of increase in kinetic energy per unit volume	$=$	$-\Delta \cdot \left(\frac{1}{2} \rho v^2 \mathbf{v} \right)$ net rate of input of kinetic energy by virtue of bulk flow	$-p(-\Delta \cdot \mathbf{v})$ rate of work done by pressure of surroundings on volume element	$-p(-\Delta \cdot \mathbf{v})$ rate of <i>reversible</i> conversion to internal energy
			$-\Delta \cdot [\boldsymbol{\tau} \cdot \mathbf{v}]$ rate of work done by viscous forces on volume element	$-(-\boldsymbol{\tau} : \Delta \mathbf{v})$ rate of <i>irreversible</i> conversion to internal energy
		$+\rho(\mathbf{v} \cdot \mathbf{g})$ rate of work done by gravity force on volume element		

(2.70)

The various quantities that make up this equation have been written using tensor notation. As we do not intend to evaluate these terms, we have given the physical significance of each term. By integrating Eq. 2.70 over the volume of a region one can obtain Eq. 2.69. Equation 2.70 is used to determine the power requirements for a piece of processing equipment.

Example 2.4. Radial Flow of a Newtonian Fluid Between Two Parallel Disks

Determine the velocity field and the pressure distribution for the flow of an incompressible Newtonian fluid between two disks as shown in Figure 2.13. Flows similar to this occur in several polymer processes including injection molding in a center-gated disk mold or compression molding.

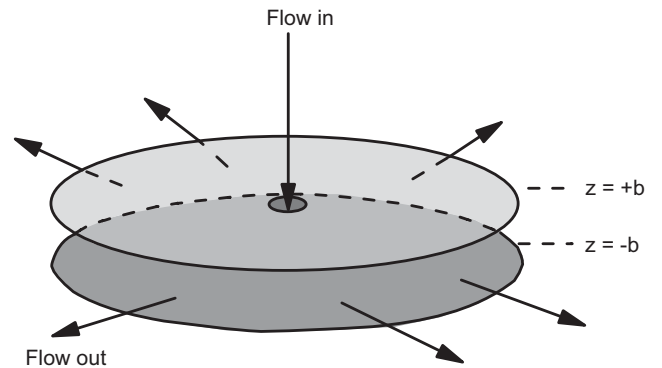


FIGURE 2.13 Radial flow between two parallel disks.

Solution. We start with the postulates for the velocity and pressure fields:

$$v_r = v_r(z, r) \quad p = p(r) \quad (2.71)$$

Next one decides on which components of stress arise for a given constitutive equation. Here the Newtonian fluid model is selected, and one uses Table 2.8 to determine the components of $\dot{\gamma}$. Because $\tau_{ij} = -\mu\dot{\gamma}_{ij}$, then based on Eq. 2.71 one finds the following components for τ :

$$\tau_{rr} = -2\mu(\partial v_r/\partial r) \quad (2.72)$$

$$\tau_{\theta\theta} = -2\mu v_r/r \quad (2.73)$$

$$\tau_{rz} = \tau_{zr} = -\mu(\partial v_r/\partial z) \quad (2.74)$$

The equation of continuity reduces to

$$\frac{1}{r} \frac{\partial}{\partial r}(rv_r) = 0 \quad (2.75)$$

It is indicated by Eq. 2.5 that rv_r must be a function of z only, $\Phi(z)$. Hence, from Eq. 2.75 one finds

$$v_r = \Phi(z)/r \quad (2.76)$$

This reduces the expressions for the stresses to the following equations:

$$\tau_{\theta\theta} = -2\mu \frac{\phi(z)}{r^2} \quad \tau_{rr} = +2\mu \frac{\phi(z)}{r^2} \quad \tau_{zr} = -\frac{\mu}{r} \frac{d\phi(z)}{dz} \quad (2.77)$$

The equation of motion, using Table 2.7, becomes (note that the inertial terms are neglected)

$$-\frac{1}{r} \frac{\partial}{\partial r}(r\tau_{rr}) - \frac{\partial}{\partial z}\tau_{zr} + \frac{\tau_{\theta\theta}}{r} - \frac{\partial p}{\partial r} = 0 \quad (2.78)$$

Substituting Eq. 2.77 into Eq. 2.78 and making use of Eq. 2.75, one obtains the following differential equation for $\Phi(z)$:

$$0 = -\frac{dp}{dr} + \frac{\mu}{r} \frac{d^2\phi}{dz^2} \quad (2.79)$$

We can integrate this equation to find ϕ , since dp/dr is a function of r , and the constants of integration can be solved for using the following boundary conditions:

$$\text{B.C.1: at } z = +b, \quad \phi(z) = 0 \text{ for all } r \quad (2.80)$$

$$\text{B.C.2: at } z = -b, \quad \phi(z) = 0 \text{ for all } r \quad (2.81)$$

Furthermore, one can find the pressure difference using

$$\text{B.C.3: at } r = r_1, \quad p = p_1 \quad (2.82)$$

$$\text{B.C.4: at } r = r_2, \quad p = p_2 \quad (2.83)$$

The velocity field is then given as

$$v_r(r, z) = \frac{b^2 \Delta p}{2\mu r \ln(r_2/r_1)} [1 - (z/b)^2] \quad (2.84)$$

The volumetric flow rate, Q , is found by integrating v_r over the cross-sectional area:

$$Q = \int_0^{2\pi} \int_{-b}^b v_r(r, z) r \, d\theta \, dz = \frac{4\pi b^2 \Delta p}{3\mu \ln(r_2/r_1)} \quad (2.85)$$

The key points of this example are that the continuity equation helps us find the form of $v_r(r, z)$ and that there are normal stresses for this flow. The values of τ_{rr} and $\tau_{\theta\theta}$ come from the extensional deformations generated in this flow. It is noted because of the sign convention, tensile stresses are negative. ■

Example 2.5. Radial Flow of a Power-Law Fluid

Do Example 2.4 for a power-law fluid.

Solution. For a power-law fluid the same postulates and assumptions that are made for the Newtonian case are used. In particular, Eq. 2.76 holds as well as those for the stress components. The difference is that μ must be replaced by η , which depends on $\dot{\gamma}$. $\dot{\gamma}$ for this flow is

$$\dot{\gamma} = \sqrt{2\left(\frac{\partial v}{\partial r} r\right)^2 + 2\left(\frac{v}{r} r\right)^2 + \left(\frac{\partial v}{\partial z} r\right)^2} \quad (2.86a)$$

$$= \sqrt{2\frac{\phi^2}{r^4} + \frac{2\phi^2}{r^4} + \frac{1}{r^2} \left(\frac{d\phi}{dz}\right)^2} \quad (2.86b)$$

The stresses are then

$$\tau_{rr} = +2m|\dot{\gamma}|^{n-1} \frac{\phi(z)}{r^2} \quad (2.87)$$

$$\tau_{\theta\theta} = -2m|\dot{\gamma}|^{n-1} \frac{\phi(z)}{r^2} \quad (2.88)$$

$$\tau_{zr} = -m|\dot{\gamma}|^{n-1} \frac{d\phi(z)}{dz} \frac{1}{r} \quad (2.89)$$

When these are substituted into Eq. 2.78, one obtains a nonlinear differential equation for $\Phi(z)$. Hence, the use of the GNF model for the stress components leads to a complex differential equation. ■

2.4 USEFUL APPROXIMATIONS

The radial flow example illustrates how rapidly problems involving the flow of non-Newtonian fluids become mathematically complicated. There are a number of times when the analysis can be simplified. There are two useful approximations that simplify the differential equations that arise out of the equations of motion. These neglect the effect of curvature and the lubrication approximation. The solutions of several problems, which have already been dealt with, are used to illustrate these approximations. First, we examine how neglecting curvature can lead to a simplification of the differential equations. This is followed by the handling of geometries in which a variation in the dimension transverse to the flow direction occurs, such as the case of a tapered tube.

The extrusion of a polymer melt for film blowing is usually carried out using an annular die with a thin gap such that $\kappa > 0.90$. For example, a film blowing die may have an outer diameter of 0.045 m and an inner diameter of 0.0449 m. Hence, κ is about 0.998. The equation of motion for this flow is

$$\frac{d}{dr}(r\tau_{rz}) = (P'_0 - P'_L)r/L \quad (2.90)$$

For a power-law fluid, τ_{rz} is given by Eq. 2.32. One now expands the derivative in Eq. 2.90 and compares the order of each term:

$$\frac{d\tau_{rz}}{dr} + \frac{\tau_{rz}}{r} = \frac{P'_0 - P'_L}{L} \quad (2.91)$$

where τ_{rz} is given by the following expression:

$$\tau_{rz} = -m(dv_z/dr)^n \quad (2.92)$$

in the region $\kappa R < r < \beta R$. We now approximate the derivatives as follows:

$$\frac{dv_z}{dr} \approx \frac{v_{\max} - 0}{\beta R - \kappa R} = \frac{v_{\max}}{(\beta - \kappa)R} \quad (2.93)$$

$$\tau_{rz} \approx -m \left(\frac{v_{\max}}{(\beta - \kappa)R} \right)^n \quad (2.94)$$

$$\frac{d\tau_{rz}}{dr} \approx -mn \left(\frac{v_{\max}}{(\beta - \kappa)R} \right)^{n-1} \frac{v_{\max}}{R^2(\beta - \kappa)^2} \quad (2.95)$$

One can compare the order of each term on the left side of Eq. 2.91 to determine if one or the other is dominant. Given the conditions in the example, βR will be about $0.5R(1 - \kappa)$ or $\beta = 0.999$. Hence,

$$\frac{\tau_{rz}}{r} \approx -m \left(\frac{v_{\max}}{(\beta - \kappa)R} \right)^n \frac{1}{R} \quad (2.96)$$

$$\frac{d\tau_{rz}}{dr} \approx -mn \left(\frac{v_{\max}}{(\beta - \kappa)R} \right)^n \frac{1}{R(0.001)} \quad (2.97)$$

Therefore, $d\tau_{rz}/dr$ is about 1000 times greater than τ_{rz}/r and one neglects the second term in Eq. 2.91. Now we integrate Eq. 2.91 to find the stress field:

$$\tau_{rz} = [(P'_0 - P'_L)/L]r + C_1 \quad (2.98)$$

At $r = \beta R$, $\tau_{rz} = 0$ and $C_1 = -(P'_0 - P'_L)/L(\beta R/L)$. Before continuing it is noted that Eq. 2.98 is exactly that which is solved for flow between flat plates. One now substitutes the expression for τ_{rz} based on the power-law fluid into Eq. 2.98 to find $v_z(r)$:

for

$$\kappa R < r < \beta R, \quad -m \left(\frac{dv_z}{dr} \right)^n = \left(\frac{P'_0 - P'_L}{L} \right) [r - \beta R] \quad (2.99)$$

and for

$$\beta R < r < R, \quad +m \left(\frac{dv_z}{dr} \right)^n = \left(\frac{P'_0 - P'_L}{L} \right) [r - \beta R] \quad (2.100)$$

These equations are integrated using the no-slip boundary conditions as before to give $v_z(r)$:

$$v_z^<(\xi) = \left(\frac{(P'_0 - P'_L)R}{mL} \right)^{1/n} \frac{Rn}{n+1} [(\beta - \kappa)^{1/n+1} - (\beta - \xi)^{1/n+1}] \quad (2.101)$$

$$v_z^>(\xi) = \left(\frac{(P'_0 - P'_L)R}{mL} \right)^{1/n} \frac{Rn}{n+1} [(1 - \beta)^{1/n+1} - (\xi - \beta)^{1/n+1}] \quad (2.102)$$

With the condition that $v_z^< = v_z^>$ at $r = \beta R$, one finds that $\beta = (1 + \kappa)/2$ or that for small gaps β is at the center of the gap. Hence, for small gaps one finds an analytical solution for $v_z(r)$. This solution is expected to apply for values of κ down to about 0.8. Obviously the expressions in Eqs. 2.101 and 2.102 can be integrated to find Q :

$$Q = \left(\frac{\pi R^3}{s+2} \right) \left(\frac{R \Delta P}{2mL} \right)^s (1 - \kappa)^{s+2} \frac{(1 + \kappa)}{2} \quad (2.103)$$

where $s = 1/n$ and $\Delta P = P'_0 - P'_L$.

This same expression could be found by using the expression for slit flow in Table 2.5 and replacing the width, W , by $\pi R(1 + \kappa)$ and the height, H , by $R(1 - \kappa)$ (see Problem 2B.4). In essence, the annular region is opened up and treated as plane slit flow. One will find this a useful approach throughout the design of polymer processes.

There are many geometries in polymer processing where the dimensions change along the flow direction: for example, in extrusion through a tapered die, in calendaring, and the

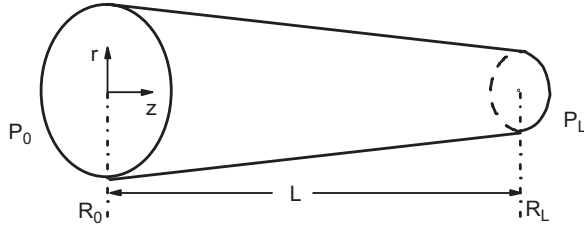


FIGURE 2.14 Flow through a tapered tube.

channel of an extrusion screw. Solving the differential equations associated with these geometries would lead to non-linear partial differential equations. However, by introducing an approximation known as the *lubrication approximation*, one can simplify the differential equation. To illustrate this method, flow through a tapered tube, as shown in Figure 2.14, is considered. Based on this geometry one would postulate velocity and pressure fields as follows:

$$v_z = v_z(r, z) \quad p = p(z) \quad (2.104)$$

This would lead to the following form of the equation of motion:

$$-\frac{1}{r} \frac{\partial}{\partial r} (r \tau_{rz}) - \frac{\partial}{\partial z} \tau_{zz} - \frac{\partial p}{\partial z} = 0 \quad (2.105)$$

If one evaluated $\partial \tau_{zz} / \partial z$ relative to the other term, we would find that for small amounts of taper this term would be small compared to the other term. One would follow the same analysis as in the previous example to show the derivative is small. Hence, one neglects $\partial \tau_{zz} / \partial z$ and solves the following equation:

$$\frac{1}{r} \frac{\partial}{\partial r} (r \tau_{rz}) - \frac{\partial p}{\partial z} = 0 \quad (2.106)$$

This is just the equation that would be solved for a straight tube. Hence, the solution to this equation is

$$v_z(r) = \frac{R}{1+s} \left(\frac{R \Delta P}{2mL} \right)^{1/n} \left[1 - \left(\frac{r}{R} \right)^{\frac{1}{n}+1} \right] \quad (2.107)$$

However, the solution is applied at each distance z down the tube. One replaces R by $R(z)$, which is obtained from the geometry of the tube as follows:

$$R(z) = -[(R_0 - R_L)L]z + R_0 \quad (2.108)$$

At any z position, one can integrate Eq. 2.107 over the cross section of the tube to find Q :

$$Q = \left(\frac{\pi R^3}{s+3} \right) \left(\frac{R \Delta P}{2mL} \right)^s \quad (2.109)$$

$\Delta P/L$ is replaced by $-dp/dz$ and R by Eq. 2.108. This gives a first order differential equation for finding p :

$$2m \left(\frac{Q(s+3)}{\pi} \right)^n R^{-3n-1} = -\frac{dp}{dz} \quad (2.110)$$

Equation 2.110 can be integrated using the conditions that at $z=0$, $p=P_0$ and at $z=L$, $p=P_L$ to give

$$P_0 - P_L = \frac{2mL}{3n} \left[\frac{Q}{\pi} \left(\frac{1}{n+3} \right) \right]^n \left(\frac{R_L^{-3n} - R_0^{-3n}}{R_0 - R_L} \right) \quad (2.111)$$

This approximation is probably adequate for tapers of less than 30° , but for more abrupt contractions the viscoelastic nature of polymeric fluids may make the pressure drop higher (see Section 7.2). However, for the most part the lubrication approximation will be extremely useful in the design of extrusion processes (i.e., the design of extrusion dies and screw design).

2.5 SOLUTION TO DESIGN PROBLEM I

The solution to Design Problem I is presented in this section. The lubrication approximation is used first to obtain a solution. This is followed by a numerical approach in which the die is broken into a series of annuli.

2.5.1 Lubrication Approximation Solution

The solution will proceed as follows: (1) the dimensions of the die will be determined; (2) an expression for ΔP versus Q will be determined using the lubrication approximation; (3) from this relation one can calculate Q for the given ΔP and the average velocity $\langle v_z \rangle$; and (4) the time required to extrude the parison is calculated.

The following information is given in the problem statement:

- Parison weight: 90 g
- Parison thickness (t_p): 3.81×10^{-4} m
- Parison diameter (D_p): 0.127 m
- Parison density (ρ_p): 965 kg/m^3

From this information and the equation for the mass of the parison (m_p),

$$m_p = \rho_p L_p \pi \left(R_{0,p}^2 - R_{i,p}^2 \right) \quad (2.112)$$

one can calculate the desired length of the parison (L_p), which is 0.615 m. Since the phenomenon of die swell (see Section 3.2) is neglected, the final thickness and diameter of

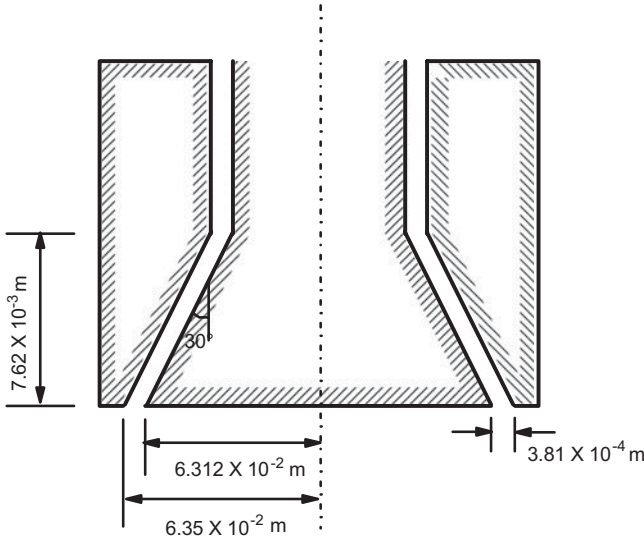


FIGURE 2.15 Conical region of the blow molding die showing the dimensions required to produce the parison as requested in Design Problem I.

the die are assumed to be the same as those of the parison. The dimensions of the die geometry are then as shown in Figure 2.15.

The next goal is to determine an expression that will allow one to calculate Q and the average velocity, $\langle v_z \rangle$, for the maximum allowable pressure drop. To do this the lubrication approximation is used. The flow region of interest is shown in Figure 2.16. With the assumption that the gap is small relative to the radius (which is acceptable over most of the length of the die), the annular region can be opened up to the planar region shown in Figure 2.16. For a Newtonian fluid the expression for Q for flat plates (see Table 2.3) is

$$Q = \frac{WH^3 \Delta P}{12\mu L} \quad (2.113)$$

$\Delta P/L$ is replaced by $-dp/dz$. H is the gap which is constant and is $R_0(1 - \kappa_0)$ or $R_L(1 - \kappa_L)$, where R_0 and R_L are the outer radii of the tapered annulus at $z = 0$ and $z = L$, respectively. It is also noted that although the gap is constant, the ratio of the inner to outer radii, κ , varies slightly with the distance

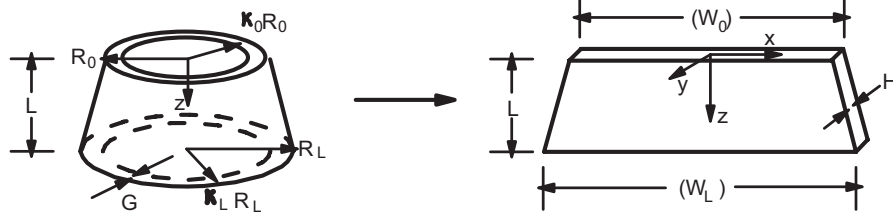


FIGURE 2.16 Three-dimensional view of a conical die unfolded into a planar die.

z (e.g., the value of κ at $z = L$ is defined as κ_L). W varies linearly with z as given below:

$$W = W_0 + \frac{W_L - W_0}{L}z \quad (2.114)$$

where $W_0 = \pi R_0(1 + \kappa_0)$ and $W_L = \pi R_L(1 + \kappa_L)$. On substituting the expression for W into Eq. 2.113 and replacing $\Delta P/L$ by $-dp/dz$, Eq. 2.113 becomes

$$Q = \left(W_0 + \frac{W_L - W_0}{L}z \right) \frac{H^3}{12\mu} \left(\frac{-dp}{dz} \right) \quad (2.115)$$

Separating variables and integrating, Eq. 2.115 becomes

$$\int_{P_0}^{P_L} (-dp) = \int_0^L \frac{12\mu Q}{H^3 [W_0 + (W_L - W_0)z/L]} dz \quad (2.116)$$

Carrying out the integration one obtains the following expression:

$$P_L - P_0 = \frac{12\mu QL}{H^3(W_L - W_0)} \ln \left(\frac{W_L}{W_0} \right) \quad (2.117)$$

Equation 2.117 is now rearranged to give the following expression for Q :

$$Q = \frac{(P_L - P_0)H^3(W_L - W_0)}{12\mu L \ln(W_L/W_0)} \quad (2.118)$$

Before using Eq. 2.118 to answer the questions associated with Design Problem I, a similar expression will be obtained for a fluid whose viscosity function is described by the power law. Again, using Table 2.3, the expression for pressure-driven flow of a power-law fluid through parallel plates is

$$Q = \frac{WH^2}{2(s+2)} \left(\frac{H \Delta P}{2\mu L} \right)^s \quad (2.119)$$

where $s = 1/n$. Following the same approach as for the Newtonian fluid, one obtains

$$\left(\frac{-dp}{dz} \right)^s = \frac{2Q(s+2)}{(W_0 + (W_L - W_0)z/L) H^2} \left(\frac{2m}{H} \right)^s \quad (2.120)$$

The n th power is taken of both sides of Eq. 2.120 to obtain

$$-\frac{dp}{dz} = \left(\frac{2Q(s+2)}{(W_0 + (W_L - W_0)z/L)H^2} \right)^{1/s} \left(\frac{2m}{H} \right) \quad (2.121)$$

Equation 2.121 is integrated to find $P_0 - P_L$:

$$P_0 - P_L = \left(\frac{2Q(s+2)}{H^2} \right)^n \left(\frac{2mL}{H} \right) \left(\frac{1}{1-n} \right) \times \left(\frac{W_L^{1-n} - W_0^{1-n}}{W_L - W_0} \right) \quad (2.122)$$

Equation 2.122 is rearranged to give the following expression for Q :

$$Q = \frac{(P_0 - P_L)^s H^2}{\left[2(s+2)(H/2mL)^s \left(\frac{1}{1-n} \right)^s \left(\frac{W_L^{1-n} - W_0^{1-n}}{W_L - W_0} \right)^s \right]} \quad (2.123)$$

Equations 2.118 and 2.123 are now used to make the decisions required to solve Design Problem I. The pressure drop at the onset of melt fracture is obtained from the expression for the wall shear stress in Table 2.3:

$$P_0 - P_L = \frac{\tau_w L}{\cos \theta} \frac{2}{H} = \frac{(1.4 \times 10^5 \text{ Pa})(3.81 \times 10^{-4} \text{ m})40}{0.866(3.81 \times 10^{-4} \text{ m})} = 6.467 \times 10^6 \text{ Pa} \quad (2.124)$$

The value of $P_0 - P_L$ is the same whether the fluid is assumed to be described by a Newtonian or power-law model. Equation 2.118 is used to find Q and $\langle v_z \rangle = Q/A$ for the Newtonian case:

$$Q = \frac{(6.467 \times 10^6 \text{ Pa})(3.81 \times 10^{-4})^3}{(3.978 \times 10^{-1} \text{ m} - 3.632 \times 10^{-1} \text{ m})} = 7.08 \times 10^{-7} \text{ m}^3/\text{s}$$

$$Q/A = \frac{7.08 \times 10^{-7} \text{ m}^3/\text{s}}{(3.805 \times 10^{-1} \text{ m})(3.81 \times 10^{-4} \text{ m})} = 4.8 \times 10^{-3} \text{ m/s} \quad (2.125)$$

For the power law Eq. 2.123 is used to find Q and $\langle v_z \rangle$:

$$Q = 2.47 \times 10^{-6} \text{ m}^3/\text{s}$$

$$Q/A = \frac{2.47 \times 10^{-6}}{1.45 \times 10^{-4}} \text{ m/s} = 1.704 \times 10^{-2} \text{ m/s} \quad (2.126)$$

Hence, one can see that there is a significant difference in the values for the Newtonian and power-law cases.

Finally, the length of time to “hang the parison” is determined. Based on the parison weight, the required parison

length is calculated to be 0.615 m. If it is assumed that the parison does not sag under its own weight, then the hang time, t_H , is

$$\text{Newtonian: } t_H = \frac{L}{\langle v_z \rangle} = \frac{0.615 \text{ m}}{4.88 \times 10^{-3} \text{ m/s}} = 126.0 \text{ s}$$

$$\text{Power law: } t_H = \frac{0.615 \text{ m}}{1.704 \times 10^{-2} \text{ m/s}} = 36.1 \text{ s} \quad (2.127)$$

Again there is a significant difference between the hang times for the Newtonian and power-law cases.

In practice, the polymer swells as it leaves the die, giving a wall thickness and parison diameter greater than would be expected. Furthermore, the weight of the parison causes the extruded material to sag under its own weight. This reduces the wall thickness. If the sag is too great, the parison may fail when blown or the wall thickness will vary considerably over the length of the parison. These factors will be dealt with in the next chapter.

2.5.2 Computer Solution

In the second part of Design Problem I, a computer solution is requested. This solution is outlined here, and the program listing is given in the accompanying website under “Numerical Solutions, Chapter 2.” The computer solution allows one to deal with dies having a variable gap (in Fig. 2.2, this corresponds to angle $\alpha \neq 0$). Although one could extend the parallel plate solution to annular dies of variable gap, the computer solution outlined here uses the solution for annular die flow (Table 2.5) applied to segments of length Δz .

The solution proceeds as described below. $\Delta P/\Delta z$ is calculated using Eq. 2.41 for a segment of length Δz :

$$\frac{\Delta P}{\Delta z'} = \left(\frac{Q(s+3)}{\pi R^3(z')} \right)^n \frac{2m}{[(1-\beta^2)^{1+s} - \kappa^{1-s}(\beta^2 - \kappa^2)^{1+s}]^n} \quad (2.128)$$

where $\Delta z' = \Delta z/\cos \theta$ and $z' = z/\cos \theta$. R^o is the outer radius of the annular segment and is given by the following:

$$R^o = R_0^o + \tan \theta z \quad (2.129)$$

while κ is ratio of the inner radius to outer radius at each segment given by

$$\kappa = \frac{R^i(z)}{R^o(z)} = \frac{R_0^i + z \tan \theta}{R_0^o + z \tan \theta} \quad (2.130)$$

Here R is R^o at $z = 0$. β must also be determined for each step and this is done for each segment using Eq. 2.39. Because neither $P_0 - P_L$ nor Q is known, one must use the equation for $\tau_{rz}(R)$ in Table 2.5 to determine $\Delta P/\Delta z'$ over the last segment

TABLE 2.9 Comparison of Predictions for Different Methods of Computation

Approximation Fluid	Flat Plate ^a (Variable Width and Separation)		Series of Annuli ^b	
	Newtonian	Power Law	Power Law	Power Law
Q [m ³ /s]	5.608×10^{-6}	6.638×10^{-5}	20 sections: 1.174×10^{-4}	100 sections: 1.1652×10^{-4}
$\frac{dP}{dz} _{\text{EXIT}}$ [Pa/m]	-8.630×10^9	-5.397×10^9	-4.8504×10^9	-5.7050×10^9
$\tau_{w\text{EXIT}}$ [Pa]	1.490×10^5	9.318×10^5	10.217×10^5	11.091×10^5
Melt fracture?	Yes	Yes	Yes	Yes
$\langle v_z \rangle$ [m/s]	4.083×10^{-2}	4.832×10^{-1}	1.589×10^{-1}	1.553×10^{-1}
t , time required to extrude parison [s]	15.11	1.277	3.884	3.974

^aResults obtained from Computer Code DIEFPA. for (flat plate approximation).

^bResults obtained from Computer Code SERADA (series annular dies approximation).

of the annulus. One can then guess at Q and calculate ΔP over each segment using Eq. 2.118. If ΔP does not match the value at the end segment based on the limit due to melt fracture, then Q is changed and the iteration procedure is started all over. When $\alpha = 0$ and the gap is small, one would expect that this improved method of computation would not be necessary.

The computer solution is compared against the plate solution for the case when $\alpha = 10^\circ$ (note in Section 2.5.1 α was taken as zero) in Table 2.9. First we observe that $\langle v_z \rangle$ or Q is about 10 times greater for the power-law case than for the Newtonian case. The computer solution based on breaking the die up into annular segments (100 sections) leads to values of $\langle v_z \rangle$ that are only about one-third of those calculated using the flat plate. Hence, at the beginning of the conical region there must be a large error in neglecting the curvature in the geometry. We also observe that the taper ($\alpha = 10^\circ$) has a significant effect on the flow rate. The parison hang times vary significantly from the flat plate to annular segment approach. Hence, more accurate solutions may only be obtained by use of a numerical solution and the computer.

PROBLEMS

A. Applications

2A.1 *Power-Law Parameters from the Ellis Model.* Ellis model parameters for a polypropylene sample at 200 °C are $\eta_0 = 1.24\text{E}+04$ Pa·s, $\tau_{1/2} = 6.90\text{E}+03$ Pa, and $\alpha = 2.82$. Estimate m and n in the power-law model using these values of the parameters in the Ellis model.

2A.2 *Flow of HDPE Through Parallel Plates*

- (a) Compare the predictions at $\tau_w = 1.0\text{E}+05$ Pa for the volumetric flow rate for HDPE at 180 °C

for flow through parallel plates (Table 2.3) for Newtonian, power-law, and Ellis models. Use the parameters given in Table 2.2. The plate dimensions are $H = 2.54\text{E}-03$ m, $W = 2.54\text{E}-02$ m, and $L = 5.08\text{E}-02$ m.

- (b) Determine the pressure drop in each case.
(c) Determine the wall shear rate, $\dot{\gamma}_w$, for each model.

2A.3 *Pressure Transducer Selection.* It is desired to select pressure transducers to be mounted on the upper wall of the plates described in Problem 2A.2. The accuracy of the transducers depends on the range of pressure that must be measured. For the conditions described in Problem 2A.2, what is the maximum pressure that would have to be measured for pressure transducers mounted at the entrance, halfway down the channel, and at a distance of H from the exit?

2A.4 *Change in Wire Coating Conditions.* For the wire coating problem described in Section 2.2.2 it is found that one can actually pass through melt fracture by increasing the wire speed to the point where the wall shear stress (τ_w) = 2.2E+05 Pa (on increasing to higher values of τ_w another form of melt fracture occurs). Using the same die radius as calculated in Example 2.3, find the wire coating thickness, δ , and the wire speed, V , for $\tau_w = 2.2\text{E}+05$ Pa. Use the rheological parameters given for HDPE at 200 °C in Table 2.2.

2A.5 *Flow Through a Tubing Die.* A polypropylene is extruded through an annular die at 210 °C to make tubing for various biomedical applications. The die dimensions are $D = 3.175\text{E}-03$ m, $\kappa = 0.7$, and $L = 3.175\text{E}-02$ m. The extruder can feed a

maximum of 22 kg/h to the die. With the following rheological parameters given calculate ΔP and determine the maximum wall shear stress: $m = 3.21\text{E}+04 \text{ Pa}\cdot\text{s}^n$, $n = 0.25$, $\eta_0 = 3.5\text{E}+04 \text{ Pa}\cdot\text{s}$, $\tau_{1/2} = 3.35\text{E}+04 \text{ Pa}$, and $\alpha = 4.19$. Density values can be determined using Table 5.6.

2A.6 Pressure Drop Across a Pelletizing Die. Polypropylene is mixed with pigments (1.0 wt%) in a single-screw extruder and then pumped through a pelletizing die consisting of ten capillaries ($D = 3.175\text{E}-03 \text{ m}$ and $L = 3.175\text{E}-02 \text{ m}$). The ten strands are quenched in a water bath and then cut into pellets $6.35\text{E}-03 \text{ m}$ in length. Given that the polymer has the same properties as described in Problem 2A.5 and that the extruder is capable of delivering 50 kg/h, determine the pressure drop, ΔP , across the die (neglect the pressure drop across the distribution system) and the wall shear stress at the maximum mass flow rate.

B. Principles

2B.1 Flow Between Parallel Plates of a Newtonian Fluid. The solution to the flow between parallel plates as shown in Figure 2.17 is frequently used in the analysis of polymer processes.

- (a) Make a differential force (or momentum) balance and obtain expressions for the distributions of shear stress (or momentum flux) and velocity for a Newtonian fluid. (Note: These expressions are given in Table 2.3.)
- (b) Start with the equations of motion (see Tables 2.7 and 2.8) and obtain the velocity distribution.
- (c) Obtain an expression for the volumetric flow rate, Q .

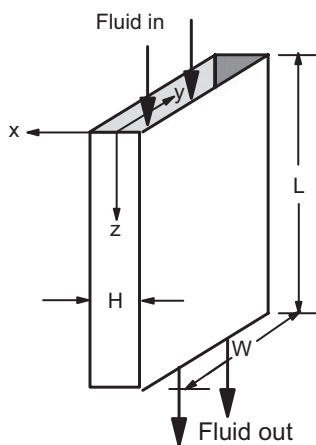


FIGURE 2.17 Flow through a set of parallel plates.

2B.2 Flow Between Parallel Plates of a Non-Newtonian Fluid

- (a) Use the equations of motion (Table 2.7) and the power-law empiricism for viscosity to find the shear stress and velocity distributions for the flow of a non-Newtonian fluid through parallel plates (see Fig. 2.17). Also determine expressions for $\dot{\gamma}$ and Q .
- (b) Do the same as in part (a), but use the Ellis model. (Note: Both solutions are given in Table 2.3.)
- (c) Formulate the problem using the Cross model, Eq. 2.13, and specify whether it is possible to get an analytical solution.

2B.3 Flow of a Non-Newtonian Fluid Through a Tube

- (a) Obtain an expression for Q for the flow of a power-law fluid through a tube of radius R . (Confirm your expression with that in Table 2.4.)
- (b) Derive an express for Q for the Ellis model (see Table 2.4.)
- (c) Show that in the limit as s goes to one and $m = \mu$, one obtains the Newtonian solution.
- (d) Formulate the solution using the Carreau model, Eq. 2.67a, and specify whether it is possible to obtain an analytical solution.

2B.4 Adapting the Parallel Plate Solution to Annular Flow. For small annular gaps (e.g., $\kappa = 0.9$) the expression for Q for flow through a slit of a power-law fluid (Problem 2B.3) can be used to obtain an expression for Q for annular flow. Adapt the parallel plate flow solution for the power-law model to that for flow through an annulus with a small gap (you should obtain the expression in Eq. 2.103).

2B.5 Wire Coating with an Imposed Pressure. In practice there is always a pressure drop across a wire coating die as the result of polymer melt being pumped by an extruder. By imposing a pressure drop the coating thickness can be controlled independently of the wire speed.

- (a) For the situation shown in Figure 2.11 obtain the following expression for the volumetric flow rate for a Newtonian fluid:

$$Q = \frac{\pi R^2 V}{2} \left(\frac{1 - \kappa^2}{\ln(1/\kappa)} - 2\kappa^2 \right) + \frac{\pi \Delta P R^4}{8\mu L} \times \left[1 - \kappa^4 - \frac{(1 - \kappa^2)^2}{\ln(1/\kappa)} \right] \quad (2.131)$$

- (b) Show that the coating thickness for a Newtonian fluid is given by

$$\delta' = \frac{\delta}{R_i} = (1 + f_d + f_p)^{1/2} - 1 \quad (2.132)$$

where

$$f_d = \frac{\rho'}{\rho} \left(\frac{1 - \kappa^2}{2\kappa^2 \ln(1/\kappa)} - 1 \right)$$

$$f_p = \frac{\rho'}{\rho} \phi \frac{1}{8\kappa^2} \left[1 - \kappa^4 - \frac{(1 - \kappa^2)^2}{\ln(1/\kappa)} \right] \quad (2.133)$$

and where

$$\phi = \frac{\Delta P R^2}{\mu \nu L}$$

ρ' is the density of the polymer at 25 °C.

- (c) Solve the problem for the power-law model. (Can one obtain an analytical expression for Q in this case?)
- (d) Obtain a solution for the power-law model for the case of small gaps.

2B.6 Tangential Annular Flow

- (a) Determine the stress and velocity field for tangential annular flow (see Fig. 2.18) of a power-law fluid.
- (b) Determine the torque required to turn the inner cylinder and the power required.
- (c) Obtain the velocity field for the case of small gaps.

Inner cylinder rotating

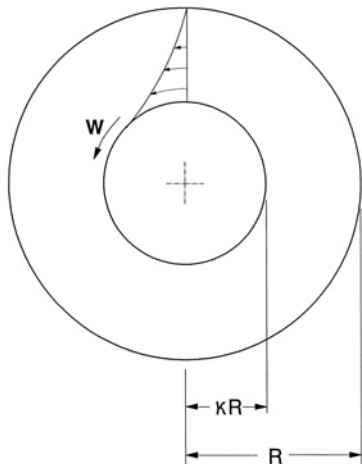


FIGURE 2.18 Flow between two coaxial cylinders with the inner cylinder rotating.

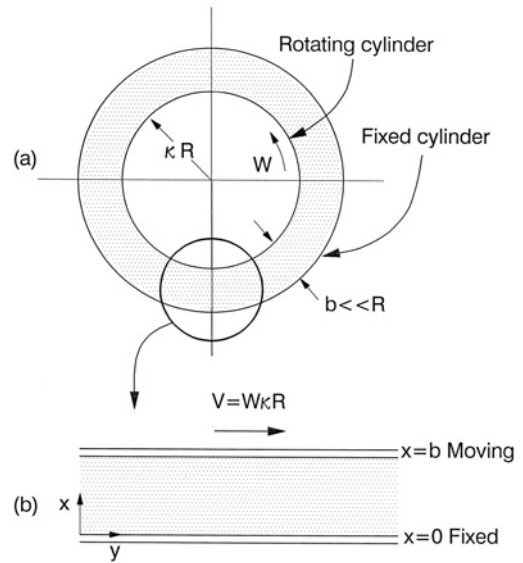


FIGURE 2.19 Creeping flow between two stationary concentric spheres.

2B.7 Flow Through an Annulus with a Rotating Mandrel. In some processes involving pressure-driven flow of polymer melts through an annulus the outer or inner cylinder (mandrel) is rotated as shown in Figure 2.19.

- (a) Show that for a Newtonian fluid the velocity field consists of two independent components $v_z(r)$ and $v_\theta(r)$.
- (b) Show that the expression for Q for a Newtonian fluid is identical to that for flow through an annulus given in Eq. 2.31.
- (c) Show that for a power-law fluid $v_z(r)$ and $v_\theta(r)$ are coupled and can't be obtained analytically.
- (d) Find $v_z(r)$ and $v_\theta(r)$ for a power-law fluid for the case of a small gap (i.e., when κ approaches 1.0), when the inner cylinder is rotated.

2B.8 Force for Pulling a Wire Through a Coating Die. In Section 2.2.2 an approximation to flow in a wire coating die was discussed. Use the velocity field given in Eq. 2.51 to determine the force required to pull a wire through a die such as that shown in Figure 2.10.

- (a) Obtain the expression for τ_{rz} given in Eq. 2.52 from the velocity field.
- (b) Obtain an expression for the force, F_z , required to pull the wire through the die by integrating the shear stress over the area of the wire.
- (c) For HDPE at 180 °C (use power-law parameters in Table 2.2) calculate F_z for the following conditions: $V = 0.5$ m/s, $R = 5.0E-03$ m, $L = 0.1$ m, and $\kappa = 0.8$.

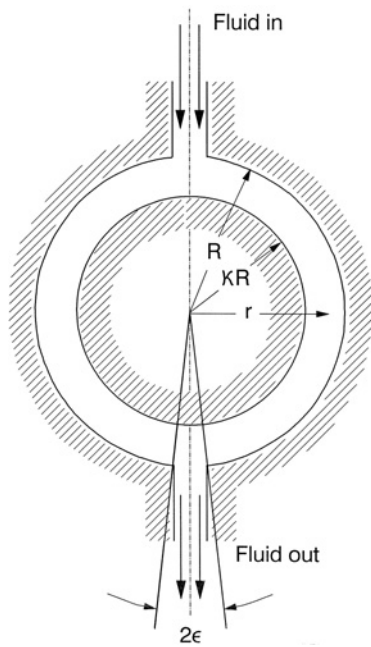


FIGURE 2.20

- 2B.9** *Stress Components for Flow Between Two Concentric Spheres.* (Bird et al., 1960, p. 117). An idealized flow of a Newtonian fluid between two concentric spheres is shown in Figure 2.20. The pressure drop and the velocity field for this flow are given below:

$$\Delta p = B \ln \left(\frac{1 - \cos \varepsilon}{1 + \cos \varepsilon} \right) = -BE(\varepsilon)$$

$$v_\theta \sin \theta = u = \frac{R \Delta P}{2\mu E(\varepsilon)} \left[\left(1 - \frac{r}{R} \right) + \kappa \left(1 - \frac{R}{r} \right) \right]$$

- (a) From the velocity field determine expressions for the stress components and specify those acting in tension and those in compression.
- (b) Obtain an expression for the net z force acting on the inner sphere.
- 2B.10** *Flow Between Tapered Plates.* Obtain an expression for the volumetric flow rate for tapered plates similar to that for a tapered tube (Eq. 2.111) using the lubrication approximation. The plates have an initial height H_0 and a final height of H_L as shown in Figure 2.21.
- 2B.11** *Power Input for Annular Flow with a Rotating Mandrel.* The integration of the mechanical energy equation (Eq. 2.70) over a fixed volume with an inlet and an outlet stream gives Eq. 2.69.

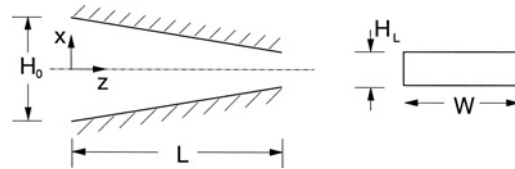


FIGURE 2.21 Pressure-driven flow through tapered plates.

- (a) Show for flow through an annulus of length L with a rotating inner mandrel that Eq. 2.70 reduces to

$$Q \Delta P - W - E_v = 0$$

where $\Delta P = P_0 - P_L$, W is the energy input into the system through the mandrel, and E_v is the viscous dissipation. (Hint: Integrate Eq. 2.70 over the volume and use the divergence theorem.)

- (b) Determine an expression for W for a Newtonian fluid. (Hint: $W = \int (\boldsymbol{\tau} \cdot \mathbf{n}) \cdot \mathbf{v} dA = \int_0^{2\pi} \int_0^L \tau_{r\theta}(\kappa R) v_\theta(\kappa R) \kappa R d\theta dz$.)
- (c) Determine an expression for W for a power-law fluid for a small gap. (Note: Evaluation of the expression will require numerical integration.)

C. Numerical Problems

- 2C.1** *Carreau–Yasuda Model Parameters from Regression Analysis.* Use either *Solve* in Excel or the IMSL subroutine RNLIN (Example 2.1) to find the Carreau–Yasuda model parameters [Eq. 2.8 with $(n - 1)/2$ replaced with $(n - 1)/a$] for LLDPE at 170 °C (viscosity data are given in Appendix A.3) and compare the results with those given in Table 2.1.
- 2C.2** *Best Fit of Viscosity Data for a Glass Filled Nylon 6,6.* Use either *Solve* in Excel or the IMSL subroutine RNLIN (Example 2.1) to determine whether the Bingham or power-law model gives the best fit to the viscosity data given in Appendix A.4 for a mineral filled nylon 6,6 melt at 285 °C.
- 2C.3** *Velocity Maximum in Annular Flow for Integer Values of the Power-Law Index.* The velocity passes through a maximum in annular flow at βR . β is found using Eq. 2.39 for specified values of κ . When s is an integer, Eq. 2.39 can be integrated analytically giving a nonlinear algebraic equation for determining β . For $s = 2$ (i.e., $n = 0.5$) and $\kappa = 0.5$, find a polynomial expression for determining β and then use either *Solve* in Excel or the IMSL subroutine NEQNF to find β .

2C.4 *Velocity Maximum in Annular Flow for Noninteger Values of the Power-Law Index.* Equation 2.39 is used to find the position of the maximum in the velocity field for flow through an annulus. For $n = 0.59$ and $\kappa = 0.5$ and 0.8 , determine β using the IMSL numerical integration subroutine QDAGS described in Appendix D.5 or *quad* in MATLAB.

2C.5 *Velocity Profile for Flow in a Capillary.* Although the Carreau model describes the viscosity behavior of polymer melts accurately, it is not possible to obtain analytical expressions for the velocity field for one-dimensional flows such as occur in a capillary. Obtain the velocity field for HDPE at 180°C . (Use the Carreau model parameters in Table 2.2 by using the IMSL subroutine BVPFD, which is described in Appendix D.9 or *BVP4C* in MATLAB.)

- (a) Show that the following nonlinear ordinary differential equation is obtained on substituting the GNF model with the Carreau empiricism for viscosity into the momentum balance:

$$\begin{aligned} \left(\frac{dv_z}{dr}\right)^{2/(n-1)} + \lambda^2 \left(\frac{dv_z}{dr}\right)^{2n/(n-1)} \\ = \left(\frac{-\Delta P}{2\eta_0 L}\right)^{2/(n-1)} r^{2/(n-1)} \end{aligned}$$

- (b) At $\tau_w = 1.0\text{E}+05$ Pa and for a capillary of $D = 3.175\text{E}-03$ m and $L = 3.175\text{E}-01$ m, use the IMSL subroutine BVPFD or the MATLAB function *BVP4C* to solve the differential equation shown above.
- (c) Compare the velocity profile to that obtained for the power-law case.

2C.6 *Flow Through a Rectangular Channel*

- (a) Show for the flow of a Newtonian fluid through a rectangular channel (see Fig. 2.22) that the equations of motion along with the use of the

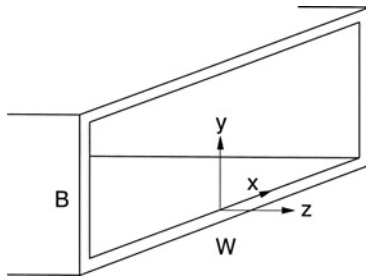


FIGURE 2.22 Pressure-driven flow through a rectangular channel having an aspect ratio $W/B < 10$.

constitutive equation for a Newtonian fluid lead to the following differential equation:

$$\frac{\partial^2 v_z}{\partial x^2} + \frac{\partial^2 v_z}{\partial y^2} = -\frac{1}{\mu} \frac{\Delta P}{L}$$

- (b) For the rectangular channel shown in Figure 2.22 use the IMSL subroutine FPS2H (Appendix D.10) or to find the velocity profile for $\Delta P/L = 1.0\text{E}+03$ Pa/m. $W/H = 5$ and $H = 0.2$ cm.
- (c) Calculate the volumetric flow rate by using the IMSL subroutine TWODQ (Appendix D.6) to numerically integrate the velocity profile obtained in part (b).
- (d) Compare the results to the series solution for flow in a rectangular channel.

2C.7 *Numerical Solution of Problem 2B.7.* For the case of a thin gap the components of the velocity field are given by the following two integrals:

$$\bar{v}_y = \int_0^{\bar{x}} C_1 [C_1^2 + (C_2 - a\bar{x})^2]^{(1-n)/2n} d\bar{x} \tag{2.134}$$

$$\bar{v}_z = \int_0^{\bar{x}} (C_2 - a\bar{x}) [C_1^2 + (C_2 - a\bar{x})^2]^{(1-n)/2n} d\bar{x} \tag{2.135}$$

where $\bar{x} = x/b$, $\bar{v}_i = v_i/V$, and $a = (\Delta P/mL)$ (b^{n+1}/ν^n). From the boundary condition that $d\bar{v}_z/d\bar{x} = 0$ at $\bar{x} = 1/2$ it is found that $C_2 = a/2$. $V = KRW$.

- (a) Use the IMSL subroutine QDAGS or *quad* in MATLAB to numerically integrate Eqs. 2.134 and 2.135 above to find \bar{v}_y and \bar{v}_z . Assume $n = 0.59$ and take arbitrary values of C_1 from 0.01 to 10 and a from 0.5 to 30.
- (b) Numerically integrate the results above to find Q . (Note: $Q = 2\pi WbR^2 \int_0^1 \bar{v}_z d\bar{x}$.)

REFERENCES

Billo, J. E. 2007. *Excel for Scientists and Engineers* (Wiley, Hoboken, NJ).
 Bird, R. B., W. E. Stewart, and E. N. Lightfoot. 1960. *Transport Phenomena* (Wiley, Hoboken, NJ).
 Bird, R. B., R. C. Armstrong, and O. Hassager. 1987. *Dynamics of Polymeric Liquids. Volume I: Fluid Mechanics*, 2nd Edition (Wiley, Hoboken, NJ).

- Bird, R. B., W. E. Stewart, and E. N. Lightfoot. 2007. *Transport Phenomena* (Wiley, Hoboken, NJ).
- Dealy, J. M. and K. F. Wissbrun. 1990. *Melt Rheology and Its Role in Plastics Processing* (Van Nostrand Reinhold, New York).
- Frankland, J. D. 1975. *Trans. Soc. Rheol. (J. Rheol.)*, **19**, 371.
- Larson, R. G. 1999. *The Structure and Rheology of Complex Fluids* (Oxford University Press, Oxford).
- Meissner, J. 1971. *Kunststoffe*, **61**, 576.
- Tadmor, Z. and C. G. Gogos. 1979. *Principles of Polymer Processing* (Wiley, Hoboken, NJ).
- Tadmor, Z. and C. G. Gogos. 2007. *Principles of Polymer Processing*, 2nd edition (Wiley, Hoboken, NJ).

3

VISCOELASTIC RESPONSE OF POLYMERIC FLUIDS AND FIBER SUSPENSIONS

DESIGN PROBLEM II DESIGN OF A PARISON DIE FOR A VISCOELASTIC FLUID

In extrusion blow molding a cylindrical tube of polymer is formed by extrusion of polymer melt through an annular die as shown in Figure 3.1. As discussed in Chapter 1, the tube of polymer is expanded by gas pressure into a mold to form a shaped object such as a bottle. Design a die that will allow one to extrude at the highest rate possible a parison of low density polyethylene, LDPE (NPE 953), at 170 °C having a diameter, D_p , of 6.13 cm and a thickness, H_p , of 0.565 cm. In particular, specify the diameter, D_o , and the gap, H_o . Take the length to be 10 H_o . The extruder feeding melt to the die is capable of delivering a maximum of 300 lb/h. As a result of a flow instability, called *melt fracture* (discussed in Chapter 7), the maximum wall shear stress that can be reached is 1.13×10^5 Pa. In your calculations consider the swell of the extrudate as shown in Figure 3.1 (i.e., consider the increase in the diameter and thickness of the parison relative to the die dimensions as a result of the viscoelastic nature of the melt). Rheological data for the polymer are given in the tables in Appendix A.1. ρ is 772 kg/m³ at 170 °C.

In Chapter 2 the pseudoplastic behavior of polymeric fluids was emphasized. In this chapter the viscoelastic behavior of polymer melts is discussed. It is this property that not only allows one to process these materials by a number of different ways such as blow molding and film blowing but also

causes many problems in the design of polymer processes. By viscoelastic behavior it is meant that polymeric fluids can exhibit a response resembling that of an elastic solid under some circumstances, while under others they can act as viscous liquids. The macromolecular nature of polymeric molecules along with physical interactions called entanglements leads to the elastic behavior. Deformed molecules are driven by thermal motions to return to their undeformed states, giving the bulk fluid elastic recovery. Phenomena associated with the viscoelastic nature of polymers such as “die swell” or “extrudate swell,” rod-climbing, and elastic recoil won’t be discussed here. A qualitative description of the flow of polymeric fluids can be found elsewhere (Bird et al., 1987a).

In Section 3.1 we define two basic flows used in the characterization of polymeric fluids along with the appropriate material functions. These basic flows are also found in polymer processes. In Section 3.2 several constitutive equations capable of describing the viscoelastic behavior of polymer melts are presented. The emphasis in this section is on manipulating these equations for flows in which the deformation history is known. In this section we have added discussion of fiber suspensions as they are commonly processed to yield materials with increased stiffness and strength. In Section 3.3 an introduction into the methods for measuring rheological properties is presented. In Section 3.4 several useful relationships between material functions are presented. These relationships (or correlations) are important as they allow one to obtain estimates, for example, of steady shear material functions from linear viscoelastic data. Because

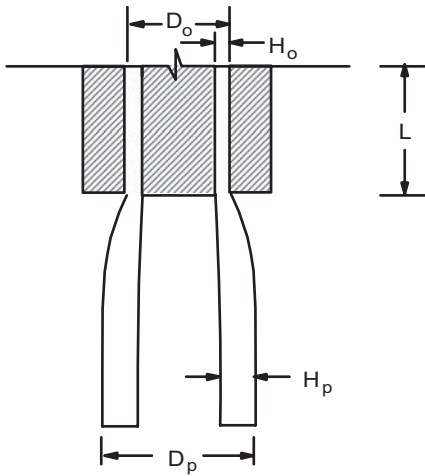


FIGURE 3.1 Quantities used to define annular extrudate swell.

quantitative design work requiring the use of nonlinear viscoelastic constitutive equations is mathematically very difficult, in Section 3.5 the value of making qualitative decisions about the processability of polymers through the measurement of the nonlinear rheological properties is discussed. Finally, in Section 3.6 a solution to Design Problem II is presented.

3.1 MATERIAL FUNCTIONS FOR VISCOELASTIC FLUIDS

3.1.1 Kinematics

There are two basic flows used to characterize polymers: shear and shear-free flows. (It so happens that processes are usually a combination of these flows or sometimes are dominated by one type or the other.) The velocity field for rectilinear shear flow is given below:

$$v_x = \dot{\gamma}(t)y \quad v_y = v_z = 0 \quad (3.1)$$

where $\dot{\gamma}(t)$ may be constant or a function of time. The velocity field for shear-free flows can be given in a general form as

$$v_x = -\frac{1}{2}\dot{\epsilon}(1+b)x \quad v_y = -\frac{1}{2}\dot{\epsilon}(1-b)y \quad v_z = +\dot{\epsilon}z \quad (3.2)$$

where $\dot{\epsilon}$ is the extension rate and b is a constant which is either 0 or 1. When $b = 0$ and $\dot{\epsilon} > 0$, the flow is *uniaxial* extensional flow. When $b = 0$, but $\dot{\epsilon} < 0$, the flow is *equibiaxial* extensional flow. When $b = 1$ and $\dot{\epsilon} > 0$, the flow is called *planar* extensional flow.

The deformational types are shown for a unit cube of incompressible material in Figure 3.2. In shear flow, the unit cube is merely skewed with the degree of strain given by the angle, $\dot{\gamma}(t_2 - t_1)$, the edge makes with the y axis. $\dot{\gamma}(t_2 - t_1)$

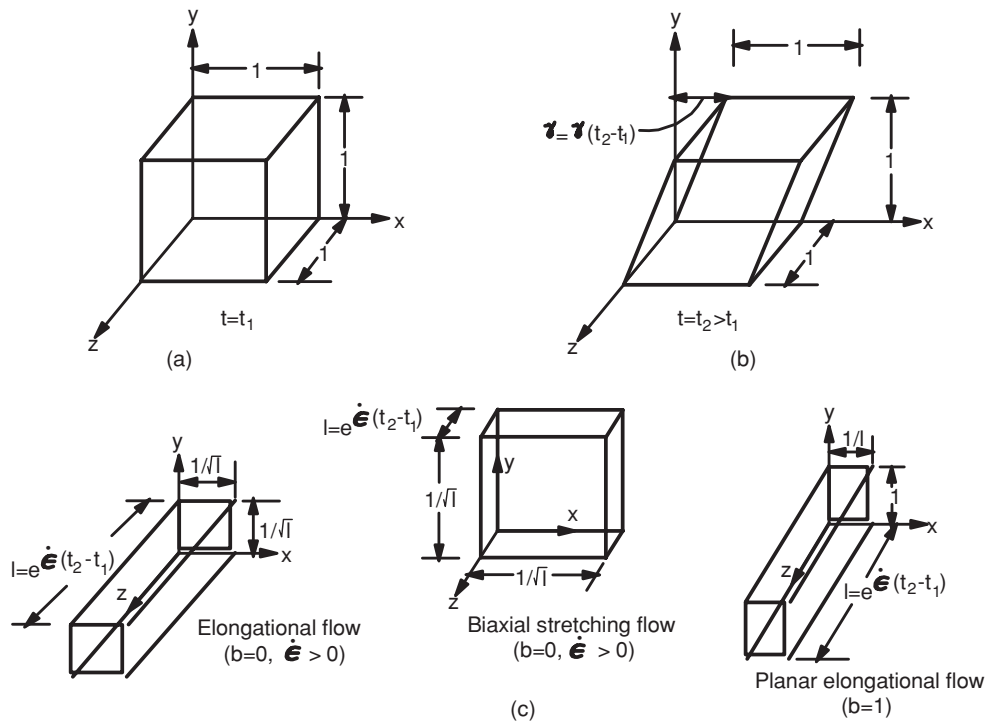


FIGURE 3.2 The deformation of (a) a unit cube of material from time t_1 to t_2 ($t_2 > t_1$) in (b) steady simple shear flow and (c) three kinds of shear-free flow. The volume of material is preserved in all of these flows. (Reprinted by permission of the publisher from Bird et al., 1987a.)

is the shear strain. There are three types of shear-free flow described in Figure 3.2. In uniaxial extensional flow the unit cube is stretched along the z axis while it contracts uniformly along the x and y axes in such a manner that mass is conserved. The elongational strain is given by $\dot{\epsilon}(t_2 - t_1)$. In biaxial elongational flow, the unit cube is stretched equally along the x and y directions but must contract in the z direction in such a way that mass is conserved. In planar extensional flow, the unit cube is stretched along the z axis but is constrained so that it contracts only in the x direction.

There are significant differences in the behavior of polymeric fluids in these two types of deformation, and each type of deformation has a different effect on the orientation of macromolecules. For example, uniaxial and planar extensional flows impart significant molecular orientation in polymers during flow compared to shear flows. On the other hand, biaxial extensional flow is a weak flow and does not lead to a strong degree of molecular orientation. Furthermore, the rheological response can be significantly different for a polymer in extensional flow versus shear flow. We demonstrate these differences later in this chapter.

For these two types of flows, the components of the rate deformation tensor (Table 2.8) take on a distinct form. For shear flow the components of the rate of deformation tensor are

$$\dot{\gamma}_{ij} = \dot{\gamma}(t) \begin{pmatrix} 0 & 1 & 0 \\ 1 & 0 & 0 \\ 0 & 0 & 0 \end{pmatrix} \quad (3.3)$$

It is noted that only the off-diagonal components of this tensor exist. For shear-free flow the rate of deformation tensor also takes on a distinct form. In particular, the components are

$$\dot{\gamma}_{ij} = \begin{pmatrix} -\dot{\epsilon}(1+b) & 0 & 0 \\ 0 & -\dot{\epsilon}(1-b) & 0 \\ 0 & 0 & 2\dot{\epsilon} \end{pmatrix} \quad (3.4)$$

Here it is seen that only diagonal components exist. The physical significance of these matrices is that in shear flow the velocity gradient is transverse to the flow direction while in shear-free flow it is in the same direction as flow.

3.1.2 Stress Tensor Components

In general, the state of stress in a flowing material in rectangular Cartesian coordinates is

$$\begin{pmatrix} \tau_{xx} + p & \tau_{xy} & \tau_{xz} \\ \tau_{yx} & \tau_{yy} + p & \tau_{yz} \\ \tau_{zx} & \tau_{zy} & \tau_{zz} + p \end{pmatrix} \quad (3.5)$$

where p is the isotropic pressure. The components such as $\tau_{xx} + p$, $\tau_{yy} + p$, and $\tau_{zz} + p$ are the normal stresses, and when the fluid is incompressible, p is unknown. Furthermore,

τ_{xx} , τ_{xy} , and so on are referred to as the *extra* or *molecular* stresses, while

$$\pi_{xx} = \tau_{xx} + p, \quad \pi_{xy} = \tau_{xy}, \quad \pi_{xz} = \tau_{xy}, \quad \text{etc.} \quad (3.6)$$

are called the *total stress components*. If one lets x , y , and z correspond to 1, 2, and 3, respectively, then we can also write out the stress components in terms of the following notation:

$$\pi_{ij} = \tau_{ij} + p\delta_{ij} \quad \text{for } i, j = 1, 2, \text{ or } 3 \quad (3.7)$$

π_{ij} is interpreted as the ij th component of the total stress tensor while τ_{ij} is the ij th component of the extra stress tensor. δ_{ij} is the Kronecker delta and is defined as

$$\delta_{ij} = \begin{cases} 1 & \text{if } i = j \\ 0 & \text{if } i \neq j \end{cases} \quad (3.8)$$

The number of components in the matrix in Eq. 3.5 is reduced for an incompressible Newtonian fluid in shear flow. Referring to Table 2.8, the definition of a Newtonian fluid, and Eq. 3.1 (the kinematics for shear flow) one can show that the stress components are

$$\begin{pmatrix} p & \tau_{xy} & 0 \\ \tau_{yx} & p & 0 \\ 0 & 0 & p \end{pmatrix} \quad (3.9)$$

where $\tau_{xy} = \tau_{yx} = -\mu\dot{\gamma}(t)$.

On the contrary, we have not yet discussed a constitutive equation for viscoelastic fluids, and we must resort to another method to find the stress components. Without proof it can be shown using symmetry arguments that, in general, for a viscoelastic fluid in shear flow the stress tensor must be of the form

$$\begin{pmatrix} \tau_{xx} + p & \tau_{xy} & 0 \\ \tau_{yx} & \tau_{yy} + p & 0 \\ 0 & 0 & \tau_{zz} + p \end{pmatrix} \quad (3.10)$$

We note that in shear flow additional normal stresses are generated which don't appear for a Newtonian fluid. Because polymeric fluids are considered to be incompressible, the components $\tau_{ii} + p$ have no direct rheological significance. Therefore, we define three independent quantities of stress of rheological significance:

$$\begin{aligned} \tau_{yx} = \tau_{xy}, \quad \pi_{xx} - \pi_{yy} = \tau_{xx} - \tau_{yy} = N_1 \\ \pi_{yy} - \pi_{zz} = \tau_{yy} - \tau_{zz} = N_2 \end{aligned} \quad (3.11)$$

where N_1 and N_2 are called the primary and secondary normal stress differences, respectively. These additional stresses are thought to be related to phenomena such as die swell, elastic

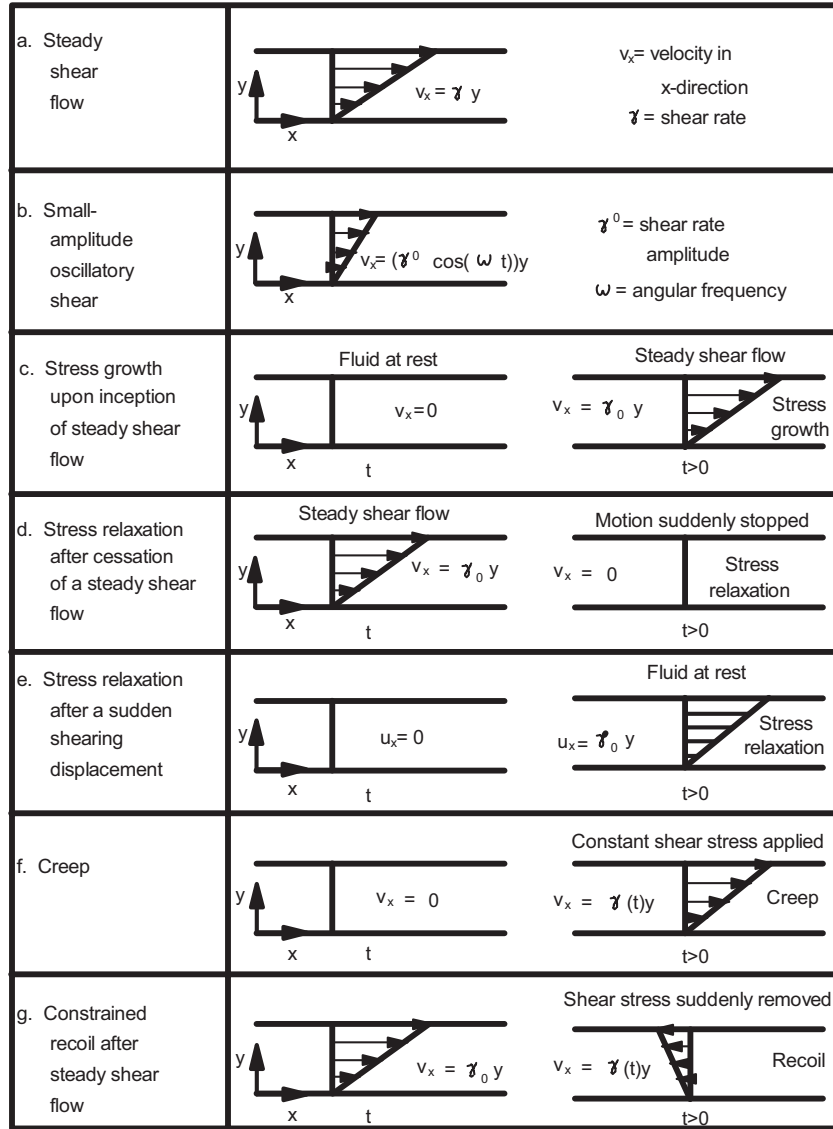


FIGURE 3.3 Shear flow experiments.

recoil, and rod climbing (the climbing of polymer fluid up a mixing blade) and hence are associated with the ideas of elasticity.

For shear-free flows it can be shown using symmetry arguments again that the extra stress tensor is of the form

$$\begin{pmatrix} \tau_{xx} + p & 0 & 0 \\ 0 & \tau_{yy} + p & 0 \\ 0 & 0 & \tau_{zz} + p \end{pmatrix} \quad (3.12)$$

For incompressible polymeric fluids there are two normal stress differences of rheological interest:

$$\tau_{zz} - \tau_{xx} \quad \text{and} \quad \tau_{yy} - \tau_{xx} \quad (3.13)$$

When $b = 0$ in Eq. 3.2, then there is only one quantity of rheological significance,

$$\tau_{zz} - \tau_{xx} \quad (3.14)$$

It is important to realize that these normal stress differences are not N_1 or N_2 as they are generated under different flow conditions.

3.1.3 Material Functions for Shear Flow

Various types of shear flow experiments are used in the characterization of polymeric fluids, and some of the more commonly used ones are shown in Figure 3.3. When $\dot{\gamma}(t)$ is a constant, that is, $\dot{\gamma}_{yx} = \dot{\gamma}_0$, then we can define three material

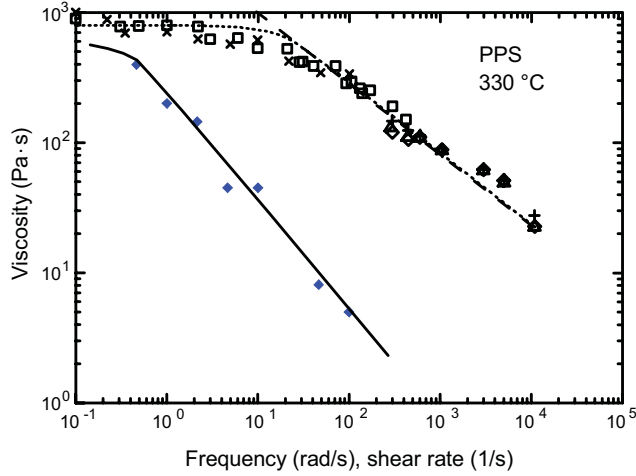


FIGURE 3.4 Viscosity (steady and complex) versus shear rate or angular frequency (ω) and the primary normal stress difference coefficient versus shear rate for polyphenylenesulfide at 330 °C. Values of Ψ_1 (\blacktriangle), η^* (\square), and η (\times) were obtained by means of a cone and plate device. All other values of η were obtained by means of a capillary rheometer.

functions in steady shear flow:

$$\tau_{xy} = -\eta(\dot{\gamma}) \dot{\gamma}_0 \quad (3.15)$$

$$\tau_{xx} - \tau_{yy} = -\Psi_1(\dot{\gamma}) \dot{\gamma}_0^2 \quad (3.16)$$

$$\tau_{yy} - \tau_{zz} = -\Psi_2(\dot{\gamma}) \dot{\gamma}_0^2 \quad (3.17)$$

where η is the viscosity, Ψ_1 is the primary normal stress difference coefficient, and Ψ_2 is the secondary normal stress difference coefficient. Some representative values for η and Ψ_1 are presented in Figure 3.4. We observe that Ψ_1 is more shear rate sensitive than is η . Furthermore, it is reported that $-\Psi_2/\Psi_1$ is in the range of 0.1 to 0.2. Because there is no concrete evidence that Ψ_2 plays a direct role in processing, we don't include Ψ_2 in any further discussions in this book.

There are numerous transient shear flows in which $\dot{\gamma}(t)$ varies in a specific way with time. One of the most frequently used experiments is when $\dot{\gamma}(t)$ varies sinusoidally with time:

$$\dot{\gamma}_{yx} = \dot{\gamma}_0 \cos \omega t \quad (3.18)$$

where $\dot{\gamma}_0$ is the amplitude and ω is the angular frequency. Because polymeric fluids are viscoelastic, the stress lags behind the input frequency. One component of the stress is in phase with the rate of deformation given by Eq. 3.18 and one is out of phase. Mathematically we represent the shear stress as

$$\tau_{yx} = -B(\omega) \dot{\gamma}_0 \cos(\omega t - \phi) \quad (0 \leq \phi \leq \pi/2) \quad (3.19)$$

By expanding Eq. 3.19 using a trigonometric identity (i.e., $\cos(A - B) = \cos A \cos B + \sin A \sin B$), we find that

$$\tau_{yx} = -B(\omega) \dot{\gamma}_0 \cos \phi \cos \omega t - B(\omega) \dot{\gamma}_0 \sin \phi \sin \omega t \quad (3.20)$$

This allows us to define a complex viscosity, η^* , as follows:

$$\eta^* = \eta' - i\eta'' \quad (3.21)$$

where $\eta' = B(\omega)\dot{\gamma}_0 \cos \phi$ is the dynamic viscosity (viscous contribution) and $\eta'' = B(\omega)\dot{\gamma}_0 \sin \phi$ is the elastic contribution associated with energy storage per cycle of deformation. Hence, we see that η' is in-phase with $\dot{\gamma}_{yx}(t)$ while $-\eta''$ is out of phase. Representative values for η^* are given in Figure 3.4. We note here the close correlation between η^* and η , which will be discussed in Section 3.4.

Some prefer to treat polymeric fluids as viscoelastic solids and thereby represent τ_{yx} as

$$\tau_{yx} = -A(\omega)\dot{\gamma}_0 \sin(\omega t + \delta) \quad (3.22)$$

where $\dot{\gamma}_0$ is the strain amplitude given as

$$\dot{\gamma} = \dot{\gamma}_0/\omega \quad (3.23)$$

Again using trigonometric identities and defining the complex shear modulus as

$$G^* = i\omega\eta^* = G' + iG'' \quad (3.24)$$

we find $G' = A(\omega)\dot{\gamma}_0 \sin \delta$ and $G'' = A(\omega)\dot{\gamma}_0 \cos \delta$, where G' is the storage modulus and G'' is the loss modulus. Representative values of G' and G'' for polyphenylenesulfide (PPS) are given in Figure 3.5. Part of the value of the G' measurements rests on the fact there is a good correlation between $2G'$ and N_1 as shown in Figure 3.6 and discussed in Section 3.4. It

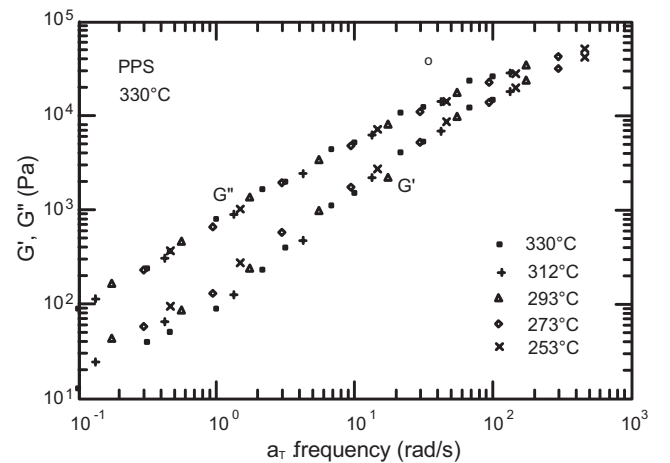


FIGURE 3.5 Values of the storage (G') and loss (G'') moduli versus the product the shift factor and angular frequency (ω) for polyphenylenesulfide (PPS) shifted to a reference temperature of 330 °C.

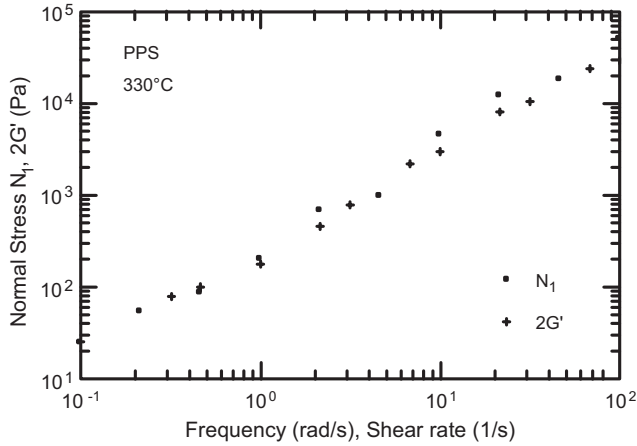


FIGURE 3.6 Values of N_1 and $2G'$ versus shear rate and angular frequency, respectively, for PPS at 330 °C.

should also be pointed out that η' and G'' and η'' and G' are interrelated: that is, $\eta'\omega = G''$ and $\eta''\omega = G'$.

The stress growth experiment (Fig. 3.3c) is also used to characterize polymeric fluids. In this experiment the fluid that is at rest is suddenly set in motion and the stresses are measured as a function of time. $\dot{\gamma}_{yx}(t)$ is given mathematically as

$$\dot{\gamma}_{yx} = \dot{\gamma}_0 H(t) \quad (3.25)$$

where $H(t)$ is the unit step function, which is defined as

$$\begin{aligned} H(t) &= 0, & t < 0 \\ H(t) &= 1, & t \geq 0 \end{aligned} \quad (3.26)$$

The following material functions are defined for this flow:

$$\tau_{yx} = -\eta^+(t, \dot{\gamma}_0) \dot{\gamma}_0 \quad (3.27)$$

$$\tau_{xx} - \tau_{yy} = -\psi_1^+(t, \dot{\gamma}_0) \dot{\gamma}_0^2 \quad (3.28)$$

$$\tau_{yy} - \tau_{zz} = -\psi_2^+(t, \dot{\gamma}_0) \dot{\gamma}_0^2 \quad (3.29)$$

Representative data are presented in Figure 3.7 for a PPS melt. We note that τ_{yx} and N_1 overshoot their equilibrium values and that the maximum in N_1 usually occurs later than that in τ_{yx} at the same value of $\dot{\gamma}_0$. Because many processes take place in short time intervals, it may be that the transient properties are more important than the steady shear ones. More will be discussed about the importance of the transient behavior in Section 3.2, when we define a dimensionless group called the *Deborah number*.

Another important experiment is that of stress relaxation following steady shear flow. This experiment is shown

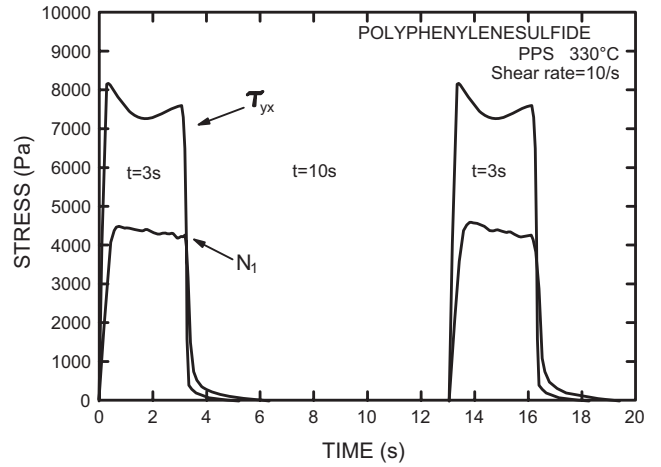


FIGURE 3.7 Transient shear behavior of PPS at 330 °C. The shear and primary normal stress difference are recorded at the startup of shear flow and on cessation of flow. After 10 s the stress growth experiment is repeated.

schematically in Figure 3.3d, and the deformation history is given mathematically as follows:

$$\dot{\gamma}_{yx}(t) = \dot{\gamma}_0 [1 - H(t)] \quad (3.30)$$

In this experiment, on cessation of steady shear flow the stresses are monitored with time. The material functions are defined as

$$\tau_{yx} = -\eta^-(\dot{\gamma}_0, t) \dot{\gamma}_0 \quad (3.31)$$

$$\tau_{xx} - \tau_{yy} = -\Psi_1^-(\dot{\gamma}_0, t) \dot{\gamma}_0^2 \quad (3.32)$$

$$\tau_{yy} - \tau_{zz} = -\Psi_2^-(\dot{\gamma}_0, t) \dot{\gamma}_0^2 \quad (3.33)$$

Representative behavior is also presented in Figure 3.7. It is observed that τ_{yx} relaxes faster than $\tau_{xx} - \tau_{yy}$. Furthermore, it is known that as $\dot{\gamma}_0$ increases the time for τ_{yx} and N_1 to relax to zero is shorter. After relaxation is complete, the stress growth and relaxation experiment are repeated as shown in Figure 3.7, and it is observed that the behavior is repeatable. Although the stresses relax within 2.0 s, higher molecular weight polymers may take 10 to 20 s before the stresses completely relax. Residual stresses in an injection-molded part can lead to the warpage of parts.

The fact that the normal stresses are relatively large compared to τ_{yx} is shown in Figure 3.8, where the ratio of $\tau_{xx} - \tau_{yy} / 2\tau_{yx}$ and G'/G'' are plotted versus shear rate and ω , respectively, for PPS. Here we see that $\tau_{xx} - \tau_{yy}$ increases monotonically with $\dot{\gamma}$, and that it reaches values where $\tau_{xx} - \tau_{yy}$ is about twice as large as τ_{yx} . Hence, $\tau_{yy} - \tau_{xx}$ can exceed the magnitude of τ_{yx} . This dimensionless ratio divided by a factor of two is equivalent to a quantity called the *Weissenberg number*, We_e , and is a measure of fluid elasticity. For

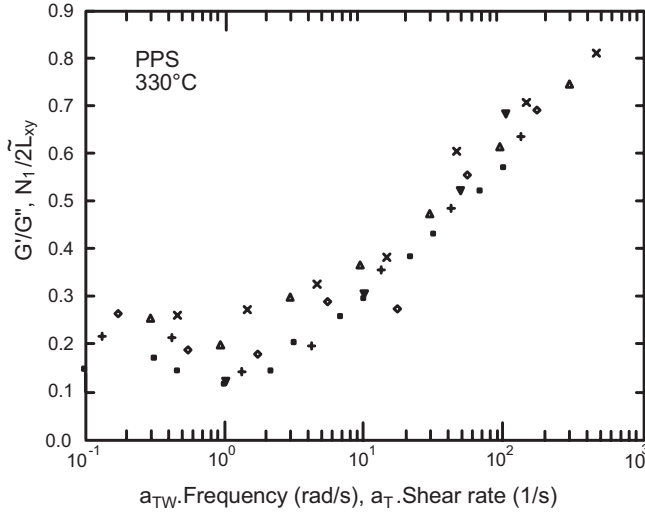


FIGURE 3.8 Values of G'/G'' and $N_1/2\tau_{xy}$ versus $a_T\omega$ and a_T , respectively, for PPS at 330 °C. Dynamic data were obtained at various temperatures and shifted to a reference temperature of 330 °C: (□) 330; (+) 312; (◇) 312; (△) 273; (x) 253 °C.

most polymers it has been observed that W_e reaches a plateau at higher values of $\dot{\gamma}$, leveling off in a range of from 1.0 to 2.0 (Bird et al., 1987a).

3.1.4 Shear-Free Flow Material Functions

Similar flow histories for shear-free flows as described for shear flows in Figure 3.3 can also be used. Here we discuss only steady and stress growth shear-free flows. For steady simple (i.e., homogeneous deformation) shear-free flows two viscosity functions, $\bar{\eta}_1$ and $\bar{\eta}_2$, are defined based on the two normal stress differences given in Eq. 3.13:

$$\tau_{zz} - \tau_{xx} = -\bar{\eta}_1(\dot{\epsilon}, b)\dot{\epsilon} \quad (3.34)$$

$$\tau_{yy} - \tau_{xx} = -\bar{\eta}_2(\dot{\epsilon}, b)\dot{\epsilon} \quad (3.35)$$

For uniaxial extensional flow where $b = 0$ and $\dot{\epsilon} > 0$, $\bar{\eta}_2 = 0$, and $\bar{\eta}_1$ is called the elongational viscosity, $\bar{\eta}$:

$$\bar{\eta}(\dot{\epsilon}) = \bar{\eta}_1(\dot{\epsilon}, 0) \quad (3.36)$$

For stress growth the two viscosity functions are defined as

$$\tau_{zz} - \tau_{xx} = -\bar{\eta}_1^+(\dot{\epsilon})\dot{\epsilon} \quad (3.37)$$

$$\tau_{yy} - \tau_{xx} = -\bar{\eta}_2^+(\dot{\epsilon})\dot{\epsilon} \quad (3.38)$$

Likewise for uniaxial extensional flow $\bar{\eta}_2^+ = 0$ and $\bar{\eta}_1^+ = \bar{\eta}^+$.

Representative data for $\bar{\eta}$ and $\bar{\eta}^+$ are shown in Figures 3.9 and 3.10, respectively. In Figure 3.9, $\bar{\eta}$ versus tensile

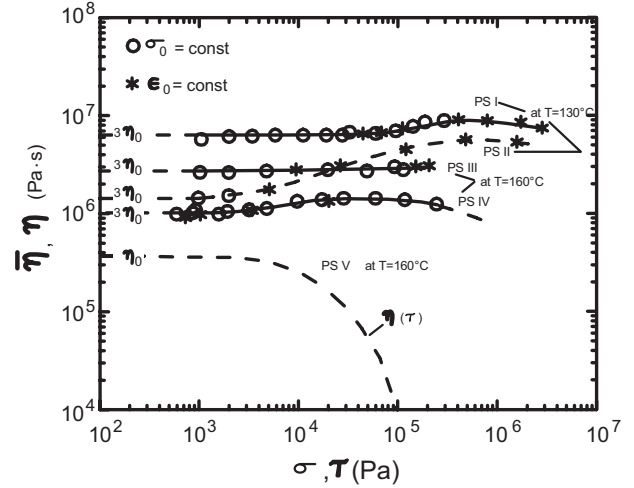


FIGURE 3.9 Steady shear (η) and elongational viscosity ($\bar{\eta}$) versus shear stress (τ) and tensile stress (σ) for four polystyrene melts:

	\bar{M}_w	\bar{M}_w/\bar{M}_n
PS I	7.4×10^4	1.2
PS II	3.9×10^4	1.1
PS III	2.53×10^5	1.9
PS IV	2.19×10^5	2.3

(Reprinted by permission of the publisher from Mündstedt, 1980.)

stress and η versus shear stress values are compared for a polystyrene melt (see Mündstedt, 1980, for detailed molecular weight (MW) features of the polymers). At low stress values, $\bar{\eta} = 3\eta_0$. However, when η shear thins, $\bar{\eta}$ tends to increase slightly with stress and then decrease. At higher values of stress, η is several decades lower than $\bar{\eta}$. Linear

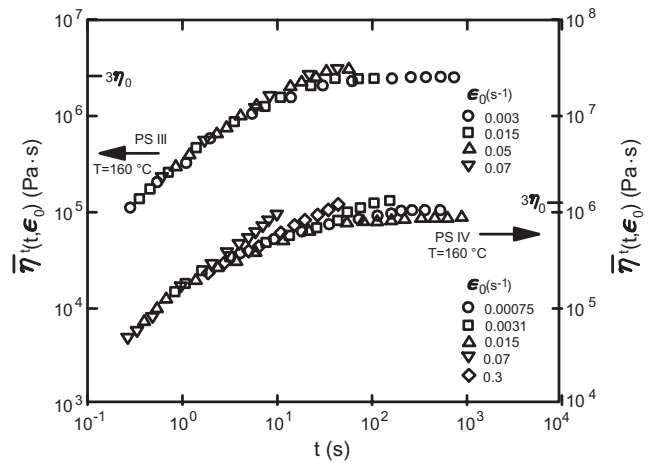


FIGURE 3.10 Time dependence \bar{M}_w of the elongational viscosity at the startup of simple elongational flow for two polystyrene samples (PS III and PS IV). (Reprinted by permission of the publisher from Mündstedt, 1980.)

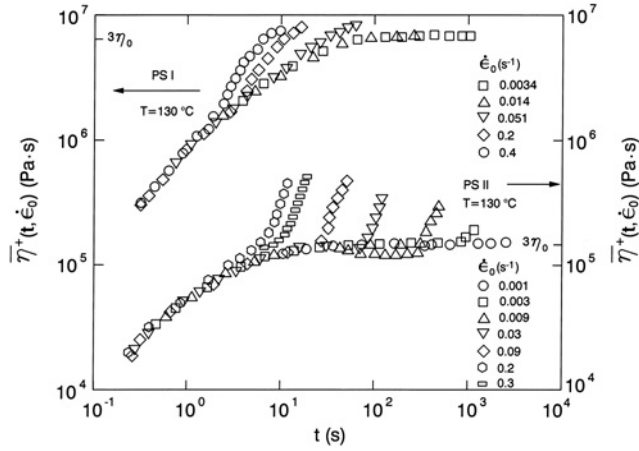


FIGURE 3.11 Time dependence of the elongational viscosity at the startup of simple elongational flow for two polystyrene samples (PS I and PS II). (Reprinted by permission of the publisher from Mündstedt, 1980.)

polymers tend to reach an equilibrium stress in the stress growth experiment as shown in Figure 3.10 for PS III. However, if there is branching or small amounts of high molecular weight tail in the polymer, then the stresses tend not to reach a steady state (at least for the strains experimentally accessible). As shown in Figure 3.10 for PS IV and Figure 3.11 for PS II, $\bar{\eta}^+$ tends to increase without bound (especially for PS II). In this case the cause of the “strain hardening” (i.e., the increase in $\bar{\eta}^+$ with time or strain, ϵt) is due to the presence of a small amount of high molecular weight PS in the MW distribution.

3.2 NONLINEAR CONSTITUTIVE EQUATIONS

In the last section it was learned that viscosity is not adequate to characterize polymeric fluids, but that many different material functions must be used. Furthermore, the generalized Newtonian fluid (GNF) model is not adequate to describe the rheological properties of polymer melts as it can only describe their shear-thinning viscosity behavior. In this section several constitutive equations capable of describing some of the nonlinear behavior of polymer melts are described. There is no intention to cover completely the topic of constitutive equations as this is done elsewhere (Bird et al., 1987a,b; Larson, 1988, 1999). The only intention is to present several realistic possibilities, show how to manipulate them algebraically, and then illustrate their use. Because of the importance of the processing of polymer melts containing fibers, we introduce the topic in this section. In particular, we are interested in the relation of fiber orientation to rheological behavior and flow during processing.

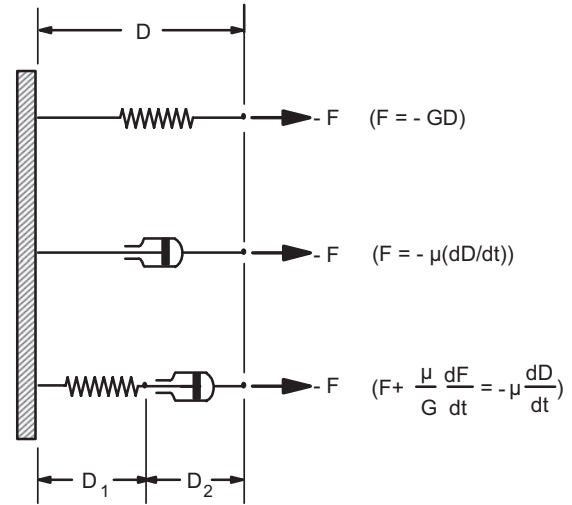


FIGURE 3.12 Spring and dashpot analogs for rheological equations: top, spring element; middle, dashpot element; bottom, spring and dashpot element in series.

3.2.1 Description of Several Models

The deformational behavior of polymeric fluids is qualitatively described by the spring and dashpot model shown in Figure 3.12. The ratio of the dashpot resistance, μ , to the spring modulus, G , has the units of time. Hence, μ/G is equivalent to a relaxation time, λ . If the deformation rate, $\dot{\gamma}$, is a lot less than $1/\lambda$, then the dashpot dominates and the material flows like a Newtonian fluid. On the other hand, if $\dot{\gamma} \gg 1/\lambda$, then the spring dominates, and the material behaves like an elastic solid. In one dimension the relation between force (per unit area) and rate of deformation is $(F/A) + \lambda d(F/A)/dt = -\mu\dot{\gamma}$. This one-dimensional model can be generalized to give the linear viscoelastic model for the spring–dashpot element shown in Figure 3.12:

$$\tau_{ij} + \lambda \frac{\partial \tau_{ij}}{\partial t} = -\mu \dot{\gamma}_{ij} \quad (3.39)$$

Note this is again a shorthand notation for representing the six components of the stress tensor. For steady shear flow this model predicts no normal stresses and a constant viscosity. The material functions predicted by this model are summarized in Table 3.1. Obviously this model as it stands is wholly inadequate to describe the behavior of polymeric melts under processing conditions.

By replacing the partial time derivative with a nonlinear time derivative, which is based on a codeforming and translating coordinate system, the constitutive equation given in Eq. 3.1 now becomes (Bird et al., 1987a):

$$\tau_{ij} + \lambda \hat{\tau}_{ij} = -\mu \dot{\gamma}_{ij} \quad (3.40)$$

TABLE 3.1 Predictions of Viscoelastic Models for Steady Shear and Elongational Flow

Model	Steady Shear Flow	Steady Extensional Flow
Maxwell	$\eta = \mu, \psi_1 = \psi_2 = 0$	$\bar{\eta} = 3\mu$
Upper convected Maxwell	$\eta = \mu, \psi_1 = 2\mu\lambda, \psi_2 = 0$	$\bar{\eta} = \frac{3\mu}{(1 + \lambda\dot{\epsilon})(1 - 2\lambda\dot{\epsilon})}$
White–Metzner	$\eta = \eta(\dot{\gamma})$ $\psi_1 = 2\eta(\dot{\gamma})\lambda(\dot{\gamma})$ $\psi_2 = 0, \lambda = \eta(\dot{\gamma})/G$	$\bar{\eta} = \frac{3\eta}{(1 + \lambda\dot{\epsilon})(1 - 2\lambda\dot{\epsilon})}$
Phan-Thien–Tanner (single relaxation time)	$\eta = \frac{\eta_0}{1 + \xi(2 - \xi)(\lambda\dot{\gamma})^2}$ $\psi_1 = \frac{2\eta\lambda}{1 + \xi(2 - \xi)(\lambda\dot{\gamma})^2}$ $\psi_2 = -\frac{\xi}{2}\psi_1$	— ^a

^aNo analytical solution is available. The following nonlinear algebraic equations must be solved to find $\bar{\eta}$:

$$\exp\left[\frac{-\varepsilon\lambda}{\eta_0}(\tau_{11} + 2\tau_{22})\right]\tau_{11} - 2\lambda\dot{\epsilon}(1 - \xi)\tau_{11} = -2\eta_0\dot{\epsilon}$$

$$\exp\left[\frac{-\varepsilon\lambda}{\eta_0}(\tau_{11} + 2\tau_{22})\right]\tau_{22} + \lambda\dot{\epsilon}(1 - \xi)\tau_{22} = +\eta_0\dot{\epsilon}$$

$\hat{\tau}_{ij}$ is given as follows:

$$\hat{\tau}_{ij} = \frac{\partial \tau_{ij}}{\partial t} + (\mathbf{v} \cdot \nabla \boldsymbol{\tau})_{ij} - [(\nabla \mathbf{v})_{jk} \tau_{ki} + \tau_{ik} (\nabla \mathbf{v})_{kj}] \quad (3.41)$$

This constitutive equation is referred to as the *upper convected Maxwell (UCM) model*. In Example 3.1 this time derivative will be written out for simple shear and shear-free flows. The predictions of this model for steady shear

and shear-free flows are summarized in Table 3.1, and the predicted material functions are fit to shear flow data in Figures 3.13 and 3.14. The most important points to be made are that the small amplitude dynamic mechanical properties are the same as those predicted by the linear viscoelastic model (Eq. 3.39). However, for shear flow one now sees that the model predicts normal stresses, but that both η and ψ_1 are constant rather than functions of $\dot{\gamma}$. Furthermore, $\bar{\eta}$ is observed to be equal to $3\eta_0$ at low $\dot{\epsilon}$, but when $\lambda\dot{\epsilon} = \frac{1}{2}$, then $\bar{\eta}$

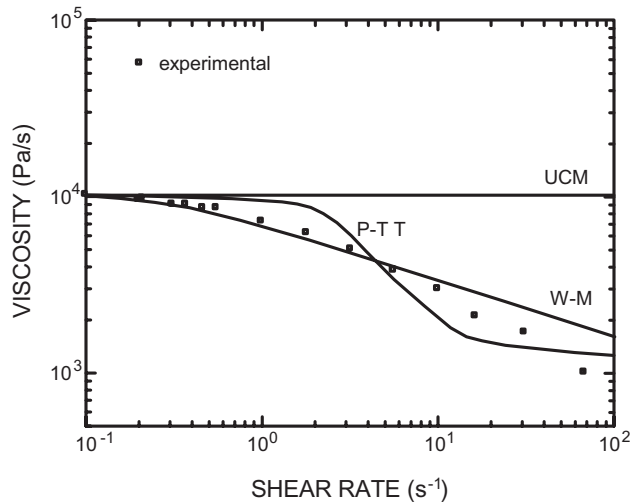


FIGURE 3.13 Comparison of the predictions for viscosity for the White–Metzner, upper convected Maxwell, and Phan–Thien–Tanner models with experimental data for polystyrene (Styron 678, Dow Chemical Company) at 190 °C. (Data from Gotsis, 1987.)

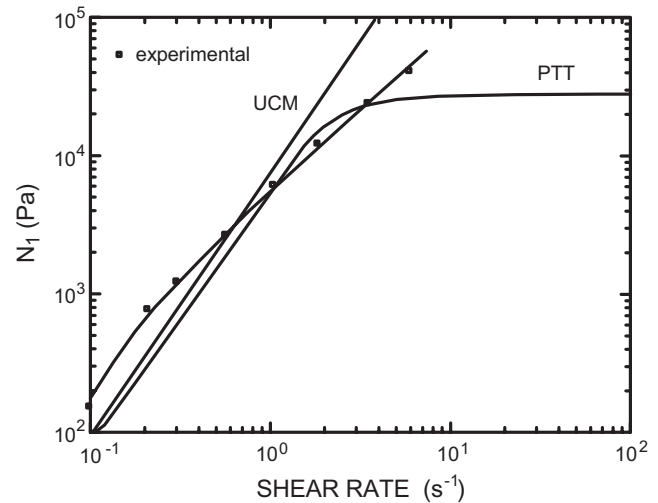


FIGURE 3.14 Comparison of the predictions for N_1 for three different constitutive equations (WM, PTT, and UCM) with experimental data for polystyrene (Styron 678) at 190 °C. (Data from Gotsis, 1987.)

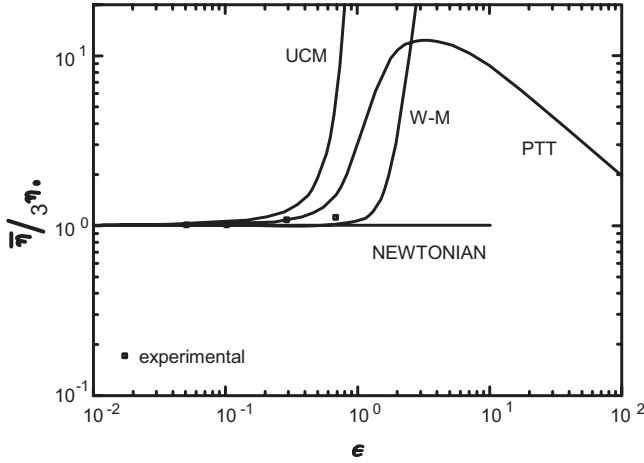


FIGURE 3.15 Comparison of predictions for extensional viscosity ($\bar{\eta}$) for three constitutive equations (WM, UCM, and PTT) with experimental data for polystyrene (Styron 678) at 190 °C. (Data from Gotsis, 1987.)

risers in an unbounded manner (see Fig. 3.15). Yet, we see that this model is not adequate either, as it fails to predict even the most basic property of polymeric fluids, shear-thinning viscosity.

One way to at least make the UCM model predict realistic steady shear flow properties is to replace the material properties μ and $\lambda = \mu/G$ by functions that depend on $\dot{\gamma} = \sqrt{\frac{1}{2}\Pi\dot{\gamma}}$. If one replaces μ by any of the empiricisms for η discussed in Section 2.1, then the constitutive equation, which is known as the White–Metzner (WM) model, can be written as

$$\tau_{ij} + \lambda\tau_{ij} = -\eta\dot{\gamma}_{ij} \quad (3.42)$$

The material properties predicted by this model are summarized in Table 3.1. In particular, in shear flow it is observed that the following stresses are predicted:

$$\tau_{yx} = -\eta\dot{\gamma}_{yx} \quad (3.43)$$

$$\tau_{xx} - \tau_{yy} = -2\lambda\eta\dot{\gamma}_{yx}^2 \quad (3.44)$$

For this model $\lambda = \eta/G$, and G is a constant shear modulus. This model predicts a value of Ψ_1 which is proportional to η^2 . However, Ψ_1 usually shear-thins more rapidly than this. For numerical calculations it is best to fit the Ψ_1 data exactly and then obtain λ as a function of $\dot{\gamma}$. In the case of extensional flow, $\bar{\eta}$ is predicted to rise in an unbounded manner, but the critical extension rate is postponed to higher values of $\dot{\epsilon}$ relative to that for the UCM model (see Fig. 3.15).

The choice of constitutive equation cannot be determined solely by whether it predicts the appropriate steady shear

flow behavior. The only way that one can really assess the value of a constitutive relation is to use it in conjunction with the equations of motion to predict stress and velocity fields. Then these results must be confirmed by experiments using flow visualization and birefringence techniques to obtain the velocity fields or streamlines and the stress fields, respectively. This has been done by White and Baird (1988) for flow of two polymer melts through a planar contraction. They found that the observed behavior could be predicted if the constitutive equation used in the computations predicted accurately both the shear and extensional flow properties of the melt.

For this reason the Phan-Thien–Tanner (PTT) model is discussed next. This model allows one to describe the various types of behavior observed while still describing the shear-thinning viscosity. The Phan-Thien–Tanner (PTT) model (Phan-Thien and Tanner, 1977) is given below:

$$Z(\text{tr } \boldsymbol{\tau})\boldsymbol{\tau} + \lambda\boldsymbol{\tau} + \frac{\xi}{2}\lambda(\dot{\boldsymbol{\gamma}} \cdot \boldsymbol{\tau} + \boldsymbol{\tau} \cdot \dot{\boldsymbol{\gamma}}) = -\eta_0\dot{\boldsymbol{\gamma}} \quad (3.45)$$

The function $Z(\text{tr } \boldsymbol{\tau})$, where $\text{tr } \boldsymbol{\tau}$ is the trace of the stress tensor, is given by one of the following functions:

$$Z = \begin{cases} 1 - \varepsilon\lambda \text{tr } \boldsymbol{\tau} / \eta_0 \\ \text{or} \\ \exp(-\varepsilon\lambda \text{tr } \boldsymbol{\tau} / \eta_0) \end{cases} \quad (3.46)$$

Here λ , η_0 , and ξ are found from steady shear and dynamic data. The parameter ε is obtained from extensional viscosity data and has little effect on the prediction of the shear flow properties. Actually, η_0 can be replaced by $\eta(\dot{\gamma})$ or a set of values for η_i and λ_i . Predictions of the model for steady shear and uniaxial extensional flows are summarized in Table 3.1. The choice of the exponential function allows one to predict values of $\bar{\eta}$ which increase with $\dot{\epsilon}$ and then pass through a maximum.

A few additional comments should be made pertaining to this model. The model as it stands has a problem in that the shear stress passes through a maximum at critical value of $\dot{\gamma}$ (this leads to instabilities in any numerical calculation). This problem is overcome by several different methods. One is to use a spectrum of relaxation times and viscosities, λ_i and η_i , respectively. (This is referred to as a multimode approach.) Another is to add a Newtonian viscosity term (i.e., $\tau_p = \tau_s + \tau_p$, where τ_p is given by Eq. 3.45 and $\tau_s = -\mu_s\dot{\boldsymbol{\gamma}}$). Furthermore, one can replace η by one of the empiricisms for viscosity discussed in Section 2.4. Finally, there are no problems that can be solved analytically using this model (or with the others for that matter), and numerical methods are usually required.

The predictions of these models and their fit to rheological data for a polystyrene melt are summarized in Figures 3.13,

3.14, and 3.15. Here it can be seen how well each model fits experimental data. Certainly if a spectrum of relaxation times were used, the PTT model would fit the steady shear data even better. In Figure 3.15 the predictions of $\bar{\eta}$ are presented. In fact, for the PTT model the predictions for $\bar{\eta}$ versus $\dot{\epsilon}$ can be changed by the values chosen for ε . With $\varepsilon = 0.01$, $\bar{\eta}$ strain rate hardens, passes through a maximum, and then decreases with increasing $\dot{\epsilon}$. If $\varepsilon > 0.1$, $\bar{\eta}$ starts at $3\eta_0$ and then decreases with increasing $\dot{\epsilon}$. It is believed that these two different types of behavior for $\bar{\eta}$ are related to differences in the processability of polymers, especially in cases where extensional deformations are important. Over the range for which N_1 data is available, all the models predict reasonable values of N_1 (see Fig. 3.14). However, it is observed that the PTT model predicts values of N_1 which become independent of shear rate (when a Newtonian limiting viscosity is included), which may be a more realistic prediction at high shear rates. (*Note:* Values of N_1 at values of $\dot{\gamma} > 100$ are not readily available.)

It should be noted that the constitutive equations that are discussed here represent only a few of the plethora of equations from which to choose. The choice of the PTT model has been justified because of its ability to fit the extensional flow behavior of polymeric fluids in a manner nearly independent of the shear flow behavior. There are several other possibilities for constitutive equations which might behave in a similar manner to the PTT model. In particular, we note the Giesekus model (see Problem 3B.5) and a couple of integral models (Bird et al., 1987a). In Problem 3B.8, the ‘‘pom-pom-model’’ of McLeish and Larson (1998) is evaluated and we note that it behaves in a manner similar to that of the PTT model but the parameter that leads to strain hardening is associated with the degree of long chain branching. As there is no intention in this book to include the additional mathematical complexities associated with integral models, they will not be discussed.

As there is no intention in this book to use the nonlinear constitutive equations in conjunction with the equations of motion to solve polymer processing problems, we at least show in the next several examples how one determines the predictions of a nonlinear model for flows in which the kinematics are known. In particular, we consider shear and shear-free flows. Furthermore, we show how one goes about finding the material parameters in a constitutive equation from rheological data for a polymer melt.

Example 3.1. Shear Flow Predictions for the White–Metzner Model

Calculate the material functions for the White–Metzner model in simple shear flow (i.e., $v_x = \dot{\gamma}_{xy}(t)y$, $v_y = v_z = 0$) including the startup of simple shear flow (SF), steady simple SF, and stress relaxation following steady SF.

Solution. For an unsteady simple shear flow the terms in Eq. 3.42 are given below:

$$\tau_{ij} = \begin{pmatrix} \tau_{xx} & \tau_{yx} & 0 \\ \tau_{yx} & \tau_{yy} & 0 \\ 0 & 0 & \tau_{zz} \end{pmatrix} \quad (3.47)$$

$$\begin{aligned} \tau &= \frac{\partial}{\partial t} \begin{pmatrix} \tau_{xx} & \tau_{yx} & 0 \\ \tau_{yx} & \tau_{yy} & 0 \\ 0 & 0 & \tau_{zz} \end{pmatrix} + v_x \frac{\partial}{\partial x} \begin{pmatrix} \tau_{xx} & \tau_{yx} & 0 \\ \tau_{yx} & \tau_{yy} & 0 \\ 0 & 0 & \tau_{zz} \end{pmatrix} \\ &\quad - \begin{pmatrix} 0 & \dot{\gamma}_{yx} & 0 \\ 0 & 0 & 0 \\ 0 & 0 & 0 \end{pmatrix} \begin{pmatrix} \tau_{xx} & \tau_{yx} & 0 \\ \tau_{yx} & \tau_{yy} & 0 \\ 0 & 0 & \tau_{zz} \end{pmatrix} - \begin{pmatrix} \tau_{xx} & \tau_{yx} & 0 \\ \tau_{yx} & \tau_{yy} & 0 \\ 0 & 0 & \tau_{zz} \end{pmatrix} \begin{pmatrix} 0 & 0 & 0 \\ \dot{\gamma}_{yx} & 0 & 0 \\ 0 & 0 & 0 \end{pmatrix} \\ &= \frac{\partial}{\partial t} \begin{pmatrix} \tau_{xx} & \tau_{yx} & 0 \\ \tau_{yx} & \tau_{yy} & 0 \\ 0 & 0 & \tau_{zz} \end{pmatrix} - \dot{\gamma}_{yx} \begin{pmatrix} 2\tau_{yx} & \tau_{yy} & 0 \\ \tau_{yy} & 0 & 0 \\ 0 & 0 & 0 \end{pmatrix} \quad (3.48) \end{aligned}$$

$$\dot{\gamma}_{ij} = \begin{pmatrix} 0 & \dot{\gamma}_{yx} & 0 \\ \dot{\gamma}_{yx} & 0 & 0 \\ 0 & 0 & 0 \end{pmatrix} \quad (3.49)$$

Note the underlined term in Eq. 3.48 is zero for a homogeneous flow (i.e., a flow in which $\dot{\gamma}_{xy}$ is not a function of x , y , or z). This leads to the following matrix equation for determining τ_{ij} :

$$\begin{aligned} \begin{pmatrix} \tau_{xx} & \tau_{yx} & 0 \\ \tau_{yx} & \tau_{yy} & 0 \\ 0 & 0 & \tau_{zz} \end{pmatrix} + \frac{\eta(\dot{\gamma})}{G} \left[\frac{d}{dt} \begin{pmatrix} \tau_{xx} & \tau_{yx} & 0 \\ \tau_{yx} & \tau_{yy} & 0 \\ 0 & 0 & \tau_{zz} \end{pmatrix} \right. \\ \left. - \dot{\gamma}_{yx} \begin{pmatrix} 2\tau_{yx} & \tau_{yy} & 0 \\ \tau_{yy} & 0 & 0 \\ 0 & 0 & 0 \end{pmatrix} \right] = -\eta(\dot{\gamma}) \begin{pmatrix} 0 & \dot{\gamma}_{yx} & 0 \\ \dot{\gamma}_{yx} & 0 & 0 \\ 0 & 0 & 0 \end{pmatrix} \quad (3.50) \end{aligned}$$

From this matrix equation one obtains a set of coupled ordinary differential equations for the stress components:

$$\left(1 + \frac{\eta(\dot{\gamma})}{G} \frac{d}{dt}\right) \tau_{xx} - \frac{2\eta(\dot{\gamma})}{G} \tau_{yx} \dot{\gamma}_{yx} = 0 \quad (3.51)$$

$$\left(1 + \frac{\eta(\dot{\gamma})}{G} \frac{d}{dt}\right) \tau_{yy} = 0 \quad (3.52)$$

$$\left(1 + \frac{\eta(\dot{\gamma})}{G} \frac{d}{dt}\right) \tau_{yx} + \dot{\gamma}_{yx} \tau_{yy} = -\eta(\dot{\gamma}) \dot{\gamma}_{yx} \quad (3.53)$$

$$\left(1 + \frac{\eta(\dot{\gamma})}{G} \frac{d}{dt}\right) \tau_{zz} = 0 \quad (3.54)$$

From Eqs. 3.52 and 3.54 one sees that τ_{yy} and τ_{zz} are zero for all time-dependent simple shear flows. (This follows from $\tau_{zz} = \tau_{yy} = 0$ at $t = -\infty$.) One can now solve for τ_{xx} and τ_{xy} .

First using Eq. 3.53 one solves for τ_{yx} using an integrating factor:

$$d/dt(e^{t/\lambda} \tau_{yx}) = -G \exp(t/\lambda) \dot{\gamma}_{yx}(t) \quad (3.55)$$

This gives the following expression for τ_{yx} on integration:

$$\tau_{yx}(t) = -G \int_{-\infty}^t \exp[-(t-t')/\lambda] \dot{\gamma}_{yx}(t') dt' \quad (3.56)$$

Note that the integration starts at $-\infty$ where the stresses are assumed to be zero. Likewise one can find an expression for $\tau_{xx}(t)$:

$$\tau_{xx}(t) = -2G \int_{-\infty}^t e^{-(t-t')/\lambda} \tau_{yx}(t') dt' \quad (3.57)$$

We now considers the three special cases requested in this example.

Stress Growth. For startup of shear flow (the stress growth experiment), $\dot{\gamma}_{yx}(t)$ is given by

$$\dot{\gamma}_{yx}(t) = \dot{\gamma}_0 H(t) \quad (3.58)$$

where $H(t)$ is the unit step function. When Eq. 3.58 is substituted into Eqs. 3.56 and 3.57 one obtains the following expressions for the stress components:

$$\tau_{yx} = -\eta(\dot{\gamma}) \dot{\gamma}_0 [1 - e^{-t/\lambda}] \quad (3.59)$$

$$\tau_{xx}(t) = -2\eta(\dot{\gamma}) \dot{\gamma}_0^2 \lambda [1 - t/\lambda e^{-t/\lambda}] \quad (3.60)$$

It is observed from these equations that the stresses rise monotonically to their steady-state values.

Steady Shear Flow. For steady shear flow one starts with Eqs. 3.56 and 3.57 and with $\dot{\gamma}_{yx}(t) = \dot{\gamma}_0$ one finds

$$\tau_{yx}(t) = -G \int_{-\infty}^t e^{-(t-t')/\lambda} \dot{\gamma}_0 dt' \quad (3.61)$$

Next one replaces the integration variable t' by $s = t - t'$ to give

$$\tau_{yx}(t) = -G \int_{-\infty}^t e^{-s/\lambda} \dot{\gamma}_0 ds \quad (3.62)$$

which can be further integrated to give

$$\tau_{yx} = -\eta(\dot{\gamma}) \dot{\gamma}_0 \quad (3.63)$$

One can carry out the same procedure to find τ_{xx} :

$$\tau_{xx} = -2\eta(\dot{\gamma}) \lambda \dot{\gamma}_0^2 \quad (3.64)$$

Hence, it is seen by replacing $\eta(\dot{\gamma})$ by an appropriate function one can fit the viscosity data exactly. The normal stress is predicted to be proportional to η^2 , if λ is replaced by η/G . However, this is not quite what is observed experimentally.

Stress Relaxation Following Steady Shear Flow. For this flow one uses $\dot{\gamma}_{xy} = \dot{\gamma}_0(1 - H(t))$. Returning to Eqs. 3.56 and 3.57 one obtains the following expressions:

$$\tau_{yx}(t) = -G \int_{-\infty}^t e^{-(t-t')/\lambda} \dot{\gamma}_0 (1 - H(t')) dt' \quad (3.65)$$

$$\tau_{xx}(t) = -2 \int_{-\infty}^t e^{-(t-t')/\lambda} \tau_{yx}(t') \dot{\gamma}_0 (1 - H(t')) dt' \quad (3.66)$$

Equation 3.65 is integrated by parts to obtain $\tau_{yx}(t)$:

$$\tau_{yx}(t) = -\eta(\dot{\gamma}) \dot{\gamma}_0 e^{-t/\lambda} \quad (3.67)$$

Now one substitutes Eq. 3.67 into Eq. 3.66 to obtain

$$\tau_{xx}(t) = -2\eta(\dot{\gamma}) \lambda \dot{\gamma}_0^2 e^{-t/\lambda} \quad (3.68)$$

It is indicated by these equations that on cessation of flow the stresses decay exponentially with time. At higher $\dot{\gamma}_{yx}$, the stresses relax faster as a result of a decrease in λ . This is in agreement with experimental observations. However, the model predicts that τ_{yx} and τ_{xx} relax at the same rate, which is not what is observed in general. ■

Example 3.2. Predictions of the PTT Model in Steady Simple Shear and Steady Shear-Free Flow

- Determine the predictions for the material functions in steady simple shear flow for the PTT model.
- Do the same for steady shear-free flow (SSFF) and then show the results for simple elongational flow.

Solution. (a) The PTT model requires additional manipulations relative to the White–Metzner model. Quantities such as $\text{tr } \boldsymbol{\tau}$ and $\dot{\boldsymbol{\gamma}} \cdot \boldsymbol{\tau}$ must be determined. $\boldsymbol{\tau}$ is given in Eq. 3.48. The trace of $\boldsymbol{\tau}$ (i.e., $\text{tr } \boldsymbol{\tau}$) is the sum of the diagonal components of $\boldsymbol{\tau}$, which is

$$\text{tr } \boldsymbol{\tau} = \tau_{xx} + \tau_{yy} + \tau_{zz} \quad (3.69)$$

Hence, the first term in Eq. 3.45 is

$$Z(\text{tr } \boldsymbol{\tau}) \boldsymbol{\tau} = \exp[-\varepsilon \lambda (\tau_{xx} + \tau_{yy} + \tau_{zz}) / \eta_0] \boldsymbol{\tau} \quad (3.70)$$

The third term in Eq. 3.45 is

$$\begin{aligned}
 & (\xi\lambda/2)[\dot{\boldsymbol{\gamma}} \cdot \boldsymbol{\tau} + \boldsymbol{\tau} \cdot \dot{\boldsymbol{\gamma}}] \\
 &= \left(\frac{\xi\lambda}{2}\right) \begin{pmatrix} 0 & \dot{\gamma}_0 & 0 \\ \dot{\gamma}_0 & 0 & 0 \\ 0 & 0 & 0 \end{pmatrix} \begin{pmatrix} \tau_{xx} & \tau_{xy} & 0 \\ \tau_{yx} & \tau_{yy} & 0 \\ 0 & 0 & \tau_{zz} \end{pmatrix} \\
 &+ \begin{pmatrix} \tau_{xx} & \tau_{xy} & 0 \\ \tau_{yx} & \tau_{yy} & 0 \\ 0 & 0 & \tau_{zz} \end{pmatrix} \begin{pmatrix} 0 & \dot{\gamma}_0 & 0 \\ \dot{\gamma}_0 & 0 & 0 \\ 0 & 0 & 0 \end{pmatrix} \\
 &= \frac{\xi\lambda}{2} \dot{\gamma}_0 \begin{pmatrix} 2\tau_{yx} & \tau_{yy} + \tau_{xx} & 0 \\ \tau_{xx} + \tau_{yy} & 2\tau_{xy} & 0 \\ 0 & 0 & 0 \end{pmatrix} \quad (3.71)
 \end{aligned}$$

Finally, we put all the terms together to obtain the following matrix equation:

$$\begin{aligned}
 Z(\text{tr } \boldsymbol{\tau}) \begin{pmatrix} \tau_{xx} & \tau_{xy} & 0 \\ \tau_{yx} & \tau_{yy} & 0 \\ 0 & 0 & \tau_{zz} \end{pmatrix} + \frac{\xi\lambda}{z} \dot{\gamma}_0 \begin{pmatrix} 2\tau_{yx} & \tau_{yy} + \tau_{xx} & 0 \\ \tau_{xx} + \tau_{yy} & 2\tau_{xy} & 0 \\ 0 & 0 & 0 \end{pmatrix} \\
 -\lambda \dot{\gamma}_0 \begin{pmatrix} 2\tau_{yx} & \tau_{yy} & 0 \\ \tau_{yy} & 0 & 0 \\ 0 & 0 & 0 \end{pmatrix} = -\eta_0 \begin{pmatrix} 0 & \dot{\gamma}_0 & 0 \\ \dot{\gamma}_0 & 0 & 0 \\ 0 & 0 & 0 \end{pmatrix} \quad (3.72)
 \end{aligned}$$

From this matrix equation we obtain a set of coupled algebraic equations for the stress tensor components:

$$\tau_{xx} : Z(\text{tr } \boldsymbol{\tau}) \tau_{xx} + \xi\lambda \dot{\gamma}_0 \tau_{yx} - 2\lambda \dot{\gamma}_0 \tau_{yx} = 0 \quad (3.73)$$

$$\tau_{xy} : Z(\text{tr } \boldsymbol{\tau}) \tau_{xy} + \frac{\xi\lambda}{2} \dot{\gamma}_0 (\tau_{yy} + \tau_{xx}) - \lambda \dot{\gamma}_0 \tau_{xy} = -\eta_0 \dot{\gamma}_0 \quad (3.74)$$

$$\tau_{yy} : Z(\text{tr } \boldsymbol{\tau}) \tau_{yy} + \xi\lambda \dot{\gamma}_0 \tau_{xy} = 0 \quad (3.75)$$

$$\tau_{zz} : Z(\text{tr } \boldsymbol{\tau}) \tau_{zz} = 0 \quad (3.76)$$

In the form above the equations are coupled nonlinear algebraic equations, and one would have to use Newton's method to solve these equations. However, they can be simplified by the fact that for shear flow (this is called a weak flow in the continuum mechanics literature) $\text{tr } \boldsymbol{\tau}$ is small and the term $\varepsilon\lambda \text{tr } \boldsymbol{\tau}/\eta_0$ approaches zero. Hence, $Z(\text{tr } \boldsymbol{\tau}) \approx 1.0$ (where " \approx " means approximately). We also note that $\tau_{xy} = \tau_{yx}$, because the stress tensor is symmetric. Solving the above equations we find that

$$\tau_{xy} = \frac{-\eta_0 \dot{\gamma}_0}{[1 + \xi(2 - \xi)(\lambda \dot{\gamma}_0)^2]} \quad (3.77)$$

$$\tau_{xx} = \frac{-\lambda \dot{\gamma}_0^2 (2 - \xi) \eta_0}{[1 + \xi(2 - \xi)(\lambda \dot{\gamma}_0)^2]} \quad (3.78)$$

$$\tau_{yy} = \frac{+\xi\lambda \eta_0 \dot{\gamma}_0^2}{[1 + \xi(2 - \xi)(\lambda \dot{\gamma}_0)^2]} \quad (3.79)$$

$$\tau_{zz} = 0 \quad (3.80)$$

Using the definitions in Section 3.1 for η , ψ_1 , and ψ_2 , we obtain the entries which are given in Table 3.1.

(b) For simple shear-free flow the approach is the same. The matrix equation for the stresses is

$$\begin{aligned}
 Z(\text{tr } \boldsymbol{\tau}) \begin{pmatrix} \tau_{xx} & 0 & 0 \\ 0 & \tau_{yy} & 0 \\ 0 & 0 & \tau_{zz} \end{pmatrix} - \lambda \dot{\varepsilon}_0 \begin{pmatrix} -(1+b)\tau_{xx} & 0 & 0 \\ 0 & -(1-b)\tau_{yy} & 0 \\ 0 & 0 & 2\tau_{zz} \end{pmatrix} \\
 + \xi\lambda \dot{\varepsilon}_0 \begin{pmatrix} -(1+b)\tau_{xx} & 0 & 0 \\ 0 & -(1-b)\tau_{yy} & 0 \\ 0 & 0 & 2\tau_{zz} \end{pmatrix} \\
 = -\eta_0 \dot{\varepsilon}_0 \begin{pmatrix} -(1+b) & 0 & 0 \\ 0 & -(1-b) & 0 \\ 0 & 0 & 2 \end{pmatrix} \quad (3.81)
 \end{aligned}$$

In this case the factor $Z(\text{tr } \boldsymbol{\tau})$ does not reduce to one and hence must be maintained. The stress components are

$$\begin{aligned}
 \exp\left[\frac{-\varepsilon\lambda}{\eta_0}(\tau_{xx} + \tau_{yy} + \tau_{zz})\right] \tau_{xx} + \lambda \dot{\varepsilon}_0 (1+b) \tau_{xx} \\
 - \xi\lambda \dot{\varepsilon}_0 (1+b) \tau_{xx} = +\eta_0 \dot{\varepsilon}_0 (1+b) \quad (3.82)
 \end{aligned}$$

$$\begin{aligned}
 \exp\left[\frac{-\varepsilon\lambda}{\eta_0}(\tau_{xx} + \tau_{yy} + \tau_{zz})\right] \tau_{yy} + \lambda \dot{\varepsilon}_0 (1+b) \tau_{yy} \\
 - \xi\lambda \dot{\varepsilon}_0 (1-b) \tau_{yy} = +\eta_0 \dot{\varepsilon}_0 (1-b) \quad (3.83)
 \end{aligned}$$

$$\begin{aligned}
 \exp\left[\frac{-\varepsilon\lambda}{\eta_0}(\tau_{xx} + \tau_{yy} + \tau_{zz})\right] \tau_{zz} - 2\lambda \dot{\varepsilon}_0 \tau_{zz} \\
 + 2\xi\lambda \dot{\varepsilon}_0 \tau_{zz} = -2\eta_0 \dot{\varepsilon}_0 \quad (3.84)
 \end{aligned}$$

For steady elongational flow, $b = 0$, $\dot{\varepsilon}_0 > 0$, and we see that $\tau_{xx} = \tau_{yy}$. Hence, the equations become

$$\begin{aligned}
 \exp\left[\frac{-\varepsilon\lambda}{\eta_0}(2\tau_{xx} + \tau_{zz})\right] \tau_{xx} + \lambda \dot{\varepsilon}_0 (1 - \xi) \tau_{xx} = -\eta_0 \dot{\varepsilon}_0 \\
 \quad (3.85)
 \end{aligned}$$

$$\begin{aligned}
 \exp\left[\frac{-\varepsilon\lambda}{\eta_0}(2\tau_{xx} + \tau_{zz})\right] \tau_{zz} + 2\lambda \dot{\varepsilon}_0 (1 - \xi) \tau_{zz} = -2\eta_0 \dot{\varepsilon}_0 \\
 \quad (3.86)
 \end{aligned}$$

In this case we cannot obtain an analytical expression for $\bar{\eta}$, but Eqs. 3.85 and 3.86 must be solved numerically for specified values of $\dot{\varepsilon}_0$, $\dot{\varepsilon}$, λ , and η_0 . ■

Example 3.3. Material Parameters for the Phan-Thien–Tanner (PTT) Model

Obtain the material parameters (i.e., η_0 , λ , ξ , ε) in the PTT model for LDPE (NPE 953) at 170 °C for which rheological data is given in Appendix A.1.

- (a) First obtain the parameters by any method desired.
- (b) Determine the model parameters using nonlinear regression analysis. In particular, use either the IMSL (International Mathematics and Statistics Libraries) subroutine RNLIN (see Appendix E.3) in the folder, “IMSL Documentation-Appendix E;” on the accompanying website or Excel and the *Solve* function.
- (c) Compare the methods in terms of how well they fit the data and comment on the ability of the PTT model to fit the data.

Solution. (a) From the stress quantities given in Eqs. 3.77 to 3.79 the viscosity function is

$$\eta = \frac{\eta_0}{1 + \xi(2 - \xi)(\lambda \dot{\gamma}_0)^2} \quad (3.87)$$

while N_1 is given by

$$N_1 = \frac{-2 \eta_0 \lambda \dot{\gamma}_0^2}{1 + \xi(2 - \xi)(\lambda \dot{\gamma}_0)^2} \quad (3.88)$$

Working with Eq. 3.87, we can obtain η_0 directly from the viscosity data in Appendix A.1. In this case we take η_0 to be 23,100 Pa·s (i.e., we used η at the lowest $\dot{\gamma}_0$). To obtain ξ and λ we plot η/η_0 versus $\lambda \dot{\gamma}_0$, which is a dimensionless shear rate, for different values of ξ . The dimensionless viscosity curves (or “master curves”) for each value of ξ are then superimposed on plots of η/η_0 versus $\dot{\gamma}_0$ or η^*/η_0 versus ω based on data taken from Appendices A.1 and A.2, respectively. The curves are then shifted horizontally until the “best fit” is obtained between the experimental results and the theoretical curves. The parameter that shifts the experimental data on to the master curve is λ . Curves for three different values of λ are shown in Figure 3.16. The best fit seems to be obtained by selecting a value of $\lambda = 0.5$.

In Figure 3.17 we plot predicted values of N_1 (Eq. 3.88) versus $\dot{\gamma}_0$ and compare them against experimental values of N_1 and $2G'$. At low $\dot{\gamma}_0$ the predicted values of N_1 agree well with the experimental values. The agreement between N_1 and $2G'$ is not good, and hence one would not expect good agreement between the predicted values of N_1 and $2G'$ at high $\dot{\gamma}_0$ (for an alternate relation between N_1 and G' see Eq. 3.148).

It is difficult to fit Eq. 3.87 to the viscosity data because the shape of the curve is not quite what is observed experimentally. In particular, the slope of $\ln \eta$ versus $\ln \dot{\gamma}_0$ is less than -1.0 , which is physically unrealistic (this means that τ_{yx} passes through a maximum, and for flow through a capillary it would mean there could be more than one flow rate

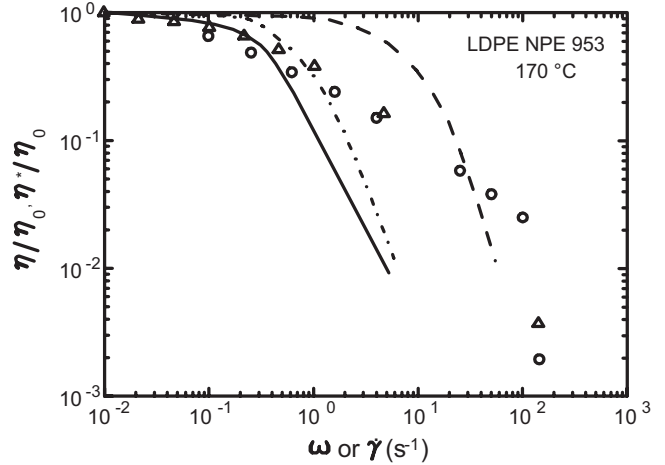


FIGURE 3.16 Reduced viscosity versus shear rate or angular frequency (ω) for LDPE (NPE 953) at 170 °C. The curves represent the PTT model viscosity function for three sets of parameters: (—) $\xi = 0.05$, $\lambda = 2.7$; (---) $\xi = 0.05$, $\lambda = 0.5$; and (-·-) $\xi = 0.038$, $\lambda = 5.47$.

possible for a given pressure drop). However, in an effort to improve on the fit of Eq. 3.87 to the viscosity data, we use a nonlinear regression analysis to obtain a set of coefficients that fit the data in a least-squares sense.

(b) The method used in part (a) to obtain the coefficients is in essence a least-squares approach, but it is somewhat subjective. The method of nonlinear regression analysis is used to find the parameters that minimize the sum of the residual errors between the predicted and experimental values. The solution to this problem is given on the accompanying website in the folder under “Numerical Examples, Chapter 3.”

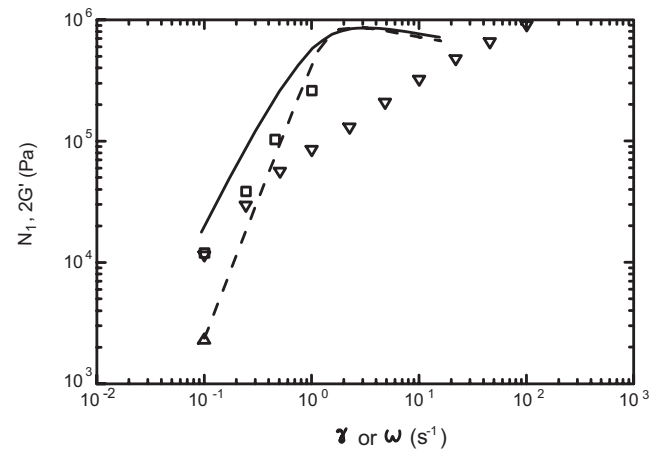


FIGURE 3.17 Comparison of predicted values of N_1 (PTT model) with experimental values of N_1 and $2G'$ for LDPE (NPE 953) at 170 °C: (—) $\xi = 0.038$, $\lambda = 5.47$ s; (---) $\xi = 5.00E-02$, $\lambda = 2.70$ s; (▽) $2G'$; (□) N_1 .

In this solution, we use the IMSL subroutine RNLIN (see EX3-3-Fortran) or the *Solve* function in Excel (see EX3-3-Excel.xlsx) to find η_0 , ξ , and λ . The values for η_0 , ξ , and λ obtained in a least-squares sense (called theta (1), theta (2), and theta (3) in the Fortran code, respectively, but listed as theta in the solution) are 23,100 Pa·s, 0.038, and 5.475 s, respectively. It is also observed that it was difficult to fit the PTT viscosity function to the experimental data. The function does not fit the data well as the sum of the squares of the errors (SSE) is very large. By using the values for η_0 , ξ , and λ , Eq. 3.87 is evaluated and η/η_0 is plotted versus $\lambda\dot{\gamma}_0$ in Figure 3.16. Here we see that the fit is very good at low $\dot{\gamma}_0$, but at high $\dot{\gamma}_0$ there is considerable disagreement. Furthermore, this curve is very close to the “eyeballed” curve for $\xi = 0.05$ and $\lambda = 2.7$. In the case of the use of Excel, the values obtained for ξ and λ are 0.035 and 0.44, respectively.

Values of N_1 calculated from Eq. 3.88 using the coefficients determined by means of the subroutine RNLIN are plotted in Figure 3.17 and compared against the experimental values. Values based on Eq. 3.88 and the eyeballed values of η_0 , ξ , and λ are also plotted in Figure 3.17. The statistically determined values lead to a better prediction of N_1 at low $\dot{\gamma}_0$, but the values seem to converge at higher $\dot{\gamma}_0$.

The parameter ε is determined from extensional data and requires the solution of ordinary differential equations for various values of ε . This is done in the solution to Problem 3C.3.

(c) Finally, we recognize that the PTT model in its present form does not fit the viscosity data well because it predicts a function for η which is too highly shear rate dependent. By adding a Newtonian viscosity to the function in Eq. 3.87, the fit can be made better and η does not shear-thin in an unrealistic manner.

It is clear that viscoelastic fluids require a constitutive equation that is capable of describing time-dependent rheological properties, normal stresses, elastic recovery, and an extensional viscosity which is independent of the shear viscosity. It is not clear at this point exactly as to how a constitutive equation for a viscoelastic fluid, when coupled with the equations of motion, leads to the prediction of behavior (i.e., velocity and stress fields) which is any different from that calculated for a Newtonian fluid. As the constitutive relations for polymeric fluids lead to nonlinear differential equations that cannot easily be solved, it is difficult to show how their use affects calculations. Furthermore, it is not clear how using a constitutive equation, which predicts normal stress differences, leads to predictions of velocity and stress fields which are significantly different from those predicted by using a Newtonian fluid model. Finally, there are numerous possibilities of constitutive relations from which to choose. The question is then: When and how does one use a viscoelastic constitutive relation in design calculations especially when sophisticated numerical methods such as finite element methods are not available to the student at this point? For the

time being, it appears that the most important material functions which the model must describe accurately are the shear and extensional viscosity. The design calculations for which one must use a viscoelastic constitutive relation are those involving shear-free flows such as film blowing, expansion of a parison in blow molding, squeezing flow, film casting, and fiber spinning. Furthermore, a viscoelastic model can be useful for estimating extrudate swell, which is the expansion of a polymeric fluid on leaving a die. It has been suggested that die swell can be correlated to N_1 . One commonly used relation proposed by Tanner (1970) is

$$\frac{D_p}{D_0} = 0.1 + \left[1.0 + \frac{1}{2} \left(\frac{N_{1,w}}{2\tau_w} \right)^2 \right]^{1/6} \quad (3.89)$$

where D_p is the diameter of the extrudate and D_0 is the capillary diameter. (Further discussion of extrudate or “die” swell is presented in Chapter 7.) Hence, in this book we will primarily use nonlinear viscoelastic models for estimating values of N_1 at high shear rates and when the kinematics are known. It is beyond the level of this book to solve problems in which nonlinear constitutive equations are used in conjunction with the equations of motion.

A few additional comments about when and under what conditions one must use a nonlinear viscoelastic constitutive equation are discussed here. At this time it seems that whenever the flow is unsteady in either a Lagrangian ($D\mathbf{v}/Dt \neq 0$) or a Eulerian ($\partial\mathbf{v}/\partial t \neq 0$) sense, then viscoelastic effects become important. In the former case one finds flows of this nature whenever inhomogeneous shear-free flows arise (e.g., flow through a contraction) and in the latter case in the startup of flows. However, even in simple flows, such as in capillaries or slit dies, viscoelastic effects can be important, especially if the residence time of the fluid in the die is less than the longest relaxation time of the fluid. Then factors such as stress overshoot could lead to an apparent viscosity that is higher than the steady-state viscosity. In line with these ideas one defines a dimensionless group referred to as the Deborah number:

$$De = \lambda/t_{av} \quad (3.90)$$

where t_{av} is the process time and λ is the relaxation time. If $De \geq 1$, then transient effects are important. Another place where viscoelastic effects are important would be in injection molding where the stresses in the melt may relax slowly relative to the heat transfer rate, and in which case residual stresses are frozen into the part. Hence, even when the flows are steady, the viscoelastic nature of the fluid can be important. Certainly for the most part to consider viscoelastic effects in design calculations, it will be necessary to use numerical techniques. ■

3.2.2 Fiber Suspensions

Polymer melts containing glass and other types of chopped fibers are commonly processed by means of injection and compression molding to form parts with enhanced strength and stiffness. As these materials are commonly processed by means used for polymer melts, it is necessary to introduce their flow behavior and to introduce theory for handling their rheological behavior and predicting evolution of fiber orientation. This chapter is not intended to provide a complete overview of the topic of fiber suspension rheology, which can be found elsewhere (Eberle et al., 2008), but to provide a quantitative approach to predicting fiber orientation for what are considered as rigid fiber systems.

Before discussing theoretical models for the rheology of fiber suspensions and its connection to fiber orientation, there are three topics that must be discussed: Brownian motion, concentration regimes, and fiber flexibility. Brownian motion refers to the random movement of any sufficiently small particle as a result of the momentum transfer from suspending medium molecules. The relative effect that Brownian motion may have on orientation of anisotropic particles in a dynamic system can be estimated using the rotary Peclet number, $Pe \equiv \dot{\gamma}/D_{ro}$, where $\dot{\gamma}$ is the shear rate and D_{ro} is the rotary diffusivity, which defines the ratio of the thermal energy in the system to the resistance to rotation. Doi and Edwards (1988) estimated the rotary diffusivity, D_{ro} , to be

$$D_{ro} = 3k_B T [\ln(a_r) - \Omega] / \pi \eta_s L^3 \quad (3.91)$$

where k_B is Boltzmann's constant, T is absolute temperature, a_r is the fiber aspect ratio (L/d), and Ω is estimated to be 0.8. We use the scaling argument that when $Pe \gg 1$ Brownian effects can be neglected, which, in general, is true for particles whose longest dimension is $\geq 10 \mu\text{m}$. In this section we are only interested in fiber suspensions, which can be considered non-Brownian. The reader is referred to the work of Doi and Edwards (1988) on the dynamics of Brownian rods for the coverage of such topics.

Fiber suspensions are typically classified into three concentration regimes: dilute, semidilute, and concentrated, which are based on their volume fraction, $\phi = \pi n L^3 / 4 a_r^2$, where n is the number of fibers per unit volume. The dilute regime is such that the fibers within the suspension are free to both rotate and translate without hydrodynamic interaction or direct contact. Theoretically, this occurs when the average distance between the center of mass of two fibers is greater than L leading to the constraint of $n < 1/L^3$ or $\phi < a_r^{-2}$. The transition to the semidilute region occurs just above the dilute upper limit. Here hydrodynamic interaction is the predominant phenomenon with little fiber contact. However, the suspension orientation state is not subject to

geometric constraints, which can constrict orientation states. Interaction between fibers becomes theoretically possible for homogeneously dispersed fibers when $n > 1/L^3$, but when the mean spacing between fibers, S_m , is on the order of the fiber diameter (d), physical contact becomes an increasingly significant phenomenon. Therefore, the upper limit is subject to the constraint $S_m \gg d$ (Doi and Edwards, 1988). The mean spacing between fibers is a function of the orientation state of the fibers within the suspension. For a random orientation state the mean spacing is estimated as $S_m \cong 1/nL^2$ and for a suspension whose fibers are completely aligned the mean spacing is of the order $S_m \cong (nL)^{-1/2}$. This leads to two upper limits: $n \ll 1/dL^2$ for random and $n \ll 1/d^2L$ for aligned orientation.

The concentrated regime is where $n \geq 1/dL^2$ or $\phi \geq a_r^{-1}$. In this range the dynamic properties of the fibers can be severely affected by fiber–fiber interactions and can lead to solid-like behavior. It is interesting to note that most fiber composites of industrial interest typically have fiber concentrations of $\phi > 0.1$ and fall within the concentrated regime. In addition to the three regimes defined above, molecular theories define a critical concentration in which molecules will preferentially align to form a nematic liquid crystalline phase, a phase intermediate to a purely crystalline phase and an isotropic liquid phase. However, it has yet to be proved that fiber suspensions will also go through this transition (Larson, 1999).

The final aspect deals with the term “flexibility”, which will be used to describe how stiff a fiber behaves in the presence of flow. In this context, a fiber exhibiting a larger degree of flexibility is easier to bend within a specified flow field. The flexibility of a fiber commonly leads to two classes of materials—short and long. Short fiber suspensions are defined as those that remain rigid within a specified shear field, while long fiber suspensions consist of fibers that flex or bend. Switzer and Klingenberg (2003) characterized the flexibility of a fiber using an effective stiffness dimensionless number (S^{eff}) defined as

$$S^{\text{eff}} \equiv \frac{E_Y \pi}{4 \eta_s \dot{\gamma} a_r^4} \quad (3.92)$$

where E_Y is the Young's modulus, and η_s is the suspending medium viscosity. From this expression, the flexibility of a fiber can be seen to increase with aspect ratio for a material with a given Young's modulus. In this section we are primarily concerned with stiff fibers, which in the case of glass involves fibers of length less than 1 mm.

In most theoretical work, fiber orientation has been formulated using the orientation tensors that define an averaged orientational state of the system, often referred to as structure tensors. The structure tensors of interest with respect to modeling orientation for fiber suspensions are the

second- and fourth-order tensors defined as

$$\mathbf{A}(t) = \int \mathbf{u}\mathbf{u}\psi(\mathbf{u}, t) d\mathbf{u} \quad (3.93)$$

$$\mathbf{A}_4(t) = \int \mathbf{u}\mathbf{u}\mathbf{u}\mathbf{u}\psi(\mathbf{u}, t) d\mathbf{u} \quad (3.94)$$

where \mathbf{u} is the unit vector along the fiber and ψ is the orientation distribution function. The trace of \mathbf{A} is always equal to 1 and for a completely random orientation state $\mathbf{A} = \frac{1}{3}\mathbf{I}$, where \mathbf{I} is the unity tensor. In the limit that all the fibers are perfectly aligned in the x_1 direction, the only nonzero component is $A_{11} = 1$. The fourth-order tensor arises in the theoretical analysis for both the particle motion and in calculating the contribution of the hydrodynamic interaction of the fibers to the extra stress. For a more complete description of orientation tensors and their use in representing fiber suspensions, the reader is referred to Advani and Tucker (1990).

The origin of an evolution equation in a form containing \mathbf{A} is described elsewhere (Bird et al., 1987a; Advani and Tucker, 1990) but essentially consists of performing a balance on configuration or orientation and a momentum balance to obtain governing equations for ψ and $\dot{\mathbf{u}}$. These equations are combined to give the following equation for the orientation tensor \mathbf{A} for rigid particles not influenced by Brownian motion:

$$\begin{aligned} \frac{D\mathbf{A}}{Dt} = & (\mathbf{W} \cdot \mathbf{A} - \mathbf{A} \cdot \mathbf{W}) \\ & + \lambda(\dot{\gamma} \cdot \mathbf{A} + \mathbf{A} \cdot \dot{\gamma} - \dot{\gamma} \cdot \mathbf{A} - \dot{\gamma} : \mathbf{A}_4) \end{aligned} \quad (3.95)$$

where $\mathbf{W} = [(\nabla\mathbf{v})^t - \nabla\mathbf{v}]$ is the vorticity tensor and λ is a parameter related to the shape of the rigid particle and discussed below. To solve this equation a closure approximation is need to express \mathbf{A}_4 in terms of \mathbf{A} . The fourth-order tensor \mathbf{A}_4 has been the subject of much research because in order to complete the analysis one must use a closure or decoupling approximation to express the fourth-order tensor in terms of the second-order tensor. A closure approximation is some function that approximates a higher order orientation tensor with lower order orientation tensors and/or the invariants of lower order orientation tensors. The closure approximation is vital in establishing an equation of change for the average orientation state of the system and in calculating the extra stress contribution as a result of the hydrodynamic drag discussed later. In addition, the higher order orientation tensors (tensors greater than second order) arise in any continuum model that describes the mechanical or rheological properties of a two-phase system containing particles whose orientation can be anisotropic. Numerous closure approximations have been suggested and tested which is beyond the scope of this

text (Advani and Tucker, 1990). For simplicity we will use the quadratic closure approximation:

$$\mathbf{A}_4 = \mathbf{A}\mathbf{A} \quad (3.96)$$

In semidilute suspensions the oscillations present in the dilute suspensions are less common. This is a direct result of the contributing factors that can dampen the oscillations being more prevalent as the fiber concentration is increased. The common approach to predict this behavior relies on Jeffery's equation for the fiber orientation with the assumption that the fiber is infinitely long or $\lambda = 1$, in which case,

$$\frac{D\mathbf{A}}{Dt} = (\mathbf{W} \cdot \mathbf{A} - \mathbf{A} \cdot \mathbf{W}) + (\dot{\gamma} \cdot \mathbf{A} + \dot{\gamma} \cdot \mathbf{A} - \dot{\gamma} : \mathbf{A}_4) \quad (3.97)$$

The predictions are no longer periodic but transient in that the fibers will rotate from their initial orientation state to align in the flow direction.

In the first attempts at simulating the fiber orientation of concentrated suspensions in mold filling, Jeffery's equation for infinitely long fibers, Eq. 3.97, was used. Comparison between fiber orientation measurements of injection-molded parts and simulation results suggested Jeffery's equation overpredicts the degree of alignment and the shear strain needed to align the fibers. As a result, Folgar and Tucker (1984) modified Jeffery's theory to include a phenomenological term that prevents full alignment of fiber orientation, termed the Folgar–Tucker (FT) model. The Folgar–Tucker (FT) model can be written in terms of \mathbf{A} as follows:

$$\begin{aligned} \frac{D\mathbf{A}}{Dt} = & (\mathbf{W} \cdot \mathbf{A} - \mathbf{A} \cdot \mathbf{W}) + (\dot{\gamma} \cdot \mathbf{A} + \mathbf{A} \cdot \dot{\gamma} - \dot{\gamma} : \mathbf{A}_4) \\ & + C_1\dot{\gamma}(\mathbf{I} - 3\mathbf{A}) \end{aligned} \quad (3.98)$$

where C_1 is a phenomenological parameter. The last term on the right-hand side of the equation is similar to the isotropic diffusivity term in theories for Brownian rods (Doi and Edwards, 1988). The FT model allows for the control of the steady-state fiber orientation through the magnitude of C_1 , but the rate of fiber reorientation is dominated by the flow field for the case of small C_1 , which is typically in the range of 0.016–0.0001. Currently, there is no theoretical approach to calculate the interaction coefficient, C_1 , in the FT model, and it is determined by fitting predictions to experimental results, which can be time intensive to produce. Bay and Tucker (1992) developed an empirical expression for concentrated suspensions that is a function of the fiber volume fraction and aspect ratio:

$$C_1 = 0.0184 \exp(-0.7148\phi a_r) \quad (3.99)$$

Equation 3.99 predicts that C_1 decreases for increasing ϕa_r and represents fiber screening. Phan-Thien et al. (2002) proposed a model in which C_1 increases with increasing ϕa_r as

$$C_1 = m_1 [1.0 - \exp(-m_2 \phi a_r)] \quad (3.100)$$

where m_1 and m_2 are fit parameters, which they found to be $m_1 = 0.03$ and $m_2 = 0.224$.

The FT model improves the predictions of the steady-state fiber orientation but has little effect on the strain at which the steady-state orientation occurs. In an attempt to control the rate of fiber reorientation, Sepehr et al., (2004) included a term to reduce the rate of fiber orientation termed the strain reduction factor or the slip coefficient. The slip coefficient, α , can be added to the FT model as follows,

$$\frac{D\mathbf{A}}{Dt} = \alpha[(\mathbf{W} \cdot \mathbf{A} - \mathbf{A} \cdot \mathbf{W}) + (\dot{\boldsymbol{\gamma}} \cdot \mathbf{A} + \mathbf{A} \cdot \boldsymbol{\gamma} - \dot{\boldsymbol{\gamma}} : \mathbf{A}_4) + C_1 \dot{\boldsymbol{\gamma}}(\mathbf{I} - 3\mathbf{A})] \quad (3.101)$$

and has a value $0 < \alpha < 1$ (Eberle et al., 2010). However, the addition of the slip or strain reduction factor to the equations governing fiber motion results in a loss of objectivity of the equation. This becomes important when the coordinate frame is translated or rotated, but the physical aspects of the predictions, in the case of simple shear flow, are still acceptable.

In order to solve the equations above, such as Eq. 3.101, for fiber orientation, the flow kinematics, which depend on the rheology of the fiber suspensions, must be known. One way to solve the equations for fiber orientation has been to use the bulk rheology of the suspensions (e.g., power-law model fit to the viscosity of the suspension). A more rigorous way is to couple the fiber orientation with the stress tensor and thereby calculate the rheology as a function of fiber orientation. A general expression for the total stress in a dilute suspension of high aspect ratio non-Brownian particles can be derived from the theories of Hand and Giesekus and is commonly referred to as the Lipscomb model (Lipscomb et al., 1988; Sepehr et al., 2004):

$$\boldsymbol{\Pi} = P\mathbf{I} - \eta_s \dot{\boldsymbol{\gamma}} - c_1 \phi \eta_s \dot{\boldsymbol{\gamma}} - \phi \eta_s N \dot{\boldsymbol{\gamma}} : \mathbf{A}_4 \quad (3.102)$$

where $\boldsymbol{\Pi}$ is the total stress, η_s is the suspending medium viscosity, c_1 is a constant, and N is a dimensionless parameter that represents the coupling between hydrodynamic stress contribution and the fiber orientation. The third term on the right side of the equation is the viscosity enhancement as a result of the fiber. Lipscomb et al. (1988) give c_1 to be equal to 2. The fourth term on the right side of the equation is the contribution to stress from the hydrodynamic drag of the fluid over the fiber.

As in the equation for evolution of fiber orientation, a closure approximation is needed in Eq. 3.102 to express \mathbf{A}_4 in terms of \mathbf{A} . Using Eq. 3.102 it is straightforward to show that the shear stress growth coefficient, η^+ , and the first normal stress growth function, N_1^+ , are

$$\eta^+ = \sigma_{12}/\dot{\boldsymbol{\gamma}} = \eta_s [1 + \phi (c_1 + 2NA_{1212})] \quad (3.103)$$

$$N_1^+ = 2\phi \eta_s \dot{\boldsymbol{\gamma}} N (A_{1112} - A_{2212}) \quad (3.104)$$

where the fourth-order tensor components are a function of time. In Example 3.5 below, we will use the closure approximation in Eq. 3.96 to find the predictions of Eq. 3.102 for simple shear flow.

For dilute suspensions Lipscomb et al. (1988) give N to be a function of fiber aspect ratio,

$$N = \frac{a_r^2}{2 \ln a_r} \quad (3.105)$$

Other works for dilute suspensions give N to be a function of the number of fibers per unit volume, n , and/or fiber length, L , and aspect ratio:

$$N = \frac{a_r^2}{3 \ln(2a_r)} f(\varepsilon), \quad f(\varepsilon) = \frac{1 + 0.64\varepsilon}{1 - 1.5\varepsilon} + 1.659\varepsilon^2, \quad \varepsilon = [\ln(2a_r)]^{-1} \quad (3.106)$$

Currently, there is no theory for concentrated suspensions that accounts for fiber contact. However, semidilute theory has been used to some extent to model their stress behavior, in which case N is fit to the rheological material functions of a fluid instead of calculating N from theory. In the majority of fiber composites of industrial significance, the matrix is polymeric and exhibits nontrivial viscoelastic behavior, which increases the complexity of modeling such suspensions. The first attempts ignore the fiber and treat the suspension as a homogeneous viscoelastic fluid.

Example 3.4. Predictions of Fiber Orientation in Simple Shear Flow

From Eq. 3.101 obtain the system of ordinary differential equations for determining the components of the orientation tensor, \mathbf{A} , at the start of flow and under steady-state conditions for steady-state shear flow. In particular, find the equations for determining A_{11} , A_{22} , A_{33} , $A_{12} = A_{21}$, and A_{13} . \mathbf{A} is a symmetric tensor such that $A_{ij} = A_{ji}$. The initial orientation of the fibers is taken as random, which means $A_{11} = A_{22} = A_{33} = \frac{1}{3}$.

Solution.

$$\begin{aligned}
& \frac{d}{dt} \begin{pmatrix} A_{11} & A_{12} & A_{13} \\ A_{21} & A_{22} & A_{23} \\ A_{31} & A_{32} & A_{33} \end{pmatrix} \\
&= \alpha \left[\begin{pmatrix} 0 & \dot{\gamma} & 0 \\ -\dot{\gamma} & 0 & 0 \\ 0 & 0 & 0 \end{pmatrix} \cdot \begin{pmatrix} A_{11} & A_{12} & A_{13} \\ A_{21} & A_{22} & A_{23} \\ A_{31} & A_{32} & A_{33} \end{pmatrix} \right. \\
&- \begin{pmatrix} A_{11} & A_{12} & A_{13} \\ A_{21} & A_{22} & A_{23} \\ A_{31} & A_{32} & A_{33} \end{pmatrix} \cdot \begin{pmatrix} 0 & \dot{\gamma} & 0 \\ -\dot{\gamma} & 0 & 0 \\ 0 & 0 & 0 \end{pmatrix} + \begin{pmatrix} 0 & \dot{\gamma} & 0 \\ \dot{\gamma} & 0 & 0 \\ 0 & 0 & 0 \end{pmatrix} \cdot \begin{pmatrix} A_{11} & A_{12} & A_{13} \\ A_{21} & A_{22} & A_{23} \\ A_{31} & A_{32} & A_{33} \end{pmatrix} \\
&+ \begin{pmatrix} A_{11} & A_{12} & A_{13} \\ A_{21} & A_{22} & A_{23} \\ A_{31} & A_{32} & A_{33} \end{pmatrix} \cdot \begin{pmatrix} 0 & \dot{\gamma} & 0 \\ \dot{\gamma} & 0 & 0 \\ 0 & 0 & 0 \end{pmatrix} - (2\dot{\gamma}A_{21}) \begin{pmatrix} A_{11} & A_{12} & A_{13} \\ A_{21} & A_{22} & A_{23} \\ A_{31} & A_{32} & A_{33} \end{pmatrix} \\
&\left. + (C_1\dot{\gamma}) \left[\begin{pmatrix} 1 & 0 & 0 \\ 0 & 1 & 0 \\ 0 & 0 & 1 \end{pmatrix} - 3 \begin{pmatrix} A_{11} & A_{12} & A_{13} \\ A_{21} & A_{22} & A_{23} \\ A_{31} & A_{32} & A_{33} \end{pmatrix} \right] \right] \quad (3.107)
\end{aligned}$$

The system of coupled ordinary differential equations for the various components of \mathbf{A} become

$$\frac{dA_{11}}{dt} = \alpha\dot{\gamma}[4A_{12} - 2A_{12}A_{11} + C_1(1 - 3A_{11})] \quad (3.108)$$

$$\frac{dA_{12}}{dt} = \alpha\dot{\gamma}[2A_{22} - 2A_{12}A_{12} - 3C_1A_{12}] \quad (3.109)$$

$$\frac{dA_{22}}{dt} = \alpha\dot{\gamma}[-2A_{12}A_{22} + C_1(1 - 3A_{22})] \quad (3.110)$$

$$\frac{dA_{33}}{dt} = \alpha\dot{\gamma}[-2A_{12}A_{33} + C_1(1 - 3A_{33})] \quad (3.111)$$

$$\frac{dA_{13}}{dt} = \alpha\dot{\gamma}[2A_{23} - 2A_{12}A_{13} - 3C_1A_{13}] \quad (3.112)$$

$$\frac{dA_{23}}{dt} = \alpha\dot{\gamma}[2A_{12}A_{23} - 3C_1A_{23}] \quad (3.113)$$

The solution under steady-state conditions is found by setting all the time derivatives to zero and solving the system of algebraic equations for the A_{ij} . For example, to find A_{11} , A_{22} , and $A_{12} = A_{21}$ we solve the following three equations:

$$4A_{12} - 2A_{12}A_{11} + C_1(1 - 3A_{11}) = 0 \quad (3.114)$$

$$2A_{22} - 2A_{12}A_{12} - 3C_1A_{12} = 0 \quad (3.115)$$

$$-2A_{12}A_{22} + C_1(1 - 3A_{22}) = 0 \quad (3.116)$$

This system of algebraic equations is solved in Problem 3C.5. ■

Example 3.5. Startup of Simple Shear Flow Predictions for the Lipscomb–Denn Model, Eq. 3.102, and the Quadratic Closure Approximation

Solution. Equation 3.102 becomes for the startup of shear flow

$$\begin{aligned}
\Pi_{ij} = P\delta_{ij} - \eta_s \begin{pmatrix} 0 & \dot{\gamma} & 0 \\ \dot{\gamma} & 0 & 0 \\ 0 & 0 & 0 \end{pmatrix} - c_1\phi\eta_s \begin{pmatrix} 0 & \dot{\gamma} & 0 \\ \dot{\gamma} & 0 & 0 \\ 0 & 0 & 0 \end{pmatrix} \\
- 2\phi\eta_s N\dot{\gamma} A_{21} \begin{pmatrix} A_{11} & A_{12} & A_{13} \\ A_{21} & A_{22} & A_{23} \\ A_{31} & A_{32} & A_{33} \end{pmatrix} \quad (3.117)
\end{aligned}$$

Remembering that \mathbf{A} is a symmetric tensor, then $A_{12} = A_{21}$, and so on. The shear stress and the primary normal stress difference, which are a function of time, become

$$\Pi_{12} = \Pi_{21} = -\eta_s\dot{\gamma} - c_1\phi\eta_s\dot{\gamma} - 2\phi\eta_s N A_{12}^2 \quad (3.118)$$

$$\Pi_{11} - \Pi_{22} = -2\phi\eta_s N\dot{\gamma} A_{12}(A_{11} - A_{22}) \quad (3.119)$$

One now solves Eqs. 3.108 to 3.110 to find $A_{12}(t)$, $A_{11}(t)$, and $A_{22}(t)$ and substitutes these into Eqs. 3.118 and 3.119 to find the stresses as a function of time. ■

3.3 RHEOMETRY

Of all the transport properties of polymeric materials, the rheological properties are probably the most important to the design of polymer processes. While the other transport properties such as thermal conductivity, heat capacity, and density remain nearly constant with changes in molecular structure such as molecular weight and branching, slight changes in molecular structure can alter the rheological properties and, hence, processing behavior of a polymer significantly. As one can imagine, variations in molecular structure from batch to batch of a polymer are quite common. Hence, one cannot expect to have available a set of rheological data such as would be found in a handbook which could be used for design calculations. It is necessary that the rheological behavior of polymeric fluids be determined on a regular basis. For this reason it is necessary to know how rheological properties are measured.

It is not the intention here to give an in-depth description of the techniques used in measuring rheological properties of polymer melts as these details can be found elsewhere (Dealy, 1982; Macosko, 1994; Walters, 1975). The goal is to make sure that one is aware of at least the most common methods, how data is manipulated to obtain material functions, and the limitations of various techniques. Methods for measuring shear flow properties are discussed first followed by methods for measuring shear-free flow properties.

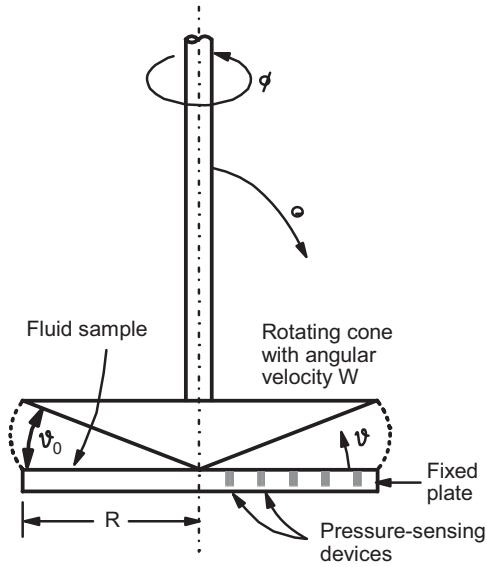


FIGURE 3.18 Cone-and-plate rheometer. The cone turns with an angular velocity, W . The torque, T , and normal force, F , measurements are used to determine η and ψ_1 , respectively, as given:

$$\eta = \frac{3T}{2\pi R^3 \dot{\gamma}} \quad \psi_1 = \frac{2F}{\pi R^2 \dot{\gamma}^2} \quad \dot{\gamma} = \frac{W}{\phi_0}$$

In some instances pressure transducers are mounted along the bottom plate to measure the pressure distribution from which ψ_2 is obtained.

3.3.1 Shear Flow Measurements

Measurements of rheological properties at low shear rates are usually carried out in rotary rheometers such as the cone-and-plate (C-P) or plate-plate (P-P) systems shown in Figures 3.18 and 3.19, respectively. In rotary rheometers one of

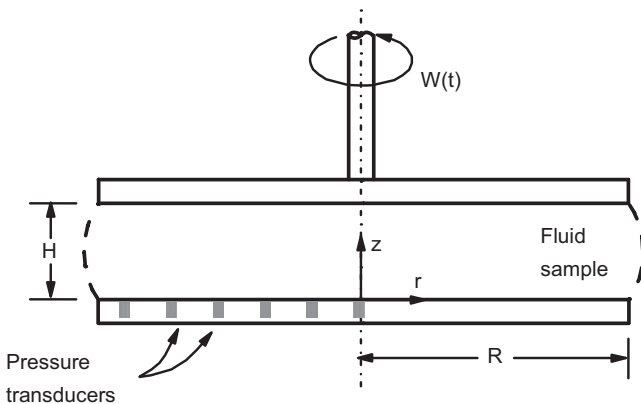


FIGURE 3.19 Plate-plate rheometer. The torque, T , and normal force, F , measurements are used to determine η and $\psi_1 - \psi_2$:

$$\eta = \frac{(T/2\pi R^3 \dot{\gamma} R)[3 + d \ln(T/2\pi R^3)/d \ln \dot{\gamma}_R]}{d \ln \dot{\gamma}_R}$$

$$\psi_1 - \psi_2 = \frac{(F/\pi R^2 \dot{\gamma}_R^2)[2 + d \ln(F/\pi R^2)/d \ln \dot{\gamma}_R]}{d \ln \dot{\gamma}_R}$$

$$\dot{\gamma}_R = \frac{WR}{H}$$

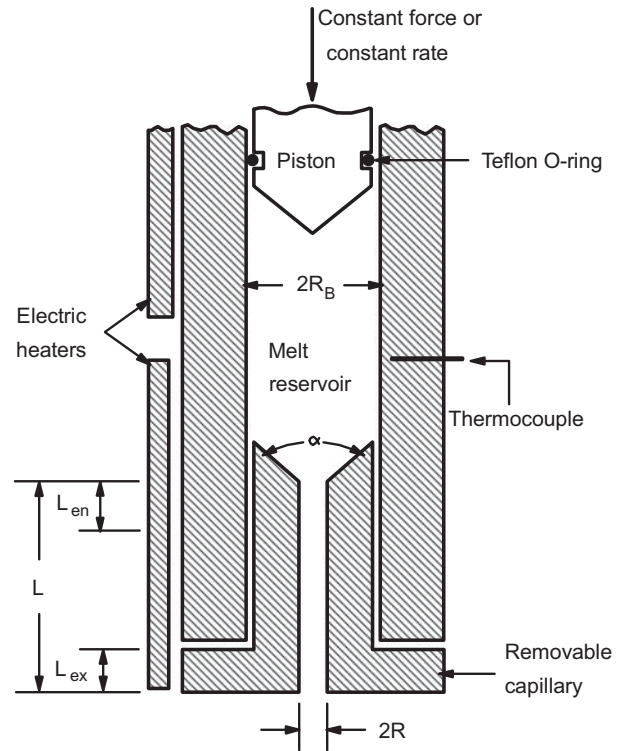


FIGURE 3.20 Capillary rheometer. Polymer is melted by conduction in the reservoir and then pushed through the capillary by the plunger. Viscosity data are obtained from ΔP and Q measurements.

the members of the system is driven, which transmits forces through the fluid to the bottom plate. The torque, T , and the normal force, F , are recorded at the bottom member by means of transducers. The cone-and-plate has the advantage that the shear rate, $\dot{\gamma}$, is nearly uniform through the gap, and hence the material properties of the polymeric fluid can be measured at each $\dot{\gamma}$ directly. The equations for determining the material functions, η and ψ_1 , are given in the caption of Figure 3.18. Because $\dot{\gamma}$ is uniform throughout the gap, it is possible to use the C-P to measure the transient response of polymeric fluids. For the case of the P-P device (Fig. 3.19), $\dot{\gamma}$ is found to vary with the distance r from the center of the plates. Hence, one must make a series of measurements at various shear rates before obtaining values of η and $\psi_1 - \psi_2$ at specific values of $\dot{\gamma}$. For the C-P device the maximum $\dot{\gamma}$ for which measurements are possible (the melt usually fractures and comes out of the gap) is about 10 s^{-1} while slightly higher values of $\dot{\gamma}$ are possible with the P-P device.

The capillary rheometer (Fig. 3.20) is commonly used to obtain η at high shear rates. Basically the device consists of a barrel for melting the polymer and a plunger that pushes the melt through the capillary. The data obtained from this device consist of the pressure required to push the melt through the capillary and the volumetric flow rate (plunger speed and cross-sectional area). Two corrections are applied to this data.

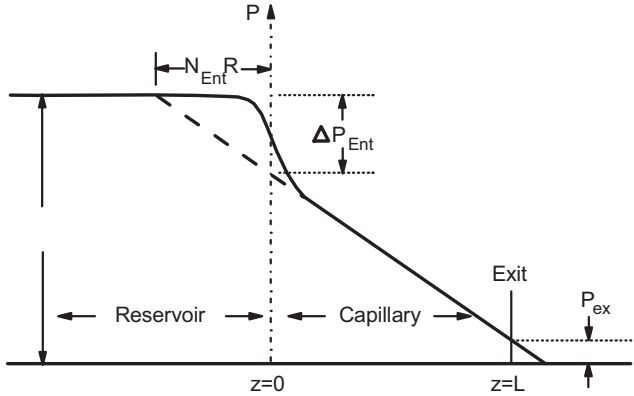


FIGURE 3.21 Pressure profile in a capillary rheometer. The various pressures are defined in the figure including the exit pressure, P_{ex} , and the entrance pressure, ΔP_{ent} .

First, the pressure drop must be corrected for the additional pressure required for the melt to pass through the contraction between the barrel and the capillary. For any fluid, the wall shear stress is given by

$$\tau_R = \left(\frac{-dp}{dz} \right) \frac{R}{2} \quad (3.120)$$

where dp/dz is the pressure gradient in the capillary. Usually dp/dz is approximated by $-\Delta P/L$, where ΔP is the pressure drop across the whole capillary including the entrance and L is the capillary length. For a Newtonian fluid the pressure gradient is nearly constant over the length of the capillary. For polymeric fluids the pressure drop is shown schematically in Figure 3.21. The pressure gradient is nonlinear for polymeric materials and approximating it as $-\Delta P/L$ would lead to large errors in the determination of τ_R . The difference between the pressure extrapolated from the linear region and the true pressure is called the entrance pressure, ΔP_{ent} . There may be residual pressure at the die exit, called the exit pressure, ΔP_{ex} , but it is quite small relative to ΔP_{ent} and hence is neglected. If there is additional pressure at the die exit, then the method used to obtain ΔP_{ent} actually includes ΔP_{ex} . The total pressure correction for exit and entrance regions is called the end pressure, ΔP_{end} , that is,

$$\Delta P_{end} = \Delta P_{ex} + \Delta P_{ent} \quad (3.121)$$

The true wall shear stress, τ_R , is then obtained by plotting the total pressure, ΔP_{tot} , versus L/D at each value of $\dot{\gamma}$ for several L/D values (see Fig. 3.22). The extrapolation of ΔP_{tot} to $L/D = 0$ is ΔP_{end} . One now obtains τ_R as follows:

$$\tau_R = \left(\frac{\Delta P_{tot} - \Delta P_{end}}{L} \right) \frac{R}{2} \quad (3.122)$$

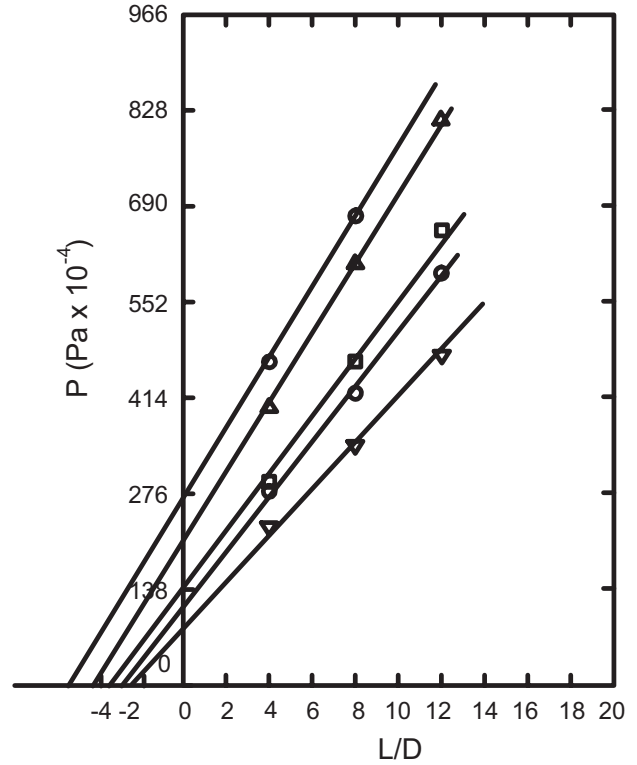


FIGURE 3.22 Total pressure drop, ΔP_{tot} , versus L/D for various shear rates for PP at 200 °C: (∇) 131; (\circ) 235; (\square) 289; (Δ) 569; (\diamond) 724 s^{-1} . These plots are sometimes referred to as Bagley plots.

One may also correct for ΔP_{end} by calculating the equivalent die length required to produce ΔP_{tot} . Referring again to Figure 3.22, one finds the additional length by extrapolating ΔP_{tot} versus L/D to $\Delta P_{tot} = 0$. The additional length required is given as a factor, N_{ent} , times the radius; that is,

$$(L/D)_c = (L + N_{ent}D/2)/D \quad (3.123)$$

where $(L/D)_c$ is the corrected value of L/D . τ_R is now given as

$$\tau_R = 4\Delta P_{tot}/(L/D)_c \quad (3.124)$$

Because the velocity profile is nonparabolic, one must correct the apparent wall shear rate, $\dot{\gamma}_a$, defined as $4Q/\pi R^3$. The correction is obtained by integrating the volumetric flow rate, Q , by parts:

$$Q = 2\pi \int_0^R v_z(r)r dr \quad (3.125)$$

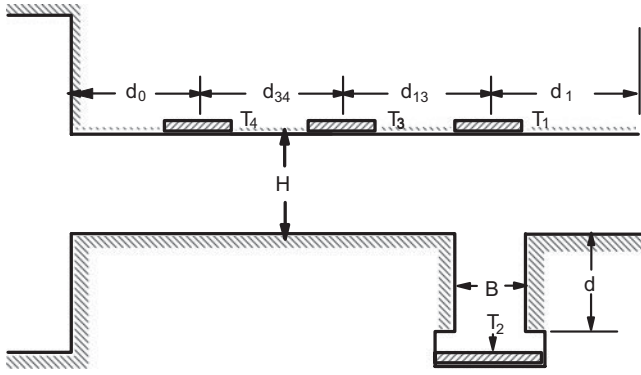


FIGURE 3.23 Slit-die rheometer showing the position of the pressure transducers (T_i).

and then differentiating with respect to τ_R using Leibnitz's rule to give (see Problem 3B.1)

$$\dot{\gamma}_w = \frac{\dot{\gamma}_a}{4} \left(3 + \frac{d \ln \dot{\gamma}_a}{d \ln \tau_R} \right). \quad (3.126)$$

Hence, by plotting τ_R versus $\dot{\gamma}_a$ on a ln–ln plot, one obtains the reciprocal of the required correction factor. It turns out that this value is just $1/n$, where n is the power-law index.

Slit-die rheometers (see Fig. 3.23) are useful devices for measuring the viscosity of polymer melts because it is possible to measure the pressure gradient directly. The geometry is that of two flat plates with a rectangular cross section. If the aspect ratio, W/H , is greater than or equal to 10, then there is no side wall effect. The wall shear stress, τ_w , is then

$$\tau_w = \left(\frac{-dp}{dz} \right) \frac{H}{2} = \frac{P_3 - P_1}{d_{31}} \frac{H}{2} \quad (3.127)$$

where P_3 and P_1 are the pressures recorded by transducers T_3 and T_1 , respectively, and d_{31} is the distance between the center of the transducers. The wall shear rate, $\dot{\gamma}_w$, is obtained from the following relation:

$$\dot{\gamma}_w = \frac{\dot{\gamma}_a}{3} \left[2 + \frac{d \ln \dot{\gamma}_a}{d \ln \tau_w} \right] \quad (3.128)$$

where $\dot{\gamma}_a = 6Q/WH^2$ (this is just the wall shear rate for a Newtonian fluid) for flow through flat plates.

The slit-die rheometer also offers the possibility of obtaining values of N_1 at high shear rates (Baird, 2008). The method is based on the measurement of a quantity called the hole pressure, P_H , which is the difference of pressures P_1 and P_2 , where P_2 is the pressure measured by transducer T_2 mounted

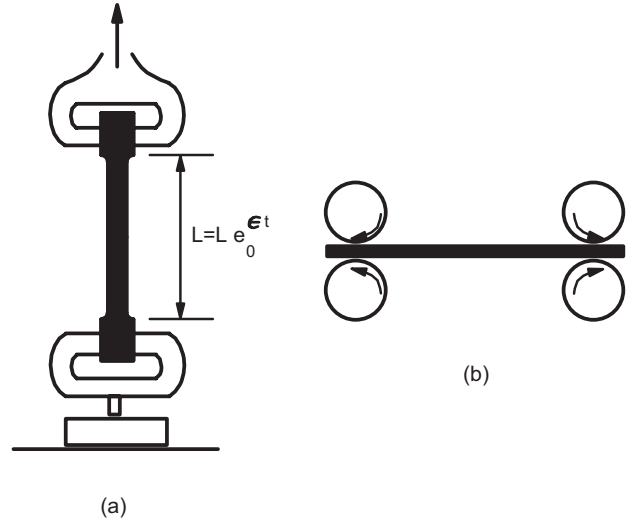


FIGURE 3.24 Two methods for generating uniaxial extensional flow.

at the bottom of a rectangular slot placed perpendicular to the flow direction; that is,

$$P_H = P_1 - P_2 \quad (3.129)$$

N_1 is obtained from the following equation (Baird, 2008):

$$N_1 = 2\tau_w (dP_H/d\tau_w) \quad (3.130)$$

Hence, from data of P_H versus τ_w one can obtain N_1 as a function of τ_w . (Accurate measurements of P_H are quite difficult and great care must be taken to make these measurements.)

3.3.2 Shear-Free Flow Measurements

Two techniques for measuring uniaxial extensional viscosity of polymer melts are shown in Figure 3.24. In the first technique (Ballman method) polymer melt is either glued or clamped at both ends, and then one end is moved in such a manner as to generate either a uniform extension rate, $\dot{\epsilon}$, or a constant tensile stress. In the Meissner method, both ends of the melt are pulled at a constant velocity either to achieve a uniform extension rate or to provide a constant stress.

In the Ballman method, to generate a uniform $\dot{\epsilon}$ throughout the sample, one end of the sample must be deformed such that the length of the sample is increased exponentially with time: that is, $L = L_0 e^{\dot{\epsilon}t}$. An apparatus based on the Ballman method is shown in Figure 3.25. The sample must be supported in an oil of similar density as shown in Figure 3.25. The limitations of the technique include (1) the availability of a suitable adhesive for gluing the sample to metal clips;

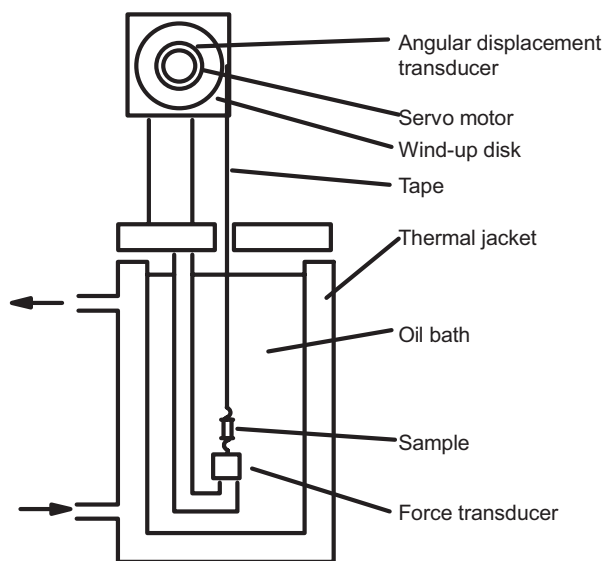


FIGURE 3.25 Extensional rheometer for polymer melts based on the Ballman method. The length of the sample is increased exponentially with time to generate a constant extension rate.

(2) the ability of the sample to deform uniformly without necking; (3) the availability of an oil of similar density as the polymer melt (unless the sample is deformed in a horizontal plane); and (4) low strains ($\dot{\epsilon}t$) of only about 3.9. In spite of the limitations of the method, valuable data, especially for polyolefins, can be obtained.

The Meissner method has several advantages and disadvantages relative to the Ballman method. First, it is possible to reach very high strains (on the order of 7.0). Second, the sample is usually deformed horizontally so that the matching of the oil density with that of the polymer melt is not as critical. Finally, finding a suitable glue is not necessary. On the other hand, the construction of the apparatus is more complicated and expensive. Larger samples are required, and they must be nearly free of inhomogeneities.

A variation of the Meissner method is the Sentmanat dual-roller device, which is an attachment for rotational rheometers (Sentmanat, 2004). When η_0 of the polymer melt is greater than about 5000 Pa·s, then the sample can be stretched without supporting it in an oil bath. Hencky strains on the order of 4.0 and extension rates of about 30 s⁻¹ can be reached. A rectangular sample (8–10 mm width, 1.2–1.4 mm thickness, and 15–20 mm length) is placed on the dual counterrotating windup drums where rotation is resisted by the stretching material. The resistance to rotation force is measured by the rheometer torque transducer. Sample sizes of only 1.0 to 2.0 g are needed for use in this device.

For both methods the technique for obtaining the extensional viscosity, $\eta^+(\dot{\epsilon}, t)$ is similar. With the assumption that the surroundings of the sample are at atmospheric pressure, p_a , the total force per unit area exerted by the load cell and

atmospheric pressure on the sample must be balanced by Π_{zz} ; that is,

$$\Pi_{zz} = -(F(t)/A(t)) + p_a \quad (3.131)$$

where A is the instantaneous cross-sectional area of the sample. A force balance in the radial direction gives the normal stress difference as a function of time:

$$\tau_{zz} - \tau_{rr} = -F(t)/A(t) \quad (3.132)$$

$\bar{\eta}^+$ is then obtained from

$$\bar{\eta}^+ = -\frac{\tau_{zz} - \tau_{rr}}{\dot{\epsilon}} = \frac{F(t) e^{\dot{\epsilon}t}}{A_0 \dot{\epsilon}} \quad (3.133)$$

where A_0 is the initial cross-sectional area.

In the event the devices for measuring are not available, there are two methods for obtaining approximate values of $\bar{\eta}$. The first method is based on the fiber spinning technique as shown in Figure 3.26. (The device is known as the Rheotens.) Without any discussion of the theory the extension rate is given by

$$\dot{\epsilon} = \frac{2\pi\nu R_w}{H} \ln \left[\frac{8\pi\nu R_w}{\dot{\gamma}_a R} \right] \quad (3.134)$$

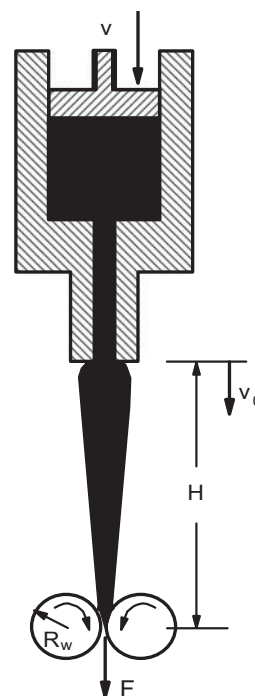


FIGURE 3.26 Rheotens apparatus for estimating the uniaxial extensional viscosity.

where ν is the angular velocity (radians per second) of the wheel of radius, R_w , H is the distance of the capillary to the wheel, $\dot{\gamma}_a$ is the apparent shear rate in the capillary, and R is the radius of the capillary. The normal stress difference is given by

$$\tau_{zz} - \tau_{rr} = -8\nu R_w F/R_a^3 \quad (3.135)$$

where F is the tensile force determined by the tension transmitted through the melt strand to the take-up wheels. Finally, the stretch ratio, Λ , is given as

$$\Lambda = 8\pi\nu R_w/R_a \quad (3.136)$$

Obviously, $\bar{\eta}$ is obtained from the values calculated using Eqs. 3.134 and 3.135.

The second method for estimating $\bar{\eta}$ is based on entrance pressure data (Cogswell, 1978). The extension rate is given as

$$\dot{\epsilon} = \frac{4\dot{\gamma}_a^2 \eta_a}{3(n+1)\Delta P_{\text{ent}}} \quad (3.137)$$

where n is the power-law index and η_a is the apparent viscosity ($\eta_a = \tau_w/\dot{\gamma}_a$). The normal stress difference is

$$\tau_{zz} - \tau_{rr} = -3(n+1)\Delta P_{\text{ent}}/8 \quad (3.138)$$

and hence

$$\bar{\eta} = 9(n+1)^2 \Delta P_{\text{ent}}^2 / 32 \dot{\gamma}_a^2 \eta_a \quad (3.139)$$

It must be emphasized that these two methods will give only approximate values for $\bar{\eta}$.

3.4 USEFUL RELATIONS FOR MATERIAL FUNCTIONS

In this section three topics are discussed: (1) the molecular weight dependence of the rheological properties; (2) the interrelation between steady shear and dynamic oscillatory shear measurements; and (3) the effect of branching. The importance of the second topic rests on the fact that dynamic oscillatory properties are easier to measure and can be obtained at higher equivalent shear rates than are possible for the steady shear flow properties obtained by means of rotary rheometers.

3.4.1 Effect of Molecular Weight

Molecular weight, M , has a significant effect on the magnitude of the rheological properties. At low molecular weight,

that is, below some critical molecular weight (M_c), for flexible chain polymers η_0 depends on M , and on M to the 3.4 power above M_c :

$$\begin{aligned} \eta_0 &\propto M \quad (M < M_c) \\ \eta_0 &\propto M^{3.4} \quad (M > M_c) \end{aligned} \quad (3.140)$$

The 3.4 power dependence has been observed experimentally and predicted theoretically. Furthermore, the primary normal stress difference coefficient in the limit as $\dot{\gamma}$ goes to zero, $\Psi_{1,0}$, is observed to be proportional to M raised to the 7.0 power; that is,

$$\Psi_{1,0} \propto \eta_0^2 \propto M^{7.0} \quad (3.141)$$

Usually M is replaced by \bar{M}_w which is the weight average molecular weight (which is the second moment of the molecular weight distribution). In the case of $\Psi_{1,0}$ there is not as much experimental confirmation as there is for η_0 . For rod-like molecules there is some evidence that the following relations hold (Baird and Ballman, 1979):

$$\begin{aligned} \eta_0 &\propto \bar{M}_w^{6.8} \quad (M > M_c) \\ \Psi_{1,0} &\propto \bar{M}_w^{13.0} \end{aligned} \quad (3.142)$$

The change in the linear dependence of η_0 on M to the 3.4 power dependence for flexible chain polymers is believed to be due to the formation of an "entanglement" network or temporary physical junctions between the polymer chains. In the case of rod-like molecules, the hindrance of free rotation of the rod-like molecule by neighboring molecules serves as the entanglements.

In addition to the dependence of the magnitude of η_0 and $\Psi_{1,0}$ on M , the onset of shear-thinning behavior is affected by M . In particular, as M increases, the shear rate at which shear-thinning behavior starts, $\dot{\gamma}_0$, decreases. The relation between $\dot{\gamma}_0$ at M_1 and M_2 where $M_2 > M_1$ is

$$\dot{\gamma}_0(M_1) = a_M \dot{\gamma}_0(M_2) \quad (3.143)$$

where

$$a_M = \frac{\eta_0(M_2)}{\eta_0(M_1)} \quad (3.144)$$

Temperature leads to a similar effect and in Section 4.1 the temperature dependence of a_T will be discussed. Hence, within a given series of the same polymer, it is possible to generate the flow curves at all other molecular weights given the relation between η_0 and M and the flow curve of a sample at a given M . (*Note:* The breadth of the molecular weight distribution must be the same.)

3.4.2 Relations Between Linear Viscoelastic Properties and Viscometric Functions

It has been observed experimentally for many polymers that the magnitude of the complex viscosity, $|\eta^*(\omega)|$, and the shear viscosity, $\eta(\dot{\gamma})$, evaluated at the same values of ω and $\dot{\gamma}$, respectively, are identical; that is,

$$\eta(\dot{\gamma}) = |\eta^*(\omega)|_{\omega=\dot{\gamma}} \quad (3.145)$$

This relation is known as the Cox–Merz rule (Cox and Merz, 1958). When $\eta(\dot{\gamma})$ is not available, the Cox–Merz rule serves as a useful way to obtain $\eta(\dot{\gamma})$, especially for linear polymers (i.e., those without branching). When dealing with filled polymers, polymer blends, fiber suspensions, or highly branched polymers, the Cox–Merz rule may not hold.

An alternative to the Cox–Merz rule is Gleiselle’s mirror relation (Gleiselle, 1980):

$$\eta(\dot{\gamma}) = \eta^+(t)|_{t=1/\dot{\gamma}} \quad (3.146)$$

where $\eta^+(t)$ is the limiting curve of $\eta^+(\dot{\gamma}, t)$ as $\dot{\gamma} \rightarrow 0$. This relation has been tested for a wide variety of polymers including PE, polyisobutylene (PIB), and silicone oils.

It is desirable to be able to estimate N_1 , as measurements of this quantity at high $\dot{\gamma}$ are also difficult. At low values of $\dot{\gamma}$ and ω it is observed for a number of polymers that

$$(N_1/2)|_{\dot{\gamma}=\omega} = G' \quad (3.147)$$

At higher shear rates it is observed that this relation fails for some polymers. Laun (1986) suggested another empiricism for N_1 which seems to fit data over a wider range of shear rates:

$$N_1 = 2\omega\eta''(\omega) \left[1 + \left(\frac{\eta''}{\eta'} \right)^2 \right]^{0.7} \bigg|_{\omega=\dot{\gamma}} \quad (3.148)$$

where η' is the dynamic viscosity and η'' is associated with the elastic energy stored per cycle of deformation (it is noted that G' , G'' , η' , and η'' are interrelated with $G' = \omega\eta''$). The empiricism in Eq. 3.148 has been tested for PS, LDPE, HDPE, and PP and the agreement between N_1 values and those estimated from linear viscoelastic data was found to be excellent (Laun, 1986).

3.4.3 Branching

Branching is known to have a significant effect on the rheology of polymeric fluids especially on the extensional behavior. Polyethylene is known to have various degrees of branch-

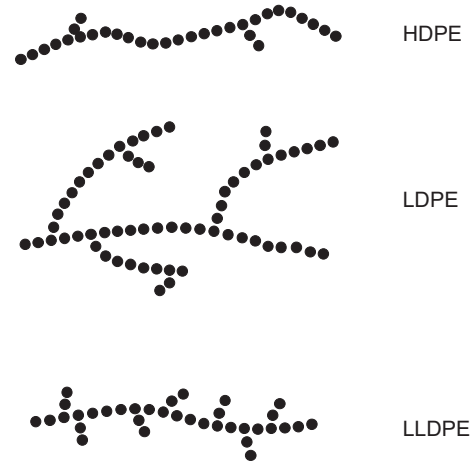


FIGURE 3.27 Branching characteristics exhibited by various types of polyolefins.

ing depending on the method of polymerization as shown in Figure 3.27. LDPE is believed to have very long branches while LLDPE is believed to have numerous short branches. On the other hand, HDPE has only a few short branches. Values of $\bar{\eta}^+$ are shown for LDPE and HDPE in Figure 3.28. Here we see that $\bar{\eta}^+$ for LDPE deviates drastically from the linear viscoelastic limit while that for HDPE shows only a slight deviation. LLDPE tends to approach equilibrium with very little deviation from the linear viscoelastic behavior, much in the same manner reported for PS in Figure 3.28.

When the MW of the branch arm, M_b , is greater than M_c , which is referred to as long chain branching, LCB, then LCB can have a significant effect on the shear rheology of polymer melts. For example, it has been observed that for a MW of 100,000 g/gmol that η_0 will pass through a maximum (which is two orders of magnitude higher than that of the linear polymer) at approximately one-half branch per molecule (i.e., one in two chains containing a branch) and then decrease as the branching level increases. At three branches per chain, η_0 can be suppressed by about two orders of magnitude. Significant effects on N_1 and the onset of shear thinning have also been observed (Doerpinghaus and Baird, 2003). Janzen and Colby (1999) proposed a phenomenological expression for η_0 and its relation to molecular weight and levels of branching:

$$\eta_0 = AM_b \left[1 + \left(\frac{M_b}{M_c} \right)^{2.4} \right] \left(\frac{M_w}{M_b} \right)^{s/\gamma} \quad \text{for } M_c \leq M_b \leq M_w \quad (3.149)$$

Here, A is a numerical prefactor having units of (Pa·s·mol)/g and is specific to molecular composition and temperature, M_b is the molecular weight (MW) between branch points, M_c is the critical MW for entanglements, M_w is the weight

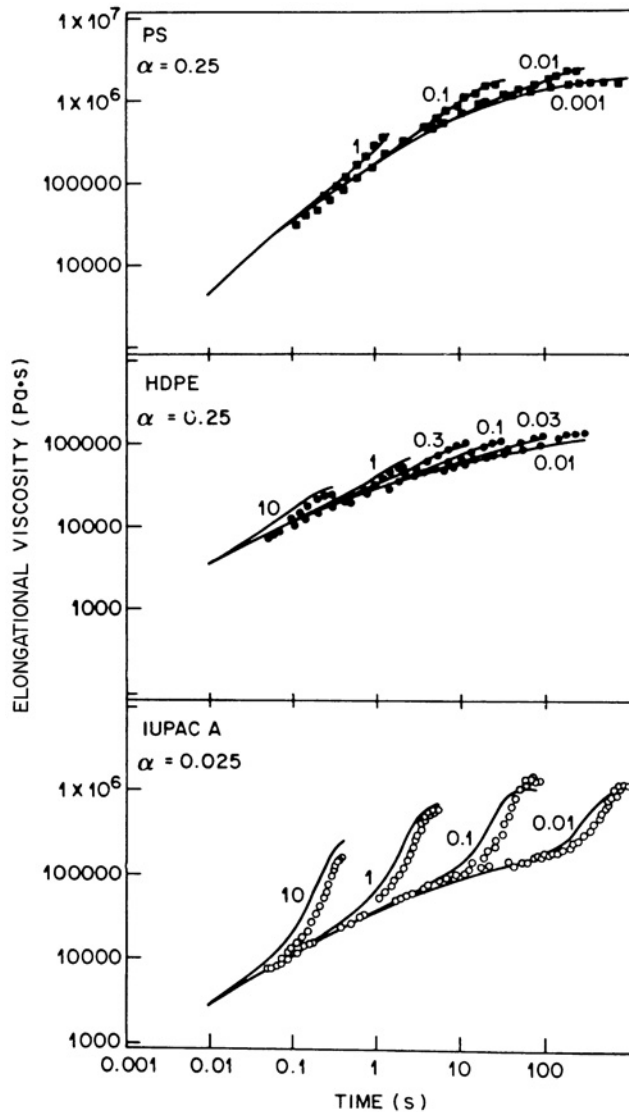


FIGURE 3.28 Extensional growth viscosity versus time for polystyrene (top), LDPE, and HDPE. (Reprinted by permission of the publisher from Khan et al., 1987.)

average MW, and s/γ is an exponent that depends on M_b as shown in Eq. 3.150 below:

$$\frac{s}{\gamma} = \max \left[1, \frac{3}{2} + \frac{9B}{8} \ln \left(\frac{M_b}{90M_{\text{Kuhn}}} \right) \right] \quad (3.150)$$

where B is a material specific constant and M_{Kuhn} is the MW of a statistical Kuhn segment. For polyethylene, the values of the coefficients taken from Janzen and Colby (1999) are $A(150^\circ\text{C}) = 5.22 \times 10^{-6}$ (Pa·s·mol/g), $B = 6.0$, M_0 (repeat unit MW) = 14.027 g/mol, $M_c = 2100$ g/mol, and $M_{\text{Kuhn}} = 145.9$ g/mol. For a branching architecture referred to as a Cayley tree (which is used to approximate random

branching), α , the fraction of the total carbons that are long-branch vertexes is given by (Colby and Janzen, 1999)

$$\alpha = \frac{M_0}{2} [M_b^{-1} - M_w^{-1}] \quad (3.151)$$

In summary, with the relations given in this section it is possible to obtain steady shear rheological data from linear viscoelastic data over a wide range of shear rates using Eqs. 3.146 and 3.148. Furthermore, within a given series of polymers of different molecular weights, it is possible to obtain $\eta(\dot{\gamma})$ and $N_1(\dot{\gamma})$ data at any M using Eq. 3.144 and data at two values of M . Branching has a significant effect on the extensional rheology of polymer melts, but its effect on shear properties seems even more significant especially in the case of sparse LCB. Equations 3.149, 3.150, and 3.151 allow us to estimate how we can substantially increase or decrease the viscosity by incorporating a few long chain branches.

3.5 RHEOLOGICAL MEASUREMENTS AND POLYMER PROCESSABILITY

The emphasis so far in this chapter has been on quantitative relations between stress and deformation rate or constitutive equations and methods for measuring rheological properties. It is clear that any attempts to carry out quantitative design work using nonlinear constitutive equations is met quite often with mathematical difficulties. However, certain rheological measurements of a polymeric fluid may provide a tool for assessing differences in processability when most standard methods fail. To illustrate this idea a case study (Meissner, 1979) is considered, which is concerned with the effect of branching on the processing performance of LDPE.

The following case study is concerned with the processing of LDPE using the technique of film blowing (Meissner, 1979). As shown in Table 3.2 two of the resins (identified as B and C) could be drawn down at the same critical rate of 23 m/min leading to a film thickness at break of 10 μm . Resin A, on the other hand, could not be drawn down as much (critical draw down rate of 13 to 18 m/min depending on which group made the measurements). Once a processing difference was detected the next goal was to characterize the three resins using standard techniques to determine if any differences could be detected. As far as the molecular weight distribution was concerned (Fig. 3.29) the samples were identical. The standard rheological measurements usually made in industry as shown in Table 3.3 provided no clue as to the differences in the samples. For example, it was indicated by the melt flow index (now referred to as the melt index, MI*)

*The melt index(MI) is a characterization parameter provided by companies and is the amount of polymer in grams that passes through a capillary of specified radius in 10 minutes when subjected to a fixed pressure drop. More details are found regarding this topic in Pr. 3A.1.

TABLE 3.2 Critical Film Draw Down Speed and Thickness for LDPE

Participant	Melt Temperature.		A	B	C
IV	180 °C	Critical film draw down (m/min)	18	23	23
		film thickness at break (μm)	15	10	10
IV	150 °C	Critical film draw down (m/min)	13	23	23
		film thickness at break (μm)	20	10	10

Source: Data from Meissner, 1979.

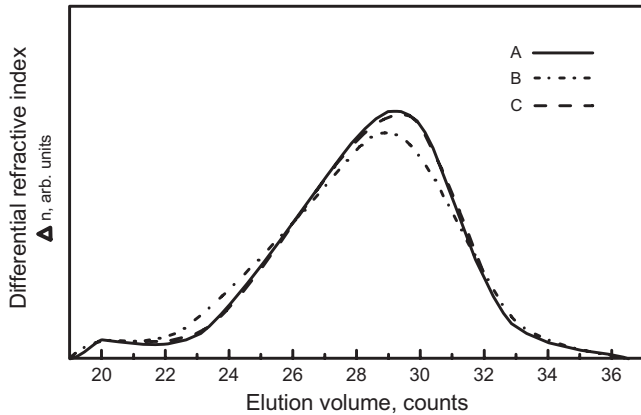


FIGURE 3.29 Molecular weight distribution of three LDPE samples as determined by means of gel permeation chromatography. (Reprinted by permission of the publisher from Meissner, 1979.)

that A and B are similar. It was suggested by the melt memory index, which is a measure of die swell measured under specified conditions, that A and C were similar polymers. It was indicated by the zero shear viscosity that A and B were identical but that C was slightly different. Hence, as far as the more standard measurements were concerned, there was no way to differentiate between the three samples.

The measurement of the full flow curve is less commonly made in industry, but it might provide more information as to differences in polymer systems. However, as shown in Figure 3.30, the flow curves for the three samples are, for all practical purposes, identical. One difference in the samples is noted and that is the onset of melt fracture. (Melt fracture is associated with flow instabilities and is discussed in Chapter 7.) It appears that B and C undergo melt fracture at a higher shear rate than does sample A. It is not clear as to the significance of this observation at this point, but it may

TABLE 3.3 Melt Flow Characteristics for Three LDPE Samples

Characteristic	A	B	C
Melt flow index (g/10 min)	1.37	1.41	1.59
Melt memory index (% die swell)	54	59	53
Zero shear viscosity (150 °C)(× 10 ⁵ poise)	4.7	4.7	4.9

Source: Data from Meissner, 1979.

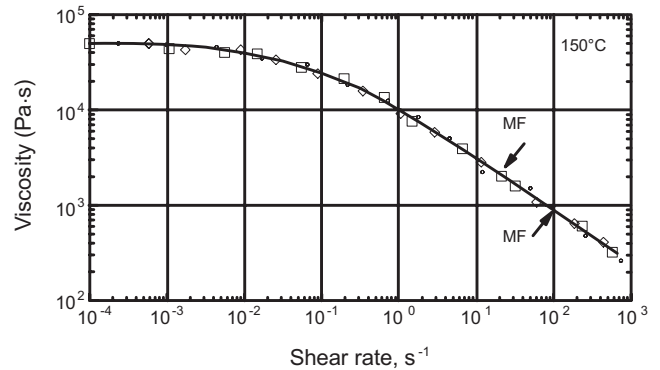


FIGURE 3.30 Viscosity versus shear rate data for three LDPE samples obtained by various investigators. The letters “MF” indicate the onset of melt fracture: symbols are the same as in Figure 3.32. (Reprinted by permission of the publisher from Meissner, 1979.)

be due to differences in the flow behavior of these resins in the die entry (see Section 7.1).

Whereas the standard measurements provided no clue as to the differences in the samples, the nonlinear measurements provided some insight into the differences in the samples. In Figure 3.31 is shown the stress growth behavior of the three polymers. The shear stress growth curves of the three samples at the same shear rate are essentially the same. However, $N_1(\dot{\gamma}, t)$ for sample A apparently rises to a higher value than it does for either sample B or C. This is the first material property which indicated there was a difference in the three samples.

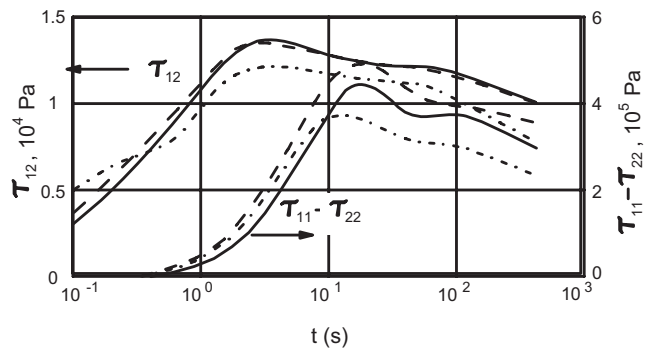


FIGURE 3.31 Stress growth behavior of three LDPE samples at 150 °C: (---) A; (—) B; (---) C. (Reprinted by permission of the publisher from Meissner, 1975.)

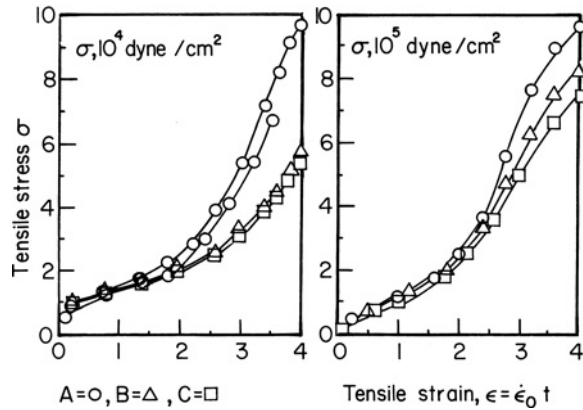


FIGURE 3.32 Extensional stress growth versus strain at two extension rates ($\dot{\epsilon}_0 = 0.001 \text{ s}^{-1}$ and 0.01 s^{-1}) for the three LDPE samples: (○) A; (△) B; (□) C. (Reprinted by permission of the publisher from Meissner, 1979.)

The most enlightening difference occurred in the extensional viscosity and ΔP_{ent} data. In Figure 3.32 values of the tensile stress (i.e., $\tau_{zz} - \tau_{rr}$) are plotted versus strain for two values of $\dot{\epsilon}$. Sample A was observed to exhibit higher values of stress than did either sample B or C especially at lower extension rates. Furthermore, entrance pressure behavior in the form of end correction (N_{ent}) data (Fig. 3.33) reflected the same tendency as the extensional data; that is, N_{ent} of sample A was higher than N_{ent} of samples B and C. This is reasonable in light of the discussion in Section 3.4 in which $\bar{\eta}$ can be estimated from ΔP_{ent} data. Hence, the quantities related to extensional viscosity seem to be the most sensitive in distinguishing differences in these polymers.

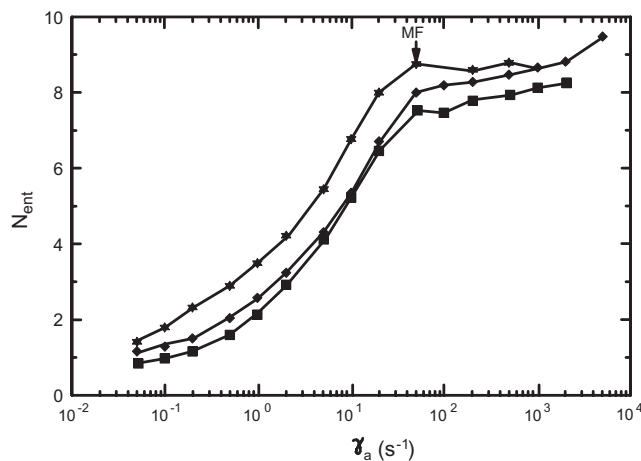


FIGURE 3.33 End correction versus apparent shear rate for three LDPE samples at 150°C . The arrow indicates the onset of melt fracture. (Reprinted by permission of the publisher from Meissner, 1979.)

At a later date it was revealed what the difference was in the three samples. The difference was that the degree of long chain branching was varied, with sample A having more branches than polymers B and C. Hence, extensional viscosity is apparently sensitive to changes in the degree of chain branching.

3.6 SOLUTION TO DESIGN PROBLEM II

Design Problem II at the beginning of this chapter requires you to design an annular die for LDPE at 170°C considering the fact that the extrudate increases in both thickness and diameter on leaving the die. The die dimensions must therefore be less than those of the extrudate. The constraints are the output from the extruder or the onset of melt fracture.

The basic idea is to determine the dimensions of the annular die, which will yield the extrudate with the desired dimensions at the highest extrusion rate possible. The extrudate leaves the die with dimensions (i.e., diameter and thickness) greater than those of the die. This increase in dimensions is due to a phenomenon called extrudate swell, which is associated with elastic recovery. For flow through a capillary, Eq. 3.89 has been proposed for predicting extrudate swell. The questions we are faced with in carrying out this design are: (1) Can one extend Eq. 3.89 to other geometries? (2) What is the relation between extrudate swell and diameter and thickness swell for an annular geometry? (3) How can one obtain the appropriate rheological data at high shear rates?

The starting point is Eq. 3.89, which gives the increase in diameter of an extrudate emerging from a capillary as a function of $N_1(\tau_w)$ and τ_w . It is assumed that Eq. 3.89 applies to both the increase in diameter and thickness of the annular extrudate. Based on the dimensions of the desired extrudate we can expect the ratio of the inner radius, κR_o , to outer radius, R_o , to be in the range of 0.8 (2.5 cm/3.065 cm), and hence we can treat the annulus to a first approximation as a slit of width $W_0 = \pi(R_o + \kappa R)$, and height $H_0 = R_o - \kappa R_o$. If an appropriate constitutive equation was available, one could in principle substitute expressions for N_1 and τ_w (e.g., see entries in Table 3.5) into Eq. 3.89 and thereby obtain values for the thickness swell, H_p/H_0 , as a function of the wall shear rate, $\dot{\gamma}_w$, or the wall shear stress. The PTT model in its present form (see Table 3.1 for the predictions in shear and shear-free flows) cannot be used because τ_{xy} passes through a maximum and then decreases, which leads to abnormally high values of extrudate swell. The viscosity can be described by the following expression (Crochet and Bezy, 1979):

$$\eta = \frac{\eta_1}{1 + \xi(2 - \xi)(\lambda\dot{\gamma})^2} + \eta_2 \quad (3.152)$$

TABLE 3.4 Predicted Values of N_1 , $N_1/2\tau_{yx}$, and Extrudate Swell (H_p/H_0) for LDPE (NPE 953) at 170 °C Using the Phan-Thien–Tanner Model

$\dot{\gamma}$ (s ⁻¹)	τ_{yx} (Pa)	N_1 (Pa)	$N_1/2\tau_{yx}$	H_p/H_0^a
0.1	1.74E + 03	1.90E + 03	0.55	1.12
1.0	7.50E + 03	2.09E + 03	1.40	1.22
10.0	2.77E + 04	8.69E + 04	1.57	1.24
100.0	1.90E + 05	8.73E + 04	0.23	1.10
553.0	1.98E + 05	8.73E + 04	0.22	1.10

$\eta = 17,753$ Pa·s, $\eta_2 = 1975$ Pa·s, $\lambda = 5.475$, and $\xi = 0.0379$.
^aNote: Calculated using Eq. 3.89.

where η_2 is a high shear rate limit viscosity. The addition of η_2 makes τ_{xy} increase monotonically with $\dot{\gamma}$. By using nonlinear regression (Example 3.3) the following parameters were obtained:

$$\eta_1 = 17,753 \text{ Pa} \cdot \text{s}, \eta_2 = 1975 \text{ Pa} \cdot \text{s}, \xi = 0.0379, \lambda = 5.47 \text{ s}$$

Values of $N_1/2\tau_{yx}$ and H_p/H_0 are calculated and listed in Table 3.4, but they are unreasonably low at high shear rates. This is due to the predictions of the PTT model at high shear rates when only a single relaxation time is used. Hence, the PTT model does not allow us to properly estimate thickness swell.

One would like to go directly to experimental data, but values of N_1 are usually not available at values of $\dot{\gamma}$ greater than 10 s⁻¹. Hence, we use the approximation given in Eq. 3.118 along with dynamic mechanical data given in Appendix A.1, Table A.2. Estimated values of N_1 presented in Table 3.5 are used to calculate values of $N_1/2\tau_{yx}$ and H_p/H_0 . These values seem to be more realistic and in-line with present knowledge. However, values of H_p/H_0 at shear rates higher than 100 s⁻¹ are not available. To obtain these values, one can only extrapolate values of $N_1/2\tau_{yx}$ versus $\dot{\gamma}$ to higher shear rates. In fact, values of N_1 versus τ_{xy} are plotted in Figure 3.34, and it is observed that on a plot of $\ln N_1$ versus $\ln \tau_{xy}$ the relation is linear. Hence, we fit a function of the form $N_1 = A\tau_{xy}^b$ to the data.

Finally, one other approach is to use the White–Metzner model (see Table 3.1), as at least the viscosity function can be fit to the viscosity data (parameters for the Carreau viscosity model are found using nonlinear regression and are $\eta_0 = 23,000$ Pa·s, $n = 0.587$, and $\lambda = 19.7$ s). Values of N_1 cannot

TABLE 3.5 Experimental Values of N_1 and $N_1/2\tau_{yx}$ for LDPE and Calculated Values of H_p/H_0 (Eq. 3.51)

$\dot{\gamma}$ (s ⁻¹)	τ_{yx} (Pa)	N_1 (Pa)	N_1 (Pa)	$N_1/2\tau_{yx}$	H_p/H_0
0.1	6.9E + 02	1.48E + 03	1.32E + 03	1.07	1.18
1.0	6.35E + 03	1.32E + 04	1.084E + 04	0.85	1.15
10.0	2.11E + 04	8.66E + 04	5.40E + 04	1.28	1.20
100.0	5.65E + 04		1.875E + 05	1.66	1.26

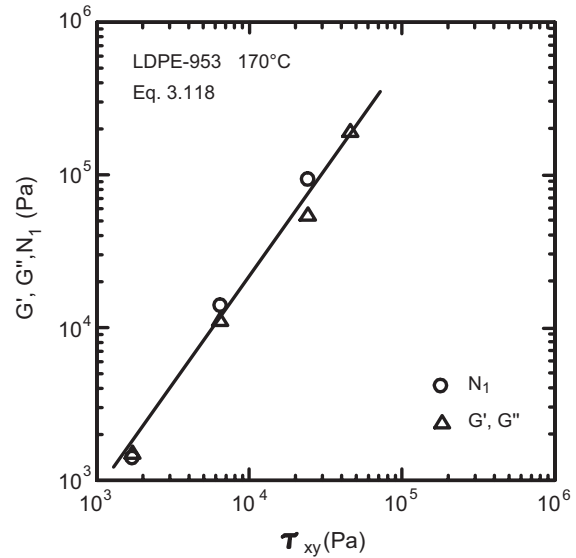


FIGURE 3.34 N_1 versus τ_{xy} for LDPE (NPE 953) at 170 °C: (○) measured values of N_1 ; (Δ) estimated values of N_1 from Eq. 3.118 and values of G' and G'' .

be predicted directly from η but the modulus, G , is required. G is determined usually at each $\dot{\gamma}$ by fitting the predictions for N_1 ($= 2 \eta^2/G$) to data. For $\dot{\gamma}$ greater than 100 s⁻¹ this data is not available, and hence we use G determined at 100 s⁻¹ for predicting values of N_1 at higher shear rates. As shown in Table 3.6, the values of $N_1/2\tau_{yx}$ increase at least

TABLE 3.6 Predicted Values of N_1 , $N_1/2\tau_{yx}$, and Thickness Swell (H_p/H_0) for LDPE (NPE 953) Using the White–Metzner Model

(s ⁻¹)	τ_{xy} (Pa)	N_1 (Pa)*	$N_1/2\tau_{yx}$	H_p/H_0
0.1	1.66E + 03	1.45E + 03	0.44	1.12
1.0	6.71E + 03	1.08E + 04	0.80	1.15
10.0	2.59E + 04	5.40E + 04	1.04	1.18
100.0	1.00E + 05	1.88E + 05	0.94	1.16
553.0	2.74E + 05	1.40E + 06	2.6	1.37

* N_1 calculated from Eq. 3.148 and dynamic oscillatory shear data.

monotonically with increasing τ_{xy} , but they are lower than values based on experimental results.

We are now in position to estimate the diameter and gap of the die. First we observe that H_o and D_o are a function of shear rate and hence the die dimensions will change with changes in the mass throughput. Based on the information given in the problem, our limits are the extruder output or the onset of melt fracture, which occurs at a wall shear stress of 1.13×10^5 Pa for LDPE. Based on the results in Table 3.6 (note that we arbitrarily choose the experimental data over the estimated values given in Table 3.6), then we predict the following dimensions:

$$\begin{aligned} H_o &= H_p/1.317 = 0.429 \text{ cm} \\ D_o &= D_p/1.317 = 4.655 \text{ cm} \end{aligned}$$

Using these dimensions and the wall shear stress of 1.13×10^5 Pa, the mass flow rate is found using the appropriate expression for the power-law case in Table 2.5:

$$\begin{aligned} \rho Q &= \frac{\rho W_0 H_0^2}{2(s+2)} \left(\frac{\tau_w}{m}\right)^s = \frac{772(4.29 \times 10^{-3})^2(0.1327)}{2(3.704)} \\ &\times \left(\frac{1.13 \times 10^5}{5.17 \times 10^3}\right)^{1.704} = 4.88 \times 10^{-2} \text{ kg/s} \\ &= 3.87 \times 10^2 \text{ lb/hr} \end{aligned} \quad (3.153)$$

Here we have used $m = 5.17 \times 10^3 \text{ Pa}\cdot\text{s}^n$ and $n = 0.587$, which were obtained by fitting the power-law expressions to viscosity data using nonlinear regression. The value of ρQ exceeds that which is possible with the given extruder. Hence, it is necessary to recalculate the die dimensions using the maximum flow rate of 300 lb/h. From the expression for ρQ (Eq. 3.120 above or Table 2.4), τ_w at $\rho Q = 300 \text{ lb/h}$ is calculated:

$$\begin{aligned} \tau_w &= m \left[\frac{2\rho Q(s+2)}{\rho W_0 H_0^2} \right]^n \\ &= (5.17 \times 10^3) \left[\frac{(2)(3.78 \times 10^{-2})(3.704)}{(772)(0.1327)(4.29 \times 10^{-3})^2} \right]^{0.587} \\ &= 9.735 \times 10^4 \text{ Pa} \end{aligned} \quad (3.154)$$

Using the relation $N_1 = A\tau_{xy}^b$ with $A = 0.119$ and $b = 1.304$ (these values were obtained by regression analysis of data plotted in Fig. 3.34), we calculate N_1 to be 3.8×10^5 Pa. Using Eq. 3.89 we calculate the thickness and diameter swell to be

$$H_p/H_o = 1.294 \quad D_p/D_o = 1.294$$

Using the required extrudate dimensions $H_o = 0.436 \text{ cm}$ and $D_o = 4.737 \text{ cm}$ and the expression for ρQ (Eq. 3.153), we calculate ρQ to be 315.9 lb/h. This still exceeds the maximum flow rate possible, and hence we repeat the above process. τ_w is recalculated and found to be $9.45 \times 10^4 \text{ Pa}$. N_1 is estimated to be $3.66 \times 10^5 \text{ Pa}$. The new dimensions based on an extrudate swell of 1.292 are $H_o = 0.437 \text{ cm}$ and $D_o = 4.743 \text{ cm}$. The mass flow rate for these conditions is 302 lb/h. Another iteration of this process would be required to determine the exact dimensions. However, one is now close enough, for all practical considerations, to the final die dimensions.

Before leaving Design Problem II a few additional comments are required. The die design typically used is more similar to that shown in Design Problem I. For this type of die the flow is more complex than just shear flow and hence extrudate swell will be different from what is expected. Extrudate swell, which is described in Chapter 7, is a complex function of several variables and not just $N_1/2\tau_{yx}$. Furthermore, there is not always a simple relation between capillary swell, thickness swell, and diameter swell. The approach we have used in solving Design Problem II is at best a crude approximation.

PROBLEMS

A. Applications

3A.1 *Viscosity from the Melt Flow Index for LDPE.* The melt flow index (MFI) is in essence a single point viscosity used by industry to characterize a polymer within a family of resins. Most resins are bought and sold based on the MFI. The device used to measure the MFI, which is shown in Figure 3.35, is basically a capillary rheometer in which a known force is applied to the polymer melt and the mass of polymer leaving the capillary of known dimensions is measured over a 10 min period. Determine the viscosity and wall shear rate corresponding to a 2.0 MFI LDPE (NPE 953) at 190 °C. The following information is given:

$$\begin{aligned} 2.0 \text{ MFI} &= 2.0 \text{ g/10 min}; D = 2.095 \text{ mm}; L = 8.00 \text{ mm} \\ \text{weight} &= 2.16 \text{ kg}; \text{reservoir diameter} = 9.53 \text{ mm}; \\ \rho &= 820 \text{ kg/m}^3 \end{aligned}$$

Hint: The data in Appendix A.1.2 could be useful.

3A.2 *Increase in Wire Coating Thickness Due to Extrudate Swell.* LDPE (NPE 953) melt at 170 °C is used to coat a wire as shown in Figure 2.10. Given that $R = 5.0\text{E}-03 \text{ m}$, $\kappa = 0.85$, and the wire speed $V_w = 15 \text{ m/min}$, calculate the thickness of the coating at the

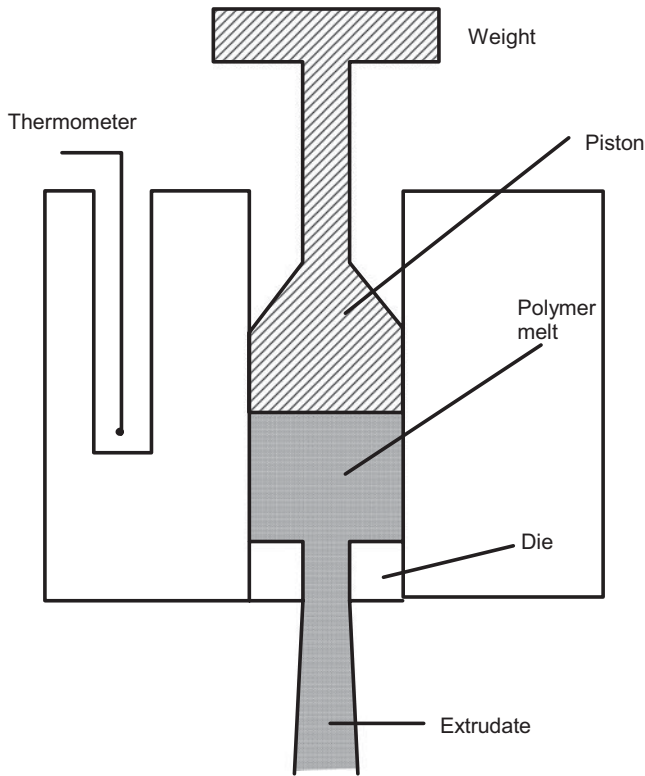


FIGURE 3.35 Melt index (MI) device.

die exit taking into account extrudate swell. List any assumptions you make.

- 3A.3** *Viscosity from Capillary Rheometer Data for LLDPE.* From values of the apparent wall shear stress, τ_a , and the apparent wall shear rate, $\dot{\gamma}_a$, given in Appendix A.3.3 calculate the viscosity as a function of shear rate and compare your results to those which can be obtained directly from the data in Appendix A.3.3 (i.e., τ_c and $\dot{\gamma}_c$ where τ_c and $\dot{\gamma}_c$ are the corrected wall shear stress and rates, respectively). In particular, use the values of τ_a at each L/D to obtain ΔP_{ent} at each shear rate. Correct the values of ΔP_{tot} to obtain τ_w . Determine $\dot{\gamma}_w$ by correcting $\dot{\gamma}_a$ for the nonparabolic velocity profile using Eq. 3.3-7.
- 3A.4** *Estimate the Primary Normal Stress Difference from Dynamic Data.* Use Eq. 3.148 and the dynamic oscillatory data given in Appendix A.3, Table A.8 to estimate N_1 for LLDPE at 170 °C. Compare your values with those given in Appendix A.3, Table A.7.
- 3A.5** *Estimate Extensional Viscosity from Capillary Rheometer Data*
- (a) Use Eq. 3.138 and capillary rheometer data given in Appendix A.1, Table A.3 for LDPE and in Appendix A.3, Table A.9 for LLDPE to calculate

the extensional viscosity as a function of extension rate.

- (b) Normalize the values of $\dot{\gamma}$ by dividing them by η_0 and compare the normalized values for the two polymers. Is there any significant difference between the values for the two polymers?

B. Principles

3B.1 *Corrected Wall Shear Rate in a Capillary (No-Slip Case).* The wall shear rate for a Newtonian fluid is given by $4Q/\pi R^3$, which is called the apparent shear rate, $\dot{\gamma}_a$, for a polymeric fluid. Because of the shear-thinning viscosity exhibited by a polymeric fluid, $\dot{\gamma}_a$ does not represent the wall shear rate, $\dot{\gamma}_w$, for a polymeric fluid. A correction procedure is needed which allows one to determine $\dot{\gamma}_w$ without any knowledge of the viscosity of the fluid.

- (a) Show that if there is no slip of the fluid at the capillary walls then the integral for the volume rate of flow may be integrated by parts to give

$$Q = -\pi \int_0^R \frac{dv_z}{dr} r^2 dr \quad (3.155)$$

- (b) Introduce the change of variable $r/R = \tau_{rz}/\tau_R$ (where $\tau_R = (P_0 - P_L)R/2L$ is the wall shear stress) and rewrite the integral in part (a) in terms of the integration variable τ_{rz} .
- (c) Differentiate the integral obtained in part (b) with respect to τ_R to obtain the following equation:

$$\left(-\frac{dv_z}{dr} \right)_{r=R} = \frac{1}{\pi R^3 \tau_R^2} \frac{d}{d\tau_R} (\tau_R^3 Q) \quad (3.156)$$

- (d) Show how to obtain Eq. 3.128 in the text from Eq. 3.155.

3B.2 *Wall Shear Rate in a Capillary with Slip.* Very viscous polymeric materials such as rubber, highly filled polymers, and polymers containing processing aids do not readily adhere to the walls of a capillary, leading to slip.

- (a) Assuming the slip velocity is v_s (and is independent of τ_R) show that the integral for the volume rate of flow may be integrated by parts to give:

$$Q = \pi R^2 v_s - \pi \int_0^R \frac{dv_z}{dr} r^2 dr$$

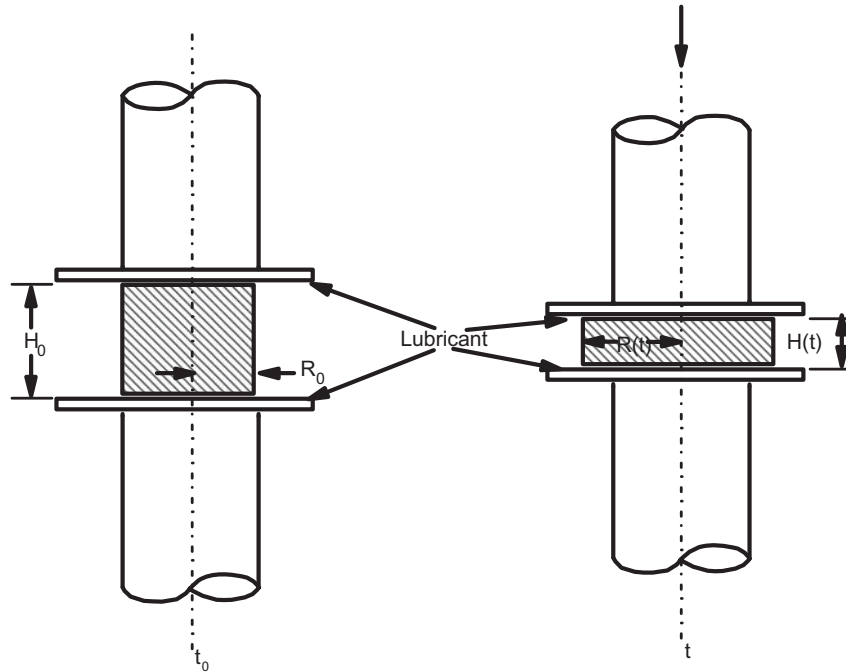


FIGURE 3.36 Lubricated squeezing flow between two parallel disks. The figure at the left shows the initial configuration while the figure at the right shows the material at some other time $t > t_0$. (Reprinted by permission of the publisher from Soskey and Winter, 1985.)

- (b) Introduce a change of variable as in part (b) of Problem 3B.1 and rewrite the integral in part (a) in terms of the variable τ_{rz} .
- (c) Differentiate the integral in part (b) with respect to τ_R to obtain the following equation:

$$-\dot{\gamma}_w = (\dot{\gamma}_a / 4)[3 + d \ln \dot{\gamma}_a / d \ln \tau_R] - 3 v_s / R \tag{3.157}$$

- (d) Explain how you would use Eq. 3.157 to obtain v_s .

3B.3 Squeezing Flow Between Lubricated Disks. Biaxial stretching flow can be generated in lubricated squeezing flow which is shown in Figure 3.36. A thin layer of lubricant applied to the upper and lower disks prevents the fluid from sticking to the plates.

- (a) Assuming that the squeezing rate, $\dot{\epsilon}$, is constant throughout the gap, use the equation of continuity to show that the velocity field is

$$v_z = -\dot{\epsilon}z \quad v_r = \frac{1}{2}\dot{\epsilon}r$$

- (b) How must the gap, $H(t)$, change with time to make $\dot{\epsilon}$ constant?
- (c) Determine the components of the rate of deformation tensor for this flow.
- (d) Which components of stress exist for any fluid?

- (e) Find $\bar{\eta}_1$ and $\bar{\eta}_2$ for a Newtonian fluid. In particular, show that $\bar{\eta}_1 = 6\bar{\eta}_0$ ($\bar{\eta}_1$ is called the biaxial extensional viscosity in this case).
- (f) Show that the normal stress difference is related to the force F by the following expression:

$$\tau_{zz} - \tau_{rr} = \frac{F(t)}{\pi[R(t)]^2}$$

3B.4 Tangential Annular Flow for a Polymeric Liquid. Tangential annular flow was analyzed in Problem 2B.6 for a power-law fluid. Carry out a similar analysis for a viscoelastic fluid.

- (a) Show that the components of the equation of motion are

$$\frac{\partial}{\partial r}(r^2 \tau_{r\theta}) = 0 \tag{3.158}$$

$$\frac{-\rho v_\theta^2}{r} = -\frac{\partial p}{\partial r} - \frac{1}{r} \frac{\partial}{\partial r}(r \tau_{rr}) + \frac{\tau_{\theta\theta}}{r} \tag{3.159}$$

- (b) What is the relation between torque, T , and $\tau_{r\theta}$?
- (c) Use Eq. 3.159 to show how one can obtain the primary normal stress difference.

3B.5 Steady Shear Material Functions for the Giesekus Model. The Giesekus model (Giesekus, 1982) is a

nonlinear constitutive equation with a quasimolecular basis, which is written as

$$\begin{aligned} \boldsymbol{\tau} + \lambda_1 \frac{\Delta}{\tau} - a \frac{\lambda_1}{\eta_0} \{\boldsymbol{\tau} \cdot \boldsymbol{\tau}\} - a \lambda_2 \{\dot{\boldsymbol{\gamma}} \cdot \boldsymbol{\tau} + \boldsymbol{\tau} \cdot \dot{\boldsymbol{\gamma}}\} \\ = -\eta_0 \left[\dot{\boldsymbol{\gamma}} + \lambda_\gamma \frac{\Delta}{\gamma} - a \frac{\lambda_2^2}{\lambda_1} \{\dot{\boldsymbol{\gamma}} \cdot \dot{\boldsymbol{\gamma}}\} \right] \end{aligned} \quad (3.160)$$

The model contains four parameters: α , λ_1 , λ_2 , and η_0 and $a = \alpha/(1 - \lambda_2/\lambda_1)$. The model is capable of describing many of the observed rheological properties of polymeric fluids. Show that the steady shear material functions are

$$\frac{\eta}{\eta_0} = \frac{\lambda_2}{\lambda_1} + \left(1 - \frac{\lambda_2}{\lambda_1}\right) \frac{(1-f)^2}{1 + (1-2\alpha)f} \quad (3.161)$$

$$\frac{\Psi_1}{2\eta_0(\lambda_1 - \lambda_2)} = \frac{f(1-\alpha f)}{(\lambda_1 \dot{\gamma})^2 \alpha(1-f)} \quad (3.162)$$

$$\frac{\Psi_2}{\eta_0(\lambda_1 - \lambda_2)} = \frac{-f}{(\lambda_1 \dot{\gamma})^2} \quad (3.163)$$

where

$$\begin{aligned} f &= \frac{1 - \chi}{1 + (1 - 2\chi)_\chi}; \\ \chi^2 &= \frac{(1 + 16\alpha(1 - \alpha)(\lambda_1 \dot{\gamma})^2)^{1/2} - 1}{8\alpha(1 - \alpha)(\lambda_1 \dot{\gamma})^2} \end{aligned}$$

3B.6 *Steady Elongational Flow for the Giesekus Model.* Show that in steady elongational flow the extensional viscosity for the Giesekus model is given by

$$\begin{aligned} \frac{\bar{\eta}}{3\eta_0} &= \frac{\lambda_2}{\lambda_1} \\ &+ \left(1 - \frac{\lambda_2}{\lambda_1}\right) \frac{1}{6\alpha} \left[3 + \frac{1}{\lambda_1 \dot{\epsilon}} \{ [1 - 4(1 - 2\alpha)\lambda_1 \dot{\epsilon} \right. \\ &\left. + 4\lambda_1^2 \dot{\epsilon}^2]^{1/2} - [1 + 2(1 - 2\alpha)\lambda_1 \dot{\epsilon} + \lambda_1^2 \dot{\epsilon}^2]^{1/2} \} \right] \end{aligned} \quad (3.164)$$

3B.7 *Predictions of Fiber Orientation in the Startup of Shear-Free Flow.* From Eq. 3.101 obtain the system of ordinary differential equations for determining the components of the orientation tensor, \mathbf{A} , at the start of shear-free flow and under steady state conditions. In particular, find the equations for determining A_{11} , A_{22} , and A_{33} . The initial orientation of the fibers is taken as random which means $A_{11} = A_{22} = A_{33} = 1/3$.

TABLE 3.7 Pom-Pom Constitutive Equation for Branched Polymers

Stress	$\boldsymbol{\sigma} = \sum_i \boldsymbol{\sigma}_i = 3 \sum_i g_i \lambda_i^2 \mathbf{S}_i$	(1)
Orientation	$\mathbf{S}_i = \frac{\mathbf{A}_i}{\text{tr } \mathbf{A}_i}$	(2a)
	$\frac{D}{Dt} \mathbf{A}_i = \mathbf{K} \cdot \mathbf{A}_i + \mathbf{A}_i \cdot \mathbf{K}^T - \frac{1}{\tau_{bi}} (\mathbf{A}_i - \mathbf{I})$	(2b)
Stretch	$\frac{D}{Dt} \lambda_i = \lambda_i (\mathbf{K} : \mathbf{S}_i) - \frac{1}{\tau_{si}} (\lambda_i - 1) e^{\nu_i^* (\lambda_i - 1)}$	(3)

Source: McLeish and Larson, 1998.

3B.8 *Predictions of the McLeish–Larson Constitutive Equation for Branched Polymers* (McLeish and Larson, 1998). The stress tensor for a branched polymer, which is given in Table 3.7, is a function of the dynamic variable \mathbf{S} , which describes the average backbone orientation, and λ , which describes the average backbone stretch. The model described in the table is written for multiple relaxation modes and represents the simplest model for a branched polymer. Dynamic expressions for \mathbf{S} and λ for each relaxation mode are given in Eqs. 2 and 3 in Table 3.7. τ_{bi} is the i th mode of the backbone relaxation time and τ_{si} is the backbone stretch orientation time. ν^* is taken as $2/q$, where q is the number of branch arms associated with a given τ_s .

- For small strain oscillatory shear flow write out the expression for G' and G'' .
- Write out the expressions for η^+ and N_1^+ at the startup of shear flow.
- Write out the expression for extensional viscosity for the startup of uniaxial extensional flow.

C. Numerical Problems

3C.1 *Steady Extensional Viscosity for the Phan-Thien–Tanner Model.* Two nonlinear algebraic equations must be solved as shown in Table 3.1 to determine $\bar{\eta}$ for the PTT model. Using the values of $\eta_0 = 17,753$ Pa·s and $\lambda = 5.47$ s for LDPE at 170 °C, determine $\bar{\eta}$ at $\dot{\epsilon} = 0.01, 0.1, 1, 10,$ and 100 s^{-1} for values of $\epsilon = 0.001, 0.01,$ and 1.0 .

3C.2 *Transient Extensional Stress Growth for the PTT Model.* For the startup of uniaxial extensional flow two coupled ordinary differential equations are obtained as shown below for the PTT model:

$$\begin{aligned} \lambda \frac{d\tau_{11}}{dt} + \exp \left[-\frac{\epsilon \lambda}{\eta_0} (\tau_{11} + 2\tau_{22}) \right] \tau_{11} - 2\lambda \dot{\epsilon} (1 - \xi) \tau_{11} \\ = -2\eta_0 \dot{\epsilon} \end{aligned} \quad (3.165)$$

$$\lambda \frac{d\tau_{22}}{dt} + \exp\left[-\frac{\varepsilon\lambda}{\eta_0}(\tau_{11} + 2\tau_{22})\right]\tau_{22} + \lambda\dot{\varepsilon}(1 - \dot{\varepsilon})\tau_{22} = \eta_0 \dot{\varepsilon} \quad (3.166)$$

Using either the IMSL subroutine IVPAG or an ordinary differential equation solver in MATLAB, solve these equations for τ_{11} and τ_{22} as a function of time and calculate $\bar{\eta}$ as a function of time. Take $\dot{\varepsilon} = 0.2$, $\varepsilon = 0.01$, and the rest of the parameters as given in Problem 3C.1. Compare the predicted values with the experimental ones for LDPE given in Appendix A.1, Table A.4.

- 3C.3** *Fit of Giesekus Model to Rheological Data.* The steady shear material functions for the Giesekus model are given in Problem 3B.5. Find the parameters in this model which give the best fit of the steady shear and dynamic oscillatory data at 170 °C given for LDPE in Appendix A.1, Tables A.1 and A.2.
- 3C.4** *Regression Analysis of Capillary Rheometer Measurements.* Capillary rheometer data are given for LDPE in Appendix A.1, Table A.1. Using the apparent values of wall shear stress, τ_a , and shear rate, $\dot{\gamma}_a$, for three different L/D capillaries determine ΔP_{ent} . Use these values to find the corrected values of the wall shear stress. Correct the apparent wall shear rate values. Compare your values with those given in Appendix A.1, Table A.3. Use the linear regression analysis subroutine, RCURV (in SSTAT2B.LIB), or MATLAB to determine values of ΔP_{ent} .
- 3C.5** *Numerical Solution of Example 3.4.* Solve the system of equations given in Example 3.4 using either one of the ordinary differential equation solvers in MATLAB or IVPAG in the IMSL subroutines. Assume initially that the rods are randomly oriented.
- 3C.6** *Fiber Orientation at the Startup of Shear-Free Flow.* Solve the system of ordinary differential equations developed in Problem 3B.7 for the case of equibiaxial extensional flow (i.e., $b = 0$ and $\dot{\varepsilon} = -1.0$) Take $\alpha = 0.3$ and $C_1 = 0.002$. Use either one of the ordinary differential equation solvers in MATLAB or IVPAG in the IMSL subroutines.
- 3C.7** *Branching Frequency of Two Sparsely Branched LLDPEs*
- (a) Two commercial LLDPEs are believed to contain sparse long chain branching, LCB. Their M_w and η_0 values are given, respectively, below:

Dow Affinity PL 1840: 87,900 g/gmol and 46,800 Pa·s (at 150 °C)

Dow Affinity PL 1880: 116,400 g/gmol and 45,370 Pa·s (at 150 °C)

Using Eqs. 3.149, 3.150, and 3.151 and the parameters $A(150\text{ °C}) = 5.22 \times 10^{-6}$ (Pa·s mol/g), $B = 6.0$, $M_0(\text{repeat unit MW}) = 14.027$ g/mol, $M_c = 2100$ g/mol, and $M_{\text{Kuhn}} = 145.9$ g/mol, find α , the branching frequency (i.e., the fraction of carbon atoms containing LCBs).

- (b) Determine α for making η_0 a maximum and convert this to the number of branches per molecule for PL 1840.

D. Design Problems

- 3D.1** *Slit-Die Rheometer Design for a Viscoelastic Fluid.* Design a slit-die rheometer for measuring the viscosity and N_1 for HDPE (rheological data are given in Appendix A.2, Tables A.5 and A.6) for shear rates from 1.0 to 100 s⁻¹ at 170 °C. Pressure transducers having full pressure ranges of 500, 1000, and 3000 psi are available. If the pressure transducers are calibrated in the die, then pressures can be measured as accurately as 1.0% of the reading. The extruder and gear pump system used to feed the die can provide up to 25.0 kg/h. In your design specify the placement of the transducers and the dimensions of the die.
- 3D.2** *Design of a Parison Stretching Process.* A parison of LDPE (NPE 953 at 170 °C) having an outside diameter of 0.127 m, thickness of 3.81×10^{-4} m, and length of 0.615 m is stretched to twice its original length before being blown. The end of the parison is stretched to its final length in 1.0 s by pulling on the end of the parison at a constant velocity. Determine the maximum force required to stretch the parison under the conditions given and the minimum clamping force required to hold the parison if the friction coefficient between the grips and the polymer is 0.3.

REFERENCES

- Advani, S. G. and C. L. Tucker. 1990. "Closure Approximations for Three-Dimensional Structure Tensors." *J. Rheol.*, **34**(3), 367–386.
- Advani, S. G. and E. M. Sozer. 2003. *Process Modeling in Composites Manufacturing* (Marcel Dekker, New York).
- Baird, D. G. 2008. "Primary Normal Stress Difference Measurements for Polymer Melts at High Shear Rates in a Slit-Die Using Hole and Exit Pressure Data." *J. Non-Newtonian Fluid Mech.*, **148**, 13–23.
- Baird, D. G. and R. L. Ballman. 1979. "Comparison of the Rheological Properties of Concentrated Solutions of a Rodlike and a Flexible Chain Polyamide." *J. Rheol.*, **23**(4), 505–524.
- Bay, R. S. and C. L. Tucker III. 1992. "Fiber Orientation in Simple Injection Moldings. Part I: Theory and Numerical Methods." *Polym. Compos.*, **13**, 332–341.

- Bird, R. B., R. C. Armstrong, and O. Hassager. 1987a. *Dynamics of Polymeric Liquids: Volume 1, Fluid Mechanics*, 2nd edition (Wiley, Hoboken, NJ).
- Bird, R. B., R. C. Armstrong, and O. Hassager. 1987b. *Dynamics of Polymeric Liquids: Volume 2, Kinetic Theory* (Wiley, Hoboken, NJ).
- Chung, D. H. and T. H. Kwon. 2001. "Improved Model of Orthotropic Closure Approximation for Flow Induced Fiber Orientation." *Polym. Compos.*, **22**, 636–649.
- Cogswell, F. N. 1978. "Converging Flow and Stretching Flow: A Compilation." *J. Non-Newtonian Fluid Mech.*, **4**, 23.
- Cox, W. P. and E. H. Merz. 1958. "Correlation of the Complex Viscosity with Steady Shear Viscosity." *J. Polym. Sci.*, **28**, 619.
- Crochet, M. J. and M. Bezy. 1979. "Numerical Solution for the Flow of Viscoelastic Fluids." *J. Non-Newtonian Fluid Mech.*, **5**, 201.
- Dealy, J. M. 1982. *Rheometers for Molten Plastics* (Van Nostrand Reinhold, New York).
- Doerpinghaus, P. J. and D. G. Baird. 2003. "Separating the Effects of Sparse Long-Chain Branching on Rheology from Those Due to Molecular Weight in Polyethylenes." *J. Rheol.*, **47**(3), 717–736.
- Doi, M. and S. F. Edwards. 1988. *The Theory of Polymer Dynamics* (Oxford University Press, New York).
- Eberle, A. P. R., D. G. Baird, and P. Wapperom. 2008. "The Rheological Properties of Non-Newtonian Fluids Containing Glass Fibers: A Review of Experimental Literature." *Ind. Eng. Chem.*, **47**(9), 2849–2872.
- Eberle, A. P. R., G. M. Velez-Garcia, D. G. Baird, and P. Wapperom. 2010. "Fiber Orientation Kinetics of a Concentrated Short Glass Fiber Suspension in Startup of Simple Shear Flow." *J. Non-Newtonian Fluid Mech.*, **165**, 110–119.
- Folgar, F. P. and C. L. Tucker III. 1984. "Orientation Behavior of Fibers in Concentrated Suspensions." *J. Rein. Plast. Comp.*, **3**, 98–119.
- Giesekus, H. 1982. "A Simple Constitutive Equation for Polymer Fluids Based on the Concept of the Deformation-Dependent Tensorial Mobility." *J. Non-Newtonian Fluid Mech.*, **11**, 69–109.
- Glissele, W. 1980. *Rheology*, Vol. 2 (Plenum Press, New York), p. 457.
- Gotsis, A. D. 1987. *Study of the Numerical Simulation of Viscoelastic Flow: Effect of the Rheological Model and the Mesh* (Ph.D. Thesis, Department of Chemical Engineering, Virginia Polytechnic Institute and State University, Blacksburg, VA.)
- Han, C. D. 1976. *Rheology in Polymer Processing* (Academic Press, New York).
- Janzen, J. and R. J. Colby. 1999. "Diagnosing Long-Chain Branching in Polyethylenes." *J. Mol. Struct.*, **48**, 569–584.
- Khan, S. A., R. K. Prud'homme, and R. G. Larson. 1987. "Comparison of the Rheology of Polymer Melts in Shear and Biaxial and Uniaxial Extensions." *Rheol. Acta*, **26**, 44.
- Larson, R. G. 1988. *Constitutive Equations for Polymer Melts and Solutions* (Butterworths, Boston).
- Larson, R. G. 1999. *The Structure and Rheology of Complex Fluids* (Oxford University Press, New York).
- Laun, H. M. 1986. "Prediction of Elastic Strains of Polymer Melts in Shear and Elongation." *J. Rheol.*, **30**, 459.
- Lipscomb, G. G. II, M. M. Denn, D. U. Hur, and D. V. Boger. 1988. "The Flow of Fiber Suspensions in Complex Geometries." *J. Non-Newtonian Fluid Mech.*, **26**, 297–325.
- Macosko, W. W. 1994. *Rheology Principles, Measurements and Applications* (VCH Publishers, New York).
- McLeish, T. C. B. and R. G. Larson. 1998. "Molecular Constitutive Equations for a Class of Branched Polymers: The Pom-Pom Polymer." *J. Rheol.*, **42**, 82–112.
- Meissner, J. 1979. "Basic Parameters, Melt Rheology, Processing, and End-Use Properties of Three Low-Density Polyethylene Samples." *J. Pure Appl. Chem.*, **42**, 553–612.
- Münstedt, H. 1980. "Dependence of the Elongational Behavior of Polystyrene Melts on Molecular Weight and Molecular Weight Distribution." *J. Rheol.*, **24**, 847–867.
- Phan-Thien, N. and R. I. Tanner. 1977. "A New Constitutive Equation Derived from Network Theory." *J. Non-Newtonian Fluid Mech.*, **2**, 255–270.
- Phan-Thien, N., X. J. Fan, R. I. Tanner, and R. Zheng. 2002. "Folgar–Tucker Constant for a Fiber Suspension in a Newtonian Fluid." *J. Non-Newtonian Fluid Mech.*, **103**, 251–260.
- Sentmanat, M. L. 2004. "Miniature Universal Testing Platform: From Extensional Melt Rheology to Solid-State Deformation Behavior." *Rheol. Acta*, **43**, 657–669.
- Sepehr, M., G. Ausias, and P. J. Carreau. 2004. "Rheological Properties of Short Fiber Filled Polypropylene in Transient Shear Flow." *J. Non-Newtonian Fluid Mech.*, **123**, 19–32.
- Soskey, P. R. and H. H. Winter. 1985. *J. Rheol.*, **29**, 493.
- Switzer, L. H. and D. J. Klingenberg. 2003. "Rheology of Sheared Flexible Fiber Suspensions Via Fiber-Level Simulations." *J. Rheol.*, **47**(3), 759–778.
- Tanner, R. I. 1970. "Theory of Die Swell." *J. Polym. Sci.*, **A8**, 2067.
- Walters, K. 1975. *Rheometry* (Chapman and Hall, London).
- White, S. A. and D. G. Baird. 1988. "Numerical Simulation Studies of the Planar Entry Flow of Polymer Melts." *J. Non-Newtonian Fluid Mech.*, **30**, 47–71.

4

DIFFUSION AND MASS TRANSFER

DESIGN PROBLEM III DESIGN OF A DRY-SPINNING SYSTEM

One of the production methods for fiber formation includes the evaporation of a solvent from the spinning line and the resulting solidification of the fiber. This method is called dry spinning (Ohzawa et al., 1969; Ziabicki, 1976), and it finds application to polymers that do not form thermally stable and viscous melts. These polymers are dissolved in low-molecular-weight volatile solvents (ether, acetone, dimethylformamide, alcohols, etc.). The method consists of extruding the polymer solution into a vertical cell of jets. These jets after leaving the spinneret come into contact with hot air, Figure 4.21 (p. 100), in which the solvent evaporates; and thus the concentration of the polymer increases and the spinning line solidifies.

Consider the system of polyacrylonitrile (PAN) and dimethylformamide (DMF). This solution is fed into the dry-spinning apparatus (Fig. 4.21), and the solvent DMF evaporates into the hot air. Three mechanisms account for the mass transfer of the solvent to the air: flash vaporization, diffusion within the spinning line, and convective mass transfer from the spinning line surface to the air. It is expected that the first and third mechanisms are important in the region close to the spinneret. Analyze the region where the diffusion within the spinning line is the controlling mass transfer mechanism, and calculate the axial distance the fiber travels before all the solvent is removed. For the system of PAN–DMF the following data are given (Ohzawa and Nagano, 1970): dope output $\dot{m}_P = 2.0 \times 10^{-2}$ g/s; dope solvent mass fraction $\bar{w}_{Ad} = 0.74$;

dope temperature $T_d = 100$ °C; air temperature $T_\infty = 200$ °C; velocity of cross air flow $V_{C\infty} = 2$ m/s; velocity of parallel air flow $V_{P\infty} = 50$ cm/s; solvent mole fraction in the air $x_{A\infty} = 0$; diffusivity of DMF in PAN in cm^2/s , $\mathcal{D}_{AP} = 9.03 \times 10^{-4} \exp[-2360/T]$; dope cross-sectional area = 0.001 cm^2 ; and final cross-sectional area = 1.56×10^{-5} cm^2 .

The mass transfer coefficients for parallel and cross air flow, respectively, are given below:

$$k_{c,P} = 0.26 \left[\mathcal{D}_{\text{Air}} \left(\frac{\mu}{\rho} \right)^{-1/3} \right] \left(\frac{\text{Sc}}{\text{Pr}} \right)^{1/2} R(z)^{-2/3} V_{P\infty}^{1/3}$$

$$k_{c,C} = 0.52 \left[\mathcal{D}_{\text{Air}} \left(\frac{\mu}{\rho} \right)^{-1/3} \right] \left(\frac{\text{Sc}}{\text{Pr}} \right)^{1/2} R(z)^{-2/3} V_{C\infty}^{1/3}$$

where Sc and Pr are the Schmidt and Prandtl numbers, respectively, and $R(z)$ is the radius of the spinning line at every z distance. For DMF in air and for the conditions previously described, Sc = 1.81 and Pr = 0.69.

Chapters 2 and 3 dealt with momentum transfer and rheological equations of state and their applications to polymer processing. In this chapter and the next one we are concerned with the other two transfers: mass and heat. A substantial number of polymer processes involve changes of composition of the component materials through mass diffusion and convection methods. In many cases these changes of composition do not necessarily involve chemical reactions. We describe some of these polymer processes below.

Mass transfer operations can be found in a number of polymer processing operations. For example, in the dry spinning of polymer solutions to form fibers we find operations, such as diffusion of the solvent within the filaments and convective mass transfer from the filament surfaces to a flowing gas. In the wet spinning of polymer solutions, the viscous polymer solution is extruded through a spinneret submerged in a bath of a nonsolvent. As the filament passes through the bath of liquid, the nonsolvent diffuses into the filament, while the solvent diffuses out. As a result, the fiber is solidified. Foaming of polymer materials in an extruder involves the diffusion of the physical blowing agent to the nucleation sites and subsequent growth of gas bubbles. The formation of a microfoam, that is, a foam with a final bubble size of about 10 μm and less, is controlled by the diffusional aspects of the blowing agent (usually nitrogen or carbon dioxide gas). Drying of polymer pellets before processing is an example of the use of mass transfer in preprocessing stages. The presence of extensive moisture in the pellets can render the final product unacceptable. The size of the dispersed phase in a polymer blend and consequently its mechanical properties are controlled by the mutual diffusivity and time of the mixing step. Finally, mass transfer occurs in the removal of volatiles from polymers inside an extruder (this process is called devolatilization), where residual monomers or volatile fluids diffuse out of the polymer.

In addition to polymer processing operations, mass transfer is involved in many applications of polymers. For example, successful packaging of food and beverages is made possible through the use of barrier polymers, which impede the diffusion of gases, such as oxygen and carbon dioxide, as well as flavors, aroma, and odors. Plastic fuel tanks are made possible by exploiting the barrier properties of some polymers to hydrocarbons. Similarly, drug packages contain layers of various polymers that can provide a controlled drug release. Welding and crack healing of polymers can be modeled as a diffusional process.

We do not intend in this chapter to present an extensive analysis of mass transfer concepts but, rather, to summarize the basics of mass transfer as required in the design and analysis of polymer processing operations. In this regard, we give only an extensive overview of the estimation techniques for the diffusivity, solubility, and permeability of solvents in polymers. The laws of diffusional mass transfer, as well as the relationships for convective mass transfer, remain the same as applied to any material. The books by Perry and Chilton (1973), Reid et al. (1977), and Brandrup and Immergut (1989) provide an extensive overview of experimental data and formulas for the calculation of diffusivity, solubility, and permeability of various polymer systems.

This chapter is organized as follows. In Section 4.1 we describe the fundamentals of mass transfer, such as the various definitions for concentrations and velocities, Fick's first law of diffusion, and the microscopic mass balance principle.

In this section the analogy between heat and mass transfer is introduced and used to solve problems. The specific estimation relationships for permeants in polymers are discussed in Section 4.2 with the emphasis placed on gas-polymer systems. This section provides the necessary formulas for a first approximation of the diffusivity, solubility, and permeability, and their dependence on temperature. Non-Fickian transport, which is frequently present in high activity permeants in glassy polymers, is introduced in Section 4.3. Convective mass transfer coefficients are discussed in Section 4.4, and the analogies between mass and heat transfer are used to solve problems involving convective mass transfer. Finally, in Section 4.5 the solution to Design Problem III is presented.

4.1 MASS TRANSFER FUNDAMENTALS

This section includes the terminology for concentrations, velocities, and fluxes and their relationships. Although the discussion of new physical situations is limited, knowledge of the definitions is necessary for the next sections. Fick's first and second laws and the microscopic mass balance principle are introduced. Finally, simple cases based on the analogy between heat and mass transfer are analyzed.

4.1.1 Definitions of Concentrations and Velocities

The concentrations of the species in a multicomponent system can be expressed in various forms. Four of these forms, which are the most frequently used, are the following. *Mass concentration*, ρ_i , is the mass of species i per unit volume of the solution. Similarly, *molar concentration*, C_i , is the number of moles of species i per unit volume of the solution. *Mass fraction*, ω_i , is the mass of species i divided by the total mass of the solution. Finally, the *mole fraction*, x_i , is the number of moles of species i divided by the total number of moles of the solution. The total mass and molar concentrations are ρ and C , respectively, so that ω_i and x_i are given as

$$\omega_i = \frac{\rho_i}{\rho} \quad \text{and} \quad x_i = \frac{C_i}{C} \quad (4.1)$$

Table 4.1 presents the above definitions and some of their relations for a binary system.

The species in a diffusing mixture move with different velocities. If \mathbf{v}_i is the velocity of the i th species with respect to a fixed coordinate system, then the *mass average bulk velocity*, \mathbf{v} , is defined as

$$\mathbf{v} \equiv \frac{\sum_{i=1}^n \rho_i \mathbf{v}_i}{\sum_{i=1}^n \rho_i} = \frac{\sum_{i=1}^n \rho_i \mathbf{v}_i}{\rho} \quad (4.2)$$

TABLE 4.1 Definitions for Concentrations in Binary Systems

$\rho = \rho_A + \rho_B =$ mass density of solution (g/cm ³)	(A)
$\rho_A = C_A M_A =$ mass concentration of A (g of A/cm ³ of solution)	(B)
$\omega_A = \frac{\rho_A}{\rho} =$ mass fraction of A	(C)
$C = C_A + C_B =$ molar density of solution (g-moles/cm ³)	(D)
$C_A = \frac{\rho_A}{M_A} =$ molar concentration of A (g-moles of A/cm ³ of solution)	(E)
$x_A = \frac{C_A}{C} =$ mole fraction of A	(F)
$M = \frac{\rho}{C} =$ number-mean molecular weight of mixture	(G)
$x_A + x_B = 1$	(H)
$\omega_A + \omega_B = 1$	(I)
$x_A M_A + x_B M_B = M$	(J)
$\frac{\omega_A}{M_A} + \frac{\omega_B}{M_B} = \frac{1}{M}$	(K)
$x_A = \frac{\frac{\omega_A}{M_A}}{\frac{\omega_A}{M_A} + \frac{\omega_B}{M_B}}$	(L)
$\omega_A = \frac{x_A M_A}{x_A M_A + x_B M_B}$	(M)

Source: Bird et al., 1960.

where n is the total number of species in the system. Similarly, the *molar average bulk velocity*, \mathbf{v}^* , is defined as

$$\mathbf{v}^* \equiv \frac{\sum_{i=1}^n C_i \mathbf{v}_i}{\sum_{i=1}^n C_i} = \frac{\sum_{i=1}^n C_i \mathbf{v}_i}{C} \quad (4.3)$$

Finally, the *volume average bulk velocity*, \mathbf{v}^\bullet , is defined as

$$\mathbf{v}^\bullet = \sum_{i=1}^n \rho_i \mathbf{v}_i \frac{\bar{V}_i}{M_i} \quad (4.4)$$

where \bar{V}_i and M_i are the molar volume and molecular weight of component i , respectively. Note that $\rho \mathbf{v}$ and $C \mathbf{v}^*$ represent the local rates of mass and molar transport through planes perpendicular to \mathbf{v} and \mathbf{v}^* , respectively.

The velocity of the i th species, \mathbf{v}_i , can also be written as

$$\mathbf{v}_i = (\mathbf{v}_i - \mathbf{v}) + \mathbf{v} \quad (4.5)$$

This implies that the total mass flux of the i th species relative to a fixed coordinate system consists of two fluxes: one is due to the molecular diffusion (diffusion velocity: $\mathbf{v}_i - \mathbf{v}$) and the other is due to bulk movement (bulk velocity: \mathbf{v}). Similar arguments hold for the total molar and volume fluxes. This partitioning is necessary, because interdiffusion of unequal size molecules of two components causes bulk flow, even in the absence of an external bulk flow. Table 4.2 summarizes the definitions of the average velocities and their relations. The following example (basic features of which are drawn

TABLE 4.2 Definitions for Velocities in Binary Systems

Basic Definitions	
$\mathbf{v}_A =$ velocity of species A relative to fixed coordinates	(A)
$\mathbf{v}_A - \mathbf{v} =$ diffusion velocity of species A relative to \mathbf{v}	(B)
$\mathbf{v}_A - \mathbf{v}^* =$ diffusion velocity of species A relative to \mathbf{v}^*	(C)
$\mathbf{v}_A - \mathbf{v}^\bullet =$ diffusion velocity of species A relative to \mathbf{v}^\bullet	(D)
$\mathbf{v} =$ mass average velocity =	(E)
$(1/\rho)(\rho_A \mathbf{v}_A + \rho_B \mathbf{v}_B) = \omega_A \mathbf{v}_A + \omega_B \mathbf{v}_B$	
$\mathbf{v}^* =$ molar average velocity =	(F)
$(1/C)(C_A \mathbf{v}_A + C_B \mathbf{v}_B) = x_A \mathbf{v}_A + x_B \mathbf{v}_B$	
$\mathbf{v}^\bullet =$ volume average velocity =	(G)
$\rho_A \mathbf{v}_A \bar{V}_A / M_A + \rho_B \mathbf{v}_B \bar{V}_B / M_B$	
Additional Relations	
$\mathbf{v} - \mathbf{v}^* = \omega_A (\mathbf{v}_A - \mathbf{v}^*) + \omega_B (\mathbf{v}_B - \mathbf{v}^*)$	(H)
$\mathbf{v}^* - \mathbf{v} = x_A (\mathbf{v}_A - \mathbf{v}) + x_B (\mathbf{v}_B - \mathbf{v})$	(I)

Source: Bird et al., 1960.

from Bird et al., 1960) illustrates the meaning of the various velocities for a binary mixture.

Example 4.1. Velocities and Their Meaning

Consider a long tube that contains liquid A and vapor B (Fig. 4.1). The liquid starts evaporating, and it moves in the region initially filled with B. Calculate the velocity vectors \mathbf{v} and \mathbf{v}_B , for $x_A = 1/6$, $\mathbf{v}^* = 12$, $\mathbf{v}_A = 15$, and $M_A = 5M_B$. How do \mathbf{v} and \mathbf{v}_B change if $M_A = M_B$?

Solution. Figure 4.1a shows the schematic of the system. A and B diffuse along the z axis in the positive and negative directions, respectively. At the z position where $x_A = 1/6$ the velocities are found as follows:

$$\mathbf{v}_B = \frac{\mathbf{v}^* - x_A \mathbf{v}_A}{x_B} = \frac{57}{5} \quad (4.6)$$

The ratios of the component molecular weight to the number-mean molecular weight of the mixture are

$$\frac{M_A}{M} = 3, \quad \frac{M_B}{M} = \frac{3}{5} \quad (4.7)$$

and, thus, the mass average velocity \mathbf{v} is calculated as

$$\mathbf{v} = 3x_A \mathbf{v}_A + \frac{3}{5}x_B \mathbf{v}_B = \frac{66}{5} \quad (4.8)$$

The velocity vectors for both components are shown in Figure 4.1b. For component A, the diffusion velocity accounts for only 12% of the velocity of that component with respect to a fixed coordinate system with the remaining 88% being attributed to the bulk flow. The diffusion velocity for component B is negative (about 14% of \mathbf{v}), because it flows in the negative z direction. $\mathbf{v} = \mathbf{v}^*$ when the molecular weights of the components are equal. In that case, the

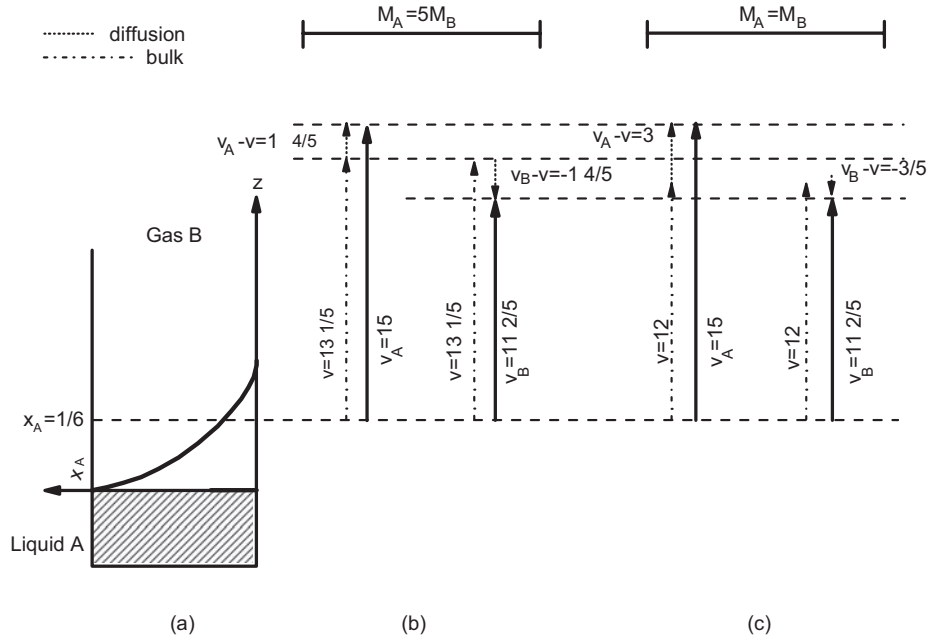


FIGURE 4.1 (a) Long tube for diffusion experiments. (b) Velocity vectors for the case of $M_A/M_B = 5$. (c) Velocity vectors for the case of $M_A/M_B = 1$.

diffusion velocity for component A accounts for 20% of v_A (Fig. 4.1.c), and the diffusion velocity for component B is negative and close to zero (about 5% of v). ■

4.1.2 Fluxes and Their Relationships

Once the velocities are known, the fluxes, both mass and molar, can be evaluated. The flux is a vector quantity, and its magnitude denotes the mass (or moles) passing through a unit area per unit time. Depending on the velocity we choose, we can define mass and molar fluxes *relative to stationary coordinates, relative to the mass average velocity, v, and relative to the molar average velocity, v**. Thus, the mass and molar fluxes relative to fixed coordinates are defined as

$$\begin{aligned} \mathbf{n}_i &= \rho_i \mathbf{v}_i && \text{mass} \\ \mathbf{N}_i &= C_i \mathbf{v}_i && \text{molar} \end{aligned} \tag{4.9}$$

Similarly, the fluxes with respect to the mass average velocity, v , are defined as

$$\begin{aligned} \mathbf{j}_i &= \rho_i (\mathbf{v}_i - \mathbf{v}) && \text{mass} \\ \mathbf{J}_i &= C_i (\mathbf{v}_i - \mathbf{v}) && \text{molar} \end{aligned} \tag{4.10}$$

and the fluxes with respect to the molar average velocity are defined as

$$\begin{aligned} \mathbf{j}_i^* &= \rho_i (\mathbf{v}_i - \mathbf{v}^*) && \text{mass} \\ \mathbf{J}_i^* &= C_i (\mathbf{v}_i - \mathbf{v}^*) && \text{molar} \end{aligned} \tag{4.11}$$

The mass and molar fluxes with respect to the volume average velocity v^* can be formulated similarly, but their uses are limited, and thus we omit them. Table 4.3 summarizes the various definitions and relations for the mass and molar fluxes of a binary system. The most frequently used definitions are those of molar fluxes N_i and J_i^* , and mass flux j_i . Actually, N_i is used in engineering applications, because it offers the advantage of a fixed coordinate system, whereas the fluxes j_i and J_i^* are the usual measures of diffusion rates. Both definitions will be used in the subsequent analysis of mass transfer.

4.1.3 Fick’s First Law of Diffusion

In analogy with momentum and heat transfer, mass transfer is governed by a simple law of diffusion, Fick’s first law. This law states that component A moves relative to the bulk motion (diffuses) in the direction of decreasing mole fraction of A:

$$\mathbf{J}_A^* = -D_{AB} \nabla C_A \tag{4.12}$$

where D_{AB} is the *mutual diffusion coefficient* or *mass diffusivity* or *interdiffusion coefficient* or simply *diffusion coefficient* in the binary system of A and B. Note that in a binary system $D_{AB} = D_{BA}$.

Table 4.4 summarizes some of the different expressions for Fick’s first law. In principle, any of these expressions can be used to solve a diffusion problem, but the right choice of the expression helps in reducing the mathematical complexities involved. The right choice depends on the specific

TABLE 4.3 Mass and Molar Fluxes in Binary Systems

Quantity	With Respect to Stationary Axes		With Respect to \mathbf{v}		With Respect to \mathbf{v}^*
Basic Definitions					
Velocity of species A (cm/s)	\mathbf{v}_A	(A)	$\mathbf{v}_A - \mathbf{v}$	(B)	$\mathbf{v}_A - \mathbf{v}^*$ (C)
Mass flux of species A (g/cm ² ·s)	$\mathbf{n}_A = \rho_A \mathbf{v}_A$	(D)	$\mathbf{j}_A = \rho_A (\mathbf{v}_A - \mathbf{v})$	(E)	$\mathbf{j}_A^* = \rho_A (\mathbf{v}_A - \mathbf{v}^*)$ (F)
Molar flux of species A (g-moles/cm ² ·s)	$\mathbf{N}_A = C_A \mathbf{v}_A$	(G)	$\mathbf{J}_A = C_A (\mathbf{v}_A - \mathbf{v})$	(H)	$\mathbf{J}_A^* = C_A (\mathbf{v}_A - \mathbf{v}^*)$ (I)
Relations Among the Fluxes					
Sum of mass fluxes (g/cm ² ·s)	$\mathbf{n}_A + \mathbf{n}_B = \rho \mathbf{v}$	(J)	$\mathbf{j}_A + \mathbf{j}_B = 0$	(K)	$\mathbf{j}_A^* + \mathbf{j}_B^* = \rho (\mathbf{v} - \mathbf{v}^*)$ (L)
Sum of molar fluxes (g-moles/cm ² ·s)	$\mathbf{N}_A + \mathbf{N}_B = C \mathbf{v}^*$	(M)	$\mathbf{J}_A + \mathbf{J}_B = C (\mathbf{v}^* - \mathbf{v})$	(N)	$\mathbf{J}_A^* + \mathbf{J}_B^* = 0$ (O)
Fluxes in terms of \mathbf{n}_A and \mathbf{n}_B	$\mathbf{N}_A = \frac{\mathbf{n}_A}{M_A}$	(P)	$\mathbf{j}_A = \mathbf{n}_A - \omega_A (\mathbf{n}_A + \mathbf{n}_B)$	(Q)	$\mathbf{j}_A^* = \mathbf{n}_A - x_A \left(\mathbf{n}_A + \frac{M_A}{M_B} \mathbf{n}_B \right)$ (R)
Fluxes in terms of \mathbf{N}_A and \mathbf{N}_B	$\mathbf{n}_A = \mathbf{N}_A M_A$	(S)	$\mathbf{J}_A = \mathbf{N}_A - \omega_A \left(\mathbf{N}_A + \frac{M_B}{M_A} \mathbf{N}_B \right)$	(T)	$\mathbf{J}_A^* = \mathbf{N}_A - x_A (\mathbf{N}_A + \mathbf{N}_B)$ (U)
Fluxes in terms of \mathbf{j}_A and \mathbf{v}	$\mathbf{n}_A = \mathbf{j}_A + \rho_A \mathbf{v}$	(V)	$\mathbf{J}_A = \frac{\mathbf{j}_A}{M_A}$	(W)	$\mathbf{J}_A^* = \frac{M}{M_B} \mathbf{j}_A$ (X)
Fluxes in terms of \mathbf{J}_A^* and \mathbf{v}^*	$\mathbf{N}_A = \mathbf{J}_A^* + C_A \mathbf{v}^*$	(Y)	$\mathbf{J}_A = \frac{M_B}{M} \mathbf{J}_A^*$	(Z)	$\mathbf{J}_A^* = \mathbf{J}_A^* M_A$ (AA)

Source: Reprinted by permission of the publisher from Bird et al., 1960.

problem. One of the most frequently used expressions relates the molar flux to the mole fraction of component A as follows (see also Problem 4A.1):

$$\mathbf{N}_A = x_A (\mathbf{N}_A + \mathbf{N}_B) - C \mathcal{D}_{AB} \nabla x_A \quad (4.13)$$

This equation shows that the molar flux of one component is the sum of two contributions: one from the bulk motion of the fluid and the other from the molar flux of the component due to diffusion.

The equations for mass, heat, and momentum transfer, that is, Eqs. 4.12, 5.18 and 2.3, are analogous. All state that

TABLE 4.4 Forms of Fick's First Law of Diffusion in Binary Systems

Flux	Gradient	Form of Fick's First Law
\mathbf{n}_A	$\nabla \omega_A$	$\mathbf{n}_A - \omega_A (\mathbf{n}_A + \mathbf{n}_B) = -\rho \mathcal{D}_{AB} \nabla \omega_A$ (A)
\mathbf{N}_A	∇x_A	$\mathbf{N}_A - x_A (\mathbf{N}_A + \mathbf{N}_B) = -C \mathcal{D}_{AB} \nabla x_A$ (B)
\mathbf{j}_A	$\nabla \omega_A$	$\mathbf{j}_A = -\rho \mathcal{D}_{AB} \nabla \omega_A$ (C)
\mathbf{J}_A^*	∇x_A	$\mathbf{J}_A^* = -C \mathcal{D}_{AB} \nabla x_A$ (D)
\mathbf{j}_A	∇x_A	$\mathbf{j}_A = -\left(\frac{C^2}{\rho} \right) M_A M_B \mathcal{D}_{AB} \nabla x_A$ (E)
\mathbf{J}_A^*	$\nabla \omega_A$	$\mathbf{J}_A^* = -\left(\frac{\rho^2}{C M_A M_B} \right) \mathcal{D}_{AB} \nabla \omega_A$ (F)

Source: Bird et al., 1960.

mass, energy, and momentum are transferred because of a gradient in concentration, temperature, and velocity, respectively. Also, the proportionality constants in all these equations (mass and thermal diffusivity and kinematic viscosity) have the same dimensions of length²/time. These analogies break down in two- and three-dimensional problems, because stress is a tensorial quantity, whereas heat and mass (or molar) fluxes are vectors.

Example 4.2. Mass Flux in a Polymer Membrane-Penetrant System

Calculate the mass flux of a penetrant diffusing through a polymer membrane as a function of the penetrant mass fraction. Start with the definition of the mass flux with respect to the mass average velocity.

Solution. For the binary system of the polymer membrane (P) and the diffusing species (A) Eq. 4.10 yields

$$\mathbf{j}_A = \rho_A (\mathbf{v}_A - \mathbf{v}) = \rho_A \mathbf{v}_A - \frac{\rho_A}{\rho} (\rho_A \mathbf{v}_A + \rho_P \mathbf{v}_P) \quad (4.14)$$

The velocity of the membrane with respect to a fixed reference system, \mathbf{v}_P , is zero. Hence,

$$\mathbf{j}_A = \mathbf{n}_A - \omega_A \mathbf{n}_A = -\rho \mathcal{D}_{AB} \nabla \omega_A \quad (4.15)$$

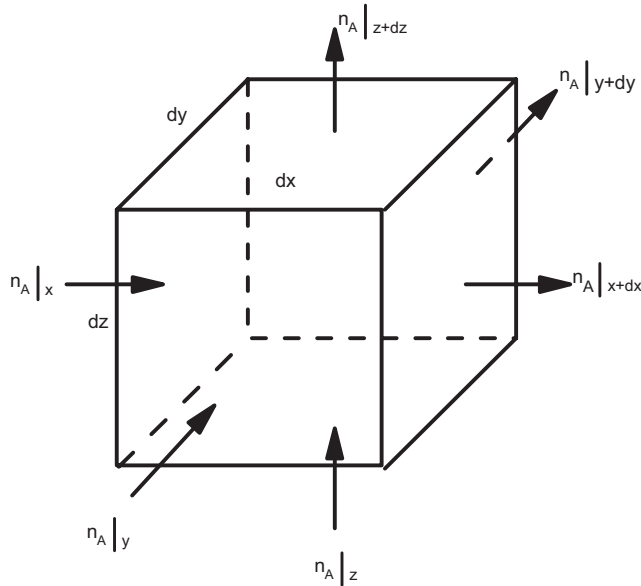


FIGURE 4.2 Differential volume element for the microscopic material balance.

and thus,

$$\mathbf{n}_A = \frac{-\rho D_{AB}}{1 - \omega_A} \nabla \omega_A \quad (4.16)$$

In typical polymer membrane–gas systems, the term $1/(1 - \omega_A)$ is approximately equal to 1, so that Eq. 4.16 is further simplified. However, in polymer membrane–solvent systems, ω_A can be significant, and it cannot be neglected in Eq. 4.16. ■

4.1.4 Microscopic Material Balance

Microscopic material balance is based on the conservation of mass. The law of conservation of mass for material A flowing in and out of a differential volume element $dx \, dy \, dz$ (Fig. 4.2) in its rate form states that

$$\begin{aligned} \text{(Rate of accumulation in the element)} &= \\ & \text{(Rate of transport into the element)} \\ & - \text{(Rate of transport out of the element)} \\ & + \text{(Rate of generation in the element)} \\ & - \text{(Rate of consumption in the element)} \end{aligned} \quad (4.17)$$

This mass balance is similar to Eqs. 2.15 and 5.15, which contain the momentum and energy balances, respectively.

The rate of generation and consumption (net rate of mass production) of material A in Eq. 4.17 refers to chemical reactions, and it will be denoted as \dot{r}_A (dimensions: mass/volume-time). If we consider that the volume element

of Figure 4.2 is fixed in space (*Eulerian approach*) Eq. 4.17 can be written as

$$\begin{aligned} dx \, dy \, dz \frac{\partial \rho_A}{\partial t} &= (n_{Ax|x} - n_{Ax|x+dx}) \, dy \, dz \\ &+ (n_{Ay|y} - n_{Ay|y+dy}) \, dx \, dz \\ &+ (n_{Az|z} - n_{Az|z+dz}) \, dx \, dy + \dot{r}_A \, dx \, dy \, dz \end{aligned} \quad (4.18)$$

Dividing this equation by $dx \, dy \, dz$ and shrinking the differential volume to zero, we get the microscopic mass balance (or *continuity*) equation as follows:

$$\frac{\partial \rho_A}{\partial t} + \frac{\partial n_{Ax}}{\partial x} + \frac{\partial n_{Ay}}{\partial y} + \frac{\partial n_{Az}}{\partial z} - \dot{r}_A = 0 \quad (4.19)$$

or in vector notation,

$$\frac{\partial \rho_A}{\partial t} + \nabla \cdot \mathbf{n}_A - \dot{r}_A = 0 \quad (4.20)$$

Obviously, a similar expression holds for every component i of a multicomponent system. Table 4.5 summarizes the continuity equations in terms of mass fluxes for component A in rectangular, cylindrical, and spherical coordinates. In terms of molar fluxes, Eq. 4.20 becomes

$$\frac{\partial C_A}{\partial t} + \nabla \cdot \mathbf{N}_A - \dot{R}_A = 0 \quad (4.21)$$

where \dot{R}_A is the net molar production of component A in mol/volume-time. Table 4.6 summarizes the continuity equations in terms of molar fluxes for component A in rectangular, cylindrical, and spherical coordinates.

By summing all the continuity equations for each component i and noting that the sum of all net mass productions due to reaction, $\sum \dot{r}_i$, is equal to zero, we get

$$\frac{\partial \rho}{\partial t} + \nabla \cdot (\rho \mathbf{v}) = 0 \quad (4.22)$$

where use of Table 4.3 was made. This is the *continuity equation for the mixture*. For a fluid mixture with constant density we note that Eq. 4.22 becomes

$$\nabla \cdot \mathbf{v} = 0 \quad (4.23)$$

which is the familiar continuity equation for incompressible flow (e.g., Eq. 2.58 or Table 2.8). If we use molar fluxes in place of mass fluxes, the equivalent continuity equation for the mixture becomes

$$\frac{\partial C}{\partial t} + \nabla \cdot (C \mathbf{v}^*) - \sum_{i=1}^n \dot{R}_i = 0 \quad (4.24)$$

Note that, in general, the sum of the rates of molar productions by chemical reactions cannot be set equal to zero unless

TABLE 4.5 Forms of Continuity Equation of Species A with Mass Fluxes (No Chemical Reactions)
A. Continuity Equation of Species A in Various Coordinate Systems

Rectangular coordinates:

$$\frac{\partial \rho_A}{\partial t} + \left(\frac{\partial n_{Ax}}{\partial x} + \frac{\partial n_{Ay}}{\partial y} + \frac{\partial n_{Az}}{\partial z} \right) = 0 \quad (\text{A})$$

Cylindrical coordinates:

$$\frac{\partial \rho_A}{\partial t} + \left(\frac{1}{r} \frac{\partial (r n_{Ar})}{\partial r} + \frac{1}{r} \frac{\partial n_{A\theta}}{\partial \theta} + \frac{\partial n_{Az}}{\partial z} \right) = 0 \quad (\text{B})$$

Spherical coordinates:

$$\frac{\partial \rho_A}{\partial t} + \left(\frac{1}{r^2} \frac{\partial (r^2 n_{Ar})}{\partial r} + \frac{1}{r \sin \theta} \frac{\partial (n_{A\theta} \sin \theta)}{\partial \theta} + \frac{1}{r \sin \theta} \frac{\partial n_{A\phi}}{\partial \phi} \right) = 0 \quad (\text{C})$$

B. Continuity Equation of Species A for Constant ρ and \mathcal{D}_{AB}

Rectangular coordinates:

$$\frac{\partial \rho_A}{\partial t} + \left(v_x \frac{\partial \rho_A}{\partial x} + v_y \frac{\partial \rho_A}{\partial y} + v_z \frac{\partial \rho_A}{\partial z} \right) = \mathcal{D}_{AB} \left(\frac{\partial^2 \rho_A}{\partial x^2} + \frac{\partial^2 \rho_A}{\partial y^2} + \frac{\partial^2 \rho_A}{\partial z^2} \right) \quad (\text{D})$$

Cylindrical coordinates:

$$\frac{\partial \rho_A}{\partial t} + \left(v_r \frac{\partial \rho_A}{\partial r} + v_\theta \frac{1}{r} \frac{\partial \rho_A}{\partial \theta} + v_z \frac{\partial \rho_A}{\partial z} \right) = \mathcal{D}_{AB} \left(\frac{1}{r} \frac{\partial}{\partial r} \left(r \frac{\partial \rho_A}{\partial r} \right) + \frac{1}{r^2} \frac{\partial^2 \rho_A}{\partial \theta^2} + \frac{\partial^2 \rho_A}{\partial z^2} \right) \quad (\text{E})$$

Spherical coordinates:

$$\begin{aligned} \frac{\partial \rho_A}{\partial t} + \left(v_r \frac{\partial \rho_A}{\partial r} + v_\theta \frac{1}{r} \frac{\partial \rho_A}{\partial \theta} + v_\phi \frac{1}{r \sin \theta} \frac{\partial \rho_A}{\partial \phi} \right) \\ = \mathcal{D}_{AB} \left(\frac{1}{r^2} \frac{\partial}{\partial r} \left(r^2 \frac{\partial \rho_A}{\partial r} \right) + \frac{1}{r^2 \sin \theta} \frac{\partial}{\partial \theta} \left(\sin \theta \frac{\partial \rho_A}{\partial \theta} \right) + \frac{1}{r^2 \sin^2 \theta} \frac{\partial^2 \rho_A}{\partial \phi^2} \right) \end{aligned} \quad (\text{F})$$

TABLE 4.6 Forms of Continuity Equation of Species A with Molar Fluxes (No Chemical Reactions)
A. Molar Flux of Species A in Various Coordinate Systems

Rectangular coordinates:

$$\frac{\partial C_A}{\partial t} + \left(\frac{\partial N_{Ax}}{\partial x} + \frac{\partial N_{Ay}}{\partial y} + \frac{\partial N_{Az}}{\partial z} \right) = 0 \quad (\text{A})$$

Cylindrical coordinates:

$$\frac{\partial C_A}{\partial t} + \left(\frac{1}{r} \frac{\partial (r N_{Ar})}{\partial r} + \frac{1}{r} \frac{\partial N_{A\theta}}{\partial \theta} + \frac{\partial N_{Az}}{\partial z} \right) = 0 \quad (\text{B})$$

Spherical coordinates:

$$\frac{\partial C_A}{\partial t} + \left(\frac{1}{r^2} \frac{\partial (r^2 N_{Ar})}{\partial r} + \frac{1}{r \sin \theta} \frac{\partial (N_{A\theta} \sin \theta)}{\partial \theta} + \frac{1}{r \sin \theta} \frac{\partial N_{A\phi}}{\partial \phi} \right) = 0 \quad (\text{C})$$

B. Continuity Equation of Species A for Constant ρ and \mathcal{D}_{AB}

Rectangular coordinates:

$$\frac{\partial C_A}{\partial t} + \left(v_x \frac{\partial C_A}{\partial x} + v_y \frac{\partial C_A}{\partial y} + v_z \frac{\partial C_A}{\partial z} \right) = \mathcal{D}_{AB} \left(\frac{\partial^2 C_A}{\partial x^2} + \frac{\partial^2 C_A}{\partial y^2} + \frac{\partial^2 C_A}{\partial z^2} \right) \quad (\text{D})$$

Cylindrical coordinates:

$$\frac{\partial C_A}{\partial t} + \left(v_r \frac{\partial C_A}{\partial r} + v_\theta \frac{1}{r} \frac{\partial C_A}{\partial \theta} + v_z \frac{\partial C_A}{\partial z} \right) = \mathcal{D}_{AB} \left(\frac{1}{r} \frac{\partial}{\partial r} \left(r \frac{\partial C_A}{\partial r} \right) + \frac{1}{r^2} \frac{\partial^2 C_A}{\partial \theta^2} + \frac{\partial^2 C_A}{\partial z^2} \right) \quad (\text{E})$$

Spherical coordinates:

$$\begin{aligned} \frac{\partial C_A}{\partial t} + \left(v_r \frac{\partial C_A}{\partial r} + v_\theta \frac{1}{r} \frac{\partial C_A}{\partial \theta} + v_\phi \frac{1}{r \sin \theta} \frac{\partial C_A}{\partial \phi} \right) \\ = \mathcal{D}_{AB} \left(\frac{1}{r^2} \frac{\partial}{\partial r} \left(r^2 \frac{\partial C_A}{\partial r} \right) + \frac{1}{r^2 \sin \theta} \frac{\partial}{\partial \theta} \left(\sin \theta \frac{\partial C_A}{\partial \theta} \right) + \frac{1}{r^2 \sin^2 \theta} \frac{\partial^2 C_A}{\partial \phi^2} \right) \end{aligned} \quad (\text{F})$$

the reaction is equimolar (i.e., for every mole of component i consumed one mole of component j is produced, etc.). For a fluid of constant molar density C , Eq. 4.24 yields

$$C \nabla \cdot \mathbf{v}^* = \sum_{i=1}^n \dot{R}_i \quad (4.25)$$

Neither form of the continuity equation for species A, that is, Eq. 4.20 or 4.21, are very useful as they stand. They can be written in terms of the mass and molar average velocities by combining Eqs. 4.10, 4.11, 4.20, and 4.21 as follows:

$$\frac{\partial \rho_A}{\partial t} + \nabla \cdot \mathbf{j}_A + \nabla \cdot (\rho_A \mathbf{v}) - \dot{r}_A = 0 \quad (4.26)$$

and

$$\frac{\partial C_A}{\partial t} + \nabla \cdot \mathbf{J}_A^* + \nabla \cdot (C_A \mathbf{v}^*) - \dot{R}_A = 0 \quad (4.27)$$

Combining these equations and the equations for \mathbf{n}_A and \mathbf{N}_A from Table 4.4 we get

$$\frac{\partial \rho_A}{\partial t} + \nabla \cdot (\rho_A \mathbf{v}) - \nabla \cdot (\mathcal{D}_{AB} \nabla \rho_A) - \dot{r}_A = 0 \quad (4.28)$$

and

$$\frac{\partial C_A}{\partial t} + \nabla \cdot (C_A \mathbf{v}^*) - \nabla \cdot (\mathcal{D}_{AB} \nabla C_A) - \dot{R}_A = 0 \quad (4.29)$$

These equations are valid for variable mass or molar density, ρ or C , and variable diffusion coefficient \mathcal{D}_{AB} . Their generality can be reduced in certain cases as is shown below.

Constant ρ and \mathcal{D}_{AB} and No Chemical Reaction. For that case, Eq. 4.28 becomes (using also the continuity Eq. 4.23)

$$\frac{\partial \rho_A}{\partial t} + \mathbf{v} \cdot \nabla \rho_A = \mathcal{D}_{AB} \nabla^2 \rho_A \quad (4.30)$$

This equation is typically used for diffusion in *dilute solutions*, and it is similar to equations used in momentum (Table 2.9 or Eq. 5.58) and heat transfer (Table 5.3 or Eq. 5.59). Table 4.5 summarizes the expressions for Eq. 4.30 for the three coordinate systems. Division of all terms of Eq. 4.30 by the molecular weight of A gives the forms of the continuity equation shown in Table 4.6. Finally, note that the left side of Eq. 4.30 can be written as $D(\rho_A)/Dt$, where D/Dt notes the material derivative.

Zero Mass or Molar Average Velocity and No Chemical Reaction. For this case, Eq. 4.28 (or Eq. 4.29) becomes

$$\frac{\partial \rho_A}{\partial t} = \nabla \cdot (\mathcal{D}_{AB} \nabla \rho_A) \quad (4.31)$$

which for constant \mathcal{D}_{AB} yields

$$\frac{\partial \rho_A}{\partial t} = \mathcal{D}_{AB} \nabla^2 \rho_A \quad (4.32)$$

which is called *Fick's second law of diffusion* or simply the *diffusion equation*. Note again that this equation is used in cases where \mathbf{v} is zero (i.e., diffusion in solids or stationary liquids) or \mathbf{v}^* is zero (i.e., equimolar counterdiffusion in gases). The similarity between Eq. 4.32 and the heat conduction equation is the basis for the similarity of solutions to these equations.

4.1.5 Similarity with Heat Transfer: Simple Applications

The majority of diffusion problems can be solved by recognizing their similarity to heat transfer problems. For example, Eqs. 4.30 and 4.32 are directly analogous to the heat transfer equations, as is illustrated in Table 4.7. Note that for this analogy to hold one should make the following substitutions: ρ_A or C_A in place of T and \mathcal{D}_{AB} in place of α (thermal diffusivity). More specifically, Figures 5.10, 5.11, 5.12, and 5.13, which present the graphical solutions of the unsteady heat conduction equation (see Table 4.7) for infinite slabs and cylinders, are equally well applicable to the unsteady diffusion equation (Eq. 4.32) for the same geometries and boundary conditions. For example, Figures 5.10 and 5.11 can also be considered to show the dimensionless concentration as a function of time and relative position in a slab and a cylinder, respectively, when their surfaces are kept at a constant concentration.

Furthermore, Figures 5.12 and 5.13 can also be used to show the dimensionless concentration as a function of dimensionless time and position for the case in which there is resistance to mass transfer at the interface between a solid and a fluid: $-\mathcal{D}_{AB} (\partial C_A / \partial z) = k_c (C_{Ai} - C_{A\infty})$, where k_c is the convective mass transfer coefficient (Section 4.4), C_{Ai} is the concentration of species A at the interface in the fluid side, and $C_{A\infty}$ is the concentration of species A in the fluid far away from the interface. Note that the constant concentration boundary condition referred to in the previous paragraph could be considered as a special case of the convective-type boundary condition for a Sherwood number, Sh (or Nusselt number for diffusion), equal to ∞ . Also, in Figures 5.12 and 5.13, the Biot (or Nusselt) number for heat transfer should be replaced by $(k_c b / \mathcal{D}_{AB}) (1/K) = (Sh/K) = Sh'$, where K is the ratio of the equilibrium concentration in the solid to the

TABLE 4.7 Analogy Between Heat Conduction and Mass Diffusion

Unsteady-State Nonflow	Steady-State Flow	Steady-State Nonflow
$\frac{\partial T}{\partial t} = \alpha \nabla^2 T$	$(\mathbf{v} \cdot \nabla T) = \alpha \nabla^2 T$	$\nabla^2 T = 0$
Heat conduction in solids	Heat conduction in laminar incompressible flow	Steady heat conduction in solids
1. $k = \text{constant}$	1. $k, \rho = \text{constants}$	1. $k = \text{constant}$
2. $\mathbf{v} = 0$	2. No viscous dissipation	2. $\mathbf{v} = 0$
	3. Steady state	3. Steady State
$\frac{\partial C_A}{\partial t} = \mathcal{D}_{AB} \nabla^2 C_A$	$(\mathbf{v} \cdot \nabla C_A) = \mathcal{D}_{AB} \nabla^2 C_A$	$\nabla^2 C_A = 0$
Diffusion of traces of A through B	Diffusion in laminar flow (dilute solutions of A in B)	Steady diffusion in solids
1. $\mathcal{D}_{AB}, \rho = \text{constants}$	1. $\mathcal{D}_{AB}, \rho = \text{constants}$	1. $\mathcal{D}_{AB}, \rho = \text{constants}$
2. $\mathbf{v} = 0$	2. Steady state	2. Steady state
3. No chemical reactions	3. No chemical reactions	3. No chemical reactions
		4. $\mathbf{v} = 0$
OR Equimolar counterdiffusion in low-density gases		
1. $\mathcal{D}_{AB}, C = \text{constants}$		
2. $\mathbf{v}^* = 0$		
3. No chemical reactions		

Source: Reprinted by permission of the publisher from Bird et al., 1960.

concentration in the surrounding fluid (also called partition coefficient or equilibrium distribution coefficient; it is a form of the Henry’s law constant of Section 4.2.1), and b is the half-thickness of the slab.

Figures 4.3 and 4.4 show the graphical solutions of the unsteady diffusion problem for a sphere, which is not covered in the heat transfer Chapter 5. C_{A0} and $C_{A\infty}$ in Figure 4.3 correspond to T_0 and T_1 , respectively, in Figures 5.12 and 5.13. Similarly, T_0 in Figures 5.12 and 5.13 should be replaced by

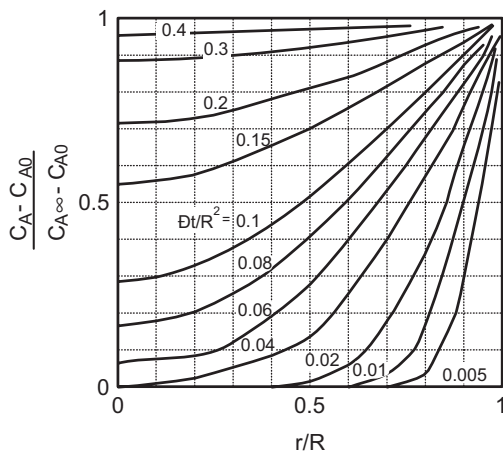


FIGURE 4.3 Concentration profiles for unsteady mass diffusion in a sphere of radius R . $C_A(R, t) = C_{A\infty}$; $C_A(r, 0) = C_{A0}$. (Reprinted by permission of the publisher from Crank, 1956.)

C_{A0} . Finally, in Figure 4.4, $C_{A\infty}^*$, which is the concentration of A in the solid in equilibrium with the concentration of A in the fluid $C_{A\infty}$ (i.e., $C_{A\infty}^* = K C_{A\infty}$), is used in place of $C_{A\infty}$.

One additional feature of mass transfer is the calculation of the amount absorbed or desorbed at time t , M_t , and its comparison to the total possible amount absorbed or desorbed, M_∞ (see also Problem 4B.1). Such comparisons as a function of the diffusivity, time, and length scale of the geometry are shown in Figure 4.5, for a slab, cylinder, and sphere. The parameter in this figure is the Sherwood number (or Sh'). The following examples illustrate the similarity between heat and mass transfer for the case of unsteady transfer in simple geometries.

Example 4.3. Diffusion in a Slab

An infinite slab of polypropylene (PP) is exposed to high-pressure nitrogen at time equal to zero. Calculate the exposure time required for the nitrogen concentration at the slab’s axis to reach 90% of its equilibrium value. The slab thickness is 0.318 cm and the diffusivity of nitrogen in PP is $3.87 \times 10^{-8} \text{ cm}^2/\text{s}$ at room temperature.

Solution. Figure 5.8 shows the PP slab exposed to constant concentration nitrogen gas. We assume that the slab edges are kept at this constant nitrogen concentration, which is also the equilibrium concentration of the whole slab. From

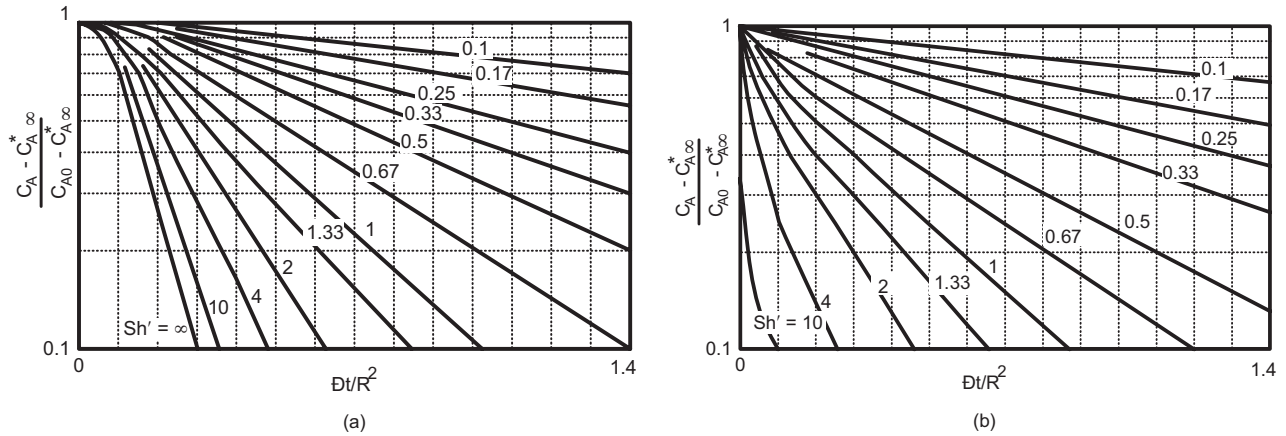


FIGURE 4.4 Dimensionless concentration in sphere (radius R) subjected to step change in surface concentration. $Sh' = k_c R / \mathcal{D}K$; $C_{A\infty}^* = K C_{A\infty}$ (a) Center of sphere. (b) Surface of sphere. (Reprinted by permission of the publisher from Boelter et al. 1965.)

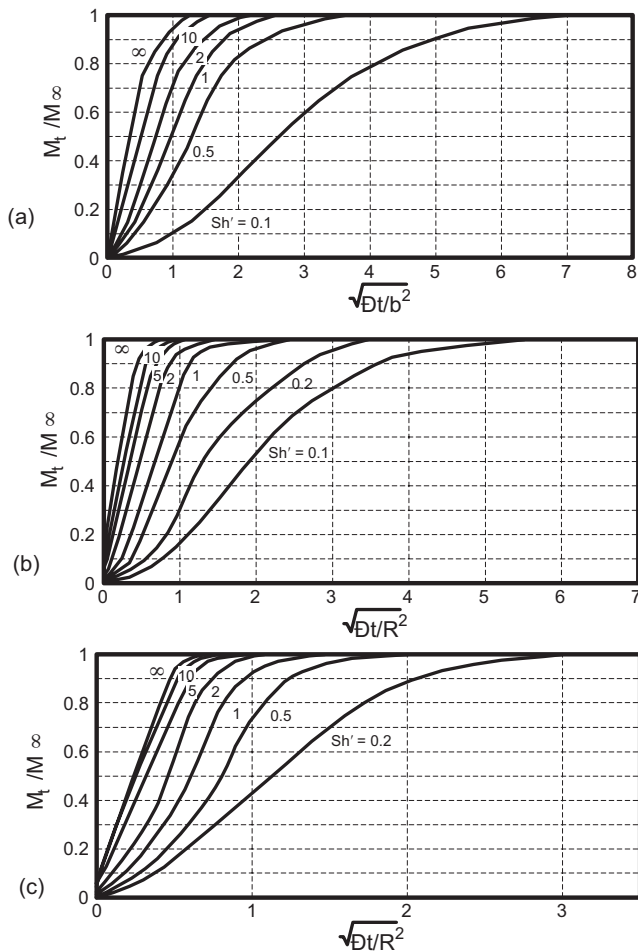


FIGURE 4.5 Ratio of the amount absorbed (or desorbed) at time t , M_t , to the total amount absorbed, M_∞ , as a function of time, for various values of $Sh' = k_c R / \mathcal{D}K$. (a) Slab of thickness $2b$. (b) Cylinder of radius $R = b$. (c) Sphere of radius $R = b$. (Reprinted by permission of the publisher from Crank, 1956.)

Figure 5.10, the 90% concentration at the centerline corresponds to $\mathcal{D}t/b^2 = 1.0$. Thus,

$$t = \frac{b^2}{\mathcal{D}} = \frac{(0.318/2)^2}{3.87 \times 10^{-8}} \text{s} = 7.56 \text{ days} \quad (4.33)$$

One way to reduce this long time is to increase the temperature of the experiment so that the diffusivity increases. ■

The graphical solutions in Figures 5.10, 5.11, and 4.3 can be combined to give solutions to multidimensional problems. For example, unsteady diffusion into a short cylindrical pellet is considered to consist of mass transfer in both the radial and axial directions. Thus, the solution for a short cylinder is

$$\left[\frac{C_A - C_{A\infty}}{C_{A0} - C_{A\infty}} \right]_{\text{short cylinder}} = \left[\frac{C_A - C_{A\infty}}{C_{A0} - C_{A\infty}} \right]_{\text{infinite cylinder}} \times \left[\frac{C_A - C_{A\infty}}{C_{A0} - C_{A\infty}} \right]_{\text{flat plate}} \quad (4.34)$$

where C_{A0} is the concentration in the short cylinder at time equal to zero and $C_{A\infty}$ is the concentration at equilibrium (or infinite time) with the surrounding medium (Hines and Maddox, 1985). Note that the ratio $(C_A - C_{A\infty}) / (C_{A0} - C_{A\infty})$ determines the difference of the concentration of species A at a certain point inside the cylinder from the equilibrium value in a percentage form. Similarly, diffusion in a parallelepiped consists of mass transfer in all three directions x , y , and z , and as such the solution is represented by the product of the flat plate solutions in each direction.

Example 4.4. Unsteady Diffusion in Multidimensional Objects

PP is extruded and pelletized into small cylindrical pellets. Pellets can be produced of three different sizes or surface areas. Pellets I have a diameter of $2R = 3 \text{ mm}$ and a length

of $2b = 3$ mm, pellets II have respective dimensions 2 mm and 6.75 mm, and pellets III have respective dimensions 2 mm and 5.75 mm. Thus, pellets I have the same surface area and larger volume than pellets III, and pellets I have the same volume and larger surface area than pellets II. These PP pellets should be saturated with nitrogen gas and then processed. Which type pellet will have a concentration closer to equilibrium saturation after 86,400 s (24 h) exposure to nitrogen? \mathcal{D} for nitrogen in PP at room temperature is 3.87×10^{-8} cm²/s.

Solution. For type I pellets at 86,400 s

$$\frac{\mathcal{D}t}{R^2} = 0.15; \quad \frac{\mathcal{D}t}{b^2} = 0.15 \quad (4.35)$$

and therefore the corresponding concentrations at the centerline are

$$\left[\frac{C_A - C_{A\infty}}{C_{A0} - C_{A\infty}} \right]_{\text{infinite cylinder}} = 0.34 \quad (4.36)$$

and

$$\left[\frac{C_A - C_{A\infty}}{C_{A0} - C_{A\infty}} \right]_{\text{plate}} = 0.15$$

The infinite cylinder value was obtained from Figure 5.11, while the plate value was obtained from Figure 5.10. Thus,

$$\left[\frac{C_A - C_{A\infty}}{C_{A0} - C_{A\infty}} \right]_{\text{pellets I}} = (1 - 0.34) \times (1 - 0.15) = 0.56 \quad (4.37)$$

Similarly,

$$\left[\frac{C_A - C_{A\infty}}{C_{A0} - C_{A\infty}} \right]_{\text{pellets II}} = (1 - 0.7) \times (1 - 0) = 0.3 \quad (4.38)$$

and

$$\left[\frac{C_A - C_{A\infty}}{C_{A0} - C_{A\infty}} \right]_{\text{pellets III}} = (1 - 0.7) \times (1 - 0) = 0.3 \quad (4.39)$$

Type I pellets are the closer to equilibrium saturation, and then come pellets II and III. ■

Example 4.5. Diffusion into a Falling Polymer Film

Consider the sorption of a dye, A, into a falling thin polymer film as shown in Figure 4.6. Assume that the flow of the film is fully developed and laminar, the process is at steady-state conditions, the solubility of the dye in the polymer is low, and no chemical reaction is present. Calculate the dye concentration profile in the polymer film as a function of time.

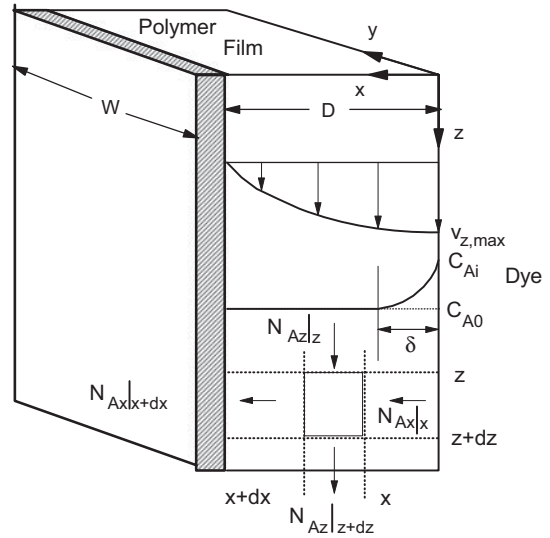


FIGURE 4.6 Diffusion of dye into a falling polymer film. Differential element and the fluxes.

Solution. In this example we will illustrate the use of the microscopic balances in solving mass transfer problems. Figure 4.6 shows the falling polymer film, its velocity profile, the concentration of the dye, and a microscopic element $dx dz$. It is evident from this figure that dye is transferred in both the x and z directions, so that a molar balance on the differential element yields

$$(N_{Ax|x} - N_{Ax|x+dx})W dz + (N_{Az|z} - N_{Az|z+dz})W dx = 0 \quad (4.40)$$

where W is the width of the film. Equation 4.40 becomes, on dividing by the volume of the element and taking the limit as dx and dz go to zero,

$$\frac{\partial N_{Ax}}{\partial x} + \frac{\partial N_{Az}}{\partial z} = 0 \quad (4.41)$$

Note that this equation could have been taken directly from Table 4.6.

The concentration of the dye at the film–dye solution interface is C_{Ai} , and in the main bulk of the film it is equal to C_{A0} (in this example $C_{A0} = 0$). If the dye is considered to be slightly soluble in the polymer (low concentrations are adequate for dyeing), it is logical to consider the thickness, δ , over which the concentration changes from C_{Ai} to C_{A0} , to be small relative to the film thickness, D . Consequently, the boundary conditions are

$$\text{B.C.1: } C_A = C_{A0} \quad \text{at } z = 0 \quad \text{for all } x \quad (4.42)$$

$$\text{B.C.2: } C_A = C_{A0} \quad \text{at } x = \infty \quad \text{for all } z \quad (4.43)$$

$$\text{B.C.3: } C_A = C_{Ai} \quad \text{at } x = 0 \quad \text{for all } z \quad (4.44)$$

Equation 4.13 can be written for the x coordinate as

$$N_{Ax} = -\mathcal{D}_{AP} \frac{\partial C_A}{\partial x} + x_A (N_{Ax} + N_{Px}) \quad (4.45)$$

Because the dye is slightly soluble, $x_A \cong 0$, and hence we can write

$$N_{Ax} \cong -\mathcal{D}_{AP} \frac{\partial C_A}{\partial x} \quad (4.46)$$

Similarly, in the z direction

$$N_{Az} = -\mathcal{D}_{AP} \frac{\partial C_A}{\partial z} + C_A v_z^* \quad (4.47)$$

In this direction we postulate that the convective flow is the predominant one, so that

$$N_{Az} \cong C_A v_z^* \quad (4.48)$$

Also, because the penetration, δ , of the dye into the film is small, we will be concerned only with the velocity at the surface, so that

$$N_{Az} \cong C_A v_{z,\max} \quad (4.49)$$

Equations 4.41, 4.46, and 4.49 can be combined as

$$\mathcal{D}_{AP} \frac{\partial^2 C_A}{\partial x^2} = \frac{\partial C_A}{\partial t} \quad (4.50)$$

where $t = z/v_{z,\max}$. Note that this equation represents unsteady-state diffusion and that we could have obtained this equation if we had allowed the differential element $dx dz$ to move with velocity $v_{z,\max}$. Also, note that Eq. 4.42 should be considered now as an initial condition, because $z = 0$ is equivalent to $t = 0$. The solution to Eq. 4.50 can be obtained by transforming it to an ordinary differential equation (see Bird et al., 1960, p. 125). After some algebraic manipulations this equation gives

$$\frac{C_A - C_{A0}}{C_{Ai} - C_{A0}} = 1 - \frac{2}{\sqrt{\pi}} \int_0^\eta e^{-\eta^2} d\eta = 1 - \text{erf}(\eta) \quad (4.51)$$

where $\eta = x/\sqrt{4\mathcal{D}_{AP}t}$ and $\text{erf}(\cdot)$ is the *error function*, which is tabulated in mathematical handbooks. Another type of problem treated with the same technique is that of diffusion in a semi-infinite slab (see Problem 4C.3a). Finally, note that this approach can be applied to the problem of devolatilization of a falling polymer film. ■

4.2 DIFFUSIVITY, SOLUBILITY, AND PERMEABILITY IN POLYMER SYSTEMS

In this section we analyze diffusive mass transport, as applied to polymer processing applications. The focus is on the estimation of the diffusion coefficient and solubility in the following three systems: gas–polymer, liquid–polymer, and polymer–polymer. The goal of this section is for the reader to be able to estimate the parameters of diffusional mass transfer for any polymer system using formulas and tables. Note that the diffusion coefficient is one of the two primary parameters of mass transfer, the other being the convective mass transfer coefficient discussed in Section 4.4. Typical values of diffusivity, solubility, and permeability can be found in the extensive collection by Brandrup and Immergut (1989).

4.2.1 Diffusivity and Solubility of Simple Gases

Simple gases in the following context are the noneasily condensable gases (low boiling and critical points) with weak molecular interactions. Typical examples are nitrogen, oxygen, helium, and so on at relatively low pressures or equivalently low activities. These gases can also be called *permanent gases*. Carbon dioxide (CO_2), sulfur dioxide (SO_2), methane (CH_4), and other similar gases can also be considered simple gases at relatively low pressures, although they are condensable. The model law, which finds direct application to the diffusivity and solubility of simple gases, is the *Lennard-Jones* equation:

$$\phi(r) = 4\epsilon \left[\left(\frac{\sigma}{r} \right)^{12} - \left(\frac{\sigma}{r} \right)^6 \right] \quad (4.52)$$

where $\phi(r)$ is the intermolecular energy of two molecules r distance apart, ϵ is the potential energy constant, and σ is the potential length constant. Note that ϵ and σ are also called the *Lennard-Jones scaling factors*. Division of ϵ by the Boltzmann constant k gives the *Lennard-Jones temperature* ϵ/k in Kelvin units, and σ is also called the *collision diameter* of the molecule. Properties of simple gases can be found in Table 4.8 and an extensive collection appears in Reid et al. (1977).

Simple gases interact weakly with polymers with a consequence that their diffusion behavior is *Fickian*. This means that the diffusion coefficient \mathcal{D} does not depend on concentration and time but only on temperature. The dependence on temperature is expressed by an Arrhenius type equation as

$$\mathcal{D} = \mathcal{D}_0 \exp(-E_{\mathcal{D}}/R_g T) \quad (4.53)$$

because diffusion of gases is considered to be a thermally activated process. \mathcal{D}_0 and $E_{\mathcal{D}}$ are constants for the particular gas–polymer system. $E_{\mathcal{D}}$ is the activation energy of diffusion, R_g is the universal gas constant, and \mathcal{D}_0 is the pre-exponential

TABLE 4.8 Boiling (T_b , K), Critical (T_{cr} , K), and Lennard-Jones (ϵ/k , K) Temperatures and Collision Diameter (σ , nm) of Various Gases

Gas	T_b (K)	T_{cr} (K)	ϵ/k (K)	σ (nm)
He	4.2	5.2	10.22	25.51
Air	—	—	78.6	37.11
N ₂	77.4	126.2	71.4	37.98
O ₂	90.2	154.6	106.7	34.67
H ₂	20.4	33.2	59.7	28.27
CO ₂	194.7	304.2	195.2	39.41
CO	81.7	132.9	91.7	36.90
Ar	87.3	150.8	93.3	35.42
CCl ₄	349.7	556.4	322.7	59.47
CH ₄	111.7	190.6	148.6	37.58
HCl	188.1	324.6	344.7	33.39
Cl ₂	238.7	417.0	316.0	42.17
H ₂ O	373.2	647.3	809.1	26.41
NH ₃	239.7	405.6	558.3	29.00
<i>o</i> -Xylene	417.6	630.2	532.30	60.00
C ₆ H ₆	353.3	562.1	412.3	53.49
<i>n</i> -C ₆ H ₁₄	341.9	507.4	399.3	59.49
<i>n</i> -C ₄ H ₁₀	272.7	425.2	531.4	46.87
C ₃ H ₈	231.1	369.8	237.1	51.18
<i>n</i> -C ₅ H ₁₂	309.2	469.6	341.1	57.84
CClF ₃ (CFC-13)	191.7	302.0	248.24	46.40
CCl ₂ F ₂ (CFC-12)	243.4	385.0	316.20	49.48
C ₂ Cl ₂ F ₄ (CFC-114)	276.9	418.9	349.64	54.87
CHClF ₂ (CFC-22)	232.4	369.2	305.66	45.77

Source: Reid et al., 1977.

factor in the same units as \mathcal{D} . The estimation of these two parameters follows.

The activation energy of diffusion, $E_{\mathcal{D}}$, is the most important parameter in the diffusion process. It is the energy necessary for the gas molecule to jump into a new position ("hole"). It is thus obvious that the larger the size of the diffusant molecule, the higher the activation energy and the lower the diffusivity are. The size of the gas molecule, x , is determined by its collision diameter, σ_x . If nitrogen gas is taken as the standard diffusing gas, then the activation energy is given by the following relations (Van Krevelen, 1990) for elastomers (and for polymers in the rubbery state):

$$10^{-3} \frac{E_{\mathcal{D}}}{R_g} = \left(\frac{\sigma_x}{\sigma_{N_2}} \right)^2 [7.5 - 2.5 \times 10^{-4}(298 - T_g)^2] \pm 0.6 \quad (4.54)$$

and for glassy amorphous polymers:

$$10^{-3} \frac{E_{\mathcal{D}}}{R_g} = \left(\frac{\sigma_x}{\sigma_{N_2}} \right)^2 [7.5 - 2.5 \times 10^{-4}(T_g - 298)^{3/2}] \pm 1.0 \quad (4.55)$$

In the above equations, $R_g = 8.314$ J/mol·K, and $E_{\mathcal{D}}$ is in kilojoules (kJ), so that the ratio $E_{\mathcal{D}}/R_g$ is in 1000 K. Also, T_g is in Kelvin units (K).

The other important parameter is the constant \mathcal{D}_0 . This was found to correlate with $E_{\mathcal{D}}$ rather well (Van Krevelen, 1990). For elastomers and glassy amorphous materials the correlations are

$$\log \mathcal{D}_0 = \frac{E_{\mathcal{D}} \times 10^{-3}}{R_g} - 4.0 \pm 0.4 \quad \text{for elastomers} \quad (4.56)$$

and

$$\log \mathcal{D}_0 \cong \frac{E_{\mathcal{D}} \times 10^{-3}}{R_g} - 5.0 \pm 0.8 \quad (4.57)$$

for glassy amorphous polymers

In these equations \mathcal{D}_0 is in cm²/s.

Finally, the diffusivity of a semicrystalline material, \mathcal{D}_{sc} , can be approximated as follows:

$$\mathcal{D}_{sc} \cong \mathcal{D}_a (1 - \phi_c) \quad (4.58)$$

where ϕ_c is the crystallinity of the material, and \mathcal{D}_a is the diffusivity of the corresponding completely amorphous material. In other words, the crystalline regions are considered impermeable to the gas. A number of diffusivity data for common gas-polymer systems at room temperature (25 °C) are compiled in Table 4.9. Brandrup and Immergut (1989), Duda et al. (1973) and Durrill and Griskey (1966) present some other data of gas diffusivities in polymers at elevated temperatures.

Example 4.6. Estimation of \mathcal{D}

Estimate the diffusivity of oxygen in polycarbonate at 298 K.

Solution. The collision diameter of oxygen is 34.67 nm (from Table 4.8) and the T_g of polycarbonate (PC) is 150 °C = 423 K (glassy amorphous polymer). From Eq. 4.55 we estimate the activation energy as

$$10^{-3} \frac{E_{\mathcal{D}}}{R_g} = \left(\frac{34.67}{37.98} \right)^2 [7.5 - 2.5 \times 10^{-4}(423 - 298)^{3/2}] \pm 1.0 = 5.96 \pm 1.0 \quad (4.59)$$

which gives $E_{\mathcal{D}} = 49.6 \pm 8.3$ kJ/mol. This value is higher than the experimentally observed value of 32.2 kJ/mol (Brandrup and Immergut, 1989). \mathcal{D}_0 (in cm²/s) is calculated from

TABLE 4.9 Diffusivity (\mathcal{D} , 10^{-6} cm²/s) and Activation Energy of Diffusion ($E_{\mathcal{D}}/R_g$, 10^3 K) for Various Gas Polymer Systems at 298 K

Gas/Polymer	N ₂		O ₂		CO ₂	
	\mathcal{D}	$E_{\mathcal{D}}/R_g$	\mathcal{D}	$E_{\mathcal{D}}/R_g$	\mathcal{D}	$E_{\mathcal{D}}/R_g$
Polybutadiene	1.1	3.60	1.5	3.40	1.05	3.65
Polychloroprene (Neoprene rubber)	0.24	5.18	0.38	4.74	0.23	5.40
<i>cis</i> -1,4-Polyisoprene (natural rubber)	1.1	2.60	1.73	4.03	1.25	4.13
Silicone rubber	15	1.35	25	1.10	15	1.35
HDPE	0.10	4.5	0.17	4.40	0.12	4.25
LDPE	0.35	4.95	0.46	4.80	0.37	4.60
PETP	0.0014	5.25	0.0036	5.50	0.0015	5.95
PS	0.06	4.25	0.11	4.15	0.06	4.35
PVC, unplasticized	0.0038	7.45	0.012	6.55	0.0025	7.75
PVAc	0.03	6.15	0.056	7.30	—	—
PC	0.015	4.35	0.021	3.85	0.005	4.50
Poly(ethyl methacrylate)	0.17	5.14	0.89	3.82	3.79	3.98
Polytetrafluoroethylene	0.088	2.93	0.152	3.16	0.095	3.44
Teflon (FEP)	0.0948	4.63	0.184	4.17	0.105	4.40

Source: Brandrup and Immergut, 1989.

Eq. 4.57 as: $\log \mathcal{D}_0 = 0.96 \pm 0.8$. Finally, Eq. 4.53 gives the diffusivity at 298 K as

$$\mathcal{D}(298) = 10^{0.96} \exp\left(\frac{-5960}{298}\right) = 1.8 \times 10^{-8} \text{ cm}^2/\text{s} \quad (4.60)$$

which compares very well with the value given in Table 4.9. ■

Solubility, S , is the amount of gas dissolved in a polymer matrix at equilibrium with a partial pressure, P , and it is defined as

$$\frac{V_A}{V_P} = S(P)P \quad (4.61)$$

where V_A is the volume of gas (at standard temperature (298 K) and pressure, 0.1013 MPa = 1 atm, conditions; STP) dissolved into the polymer per unit volume of the solution, and V_P is the volume of polymer per unit volume of the solution. V_A is related to ρ_A via the expression: $\rho_A = d_A V_A$, where d_A is the density of species A in g/cm³. The units of S are cm³(STP)/cm³·Pa. Equation 4.61, for $S(P) = \text{constant}$, is also called *Henry's law*, and it is generally followed by substances at low concentrations. For organic vapors, the solubility is usually expressed in weight of vapor per weight of polymer per unit pressure, and the definition is similar to Eq. 4.61 with the substitution of ρ_A and ρ_P in place of V_A and V_P , respectively. The solubility, S , follows an Arrhenius type expression with temperature:

$$S = S_0 \exp(-\Delta \bar{H}_S / R_g T) \quad (4.62)$$

where S_0 is the pre-exponential factor, and $\Delta \bar{H}_S$ is the molar heat of sorption. Note that the ratio $\Delta \bar{H}_S / R_g$ has the units of temperature (K).

The diffusivity was described as a function of the glass transition temperature, T_g , and degree of crystallinity, ϕ_c , of the polymer and the Lennard-Jones temperature, ε/k , of the gas. Similarly, the solubility can be estimated with good accuracy from the same variables. The pertinent expressions are (Van Krevelen, 1990), for elastomers (and for polymers in the rubbery state):

$$10^{-3} \frac{\Delta \bar{H}_S}{R_g} = 1.0 - 0.010 \frac{\varepsilon}{k} \pm 0.5 \quad (4.63)$$

$$\log S_0 = -5.5 - 0.005 \frac{\varepsilon}{k} \pm 0.8 \quad (4.64)$$

and for glassy amorphous polymers:

$$10^{-3} \frac{\Delta \bar{H}_S}{R_g} = 0.5 - 0.010 \frac{\varepsilon}{k} \pm 1.2 \quad (4.65)$$

$$\log S_0 = -6.65 - 0.005 \frac{\varepsilon}{k} \pm 1.8 \quad (4.66)$$

Finally, the solubility of semicrystalline polymers, S_{sc} , depends on the degree of crystallinity, ϕ_c , and the solubility of the completely amorphous polymers, and it can be approximated as follows:

$$S_{sc} = S_a(1 - \phi_c) \quad (4.67)$$

In other words, the gas is soluble in the amorphous regions only.

TABLE 4.10 Solubility (S , 10^{-6} cm³(STP)/cm³·Pa) and Heat of Sorption ($\Delta\bar{H}_S/R_g$, 10^3 K) for Various Gas–Polymer Systems at 298 K

Gas/Polymer	N ₂		O ₂		CO ₂	
	S	$\Delta\bar{H}_S/R_g$	S	$\Delta\bar{H}_S/R_g$	S	$\Delta\bar{H}_S/R_g$
Polybutadiene	0.44	0.51	0.96	0.14	9.87	-1.06
Polychloroprene (Neoprene rubber)	0.36	0.16	0.74	0.25	8.19	-1.15
<i>cis</i> -1,4-Polysisoprene (natural rubber)	0.55	0.25	1.02	-0.51	9.20	-1.50
Silicone rubber	0.81	—	1.26	—	4.30	—
HDPE	0.15	0.24	0.18	-0.20	0.22	-0.66
LDPE	0.23	0.95	0.47	0.30	2.54	0.05
PETP	0.39	-1.37	0.69	-1.56	13.0	-3.78
PS	—	—	0.55	—	6.5	—
PVC, unplasticized	0.23	0.85	0.29	0.14	4.7	-0.94
PVAc	0.2	—	0.64	-0.55	—	—
PC	0.28	—	5.03	-1.55	1.24	-2.62
Poly(ethyl methacrylate)	0.57	-0.25	0.84	0.55	11.3	-0.51
Polytetrafluoroethylene	1.20	-0.66	2.1	-0.87	9.2	-1.76
Teflon (FEP)	1.25	-0.95	2.02	-1.11	9.08	-1.89

Source: Brandrup and Immergut, 1989.

At 298 K, the solubility of gases in elastomers and glassy amorphous polymers can be expressed as (S in cm³/cm³·Pa)

$$\log S(298) = -7.0 + 0.010 \frac{\varepsilon}{k} \pm 0.25 \quad (4.68)$$

for elastomers, and as

$$\log S(298) = -7.4 + 0.010 \frac{\varepsilon}{k} \pm 0.6 \quad (4.69)$$

for glassy amorphous polymers. The nature of the polymer affects the solubility slightly, and the size of the gas molecules affects the sign of the heat of sorption: dissolution of small gas molecules is endothermic (positive $\Delta\bar{H}_S$), whereas larger gas molecules cause exothermic dissolution (negative $\Delta\bar{H}_S$). Table 4.10 summarizes some data on solubility for common gas–polymer systems. More data can be found in Brandrup and Immergut (1989), Gorski et al. (1985), Cheng and Bonner (1978), Stiel and Harnish (1976), Duda et al. (1973), and Durrill and Griskey (1966) and (1969). As a rule of thumb with the solubility of nitrogen taken as 1, that of oxygen is about 2, and that of carbon dioxide is 25.

Example 4.7. Estimation of S

Estimate the solubility of oxygen in polycarbonate and poly(vinyl acetate) (PVAc) at 298 K.

Solution. From Table 4.8 we get $\varepsilon/k = 106.7$ K for oxygen. Thus, Eq. 4.69 gives for both polymers (they are in the glassy amorphous state) the mean value for solubility as

$$S(298) = 4.64 \times 10^{-7} \text{ cm}^3(\text{STP})/\text{cm}^3 \cdot \text{Pa} \quad (4.70)$$

with the values at the extremes being 1.9×10^{-6} and 1.2×10^{-7} cm³/cm³·Pa. Table 4.10 shows that the theoretical and experimental values for PVAc are very close, and that the experimental value for PC is a little higher than the upper limit of the theoretical value. ■

4.2.2 Permeability of Simple Gases and Permachor

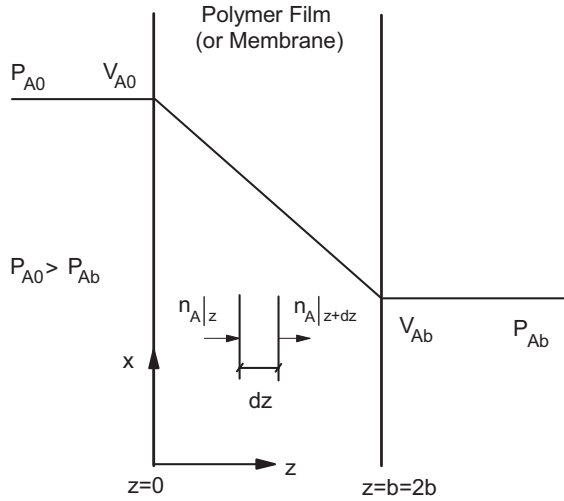
The product of the diffusivity and the solubility is called permeability, \bar{P} :

$$\bar{P} \equiv DS \quad (4.71)$$

It determines the amount of the diffusing species passing through a polymer film of unit thickness per unit cross-sectional area, per unit time, and at a unit pressure difference. Its primary applications are in polymer membrane separations and polymer film packaging. More specifically, the ability of certain polymer films to allow only minimal amounts of gases (e.g., oxygen, carbon dioxide, moisture, flavors, and odors) to be transported across them makes these films useful for food and beverage packaging. In this case the polymers are called *barrier* polymers.

The physical meaning of permeability is better understood from the schematic in Figure 4.7. Consider a polymer film (or membrane) of thickness $\ell = 2b$ and a diffusing gas A. This film separates two regions of different pressures (or concentrations) of species A. The left region contains high pressure and the right low pressure, so that the diffusion takes place from left to right. At steady state and in cases of low mass fractions of A inside the film, Eq. 4.16 simplifies to

$$n_{Az} = -\rho D_{AP} \frac{d\omega_A}{dz} = \frac{\rho D_{AP}}{2b} (\omega_{A0} - \omega_{A\ell}) \quad (4.72)$$


FIGURE 4.7 Permeation across a polymer film (or membrane).

By transforming ω to V and using Eq. 4.61, Eq. 4.72 becomes

$$n_{Az} = \mathcal{D}_{AP} \frac{dA}{2b} (V_{A0} - V_{Ab}) = \mathcal{D}_{AP} S \frac{d_A V_P}{2b} (P_{A0} - P_{Ab}) \quad (4.73)$$

Finally, combining Eqs. 4.71 and 4.72 yields

$$n_{Az} = \bar{P} \frac{d_A V_P}{2b} \Delta P \cong \bar{P} \frac{d_A}{2b} \Delta P \quad (4.74)$$

where ΔP is the difference in pressures of species A of the left and the right regions, and the approximate relation holds for $V_P \cong 1$.

Equation 4.74 shows clearly that the mass transfer through the membrane or film depends on the permeability \bar{P} of the gas A through the polymer. The units of \bar{P} are $\text{cm}^3(\text{STP}) \cdot \text{cm}^2/\text{s} \cdot \text{cm}^3 \cdot \text{Pa}$ or $\text{cm}^2/\text{s} \cdot \text{Pa}$. Also, the unit of *Barrer* is frequently used in the literature: 1 *Barrer* = $10^{-10} \text{cm}^3(\text{STP}) \cdot \text{cm}/\text{cm}^2 \cdot \text{s} \cdot \text{cm Hg} = 7.5 \times 10^{-14} \text{cm}^2/\text{s} \cdot \text{Pa}$. Combining Eqs. 4.53, 4.62, and 4.71 we get

$$\bar{P} = \bar{P}_0 \exp\left(\frac{-E_{\bar{P}}}{R_g T}\right) = \mathcal{D}_0 S_0 \exp\left(-\frac{E_{\mathcal{D}} + \Delta \bar{H}_S}{R_g T}\right) \quad (4.75)$$

so that the activation energy for permeability is the sum of the activation energies for diffusion and solubility, that is, $E_{\bar{P}} = E_{\mathcal{D}} + \Delta \bar{H}_S$, and $\bar{P}_0 = \mathcal{D}_0 S_0$. From available experimental data the following relations can provide an approximation for the permeability values (Van Krevelen, 1990): for elastomers,

$$\log \bar{P}_0 = -10.1 + 10^{-3} \frac{E_{\bar{P}}}{R_g} \pm 0.25 \quad (4.76)$$

TABLE 4.11 Relative Permeability Parameters for Various Gases

Gas / Parameter	\bar{P}	$E_{\bar{P}}$
N ₂	1	1
CO	1.2	1
CH ₄	3.4	1
O ₂	3.8	0.86
He	15	0.62
H ₂	22.5	0.70
CO ₂	24	0.70
H ₂ O	(550)	0.75

Source: Van Krevelen, 1990.

and for glassy amorphous polymers,

$$\log \bar{P}_0 = -11.25 + 10^{-3} \frac{E_{\bar{P}}}{R_g} \pm 0.75 \quad (4.77)$$

Experimental values of permeability of nitrogen at room temperature through various elastomers, semicrystalline, and amorphous polymers showed great variation depending on the polymer. Thus, silicone rubber showed the highest permeability of $10^{-11} \text{cm}^2/\text{s} \cdot \text{Pa}$, whereas poly(vinylidene chloride) showed the lowest of $4 \times 10^{-17} \text{cm}^2/\text{s} \cdot \text{Pa}$. Table 4.11 provides rules of thumb on relative permeability and activation energy.

A more accurate way of predicting the barrier properties of polymers is to correlate polymer structure and morphology to permeability. Salame (1986) introduced the idea of the *permachor*, π , which assigns a value for the polymer chain based on the specific values for the various structural units of that chain. Although three gases were studied extensively (N₂, O₂, and CO₂), the approach can be extended to other gases as well. The permeability is defined as

$$\bar{P}(298) = \bar{P}^*(298) \exp(-s\pi) \quad (4.78)$$

where s is a scaling factor and \bar{P}^* is a pre-exponential permeability factor. These factors are constant for a specific gas (Table 4.12). The values reported in Table 4.12 refer to both elastomers and glassy amorphous materials. The method of

TABLE 4.12 Pre-exponential Permeability Factor, \bar{P}^* , and Scaling Factor, s

Gas / Factor	\bar{P}^* ($\text{cm}^3(\text{STP}) \cdot \text{cm}/\text{cm}^2 \cdot \text{s} \cdot \text{Pa}$)	s (cm^3/cal)
N ₂	1.16×10^{-12}	0.121
O ₂	3.42×10^{-12}	0.112
CO ₂	2.13×10^{-11}	0.122

Source: Salame, 1986.

TABLE 4.13 Group Contributions to the Molar Permachor

Group	π_i (cal/cm ³)	Group	π_i (cal/cm ³)
-CH ₂ -	15	-CH(OH)-	255
$\begin{array}{c} \\ -C- \\ \end{array}$	-50		wet 100
-CH(CH ₃)-	15	-CH(CN)-	205
-CH(C ₆ H ₅)-	39	-CHF-	85
-CH(<i>i</i> -butyl)-	-1	-CF ₂ -	120
-C(CH ₃) ₂ -	-20	-CHCl-	108
-CH=CH-	-12	-CCl ₂ -	155
-CH=C(CH ₃)-	-30	-CH(CH ₂ Cl)-	50
-CH=C(Cl)-	33	-Si(CH ₃) ₂ -	-116
-C ₆ H ₁₀ - (aromatic)	-54	-O-	70
-C ₆ H ₆ - (aromatic)	60	-COO-	102
-C ₆ H ₄ (CH ₃) ₂ - (<i>meta</i> /aromatic)	-74	-O-COO-	24
		-CO-NH-	309
			wet 210
$\begin{array}{c} \\ -CH- \\ \end{array}$	0	$\begin{array}{c} \\ -Si- \\ \end{array}$	-146

Source: Salame, 1986.

calculating π_a , that is, the permachor for completely amorphous materials, is simply

$$\pi_a = \frac{1}{n} \sum_{i=1}^n \pi_i \quad (4.79)$$

where n is the total number of individual groups per structural unit of the macromolecule, and π_i is the individual group value of the permachor. Typical π_i values are shown in Table 4.13.

For semicrystalline materials, with crystallinity ϕ_c , the permachor π_{sc} should be calculated based on the amorphous π_a as follows:

$$\pi_{sc} \cong \pi_a - 18 \ln(1 - \phi_c) \quad (4.80)$$

and for oriented crystallites the following correction should be made:

$$\bar{P}_{\text{oriented, sc}} = \frac{\bar{P}_{sc}}{\tau_0} \cong \bar{P}_{sc} \frac{(1 - \phi_c)^{1/2}}{1.13} \quad (4.81)$$

where τ_0 is the *tortuosity* of crystallites. Based on these expressions one can calculate the total permachor values, π , for various polymers (Table 4.14). Note that the permachor value scale has a zero value assigned to natural rubber (*cis*-1,4- polyisoprene) and a value of 100 assigned to oriented and crystalline poly(vinylidene chloride). The following example

TABLE 4.14 Values of the Permachor, π , for Various Polymers

Polymer	π (cal/cm ³)
Elastomers	
Silicone rubber	-23
Butyl rubber (polyisobutylene)	-2
Natural rubber (poly- <i>cis</i> -isopropene)	0
Butadiene rubber (polybutadiene)	6
Poly-4-methyl-1-pentene	7
EPR elastomer (unmodified)	15
Neoprene rubber (polychloroprene)	21
Glassy amorphous polymers	
Hydropol (hydrogenated polybutadiene)	15
Polystyrene	27
Bisphenol-A polycarbonate	31
Poly(vinyl fluoride) (quenched)	50
Poly(ethylene terephthalate)	59
Poly(vinyl acetate)	61
Poly(vinyl chloride)	61
Poly(vinylidene chloride)	86
Polyacrylonitrile	110
Semicrystalline polymers	
Low-density polyethylene ($\phi_c = 0.43$)	25
Polypropylene ($\phi_c = 0.60$)	31
High-density polyethylene ($\phi_c = 0.74$)	39
Poly(vinyl fluoride) ($\phi_c = 0.40$)	59
Poly(ethylene terephthalate) ($\phi_c = 0.30$)	65
Nylon 6,6 ($\phi_c = 0.40$)	73 (dry)
	60 (wet)
Nylon 6 ($\phi_c = 0.60$)	80 (dry)
	67 (wet)
Poly(vinylidene chloride) (oriented and crystalline)	100
Poly(vinyl alcohol) (dry, $\phi_c = 0.70$)	157

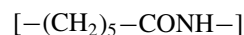
Source: Salame, 1986.

illustrates the application of the permachor algorithm to estimate the permeability of gas-polymer systems.

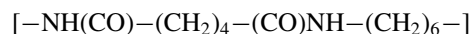
Example 4.8. Permeability of Nylon 6 and Nylon 6,6 Films to CO₂

Calculate the CO₂ permeability of Nylon 6 and Nylon 6,6 films with 40% crystallinity at room temperature and compare it with the literature value (Brandrup and Immergut, 1989) of 5.2×10^{-15} cm²/s·Pa. Use the permachor estimation algorithm.

Solution. The structural unit of Nylon 6 is



and that of Nylon 6,6 is



Their permachor is easily proved to be the same, and so we continue our calculations with Nylon 6,6 only. The permachor is calculated as follows (Table 4.13):

$$\begin{array}{lll} 10 & -\text{CH}_2- & = 10 \times 15 = 150 \text{ cal/cm}^3 \\ 2 & -\text{NH}-\text{CO}- & = 2 \times 309 = 618 \text{ cal/cm}^3 \\ n & & = 12 \sum \pi_i = 768 \text{ cal/cm}^3 \end{array}$$

Thus, $\pi_a = 768/12 = 64 \text{ cal/cm}^3$. The value for the 40% crystalline Nylon 6,6 is calculated from Eq. 4.80 as: $\pi_{sc} = 64 - 18 \ln(1 - 0.4) = 73 \text{ cal/cm}^3$ (see also Table 4.14). The permeability of this film to CO_2 is calculated with the aid of Eq. 4.78 and Table 4.12 as

$$\begin{aligned} \bar{P} &= 2.48 \times 10^{-11} \exp(-0.122 \times 73) \\ &= 3.4 \times 10^{-15} \text{ cm}^2/\text{s} \cdot \text{Pa} \end{aligned} \quad (4.82)$$

That value compares well with the literature value of $5.2 \times 10^{-15} \text{ cm}^2/\text{s} \cdot \text{Pa}$ taking into consideration that the literature value is not referred to any specific crystallinity. ■

Finally, there exists one more technique that predicts the transport properties of polymers by performing summations over atom and bond contributions defined in terms of connectivity indices. For more about this technique the reader is referred to Bicerano (1993).

4.2.3 Moisture Sorption and Diffusion

The diffusivity and solubility of water in polymers differs from that of simple gases to the extent that the water molecule interacts with the polymer. Based on this interaction, the polymer molecules are classified as *hydrophilic* or *hydrophobic*. The solubility of water in hydrophobic polymers, such as polyolefins and some polyesters, is very low and the diffusivity follows the rules of the other simple gases mentioned in Section 4.2.1. On the other hand, hydrophilic polymers, such as cellulose, poly(vinyl alcohol), and proteins, interact strongly with water, and water diffusivity increases with its content. A good approximation for this situation is (Van Krevelen, 1990)

$$\log \mathcal{D}_w = \log \mathcal{D}_{w=0} + 0.08 w \quad (4.83)$$

where w is the water content in weight percent. The pre-exponential factor, \mathcal{D}_{0w} , is taken as

$$\log \mathcal{D}_{0w} \cong \frac{E_{\mathcal{D}} \times 10^{-3}}{R_g} - 7 \quad (4.84)$$

where $E_{\mathcal{D}}$ is in J/mol. In between the extremes of hydrophobic and hydrophilic polymers are less hydrophilic polymers,

such as polyethers and polymethacrylates. Although the pre-exponential factor \mathcal{D}_{0w} depends on $E_{\mathcal{D}}$ as in simple gases, the diffusivity itself decreases with water content as

$$\log \mathcal{D}_w = \log \mathcal{D}_{w=0} - 0.08 w \quad (4.85)$$

The solubility of water in polymers can be estimated from contributions from individual groups of the structural unit. Table 4.15 presents these molar water contributions of various groups (Van Krevelen, 1990) in a manner similar to the permachor. The solubility in g/g or $\text{cm}^3(\text{STP})/\text{g}$ can easily be calculated from the contributions of Table 4.15. The molar volume of the structural unit is needed in the case where the solubility is needed in $\text{cm}^3(\text{STP})/\text{cm}^3$. Finally, the heat of sorption is about 25 kJ/mol for nonpolar polymers and about 40 kJ/mol for polar polymers.

Example 4.9. Estimation of the Saturation Moisture Content of Polymers

Estimate the saturation moisture content of poly(methyl acrylate) (PMA) and polystyrene (PS) at 25 °C and relative humidity of 50%. Compare these values with experimental values from Crank and Park (1968, p. 263).

Solution. The structural unit of PMA is



and from Table 4.15 the molar moisture content at 50% relative humidity is $(0.05 + 7.5 \times 10^{-5}) \cong 0.05$ or equivalently $0.05 \times 18/100 = 0.9/100 \text{ g}$ of water per g of polymer. This value compares really well with the experimental value of 0.99/100. Similarly, the weight percent of water in PS is calculated to be 0.032%, which is identical to the experimental value of 0.032%. ■

4.2.4 Permeation of Higher-Activity Permeants

We considered the ideal cases in terms of diffusion and solubility, that is, Fickian diffusion and constant solubility (Henry's law), in Sections 4.2.1, 4.2.2, and 4.2.3. However, complexities might arise at higher penetrant activities, because the high solubility in these cases can cause swelling of the polymer and nonlinearities of the coefficients of diffusion and solubility. In this section, we restrict ourselves to the outline of the nonlinear behavior of some systems without going into the details.

A typical example for amorphous rubbery polymers is given in Figure 4.8 with the sorption isotherms of ethylene, carbon dioxide, methane, and nitrogen in silicone rubber at 35 °C (Koros and Hellums, 1990). Methane and nitrogen obey Henry's law at all pressures, whereas ethylene and

TABLE 4.15 Molar Water Content per Structural Group at Various Relative Humidities at 25 °C

Group	Relative Humidity				
	0.3	0.5	0.7	0.9	1.0
-CH ₃	(1.5 × 10 ⁻⁵)	(2.5 × 10 ⁻⁵)	(3.3 × 10 ⁻⁵)	(4.5 × 10 ⁻⁵) (5 × 10 ⁻⁵)	
-CH ₂ -	(1.5 × 10 ⁻⁵)	(2.5 × 10 ⁻⁵)	(3.3 × 10 ⁻⁵)	(4.5 × 10 ⁻⁵) (5 × 10 ⁻⁵)	
$\begin{array}{c} \text{H} \\ \\ -\text{C}- \\ \end{array}$	(1.5 × 10 ⁻⁵)	(2.5 × 10 ⁻⁵)	(3.3 × 10 ⁻⁵)	(4.5 × 10 ⁻⁵) (5 × 10 ⁻⁵)	
-C ₆ H ₆ - (aromatic)	0.001	0.002	0.003	0.004	0.005
-CO-	0.025	0.055	(0.11)	(0.20)	(0.3)
-COO-	0.025	0.05	0.075	0.14	0.2
-O-	0.006	0.01	0.02	0.06	0.1
-OH	0.35	0.5	0.75	1.5	2
-NH ₂ -	0.35	0.5	0.75	(1.5)	(2)
-NH ₃ ⁺	—	—	2.8	5.3	—
-COOH	0.2	0.3	0.6	1.0	1.3
-COO-	1.1	2.1	4.2	—	—
-CONH-	0.35	0.5	0.75	1.5	2
-Cl	0.003	0.006	0.015	0.06	(0.1)
-CN	0.015	0.02	0.065	0.22	(0.3)

Source: Reprinted by permission of the publisher from Van Krevelen, 1990.

carbon dioxide obey it at low pressures and deviate positively (from the initial slope) at high pressures. This positive deviation is called the *Flory-Huggins swelling behavior*. This behavior is mathematically expressed as

$$\ln \frac{P}{P_0} = \ln \phi_A + (1 - \phi_A) + \chi(1 - \phi_A)^2 \quad (4.86)$$

where P is the solvent partial pressure, P_0 is the pure solvent vapor pressure, ϕ_A is the solvent volume fraction, and χ

is the interaction parameter of the solvent-polymer system. Equation 4.86 is valid in the absence of crosslinking and for a high degree of polymerization of the polymer. Furthermore, the permeability of silicone rubber to carbon dioxide and ethylene (Fig. 4.9) increases with pressure, while for helium and nitrogen it decreases with increasing pressure, and the pressure has no effect on the permeability to methane. Note that the critical temperature of the first two gases is high, of the next two is low, and that of methane is intermediate.

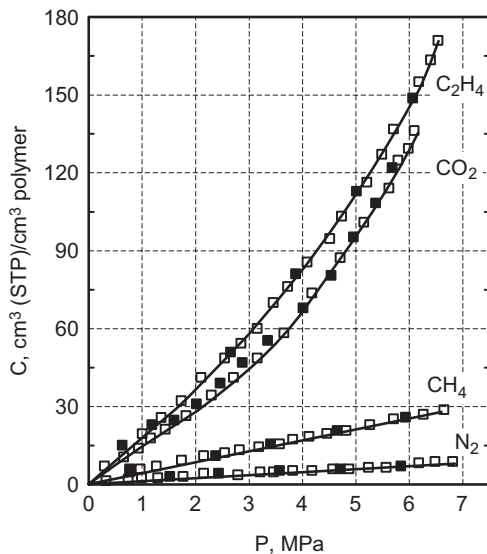


FIGURE 4.8 Sorption isotherms of various gases in silicone rubber at 35 °C. □ sorption; ■ desorption. (Reprinted by permission of the publisher from Koros and Hellums, 1989.)

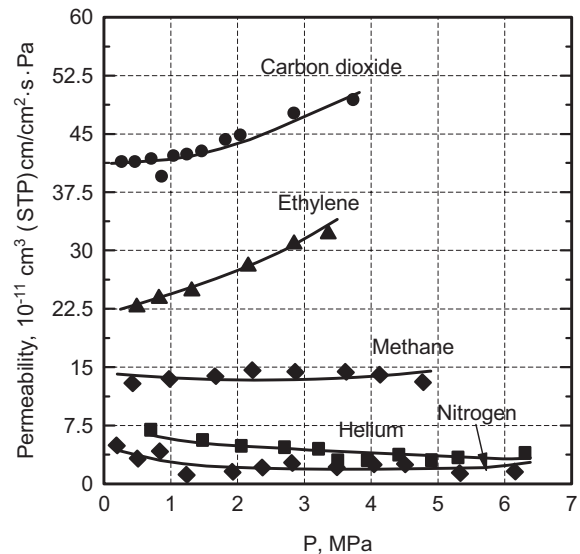


FIGURE 4.9 Permeability of silicone rubber to various gases at 35 °C. (Reprinted by permission of the publisher from Koros and Hellums, 1989.)

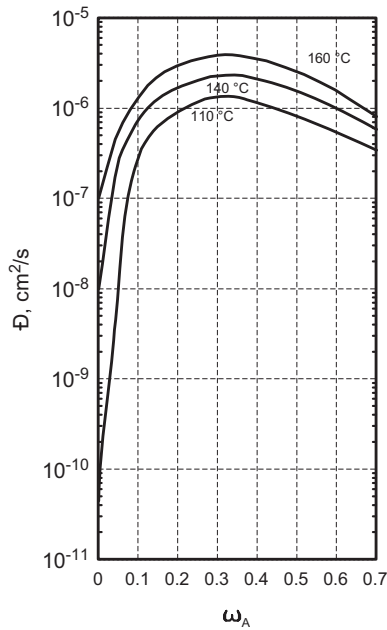


FIGURE 4.10 Diffusion coefficient of toluene in the toluene-polystyrene system, as a function of the toluene mass fraction. (Reprinted by permission of the publisher from Vrentas et al., 1982.)

The strong dependence of the diffusivity on the mass fraction of the diffusant, for intermediate size molecules, such as organic solvents in rubbery materials, is shown in Figure 4.10. The sorption isotherms of various gases in PC are shown in Figure 4.11. The solubility of helium and nitrogen in PC varies linearly with pressure even at relatively high pressures, whereas the solubility of carbon dioxide and methane varies linearly with pressure only at relatively low

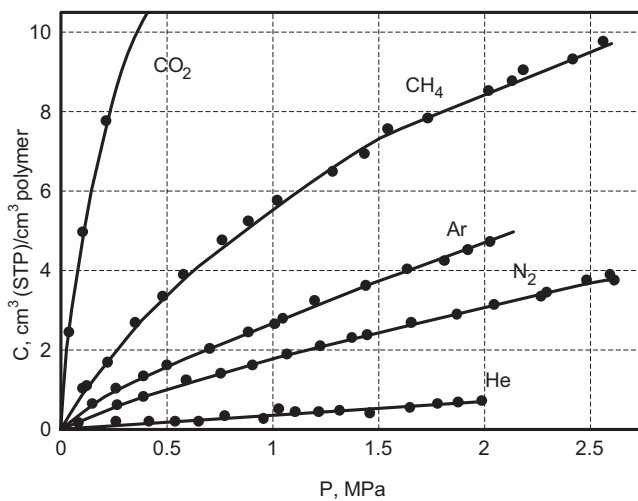


FIGURE 4.11 Sorption isotherms of various gases in polycarbonate at 35 °C. (Reprinted by permission of the publisher from Koros and Hellums, 1989.)

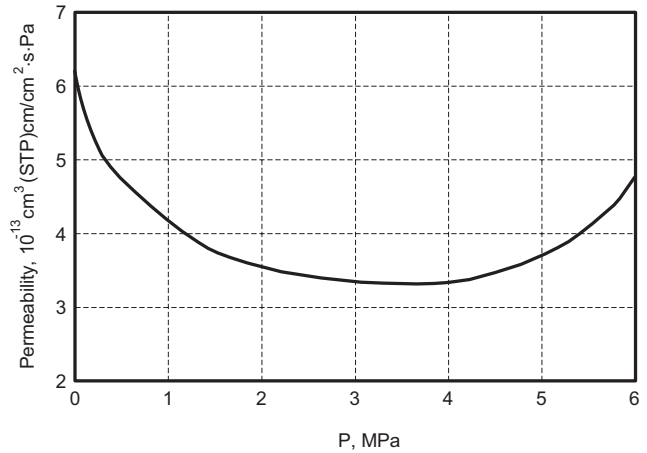


FIGURE 4.12 Permeability of polycarbonate at 35 °C to carbon dioxide. (Reprinted by permission of the publisher from Koros and Hellums, 1989.)

and high pressures. Argon shows intermediate behavior. Note that the shape of the CO₂ isotherm in PC is different from the shape of the CO₂ isotherm in silicone rubber (Fig. 4.8), that is, it shows negative deviation from the initial slope in PC and positive deviation in silicone rubber. The sorption isotherm of CO₂ in PC is called the *Langmuir isotherm* (see also Problem 4C.6b or Vieth, 1991). Finally, the permeability of PC to carbon dioxide is shown in Figure 4.12.

Diagrammatically, the effect of the penetrant activity on the transport properties is shown in Figure 4.13 (Hopfenberg and Frisch, 1969), which is valid for amorphous polymers. Concentration-independent diffusion takes place at any

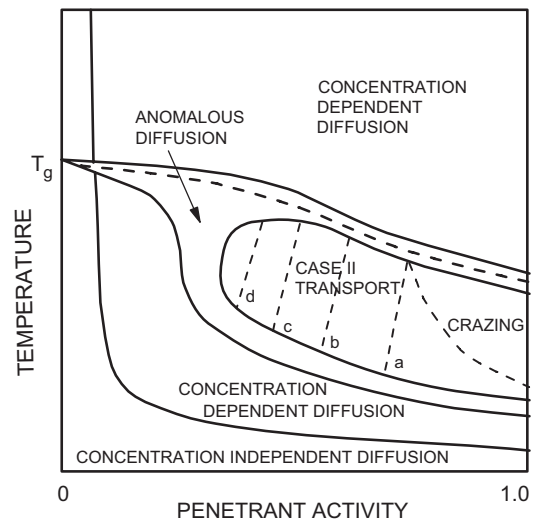


FIGURE 4.13 Transport regions in the temperature-penetrant activity plane. Lines a, b, c, and d are lines of constant activation energy and decreasing in that order. (Reprinted by permission of the publisher from Hopfenberg and Frisch, 1969.)

temperature and low penetrant activities or at low temperatures and high activities. At high penetrant activities and temperatures lower than T_g , the transport of the penetrant causes high stresses and thus crazing and failure of the polymer. The so-called Case II (or relaxation-controlled; see also Section 4.3) transport takes place at medium to high activities and temperatures below T_g . Finally, at lower temperatures, both relaxation and diffusion mechanisms are present causing anomalous behavior.

In conclusion, permeation at relatively high pressures of higher activity permeants, such as condensable gases, intermediate size vapors, and liquids, presents deviations from the simple Henry's law. The Flory–Huggins and the Langmuir isotherms are two such deviations observed in rubbery and glassy materials, respectively. In terms of the permeability as a function of pressure, a single gas can exhibit all possible behaviors, such as increasing, decreasing, and being constant, in a single graph. Finally, as a rule of thumb, the diffusivity of liquids in polymers is inversely proportional to the viscosity of the liquid.

4.2.5 Polymer–Polymer Diffusion

Diffusion in polymer–polymer systems is important in many practical applications, such as crack healing, polymer blending, welding, adhesion, elastomer tack, polymer fusion, and many others. However, diffusion coefficient data is lacking due to the complexity of the polymer diffusion process. Typical techniques employed are infrared spectroscopy, spectroscopic ellipsometry, and optical schlieren. Only a few studies of interdiffusion in polymer pairs are reported. Depending on the temperature and other physical parameters of the system, Fickian and Case II diffusions (see Section 4.3) can be observed with varying relative importance (Jabbari and Peppas, 1993).

In polymer melts it is customary to measure the *self-diffusion*, \mathcal{D}_s , and the *tracer diffusion*, \mathcal{D}^* , coefficients (Kausch and Tirrell, 1989). The self-diffusion refers to the diffusion of a macromolecule in a background of identical macromolecules. On the other hand, tracer diffusion refers to the diffusion of a small number of identical macromolecules (i.e., at the tracer level; usually in a tagged state) in a background which consists of macromolecules, all of which are not identical to the diffusing macromolecules. Note that in a binary system of species A and B, which approaches infinite dilution of species A, the diffusion coefficient of A and B becomes equal to the tracer diffusion coefficient of A, that is, $\mathcal{D}_{AB} = \mathcal{D}_A^*$. Finally, the self-diffusion coefficients can be combined to yield the mutual diffusion coefficient of species A and B.

Typical diffusivity values are in the range from 10^{-16} to 10^{-6} cm^2/s . Figures 4.14 and 4.15 present the self-diffusion data for the two polymers studied extensively in the literature, PE and PS, respectively. The correlations in these two

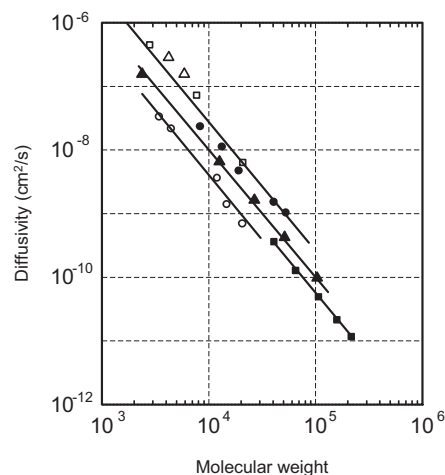


FIGURE 4.14 Self-diffusion coefficient of molten polyethylene (PE) as a function of molecular weight at 176 °C. Lines drawn have slope -2 . (Reprinted by permission of the publisher from Tirrell, 1984.)

figures show that the self-diffusion coefficient depends on the molecular weight of the diffusing species as follows (see also Problem 4B.6):

$$\mathcal{D}_s \propto (\text{MW})^{-2} \quad (4.87)$$

The activation energy for self-diffusion of PE is about 23 kJ/mol, whereas that of PS varies widely, from 62.2 to 167 kJ/mol (Tirrell, 1984). There are no more extensive data in the literature for any other polymer system.

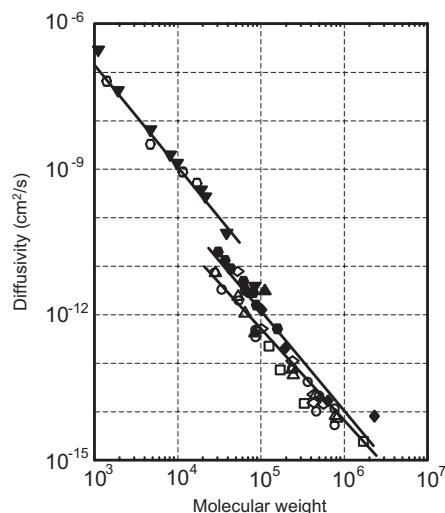


FIGURE 4.15 Self-diffusion coefficient of molten polystyrene (PS) as a function of molecular weight at or near 175 °C. Lines drawn have slope -2 . (Reprinted by permission of the publisher from Tirrell, 1984.)

Equation 4.87 agrees with the predictions of the reptation theory applied to entangled polymer systems. According to this theory, each polymer chain is confined to a tube surrounding its own contour, whose walls are made up by the neighboring chains. The diffusion of the polymer chain is assumed to proceed primarily by reptation, which is similar to the motion of snakes as they move through a fixed set of obstacles. This diffusion path is the one that offers the least resistance, because the tube walls impede the lateral motions of the polymer chain. Finally, the molecular weight dependence of the self-diffusion coefficient is calculated from the molecular weight dependencies of the radius of gyration, R_G , and the longest relaxation time, τ , and by recognizing that the center of mass of the polymer chain will move a distance approximately equal to R_G in time equal to τ (Tirrell, 1984, and Problem 4B.6).

4.2.6 Measurement Techniques and Their Mathematics

This section is concerned with measurement techniques of the diffusivity and solubility from which the permeability can easily be calculated. In the following analysis we restrict ourselves to the measurement of constant values of \mathcal{D} . Concentration- and position-dependent diffusivities are analyzed in Crank and Park (1968) and Crank (1975). Generally, the techniques are: for permeability, steady-state and time lag techniques; and for diffusivity, sorption and desorption kinetics and concentration–distance curves. For self-diffusivity in polymer melts the techniques are (Tirrell, 1984) nuclear magnetic resonance, neutron scattering, radioactive tracer, and infrared spectroscopy.

In the steady-state permeation method, the surfaces of a polymer film of thickness $\ell = 2b$ are kept at constant gas pressures P_{A0} and $P_{A\ell}$. At steady state Eq. 4.75 applies, and the permeability \bar{P} is found from this equation. If the solubility is known, then the diffusivity can be found from Eq. 4.71. For hollow cylinders and spheres, expressions similar to Eq. 4.74 hold. On the other hand, in the time lag method we deal with the unsteady-state permeation of a diffusant through a slab of thickness $2b$. The surfaces of the slab are kept at concentrations C_{A0} and at zero. The accumulated amount of gas which has passed through the slab in time t ,

$$Q_t = -\mathcal{D} \int_0^t \left(\frac{\partial C_A}{\partial z} \right)_{z=0} dt$$

is given by

$$\frac{Q_t}{2bC_{A0}} = \frac{\mathcal{D}t}{(2b)^2} - \frac{1}{6} - \frac{2}{\pi^2} \sum_{n=1}^{\infty} \frac{(-1)^n}{n^2} \exp\left(\frac{-\mathcal{D}n^2\pi^2 t}{4b^2}\right) \quad (4.88)$$

At long times (i.e., when steady state is achieved) the exponential term becomes negligible, so that

$$Q_t = \frac{\mathcal{D}C_{A0}}{2b} \left(t - 4\frac{b^2}{6\mathcal{D}} \right) \quad (4.89)$$

The intercept of the above equation with the time axis gives the so-called time lag as

$$t_{\text{lag}} = \frac{4b^2}{6\mathcal{D}} \quad (4.90)$$

Similar relations hold for cylinders and spheres.

In the sorption kinetics techniques, the mass uptake of a slab of thickness $2b$ at time t ,

$$M_t = 2 \int_0^b (C_A - C_{A0}) dz$$

relative to the maximum mass uptake, $M_{\infty} = 2b(C_{A\infty} - C_{A0})$, is given by

$$\frac{M_t}{M_{\infty}} = 4 \left(\frac{\mathcal{D}t}{(2b)^2} \right)^{1/2} \left(\frac{1}{\sqrt{\pi}} + 2 \sum_{n=0}^{\infty} (-1)^n \text{ierfc} \left(\frac{2nb}{\sqrt{4\mathcal{D}t}} \right) \right) \quad (4.91)$$

where C_{A0} is the initial concentration in the slab, $C_{A\infty}$ is the final concentration in the slab, and the function $\text{ierfc}(\cdot)$ is given by

$$\text{ierfc}(x) = \int_x^{\infty} \text{erfc}(x') dx' \quad (4.92)$$

where $\text{erfc}(\cdot)$ is the *complementary error function*, which is equal to $1 - \text{erf}(\cdot)$. Equation 4.91 is more accurate at short times (i.e., for $M_t/M_{\infty} \leq 0.6$, even if the infinite summation term is neglected), whereas the expression given in Problem 4B.1 is more accurate for $M_t/M_{\infty} > 0.6$, even if only the first term in the summation is used. Figure 4.16 shows a typical graph of mass uptake in a slab. At $t \rightarrow 0$ Eq. 4.91 yields

$$\mathcal{D} = \frac{\pi(2b)^2}{16t} \left(\frac{M_t}{M_{\infty}} \right)^2 \quad (4.93)$$

Thus, \mathcal{D} can be estimated from the slope of Figure 4.16 at $t = 0$. Another way to determine \mathcal{D} using the data from the same figure is to evaluate it at $M_t/M_{\infty} = \frac{1}{2}$ as follows

$$\mathcal{D} = 0.04919 \frac{(2b)^2}{t_{1/2}} \quad (4.94)$$

A desorption experiment is similar to the sorption experiment just described. Experimentally, the mass gain or loss is

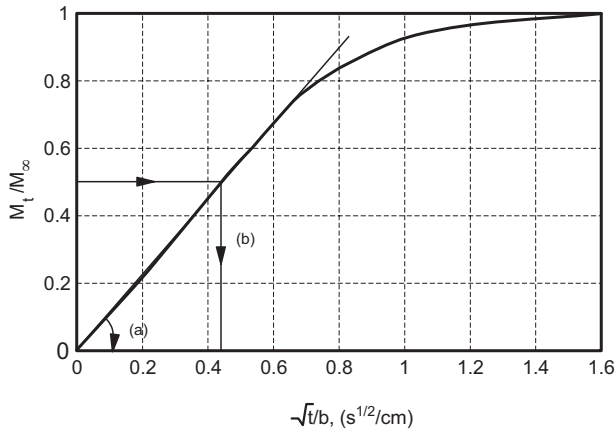


FIGURE 4.16 Relative mass uptake, M_t/M_∞ , of a slab with constant surface concentration. The diffusivity can be calculated by either (a) the slope at $t = 0$ or (b) at $M_t/M_\infty = \frac{1}{2}$.

plotted as a function of time, and the diffusivity is calculated from that plot.

Finally, the diffusion coefficient can also be deduced from the concentration–distance curves in the case of two semi-infinite media brought together and interdiffusing. For example, a polymer sheet and a solvent or even two polymer sheets are brought in contact, and the concentration–distance curves are calculated by measuring the refractive index or by analyzing the radioactivity of a tracer (Crank and Park, 1968). Problem 4C.3 presents an example of the concentration–distance curve, which is shown in Figure 4.17 and mathematically given by

$$C_A = \frac{1}{2}C_{A0}\operatorname{erfc}\left(\frac{x}{2\sqrt{Dt}}\right) \quad (4.95)$$

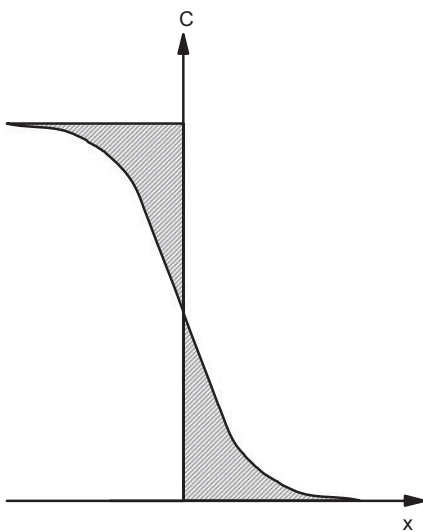


FIGURE 4.17 Schematic of the concentration–distance curve used in the calculation of the diffusivity.

where C_{A0} is the initial concentration of the radioactive tracer in one of the semi-infinite media.

4.3 NON-FICKIAN TRANSPORT

In some cases, solvents cause swelling of the polymers and consequently the penetrant transport cannot be described by Fick's law even with a concentration-dependent diffusivity. Generally, this case is most frequently encountered during sorption in glassy polymers, whereas desorption from glassy polymers and either desorption or sorption in rubbery polymers exhibit mostly Fickian diffusion. To better understand the effect of the type of polymer on the diffusion process, we need to visualize the diffusion process as a sequence of creation of bulges between two macromolecules, diffusional jumps of the penetrant molecules to these bulges, and relaxation of the original bulges containing the penetrant molecules before the jumps. In the rubbery state, both creation of a new bulge (by activation) and the relaxation of the original bulge are completed in short time scales (short relaxation times), so that they do not cause any diffusion anomalies. However, in the glassy state the relevant time scales are long and the behavior is time dependent. As temperature and/or penetrant concentration increase, the relaxation times of the glassy material shorten, and the diffusional behavior tends to resemble that of a rubbery material.

A convenient method of predicting whether the transport of a solvent in an amorphous polymer is Fickian or non-Fickian is to examine the diffusional Deborah number, De_D . This number is defined as the ratio of a characteristic relaxation time for the polymer–solvent system to the characteristic time of the diffusion process (Vrentas et al., 1975). Fickian transport is observed when either $De_D < 0.1$ or $De_D > 10$, whereas non-Fickian transport is observed when $De_D \cong 1$.

Alfrey et al. (1966) proposed the following classification of the diffusional processes:

1. Case I, or Fickian transport: the diffusion time scale is much longer than the relaxation time scale. (Rubbery polymers usually exhibit such behavior.)
2. Case II diffusion: this is the other extreme of Case I, and it refers to the diffusion time scale being much shorter than the relaxation time scale.
3. Non-Fickian or anomalous transport: this process occurs when the diffusion and relaxation time scales are comparable.

Case II diffusion has been associated with advancing fronts of the penetrant material, where these fronts also mark the regions of swollen and glassy polymers. An exponential dependence of the diffusivity on the concentration for large values of the exponential constant can produce advancing

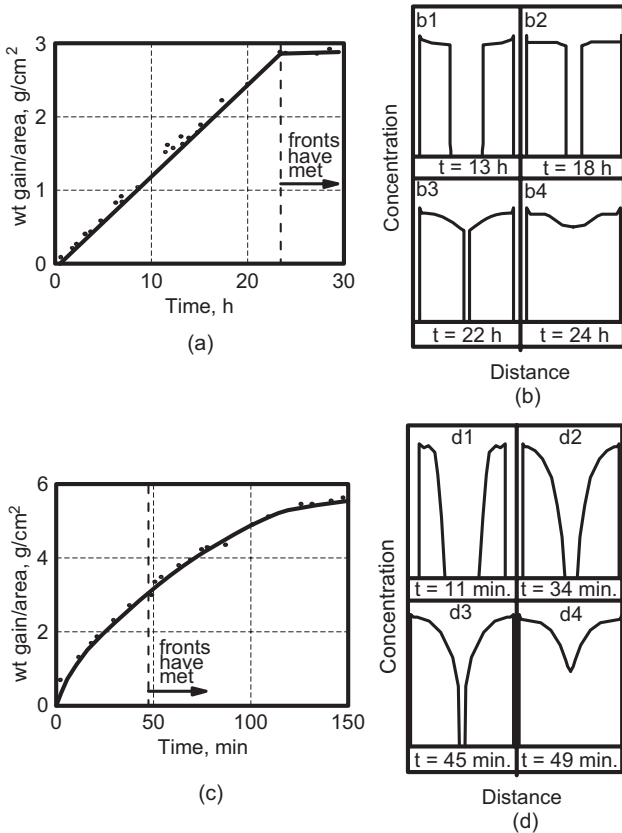


FIGURE 4.18 Case II diffusion in the system PMMA–methanol. PMMA sheets are submerged into liquid methanol. (a) Mass uptake per unit area against time at 30 °C. (b) Concentration of methanol in the PMMA sheets as a function of time at 30 °C. (c) Mass uptake per unit area against time at 60 °C. (d) Concentration of methanol in the PMMA sheets as a function of time at 60 °C. (Reprinted by permission of the publisher from Thomas and Windle, 1978.)

fronts. Both Cases I and II are considered simple diffusion cases, because they are described by a constant, which is the diffusivity in Case I and the constant velocity of the advancing front of the penetrant in Case II (see also Problem 4C.8). In terms of the sorption kinetics, the mass uptake of a semi-infinite slab in Case I was shown (Fig. 4.16) to be proportional to $t^{1/2}$, in the early stages of the sorption process, whereas in Case II it is primarily proportional to t (although at the very beginning it may include a term proportional to the square root of time). Non-Fickian systems lie between those two cases with the mass uptake being proportional to t^n , where $\frac{1}{2} < n \leq 1$, or changing from one case to another. Also, non-Fickian systems require two or more parameters for their description.

A typical example of Case II diffusion is observed in the system PMMA–methanol (Thomas and Windle, 1978, 1982; Sarti and Doghieri, 1994). At 30 °C and below, the system shows linear mass uptake with time (Fig. 4.18a) and sharp concentration profiles (Fig. 4.18b), whereas at 60 °C (boiling

point of methanol is 65 °C) the mass uptake is not linear but curved, and PMMA continues to sorb methanol after the two fronts meet (Fig. 4.18c). Also, at 60 °C the concentration profiles are not as sharp as before (Fig. 4.18d). Finally, an example of combination of Fickian and Case II diffusions, with relative importance depending on the temperature, is presented by Jabbari and Peppas (1993) for the interdiffusion of polystyrene and poly(vinyl methyl ether) at either 85 °C or 105 °C.

In conclusion, Case II and non-Fickian transport behaviors are frequently present in glassy polymer systems. Case II transport particularly was found to be associated with sharp penetrant fronts and linear mass uptake with time, whereas in the non-Fickian transport the mass uptake is proportional to t^n , where $\frac{1}{2} < n \leq 1$. Methanol absorbed in PMMA exhibits Case II diffusion characteristics at relatively low temperatures, whereas at higher temperatures a more peculiar behavior is noticed.

4.4 MASS TRANSFER COEFFICIENTS

In the preceding sections of this chapter we considered mass transfer inside a medium, and we presented correlations for the solubility and diffusivity of various penetrants in polymers. This approach is the most general and fundamental. However, mass transfer can also be described in an empirical and a simpler way using a mass transfer coefficient. The two approaches (i.e., the first one based on the diffusivity and the second one on the mass transfer coefficient) are practically equivalent and the choice between them depends on the difficulty of obtaining the respective data. A more thorough discussion of this topic is given by Bird et al. (1960) and Hines and Maddox (1985).

4.4.1 Definitions

Consider the steady-state diffusion of solute A through a polymer membrane and into a stream with concentration $C_{A\infty}$ as shown in Figure 4.19a. The interface concentration is C_{Ai} . Similar to the definition of the heat transfer coefficient, Eq. 5.122, the mass transfer coefficient is defined as

$$k_c^* \equiv \frac{J_{Az}^*}{C_{Ai} - C_{A\infty}} = -\frac{D(\partial C_A / \partial z)_{z=0}}{C_{Ai} - C_{A\infty}} \quad (4.96)$$

where k_c^* is the convective local mass transfer coefficient (or simply the mass transfer coefficient). This coefficient depends also on the molar transfer rate of species A and B as (Table 4.3, Eq. U)

$$k_c^* = \frac{N_A - x_A(N_A + N_B)}{C_{Ai} - C_{A\infty}} \quad (4.97)$$

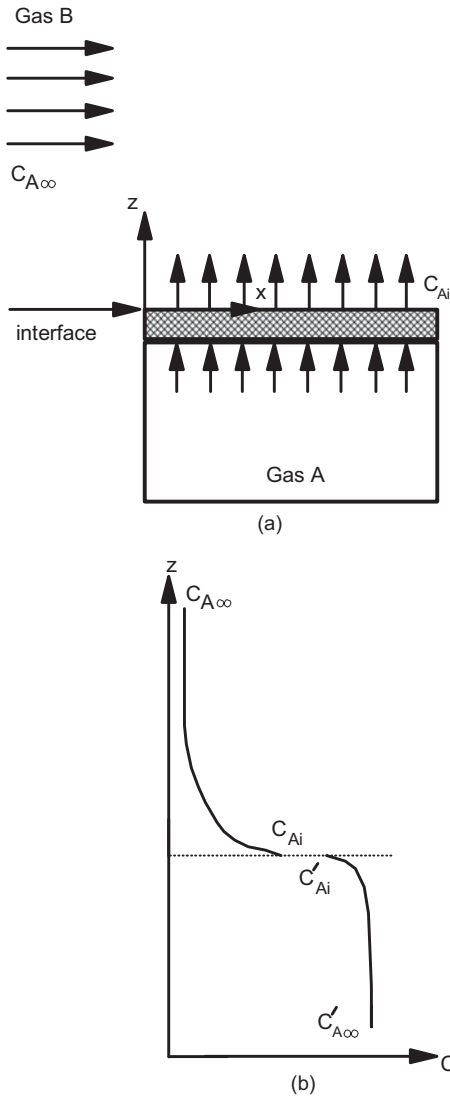


FIGURE 4.19 (a) Mass transfer across a polymer film–fluid interface. (b) Mass transfer across an interface with two resistances present: the first in one side of the interface ($C'_{A\infty}$ to C'_{Ai}), and the second in the other side of the interface (C_{Ai} to $C_{A\infty}$). Henry's law is applicable at the interface, between C_{Ai} and C'_{Ai} .

where we have dropped the z dependence of the molar rate, for simplicity. A similar expression holds for the convective local mass transfer coefficient k'_x (based on x_{Ai} and $x_{A\infty}$). The units of k'_c and k'_x are cm/s and mol/cm²·s, respectively.

The dependence of the mass transfer coefficients on the mass transfer rate distinguishes them from the heat transfer coefficients. However, in the majority of applications, this dependence is negligible and the mass transfer coefficients k'_c and k'_x can be replaced by k_c and k_x , respectively. In such cases,

$$N_A = k_c (C_{Ai} - C_{A\infty}) = k_x (x_{Ai} - x_{A\infty}) \quad (4.98)$$

The units of k_c and k_x are the same as the respective units of k'_c and k'_x . Finally, the average mass transfer coefficients, \bar{k}_c and \bar{k}_x , are defined as

$$N_A - x_{Ai} (N_A + N_B) = \bar{k}_c A_s (C_{Ai} - C_{A\infty}) \quad (4.99)$$

$$N_A - x_{Ai} (N_A + N_B) = \bar{k}_x A_s (x_{Ai} - x_{A\infty}) \quad (4.100)$$

where A_s is the area across which the mass transfer takes place, and N_A and N_B are the molar rates over the entire interface, in mol/s. The units of \bar{k}_c and \bar{k}_x are cm/s and mol/cm²·s, respectively.

The definitions for the mass transfer coefficients can be used to theoretically predict them using the diffusivity, concentrations, length scales, and fluid flow characteristics, thus rendering the two mass transfer approaches equivalent. This can easily be done in the cases of equimolar counterdiffusion ($N_{Az} + N_{Bz} = 0$) and diffusion of A through a stagnant film ($N_{Bz} = 0$) (Hines and Maddox, 1985, p. 140). Also, the theoretical models of film, penetration, surface renewal, and film penetration have been proposed for the estimation of the mass transfer coefficients at a fluid–fluid interface (Hines and Maddox, 1985, pp. 146–151).

Finally, Figure 4.19b shows the concentration profile across an interface where a concentration difference ($C'_{A\infty}$ to C'_{Ai}) is followed by a change in interfacial concentrations (Henry's law) and another concentration difference (C_{Ai} to $C_{A\infty}$). Thus, the interface offers two resistances, one on every side of the interface. A typical example that fits into this description is the drying of polymer pellets by air flowing over them. The concentration difference inside the pellet is due to diffusional resistance, while the same difference in the air is due to convective mass transfer. The discussion of Design Problem III (Section 4.5) elaborates on the two resistances and their relative importance.

4.4.2 Analogies Between Heat and Mass Transfer

Similar to the heat transfer problems, the dimensionless groups in the mass transfer processes are

$$\text{Sherwood number: } Sh = \frac{k_c \ell}{D}; \quad \frac{k_x \ell}{C D} \quad (4.101)$$

$$\text{Schmidt number: } Sc = \frac{\mu}{\rho D} \quad (4.102)$$

$$\text{Grashof number: } Gr_D = \frac{\ell^3 \rho^2 g \zeta (x_{Ai} - x_{A\infty})}{\mu^2} \quad (4.103)$$

$$\text{Stanton number: } St_D = \frac{Sh}{Re Sc} = \frac{k_c}{\nu}; \quad \frac{k_x}{C \nu} \quad (4.104)$$

$$\text{Peclet number: } Pe_D = Re Sc = \frac{\ell \nu}{D} \quad (4.105)$$

TABLE 4.16 Analogies Between Heat and Mass Transfer at Low Mass Transfer Rates (ℓ Is the Length Scale)

	Heat Transfer Quantities	Binary Mass Transfer Quantities
Profiles	T	x_A
Diffusivity	$\alpha = \frac{k}{\rho \bar{C}_p}$	\mathcal{D}_{AB}
Effect of profiles on density	$\beta = -\frac{1}{\rho} \left(\frac{\partial \rho}{\partial T} \right)_{p, x_A}$	$\zeta = -\frac{1}{\rho} \left(\frac{\partial \rho}{\partial x_A} \right)_{p, T}$
Flux	q	$\mathbf{J}_A^* = \mathbf{N}_A - x_A (\mathbf{N}_A + \mathbf{N}_B)$
Transfer rate	Q	$N_A - x_A (N_A + N_B)$
Transfer coefficient	$h = \frac{Q}{A_s \Delta T}$	$\bar{k}_x = \frac{N_A - x_A (N_A + N_B)}{A_s (x_{Ai} - x_{A\infty})}$
Dimensionless groups that are the same in both correlations	$Re = \frac{\ell v \rho}{\mu}$ $Fr = \frac{v^2}{g \ell}$	$Re = \frac{\ell v \rho}{\mu}$ $Fr = \frac{v^2}{g \ell}$
Basic dimensionless groups that are different	$Nu = \frac{h \ell}{k}$ $Pr = \frac{\bar{C}_p \mu}{k} = \frac{\mu}{\rho \alpha}$ $Gr_H = \frac{\ell^3 \rho^2 g \beta \Delta T}{\mu^2}$ $St_H = \frac{Nu}{Re Pr} = \frac{h}{\rho \bar{C}_p v}$	$Sh = \frac{k_x \ell}{C \mathcal{D}_{AB}}; \frac{k_c \ell}{\mathcal{D}_{AB}}$ $Sc = \frac{\mu}{\rho \mathcal{D}_{AB}}$ $Gr_B = \frac{\ell^3 \rho^2 g \zeta \Delta x_A}{\mu^2}$ $St_B = \frac{Sh}{Re Sc} = \frac{k_x}{C v}; \frac{k_c}{v}$
Special combinations of dimensionless groups	$Pe_H = Re Pr = \frac{\ell v \rho \bar{C}_p}{k}$ $j_H = Nu Re^{-1} Pr^{-1/3}$ $= \frac{h}{\rho \bar{C}_p v} \left(\frac{\bar{C}_p \mu}{k} \right)^{2/3}$	$Pe_B = Re Sc = \frac{\ell v}{\mathcal{D}_{AB}}$ $j_B = Sh Re^{-1} Sc^{-1/3}$ $= \frac{k_x}{C v} \left(\frac{\mu}{\rho \mathcal{D}_{AB}} \right)^{2/3}; \frac{k_c}{v} \left(\frac{\mu}{\rho \mathcal{D}_{AB}} \right)^{2/3}$

Source: Reprinted by permission of the publisher from Bird et al., 1960.

and

$$j_B = Sh Re^{-1} Sc^{-1/3} = \frac{k_c}{v} \left(\frac{\mu}{\rho \mathcal{D}} \right)^{2/3}; \frac{k_x}{C v} \left(\frac{\mu}{\rho \mathcal{D}} \right)^{2/3} \quad (4.106)$$

where Sh in mass transfer corresponds to Nu in heat transfer and j_B is the mass transfer Chilton–Colburn j -factor, ℓ is the length scale of the system, and ζ is the concentration coefficient of volumetric expansion (see Table 4.16 for the definition). Table 4.16 summarizes all the definitions of variables and dimensionless numbers and their correspondence to their respective entities in the heat transfer area. Note that the analogy of Table 4.16 holds for low mass transfer rates.

The analogies between heat and mass transfer in either form, forced or free convection, can be visualized as follows (Bird et al., 1960):

Forced convection:

$$\begin{aligned} Nu &= \text{a function of } (Re, Pr, \text{ geometry}) \\ Sh &= \text{a function of } (Re, Sc, \text{ geometry}) \end{aligned} \quad (4.107)$$

Free convection around submerged objects:

$$\begin{aligned} Nu &= \text{a function of } (Gr_H, Pr) \\ Sh &= \text{a function of } (Gr_B, Sc) \end{aligned} \quad (4.108)$$

As examples of the application of these analogies we illustrate their use in flow over a flat plate, around a submerged cylinder, and in free convection problems. Thus, Eq. 5.123 can be used directly for mass transfer problems for flow over a smooth flat plate as

$$Sh = 0.332 Re^{1/2} Sc^{1/3} \quad (4.109)$$

For transverse flow over a long cylinder (e.g., fiber spinning) the relevant equations (analogous to Eqs. 5.125 and 5.126) are

$$\begin{aligned} Sh &= (0.43 + 0.50 Re^{1/2}) Sc^{0.38} & \text{for } 1 < Re < 10^3 \\ Sh &= 0.25 Re^{0.6} Sc^{0.38} & \text{for } 10^3 < Re < 2 \times 10^5 \end{aligned} \quad (4.110)$$

For free convection problems, Eqs. 5.130, 5.131, and 5.132 can easily be translated to mass transfer applications using Table 4.16.

Example 4.10. Solution Casting

Figure 4.20 shows the process of production of solution-cast films. A polymer solution is cast onto a rotating roll (Middleman, 1977), and the solvent is removed by air flowing in the opposite direction. Then, the dry film is removed from the roll and goes into the next processing step. Estimate the convective mass transfer coefficient of the solvent into the air and the time needed for 80% solvent removal. The air speed, V , is 1 m/s; the radius of the roll, R , is 30 cm, and the thicknesses of the film, L , and the air duct, L' , are 2 mm. The polymer solution is in contact with the roll for one-fifth of its periphery. The average air temperature is 50 °C and a typical value for the diffusivity of the solvent into the air stream is $\mathcal{D}_{\text{Air}} = 1 \times 10^{-5} \text{ cm}^2/\text{s}$ and the diffusivity of the solvent in the solution is $\mathcal{D}_{\text{Aliq}} = 1 \times 10^{-6} \text{ cm}^2/\text{s}$.

Solution. In this problem, two mass transfer operations take place: diffusion of the solvent in the polymer solution (I) and into the air stream (II). The importance of these two operations is evaluated from the value of the Sherwood number, Sh :

$$Sh = \frac{k_c \ell}{\mathcal{D}_{\text{Air}}} \quad (4.111)$$

We first calculate the mass transfer coefficient, and then we solve the transient diffusion equation for the solvent in the solution.

Because the thickness of the solution on the roll is very small compared to the radius of the roll, we assume that the solution forms a plate over which an air stream flows and removes the solvent. Then, Eq. 4.109 is directly applicable to our case. The concentration of the solvent in the air is assumed small, so that the properties of the air remain unaltered. The density and viscosity of the air, at 50 °C, are $\rho =$

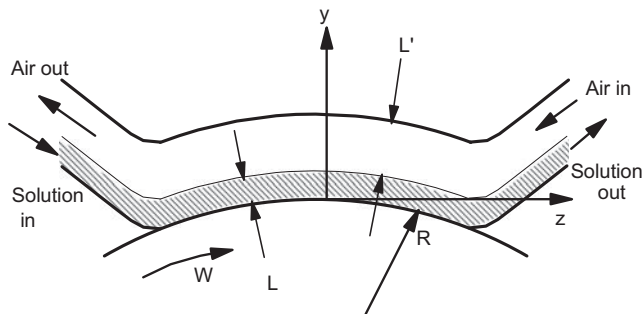


FIGURE 4.20 Solution-cast film geometry.

0.0011 g/cm³ and $\mu = 0.019 \text{ mPa}\cdot\text{s}$ (from Perry and Chilton, 1973). The contact length of the solution onto the roll is $l = 2\pi R/5 = 37.7 \text{ cm}$. The Reynolds number is calculated as

$$Re = \frac{100 \times 37.7 \times 100 \times 0.0011}{0.019} = 21,826 \quad (4.112)$$

Similarly, the Schmidt number is

$$Sc = \frac{0.019}{100 \times 0.0011 \times 0.00001} = 17,273 \quad (4.113)$$

Thus, the Sherwood number for the solvent transfer into the air, Sh , is calculated from Eq. 4.109 as

$$Sh = 0.332 \times 21,826^{1/2} \times 17,272^{1/3} = 1268 \quad (4.114)$$

and from this value the mass transfer coefficient k_c is calculated as

$$k_c = \frac{Sh \mathcal{D}}{\ell} = 3.26 \times 10^{-4} \text{ cm/s} \quad (4.115)$$

Assuming that the solution is moving in the z direction with a flat velocity profile of magnitude V , the term for the convective mass transfer in the z direction in Fick's second law, $V(\partial/\partial z)$, is equivalent to the unsteady term, $(\partial/\partial t)$. Furthermore, the boundary condition at $y = L$ is of the convective type, with Sh equal to 1268 (Eq. 4.114), which is equivalent to ∞ in Figure 4.5. From the same figure, for 80% removal

$$\frac{\mathcal{D}_{\text{Aliq}} t}{L^2} = 0.6^2 \Rightarrow t = 14,400 \text{ s} \quad (4.116)$$

Thus, the time is approximately 4 hours and some changes should be made to shorten this time. ■

4.5 SOLUTION TO DESIGN PROBLEM III

Figure 4.21 shows the schematic of one jet in dry-spinning conditions of fiber production. In the following analysis we solve the problem of one jet and assume that the solution is valid for all the jets together. We assume that the fiber at any axial distance is round, and thus we solve the problem using cylindrical coordinates. As the polymer solution exits the spinneret, it expands, and at the point of maximum cross-sectional area (dope) we put the origin of the coordinate system. As z increases, the cross-sectional area decreases due to the loss of solvent and the tension from the windup roll. At z_w (i.e., at the windup roll) the solvent should have been evaporated and the fiber solidified. The complete solution of the dry-spinning problem should include the momentum, energy, and mass balance equations along with the appropriate boundary conditions. The resulting system of equations

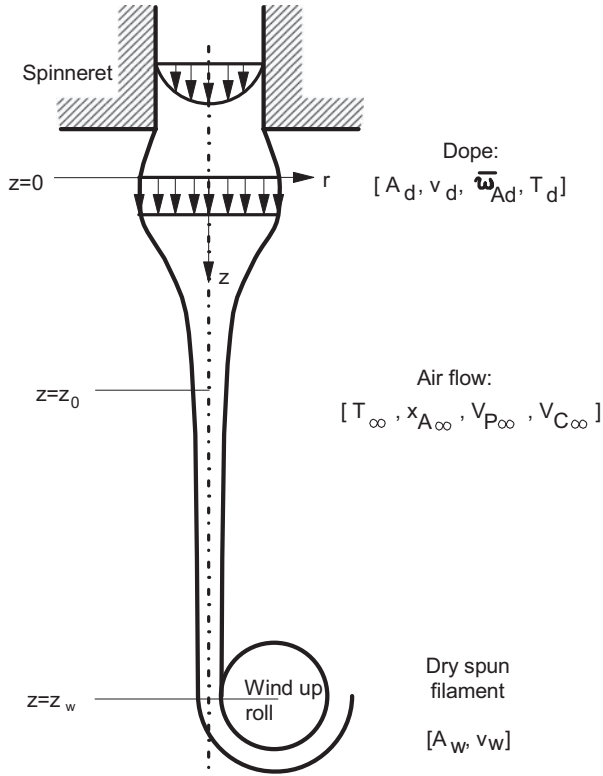


FIGURE 4.21 Dry-spinning system.

is very complex and in the present analysis we use some simplifying assumptions. We consider isothermal conditions and that the flash vaporization takes place at the spinneret exit, and thus it will not affect our discussion of the later stages.

The solvent diffuses from the spinning line (or filament) to the spinning line surface with diffusivity \mathcal{D}_{AP} , and it is carried away by the flowing air in a convective mode. Air is flowing at a cross direction to the fiber movement, but due to the high speed of the fiber air is also entrained in the parallel direction. Consequently, the convective mass transfer is taking place in the r as well as in the z directions. Because the cross-flow velocity is four times the parallel-flow velocity, the mass transfer coefficient of the cross flow is $3.17 (= 0.52 \times 4^{1/3}/0.26)$ times that of the parallel flow. Consequently, the controlling mass transfer coefficient is that of parallel flow.

To calculate this coefficient we need to estimate the properties of the air-DMF mixture at 200°C . We further assume that the properties of the mixture are very close to those of plain air. From Perry and Chilton (1973) we get that $\mu = 2.5 \times 10^{-5} \text{ Pa}\cdot\text{s}$, and from simple calculations from the law of ideal gases we get that $\rho = 7.47 \times 10^{-4} \text{ g/cm}^3$. Based on these values and the value of Sc we get that $\mathcal{D}_{\text{Air}} = 0.18 \text{ cm}^2/\text{s}$. Thus,

$$k_{c,P} = 0.402R(z)^{-2/3} \text{ cm/s} \quad (4.117)$$

The extreme values of $R(z)$ are 0.0178 cm at the dope and 0.0022 cm at the windup roll, so that the convective mass transfer coefficient varies from 5.9 to 23.8 cm/s . Therefore, the resistance to mass transfer in the air flow scales as $0.17 (=1/5.9)$ to $0.04 (=1/23.8)$.

The resistance to diffusion inside the spinning line is scaled as R/\mathcal{D}_{AP} . For an average spinning line temperature of 90°C , the diffusivity of DMF in PAN is calculated as

$$\begin{aligned} \mathcal{D}_{AP} &= 9.03 \times 10^{-4} \exp\left(\frac{-2360}{273 + 90}\right) \\ &= 1.36 \times 10^{-6} \text{ cm}^2/\text{s} \end{aligned} \quad (4.118)$$

Note that due to lack of more data we assume that the polymer fraction of the spinning line has no effect on the diffusivity of the DMF within the spinning line. Therefore, the diffusive resistance varies from 1620 to $13,130$, which represents from 4 to 6 orders of magnitude higher resistance within the spinning line than in the air flow. It is thus permissible to neglect the mass transfer in the air and to solve the diffusion equation within the spinning line with a boundary condition at the spinning line surface of zero DMF concentration.

The region where the solution which follows is applicable is somewhat away from the spinneret and its beginning is denoted by z_0 in Figure 4.21. A fluid element is located at z_0 at time $t = 0$. Finally, we arbitrarily set the average mass fraction of solvent at that point equal to 0.25 .

As a fluid element in the spinning line moves in the z direction, it changes its radius due to two reasons: tension from the windup roll and mass change due to solvent removal. Assuming that the mass change due to solvent removal is negligible we can consider the DMF diffusion within the spinning line as taking place in a stationary liquid ($v_r = 0$ or very small compared to v_z). Consequently, the diffusion equation in cylindrical coordinates for constant ρ becomes (Table 4.5)

$$\frac{\partial \omega_A}{\partial t} = \frac{1}{r} \frac{\partial}{\partial r} \left(r \mathcal{D}_{AP} \frac{\partial \omega_A}{\partial r} \right) \quad (4.119)$$

with initial and boundary conditions:

$$\begin{aligned} \text{I.C.:} \quad & \omega_A(r, 0) = \omega_{A0} \\ \text{B.C.1:} \quad & \omega_A(R, t) = 0 \\ \text{B.C.2:} \quad & \left(\frac{\partial \omega_A}{\partial r} \right)_{r=0} = 0 \end{aligned} \quad (4.120)$$

The solution to Eq. 4.119 subjected to the boundary and initial conditions given in Eq. 4.120 is given in many places

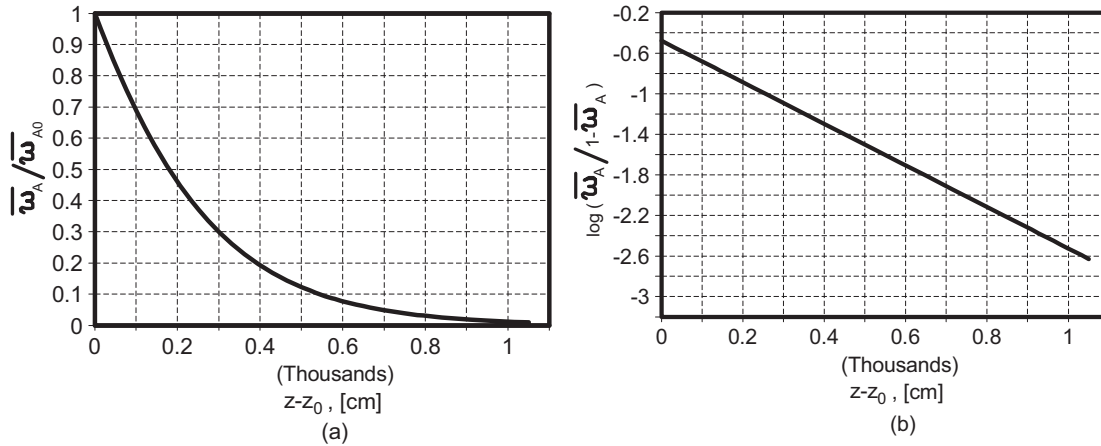


FIGURE 4.22 (a) Average mass fraction of the solvent DMF divided by the initial average mass fraction (at z_0) as a function of the axial distance from the reference point z_0 , for the system PAN–DMF. (b) The logarithm of the relative solvent concentration $\bar{w}_A/(1 - \bar{w}_A)$ as a function of the axial distance from the reference point z_0 , for the system PAN–DMF.

(e.g., Crank, 1975). If we average the solvent mass fraction over the cross-sectional area we get

$$\frac{\bar{w}_A}{\bar{w}_{A0}} = 4 \sum_{k=1}^{\infty} \mu_k^{-2} \exp\left(\frac{-\mu_k^{-2} \mathcal{D}_{AP} t}{R^2}\right) \quad (4.121)$$

where μ_k are the roots of the Bessel function $J_0(\mu_k) = 0$. If the series in Eq. 4.121 converges rapidly, we can keep only the first term, so that we get

$$\frac{\bar{w}_A}{\bar{w}_{A0}} = \frac{4}{\mu_1^2} \exp\left(\frac{-\mu_1^{-2} \mathcal{D}_{AP} t}{R^2}\right) \quad (4.122)$$

where $\mu_1 = 2.4048$.

Time, t , in Eq. 4.122 can be replaced by

$$t = \frac{z - z_0}{\bar{V}} \quad (4.123)$$

where \bar{V} is the velocity of the filament, which is considered to move as in plug flow. The mass flow rate of the polymer, \dot{m}_P , follows the relation

$$\dot{m}_P = \pi \rho R^2 \bar{V} (1 - \bar{w}_A) \quad (4.124)$$

Combining Eqs. 4.122–4.124, we get the following equation:

$$\frac{d\bar{w}_A}{dz} = - \left(\frac{\pi \rho \mu_1^2 \mathcal{D}_{AP}}{\dot{m}_P} \right) (1 - \bar{w}_A) \bar{w}_A \quad (4.125)$$

which is subject to the following boundary condition:

$$\text{B.C. : } \bar{w}_A(z_0) = \bar{w}_{A0} \quad (4.126)$$

Equation 4.125 subject to the boundary condition in Eq. 4.126 was solved and the results are shown in Figure 4.22. In Figure 4.22a the ratio of the average solvent mass fraction at the axial position z relative to that at z_0 is plotted against the

axial distance, and in Figure 4.22b the same data are formed in terms of the logarithm of the ratio of the average solvent mass fraction to the polymer mass fraction. The straight line in Figure 4.22b has also been experimentally observed (Ziabicki, 1976) for the region away from the spinneret. Figure 4.22a shows that the complete removal of the solvent is achieved at about 10 m away from the point where $\bar{w}_{A0} = 0.25$.

PROBLEMS

A. Applications

4A.1 Relationships Between Fluxes. Prove the following:

- The sum of the molar fluxes with respect to the molar average velocity is equal to zero in a multicomponent system,
- The sum of the mass fluxes with respect to the mass average velocity is equal to zero, and

$$\text{(c) } \mathbf{J}_i^* = \mathbf{N}_i - x_i \sum_{j=1}^n \mathbf{N}_j.$$

4A.2 Saturation of PP with Nitrogen Gas. A very thin disk (thickness: 0.159 cm) of PP is used for microcellular foaming experiments. The disk sits at the bottom of a cylindrical pressure vessel and it is exposed to high pressure nitrogen gas. Calculate the time necessary for nitrogen gas to diffuse into PP so that its concentration at the PP surface facing the bottom of the vessel reaches 90% of its equilibrium value. The diffusion coefficient of nitrogen in PP is $\mathcal{D} = 3.87 \times 10^{-8} \text{ cm}^2/\text{s}$. Assume that the high pressure does not affect the type of the diffusion process (i.e., it is still Fickian) and the value of the diffusivity.

4A.3 *Diffusion of Gas into Polymer Droplets and Fibers.* Consider a molten polymer blend with the minor component in the form of small spheres of radius 5 μm . Calculate the time it takes for the diffusion of these spheres from the major component to reach 90% equilibrium. Repeat the same calculations when the minor component is in the form of long fibers with the same radius as the spherical droplets. $D = 10^{-8} \text{ cm}^2/\text{s}$.

4A.4 *Economics of Barrier Polymers.* Four polymers are being considered for an oxygen barrier application. The polymers are: (1) Barex (trademark of Vistron Co.), which is an amorphous copolymer of acrylonitrile 70% mol/mol $[-\text{CH}(\text{CN})-\text{CH}_2-]$ and methyl acrylate $[-\text{C}(\text{CH}_3)(\text{COOCH}_3)-\text{CH}_2-]$, (2) EVAL-F (trademark of Kuraray Co.), which is a copolymer of ethylene (23% weight) and vinyl alcohol $[-\text{CH}(\text{OH})-\text{CH}_2-]$ with 70% crystallinity, (3) amorphous polyvinylidene chloride (PVDC) $[-\text{C}(\text{Cl}_2)-\text{CH}_2-]$ and (4) Nylon 6,6 with 40% crystallinity. Their density and cost per weight are as follows:

Barex	1.15 g/cm ²	2.76 \$/kg
EVAL-F	1.16 g/cm ²	4.85 \$/kg
PVDC	1.70 g/cm ²	2.76 \$/kg
Nylon 6,6	1.19 g/cm ²	3.75 \$/kg

Which is the most advantageous material for that application?

4A.5 *Plastic Automotive Fuel Tanks.* The North American auto industry is converting to plastic automotive fuel tanks from blow-molded HDPE. The advantages of HDPE tanks over the usual steel tanks are: no corrosion, lighter than steel, easily shaped to fit in the car, and more puncture resistant than steel. However, the HDPE tanks suffer from high permeability to liquid gasoline.

(a) Calculate the average mass loss of gasoline per day at steady state from an HDPE 60 liter tank with wall thickness of 1 mm, and compare it with the EPA standard of 2 g/day. Assume Fickian diffusion of gasoline in the HDPE wall and that the gasoline uptake by the wall via Langmuir sorption is zero. Simulate the tank with an equal volume cubic structure and assume that the tank is emptied with equal gasoline consumption each day. At 29 °C the following data is given (Kathios and Ziff, 1991): constant diffusivity and solubility of gasoline in HDPE equal to $7 \times 10^{-8} \text{ cm}^2/\text{s}$ and $0.066 \text{ g/cm}^3 \cdot \text{atm}$, respectively. Assume that the pressure in the tank is 1 atm and that the density of gasoline is 1 g/cm^3 .

(b) The most promising barrier technology to correct this high permeability is the coextrusion of

HDPE and polyamide to form a laminated structure. Thus, consider two adjacent layers of HDPE and polyamide. If the permeability of gasoline in polyamide is one-tenth of that in HDPE, what should the thickness of the polyamide layer be for the tank to conform with the EPA regulation?

4A.6 *Unsteady Diffusion in Cubes and Spheres.* Consider the unsteady diffusion of a gas into two polymer pellets: the first is a cube and the other is a sphere. Calculate the time needed for 90% saturation of the pellets at their centers, for the following cases: (a) same linear dimension, (b) same surface area, and (c) same volume of both pellets.

4A.7 *Poly(ethylene terephthalate) (PET) Pellet Drying.* PET is a relatively hydrophobic polymer (Myers et al., 1961), which still needs drying before processing. Calculate the temperature of the drying oven, so that the drying of spherical pellets, 3 mm in diameter, does not take more than 11 hours. Assume that the pellets were initially in equilibrium with air having 70% relative humidity.

B. Principles

4B.1 *Mass Uptake by Slabs and Spheres.* Consider a polymer slab at initial solute concentration C_{A0} and thickness $2b$. A solution with solute concentration $C_{A\infty}$ is brought in contact with the slab, so that the slab surface solute concentration is considered to be equal to $C_{A\infty}$. Prove that the mass uptake of solute, M_t , at time t is equal to

$$\left[\frac{M_t}{M_\infty} \right]_{\text{slab}} = 1 - \frac{8}{\pi^2} \sum_{n=0}^{\infty} \frac{1}{(2n+1)^2} \exp\left(-\frac{(2n+1)^2 \pi^2 D t}{4b^2}\right)$$

where M_∞ is the maximum uptake, which is equal to $2b(C_{A\infty} - C_{A0})$. Note that the left-hand side of the above equation is also equal to $(\bar{C}_A - C_{A0}) / (C_{A\infty} - C_{A0})$, where \bar{C}_A is the average concentration of A in the slab. Also, prove that a similar expression holds for a polymer sphere, that is,

$$\left[\frac{M_t}{M_\infty} \right]_{\text{sphere}} = 1 - \frac{6}{\pi^2} \sum_{n=0}^{\infty} \frac{1}{n^2} \exp\left(-\frac{n^2 \pi^2 D t}{R^2}\right).$$

4B.2 *Saturation of Polyetheretherketone (PEEK) with Carbon Dioxide Gas.* PEEK (see Table 5.8) is used in foaming experiments with carbon dioxide as the foaming agent. The description of the experiment is the same as in Problem 4A.2. Calculate the diffusion

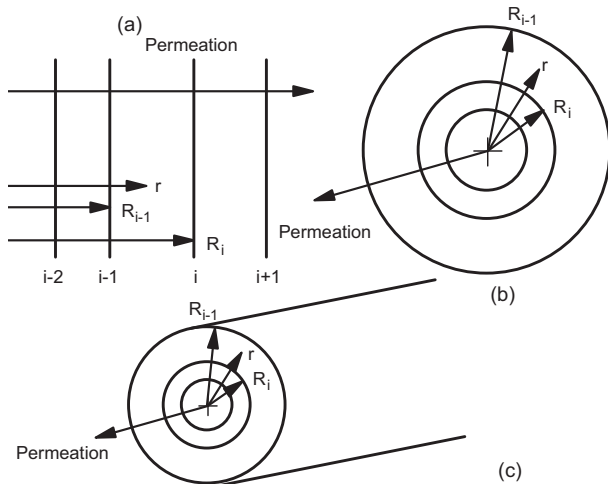


FIGURE 4.23 Structures of laminar composites in permeation experiments: (a) slabs, (b) hollow cylinders, and (c) spherical shells.

coefficient of CO₂ in PEEK at room temperature and then calculate the time needed for 90% saturation of the bottom surface. At which temperature is the time span of the experiment one day? Assume $\phi_c = 50\%$.

4B.3 *PET Bottles for Carbonated Beverages—Steady-State Simulation.* Amorphous PET is extensively used in the production of bottles for carbonated beverages. Consider such a bottle with radius of 6 cm and with a headspace equal to 6% of the volume of the beverage. Assume that the bottle loses carbon dioxide through the sides only and that the wall thickness is much smaller than the bottle radius. The beverage inside the bottle is considered nonmarketable if the partial pressure differential between inside and outside of the bottle drops to about 90% of the initial pressure differential in three months. Calculate the minimum wall thickness to achieve such partial pressure drop at steady state if the bottle is left on the shelf for three months at 25 °C. The structural unit of PET is $[-O-CH_2-CH_2-O-CO-C_6H_4-CO-]$. Assume that Henry’s law is applicable, and neglect any carbon dioxide uptake by the bottle walls via Langmuir sorption. The solubility of carbon dioxide into the beverage obeys Henry’s law with a coefficient of $3.28 \times 10^{-5} \text{ mol/cm}^3 \cdot \text{atm}$.

4B.4 *Permeability of Composite Laminates.* Consider a laminar composite structure, in which the laminae, L_i , are normal to the direction of permeation. These laminae can be either slabs, or hollow cylinders, or spherical shells (Fig. 4.23). Prove that the composite permeability, \bar{P} , is given by the relationship

$$\frac{I_v(R_0, R_n)}{\bar{P}} = \sum_{i=1}^n \frac{I_v(R_{i-1}, R_i)}{\bar{P}_i}$$

where n is the total number of laminates and R represents the linear dimension of the composite structure. I_v is given by

$$I_v(R_{i-1}, R_i) = \int_{R_{i-1}}^{R_i} \frac{1}{r^{v-1}} dr$$

where v is the *order* of the structure, that is, 1 for slabs, 2 for cylinders, and 3 for spheres.

4B.5 *Diffusivity of a Polymer Blend.* Model a polymer blend by a lattice of rectangular parallelepipeds (Barrer and Petropoulos, 1961) suspended in a polymer matrix, Figure 4.24. Using geometrical arguments and Fick’s first law, calculate the blend diffusivity, D_{blend} , as a function of the diffusivities of both phases and geometrical constants. Simplify the expression for the cases of (a) impermeable dispersed phase, (b) dispersion of platelets, and (c) extremely permeable dispersed phase in the form of platelets.

4B.6 *Crack Healing of PMMA.* Similar to the hot-melt adhesive bonding of polyethylene (see Problem 4C.4) is the problem of welding (healing) a crack at elevated temperatures with the application of a slight pressure (Jud et al., 1981). The success of the healing process is judged by comparing the fracture toughness of the healed sample, K_{Ii} , to the original fracture toughness, Figure 4.25. Calculate the penetration depth of the PMMA macromolecules for successful healing and compare it to the radius of gyration of PMMA. According to Graessley (1980) and based on the reptation theory for the diffusion of macromolecules (“snake-like movements”) the self-diffusion coefficient is given by

$$D_s = \frac{G_N^0}{135} \left(\frac{\rho R_g T}{G_N^0} \right)^2 \left(\frac{R^2}{MW} \right) \frac{M_{cr}}{(MW)^2 \eta_0(M_{cr})}$$

where the symbols, their names, and their values for PMMA at 390 K are as follows (Jud et al., 1981):

G_N^0	Plateau modulus	6.36×10^4 N/m ²
ρ	Density	1.14 g/cm ³
MW	Molecular weight	120,000
R^2/MW	Mean square end-to-end distance/MW	4.56×10^{-19} m ² · mol/g
M_{cr}	Critical MW for entanglements	30,000
$\eta_0(M_{cr})$	Zero shear viscosity for M_{cr}	2.14×10^7 Pa·s

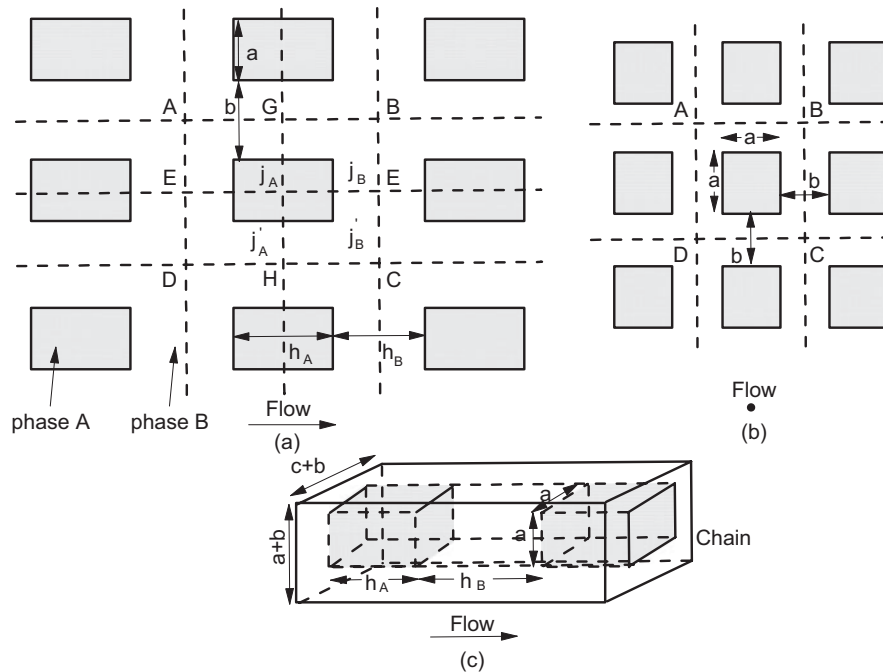


FIGURE 4.24 Lattice of rectangular parallelepipeds. (a) Side view. (b) End-on view. (c) Three-dimensional view. (Reprinted by permission of the publisher from Barrer and Petropoulos, 1961.)

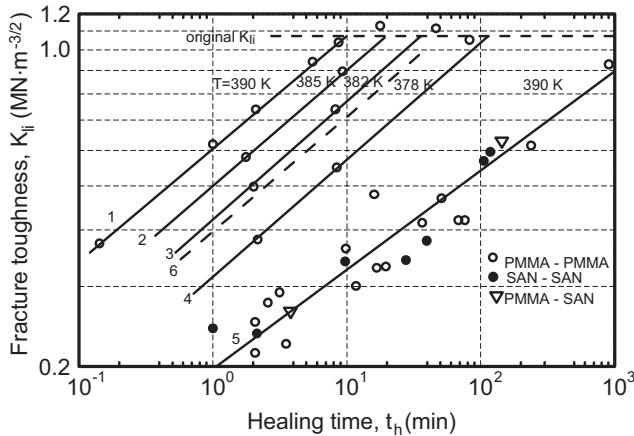


FIGURE 4.25 Fracture toughness against healing time. Curves 1–4: healing of broken PMMA immediately after fracture. Curve 5: surfaces welded after vacuum drying and polishing. Curve 6: healing at 390 K immediately after fracture of dried PMMA samples. (Reprinted by permission of the publisher from Jud et al., 1981.)

C. Numerical Problems

4C.1 Dissolution of a Bubble into a Molten Polymer Matrix. Consider a molten polymer matrix with dispersed bubbles of radius $R_0 = 10 \mu\text{m}$. Calculate the dissolution time of the bubble, t_{dis} , using Fick’s second law of diffusion in spherical coordinates and moving (shrinking) boundaries. As the gas (species A) diffuses out the radius of the bubble decreases. Also,

consider that (Epstein and Plesset, 1950) the initial mass fraction of the gas into the polymer matrix is equal to zero, and neglect any surface tension effects as well as the hydrodynamic response of the polymer melt to the bubble shrinkage. Then,

1. Write Fick’s second law of diffusion.
2. Introduce a new dependent variable $u = r(\rho_A - \rho_{As})$, where ρ_{As} is the gas concentration at the interface.
3. Solve the resulting equation and calculate the flux of gas at the surface of the bubble.
4. Relate the change in radius to the flux.
5. Solve the resulting differential equation, using a simplifying assumption (constant term in the equation vanishes). Show that the approximate complete dissolution time is given by

$$t_{\text{dis}} = \frac{R_0^2}{2DK}$$

where K is the partition coefficient of the gas at the interface and the gas inside the bubble. Also show that $t_{\text{dis}} = 250 \text{ s}$ for $\mathcal{D} = 10^{-7} \text{ cm}^2/\text{s}$ and $K = SR_gT/MW = 0.02$, where S is the Henry’s law constant for the gas–polymer system in $\text{g}/\text{cm}^3 \cdot \text{atm}$.

4C.2 Nylon 6 Pellet Drying. Nylon 6 is a relatively hydrophilic polymer. Asada and Onogi (1963) measured the diffusion coefficient of water vapor in Nylon

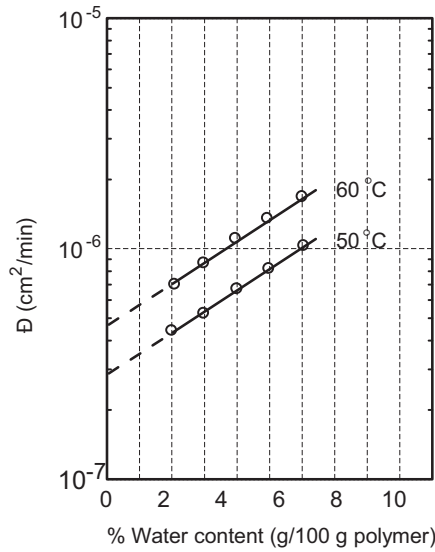


FIGURE 4.26 Diffusion coefficient of moisture in Nylon 6 as a function of moisture content. (Reprinted by permission of the publisher from Asada and Onogi, 1963.)

6 and their data are shown in Figure 4.26. The polymer pellets are to be dried to 0.15% g/g with dehumidified air at temperatures less than 80 °C. Calculate the dehumidification time for spherical pellets 3 mm in diameter. Nylon 6 has 70% crystallinity and in this particular case was in equilibrium with air at 70% relative humidity. $\rho = 1.13 \text{ g/cm}^3$ for Nylon 6.

4C.3 Mutual Diffusion of Polymers in Contact (Adhesion).

Diffusion theory is one of the theories of adhesion. According to this theory, the molecules of two polymers in mutual contact diffuse across the interface (Fig. 4.27), so that after some time the interface does not exist. The strength of the joint will then depend on the distance the macromolecules have interpenetrated each other. Crack healing is also based on the theory of diffusion.

(a) Consider two semi-infinite polymer slabs. One of the slabs is doped with a diffusant at concentration C_{A0} , whereas the other one is diffusant free. At time $t = 0$, the two slabs are brought into contact at $x = 0$. Calculate the diffusant concentration profile as a function of time as shown in Figure 4.28.

(b) An infrared spectrometer is used to measure the interdiffusion of poly(vinyl methyl ether) (PVME) and polystyrene (PS) (Jabbari and Pepas, 1993). The assembly consists of a solution-cast PS thin film on top of a germanium crystal, and a solution-cast PVME film on top of the PS film. The thickness of the PS film is 1 μm . Calculate the time it takes for the PVME molar

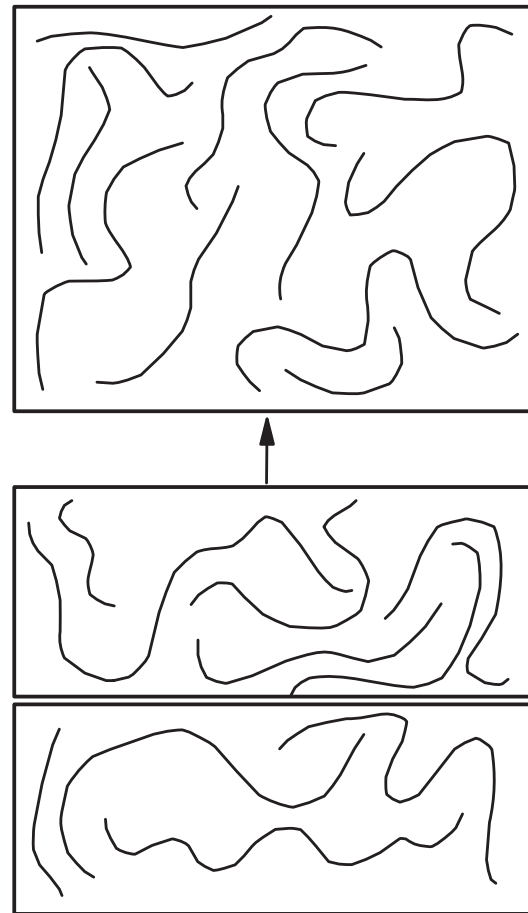


FIGURE 4.27 Diffusion across the interface between two polymers in contact. The interface becomes diffuse as the mutual diffusion takes place.

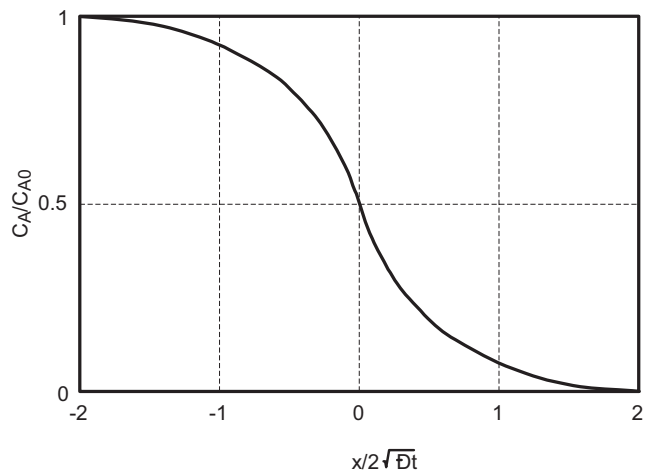


FIGURE 4.28 Diffusant concentration as a function of distance for two semi-infinite slabs in contact. Initially only one of them had nonzero diffusant concentration.

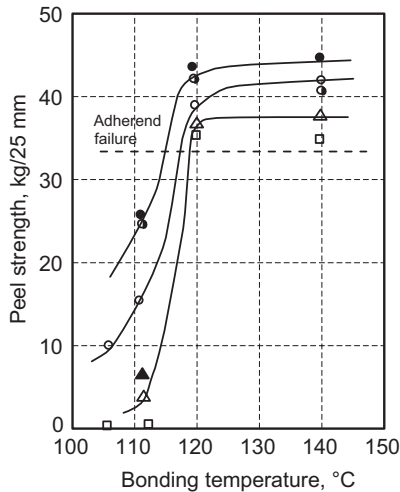


FIGURE 4.29 Peel strength at 23 °C as a function of the bonding temperature. The symbols represent the various types of thermoplastic adhesives (ethylene copolymers) used to adhere two sheets of polyethylene for 300 s. (Reprinted by permission of the publisher from Yamakawa, 1976.).

concentration at the crystal–PS interface to reach 80% of its equilibrium value. Assume Fickian diffusion and diffusivity equal to 1.1×10^{-12} cm²/s.

4C.4 Adhesive Bond Strength and Diffusion. Yamakawa (1976) studied the effect of bonding temperature on the peel strength of two polyethylene sheets bonded with an ethylene copolymer as the bonding agent (Fig. 4.29). Assume that (1) the thicknesses of the polyethylene sheets and the adhesive bond are considered as infinite compared to the penetration depth of the adhesive; (2) $\mathcal{D}_{AP}(140\text{ °C}) = 5 \times 10^{-11}$ cm²/s and $E_{\mathcal{D}} = 50$ kJ/mol; and (3) the adhesive bonding is satisfactory (leveled portion of curves in Fig. 4.29) when the penetration depth of the adhesive (at 10% concentration change) exceeds a threshold value. Calculate that threshold value and the bonding time for successful bonding of the two polyethylene sheets at 110 °C.

4C.5 Mass Uptake in Slabs, Spheres, and Cylinders. Solve Problem 4B.1 for slabs, spheres, and cylinders using numerical methods.

4C.6 Transient Diffusion and Dual-Mode Sorption

- Rework Problem 4B.3 in the transient mode, assuming again that the carbon dioxide uptake by the PET wall via Langmuir sorption is zero. Assume $\mathcal{D} = 1.10 \times 10^{-9}$ cm²/s, and wall thickness, b , equal to 0.57 mm.
- Sorption and diffusion of gases in glassy polymers might be described by the dual-mode sorption

model (Vieth, 1991). The basic assumptions of the model are as follows:

- Two modes of sorption, Henry's law sorption, $C_{\mathcal{D}} = S_{\mathcal{D}}P$, and Langmuir sorption (or "microvoid filling" sorption; Section 4.2.4), $C_{\text{H}} = C'_{\text{H}}b'P/(1 + b'P)$, occur simultaneously. $S_{\mathcal{D}}$ is the Henry's law constant in mol/cm³·atm, C'_{H} is the microvoid saturation constant in mol/cm³, b' is the microvoid affinity constant in atm⁻¹, and P is the pressure in atm.
- The two modes are in local equilibrium throughout the glassy polymer.
- The gas sorbed in the Langmuir mode is completely immobilized.
- Henry's mode is the only diffusion mode.
- The diffusion coefficient is constant.

Based on these assumptions show that Fick's second law is now expressed as

$$\mathcal{D} \frac{\partial^2 C_{\mathcal{D}}}{\partial x^2} = \frac{\partial C_{\mathcal{D}}}{\partial t} \left[1 + \frac{C'_{\text{H}}b'/S_{\mathcal{D}}}{(1 + C_{\mathcal{D}}b'/S_{\mathcal{D}})^2} \right]$$

and then rework part (a) of this problem, using the following data (Masi and Paul, 1982): the initial pressure in the headspace is equal to 4.0 atm, $S_{\mathcal{D}} = 1.48 \times 10^{-5}$ mol/cm³·atm, $C'_{\text{H}} = 3.235 \times 10^{-4}$ mol/cm³, and $b' = 0.351$ atm⁻¹.

4C.7 Interdiffusion in a Polymer Blend. A dilute polymer blend consists of a minor component A, which is dispersed in the form of droplets 2 μm in diameter, and a major component B. The volume fraction of A is $\phi_{\text{A}} = 1.56\%$. Calculate the time it takes for the molar concentration of A at the center of a droplet to decrease by 95% of its original concentration, assuming Fickian interdiffusion and constant $\mathcal{D} = 1 \times 10^{-12}$ cm²/s.

4C.8 Combination of Fickian and Case II Transports. During the sorption of acetone in a poly(vinyl chloride) (PVC) slab of thickness $2b$, submerged into a large acetone bath at room temperature, the slab is divided into two regions. The first one is the gel-like region, which is in direct contact with the acetone bath and where the transport of acetone can be described by a combination of a Fickian diffusion, with diffusion coefficient \mathcal{D} , and a Case II diffusion, with velocity of the advancing front V . The second region is the glass region, where the transport is described by a Fickian diffusion, with diffusion coefficient \mathcal{D}_{g} . For $\mathcal{D} \gg \mathcal{D}_{\text{g}}$ only the transport of acetone in the gel-like region is considered. According to Kwei et al. (1972) the

one-dimensional transport equation for the gel-like region is

$$D \frac{\partial^2 C}{\partial x^2} - V \frac{\partial C}{\partial x} = \frac{\partial C}{\partial t}$$

where C is the molar concentration of acetone. The advancing acetone front is located at $\theta_x = C_x/C_0 = 0.068$, where $C_0 = 8.62 \times 10^{-3} \text{ mol/cm}^3$ is the equilibrium molar concentration of acetone in the gel-like region. Calculate the acetone molar concentration profile and the mass uptake as a function of distance and time for swelling number $Sw = Vb/D$ equal to 3.87, and compare it with the simple Fickian case (i.e., where $Sw = 0$).

D. Design Problems

4D.1 Microcellular Foaming. Microcellular foam is a kind of plastic foam with bubble size less than 10 μm , which is much less than the conventional foam. Indications of improvement of the properties of the polymer matrix by microcellular foaming have given importance to this relatively new process. One technique to produce microcellular foam is the gas supersaturation technique, which for amorphous materials consists of three steps: gas saturation, supersaturation, and foaming. In the first step the polymer matrix is saturated with the foaming gas (nitrogen, carbon dioxide, etc). In the second step the gas pressure is released creating supersaturation conditions, but the polymer matrix does not foam because the temperature is low (above room temperature but below the glass transition temperature of the polymer matrix). Foaming takes place in the final step, during which the sample is submerged into an oil bath kept at a temperature above the glass transition temperature of the polymer matrix. During this step the bubble can be initiated either at a heterogeneous nucleation site or at a microcrack of the matrix created during the forming process.

- (a) Follow the steps outlined in Problem 4C.1 and calculate the radius of the bubble as a function of foaming time, for a diffusion-controlled process (Fig. 4.30); that is, the hydrodynamic force which resists bubble growth is considered negligible compared to the diffusion force. Neglect the effects of surface tension, and assume that the bubble is suspended in an infinite sea of polymer matrix ($S(t) \rightarrow \infty$).
- (b) As a numerical example consider PS as the polymer matrix at 188 °C, and the following gases

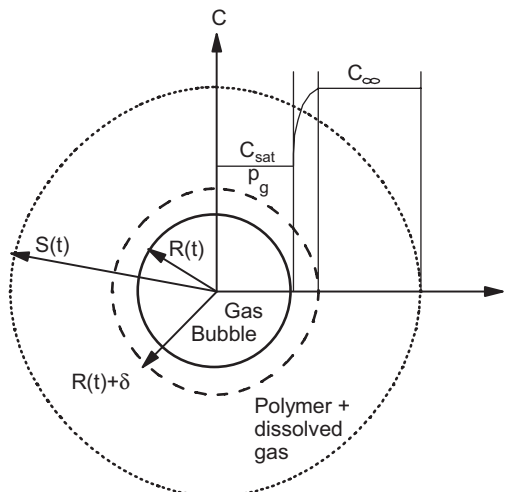


FIGURE 4.30 Gas bubble growing in an infinite sea of polymer matrix. $S(t)$ presents the radius of the cell assigned to each growing bubble (∞ in our problem). δ presents the thickness of the concentration layer, where the gas concentration changes from its undisturbed value C_∞ to C_{sat} .

with their corresponding Henry’s law constants (Durill and Griskey, 1966) in $\text{cm}^3(\text{STP})/\text{g}\cdot\text{atm}$:

Nitrogen	0.049
Carbon dioxide	0.220
CFC-22	0.388
Argon	0.093
Helium	0.029

The saturation pressure is 1000 psi (6.9 MPa), and the pressure inside the growing bubble is the ambient pressure. Neglect the surface tension forces between the bubble and the polymer. Which gas is the most promising for microcellular foaming?

- (c) Propose changes in the above experimental procedure that might bring more controllability to the foaming process.

4D.2 Precipitation Foams. The insulation of a wire is achieved by a solution coating process, which also involves a precipitation foaming process. The whole process consists of the following four steps.

1. *Coating (coating of the conductor).* A copper conductor is passed through a crosshead die where it is coated with a solution of about 30% HDPE in xylene at 130 °C.
2. *Whitening.* The coated conductor passes through water at about 80 °C and thus the HDPE crystallizes, precipitates out, and whitens the solution.
3. *Drying.* The whitened insulation on the conductor is dried by passing through an air duct where the

air temperature and the air speed are controlled at about 55 °C and 4 m/s, respectively.

4. *Inversion*. The final foamed structure is created by sintering and fusion of the polyethylene particles. If the radius of the copper wire is 150 μm and the radius of the insulation is 350 μm, calculate the time of the drying step, neglecting any shrinkage of the insulation during this step.

REFERENCES

- Alfrey, T., E. F. Gurnee, and W. G. Lloyd. 1966. "Diffusion in Glassy Polymers." *J. Polym. Sci.: Part C*, **12**, 249–261.
- Asada, T. and S. Onogi. 1963. "The Diffusion Coefficient for the Nylon 6 and Water System." *J. Colloid Sci.*, **18**, 784–792.
- Barrer, R. M. and J. H. Petropoulos. 1961. "Diffusion in Heterogeneous Media: Lattices of Parallelepipeds in a Continuous Phase." *Br. J. Appl. Phys.*, **12**(12), 691–697.
- Biceramo, J. 1993. *Prediction of Polymer Properties* (Marcel Dekker, New York).
- Bird, R. B., W. E. Stewart, and E. N. Lightfoot. 1960. *Transport Phenomena* (Wiley, Hoboken, NJ).
- Boelter, L. M., V. H. Cherry, H. A. Johnson, and R. C. Martinelli. 1965. *Heat Transfer Notes* (McGraw Hill, New York).
- Brandrup, J. and E. H. Immergut, Eds. 1989. *Polymer Handbook*, 3rd edition. (Wiley, Hoboken, NJ).
- Cheng, Y. L. and D. C. Bonner. 1978. "Solubility of Nitrogen and Ethylene in Molten Low-Density Polyethylene to 69 Atmospheres." *J. Polym. Sci.*, **16**, 319–333.
- Comyn, J., Ed. 1985. *Polymer Permeability* (Elsevier, New York).
- Crank, J. 1956. *The Mathematics of Diffusion* (Oxford University Press, Oxford).
- Crank, J. 1975. *The Mathematics of Diffusion*, 2nd edition. (Oxford University Press, Oxford).
- Crank, J. and G. S. Park, Eds. 1968. *Diffusion in Polymers* (Academic Press, New York).
- Duda, J. L., G. K. Kimmerly, W. L. Sigelco, and J. S. Vrentas. 1973. "Sorption Apparatus for Diffusion Studies with Molten Polymers." *Ind. Eng. Chem. Fundam.*, **12**(1), 133–136.
- Durrill, P. L. and R. G. Griskey. 1966. "Diffusion and Solution of Gases in Thermally Softened or Molten Polymers: Part I. Development of Technique and Determination of Data." *AIChE J.*, **12**(6), 1147–1151.
- Durrill, P. L. and R. G. Griskey. 1969. "Diffusion and Solution of Gases into Thermally Softened or Molten Polymers: Part II. Relation of Diffusivities and Solubilities with Temperature, Pressure, and Structural Characteristics." *AIChE J.*, **15**(1), 106–110.
- Epstein, P. S. and M. S. Plesset. 1950. "On the Stability of Gas Bubbles in Liquid–Gas Solutions." *J. Chem. Phys.*, **18**(11), 1505–1509.
- Gorski, R. A., R. B. Ramsey, and K. T. Dishart. 1985. "Physical Properties of Blowing Agent Polymer Systems—I. Solubility of Fluorocarbon Blowing Agents in Thermoplastic Resins." 29th Annual Tech./Mark. Conference, SPI Polyurethane Division, pp. 286–299.
- Graessley, W. W. 1980. "Some Phenomenological Consequences of the Doi–Edwards Theory of Viscoelasticity." *J. Polym. Sci.: Polym. Phys. Ed.*, **18**, 27–34.
- Hines, A. L. and R. N. Maddox. 1985. *Mass Transfer* (Prentice Hall, Englewood Cliffs, NJ).
- Hopfenberg, H. B. and H. L. Frisch. 1969. "Transport of Organic Macromolecules in Amorphous Polymers." *Polym. Lett.*, **7**, 405–409.
- Jabbari, E. and N. A. Peppas. 1993. "Use of ATR-FTIR to Study Interdiffusion in Polystyrene and Poly(vinyl methyl ether)." *Macromolecules*, **26**, 2175–2186.
- Jud, K., H. H. Kausch, and J. G. Williams. 1981. "Fracture Mechanics Studies of Crack Healing and Welding of Polymers." *J. Mater. Sci.*, **16**, 204–210.
- Kathios, D. J. and R. M. Ziff. 1991. "Permeation of Gasoline–Alcohol Fuel Blends Through High Density Polyethylene Fuel Tanks." 49th SPE Annual Technical Conference, Montreal, **37**, 1509–1511.
- Kausch, H. H. and M. Tirrell. 1989. "Polymer Interdiffusion." *Annu. Rev. Mater. Sci.*, **19**, 341–377.
- Koros, W. J. and M. W. Hellums. 1989. "Transport Properties." In H. F. Mark et al., Eds., *Encyclopedia of Polymer Science and Technology*, Supplement, pp. 724–802 (Wiley, Hoboken, NJ).
- Kwei, T. K., T. T. Wang, and H. M. Zupko. 1972. "Diffusion in Glassy Polymers. V. Combination of Fickian and Case II Mechanisms." *Macromolecules*, **5**(5), 645–646.
- Masi, P. and D. R. Paul. 1982. "Modeling Gas Transport in Packaging Applications." *J. Membr. Sci.*, **12**, 137–151.
- Middleman, S. 1977. *Fundamentals of Polymer Processing* (McGraw-Hill, New York).
- Myers, A. W., J. A. Meyer, C. E. Rogers, V. Stannett, and M. Szwarc. 1961. "Studies in the Gas and Vapor Permeability of Plastic Films and Coated Papers." *Tappi*, **44**(1), 58–64.
- Ohzawa, Y., and Y. Nagano. 1970. "Studies on Dry Spinning. II. Numerical Solutions for Some Polymer–Solvent Systems Based on the Assumption that Drying is Controlled by Boundary-Layer Mass Transfer." *J. Appl. Polym. Sci.*, **14**, 1979–1999.
- Ohzawa, Y., Y. Nagano, and T. Matsuo. 1969. "Studies on Dry Spinning. I. Fundamental Equations." *J. Appl. Polym. Sci.*, **13**, 257–283.
- Perry, R. H. and C. H. Chilton, Eds. 1973. *Chemical Engineers' Handbook*, 5th edition. (McGraw Hill, New York).
- Reid, R. C., J. M. Prausnitz, and T. K. Sherwood. 1977. *The Properties of Gases and Liquids*, 3rd edition. (McGraw Hill, New York).
- Salame, M. 1986. "Prediction of Gas Barrier Properties of High Polymers." *Polym. Eng. Sci.*, **26**(22), 1543–1546.
- Sarti, G. C. and F. Doghieri. 1994. "Non-Fickian Transport of Alkyl Alcohols Through Prestretched PMMA." *Chem. Eng. Sci.*, **49**(5), 733–748.
- Stiel, L. I. and D. F. Harnish. 1976. "Solubility of Gases and Liquids in Molten Polystyrene." *AIChE J.*, **22**(1), 117–122.

- Thomas, N. and A. H. Windle. 1978. "Case II Swelling of PMMA Sheet in Methanol." *J. Membr. Sci.*, **3**, 337–342.
- Thomas, N. and A. H. Windle. 1982. "A Theory of Case II Diffusion." *Polymer*, **23**, 529–542.
- Tirrel, M. 1984. "Polymer Self-Diffusion in Entangled Systems." *Rubber Chem. Technol.*, **57**, 523–556.
- Van Krevelen, D. W. 1990. *Properties of Polymers*, 3rd edition. (Elsevier, New York).
- Vieth, W. R. 1991. *Diffusion In and Through Polymers* (Hanser, Munich).
- Vrentas, J. S., C. M. Jarzebski, and J. L. Duda. 1975. "A Deborah Number for Diffusion in Polymer–Solvent Systems." *AIChE J.*, **21**, 894–901.
- Vrentas, J. S., J. L. Duda, and M. K. Lau. 1982. "Solvent Diffusion in Molten Polyethylene." *J. Appl. Polym. Sci.*, **27**, 3987–3997.
- Yamakawa, S. 1976. "Hot-Melt Adhesive Bonding of Polyethylene with Ethylene Copolymers." *Polym. Eng. Sci.*, **16**(6), 411–418.
- Ziabicki, A. 1976. *Fundamentals of Fibre Formation* (Wiley, Hoboken, NJ).

5

NONISOTHERMAL ASPECTS OF POLYMER PROCESSING

DESIGN PROBLEM IV CASTING OF POLYPROPYLENE FILM

Polypropylene is extruded at 200 °C from a film die having lips 76.2 cm wide and 0.1016 cm thick (see Fig. 5.1). The extruded film is drawn down to a width of 60.96 cm and a thickness of 0.005 cm. The distance from the die face to the casting drum is 2.54 cm. The film is in contact with the drum over a length of 70% of the circumference of the drum. The air temperature is taken as 25 °C and the line speed is 60 m/min. The radius of the drum is 0.45 m. Determine the heat transfer coefficient required at the drum surface to produce a clear film. The requirement for a clear film is based on keeping the crystallinity at the center to be less than 3% and the spherulite size less than 5000 μm . Tap water at 12 °C is available for cooling.

Most polymer processes involve heat transfer. Polymers must usually be heated above their melting points before shaping and then cooled to maintain the desired shape. It is during the cooling phase of the process that the physical properties of the polymer can drastically be altered. Because the thermodynamic and thermal properties of most polymers are rather similar to other materials, it is not necessary to develop any new laws as it was for the flow of polymers. Hence, this chapter serves mostly as a review of heat transfer with emphasis on those topics pertinent to polymer processing. The main aspects that require additional discussion and that set polymers apart from other materials are their crystallization behavior and the ability to control molecular orientation during processing.

We begin by summarizing how one handles the temperature dependence of rheological properties of polymer melts in Section 5.1. In Section 5.2 the shell balance approach is used to set up one-dimensional nonisothermal problems encountered in polymer processing. In this same section we summarize the nonisothermal equations of change and their use in polymer processing. The thermal transport properties that occur in these equations include heat capacity, thermal conductivity, density, and for semicrystalline polymers, heat of fusion. These topics are addressed in Section 5.3. In Section 5.4 the solutions to well-known problems in heat transfer are presented as well as a summary of charts for heat transfer coefficients for commonly encountered geometries. As radiation heat transfer is encountered in a number of processes, this form of heat transfer is also reviewed in Section 5.4. The mechanical properties of polymers depend on the morphology and orientation that are generated during the cooling process and in Section 5.5 these topics are discussed. Finally, in Section 5.6 the solution to Design Problem IV is presented.

5.1 TEMPERATURE EFFECTS ON RHEOLOGICAL PROPERTIES

The rheological properties of polymer melts and solutions are highly dependent on temperature. This is clearly illustrated by the data presented in Figure 2.5 (p. 12), where the zero shear rate viscosity, η_0 , drops by two orders of magnitude as the temperature is raised from 115 °C to 240 °C. In general, as illustrated in this same figure, the shape of the curves remains nearly unchanged at each temperature. Because of this similarity in the shape of the flow curves, it is possible to

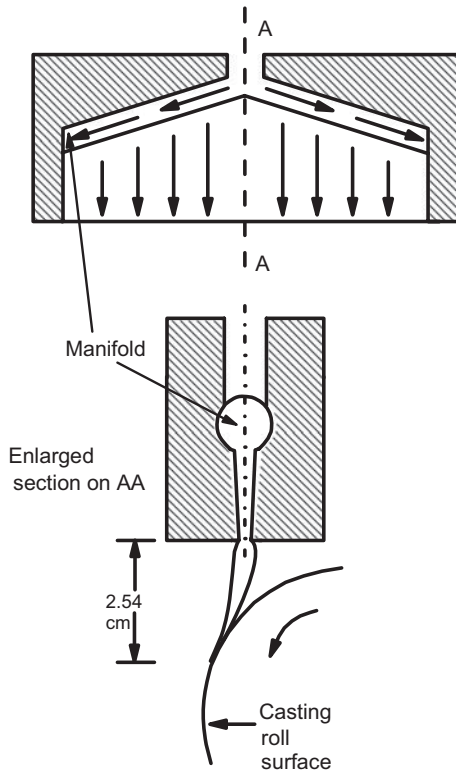


FIGURE 5.1 Schematic of a film casting process showing the polymer film being cast onto a rotating drum.

represent the viscosity versus $\dot{\gamma}$ data by a single curve, as is shown in Figure 3.4 (p. 41) by plotting the reduced viscosity, η_r , versus the reduced shear rate, $\dot{\gamma}_r$, where

$$\eta_r = \eta(\dot{\gamma}, T) \frac{\eta_0(T_0)}{\eta_0(T)} \quad (5.1)$$

and

$$\dot{\gamma}_r = a_T \dot{\gamma} \quad (5.2)$$

$\eta_0(T_0)$ and $\eta_0(T)$ are the zero shear viscosities measured at temperatures T_0 and T , respectively. The *shifting factor*, a_T , is given as

$$a_T = \frac{\eta_0(T) T_0 \rho_0}{\eta_0(T_0) T \rho} \quad (5.3)$$

where ρ_0 and ρ are the densities of the melt at T_0 and T , respectively. Actually the ratio $T_0 \rho_0 / T \rho$ is about unity so that

$$a_T = \frac{\eta_0(T)}{\eta_0(T_0)} \quad (5.4)$$

The value of the reduced variables approach is that given the flow curve at one temperature, we can find the complete flow curve at any other temperature, if we know the ratio of the zero shear viscosities at the two temperatures.

If η_0 at T or T_0 is not known, then one can use the insensitivity of shear stress to temperature to find a_T . From Eqs. 5.2 and 5.3 we define the reduced shear stress, τ_r , as

$$\tau_r(\dot{\gamma}, T_0) = \tau_{yx}(\dot{\gamma}, T) \frac{T_0 \rho_0}{T \rho} \quad (5.5)$$

Hence, because $T_0 \rho_0 / T \rho$ is about unity, this implies that τ_{yx} is insensitive to temperature. The horizontal shifting of different $\tau_r(\dot{\gamma}, T_0)$ curves gives a master curve of $\tau_r(\dot{\gamma}_r, T_0)$ with the amount of shifting along the shear rate axis at each temperature being a_T .

The temperature dependence of a_T is shown in Figure 5.2 for two polymer melts. In this figure $\ln a_T$ is plotted versus $1/T$ (note T is in kelvin units, K), which suggests that a_T has the following form:

$$a_T = \exp \left[\frac{\Delta E}{R} \left(\frac{1}{T} - \frac{1}{T_0} \right) \right] \quad (5.6)$$

where ΔE is the activation energy for flow. Most polymer melts seem to follow this behavior. Values of $\Delta E/R$ are reported to be 4.5×10^3 K, 2.83×10^3 K, 5.14×10^3 K, 6.34×10^3 K, and 4.98×10^3 K for LDPE, HDPE, polypropylene (PP), polyphenylenesulfide, and polyetheretherketone, respectively.

Another way to estimate a_T is through the WLF equation, which has been found to hold for a wide variety of polymers for temperatures between the glass transition temperature,

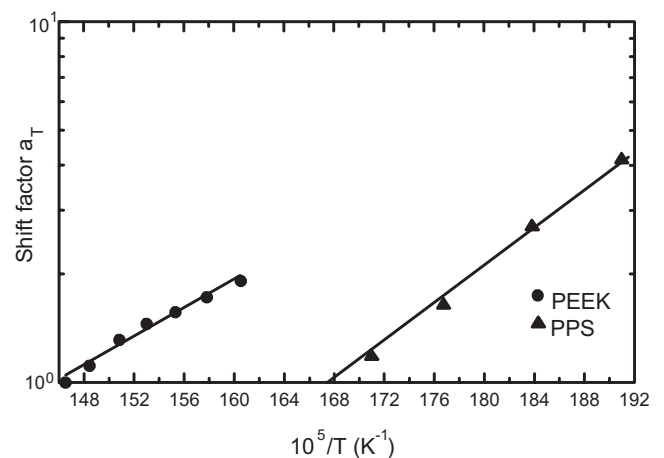


FIGURE 5.2 The shift factor versus reciprocal temperature for polyphenylene sulfide (PPS) and polyetheretherketone (PEEK).

T_g , and $T_g + 100$ (Williams et al., 1955). This equation is given as

$$\log a_T = \frac{-C_1^0(T - T_0)}{C_2^0 + (T - T_0)} \quad (5.7)$$

If T_0 is taken as the glass transition temperature, T_g , then $C_1^0 = 17.44$ and $C_2^0 = 51.6$ K for a wide variety of polymers. When some data are available, then it is recommended to take $C_1^0 = 8.86$ and $C_2^0 = 101.6$ K and then choose T_0 to give the best fit of the data.

The primary normal stress difference and other quantities are handled in a manner similar to that used for τ_r :

$$N_{1,r}(\dot{\gamma}, T_0) = N_1(\dot{\gamma}, T) \frac{T_0 \rho_0}{T \rho} \quad (5.8)$$

Thus, Ψ_1 is reduced as follows:

$$\Psi_{1,r}(\dot{\gamma}, T_0) = \Psi_1 T_0 / a_T^2 T \quad (5.9)$$

where $T_0 \rho_0 / T \rho \sim 1$. The dynamic oscillatory functions can be reduced in the same manner:

$$G'_r(\omega, T_0) = G'(\omega, T) \frac{T_0 \rho_0}{T \rho} \quad (5.10)$$

$$G''_r(\omega, T_0) = G''(\omega, T) \frac{T_0 \rho_0}{T \rho} \quad (5.11)$$

with $\omega_r = a_T \omega$.

The temperature dependence of viscosity can be incorporated into the empiricisms for viscosity. For example, the temperature dependence of the power law coefficients is given as

$$m = m^0 \exp[-B(T - T_0)] \quad (5.12)$$

$$n = n^0 + C(T - T_0) \quad (5.13)$$

where m^0 and n^0 are the values of the parameters at the reference temperature, T_0 , and B and C are constants. Although m is a strong function of T , n is not. It is customary to assume that n is constant for most computations. For the Carreau model we can replace $\eta_0(T)$ by $a_T \eta_0(T_0)$ and λ by $\lambda(T_0) a_T$. Hence, the Carreau model becomes

$$\eta(T, \dot{\gamma}) = \eta_0(T_0) a_T [1 + (\lambda(T_0) a_T \dot{\gamma})^2]^{(n-1)/2} \quad (5.14)$$

From Eq. 5.14 one can calculate the flow curve at any other temperature provided η_0 and λ are known at the reference temperature, T_0 , and a_T is known. Computations must be done numerically with this model.

5.2 THE ENERGY EQUATION

5.2.1 Shell Energy Balances

In this section we set up shell energy balances for flowing polymeric fluids. This material should be helpful in conceptualizing the nonisothermal equations of change. The basic principle that is used is the conservation of thermal energy as applied to a thin shell of fluid, which is stated below:

$$\begin{aligned} \left(\begin{array}{c} \text{Net rate of gain of} \\ \text{thermal energy} \end{array} \right) &= \left(\begin{array}{c} \text{Rate of thermal} \\ \text{energy in} \end{array} \right) \\ - \left(\begin{array}{c} \text{Rate of thermal} \\ \text{energy out} \end{array} \right) &+ \left(\begin{array}{c} \text{Rate of thermal} \\ \text{energy production} \end{array} \right) \end{aligned} \quad (5.15)$$

Applying this principle to a differential volume element and taking the limit as the volume element goes to zero leads to a differential equation for the temperature distribution. The procedure is described in more detail elsewhere (Bird et al., 1960, 2007, Chapter 9). We illustrate the use of Eq. 5.15 through the following example.

Example 5.1. Cooling of Polypropylene Film

As shown in the figure associated with Design Problem IV (Fig. 5.1) a film of polypropylene (PP) 0.1016 cm in thickness is extruded from a 0.162 m wide film die onto a casting drum 2.54 cm below the die. The temperature of the film drops as a result of forced convection at the film surface. Determine the temperature of the film surface when it contacts the casting drum. The melt temperature as it leaves the die is 200°C. The heat transfer coefficient is 100 W/m² · K. Neglect die swell and use an average film thickness of 2.54×10^{-2} cm. (The film thickness is not uniform, and this aspect is discussed in Chapter 9.) In Figure 5.3 is shown a model of the region of interest.

Solution. The model of the region to be analyzed is shown in Figure 5.3. The heat is removed primarily by forced convection at the surfaces due to air at 25°C moving over the sheet. (But in principle one should consider radiation effects as is discussed in Section 5.4.) An energy balance is performed on the element shown in Figure 5.3 to give

$$\begin{aligned} V_0 \rho \bar{C}_p (T - T_R)|_x W \Delta y - V_0 \rho \bar{C}_p (T - T_R)|_{x+\Delta x} \\ W \Delta y + q_x|_x W \Delta y - q_x|_{x+\Delta x} (W \Delta y) \\ + (q_y|_y - q_y|_{y+\Delta y}) W \Delta x = 0 \end{aligned} \quad (5.16)$$

where T_R is a reference temperature, \bar{C}_p is the constant pressure heat capacity per unit mass, V_0 is the film velocity, W is the film width, and ρ is the density. We divide Eq. 5.16 by

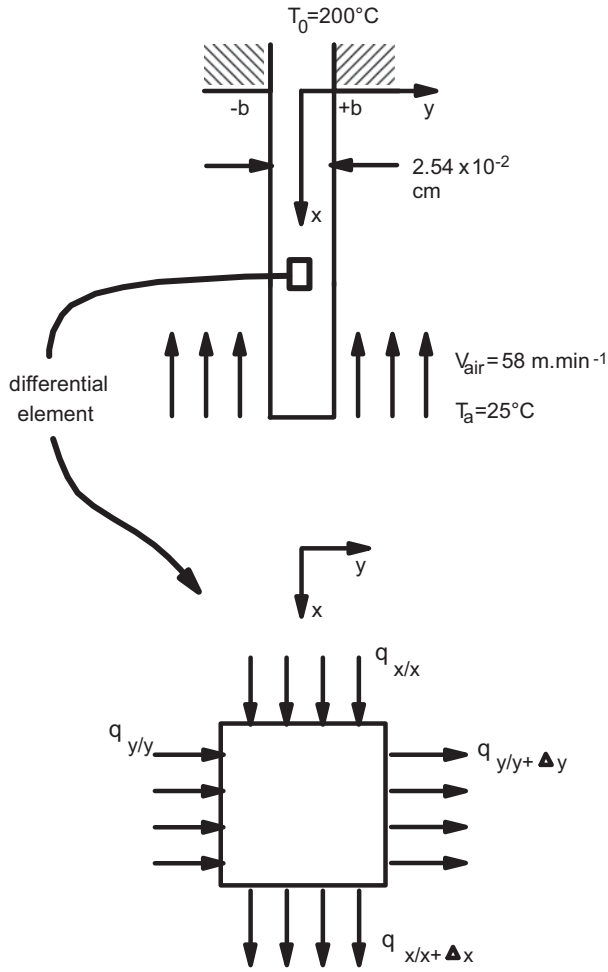


FIGURE 5.3 Model of region between the film die and casting drum (top) and expanded element on which energy balance is performed (bottom).

the volume of the element, $W \Delta x \Delta y$, and take the limit as Δx and Δy go to zero to give

$$-V_0 \rho \bar{C}_p \frac{\partial T}{\partial x} - \frac{\partial q_x}{\partial x} - \frac{\partial q_y}{\partial y} = 0 \quad (5.17)$$

To obtain a differential equation in terms of temperature rather than the heat fluxes, q_x and q_y , we use Fourier's law of heat conduction (Bird et al., 1960, 2007, Chapter 9):

$$q_x = -k \frac{\partial T}{\partial x} \quad q_y = -k \frac{\partial T}{\partial y} \quad (5.18)$$

where k is the thermal conductivity. Substitution of the expressions in Eq. 5.18 into Eq. 5.17 gives

$$V_0 \rho \bar{C}_p \frac{\partial T}{\partial x} - k \frac{\partial^2 T}{\partial x^2} - k \frac{\partial^2 T}{\partial y^2} = 0 \quad (5.19)$$

where it has been assumed that k is constant. Equation 5.19 must be solved along with the following boundary and initial conditions:

$$\text{B.C.1: at } y = +b, \quad q_y = -k \frac{\partial T}{\partial y} = h(T(b) - T_a)$$

$$\text{B.C.2: at } y = -b, \quad q_y = -k \frac{\partial T}{\partial y} = h(T_a - T(-b))$$

$$\text{I.C.: at } x = 0, \quad T = T_0 = 200^\circ\text{C} \quad (5.20)$$

Here T_a is the air temperature.

We next try to determine whether Eq. 5.19 can be reduced or simplified. By writing Eq. 5.19 and the boundary and initial conditions in dimensionless form it is much easier to determine which terms in the differential equation are most important. The dependent and independent variables are written in dimensionless form by dividing them by an appropriate characteristic quantity. In particular, we introduce the following dimensionless quantities:

$$\zeta = \frac{x}{b}, \quad \xi = \frac{y}{b}, \quad \theta = \frac{T - T_a}{T_0 - T_a} \quad (5.21)$$

Equation 5.19 in dimensionless form becomes

$$\frac{bV_0\rho\bar{C}_p}{k} \frac{\partial \theta}{\partial \zeta} = \frac{\partial^2 \theta}{\partial \zeta^2} + \frac{\partial^2 \theta}{\partial \xi^2} \quad (5.22)$$

The term multiplying $\partial \theta / \partial \zeta$ is also dimensionless and is called the Peclet number, Pe , and represents the ratio of the heat transfer by forced convection to that by conduction. The boundary and initial conditions given in Eq. 5.20 become

$$\text{B.C.1: at } \xi = 1, \quad \frac{\partial \theta}{\partial \xi} = \frac{hb}{k} \theta \Big|_{\xi=1}$$

$$\text{B.C.2: at } \xi = -1, \quad \frac{\partial \theta}{\partial \xi} = \frac{-hb}{k} \theta \Big|_{\xi=-1} \quad (5.23)$$

$$\text{I.C.: at } \zeta = 0, \quad \theta = 1$$

The combination of terms, hb/k , is called the nusselt number, Nu , and it is basically a dimensionless temperature gradient averaged over the heat transfer surface.

We are now in a position to evaluate which terms could be eliminated from Eq. 5.22. First we compare the order of $\partial \theta / \partial \zeta$ and $\partial^2 \theta / \partial \zeta^2$. Evaluating Pe using data in Table 5.4 we find $Pe = 2100$. Hence, $Pe \partial \theta / \partial \zeta \gg \partial^2 \theta / \partial \zeta^2$, and we can eliminate $\partial^2 \theta / \partial \zeta^2$ from Eq. 5.22. The equation which is to be solved is

$$Pe \frac{\partial \theta}{\partial \zeta} = \frac{\partial^2 \theta}{\partial \xi^2} \quad (5.24)$$

Except when dealing with molten metals it is common to neglect conduction in the flow direction as heat transfer by this manner is small relative to convection. The solution to

this equation requires the use of the separation of variables and the solution is presented in graphical form in Figure 5.12.

We can try to reduce the equation further in order to obtain an analytical solution. Since $Pe \gg 1$, heat transfer is dominated by forced convection rather than conduction, and it is possible to assume that the temperature distribution through the thickness of the sheet is nearly uniform, except near the outer edges. In order to reduce Eq. 5.24 to an ordinary differential equation (ODE) we first define the mean temperature, $\bar{\theta}$:

$$\bar{\theta} = \int_{-1}^1 \theta d\xi / \int_{-1}^1 d\xi \quad (5.25)$$

Next, we integrate Eq. 5.24 over the thickness of the sheet and use Eq. 5.25 to obtain

$$Pe \frac{\partial \bar{\theta}}{\partial \zeta} = \frac{1}{2} \int_{-1}^1 \frac{\partial}{\partial \xi} \frac{\partial \theta}{\partial \xi} d\xi \quad (5.26)$$

As

$$\frac{\partial \theta}{\partial \xi} = \frac{-q_y b}{k(T_0 - T_a)} \quad (5.27)$$

Equation 5.26 becomes

$$Pe \frac{\partial \bar{\theta}}{\partial \zeta} = \frac{(-b)}{k(T_0 - T_a)} \int_{q_y(-1)}^{q_y(+1)} dq_y \quad (5.28)$$

Using the boundary conditions in Eq. 5.23, we now obtain

$$Pe \frac{\partial \bar{\theta}}{\partial \zeta} = -\frac{hb}{k} \bar{\theta} \quad (5.29)$$

The solution to Eq. 5.29 can be found by using either an integrating factor or separating variables and is

$$\bar{\theta} = C_1 e^{-C\zeta} \quad (5.30)$$

where C_1 is an integration constant and $C = h/\rho C_p V_0$. C_1 is obtained from the I.C. (Eq. 5.23) and is 1.0. Using the material properties for PP given in Table 5.4 and the conditions given in the problem, $\theta = 0.999$ or the change in the film temperature over a distance of 2.54 cm is insignificant. ■

Example 5.2. Temperature Rise Due to Viscous Dissipation for HDPE in a Cone-and-Plate Rheometer

Determine the maximum temperature rise for HDPE in a cone-and-plate rheometer at a shear rate of 10 s^{-1} . The diameter of the plate is 2.54 cm and the cone angle is 0.1 radian.

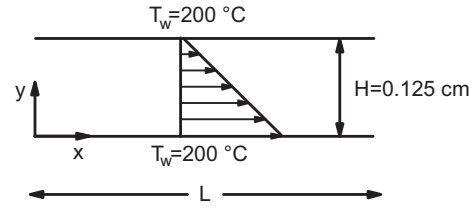


FIGURE 5.4 Approximation of flow in a cone-and-plate rheometer.

The properties are assumed to be independent of temperature and are given below:

$$\begin{aligned} \rho &= 782 \text{ kg/m}^3 & k &= 0.255 \text{ W/m} \cdot \text{K} \\ m &= 4.68 \times 10^3 \text{ Pa} \cdot \text{s}^n & n &= 0.54 & C_p &= 2650 \text{ J/kg} \cdot \text{K} \end{aligned}$$

The plate and melt temperatures are taken to be 200°C , and no heat transfer is assumed to occur at the free surface.

Solution. Based on the description of the cone-and-plate rheometer in Section 3.3 we can consider the flow to be as shown in Figure 5.4. Based on the dimensions given, the height, H , at the edge is 0.125 cm. An energy balance is performed on the slab of thickness Δy and unit width. It is assumed that heat is generated by viscous dissipation, which is the conversion of mechanical energy into heat. The viscous dissipation per unit volume is

$$\dot{S} = -\tau_{yx} \frac{dv_x}{dy} \quad (5.31)$$

and is analogous to the rate of work in moving a single particle (i.e., $W = F_x v_x$). The heat that is generated is conducted out of the melt through the metal plates by means of conduction in the y direction. The energy balance per unit width is

$$q_y|_y L - q_y|_{y+\Delta y} L + \dot{S} L \Delta y = 0 \quad (5.32)$$

Next, we divide through by the volume of the element (i.e., $1 \cdot \Delta y \cdot L$) and take the limit as $\Delta y \rightarrow 0$. This gives the following differential equation:

$$-\frac{dq_y}{dy} + \dot{S} = 0 \quad (5.33)$$

We now replace q_y with $-k dT/dy$, which is Fourier's law, and S with Eq. 5.31:

$$k \frac{d^2 T}{dy^2} - \tau_{yx} \frac{dv_x}{dy} = 0 \quad (5.34)$$

Substituting in for τ_{yx} , which is

$$\tau_{yx} = +m \left(-\frac{dv_x}{dy} \right)^n = +m \dot{\gamma}^n \quad (5.35)$$

we obtain the following differential equation:

$$k \frac{d^2 T}{dy^2} + m \dot{\gamma}^{n+1} = 0 \quad (5.36)$$

Equation 5.36 can be integrated to give

$$T = -\frac{m}{k} (\dot{\gamma})^{n+1} \left(\frac{y^2}{2} \right) + C_1 y + C_2 \quad (5.37)$$

The boundary conditions required for finding C_1 and C_2 are

$$\text{B.C.1: at } y = 0, \quad T = T_w = 200 \text{ }^\circ\text{C} \quad (5.38)$$

$$\text{B.C.2: at } y = H, \quad T = T_w = 200 \text{ }^\circ\text{C} \quad (5.39)$$

Using Eqs. 5.39 and 5.38, Eq. 5.37 becomes

$$T = -\frac{H^2 m \dot{\gamma}^{n+1}}{2k} \left(\frac{y}{H} \right)^2 + \frac{H^2 m \dot{\gamma}^{n+1}}{2k} \frac{y}{H} + T_w \quad (5.40)$$

From this equation it is found that the temperature is a maximum at $H/2$ and for $\dot{\gamma} = 10 \text{ s}^{-1}$, $T - T_w$ is $6.50 \text{ }^\circ\text{C}$. Hence, at this shear rate there is a significant rise in the melt temperature and the viscosity measurements would be affected. Furthermore, this would be enough of a temperature rise to significantly affect the measurement of N_1 because of the increase in volume, which causes the plates to be pushed apart. ■

The next example is more complicated and involves the flow of HDPE through a pipe die. It is important to minimize the temperature increase in a melt due to viscous dissipation. In this case the velocity profile may not be known a priori as it may be affected by the temperature distribution.

Example 5.3. Nonisothermal Flow of HDPE Through a Pipe Die

Returning to Section 2.2.1 we now ask whether the melt temperature will remain at 453 K as HDPE passes through the pipe die at the upper extrusion limit. We assume that the melt enters the die at $T_0 = 453 \text{ K}$ and that the wall temperature at R is 453 K. The inner wall is also maintained at 453 K. The rheological properties for this melt were given in Table 2.3 (p. 20). The thermal properties are given in Table 5.6 (p. 122). For this problem we take these properties to be independent of temperature and use $\rho = 782 \text{ kg/m}^3$, $C_p = 2650 \text{ J/kg} \cdot \text{K}$, and $k = 0.255 \text{ W/m} \cdot \text{K}$.

Solution. For pedagogical purposes we solve this problem using the forced convection assumption in which it is assumed that the velocity profile is unaffected by changes in the viscosity as a result of changes in temperature. With

this assumption, the velocity profile remains unchanged from that of the isothermal case and the equation of motion can be used independently of the energy balance. The equation of motion for this problem was given in Eq. 2.10 and is repeated below:

$$\frac{d}{dr}(r\tau_{rz}) = -\left(\frac{dp}{dz}\right)r = \frac{(P_0 - P_L)}{L}r \quad (5.41)$$

For a GNF model using the power-law empiricism for viscosity, the velocity field was given in Eqs. 2.28 and 2.29. Taking $n = 0.5$ (actually it is 0.56, but this allows us to obtain an analytical solution) we find $v_z^<$ and $v_z^>$ to be, respectively:

$$\begin{aligned} v_z^< &= R \left[\frac{(P_0 - P_L)R}{2mL} \right]^s \left[(\xi - \kappa) \left(\frac{\beta^4}{\xi} - 2\beta^2 \right) \right. \\ &\quad \left. + \frac{1}{3}(\xi^3 - \kappa^3) \right] \\ v_z^> &= R \left[\frac{(P_0 - P_L)R}{2mL} \right]^s \left[(1 - \xi) \left(\frac{\beta^4}{\xi} - 2\beta^2 \right) \right. \\ &\quad \left. + \frac{1}{3}(1 - \xi^3) \right] \end{aligned} \quad (5.42)$$

We next carry out an energy balance on the differential (doughnut) element shown in Figure 5.5. The sources of energy transport consist of heat transfer into and out of the element by convection due to flow in the z direction, conduction of heat into and out of the element in both the z and r directions, and heat generated by viscous dissipation. When an energy balance is applied to the element shown in Figure 5.5 the following equation is obtained:

$$\begin{aligned} \rho \bar{C}_p (T - T_R)|_z v_z 2\pi r \Delta r - \rho \bar{C}_p (T - T_R)|_{z+\Delta z} v_z 2\pi r \Delta r \\ + (q_z|_z - q_z|_{z+\Delta z}) 2\pi r \Delta r \\ + (q_r r|_r - q_r r|_{r+\Delta r}) 2\pi r \Delta z + \dot{S} 2\pi r \Delta r \Delta z = 0 \end{aligned} \quad (5.43)$$

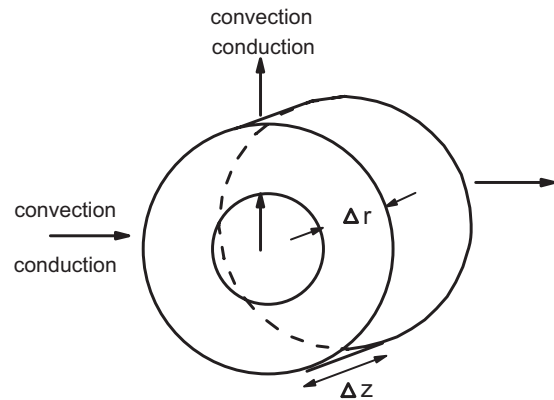


FIGURE 5.5 Cylindrical element on which the energy balance is performed in Example 5.3.

Here \overline{C}_p is the constant pressure heat capacity per unit mass, T_R is a reference temperature, q_z and q_r are the heat fluxes due to conduction in the z and r directions, respectively, and \dot{S} is a source term in units of energy per unit time per unit volume. In this example there is no chemical reaction, but because of the high viscosity of the fluid, there may be significant viscous dissipation. Viscous dissipation is given by

$$\dot{S} = -\tau_{rz} \frac{dv_z}{dr} \quad (5.44)$$

We now divide all the terms in Eq. 5.43 by the volume of the element, $2\pi r \Delta r \Delta z$, and then take the limit as Δr and $\Delta z \rightarrow 0$. This leads to the following differential equation:

$$\rho \overline{C}_p v_z \frac{\partial T}{\partial z} = -\frac{\partial q_z}{\partial z} - \frac{1}{r} \frac{\partial}{\partial r} (r q_r) + \dot{S} \quad (5.45)$$

In order to put Eq. 5.45 into a form that can be solved for T , two substitutions are required. We first replace q_z and q_r by the following expressions, which come from Fourier's law of heat conduction (Bird et al., 1960, 2007):

$$q_z = -k \frac{\partial T}{\partial z} \quad q_r = -k \frac{\partial T}{\partial r} \quad (5.46)$$

Furthermore, we replace S by $-\tau_{rz}(dv_z/dr)$, which for a power-law fluid becomes

$$-\tau_{rz} \frac{dv_z}{dr} = +m \left| \frac{dv_z}{dr} \right|^{n-1} \left(\frac{dv_z}{dr} \right)^2 \quad (5.47)$$

This leads to a partial differential equation for the temperature distribution,

$$\rho \overline{C}_p v_z(r) \frac{\partial T}{\partial z} = k \frac{\partial^2 T}{\partial z^2} + \frac{k}{r} \frac{\partial}{\partial r} \left(r \frac{\partial T}{\partial r} \right) + m \left| \frac{dv_z}{dr} \right|^{n-1} \left(\frac{dv_z}{dr} \right)^2 \quad (5.48)$$

Because of the forced convection assumption we can solve Eq. 5.48 independently of the equation of motion. However, these two equations would ordinarily be coupled because of the dependence of $v_z(r)$ on η , which is highly temperature dependent, and hence numerical methods would be required.

In order to estimate whether a significant temperature rise will occur, we make three further simplifications. Because $\kappa = 0.83$, we can neglect curvature and treat the annular die as if it is parallel plate geometry of height $H = R(1 - \kappa)$ and width $W = \pi R(1 + \kappa)$. Equation 5.48 becomes

$$\rho \overline{C}_p v_z(y) \frac{\partial T}{\partial z} = k \frac{\partial^2 T}{\partial y^2} + m \left| \frac{dv_z}{dy} \right|^{n-1} \left(\frac{dv_z}{dy} \right)^2 \quad (5.49)$$

where again it is assumed that the conduction term in the flow direction (z direction) is insignificant relative to the convection term. The highest possible temperature rise will occur if there is no heat conducted through the walls of the die (this is referred to as adiabatic conditions). This is equivalent to saying that $q_y = 0$ at both walls. Using the velocity profile for flow through parallel plates given in Table 2.5 (p. 22), Eq. 5.49 becomes

$$\rho \overline{C}_p v_{\max} \left[1 - \left(\frac{y}{H/2} \right)^{s+1} \right] \frac{\partial T}{\partial z} = k \frac{\partial^2 T}{\partial y^2} + m \left[\frac{v_{\max}(s+1)}{H/2} \right]^{n+1} \left(\frac{y}{H/2} \right)^{1+s} \quad (5.50)$$

subject to the following boundary and initial conditions:

$$\text{B.C.1:} \quad \text{at } y = 0, \quad q_y = 0 \quad (5.51)$$

$$\text{B.C.2:} \quad \text{at } y = H/2, \quad q_y = 0 \quad (5.52)$$

$$\text{I.C.:} \quad \text{at } z = 0, \quad T = T_0 \quad (5.53)$$

We next average Eq. 5.50 over the cross-sectional area using the boundary conditions above to yield

$$\rho \overline{C}_p \langle v_z \rangle HW \frac{dT}{dz} = \frac{WHm}{s+2} \left[\frac{v_{\max}(s+1)}{H/2} \right]^{n+1} z \quad (5.54)$$

This is a first-order ordinary differential equation, which we can now integrate to find the temperature rise at the exit of the die:

$$T - T_0 = \frac{m}{\rho \overline{C}_p \langle v_z \rangle (s+2)} \left[\frac{v_{\max}(s+1)}{H/2} \right]^{n+1} z \quad (5.55)$$

Using the results from Section 2.2.2 and the values given in the problem statement, we find

$$\begin{aligned} T - T_0 &= \frac{6.19\text{E} + 03 \text{ Pa} \cdot \text{s}^n (3.33\text{E} + 03)}{(782 \text{ kg/m}^3)(26,503/\text{kg} \cdot \text{K})(0.112 \text{ m/s})(3.786)} z \\ &= 14.6 z \end{aligned} \quad (5.56)$$

With the length of the die given as 6.35×10^{-3} m, the temperature rise is only 0.92 K. Hence, for the case at hand there is no significant rise in temperature as a result of viscous heating. However, if the die length was increased to $L = 0.635$ m, then there would be a 9.2 K increase in temperature which could be significant. ■

5.2.2 Equation of Thermal Energy

As in Chapter 2 for the equation of motion it is more convenient to use the general form of the thermal energy equation

TABLE 5.1 The Equation of Thermal Energy in Terms of Energy and Momentum Fluxes

Rectangular coordinates:

$$\rho \hat{C}_v \left(\frac{\partial T}{\partial t} + v_x \frac{\partial T}{\partial x} + v_y \frac{\partial T}{\partial y} + v_z \frac{\partial T}{\partial z} \right) = - \left[\frac{\partial q_x}{\partial x} + \frac{\partial q_y}{\partial y} + \frac{\partial q_z}{\partial z} \right] - T \left(\frac{\partial p}{\partial T} \right)_\rho \left(\frac{\partial v_x}{\partial x} + \frac{\partial v_y}{\partial y} + \frac{\partial v_z}{\partial z} \right) - \left\{ \tau_{xx} \frac{\partial v_x}{\partial x} + \tau_{yy} \frac{\partial v_y}{\partial y} + \tau_{zz} \frac{\partial v_z}{\partial z} \right\} - \left\{ \tau_{xy} \left(\frac{\partial v_x}{\partial y} + \frac{\partial v_y}{\partial x} \right) + \tau_{zz} \left(\frac{\partial v_x}{\partial z} + \frac{\partial v_z}{\partial x} \right) + \tau_{yz} \left(\frac{\partial v_y}{\partial z} + \frac{\partial v_z}{\partial y} \right) \right\} \quad (\text{A})$$

Cylindrical coordinates:

$$\rho \hat{C}_v \left(\frac{\partial T}{\partial t} + v_r \frac{\partial T}{\partial r} + \frac{v_\theta}{r} \frac{\partial T}{\partial \theta} + v_z \frac{\partial T}{\partial z} \right) = - \left[\frac{1}{r} \frac{\partial}{\partial r} (r q_r) + \frac{1}{r} \frac{\partial q_\theta}{\partial \theta} + \frac{\partial q_z}{\partial z} \right] - T \left(\frac{\partial p}{\partial T} \right)_\rho \left(\frac{1}{r} \frac{\partial}{\partial r} (r v_r) + \frac{1}{r} \frac{\partial v_\theta}{\partial \theta} + \frac{\partial v_z}{\partial z} \right) - \left\{ \tau_{rr} \frac{\partial v_r}{\partial r} + \tau_{\theta\theta} \frac{1}{r} \left(\frac{\partial v_\theta}{\partial \theta} + v_r \right) + \tau_{zz} \frac{\partial v_z}{\partial z} \right\} - \left\{ \tau_{r\theta} \left[r \frac{\partial}{\partial r} \left(\frac{v_\theta}{r} \right) + \frac{1}{r} \frac{\partial v_r}{\partial \theta} \right] + \tau_{rz} \left(\frac{\partial v_z}{\partial r} + \frac{\partial v_r}{\partial z} \right) + \tau_{\theta z} \left(\frac{1}{r} \frac{\partial v_z}{\partial \theta} + \frac{\partial v_\theta}{\partial z} \right) \right\} \quad (\text{B})$$

Spherical coordinates:

$$\rho \hat{C}_v \left(\frac{\partial T}{\partial t} + v_r \frac{\partial T}{\partial r} + \frac{v_\theta}{r} \frac{\partial T}{\partial \theta} + \frac{v_\phi}{r \sin \theta} \frac{\partial T}{\partial \phi} \right) = - \left[\frac{1}{r^2} \frac{\partial}{\partial r} (r^2 q_r) + \frac{1}{r \sin \theta} \frac{\partial}{\partial \theta} (q_\theta \sin \theta) + \frac{1}{r \sin \theta} \frac{\partial q_\phi}{\partial \phi} \right] - T \left(\frac{\partial p}{\partial T} \right)_\rho \left(\frac{1}{r^2} \frac{\partial}{\partial r} (r^2 v_r) + \frac{1}{r \sin \theta} \frac{\partial}{\partial \theta} (v_\theta \sin \theta) + \frac{1}{r \sin \theta} \frac{\partial v_\phi}{\partial \phi} \right) - \left\{ \tau_{rr} \frac{\partial v_r}{\partial r} + \tau_{\theta\theta} \left(\frac{1}{r} \frac{\partial v_\theta}{\partial \theta} + \frac{v_r}{r} \right) + \tau_{\phi\phi} \left(\frac{1}{r \sin \theta} \frac{\partial v_\phi}{\partial \phi} + \frac{v_r}{r} + \frac{v_\theta \cot \theta}{r} \right) \right\} - \left\{ \tau_{r\theta} \left(\frac{\partial v_\theta}{\partial r} + \frac{1}{r} \frac{\partial v_r}{\partial \theta} - \frac{v_\theta}{r} \right) + \tau_{r\phi} \left(\frac{\partial v_\phi}{\partial r} + \frac{1}{r \sin \theta} \frac{\partial v_r}{\partial \phi} - \frac{v_\phi}{r} \right) + \tau_{\theta\phi} \left(\frac{1}{r} \frac{\partial v_\phi}{\partial \theta} + \frac{1}{r \sin \theta} \frac{\partial v_\theta}{\partial \phi} - \frac{\cot \theta}{r} v_\phi \right) \right\} \quad (\text{C})$$

Source: Reprinted by permission of the publisher from Bird et al., 1960.

rather than use the shell energy balance approach. The thermal energy equation is given in terms of energy and momentum fluxes in Table 5.1. When the components of the heat flux, \mathbf{q} , which are given in Table 5.2, and the GNF model are substituted into the equations given in Table 5.1, we obtain the energy equation in terms of transport properties. This form of the equation with the assumption of constant properties is given in Table 5.3. (In this table we replace μ by η .) These tables are much more convenient to use than the shell energy balance approach.

We solve the following set of equations written in vector notation:

$$\text{Continuity:} \quad \nabla \cdot \rho \mathbf{v} = 0 \quad (5.57)$$

$$\text{Motion:} \quad \rho \frac{D\mathbf{v}}{Dt} = -\nabla p + \nabla \cdot \boldsymbol{\eta} \dot{\boldsymbol{\gamma}} + \rho \mathbf{g} \quad (5.58)$$

$$\text{Energy:} \quad \rho \bar{C}_p \frac{DT}{Dt} = (\nabla \cdot \mathbf{k} \nabla T) + \frac{1}{2} \eta (\dot{\boldsymbol{\gamma}} : \dot{\boldsymbol{\gamma}}) + \dot{S} \quad (5.59)$$

TABLE 5.2 Components of the Energy Flux q

Rectangular	Cylindrical	Spherical
$q_x = -k \frac{\partial T}{\partial x}$	$q_r = -k \frac{\partial T}{\partial r}$	$q_r = -k \frac{\partial T}{\partial r}$
$q_y = -k \frac{\partial T}{\partial y}$	$q_\theta = -k \frac{1}{r} \frac{\partial T}{\partial \theta}$	$q_\theta = -k \frac{1}{r} \frac{\partial T}{\partial \theta}$
$q_z = -k \frac{\partial T}{\partial z}$	$q_z = -k \frac{\partial T}{\partial z}$	$q_\phi = -k \frac{1}{r \sin \theta} \frac{\partial T}{\partial \phi}$

Here D/Dt is the material time derivative or the time derivative following the fluid motion. These equations have been written in a form which demonstrates the temperature dependence of the viscosity and thermal conductivity. Furthermore, the equations have been written with the assumption that the rheological properties are described by the GNF model. We now use the nonisothermal equations of change to resolve the examples in Section 5.2.1.

TABLE 5.3 The Equation of Thermal Energy in Terms of the Transport Properties (for Newtonian Fluids of Constant ρ and k)

Rectangular coordinates:

$$\begin{aligned} \rho \hat{C}_p \left(\frac{\partial T}{\partial t} + v_x \frac{\partial T}{\partial x} + v_y \frac{\partial T}{\partial y} + v_z \frac{\partial T}{\partial z} \right) = k \left[\frac{\partial^2 T}{\partial x^2} + \frac{\partial^2 T}{\partial y^2} + \frac{\partial^2 T}{\partial z^2} \right] + 2\mu \left\{ \left(\frac{\partial v_x}{\partial x} \right)^2 + \left(\frac{\partial v_y}{\partial y} \right)^2 + \left(\frac{\partial v_z}{\partial z} \right)^2 \right\} \\ + \mu \left\{ \left(\frac{\partial v_x}{\partial y} + \frac{\partial v_y}{\partial x} \right)^2 + \left(\frac{\partial v_x}{\partial z} + \frac{\partial v_z}{\partial x} \right)^2 + \left(\frac{\partial v_y}{\partial z} + \frac{\partial v_z}{\partial y} \right)^2 \right\} \end{aligned} \quad (\text{A})$$

Cylindrical coordinates:

$$\begin{aligned} \rho \hat{C}_p \left(\frac{\partial T}{\partial t} + v_r \frac{\partial T}{\partial r} + \frac{v_\theta}{r} \frac{\partial T}{\partial \theta} + v_z \frac{\partial T}{\partial z} \right) = k \left[\frac{1}{r} \frac{\partial}{\partial r} \left(r \frac{\partial T}{\partial r} \right) + \frac{1}{r^2} \frac{\partial^2 T}{\partial \theta^2} + \frac{\partial^2 T}{\partial z^2} \right] + 2\mu \left\{ \left(\frac{\partial v_r}{\partial r} \right)^2 + \left[\frac{1}{r} \left(\frac{\partial v_\theta}{\partial \theta} + v_r \right) \right]^2 + \left(\frac{\partial v_z}{\partial z} \right)^2 \right\} \\ + \mu \left\{ \left(\frac{\partial v_\theta}{\partial z} + \frac{1}{r} \frac{\partial v_z}{\partial \theta} \right)^2 + \left(\frac{\partial v_z}{\partial r} + \frac{\partial v_r}{\partial z} \right)^2 + \left[\frac{1}{r} \frac{\partial v_r}{\partial \theta} + r \frac{\partial}{\partial r} \left(\frac{v_\theta}{r} \right) \right]^2 \right\} \end{aligned} \quad (\text{B})$$

Spherical coordinates:

$$\begin{aligned} \rho \hat{C}_p \left(\frac{\partial T}{\partial t} + v_r \frac{\partial T}{\partial r} + \frac{v_\theta}{r} \frac{\partial T}{\partial \theta} + \frac{v_\phi}{r \sin \theta} \frac{\partial T}{\partial \phi} \right) = k \left[\frac{1}{r^2} \frac{\partial}{\partial r} \left(r^2 \frac{\partial T}{\partial r} \right) + \frac{1}{r^2 \sin \theta} \frac{\partial}{\partial \theta} \left(\sin \theta \frac{\partial T}{\partial \theta} \right) + \frac{1}{r^2 \sin^2 \theta} \frac{\partial^2 T}{\partial \phi^2} \right] \\ + 2\mu \left\{ \left(\frac{\partial v_r}{\partial r} \right)^2 + \left(\frac{1}{r} \frac{\partial v_\theta}{\partial \theta} + \frac{v_r}{r} \right)^2 + \left(\frac{1}{r \sin \theta} \frac{\partial v_\phi}{\partial \phi} + \frac{v_r}{r} + \frac{v_\theta \cot \theta}{r} \right)^2 \right\} \\ + \mu \left\{ \left[r \frac{\partial}{\partial r} \left(\frac{v_\theta}{r} \right) + \frac{1}{r} \frac{\partial v_r}{\partial \theta} \right]^2 + \left[\frac{1}{r \sin \theta} \frac{\partial v_r}{\partial \phi} + r \frac{\partial}{\partial r} \left(\frac{v_\phi}{r} \right) \right]^2 \right. \\ \left. + \left[\frac{\sin \theta}{r} \frac{\partial}{\partial \theta} \left(\frac{v_\phi}{\sin \theta} \right) + \frac{1}{r \sin \theta} \frac{\partial v_\theta}{\partial \phi} \right]^2 \right\} \end{aligned} \quad (\text{C})$$

Source: Reprinted by permission of the publisher from Bird et al., 1960.

Example 5.4. Use of the Nonisothermal Equations of Change

Reformulate Examples 5.1, 5.2, and 5.3 using the nonisothermal equations of change.

Solution to Example 5.1. We start by making postulates pertaining to the velocity and temperature fields:

$$v_x = \text{const.} = v_0 \quad T = T(x, y) \quad (5.60)$$

From these postulates and Fourier's law (Table 5.2) the following fluxes exist:

$$q_x = -k \frac{\partial T}{\partial x} \quad q_y = -k \frac{\partial T}{\partial y} \quad (5.61)$$

The equation of thermal energy becomes

$$\rho C_p v_x \frac{\partial T}{\partial x} = -\frac{\partial q_x}{\partial x} - \frac{\partial q_y}{\partial y} \quad (5.62)$$

Similar arguments as presented in Example 5.1 can be used to reduce Eq. 5.62 to Eq. 5.29. ■

Solution to Example 5.2. Again postulates pertaining to the velocity and temperature fields are made:

$$v_x = v_x(y) \quad T = T(y) \quad (5.63)$$

The equation of motion is

$$-\frac{\partial \tau_{yx}}{\partial x} = 0 \quad (5.64)$$

For the GNF model with the power-law empiricism for viscosity

$$\tau_{yx} = -m \left(\frac{dv_x}{dy} \right)^n \quad (5.65)$$

Hence, the velocity profile is

$$v_x = \frac{V_0}{H} y \quad (5.66)$$

 and for this flow v_x is unaffected by the temperature profile. The energy equation for constant properties becomes

$$k \frac{\partial^2 T}{\partial y^2} + \eta \left(\frac{dv_x}{dy} \right)^2 = 0 \quad (5.67)$$

This equation can be solved as in Example 5.2. We again assume that all the physical properties are constant. ■

Solution to Example 5.3. The following postulates are made for v_z and T :

$$v_z = v_z(r) \quad T = T(r, z) \quad (5.68)$$

The equation of motion becomes

$$-\frac{dp}{dz} = +\frac{1}{r} \frac{d}{dr}(r\tau_{rz}) \quad (5.69)$$

or with $\tau_{rz} = -\eta(dv_z/dr)$, we obtain

$$\frac{dp}{dz} = \frac{1}{r} \frac{d}{dr} \left(r\eta \frac{dv_z}{dr} \right) \quad (5.70)$$

The energy equation is

$$\rho \bar{C}_p v_z \frac{\partial T}{\partial z} = -\frac{1}{r} \frac{\partial}{\partial r}(rq_r) - \frac{\partial q_z}{\partial z} - \tau_{rz} \frac{dv_z}{dr} \quad (5.71)$$

With the substitution of Fourier's law of heat conduction and the GNF model we obtain

$$\rho \bar{C}_p v_z \frac{\partial T}{\partial z} = +\frac{1}{r} \frac{\partial}{\partial r} \left(kr \frac{\partial T}{\partial r} \right) + \frac{\partial}{\partial z} \left(k \frac{\partial T}{\partial z} \right) + \eta \left(\frac{dv_z}{dr} \right)^2 \quad (5.72)$$

With the assumption of constant physical properties, Eq. 5.72 would be the same as that obtained by means of the shell energy balance (Eq. 5.48). ■

5.3 THERMAL TRANSPORT PROPERTIES

The material properties that appear in the thermal energy equation are the density, ρ , the constant pressure heat capacity, \bar{C}_p (note that when ρ is constant $\bar{C}_p \approx \bar{C}_v$), and the thermal conductivity. In addition, because a number of polymers are semicrystalline, energy can be absorbed during melting or given up when crystallization occurs on cooling. The energy absorbed is referred to as the heat of fusion ($\Delta \bar{H}_f$) while the energy released is the heat of crystallization ($\Delta \bar{H}_c$). In this section representative values for both common commercial polymers as well as high performance engineering thermoplastics are presented. Later in Chapter 11, because of the interest in using what are referred to as compostable polymers (i.e., polymers that are biodegradable) and polymers from renewable resources, values of their thermal properties are given for a few of the major polymers. Methods for

estimating thermal properties for composite systems (i.e., filled polymers and polymer blends) are also discussed.

5.3.1 Homogeneous Polymer Systems

Representative thermal properties for an amorphous polymer, in this case polycarbonate, are shown in Figure 5.6 as a function of temperature. Here it is observed that all the quantities except \bar{C}_p change continuously with increasing temperature. At about 153°C, there is a discontinuity in \bar{C}_p which is associated with the glass transition temperature, T_g . Above T_g , the polymer becomes more easily deformable and is usually processed above T_g . It is observed that above T_g there is very little change in the properties. For example, \bar{C}_p changes from 0.46 kcal/g·K at 435 K to 0.5 kcal/g·K at 480 K. The thermal conductivity changes even less.

Representative values of ρ , k , and \bar{C}_p are shown in Figure 5.7 for a semicrystalline polymer. Here it is observed that \bar{C}_p increases rapidly with temperature, passing through a maximum and then decreasing with temperature. The temperature at the peak value is taken as the melting point, T_m . The area under the curve is associated with the melting of the crystalline phase and is referred to as the heat of fusion, $\Delta \bar{H}_f$. Above T_m the thermal properties are observed not to change significantly with temperature. For computational purposes above T_m , we take ρ , \bar{C}_p , k , and α ($= k/\rho \bar{C}_p$) to be independent of temperature.

Values of ρ , \bar{C}_p , and k are presented for a number of commercially available polymers at 25°C in Table 5.4 and at 150°C in Table 5.5. Here it is observed that the values

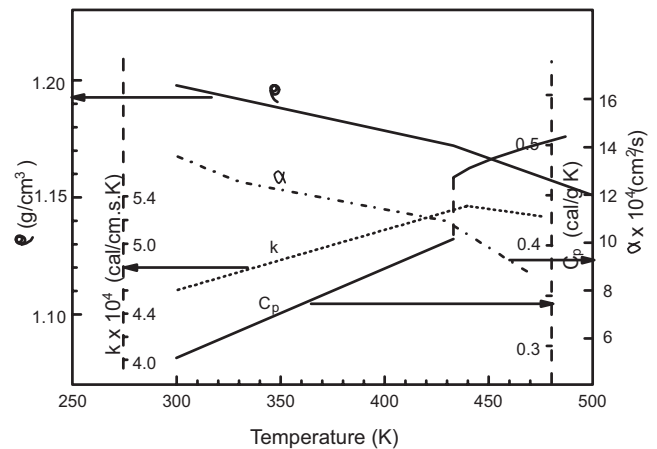


FIGURE 5.6 Coefficient of thermal conductivity, heat capacity, thermal diffusivity, and density for polycarbonate, a glassy polymer. (Reprinted with permission of the publisher from Tadmor and Gogos, 1979, p. 132.)

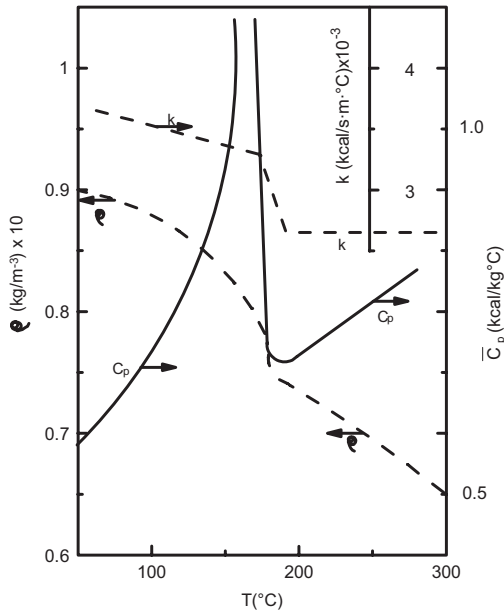


FIGURE 5.7 Thermal property data for a semicrystalline polymer, polypropylene (Data from Wanger, 1969.)

all lie within a fairly narrow range. For more rigorous computations the temperature dependence of \bar{C}_p , ρ , and k is presented for three commercial polymers in Table 5.6. Here all properties are given as polynomial functions of temperature. Thermal properties can be difficult to obtain, but many values can be found in the book by Van Krevelen (1990) and *The Polymer Handbook* (Brandrup and Immergut, 1981). A method for estimating \bar{C}_p is given in Appendix C. Data are presented for three high performance engineering thermoplastics in Table 5.7. These polymers typically have higher T_g and T_m values and densities than those of the commodity resins, but similar values of \bar{C}_p and k . They are used primarily in applications where high strength and stiffness are required at elevated temperatures. Furthermore, they are frequently used in combination with carbon or other stiff fibers to form thermoplastic composites. A more complete list of engineering thermoplastics is given in Table 5.8. In this table their chemical structures along with their T_g and T_m values are given. Additional information on these polymers as well as others can be found in the book by Van Krevelen (1990).

TABLE 5.4 Density, Thermal Conductivity, and Heat Capacity of Some Polymers at Room Temperature

Polymer	Density (kg/m^3) $\times 10^{-3}$	Thermal Conductivity ($\text{J/m} \cdot \text{s} \cdot \text{K}$)	T_g ($^{\circ}\text{C}$)	T_M ($^{\circ}\text{C}$)	Heat Capacity ($\text{kJ/kg} \cdot \text{K}$)
ABS	1.16	0.188–0.335	80		1.25–1.67
Nylon 66	1.13–1.15	0.243	57	240	0.46
Polycarbonate	1.2	0.192	149		1.25
Polyester (PETP)	1.37	0.289	80	249	1.25
LDPE	0.910–0.925	0.335			2.30
HDPE	0.940–0.965	0.460–0.519	–78	141	2.30
PMMA	1.17–1.20	0.167–0.251			1.46
Polyoxymethylene	1.42	0.230	–82	183	1.46
PS	1.04–1.09	0.100–0.138	107		1.34
PTFE	2.0–2.14	0.250			1.05
Polyurethane (thermoplastic)	1.05–1.25	0.070–0.310	–46 to –18		1.67–1.88
PVC (rigid)	1.30–1.45	0.125–0.293			0.84–1.25
PP	0.91	0.172	–10	165	2.14

Source: Data from Van Krevelen, 1990, and H. H. Winter, 1977.

TABLE 5.5 Thermal Conductivity and Heat Capacity of Some Polymers at 150 $^{\circ}\text{C}$

Polymer	k ($\text{W/m} \cdot \text{K}$)	C_p ($\text{kJ/kg} \cdot \text{K}$)	ρ (10^{-3}kg/m^3)	
LDPE	Low-density polyethylene	0.241	2.57	0.782
HDPE	High-density polyethylene	0.255	2.65	0.782
PP ^a	Polypropylene	0.142	2.80	0.867
PVC	Polyvinyl chloride	0.166	1.53	1.31
PS	Polystyrene	0.167	2.04	0.997
PMMA	Polymethylmethacrylate	0.195		1.11

^aPP data are at 180 $^{\circ}\text{C}$ ($T_m = 165^{\circ}\text{C}$).

Source: Data from H. H. Winter, 1977.

TABLE 5.6 Temperature Dependence of Physical Properties of Several Polymers^a

Property	Polymer	Temperature Range (°C)	Coefficients in Polynomial Representation ^b					
			A	B	C	D	E	F
k (W/m · K)	HDPE	10–143	0.453	-8.59×10^{-4}	-5.29×10^{-6}	4.12×10^{-8}	-1.98×10^{-8}	
		143–200	0.26					
	LDPE	10–126	0.365	-4.07×10^{-4}	-7.34×10^{-6}	8.28×10^{-8}	-5.53×10^{-8}	
		126–200	0.223					
	PVC	0–200	0.168					
	HDPE	10–88	1.597	3.61×10^{-3}	5.96×10^{-5}	-3.44×10^{-8}	9.77×10^{-9}	
		88–121	-1.983×10^2	6.17	-6.34×10^{-2}	2.19×10^{-4}		
		121–130	-2.837×10^2	2.41				
		130–133	1.208×10^3	-9.07				
		133–200	1.984	3.88×10^{-3}				
10–90		1.943	5.39×10^{-2}	2.56×10^{-2}	-3.23×10^{-6}	3.53×10^{-8}		
LDPE	90–105	8.497×10^1	-1.84	1.04×10^{-2}				
	105–110	-1.29×10^2	1.3					
	110–113.5	3.786×10^2	-3.31					
	113.5–200	1.98	3.70×10^{-3}					
	10–67	0.75	4.66×10^{-3}	1.21×10^{-1}	-9.71×10^{-4}	2.90×10^{-6}		
	67–96	1.361×10^2	-6.64					
ρ^{-1} (cm ³ /g)	HDPE	96–200	1.208	2.96×10^{-3}				
		10–133	1.033	17.87×10^{-4}	-7.19×10^{-5}	16.11×10^{-7}	-15.45×10^{-9}	5.58×10^{-11}
	LDPE	133–200	1.158	8.09×10^{-4}				
		10–113.5	1.078	1.24×10^{-4}	2.68×10^{-5}	-3.95×10^{-7}	2.35×10^{-9}	
	PVC	113.5–200	1.158	8.09×10^{-4}				
		10–110	0.7154	1.02×10^{-4}	0.0781×10^{-5}	-0.0167×10^{-7}	0.0524×10^{-9}	
		110–200	0.6791	5.67×10^{-4}				

^aAll properties are given as polynomials of the form $A + BT + CT^2 + \dots$ in which T is the temperature in degrees centigrade.

^bThe coefficients in this table were taken from U. Kleindienst, Doctoral Dissertation, Stuttgart University, 1976.

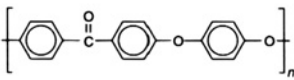
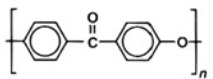
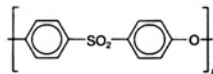
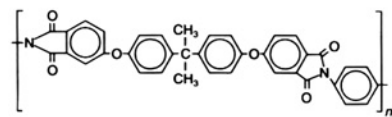
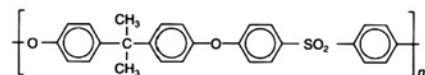
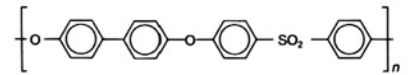
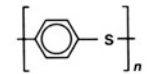
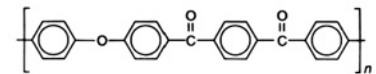
TABLE 5.7 Thermal Properties for Three Semicrystalline Engineering Thermoplastics at Room Temperature

Polymer	T_g (°C)	T (°C)	T_m (°C)	k (W/m · K)	C_p (kJ/kg · K)	ρ (10^{-3} kg/m ³)
PEEK (polyetheretherketone)	144	390	334–343	0.251	1.34	1.401 (cry) ^a 1.263 (amor) ^a
PPS (polyphenylene sulfide)	88	315	285–290	0.289	1.09	1.34 (amor) 1.44 (cry)
PEKK (poly(aryl ether ketone ketone))	156	354	330–339	—	—	—

^acry = crystalline; amor = amorphous.

For semicrystalline polymers it is observed that melting occurs leading to the absorption of energy. The energy associated with the change from the crystalline phase to the completely amorphous state is obtained by integrating the area under the curve of \bar{C}_p versus temperature

TABLE 5.8 Structure of a Number of Engineering Thermoplastics and Their Glass Transition and Melt Temperatures

PEEK—Polyetheretherketone		T_g (°C) = 144 T_m (°C) = 334
PEK—Polyetherketone		T_g (°C) = 154 T_m (°C) = 367
VITREX PES 200P—Polyethersulfone		T_g (°C) = 220
ULTEM—Polyetherimide		T_g (°C) = 220
UDEL P-1700—Polysulfone		T_g (°C) = 190
RADEL—Polyarylsulfone		T_g (°C) = 220
RYTON—Polyphenylene sulfide		T_g (°C) = 85 T_m (°C) = 285
PEKK—Polyetherketoneketone		

data.* The energy associated with this phase transition is called the heat of fusion, ΔH_f . Values of ΔH_f are presented in Table 5.9 for a number of commercially available polymers as well as two high performance polymers used in the formation of thermoplastic composites. It should also be noted that the melting point is not really distinct, but covers a broad temperature range. When carrying out calculations involving melting, it may be more appropriate to use C_p as a function of temperature rather than treat the polymer as having a distinct phase change.

The cooling of a semicrystalline polymer from a temperature above T_m to some lower temperature leads to crystallization. The energy associated with crystallization, called the heat of crystallization (ΔH_c), is affected by the temperature at which crystallization takes place. Representative data for PPS are presented in Table 5.10. Here it is observed that the heat of crystallization, ΔH_c , depends on \bar{M}_w and temperature. Furthermore, the values of ΔH_c are somewhat lower than those of ΔH_f . Unless data are available, it is customary to consider $\Delta H_f = \Delta H_c$. Values of ΔH_c for some common polymers are given in Appendix C and can be found for other polymers in the books by Van Krevelen (1990) and Brandrup and Immergut (1989).

5.3.2 Thermal Properties of Composite Systems

By composite systems we mean any combination of a polymer system (called the matrix) with another polymer, fillers such as glass fibers, nanoclays or carbon black (particulates), or long continuous fibers used in the formation of thermoplastic prepregs (a prepreg is a sheet of polymer that is reinforced with fiber and can later be processed by forming techniques). Blending rules are usually used to weight the contribution of each component. The rules consider the thermal properties to be in either a series or a parallel arrangement of the matrix and second component (Richardson, 1977). The series arrangement is

$$1/\Gamma_b = \phi_1/\Gamma_1 + \phi_2/\Gamma_2 \quad (5.73)$$

*Values of \bar{C}_p versus temperature are most often obtained by means of differential scanning calorimetry (DSC). This technique is based on monitoring the heat flow to or from the polymer sample from a standard, both of which are increased in temperature at the same rate. The properties of the standard are rigorously known.

TABLE 5.9 Heat of Fusion of Some Polymers

Polymer	ΔH_f (J/kg) $\times 10^{-4}$	Reference
Polyoxymethylene	24.9	Starkweather and Boyd, 1960
Polybutene-1	24.7	Nielsen, 1962
HDPE ("Super Dylan")	24.5	Ke, 1960
PP	23.4	Nielsen, 1962
HDPE ("Marlex 50")	21.8	Ke, 1960
Nylon 66	20.5	Nielsen, 1962
LDPE	13.8	Nielsen, 1962
PET	13.7	Nielsen, 1962
Natural rubber (<i>cis</i> -poly- isoprene)	6.4	Nielsen, 1962
PTFE	5.7	Starkweather and Boyd, 1960
PEEK	13.0	Velisaris and Saferis, 1988
PPS	10.5	Lopez and Wilkes, 1988

TABLE 5.10 Heats of Crystallization for Polyphenylene Sulfide as a Function of \bar{M}_w and Crystallization Temperature, T_c

T_c ($^{\circ}\text{C}$)	ΔH_c ($M_w = 24,000$) (J/kg) $\times 10^{-4}$	ΔH_c ($M_w = 63,000$) (J/kg) $\times 10^{-4}$
225	4.3	3.7
235	4.6	4.2
245	4.7	4.4
255	5.1	4.7

Source: Data from Lopez and Wilkes, 1988.

where

- Γ_b = bulk composite property (\bar{C}_p or k)
- Γ_1 = matrix property (\bar{C}_p or k)
- Γ_2 = second component property (\bar{C}_p or k)
- ϕ_1 = volume fraction of the matrix
- ϕ_2 = volume fraction of the second component

TABLE 5.11 Thermal Properties of PEEK and PEEK/Carbon Fiber Composites

Material	Density (kg/m ³)	Mass Fraction (kg matrix/kg)	Volume Fraction (m ³ matrix/m ³)	C_p (kJ/kg · K)	k (W/m · K)	$\alpha \times 10^7$ (m ² /s)
Matrix	1263 (amor) 1401 (cryst)			1.34	0.251	1.485
Carbon fiber	1790			1.26	0.427	1.899
Composite APC-1	1534	0.40	0.48	1.30	0.318	1.598
Composite APC-2	1579	0.32	0.32	1.30	0.339	1.655

Source: Data from Velisaris and Seferis, 1986.

The parallel arrangement of the matrix and second component properties is

$$\Gamma_b = \phi_1 \Gamma_1 + \phi_2 \Gamma_2 \quad (5.74)$$

Actually the series arrangement represents the highest limit for the bulk composite property while the parallel arrangement represents the lowest limit.

For a PEEK and carbon fiber composite, the thermal conductivity was found to be best determined using Eq. 5.73 while the heat capacity was best determined using Eq. 5.74 but with mass fractions instead of volume fractions (Velisaris and Seferis, 1988). Values for ρ , k , and \bar{C}_p are given in Table 5.11. It is interesting to note that the values of \bar{C}_p for the matrix and carbon fiber are similar while the values of k are lower for the matrix. The bulk values of k for the composite are then increased somewhat over those of the matrix. Although it is not certain that these rules apply to polymer blends, filled polymers, or other composite structures, they at least represent the starting point for estimating the thermal transport properties of composite systems.

5.4 HEATING AND COOLING OF NONDEFORMING POLYMERIC MATERIALS

Heat transfer is as important as polymer rheology in the processing of polymeric materials. Polymers usually start as solids and then are heated to temperatures above T_g or T_m before being shaped. During or immediately after the shaping process the cooling process starts, and it is here that the morphology and structure and associated physical properties are developed. In this section three methods of heat transfer are summarized: conduction, convection, and radiation. First, solutions to well-known problems are presented in graphical form in Section 5.4.1, as many processes can be modeled as one of these basic heat transfer processes. From the graphical solutions we proceed directly to numerical solutions of heat transfer problems. In Section 5.4.2 the important heat transfer coefficients commonly found in polymer processing are summarized. Radiation heat transfer is discussed in Section 5.4.3 as this technique is used frequently to heat polymers up rapidly before applying shaping operations such as thermoforming and blow molding.

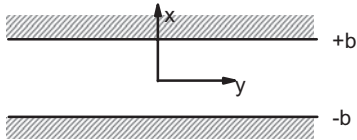


FIGURE 5.8 One-dimensional heat transfer in a slab with the heat flux in the x direction. Common boundary conditions are (a) constant wall temperatures at $x = +b$ and $-b$ and (b) heat flux at $x = +b$ and $-b$ due to thermal resistance between a fluid and the slab surface.

5.4.1 Transient Heat Conduction in Nondeforming Systems

When no deformation occurs, the thermal energy equation reduces to the following form:

$$\rho \bar{C}_p \frac{\partial T}{\partial t} = \nabla \cdot k \nabla T + \dot{S} \quad (5.75)$$

Here the source term, \dot{S} , could represent the rate of energy generated per unit volume due to a phase change, absorbed radiation, or a chemical reaction. For a number of problems encountered in polymer processing this equation takes on two relatively simple forms for planar and cylindrical geometries. For a planar geometry (see Fig. 5.8), Eq. 5.75 becomes

$$\rho \bar{C}_p \frac{\partial T}{\partial t} = k \frac{\partial^2 T}{\partial x^2} + \dot{S} \quad (5.76)$$

which is the one-dimensional heat conduction equation for a slab. Examples of processes that are described by this equation include the cooling of an expanded parison as it contacts a cold mold wall, the cooling of an injection-molded part, cooling of a laminated thermoplastic composite prepreg in a mold, and cooling of a cast film on a metal drum. For cylindrical geometries (see Fig. 5.9), Eq. 5.75 reduces to

$$\rho \bar{C}_p \frac{\partial T}{\partial t} = k \frac{1}{r} \frac{\partial}{\partial r} \left[r \frac{\partial T}{\partial r} \right] + \dot{S} \quad (5.77)$$

which is the heat conduction equation for a cylinder in which heat transfer occurs only in the r direction. Examples of processes that are described by Eq. 5.77 include cooling



FIGURE 5.9 One-dimensional heat transfer in a cylinder in the r direction. Common boundary conditions are (1) constant wall temperature at $r = R$ and a zero heat flux in the r direction at the center (i.e., $q_r = 0$); and (2) heat flux at $r = R$ due to thermal resistance between a fluid and the cylinder surface.

of a strand of polymer in a pelletizing process, of a polymer coated metal wire, and an injection-molded part of cylindrical cross section (e.g., a cylindrical preform that is later blow molded).

The solutions of Eqs. 5.76 and 5.77 are subject to various boundary conditions. For a slab of finite thickness (thickness $2b$, with the axis at the center of the slab) the boundary conditions are usually given as constant surface temperatures or a step change in the surface temperature due to convection at the free surfaces. Mathematically for the first case the boundary and initial conditions are given as

$$\text{B.C.1: at } x = +b, \quad T(b, t) = T_w \quad (5.78)$$

$$\text{B.C.2: at } x = -b, \quad T(-b, t) = T_w \quad (5.79)$$

$$\text{I.C.: at } t = 0, \quad T(x, 0) = T_0 \quad (5.80)$$

In the second case the boundary and initial conditions are given as

$$\begin{aligned} \text{B.C.1: at } x = -b, \quad q_x(-b, t) &= -k \left. \frac{\partial T}{\partial x} \right|_{-b} \\ &= h[T_a - T(-b)] \end{aligned} \quad (5.81)$$

$$\begin{aligned} \text{B.C.2: at } x = +b, \quad q_x(b, t) &= -k \left. \frac{\partial T}{\partial x} \right|_{+b} \\ &= h[T(+b) - T_a] \end{aligned} \quad (5.82)$$

$$\text{I.C.: at } t = 0, \quad T(x, 0) = T_0 \quad (5.83)$$

T_a here is the temperature of the cooling fluid. In the case of the cylindrical geometry the corresponding boundary and initial conditions for the constant surface temperature (step change in temperature) or the step change in surface temperature due to convection are written, respectively, as

$$\text{B.C.1: } T(R, t) = T_1 \quad (5.84)$$

$$\text{B.C.2: } \left. \frac{\partial T}{\partial r} \right|_{r=0} = 0 \quad (5.85)$$

$$\text{I.C.: } T(r, 0) = T_0 \quad (5.86)$$

or

$$\text{B.C.1: } q_r(R, t) = -k \left. \frac{\partial T}{\partial r} \right|_{r=R} = h(T(R) - T_a) \quad (5.87)$$

$$\text{B.C.2: } q_r(0, t) = -k \left. \frac{\partial T}{\partial r} \right|_{r=0} = 0 \quad (5.88)$$

$$\text{I.C.: } T(r, 0) = T_0$$

The solutions of Eqs. 5.76 and 5.77 are dependent on the boundary conditions. For constant coefficients (i.e., constant values of ρ , \bar{C}_p , and k) the solutions are well known and can be found in many books on heat transfer. We note here, in particular, the book by Carslaw and Jaeger (1973). Rather than reproduce the solutions, which are based on the method

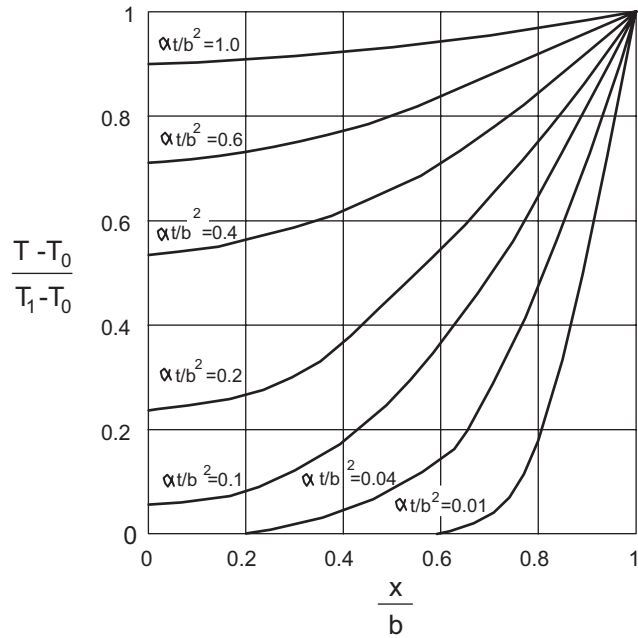


FIGURE 5.10 Dimensionless temperature versus dimensionless distance for a slab subjected to a step change in surface temperature (no thermal resistance). The parameter is the dimensionless time, t^* . T_0 is the initial temperature and T_1 is the wall temperature.

of separation of variables, we provide graphical solutions of some of the more commonly encountered cases. For example, Figure 5.10 shows the transient temperature profiles for a slab with constant surface temperatures. The parameter is the dimensionless time, $t^* = \alpha t/b^2$. In Figure 5.11 the corresponding case is given for the infinite cylinder. For a slab in which there is resistance to heat transfer at the interface between a solid and liquid the solution is graphically presented in Figure 5.12. Graphs are given for two positions, $x/b = 0$ and 1.0 . The parameter is the reciprocal of the Biot number, $Bi^{-1} = k/hb$. Similar plots are given in Figure 5.13 for an infinite cylinder. These figures can be used to make estimates for heating and cooling times for polymeric materials.

For constant coefficients, the temperature profiles for various geometries such as flat plates, infinite cylinders, and spheres are given in terms of infinite series. For example, for flat plates with surface resistance to heat transfer the equation to be solved is the one-dimensional heat transfer equation subject to the following boundary conditions:

$$\text{B.C.1: at } x = b, \quad -\frac{\partial T}{\partial x}(b, t) = (h/k)[T(b, t) - T_1] \tag{5.89}$$

$$\text{B.C.2: at } x = -b, \quad -\frac{\partial T}{\partial x}(-b, t) = (h/k)[T_1 - T(-b, t)]$$

$$\text{I.C.: at } t = 0, \quad T(x, 0) = T_0 \tag{5.90}$$

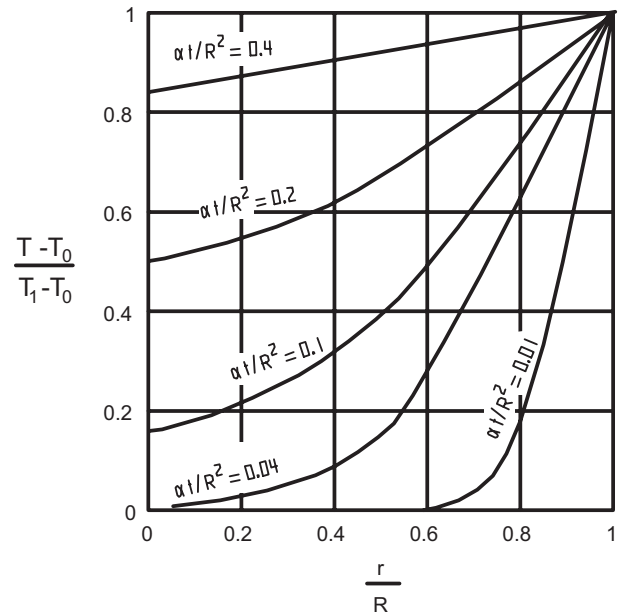


FIGURE 5.11 Dimensionless temperature profiles versus dimensionless distance for a cylinder subjected to a step change in surface temperature (no thermal resistance). The parameter is the dimensionless time, t^* . T_0 is the initial temperature and T_1 is the wall temperature.

The solution is

$$\frac{T_1 - T}{T_1 - T_0} = \sum_{n=1}^{\infty} \frac{2 \left(\frac{hb}{k}\right) \cos\left(\beta_n \frac{x}{b}\right)}{\left[\beta_n^2 + \frac{hb}{k} + \left(\frac{hb}{k}\right)^2\right] \cos \beta_n} \times \exp\left(-\frac{\beta_n^2 \alpha t}{b^2}\right) \tag{5.92}$$

where the eigenvalues, β_n , are given by

$$\beta_n \tan \beta_n = (hb/k) \tag{5.93}$$

To use the series solution, numerical techniques are needed to find β_n .

Rather than reproduce the series solutions for the various cases encountered in polymer processing, we use numerical techniques. Once we add factors such as temperature-dependent properties, chemical reactions, viscous dissipation, or enthalpy changes due to a phase change, then the series solutions become of little use. We use several different approaches to obtain a numerical solution. First we use the IMSL subroutine MOLCH (see Appendix E.8 in the folder entitled “IMSL Documentation-Appendix E” on the accompanying website for a description of this numerical subroutine), which solves one-dimensional partial differential equations of the parabolic type found in heat and mass transfer. This subroutine is capable of handling the case of a step change in surface temperature when there is no resistance

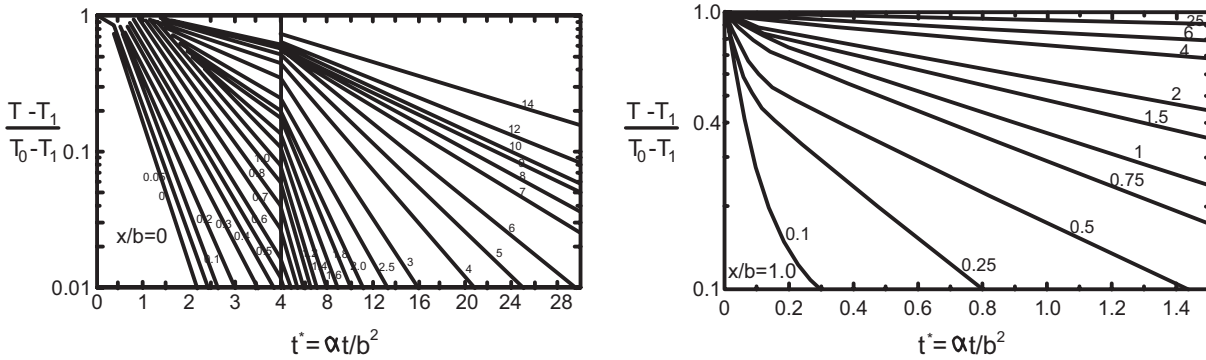


FIGURE 5.12 Dimensionless temperature versus dimensionless time for a slab subjected to a step change in surface temperature with thermal resistance at the interface between a fluid and a solid surface. $x/b = 0$ is at the centerline and $x/b = 1$ is at the surface. The parameter is the reciprocal of the Biot number, $\text{Bi}^{-1} = k/hb$. T_0 is the initial temperature, and T_1 is the temperature of the cooling fluid.

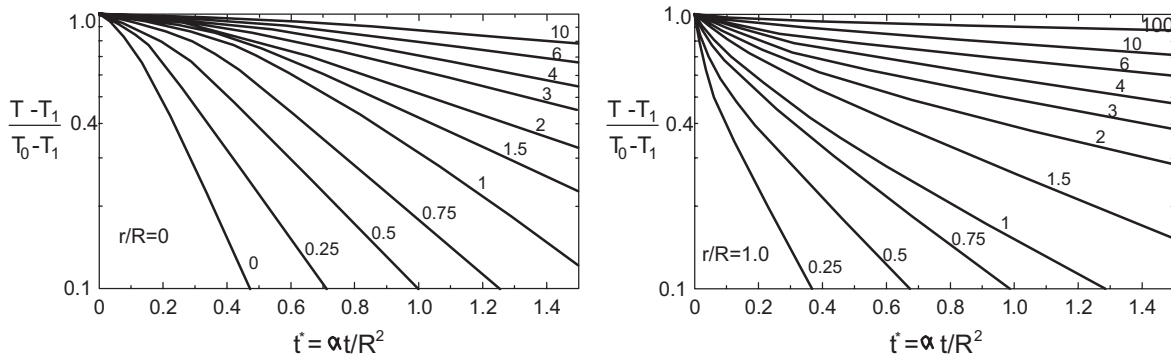


FIGURE 5.13 Dimensionless temperature versus dimensionless time for a cylinder subjected to a step change in surface temperature with thermal resistance. The parameter is $\text{Bi}^{-1} = k/hR$. T_0 is the initial temperature, and T_1 is the temperature of the cooling fluid.

to heat transfer. The only shortcoming is that the initial condition must satisfy the boundary conditions, which is difficult for situations in which there is a step change in temperature. The use of MOLCH is illustrated in the program “EX5-5-Fortran-MOLCH.doc.” In particular, one should note how we handle the initial condition so that it satisfies the boundary conditions. For the case of resistance at the surface the function (or subroutine) PDPDE in MATLAB is also used to solve partial differential equations of the parabolic type and its use in solving Example 5.5 is given in “EX5-5-PDEPE-MATLAB.doc” on the accompanying website. Finally, Excel is used to solve the parabolic partial differential equation that arises in Example 5.5 (“EX5-5-Excel.doc”).

Example 5.5. Cooling of an Injection-Molded Slab of HDPE

HDPE is injection molded into a rectangular cavity having dimensions of 10 cm by 10 cm by 0.32 cm thick. HDPE enters the cavity at 200 °C and the filling process occurs so

rapidly that the drop in temperature during filling can be considered to be negligible. Determine the time required to drop the centerline temperature of the melt to 130 °C (neglect crystallization) if the mold temperature is 25 °C and the heat transfer coefficient between the mold wall and the polymer is 25 W/m² · K.

Solution. The temperature variation in the polymeric melt is described by the one-dimensional heat transfer equation

$$\rho \bar{C}_p \frac{\partial T}{\partial t} = k \frac{\partial^2 T}{\partial x^2} \quad (5.94)$$

If it is assumed there is perfect thermal contact between the cooling medium and the melt, then the boundary and initial conditions are as follows:

$$\text{B.C.1:} \quad \text{at } x = b, \quad T(b, t) = 25 \text{ }^\circ\text{C} \quad (5.95)$$

$$\text{B.C.2:} \quad \text{at } x = 0, \quad \left. \frac{\partial T}{\partial x} \right|_0 = 0 \quad (5.96)$$

$$\text{I.C.:} \quad \text{at } t = 0, \quad T(x, 0) = 200 \text{ }^\circ\text{C} \quad (5.97)$$

When thermal contact is poor, then there is a flux of thermal energy at the surface given by

$$q_x(b, t) = -k \left. \frac{\partial T}{\partial x} \right|_b = h[T(b, t) - 25^\circ\text{C}] \quad (5.98)$$

We now introduce the following dimensionless variables:

$$\xi = x/b \quad \theta = \frac{T - T_1}{T_0 - T_1} \quad (5.99)$$

where $T_1 = 25^\circ\text{C}$ and $T_0 = 200^\circ\text{C}$. Equation 5.94 becomes

$$\frac{\partial \theta}{\partial t} = \frac{k}{\rho \bar{C}_p b^2} \frac{\partial^2 \theta}{\partial \xi^2} \quad (5.100)$$

with boundary and initial conditions

$$\text{B.C.1: at } \xi = 1, \quad \theta(1, t) = 0 \quad (5.101)$$

$$\text{B.C.2: at } \xi = 0, \quad \left. \frac{\partial \theta}{\partial \xi} \right|_0 = 0 \quad (5.102)$$

$$\text{I.C.: at } t = 0, \quad \theta(\xi, 0) = 1 \quad (5.103)$$

or for a heat flux at the surface

$$\text{B.C.1: at } \xi = 1, \quad \left. \frac{\partial \theta}{\partial \xi} \right|_1 = \frac{hb}{k} \theta(1, t) \quad (5.104)$$

$$\text{B.C.2: at } \xi = 0, \quad \left. \frac{\partial \theta}{\partial \xi} \right|_0 = 0 \quad (5.105)$$

$$\text{I.C.: at } t = 0, \quad \theta(\xi, 0) = 1 \quad (5.106)$$

Time can be made dimensionless by introducing

$$t^* = t \rho \bar{C}_p b^2 / k \quad (5.107)$$

The solutions are given in Figures 5.10 and 5.12 for the two cases.

For the temperatures given

$$\theta = \frac{130 - 25}{200 - 25} = 0.6 \quad (5.108)$$

At $x/b = 0$ and $\theta = 0.6$,

$$\alpha t / b^2 = t^* \approx 0.44 \quad (5.109)$$

We note that it was necessary to estimate the value of t^* , because it falls between the values of 0.4 and 0.6 given on the graph. Using values of ρ , C_p , and k given in Table 5.5,

which appear to be nearly independent of temperature over the range of interest, we find

$$t = \frac{b^2(0.44)}{\alpha} = \frac{(2.56 \times 10^{-6})(0.44)}{1.2305 \times 10^{-7}} = 9.15 \text{ s} \quad (5.110)$$

For the case when there is a heat flux at the surface we use Figure 5.12. In Figure 5.12 the dimensionless temperature is plotted versus dimensionless time with the parameter being the reciprocal of the Biot number, $\text{Bi}^{-1} = k/hb$. With a dimensionless temperature of $\theta = 0.6$,

$$t = \frac{b^2 t^*}{\alpha} = \frac{(2.56 \times 10^{-6})(4.0)}{1.2305 \times 10^{-7}} = 83.3 \text{ s} \quad (5.111)$$

Hence, it takes about 13 times as long to cool the polymer melt down to 130°C if there is significant resistance at the surface.

The problem is also solved numerically using the subroutine MOLCH, which is described in the accompanying website under the file "IMSL Subroutines." The subroutine has been made as "user friendly" as possible so that one does not have to really understand the numerical method. However, because of this, there is one limitation which requires the initial condition satisfy the boundary condition. For the case at hand this presents a problem (i.e., the initial condition of $T(x, 0) = T_0$ satisfies B.C.2 but does not satisfy B.C.1, which is $T(b, t) = T_1$). For the dimensionless temperature, θ , we introduce the following function:

$$\theta(\xi, 0) = 1 - \xi^{20} \quad (5.112)$$

This function satisfies $\partial \theta / \partial \xi = 0$ at $\xi = 0$ and $\theta = 0$ at $\xi = 1$ while being approximately 1.0 over the region $0 \leq \xi \leq 1$. Other exponents can be used without affecting the results significantly. The calling program is given on the accompanying website in the file "Numerical Solutions, Chapter 5" in the document "Example 5-5-MOLCH-Fortran" and the results are given in Table 5.12. The first column corresponds to the dimensionless temperature at the centerline. At $t = 7.0$ s, $\theta = 0.58462$, which corresponds to a temperature of 128°C . Actually, t is less than 7.0 s. An identical solution is obtained by using PDPDE in MATLAB (see the file "EX5-5-PDPDE-MATLAB.doc" on the accompanying website).

The partial differential equation in Eq. 5.100 is referred to as a parabolic partial differential equation. When the boundary conditions involve resistance at the interface (i.e., a boundary condition as given in Eq. 5.104), then the temperature at the interface between the slab and gas or fluid is changing. The IMSL numerical subroutine MOLCH is not capable of handling this boundary condition. By introducing a finite difference operator for the spatial derivative

TABLE 5.12 Numerical Output for a Step Change in Temperature

Time(s)	1	2	3	4	5	6
1.00	0.99618	0.97742	0.91180	0.74588	0.43256	0.00006
2.00	0.94835	0.91236	0.80682	0.61546	0.33646	0.00006
3.00	0.87437	0.83301	0.71885	0.53252	0.28449	0.00006
4.00	0.79491	0.75395	0.64380	0.47096	0.24912	0.00006
5.00	0.71863	0.68009	0.57804	0.42055	0.22150	0.00006
6.00	0.64834	0.61275	0.51967	0.37716	0.19827	0.00006
7.00	0.58462	0.55195	0.46754	0.33892	0.17801	0.00006
8.00	0.52720	0.49728	0.42089	0.30489	0.16007	0.00006
9.00	0.47562	0.44820	0.37909	0.27448	0.14405	0.00006
10.00	0.42935	0.40418	0.34161	0.24723	0.12972	0.00006

(i.e., $\partial^2 T / \partial x^2$) the partial differential equation becomes a system of ordinary differential equations, which can be solved using the IMSL subroutines IVPAG or DIVPAG (see the file “IMSL Subroutines” on the accompanying website). The procedure for converting Eq. 5.100 to a system of ordinary differential equations is as follows. The region $0 \leq \xi \leq 1$ is divided up into N nodes or spatial points. In the case of the slab, the node at the center is taken as 0 and the node at the mold wall is numbered as $\text{NEQ} + 1 = N$. The differential equation (Eq. 5.100) at the interior nodes becomes, using a central difference approximation (Riggs, 1988; Matthews and Fink, 2004),

$$\frac{d\theta_i}{dt} = \alpha' \left[\frac{\theta_{i-1} - 2\theta_i + \theta_{i+1}}{\Delta\xi^2} \right] \quad (5.113)$$

where $\alpha' = k/\rho C_p b^2$ and $\Delta\xi$ is the distance between the nodes and i runs from 2 to $\text{NEQ} - 1$. At node 0 using Eq. 5.105 and a forward difference approximation; for $\partial\theta/\partial\xi$ we find that

$$\frac{\partial\theta}{\partial\xi} = 0 = \frac{-3\theta_0 + 4\theta_1 - \theta_2}{2\Delta\xi} \quad (5.114)$$

or

$$\theta_0 = \frac{1}{3}(4\theta_1 - \theta_2) \quad (5.115)$$

At the mold wall Eq. 5.100 can be expressed using a backward difference approximation; that is,

$$\frac{\partial\theta}{\partial\xi} = \frac{3\theta_i - 4\theta_{i-1} + \theta_{i-2}}{2\Delta\xi} \quad (5.116)$$

to give

$$\theta_{\text{NEQ}+1} = \frac{4\theta_{\text{NEQ}} - \theta_{\text{NEQ}-1}}{3 + (2\Delta\xi hb)/k} \quad (5.117)$$

The PDE at node 1 becomes

$$\frac{d\theta_2}{dt} = \left(\frac{\alpha'}{\Delta\xi^2} \right) \left[-\frac{2}{3}\theta_2 + \frac{2}{3}\theta_3 \right] \quad (5.118)$$

while that at node NEQ is

$$\frac{d\theta_{\text{NEQ}}}{dt} = \frac{\alpha'}{\Delta\xi^2} \left[\theta_{\text{NEQ}-1} - 2\theta_{\text{NEQ}} + \frac{4\theta_{\text{NEQ}} - \theta_{\text{NEQ}-1}}{3 + (2\Delta\xi hb)/k} \right] \quad (5.119)$$

Hence, a system of NEQ ordinary differential equations are solved. The temperature at each boundary node is calculated at each time step using the algebraic expressions in Eqs. 5.115 and 5.117.

The calling program is given in the file “EX5-5-Resistance-IMSL-Fortran.doc” on the accompanying website. To solve Eq. 5.100 the region from the centerline of the slab to the surface of the slab is broken up into 10 segments (one should try other nodal spacings). The node at the center is numbered 1 while that at the surface is numbered 11. The differential equation at node 2 is given by Eq. 5.118 while that at node 10 is given by

$$\frac{d\theta_{10}}{dt} = \frac{\alpha'}{\Delta\xi^2} \left[\theta_9 - 2\theta_{10} + \frac{4\theta_{10} - \theta_9}{3 + (2\Delta\xi hb)/k} \right] \quad (5.120)$$

The differential equations for the remaining nodes (3 through 9) are given by Eq. 5.113. These equations are written in subroutine FCN. The values of θ at the boundaries, θ_1 and θ_{11} , are calculated after each time step (or call to DIVPAG) using Eq. 5.115 for θ_1 and the following equation for θ_{11} (see Eq. 5.117):

$$\theta_{11} = \frac{4\theta_{10} - \theta_9}{3 + (2\Delta\xi hb)/k} \quad (5.121)$$

The output from the numerical solutions (using any of the three methods: IMSL, Excel, or MATLAB, which are

TABLE 5.13 Numerical Output for Resistance at the Interface Between the Mold Walls and Melt

Time(s)	1	2	3	4	5	6	7	8	9	10	11
0.0	1.00	1.00	1.00	1.00	1.00	1.00	1.00	1.00	1.00	1.00	1.00
10.0	0.953	0.953	0.950	0.947	0.942	0.936	0.928	0.919	0.909	0.897	0.884
20.0	0.888	0.887	0.885	0.887	0.882	0.871	0.864	0.855	0.846	0.835	0.822
30.0	0.826	0.826	0.824	0.821	0.817	0.811	0.804	0.796	0.787	0.777	0.766
40.0	0.769	0.769	0.767	0.764	0.760	0.755	0.749	0.741	0.733	0.723	0.713
50.0	0.716	0.716	0.714	0.711	0.708	0.703	0.697	0.690	0.682	0.673	0.664
60.0	0.667	0.666	0.665	0.662	0.659	0.654	0.649	0.643	0.635	0.627	0.618
70.0	0.621	0.620	0.619	0.617	0.613	0.609	0.604	0.598	0.591	0.584	0.575
80.0	0.578	0.577	0.576	0.574	0.571	0.567	0.562	0.557	0.551	0.543	0.535
90.0	0.538	0.538	0.536	0.534	0.532	0.528	0.524	0.518	0.513	0.506	0.498

described in the accompanying website in “Numerical Solutions, Chapter 5”) is given in Table 5.13. The nodal values for dimensionless temperature are given at each time step in the output. A centerline temperature of 130 °C corresponds to $\theta = 0.6$. From Table 5.13 we see that it takes about 75 s to reach this temperature, which is somewhat different from the value obtained using Figure 5.12. However, this difference is due to the inability to accurately extrapolate values from the graph in Figure 5.12. ■

5.4.2 Heat Transfer Coefficients

The equation of thermal energy presented in the last section is usually solved along with prescribed boundary conditions. We either specify (1) the surface (or boundary) temperature or (2) the heat flux at the surface. This section is concerned with empiricisms for heat transfer coefficients which allow us to deal with the difference in temperature between a fluid and a solid interface as a result of thermal resistance.

The heat flux is usually given in terms of heat transfer coefficients, defined by Newton’s law of cooling as

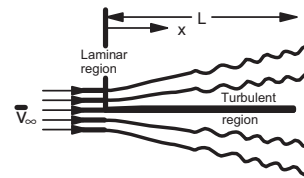
$$q_n|_s = -k \frac{\partial T}{\partial n} |_s = h[T(s) - T_a] \quad (5.122)$$

where $q_n|_s$ is the heat flux in the direction normal to the surface and evaluated at the surface and h is the heat transfer coefficient. T_a is the temperature of the ambient fluid (gas or liquid) and $T(s)$ is the local surface temperature of the solid or molten polymer. In the case of forced convection, correlations for h with the Reynolds number, Re , are well known for certain common geometries.

In particular, we note several cases that occur frequently in polymer processing. For flow of a fluid over a smooth flat plate (see Fig. 5.14) the local heat transfer coefficient, h_x , is given in terms of the Prandtl number, Pr , and local Reynolds number, Re_x , as

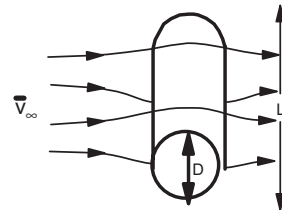
$$\frac{h_x x}{k} = 0.332 Pr^{1/3} Re_x^{1/2} \quad (5.123)$$

where $Pr = (\mu \bar{C}_p / k)_f$ and $Re_x = (v_\infty \rho x / \mu)_f$. The subscript f implies to evaluate the properties of the fluid at the film temperature, T_f , where $T_f = \frac{1}{2} (T_0 + T_\infty)$, where T_0 is the surface temperature of the solid and T_∞ is the temperature of the approaching fluid. The relation in Eq. 5.123 is valid for



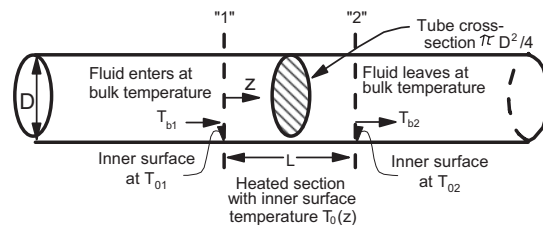
$$h_x x / k = 0.332 (\rho \bar{C}_p / k)_f^{1/3} (v_\infty \rho x / \mu)_f^{1/2}$$

$$\bar{h} = 2h|_{x=L}, Re = 10^6$$



$$Nu = hD/k = (0.43 + 0.5 Re^{0.5}) Pr^{0.38} (Pr_f / Pr_w)^{0.25} \quad 1 < Re < 10^3$$

$$Nu = 0.25 Re^{0.6} Pr^{0.38} (Pr_f / Pr_w)^{0.25} \quad 10^3 < Re < 2 \times 10^5$$



$$h_{in} D / k_b = 0.026 (DG / \mu_b)^{0.9} (\bar{C}_p \mu / k)^{0.5} (\mu_b / \mu_0)^{0.14} \quad Re > 20,000$$

$$h_{in} D / k_b = 0.026 (Re_f Pr_b D / L)^{0.5} (\mu_b / \mu_0)^{0.14} \quad Re < 2200$$

FIGURE 5.14 Forced convection heat transfer coefficients for three commonly encountered geometries.

$Re < 10^6$. The average heat transfer coefficient, \bar{h} , over the length of the plate is found by averaging Eq. 5.123 over the length of the plate, L , and is

$$\bar{h} = 2h|_{x=L} \quad (5.124)$$

In the processing of polymers the relations in Eqs. 5.123 and 5.124 are usually applied for situations where the temperature along the plate is not constant, but the fluid temperature is. Hence, with the availability of numerical methods we can use h_x . The correlation in Eq. 5.123 should be applicable to processes such as film blowing and the extrusion of flat sheet.

Another common geometry encountered in polymer processing is the cooling of long cylinders such as might occur in fiber spinning. The heat transfer coefficient for transverse flow over a long cylinder (see Fig. 5.14) is given in terms of Re and Pr as

$$Nu = \frac{hD}{k_f} = (0.43 + 0.50 Re^{1/2}) Pr^{0.38} \left(\frac{Pr_f}{Pr_0} \right)^{0.25}, \quad \text{for } 1 < Re < 10^3 \quad (5.125)$$

$$Nu = 0.25 Re^{0.6} Pr^{0.38} \left(\frac{Pr_f}{Pr_0} \right)^{0.25}, \quad \text{for } 10^3 < Re < 2 \times 10^5 \quad (5.126)$$

where the subscript f implies to evaluate the fluid properties at the film temperature, $T_f = (T_0 + T_\infty)/2$. T_∞ is the temperature of the approaching fluid and T_0 is the surface temperature of the cylinder. For gases the ratio Pr_f/Pr_0 , where Pr_0 is Pr evaluated at T_0 , is dropped and the fluid properties are evaluated at T_f . For fluids the ratio is retained with the fluid properties evaluated at T_∞ . Correlations for tube banks are also available (Holman, 1981). This situation might more closely resemble fiber spinning processes in which many filaments are spun from a spinneret.

Cooling of metal surfaces, such as occurs in the cooling of injection molding tooling, is usually done by circulating cooling fluid through channels located just beneath the metal surface. This requires the knowledge of heat transfer coefficients for fully developed flow in smooth pipes (see Fig. 5.14). For highly turbulent flow, for $L/D > 10$ and $Re > 20,000$, the logarithmic mean heat transfer coefficient is given by

$$\frac{h_{ln} D}{k_b} = 0.026 \left(\frac{DG}{\mu_b} \right)^{0.9} \left(\frac{\bar{C}_p \mu}{k} \right)^{1/2} \left(\frac{\mu_b}{\mu_0} \right)^{0.14} \quad (5.127)$$

For laminar flow h_{ln} is given by

$$\frac{h_{ln} D}{k_b} = 1.86 (Re_b Pr_b D/L)^{1/2} (\mu_b/\mu_0)^{0.14} \quad (5.128)$$

where D is the tube diameter and G is $< \rho v_z >$. The subscript b means to evaluate μ at $\frac{1}{2} (T_{b1} + T_{b2})$ while the subscript 0 means to evaluate μ at $T = \frac{1}{2} (T_{01} + T_{02})$. For highly turbulent flow the results in Eq. 5.127 can be extended to noncircular cross sections by replacing the diameter with $4R_H$, where R_H is the mean hydraulic radius.

There are situations in which heat transfer by free convection could be important such as the cooling of a slowly moving strand of polymer in a water bath and the cooling of a parison as it hangs from a die before being blown. For those who have studied heat transfer, it is known that the dimensionless heat transfer coefficient, Nu , is given as a function of the Grashof number, Gr , and the Prandtl number:

$$Nu_m = Nu(Gr, Pr) \quad (5.129)$$

where Nu_m is based on the heat transfer coefficient for the total surface, h_m , of the submerged object, $Gr = L^3 \rho^2 g \beta \Delta T / \mu^2$ and $Pr = C_p \mu / k$. β is the volume coefficient of expansion of the fluid and $\Delta T = T_0 - T_\infty$. For a long horizontal cylinder in an infinite fluid,

$$Nu_m = 0.518 (Gr_f Pr_f)^{0.25} \quad (5.130)$$

where $Gr_f = D^3 \rho^2 f g \beta_f \Delta T / \mu_p^2$ and $Pr_f = \bar{C}_p \mu_f / k_f$. Equation 5.130 is valid for $Gr Pr > 10^4$. An equation similar to Eq. 5.130 can be applied to horizontal flat plates:

$$Nu_m = 0.6 (Gr_f Pr_f)^{1/4} \quad (5.131)$$

with D replaced by $L = L_n L_v / (L_n + L_v)$, where L_n is the horizontal length and L_v is the thickness of the plate. For vertical plates and cylinders suspended in air,

$$Nu_m = 0.59 (Gr_f Pr_f)^{1/4} \quad (5.132)$$

for $10^4 < Gr Pr < 10^9$. For a flat plate D^3 is replaced by L^3 (length of the plate).

We have attempted to list only a few of the more pertinent heat transfer coefficients. Certainly correlations for other geometries and situations will be used in polymer processing. Furthermore, the use of correlations between Nu and Gr and Pr have ranges of applicability. There are numerous references that should be consulted for more details concerning the use of heat transfer coefficients and for other correlations (Bird et al., 1960, 2007; Whitaker, 1977; McAdams, 1954; Holman, 1981).

Example 5.6. Cooling of a Strand in a Pelletizing Bath

Ten strands of PP having a diameter of 3.175×10^{-3} m are extruded at 200°C from a pelletizing die into a water bath at the rate of 3 m/min. In order to determine the length of the

bath required to drop the temperature of a strand to 75 °C, it is necessary to determine a heat transfer coefficient. Determine the heat transfer coefficient if the water temperature is 12 °C.

Solution. Heat transfer may occur by both free convection transverse to the filament surface and by forced convection as the strand moves through the water. We first estimate h for free convection from a horizontal cylinder using Eq. 5.130. The properties of water are needed at T_f , but T_f changes along the length of the strand. We calculate Nu_m at the beginning and end of the bath. At the beginning

$$T_f = \frac{200 + 12}{2} = 106 \text{ }^\circ\text{C}$$

From Table C.6 (Appendix C)

$$Pr Gr = 7.40 \times 10^5$$

Using Eq. 5.130,

$$Nu_m = 0.518 (7.40 \times 10^5)^{0.25} = 15.2$$

$$h = \frac{(15.2)(0.684)}{3.175 \times 10^{-3}} = 3273 \text{ W/m} \cdot \text{ }^\circ\text{C}$$

At the end of the bath

$$T_f = \frac{75 + 12}{2} = 43.5 \text{ }^\circ\text{C}$$

Again referring to Table C.6 in Appendix C.6, we find

$$Pr Gr = 9.86 \times 10^4$$

and hence $Nu_m = 9.18$ and $h_m = 1842 \text{ W/m}^2 \cdot \text{ }^\circ\text{C}$.

For forced convection there are no correlations for flow along a cylinder, and hence we use the correlation for flow over a flat plate (Eqs. 5.123 and 5.124). Using the data in Appendix C.6, we calculate Pr and Re at $T_f = 106 \text{ }^\circ\text{C}$:

$$Pr_f = (\mu \bar{C}_p / k)_f = (2.67 \times 10^{-4})(4216)/0.684 = 1.66$$

$$Re_f = (v_\infty \rho L / \mu)_f = (0.05)(955)(1)/(2.67 \times 10^{-4})$$

$$= 1.79 \times 10^5$$

We arbitrarily estimate L to be 1 m in the above calculation. Using Eq. 5.123 we calculate

$$h|_{x=L} = (k/l)(0.332)(1.646)^{1/3}(1.788 \times 10^5)^{1/2}$$

$$= 113.4 \text{ W/m}^2 \cdot \text{ }^\circ\text{C}$$

$$\bar{h} = 2h|_{x=L} = 226.8 \text{ W/m}^2 \cdot \text{ }^\circ\text{C}$$

Hence, it is apparent that the dominant form of heat transfer for the conditions given is that of free convection.

If one were required to design a pelletizing bath it would be necessary to solve the equation of energy using a heat flux boundary condition at the strand surface. h changes significantly along the length of the strand as shown in the calculations. Certainly for the most rigorous calculations we would attempt to calculate h as a function of temperature. As a first approximation we could use a simple average value based on the two extremes. ■

5.4.3 Radiation Heat Transfer

Thermal radiation is often used to heat up preforms used in blow molding or plastic sheets used in thermoforming. Furthermore, in processes such as fiber spinning considerable cooling of the outer filaments can occur through radiation heat transfer. We review here the basic ideas of radiation heat transfer.

The heat flux at a surface associated with radiation heat transfer when the radiation is completely absorbed at the surface is given as

$$q_n(t, s) = -k \left. \frac{\partial T}{\partial n} \right|_{s,t} = -\sigma F [T_r^4 - T^4(s, t)] \quad (5.133)$$

where T_r is the temperature of the radiation source and F is the combined configuration emissivity factor (i.e., eF' , where F' is related to the surface geometry and is called the view factor and e is the emissivity). σ is the Stefan–Boltzmann radiation constant given as $5.6697 \times 10^{-8} \text{ W/m}^2 \cdot \text{K}^4$ or $0.1712 \times 10^{-8} \text{ Btu/h} \cdot \text{ft}^2 \cdot \text{ }^\circ\text{R}^4$. For most polymers the emissivity, e , is $0.9 < e < 1.0$. If $T_r \gg T(s, t)$, then we assume a constant heat flux.

The combined shape factors, F , take on various forms depending on the geometry of the emitting and absorbing surfaces. Several common situations are listed below while other geometries can be found in the books by Holman (1981), Rohsenow and Hartnett (1973), and Siegal and Howell (1981). For parallel flat plates F is given by

$$F = (1/e_1 + 1/e_2 - 1)^{-1} \quad (5.134)$$

where e_1 and e_2 are the emissivities of the sheet and source, respectively. If one cylindrical surface is enclosed by another such as for a rod, wire, or pipe exposed to a source (e.g., two parallel banks of lights), then

$$F = [1/e_1 + (A_1/A_2)/(1/e_2 - 1)]^{-1} \quad (5.135)$$

where A_1 is the area of the polymer and A_2 is the area of the source. As $A_1/A_2 \rightarrow 0$, then $F = e_1$.

In some cases in which radiation heating is used, convection may also be employed. This is because in the case of radiation heating the surface of a polymer may reach temperatures well above the degradation temperature and convection

can be used intermittently to cool the surface. The total heat flux at the surface in this case is given as

$$q_n|_s = (h_c + h_r)(T_1 - T_2) \quad (5.136)$$

where h_c is the convection heat transfer coefficient and h_r is the radiant heat transfer coefficient. The value of h_r is calculated from the following expression:

$$q_n|_s = h_r(T_1 - T_2) = F\sigma(T_1^4 - T_2^4) \quad (5.137)$$

where the subscript "1" pertains to the polymer and the subscript "2" to the heating source. From this equation we find

$$h_r = F\sigma(T_1^2 + T_2^2)(T_1 + T_2) \quad (5.138)$$

Example 5.7. Radiation Heating of a Sheet (Thermoforming)

Prior to thermoforming a polymer (PVC) sheet it is heated on both sides by radiation from an initial temperature, T_0 , of 90 °F to a final centerline temperature, T_f , of 390 °F. Determine how long it will take for the centerline of the sheet to reach 390 °F for the following set of data.

Polymer sheet: $k = 0.14$ Btu/h · ft · °F, $F = 0.9$

Thickness ($2b$) = 0.24 in.; $\rho C_p/k = \alpha = 5 \times 10^{-3}$ ft²/h

Radiation source: $T_s = 1740$ °F and is a bank of heating elements which can be considered as a parallel plate radiation source

Solution. The differential equation to be solved along with the appropriate boundary conditions are

$$\rho \tilde{C}_p \frac{\partial T}{\partial t} = k \frac{\partial^2 T}{\partial x^2}$$

$$\text{I.C.: at } t = 0, \quad T = T_0$$

$$\text{B.C.1: at } x = b, \quad q_x|_b = -k \frac{\partial T}{\partial x}|_{x=b} = h_r(T_1 - T_2)$$

$$\text{B.C.2: at } x = -b, \quad q_x|_b = -k \frac{\partial T}{\partial x}|_{x=-b} = h_r(T_2 - T_1)$$

or we can also use

$$\text{B.C.2: at } x = 0, \quad q_x = 0$$

The solution to this problem can be obtained numerically or by separation of variables if the coefficients are constant.

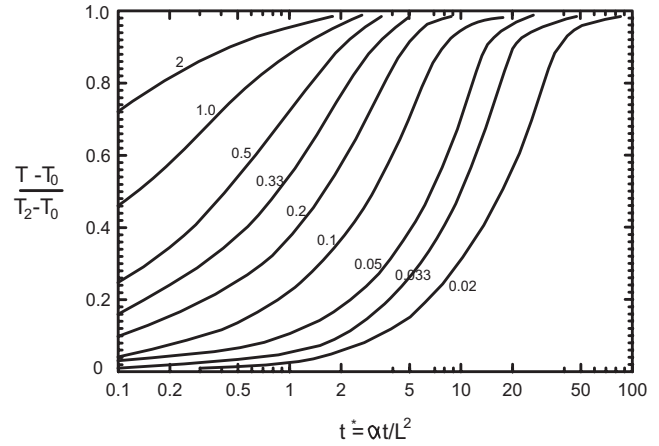


FIGURE 5.15 Dimensionless temperature versus dimensionless time for a slab subjected to radiation energy input at the surface ($x/b = 1$). The parameter is the radiative Biot number, $Bi_r = \sigma F T_s^3 L/k$. The curves are for a specific ratio of $T_0/T_2 = 1/4$, where T_0 and T_2 are given in absolute units.

Since α is given as constant, we can use the separation of variables solution, which is presented in graphical form in Figures 5.15 and 5.16 for the case when $T_0/T_2 = 0.25$ (based on absolute temperatures). Solutions for other parameters are given in the *Handbook of Heat Transfer* (Rohsenow and Hartnett, 1973). We assume here $T_2 \gg T_1$, in which case $h_r = F\sigma T_2^3$. The radiative Biot number, Bi_r , is then defined as

$$Bi_r = \frac{h_r b}{k} = \frac{F\sigma T_2^3 b}{k}$$

which comes from the dimensionless temperature gradient. From the data given in this problem we obtain the following

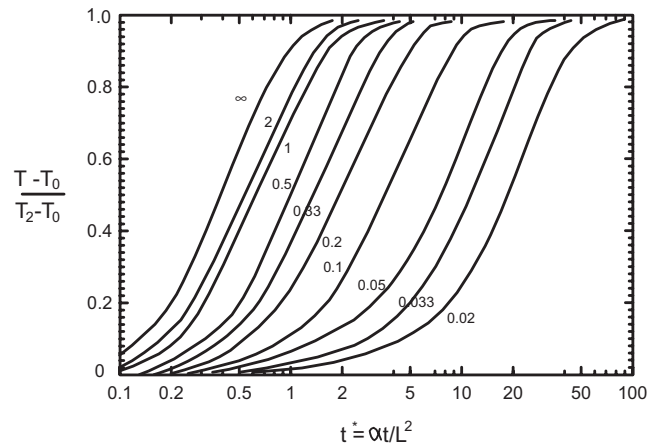


FIGURE 5.16 Dimensionless temperature versus dimensionless time for a slab subjected to radiation energy input at the centerline ($x/b = 0$) as in Figure 5.15.

quantities:

$$(T - T_0)/(T_2 - T_0) = (390^\circ\text{F} - 90^\circ\text{F})/(1740^\circ\text{F} - 90^\circ\text{F}) = 0.182$$

$$\text{Bi}_r = (0.172 \times 10^{-8})(0.9)(0.12/12) \times (2200)^3/0.14 = 1.18$$

From Figure 5.16, we read the dimensionless time from the abscissa:

$$0.3 = \alpha t/L^2$$

From this we solve for t and find that $t = 6 \times 10^{-3}$ h.

The surface temperature of the sheet during the time of heating will reach $(0.7 = (T - T_0)/(T_2 - T_0))$ 824.5°F , which may degrade the sheet surface. In practice we would use forced convection to cool the surface of the sheet. We could then use the combined heat transfer coefficient and resolve the problem. A more accurate solution to this problem can be obtained numerically, and this is done in Problem 5C.5. ■

In Eq. 5.138 it is assumed that all the radiation from the light source is absorbed at the surface. However, this is not always the case as some materials transmit portions of the incident radiation of certain wavelengths rather than absorb it. In Figure 5.17 is shown the transmittance curve for a 3.8 mm thick sample of PET, and here we observe that for wavelengths beyond 2.25 μm no light is transmitted (i.e., for wavelengths of light greater than 2.25 μm PET of thickness 3.80 mm is opaque). Assuming that the power

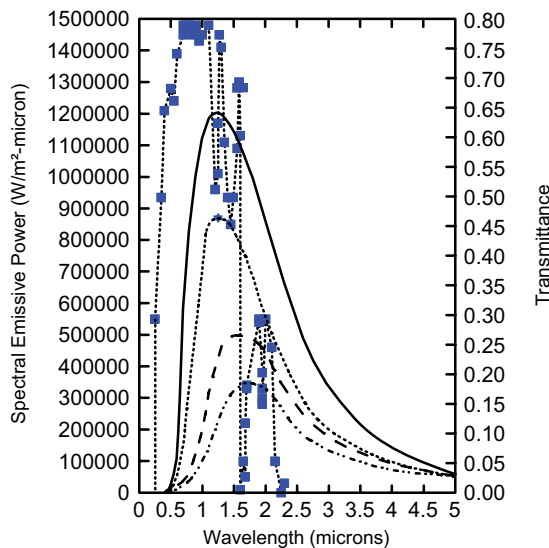


FIGURE 5.17 Blackbody radiation spectral distributions superimposed on the transmittance curve for a 3.8 mm thick PET sample. (Data from Shelby, 1991.)

output of a typical quartz lamp has a specular distribution that can be approximated by a blackbody emitter, the spectral emissive power of a blackbody source can be described by Planck's distribution:

$$P(\lambda) = BE(\lambda) = C_1\lambda^{-6}/[\exp(C_2/\lambda T) - 1] \quad (5.139)$$

where B is a scaling constant relating the fraction of $E(\lambda)$ that reaches the sample, λ is the wavelength in μm , and C_1 and C_2 are constants having values of $3.742 \times 10^6 \text{ W} \cdot \mu\text{m}^4/\text{m}^2$ and $1.439 \times 10^4 \mu\text{m} \cdot \text{K}$, respectively. The spectral emissive power is superimposed on Figure 5.17 for various lamp temperatures. Here we see that for the two highest lamp temperatures most of the incident energy has wavelengths that overlap with the region where PET transmits the radiation rather than absorbs it. Hence, we might expect it difficult to heat a semitransparent parison such as PET by means of radiation.

Actually there are advantages in having the polymer partially transparent to the incident radiation. This is because the radiation is absorbed internally in the polymer sample, which provides a more uniform heating of the material relative to that produced when the radiation is absorbed only at the surface.

Mathematically the absorbing of radiation is treated as a source term in the equation of energy. The intensity of the incident radiation as a function of depth, x , for a planar slab is given by Beer's law (Holman, 1981):

$$\frac{I_x(\lambda)}{I_s(\lambda)} = e^{-k(\lambda)x} \quad (5.140)$$

where $I_s(\lambda)$ is the intensity of the radiation at the surface for a given wavelength and $k(\lambda)$ is the absorption coefficient. Noting that $I(\lambda)$ has dimensions of energy per unit area per unit time, we can perform an energy balance to find the energy generated per unit volume per unit time. For a slab of area A and thickness Δx the energy balance is (note that $x = 0$ is taken at the surface here)

$$(I_x|_x - I_x|_{x+\Delta x})A = \dot{S}A\Delta x \quad (5.141)$$

Dividing by Δx and taking the limit as $\Delta x \rightarrow 0$, we obtain an expression for the energy generated per unit time and volume:

$$-\frac{dI_x}{dx} = \dot{S} = I_s k(\lambda)e^{-k(\lambda)x} \quad (5.142)$$

For heating cylindrical geometries such as parisons, a similar approach can be used to find \dot{S} :

$$\dot{S} = \frac{1}{r} \frac{d}{dr}(rI_r) \quad (5.143)$$

TABLE 5.14 Effective Values of the Absorption Coefficient for PET as a Function of Lamp Temperature

Lamp Temperature (°C)	\bar{k} (m ⁻¹)
2200	1300
2040	1460
1900	1610
1750	1790

Source: Shelby, 1991.

In cylindrical coordinates Eq. 5.140 becomes

$$\frac{I_r(\lambda)}{I_s(\lambda)} = \exp[-k(\lambda)(R_s - r)] \quad (5.144)$$

where R_s is the radius of the outer surface. Substituting Eq. 5.144 into Eq. 5.143, we find \dot{S} for cylindrical coordinates:

$$\dot{S} = I_s(k(\lambda)/r) \exp[-k(\lambda)(R_s - r)] \quad (5.145)$$

Provided we know $k(\lambda)$ and I_s we now have the energy generated per unit volume per unit time as the result of absorbed radiation.

A few comments need to be made regarding the determination of $k(\lambda)$ and I_s . $k(\lambda)$ is related to the transmittance, $\tau(\lambda)$, and the thickness of the sample, L , by

$$k(\lambda) = -\ln \tau(\lambda)/L \quad (5.146)$$

Shelby (1991, p. 1420) obtained an effective value of $k(\lambda)$, \bar{k} , for PET by measuring $\tau(\lambda)$ and then averaging the values over all wavelengths weighted with the blackbody spectral emission curve corresponding to the given lamp temperature. Values of \bar{k} for PET are given in Table 5.14. This type of data does not appear to be readily available in the literature for other polymers but must be measured for polymers that are semitransparent. $I_s(\lambda)$ for different lamp temperatures was given for PET and the lamp arrangement to be

$$I_s(T_2) = 12,000 (T_s/2473 \text{ K})^4 \quad (5.147)$$

Example 5.8. Radiation Heating of a Semitransparent Sheet

A sheet of (3.8 mm thick, 10 cm × 12 cm) amorphous PET is heated on both sides by a bank of quartz lamps (eight Fostoria T-3 quartz lamps per bank) rated at 500 watts with a peak filament temperature of 2250 °C at 120 volts. Formulate the equations and boundary and initial conditions which must be solved to find the time to heat the sheet up to

120 °C at the centerline. The following properties are given for PET:

$$\begin{aligned} \rho &= 1350 \text{ kg/m} & k &= 0.29 \text{ J/m} \cdot \text{s} \cdot ^\circ\text{C} \\ \bar{C}_p &= 1250 + 2.0 T \text{ J/kg} \cdot ^\circ\text{C} & & 20 \leq T \leq 60 ^\circ\text{C} \\ \bar{C}_p &= 1370 + (T - 60)^2 (0.95) \text{ J/kg} \cdot ^\circ\text{C} & & 60 \leq T \leq 80 ^\circ\text{C} \\ \bar{C}_p &= 1750 \text{ J/kg} \cdot ^\circ\text{C} & & T \geq 80 ^\circ\text{C} \end{aligned}$$

At 111 volts the lamp temperature is given as 2200 °C. Free convection is assumed to occur at the sheet surfaces with h taken to be 17 W/m² · °C. The ambient air temperature is 35 °C, while the initial temperature of the preform is 25 °C.

Solution. Taking the coordinates to be at the center of the sheet and the thickness to be $2b$, the energy equation is

$$\rho \bar{C}_p \frac{\partial T}{\partial t} = k \frac{\partial^2 T}{\partial x^2} + I_s k(\lambda) e^{-k(\lambda)x}$$

The boundary and initial conditions are

$$\begin{aligned} \text{B.C.1:} \quad & \text{at } x = b, \quad q_x = -k \frac{\partial T}{\partial x} = h(T_a - T(b, t)) \\ \text{B.C.2:} \quad & \text{at } x = -b, \quad q_x = -k \frac{\partial T}{\partial x} = h(T(-b, t) - T_a) \\ \text{I.C.:} \quad & \text{at } t = 0, \quad T = T_0 (= 25 ^\circ\text{C}) \end{aligned}$$

Even if the thermal properties are all taken as constant, one would have to solve the problem numerically because of the source term. ■

5.5 CRYSTALLIZATION, MORPHOLOGY, AND ORIENTATION

The physical properties of a given semicrystalline polymer depend on the size of the crystallites, morphology of the crystalline and amorphous regions, and the molecular orientation within the crystalline and amorphous regions. The above factors, which control the physical properties of polymers, are related to crystallization kinetics, cooling rate (heat transfer), and the deformation history. The physical properties of polymers are thought to be associated with the ordering and packing of the molecules, which can be affected by processing conditions as illustrated in Table 5.15. In this table it is observed that the modulus of HDPE can be increased from 7 to 70 GPa by the processing technique used, but this is still far from the theoretical limit. Furthermore, the modulus of some organic materials can reach the level of steel, but when compared on a weight basis the organic materials are much stiffer. In this section we first review some qualitative features of crystallization and then the kinetics of crystallization under quiescent conditions. Our goal in this section is to

TABLE 5.15 Tensile Moduli of Polymers and Other Engineering Materials at 25°C

Material	Modulus, E ($\text{N/m}^2 \times 10^{-9}$)	Density, ρ ($\text{kg/m}^3 \times 10^{-3}$)	Specific Modulus, E/ρ ($\times 10^{-6}$)
Polymers			
Commonly processed HDPE (Southern and Porter, 1970)	1–7	1	1–7
Extrusion drawn HDPE fibers (Southern and Porter, 1970)	~70	1	~70
Specially cold drawn HDPE fibers (Capaccio and Ward, 1975)	68	1	68
DuPont Kevlar fibers (rod-like molecules)	132	1.45	92
Theoretical limit of HDPE and PVA—fully extended (Sakurada et al., 1966)	240–250	1	240–250
Other materials			
Aluminum alloys	< 70		
“E” glass fiber	63	2.54	35
Steels	~200	~7.0	~29
RAE carbon filaments	420	2.0	210

emphasize the fact that the processing conditions can have a significant effect on the properties of a polymer, which in turn affect its end uses.

5.5.1 Crystallization in the Quiescent State

Because polymers are only semicrystalline, which means both crystalline and amorphous phases exist, we must define the degree of crystallinity, ϕ_c . The degree of crystallinity is the volume fraction of crystallinity and is given by

$$\phi_c = N\bar{a}f \quad (5.148)$$

where N is the number of crystalline units (usually they are called spherulites) per unit volume, \bar{a} is the average diameter of the crystallites, and f is the packing factor. f varies between 0.5 and 1.0 depending on the shape of the crystallites. For example, if the crystallites are spherical, the closest packing is that when the spheres are arranged in a face centered cubic structure. f for this arrangement is $\pi/3\sqrt{2}$ (0.741).

The manner in which individual molecules crystallize depends on the conformation of the chains. Flexible chain polymers, as shown schematically in Figure 5.18, fold to form microlamellar plates. Rigid chain polymers form bundles of rod-like structures. The bulk structure or macrostructure of the polymer depends on whether crystallization occurs from dilute solution or from the melt state. When crystallization occurs under quiescent conditions in a dilute solution, then single crystals consisting of folded chains arise. When crystallization from the melt occurs under quiescent

conditions, chain folding occurs rapidly in all directions leading to a spherical structure. These structures are shown schematically in Figure 5.18. Stress has a significant influence on the macrostructure or morphology. For both dilute solutions and melts of flexible chain polymers the “shish-kebab” structure is observed. Folded chains seem to emanate from rows of highly extended chains as shown in Figure 5.18.

The only theory available for describing the conversion of polymer melts to crystalline materials deals with flexible chain polymer melts crystallizing under quiescent (no deformation) conditions. The rate of crystallization (i.e., the rate of conversion of the volume of amorphous material into crystalline material) consists of two processes as shown in Figure 5.19: nucleation and growth. *Nucleation* is the initiation of a very small amount of crystalline material emerging from the melt by fluctuation processes. The number of nucleation sites determines the morphology of the growing crystallites as a large number of nucleation centers would lead to a large number of small crystallites. Nucleation may be homogeneous or heterogeneous. Homogeneous nucleation occurs in the absence of a second phase while heterogeneous nucleation is due to the presence of a second phase. In practice heterogeneous nucleation is the rule as most polymer melts contain heterogeneities such as impurities, residues of unmelted polymer, and nucleating agents. Growth proceeds also by a nucleation mechanism. Nucleation in this case is a surface process. The whole crystallization process is a continuous interplay between nucleation and diffusive transport of matter to a surface. The rate of overall crystallization depends on the number of available nuclei and on the rate of transport of molecules.

TYPE OF MACROMOLECULE	CONFORMATION	MICROSTRUCTURAL UNIT	CONDITIONS	MACROSTRUCTURE	PATTERN (CROSS-SECTION)
FLEXIBLE MACROMOLECULE IN QUIESCENT CONDITIONS	RANDOM COIL	FOLDED CHAIN LAMELLAE	VERY DILUTE QUIESCENT SOLUTION	SINGLE CRYSTAL	
			MELT	SPHERULITE	
FLEXIBLE MACROMOLECULE IN FIELDS OF FORCE (FLOW)	DEFORMED COIL	CORE OF ALIGNED CRYSTALS (ROW) + LAMELLAR "SIDE PLATES"	DILUTE STIRRED SOLUTION	SHISH-KEBAB	
			EXTRUDED "MELT"	ROW NUCLEATED STRUCTURE	
RIGID MACROMOLECULE	ROD (LIQUID CRYSTAL)	MICROFIBRIL (RODLET)	SPINNING FROM SOLUTION WITHOUT SPECIAL CONDITIONS	MOSAIC OF RANDOMLY ORIENTED MICROFIBRILS	
			SPINNING WITH MAINTENANCE OF FULL ORIENTATION	HIGHLY AND SYMMETRICALLY ORDERED MICROFIBRILS	

FIGURE 5.18 Morphology of crystallites in polymers. (Reprinted with permission of the publisher from Van Krevelen, 1990.)

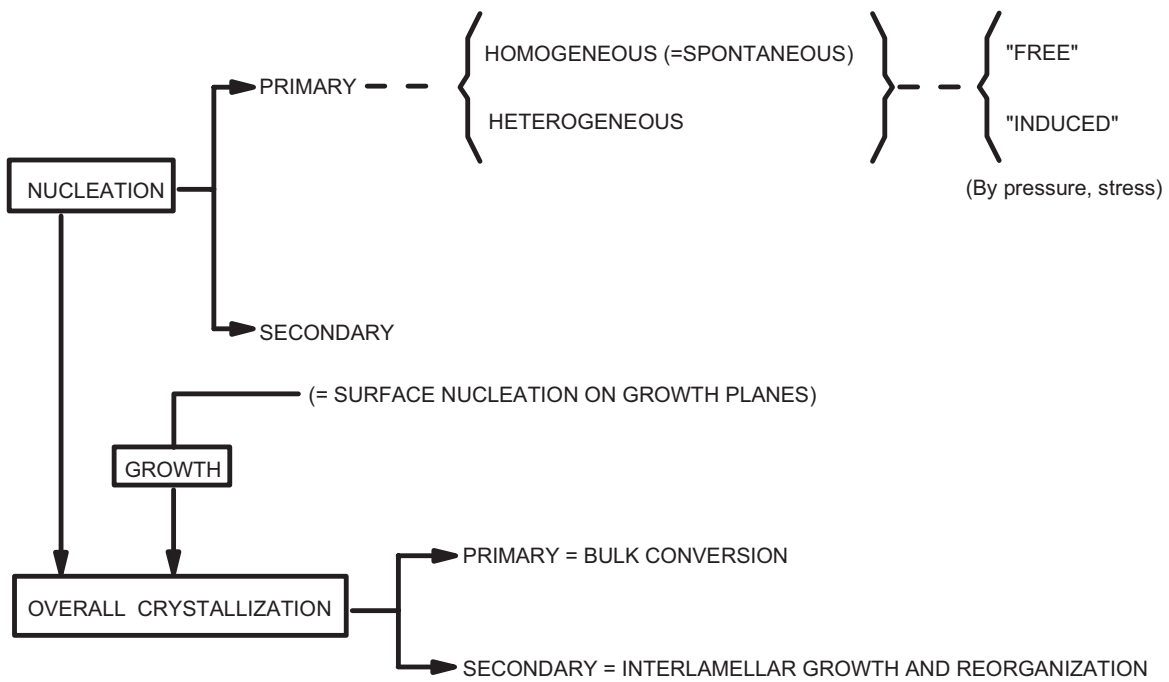


FIGURE 5.19 Description of the crystallization process for polymers. (Data from Van Krevelen, 1978.)

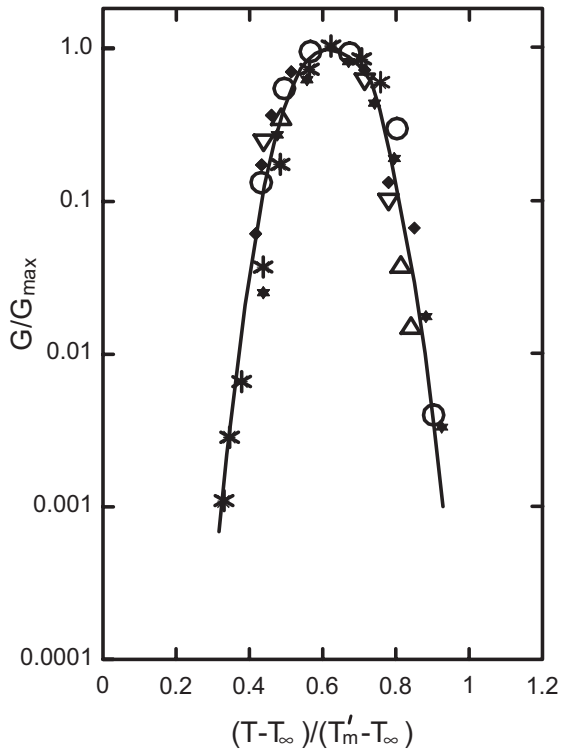


FIGURE 5.20 Plot of dimensionless linear growth rate of crystallization versus dimensionless temperature. (Reprinted with permission of the publisher from Gandica and Magill, 1972.)

Free crystallization (i.e., no strain or stress) starts from a number of point nuclei and progresses in all directions at equal linear rates (i.e., the rate of increase of the radius of a spherulite, G , is linear with time). The rate of growth is very dependent on the temperature of crystallization. In particular, $G = 0$ at T_g and T_m and passes through a maximum at some intermediate temperature, T_K . According to Gandica and Magill (1972) the crystallization process of all the normal polymers follows a master curve. This master curve is a plot of G/G_{max} versus a dimensionless temperature, θ :

$$\theta = (T - T_\infty)/(T'_m - T_\infty) \quad (5.149)$$

where

$$T_\infty = T_g - 50 \quad (5.150)$$

and T'_m is the thermodynamic equilibrium melting temperature. This master curve is shown in Figure 5.20. G/G_{max} passes through a maximum when θ is 0.635, which corresponds approximately to

$$T_K \approx 0.5(T'_m + T_g) \quad (5.151)$$

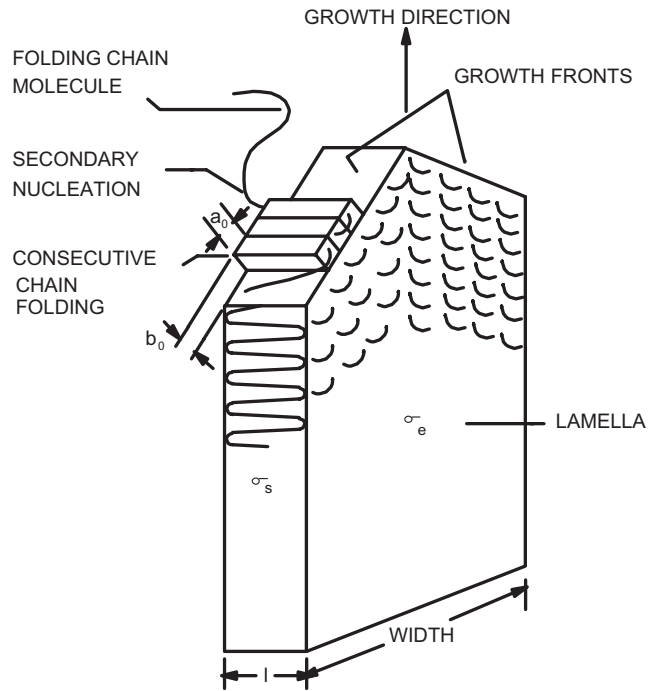


FIGURE 5.21 Model of lamellar growth front assuming regular chain folding. (Adapted from Bright, 1975.)

The quantitative theory of crystallization starts with the linear rate of growth, G , which is given by (Lauritzen and Hoffman, 1964)

$$G = G_0 \exp[-E_D/RT] \exp[-\Delta F_n^*/k_B T] \quad (5.152)$$

G_0 is the molecular jump frequency and is given by $b_0 k_B T/h_P$ where k_B and h_P are the Boltzman and Planck constants, respectively. b_0 is a crystal dimension (see Fig. 5.21), values of which are given in Table 5.16 for PP and in Appendix C for a number of other polymers. The quantity $(-E_D/RT)$ represents the diffusive transport of the molecules in the melt while ΔF_n^* is the free energy of a nucleus with n -dimensional

TABLE 5.16 Thermal-Physical Properties of Polypropylene

Parameter	Value	Units
T'_m	447	K
T_g	267	K
ΔH_c	45	cal/g
ρ_m	0.867	g/cm ³
ρ_c	0.938	g/cm ³
b_0	5.40×10^{-8}	cm
a_0	3.35×10^{-8}	cm
σ	9.54	ergs/cm ²
σ_e	47.7	ergs/cm ²
$\sigma\sigma_e$	455	ergs ² /cm ⁴
ϕ_∞	0.62	

Source: Data from Bright, 1975.

growth. E_D is the activation energy, R is the gas law constant, and T is the absolute temperature.

Near T_g the term (E_D/RT) is given by the WLF equation:

$$\frac{E_D}{RT} = \frac{C_1}{R(C_2 + T - T_g)} \quad (5.153)$$

where $C_1 = 17.2$ kJ/mol and $C_2 = 51.6$ K. Near the maximum crystallization temperature the following expression is suggested:

$$\frac{E_D}{R} = C_D \frac{T_m'^2}{T_m' - T_g} \quad (5.154)$$

where $C_D \approx 5.0$. The nucleation factor, $\Delta F_n^*/k_B T$, has the following form:

$$\frac{\Delta F_n^*}{k_B T_x} = \frac{C}{T_x} \left(\frac{T_m'}{T_x}\right)^{n-1} \left(\frac{T_m'}{\Delta T}\right)^{n-1} \approx \frac{C}{T_x} \left(\frac{T_m'}{\Delta T}\right)^{n-1} \quad (5.155)$$

where

- T_x = crystallization temperature (K)
- $\Delta T = T_m' - T_x$ (undercooling)
- n = dimensionality of the nucleation process which is usually taken as 2.0
- C = a characteristic constant for every polymer; for a number of polymers $C = 265$ K
- T_m' = thermodynamic equilibrium melting point (note that this value is slightly different from T_m)

C can actually be determined theoretically from the following expression:

$$C = \frac{4b_0\sigma_s\sigma_e}{k_B\Delta\bar{H}_f\rho_c} \quad (5.156)$$

where the various parameters are shown in Figure 5.21. $\Delta\bar{H}_f$ is the heat of fusion and ρ_c is the density of the crystalline plane. σ_s is the side surface energy and σ_e is the end surface energy associated with lamellar growth as shown in Figure 5.21.

The linear growth rate is now obtained for two temperature ranges. Using $\xi = T_m'/T_x$ and $\delta = T_g/T_m'$, one obtains for $T_x > T_K$ the following expression:

$$\log G = \log G_0 - 2.3 \frac{\xi}{1 - \delta} - \frac{115}{T_m'} \frac{\xi^2}{\xi - 1} \quad (5.157)$$

and for $T_x \ll T_K$

$$\log G = \log G_0 - \frac{895\xi}{51.63\xi + T_m'(1 - \delta\xi)} - \frac{115}{T_m'} \frac{\xi^2}{\xi - 1} \quad (5.158)$$

G_0 is taken as 10^{12} nm/s. (Note: G_0 depends on \bar{M}_w and the presence of nucleating agents.) Equation 5.157 follows

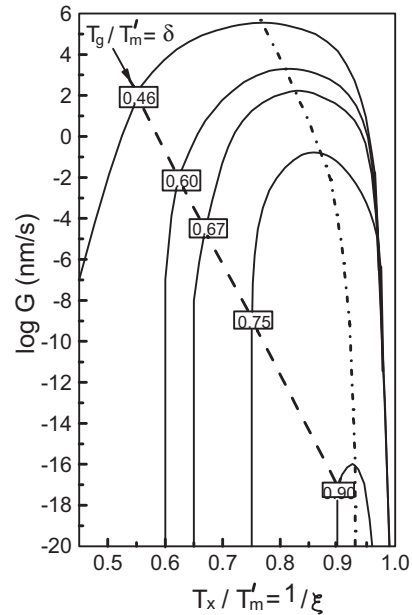


FIGURE 5.22 Universal master curve of the rate of growth of spherulites as a function of the dimensionless parameters T_x/T_m and T_g/T_m for $T_m = 473$ K. (Reprinted with permission of the publisher from Van Krevelen, 1978.)

by substituting Eq. 5.154 into Eq. 5.152 while Eq. 5.158 follows by substituting Eq. 5.153 into Eq. 5.152. Equations 5.157 and 5.158 are presented in graphical form in Figure 5.22. Here T_m' was arbitrarily selected as 473 K so that a two-dimensional plot could be constructed. For every 10°C change in T_m' , G will be 0.1 times higher or lower than given in the graph. Furthermore, it is seen that T_g/T_m' has a great influence on the absolute value of G .

For symmetrical polymers such as PE, G is high ($T_g/T_m' \sim 0.5$), whereas for asymmetrical polymers such as isotactic polystyrene with $\delta = 0.75$, G is very low. Some numerical values of G for several polymers are presented in Table 5.17. Using these values, we can estimate the length of time for a spherulite to grow to a radius of 10 cm for the various polymers:

PE	1 hour
Nylon 66	1 day
PETP	1 month
IPS	1 year

TABLE 5.17 Maximum Growth Rates for Some Polymers

Polymer	T_g/T_m'	Maximum Growth Rate (nm/s)
High-density polyethylene	0.47	3×10^4
Nylon 6	0.6	3×10^3
Polyester (PETP)	0.64	1×10^2
Isotactic polystyrene (IPS)	0.73	3×10^0

Hence, one can more fully appreciate the relative rates of spherulitic growth.

The overall rate of crystallization under isothermal conditions is given by the Avrami equation (Avrami, 1939, 1940, 1941):

$$\phi_c/\phi_\infty = 1 - \exp(-Kt^n) \quad (5.159)$$

Here ϕ_c is the volume fraction of crystallinity and is given by

$$\phi_c = (\rho - \rho_a)/(\rho_c - \rho_a) \quad (5.160)$$

where ρ is the density of the sample containing both crystalline and amorphous phases, ρ_a is the density of the amorphous phase, and ρ_c is the density of the spherulitic phase. ϕ_∞ is the equilibrium volume fraction of crystallinity (this value is usually less than 1.0). n is a constant that is in the neighborhood of 3.0 but can be determined using differential scanning calorimetry, DSC, for each polymer. $n = 3.0$ for spherulitic growth, but in practice n may be less than 3.0. For PPS n falls between 3.1 and 2.6 for different crystallization temperatures. For PEEK, on the other hand, n is about 2.5 but changes to 1.5 at high values of ϕ . K is the overall rate constant of crystallization and is determined by fitting DSC data or estimated by the number of nuclei and the linear growth rate as

$$K = \frac{4}{3}\pi NG^3 \quad (5.161)$$

K is related to the half-time for crystallization, $t_{1/2}$, by $t_{1/2} = (\ln 2/K)^{1/n}$.

For nonisothermal crystallization a modified form of Eq. 5.159 is used:

$$\phi_c/\phi_\infty = 1 - \exp\left[-\int_0^t K(T)nt^{n-1}dt\right] \quad (5.162)$$

Here it is assumed that the contributions to the crystallization process are additive (i.e., at each temperature Eq. 5.159 holds over each temperature interval, ΔT , as the temperature is decreased). One approximation for $K(T)$ is (Velisaris and Seferis, 1988)

$$K(T) = C_1 T \exp[-C_2/(T - T_g + 51.6)] \times \exp[C_3/T(T'_m - T)^2] \quad (5.163)$$

In this equation C_1 , C_2 , and C_3 are coefficients which are obtained by fitting the function to crystallization data. (For example, for PEEK, C_1 , C_2 , and C_3 are $2.08 \times 10^{10} \text{ S}^{-n} \cdot \text{K}^{-1}$, 4050 K, and $1.8 \times 10^7 \text{ K}^3$, respectively). The function given in Eq. 5.163 is based on the assumption that $K(T)$ takes on the same form as G .

TABLE 5.18 Yield Stress for Nylon 66 as a Function of Spherulite Size

Spherulite Size (μm)	Yield Stress, P (psi)	$\text{Pa} \times 10^{-6}$
50	10,250	72
10	11,800	83
5	12,700	89
3	14,000	98

Source: Data from Van Krevelen, 1978.

As K is proportional to the number of nuclei, some estimate of this number is needed. According to Van Krevelen (1978), $N = 3 \times 10^4 \text{ cm}^{-3}$ when a polymer is quenched from the melt to T_x and $N = 3 \times 10^{11} \text{ cm}^{-3}$ when a sample is heated from the solid state to T_x . In other words, there are many more nuclei when starting from the solid state. Since 1 cm^3 contains about 10^{18} molecules, the number of nuclei as a fraction of the molecules is extremely small. Starting from the melt there are 3 nuclei per 10^{13} molecules while in starting from the solid state there are 3 nuclei in 10^6 molecules.

N determines the maximum size of the spherulites once the whole sample is converted into crystalline material. Since $\phi_c = \frac{4}{3}\pi R_{\text{max}}^3 N$ and if $\phi_c = 1$, then $R_{\text{max}} N^{1/3} \approx 0.62$. Hence, the more nuclei the smaller the radius of the spherulites.

The properties of a polymer are dependent on the size of the crystallites. In particular, polymeric materials are brittle when they consist of large spherulites. Hence, it might be better that the spherulites be as small as possible. Although there is very little quantitative data available in the literature in which correlations between spherulite size and mechanical properties are made, some data is presented in Table 5.18 for nylon 66. Here it is observed that the yield stress increases as the spherulite size decreases.

Example 5.9. Maximum Crystallization Values for Polypropylene

Determine the maximum crystallization temperature, T_K , and the maximum rate of crystallization for polypropylene.

Solution. As a first approximation we can use Eq. 5.151, which gives

$$T_K = 0.5(170^\circ\text{C} - 10^\circ\text{C}) = 80^\circ\text{C}$$

To obtain a more accurate value we differentiate Eq. 5.157 with respect to ξ (after converting to natural logarithms) and set the derivative equal to zero:

$$\frac{1}{G} \frac{\partial G}{\partial \xi} = -\frac{2.3}{1-\delta} - \frac{115}{T'_m} \left[\frac{\xi^2 - 2\xi}{(\xi - 1)^2} \right] = 0$$

Rearranging this equation we obtain

$$-\left[\frac{2.3T'_m}{115(1-\delta)} + 1\right]\xi^2 + 2\left[\frac{2.3T'_m}{115(1-\delta)}\right]\xi - \left[\frac{2.3T'_m}{115(1-\delta)}\right] = 0$$

Using the values in Table 5.16 for T_g and T'_m , this equation becomes

$$-23.184\xi^2 + 46.386\xi - 22.184 = 0$$

The roots of this equation are $\xi = 1.207$ and 0.792 . Because $\xi = T_m/T_x$, we use 1.207 to find that $T_K = 93^\circ\text{C}$.

Substituting T_K back into Eq. 5.157 we can now find G_{\max} :

$$\begin{aligned} \ln G &= \ln(1 \times 10^{12}) - \frac{(2.303)(2.3)(1.207)}{0.403} \\ &\quad - \frac{(2.303)(115)(1.207)^2}{447(0.207)} = 7.645 \\ G_{\max} &= 2.09 \times 10^3 \text{ nm/s} \end{aligned}$$

Finally, using Eq. 5.161 we estimate K_{\max} to be

$$\begin{aligned} K_{\max} &= \frac{4}{3}\pi(3 \times 10^4 \text{ cm}^{-3})(2.09 \times 10^{-4} \text{ cm/s})^3 \\ &= 1.15 \times 10^{-6} \text{ s}^{-3} \end{aligned}$$

In this calculation we have used the values of $G_0 = 10^{12}$ nm/s and $N = 3 \times 10^4$ cm⁻³, which seem to be average values for a number of polymers. To obtain more accurate values, experimental values of K and G_0 are required (these values are usually determined from DSC measurements). ■

Example 5.10. Calculation of the Amount of Crystallization

Determine the volume fraction of crystallinity in PP crystallized at $T_{\max} = 93^\circ\text{C}$ for 2 minutes and the size of the spherulites. $\phi_\infty = 0.62$ for PP.

Solution. Using Eq. 5.159 with $n = 3$ for spherulitic growth we find

$$\phi_c = \phi_\infty(1 - \exp[-1.15 \times 10^{-6}(120)^3]) = 0.535$$

The spherulite size is obtained using Eq. 5.161.

$$\begin{aligned} G &= \frac{dR}{dt} = [K(3/4\pi)/N]^{1/3} = 2.09 \times 10^{-4} \text{ cm/s} \\ R &= (2.09 \times 10 \text{ cm/s}) 120 \text{ s} = 2.51 \times 10^{-2} \text{ cm} \end{aligned}$$

■

Example 5.11. Effect of Heat of Crystallization on the Temperature Profile

A film of PP 0.005 cm thick is cooled from a melt temperature of 220°C to a temperature of 50°C on a casting drum. Determine whether the temperature profile in the film is affected by the heat released during the crystallization process.

Solution. The energy equation for this situation is

$$\rho\bar{C}_p \frac{\partial T}{\partial t} = k \frac{\partial^2 T}{\partial x^2} + \rho_c \Delta\bar{H}_c \frac{d\phi_c}{dt}$$

where the last term in the differential equation is the heat released per unit time per unit volume as a result of crystallization. This comes from the fact that

$$\dot{S} = \frac{\Delta\bar{H}_c}{v} \left(\frac{dw_c}{dt} \right)$$

where w_c is the mass of crystalline material and dw_c/dt is the rate of conversion of amorphous to crystalline phase. Using $\phi_c = v_c/v$ and $\rho_c = w_c/v_c$, where v_c is the volume of the crystalline phase, it is now clear how the source term was obtained. Rather than solve the differential equation at this time, we cast it into dimensionless form and evaluate the dimensionless groups that arise. Introducing the following dimensionless groups:

$$\theta = \frac{T - T_0}{T_w - T_0} \quad \xi = \frac{x}{b} \quad t^* = tK^{1/3}$$

the differential equation becomes

$$\frac{\partial \theta}{\partial t^*} = \left(\frac{kK^{-1/3}}{\rho\bar{C}_p b^2} \right) \frac{\partial^2 \theta}{\partial \xi^2} + \left(\frac{\rho_c \Delta\bar{H}_c}{\rho\bar{C}_p \Delta T} \right) \frac{d\phi_c}{dt^*}$$

where $\Delta T = T_w - T_0$, $2b$ is the thickness, and K is the rate constant of crystallization. The dimensionless groups in parentheses can now be used to help us decide whether we should include the source term in the differential equation. Using the values in Table 5.16 and K_{\max} calculated in Example 5.9 we find the following:

$$\left(\frac{kK^{1/3}}{\rho\bar{C}_p b^2} \right) = \frac{(0.142)(95.4)}{(902)(2.8 \times 10^4)(6.25 \times 10^{-10})} = 86.0$$

$$\left(\frac{\rho_c \Delta\bar{H}_c}{\rho\bar{C}_p \Delta T} \right) = \frac{(938)(18.8 \times 10^4)}{(902)(2.8 \times 10^4)(150)} = 0.46$$

Hence, we see that the coefficient multiplying $d\phi_c/dt^*$ is about two orders of magnitude smaller than the coefficient

multiplying $d^2\theta/d\xi^2$, and thus there should be little contribution to the temperature profile from the heat of crystallization for the conditions given in the problem. We can see that K would have to become extremely large or the polymer sample quite thick (e.g., $b = 0.3$ cm) before the coefficients would be of similar magnitude. ■

5.5.2 Other Factors Affecting Crystallization

Other factors that affect crystallization processes include pressure and stress. Increasing the static pressure has the effect of raising T_m as shown by the Clapeyron equation:

$$\frac{dT_m}{dP} = T_m \frac{\Delta \bar{V}_m}{\Delta \bar{H}_m} \tag{5.164}$$

where T_m^0 is the melting point at atmospheric conditions, and ΔV_m and ΔH_m are the volume and enthalpy changes, respectively, of the melting process. For large pressure variations the change in T_m is given by the Simon equation,

$$P - P_0 = a \left[\left(\frac{T_m}{T_m^0} \right)^c - 1.0 \right] \tag{5.165}$$

where P_0 and T_m^0 are the pressure and melting temperature at the reference conditions and a and c are coefficients. For example, for PE, $T = 409$ K (136°C), $a = 3$ kbar, and $c = 4.5$. From this equation, it can be determined that T_m can be raised by 100°C at pressures of 5 kbar. As a result of the increase in T_m , the fold length of the chains increases. Unfortunately, the physical properties of polymers crystallized under extreme pressure are poor.

Stress, on the other hand, where deformation is involved, has a considerable effect on crystallization kinetics and morphology. Polymer molecules become oriented during deformation. If the temperature is reduced enough before the molecules relax, then they may crystallize in this oriented state. For polymer melts it is not so easy to create stress-induced crystallization. However, if the product of the relaxation time, λ , and the time, t , for the melt temperature to drop to T_x is approximately equal to 1.0, then we can expect the crystallization of oriented molecules.

Extensional flow is known to have more of an effect on chain extension than shear flow. We illustrate this idea by data obtained in the spinning of PET. Below spinning speeds of 3500 m/min there is very little crystallinity, but above this speed significant crystallinity is observed as shown in Figure 5.23. The processing time at these spinning speeds is a few milliseconds whereas $t^{1/2} = 50$ s. Hence, the crystallization rate must be many decades faster than in the quiescent state.

The stretching of fibers in the neighborhood of T_g is called cold drawing. An example of results for PET is shown in Figure 5.24. It is noted that at a draw ratio of about 2.5

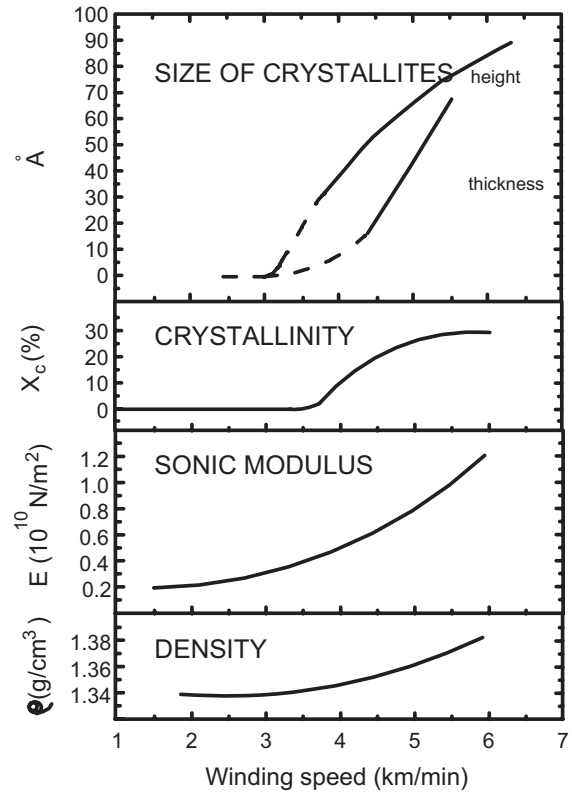


FIGURE 5.23 Physical properties of PET yarns wound at various speeds. (Data are from Huisman and Henvel, 1978.)

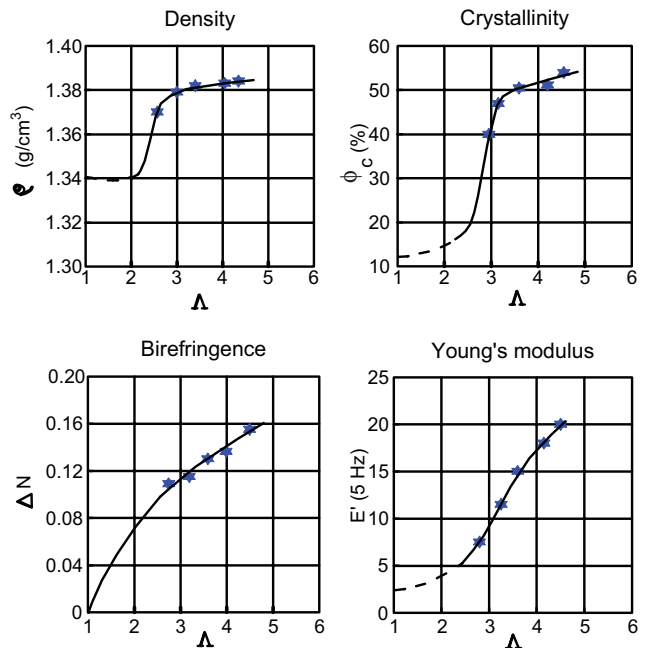


FIGURE 5.24 Physical properties of PET as a function of the drawing ratio. (Adapted from Van der Meer, 1971.)

there is a sudden change in the amount of crystallinity and hence the density. However, whereas ρ and ϕ_c become only slightly dependent, Young's modulus continues to increase with increasing draw ratio. We also note that as ΔN , the birefringence, increases so does Young's modulus, E . Crystallinity is not directly correlated with E , but ΔN is. As ΔN is related to molecular orientation as discussed in the next section, then E is related to orientation.

One way to incorporate the effect of stress on crystallization is described here (Katayama and Yoon, 1985). One starts with the generalized Avrami equation:

$$\phi_c/\phi_\infty = 1 - \exp\left[-\left(\int_0^t K(T, \Delta N)d't\right)^n\right] \quad (5.166)$$

where $K(T, \Delta N)$ is a crystallization rate constant dependent on T and ΔN . From the stress optic law ($\Delta N C' = \sigma_1 - \sigma_2$), one can relate orientation to stress. According to the theory of Hoffman the ratio of the oriented (G_{or}) to unoriented (G_{un}) linear growth rates is

$$\frac{G_{or}}{G_{un}} = \exp\left[-\frac{4B_0\sigma_s\sigma_e}{KT^{(K)}}\left(\frac{1}{\Delta G_{or}} - \frac{1}{\Delta G_{un}}\right)\right] \quad (5.167)$$

ΔG_{un} is the free energy difference between the amorphous and crystalline states under random orientation and ΔG_{or} is the free energy difference in the oriented state. $T^{(K)}$ is the absolute temperature. The free energy expressions are

$$\Delta G_{un}/\rho = \Delta H_{un} - T^{(K)}\Delta S_{un} = \Delta H(\Delta T/T_m^{(K)}) \quad (5.168)$$

$$\Delta G_{or}/\rho = \Delta H_{or} - T^{(K)}\Delta S_{or} = \Delta H(\Delta T/T_m^{(K)}) + T^{(K)}(\Delta S_{or} - \Delta S_{un}) \quad (5.169)$$

where ΔS_{un} is the entropy difference between the amorphous and crystalline states under random orientation, ΔT is the undercooling, $T_m^{(K)}$ is the melting point in K, $\Delta H_{or} = \Delta H_{un} = \Delta H$, and $\Delta S_{or} - \Delta S_{un}$ is the entropy difference between the oriented and the unoriented amorphous states.

The next step is to relate $\Delta S_{or} - \Delta S_{un}$ to some quantity such as orientation. This requires a constitutive equation. Most have used the theory of rubber elasticity, which is not acceptable for polymer melts, but which gives

$$\Delta S_{or} - \Delta S_{un} \propto v^2 + 2/v - 3 \quad (5.170)$$

where v is the extension ratio. For $v = 1$ (i.e., small deformations), $\Delta S_{or} - \Delta S_{un} \propto (\Delta N)^2$. Using this relation and Eqs. 5.168 and 5.169, Eq. 5.167 becomes

$$\frac{G_{or}}{G_{un}} = \exp\left\{\frac{C_1}{T^{(K)}\Delta T}\left(1 - \frac{1}{1 + C_2(T^{(K)}/\Delta T)(\Delta N)^2}\right)\right\} \quad (5.171)$$

where C_1 and C_2 are constants. Because K is related to G (see Eq. 5.161), $K(T, \Delta N)$ in Eq. 5.166 is now replaced by Eq. 5.171. There is, however, no significant verification of this approach and one must use the equation with crystallization data obtained from samples processed under high stress conditions.

5.5.3 Polymer Molecular Orientation

The physical properties, in particular, the modulus, depend on the degree to which the polymer chains lie along a particular direction. In the case of fiber spinning, the degree to which the chains lie along the fiber axis determines the stiffness and strength of the fiber. In this section we define molecular orientation and briefly describe how it is determined.

We first must remember that most polymers are semicrystalline (although some are just amorphous), and so we must define orientation for both the crystalline and amorphous regions. For the crystalline regions wide angle X-ray scattering (WAXS) is used to determine orientation. X-rays scatter off the crystallographic planes and are reflected back to the photographic film or a detector. Because polymers are polycrystalline, and if they are unoriented, the reflections are cones having the incident beam as their axis. As the sample is drawn to create orientation, the circles become arcs and then just dots. This is shown in Figure 5.25.

To quantify the degree of orientation, we define orientation functions. To do this we need to know what the unit cell is. For polyethylene (PE), the unit cell is orthorhombic in which the three crystallographic axes, a , b , and c , are mutually perpendicular. The orientation functions are

$$f^a = \frac{\overline{3\cos^2\phi_{a,z}} - 1}{2} \quad (5.172a)$$

$$f^b = \frac{\overline{3\cos^2\phi_{b,z}} - 1}{2} \quad (5.172b)$$

$$f^c = \frac{\overline{3\cos^2\phi_{c,z}} - 1}{2} \quad (5.173)$$

The angles $\phi_{i,z}$ are the angles each crystallographic axis makes with the z axis (which is the stretch direction). The values $\overline{\cos^2\phi_{i,z}}$, where $i = a, b, \text{ or } c$, are evaluated as follows:

$$\overline{\cos^2\phi_{i,z}} = \frac{\int_0^{\pi/2} I_{hkl}(\phi_{i,z})\cos^2\phi_{i,z}\sin\phi_{i,z}d\phi_{i,z}}{\int_0^{\pi/2} I_{hkl}(\phi_{i,z})\sin\phi_{i,z}d\phi_{i,z}} \quad (5.174)$$

$I_{hkl}(\phi_{i,z})$ is the intensity diffracted from the (hkl) planes, which are normal to the i crystallographic axis. For orthogonal unit cells the orientation functions are related as follows:

$$f^a + f^b + f^c = 0 \quad (5.175)$$

$$\sum_{i=1}^3 \overline{\cos^2\phi_{i,z}} = 1 \quad (5.176)$$

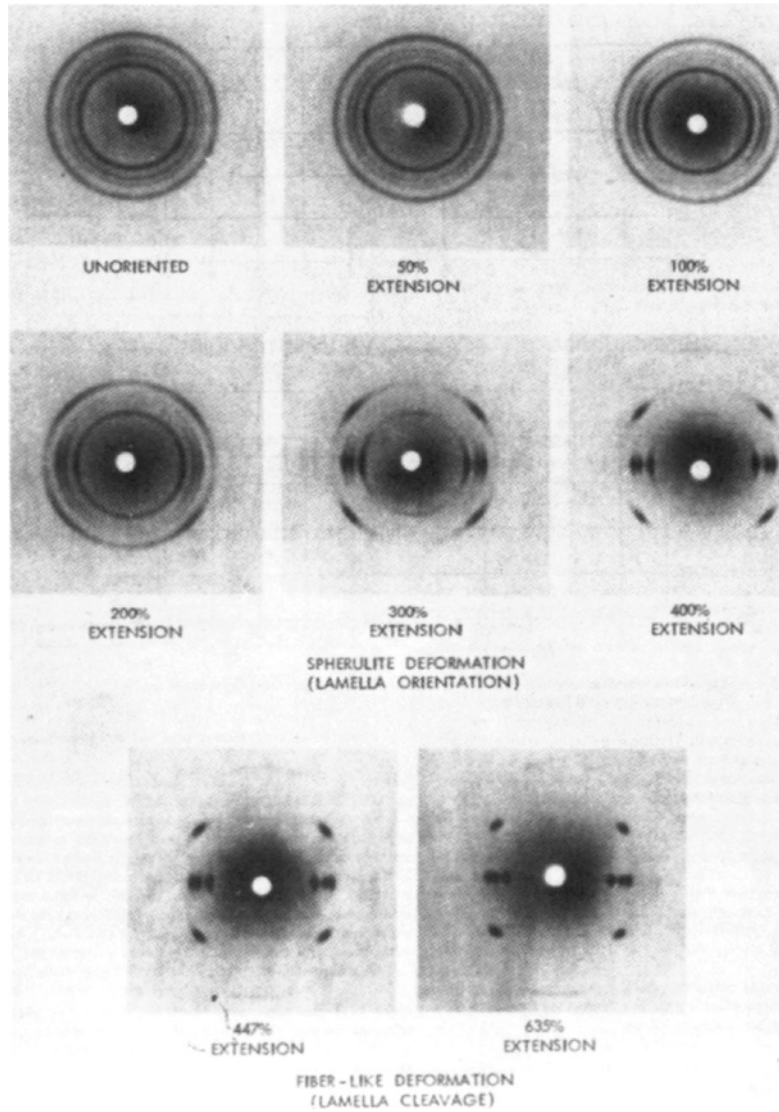


FIGURE 5.25 Effect of isotactic polypropylene film extension on the wide-angle X-ray diffraction patterns. (Reprinted with permission of the publisher from Samuels, 1974, p. 27.)

When a crystallographic axis (e.g., c) is perpendicular to z , $f^c = -0.5$; when it is parallel, $f^c = 1.0$, and when it is randomly oriented with respect to z , $f^c = 0$. The orientation functions are defined in terms of the cosine squared otherwise the integral would always be zero.

For the amorphous regions, we can use sonic waves or birefringence to determine orientation. (Certainly there are several methods, but our intention is not to review all these nor to say which is best.) To use birefringence we must know the intrinsic birefringence, ΔN^0 , which is either calculated or measured on a perfectly oriented sample. The birefringence, ΔN , is related to the stress field through the stress/optic law. In particular, the law reads:

$$\Delta N = C \Delta \sigma \tag{5.177}$$

where C is the stress optic coefficient and $\Delta \sigma = \sigma_1 - \sigma_2$ is the difference between the principal stresses. (Note that in shear flow $\sigma_1 - \sigma_2 = \sqrt{N_1^2 + 4\tau_{yx}^2}$.) For uniaxial stretching flows such as in fiber spinning or drawing then

$$\Delta N = C \Delta \sigma = C(\tau_{zz} - \tau_{rr}) \tag{5.178}$$

Because the melt is amorphous

$$\Delta N = \Delta N_{am}^0 f_{am} \tag{5.179}$$

and

$$f_{am} = (C/\Delta N_{am}^0) \Delta \sigma \tag{5.180}$$

The quantity $(C/\Delta N_{\text{am}}^0)$ turns out to be a constant for all polymers. Thus, f_{am} is proportional to $\Delta\sigma$, which arises during flow. We must remember that stresses relax when the flow is stopped so that unless the cooling is rapid enough, we will lose a considerable amount of the orientation. For shear flows the same stress/optic law holds; that is,

$$C \Delta\sigma = C(\sigma_1 - \sigma_2) = \Delta N \quad (5.181)$$

where σ_1 and σ_2 are the principal stresses, C is the stress optic coefficient, and ΔN is the birefringence. By a transformation of the coordinates we can relate the stress components in the laboratory coordinates to those in terms of the principal axes. For shear flow the relations are

$$\tau_{yx} = \frac{1}{2} \Delta\sigma \sin 2\chi \quad (5.182)$$

$$\tau_{xx} - \tau_{yy} = \Delta\sigma \cos 2\chi \quad (5.183)$$

$$\Delta\sigma = \sigma_1 - \sigma_2 \quad (5.184)$$

With the assumption that the principal directions and the optical directions coincide—that is,

$$\chi_{\text{opt}} = \chi_{\text{stress}} = \chi \quad (5.185)$$

and introducing Eq. 5.182 into Eqs. 5.183 and 5.184, we obtain the following relations:

$$\tau_{yx} = \frac{1}{2} \frac{\Delta N}{C} \sin 2\chi \quad (5.186)$$

$$\tau_{xx} - \tau_{yy} = (\Delta N/C) \cos 2\chi \quad (5.187)$$

Hence, from the stress field generated during flow we can estimate the degree of molecular orientation. In particular, we find from Eqs. 5.186 and 5.187 that

$$\tan 2\chi = \frac{2\tau_{yx}}{\tau_{xx} - \tau_{yy}} \quad (5.188)$$

In extensional flow it is assumed that $\chi_{\text{opt}} = \chi_{\text{stress}} = \chi = 0$, and hence $\tau_{xx} - \tau_{yy} = \sigma_1 - \sigma_2 = \Delta N/C$. So in extensional flow, the molecules are oriented in the flow direction. Values of C for several polymers are listed in Table 5.19.

If we were to measure the birefringence, ΔN , of a polycrystalline material in the solid state, it would not represent the overall orientation. ΔN consists of contributions from the amorphous and crystalline regions:

$$\Delta N = \phi_c \Delta N_{\text{cr}}^0 f_{\text{cr}} + (1 - \phi_c) \Delta N_{\text{am}}^0 f_{\text{am}} \quad (5.189)$$

where ΔN_{cr}^0 and ΔN_{am}^0 are the birefringence values of the perfectly oriented crystalline and amorphous regions and ϕ_c is the crystalline volume fraction. (It also should be added that shrinkage measurements upon annealing are a widely

TABLE 5.19 Stress-Optical Coefficients

Materials	Temperature (°C)	C (10^{-9} m ² /N)
Polystyrenes		
Styron 666	190	-4.1
Styron 678	190	-4.8
BASF 3	178	-4.5
	188	-4.6
	200	-4.4
	214.5	-4.2
Polyethylenes		
HD	150	2.4
	190	1.8
LD	150	2.0
IUPAC A	150	2.1
Polypropylenes		
PP	210	0.9

Source: Data from Janeschitz-Kriegl, 1969, 1983.

used method for determining macromolecular orientation in processed articles. The idea is that stretched oriented chains will become randomized on annealing above T_g .)

The reason for the discussion of orientation is because physical properties are closely tied to orientation. Our goal is to point out that molecular orientation and morphology are related to flow and deformation history, and hence physical properties are related to processing history. Our discussions of orientation serve only to quantify and define orientation. Likewise they serve to show that at least for amorphous polymers and for polymer melts there is a direct correlation between stress and orientation.

5.6 SOLUTION TO DESIGN PROBLEM IV

The solution to Design Problem IV proceeds as follows. We first develop the form of the energy equation that must be solved. We then determine whether heat transfer from the polymer film to air is important relative to that which occurs at the drum surface. The temperature profile along the film (or in essence as a function of time following a fluid element) is then determined. This can then be substituted into the equation for nonisothermal crystallization to give the percent crystallinity for a given heat transfer coefficient at the drum surface. Assuming spherulitic growth, which is reasonable for PP, we can estimate the spherulite radius from the linear growth rate.

We first determine the form of the energy equation. Following Examples 5.1 and 5.11, the energy equation is

$$\text{Pe} \frac{\partial \bar{\theta}}{\partial \zeta} = \frac{-b}{2k} [h_1(T(1) - T_a)/(T_0 - T_a) + h_2(T(-1) - T'_a)/(T_0 - T_a)] \quad (5.190)$$

where h_1 and h_2 are the heat transfer coefficients at the film–drum surface and at the film–air interface, respectively, and T is the temperature of the air.

It is not certain whether h_2 is significant at this point. Using Eqs. 5.123 and 5.124 for forced convection heat transfer involving flow over a flat plate and the conditions given in the problem, we estimate $h_2 = 2.8 \text{ W/m}^2 \cdot \text{K}$, which is quite small. For free or natural convection from a vertical flat plate we use Eq. 5.132 to find $h_2 = 3.87 \text{ W/m}^2 \cdot \text{K}$, which again is small. Hence, we consider only the heat transfer at the film–drum surface and Eq. 5.190 becomes

$$\text{Pe} \frac{\partial \bar{\theta}}{\partial \zeta} = -\frac{bh_1}{2k} \bar{\theta} \quad (5.191)$$

where we have introduced the average dimensionless temperature,

$$\bar{\theta} = \frac{\bar{T} - T_a}{T_0 - T_a} = \frac{T(1) - T_a}{T_0 - T_a} \quad (5.192)$$

because there is little variation of T over the film thickness.

We next estimate the magnitude of h_1 required to keep the crystallinity below 3.0%. To do this we first estimate what value of h_1 is needed to drop the film temperature from 200 °C (we expect an insignificant drop in film temperature from the die to the drum based on Example 5.1) to 25 °C. This temperature is arbitrary and we may find that we would like to keep the temperature higher as the film is drawn after leaving the chill roll. Equation 5.191 becomes

$$\frac{\partial \bar{\theta}}{\partial \zeta} = -\frac{h_1 \bar{\theta}}{2\rho \bar{C}_p V_0} \quad (5.193)$$

If we follow an element of the film, then we can recast Eq. 5.193 as a transient heat conduction problem. With $\zeta = z/b$, where b is one-half the film thickness and $t = z/V_0$, we are now solving the following DEQ (differential equation):

$$\frac{\partial \bar{\theta}}{\partial t} = -\frac{h_1 \bar{\theta}}{2b\rho \bar{C}_p} \quad (5.194)$$

with I.C. at $t = 0$, $\bar{\theta} = 1.0$.

Equation 5.194 can easily be solved if h_1 , ρ , and \bar{C}_p are taken to be independent of temperature. Most likely one would use channels carrying a cooling fluid just below the surface and hence h_1 might change slightly across the drum. According to Table 5.6 ρ is not expected to change much, but \bar{C}_p is somewhat temperature dependent. (We could use Eq. C.2 and Table C.9 in Appendix C if we want to improve the results.) Taking \bar{C}_p to be $2.80 \times 10^3 \text{ kg}^{-1} \cdot \text{K}^{-1}$ and ρ to be 867 kg/m^3 we can estimate what h_1 should be. Given the line speed and drum diameter we find that the time the film

is in contact with the drum is 1.98 s. With the assumption of constant coefficients the solution to Eq. 5.194 is

$$\bar{\theta} = \exp \left[-\frac{h_1 t}{2b\rho \bar{C}_p} \right] \quad (5.195)$$

When $\bar{T} = 25 \text{ }^\circ\text{C}$, $\bar{\theta} = 0.069$; then $h_1 = 164 \text{ W/m}^2 \cdot \text{K}$.

Although we have an estimate for h_1 , we don't know whether this value will keep the amount of crystallinity below the level of 3.0%. To find this out we use Eqs. 5.161 and 5.162:

$$\phi_c/\phi_\infty = 1 - \exp \left[-\int_0^t \left(\frac{4}{3}\right) \pi N G^3 n t'^{(n-1)} dt' \right] \quad (5.196)$$

where G is given by either Eq. 5.157 or Eq. 5.158. T_K has been calculated in Example 5.9 to be 93 °C. In principle we should use Eq. 5.157 for $93 \leq T \leq 200 \text{ }^\circ\text{C}$ and Eq. 5.168 for $25 \leq T \leq 93 \text{ }^\circ\text{C}$, but we will use Eq. 5.157 over the whole temperature interval. For PP Eq. 5.157 becomes

$$\ln G = \ln G_0 - (2.303) \left[(2.553 \times 10^3/T) + \frac{5.141 \times 10^4}{T(447 - T)} \right] \quad (5.197)$$

or

$$G = G_0 \exp \left[-(2.303) \left((2.553 \times 10^3/T) + 5.141 \times 10^4/T(447 - T) \right) \right] \quad (5.198)$$

From Eq. 5.195 we know how T changes with time and hence we can calculate ϕ_c by substituting Eq. 5.198 in Eq. 5.196. Before doing this we make a change of variables in Eq. 5.196 from time to temperature using Eq. 5.195, and we express Eq. 5.196 as

$$\begin{aligned} \ln(1 - \phi_c/\phi_\infty) &= -\int_0^t \frac{4}{3} \pi N G^3 n t'^{(n-1)} dt' \quad (5.199) \\ &= \int_{T_0}^{T_f} -C \exp \left[-(3)(2.303) \left((2.553 \times 10^3/T) \right. \right. \\ &\quad \left. \left. + 5.141 \times 10^4/T(447 - T) \right) \right] (\ln\{(T - T_a)/ \\ &\quad (T_0 - T_a)\})^2 (1/(T - T_a)) dT \quad (5.200) \end{aligned}$$

where $T_f = 298 \text{ K}$ and $T_0 = 473 \text{ K}$ and $C = \frac{4}{3} \pi N G (3)(2b\rho \bar{C}_p/h_1)^3$. To integrate the expression on the right-hand side (R.H.S.) of Eq. 5.200 numerical techniques are required. This is done by using either the IMSL subroutine QDAGS as described in the file "DesignPR4-IMSL-Fortran" or the MATLAB function "Quad" as described in the file "DesignPR4-MATLAB-Quad" on the accompanying website. Furthermore, we find it necessary to use the double

precision form of the subroutine because of the magnitude of the terms in Eq. 5.200. For the conditions given and the assumed final temperature of 25 °C, $\phi_c \approx 0.0$ for all practical purposes (i.e., $\ln(1 - \phi_c/\phi_\infty) = -0.36 \times 10^{-8}$). Hence, a value of $h_1 = 164 \text{ W/m}^2 \cdot \text{K}$ will keep the crystallinity below 3.0%.

We have only found a desired heat transfer coefficient. Whether we can achieve these conditions is another matter. The design of a cooling system to obtain the desired heat transfer coefficient may be difficult. Two methods that are used presently are the spraying of water on the inside of the drum surface and the circulation of water through channels beneath the drum surface.

The other question of concern in this problem was spherulite size. Because ϕ_c is negligible, there is no need to calculate the radius of a spherulite. However, if this was necessary, we would use Eqs. 5.198 and Eq. 5.153 to obtain a differential equation for determining R . We would then use the IMSL ordinary differential equation solver, IVPAG, or a MATLAB solver such as "ode15s" to find the radius, R , as a function of time.

PROBLEMS

A. Applications

- 5A.1** *Temperature Shifting of Rheological Data.* Viscosity versus shear rate data are given in Appendix A, Table A.12 for PPS at various temperatures. Use the shift factors given in Appendix A.5 as well as the rheological data to obtain values of η and N_1 at 330 °C at higher shear rates than given. Compare the shifted values to the measured values where overlap of the shear rates exists.
- 5A.2** *Shift Factor Determined Using the WLF Equation.* Calculate the shift factor for PPS at 293 °C for a reference temperature of 330 °C using the WLF equation (Eq. 5.7) and compare it with the experimental value of 1.708.
- 5A.3** *Viscous Heating in a Slit Die.* Determine the maximum temperature rise in the slit die shown in Figure 3.23 (p. 58) for HDPE at 170 °C at a wall shear rate of 100 s^{-1} . Use the rheological parameters given in Table 2.3 (p. 20) and Eq. 5.55. Take the die length to be 100 mm and the height to be 2.5 mm.
- 5A.4** *Pressure Profile in the Presence Viscous Heating.* Determine the effect of viscous heating on the pressure profile in the slit die in Problem 5A.3.
- 5A.5** *Heat Transfer Coefficients in High Speed Wire Coating.* A copper wire coated with LDPE leaves a wire coating die at 165 °C. The diameter of the metal wire and coating is 0.09 cm and the coating thickness is 0.02 cm. The line speed is 2000 m/min. The cooling medium is water at 25 °C and the final temperature of the surface of the coating is 25 °C. Determine the heat transfer coefficient as the wire enters the cooling bath.
- 5A.6** *Heat Transfer Coefficient During the Heating of PETP Preforms.* A 57 g PETP preform is heated from 25 °C to 120 °C using a radiant heat source. The outer diameter of the preform is 2.54 cm and the wall thickness is 0.32 cm. The air temperature is 25 °C. Determine the convective part of the heat transfer coefficient at the outside surface of the preform assuming that the source of heat transfer is free convection.
- 5A.7** *Effect of Carbon Fiber on the Cooling Time of a Composite.* A 0.4064 cm thick laminate (layers of polymer sheet reinforced with long continuous fibers) consisting of 60 volume % carbon fiber and 40 volume % PEEK is cooled from 350 °C to 100 °C in a mold with the wall temperatures set at 75 °C. Neglecting crystallization and assuming constant thermal properties, determine how much faster the composite cools down to the final temperature relative to the pure matrix of the same thickness. The properties of the fiber and matrix are given in Table 5.11.
- 5A.8** *Crystallization of LDPE.* Determine the temperature at which the maximum rate of crystallization occurs and $K(T)_{\max}$ for HDPE. Which crystallizes faster, PP or HDPE?
- 5A.9** *Orientation of a Polymer Melt in Shear Flow.* LDPE (NPE-953) is extruded through a film die at 170 °C at a wall shear stress of $1.2 \times 10^5 \text{ Pa}$. The film die consists of parallel plates having a width of 1.0 m and a height of 0.05 cm. Determine the amorphous orientation function as a function of distance from the center to the die wall in the region where steady shear flow exists.
- 5A.10** *Radiation Heating of Carbon Fiber Tow.* Before impregnating carbon fiber (black in color) with the matrix it is heated on both sides by means of a bank of quartz lamps having a filament temperature of 1492 °C. The carbon fiber bundles (called tows) are spread to a width of 20 cm and a thickness of 0.25 cm. Treating the bank of lights and the spread carbon fiber as parallel flat plates, determine the time required to heat the centerline of the carbon fibers from 100 °C to 300 °C. What will the surface temperature of the filaments be when the center is 300 °C?

5A.11 *Factors Affecting Spherulitic Crystallization*

- (a) The overall rate of crystallization, $r_c = d\phi_c/dt$, is proportional to $(t_{1/2})^{-1}$, where $t_{1/2} = (\ln 2/K)^{1/3}$ for spherulitic crystallization. Show that $r_c \propto 1.5N^{1/3}$, where N is the number of nucleation sites.
- (b) Based on the expression above list four factors on which r_c depends.
- (c) Which two of these factors can be altered by processing conditions?
- (d) Which two of these factors are determined by the polymer structure?

B. Principles

5B.1 *Viscous Heating in Tangential Annular Flow.* Determine the temperature distribution in an incompressible power-law fluid between two coaxial cylinders (see Problem 2B.6) each assumed to be at the same temperature, T_w . Assume that the forced convection assumption holds and that μ , ρ , and k are constant. (Note: The equations of motion and energy can be solved independently.)

- (a) Show that the equation of energy is

$$0 = k \frac{1}{r} \frac{d}{dr} \left(r \frac{dT}{dr} \right) + m \left[r \frac{d}{dr} \left(\frac{v_\theta}{r} \right) \right]^{n+1} \quad (5.201)$$

- (b) Using the velocity profile determined in Problem 2B.6, show that Eq. 5.201 becomes

$$0 = k \frac{1}{r} \frac{d}{dr} \left(r \frac{dT}{dr} \right) + m \left[\frac{-2WR^{2/n}k^{2/n}}{n(1-k^{2/n})} \right]^{n+1} r^{-2(1+s)} \quad (5.202)$$

- (c) Solve Eq. 5.202 for the temperature distribution.
- (d) Under what conditions might we expect a significant temperature rise, say, on the order of 10 °C, if the fluid has the properties of HDPE given in Table 2.3 (p. 20)?

5B.2 *Viscous Heating in a Wire Coating Die.* In Example 2.3 in Chapter 2 (p. 18) determine whether any significant rise in temperature will occur for the conditions given. Assume the melt enters the die at 200 °C and the wall and wire temperatures are also 200 °C. Repeat the calculations for a wire speed of 2000 m/min.

5B.3 *Forced Convection Heat Transfer in Tubes—Short Contact Times.* A polymeric fluid whose viscosity function is described by the Ellis model is flowing through the tube as shown in Figure 5.26. Determine the temperature profile and the wall heat flux for the

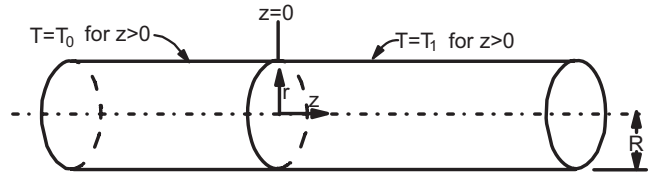


FIGURE 5.26 Pipe with sudden change in wall temperature.

case of short contact times in which the heat does not penetrate very far into the fluid.

- (a) Obtain the velocity profile.
- (b) Obtain the differential equation for $T(r, z)$ by carrying out an energy balance and by using the equation of thermal energy.
- (c) Set $s = R - r$ and discard any terms that are not important in the vicinity of the wall to obtain the following differential equation:

$$\rho \bar{C}_p \left[(\tau_R/\eta_0) + \left(\tau_R^\alpha/\tau_{1/2}^{\alpha-1} \eta_0 \right) \right] s \frac{\partial T}{\partial z} = k \frac{\partial^2 T}{\partial s^2} \quad (5.203)$$

in which τ_R is the momentum flux at $r = R$.

- (d) Under what conditions is it possible to make the substitution suggested in part (c)?
- (e) Introduce the following dimensionless variables and rewrite Eq. 5.203:

$$\theta = \frac{T - T_0}{T_1 - T_0}, \quad \zeta = \frac{z}{R}, \quad \sigma = \frac{s}{R},$$

$$N = \frac{\rho \bar{C}_p R^2}{k} \left[(\tau_R/\eta_0) + \left(\tau_R^\alpha/\tau_{1/2}^{\alpha-1} \eta_0 \right) \right] \quad (5.204)$$

- (f) Show that if a solution of the following form is assumed,

$$\theta = f(\eta), \quad \text{where } \eta = \left(\frac{N\sigma^3}{9\zeta} \right)^{1/3} \quad (5.205)$$

the partial differential equation in part (c) is transformed into the ordinary differential equation

$$f'' + 3\eta^2 f' = 0 \quad (5.206)$$

in which the prime indicates differentiation with respect to η .

- (g) What boundary conditions are required to solve Eq. 5.206?

(h) Solve Eq. 5.206 and get

$$f = [\Gamma(4/3)]^{-1} \int_{\eta}^{\infty} e^{-\eta^3} d\eta \quad (5.207)$$

in which $\Gamma(4/3)$ is the gamma function evaluated at $4/3$.

- (i) From the temperature distribution in part (h), evaluate the wall heat flux as a function of the distance down the tube.
- (j) Integrate the result in part (i) to obtain the total heat flow through the pipe surface between $z = 0$ and $z = L$: that is, show that

$$Q = 4\pi Rk(T_1 - T_0) \left(\frac{N}{9}\right)^{1/3} \left(\frac{L}{R}\right)^{2/3} \left[\Gamma\left(\frac{7}{3}\right)\right]^{-1} \quad (5.208)$$

5B.4 Solidification of a Polymer Melt During Injection Molding. A thin rectangular mold is filled with a polymer melt having an initial temperature of T_0 . The melt is assumed to make perfect thermal contact with the mold walls, which are set at T_w . Determine the rate of solidification (i.e., $W_a = \rho_s dX_s/dt$) and the time it takes for the centerline to reach the crystallization temperature, T_c . Consider the melt to have a distinct crystallization temperature, T_c . The heat of crystallization is taken as $\Delta\bar{H}_c$. Assume that there is enough flow into the center of the molten polymer so that the solid polymer always makes contact with the walls of the mold. Use the notation given in Figure 5.27 and carry out the following steps:

- (a) Assuming that each region is a finite slab, obtain the differential equations for the temperature distribution and the corresponding initial and boundary conditions for the liquid and solid phases.
- (b) To relate the temperature distributions in the two phases, carry out an energy balance at the interface to obtain

$$k_s \frac{\partial T_s}{\partial x_s} \Big|_{x_s} - k_l \frac{\partial T_l}{\partial x_l} \Big|_{x_l} = \rho_s \Delta\bar{H}_c \frac{dX_s}{dt} \quad (5.209)$$

- (c) Substitute the series solutions to the differential equations in part (a) into Eq. 5.209 and explain how this equation can be used to find the solidification rate.

5B.5 Relation of Volume Fraction of Crystallinity to Density. Show that ϕ_c is related to ρ , ρ_c , and ρ_a by the following relation:

$$\phi_c = (\rho - \rho_a)/(\rho_c - \rho_a)$$

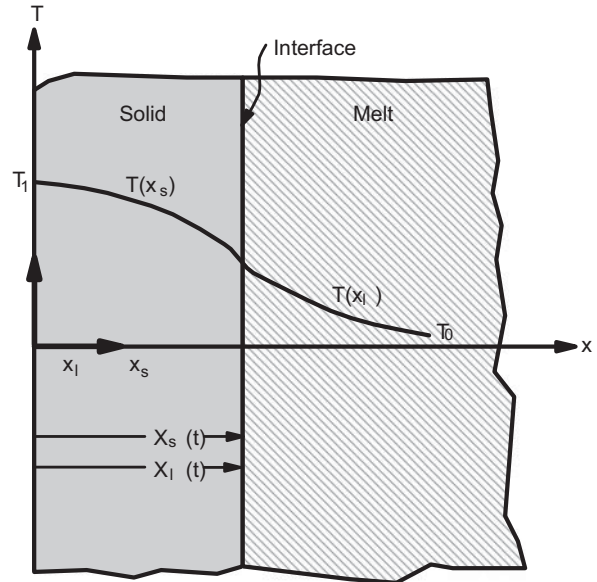


FIGURE 5.27 Crystallization of a semi-infinite melt.

where ρ is the density of the semicrystalline material, ρ_a is the density of the amorphous phase, and ρ_c is the density of the crystalline phase.

5B.6 Density and Heat Capacity in a Crystallizing Polymer. During crystallization the density and heat capacity change as the polymer is converted from amorphous melt to crystalline solid. Obtain expressions for ρ and \bar{C}_p of the semicrystalline composite material in terms of ϕ , ϕ_c , ϕ_a , and the corresponding crystalline and amorphous values of ρ_c , ϕ_a , $\bar{C}_{p,c}$, and $\bar{C}_{p,a}$.

C. Numerical Problems

5C.1 Numerical Solution of Heat Conduction in a Slab. Do Example 5.5 for the case in which the boundary conditions are given in terms of a heat transfer coefficient and the thermal coefficients are temperature dependent (see Table 5.6). Compare the results to those obtained in Example 5.5 in which constant thermal coefficients were used.

5C.2 Numerical Solution of Heat Conduction in a Slab. Solve Example 5.5 for the case in which the boundary conditions are given in terms of a flux through a heat transfer coefficient. Use the IMSL subroutine MOLCH or the function “pdpdf” in MATLAB to obtain the time to cool the centerline to 130°C.

5C.3 Nonisothermal Crystallization of PEEK. The temperature of a PEEK/carbon fiber composite

(containing 60% by weight of carbon fiber) is reduced from 350 °C to 75 °C at the rate of 20 °C/min. The thickness of the composite is 0.3175 cm. Determine ϕ_c using Eqs. 5.162 and 5.163.

5C.4 *Film Casting of LDPE.* It is desired to use the same film casting equipment as is used for polypropylene (see Design Problem IV). Using the same conditions as given in Design Problem IV, except the initial temperature for LDPE is 175 °C, determine whether ϕ_c can be maintained below 3.0%.

5C.5 *Radiation Heating of a Sheet.* Do Example 5.7 numerically using the approach described in Example 5.5. Do the problem for both the cases of constant and temperature-dependent thermal properties. (The material is PVC.)

5C.6 *Bonding of Polymer to a Metal Sheet.* PPS sheets (0.018 cm thick) are bonded to both sides of a copper sheet (0.05 cm thick) by heating the materials from 25 °C to 310 °C in a press as shown in Figure 5.28. The platens of the press are held at 330 °C. Determine the time required to heat the interface between PPS and copper to 310 °C. The following properties are given for Cu:

$$k_c = 377 \text{ W/m} \cdot \text{K}, \quad \rho_c = 8954 \text{ kg/m}^3, \\ \bar{C}_{p,c} = 0.381 \text{ kJ/m} \cdot \text{°C}$$

- Formulate the differential equation and boundary and initial conditions required to find the time to heat the interface between PPS and Cu up to 310 °C.
- Find an analytical solution to this problem if possible.
- Solve the problem numerically.

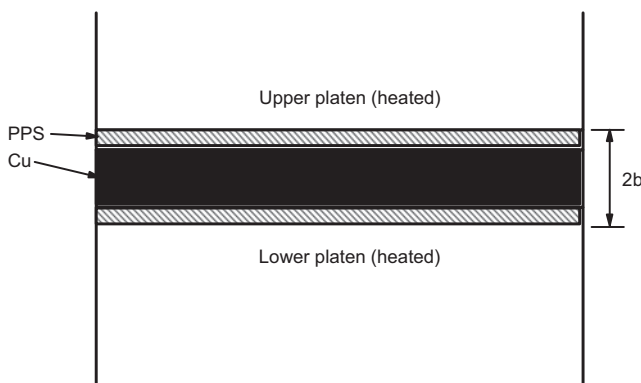


FIGURE 5.28 Lamination of two films of PPS to a copper sheet.

D. Design Problems

5D.1 *Design of a Pelletizing Bath.* Based on the conditions given in Example 5.6, determine the minimum bath length required to drop the centerline temperature of the strand to 75 °C. In your calculations determine the length for three conditions: (1) no thermal resistance at the polymer–water interface; (2) use a heat transfer coefficient based on a mean value calculated at the beginning and end of the bath; and (3) use a variable heat transfer coefficient that depends on temperature.

5D.2 *Cooling of a Blow Molded Gas Tank.* A coextruded parison consisting of HDPE and nylon 6 are blow molded to form a gasoline tank for an automobile. The nylon 6 serves as a barrier to gasoline fumes. In order for the tank to exhibit adequate impact properties, the spherulite size must be maintained below 10 microns in both resins and ϕ_c for both resins should approach 75% of ϕ_∞ . Determine the heat transfer coefficient required at the mold wall to provide these conditions. The thickest section of the parison as it contacts the wall is 0.50 cm with nylon 6 representing 1/5 of the thickness. Treat the composite material as a slab and assume that there is no heat transfer at the inner surface. The mold is to be cooled by channels with circulating water at 12 °C. In your design you must consider that it is necessary to use the shortest time possible to cool the part down.

REFERENCES

- Avrami, M. 1939. "Kinetics of Phase Change. I: General Theory." *J. Chem. Phys.*, **7**, 1103.
- Avrami, M. 1940. "Kinetics of Phase Change. II: Transformation–Time Relations for Random Distribution of Nuclei." *J. Chem. Phys.*, **8**, 212.
- Avrami, M. 1941. "Kinetics of Phase Change. III: Granulation, Phase Change, and Microstructure." *J. Chem. Phys.*, **9**, 177.
- Bird, R. B., W. E. Stewart, and E. N. Lightfoot. 1960. *Transport Phenomena* (Wiley, Hoboken, NJ).
- Bird, R. B., W. E. Stewart, and E. N. Lightfoot. 2007. *Transport Phenomena*, 2nd edition (Wiley, Hoboken, NJ).
- Brandrup, J. and E. H. Immergut, Eds. 1989. *Polymer Handbook*, 3rd edition (Wiley, Hoboken, NJ).
- Bright, D.G. 1975. *Quantitative Studies of Polymer Crystallization Under Nonisothermal Conditions* (Ph.D. dissertation, Georgia Institute of Technology.)
- Capaccio, G. and I. M. Ward. 1975. "Ultra-High Modulus Linear Polyethylene Through Controlled Molecular Weight and Drawing." *Polym. Eng. Sci.*, **15**, 219.
- Carlsaw, H. S. and J. C. Jaeger. 1973. *Conduction of Heat in Solids*, 2nd edition (Oxford University Press, New York).

- Fand, R. M. and K. K. Keswani. 1973. "Combined Natural and Forced Convection Heat Transfer from Horizontal Cylinders to Water." *Int. J. Heat Mass Transfer*, **16**, 175.
- Gandica, A. and J. H. Magill. 1972. "A Universal Relationship for the Crystallization Kinetics of Polymer Materials." *Polymer*, **13**, 595.
- Holman, J. P. 1981. *Heat Transfer*, 5th edition (McGraw Hill, New York).
- Huisman, R. and H. M. Henvel. 1978. *J. Appl. Polym. Sci.*, **22**, 943.
- Janeschitz-Kriegl, H. 1969. "Flow Birefringence of Elastico-viscous Polymer Systems." *Adv. Polym. Sci.*, 170–318.
- Janeschitz-Kriegl, H. 1983. *Polymer Melt Rheology and Flow Birefringence* (Springer-Verlag, Berlin).
- Ke, B. 1960. "Characterization of Polyolefins by Differential Thermal Analysis." *J. Polym. Sci.*, **42**, 15.
- Katayama, K. and M. Yoon. 1985. In A. Ziabicki and H. Kawai, Eds. *High Speed Fiber Spinning* (Wiley, Hoboken, NJ).
- Lauritzen, I. Jr. and J. D. Hoffman. 1964. *J. Res. Natl. Bur. Stand. (A)*, **64**, 73.
- Lopez, L. C. and G. L. Wilkes. 1988. "Crystallization Kinetics of Poly(*p*-phenylene sulphide): Effect of Molecular Weight." *Polymer*, **29**, 106.
- Matthews, J. H. and K. D. Fink. 2004. *Numerical Methods Using MATLAB* (Pearson Prentice Hall, Upper Saddle River, NJ).
- McAdams, W. H. 1954. *Heat Transmission* (McGraw Hill, New York).
- Nielsen, L. 1962. *Mechanical Properties of Polymers* (Reinhold, New York).
- Richardson, M. O. W. 1977. *Polymer Engineering Composites* (Applied Science Publishers Ltd, London).
- Riggs, J. B. 1988. *An Introduction to Numerical Methods for Chemical Engineers* (Texas Tech University Press, Lubbock, TX).
- Rohsenow, W. M. and J. P. Hartnett, Eds. 1973. *Handbook of Heat Transfer* (McGraw Hill, New York).
- Rudnik, E. 2008. *Compostable Polymer Materials* (Elsevier, Amsterdam).
- Sakurada, I., T. Ito, and K. Nakamae. 1966. *J. Polym. Sci.*, **C15**, 75.
- Samuels, R. J. 1974. *Structured Polymer Properties* (Wiley, Hoboken, NJ).
- Shelby, M. D. 1991. "Effects of Infrared Lamp Temperature and Other Variables on the Reheat Rate of PET." *Soc. Plastics Eng. Tech. Papers*, **37**, 1420.
- Siegel, R. and J. R. Howell. 1981. *Thermal Radiation Heat Transfer* (McGraw Hill, New York).
- Southern, J. H. and R. S. Porter. 1970. "The Properties of PETP Crystallized Under the Orientation and Pressure Effects of Pressure Capillary Rheometer." *J. Appl. Polym. Sci.*, **14**, 2305.
- Starkweather, H. W. Jr. and R. H. Boyd. 1960. *J. Phys. Chem.*, **64**, 410.
- Tadmor, Z. and C. G. Gogos. 1979. *Principles of Polymer Processing* (Wiley, Hoboken, NJ).
- Van der Meer, S. J. 1971. (Ph.D. dissertation, Delft University, Delft, The Netherlands).
- Van Krevelen, D. W. 1978. "Crystallization of Polymers and the Means to Influence the Crystallization Process." *Chimia*, **32**(8), 279.
- Van Krevelen, D. W. 1990. *Properties of Polymers* (Elsevier, Amsterdam).
- Van de Manakker, F., T. Vermonden, C. F. van Nostrum, and W. E. Hennink 2009. "Cyclodextrin-Based Polymeric Materials: Synthesis, Properties, and Pharmaceutical/Biomedical Applications." *Bio-Macromolecules*, **10**, 3157.
- Velisaris, C. N. and J. C. Seferis. 1988. "Heat Transfer Effects on the Processing–Structure Relationships of Polyetheretherketone (PEEK) Based Composites." *Polym. Eng. Sci.*, **9**(28), 583.
- Wanger, W. H. Jr. 1969. *Cooling of Polymer Filaments During Melt Spinning* (Ph.D. dissertation, University of Denver).
- Whitaker, S. 1977. *Fundamental Principles of Heat Transfer* (Pergamon Press, New York).
- Williams, M. L., R. F. Landel, and J. D. Ferry. 1955. "The Temperature Dependence of Relaxation Mechanisms in Amorphous Polymers." *J. Am. Chem. Soc.*, **77**, 3701.
- Winter, H. H. 1977 *Adv. Heat Transfer*, **13**, 205–267.

6

MIXING

DESIGN PROBLEM V DESIGN OF A MULTILAYERED EXTRUSION DIE

Coextrusion is an important process for manufacturing layered plastic composites, such as film, sheet, and tubing (Middleman, 1977; Schrenk and Alfrey, 1983; Schrenk et al., 1963). A costly alternative would be the fabrication of individual layers of plastics followed by conventional lamination and coating. An additional advantage of the coextrusion technique is its ability to handle extremely thin films on the order of $10\ \mu\text{m}$. One of the most “colorful” applications of this technique is the iridescent film, which consists of hundreds of very thin layers of alternating low and high refractive indices. A typical example of this type of film consists of 116 layers of poly(methyl methacrylate) (PMMA) with refractive index 1.49 and 115 layers of polystyrene (PS) with refractive index 1.59 and total film thickness of about $20\ \mu\text{m}$ (Radford et al., 1973).

We seek to produce a multilayered film of two polymers from a coextrusion blown film apparatus. The die is of the annular type with the mandrel rotating (see Fig. 6.31a) and its dimensions are: $\kappa R = 4.8\ \text{cm}$, $R = 5.0\ \text{cm}$, and $L = 15\ \text{cm}$. The two polymers, which are presented in the schematic by black and white colors, have the same Newtonian viscosity, $\mu = 500\ \text{Pa}\cdot\text{s}$, at the extrusion temperature. The pressure drop in the die is $\Delta P = 3.45\ \text{MPa}$ (500 psi) and the total volumetric flow rate is $Q = 9.43\ \text{cm}^3/\text{s}$. The feedport system consists of 20 equal-size ports in total, 10 for the first polymer (black) and the other 10 for the second polymer (white). A similar feedport system with 16 ports in total is shown in

Figure 6.31. Calculate the minimum rotational frequency of the mandrel for the maximum layer thickness not to exceed $5\ \mu\text{m}$ at the end of the die. To solve this problem follow both the geometrical and the kinematical approaches. Also, calculate the power to rotate the mandrel and introduce changes necessary for the reduction of the power consumption.

In the preceding four chapters momentum, mass, and heat transfers were analyzed, as they apply to polymer processing. This is the first chapter among the last five concerned with the specifics of various types of processes. Primarily, mixing in polymer processing addresses two tasks: addition of various ingredients (additives) and production of polymer blends and alloys. The additives are used to alter the properties of the matrix polymer, such as impact strength, flexural modulus, modulus of elasticity, foaming ability, and cost. These additives are called modifying additives. Additives are also used to prevent polymer degradation, and they are called protective additives. The other important task of mixing at present is the blending of other polymers with the given polymer to obtain a desired improvement in the given polymer. For example, the blending of polypropylene (PP) and compatibilizers with Nylon 6 leads to a composition that is lower in price and has improved energy absorbing characteristics (Van Gheluwe et al., 1988). Similarly, blending of rubber with polystyrene (PS) produces a very fine dispersion of rubber particles in the PS matrix, called high-impact PS (HIPS), with great improvements in the energy absorbing characteristics (Bucknall, 1977). Although many would like to think that the properties of a blend are determined by the

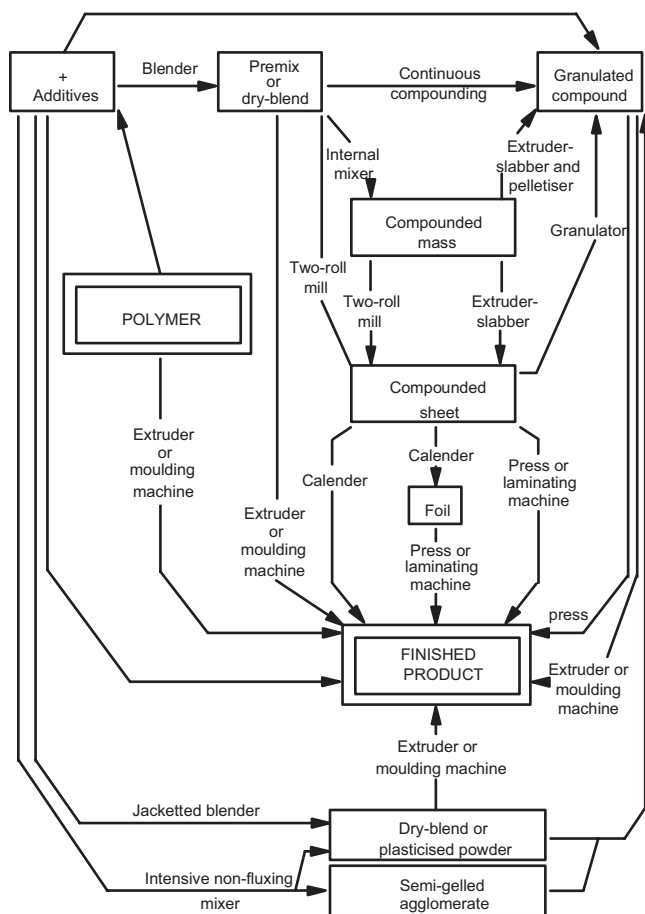


FIGURE 6.1 Mixing in the major routes for melt processing of polymers to finished products. (Reprinted by permission of the publisher from Matthews, 1982.)

thermodynamics, it turns out that the method of preparation is of utmost importance. Figure 6.1 shows the importance of mixing in polymer processing by laying out the major routes for melt processing of polymers to finished products.

Clearly, there are differences between the mixing requirements for the cases of the additives and the blending of polymers. Blending of polymers usually involves large concentrations (or weight percent) of the additive phase, various degrees of compatibility between the various phases, small density differences, and dispersion of one phase into droplets or fibers with dimensions affected by the physical characteristics of that phase and the hydrodynamics prevailing in the mixing environment. These characteristics of the polymer blending processes are contrasted with the characteristics of polymer-additive systems: low concentrations, large density differences, and solid-liquid distribution and dispersion of agglomerates into particles that cannot be divided any further.

Generally, in polymer processing we are concerned with mixing in three types of systems: liquid-liquid, solid-solid,

and liquid-solid, each with different mechanisms and kinetics of mixing. In the liquid-liquid case, mixing is concerned with either low viscosity monomers or high viscosity polymer melts. Solid-solid mixing involves blending of either two polymers or resins or an additive and a polymer. In such cases, the polymer is in granular, pelletized, powdered, or diced form. Finally, solid-liquid mixing involves blending of liquid additives and solid polymers (not melted) or solid additives (below their melting point) and melted polymers.

This chapter is organized as follows. In Section 6.1 we describe mixing with particular emphasis on polymer processing. The characterization of the state of the mixture together with the statistical analysis and the various experimental techniques are presented in Section 6.2. Laminar mixing is the only viable mixing mechanism for polymer melts due to their high viscosity, and it is analyzed in Section 6.3 using both the geometrical and kinematical approaches. In Section 6.4 we emphasize the importance of residence time and strain distributions of polymer processing equipment in understanding the degree of mixing achieved in each process. Dispersive mixing is analyzed in Section 6.5 with focus on both solid aggregates and liquid-liquid dispersions. In Section 6.6 we highlight the importance of thermodynamics in polymer processing, and in Section 6.7 we describe the fundamentals of chaotic mixing as a way to improve the degree of mixing. Finally, Section 6.8 provides the solution to Design Problem V.

6.1 DESCRIPTION OF MIXING

The term *mixing* refers to operations that have a tendency to reduce nonuniformities or gradients in concentration, temperature, size of a dispersed phase, or other properties of materials. Equivalently, a mixing operation increases the configurational entropy of the system, which becomes a maximum as the configuration becomes random. Mixing is considered to be one of the most widespread industrial unit operations, and it is found in the core of many areas in the general industry. This unit operation might be a process in itself or might be a part of a more extended sequence of processes. Typical examples can be taken from the general industry, polymerization processes, and polymer processing.

Here we restrict ourselves to the study of the mixing of two-component systems. The two components are defined as either *major* or *minor* components by the level of their total concentration. The goal of the mixing process is usually to achieve a homogeneous dispersion of the minor component into the major one, obtaining the *ultimate particle* or *sub-division* (or *volume element*) level of the minor component (McKelvey, 1962). In the mixing area, that term is used in a restricted sense, because in its general form the ultimate particle is the molecule and ultimate mixing is molecular mixing. However, in typical mixing operations the two parameters

that define the size and form of the ultimate particle are the form of the component and the level of satisfaction of the final dispersion. For example, in the mixing of carbon black agglomerates in polyethylene (PE), the ultimate particle is one particle of carbon black defined by the form of the initial agglomerates (many particles together) as well as by the satisfactory dispersion level of one carbon black particle. In general, typical ultimate particles are molecules and colloidal and microscopic particles.

Mixing is accomplished by movement of material from various parts by the flow field. This movement occurs by a combination of the following mechanisms, two of which are hydrodynamic and one is molecular (Brodkey, 1966). The first is *convective transport*. It is present in both laminar and turbulent regimes, and it can also be called *bulk diffusion*. Generally, a colored pigment being dispersed in a bucket of paint is an example of laminar mixing. In this case, layers of pigment are thinned, lumps are flattened, and threads are elongated by laminar convective flow. Stirring of cream in a cup of coffee is an example of turbulent mixing, in which the mechanism of turbulent bulk flow predominates at the first stages.

The second mechanism is *eddy diffusion*, which is produced by local turbulent mixing. This mechanism prevails at the later stages in the example of stirring of cream into a cup of coffee which was mentioned above. The turbulent eddies in the flow field create small scale mixing, which is sometimes thought to be analogous to molecular diffusion. However, eddy diffusivity is much higher than molecular diffusivity, and it occurs over longer length scales. For gases and low viscosity liquid systems eddy diffusion becomes the usual mode of mixing.

Finally, there is *molecular diffusion* or interpenetration of molecular species. It is responsible for the ultimate homogenization on a molecular scale (the ultimate particles are the molecules), and it is considered to be true mixing. This form of diffusion is driven by the chemical potential difference due to concentration variation, and it is a very slow process, because its time scale is proportional to the value of the diffusion coefficient. Thus, this mechanism becomes important in gases and low-molecular-weight, miscible liquid systems, although there are time scale differences in those two cases.

The major difference between mixing in general and in polymer processing stems from the fact that the viscosity of polymer melts is usually higher than 10^2 Pa·s, and thus mixing takes place in the laminar regime only ($Re < 2000$); to achieve such a number the polymer would have to flow down a 1 m wide channel at a velocity of 20 cm/s). This has a severe consequence which is the lack of eddy and molecular diffusion which greatly enhance the rate of mixing and reduce the scale of homogenization. Thus, all mixing theories and practices should be adjusted to the laminar regime to find applicability in the polymer processing area. This remark applies also to solid–solid mixing in polymer

processing, but it does not find application to the addition of low-molecular-weight substances into polymers, such as dyes, where molecular diffusion plays a role.

The two basic types of mixing can be identified as *extensive* and *intensive* mixing. *Distributive, convective, repetitive, simple mixing*, and *blending* are the main names with which extensive mixing is also associated, whereas *compounding, dispersive*, and *dispersing* mixing are the corresponding names associated with intensive mixing. Extensive mixing refers to processes that reduce the nonuniformity of the distribution (viewed on a scale larger than the size of the distributed components) of the minor into the major component without disturbing the initial scale of the minor component. It can be achieved through two mechanisms: rearrangement and deformation in laminar flow. The rearrangement mechanism works in plug-type flows (Tadmor and Gogos, 1979) with absence of deformation and it can be subdivided into random and ordered types as shown schematically in Figure 6.2. Also, deformation achieved in shear, elongation, and squeezing flows plays a major role in distributing the minor component.

The term intensive mixing refers to processes that break down the liquid dispersed phase or the initial particle agglomerates, and they decrease the ultimate particle of the dispersion. A typical example is the dispersion of agglomerates of colloidal carbon black particles in PE. In this case the initial ultimate particle is the agglomerate, and the final is the particle itself. Another example is the dispersion of a polymer into another polymer where the minor component should be dispersed into small droplets or elongated fibers (both of them have a length scale of about 10 μ m). The analysis of dispersive mixing follows the lines of the analysis of distributive mixing with the complication that the breakup forces should now be included.

The geometry of the mixing equipment, physical parameters, such as viscosity, density, interfacial tension, elasticity, and attractive forces for solids, operating conditions, such as temperature, speed of rotating parts, flowing velocity, and residence time are the important factors that determine the relative strengths of the mixing mechanisms. As a consequence, this relative strength affects the efficiency of mixing and the quality of the product. In almost all cases, both good distribution and good dispersion are required. In some cases, only distributive mixing can be tolerated if the next step offers dispersive characteristics and, respectively, dispersive mixing is used when a finely dispersed mixture is required and when the next step does not offer any dispersion characteristics. The distinction between good and poor dispersion and distribution is shown in Figure 6.3.

Some of the terms mentioned get a specific connotation when referred to polymer processing, and thus we give here some specific definitions (Matthews, 1982). *Compounding* refers to the process of softening, melting, and compaction of the polymer matrix and dispersion of the additive into

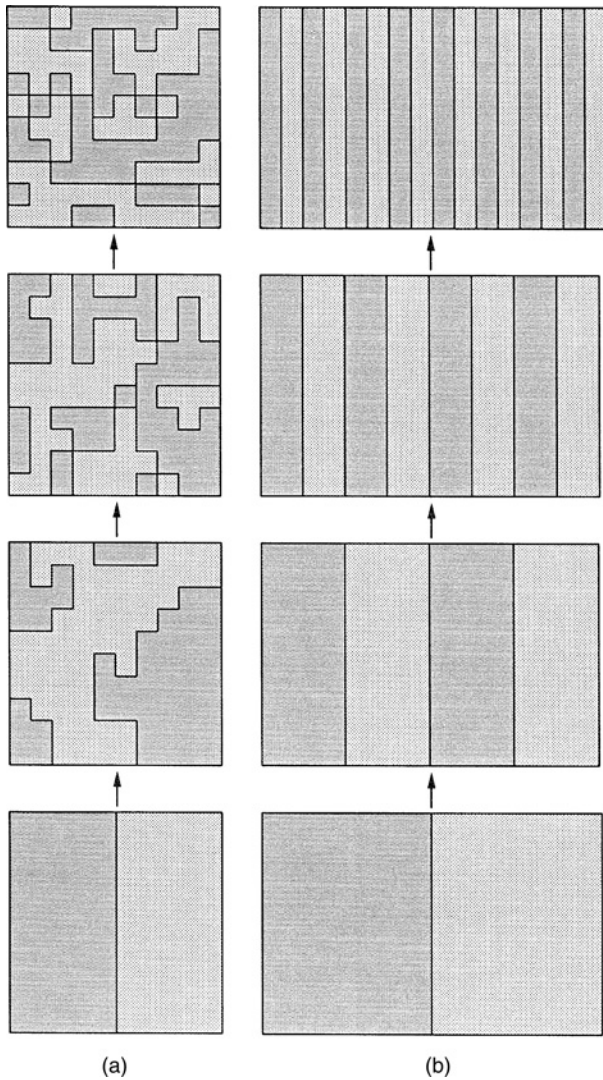


FIGURE 6.2 Distributive mixing: (a) random and (b) ordered rearrangements. (Reprinted by permission of the publisher from Tadmor and Gogos, 1979.)

that matrix. *Blending* refers to all processes in which two or more components are intermingled without significant change of their physical state. Finally, *kneading* refers to mixing achieved by compression and folding of layers over one another; *milling* refers to a combination of smearing, wiping, and possibly grinding; and *mulling* refers to wiping and rolling actions.

6.2 CHARACTERIZATION OF THE STATE OF MIXTURE

After a certain mixing process is completed, the polymer process engineer faces the question about the effectiveness of the selected process as well as about the uniformity of the product. In this section we restrict ourselves to the examination of

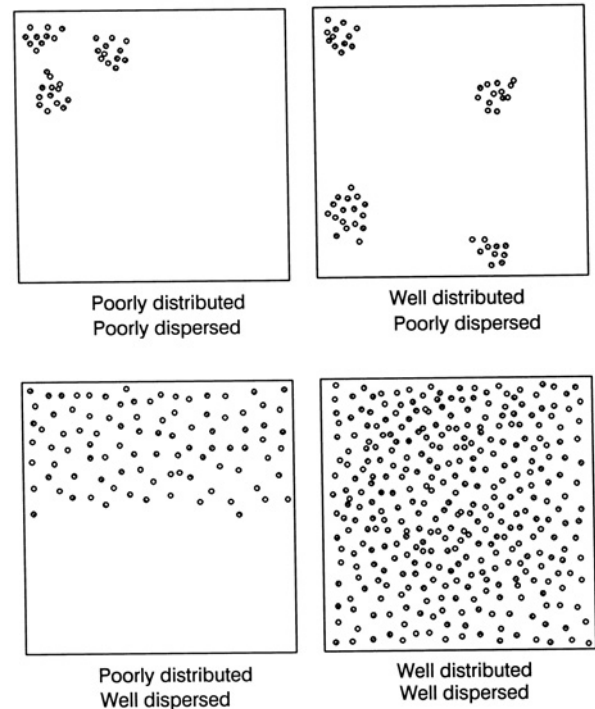


FIGURE 6.3 Quality of distributive and dispersive mixing. (Reprinted by permission of the publisher from Morton-Jones, 1989.)

the product in terms of meeting the preset specifications. In its strictest sense, this should include a detailed description of the ultimate particles (aggregates, particles, drops, and fibers) of the minor component (i.e., their number, length scales, shape, orientation, and statistical description of their spatial distribution). For example, suppose we intend to mix 1% carbon black in PE. After the mixing is carried out, we fracture a number of samples of PE in order to determine whether the initial carbon black aggregates were broken down to either smaller-size aggregates or even to individual particles and to assess the size of the existing carbon black entities and their spatial distribution. Of course, all this information will be integrated into the task of determining the sample concentration statistics and its relation to the expected 1% overall concentration. This procedure can be somewhat altered in terms of measuring the ultimate particles, because their number and size might affect some physical property whose measurement can provide a quick way of assessing the success of the mixing step.

Usually it is sufficient to characterize any mixture by its *gross uniformity*, *texture*, and *local structure*. The term *gross uniformity* can also be found in the literature as *overall uniformity* or *gross composition uniformity*. In the example of carbon black mixed into PE, the gross uniformity indicates the goodness of the concentration distribution of carbon black, and it can be evaluated by statistical analysis on a number

of fractured pellets selected randomly from a large batch of pelletized PE. In the ideal case, all the randomly selected pellets will contain the same concentration of carbon black, and thus the mixture will be called *perfectly gross uniform*. In practice, the gross uniformity is a measure of the degree of fit of the concentration distribution to the binomial distribution, which was found theoretically and proved experimentally to describe these situations.

The size of the PE pellets determines the *scale of examination* (McKelvey, 1962; Tadmor and Gogos, 1979), which can be expressed by order of magnitude fashion and in terms of length, area, or volume. When a finished product is examined for composition gross uniformity, the scale of examination is determined by the size of the sampling volume. It is obvious that the maximum scale of examination is identical to the scale of the finished product itself and that the minimum is the length scale of the ultimate particles. McKelvey (1962) introduced the ideas of fine- and coarse-grained samples depending on the ratio of the scales of examination and ultimate particles. In particular, if this ratio is very large the sampling volume contains many particles, and its appearance is fine grained, whereas if this ratio is about 10 to 100, then the sampling volume contains a few particles, and it is characterized as coarse grained.

At this point, one should not overlook the importance of the volume fraction of the minor component in commenting on the relative sizes of scales of examination and ultimate particles. To be more specific, suppose that we carry out a statistical evaluation of samples of 1% and 10% carbon black in PE and that we would like to have in our microscope eyepiece only about 30 carbon black particles. To meet that requirement we should increase our magnification in the 10% sample more than is required for the 1% sample due to its lower particle concentration.

Is there an ideal scale of examination? Besides the upper and lower limits mentioned previously, the *texture* of the mixture and its *granularity* pose another lower limit. Tadmor and Gogos (1979) define texture as nonuniformity in the forms of patches, stripes, streaks, and so on. Thus, we can narrow the large range for the scale of examination by raising the lower limit to the scale of the granularity of the texture.

The presence of texture in the samples is important in polymer processing, as (1) laminar mixing produces texture; (2) the mechanical properties of polymer blends depend on the texture (e.g., skin-core formation, fiber orientation, and distribution of voids along the thickness in structural foams); and (3) the lack or the presence of texture is required in certain products. Samples can exhibit a certain texture, and at the same time they do or do not exhibit concentration gross uniformity.

The scale of examination for textures might differ from that for gross uniformity. However, the upper and lower limits, in both cases, remain the same. When the scale of examination is about the same as the scale of the ultimate

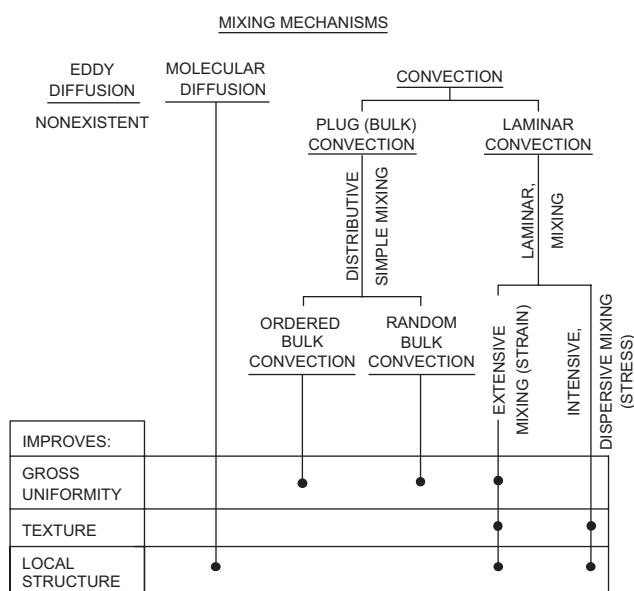


FIGURE 6.4 Mixing mechanisms and their effect on the characteristics of mixtures. (Reprinted by permission of the publisher from Hold, 1983.)

particles, we can probe the *local structure*. In conclusion, gross uniformity, texture, and local structure are the characteristics of the mixture, and their relative importance depends on the specific application. For instance, if carbon black is used for coloring purposes for PE, then its composition gross uniformity and texture are important while local structure is unimportant. However, if the purpose of mixing carbon black in PE is for UV protection (obtained by particles themselves and not aggregates), then the local structure and texture are important. The effects of the various mixing mechanisms on the three parameters of the state of mixture are shown in Figure 6.4.

6.2.1 Statistical Description of Mixing

The gross uniformity of a mixture can be analyzed by statistical methods that can also be used to define the degree of mixing or index of mixedness. For example, for a mixture of carbon black and PE we assume that there exist no agglomerates, that the carbon black particles are uniform in size (monodisperse sample), and that the PE matrix can be divided into fictitious “particles” having the size of carbon black particles. Thus, the mixture will consist of “white” PE particles and “black” carbon black particles mixed together. Solid–solid, solid–liquid, and liquid–liquid (when the dispersed liquid cannot be dispersed any further) dispersions can easily be visualized by this example. Just before mixing starts, the two components are separated inside the mixer. We assume that the diameter of the particles is very small compared to the length scale of the mixer and that there is a

large but finite number of these particles. To test for the kinetics of mixing and the gross uniformity, we need to extract, on a regular basis, small samples from the mixture. Sample size should be large enough to contain a sufficient number of particles for statistical analysis and small enough to leave the mixture undisturbed.

As mixing progresses, the black and white particles intermingle to a greater extent, and, after sufficient time passes, the mixture obtains its random mixing status. At this point the probability of finding a white particle at any point is constant and equal to the overall fraction of the white particles. If a number of samples of equal size are extracted from the mixture, the fraction of the white particles will vary from sample to sample. The mean value over all samples studied should equal the overall fraction of white particles and the distribution of values should follow the binomial or an equivalent distribution.

Consider a sample, randomly extracted from the mixture, which contains n particles, where n is large enough for statistical treatment and small enough compared to the total number of particles in the mixture itself. Let p equal the fraction of black particles in the entire mixture. Then the probability P that this randomly selected sample has exactly b black particles ($x = b/n$) is given by the binomial (or Bernoulli) distribution (Spiegel, 1991):

$$P(b; n, p) = \frac{n!}{b!(n-b)!} p^b (1-p)^{n-b} \quad (6.1)$$

The variance of that distribution is given by

$$\sigma_n^2 = \frac{p(1-p)}{n} \quad (6.2)$$

Similarly, if there are N samples tested, where N is a very large number, then the variance of the binomial distribution, for these samples, is given by the formula

$$s_N^2 = \frac{p(1-p)}{N} \quad (6.3)$$

This variance is a measure of how much the concentration differs from the mean value. The procedure to determine whether or not the mixture is grossly uniform is obvious from the above discussion: samples are extracted from the mixture, their average concentration is calculated, and finally the concentration distribution is checked against the binomial distribution. If there is a match between these two distributions, the mixture is considered to be grossly uniform or a random mixture. In the limit of zero variance the mixture attains the uniform state.

The binomial distribution is considered to approach the normal (or Gaussian) distribution if the number of

samples is large. More specifically, if the following conditions are met

$$Np > 5 \text{ and } p < 0.5 \quad (6.4)$$

then the distribution of concentrations is approximated by the continuous Gaussian form:

$$P = \frac{1}{\sigma\sqrt{2\pi}} \exp\left[-\frac{(x-p)^2}{2\sigma^2}\right] \quad (6.5)$$

Note that if the entire fraction of white particles, P , is very small, then a better approximation of the binomial distribution is the Poisson distribution:

$$P = \frac{e^{-np}(np)^b}{b!} \quad (6.6)$$

In practice, a limited number of samples are examined. Let N be the number of samples. Then, the mean, \bar{C} , is defined as

$$\bar{C} = \frac{1}{N} \sum_{i=1}^N C_i \quad (6.7)$$

where C_i represents the concentration of the i th sample. The variance, s^2 (or standard deviation s), of the measurements is defined as

$$\begin{aligned} s^2 &= \frac{1}{N-1} \sum_{i=1}^N (C_i - \bar{C})^2 \\ &= \frac{1}{N-1} \sum_{i=1}^N C_i^2 - \frac{1}{N(N-1)} \left[\sum_{i=1}^N C_i \right]^2 \end{aligned} \quad (6.8)$$

If the sampling procedure has been properly executed, then \bar{C} and p should not be significantly different. The values for the mean and the variance can be used in two ways. First, either with the confidence tests of the statistical theory we can estimate the actual mean and variance of the whole mixture, or, closely to is, with the significance theory we can answer the question, "Are the samples taken from the same mixture or not?" Second, the variance can be used in the evaluation of the mixedness or in various kinetic calculations of mixing.

Confidence intervals express (in quantitative terms) the percentage of times that the true (yet unknown) values of the mean and standard deviation will lie within a range of specified values. These values are specified based on the statistics of a limited number of samples. The confidence intervals for the mean, μ , are the following:

$$\bar{C} - z \frac{s}{\sqrt{N}} < \mu < \bar{C} + z \frac{s}{\sqrt{N}} \quad (6.9)$$

for $N \geq 30$, where the normal distribution applies (note that z is the confidence coefficient and is read from the normal distribution table), or

$$\bar{C} - t \frac{s}{\sqrt{N}} < \sigma < \bar{C} + t \frac{s}{\sqrt{N}} \quad (6.10)$$

for $N < 30$, where the t distribution with $N - 1$ degrees of freedom applies. Tables for the normal and t distributions are found in standard statistics textbooks (e.g., Spiegel, 1991). For example, if a confidence level of 95% is chosen, the z value ($z_{0.475}$) is 1.96 and the t value ($t_{0.975}$, for 2.5% of the area lying in the “tail”) is 2.26 for 9 degrees of freedom.

The confidence intervals for variances are obtained from the χ^2 distribution:

$$\frac{s\sqrt{(N-1)}}{\chi_\alpha} < \sigma < \frac{s\sqrt{(N-1)}}{\chi_{1-\alpha}} \quad (6.11)$$

For example, for 95% confidence level and $N - 1$ degrees of freedom, the values $\chi_{0.975}$ and $\chi_{0.025}$ are taken from the relevant tables of Spiegel (1991).

Example 6.1. Confidence Intervals for the Mean and Variance

Suppose that 2% carbon black is mixed with PE in a melt extruder and that the product is pelletized and shipped in 25 kg bags. We randomly select 10 bags, extract a number of pellets, and fracture and analyze them in a microscope for carbon black particle statistics. The weight fraction of carbon black is calculated from the number of particles, and their size and density, and it was found to vary as follows in the 10 bags:

Bag #	Weight Fraction of Carbon Black
1	0.0198
2	0.0185
3	0.0202
4	0.0194
5	0.0211
6	0.0200
7	0.0204
8	0.0189
9	0.0197
10	0.0210

Estimate the ranges for the mean and the variance for 95% and 99% confidence.

Solution. The mean weight fraction of carbon black is 0.0199 and the standard deviation is 0.00083 (i.e., 4.17%

of the mean value). For 95% confidence level and 9 degrees of freedom, $t_{0.975} = 2.26$, $\chi_{0.975} = \sqrt{19} = 4.36$, and $\chi_{0.025} = \sqrt{2.7} = 1.64$. Then Eqs. 6.10 and 6.11 yield

$$0.01930 < \mu < 0.02050; \quad 0.00013 < \sigma < 0.00093$$

Thus, 95% of the time mixed PE will contain carbon black in concentration between 1.93% and 2.05%. Similarly, the standard deviation will vary in the range from 0.00013 to 0.00093. For 99% of the time the corresponding values are

$$0.01904 < \mu < 0.02076; \quad 0.00011 < \sigma < 0.00145$$



The significance tests are interconnected with the concept of hypothesis testing and Type I and II errors. Type I error is made when we reject a hypothesis that should have been accepted, and Type II error is made when we accept a hypothesis that should have been rejected. The *level of significance* of testing a given hypothesis is the maximum probability that a Type I error might occur. In practice a level of significance of 5% or 1% are customary. Thus, if we accept a 5% level of significance, we are 95% confident that the right choice was made or otherwise stated; there are about 5 out of 100 chances that a Type I error was made.

In polymer processing the significance tests are used to compare the samples with some reference material that might be a hypothetical material that is perfectly mixed, and thus it constitutes the goal of the mixing process, might have a certain desirable composition, or might be a material produced in a process that is considered for scaleup. In all those instances, the mean and the variance of the samples are compared with those of the reference material and a parameter is calculated. That parameter is then compared to tabulated values for the set level of significance. If the value of that parameter is within set limits, then the difference in values of the mean and the variance between the samples and the reference material is considered statistically nonsignificant.

In the significance tests for means, the mean and the variance of the samples are calculated using Eqs. 6.7 and 6.8, and the mean and the variance of the reference material are denoted by μ and σ^2 , respectively. If the number of samples, N , is less than 30, then the Student’s t distribution is used for the means:

$$t = \frac{\bar{C} - \mu}{\sigma / \sqrt{N}} \quad (6.12)$$

This value of t is then compared to the tabulated value of t for $N - 1$ degrees of freedom and the set level of significance. The hypothesis that the sample mean is the same as the population mean μ is not rejected if the calculated t is less than the tabulated value.

The significance test for variances is relevant to cases in which we have to decide whether two samples of sizes N and M and variances s_N^2 and s_M^2 do or do not come from the same mixture. The hypothesis that the two samples come from the same mixture will be tested using the F distribution:

$$F = \frac{s_N^2}{s_M^2} \quad (6.13)$$

For example, to test the hypothesis at the 10% level, the following relationship should be used:

$$F_{0.05} \leq \frac{s_N^2}{s_M^2} \leq F_{0.95} \quad (6.14)$$

where the F values can be found in Spiegel (1991) for $N - 1$ and $M - 1$ degrees of freedom. Note that the following relationship holds: $F_{0.05} = 1/F_{0.95}$, where the first F value has $M - 1$ and $N - 1$ degrees of freedom and the other one has $N - 1$ and $M - 1$ degrees of freedom.

Example 6.2. Test of the Hypothesis

Test the hypothesis with level of significance 10% that the samples in Example 6.1 truly represent a carbon black/PE mixture with a mean carbon black weight fraction of 0.02 and a standard deviation 0.007 (i.e., 3.5% of the mean). Assume that the standard deviation of the mixture was calculated using 25 samples.

Solution. To test the hypothesis for the mean we use Eq. 6.12, and thus the t value is equal to -0.381 . The tabulated value for $t_{0.95}$ and 9 degrees of freedom is 1.83. The hypothesis, with respect to means, is not rejected because $-1.83 < -0.381 < 1.83$. As far as the standard deviation is concerned, Eq. 6.14 applies. The calculated F value is 1.41. The tabulated F values are $F_{0.05} = 0.34$, for 24 and 9 degrees of freedom, and $F_{0.95} = 2.30$, for 9 and 24 degrees of freedom. Thus, the hypothesis with respect to standard deviations is not rejected either. ■

These statistics are also useful in the discussion on the *degree of mixing*, or *mixedness*, or *admixedness*, or *goodness of mixing*. It is obvious that the goal of the mixing process is to produce a mixture where the distribution of the minor component is statistically random. The term *perfect mixing* refers exactly to that state, or, equivalently, to the state in which the probability of appearance of the minor component at any point in the mixture is constant. Therefore, the degree of mixing measures the “distance” between the mixing state of our sample and that of the statistically random sample, and it is represented mathematically by the mixing indices.

There are more than 30 different criteria of the degree of mixedness (Fan et al., 1970), and they are tied to particular

mixing situations. Because the mixing process is a random process, statistical analysis predominates in the calculations for the degree of mixing. More frequently the variance of a spot sample taken from the mixture is compared to that of the perfectly random sample:

$$M = \frac{\sigma^2}{s^2} \quad (6.15)$$

where σ^2 is the limiting minimum value of the variance of the perfectly random sample, and M is the degree of mixing.

The index of mixedness can also be expressed as:

$$M = \frac{\sigma}{s} \quad (6.16)$$

if the variances of Eq. 6.15 are substituted by the respective square roots, that is, by the standard deviations. Lacey (1954) introduced the variance of the totally unmixed state, σ_0^2 , in his definition of the mixing index:

$$M = \frac{\sigma_0^2 - s^2}{\sigma_0^2 - \sigma^2} \quad (6.17)$$

The advantage of using this definition as opposed to that of Eq. 6.15 lies in the range of the index of mixing. Equation 6.15 yields values between $1/n$ and ∞ , whereas Eq. 6.17 attains values between 0 and 1. The same idea that transformed Eq. 6.15 to Eq. 6.16 can also be applied to Eq. 6.17.

The rate of mixing can be monitored by measuring the index of mixing at various time periods. It is obvious that as time progresses (or as the number of revolutions for a rotating mixer increases) mixing is also improving and moving toward its random state. Reference to the “unmixing” or “demixing” that might take place during mixing will not be mentioned. Lacey (1954) developed the idea that all mixing mechanisms for solids, namely, convective, diffusional (see Problem 6B.1), and shear, are consistent with a first-order rate of reaction:

$$M = 1 - e^{-kt} \quad (6.18)$$

where k is the rate constant (unit of k is s^{-1}). The constant k can be calculated from experimental data of the index of mixing as a function of time and it reflects the quality of the mixer and the suitability of the chosen conditions of mixing. It is not unusual for the variance to reach an asymptotic value different from the corresponding value for the random mixture, because large density differences cause stratification inside the mixer. In such cases, the definition of the index of mixing should be altered to accommodate this difference.

The statistical description of mixing given in this section is restricted to a two-component system for simplicity. Of course, a four-component system can be considered as a

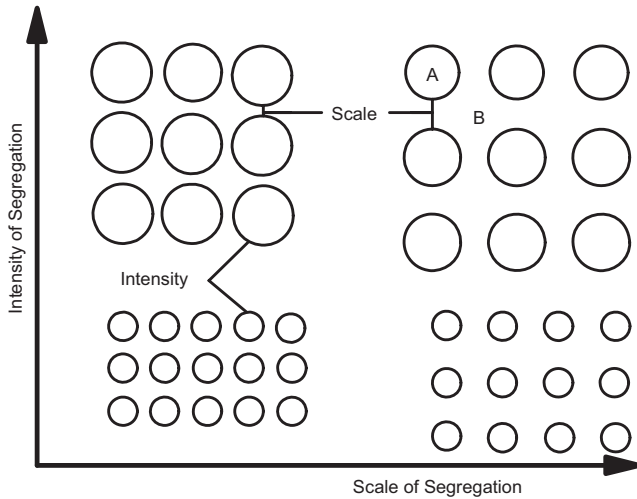


FIGURE 6.5 Intensity and scale of segregation.

two-component system if the second, third, and fourth components are considered as a single entity. If this is not an accurate description of the reality, then the use of Markov chains is inevitable, and the mathematics involved are complex. Such analysis goes beyond the scope of this textbook.

6.2.2 Scale and Intensity of Segregation

The texture of a sample is characterized by two parameters (Danckwerts, 1952): (1) *scale* and (2) *intensity* of segregation. The two parameters can be visualized as shown in Figure 6.5. We assume that we have mixed two components, A, which is included in the circles, and B, which is lying in the interstices. The scale of segregation is the measure of the distance between clumps of the same component. It can also be defined as a measure of the size of undistributed parts of the components (Mohr et al., 1957) or as the length scale of the distance between similar interfaces. By following the latter definition we see that the distance between clumps or circles of component A increases as we move toward the right in Figure 6.5, that is, the scale of segregation increases. In general, mechanical energy, through deformation, is necessary for the reduction of the scale of segregation. Typical mechanisms include shear, kneading, break up, and turbulence.

The intensity of segregation refers to the difference in concentration of one component between areas of component A and B. The intensity is reduced as component A diffuses out of the circles into the area of component B or as the size of the clumps of A is reduced due to the diffusion of A. If the two components do not have any difference in color, the intensity of segregation can be pictured as the difference in the size of clumps A (Fig. 6.5). If there is a difference in color between A (black) and B (white), then the minimum intensity of segregation is achieved when the black has been

spread into the white, producing a grey color for the sample. Clearly, as Mohr et al. (1957) pointed out, the reduction in intensity is affected only by diffusion and not by mechanical mixing. Thus, although diffusion cannot change the shape of the clumps (deformation can do that), it can produce grey color when black and white meet. Note that deformation changes spherical clumps into elongated shapes, breaks them or changes their patterns, but it never causes any diffusional process to take place.

Both reduction of scale and intensity produce uniformity, and so the quality of mixing, as far as texture is concerned, depends on both quantities. Note that the maximum reduction of the scale is achieved when the distance between interfaces approaches the length scale of the ultimate particles (or ultimately molecular scales), and the maximum reduction in intensity is obtained when the minor component is uniformly mixed throughout the major component.

Scale and intensity have also statistical representations. The intensity can be defined mathematically as

$$I = \frac{s^2}{\sigma_0^2} \quad (6.19)$$

and expresses the difference of concentration of the minor component from the average value normalized by the variance of the completely segregated (totally unmixed; Eq. 6.17) system. Its values range from 1 for a completely unmixed system to 0 for a uniformly mixed system. This definition bears resemblance to the definition of the indices of mixing. Usually the intensity for polymer systems, even in the melt state, is close to 1, because diffusion is extremely slow.

To define the scale of segregation we need to define first the correlation function, $R(\mathbf{r})$. It is very similar to the variance in the sense that the variance measures the concentration difference of a point and the mean value, whereas the correlation function considers the concentration difference between two points \mathbf{r} distance away. Thus, $R(\mathbf{r})$ is given by

$$R(\mathbf{r}) = \frac{1}{N} \sum_{i=1}^N [(C_i(\mathbf{x}) - \bar{C})(C_i(\mathbf{x} + \mathbf{r}) - \bar{C})] \quad (6.20)$$

where C_i is the concentration of the i th sample, \bar{C} is the mean concentration, and N is the total number of samples. When \mathbf{r} equals $\mathbf{0}$ then the correlation function becomes approximately (for large N) equal to the variance:

$$R(\mathbf{0}) = \frac{N-1}{N} s^2 \cong s^2 \quad (6.21)$$

The correlation coefficient is obtained by the normalization of the correlation function with the variance:

$$\rho(\mathbf{r}) = \frac{R(\mathbf{r})}{s^2} \quad (6.22)$$

so that $\rho(\mathbf{0})$ is equal to unity for sufficiently large N . The graph of the correlation coefficient is called a *correlogram*. In isotropic mixtures, we can neglect the vector form of r and substitute it with its scalar form. By doing this we presuppose that $\rho(r)$ is the average of $\rho(\mathbf{r})$ over all possible orientations of the vector \mathbf{r} .

The values of the correlation coefficient range from -1 to 1 . When the origin and the end of the vector \mathbf{r} lie in different components, the correlation coefficient attains a value of -1 , and the correlation is considered to be perfectly negative. The correlation is considered perfectly positive when both the origin and the end of the \mathbf{r} vector lie in the same component (either minor or major), and consequently the correlation coefficient equals unity. Finally, the correlation coefficient equals zero when the correlation is random or, equivalently, when knowledge of the composition at the origin provides no information about the composition at the end of the vector.

The correlation coefficient is calculated by the technique of *dipole* or *needle throwing*. Consider a mixture of carbon black in PE with \bar{C} average carbon black concentration. We fracture one pellet, and we take a photograph of the surface with the aid of a high resolution scanning electron microscope. We take a needle of length r and drop it onto the photograph. Four events can take place: (1) both ends could land in carbon black particles with probability P_{11} ; (2) both ends could land in the PE matrix with probability P_{22} ; (3) the first end lands in carbon black and the second in PE with probability P_{12} ; and (4) the opposite of the previous event with probability P_{21} . Nadav and Tadmor (1973) calculated the correlation coefficient as

$$\rho(r) = \frac{1 - \bar{C}}{\bar{C}} P_{11} + \frac{\bar{C}}{1 - \bar{C}} P_{22} - P_{12} - P_{21} \quad (6.23)$$

A typical example of the application of that formula is given in Example 6.3. Other examples and the derivation of Eq. 6.23 are given in Nadav and Tadmor (1973), Tadmor and Gogos (1979), and Tucker (1981).

Example 6.3. Calculation of the Correlation Coefficient

Consider a mixture of carbon black in PE and assume that the mixture can be represented as a set of unit cells of radius A . A carbon black particle of radius α is at the center of the cell, and it is surrounded by PE matrix. The unit cell is shown in Figure 6.6a. Approximate the correlation coefficient for this mixture based on Eq. 6.23 for small r compared to either α or A (i.e., ignore terms of order r^2 and higher).

Solution. Divide the unit cell into four regions: region I is inside the particle with radius $\alpha - r$; region II is a spherical shell with outside radius α and inside $\alpha - r$; region III is a spherical shell in the PE matrix with inside radius α and outside $\alpha + r$; and finally region IV has inside radius $\alpha + r$

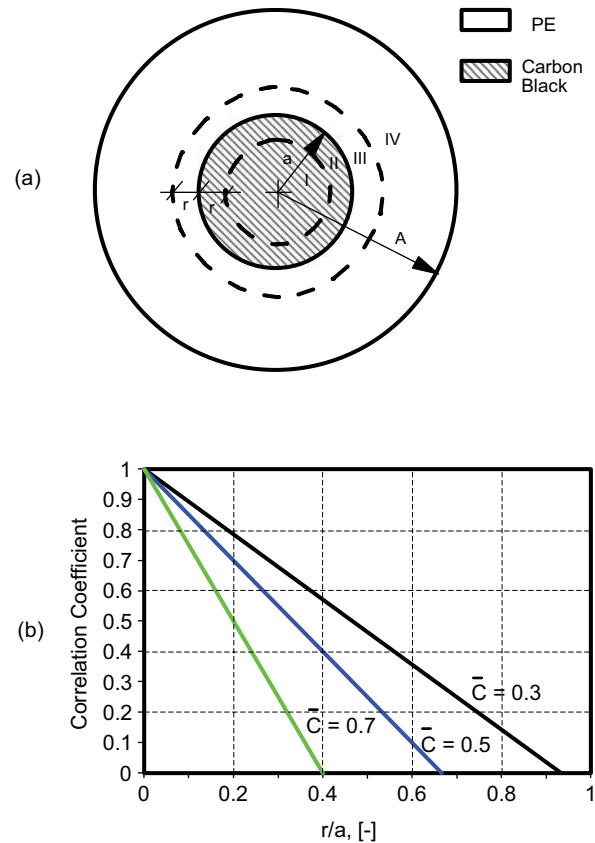


FIGURE 6.6 (a) Unit cell of a carbon black particle in a PE matrix. (b) Correlation coefficient as a function of the dimensionless radial distance.

and outside radius A . The probabilities of the various ways that a needle of length r might land on this mixture can be calculated. Note that although the cell is pictured in its two-dimensional form in Figure 6.6a, the solution will be based on the real three-dimensional picture.

The probability that both needle ends will fall in carbon black depends on the probability that the first end will fall in regions I and II in combination with the probability that the second end will fall in carbon black regions. The probability that the first end will fall in region I is the ratio of the region's volume to the total cell volume:

$$P(\text{I}) = \frac{V_{\text{I}}}{V_{\text{cell}}} = \frac{(\alpha - r)^3}{A^3} \cong \bar{C} - 3\bar{C}\frac{r}{\alpha} \quad (6.24)$$

The probability that its second end will fall in carbon black is 1. The probability that the first end will fall in region II is similarly equal to the ratio of volumes:

$$P(\text{II}) = \frac{V_{\text{II}}}{V_{\text{cell}}} = \frac{\alpha^3 - (\alpha - r)^3}{A^3} \cong 3\bar{C}\frac{r}{\alpha} \quad (6.25)$$

Now the conditional probability that the second end falls in carbon black region is $3/4$. This is calculated by drawing a sphere of radius r centered at a radial distance x from the cell center. That probability is then calculated as the ratio of the area of the sphere inside the carbon black to the total area of the sphere averaged over all possible x (i.e., from $r - \alpha$ to α).

The probability that both ends fall in carbon black is

$$P_{11} = P(\text{I})x + P(\text{II})x(3/4) \cong \bar{C} - \frac{3}{4}\bar{C}\frac{r}{\alpha} \quad (6.26)$$

The other terms in Eq. 6.23 can be calculated similarly. The correlation coefficient is thus calculated as:

$$\rho(r) \cong 1 - \frac{3}{4}\frac{r}{\alpha}\frac{1}{1 - \bar{C}} \quad (6.27)$$

The correlogram for various values of \bar{C} is shown in Figure 6.6b. It is linear and it intersects the x axis at $4\alpha(1 - \bar{C})/3$. ■

The linear scale of segregation can now be defined in terms of the correlation coefficient:

$$S_L = \int_0^{\infty} \rho(r) dr \quad (6.28)$$

and it represents the area under the correlation coefficient curve. Similarly, the volumetric scale of segregation is defined as

$$S_V = 2\pi \int_0^{\infty} \rho(r)r^2 dr \quad (6.29)$$

In the example of a clumpy mixture, the linear scale represents the average size, and the volumetric scale represents the average volume of the clumps. Note that for the same example there is no difficulty in evaluating the integral, because the correlation coefficient becomes zero above some value of r . Typical values of the ratio of the linear scale of segregation to the length scale of the structure are: (1) 0.237 for a planar checkered board pattern; (2) 0.250 for an alternating layered structure (one dimensional) of equal layer thickness; and (3) 0.380 for a collection of spheres.

An alternative description of the texture is its spectral description or power spectrum, $P(n)$ (Tucker, 1991):

$$P(n) = \int_{-\infty}^{+\infty} R(r)e^{-2\pi nr} dr \quad (6.30)$$

The importance of the power spectrum stems from the fact that it can be calculated directly from the concentration field and that it can easily be inverted into the correlation function via the fast Fourier transform (FFT) method.

6.2.3 Mixing Measurement Techniques

The goal of mixing measurement techniques is the acquisition and statistical analysis of data collected from samples in order to evaluate the quality of the process and the final product. These techniques are usually time consuming and laborious. One common problem in measurement techniques that examine a planar section of the product is that two-dimensional information should be transformed into three-dimensional information. This is done with the help of *stereology science* (Underwood, 1977).

The measurement of the variance indicates the quality of the mixing. If the mixture is homogeneous, the variance is small and the average composition is close to \bar{C} . To measure the variance we need to withdraw samples from the mixing device or cut samples from the final product. Extraction of samples with a hypodermic needle (Rotz and Suh, 1976), sampling by pumping the mixture through a special sampling device (Tucker and Suh, 1980a), and slicing of the solidified mixture (Hall and Godfrey, 1965) were reported in the literature. As far as the measurement technique is concerned, light transmittance (Nadav and Tadmor, 1973), electrical conductivity (Tucker and Suh, 1980b), titration, and particle counting are the most extensively used techniques.

Lately, computer analysis is used broadly for the evaluation of the state of mixing. Sectioning, acquisition, and analysis are the three steps involved. The acquisition of the digital image is done with a television camera, a video digitizer, and a computer. The camera is attached to the microscope, and its analog picture is translated into a digital one via the video digitizer. The digital intensity values are now stored into large arrays in a computer. That large array of numbers contains the light intensity of each pixel in terms of its red, green, and blue components. Typical image analysis systems can digitize the screen into 512×512 or 1024×1024 pixels. Howland and Erwin (1983) used the *laser line scanning technique*, which consists of illuminating the picture with a laser light source and measuring the reflectivity of the material with a photodiode.

The analysis of the image requires the knowledge of the correspondence between composition and color (if that is not linear, a calibration curve is required). Furthermore, if diffusion has not altered the composition at the various points, then each pixel is made dark (e.g., minor component) or light (e.g., major component) based on a *threshold* value. The power spectrum is now calculated from the composition data and an FFT algorithm. The correlation function is then calculated by using the inverse Fourier transform of the power spectrum and the scale and intensity of segregation are then

computed using the equations of Section 6.2.2. It should be mentioned at this point that the information which is collected with the image analysis system is limited to distances smaller than the height and the width of the screen and the resolution is bound by the size of the pixel. However, the great advantage of these systems is their ability to analyze many images fast and with minimum labor.

6.3 STRIATION THICKNESS AND LAMINAR MIXING

Mixing of polymer melts cannot be assisted by either diffusion or turbulence. The absence of diffusion makes the two components and their interface easily identifiable. Consequently, the interfacial area per unit volume (or intermaterial area density or specific interfacial area), A_v , can be used as a measurement of the extent of mixing, as was suggested by Spencer and Wiley (1951), as well as others. A special case of a polymer mixture is a layered or lamellar mixture shown in Figure 6.7. This mixture can be produced by either laminar flow (e.g., in a typical single-screw extruder) or ordered rearrangement with plug flow (e.g., motionless mixers, Fig. 6.2). Using the terminology of Section 6.2.1 the lamellar structure comprises the texture of the mixture. The scale of segregation of an equal thickness alternating structure was mentioned to be one-fourth of the thickness, but the scale is not important in this context, because it is a statistical measure, and the layered structure is ordered. Of course, the scale of segregation is important for polymer systems with a wide distribution of layer thickness.

The striation thickness concept was first introduced by Mohr et al. (1957) and analyzed extensively by Ranz (1979) and Ottino et al. (1979, 1981). The striation thickness, δ , is defined as one-half (Ottino et al., 1979) of the thickness of the repeating unit (i.e., one-half of the sum of the thickness of two adjacent layers of components A and B). Note that in some references the striation thickness is defined as the sum

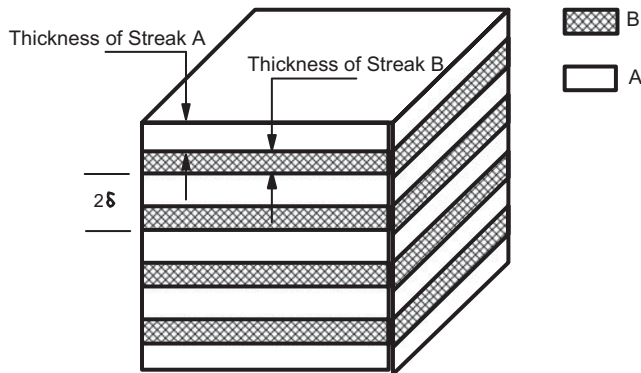


FIGURE 6.7 Layered structure and definition of striation thickness δ .

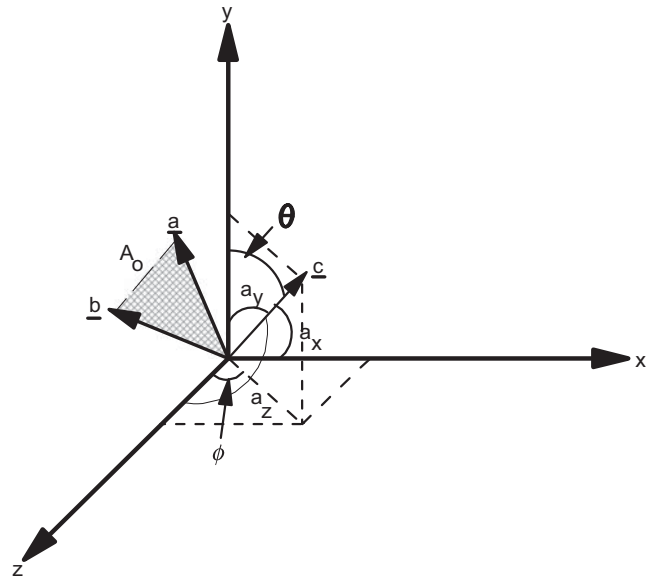


FIGURE 6.8 Interfacial element A_0 in a Cartesian coordinate system at time $t = 0$.

of the thickness of two adjacent layers and thus their striation thickness is twice that we use here. The interfacial area per unit volume, A_v , and the striation thickness, δ , are related as follows for a large number of striations:

$$A_v = \frac{1}{\delta} \tag{6.31}$$

As mixing progresses, the interfacial area per unit volume increases and the striation thickness decreases. If there is a distribution of striation thickness then not only the mean but also the variance should be taken into consideration for the quality of mixing calculations. In Section 6.3.1 the interfacial area growth, or equivalently the striation thickness reduction, is calculated from geometrical arguments.

6.3.1 Striation Thickness Reduction from Geometrical Arguments

The interfacial area per unit volume changes as a function of the strain applied to the system. Consider an interface A_0 as shown in Figure 6.8. This interface is formed by vectors **a** and **b**:

$$\mathbf{a} = x_a \delta_x + y_a \delta_y + z_a \delta_z \tag{6.32}$$

and

$$\mathbf{b} = x_b \delta_x + y_b \delta_y + z_b \delta_z \tag{6.33}$$

where δ_x , δ_y , and δ_z are the unit vectors along the x , y , and z axes, respectively, and x_a , y_a , z_a and x_b , y_b , z_b are the

components of \mathbf{a} and \mathbf{b} . The vector \mathbf{c} is perpendicular to the plane A_0 and equal to

$$\mathbf{c} = \mathbf{a} \times \mathbf{b} \quad (6.34)$$

The magnitude of \mathbf{c} is twice the area of A_0 :

$$|\mathbf{c}| = 2A_0 \quad (6.35)$$

and it forms α_x , α_y , and α_z angles with the coordinate axes x , y , and z , respectively.

The area A_0 is now subjected to strain with principal directions in the Cartesian coordinates and with principal elongation ratios λ_x , λ_y , and λ_z (Erwin, 1978a). The area A_0 will become A , and the vectors defining A are \mathbf{a}' , \mathbf{b}' , and \mathbf{c}' , so that

$$|\mathbf{a}' \times \mathbf{b}'| = |\mathbf{c}'| = 2A \quad (6.36)$$

The new vectors \mathbf{a}' and \mathbf{b}' are

$$\begin{aligned} \mathbf{a}' &= (x_a \lambda_x) \delta_x + (y_a \lambda_y) \delta_y + (z_a \lambda_z) \delta_z \\ \mathbf{b}' &= (x_b \lambda_x) \delta_x + (y_b \lambda_y) \delta_y + (z_b \lambda_z) \delta_z \end{aligned} \quad (6.37)$$

Substitution of these expressions into Eq. 6.36 yields

$$\begin{aligned} A &= \frac{1}{2} \left\{ [\lambda_y \lambda_z (y_a z_b - z_a y_b)]^2 + [\lambda_z \lambda_x (z_a x_b - x_a z_b)]^2 \right. \\ &\quad \left. + [\lambda_x \lambda_y (x_a y_b - y_a x_b)]^2 \right\}^{1/2} \end{aligned} \quad (6.38)$$

The above expression can be written equivalently as

$$A = \frac{1}{2} \sqrt{(\lambda_y \lambda_z x_c)^2 + (\lambda_z \lambda_x y_c)^2 + (\lambda_x \lambda_y z_c)^2} \quad (6.39)$$

Our primary interest is in the calculation of the change of the interface A_0 , and thus we form the ratio of the interface after mixing has started to the initial interface (at time $t = 0$), which is also called the "mixing number" frequently in the literature:

$$\left[\frac{A}{A_0} \right]^2 = \frac{(\lambda_y \lambda_z x_c)^2 + (\lambda_z \lambda_x y_c)^2 + (\lambda_x \lambda_y z_c)^2}{|\mathbf{c}|^2} \quad (6.40)$$

The angles α_x , α_y , and α_z can be expressed in terms of the components of the vector \mathbf{c} as

$$\cos \alpha_x = \frac{x_c}{|\mathbf{c}|}; \quad \cos \alpha_y = \frac{y_c}{|\mathbf{c}|}; \quad \cos \alpha_z = \frac{z_c}{|\mathbf{c}|} \quad (6.41)$$

and they follow the relationship of the directional cosines, that is,

$$\cos^2 \alpha_x + \cos^2 \alpha_y + \cos^2 \alpha_z = 1 \quad (6.42)$$

Equations 6.40 and 6.41 can be combined to give

$$\left[\frac{A}{A_0} \right]^2 = (\lambda_y \lambda_z \cos \alpha_x)^2 + (\lambda_z \lambda_x \cos \alpha_y)^2 + (\lambda_x \lambda_y \cos \alpha_z)^2 \quad (6.43)$$

If the deformation is considered to preserve the volume of the system (incompressible materials), then

$$\lambda_x \lambda_y \lambda_z = 1 \quad (6.44)$$

Substituting this equation into Eq. 6.43 yields

$$\left[\frac{A}{A_0} \right]^2 = \frac{\cos^2 \alpha_x}{\lambda_x} + \frac{\cos^2 \alpha_y}{\lambda_y} + \frac{\cos^2 \alpha_z}{\lambda_z} \quad (6.45)$$

This is similar to the expression developed by Spencer and Wiley (1951) for unidirectional shear strain. Another form of this expression can be obtained by using the equation of directional cosines, Eq. 6.42, and Eq. 6.43:

$$\begin{aligned} \left[\frac{A}{A_0} \right]^2 &= (\lambda_x \lambda_y)^2 + \lambda_y^2 (\lambda_z^2 - \lambda_x^2) \cos^2 \alpha_x \\ &\quad + \lambda_x^2 (\lambda_z^2 - \lambda_y^2) \cos^2 \alpha_y \end{aligned} \quad (6.46)$$

Next, we apply Eq. 6.46 to simple deformations to show the effect of various types of deformation on mixing.

Planar Elongation (or Pure Shear). Suppose that we stretch a material surface in the x direction while we constrain it in the z direction. The resulting flow is called planar elongational flow (plane extensional flow; plane strain; see also Section 3.1.1). The polymer fluid experiences such flow in the entrance regions to slit dies and nips between rollers. The elongation ratios are

$$\lambda_x = \lambda_0; \quad \lambda_y = \frac{1}{\lambda_0}; \quad \lambda_z = 1 \quad (6.47)$$

Equation 6.46 becomes

$$\left[\frac{A}{A_0} \right]^2 = 1 + \left(\frac{1}{\lambda_0^2} - 1 \right) \cos^2 \alpha_x + (\lambda_0^2 - 1) \cos^2 \alpha_y \quad (6.48)$$

For large elongation ($\lambda_0 \gg 1$) and for $\cos \alpha_x \neq 0$,

$$\frac{A}{A_0} = \lambda_0 |\cos \alpha_y| \quad (6.49)$$

The maximum value of the interface growth is achieved when the interface is normal to the minimum principal value; that

is, \mathbf{c} is in the direction of y ($\cos \alpha_y = 1$). The maximum value is

$$\left[\frac{A}{A_0} \right]_{\max} = \lambda_0 \quad (6.50)$$

If the orientation of the material interfaces at the entrance of the mixer is random, then the effect of planar elongation on the interfacial area is determined by averaging Eq. 6.49 over all possible orientations. To obtain that, we should evaluate the angles α_x and α_y in terms of spherical coordinates with angles ϕ and θ (see Fig. 6.8):

$$\cos \alpha_x = \sin \phi \sin \alpha_y; \quad \alpha_y = \theta \quad (6.51)$$

The average is now obtained by integration:

$$\left[\frac{A}{A_0} \right]_{\text{avg}} = \frac{1}{4\pi} \int_0^{2\pi} \int_0^\pi \sqrt{1 + \sin^2 \theta \sin^2 \phi \left(\frac{1}{\lambda_0^2} - 1 \right) + \cos^2 \theta (\lambda_0^2 - 1) \sin \theta} d\theta d\phi \quad (6.52)$$

This expression is evaluated numerically, and for large values of λ_0 it follows that

$$\left[\frac{A}{A_0} \right]_{\text{avg}} = \frac{\lambda_0}{2} \quad (6.53)$$

This means that a mixer which imposes planar elongation on initially randomly oriented fluid interfaces increases the initial interfacial area by a factor of $(\lambda_0/2) - 1$ or, equivalently, decreases the striation thickness by a factor of $(\lambda_0/2) - 1$. If the initial orientation is normal to the minimum principal elongation value, the striation thickness decreases by a factor of $\lambda_0 - 1$.

The strain, ε (equal to $\dot{\varepsilon}t$, where $\dot{\varepsilon}$ is the strain rate), imposed on the material is related to the increase of linear distance in the x direction by

$$\frac{dl}{l} = \varepsilon \quad (6.54)$$

which can be integrated to give $x = x_0 \exp(\varepsilon)$. The elongation ratio in the x direction, λ_0 , can then be related to strain, ε , by

$$\lambda_0 = e^\varepsilon = e^{\dot{\varepsilon}t} \quad (6.55)$$

Equation 6.50 can be expressed now in terms of the total strain ε :

$$\left[\frac{A}{A_0} \right]_{\max} = e^\varepsilon \quad (6.56)$$

which shows that the maximum interface growth depends on the exponential of the total applied elongation strain. Similarly, the average interface growth equals one-half the exponential of the applied strain.

Uniaxial (or Pure) Elongation. Suppose that we stretch an interface in the x direction without imposing any constraints on y and z directions. The resulting flow is called *uniaxial elongational flow* (uniaxial extensional flow; a classic example of a mixer creating pure elongational stretch is a taffy puller; see also Section 3.1.1). The elongation ratios are now

$$\lambda_x = \lambda_0; \quad \lambda_y = \lambda_z = \frac{1}{\sqrt{\lambda_0}} \quad (6.57)$$

Substitution of these ratios into Eq. 6.46 gives

$$\left[\frac{A}{A_0} \right]^2 = \lambda_0 + \left(\frac{1}{\lambda_0^2} - \lambda_0 \right) \cos^2 \alpha_x \quad (6.58)$$

If the interface is aligned with the y axis, then $\cos \alpha_x = 0$, and thus the maximum value of the interface growth is

$$\left[\frac{A}{A_0} \right]_{\max} = \sqrt{\lambda_0} \quad (6.59)$$

Equation 6.58 can be integrated numerically over all possible orientations to give, for large λ_0

$$\left[\frac{A}{A_0} \right]_{\text{avg}} \cong \frac{4}{5} \sqrt{\lambda_0} \quad (6.60)$$

Because this process is not symmetrical about $\lambda_0 = 1$, for deformations $\lambda_0 \ll 1$ it is found that

$$\left[\frac{A}{A_0} \right]_{\text{avg}} \cong \frac{4}{5} \frac{1}{\lambda_0} \quad (6.61)$$

In terms of the total applied strain, ε , the arguments are the same as those developed for planar elongation. Thus, the maximum and the average interface growth depend on $\exp(\varepsilon/2)$ for very large values of λ_0 .

Simple Shear. The most frequently encountered flow situation in mixing is that of shear. It can be imparted to the fluid by Couette or Poiseuille flow. In principle, we can follow the same ideas developed in the previous two cases, but now the

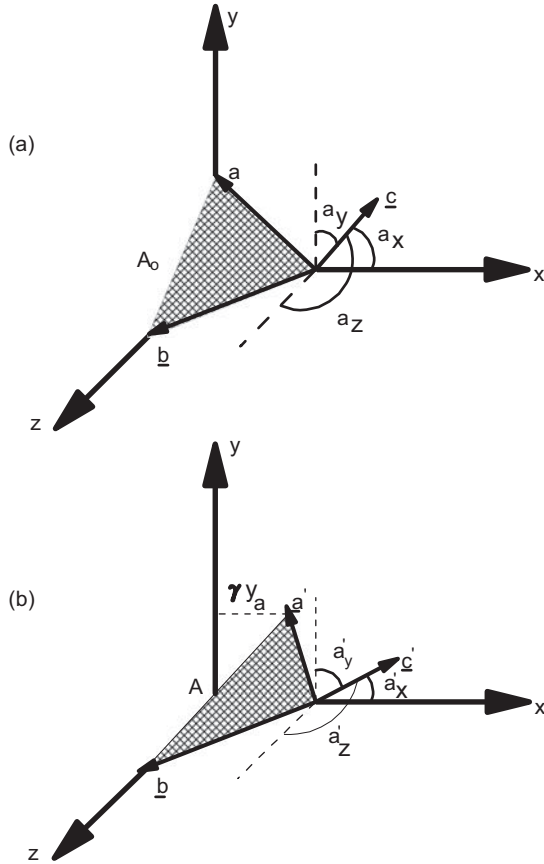


FIGURE 6.9 Interfacial element in a shearing experiment. (a) at $t = 0$. (b) After a shear strain, γ , has been applied to the interface.

principal axes change as a function of shear, and the analysis is complicated. To simplify the analysis we define the interface A_0 as in Figure 6.9a, so that \mathbf{a} lies in the x - y plane and \mathbf{b} lies in the x - z plane (McKelvey, 1962). The shear direction is along the x axis so that \mathbf{b} does not change. A shear strain γ is applied.

The new vector, \mathbf{a}' , which defines the interface A , can be expressed as (Fig. 6.9b):

$$\mathbf{a}' = (x_a + \gamma y_a)\delta_x + (y_a)\delta_y \quad (6.62)$$

so that

$$A = \frac{1}{2}\sqrt{(x_c)^2 + (y_c - \gamma x_c)^2 + (z_c)^2} \quad (6.63)$$

The interface growth function, $f(\gamma) = A/A_0$, becomes

$$\left[\frac{A}{A_0}\right]^2 = \frac{(x_c)^2 + (y_c - \gamma x_c)^2 + (z_c)^2}{|\mathbf{c}|^2} \quad (6.64)$$

Using the expressions of Eq. 6.41 for the directional cosines, we get

$$\left[\frac{A}{A_0}\right]^2 = 1 - 2\gamma \cos \alpha_x \cos \alpha_y + \gamma^2 \cos^2 \alpha_x \quad (6.65)$$

which is exactly the expression proposed by Spencer and Wiley (1951). Equation 6.65 shows that the interfacial area growth depends on its initial orientation and the magnitude of the shear strain imposed by the mixer. When $\alpha_x = 90^\circ$, vector \mathbf{c} lies in a plane parallel to the y - z plane and shear strain distorts the interface without changing its area. When $\alpha_y = 90^\circ$, vector \mathbf{c} lies in the x - z plane and shear strain distorts the interface and changes its area. In the latter case the maximum change in area occurs when the interface lies in the y - z plane.

For large values of γ , Eq. 6.65 reduces to

$$f(\gamma) = \left[\frac{A}{A_0}\right] = \gamma \cos \alpha_x \quad (6.66)$$

This equation indicates that the interfacial area growth function in a material undergoing large shear proceeds linearly with shear strain. Numerical integration of the above equation over all possible orientations following the steps described for elongational strain yields

$$f(\gamma) = \frac{\gamma}{2} \quad (6.67)$$

Equation 6.65 can be used to estimate the optimal interface orientation for a maximum in the interface growth function. Differentiation of that expression with respect to γ , at $\gamma = 0$, yields

$$\frac{dA}{d\gamma} = -A \cos \alpha_x \cos \alpha_y \quad (6.68)$$

where $A = A_0$. The maximum increase of the interfacial area is achieved at the minimum of the product of the directional cosines $\cos \alpha_x$ and $\cos \alpha_y$ (note the negative sign in Eq. 6.68). The minimum of the product occurs at $\alpha_x = 135^\circ$ and $\alpha_y = 45^\circ$, and it is equal to $-1/2$, so that

$$\left[\frac{A}{A_0}\right]_{\max} = e^{\gamma/2} \quad (6.69)$$

To achieve this maximum interface growth we should orient the interface so that its normal and the y axis form an angle of 45° and its normal and the x axis form an angle of 135° . Then, we shear the interface stepwise with step shear strain equal to a small fraction of the total shear strain γ and we reorient the interface before we proceed to the next step. This procedure is shown in the following example.

Example 6.4. Interface Growth Function with Reorientation for Simple Shear Flow

Compare the interface growth function for the following cases: (a) optimum initial orientation and one step shear strain, and (b) initial orientation $\alpha_y = 45^\circ$ and $\alpha_x = 135^\circ$, N steps, and reorientation after each step. The total shear strain is 10. Consider 5 and 20 steps for case (b).

Solution. The optimum initial orientation in case (a) is: $\alpha_x = 0^\circ$ and $\alpha_y = 90^\circ$. Equation 6.65 yields

$$\left[\frac{A}{A_0} \right]_a = \sqrt{1 + \gamma^2} \quad (6.70)$$

For $\gamma = 10$, the interface growth function is equal to 10.05 in case (a). For case (b), $\cos \alpha_y = -\cos \alpha_x = 0.707$ and the total shear strain is subdivided into N steps so that in every step the applied strain is γ/N . Thus, the interface growth function at the end of step j is calculated from Eq. 6.65 as

$$\left[\frac{A_j}{A_{0j-1}} \right]_b = \sqrt{1 + 2\frac{\gamma}{N} + \frac{1}{2} \left[\frac{\gamma}{N} \right]^2} \quad (6.71)$$

At the end of that process the total interface growth function is

$$\left[\frac{A}{A_0} \right]_b = \left[1 + 2\frac{\gamma}{N} + \frac{1}{2} \left[\frac{\gamma}{N} \right]^2 \right]^{N/2} \quad (6.72)$$

For $N = 10$ and 20 the growth function is equal to 97.66 and 128.39, respectively. Note that its maximum is $e^{10/2} = 148.41$, which is about 14 times larger than case (a). If we increase the number of steps, the growth function will approach the maximum value, because at large N the following relationship (keeping only terms of order γ/N and larger) holds:

$$\left(1 + \frac{\gamma}{N} \right)^{N/2} = \left(1 + \frac{\gamma/2}{N/2} \right)^{N/2} \rightarrow e^{\gamma/2} \quad (6.73)$$

In Table 6.1 we summarize the values of the average (integrated over all possible orientations) and maximum interface growth function $f(\gamma$ or $\varepsilon)$ for planar and uniaxial elongation,

TABLE 6.1 Interface Growth Function for Various Types of Strain

Type of Strain	Interface Growth Function A/A_0	
	Maximum	Average
Planar elongation	$\exp(\varepsilon)$	$\frac{1}{2} \exp(\varepsilon)$
Uniaxial elongation	$\exp(\varepsilon/2)$	$\frac{4}{5} \exp(\varepsilon/2)$, for $\lambda_0 \gg 1$
		$\frac{4}{5} \exp(-\varepsilon)$, for $\lambda_0 \ll 1$
Simple shear	γ	$\gamma/2$

as well as for simple shear cases. It is clear that, in terms of interface growth (or equivalently striation thickness), elongational flows are much more efficient compared to shear flows. For example, a reduction in striation thickness of 3 orders of magnitude (from a 3 mm polymer pellet down to 3 μm striations) is achieved by either a total shear strain of 2000 or a total elongation strain of about 8 for random initial orientation. This reduction in striation thickness can be obtained in 20 s in a shear field at an average shear rate of 100 s^{-1} or in 80 ms in an elongational flow field having an average rate of 100 s^{-1} .

The three strain fields, planar elongation, uniaxial elongation, and simple shear, are compared next to determine the flow pattern most favorable in terms of power consumption. High power consumption is unfavorable because of its high cost and requirements for specific equipment. Integration of the mechanical energy equation (Section 2.3) over the volume of the mixer shows that the specific power consumption (power consumption per unit volume), P_v , is equal to the viscous dissipation,

$$P_v = -\frac{1}{2} \sum_i \sum_j \tau_{ij} \dot{\gamma}_{ji} \quad (6.74)$$

where $i, j = x, y$, and z ; τ_{ij} is the ij component of the extra stress tensor $\boldsymbol{\tau}$ and $\dot{\gamma}_{ji}$ is the ji component of the rate-of-strain tensor, $\dot{\boldsymbol{\gamma}}$. Combining Eqs. 6.74, 2.59, and the components of the rate-of-strain tensor from Table 2.10, we get the following expression for the specific power of a Newtonian fluid:

$$\begin{aligned} \frac{P_v}{\mu} = 2 & \left[\left(\frac{\partial v_x}{\partial x} \right)^2 + \left(\frac{\partial v_y}{\partial y} \right)^2 + \left(\frac{\partial v_z}{\partial z} \right)^2 \right] + \left(\frac{\partial v_x}{\partial y} + \frac{\partial v_y}{\partial x} \right)^2 \\ & + \left(\frac{\partial v_y}{\partial z} + \frac{\partial v_z}{\partial y} \right)^2 + \left(\frac{\partial v_x}{\partial z} + \frac{\partial v_z}{\partial x} \right)^2 \end{aligned} \quad (6.75)$$

where μ is the fluid viscosity and v_x , v_y , and v_z are the three velocity components.

The above expression can be applied to idealized systems with three types of deformation: planar (plel), uniaxial (unel) extensional, and simple shear (ss) mixers. For a mixing device dominated by planar elongational flow, the distances along the x axis are related to strain or strain rate by

$$x = x_0 e^\varepsilon = x_0 e^{\dot{\varepsilon} t} \quad (6.76)$$

This expression, along with the expressions for the distances along the other axes, upon differentiation yield the following velocity profile:

$$v_x = \frac{dx}{dt} = \dot{\varepsilon} x; \quad v_y = -\dot{\varepsilon} y; \quad v_z = 0 \quad (6.77)$$

This velocity profile is the same as that of Eq. 3.2 if you account for the difference in axes. The specific power, P_v , is calculated by taking appropriate derivatives of the velocity field and substituting them into the power expression (Eq. 6.75):

$$(P_v)_{\text{plrel}} = 4\mu\dot{\epsilon}^2 \quad (6.78)$$

For uniaxial elongational flow we find that

$$(P_v)_{\text{unel}} = 3\mu\dot{\epsilon}^2 \quad (6.79)$$

For simple shear flow we find that

$$(P_v)_{\text{unel}} = \mu\dot{\gamma}^2 \quad (6.80)$$

We can now make an assessment of the efficiency of the three types of flows to mix materials. Suppose we need to prepare a polymer blend with striation thickness of the minor component in the final product not more than $3 \mu\text{m}$. The pellets of the minor component fed into the flowing major component have a characteristic length of 3 mm . If we allow the components to stay in the flow field no more than 10 s , the ratio of the specific power for simple shear flow to that of the uniaxial elongational flow and to that of the planar elongational flow is

$$(P_v)_{\text{ss}} : (P_v)_{\text{unel}} : (P_v)_{\text{plrel}} \cong 17,309 : 2.64 : 1 \quad (6.81)$$

Hence, shear flow is significantly less efficient than shear-free extensional flows in mixing. Similar results for a power-law fluid can be obtained (see Problem 6A.10).

6.3.2 Striation Thickness Reduction from Kinematical Arguments

A more systematic approach for the calculation of the striation thickness and mixing efficiency was presented by Ottino and co-workers (1979, 1981). They developed the mathematical formulation for the calculation of the lineal and areal stretch of a material line and area, respectively, subjected to any deformation gradient field. In this text we use the formulation for the lineal stretch because it is easier to apply and correlates to the areal stretch by a simple relation. We should emphasize at this point that the formulation is valid in the absence of interfacial forces between minor and major components. This is true for systems with negligible interfacial tension forces, such as, for systems with either negligible interfacial tension or large length scale or both.

Suppose that a polymer melt is processed in a mixer which deforms the “particles” of the melt. At time $t = 0$ we identify a differential material line at position \mathbf{x}_0 of length $|d\mathbf{x}_0|$ and orientation \mathbf{m}_0 . After a deformation (e.g., shear, elongation) is applied to the melt by the mixer, we identify the same line

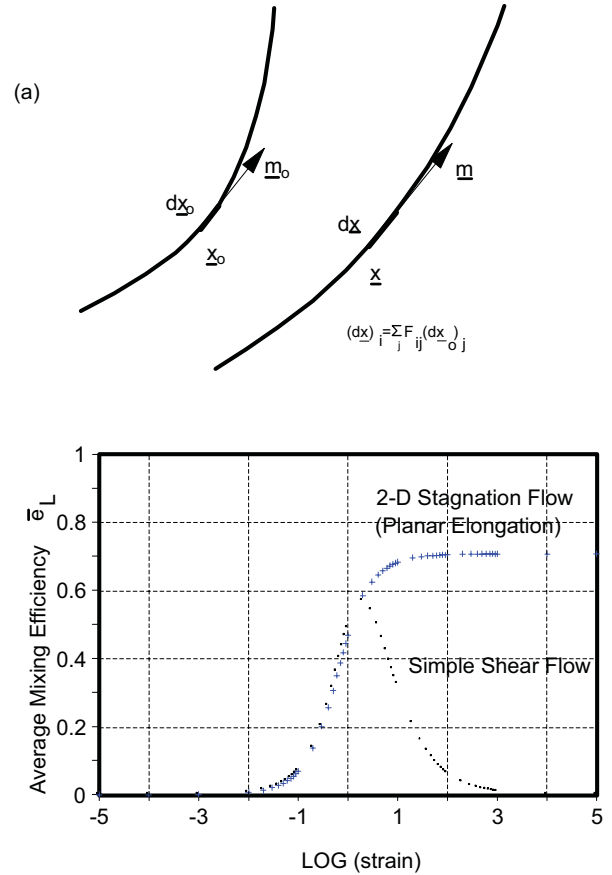


FIGURE 6.10 (a) Stretch of a material line at position \mathbf{x}_0 of length $|d\mathbf{x}_0|$ and orientation \mathbf{m}_0 at time $t = 0$ to a new line at position \mathbf{x} of length $|d\mathbf{x}|$ and orientation \mathbf{m} at present time, produced by a deformation gradient field with components F_{ij} . (b) Average mixing efficiency, \bar{e}_L , of simple shear flow and planar elongational flow, as a function of strain.

with different position, \mathbf{x} , length, $|d\mathbf{x}|$, and orientation, \mathbf{m} , (Fig. 6.10a). The lineal stretch, λ , is then defined as

$$\lambda \equiv \frac{|d\mathbf{x}|}{|d\mathbf{x}_0|} \quad (6.82)$$

The deformation applied is characterized by the deformation-gradient tensor, \mathbf{F} , with components (for a rectangular coordinate system) equal to

$$F_{ij} = \sum_i \sum_j \frac{\partial x_i}{\partial x_{0j}} \quad (6.83)$$

The transpose of the deformation gradient tensor, \mathbf{F}^T , is then given by the components

$$(F^T)_{ij} = \sum_i \sum_j \frac{\partial x_j}{\partial x_{0i}} \quad (6.84)$$

In the above two equations, as well as in the rest of the equations in this section, subscripts 1, 2, and 3 indicate x , y , and z directions, respectively. The deformation tensor and its transpose can be combined to yield the right relative Cauchy–Green strain tensor, \mathbf{C} , with components

$$C_{il} = \sum_j (F^T)_{ij} F_{jl} = \sum_j \frac{\partial x_j}{\partial x_{0i}} \frac{\partial x_j}{\partial x_{0l}} \quad (6.85)$$

The lineal stretch λ is then given by (Ottino et al., 1981)

$$\lambda^2 = \sum_i \sum_l \left(\sum_j \frac{\partial x_j}{\partial x_{0i}} \frac{\partial x_j}{\partial x_{0l}} \right) m_{0l} m_{0i} \quad (6.86)$$

and the time rate of the lineal stretch per unit of present length is

$$\frac{\dot{\lambda}}{\lambda} = \frac{1}{2} \sum_i \sum_j \dot{\gamma}_{ij} m_j m_i \quad (6.87)$$

where $\dot{\gamma}_{ij}$ are the components of the rate-of-strain tensor, $\dot{\gamma}$, and the components of the vector \mathbf{m} are given by

$$m_i = \frac{1}{\lambda} \sum_j F_{ij} m_{0j} \quad (6.88)$$

The efficiency of mixing, e_L , which relates the rate of lineal stretch and its upper bound, which is proportional to the viscous dissipation, is given by

$$e_L = 2 \frac{\dot{\lambda}/\lambda}{\sqrt{\sum_k \sum_l \dot{\gamma}_{kl} \dot{\gamma}_{lk}}} \quad (6.89)$$

and the time average efficiency of mixing, \bar{e}_L , is given by

$$\bar{e}_L = \frac{1}{t} \int_0^t e_L(t') dt' \quad (6.90)$$

Finally, for isochoric deformations (with volume conservation), the product of the areal and lineal stretches is equal to 1, and the sum of the rates of lineal and areal stretches per unit of initial length and area (respectively) is equal to zero, for the same orientation vector of the line and the area. The following example illustrates the various steps for the calculation of the striation thickness reduction function and the time average mixing efficiency for the simple shear case.

Example 6.5. Striation Thickness Reduction and Efficiency of Mixing for Simple Shear Flow

Calculate the striation thickness reduction function and the time average mixing efficiency for simple shear flow, $v_x = \dot{\gamma}y$; $v_y = v_z = 0$, for a line with orientation along the y axis, that is, with initial orientation vector $\mathbf{m}_0 = (0, 1, 0)$.

Solution. The kinematics of simple shear flow are

$$v_x = \frac{dx}{dt} = \dot{\gamma}y; \quad v_y = \frac{dy}{dt} = 0; \quad v_z = \frac{dz}{dt} = 0 \quad (6.91)$$

Integration of this equation with respect to time with initial conditions: $x = x_0$, $y = y_0$, and $z = z_0$, yields

$$x = x_0 + \gamma y_0; \quad y = y_0; \quad z = z_0 \quad (6.92)$$

where γ is the shear strain $\dot{\gamma}t$. The only nonzero components of the deformation gradient tensor are

$$F_{11} = F_{22} = F_{33} = 1; \quad F_{12} = \gamma \quad (6.93)$$

The nonzero components of the transpose of the deformation-gradient tensor are

$$(F^T)_{11} = (F^T)_{22} = (F^T)_{33} = 1; \quad (F^T)_{21} = \gamma \quad (6.94)$$

The components of the Cauchy–Green strain tensor, \mathbf{C} , are calculated from Eq. 6.85. The only nonzero components are

$$C_{11} = C_{33} = 1; \quad C_{12} = C_{21} = \gamma; \quad C_{22} = \gamma^2 + 1 \quad (6.95)$$

The lineal stretch is then calculated from Eq. 6.86 as

$$\lambda = \sqrt{1 + \gamma^2} \quad (6.96)$$

For long times, the lineal stretch varies linearly with time, that is, $\lambda \propto t$, and so shear flow is considered a *weak* flow in this respect. In extensional flows (see Problem 6B.4) the lineal stretch grows exponentially with time, that is, $\lambda \propto e^t$, and these flows are considered *strong*. The striation thickness reduction function, δ/δ_0 , which is equal to λ^{-1} , is then equal to $(1 + \gamma^2)^{-1/2}$. With the proper selection of α_x and α_y , note that Eqs. 6.65 and 6.96 are the same, so that the two approaches are equivalent.

To calculate the time average mixing efficiency of shear flow we need to calculate the components of the rate-of-strain tensor and the components of the new orientation vector, \mathbf{m} . The nonzero components of the rate-of-strain tensor are

$$\dot{\gamma}_{12} = \dot{\gamma}_{21} = \dot{\gamma} \quad (6.97)$$

The new orientation vector, \mathbf{m} , is calculated from Eq. 6.88 as

$$\mathbf{m} = \frac{1}{\lambda}(\gamma, 1, 0) \quad (6.98)$$

The rate of lineal stretch per unit of length is given by Eq. 6.87 as

$$\frac{\dot{\lambda}}{\lambda} = \frac{\dot{\gamma}^2 t}{1 + \gamma^2} \quad (6.99)$$

and the mixing efficiency is given by Eq. 6.89 as

$$e_L = \sqrt{2} \frac{\gamma}{1 + \gamma^2} = \sqrt{2} \frac{\dot{\gamma} t}{1 + \dot{\gamma}^2 t^2} \quad (6.100)$$

It can easily be proved that the initial and the final value of e_L is 0, its maximum value is $\sqrt{2}/2 = 0.707$ (at $\gamma = 1$), and at long times it decays as $1/t$. The time-average value of the mixing efficiency is calculated from Eq. 6.90 as

$$\bar{e}_L = \frac{\sqrt{2} \ln(1 + \gamma^2)}{2\gamma} \quad (6.101)$$

and it is shown graphically in Figure 6.10b. Its maximum is about 0.57, and it occurs at $\gamma \cong 2$. At long times the average efficiency decays so that simple shear flows are characterized by low efficiencies at long times. The time average mixing efficiency of a planar elongational flow (also called two-dimensional stagnation flow) is also shown in that figure. ■

Clearly, simple shear is not an effective mixing mechanism, but it is present in all mixing devices. It is difficult to maintain elongational (irrotational) flows between rigid boundaries. Also, the orientation of the interface is very important in the reduction of the striation thickness. Ng and Erwin (1981) experimentally demonstrated that an improvement in the interfacial growth function can be obtained by stepwise application of shear and reorientation of the interfaces between steps. In a single-screw extruder, the inefficiency of shear can be offset by the incorporation of “mixing sections” in the melt channel. These sections, in the form of vanes, pins, ducts, and so on, increase the pressure drop in the extruder and so the shear strain is increased. More significantly, they reorient the polymer interfaces, causing a drastic decrease of the striation thickness in the material coming out of the extruder (see Problem 6B.6; Erwin and Mokhatarian, 1983; Erwin, 1978b).

In conclusion, mixing of highly viscous liquids, such as polymer melts, is achieved mainly through laminar mixing. In this type of mixing, the interfacial area growth (or striation thickness reduction) function quantifies the degree of mixing. In simple shear laminar mixing the degree of mixing, for large strains, is proportional to the applied shear strain and the orientation of the interface. Consequently, good mixing

is obtained by the application of large strains in favorably oriented interfaces. But gross uniformity cannot be achieved through the striation thickness reduction alone. One should also distribute the interfacial elements throughout the system.

6.3.3 Laminar Mixing in Simple Geometries

In this section we discuss two examples of mixing in simple geometries: parallel plates and concentric cylinders. The parallel plate geometry is used as the basis of the analysis of the single-screw extruder and concentric cylinders are used as part of the design of rotational dies. The flow kinematics are calculated and mixing in terms of striation thickness reduction is evaluated.

Example 6.6. Mixing in Plane Couette Flow (Parallel Plate Geometry; PCF)

Consider two infinite parallel plates and a polymer blend (with equal viscosity components) filling the space between them. The discussion that follows holds for the case of both Newtonian and non-Newtonian fluids. At time $t = 0^-$ the system is at rest. Then, at time $t = 0^+$ the upper plate starts moving with velocity V_z in the positive z direction. The movement of the upper plate drags the fluid, which starts moving in the same direction. Calculate the striation thickness reduction in this geometry and the effect of reorientation in the case of initially spherical particles of the dispersed phase.

Solution. Figure 6.11 shows the parallel plate geometry. Initially, the particles of the minor component can be simulated by idealized geometries such as cubes, spheres, and rectangular parallelepipeds (with the long axis along the z or

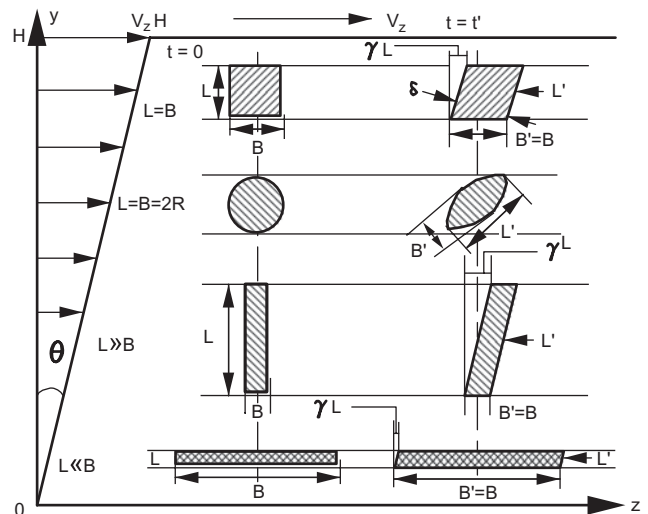


FIGURE 6.11 Effect of shear strain on striation thickness of “particles” of the minor component represented by simple geometries, in a plane Couette flow (PCF).

y directions). The shearing planes are parallel to the plates and the amount of shear strain is

$$\gamma = \dot{\gamma}t = \frac{V_z}{H}t \quad (6.102)$$

where H is the plate separation distance.

After shearing has started, the edges of the geometries transverse to the shearing planes will rotate through an angle θ . However, the edges that are parallel to the shearing planes will remain parallel and of the same length as before shearing. In the case of the sphere, the diameter transverse to the shearing plane will be transformed into the long axis of an ellipsoid. In all geometries, the initial striation thickness is the thickness B (diameter $2R$ for the sphere). After shearing, the striation thickness becomes B' . The cube and the two parallelepipeds are treated similarly. The treatment for the sphere requires one additional argument, and thus it is treated separately. The rotation angle θ and the shear strain are related as follows:

$$\tan \theta = \gamma \quad (6.103)$$

The length L' , B' , and the striation thickness, δ , for all the geometries except the sphere can be calculated from trigonometrical arguments as follows:

$$\begin{aligned} L' &= \frac{L}{\cos \theta} = L\sqrt{1 + \gamma^2} \\ B' &= B \\ \delta &= B \cos \theta = \delta_0 \cos \theta = \frac{\delta_0}{\sqrt{1 + \gamma^2}} \end{aligned} \quad (6.104)$$

In the case of a sphere that is elongated into an ellipsoid, the long axis of the ellipsoid is given by Eq. 6.104, and the short axis is calculated by equating the volume of the initial sphere ($\pi(2R)^3/6$) to the volume of the ellipsoid ($\pi L'(B')^3/6$) as

$$\delta = B' = \delta_0(1 + \gamma^2)^{-1/4} = (2R)(1 + \gamma^2)^{-1/4} \quad (6.105)$$

A comparison of Eqs. 6.104 and 6.105 shows that for the same shear strain the sphere offers the maximum reduction in striation thickness.

The generalization of these equations to the case where there is a mismatch of shear viscosity ($p = \mu_d/\mu_c \neq 1$) of the two Newtonian components is straightforward, where μ_d is the viscosity of the minor (or dispersed) component and μ_c is the viscosity of the major (or continuous) component. The stress is the same across the gap separation, and at each interface the stresses inside the major and minor components are equal (if interfacial tension is negligible). Thus,

$$\dot{\gamma}_c = p\dot{\gamma}_d \quad (6.106)$$

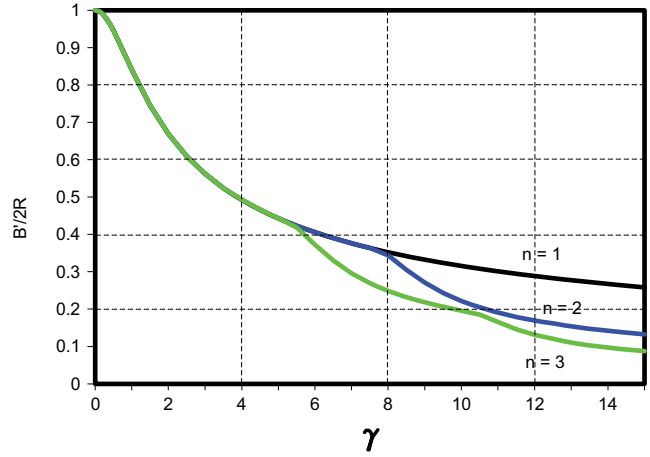


FIGURE 6.12 Effect of reorientation on the striation thickness reduction of an initially spherical particle subjected to shear strain γ . n is the number of reorientations.

where $\dot{\gamma}_c$ and $\dot{\gamma}_d$ are the shear rates in the continuous and dispersed phases, respectively. It is clear from the above that the reduction in striation thickness of the minor component is small if its viscosity is higher than that of the major component.

Finally, the effect of reorientation on the striation thickness reduction can be assessed in the example of an initially spherical particle that is deformed into an ellipsoid. Equation 6.105 gives the reduction in striation thickness as a function of the shear strain. If the ellipsoid is entering the next step with its long axis perpendicular to the shearing planes, the new striation thickness is given by the same equation. Thus, after n steps the striation thickness, δ , with reorientation is given by

$$\frac{\delta}{2R} = \prod_{j=1}^n (1 + \gamma_j^2)^{-1/4} \quad (6.107)$$

Figure 6.12 shows the effect of reorientation on the striation thickness of an initially spherical particle subjected to shear strain γ . ■

Example 6.7. Striation Thickness in Rotational Couette Flow (RCF)

Consider a rotational Couette geometry with the inside cylinder rotating, as shown in Figure 6.13a, and with the minor component represented by a black line. The position of the black line at time $t = 0$ shows the feedport of the system. After the inner cylinder starts rotating, the black line transforms into a spiral. Calculate the striation thickness as a function of the total number of revolutions of the inner cylinder and the geometry of the system.

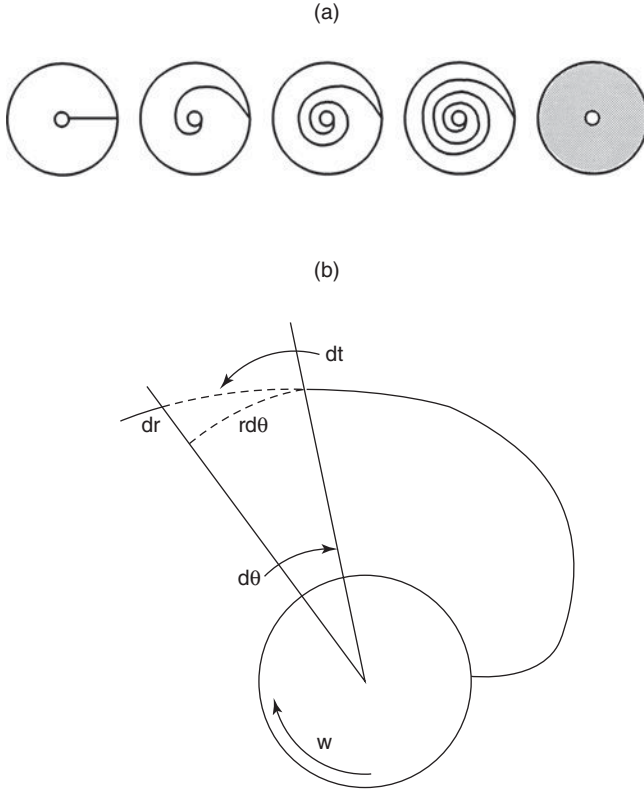


FIGURE 6.13 (a) Mixing by laminar shear flow in a rotational Couette geometry. (b) Spiral line in the annulus of a rotational Couette geometry.

Solution. A typical Couette geometry is shown in Figure 2.18. Figure 6.13b shows the geometry of a spiral line that results from the rotation of an initially straight line in a Couette geometry with the inside cylinder rotating with angular velocity W , in radians per unit time. For a power-law fluid the tangential velocity v_θ is given by (see Problem 2B.6)

$$v_\theta = rW \frac{1 - (R/r)^{2/n}}{1 - \kappa^{-2/n}} \quad (6.108)$$

where R is the radius of the outside cylinder, n is the power-law index, and κR is the radius of the inside cylinder.

Recalling that $v_\theta = r d\theta/dt$, that the counterclockwise direction in the θ coordinate is considered negative, and integrating the previous equation, we get

$$\theta = -W \frac{1 - (R/r)^{2/n}}{1 - \kappa^{-2/n}} t \quad (6.109)$$

At time $t = 2\pi/W$ one revolution of the inside cylinder is completed, and the angular displacement of two points which initially were apart by a distance dr is

$$d\theta = \frac{4\pi}{n(\kappa^{-2/n} - 1)} \frac{R^{2/n}}{r^{(n+2)/n}} dr \quad (6.110)$$

This equation was derived with the help of the approximate relation: $(r + dr)^{2/n} - r^{2/n} \cong (2/n)r^{(2-n)/n} dr$.

After N revolutions, the angular displacement will be $N(d\theta)$. Then, the total spiral length is

$$l_N = \int dl_N = \int [(dr)^2 + r^2(N d\theta)^2]^{1/2} \quad (6.111)$$

Equations 6.110 and 6.111 can be combined to give the following:

$$l_N = \int_{\kappa R}^R \left[1 + \frac{16\pi^2 N^2 R^{4/n}}{n^2(\kappa^{-2/n} - 1)^2} r^{-4/n} \right]^{1/2} dr \quad (6.112)$$

From that, the striation thickness reduction function is calculated as

$$\left[\frac{\delta}{\delta_0} \right] = \frac{R - \kappa R}{l_N} \quad (6.113)$$

For all practical purposes, $(dr)^2 \ll (rN d\theta)^2$ so that the striation thickness reduction function can be calculated from the formula

$$\left[\frac{\delta}{\delta_0} \right] = \left[\frac{2 - n}{4\pi N} \right] \left[\frac{(1 - \kappa)(\kappa^{-2/n} - 1)}{\kappa^{(n-2)/n} - 1} \right] \quad (6.114)$$

Figure 6.14 shows the effect of the total number of revolutions, ratio of inside to outside cylinder radius, and power-law index on the degree of mixing achieved in the Couette rotational device. The lines in this figure represent both the Newtonian ($n = 1$) and the power-law solution ($n = 0.5$) for $\kappa = 0.95, 0.9$, and 0.5 . It can be seen from Eq. 6.114 that the power-law index does not play a role in this formula and that δ/N is constant depending only on the κ value. ■

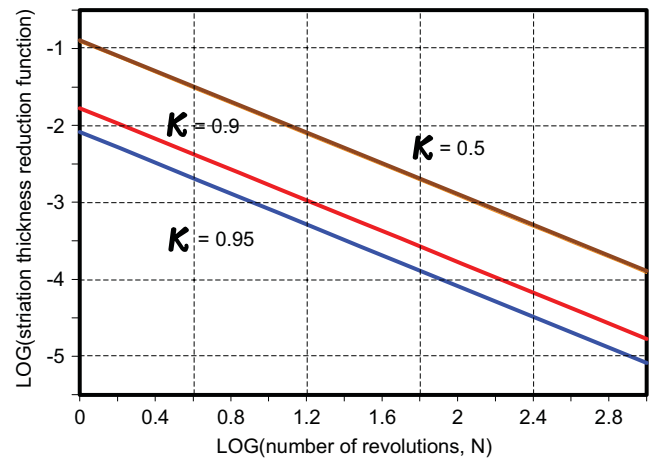


FIGURE 6.14 Striation thickness reduction function in rotational Couette flow (RCF) for various ratios of the outside to the inside radius. Newtonian and power-law fluids do not exhibit any significant difference.

6.4 RESIDENCE TIME AND STRAIN DISTRIBUTIONS

In Section 6.3 we saw that fluids in simple geometries like Couette flow in parallel plates or small gap concentric cylinders experience the same shear rate across the gap. Nevertheless, the strain history of each fluid element depends not only on the shear rate but on the time that the element has been subjected to that shear rate. Consequently, an element at a point close to the moving upper plate in a parallel plate geometry spends less time inside the apparatus than an element at a point close to the stationary lower plate, due to the different velocities at those two points. At the exit of the apparatus, the fluid collected consists of a set of fluid elements with a distribution of strain histories due to the different residence time of each element. Also, because mixing is directly related to strain, at the end of the apparatus the total mixing will exhibit a distribution. The residence time distribution (RTD) is important mainly in the areas of: (1) overall mixing efficiency, (2) degradation of temperature-sensitive polymers in processing, (3) foaming and crosslinking of polymers with the aid of temperature-sensitive foaming and crosslinking agents, and (4) backmixing, that is, mixing in the primary flow direction. A knowledge of the RTD is thus necessary for the optimization of the operation of processing equipment.

6.4.1 Residence Time Distribution

The RTD was first introduced by Danckwerts (1953), and it is defined so that $f(t)dt$ measures the fraction of the exit stream with residence time between t and $t + dt$. The cumulative RTD function or the F function, $F(t)$, is then defined as

$$F(t) = \int_{t_0}^t f(t') dt' \quad (6.115)$$

where t_0 is the minimum residence time. Clearly, $F(t)$ represents the fraction of the exit stream with residence time equal to or less than t . If Q denotes the volumetric flow rate at the exit and dQ the fraction of the volumetric exit flow rate with residence time between t and $t + dt$, then the RTD function is given by

$$f(t)dt = \frac{dQ}{Q} \quad (6.116)$$

The mean residence time, \bar{t} , is then equal to

$$\bar{t} = \int_{t_0}^{\infty} tf(t)dt \quad (6.117)$$

Extreme cases of the RTD are plug flow and perfect mixing. In the plug flow case, all elements of the fluid have

exactly the same residence time and thus “appear” at the exit at exactly the same time. In diagrams of the $F(t)$ function, the plug flow mixer is represented by a straight vertical line at $t = \bar{t}$. In reality, fluids with no slip at the walls cannot exhibit the characteristics of plug flow, but some fluids approach this behavior. Perfect mixing takes place in a stirred tank, and it will be discussed later. Example 6.8 and Problem 6A.13 illustrate the application of the above ideas to specific pressure flows.

Example 6.8. Mean Residence Time and $F(t)$ Function for Capillary Flow

Calculate the mean residence time and the cumulative RTD function for pressure (Poiseuille) flow of a power-law fluid through a circular pipe (CPPF).

Solution. The velocity profile is given in Table 2.6. Then the volumetric flow rate, dQ , with residence time between t and $t + dt$ is given by the product of the area between the circles with radii r and $r + dr$ and the velocity as

$$dQ = 2\pi r dr v_z(r) \quad (6.118)$$

and the total volumetric flow rate is given by the integral of Eq. 6.118 as

$$Q = \int dQ = 2\pi \int_0^R v_z(r)r dr \quad (6.119)$$

By substituting $v_z(r)$ into Eq. 6.119, after some calculations, we get

$$Q = \frac{\pi n R^3}{3n + 1} \left(\frac{R \Delta P}{2mL} \right)^{1/n} \quad (6.120)$$

where L is the length of the pipe. Fluid elements at the center line ($r = 0$) stay in the pipe mixer for time t_0 , which is equal to the minimum residence time:

$$t_0 = \frac{L}{v_z(r = 0)} = \frac{(1 + n)L}{nR} \left(\frac{2mL}{R \Delta P} \right)^{1/n} \quad (6.121)$$

The ratio of the residence times of fluid elements at radial distances r and 0 is

$$\frac{t}{t_0} = \frac{1}{1 - (r/R)^{(1+n)/n}} \quad (6.122)$$

The RTD function $f(t)$ is given by combining Eqs. 6.118 and 6.120 as

$$f(r) = \frac{2(1 + 3n)}{(1 + n)R^2} r \left[1 - \left(\frac{r}{R} \right)^{(1+n)/n} \right] \quad (6.123)$$

Equation 6.122 transforms $f(r)$ into $f(t)$:

$$f(t) = \frac{2n(1+3n)t_0^2}{(1+n)^2 t^3} \left(1 - \frac{t_0}{t}\right)^{(n-1)/(1+n)} \quad (6.124)$$

The mean residence time is calculated from Eq. 6.117 as

$$\bar{t} = \frac{2n(1+3n)t_0^2}{(1+n)^2} \int_{t_0}^{\infty} \frac{(1-t_0/t)^{(n-1)/(1+n)}}{t^2} dt \quad (6.125)$$

After integration by parts the mean residence time is given by

$$\bar{t} = \frac{1+3n}{1+n} t_0 \quad (6.126)$$

For Newtonian fluids $n = 1$ and, consequently, $\bar{t} = 2t_0$. For power-law fluids $\bar{t} < 2t_0$, so that these fluids approach plug flow.

The cumulative RTD function is given by combining Eqs. 6.115 and 6.124 to give

$$F(t) = \frac{2n(1+3n)t_0^2}{(1+n)^2} \int_{t_0}^t \frac{(1-t_0/t')^{(n-1)/(1+n)}}{t'^3} dt' \quad (6.127)$$

It is not difficult to complete the integration in Eq. 6.127 and to combine it with Eq. 6.126 to get

$$F(t) = \left[1 + \frac{2n}{1+3n} \frac{\bar{t}}{t}\right] \left[1 + \frac{1+n}{1+3n} \frac{\bar{t}}{t}\right]^{2n/(1+n)} \quad (6.128)$$

For Newtonian fluids, $F(t) = 1 - (1/4)(\bar{t}/t)^2$. Figure 6.15 shows the F function for a plug flow mixer and for Poiseuille

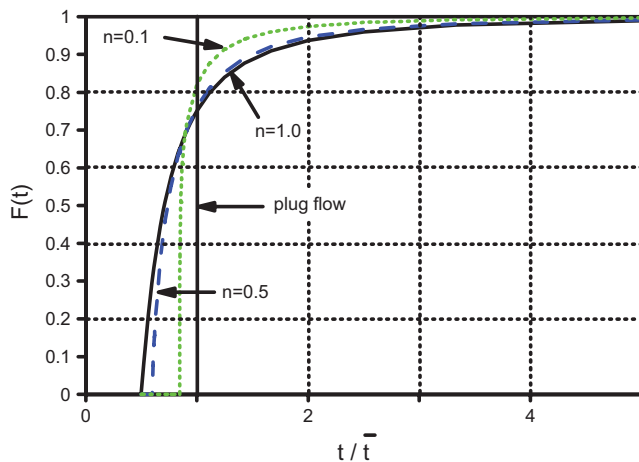


FIGURE 6.15 Cumulative residence time distribution function for Poiseuille flow of a power-law fluid in a circular pipe (CPPF).

flow in a long circular pipe for various degrees of pseudoplasticity. The more pseudoplastic the fluid is, the more the flow approaches plug flow. Also, it is evident from the figure that if we introduce a “tagged” material in a CPPF mixer, we expect to see the first trace of that material coming out of the mixer not earlier than 50% of the mean residence time (for the Newtonian case). ■

The F function is highly dependent on the flow geometry for a given fluid. For Poiseuille flow of a power-law fluid in a parallel plate geometry (PPF) the mean residence time is given by

$$\bar{t} = \frac{1+2n}{1+n} t_0 \quad (6.129)$$

and the F function by (see Problem 6A.13)

$$F(t) = \left[1 + \frac{n}{1+2n} \frac{\bar{t}}{t}\right] \left[1 + \frac{1+n}{1+2n} \frac{\bar{t}}{t}\right]^{n/(1+n)} \quad (6.130)$$

The effect of the flow geometry and flow type (Couette and Poiseuille) is shown in Figure 6.16. Note that the first trace of a “tagged” material does not come out of Poiseuille flow in parallel plate geometry earlier than 67% of the mean residence time. Finally, Poiseuille flow of Newtonian fluids in a circular pipe (CPPF) exhibits the same F function as Couette flow of Newtonian fluids in the parallel plate geometry (PCF; see Problem 6A.13).

In these two cases, Poiseuille flow in pipe and parallel plate geometries, the cumulative RTD function was obtained by calculating the velocity profile and the volumetric flow rate. However, in cases where the velocity profile is not

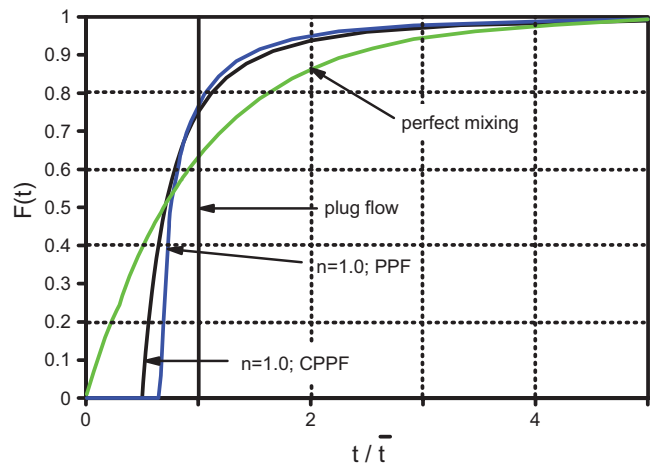


FIGURE 6.16 Cumulative residence time distribution function for plug flow, perfect mixing (complete backmixing), Poiseuille flow of Newtonian fluids in circular pipe (CPPF), and parallel plate geometries (PPF).

known, other techniques should be used to calculate the distribution of residence times. One technique is to obtain the response of the system under examination to a “step change” in influent concentration of some “tagged” material (tagged with color, pH, radioactivity, etc.). The technique works as follows. Suppose that we want to get the cumulative RTD function of a mixer with an unknown velocity profile. We connect this system with two influent pipes (one for the regular fluid and one for the tagged material with concentration C_0) through a three-way valve and we start mixing the regular fluid coming out of one of the influent pipes. After the system attains steady state (at $t = 0$) we change the valve position to allow only the tagged material to flow through the mixer and the concentration of the tagged material in the effluent stream, $C(t)$, is monitored by the appropriate technique (photometer for color as the tagging characteristic; pH meter for pH as the tagging characteristic, etc.). For the technique to work we assume that the “tagged material” flow stream exhibits the same characteristics as the main flow stream so that the flow rate is not changed within the system and that the flow enters the system in a plug flow mode.

At time t the tagged material exiting the mixer has been in the mixer for a time less than t . The volumetric flow rate of the tagged material at time t is equal to $F(t)C_0Q$, where Q is the total volumetric flow rate of the influent (or effluent) stream. The tagged material balance yields

$$QC(t) = F(t)C_0Q \quad (6.131)$$

and thus the F function is

$$F(t) = \frac{C(t)}{C_0} \quad (6.132)$$

In conclusion, the F function for systems with unknown characteristics is obtained through a step change experiment of a tagged material as the ratio of the tagged material concentrations of the incoming and outgoing streams.

Another technique for measuring the F function includes the instantaneous injection (δ function; or impulse) of a certain amount of the tagged material and the monitoring of the effluent concentration as a function of time. The difference of the two techniques lies in the way the same information is presented: the step change technique yields the $F(t)$ function whereas the “ δ function change” technique yields the $f(t)$ function.

Danckwerts (1953) distinguishes between the internal RTD function, $g(t)$, and the external RTD function, $f(t)$. The fraction of the material *in the system* with residence time between t and $t + dt$ is $g(t)dt$, whereas $f(t)dt$ refers to the fraction of the material *leaving the system*. The cumulative RTD function corresponding to $g(t)$ is denoted as $G(t)$ and it is equal to $\int_0^t g(t')dt'$. The relationship between $g(t)$

and $F(t)$ can be obtained from an imaginary step-change experiment:

$$Q - QF(t) = \frac{d}{dt} [VG(t)] \quad (6.133)$$

where V is the volume of the system occupied by the fluid, and the first, second, and third terms represent the volumetric flow rate into the system, out of the system, and change within the system, respectively. For constant Q and V and for \bar{t} equal to V/Q , Eq. 6.133 yields

$$g(t) = \frac{1 - F(t)}{\bar{t}} \quad (6.134)$$

The mean residence time of the material inside the mixer is then given by

$$\bar{t}_i = \int_0^{\infty} tg(t)dt \quad (6.135)$$

More discussion of the internal RTD functions goes beyond the scope of the present textbook.

The first extreme case, as mentioned before, is plug flow and the other extreme case is that of a “perfect mixer,” which is realized in stirred tanks. The latter case corresponds to complete backmixing, that is, mixing along the primary flow direction. Suppose that we perform a step change experiment in a stirred tank system of volume occupied by the fluid V and volumetric flow rate Q . Also, suppose that C_0 is the tagged material concentration in the influent stream and that the concentration in the effluent stream is C . Then, the material balance of the tagged component yields

$$QC_0 = QC + V\frac{dC}{dt} \quad (6.136)$$

and the initial condition is $C = 0$ at $t \leq 0$. Note that the concentration of the tagged material C in the tank and in the effluent stream is the same because perfect mixing was assumed. The solution to the first-order differential Eq. 6.136 along with the initial condition and Eq. 6.132 is

$$F(t) = 1 - e^{-t/\bar{t}} \quad (6.137)$$

where $\bar{t} = V/Q$. Figure 6.16 shows the F curve for a perfect mixer. Two notes should be made with reference to that curve: (1) the perfect mixer exhibits a broad cumulative RTD curve; and (2) there is no finite time lag, that is, the tagged material exits the mixer immediately after it is introduced to it, although at low concentrations, in contrast to pipe Poiseuille flow with time lag of $0.5\bar{t}$ and plug flow with time lag \bar{t} . Also, note that in the perfect mixer there is no

distinction between internal and external RTD functions and consequently $f(t) = g(t)$ and $F(t) = G(t)$.

The broad RTD of the perfect mixer seems to contradict the idea of perfect mixing. Caution should be exercised in this respect. The term mixing was used in this section to signify the *time distribution of material inside and outside the mixer and not the homogeneity of the effluent stream*. On the other hand, a high degree of turbulence in pipe flow produces a high degree of uniformity in the transverse direction (*transverse mixing*; radial mixing) and poor mixing in the longitudinal direction (primary flow direction; *backmixing*). Thus, although the F curves of turbulent and laminar flows in a pipe are the same, indicating the same degree of backmixing, mixing in the radial direction is greatly improved in the turbulent flow.

Two other qualities characterize the degree of mixing through the RTD of mixers: *holdback*, B , and *segregation*, S . Holdback is defined as

$$B = \frac{1}{t} \int_0^{\bar{t}} F(t) dt \quad (6.138)$$

and it represents the area under the F curve from 0 to \bar{t} . B varies from 0 for plug flow to 1 for a mixer full of dead spots, and it measures the deviation from plug flow. To understand the meaning of holdback, we borrow the example given by Danckwerts (1953). Suppose that the inflow stream changes color from white to red in a step change experiment. Then, B is equal to the fraction of the mixer which is still occupied by white color after a volume of red material equal to the mixer volume has entered the mixer. The holdback of typical flows (see Problem 6A.14) are as follows:

Plug flow	0
PPF	0.19
CPPF; PCF	0.25
Perfect mixing	0.37

Segregation, S , can be calculated from the F curves as the area between the perfect mixing and the mixer curves up to the point that these curves cross each other. S varies from $+1/e = 0.37$ for plug flow to -1 for a mixer full of dead spots. The value for the CPPF is 0.14 (see Problem 6A.14).

Finally, the average striation thickness reduction function at the exit of a mixer $\langle\langle\lambda(t)\rangle\rangle$ can be calculated using the idea of the “mixing cup” as follows (Ottino and Chella, 1983):

$$\langle\langle\lambda(t)\rangle\rangle = \left\langle\left\langle\frac{\delta}{\delta_0}(t)\right\rangle\right\rangle = \int_{t_0}^t \lambda(t') f(t') dt' \quad (6.139)$$

6.4.2 Strain Distribution

It was shown in Section 6.3 that the degree of mixing is proportional to the total shear strain for shear mixing with large applied strains. In other mixing situations the state of mixing is a function (maybe not simple) of the applied strain. However, in a mixer, the fluid particles experience different strain histories, so that the exiting fluid stream consists of particles with different degrees of mixing. The nonuniformity in the state of mixing is measured by the strain distribution function (SDF) in direct analogy with the RTD function. Note that in batch mixers, the SDF depends only on the various paths that the fluid particles have followed, whereas in continuous mixers the RTD and the variation of the path trajectories should be accounted for in the strain distribution. One should keep track of the sign of the strain, because mixing is enhanced by positive strain (along the flow direction) and reduced by negative (opposite to the flow direction) strain (demixing).

Inside continuous mixers or in batch mixers, in analogy with the RTD discussion (Eq. 6.116), the SDF, $g(\gamma)$, is calculated as the fraction of the fluid which experienced strain from γ to $\gamma + d\gamma$. The cumulative SDF, $G(\gamma)$, is then given by the integral of the SDF as in Eq. 6.115. In the exit stream of continuous mixers the SDF, $f(\gamma)d\gamma$, is defined as the fraction of the flow which has experienced strain between γ and $\gamma + d\gamma$. The cumulative SDF, $F(\gamma)$, is then calculated as

$$F(\gamma) = \int_{\gamma_0}^{\gamma} f(\gamma') d\gamma' \quad (6.140)$$

and it denotes the fraction of the exit flow stream with applied strain less than or equal to γ , where γ_0 is the minimum applied strain. The weighted average total strain, WATS (Pinto and Tadmor, 1970), and the mean total strain, $\bar{\gamma}$, are calculated by weighting the strain with the RTD function and SDF, respectively, as follows:

$$\text{WATS} \equiv \int_{t_0}^{\infty} \gamma(t') f(t') dt'; \quad \bar{\gamma} \equiv \int_{\gamma_0}^{\infty} \gamma' f(\gamma') d\gamma' \quad (6.141)$$

Obviously, the higher the value of the mean strain that is achieved, the better the mixing is. The SDF is only simply related to the RTD for the case when $\dot{\gamma}$ is constant.

Example 6.9. Cumulative SDF for PCF

Calculate the cumulative SDF for parallel plate Couette flow (PCF) of a Newtonian fluid, and show its similarity with the cumulative RTD function for Newtonian flow in PCF or CPPF configurations.

Solution. Referring to Figure 6.11 for a parallel plate geometry, we see that

$$\dot{\gamma} = \frac{V_z}{H}; \quad \gamma = \dot{\gamma}t = \frac{V_z L}{H v_z} = \frac{L}{y} \quad (6.142)$$

The minimum strain, γ_0 , corresponds to $y = H$, so that

$$\gamma_0 = \frac{L}{H} \quad (6.143)$$

The volumetric flow rate across the area $W dy$ is dQ , and it is equal to

$$dQ = W dy v_z(y) = W \frac{y}{H} V_z dy \quad (6.144)$$

The total flow rate, Q , is calculated to be $WHV_z/2$.

According to the definition of the SDF,

$$f(\gamma)d\gamma = \frac{dQ}{Q} = \frac{2}{H^2} y dy \quad (6.145)$$

With the aid of Eqs. 6.142 and 6.143, the SDF becomes

$$f(\gamma)d\gamma = 2 \frac{\gamma_0^2}{\gamma^3} d\gamma \quad (6.146)$$

which is similar to the RTD function ($2t_0^2 dt/t^3$). Note that to arrive at Eq. 6.146 we need to take into account the fact that the part of the total flow rate which experiences strain between γ and $\gamma + d\gamma$ flows through the cross-sectional area between $W(y - dy)$ and Wy . Equivalently, we can use the absolute value of dQ , because the SDF is always a positive number. The mean total strain is calculated from Eqs. 6.141 and 6.146 as

$$\bar{\gamma} = 2\gamma_0 = 2 \frac{L}{H} \quad (6.147)$$

Finally, the cumulative SDF is calculated with the aid of Eq. 6.140 as

$$F(\gamma) = 1 - \frac{1}{4} \left(\frac{\bar{\gamma}}{\gamma} \right)^2 \quad (6.148)$$

This is the same function as the cumulative RTD function of PCF and CPPF with γ_0 and γ replaced by t_0 and t , respectively. ■

In geometries and flow configurations where $\dot{\gamma}$ varies spatially, the calculations for the SDF become complicated. Example 6.10 illustrates the complexities involved.

Example 6.10. Cumulative SDF in CPPF

Show the algorithm for the calculation of the cumulative SDF of a power-law fluid flowing in a CPPF configuration. As special cases, show the final algorithm steps for a Newtonian fluid and a power-law fluid with power-law index $n = 0.5$.

Solution. The velocity profile and the shear rate are given in Table 2.6. The differential flow rate dQ passing through the “ring” $2\pi r dr$ is equal to $2\pi r v_z(r) dr$, and the total flow rate Q is then calculated as

$$Q = \int_0^R dQ = \frac{n\pi R^3}{1+3n} \left(\frac{R \Delta P}{2mL} \right)^{1/n} \quad (6.149)$$

The SDF can be calculated as a function of the variable $\xi = r/R$ from the ratio dQ/Q as

$$f(\xi)d\xi = 2 \frac{1+3n}{1+n} \xi (1 - \xi^{(n+1)/n}) d\xi \quad (6.150)$$

and the cumulative SDF is calculated as

$$F(\xi) = \frac{1+3n}{1+n} \xi^2 \left(1 - \frac{2n}{1+3n} \xi^{(n+1)/n} \right) \quad (6.151)$$

The mean total strain is calculated using the expressions for $\dot{\gamma}$, $t = L/v_z(r)$, and the SDF as

$$\bar{\gamma} = 2 \frac{L}{R} \frac{1+3n}{1+2n} \quad (6.152)$$

It is interesting to note that the mean total strain depends only on the geometry of the system (through L and R), not on the flow rate, and also that the smaller the radius or longer the pipe the higher the strain is. For Newtonian fluids, $\bar{\gamma} = 8L/3R$.

The expressions for $\dot{\gamma}$ and $\bar{\gamma}$ can be combined into the following:

$$\frac{\dot{\gamma}}{\bar{\gamma}} = \frac{(1+n)(1+2n)}{2n(1+3n)} \frac{\xi^{1/n}}{1 - \xi^{(n+1)/n}} \quad (6.153)$$

The algorithm now consists of the following steps:

1. Calculation of ξ from Eq. 6.153 for a specified $\dot{\gamma}/\bar{\gamma}$ (n th order polynomial; graphically or with the aid of software package),
2. Substitution of ξ just calculated into $F(\xi)$, and
3. Plotting of $F(\dot{\gamma}/\bar{\gamma})$ versus $\dot{\gamma}/\bar{\gamma}$.

For Newtonian fluids and for power-law fluids with $n = 0.5$, step 1 is simpler because the resulting equations are quadratic and cubic, respectively. So, for Newtonian fluids, the equations are

$$F(\xi) = 2\xi^2 \left(1 - \frac{1}{2}\xi^2\right); \quad \xi^2 + \frac{3\bar{\gamma}}{4\gamma}\xi - 1 = 0 \quad (6.154)$$

and for a power-law fluid with $n = 0.5$, the corresponding equations are

$$F(\xi) = \frac{5}{3}\xi^2 \left(1 - \frac{2}{5}\xi^2\right); \quad \xi^3 + \frac{6\bar{\gamma}}{5\gamma}\xi^2 - 1 = 0 \quad (6.155)$$

The power-law fluid shows a narrower distribution, which is expected because the velocity profile approaches that of plug flow.

Similar calculations can be repeated for the case of PPF for power-law fluids in general (see Problem 6B.9). For $\xi = 2y/H$, where H is the plate separation and $y = 0$ at the center of the separation, the SDF, cumulative SDF, and strain are given by

$$f(\xi)d\xi = \frac{1+2n}{1+n} \left(1 - \xi^{(n+1)/n}\right) d\xi \quad (6.156)$$

$$F(\xi) = \frac{1+2n}{1+n} \xi \left(1 - \frac{n}{1+2n} \xi^{(n+1)/n}\right) \quad (6.157)$$

$$\frac{\gamma}{\bar{\gamma}} = \frac{(1+n)^2}{n(1+2n)} \frac{\xi^{1/n}}{1 - \xi^{(n+1)/n}} \quad (6.158)$$

The mean total strain is equal to

$$\bar{\gamma} = 2 \frac{L}{R} \frac{1+2n}{1+n} \quad (6.159)$$

Figure 6.17 compares the cumulative SDF for Newtonian fluids in three flow situations: CPPF, PPF, and PCF.

CPPF and PPF can be compared with each other on the basis of mean total strain applied and flow rate for the same pressure drop. The ratio of the mean total strains for $H = 2R$ is calculated from Eqs. 6.152 and 6.159 as

$$\frac{\bar{\gamma}_{\text{CPPF}}}{\bar{\gamma}_{\text{PPF}}} = 2 \frac{(1+3n)(1+n)}{(1+2n)^2} \quad (6.160)$$

That ratio for Newtonian fluids is equal to 16/9, and it approaches 2 for extremely pseudoplastic fluids. Thus, the long circular pipe provides more strain for mixing, compared to a geometrically similar parallel plate configuration.

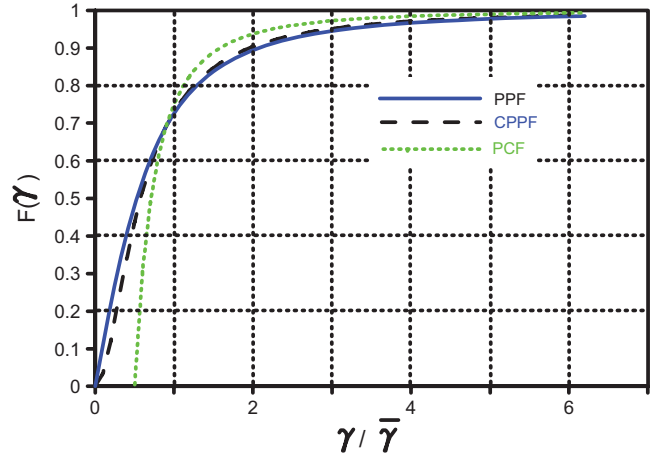


FIGURE 6.17 Comparison of the strain distribution function for circular pipe (CPPF) and parallel plate (PPF) Poiseuille flow, and parallel plate Couette flow (PCF) of Newtonian fluids.

In terms of flow rate, for the same $\Delta P/L$ and for $H = 2R$, the situation is

$$\frac{Q_{\text{CPPF}}}{Q_{\text{PPF}}} = \frac{R}{W} \frac{\pi(1+2n)}{2^{(1+n)/n}(1+3n)} \quad (6.161)$$

which for Newtonian fluids becomes $0.59R/W$. For these relationships to hold, W should be very large compared to R , so that for $W/R = 20$, the ratio of flow rates becomes 0.0295. In conclusion, CPPF incorporates more strain to the fluid but produces less flow rate than PPF with wide parallel plates. For plates with $W = 2R = H$, a shape factor should be included in the calculation of the flow rate (Middleman, 1977, p. 91), and the ratio of flow rates becomes 4.7 for Newtonian fluids.

Rotational Couette flow (RCF) is analyzed in the next example. Because the flow is confined inside the Couette flow cell and there is no exit stream, we use the nomenclature $G(\gamma)$ and $g(\gamma)d\gamma$ instead of $F(\gamma)$ and $f(\gamma)d\gamma$.

Example 6.11. SDF in RCF Configuration

Calculate the SDF for RCF, and explain the trends for Newtonian and non-Newtonian fluids.

Solution. Consider a rotational geometry with outside radius R , inside radius κR , and angular velocity of the inside cylinder, W . The velocity profile, v_θ , of the fluid in the gap for isothermal laminar flow with no gravitational and centrifugal forces and with no slip at the walls is given in Problem 2B.6. The shear rate is given (Table 2.10) by

$$\dot{\gamma} = \dot{\gamma}_{r\theta} = r \frac{\partial}{\partial r} \left(\frac{v_\theta}{r} \right) \quad (6.162)$$

as the r component of the velocity is zero. Substituting the velocity profile into Eq. 6.162, we obtain the strain:

$$\gamma = \dot{\gamma}t = \frac{2Wt}{n(1 - \kappa^{-2/n})} \left(\frac{R}{r}\right)^{2/n} \quad (6.163)$$

The minimum strain is obtained at the outside cylinder and is

$$\gamma_0 = \frac{2Wt}{n(1 - \kappa^{-2/n})} \quad (6.164)$$

and the maximum at the inside cylinder is

$$\gamma_{\max} = \frac{2Wt}{n(1 - \kappa^{-2/n})} \frac{1}{\kappa^{2/n}} \quad (6.165)$$

so that the ratio of the maximum to minimum strains is

$$\frac{\gamma_{\max}}{\gamma_0} = \frac{1}{\kappa^{2/n}} \quad (6.166)$$

For Newtonian fluids and for κ equal to 0.9, the maximum shear strain is 23% higher than the minimum, but for κ equal to 0.5 the maximum strain is 300% higher than the minimum. These differences cause a striation thickness difference inside the rotational mixer. The SDF can be computed from

$$g(r)dr = \frac{2\pi r L dr}{\pi L (R^2 - (\kappa R)^2)} \quad (6.167)$$

and Eqs. 6.163 and 6.164 as

$$g(\gamma)d\gamma = \frac{n}{1 - \kappa^2} \frac{\gamma_0^n}{\gamma^{n+1}} d\gamma \quad (6.168)$$

The mean total strain is calculated as

$$\bar{\gamma} = \int_{\gamma_0}^{\gamma_{\max}} \gamma g(\gamma) d\gamma = \gamma_0 \frac{n}{1 - n} \frac{\kappa^{2(n-1)/n}}{1 - \kappa^2} \quad (6.169)$$

for power-law fluids, whereas for Newtonian fluids it is given as

$$\bar{\gamma} = \gamma_0 \frac{2\ln(1/\kappa)}{1 - \kappa^2} \quad (6.170)$$

The cumulative SDF, $G(\gamma)$, is calculated as

$$G(\gamma) = \frac{1}{1 - \kappa^2} \left[1 - \left(\frac{1 - n}{n} \frac{1 - \kappa^2}{\kappa^{2(1-n)/n} - 1} \right)^n \left(\frac{\bar{\gamma}}{\gamma} \right)^n \right] \quad (6.171)$$

for power-law fluids, and it is calculated as

$$G(\gamma) = \frac{1}{1 - \kappa^2} \left[1 - \frac{1 - \kappa^2}{2\ln(1/\kappa)} \frac{\bar{\gamma}}{\gamma} \right] \quad (6.172)$$

for Newtonian fluids.

A number of interesting points can be revealed from the SDFs. For Newtonian fluids, only about 52% of the material is subjected to strain less than the mean strain for $\kappa = 0.9$, whereas for $\kappa = 0.5$ the corresponding value increases to 61%. For comparison with the other mixing flows the values of the percentage of the material subjected to strain less than the mean for Newtonian fluids are for CPPF and PPF 73% and for PCF 75%. The spread of the distribution depends on the gap ratio and the power-law index. The more pseudoplastic the material and the smaller the gap ratio are, the broader the distribution is. A broad distribution suggests nonuniformity in the product, because the degree of mixing will vary substantially for material layers in different parts of the rotational mixer. For power-law fluids with $n = 0.5$, 53% of the material is subjected to strain less than the mean for a gap ratio of 0.9 and 67% for a gap ratio of 0.5. Also, the distribution for power-law fluids is broader compared to that for Newtonian fluids. ■

6.5 DISPERSIVE MIXING

Dispersive mixing is the term used to describe mixing associated with some fundamental change of the physical characteristics of one or more of the components of the mixture. Generally, dispersive mixing is divided into two parts: the incorporation of the additives in terms of agglomerated particles or the second polymer component into the polymer matrix, and the dispersion (or deagglomeration) of the second phase to yield the final product. The microstructures of the blends are determined by rheological, hydrodynamic, and thermodynamic parameters. The rheological parameters are viscosity, elasticity, and yield stress of all components. The hydrodynamic parameters determine the flow fields. The thermodynamic parameters are related to solubility, adhesion, and diffusion of all components. In this section we address the dispersion of agglomerates (additives) and other polymers (liquid-liquid dispersion) into a polymer matrix.

6.5.1 Dispersion of Agglomerates

Dispersion of agglomerates has been applied in the polymer processing industry for at least 50 years. It is concerned with the incorporation and deagglomeration of additives in the polymer matrix with the ultimate goal being the reduction of the price or the improvement of the properties of the final product. Of course, if the additive exists in the form

of isolated noninteracting particles, then the task of mixing is only to distribute these particles uniformly throughout the final product. However, when the additive exists in the form of clusters of particles (interacting or noninteracting), then dispersive mixing ensures that the agglomerates break into isolated particles which then should be distributed by extensive mixing mechanisms.

The size of the particles and their ability to interact with each other characterize the type of cluster as *cohesionless* or *cohesive*. A *cohesionless* cluster is formed from noninteracting particles or from large particles (> 1 mm), and its dispersion is determined only by the total deformation of the primary phase. In this case, the dispersion is achieved by “peeling off” particles from the surface of the cluster by tangential velocity components close to the particles. On the other hand, a cohesive cluster includes interacting particles or very small particles or particles dispersed in a medium other than the polymer matrix, and its dispersion depends on the applied stresses (or equivalently on the deformation rates).

Usually, additive particles are of maximum size of about $100\ \mu\text{m}$ and the cohesive forces cannot be neglected. The significance of the cohesive forces is in the disintegration of the cluster, which requires that the hydrodynamic forces exceed the cohesive forces. Assuming the aggregates are formed by nontouching spherical particles of like material, the Bradley–Hamaker theory (Elmendorp, 1991) allows one to calculate the attractive van der Waals force between two particles as

$$F_w = \frac{2CR_1R_2A}{3} \frac{2xy - x^2 - y^2}{x^2y^2} \quad (6.173)$$

where A is the Hamaker constant ($\cong 5 \times 10^{-20}$ to 5×10^{-19} J) and $x = C^2 - (R_1 + R_2)^2$, $y = C^2 - (R_1 - R_2)^2$, and $C = R_1 + R_2 + d$. R_1 , R_2 , and d are the radii of the spheres and their distance, respectively. When the two spheres are touching each other, Eq. 6.173 reduces to

$$F_w = \frac{A}{6z^2} \frac{R_1R_2}{R_1 + R_2} \quad (6.174)$$

where z is the physical adsorption separation distance (equal to about 0.4 nm for adhering spheres). If the adhering spheres are of the same size, then $F_w = (AR)/12z^2$, and for the mean value of A we get $F_w = 0.1R$ in μN for R in μm . Rumpf (1962) showed that the tensile strength of clusters formed by equally sized randomly packed particles is

$$\sigma_T = \frac{9}{32} \frac{1 - \varepsilon}{\varepsilon} \frac{F_w}{R^2} \quad (6.175)$$

where ε is the void volume fraction or porosity of the cluster. Combining Eqs. 6.173 and 6.175 we get the cohesive force of the cluster as

$$F_c = \frac{9}{16} \frac{1 - \varepsilon}{\varepsilon} \frac{A}{12z^2R} S \quad (6.176)$$

where S is the cross-sectional contact area of the rupture plane.

The hydrodynamic forces acting to rupture the cluster can be calculated by assuming simple geometrical shapes. Tadmor and Gogos (1979) assumed that the agglomerate consisted of a dumbbell (two spheres connected with a hypothetical rod to transmit the forces between them) suspended in shear and elongational flow fields. The maximum hydrodynamic force acting on the rod to rupture the dumbbell (of equal-size spheres) was shown to be

$$F_h = \frac{3}{2} \pi \mu \dot{\gamma} LR \quad (6.177)$$

for the simple shear case, and

$$F_h = 3\pi \mu \dot{\varepsilon} LR \quad (6.178)$$

for elongational flow, where L is the distance between the center of the spheres. Note that the maximum force in the shear case is achieved when the dumbbell is oriented 45° to the direction of shear, and in the elongation case when the dumbbell is oriented along the direction of the flow. Equations 6.177 and 6.178 show that at the same shear and elongation rates elongational flow creates twice the force created in shear flows. The dumbbell is ruptured whenever the hydrodynamic force exceeds the cohesive force of Eq. 6.173. The better efficiency of the elongational field can be overcome by the shear flow, because shear devices can easily produce shear rates of $100\ \text{s}^{-1}$ and those rates cannot be achieved by elongational fields for long times. Thus, in dispersive mixing, shear is the predominant mechanism.

For a doublet of two touching equal-sized spheres suspended in an incompressible Newtonian fluid in a shear flow field, Nir and Acrivos (1973) calculated the maximum hydrodynamic force to be

$$F_h = 6.12\pi \mu \dot{\gamma} R^2 \quad (6.179)$$

Note that if the spheres are unequal in size the numerical constant of Eq. 6.179 changes. For instance, the hydrodynamic force in two touching spheres, with the diameter of one of them twice the diameter of the other, becomes equal to $2.57\pi \mu \dot{\gamma} R^2$, and for spheres with diameter ratio of 10 the force becomes $0.05\pi \mu \dot{\gamma} R^2$. By equating the maximum

hydrodynamic force on a doublet to the cohesive force of Eq. 6.174 we get the critical shear rate for breakup as

$$\dot{\gamma}_{\text{crit}} = 0.004 \frac{A}{z^2} \frac{1}{\mu R} \quad (6.180)$$

This equation shows that the smaller the particles and the lower the viscosity of the suspending medium the harder it is to break them up. The non-Newtonian character of the suspending medium can cause complications in terms of the hydrodynamic force, but this area is still under research.

The maximum hydrodynamic force acting on ellipsoidal, spherical, and highly ellipsoidal clusters of particles can be assumed to be the same as the force acting on single particles of the same shape. For spherical clusters this maximum hydrodynamic force is given (Elmendorp, 1991) as

$$F_h = \frac{5}{2} \pi \mu \dot{\gamma} R_{\text{cl}}^2 \quad (6.181)$$

where R_{cl} is the cluster radius. Equating this force to the cluster cohesive force of Eq. 6.176, we get the critical shear rate for deagglomeration:

$$\dot{\gamma}_{\text{crit}} = \frac{3}{160} \frac{S}{\pi \mu R_{\text{cl}}^2} \frac{1 - \varepsilon}{\varepsilon} \frac{A}{z^2 R} \quad (6.182)$$

which leads us to the conclusions that the more viscous the matrix and the larger the individual particles are the higher the critical shear rate is. In addition, if the agglomerate breaks at an equatorial plane (i.e., $S = \pi R_{\text{cl}}^2$), then the critical shear rate does not depend on the initial size of the cluster. The interfacial tension between the particles and the polymer matrix can act as a cohesive force of the cluster, especially when the polymer matrix does not fill completely the voids of the cluster (see Problem 6A.15).

Equation 6.179 shows the importance of high stresses ($\mu \dot{\gamma}$) in the deagglomeration process. Consequently, it is common practice in the polymer processing industry to make *masterbatches* or *superconcentrates* of the dispersed to the continuous phase and thus to increase the applied stresses by increasing the viscosity. μ in Eq. 6.181 is the viscosity of the medium, which in highly concentrated batches can be orders of magnitude higher than the viscosity of the polymer matrix. For example, the masterbatch of carbon black in PE contains about 50% carbon black while the final product contains about 2% to 5% only. The deagglomeration takes place in the masterbatch where the viscosity is high and it is followed by dilution steps in extensive type of mixing.

6.5.2 Liquid-Liquid Dispersion

The dispersion of one liquid into another is a very important mixing process for polymer blends. As mentioned in

the introduction of this chapter, dispersion of small rubber particles in PS is vital for the improvement of the impact properties of PS. Because the blending takes place in the molten state, understanding of the phenomena in a typical liquid-liquid dispersion is essential for the polymer blend business. However, a lack of agreement between the theoretical predictions and the experimental data in polymer blends should not always be used to discredit the theory, as relaxation processes can alter the structure as the blend goes from the molten to the frozen state.

Liquid-liquid dispersion is characterized by two phases, the dispersed and the continuous. The physical parameters of the two phases affecting a liquid-liquid dispersion are viscosity, elasticity, interfacial tension, solubility, and diffusion rate. For solubility, the system is considered as miscible, immiscible, or partially miscible. Interfacial tension is lowest for miscible systems and highest for immiscible systems. As mentioned in Chapter 4, all high molecular substances have a diffusion coefficient, \mathcal{D} , of about 10^{-12} to 10^{-14} cm²/s. Consequently, the diffusion rates in molten polymer systems are extremely small, and the relative penetration depths in the time scale of the blending process are extremely small.

Both the dispersed and the continuous phases are fed into the blending or compounding equipment in the form of pellets. The deformation and the dispersion starts after heating both components to temperatures above their melting point. Similarly to the dispersion of agglomerates, the hydrodynamic force is the deforming and disruptive force and the interfacial tension force is the cohesive force of the dispersed phase. The ratio of these two forces or stresses is called the *Capillary* (or *Weber*) Number, Ca :

$$Ca = \frac{F_h}{F_c} = \frac{\mu_c \dot{\gamma} R}{\gamma} \quad (6.183)$$

where R is the characteristic length (radius) of the dispersed phase and μ_c is the viscosity of the continuous phase, and γ is the interfacial tension. The initial characteristic length of the dispersed phase is the pellet radius, which is not large enough for interfacial forces, γ/R , to play any role at that stage. For example, a dispersed system with characteristic length 2 mm, interfacial tension 30 mN/m, continuous phase viscosity 100 Pa·s, and subjected to a shear rate of 100 s^{-1} experiences a viscous disruptive stress of 10,000 Pa while the resisting interfacial tension stress is only 15 Pa.

As blending proceeds, the characteristic length of the dispersed phase decreases to the point of equilibrium between the disruptive hydrodynamic and cohesive interfacial tension forces. Of course, during the blending process, dispersed droplets come in contact with each other and may coalesce, so that coalescence and breakup are two competitive mechanisms in polymer blends. In the final blending stages miscible and immiscible systems behave differently. On the one hand, in miscible systems homogenization is achieved on a very

small scale, possibly the molecular scale, if sufficient time is allowed. On the other hand, immiscible systems exhibit a two-phase structure whose characteristics depend on the physical parameters of both polymer phases.

In summary, miscible and immiscible systems show similar behavior in the initial steps of the dispersive mixing process, where hydrodynamic forces deform and disrupt the units of the dispersed phase. In the next stages, interfacial tension forces come into play and induce motion (interfacial tension driven Rayleigh or capillary disturbances). Then, at the final stages, miscible systems are expected to be homogenized at the molecular level (if sufficient time is allowed) while immiscible systems retain the coarser structure of a two-phase system.

Next, we give some fundamental ideas on drop deformation and breakup in shear and extensional fields, which are pertinent to the polymer blend area. We consider first simple shear flow. Figure 6.18a shows the deformation of an initially spherical droplet in a simple shear field. In a shear field the droplet assumes an ellipsoidal shape with long axis

L and short axis B , and it is oriented at an angle ϕ with respect to the y axis (see also Fig. 6.11). Theoretical analysis of small deformation, D , was carried out by Taylor (1934) and Cox (1969), and it applies to a single Newtonian droplet suspended in a Newtonian medium. The deformation of the droplet is defined as

$$D \equiv \frac{L - B}{L + B} \quad (6.184)$$

The above definition is appropriate for mildly deformed droplets. However, for highly deformed droplets (Fig. 6.18b) the appropriate measure of deformation is $D = L/R$, where L is now the half length and R is the radius of the undeformed droplet. The steady simple shear solution presented by Cox (1969), which in the limit of small deformation includes the theory of Taylor (1934), is

$$D = \frac{5}{4} \frac{19p + 16}{(p + 1)\sqrt{(19p)^2 + (20/\text{Ca})^2}} \quad (6.185)$$

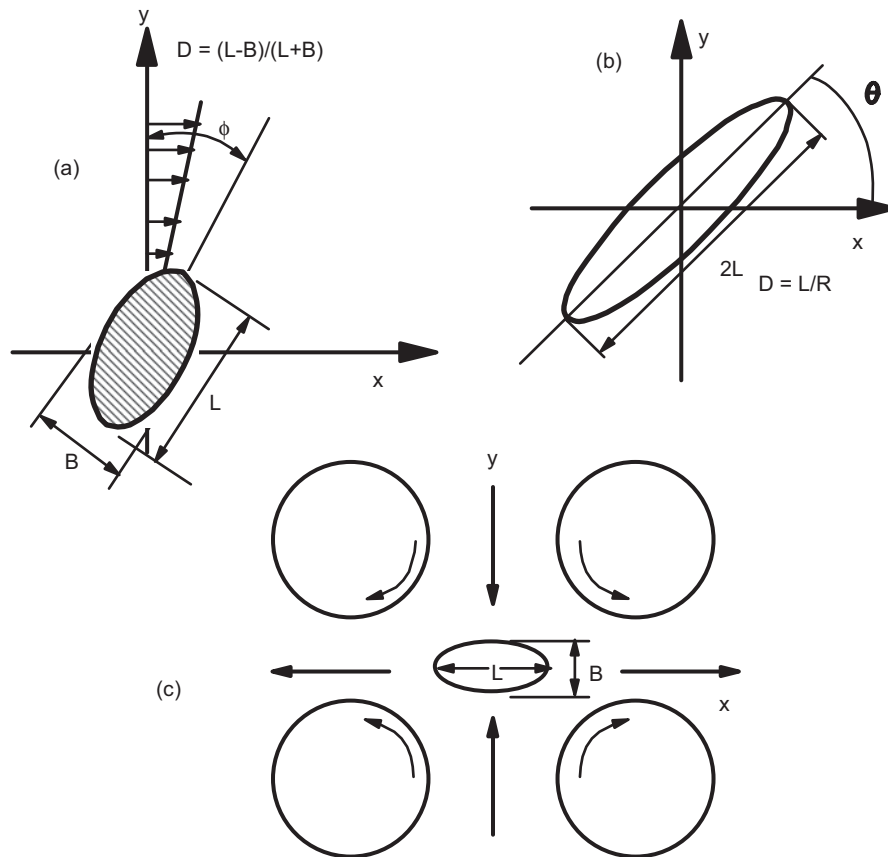


FIGURE 6.18 (a) Geometry and definition of the deformation D of a mildly deformed droplet in simple shear. (b) Geometry and definition of the deformation D of a highly extended droplet in simple shear. (c) Four-roll apparatus generating plane hyperbolic (planar extensional) flow of various strengths.

where p is the ratio of the viscosity of the dispersed to the continuous phase, μ_d/μ_c . The limiting situations of $p \rightarrow \infty$ and $Ca \rightarrow 0$ can easily be determined from Eq. 6.185 as

$$D = \frac{5}{4p} \text{ for } p \rightarrow \infty; Ca = O(1) \quad (6.186)$$

and

$$D = Ca \left(\frac{19p + 16}{16p + 16} \right) = Ca f(p) \text{ for } Ca \rightarrow 0; p = O(1) \quad (6.187)$$

where $O(1)$ stands for ‘‘on the order of magnitude of 1.’’ The orientation of the deformed droplet is

$$\phi = \frac{\pi}{4} + \frac{1}{2} \arctan \left(\frac{19p Ca}{20} \right) \quad (6.188)$$

The limitations of this theory are small deformations (much below the bursting limit), isolated droplets, and Newtonian fluids. Figure 6.19 shows the deformation, D , as a function of the parameter $\dot{\gamma}R$ for $p = 0.0037$. For small values of $\dot{\gamma}R$, the linear region corresponds to Eq. 6.187. At larger and more realistic values of the shear rate the curve is no longer linear.

As the deformation of the droplets increases, they assume elongated shapes and finally, at some value of the capillary number, called the critical capillary number, Ca_c , the disruptive forces exceed the cohesive forces and the droplets burst. An extensive experimental analysis of large deformations that lead to droplet breakup was conducted by Grace (1982) and is presented in Figure 6.20. In this figure, the critical capillary number times a function of the viscosity ratio $f(p)$, where $f(p) = (19p + 16)/(16p + 16)$, is plotted against the viscosity ratio for the two modes of bursting, that is, tip streaming (for $p < 0.1$) and regular

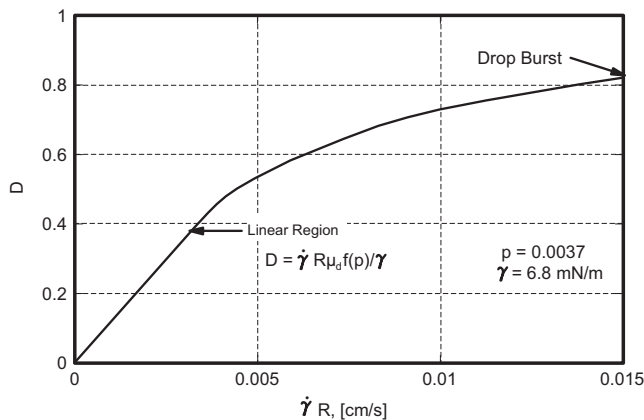


FIGURE 6.19 Deformation D of a droplet as a function of the velocity gradient across the droplet, $\dot{\gamma}R$. (Reprinted by permission of the publisher from Grace, 1982.)

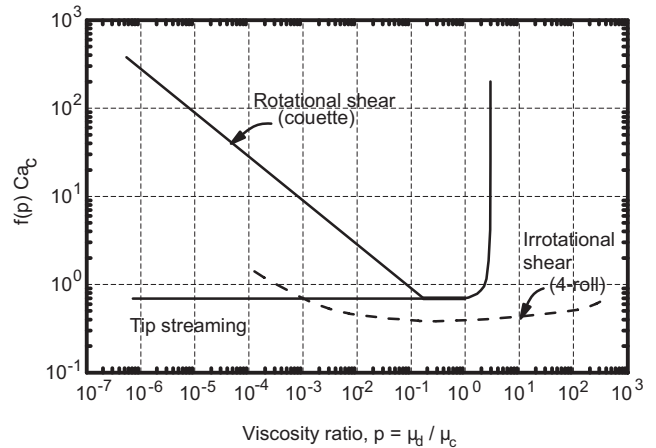


FIGURE 6.20 Critical capillary number versus viscosity ratio p . (Reprinted by permission of the publisher from Grace, 1982.)

bursting. Tip streaming refers to the situation where droplets assume a sigmoidal shape with tiny droplets shedding off the tops. The important feature shown in Figure 6.20 is the inability of shear flows to cause droplet breakup at viscosity ratios exceeding 3.5. Note that for this curve to be applicable to other systems, the increase of the shear rate should be stepwise with very small steps. If the shear increases in large steps, the droplets fragment, and the size of the fragments is not correlated by this curve. The left arm of the shear flow curve can be represented as

$$Ca_c f(p) = Ca_c \frac{19p + 16}{16p + 16} = 0.16p^{-0.16} \quad (6.189)$$

which seems to agree with some theoretical predictions.

Another important parameter of the droplet breakup process is the time necessary for the interfacial-driven instabilities to cause breakup, t_b , when the actual capillary number exceeds the critical capillary number. Grace (1982) provided this information in Figure 6.21 for Newtonian fluids. Note that the dimensionless burst time is denoted as t_b^* , which is equal to t_b/τ , where τ is the time scale of the bursting process and it is equal to $R\mu_c/\gamma$. For example, for a polymer blend with $p = 0.1$, $\gamma = 10$ mN/m, $R = 10$ μ m, $\mu_c = 1,000$ Pa·s, and $Ca/Ca_c = 10$, the dimensionless burst time is 11, and the time scale is equal to 1 s. Thus, the burst time, t_b , is equal to 11 s.

We consider next the planar elongational flow. The experimental setup is a four-roll apparatus (see Fig. 6.18c) used first by Taylor (1934). Cox (1969) developed a theory similar to that for simple shear flow:

$$D(t) = 2Ca \left(\frac{19p + 16}{16p + 16} \right) \left(1 - \exp \left(-\frac{19p}{20Ca} t \hat{\epsilon}_{\text{plel}} \right) \right) \quad (6.190)$$

where $\hat{\epsilon}_{\text{plel}}$ is the extension rate in this pure shear case, and the capillary number is defined based on the shear

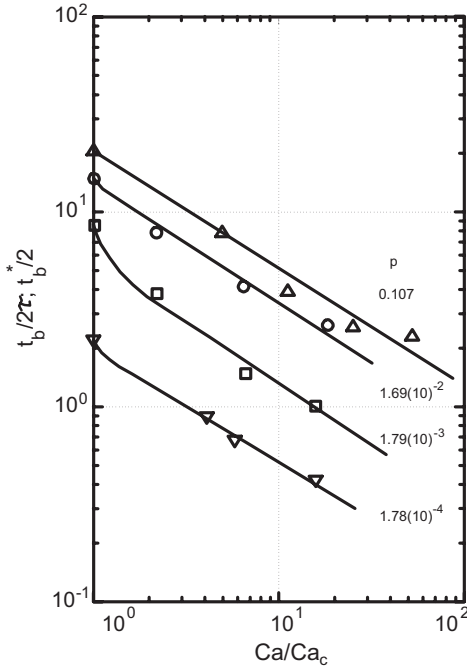


FIGURE 6.21 Effect of exceeding the critical capillary number on time to burst, t_b . $\tau = R\mu_c/\gamma$ is the time scale for burst. (Reprinted by permission of the publisher from Grace, 1982.)

viscosity and $\dot{\epsilon}_{\text{plel}}$. This equation shows that even a high-viscosity dispersed phase can be deformed. Data on pure shear are shown in Figure 6.20 as taken from Grace (1982). Two differences should be pointed out. One is the ability of pure shear flow to break droplets even at high viscosity ratios and the other is the lower value (about 1/3) of the minimum capillary number for pure shear flow compared to simple shear flow. Note that for Newtonian fluids the viscosity in pure shear is twice the simple shear viscosity, and this substitution in the capillary number in this figure will nearly bring the two curves together.

Finally, we consider the uniaxial elongational flow. This flow is more frequently encountered in practice than pure shear flow. Material flowing in a conical die experiences this type of flow. Van der Reijden-Stolk and Sara (1986) studied this flow and found that the deformation grows as

$$D(t) = \frac{3}{2} \text{Ca} \left(\frac{19p + 16}{16p + 16} \right) \left(1 - \exp \left(-\frac{19p}{20\text{Ca}} t \dot{\epsilon}_{\text{unel}} \right) \right) \quad (6.191)$$

where $\dot{\epsilon}_{\text{unel}}$ is the extension rate for uniaxial elongational flow. Comparison of the three flows in terms of the necessary extension rate to achieve the same deformation at long times, that is, comparing Eqs. 6.187, 6.190, and 6.191, shows that

$$\dot{\gamma} : \dot{\epsilon}_{\text{plel}} : \dot{\epsilon}_{\text{unel}} = 6 : 3 : 4 \quad (6.192)$$

The complete picture is formed only when we compare power expended to achieve the same deformation, with the aid of Eqs. 6.78, 6.79, and 6.80:

$$P_{\text{unel}} : P_{\text{plel}} : P_{\text{ss}} = \frac{4}{3} : 1 : 1 \quad (6.193)$$

Thus, for Newtonian fluids simple shear and planar elongational flows require the same power to produce the same deformation while uniaxial elongation requires 33% more power.

After the droplet has been deformed extensively (actual capillary number much higher than the critical capillary number) by one of the mechanisms mentioned above, it will assume a thread-like shape with long cylindrical midsection and two bulbous ends, when $p > 0.05$, and long slender shape with nearly pointed ends, when $p < 0.05$ (Stone and Leal, 1989). These shapes are unstable, because they can break up in the flow field due to interfacial tension driven instabilities (Rayleigh or capillary instabilities; Tomotika, 1935). Moreover, if the flow stops (or the thread moves to a relatively more quiescent environment) the thread can either relax or break up, depending on the extension L/R and the viscosity ratio. Figure 6.22f shows a thread relaxing back to its original droplet shape for $p = 0.01$ and $L/R = 5.3$.

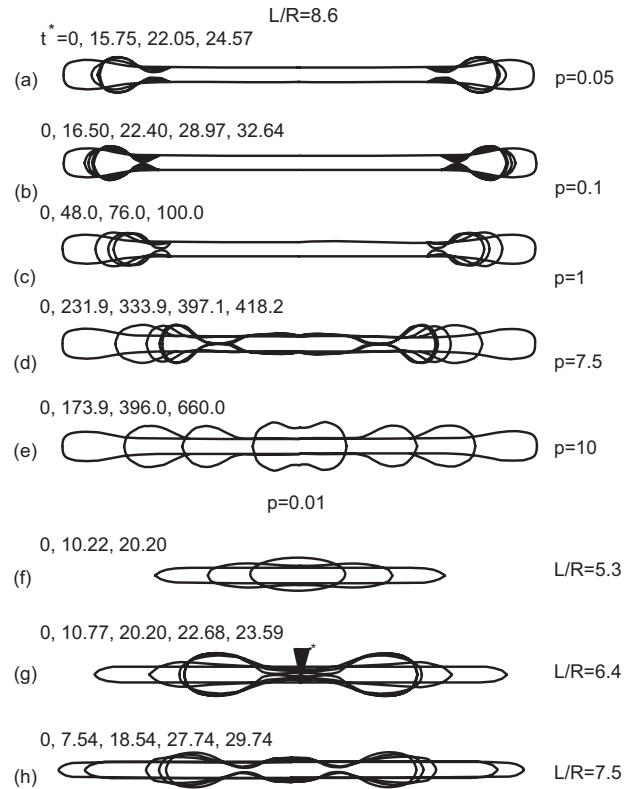


FIGURE 6.22 Relaxation and breakup of initially extended droplets in a quiescent fluid. The time scale is $\tau = R\mu_c/\gamma$. The dimensionless time t^* , equal to t/τ , is shown above each schematic. (Reprinted by permission of the publisher from Stone and Leal, 1989.)

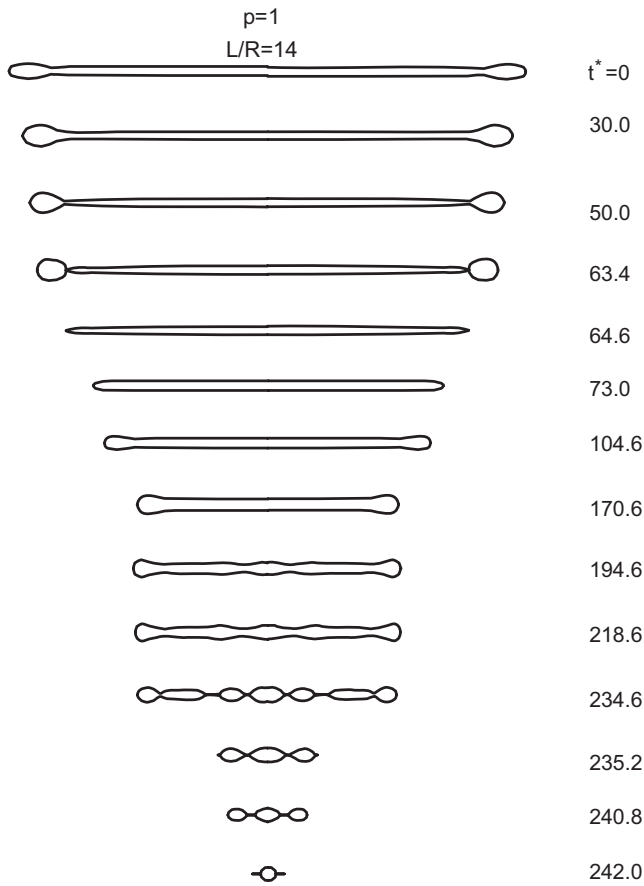


FIGURE 6.23 Evolution of end-pinching and capillary waves during the relaxation and breakup of an initially highly extended droplet suspended in a quiescent fluid. The time scale is $\tau = R\mu_c/\gamma$. The dimensionless time t^* , equal to t/τ , is shown in the side of each schematic. (Reprinted by permission of the publisher from Stone and Leal, 1989.)

Figure 6.22a–e show breakup by shedding off small droplets from the bulbous ends (“end-pinching” mechanism; Stone and Leal, 1989) for $0.05 < p < 10$ and $L/R = 8.6$. Finally, Figure 6.23 shows the combined action of instabilities and end-pinching for $p = 1$ and $L/R = 14$. Apparently, the time scale of the end-pinching mechanism is less than the time scale of the instability mechanism in cases where end-pinching prevails.

Interfacial driven disturbances on a Newtonian thread embedded in a Newtonian matrix are briefly discussed next. An initially long cylindrical thread with midsection radius R_0 is sinusoidally disturbed by a wave of interfacial tension origin as shown in Figure 6.24a. Without going into the details of the analysis we note that the burst time (Elmendorp, 1991) is given as

$$t_b = \frac{1}{q} \ln \left(\frac{0.82R_0}{a_0} \right) \quad (6.194)$$

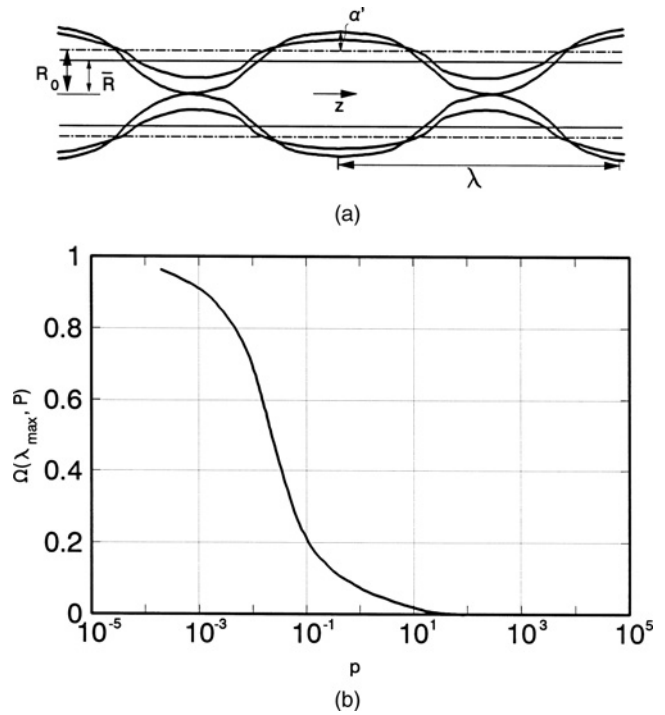


FIGURE 6.24 (a) Capillary waves in an initially uniform midsection radius thread. λ is the distortion wavelength, α' is the distortion amplitude, R_0 is the initial thread radius, \bar{R} is average thread radius, and z is the axis of the thread. (b) Dominant growth rate $\Omega(\lambda_{\max}, p)$ as a function of the viscosity ratio p . (Reprinted by permission of the publisher from Elmendorp, 1991.)

where $1/q$ is the time constant of the distortion process, and α_0 is the distortion amplitude at time equal to zero. $1/q$ is given by the equation

$$\frac{1}{q} = \frac{2\mu_c R_0}{\gamma} \frac{1}{\Omega(\lambda, p)} = \frac{2\tau}{\Omega(\lambda, p)} \quad (6.195)$$

where $\Omega(\lambda, p)$ is a complicated function of the wavelength of the distortion, λ , and the viscosity ratio, p . This function is shown in Figure 6.24b for $\lambda = \lambda_{\max}$, which is the wavelength leading to breakup. Then Eq. 6.194 becomes

$$t_b^* = \frac{t_b}{\tau} = \frac{2}{\Omega(\lambda_{\max}, p)} \ln \left(\frac{0.82R_0}{\alpha_0} \right) \quad (6.196)$$

Although the above equations apply to Newtonian systems, it was shown experimentally that they also apply to situations encountered in polymer blending (Elmendorp, 1991). The absence of the effect of viscoelasticity on polymer thread breakup is attributed to the very low deformation rates of the final stages of breakup (10^{-5} to 10^{-3} s^{-1}). At these rates it can be assumed that most polymers exhibit Newtonian behavior with viscosities equal to their zero-shear values. Examples for the use of the above equations follow.

Example 6.12. Burst Time of a Cylindrical Thread

Calculate the dimensionless and the actual burst time for a cylindrical thread of radius $5\ \mu\text{m}$, viscosity ratio 1, and interfacial tension $10\ \text{mN/m}$ submerged in a Newtonian fluid of viscosity $100\ \text{Pa}\cdot\text{s}$. What is the dimensionless burst time for $p = 0.1$?

Solution. The time scale of the bursting process is $\tau = R_0\mu_c/\gamma = 0.05\ \text{s}$. $\Omega = 0.07$ at $p = 1$ from Figure 6.24b. The amplitude of the distortion that leads to burst is usually considered to be 0.3% of the initial radius of the midsection. Then Eq. 6.196 gives the dimensionless burst time as

$$t_b^* = \frac{2}{0.07} \ln\left(\frac{0.82}{0.003}\right) = 160 \quad (6.197)$$

Thus, the actual burst time is $160 \times 0.05\ \text{s} = 8\ \text{s}$. Similarly, for viscosity ratio of 0.1 , $t_b^* = 53$. ■

Figure 6.23 can be used to compare the dimensionless times for end-pinching and instability growth. It is seen from this figure that the dimensionless time for end-pinching is about 64, whereas the dimensionless time for instability growth is 160 as calculated in Example 6.12. Figure 6.23 shows also that the dimensionless time for complete breakup is about 240.

In the analysis of drop breakup it is assumed that a single drop exists in an infinite sea of the polymer matrix. In practice, this is not the case. The effect of the volume fraction of the minor component can be double: (1) the presence of drops alters the hydrodynamics around the other drops, and (2) coalescence can take place due to increased probability of collisions. Mathematically, both phenomena can be grouped into a linear relationship (without rigid foundations; borrowed from experiments in agitated tanks):

$$R = R_T(1 + k\phi) \quad (6.198)$$

where R_T refers to the drop radius according to Taylor's theory (Eq. 6.187), k is a constant, and ϕ is the volume fraction of the minor component. Typical values of k range from 5 to 200 (Elmendorp, 1991).

Example 6.13. Blend Morphology

A PP/PS blend is formed in a roll-mill apparatus and the cooling step to temperatures below the glass transition temperature of PS ($\cong 100\ ^\circ\text{C}$) takes about 30 s. Comment on the possibility that initially in the roll-mill threads were present that later on burst to smaller droplets due to instabilities. The final morphological examination showed PP droplets of $10\ \mu\text{m}$ in size. Assume that $\gamma = 5\ \text{mN/m}$ and that the Newtonian viscosities are $\mu_c = \mu_d = 1000\ \text{Pa}\cdot\text{s}$.

Solution. We will test the scenario of small droplets (of radius $10\ \mu\text{m}$) undergoing end-pinching to form elongated threads with a thread midsection radius of about $4\ \mu\text{m}$. Then the extension ratio is $L/R = 6 \times (4/3) \times (R/R_0)^2 = 50$, if we assume that each thread produces six droplets. The calculation of the time to burst due to capillary instabilities follows exactly Example 6.12, and it is equal to 128 s. But because the extension ratio is large, both end-pinching and capillary instabilities play a role. Figure 6.23 shows that end-pinching precedes burst by capillary instabilities and that the starting time for end-pinching was one-third of the time for capillary breakup. Thus, if the same analogy holds in our system, at about 40 s two droplets will be shed off the ends of the thread. This time is slightly longer than the cooling time. For $R_0 = 3\ \mu\text{m}$, $t_b = 95\ \text{s}$. The conclusion is that the possibility of threads breaking up during the cooling step cannot totally be ruled out. ■

In the following example the application of ideas from drop breakup in extruders using a simplified flow theory is shown.

Example 6.14. Thread Breakup in Extruders

A melt-fed extruder is used for melt blending of two polymers with equal constant viscosities of $100\ \text{Pa}\cdot\text{s}$ and interfacial tension of $5\ \text{mN/m}$. The maximum shear rate in the screw channel is about $110\ \text{s}^{-1}$. The flight clearance in the extruder, δ_f , is $250\ \mu\text{m}$, the barrel diameter is $D = 2.54\ \text{cm}$, the screw rotational frequency is $N = 100\ \text{rpm}$, the flight width is $e = 0.254\ \text{cm}$, the mass flow rate is $\dot{m} = 1.4\ \text{g/s}$, the polymer density is $\rho = 1\ \text{g/cm}^3$, and the mean residence time is $\bar{t} = 138\ \text{s}$. The molten feed into the extruder consists of a dispersion of $5\ \mu\text{m}$ in radius. Assuming that the melt passes through the flight clearance once, is it possible that the final morphology consists of even a finer dispersion? Neglect any effect of extensional flows that occur as the fluid passes from the channel through the flight clearance.

Solution. The shear rate experienced by the blend when it passes through the flight clearance is calculated as (see Section 8.3.3)

$$\dot{\gamma}_{\text{clearance}} = \frac{\pi DN}{\delta_f} \cong 550\ \text{s}^{-1} \quad (6.199)$$

Using Figure 6.20, the critical capillary number for $p = 1$ and shear flow is equal to 0.79. The actual capillary number in the flight clearance is 55, so that the actual value of Ca exceeds the critical value 69 times. The dimensionless burst time for that ratio of capillary numbers is calculated using Figure 6.21 to be at least 2 (in this figure there is no entry for $p = 1$, so that the corresponding value for viscosity ratio of 0.107 is used as the lower limit). The time scale of the burst

process, τ , is equal to $R\mu_c/\gamma = 0.1$ s, and thus the actual burst time is $t_b > 4\tau = 0.4$ s. The residence time in the flight clearance is

$$\bar{t}_{\text{flight}} = \frac{\pi\rho D e \delta_f}{\dot{m}} = 0.03 \text{ s} \quad (6.200)$$

Thus, the residence time in the flight clearance is not enough for burst. However, the droplets during the flow in the flight clearance can be deformed into threads, because the shear strain in the clearance is equal to $550 \times 0.03 = 16.5$. According to Eqs. 6.104 and 6.105, the thread will have half-length and half-width to initial radius ratios of

$$\frac{L}{R} = \sqrt{1 + \gamma^2} = 16.5; \quad \frac{B}{R} = (1 + \gamma^2)^{-1/4} = 0.25 \quad (6.201)$$

So, the total length of the thread will be $160 \mu\text{m}$ and its radius $1.25 \mu\text{m}$. This thread will be subjected to end-pinch and capillary instability. The burst time due to the capillary instability is calculated as in Example 6.12. It is equal to 4 s, while the mean residence time in the extruder is 138 s. Thus, the final morphology will include finer droplets of the dispersed phase. ■

6.6 THERMODYNAMICS OF MIXING

In Section 6.5 polymer–polymer miscibility was considered to be an important parameter in the dispersion of the two polymer phases. In this respect a polymer–polymer system can be considered as miscible, immiscible, or partially miscible depending on the relative solubility of the two polymers. Total solubility characterizes a miscible system, insolubility an immiscible system, and partial solubility a partially miscible system. The degree of miscibility has important effects on the mechanical, physical, rheological, and optical properties of the resulting blend.

Measuring the glass transition temperature is the most common technique to detect miscibility. When a polymer blend is immiscible, the two constituent polymers will keep their identity and thus exhibit two distinct glass transition temperatures. However, a miscible blend will consist of one phase and exhibit a single glass transition temperature (in between the glass transition temperatures of the constituent polymers). Finally, a partially miscible system will exhibit two glass transition temperatures, shifted toward each other with respect to the original glass transition temperatures of the two polymers. Figure 6.25 shows schematically the above behavior in a typical $\tan \delta$ (δ is the loss angle) versus temperature graph.

Thermodynamically, mixing will take place when it is favored energetically, that is, when

$$\Delta G_{\text{mix}} = \Delta H_{\text{mix}} - T \Delta S_{\text{mix}} \leq 0 \quad (6.202)$$

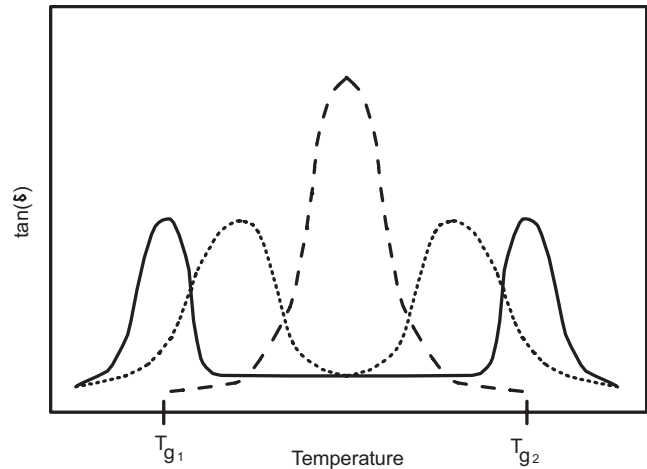


FIGURE 6.25 Loss angle, δ , as a function of temperature for various types of polymer blends: (a) miscible (dashed line), (b) immiscible (solid line), and (c) partially miscible (dotted line). The glass transition temperature, T_g , is the temperature at the peak of the loss angle.

where ΔG_{mix} , ΔH_{mix} , and ΔS_{mix} are the changes of the Gibbs free energy, enthalpy (or heat), and entropy, respectively, of mixing. The heat of mixing, ΔH_{mix} , is usually a positive quantity (endothermic process). The entropy of mixing is positive because the randomness of the mixture is higher than the randomness of the components. It should be noted that the condition of Eq. 6.202 is necessary, although not sufficient, for the formation of a stable solution. The heat of mixing is related to a parameter called the *solubility parameter*, δ , through the relationship

$$\Delta H_{\text{mix}} = V (\delta_1 - \delta_2)^2 \phi_1 \phi_2 \quad (6.203)$$

where V is the volume of the mixture and ϕ_1 and ϕ_2 are the volume fractions of the solvent and solute, respectively. If $\delta_1 = \delta_2$, then $\Delta H_{\text{mix}} = 0$ and $\Delta G_{\text{mix}} \leq 0$, and so the components will be miscible in all proportions (for equally hydrogen bonding capable polymers). Table 6.2 includes some typical

TABLE 6.2 Solubility Parameter Values for Various Polymers

Polymer	δ (MPa ^{1/2})	
	From	To
PE	15.8	12.1
PP	16.8	18.8
PS	17.4	19.0
PVC	19.2	22.1
PMMA	18.6	26.2
PAN	25.6	31.5
PB	16.6	17.6

Source: Van Krevelen, 1990.

TABLE 6.3 Interfacial Tension Values for Typical Polymer Pairs

Polymer Pairs	γ (mN/m) at 140 °C	$-d\gamma/dT$ (mN/m·°C)
PE/PP	1.1	—
PE/PS	5.9	0.020
PE/PMMA	9.7	0.018
PE/PEO	9.7	0.016
PP/PS	5.1	—

Source: Wu, 1982.

values of the solubility parameter for polymers. Finally, the interfacial tension of polymer systems was shown to be very important in the area of dispersive mixing as a determining factor of the final blend morphology. Table 6.3 summarizes interfacial tensions of polymer pairs.

6.7 CHAOTIC MIXING

A recent advance in the area of mixing is that of *chaotic mixing*. Mixing was analyzed in Section 6.3 in terms of intermaterial area generation or reduction of striation thickness. It was shown that simple shear flows, which are extensively present in the area of polymer mixing, have time decaying average mixing efficiencies (see Fig. 6.10). This flow, which is thus considered a weak mixing flow, owes its mixing inefficiency to the eventual orientation of the intermaterial area along the streamlines. However, simple flows can exhibit chaotic mixing, if they become periodic in nature. In that case, the intermaterial area increases exponentially with time, thus providing an effective means of mixing.

Aref (1984) indicated that the equations which describe the particle trajectories in a two-dimensional flow have a *Hamiltonian* structure, that is,

$$v_x = \frac{dx}{dt} = \frac{\partial \psi}{\partial y}; \quad v_y = \frac{dy}{dt} = -\frac{\partial \psi}{\partial x} \quad (6.204)$$

where ψ is the stream function. A Hamiltonian system is a physical system of particles whose motions are described by deterministic equations. If ψ in Eq. 6.204 is independent of time, then the velocity field is steady and the system cannot be chaotic. However, if ψ is time periodic, that is, depends on x , y , and t , then there is a good chance that the system will be chaotic. Aref (1984) applied this idea to the blinking vortex system, which is a system consisting of two alternating corotating vortices. These vortices switch on and off for half the cycle time.

A flow can be termed chaotic if it satisfies any of the following criteria:

1. Positive *Liapunov exponents* in a given region of the flow,

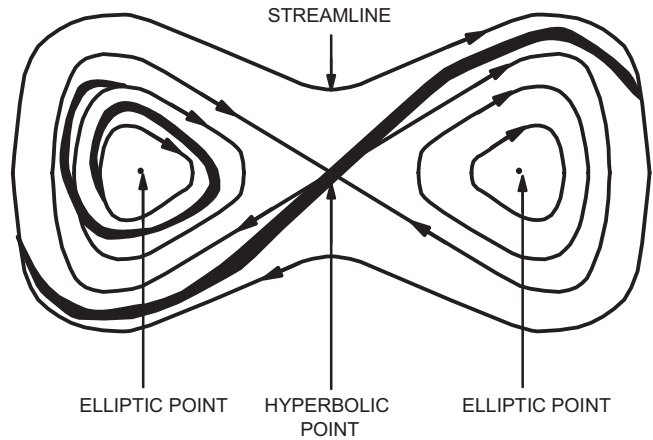


FIGURE 6.26 Elliptic and hyperbolic points. A blinking vortex system with vortex centers at the elliptic points can produce this streamline pattern.

2. Presence of *transverse homoclinic* or *heteroclinic* points, and
3. Presence of *Smale horseshoe maps*.

The Liapunov exponent, σ , is related to the long time behavior of the lineal stretch, and it is equal to:

$$\sigma = \lim_{t \rightarrow \infty} \frac{\ln(\lambda)}{t} \quad (6.205)$$

where λ is the lineal stretch given by Eq. 6.86. Note that the Liapunov exponent of a simple steady shear flow is 0, because as $t \rightarrow \infty$ the term $\ln(\dot{\gamma}t)/t$ goes to zero, and thus simple steady shear flow cannot produce chaos.

The definition of the *homoclinic* and *heteroclinic* points needs first the introduction of *hyperbolic* and *elliptic* points. A two-dimensional flow always consists of hyperbolic and/or elliptic points (Fig. 6.26). At the hyperbolic point the fluid moves toward it in one direction and away from it in another direction. At an elliptic point the fluid moves in closed pathlines. A periodic point is defined as the point at which a particle in a periodic flow returns after a number of periods. The number of periods defines also the order of the periodic point, as periodic point of period 1, 2, and so on. Note that the periodic elliptic points should be avoided should we want enhanced mixing. A point where the outflow of one hyperbolic point intersects the inflow of another hyperbolic flow is called *transverse heteroclinic* point. When the inflow and outflow refer to the same hyperbolic point, the point is called *transverse homoclinic* point.

The last identifying feature of chaos is the presence of *Smale horseshoe maps* (Fig. 6.27a). A typical map involves the stretching and folding of a square with itself. Mixing has been promoted in that sense, because the perimeter of the initial square has increased or the striation thickness has

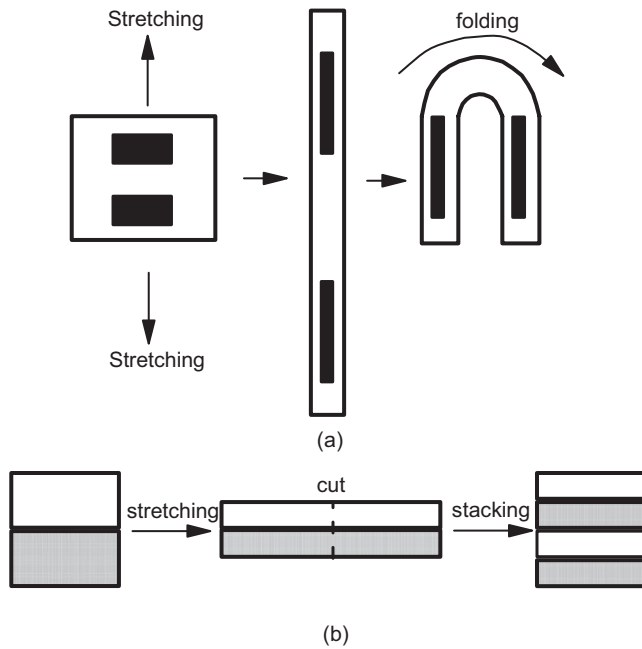


FIGURE 6.27 (a) Representation of typical Smale horseshoe map. (b) Representation of the baker's transformation.

decreased. The Smale horseshoe map is similar to the *baker's transformation*, Figure 6.27b, which involves stretching, cutting, and stacking of fluid elements (see also Spencer and Wiley, 1951), and it is considered to be the best possible mixing from the mathematical point of view.

The simplest flow that can exhibit chaos is two-dimensional flow. Ottino and co-workers (Chien et al., 1986; Khakhar et al., 1986; Leong and Ottino, 1989) produced chaotic mixing in simple prototypical devices, such as cavity flow, partitioned-pipe mixer (e.g., a Kenics static mixer as discussed in Section 8.5), and eccentric helical annular mixer with Newtonian fluids. Of prime interest in the area of polymer processing, of course, is the work in cavity flows. A typical cavity was constructed with the ability of movement of both top and bottom plates. Typical cavity flow, which is described in Chapter 8, corresponds to the steady movement of the top plate only. However, corotational (in the opposite direction) movement of both plates in a periodic fashion induces chaos in the cavity. Leong and Ottino (1989) used two types of movement: discontinuous and continuous in a sinusoidal manner (Fig. 6.28). In the discontinuous corotational flow, the top plate first moves for a half period, then it stops for 5 s, and the cycle ends with the bottom plate moving for a half period in the opposite direction. In the continuous type of movement, both plates move sinusoidally at the same time, but with a phase difference of $\pi/2$.

In terms of stretching and dispersion, mixing achieved in the discontinuous corotational periodic type of flow is superior compared to the steady flow as shown in Figure 6.29. This figure shows the streamlines of a fluorescent dye

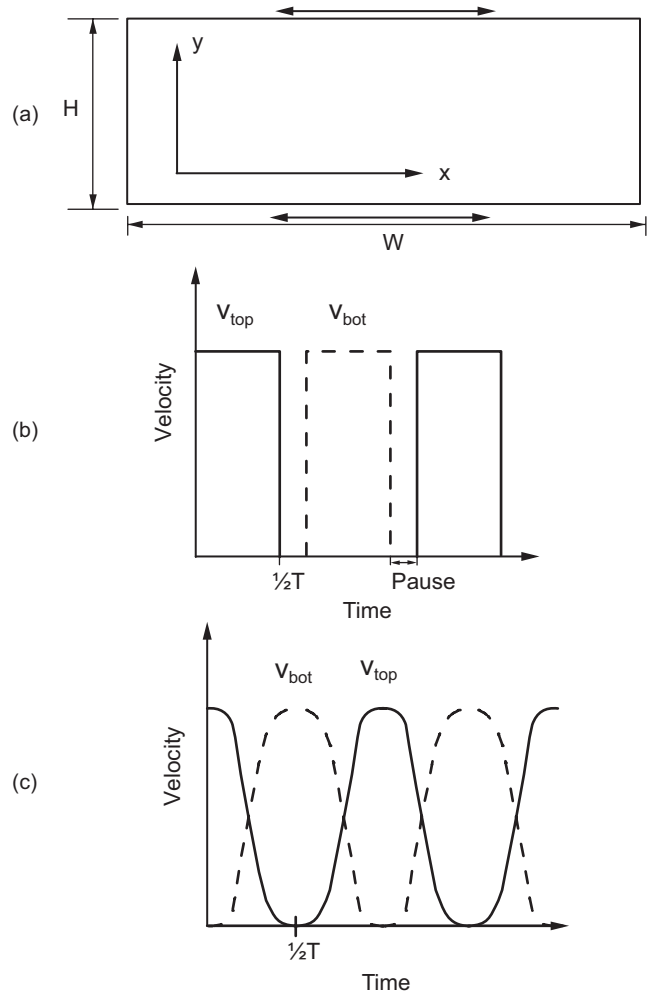


FIGURE 6.28 (a) Typical cavity used for corotational movement of both plates. (b) Top and bottom plate motion in discontinuous form. The solid line represents motion of the top plate, whereas dashed line represents motion of the bottom plate. Pause is for 5 s. (c) Top and bottom plate motion in continuous and sinusoidal form. (Reprinted by permission of the publisher from Leong and Ottino, 1989.)

injected below the top plate at the center of the cavity at time $t = 0$. The perimeter of the dye regions is indicative of the degree of mixing. Figure 6.30 shows the exponential growth of the degree of mixing for both the discontinuous and the continuous type of periodic flow and the linear growth for steady flow. Furthermore, the efficiency of the periodic flows is higher for the discontinuous case than the continuous and the form of the exponential increase is

$$P = P_0 e^{\beta t} \tag{6.206}$$

where P is the perimeter and β can be considered to be the average Liapunov exponent for the process.

A relevant question at this point is: Can we take advantage of chaos in typical polymer processing conditions? The

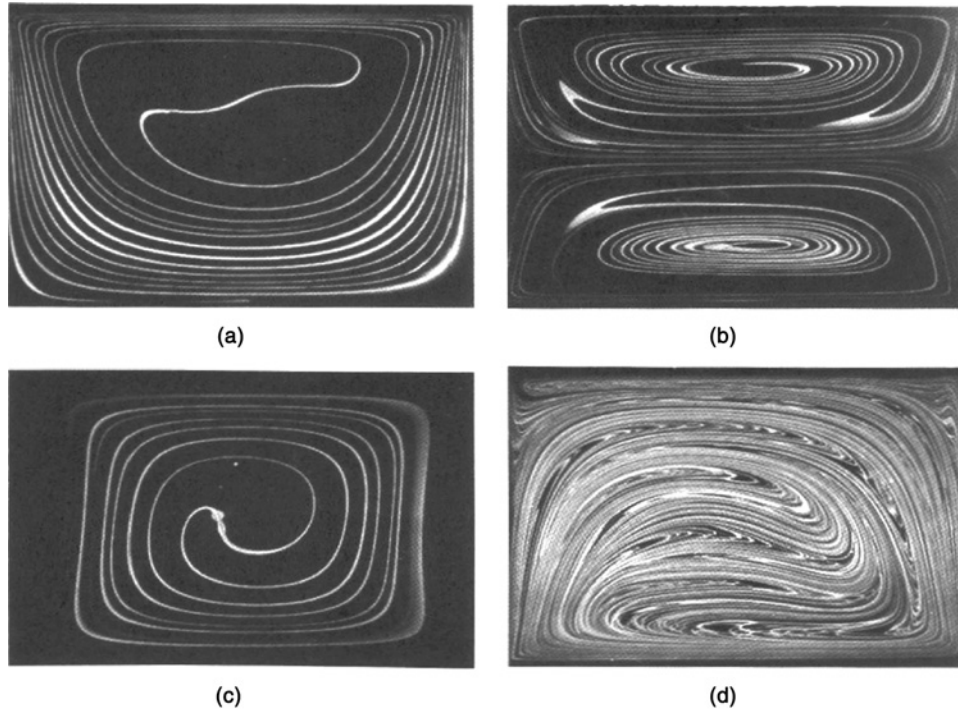


FIGURE 6.29 Comparison of the degree of mixing for steady and periodic cavity flows. Dimensionless total plate displacement per period, $N_d = DP$, where D is the dimensionless plate displacement per period and P is the total number of periods. (a) Steady flow; $Re = 1.0$; total mixing time is 300 s; $N_d = 55$. (b) Steady flow; both plates moving in the same direction; total mixing time is 300 s; $N_d = 110$. (c) Steady flow; plates moving in the opposite direction; total mixing time is 300 s; $N_d = 110$. (d) Periodic discontinuous flow; total mixing time is 280 s (4 periods); $N_d = 51.4$. (Reprinted by permission of the publisher from Leong and Ottino, 1989.)

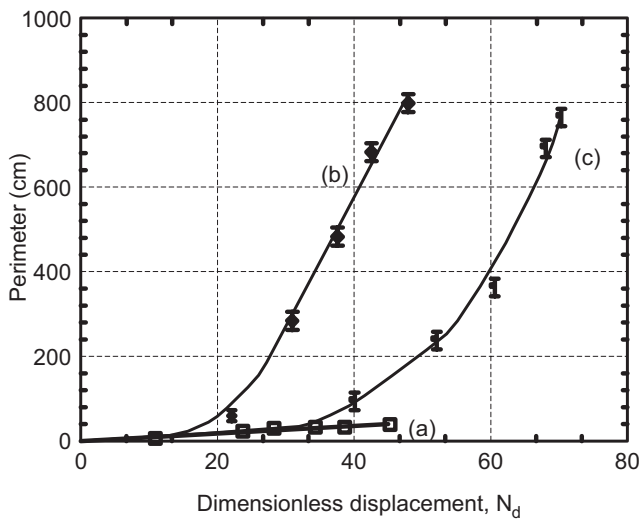


FIGURE 6.30 Perimeter growth of dye regions for steady, corotational discontinuous and continuous cavity flows, as a function of the dimensionless displacement, N_d . (a) Steady flow. (b) Discontinuous. (c) Continuous. (Reprinted by permission of the publisher from Leong and Ottino, 1989.)

answer is that we need more understanding of the chaotic processes before we can design better mixers for polymers. This design, when accomplished, will be considered as a major step forward in mixing.

6.8 SOLUTION TO DESIGN PROBLEM V

We finally return to the solution of Design Problem V (Fig. 6.31). The flow in the die is helical in nature; that is, it consists of an axial Poiseuille flow and a drag Couette rotational flow due to the rotation of the mandrel. The analysis of the striation thickness of each layer will be based on simple geometrical and kinematical arguments, and it will be shown that the two approaches give the same results. For Newtonian fluids, the axial and angular flow fields are independent and given in Tables 2.7 and Example 6.7, respectively.

The volumetric flow rate is calculated (Table 2.7) as

$$Q = \int_{kR}^R v_z(r) 2\pi r \, dr = \frac{\pi \Delta P R^4}{8\mu L} \left[1 - \kappa^4 - \frac{(1 - \kappa^2)^2}{\ln(1/\kappa)} \right] \tag{6.207}$$

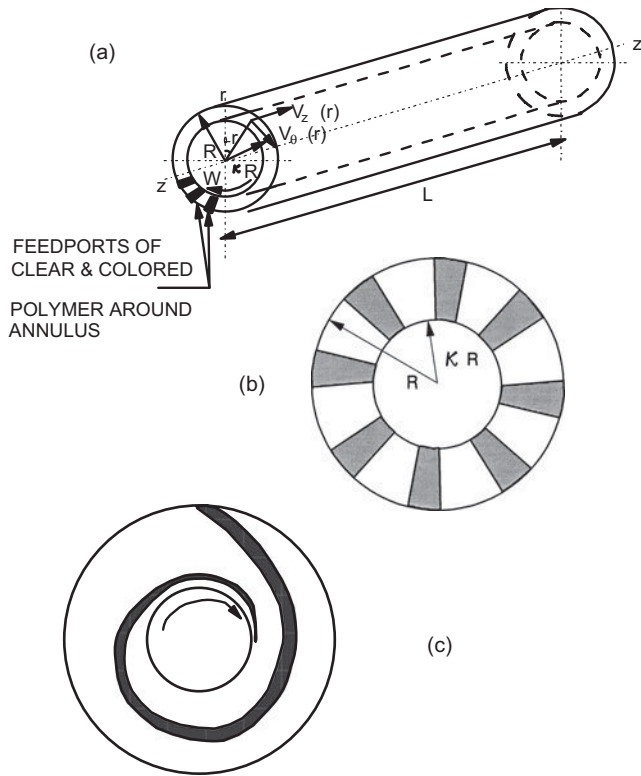


FIGURE 6.31 (a) Geometry of the continuous annular mixer die. (b) Feed distribution entering the annular die. (c) Mixing pattern generated in the die for a single feedport.

The axial velocity can now be written as

$$v_z = \frac{2Q}{\pi R^2} \frac{1 - \left(\frac{r}{R}\right)^2 + \frac{1 - \kappa^2}{\ln(1/\kappa)} \ln\left(\frac{r}{R}\right)}{1 - \kappa^4 - \frac{(1 - \kappa^2)^2}{\ln(1/\kappa)}} \quad (6.208)$$

The deformation of a material element as it rotates in a $r\theta$ plane is shown in Figure 6.32a, and as it translates down the z axis in Figure 6.32b. After time t the material has experienced both deformations. For simplicity we assume that the axial deformation is negligible compared to the rotational deformation:

$$\frac{dv_\theta}{dr} \gg \frac{dv_z}{dr} \quad (6.209)$$

Thus, the deformation in Figure 6.32b is considered negligible. From purely geometrical considerations the striation thickness, δ , and the initial striation thickness, δ_0 , are related:

$$\frac{\delta}{\delta_0} = \sin \beta \quad (6.210)$$

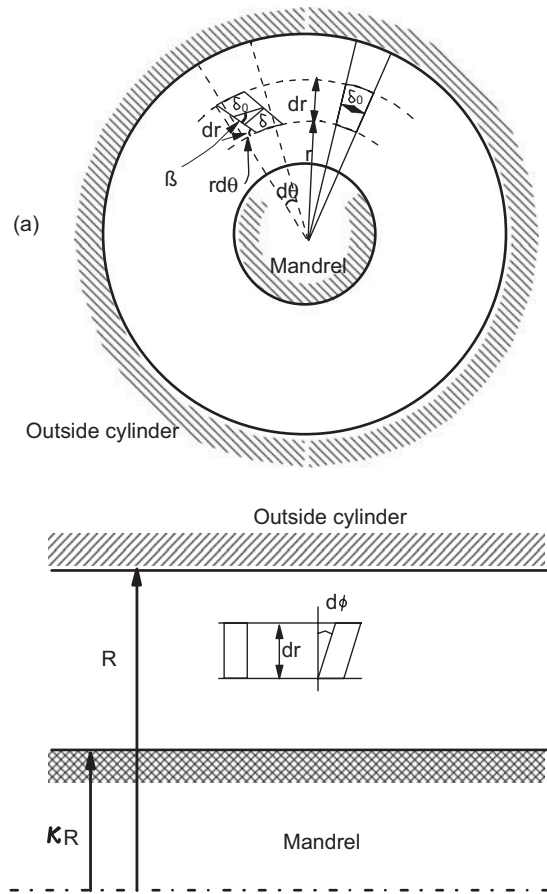


FIGURE 6.32 (a) Geometry of the material element deformation at a constant z plane. (b) Geometry of the material element deformation at a constant θ plane.

where the angle β is related to $d\theta$ through the relation

$$\tan \beta = \frac{1}{r \frac{d\theta}{dr}} \quad (6.211)$$

But $\sin \beta \cong \tan \beta$ for small β angles, and Eq. 6.210 with the aid of Eq. 6.110 becomes

$$\frac{\delta}{\delta_0} = \frac{1}{r \frac{d\theta}{dr}} = \frac{1 - \kappa^2}{2\kappa^2 W t} \left(\frac{r}{R}\right)^2 \quad (6.212)$$

The residence time t is related to the axial velocity as

$$t(r) = \frac{L}{v_z(r)} \quad (6.213)$$

and the combination of Eqs. 6.213 and 6.212 yields

$$\frac{\delta}{\delta_0} = \frac{Q}{\pi W L R^2} \frac{1 - \kappa^2}{\kappa^2} \left(\frac{r}{R}\right)^2 \frac{1 - \left(\frac{r}{R}\right)^2 + \frac{1 - \kappa^2}{\ln(1/\kappa)} \ln\left(\frac{r}{R}\right)}{1 - \kappa^4 - \frac{(1 - \kappa^2)^2}{\ln(1/\kappa)}} \quad (6.214)$$

By noting that

$$\bar{t} = \frac{\pi L R^2 (1 - \kappa^2)}{Q} \quad (6.215)$$

Eq. 6.214 reduces to

$$\begin{aligned} \frac{\delta}{\delta_0} &= \frac{1}{W \bar{t}} \frac{1 - \kappa^2}{\kappa^2} \left(\frac{r}{R}\right)^2 \frac{1 - \left(\frac{r}{R}\right)^2 + \frac{1 - \kappa^2}{\ln(1/\kappa)} \ln\left(\frac{r}{R}\right)}{1 - \kappa^4 - \frac{(1 - \kappa^2)^2}{\ln(1/\kappa)}} \\ &= \frac{f(\kappa, r/R)}{W \bar{t}} \end{aligned} \quad (6.216)$$

The radial dependence of the striation thickness reduction function is shown in Figure 6.33a for various values of the parameters κ and $W \bar{t}$. As is expected, the maximum reduction takes place at the center part of the gap, and the minimum reduction takes place at the cylinders. Also at the gap the higher the parameter $W \bar{t}$, the smaller the striation thickness is. Differentiation of Eq. 6.216 yields the radial position where the maximum reduction in striation thickness takes place, r_{\max} . The resulting equation is nonlinear

$$1 - 2 \left(\frac{r_{\max}}{R}\right)^2 + \frac{1 - \kappa^2}{\ln(1/\kappa)} \left[\ln\left(\frac{r_{\max}}{R}\right) + \frac{1}{2} \right] = 0 \quad (6.217)$$

and it can be solved as

$$r_{\max} = \phi(\kappa) R \quad (6.218)$$

so that the maximum striation thickness reduction of Eq. 6.216 becomes

$$\left(\frac{\delta}{\delta_0}\right)_{\max} = \frac{f(\kappa, \phi(\kappa))}{W \bar{t}} \quad (6.219)$$

Figure 6.33b shows the maximum striation thickness as a function of the total angular displacement in radians, $W \bar{t}$, for various values of the parameter κ . For specifications that the maximum striation thickness should not exceed a specified

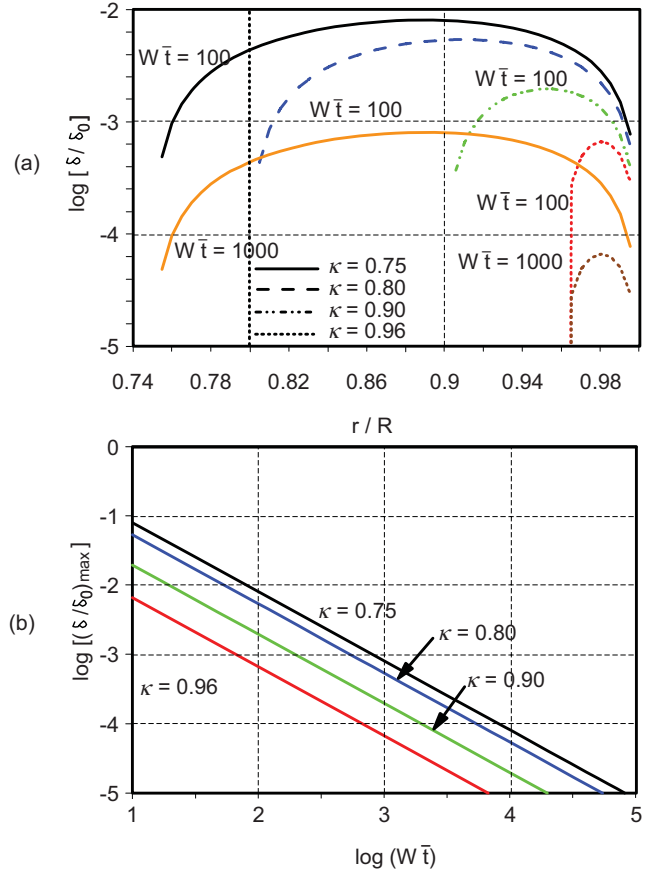


FIGURE 6.33 (a) Radial distribution of the striation thickness reduction function, for various values of the total angular displacement in radians, $W \bar{t}$. κ is the ratio of radii of the mandrel and the outside cylinder. (b) Maximum reduction of striation thickness as a function of the total angular displacement in radians, $W \bar{t}$.

value the minimum rotational frequency, N_{\min} , is calculated from Eq. 6.219 as

$$N_{\min} = \frac{Q}{2\pi^2 R^2 L (1 - \kappa^2)} f(\kappa, \phi(\kappa)) \left(\frac{\delta}{\delta_0}\right)_{\max}^{-1} \quad (6.220)$$

Using the data of Design Problem V, for $\delta_0 = (\pi R)/10$, and $\phi(0.96) = 0.98034$, we get

$$N_{\min} = 188 \text{ rev/min} \quad (6.221)$$

The validity of the above analysis was based on the assumption of Eq. 6.209 that now can be checked to be true ($|dv_\theta/dr| \cong 16|dv_z/dr|$, at $r = R(\kappa + 1)/2$). The power to rotate the mandrel is calculated as

$$P_{\text{mandrel}} = (2\pi\kappa RL)\tau_{r\theta}(\kappa R)v_\theta(\kappa R) \quad (6.222)$$

which for Design Problem V becomes $P_{\text{mandrel}} = 3.6$ kW. The pumping power is calculated to be $P_{\text{pumping}} = Q\Delta P = 32.5$ kW. Suggestions for lowering the power consumptions would be to increase the gap, the temperature, and the rotational frequency. To evaluate the new conditions one should repeat the steps.

Calculations of the striation thickness based on the kinematics developed in Section 6.3.2 and outlined in Example 6.5 require the use of *scale factors* (Bird et al., 1977). These scale factors are necessary for the calculation of the components of the deformation-gradient tensor in curvilinear coordinates. Note that Eq. 6.83 applies to rectangular coordinates only. Integration of the velocity profiles with respect to time yields:

$$\begin{aligned} r &= r_0; \quad \theta = \theta_0 + \frac{\kappa^2 W t}{\kappa^2 - 1} \left[1 - \left(\frac{R}{2} \right)^2 \right] \\ z &= z_0 + Q' \left[1 - \left(\frac{r}{R} \right)^2 + \frac{1 - \kappa^2}{\ln(1/\kappa)} \ln \left(\frac{r}{R} \right) \right] t \end{aligned} \quad (6.223)$$

where Q' is given by

$$Q' = \frac{2Q}{\pi R^2} \frac{1}{1 - \kappa^4 - \frac{(1 - \kappa^2)^2}{\ln(1/\kappa)}} \quad (6.224)$$

The only nonzero components of the deformation-gradient tensor are

$$F_{11} = F_{22} = F_{33} = 1 \quad (6.225)$$

and

$$F_{21} = -\frac{2\kappa^2 W t R^2}{1 - \kappa^2} \frac{1}{r_0^2}; \quad F_{31} = Q' \left(-2 \frac{r_0}{R^2} + \frac{1 - \kappa^2}{\ln(1/\kappa)} \frac{1}{r_0} \right) t \quad (6.226)$$

Note that the only time the scale factor was used was in the calculation of F_{21} :

$$F_{21} = r_0 \frac{\partial \theta}{\partial r_0} \quad (6.227)$$

Then, the nonzero components of the Cauchy–Green strain tensor are

$$C_{22} = C_{33} = 1; \quad C_{12} = C_{21} = F_{21}; \quad C_{13} = C_{31} = F_{31} \quad (6.228)$$

and

$$C_{11} = 1 + F_{21}^2 + F_{31}^2 \quad (6.229)$$

For a line initially oriented along the r axis, the lineal stretch, λ , is then given from Eq. 6.86 as

$$\lambda^2 = 1 + \left[\frac{-2\kappa^2 W R^2 t}{1 - \kappa^2} \frac{1}{r_0^2} \right]^2 + \left[Q' t \left(-2 \frac{r_0}{R^2} + \frac{1 - \kappa^2}{\ln(1/\kappa)} \frac{1}{r_0} \right) \right]^2 \quad (6.230)$$

The following two simplifying assumptions will be made. First, the second term on the RHS of Eq. 6.230 is much greater than 1, which is equivalent to angle β being small in the geometrical analysis. Second, the second term on the RHS of Eq. 6.230 is much greater than the third term of the same equation, which is equivalent to Eq. 6.209. Then, the analysis based on striation thickness calculations becomes

$$\frac{\delta}{\delta_0} = \frac{1}{\lambda} \cong \frac{1 - \kappa^2}{2\kappa^2 W t} \left(\frac{r}{R} \right)^2 \quad (6.231)$$

which is the same as Eq. 6.212.

PROBLEMS

A. Applications

6A.1 Probing of Local Structure. Consider a 3% carbon black dispersion in PE. Light is transmitted through a 25 μm thick sample, and the transmittance is used to characterize the local structure. Determine the required diameter of the light beam to achieve this goal, if the carbon black particle diameter is 1 μm and the density ratio of carbon black to PE mixture is 1.5.

6A.2 Confidence Intervals for Mixtures. A masterbatch of PE/carbon black is used for product formulation. The carbon black weight fraction in the masterbatch is determined by sampling a certain number of pellets from 10 bags. The weight fraction in each of these 10 bags is: 26.7, 28.0, 33.5, 27.8, 29.3, 31.9, 31.5, 33.6, 30.9, and 34.0. The masterbatch will be mixed with virgin PE to produce a blend with the following specifications: 97.5% of the blended samples should have a carbon black weight fraction of at least 10%. Calculate the additional masterbatch weight fraction that should be blended with the virgin PE due to the variation of the carbon black contained in the masterbatch.

6A.3 Statistical Description of Mixtures. Glass fibers are mixed in conventional thermoplastics (e.g., PPS) to enhance the properties of the matrices. Suppose that a requirement for the improvement of the properties is that the number density of the glass fibers is very uniform in a cross section of the final part.

Design a statistical analysis which could lead you to assure your client that the properties meet the specifications with a certain level of confidence.

6A.4 *Mixing Indices*

- (a) Prove that the values of the mixing index of Eq. 6.15 lie between $1/n$ and ∞ , where n is the size of the sample.
- (b) Calculate the mixing index for a completely uniform sample, based on Eq. 6.17, as a function of the sample size.

6A.5 *Correlation Coefficient.* Complete all the steps in Example 6.3.

6A.6 *Scale of Segregation.* Prove that the ratio of the cube of the linear scale to the volumetric scale of segregation is equal to $3/4\pi$ for the system examined in Example 6.3.

6A.7 *Power Spectrum of Spherical Clumps.* Calculate the power spectrum for the clumps shown in Figure 6.6.a and show that $P(0) = 2s^2S_L$. Comment on the relative values of the power spectra.

6A.8 *Efficiencies of Mixers and Striation Thickness Reduction.* Calculate the shear and extension rates required to reduce the striation thickness 1000 times in 10 s in the three mixers—pure shear, uniaxial extensional, and simple shear—and then prove Eq. 6.81 assuming Newtonian fluid behavior.

6A.9 *Interfacial Growth in Simple Shear.* A minor component, of volume fraction ϕ , in the form of cubic pellets is mixed with the major component. Calculate the interface growth function for large shear strains. Furthermore, extend the calculations to the case of different shear viscosities of the minor and major components and of negligible interfacial tension between the components.

6A.10 *Efficiencies of Mixers for Power-Law Fluids.* Calculate the specific power ratios, as in Eq. 6.81, for a power-law fluid with a power-law index of 0.8.

6A.11 *Effect of Viscosity Ratio on Deformation.* Consider a rectangular element of the major component and a smaller rectangular element of the minor component imbedded into the first element. Show diagrammatically the shape of both elements after a certain value of shear strain has been imposed, for all possible combinations of the viscosities of the two components.

6A.12 *Rotational Couette Flow for a Power-Law Fluid.* Prove that, for a rotational Couette geometry with the inside cylinder rotating, the striation thickness scales inversely proportional to the shear

strain, and calculate the proportionality constant for a power-law fluid rotating in a small-gap Couette geometry.

6A.13 *RTD in Poiseuille Flows.* Prove that the ratio of the mean residence times in Poiseuille flow in parallel plates to circular pipe is equal to

$$\frac{\bar{t}_{PPF}}{\bar{t}_{CPPF}} = \frac{1 + 2n}{1 + 3n} \left(\frac{1}{2}\right)^{1/n},$$

where n is the power-law index. Assume that the pressure drop per unit length is the same in both cases. Calculate also the F function for the Poiseuille flow of a power-law fluid in a parallel plate geometry.

6A.14 *Holdback and Segregation in PCF, PPF, and CPPF*

- (a) Prove that the holdback, B , for the Couette flow in the parallel plate geometry is $1/4$.
- (b) Prove that the holdback, B , for pressure-driven flow of a Newtonian fluid between parallel plates geometry is 0.19.
- (c) Prove that the segregation, S , for the Poiseuille flow in circular pipe geometry is 0.14.

6A.15 *Interfacial Tension-Driven Deagglomeration.*

Determine the critical cluster radius for the attractive van der Waals forces to become less important than the interfacial tension forces between the cluster and the polymer matrix. Assume that the voids of the cluster are not filled completely with the polymer material and the equal-sized particles are randomly packed. The physical parameters of the system are: $\gamma = 30$ mN/m, $\varepsilon = 0.9$, Hamaker constant $A = 2 \times 10^{-19}$ J, and particle radius $R = 20$ nm.

B. Principles

6B.1 *“Diffusion” of Particles in Mixers.*

Consider the geometry of the horizontal cylinder-mixer (or single-barrel mixer) of Figure 6.34. Simulate the random movement of the particles while the cylinder is rotating around its axis by the molecular diffusion in the axial direction (note that diffusion along the radius, due to the rotation of the cylinder, should be much larger than the axial diffusion). The length of the cylinder is $L = 50$ cm and the black particle concentration is 5%. Initially the black particles are concentrated in the y axis and finally their concentration is uniformly distributed inside the mixer. If the diffusion coefficient, \mathcal{D} , is equal to 10^{-2} cm²/s.

- (a) Calculate the concentration profile $C(x, t)$ at $x = 1.25, 5, 25,$ and 40 cm.
- (b) Calculate the variance $s^2(t)$ and the mixing index ($M = 1 - s^2/\sigma_0^2$).

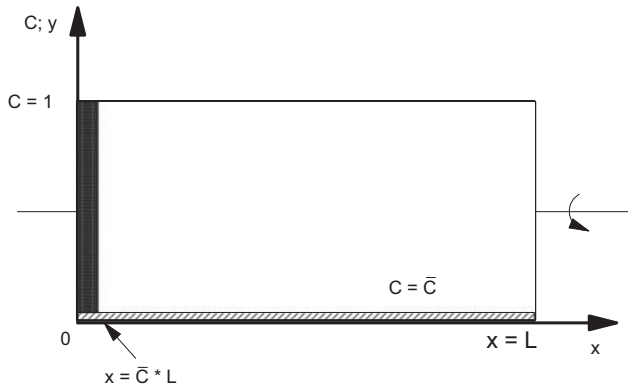


FIGURE 6.34 Geometry of a horizontal cylinder-mixer. Initially ($t = 0$) all carbon black particles are at the bottom of the cylinder that then is tumbled horizontally and starts rotating.

Also show that for long times

(c) $C(L/4, t) - \bar{C} = s(t)$.

(d) The graph of $\log(s^2(t))$ versus t has a slope of $2\pi^2 \bar{D}^2 / L^2$.

6B.2 *Diffusion in Layered Structures and Intensity of Segregation.* Consider a polymeric alternating layered structure. Calculate the time dependence of the concentration variance of the minor component and evaluate the intensity of segregation after 100 s if the diffusion time constant (square root of the ratio of diffusion coefficient to layer thickness) is equal to 400 s.

6B.3 *Striation Thickness from Kinematical Arguments.* Rework Example 6.5 for a line oriented at an angle ϕ with respect to axis x . Also, rework the same example for a two-dimensional point vortex flow with $v_r = 0$ and $v_\theta = \omega/r$.

6B.4 *Lineal Stretch Efficiency of Planar Elongational Flow.* Prove that the time average lineal stretch efficiency, \bar{e}_L , of a two-dimensional stagnation flow (planar elongational flow; Fig. 6.35) is

$$\bar{e}_L = \frac{\sqrt{2}}{4\gamma} \left[\ln \left(\frac{e^{4\gamma} + 1}{2e^{2\gamma}} \right) \right]$$

The velocity field for that type of flow is given by

$$v_x = \dot{\gamma}y; \quad v_y = \dot{\gamma}x; \quad v_z = 0$$

6B.5 *Lineal Stretch Efficiency of Uniaxial Elongational Flow.* Prove that the long time lineal stretch efficiency of uniaxial elongational flow is equal to $\sqrt{2/3}$.

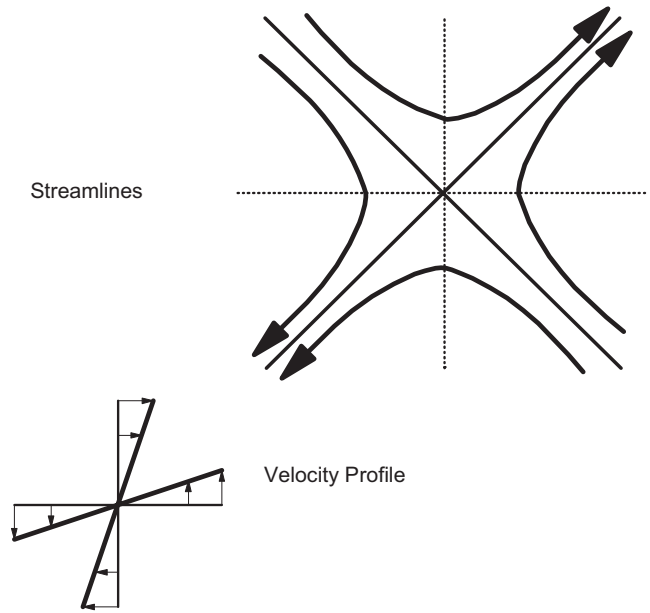


FIGURE 6.35 Streamlines and velocity profile of a two-dimensional stagnation (plane hyperbolic; planar extensional) flow.

6B.6 *Improvement of Mixing by Mixing Sections.* Consider a single-screw extruder and two types of mixing sections which function as follows: (a) randomize the orientation of the interfaces entering the section, and (b) orient the incoming interfaces perpendicular to the shearing planes. In both cases the total shear strain imparted to the fluid is equal to γ . Show that the ratio of the maximum interfacial area growth functions for type (a) and (b) mixing sections, λ , is equal to

$$\lambda = \frac{1}{2} \exp[\gamma/2e]$$

Assume that the mixing sections do not add any shearing to the fluid and that the shear strain between mixing sections is large enough for Eq. 6.66 to apply.

6B.7 *Striation Thickness in RCF with Both Cylinders Rotating.* A power-law fluid is sheared in a rotational Couette geometry with both cylinders rotating. Prove that the ratio of the striation thickness reduction of this case to the case described in Example 6.7 (only inside cylinder rotating) is equal to $(\lambda + 1)^{-1}$, where λ is the ratio of the angular velocities of the inside cylinder to the outside cylinder.

6B.8 *Striation Thickness in Axial Annular Couette Geometry.* Calculate the striation thickness reduction function for flow in axial annular Couette geometry and for a power-law fluid.

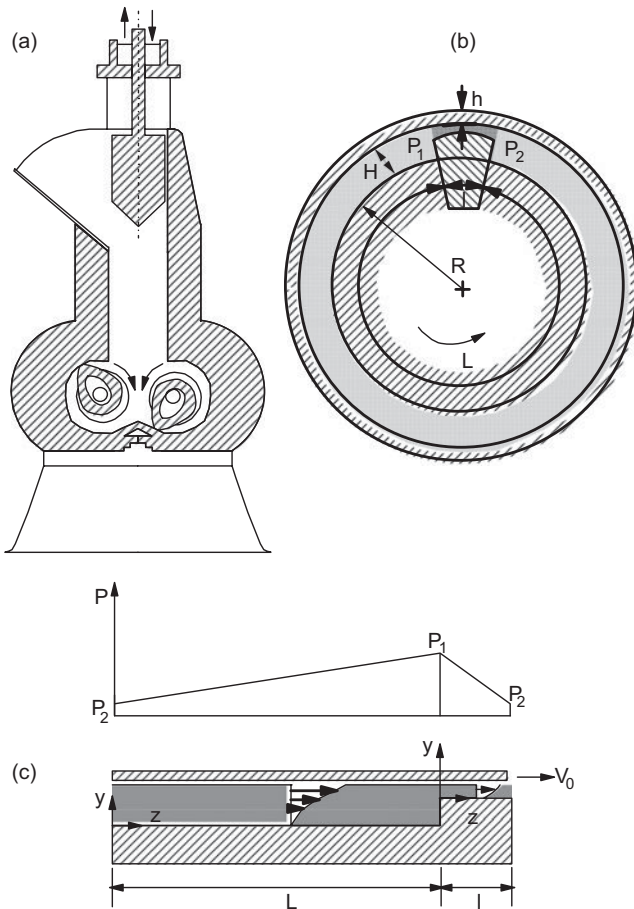


FIGURE 6.36 (a) Typical Banbury high-intensity internal mixer. (b) Idealized chamber of a Banbury mixer with a short low clearance section, consisting of two infinitely long cylinders. The inner cylinder rotates. (c) Idealization of the flow in the clearance by the flow between parallel plates with a step change in channel depth. Pressure distribution as a function of distance.

6B.9 SDF in PPF. Calculate the algorithm for determining the cumulative SDF versus $\gamma/\bar{\gamma}$ graph for a Newtonian fluid for pressure-driven flow through parallel plates. Repeat the exercise for a power-law fluid with power-law index equal to 0.5.

6B.10 Internal Banbury Mixer. Consider the high-intensity internal Banbury mixer of Figure 6.36a. It consists of a chamber shaped like a figure eight turned 90° , with two rotors counterrotating. The mixture is fed into the chamber through the vertical chute, in which the ram is located. The dispersive mixing takes place in the clearances between the rotors and the chamber walls. Simplify the flow in the chambers by the flow in the clearance of a concentric system of two infinitely long cylinders with a short low clearance section, Figure 6.36b. Furthermore, for low clearances, $H/R \ll 1$, assume

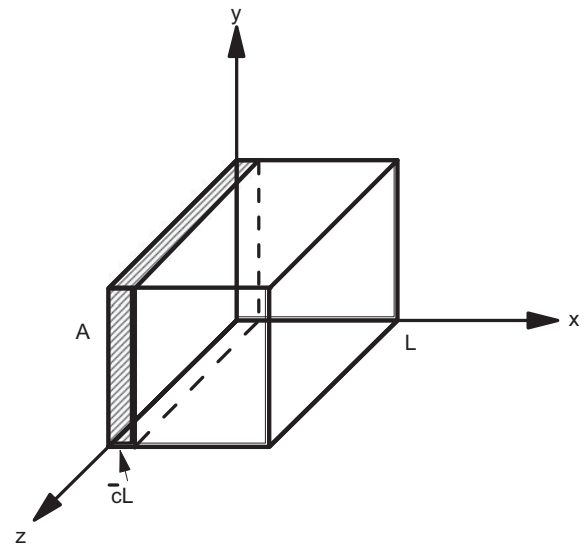


FIGURE 6.37 Cubic element of a minor component with simultaneous shear and diffusion.

that the flow is similar to the flow between parallel plates with a step change in the channel depth, Figure 6.36c. The pressure profile is given in Figure 6.36c. Calculate the shear rate and the maximum shear stress in the lower clearance section. Assume laminar isothermal flow of a Newtonian fluid, no slip at walls, and negligible entrance and exit effects.

C. Numerical Problems

- 6C.1 “Diffusion” of Particles in Mixers.** Solve Problem 6B.1 using numerical techniques.
- 6C.2 Diffusion in Layered Structures and Intensity of Segregation.** Solve Problem 4B.2 using numerical techniques.

D. Design Problem

6D.1 Simultaneous Laminar Mixing and Diffusion. Consider the case of a cubic element of the minor component (10% by volume) which is simultaneously subjected to laminar mixing and diffusion (Fig. 6.37). The minor component diffuses into the major and the thickness of the cubic element is reduced as the interface in the yz plane increases. Calculate the time necessary for the minor component to diffuse into the major component so that the concentration standard deviation is 0.11. $\mathcal{D} = 10^{-10} \text{ cm}^2/\text{s}$, $L_0 = 3 \text{ mm}$, and $\dot{\gamma} = 50 \text{ s}^{-1}$. Compare this time to the corresponding time without shearing.

REFERENCES

- Aref, H. 1984. "Stirring by Chaotic Advection." *J. Fluid Mech.*, **143**, 1–21.
- Bird, R. B., R. C. Armstrong and O. Hassanger. 1987. *Dynamics of Polymeric Liquids, Volume 1. Fluid Mechanics* (Wiley, Hoboken, NJ).
- Brockley, R. S. 1966. "Fluid Motion and Mixing." In V. H. Uhl and J.B. Gray, Eds., *Mixing, Volume 1*, Chapter 2 (Academic Press, New York).
- Bucknall, C. B. 1977. *Toughened Plastics* (Applied Science Publishers, London).
- Chien, W.-L., H. Rising and J. M. Ottino. 1986. "Laminar Mixing and Chaotic Mixing in Several Cavity Flows." *J. Fluid Mech.*, **170**, 355–377.
- Cox, R. G. 1969. "The Deformation of a Drop in a General Time-Dependent Fluid Flow." *J. Fluid Mech.*, **37**, 601–623.
- Danckwerts, P. V. 1952. "The Definition of Measurement of Some Characteristics of Mixtures." *Appl. Sci. Res. A*, **3**, 279–296.
- Danckwerts, P. V. 1953. "Continuous Flow Systems—Distribution of Residence Times." *Chem. Eng. Sci.*, **2**(1), 1–13.
- Elmendorp, J. J. 1991. "Dispersive Mixing in Liquid Systems." In C. Rauwendaal, Ed., *Mixing in Polymer Processing*, Chapter 2 (Marcel Dekker, New York).
- Erwin, L. 1978a. "Theory of Laminar Mixing." *Polym. Eng. Sci.*, **18**(13), 1044–1048.
- Erwin, L. 1978b. "Theory of Mixing Sections in Single Screw Extruders." *Polym. Eng. Sci.*, **18**(7), 572–576.
- Erwin, L. and F. Mokhtarian. 1983. "Analysis of Mixing in Modified Single Screw Extruders." *Polym. Eng. Sci.*, **23**(2), 49–60.
- Fan, L. T., S. J. Chen and C. A. Watson. 1970. "Solids Mixing." *Ind. Eng. Chem.*, **62**(7), 53–69.
- Grace, H. P. 1982. "Dispersion Phenomena in High Viscosity Immiscible Fluid Systems and Application of Static Mixers as Dispersion Devices in Such Systems." *Chem. Eng. Commun.*, **14**, 225–277.
- Hall, K. R. and J. C. Godfrey. 1965. "An Experimental and Theoretical Study of Mixing of Highly Viscous Materials." *AIChE J. Chem. Symp. Ser.*, **10**, 71–81.
- Hold, P. 1983. "Mixing of Polymers—An Overview, Part I." *Adv. Polym. Technol.*, **2**(2), 141–151.
- Howland, C. and L. Erwin. 1983. "Mixing in Counter Rotating Tangential Twin Screw Extruders." 41st SPE Annual Technical Conference, Chicago, IL, **29**, 113–116.
- Khakhar, D. V., H. Rising and J. M. Ottino. 1986. "Analysis of Chaotic Mixing in Two Model Systems." *J. Fluid Mech.*, **172**, 419–451.
- Lacey, P. M. C. 1954. "Developments in the Theory of Particle Mixing." *J. Appl. Chem., Lond.*, **4**, 257–268.
- Leong, C. W. and J. M. Ottino. 1989. "Experiments on Mixing Due to Chaotic Advection in a Cavity." *J. Fluid Mech.*, **209**, 463–499.
- Matthews, G. 1982. *Polymer Mixing Technology* (Applied Science Publishers, London).
- McKelvey, J. M. 1962. *Polymer Processing*, Chapter 12 (Wiley, Hoboken, NJ).
- Middleman, S. 1977. *Fundamentals of Polymer Processing*, Chapter 12 (McGraw Hill, New York).
- Mohr, W. D., R. L. Saxton and C. H. Jepsen. 1957. "Mixing in Laminar-Flow Systems." *Ind. Eng. Chem.*, **49**(11), 1855–1856.
- Morton-Jones, D. H. 1989. *Polymer Processing* (Chapman and Hall, London).
- Nadav, N. and Z. Tadmor. 1973. "Quantitative Characterization of Extruded Film Texture." *Chem. Eng. Sci.*, **28**, 2115–2126.
- Ng, K. Y. and L. Erwin. 1981. "Experiments in Extensive Mixing in Laminar Flow. I. Simple Illustrations." *Polym. Eng. Sci.*, **21**(4), 212–217.
- Nir, A. and A. Acrivos. 1973. "On the Creeping Motion of Two Arbitrary-Sized Touching Spheres in a Linear Shear Field." *J. Fluid Mech.*, **59**, 209–223.
- Ottino, J. M. and R. Chella. 1983. "Laminar Mixing of Polymeric Liquids; A Brief Review and Recent Theoretical Developments." *Polym. Eng. Sci.*, **23**(7), 357–379.
- Ottino, J., W. E. Ranz and C. W. Macosko. 1979. "A Lamellar Model for Analysis of Liquid-Liquid Mixing." *Chem. Eng. Sci.*, **34**, 877–890.
- Ottino, J., W. E. Ranz and C. W. Macosko. 1981. "A Framework for Description of Mechanical Mixing of Fluids." *AIChE J.*, **27**(4), 565–577.
- Pinto, G. and Z. Tadmor. 1970. "Mixing and Residence Time Distribution in Melt Screw Extruders." *Polym. Eng. Sci.*, **10**(5), 279–288.
- Radford, J. A., T. Alfrey and W. J. Schrenk. 1973. "Reflectivity of Iridescent Coextruded Multilayered Plastic Films." *Polym. Eng. Sci.*, **13**(3), 216–221.
- Ranz, W. E. 1979. "Applications of a Stretch Model to Mixing, Diffusion, and Reaction in Laminar and Turbulent Flows." *AIChE J.*, **25**(1), 41–47.
- Rotz, C. A. and N. P. Suh. 1976. "New Techniques for Mixing Viscous Reacting Liquids. Part I. Mechanical Means to Improved Laminar Mixing." *Polym. Eng. Sci.*, **16**, 664–7671.
- Rumpf, H. 1962. "The Strength of Granules and Agglomerates." In W. A. Knepper, Ed., *Agglomeration*, Chapter 15 (Interscience, New York).
- Schrenk, W. J. and T. Alfrey. 1983. "Unmixing in Rotational Laminar Shear Mixers." *Polym. Eng. Rev.*, **2**(4), 363–379.
- Schrenk, W. J., K. J. Cleereman and T. Alfrey. 1963. "Continuous Mixing of Very Viscous Fluids in an Annular Channel." *SPE Trans.*, July, 192–200.
- Spencer, R. S. and R. M. Wiley. 1951. "The Mixing of Very Viscous Liquids." *J. Colloid Sci.*, **6**, 133–145.
- Spiegel, M. R. 1991. *Probability and Statistics* (Schaum's McGraw Hill, New York).
- Stone, H. A. and L. G. Leal. 1989. "Relaxation and Breakup of an Initially Extended Drop in an Otherwise Quiescent Fluid." *J. Fluid Mech.*, **198**, 399–427.
- Tadmor, Z. and C. G. Gogos. 1979. *Principles of Polymer Processing* (Wiley, Hoboken, NJ).

- Taylor, G. I. 1934. "The Formation of Emulsions in Definable Fields of Flow." *Proc. R. Soc. Lond. A*, **146**, 501–523.
- Tomotika, S. 1935. "On the Instability of a Cylindrical Thread of a Viscous Liquid Surrounded by Another Viscous Fluid." *Proc. R. Soc. Lond. A*, **150**, 322–337.
- Tucker, C. L. 1981. "Sample Variance Measurement of Mixing." *Chem. Eng. Sci.*, **36**(11), 1829–1839.
- Tucker, C. L. 1991. "Principles of Mixing Measurement." In C. Rauwendaal, Ed., *Mixing in Polymer Processing*, Chapter 3 (Marcel Dekker, New York).
- Tucker, C. L. and N. P. Suh. 1980a. "Mixing for Reaction Injection Molding. I. Impingement Mixing of Liquids." *Polym. Eng. Sci.*, **20**(13), 875–886.
- Tucker, C. L. and N. P. Suh. 1980b. "Mixing for Reaction Injection Molding. II. Mixing of Fiber Suspensions." *Polym. Eng. Sci.*, **20**(13), 887–898.
- Underwood, E. E. 1977. *Quantitative Stereology* (Addison-Wesley, Reading, MA).
- Van der Reijden-Stolk, C. and A. Sara. 1986. "A Study on Polymer Blending Microrheology Part 3: Deformation of Newtonian Drops Submerged in Another Newtonian Fluid Flowing Through a Converging Cone." *Polym. Eng. Sci.*, **26**(18), 1229–1239.
- Van Gheluwe, P., B. D. Favis and J.-P. Chalifoux. 1988. "Morphological and Mechanical Properties of Extruded Polypropylene/Nylon-6 Blends." *J. Mater. Sci.*, **23**, 3910–3920.
- Van Krevelen, D. W. 1990. *Properties of Polymers* (Elsevier, New York).
- Wu., S. 1982 *Polymer Interfaces and Adhesion* (Marcel Dekker, New York).

7

EXTRUSION DIES

DESIGN PROBLEM VI COEXTRUSION BLOW MOLDING DIE

The blow molding of gasoline tanks for automobiles from thermoplastics offers the possibility of making more intricate shapes required to fit existing space than is possible with metals. Manufacturers would like to use HDPE, but it has poor barrier properties for gasoline vapors. However, by adding a layer of nylon 6, that is about 0.1 times the thickness of the tank wall, the material can meet the barrier requirements. The final cross-sectional shape of the gasoline tanks is to be basically as shown in Figure 7.1. Design a die having a shape similar to that of the gasoline tank as shown in Figure 7.2 for coextruding a parison consisting of 2 lb of nylon 6 and 18 lb of HDPE in the time of 5 seconds. Based on previous experience it is known that, for cylindrically shaped parisons, the maximum expansion of the tube should be no more than 2.0 (i.e., the maximum increase in the radius should be no more than a factor of 2.0). Assume that the density change on cooling and the weight of the parison are enough to offset the increase of the thickness due to extrudate swell. The extruders are horizontal, but the die must be mounted vertically. The only rheological data available are the viscosity data given in Table 2.3 for HDPE and in Table 7.3 for nylon 6. Determine the extrusion conditions required to deliver the amount of material and whether one can expect any interfacial stability problems.

Extrusion processes involve the use of extruders that melt and pump polymers and shaping devices called dies that are placed at the end of the extruder. This chapter is concerned with the design of extrusion dies while Chapter 8 deals with single- and twin-screw extruders.

Extrusion dies are metal channels that impart a specific cross-sectional shape to a polymer stream. The design difficulty centers on achieving the desired shape within set limits of dimensional uniformity at the highest production rate possible. Because of the viscoelastic nature of polymers and the associated flow behavior, it is no simple matter to design a die that will produce a smooth extrudate with the desired dimensions.

In Section 7.1 we describe briefly the origin of the nonuniformities and the factors that lead to extrudate shapes other than what is desired. In Section 7.2 we present flow phenomena associated with the viscoelastic behavior of polymers which affect the design of dies. In Section 7.3 we consider the design of sheet and flat film dies, especially with an emphasis on providing a uniform extrudate. The design of tubular dies presents somewhat different problems, and they are considered in Section 7.4. There are numerous other shapes of extrudates besides flat, round, or tubular. Extrusion of irregular shaped extrudates is referred to as profile extrusion, and this is discussed in Section 7.5. Finally, it is now common practice to extrude multiple layers of different polymers through the same die. As this presents even more complications in die design, we introduce the topic in

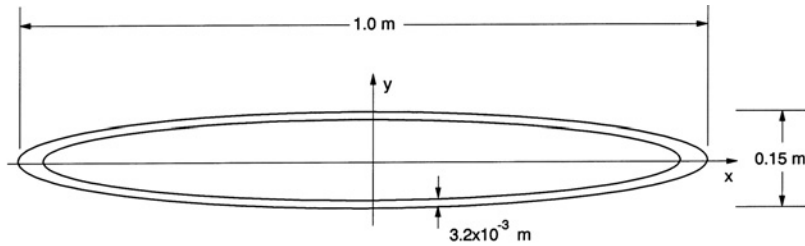


FIGURE 7.1 Cross section of an elliptically shaped parison consisting of HDPE and nylon 6 in a 9:1 ratio by weight.

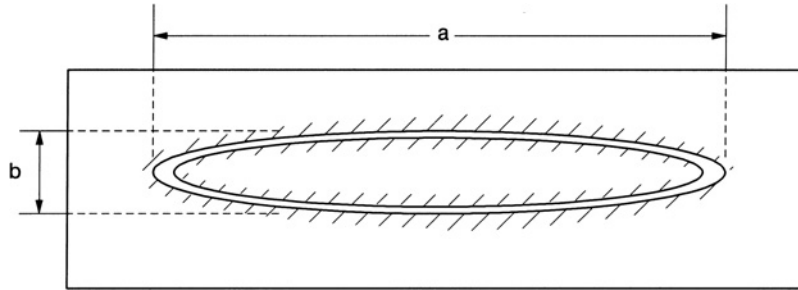


FIGURE 7.2 Exit face of the die used to produce the parison in Figure 7.1. The die opening is an elliptically shaped annulus of major axis a and minor axis b . The thickness, a , and b are determined in the solution to Design Problem VI.

Section 7.6. Finally, in Section 7.7, the solution to Design Problem VI is presented.

7.1 EXTRUDATE NONUNIFORMITIES

There are basically two types of nonuniformities. Those that occur along the machine direction (MD), or along the extrusion direction, and those that occur in the transverse direction (TD). These nonuniformities are shown in Figure 7.3 for a

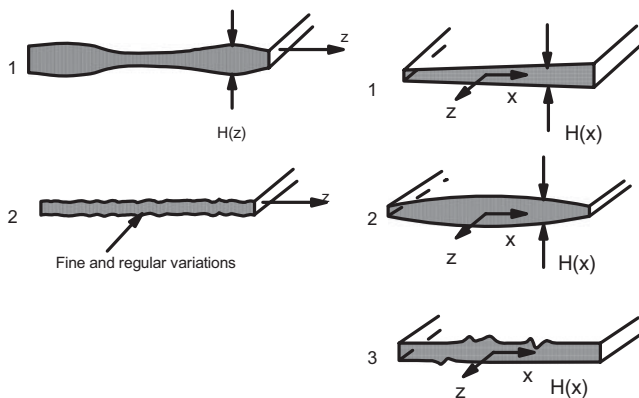


FIGURE 7.3 Irregularities in the extrusion of a sheet with those along the machine direction shown on the left and those along the transverse direction shown on the right. The extrusion direction is in the z direction.

planar geometry. The nonuniformities that arise along the MD are usually due to pressure and temperature variations, which affect the flow rate, the rheological properties of the melt, and to some degree the die design. The irregularities that occur in the TD are due nearly totally to the die design, but in some cases the rheological properties enter in.

In the case of the MD, variations in the flow rate due to pressure or temperature variations in the pumping device are the main cause of the irregularities. However, flow instabilities associated with the phenomena of melt fracture and draw resonance can lead to variations in the dimensions of the extrudate. These variations are closely connected to the rheological properties of the melt, but die design can at least alleviate the severity of the irregularities.

The TD variations are nearly totally due to die design. The first problem is to design a feed system that will distribute the melt uniformly to the shaping portion of the die. (See Fig. 7.4 for definition of parts of a die.) In the event this is not possible, then it must be possible to adjust the die lips in such a way that the fluid will leave the die with a uniform thickness. Part of the thickness variation in the TD is due to the inability to feed the die uniformly from the extruder, while the rest is due to the phenomenon of die swell. Since the degree of swell may vary nonuniformly over the cross section due to variations in the shear rate, the die lips (main shaping section) may have to be designed to compensate for this.

Before continuing we should note that a lot of the problems concerned with die design are handled empirically. Part

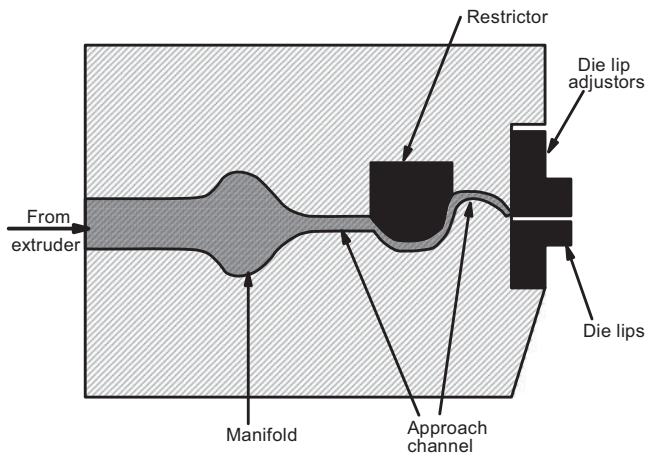


FIGURE 7.4 Schematic of a typical extrusion die showing the various parts of the die (side view). The manifold distributes the melt from the extruder uniformly over the width of the die while the restrictor can be used to compensate for variations in flow rate across the width of the die. The lips give the melt stream the desired dimensions and shape. (Note: Because of die swell the dimensions of the extrudate may be considerably different from those of the die lips.)

of this is due to the lack of the appropriate mathematical tools to simulate the flow of viscoelastic materials through dies. The lack of mathematical tools is due to both inappropriate constitutive equations to describe the rheology of polymer melts and the lack of numerical techniques for handling the nonlinear system of differential equations that must be solved. Although progress is being made to develop finite element techniques for handling die design, these codes are not fully developed or tested at this time. Even once they are developed, they may not be available for every design engineer. For this reason we present in this chapter design considerations that can be handled at this level of the educational process and at the same time present material that can be used in a qualitative fashion to improve the design of extrusion dies. It is important to recognize that most die design to date neglects the viscoelastic nature of polymeric fluids.

7.2 VISCOELASTIC PHENOMENA

There are three phenomena associated with the flow behavior of polymeric fluids which must be considered in the design of extrusion dies: pressure drops in contractions (or expansions), die swell, and melt fracture. The latter two bear a direct relation to extrudate uniformity, while the flow behavior in contractions may be related only indirectly to extrudate uniformity. In this section, for illustrative purposes, we present results based primarily on studies in the capillary geometry. One must recognize that the extension of results

from a capillary to other geometries may be difficult to make quantitatively.

7.2.1 Flow Behavior in Contractions

As discussed in Chapter 3 (Section 3.3) the pressure drop across a contraction for a polymeric fluid can be quite large relative to the pressure drop across the die land or lips. The origin of ΔP_{ent} is thought to be due to the entry flow behavior of the polymer. In some cases, such as for LDPE, the streamlines form natural entry angles as shown in Figure 7.5. The flow into the die is restricted well into the upstream region, which serves to effectively act as an extension to the capillary length and thereby increase ΔP . It is also observed that large vortices arise in the corners. For polymers such as polystyrene (see Fig. 7.6) and HDPE the streamlines only become curved a short distance from the contraction, and the vortices are quite small, as shown in Figure 7.7. In this case there is very little addition of length to the capillary and ΔP_{ent} is smaller. This explanation is in line with the results in Figure 7.7, which shows values of ΔP_{ent} normalized to the wall shear stress versus $\dot{\gamma}_a$ for various fluids. The normalization with respect to τ_w removes the difference due to differences in the magnitude of viscosity. LDPE has the highest values of $\Delta P_{\text{ent}}/\tau_w$, which is to be expected, as it forms large entry vortices. The oil, which is basically Newtonian, exhibits the lowest values. In general, linear polymers exhibit small regions of flow rearrangement and very small regions with vortices and hence lower values of $\Delta P_{\text{ent}}/\tau_w$.

The magnitude of ΔP_{ent} is a function of the rheological properties of the polymer, the contraction ratio, the cross-sectional geometry, and the degree of taper into the entry. Unfortunately, there is no known simple way to translate results from the capillary to other flow geometries, and there have been few attempts to do so. Until more information is available, we use entrance pressure measurements from capillary geometries to estimate values of ΔP_{ent} in other geometries provided we maintain at least geometric similarity.

As far as expansions are concerned, there is even less information. We assume that the pressure rise in an abrupt expansion is the same as the drop in an abrupt contraction. Certainly this will not be the same because of the viscoelastic nature of polymeric fluids.

7.2.2 Extrusion Instabilities

The limiting factor in the extrusion rate of polymeric fluids is the onset of a low Reynolds number instability called *melt fracture*. The onset of melt fracture leads to varying degrees of imperfections which may only affect the clarity of a material on one hand, while on the other may be so severe as to reduce significantly the physical properties. We first discuss the nature and origin of melt fracture and then what can be done to alleviate or at least mitigate the problem.

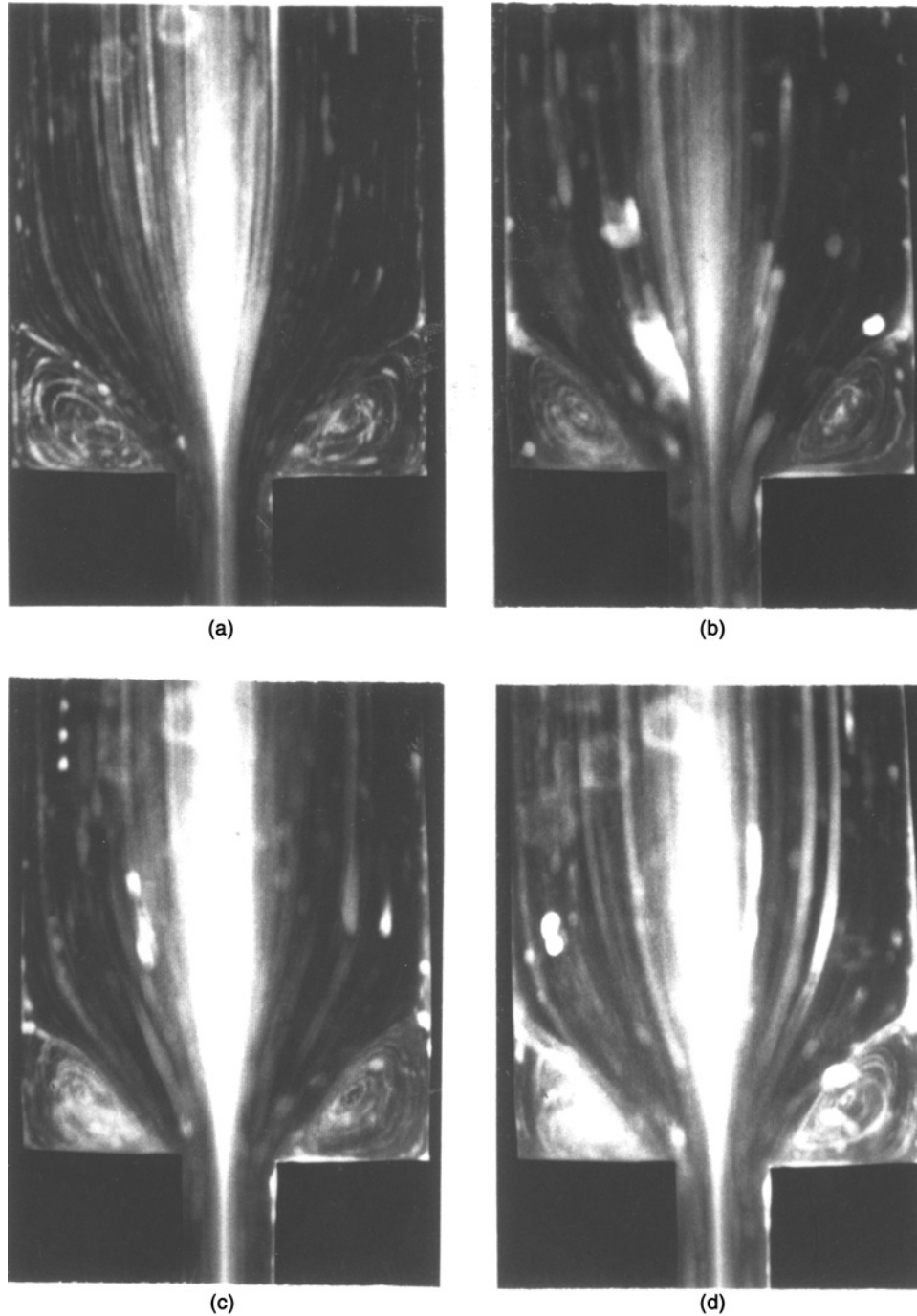


FIGURE 7.5 Streamline patterns obtained by means of streak photography for LDPE at 150 °C in a 4:1 planar contraction: (a) = 20 s⁻¹, We = 1.29; (b) = 40 s⁻¹, We = 1.35; (c) = 60 s⁻¹, We = 1.38; (d) = 80 s⁻¹, We = 1.38. (From White, 1987.)

There are basically five types of melt fracture: *sharkskin*, *ripple*, *bamboo*, *wavy*, and *severe*. These types of melt fracture are shown in Figures 7.8, 7.9, and 7.10. Sharkskin is shown in Figure 7.8 for a LLDPE. At the lowest apparent shear rate the extrudate is smooth but at $\dot{\gamma}_a = 112 \text{ s}^{-1}$, the

extrudate exhibits a mild roughness, called sharkskin, which affects the appearance of the surface. This type of fracture is extremely detrimental to the manufacture of packaging films, which must meet certain requirements for clarity. As $\dot{\gamma}_a$ is increased, another form of fracture arises. At $\dot{\gamma}_a = 750 \text{ s}^{-1}$,

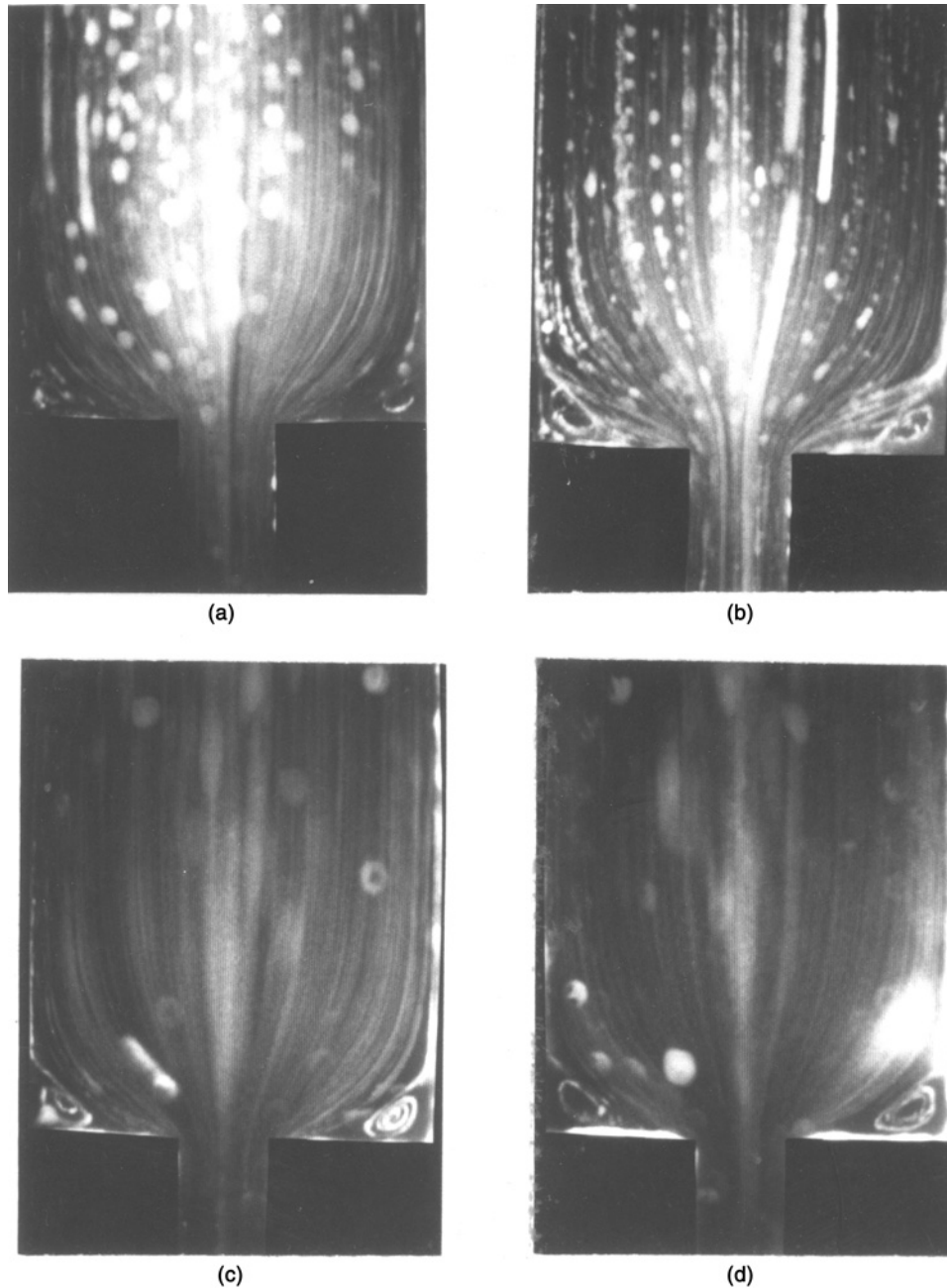


FIGURE 7.6 Streamline patterns obtained by means of streak photography for polystyrene at 190 °C in a 4:1 contraction: (a) = 5 s⁻¹, We = 0.82; (b) = 20 s⁻¹, We = 1.19; (c) = 40 s⁻¹, We = 1.39; (d) = 80 s⁻¹, We = 1.62. (From White, 1987.)

the fracture present is called bamboo. Finally, at $\dot{\gamma}_a$ of 2250 s⁻¹ the fracture is severe. LLDPE does not seem to exhibit wavy fracture.

HDPE exhibits both sharkskin and bamboo (sometimes referred to as “spurt”) fracture at lower shear rates as shown in Figure 7.9. As $\dot{\gamma}_a$ is increased, HDPE is observed to exhibit the wavy form of fracture. LDPE, on the other hand, as shown

in Figure 7.10, does not exhibit sharkskin, but only wavy and severe fracture.

In order to reduce the detrimental effect of melt fracture through die design or polymer modification, it is important to know the origin of melt fracture. The major sources for melt fracture are the die entry region, the die land, and the die exit. For a polymer such as LDPE fracture originates at

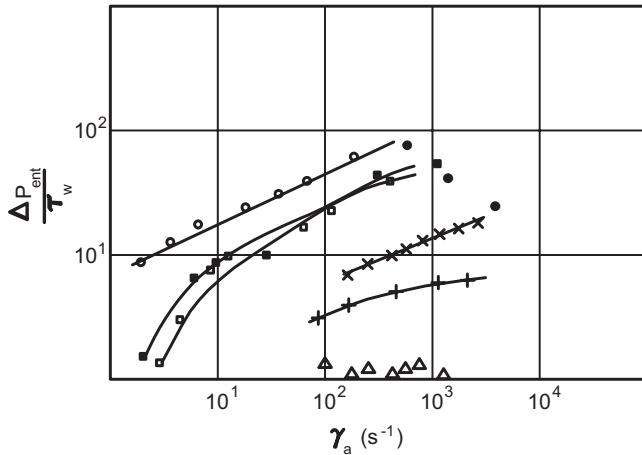


FIGURE 7.7 The ratio of entrance pressure drop to wall shear stress versus apparent shear rate, $\dot{\gamma}_a$: (■) PP; (□) PS; (○) LDPE; (+) HDPE; (●) 2.5% PIB in mineral oil; (X) 10% PIB in decalin; (Δ) NBS-OB oil. (Reprinted with permission of the publisher from White, 1973.)

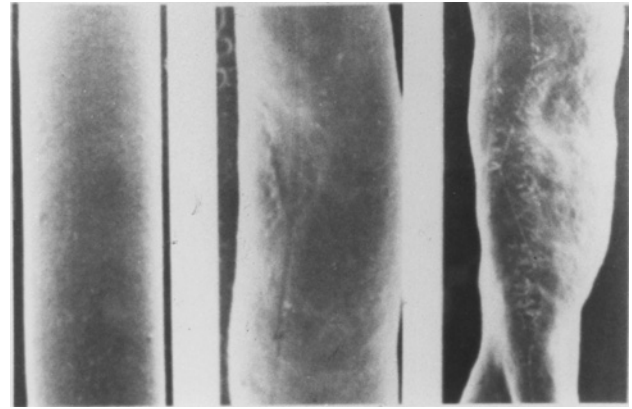


FIGURE 7.10 LDPE extrudates obtained from a capillary at different apparent shear rates, $\dot{\gamma}_a$: from left to right the values of $\dot{\gamma}_a$ are 75, 750, 2250 s^{-1} while the corresponding values of τ_a are 0.1, 0.21, 0.32 MPa. (Data from Moynihan, 1990.)

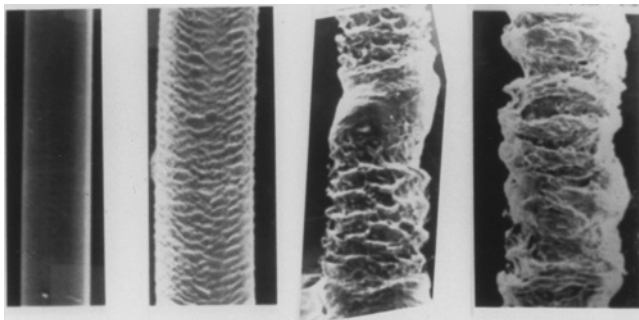


FIGURE 7.8 LLDPE extrudates obtained from a capillary at different apparent shear rates, $\dot{\gamma}_a$: from left to right the values of $\dot{\gamma}_a$ are 37, 112, 750, and 2250 s^{-1} . (Data from Moynihan, 1990.)

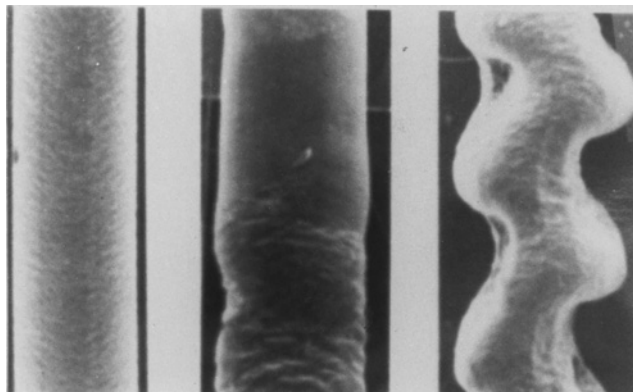


FIGURE 7.9 HDPE extrudates obtained from a capillary at different apparent shear rates, $\dot{\gamma}_a$: from left to right the values of $\dot{\gamma}_a$ are 75, 75, 2250 s^{-1} while the corresponding values of τ_a are 0.20, 0.27, 0.33 MPa. (Data from Moynihan, 1990.)

the die entry. As the extrusion rate is increased, the vortices no longer grow in size or intensity. Instead, the flow takes on a spiral motion in the die entry sending sections of the nearly stagnant fluid into the die at regular intervals. This leads to regions of various flow histories passing through the die and leaving the die exit. When this type of fracture occurs, there is no indication of the flow problems in the pressure measured along the die, and hence the wall shear stress is as shown in Figure 7.11. By streamlining the die entry or increasing the length of the die land it is possible to reduce the amplitude of the distortion, but the critical shear stress for fracture is unchanged. The critical wall shear stress for the onset of fracture for LDPE is on the order of 10^5 Pa.

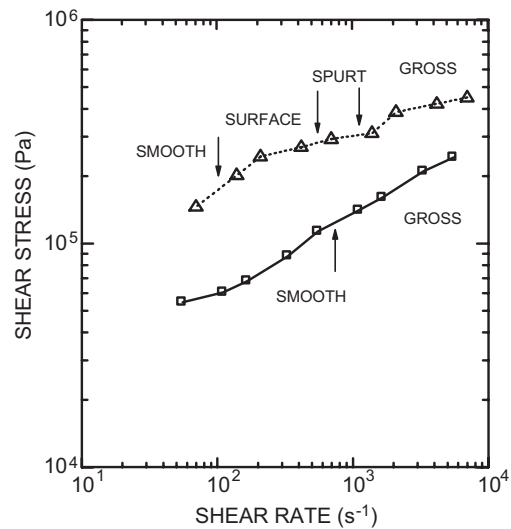


FIGURE 7.11 Shear stress versus shear rate for LDPE (lower curve) and LLDPE (upper curve). The arrows indicate the onset of various types of melt fracture. (Data from Moynihan, 1990.)

A statistical fit of the data for LDPE leads to the following empirical expression for the critical wall shear stress for fracture (Middleman, 1977):

$$\tau_{cr}/T_{abs} = 131.7 + 1.0 \times 10^7/M_w \text{ branched PE} \quad (7.1)$$

where τ_{cr} is in units of Pa and T_{abs} is in K.

On the other hand, polymers such as HDPE and LLDPE seem to slip in the die land leading to a “slip–stick” instability. There is a distinct flattening of the flow curve indicating a region where multiple flow rates are possible for the same wall shear stress. This is shown by the data presented in Figure 7.11. Eventually the flow curve appears to become normal again at high shear rates. When slip–stick fracture occurs (which results in the ripple and then bamboo types of fracture), increasing the die length just makes the degree of distortion worse.

It has been proposed that polymers such as HDPE, which is considered a linear polymer, as well as other linear polymers such as PP and PS have a similar mechanism for fracture. In fact, the molecular weight dependence of the critical shear stress (τ_{cr}) for fracture was found to be similar for linear polymers (Middleman, 1977). A statistical fit of the data for fracture gave the following relation for the critical shear stress for the onset of slip–stick melt fracture, τ_{cr} , for linear polymers:

$$\tau_{cr}/T_{abs} = 171.7 + 2.7 \times 10^7/M_w \quad (7.2)$$

It is true that linear polymers do not show large vortices in planar entry flow, although they may occur in axisymmetric flow (White et al., 1987). However, it is known that the origin of fracture for PS is the die entry. In fact, HDPE and LLDPE are the only polymers of the group presented here that readily show any indication of slip–stick in the flow curve. The rest show no indication of fracture in the flow curve, and apparently the origin of fracture is in the die entry. In spite of this, it is interesting to note that τ_{cr} for the branched polymer, LDPE, falls on a curve separate from that for the linear polymers.

The relations given in Eqs. 7.1 and 7.2 are useful for estimating the onset of gross fracture for a capillary geometry. It does not tell us, however, what will happen in an annular die or some other geometry. However, the equations are at least useful in making an estimate of limiting conditions. There are still many mysteries surrounding the origin of sharkskin melt fracture and the methods proposed to eliminate it. For example, it has been proposed that the metal used in die construction can allow one to alter τ_{cr} , while the rounding of the corners at the die exit is important. Still others recommend processing aids to increase τ_{cr} for the onset of melt fracture. (The addition of fluoroelastomers to LLDPE does eliminate both sharkskin and slip–stick fracture.) Once gross distortion

occurs, which originates in the die entry, there is very little that can be done to eliminate the problem.

7.2.3 Die Swell

The phenomenon associated with the increase of the diameter of an extrudate as a polymer leaves a capillary, known as *die swell* or *extrudate swell*, has been introduced briefly back in Section 3.2. The implication at this point is that die swell is related to unconstrained elastic recovery (S_∞) following shear flow. S_∞ is related to the ratio of the primary normal stress difference to the shear stress through the equation

$$S_\infty = N_1/2\tau_{yx} \quad (7.3)$$

Tanner’s theory for die swell (see Section 3.2) for flow through a capillary leads to

$$D_p/D_0 = 0.1 + [1 + \frac{1}{2}(S_\infty)^2]^{1/6} \quad (7.4)$$

In this section we show that die swell is more complicated than indicated by Eq. 7.4 and depends on a number of factors. We then discuss how to deal with die swell in die design.

The first fact we show is that Tanner’s theory does not accurately predict die swell in general. This is illustrated in Figure 7.12, where values of die swell for four different polymer melts are plotted versus $\frac{1}{2}S_\infty$. The solid line represents Eq. 7.4 and is generated for arbitrary values of S_∞ . There is as much as a 50% difference between the measured and predicted values of D_p/D_0 . Furthermore, the values of D_p/D_0 vary from polymer to polymer. Hence, it does not appear that die swell can be correlated simply to S_∞ .

On what else does die swell depend? It first depends on the method used to measure it. This is shown in Figure 7.13 in which values of D_p/D_0 are plotted versus shear rate for

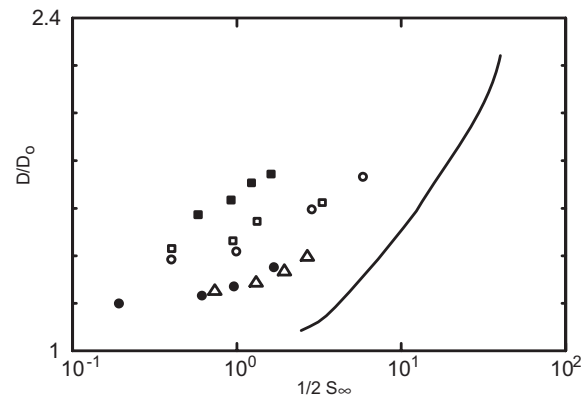


FIGURE 7.12 Capillary extrudate swell versus $\frac{1}{2}S_\infty$, the ultimate elastic recovery. (■, □) two HDPEs; (●) PS; (○) LDPE; (△) PP. (Data from White and Roman, 1976.)

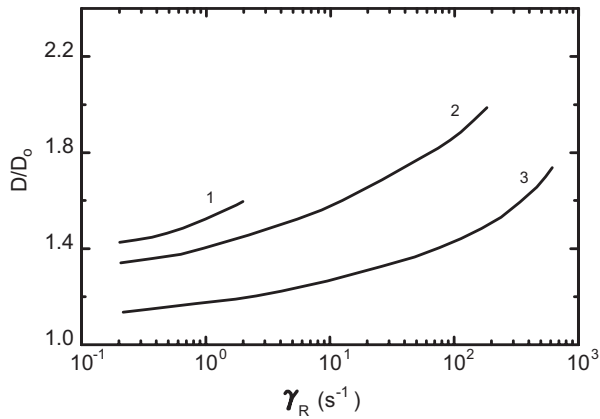


FIGURE 7.13 Effect of the method of measurement on the magnitude of die swell for HDPE extruded from a capillary at 180 °C at various wall shear rates, $\dot{\gamma}_R$: curve 1, isothermal; curve 2, annealed; curve 3, ambient air. (Data from White and Roman, 1976.)

three different methods of measurement. The highest values are obtained for polymers that are extruded isothermally into an oil bath. The lowest values are for the extrudate that is extruded into ambient air. In this case the sample is cooled down before die swell is completed. Annealing, as shown by curve 2 in Figure 7.13, allows the sample to almost reach the values obtained under isothermal conditions.

Die swell depends on the capillary L/D as shown in Figure 7.14. In this figure we see that D_p/D_0 is a function of L/D with the greatest swell being for the shortest capillary. This behavior has been attributed to the large amount of elastic energy stored during the extensional flow in the entry region.

It is also observed that die swell depends on time after the extrudate leaves the die. This is shown in Figure 7.15 in which D_p/D_0 is plotted versus time for a HDPE melt. Here we observe that a large portion of the swell occurs

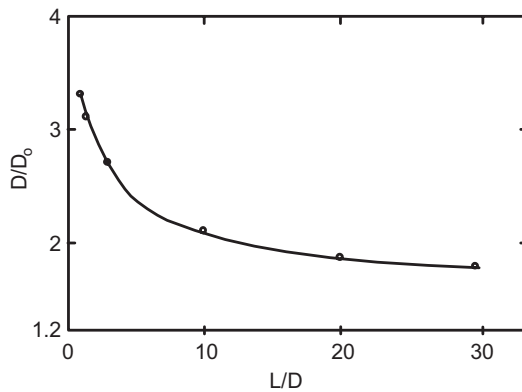


FIGURE 7.14 Extrudate swell versus capillary L/D ratio for PP extruded at 219 °C at $\dot{\gamma}_R = 700 \text{ s}^{-1}$. (Data from Mori and Funatsu, 1973.)

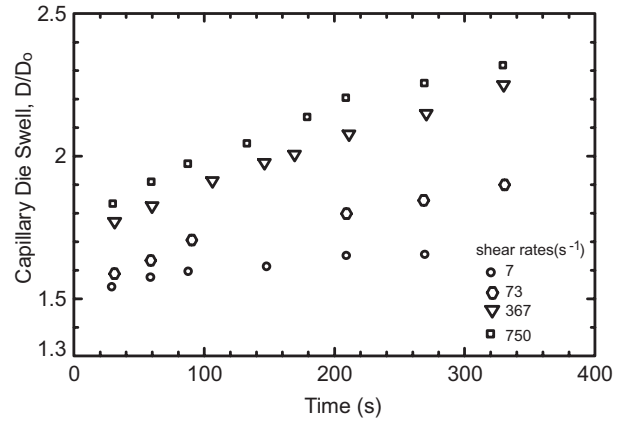


FIGURE 7.15 Capillary extrudate swell versus time for four shear rates, $\dot{\gamma}_R$, for HDPE (resin No. 27). (Data from Garcia-Rejon et al., 1982.)

instantaneously, while the remainder of the diameter increase can occur over a period of several minutes.

Finally, D_p/D_0 (equilibrium swell) is a function of the wall shear stress, τ_R . Data for a commercial polystyrene at three different temperatures when plotted versus shear rate fall on three separate curves. However, when plotted versus τ_R , the data all fall on a single curve as shown in Figure 7.16. Hence, for a given polymer the equilibrium swell can be correlated with τ_R .

In summary, capillary die swell, $B = D_p/D_0$, is a function of the following variables:

$$B = f(L/D_0, \tau_R, EG, E, t, t_p/\lambda) \quad (7.5)$$

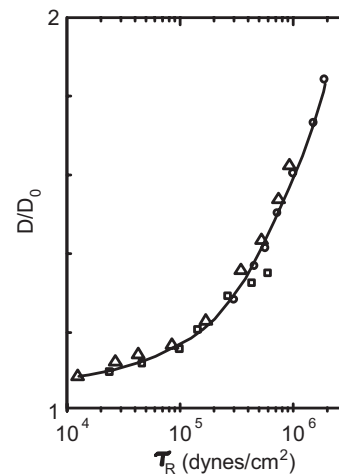


FIGURE 7.16 Capillary extrudate swell versus wall shear stress for a commercial polystyrene at three temperatures: (○) 160 °C, (Δ) 180 °C, (□) 200 °C. (Data from Graessley et al., 1970.)

TABLE 7.1 Description of Resins Studied in Annular Swell

McGill University Stock Number	Trade Name/Number	Manufacturer	Density (kg/m ³)	Melt Index (dg/min)
22	Sclair (HDPE) 59C	DuPont of Canada	960	0.42
26	40054 (HDPE)	Dow Canada	954	0.40
27	DMDJ (HDPE) 5140	Union Carbide Canada	962	0.72
28	PRO-FAX 7723 (PP)	Hercules Canada	899	0.8

Source: Data from Garcia-Rejon et al., 1982.

TABLE 7.2 Molecular Weight Parameters for Three High Density Polyethylenes

Resin Number	$M_n \times 10^{-4}$	$M_w \times 10^{-4}$	$M_z \times 10^{-4}$	M_w/M_n	M_z/M_w
22	1.8	18	140	10.7	7.9
26	1.7	12	88	7.6	7.5
27	2.1	12	74	5.8	7.0

Source: Data from Garcia-Rejon et al., 1982.

where EG is the entrance geometry, E is the exit geometry, t is the time after a fluid element leaves the die, t_p is the time required for the melt to pass through the die, and λ is the longest relaxation time for the fluid. The last quantity, λ/t_p , is referred to as the Deborah number. Certainly the ideas of elastic recovery are involved, but stresses other than those generated in shear flow (e.g., extensional flow at the die exit) must be considered.

The phenomenon of die swell is complex, and the method for incorporating it into die design calculations is unclear. In most cases the processing die geometry is considerably different from that used to make die swell measurements. For example, in the extrusion of a parison used in blow molding there is swell of both the thickness and outer diameter of the parison. How to translate die swell from a capillary to that of a parison is certainly not straightforward.

To illustrate one possible way of translating capillary die swell measurements to some other die geometry we consider the swell of extrudate leaving an annular die. In the swell of polymer extruded from an annular die as shown back in Figure 3.1 (this figure is associated with Design Problem II), there is swell of the diameter as well as the thickness of the extrudate. The two most common swell parameters are the diameter swell, B_1 , and the thickness swell, B_2 , defined, respectively, as

$$B_1 = D_p/D_0 \quad (7.6)$$

$$B_2 = H_p/H_0 \quad (7.7)$$

The thickness swell can be related to the inner (subscript 1) and outer (subscript 2) diameters as follows:

$$B_2 = (D_{p2} - D_{p1})/(D_{02} - D_{01}) \quad (7.8)$$

Sometimes the weight swell is defined, especially in the case of extruding a parison for blow molding. The weight swell, S_w , is

$$S_w = \left(D_{p2}^2 - D_{p1}^2 \right) \rho_p / \left(D_{o2}^2 - D_{o1}^2 \right) \rho_0 \quad (7.9)$$

where ρ_p is the density of the polymer extrudate and ρ_0 is the density of the melt in the die.

The questions of interest are: What are the relations between B_1 and B_2 and between B_1 and B ? To answer these questions and to illustrate the complexity of the answer, we consider the following example. Three HDPE samples of different molecular weight characteristics and a polypropylene were used in the study by Garcia-Rejon et al. (1982) (see Table 7.1 and 7.2). The steady shear and dynamic mechanical rheological properties are presented in Figures 7.17

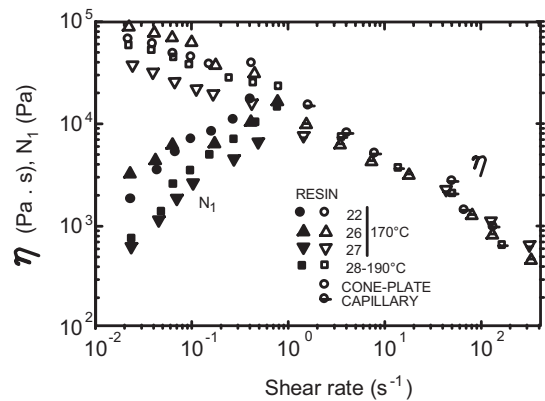


FIGURE 7.17 Steady shear viscosity and primary normal stress data for three HDPE and one PP samples described in Tables 7.1 and 7.2. (Data from Garcia-Rejon et al., 1981.)

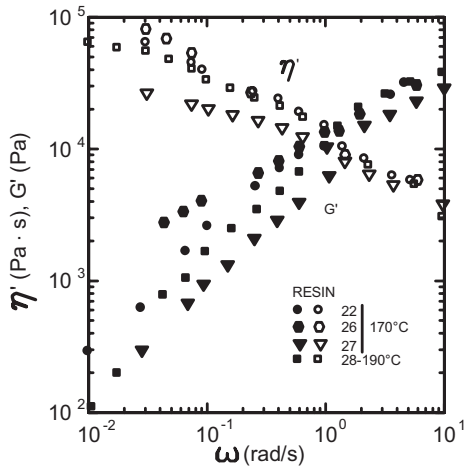


FIGURE 7.18 Dynamic viscosity and storage modulus versus angular frequency for the resins described in Tables 7.1 and 7.2. (Data from Garcia-Rejon et al., 1981.)

and 7.18, and it is seen here that η for resins 22, 26, and 28 are similar, while N_1 values are different for the three HDPEs and PP. (Note: PP is processed at 190 °C whereas the HDPE samples are processed at 170 °C.) We would expect resin 28 to have the highest values of B based on the values of η and Ψ_1 , and Eq. 7.4. Die swell data obtained from a capillary rheometer are presented in Figure 7.19, but we see this is not the case. Resin 28 exhibits the highest values of B while the other resins exhibit similar values.

We next consider how to translate the capillary swell data into values for B_1 and B_2 . To make the comparison we have to make it at either the same wall shear stress or wall shear rate. Because the ratio of $D_{01}/D_{02}(= 0.816$ in this case, Fig. 3.1)

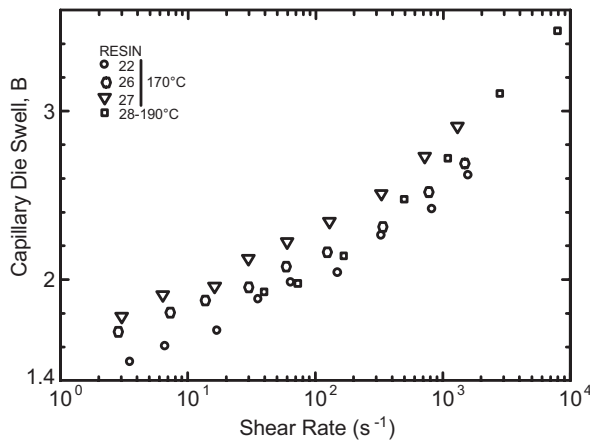


FIGURE 7.19 Capillary extrudate swell versus shear rate for the resins described in Tables 7.1 and 7.2. (Data from Garcia-Rejon et al., 1982.)

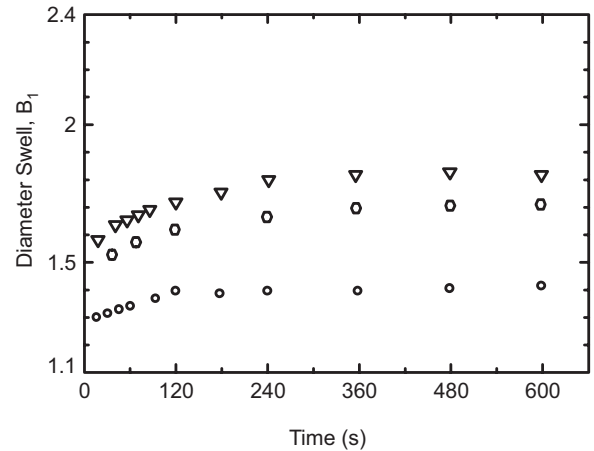


FIGURE 7.20 Annular diameter swell versus time for HDPE-22 at 170 °C and wall shear rates of (◦) 20, (◻) 121, and (Δ) 270 s⁻¹. (Data from Garcia-Rejon et al., 1982.)

approaches 1.0, we can treat the annulus as a thin slit and hence

$$\dot{\gamma}_w = 2(2 + b)Q/\pi(R_{01} + R_{02})(R_{02} - R_{01})^2 \quad (7.10)$$

where

$$b = d \ln Q/d \ln \tau_w \quad (7.11)$$

and

$$\tau_w = (R_{02} - R_{01})\Delta P/2L \quad (7.12)$$

In Figures 7.20 and 7.21 values of $B_1(t)$ and $B_2(t)$ are presented for sample HDPE-22. Here we observe that the

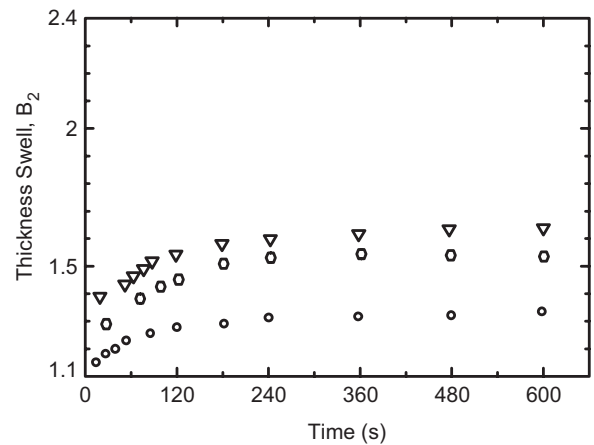


FIGURE 7.21 Annular thickness swell versus time for HDPE-22 for the same conditions as in Figure 7.20. (Data from Garcia-Rejon et al., 1982.)

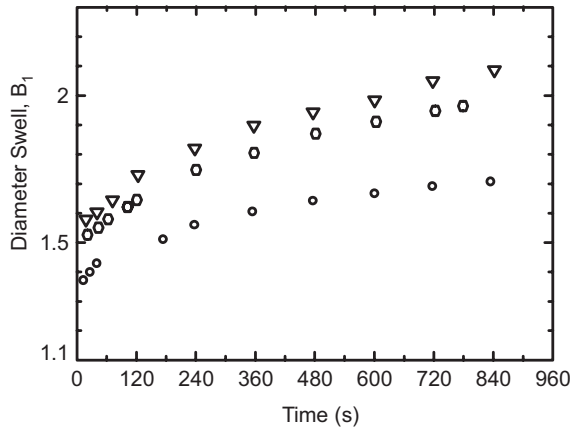


FIGURE 7.22 Annular diameter swell versus time for PP-28 at 190 °C and wall shear rates of (○) 19, (◻) 109, and (△) 231 s⁻¹. (Data from Garcia-Rejon et al., 1982.)

instantaneous swell represents about 85% of the equilibrium swell. For PP (resin #28) values of $B_1(t)$ and $B_2(t)$ are presented in Figures 7.22 and 7.23. For PP, however, the instantaneous swell is only about 75–80% of the equilibrium swell, and it takes much longer to reach the equilibrium swell. This difference cannot be accounted for merely by differences in the longest relaxation times, as they are similar for both polymers based on the viscosity data.

The first relation of interest is that between B_1 and B_2 . These results are shown in Figure 7.24 in which equilibrium values of B_2 are plotted versus B_1 for all four polymers. There are several proposed relations between B_1 and B_2 :

$$B_2 = B_1 \tag{7.13}$$

$$B_2 = B_1^2 \tag{7.14}$$

$$B_2 = B_1^2 \tag{7.15}$$

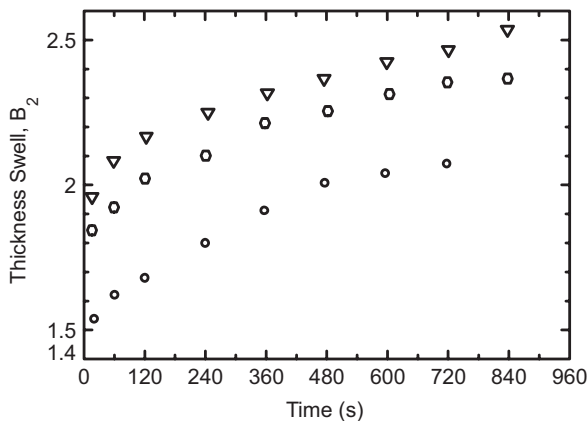


FIGURE 7.23 Annular thickness swell versus time for PP-28 for the same conditions as in Figure 7.22.

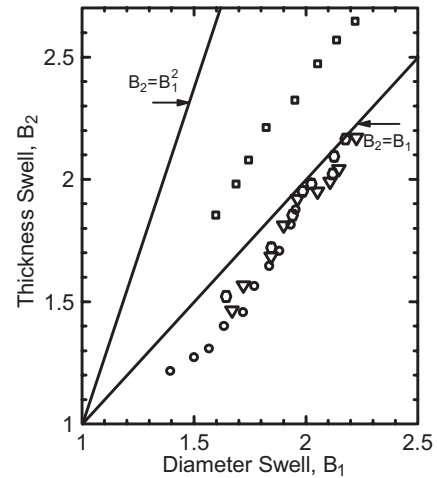


FIGURE 7.24 Equilibrium thickness swell versus equilibrium diameter swell for HDPE resins (○) 22, (◻) 26, (△) 27, and (◻) PP-28. (Data from Garcia-Rejon et al., 1982.)

The data are compared with the first two of these relations, and we see that HDPE samples follow Eq. 7.13 more closely, whereas the PP data falls in between Eqs. 7.13 and 7.14. Hence, there is apparently no universal relation between B_1 and B_2 for all polymers, and it will depend on polymer type.

Of greater interest is the relation between B_1 and B_2 and capillary extrudate swell, B . This is shown in Figures 7.25 and 7.26. In the case of diameter swell, all the data fall below the line $B_1 = B$. In the case of thickness swell, most of the data fall below the line $B_2 = B$, except for the PP data which falls more closely to the line. Again there is no general way to relate the swells.

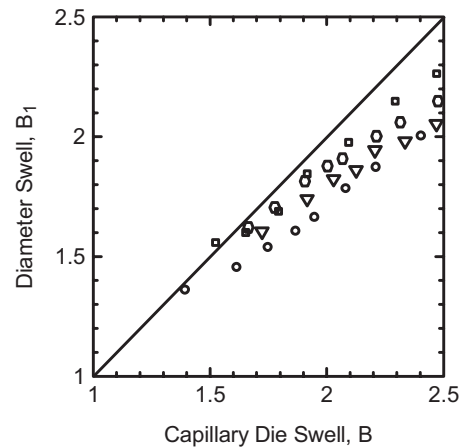


FIGURE 7.25 Annular diameter swell versus capillary swell at the same wall shear rate for resins HDPE (○) 22, (◻) 26, (△) 27, and (◻) PP-28. (Data from Garcia-Rejon et al., 1982.)

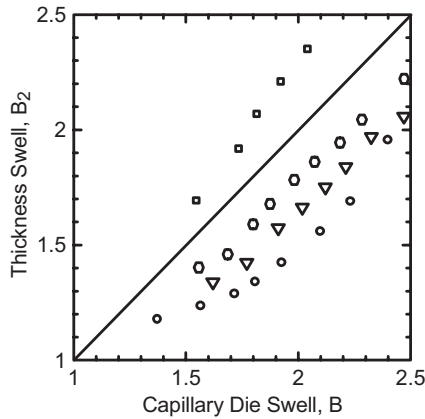


FIGURE 7.26 Annular thickness swell versus capillary swell at the same wall shear rate for HDPE resins (○) 22, (◻) 26, (△) 27, and (◻) PP-28. The line is $B_2 = B$. (Data from Garcia-Rejon et al., 1982.)

Finally, Cogswell and Lamb (1970) proposed a relation for the area swell, $B_1 B_2$, of an annular extrudate and the area swell of the extrudate from a capillary:

$$B_1 B_2 = B_A = 0.25 + 0.73 B^2 \quad (7.16)$$

This equation is compared with data in Figure 7.27, and we see here that the agreement is good for the HDPEs but not for PP. The cause of the discrepancy is not clear.

The results presented here illustrate the complexity in trying to extend die swell measurements from a capillary to other die geometries. As an initial approximation one can use the relations between B_1 , B_2 , and B given in Eqs. 7.13, 7.14, and 7.15. However, one must be aware of the fact that when significant strain hardening arises in the extensional behavior, the data will deviate more dramatically from these

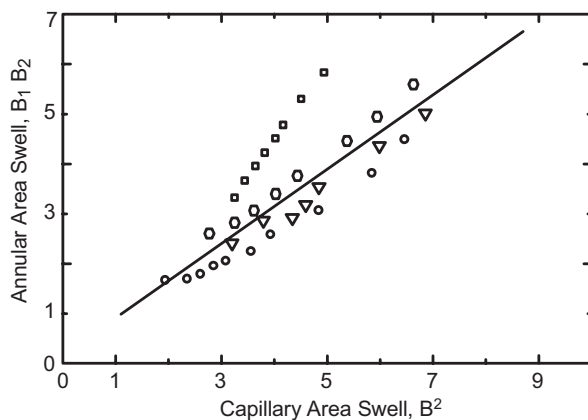


FIGURE 7.27 Annular area swell versus capillary area swell at the same wall shear rate for the same resins as in Figure 7.26. The line is Eq. 7.16. (Data from Garcia-Rejon et al., 1982.)

relations. As we proceed into more complex geometries, we will find even more problems in trying to make correlations with capillary data.

Before leaving this topic we would like to further point out the complexity of the phenomenon of extrudate swell. In Figure 7.28 are shown four different die geometries, and the corresponding extrudate swell values are given in the figure caption. Die geometry I converges to the exit while die geometry II has a capillary of constant radius at the end of the converging section. The final radius in both cases is the same, and hence, $\dot{\gamma}_W$ is the same. (Note: $\dot{\gamma}_W = (s + 3)\langle v_z \rangle / R$ and $\langle v_z \rangle$ is 7.2 mm/s for all four geometries.) However, D_p/D_0 for case I is 2.52 while it is 2.02 for case II. In die geometry III a diverging section has been added to the end of the die, while in case IV the die is straight but of the same diameter. D_p/D_0 for die geometry IV is 1.34. For die geometries III and IV, $\langle v_z \rangle$ is the same as in cases I and II, but $\dot{\gamma}_W$ is somewhat lower. In case I the additional stresses due to the converging flow lead to an increase in die swell relative to that for the straight tube. In case III the diverging section leads to a relaxation of stresses and a reduction in die swell. Hence, one can see that die design has a significant effect on extrudate swell, but there is no way at present to accurately predict this effect.

7.3 SHEET AND FILM DIES

In this section a few basic ideas behind the design of dies used in the extrusion of flat film and sheet are introduced. First some general statements about the design of these types of dies are made, and then some specific aspects are dealt with. More details about the design of sheet and film dies can be found in the book by Michaeli (1984). The distinction between sheet and flat film rests in the thickness of the extruded product. Flat film is usually less than 0.7 mm thick. Die design considerations are somewhat similar in each case, although different requirements for the properties of film and sheet exist. The main problem is that the die is fed by an extruder with a circular opening. Somehow the melt must be uniformly distributed over the width of the die so that the extrudate, which may be as wide as 400 cm, leaves the die lips being thermally homogeneous and having a uniform stress distribution. A nonuniform flow history can lead to variations in the stress distribution and extrudate thickness.

The salient features of a film (or sheet) die are shown in Figure 7.29. A film die consists of four major parts: the manifold, choker bar, the land, and the lips. The purpose of the manifold is to distribute the melt uniformly over the width of the die. The land tends to act as a resistance to flow and also promotes better flow uniformity. In the event that the manifold doesn't quite provide the required uniformity in flow rate across the die width, the choker bar can be used

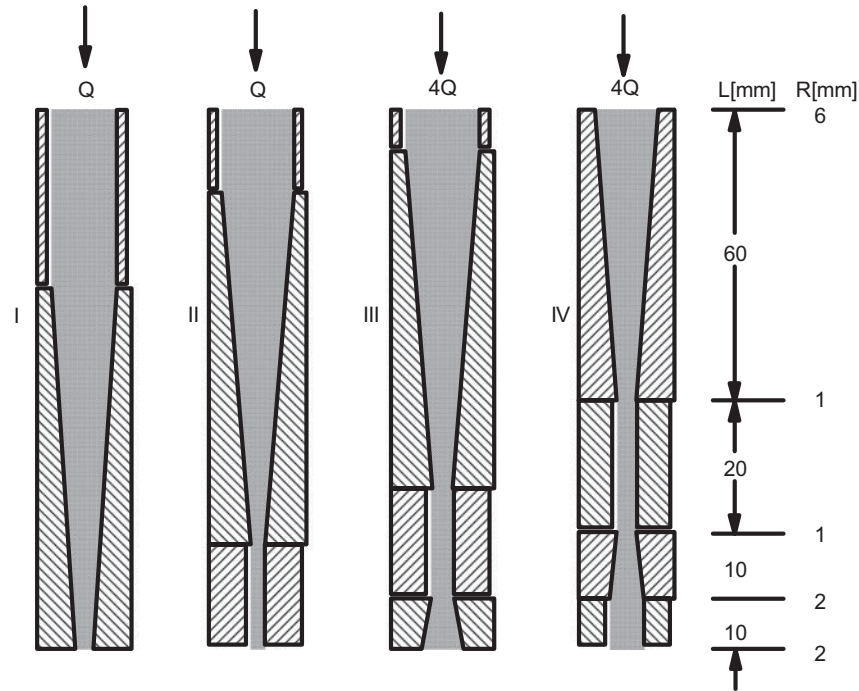


FIGURE 7.28 Influence of the die geometry on extrudate swell, D_p/D_0 , for a LDPE melt: I, $D_p/D_0 = 2.52$; II, $D_p/D_0 = 2.02$; III, $D_p/D_0 = 1.2$; IV, $D_p/D_0 = 1.34$, $\langle v_z \rangle = 7.2$ mm/s. (Data from Laun, 1989.)

to adjust the flow rate locally. The die lips provide the final film thickness and can also be adjusted locally to account for a nonuniform flow rate or nonuniform die swell.

The design of the manifold is now considered. The most widely used design is that of the coathanger type, which is shown in Figure 7.30 along with some other designs. As stated earlier the purpose of the manifold is to distribute the

melt over the width of the die in such a manner that the flow rate is the same everywhere across the width of the exit. The coathanger design is essentially a bent tube of variable radius with a slit in the side wall. A sketch of this design is shown in Figure 7.31 along with an indication of the pressure variation in the manifold and the land. The basic idea behind the design of a system like this is that in order to maintain

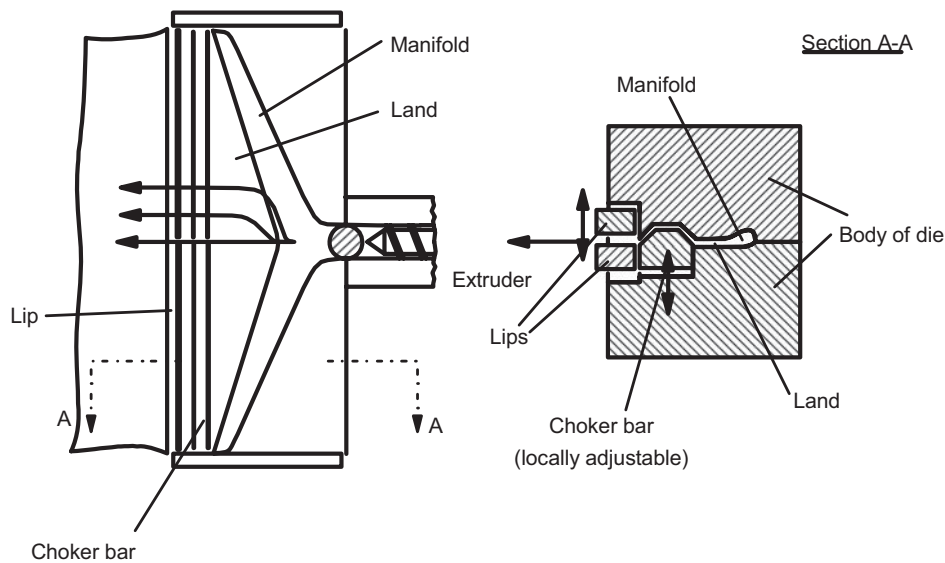


FIGURE 7.29 Slit die for sheet or film extrusion. (Data from Michaeli, 1984.)

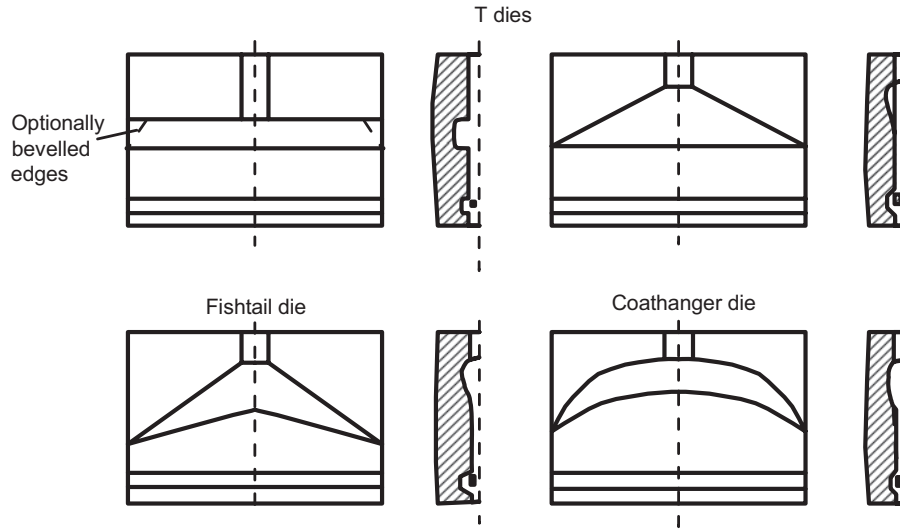


FIGURE 7.30 Commonly used manifold designs for film and sheet dies. (Data from Michaeli, 1984.)

a uniform flow rate across the width of the die the pressure gradient must be the same across the width of the die. To accomplish this the pressure gradient along any length of the manifold must equal the pressure gradient in the land. Since the pressure decreases along the manifold, it must be bent so

that the distance from the edge of the manifold decreases in such a way that the pressure gradient is constant.

To carry out the details of the design of a coathanger die, we refer to Figure 7.32. In order to maintain a uniform flow rate per unit width, q , at each distance x across the land then

$$dp/dy = G = \text{constant} \quad (7.17)$$

Next, this equation is integrated from $y = 0$ to $y = L(x)$:

$$\int_{P(0)}^{P(L)} dp = \int_{L(0)}^{L(x)} G dy \quad (7.18)$$

to give

$$P(L) - P(0) = G[L(x) - L(0)] \quad (7.19)$$

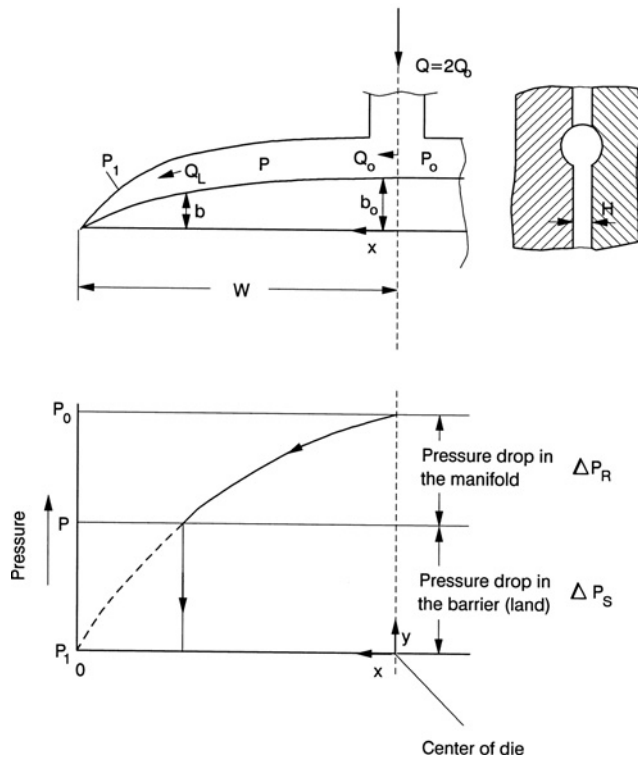


FIGURE 7.31 Geometric relationships and pressure variation in the manifold and land sections of a sheet/film die.

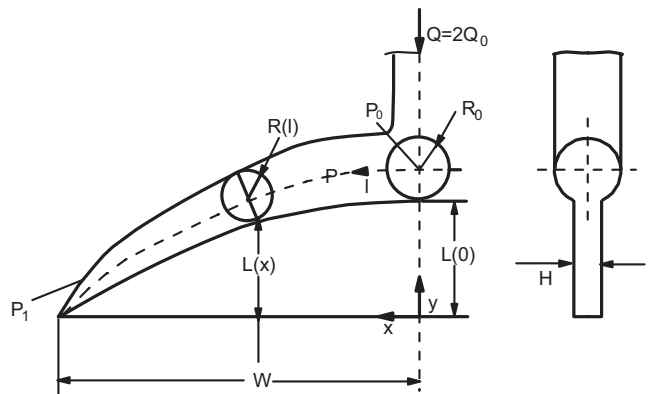


FIGURE 7.32 Geometric model of a manifold.

At $L(x)$, the pressure in the manifold at position l , $P(l)$, is assumed to equal $P(L)$. Substituting $P(l) = P(L)$ into Eq. 7.18 and differentiating with respect to l gives

$$dP(l)/dl = G dL(x)/dl \quad (7.20)$$

This is the general design equation for a coathanger manifold, which provides a uniform flow across the slit width. In this analysis, the pressure drop across the contraction has been neglected.

To complete the equation, we must specify G and dL/dl . G is determined by assuming that developed flow occurs in the land and dL/dl , which is a geometric variable, is then determined. We first solve for G assuming that the rheological properties are described by the power-law model. For slit flow the volumetric flow rate per unit width, q , is given as (see Table 2.5)

$$q = \frac{H^2}{2(s+2)} \left(\frac{H}{2m} \right)^s \left(\frac{dp}{dy} \right)^s \quad (7.21)$$

With $G = dp/dy$, we obtain

$$G = (2^{n+1}(2+s)^n m q^n)/H^{2n+1} \quad (7.22)$$

Next, flow inside the manifold is solved for. Although we will assume that the cross section is circular, in practice many times it is drop-shaped. The goal is to determine how R varies with l . To do this it is customary to use the lubrication approximation. Starting with the equation for flow of a power-law fluid through a tube, we obtain

$$-\frac{dP(l)}{dl} = \left(\frac{3+s}{\pi} \right)^n 2m Q(l)^n / R(x)^{3n+1} \quad (7.23)$$

Employing a mass balance we know that the volumetric flow rate in the manifold at any position l , $Q(l)$, must equal the volumetric flow rate in the slit from that point on until the end of the manifold:

$$Q(l) = q(W-x) \quad (7.24)$$

Combining Eqs. 7.23 and 7.24, the following expression is obtained:

$$-\frac{dP(l)}{dl} = \left[\left(\frac{3+s}{\pi} \right)^n 2m q^n (W-x)^n \right] / R(x)^{3n+1} \quad (7.25)$$

Finally, we replace $dP(l)/dl$ using Eqs. 7.20 and 7.22 to give

$$(2^n(2+s)^n/H^{2n+1})(dL/dl) + ((3+s)/\pi)^n (W-x)^n/R(x)^{3n+1} = 0 \quad (7.26)$$

For a given fluid and a slit of width of $2W$ and height H , there are two geometric variables: dL/dl and $R(x)$. For example, for a given manifold with curvature dL/dl , there exists a manifold radius profile, $R(x)$, that yields a uniform pressure at any line of constant y . On the other hand, one could specify $R(x)$ and then determine $L(l)$ or $L(x)$ such that the pressure would be constant along any line of constant y . For instructional purposes one would take dL/dl as constant. However, it is possible to apply the solution to finite segments of width ΔW and then find values of dL/dl over the segment.

Example 7.1. Design of a Coathanger Manifold

For HDPE (rheological data are given in Table 2.3) design a coathanger manifold to feed a film die having a width $2W = 1.0$ m and height of 0.0508 cm. Assume constant curvature of the manifold.

Solution. There are two unknowns in Eq. 7.26, and we must specify one and then solve for the other. We specify dL/dl and then solve for $R(x)$. Taking $dL/dl = -\tan \alpha = -0.087$ (i.e., $\alpha = 5^\circ$), rearranging Eq. 7.26, and using the value for n of 0.56, we find

$$R(x) = 0.169(W-x)^{0.209}$$

This equation gives the manifold radius (in units of cm) as a function of x . ■

Before leaving this topic a few additional comments should be made about the limitations of Eq. 7.26. First, the degree of taper (i.e., $R(x)$) and the curvature of the manifold (i.e., dL/dl) must be small enough that the lubrication approximation is not violated. Furthermore, the solution does not consider viscoelastic effects such as entrance pressure losses or the time dependence of the stresses, which might lead to higher values of viscosity than the steady-state values. We also note that the design of a coathanger manifold die is dependent on the rheological properties of the fluid. Hence, in changing from one polymer to another, or changing the melt temperature, the effectiveness of the die design will change. Thus, the choker bar and die lip opening may have to be adjusted to compensate for these changes. Finally, there may be nonuniform die swell across the width of the die as the effective land length changes with position across the die. As has been seen, die swell is strongly dependent on capillary length. Furthermore, the land length is relatively short and fully developed flow may barely be achieved. Again, the adjustable die lips can be used to compensate for the nonuniformities associated with the variations in die swell.

7.4 ANNULAR DIES

Dies with annular cross sections are used to extrude pipes, tubes, tubular films, and parisons for blow molding. Center-fed dies are commonly used for extruding pipes and tubes, while side-fed dies are used for tubular films and parisons. The four basic annular die designs in use at the present time are shown in Figure 7.33. These include (1) center-fed spider-supported mandrel dies, (2) center-fed screen pack dies, (3) side-fed mandrel dies, and (4) spiral mandrel dies. At the die exit there is usually an outer die ring which forms the die land. Only this part of the die can be analyzed simply as annular flow, while the remaining portions must be dealt with through the use of the lubrication approximation. In Section 7.4.1 we discuss the center-fed die and consider in Section 7.4.2 the side-fed and spiral mandrel die designs. Finally, wire coating dies are discussed in Section 7.4.3. Further details on die design as well as “rules of thumb” are given by Michaeli (1984).

7.4.1 Center-Fed Annular Dies

Pipes are primarily extruded using center-fed dies of the type shown in Figure 7.34. The melt stream from the extruder passes from the circular opening to the annular die by means of the mandrel support tip. The melt then passes over the “spider legs,” which support the mandrel, and through a converging annular region which for pipes is usually 10° to 15° . The converging region is followed by an annular region with parallel walls which imparts the final dimensions to the pipe. The outer diameter of the pipe can range from a few millimeters to approximately 1.6 meters. The ratio of the mandrel radius to outer wall radius usually falls in the range of 0.8 to

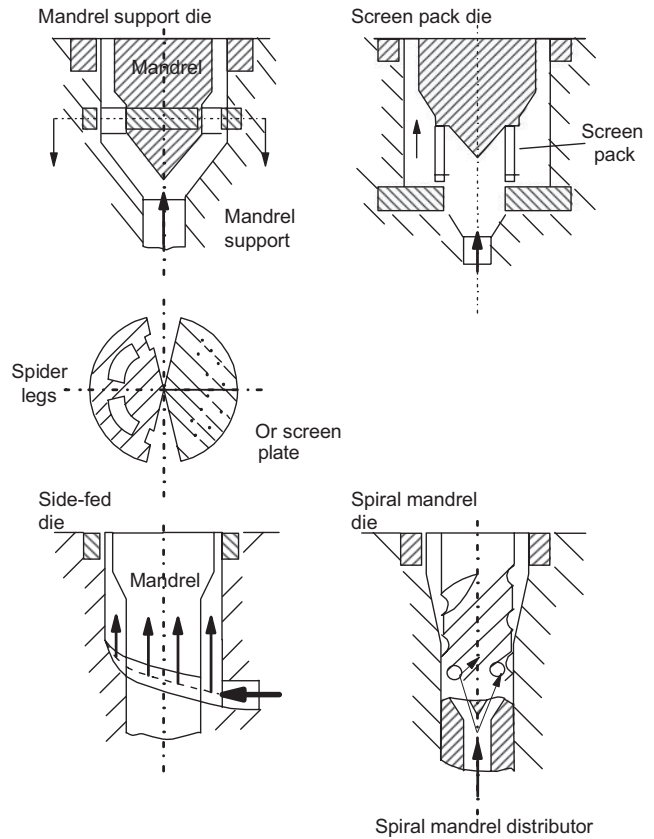


FIGURE 7.33 Four common annular die designs. (Data from Michaeli, 1984.)

0.925. This ratio is important as it implies that we can neglect curvature in the analysis of most parts of the die.

The spider legs usually lead to problems in that not only are flow markings visible, but mechanically weak regions

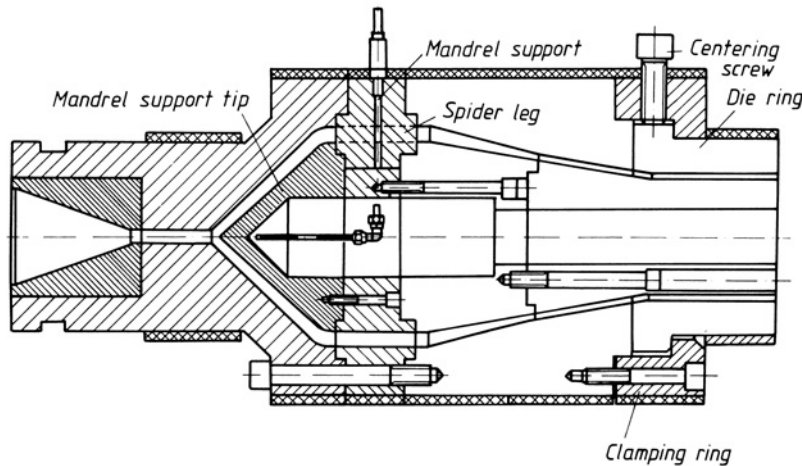


FIGURE 7.34 Typical pipe extrusion die. (Reprinted with permission of the publisher from Michaeli, 1984.)

are generated. These flow lines are also referred to as weld lines and are due to a higher degree of molecular orientation caused by the high stresses imparted to the melt and the inability of the molecules to reentangle during the time the melt spends in the die. The strength of the weld line is most likely related to the degree of reentanglement of the molecules which occurs as the melt passes through the die at the melt temperature. The reentanglement time appears to be much longer than the longest relaxation time. It has been estimated from interrupted shear experiments for polystyrene, for example, to be on the order of 300 seconds (Pissipati, 1983). It is related to self-diffusion of polymer molecules as discussed in Chapter 4.

One way of reducing the effect of the flow lines is through the design of the support system. Some spider leg systems presently used are shown in Figure 7.35. Instead of arranging the spider legs radially as shown in Figure 7.35a, a tangential arrangement as shown in Figure 7.35b will displace the defect circumferentially over the extrudate. A better way for reducing the flow marks is the use of offset spider legs as shown in Figure 7.35d. Here the flow marks do not extend all the way through the wall of the extrudate, which offers at least mechanical improvements. Finally, another way to reduce flow marks is the use of a screen plate, which is shown in

Figure 7.35c. In this design the melt passes into the annular region by first passing through a plate with many small holes bored in it. In effect the annular die is fed by multiple capillaries.

Design considerations for the center-fed dies consist of the force exerted by the melt on the mandrel support tips, the residence time in the die, the total pressure drop, the extrusion rate, die swell, and the onset of flow instabilities. The significance of the pressure exerted on the mandrel support tip rests in making sure the spider legs are strong enough. Residence time considerations are required in order to determine if sufficient time has been allowed for partial healing of the weld lines imparted by the spider legs. The relation between the shear stress and extrusion rate in the land section is also needed, as the onset of melt flow instabilities is the limiting factor in the rate of extrusion. Finally, the diameter of the extrudate as well as thickness as the result of die swell must be taken into consideration. The complete design of a center-fed die using a viscoelastic constitutive equation is not possible without the use of three-dimensional finite element methods, which is beyond the scope of this book. We can, however, estimate parts of the flow behavior needed in design work by making use of the lubrication approximation.

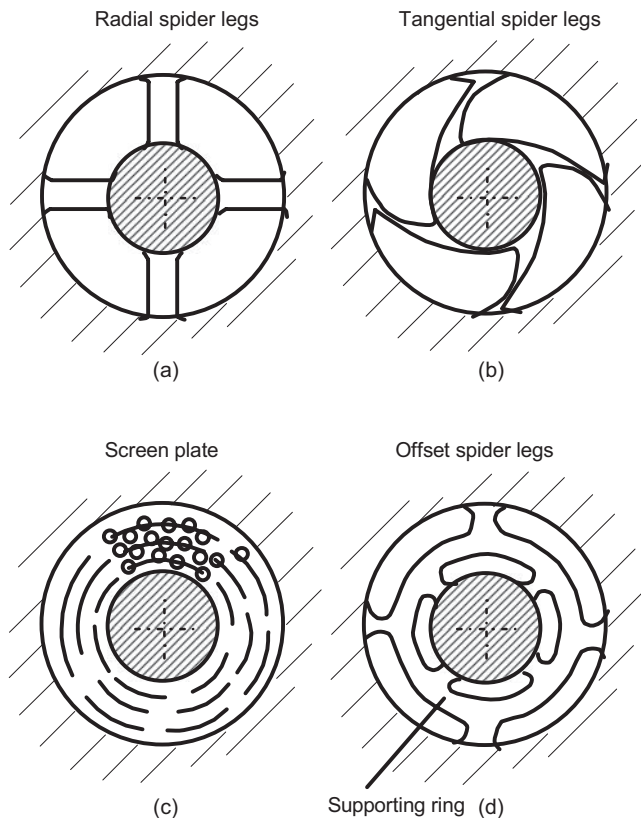


FIGURE 7.35 Typical mandrel support systems. (Data from Michaeli, 1984.)

7.4.2 Side-Fed and Spiral Mandrel Dies

The side-fed mandrel die is used in both blown film and pipe extrusion. The main consideration is to provide a uniform flow rate at the die land. This is done in much the same way as for flat film extrusion by the use of a manifold as shown in Figure 7.36. The main difficulty is in the design of the curved manifold, but one approach is to neglect curvature and consider the manifold to be like that of the flat film die but wrapped around the curved mandrel.

The spiral mandrel die seems to offer the best possibility for providing a uniform flow rate circumferentially at the annular die exit. Two specific designs of this type are shown in Figure 7.37. The die is usually fed from the extruder by means of either a star-shaped or ring-shaped distributing system. The melt then passes into spiral-shaped channels which are machined into the mandrel. The depth of the channels decreases with spiral distance which ensures that there will be mixing of the melt from channel to channel as the result of leakage. The spiral channels perform in much the same way as the single-screw extruder. Because of the design of this system there are no mandrel support elements, and hence, flow lines are eliminated completely.

7.4.3 Wire Coating Dies

Wire coating dies also involve annular cross sections. The basic sections of a wire coating die are shown in Figure 7.38. The melt usually enters from the side and so resembles the side-fed annular dies discussed in Section 7.4.1. The goal

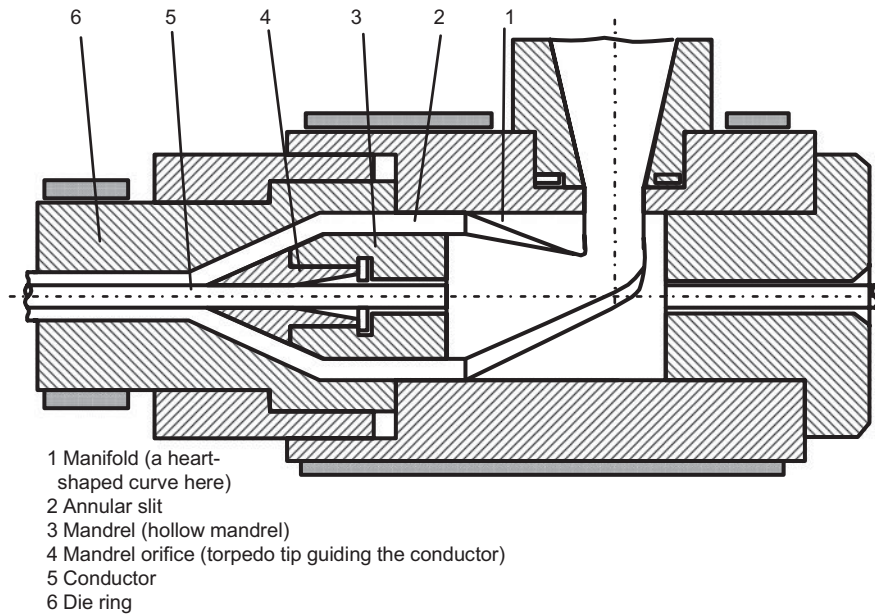


FIGURE 7.38 Basic features of a wire coating die. (Data from Michaeli, 1984.)

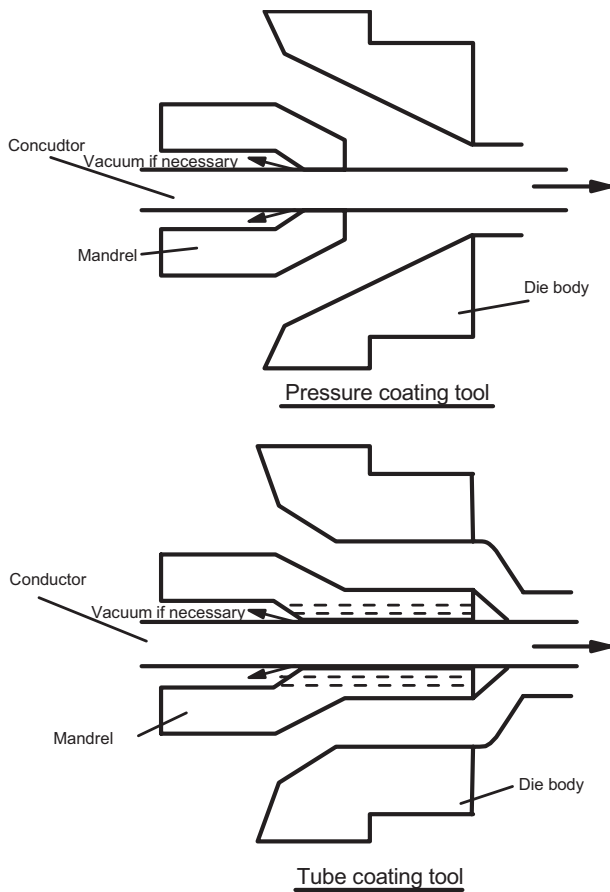


FIGURE 7.39 Two mandrel designs commonly used in wire coating dies. In the upper figure the wire is coated under pressure inside the die while in the lower figure the wire is coated outside the die.

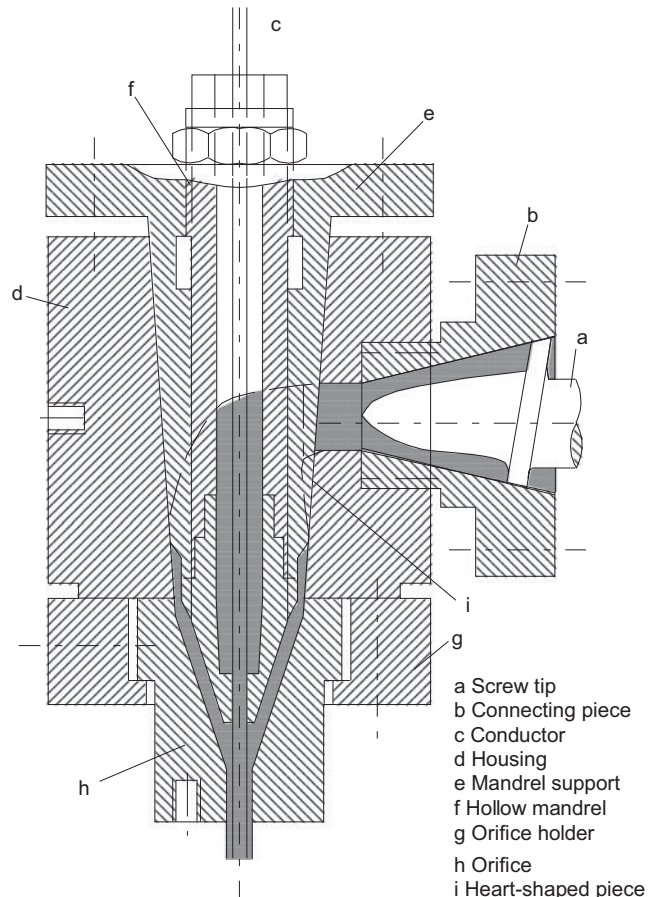


FIGURE 7.40 Wire coating die with a distribution system having heart-shaped distribution system. (Data from Michaeli, 1984.)

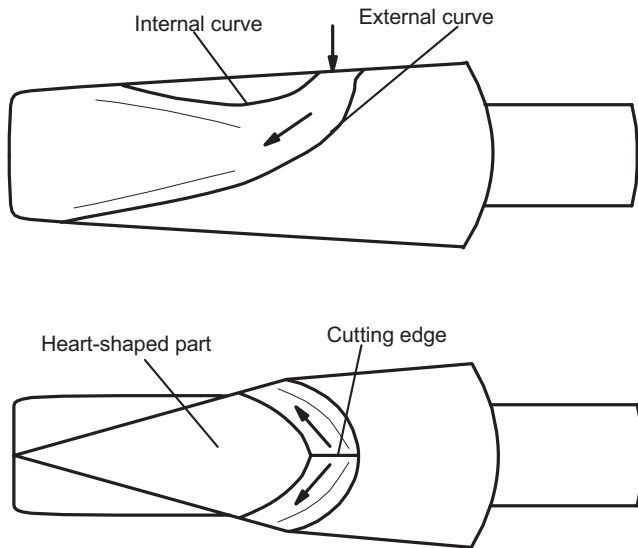


FIGURE 7.41 Deflecting distributing system with a heart-shaped piece. (Data from Michaeli, 1984.)

of the mandrel. The flow channels become wider, and their depth decreases. A heart-shaped piece, which is mounted below the bezel and elongates the flow path on the inner arc, functions as a compensating element. The length the flow edge of this heart-shaped piece is dimensioned such that the total path of the melt on the inner arc approximately corresponds to the flow path on the outer arc.

After the melt passes through the distribution system, the die housing narrows down to the wire in order to match the average velocity, $\langle v_z \rangle$, with the wire velocity. If high coating speeds are to be achieved, it is advisable to have the angle between the mandrel and the housing become constantly smaller up to the coating region. The reason for this is to suppress vortices.

Further quantitative features of the design of wire coating dies are discussed in the problems at the end of the chapter. The lubrication approximation is widely used in the design of wire coating dies.

7.5 PROFILE EXTRUSION DIES

Profile extrusion refers to the extrusion of polymer melts through dies of cross sections that are neither round, annular, nor rectangular with an aspect ratio, W/H , greater than 10.0. Because the geometries are quite complex, it is not possible to obtain analytical solutions when the generalized Newtonian fluid (GNF) or viscoelastic models are used. The use of finite element methods offers promise in solving problems associated with the design of profile dies, but the subject matter required to understand these methods is beyond the level of this text. At present, design is carried out by trial-and-error

methods. However, there are some aspects of design which can be dealt with, and these are discussed in this section.

We first consider some general aspects of profile die design. Three factors determine the dimensions of a profile die to produce an extrudate of desired dimensions. The first is the degree of die swell, which as discussed earlier (Section 7.2.3) is a function of the flow history in the die as well as the cooling conditions at the die exit. The second factor involves the shrinkage that occurs as the polymer melt solidifies. Finally, there is the shape change associated with drawing which occurs in the sizing device. Just determining the pressure drop/flow rate relation is complex enough because of the irregular boundaries. Only the pressure drop/flow rate relation for some geometries can quantitatively be dealt with at this level.

At present there are three types of profile dies used: *orifice dies*, *multistage dies*, and *tapered profile dies*. An example of an orifice die is shown in Figure 7.42. Basically the orifice die consists of a die base and a die plate in which the profile is formed. These dies are used for the extrusion of inexpensive profiles where dimensional accuracy is not necessary. Because of the abrupt change in cross-sectional area, there is usually a buildup of stagnant material behind the die plate and high extrusion rates are not possible. These dies are not commonly used for most thermoplastics but are restricted primarily to PVC and rubber.

An example of a multistage die is shown in Figure 7.43. Multistage dies exhibit step changes in the cross-sectional area of the flow channel. They consist of a series of die plates of similar geometry but of a decreasing cross-sectional area. Certainly, these represent an improvement over the orifice dies, but they still suffer from some of the same deficiencies.

Whenever profiles of high dimensional accuracy are to be produced at high extrusion rates, profile dies with a gradual change of cross-sectional area are required. An example of a profile die for producing highly accurate cross sections is shown in Figure 7.44. The design of these dies is carried out nearly on an empirical basis at present.

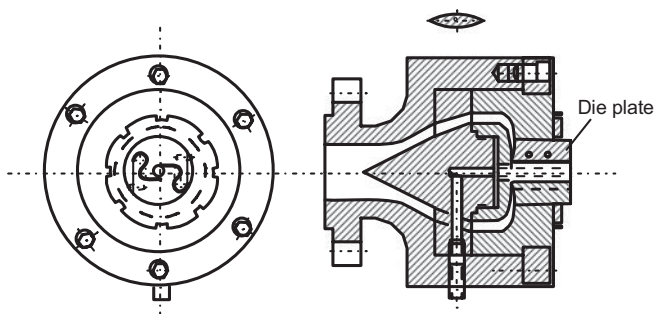


FIGURE 7.42 Profile die of the orifice type. The die plate is shown at the left. The extrudate emerges as a tube with two S-shaped flanges. (Data from Michaeli, 1984.)

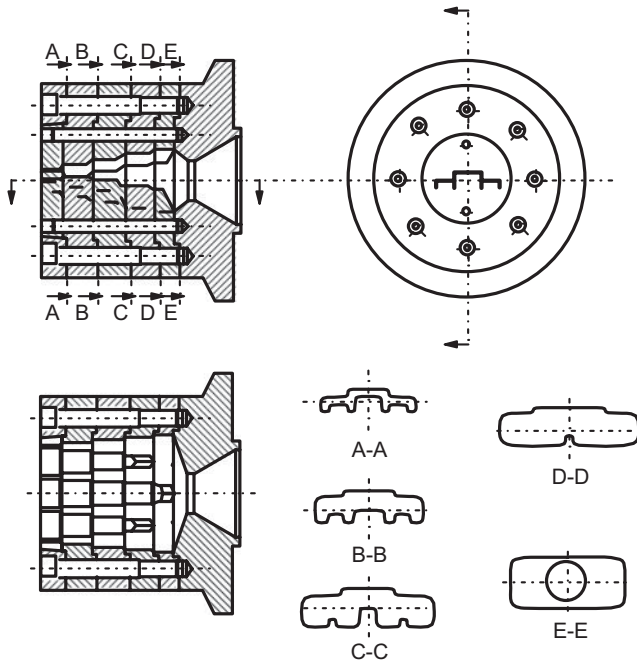


FIGURE 7.43 An example of a profile die of the multistage type. The die plate is shown in the upper right-hand figure (the extrudate is used as a window sash). In the lower right the segments making up the various stages of the die are shown. (Data from Michaeli, 1984.)

However, if one carries out empirical design work to generate profile dies on the laboratory scale, then one could use dimensional analysis for scaleup. In particular, geometric similarity would require that the following ratios be identical:

$$A_e/A_L \text{ and } L/R_H \quad (7.27)$$

where A_L is the cross-sectional area of the land and A_e is the cross-sectional area of the entry (this actually represents a contraction ratio) and R_H is the mean hydraulic radius. For dynamic similarity the Deborah (De) numbers would also have to be identical, where De is defined as

$$De = \lambda/t_p \quad (7.28)$$

λ is again the longest relaxation time of the melt and t_p is the process time, which for extrusion is $L/\langle v_z \rangle$, where $\langle v_z \rangle$ is the average velocity in the flow direction. However, because the rheological properties are for the same melt, dynamic similarity requires that

$$\langle v_z \rangle / L)_1 = \langle v_z \rangle / L)_2 \quad (7.29)$$

where the subscript "1" refers to the laboratory system and "2" the scaled-up system.

As one can imagine, it is nearly impossible at this time to carry out quantitative design work for dies such as shown in Figure 7.44. There are, however, a few considerations that can help in doing at least semiquantitative work. Some ideas concerned with die swell are considered first and then shrinkage and sizing are discussed.

The complexities associated with die swell are illustrated by the results presented in Figure 7.45. Here the extrudate shape is presented for two polymers, PVC and LDPE, as a function of the entry channel design and length to mean hydraulic radius, R_H , ratio. The mean hydraulic radius, R_H , is defined as A/P , where A is the cross-sectional area and P is the wetted perimeter. Although the die cross section is square, the extrudate shape barely reflects this. In fact, for low L/R_H ratios, the extrudate reflects the shape of the entry geometry. As the L/R_H ratio increases the extrudate reflects more closely the shape of the land section. It is also observed that the amount of swell decreases as the ratio increases. Furthermore, it is illustrated by the results in Figure 7.45 that PVC has considerably less swell than that exhibited by LDPE.

For some shapes it may be possible to carry out estimates of Q , ΔP , and extrudate swell by breaking the geometry up into a collection of simple geometries for which the flow can be analyzed. Some examples of profile geometries that can be dealt with by use of the equations derived for thin rectangular slits (Table 2.5) are presented in Figure 7.46. For example, Q for flow of a power-law fluid through a rectangular slit is given by

$$Q = \frac{WH^2}{2(s+2)} \left(\frac{H\Delta P}{2mL} \right)^s \quad (7.30)$$

We can apply Eq. 7.30 to geometry No. 3 by opening up the die to a die having a width of $2(R_o + R_i)$ and slit height, $H = R_o - R_i$. Likewise we can estimate die swell from results from a slit-die or capillary. Other geometries for which the slit formula can be used are shown in Figure 7.46 as well as replacements for W and H in Eq. 7.30.

The extruded product shrinks as it cools as a result of density changes. The amount of shrinkage can be estimated by the changes in density from the melt to the solid state. One must also assume that shrinkage occurs uniformly in all directions.

The extrudate is stretched slightly on leaving the die as it is pulled into the sizing device. In the book by Michaeli (1984) there are some suggested amounts by which the die cross-sectional area should be increased to account for the reduction in extrudate cross-sectional area generated by drawing. For example, for LDPE it is recommended that the die cross-sectional area be increased by 15–20%. However, these empirical rules-of-thumb are not very dependable.

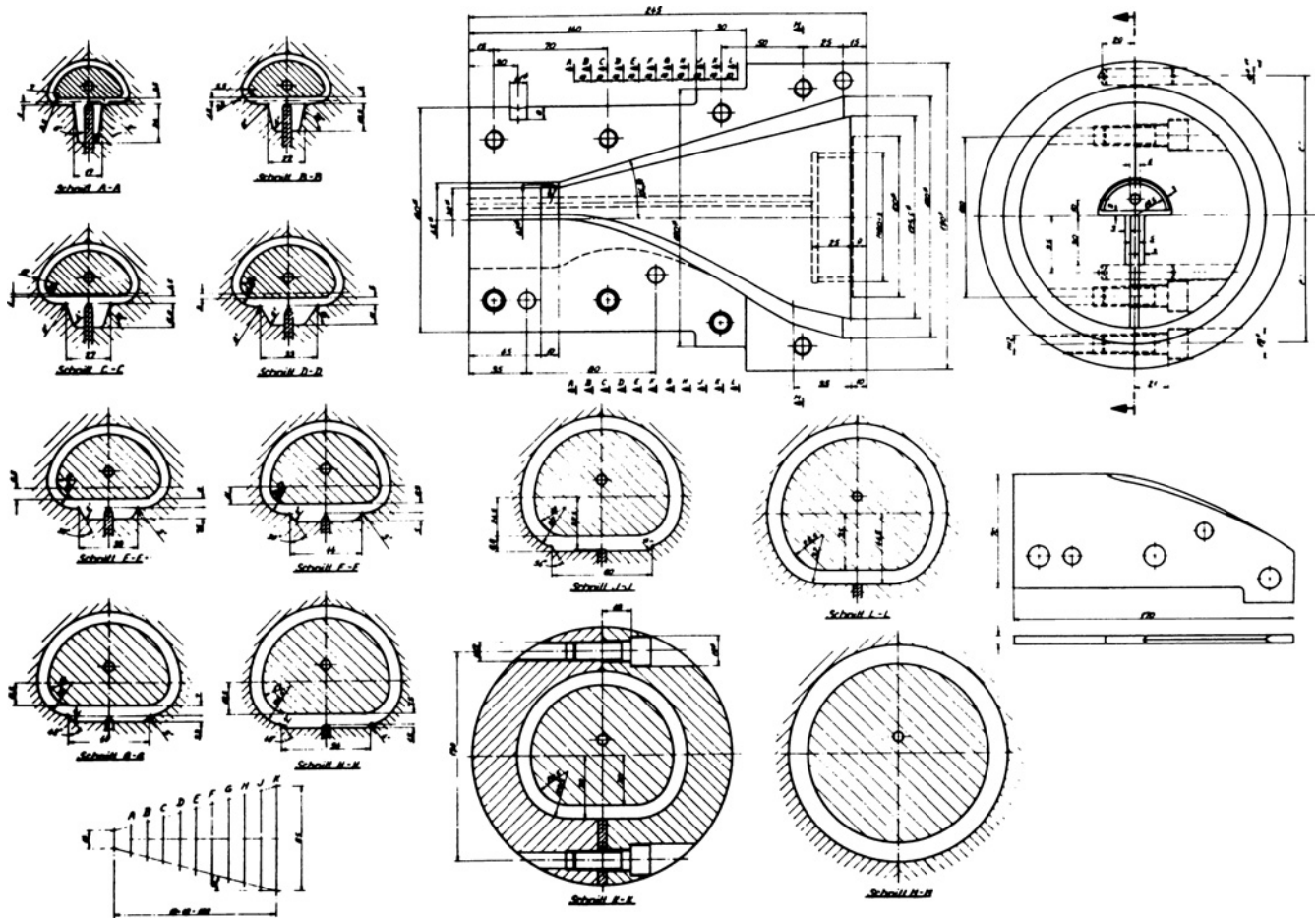


FIGURE 7.44 An example of a profile die with a gradual change of cross-sectional area for producing highly accurate shapes. (Reprinted with permission of the publisher from Michaeli, 1984.)

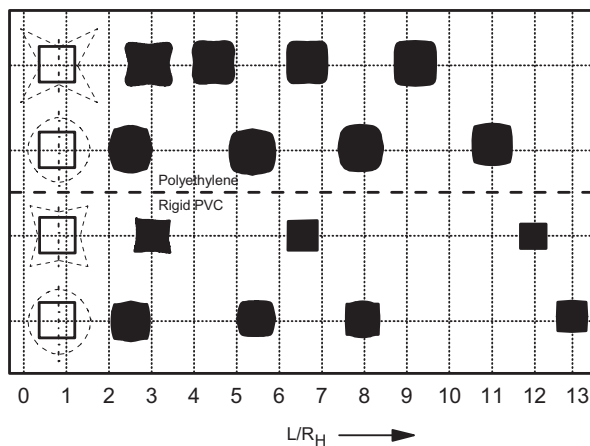


FIGURE 7.45 The effect of entrance geometry and land length (here the length is normalized by the mean hydraulic radius) on extrudate swell for LDPE (upper data) and PVC. The broken line represents the shape of the entry while the land is square. (Data from Röthemeyer, 1970.)

7.6 MULTIPLE LAYER EXTRUSION

It is becoming more common to combine multiple layers of different polymers to form products with properties which take advantage of the best properties of each component. For example, packaging film might be composed of several different types of polyethylene along with a layer of adhesive and a barrier polymer. We first discuss some general aspects of extrusion processes used for generating multiple layered products. Some quantitative aspects of die design are considered along with qualitative considerations for die design.

7.6.1 General Considerations

There are basically three types of multiple layer extrusion techniques: (1) melt streams flow separately; (2) melt streams flow separately and then together; (3) melt streams that flow together. Examples of type 1 are shown in Figure 7.47. In this process polymers A and B are extruded through separate flow channels and then joined together outside the die.

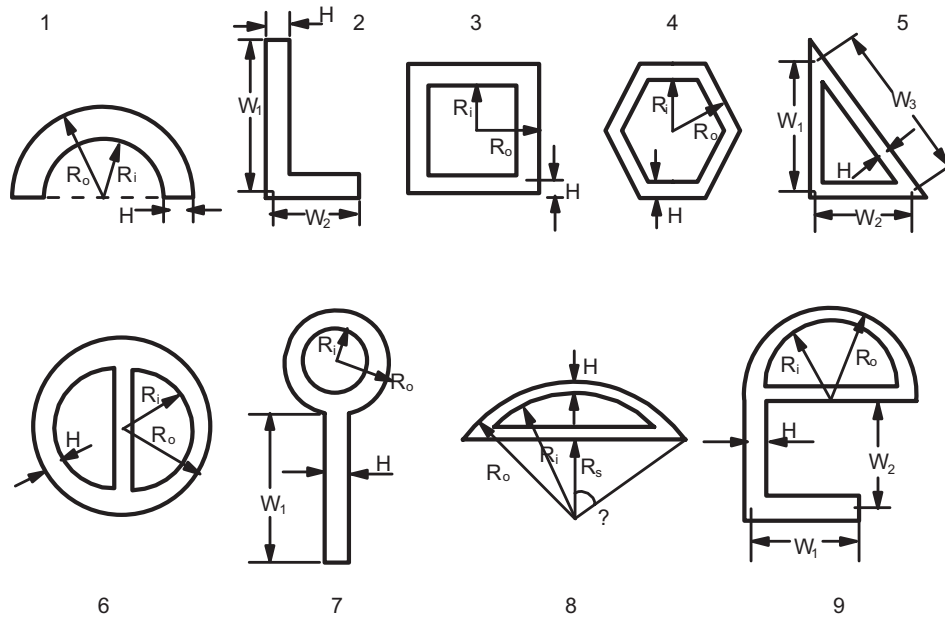


FIGURE 7.46 Profile cross-sectional shapes which can be treated as a combination of thin slits. The slit width in Eq. 7.30 is replaced by the following values in each case: 1: $W = \pi/2 (R_o + R_i)$; 2: $W = W_1 + W_2$; 3: $W = 4 (R_o + R_i)$; 4: $W = 3.46 (R_o + R_i)$; 5: $W = W_1 + W_2 + W_3$; 6: $W = \pi R_o + (2 + \pi)R_i$; 7: $W = \pi (R_o + R_i) + W$; 8: $W = (R_o + R_i)(\theta + \sin \theta)$; $\cos \theta = 2R_s / (R_o + R_i)$; 9: $W = (\pi/2)R_o + (2 + \pi/2)R_i + W_1 + W_2$. (Data from Carley, 1963.)

The advantage in this type of multilayer extrusion is that polymers with widely different processing temperatures and rheological properties can be used. The major problem is that of generating satisfactory adhesion between the components. Usually the technique is only used for two polymers.

The second technique is shown in Figure 7.48. Here the streams are brought together inside the die, and then they pass through a common land region. Because the streams are

brought together under pressure, adhesion is improved. However, it is not possible to have the streams at widely different temperatures. Likewise the rheological properties cannot be too widely different or flow instabilities will arise. Furthermore, at the point where the streams converge, interfacial instability problems may arise.

The third method is not too dissimilar from the second method as shown in Figure 7.49. Here the polymer streams

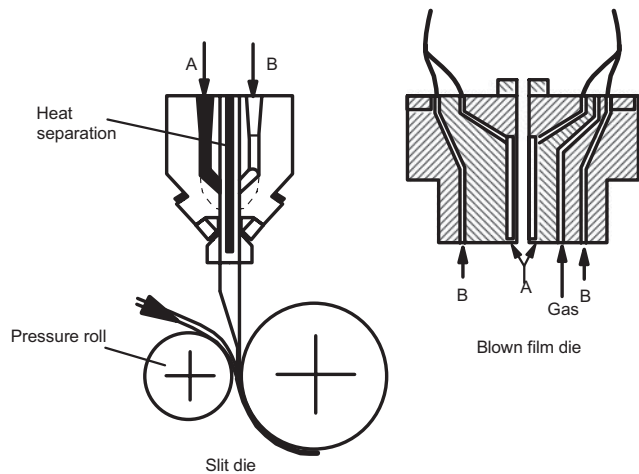


FIGURE 7.47 Coextrusion dies in which the two streams of polymer are joined outside the die.

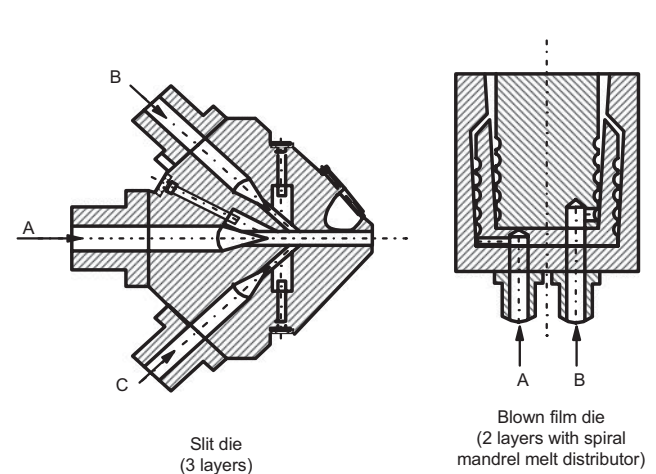


FIGURE 7.48 Coextrusion dies in which the streams are combined in the die and then pass through a common land.

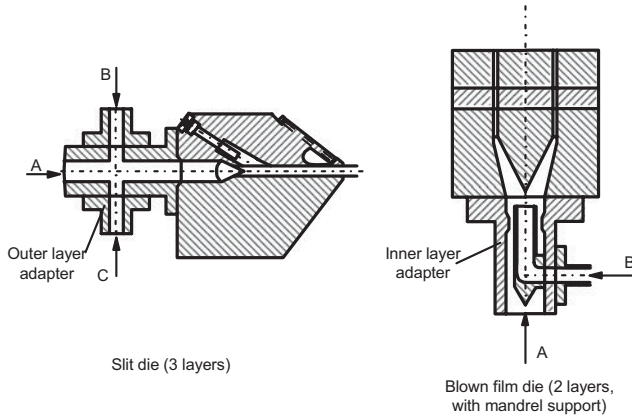


FIGURE 7.49 Coextrusion dies in which the streams are brought together in an adapter and then pass through a common die.

are brought together in an adapter, and then they pass through a common die. In this case the same die as used for single component extrusion can be used. Again the melt rheological properties cannot be too dissimilar or an instability will arise which will disrupt the laminar nature of each stream. However, this is one of the most inexpensive and simplest methods for generating multiple layer films and sheets.

7.6.2 Design Equations

The most often used die geometries in multiple layer extrusion are slits and tubular film dies. However, there are also cases in which profile dies are used. Some quantitative design work can be carried out in the case of flow through flat film and tubular dies. The factors that can be dealt with are flow rates and pressure drops required to provide a given thickness in a multilayer extrudate. The major problem in multilayer extrusion is the instability in the flow. This will be discussed in a qualitative fashion in Section 7.6.3. However, the design equations can at least be used to estimate whether the flow will be unstable.

Flow of two polymers through a slit die as shown in Figure 7.50 is considered first. It is assumed that (1) the rheological properties of the fluids are described by the power-law model; (2) the flow is stable and at steady state; and (3) the flow is isothermal. With these assumptions in hand, the goal is to determine a relation between the desired layer thickness and flow rate and pressure drop. The superscript (1) refers to that in phase 1, while the superscript (2) refers to that in phase 2. The equations of motion are then written for each phase:

$$-\frac{\partial p^{(1)}}{\partial z} - \frac{\partial \tau_{yz}^{(1)}}{\partial y} = 0 \tag{7.31}$$

$$-\frac{\partial p^{(2)}}{\partial z} - \frac{\partial \tau_{yz}^{(2)}}{\partial y} = 0 \tag{7.32}$$

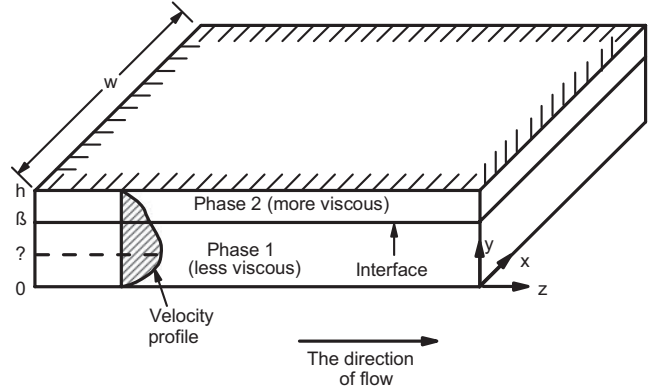


FIGURE 7.50 Flow of two polymer melts through a slit die. α is the position of the maximum in the velocity profile while β is the position of the interface between the two melts.

The pressure gradient in each phase must be identical, or there would be flow in the y direction. Equations 7.31 and 7.32 can be integrated to find $\tau_{yz}^{(1)}$ and $\tau_{yz}^{(2)}$:

$$\tau_{yz}^{(1)} = G(y - C_1) \tag{7.33}$$

$$\tau_{yz}^{(2)} = G(y - C_2) \tag{7.34}$$

where $G = -\partial p / \partial z$. At some unknown position, α , $\tau_{yz}^{(1)} = 0$, which implies that $C_1 = \alpha$. Furthermore, from the assumption that $\tau_{yz}^{(1)} = \tau_{yz}^{(2)}$ at $y = \beta$, it can be shown that $C_2 = \alpha$ also. Therefore, Eqs. 7.33 and 7.34 become

$$\tau_{yz}^{(1)} = G(y - \alpha) \tag{7.35}$$

$$\tau_{yz}^{(2)} = G(y - \alpha) \tag{7.36}$$

We need four boundary conditions in order to find $v_z^{(1)}$ and $v_z^{(2)}$:

$$\text{B.C.1: at } y = 0, \quad v_z^{(1)} = 0 \tag{7.37}$$

$$\text{B.C.2: at } y = \beta, \quad v_z^{(1)} = v_z^{(2)} \tag{7.38}$$

$$\text{B.C.3: at } y = h, \quad v_z^{(2)} = 0 \tag{7.39}$$

$$\text{B.C.4: at } y = \beta \quad \tau_{yz}^{(1)} = \tau_{yz}^{(2)} \tag{7.40}$$

Here boundary conditions 2 and 4 (B.C.4 was used already to obtain Eq. 7.36) are based on the continuity of stresses and the velocity field at the interface between the two polymer streams. Eventually, as discussed later, the cohesion between the two polymers at the interface may break down, leading to an instability.

We next need expressions for $\tau_{yz}^{(1)}$ and $\tau_{yz}^{(2)}$ in terms of velocity gradients. Because of the changes in sign of the

velocity gradient, we must break up the flow region into three parts:

$$\text{Region (1a): } 0 < y < \alpha, \quad dv_z^{(1a)}/dy > 0 \quad (7.41)$$

$$\text{Region (1b): } \alpha < y < \beta, \quad dv_z^{(1b)}/dy > 0 \quad (7.42)$$

$$\text{Region (2): } \beta < y < h, \quad dv_z^{(2)}/dy < 0 \quad (7.43)$$

Substituting the power-law expression for τ_{yz} into Eqs. 7.35 and 7.36 leads to the following differential equations for $v_z^{(1)}$ and $v_z^{(2)}$:

$$-m_1(dv_z^{(1a)}/dy)^{n_1} = G(y - \alpha) \quad (7.44)$$

$$m_1(-dv_z^{(1b)}/dy)^{n_1} = G(y - \alpha) \quad (7.45)$$

$$m_2(-dv_z^{(2)}/dy)^{n_2} = G(y - \alpha) \quad (7.46)$$

We can now integrate these equations to obtain the velocity field:

$$v_z^{(1a)} = \left(\frac{G}{m_1}\right)^{s_1} \int_0^y (\alpha - y')^{s_1} dy' \quad (7.47)$$

$$v_z^{(1b)}(\alpha) - v_z^{(1b)} = -\left(\frac{G}{m_1}\right)^{s_1} \int_\alpha^y (y' - \alpha)^{s_1} dy' \quad (7.48)$$

$$v_z^{(2)} = -\left(\frac{G}{m_2}\right)^{s_2} \int_y^h (y' - \alpha)^{s_2} dy' \quad (7.49)$$

The prime on y indicates that it is a dummy variable of integration. Carrying out the integration and using the condition that $v_z^{(1a)}(\alpha) = v_z^{(1b)}(\alpha)$ at $y = \alpha$, we find the following expressions:

$$v_z^{(1a)} = \left(\frac{G}{m_1}\right)^{s_1} \left(\frac{n_1}{n_1 + 1}\right) [\alpha^{(n_1+1)/n_1} - (\alpha - y)^{(n_1+1)/n_1}] \quad (7.50)$$

$$v_z^{(1b)} = \left(\frac{G}{m_1}\right)^{s_1} \left(\frac{n_1}{n_1 + 1}\right) [\alpha^{n_1+1/n_1} - (y - \alpha)^{(n_1+1)/n_1}] \quad (7.51)$$

We can write Eqs. 7.50 and 7.51 more succinctly as

$$v_z^{(1)} = \left(\frac{G}{m_1}\right)^{s_1} \left(\frac{n_1}{n_1 + 1}\right) [\alpha^{(n_1+1)/n_1} - |y - \alpha|^{(n_1+1)/n_1}] \quad (7.52)$$

For layer 2 we can complete the integration in Eq. 7.49 to obtain

$$v_z^{(2)} = \left(\frac{G}{m_2}\right)^{s_2} \left(\frac{n_2}{n_2 + 1}\right) [(h - \alpha)^{(n_2+1)/n_2} - (y - \alpha)^{(n_2+1)/n_2}] \quad (7.53)$$

The goal of this derivation is to obtain an expression for the volumetric flow rate in each layer and pressure drop to produce a desired thickness for each layer. The volumetric flow rate in each layer, Q_1 and Q_2 , is obtained by integrating Eqs. 7.52 and 7.53 over the cross-sectional area:

$$Q^{(1)} = W \left(\frac{G}{m_1}\right)^{s_1} \left(\frac{n_1}{n_1 + 1}\right) \times \left\{ \int_0^\alpha [\alpha^{(n_1+1)/n_1} - (\alpha - y)^{(n_1+1)/n_1}] dy + \int_\alpha^\beta [\alpha^{(n_1+1)/n_1} - (y - \alpha)^{(n_1+1)/n_1}] dy \right\} \quad (7.54)$$

$$= W \left(\frac{G}{m_1}\right)^{s_1} \left(\frac{n_1}{n_1 + 1}\right) \left[\left(\frac{n_1 + 1}{2n_1 + 1}\right) \alpha^{(2n_1+1)/n_1} + \alpha^{(n_1+1)/n_1}(\beta - \alpha) - \frac{n_1(\beta - \alpha)^{(2n_1+1)/n_1}}{2n_1 + 1} \right] \quad (7.55)$$

and

$$Q^{(2)} = W \left(\frac{G}{m_2}\right)^{s_2} \left(\frac{n_2}{n_2 + 1}\right) \int_\beta^h [(h - \alpha)^{(n_2+1)/n_2} - (y - \alpha)^{(n_2+1)/n_2}] dy \quad (7.56)$$

$$= W \left(\frac{G}{m_2}\right)^{s_2} \left(\frac{n_2}{n_2 + 1}\right) \left[(h - \alpha)^{(n_2+1)/n_2}(H - \beta) - \frac{n_2}{2n_2 + 1} (h - \alpha)^{(2n_2+1)/n_2} - (\beta - \alpha)^{(2n_2+1)/n_2} \right] \quad (7.57)$$

The total volumetric flow rate, Q , is then $Q^{(1)} + Q^{(2)}$.

To solve these equations, one more equation is needed as there are three unknowns, Q , α , and β (for a given G). The final equation is obtained from the condition

$$v_z^{(1)}(\beta) = v_z^{(2)}(\beta) \quad (7.58)$$

and is

$$\left(\frac{G}{m_1}\right)^{s_1} \left(\frac{n_1}{n_1 + 1}\right) [\alpha^{1+s_1} - (\beta - \alpha)^{1+s_1}] = \left(\frac{G}{m_2}\right)^{s_2} \left(\frac{n_2}{n_2 + 1}\right) [(h - \alpha)^{1+s_2} - (\beta - \alpha)^{1+s_2}] \quad (7.59)$$

Hence, for a given layer thickness (i.e., given β) one can use Eq. 7.59 to find α . (*Note:* One must guess at G .) Then one can calculate $Q^{(1)}$ and $Q^{(2)}$ from the values of α , β , and G . We illustrate the manipulation of these equations in the following example.

Example 7.2. Coextrusion of Two Polymers Through a Film Die

HDPE (rheological properties are given in Table 2.3) and nylon 6 (rheological properties are given in Table 7.3) are extruded through a film die both at a temperature of 220 °C. Determine the pressure gradient, G , required to produce an

TABLE 7.3 Parameters for Nylon 6, Capron™ 8200, Allied Chemical

Temperature (K)	Power Law			Carreau Model			Ellis Model		
	Range s ⁻¹	<i>m</i> Pa · s ^{<i>n</i>}	<i>n</i>	η ₀ (Pa · s)	Range (s ⁻¹)	<i>n</i>	γ (s)	α	τ _{1/2} (Pa)
498	100–2500	2.62 × 10 ³	0.63	1.6 × 10 ³	100–2000	0.63	0.27	1.64	1.06 × 10 ⁴
503	100–2000	1.95 × 10 ³	0.66	1.3 × 10 ³	100–2000	0.65	0.32	1.70	1.3 × 10 ⁴
508	100–2300	1.81 × 10 ³	0.66	1.1 × 10 ³	100–2000	0.68	0.36	1.61	1.04 × 10 ⁴

Source: Data from Tadmor and Gogos, (1979)

extrudate whose thickness is 1/5 nylon 6 (i.e., β = 0.2 h). Determine the shear rate at the interface for each component. The dimensions of the land of the die are W = 76.2 cm and h = 0.1016 cm. The line speed (i.e., linear velocity of the sheet) is 60 m/min.

Solution. The procedure for solving this problem is as follows:

1. Solve the nonlinear algebraic equation, Eq. 7.59, for α using a guess for G and the given value of β.
2. Calculate Q⁽²⁾ using Eqs. 7.56 and the values for G, α, and β.
3. Compare Q⁽²⁾ against the given value based on the line speed and the thickness, β.
4. If the difference in values is greater than a specified tolerance, ε, then return to step 1 and repeat the procedure.

An “intelligent guess” for G will accelerate the rate of convergence to the solution. Because the major component of the flow is HDPE, we use Table 2.5 and estimate G for just flow of HDPE:

$$G = -\frac{\Delta P}{L} = \left[\frac{2Q(s+2)}{WH^2} \right]^n \frac{2m}{H} = 1.653 \times 10^9 \text{ Pa/m}^{-1}$$

We then solve the nonlinear algebraic equation, Eq. 7.59, for α, which is the position of the maximum in the velocity profile (see Fig. 7.50) using either the IMSL subroutine, NEQNF, or the Solver in Excel for which the calling programs are given on the accompanying website (see “Numerical Solutions, Chapter 7”). A summary of the guesses for G and the calculated values of α and Q⁽²⁾ is given

TABLE 7.4 Calculated Values of the Parameter α and the Flow Rate for HDPE for Various Guesses of G

G (Pa/m)	α	Q ⁽²⁾ (m ³ /s)
1.653 × 10 ⁹	6.095 × 10 ⁻⁴	3.022 × 10 ⁻⁴
1.800 × 10 ⁹	6.095 × 10 ⁻⁴	3.475 × 10 ⁻⁴
2.200 × 10 ⁹	6.095 × 10 ⁻⁴	4.83 × 10 ⁻⁴
2.550 × 10 ⁹	6.095 × 10 ⁻⁴	6.194 × 10 ⁻⁴

in Table 7.4. What we observe is that after the initial guess there is no change in the predicted value of α. In other words, α is somewhat insensitive to the magnitude of G. Knowing this and Q⁽²⁾ = 6.194 × 10⁻⁴ m³/s, we can calculate G from Eq. 7.57, which we find to be 2.55 × 10⁹ Pa/m. ■

There are several other cases which are commonly encountered. For thin annular dies Eqs. 7.54 through 7.59 can be adopted directly by making appropriate replacements for W and h. For multilayer extrusion through an annulus in which the gap is too thick to apply the thin slit approximation, the appropriate equations are derived in Problem 7B.8. For more than two layers the equations for flow through parallel plates can be generalized as follows (Schrenk and Alfrey, 1976). Referring to Figure 7.51 we can obtain expressions

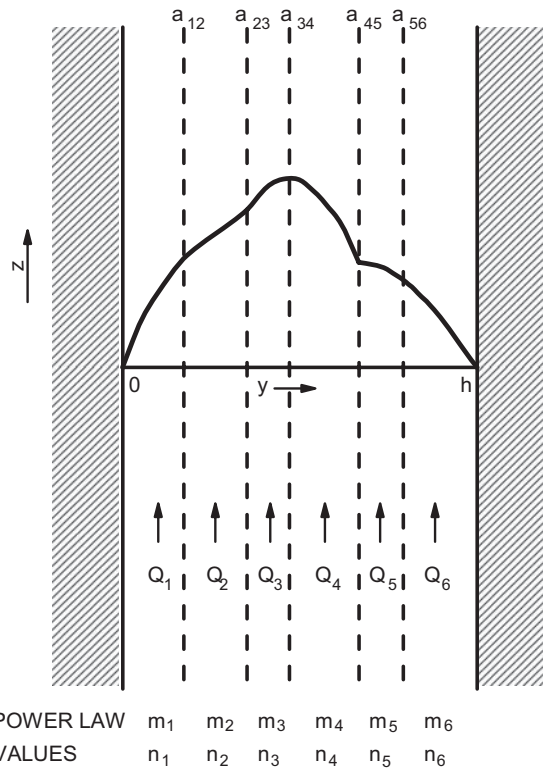


FIGURE 7.51 The velocity profile of a non-Newtonian multilayer flow through a wide narrow slit. The parameters m_i and n_i are the power-law parameters for each layer.

for the volumetric flow rate in each layer. The shear stress in each layer is

$$\tau_{yz}^{(i)} = G(y - c) \tag{7.60}$$

where c is the position where $\tau_{yz} = 0$. Expressions for the power-law model for each layer can now be substituted into Eq. 7.60 and integrated to obtain the velocity field in each layer:

$$v_M(y) = -\text{sign}(G) \left\{ \sum_{j=1}^{M-1} \frac{m_j |G|^{s_j}}{s_j + 1} [|a_{j-1,j} - \alpha|^{s_j+1} - |a_{j,j+1} - \alpha|^{s_j+1}] + \frac{m_M |G|^{s_M}}{s_M + 1} [|a_{M-1,M} - \alpha|^{s_M+1} - |y - \alpha|^{s_M+1}] \right\} \tag{7.61}$$

where $a_{j-1,j}$ is the interfacial position of layer j and $M_j = m_j^{-s_j}$. Details of the derivation required to obtain Eq. 7.61 are considered in Problem 7B.9. The volumetric flow rate in any layer is given as

$$|Q_M| = \sum_{j=1}^{M-1} \frac{m_j |G|^{s_j}}{s_j + 1} \{ |\alpha - a_{j-1,j}|^{s_j+1} - |\alpha - a_{j,j+1}|^{s_j+1} \} \times (a_{M,M+1} - a_{M-1,M}) + m_M \frac{|G|^{s_M}}{s_M + 1} \{ |\alpha - a_{M-1,M}|^{s_M+1} \} \times (a_{M,M+1} - a_{M-1,M}) + \frac{m_M |G|^{s_M}}{(s_M + 1)(s_M + 2)} \{ \text{sign}(\alpha - a_{M,M+1}) \times |\alpha - a_{M,M+1}|^{s_M+2} - \text{sign}(\alpha - a_{M-1,M}) \times |\alpha - a_{M-1,M}|^{s_M+2} \} \tag{7.62}$$

These equations are used typically to find α and a_{ij} for a given Q_M . By selecting trial values for β and α , Eq. 7.61 can be solved sequentially for a_{ij} . If $a_{M,M+1}$ does not match the location h and the calculated values of v_M do not match at the interfaces, then new trial values for a_{ij} and α are tried until the correct values are obtained. The values of Q_M can then be calculated. This process is discussed further in Problem 7C.3.

7.6.3 Flow Instabilities in Multiple Layer Flow

There are basically two problems in trying to extrude multiple layers of different fluids through the same die. First, if there are distinct viscosity differences between the fluids, then the lower viscosity component will try to encapsulate the higher viscosity component. Second, there are situations when the viscosities of two polymers are closely matched, but the interface still becomes wavy and distorted. (This type of problem is shown in Fig. 7.52.) Some general comments about each type of instability are made first followed by some attempt to estimate if an instability is imminent.

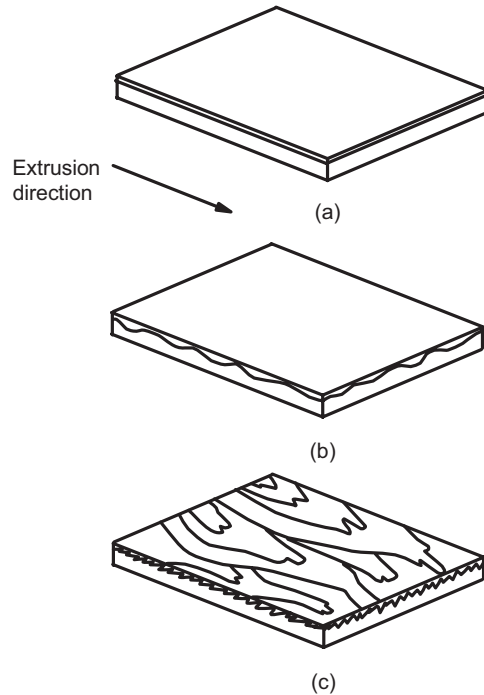


FIGURE 7.52 The appearance of two layers of sheet under (a) stable flow conditions, (b) incipient interfacial flow instability, and (c) severe instability.

The encapsulation of the high viscosity component by the low viscosity component is illustrated in Figure 7.53. Viscosity data for the two nylon 6 polymers is shown in Figure 7.54. The polymers were extruded in a side-by-side configuration through a capillary. The exit angle as well as the interface shape are shown as a function of the capillary L/D . Here it is seen that complete encapsulation does not occur until a L/D of 100 is reached. In many cases the L/D is short enough that not much rearrangement occurs. However,

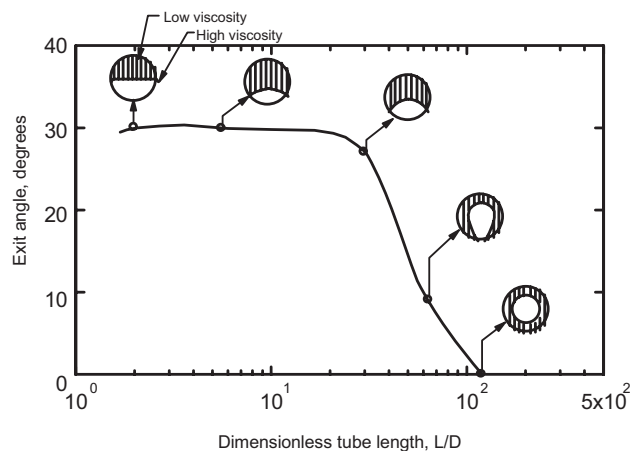


FIGURE 7.53 Extrudate interface shape and exit angle variation with tube length for two nylon 6 melts. (Data from Everage, 1975.)

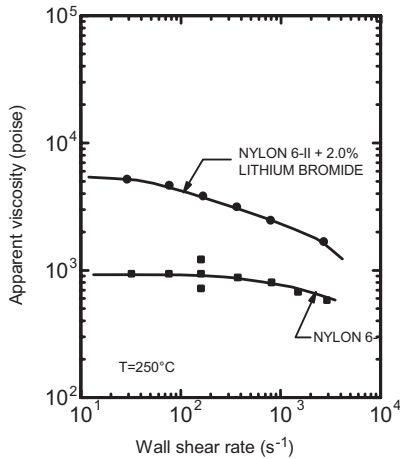


FIGURE 7.54 Apparent viscosity versus shear rate for two nylon 6 melts. (Data from Everage, 1975.)

the flow may be on the verge of an instability, and obtaining an extrudate with a straight interface may not be possible.

Although, as mentioned above, we are not in a position to determine the interface shape or the distance required for encapsulation, it is at least possible to estimate the conditions when problems are imminent. Following the procedure in Section 7.6.2 it is possible to calculate the velocity profile in tube flow in each layer for various viscosity differences. In Figure 7.55 are shown velocity profiles for two cases. First we consider the case when the viscosity of layer 2, η_{02} , is less than that of layer 1, η_{01} (Note: This is for tube flow.) When the flow is stable, the velocity profile of layer 1 is flat, whereas in layer 2 there is a large dependence of the velocity profile on the radius of the capillary. However, when $\eta_{02} > \eta_{01}$ the flow is in an unstable condition, and the velocity profile varies more strongly with r in layer 1 than in layer 2. The variation of $\dot{\gamma}$ with r is shown in Figure 7.56. When the

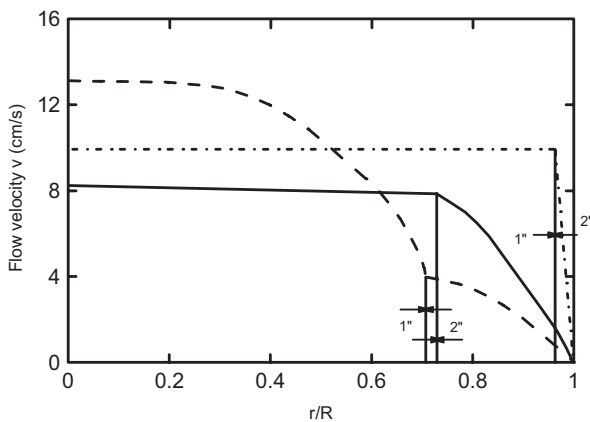


FIGURE 7.55 Velocity profiles in two component flow through a capillary for stable and unstable conditions: *stable* (—) $\eta_{02}/\eta_{01} < 1$ and (---) $\eta_{02}/\eta_{01} \ll 1$; *unstable* (- · -) $\eta_{02} > \eta_{01}$.

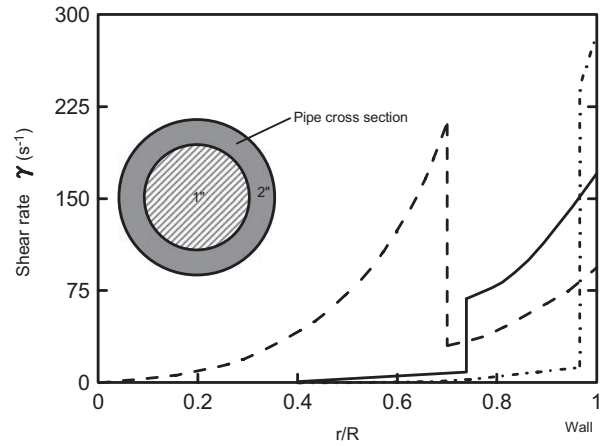


FIGURE 7.56 Shear rate versus radial position for the three conditions given in Figure 7.55.

flow is in an unstable condition, $\dot{\gamma}(r)$ is larger at the interface than at the wall. Hence, the equations presented in the last section at least can tell us if it is feasible to stably extrude a given set of polymers.

The equations developed in the last section can also be used to estimate the onset of an interfacial flow instability which leads to a rippled interface. According to Schrenk and co-workers (1976, 1978) this instability is due to slip at the interface between the polymers when a critical interfacial shear stress is exceeded. This critical stress will vary for various polymer types, but for the system of acrylonitrile-butadiene-styrene copolymer, ABS, and styron 470, this critical stress was 5.0×10^4 Pa. The analysis developed in Section 7.6.2 can be used to assess the conditions under which we might expect an interfacial instability to arise.

However, it seems that this instability may be more complicated than just a failure of adhesion between layers in shear flow. In many cases the region of fully developed shear flow is small or nonexistent and the analysis developed in Section 7.6.2 may not be applicable. The origin of the interfacial instability could be at the die exit where large stresses arise as the velocity profile undergoes a rapid rearrangement. It could also be associated with converging flow upstream of the die lips. In other words, differences in the extensional viscosity of the two polymers as well as differences in the relaxation behavior could lead to interfacial instability.

7.7 SOLUTION TO DESIGN PROBLEM VI

The following steps are used in the solution:

1. The volumetric flow rate for each component is determined from the mass and density of each component and the hang time.

2. The dimensions of the die are determined from a mass balance.
3. The curvature in the die cross section is neglected, and it is treated as a parallel plate geometry.
4. The design equations for coextrusion are used to determine the pressure gradient, G , and the position where the velocity profile passes through a maximum, α .
5. The shear rate and viscosity are calculated at the interface to determine if the flow could be unstable.
6. A manifold system is designed to feed the die.

We first calculate the volumetric flow rate of each component where $Q^{(1)}$ is Q for nylon 6 and $Q^{(2)}$ is Q for HDPE. The density of nylon 6 at 25 °C is 1132 kg/m³ while that for HDPE at 25 °C is 971 kg/m³. Given the mass of the parison is 18 lb HDPE and 2 lb nylon 6 and time for hanging the parison is 5 s, we find

$$Q^{(1)} = 8.02 \times 10^{-4} \text{ m}^3/\text{s} \quad Q^{(2)} = 8.42 \times 10^{-3} \text{ m}^3/\text{s}$$

The cross-sectional area of the gasoline tank is found by using the formula for the area of an ellipse ($A = (\pi/4)ab$, where a is the major axis and b is the minor axis of the ellipse). The cross-sectional area of the tank is

$$\begin{aligned} A_p &= (1.0)(0.15)\pi/4 - (9.936 \times 10^{-1})(0.1436)\pi/4 \\ &= 5.748 \times 10^{-3} \text{ m}^2 \end{aligned}$$

The dimensions of the die are found next. From the information given in the problem we know that the major axes of the outer wall of the elliptically shaped die are $a_o = 0.5$ m and $b_o = 0.075$ m. As the area is assumed to be conserved, we can calculate the dimensions of the die. (*Note:* There is actually extrudate swell which must be considered, but the weight of the parison causes some reduction in the thickness and the density change causes the material to shrink, which offsets some of the extrudate swell.)

$$\begin{aligned} 5.748 \times 10^{-3} &= \pi/4 [(0.5)(0.075) \\ &\quad - (0.5 - 2H_o)(0.075 - 2H_o)] \end{aligned}$$

where H_o is the gap thickness. H_o is determined to be 6.51×10^{-3} m. We open the die and treat it as flow between parallel plates having a width W_o and height H_o . Given $A_p = A_o$ and H_o , from above we find W_o to be 0.883 m.

We can now use the equations derived in Section 7.6 for coextrusion through parallel plates. Equations 7.55, 7.57, and 7.59 represent three equations for finding three unknowns. In our case, $Q^{(1)}$ and $Q^{(2)}$ are known, but G , α , and β are unknown. We could solve the three equations simultaneously using numerical techniques (e.g., the IMSL subroutine NEQNF). However, to facilitate the understanding of

the solution process, we can calculate β (i.e., the interfacial position) from the knowledge of $Q^{(1)}$ and $Q^{(2)}$ via the following expression:

$$\beta = \frac{Q^{(1)}H_o}{Q^{(2)} + Q^{(1)}} = 0.087 H_o \quad (7.63)$$

This equation is based on the fact that $Q^{(1)}/A_1 = Q^{(2)}/A_2$, where A_1 and A_2 are the areas of each stream ($A_1 = \beta H_o W_o$ and $A_2 = (H_o - \beta) H_o W_o$).

Just as in Example 7.2 we solve for α using Eq. 7.59 by estimating G . We then check to see whether Eq. 7.55 is satisfied. Before doing this we are faced with a dilemma. The melting temperature of nylon 6 is about 220 °C, and hence, rheological data are only available at temperatures higher than one would normally process HDPE. Based on the discussion of flow instabilities in coextrusion we must select conditions such that the viscosity of the two polymers is similar at the walls. With this in mind we select the HDPE stream to be at 220 °C and the nylon 6 stream to be at 225 °C. At this temperature η_0 of nylon 6 is somewhat higher than that of HDPE. However, the temperature mismatch is not so great that we would have to consider the problem to be nonisothermal.

The solution follows the approach in Example 7.2 very closely. With the conditions given we find $G = 5.9 \times 10^6$ Pa/m and $\alpha = 3.536 \times 10^{-3}$ m. From these values, β , and Eqs. 7.45 and 7.46 we find $\dot{\gamma}_w^{(1)}$ and $\dot{\gamma}_w^{(2)}$:

$$-\dot{\gamma}_w^{(1)} = \left(\frac{G}{m_1}\right)^{s_1} (H_o - \alpha)^{s_1} = 20.4 \text{ s}^{-1} \quad -\dot{\gamma}_w^{(2)} = 12.6 \text{ s}^{-1}$$

The viscosity of nylon 6 and HDPE at these conditions is

$$\eta_1(\dot{\gamma}_w^{(1)}) = 858 \text{ Pa} \cdot \text{s} \quad \eta_2(\dot{\gamma}_w^{(2)}) = 1386 \text{ Pa} \cdot \text{s}$$

Hence, there is a mismatch in viscosity with nylon 6 having a lower value at the wall. Hence, there would be a tendency for nylon 6 to encapsulate HDPE. However, by keeping the die land fairly short we can prevent this. The die length will be chosen to be $20 H_o = 6.51 \times 10^{-2}$ m.

In order to adopt the cohangar manifold design equations we must consider that two manifolds are used to feed two streams to the die (see Fig. 7.57). Hence, the direct application of Eq. 7.23 can't be made. Instead, we use Eq. 7.20 with the value of $|G| = 5.9 \times 10^6$ Pa/m. Furthermore, we use Eq. 7.23 with

$$Q(l)^n = \left[\frac{Q^{(1)}}{W} (W - x) \right]^n \quad (7.64)$$

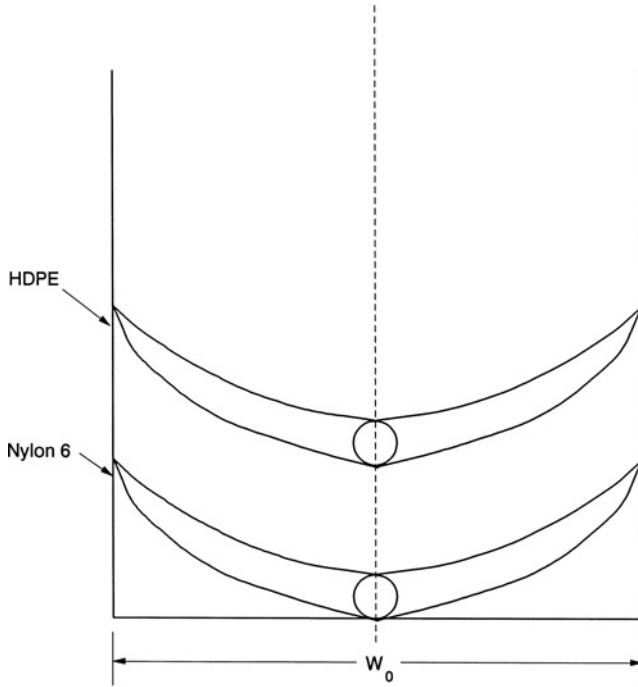


FIGURE 7.57 Planar expanded view of coathanger manifolds for HDPE and nylon 6 for feeding the elliptically shaped annular die in Design Problem VI.

The expression for $R(x)$ for each manifold now becomes

$$(R(x)^{(i)})^{3n_i+1} = -\left(\frac{3+s_i}{\pi}\right)^{n_i} 2m_i \left[\frac{Q^{(i)}}{W}(W-x)\right]^{n_i} \left(\frac{1}{G(dL/dl)}\right) \quad (7.65)$$

For nylon 6 the expression for $R(x)$ becomes (using $dL/dl = -0.087$)

$$R(x)^{(1)} = 3.15 \times 10^{-2} [W-x]^{0.223} \quad (7.66)$$

while for HDPE we find

$$R(x)^{(2)} = 7.75 \times 10^{-2} [W-x]^{0.211} \quad (7.67)$$

For example, these equations tell us that the initial openings of the manifolds ($x = 0$) should be 2.62 cm for nylon 6 and 6.52 cm for HDPE, which seem reasonable in light of the relative flow rates.

PROBLEMS

A. Applications

7A.1 *Pressure Drop in Segmented Dies: Constant Radius.* Calculate the pressure drop across dies II and IV

in Figure 7.28 and the wall shear rate at the die exit. Calculate the die swell based on Tanner’s equation, Eq. 7.4, and compare it with the experimental value. Use the rheological data given for NPE 953 in Appendix A, Table A.1 at 170 °C. The average velocity at the die exit in all cases is 7.2 mm/s. The dimensions of die II can be obtained by scaling the dimensions from die IV.

7A.2 *Pressure Drop in Segmented Dies: Tapered Radius.* Calculate the pressure drop across dies I and III in Figure 7.28 and the wall shear rate at the die exit. Estimate the die swell using Eq. 7.4. Use the rheological data given for NPE 953 in Appendix A, Table A.1. The dimensions can be obtained by scaling the dimensions from die IV.

7A.3 *Scaleup of an Extrusion Die.* A die similar to die III in Figure 7.28 is to be designed so that the final diameter is 10 mm rather than 2 mm. Determine the flow rate and the remaining dimensions of the larger diameter die such that die swell will be the same as for the smaller diameter die.

7A.4 *Pressure Drop Across a Coathanger Die.* Determine the pressure drop across the coathanger manifold and land for the sheet die discussed in Example 7.1. The extrusion rate is 200 kg/h. (Note: The pressure drop in the whole of the manifold system is calculated by calculating the pressure drop at the center of the die; that is, $y = L(0)$ and $x = 0$ in Fig. 7.32.)

7A.5 *Profile Extrusion: Square Duct.* A square duct is to be extruded from a profile die, die shape No. 3 in Figure 7.46. The dimensions of the die are $R_i = 10.0$ cm and $R_o = 10.5$ cm. The resin to be used is HDPE, resin No. 27 in Figure 7.17, and the material is extruded at 170 °C at the rate of 200 kg/h. Using the rheological data given in Figure 7.17 and the die swell data given in Figure 7.19, estimate the dimensions of the duct at 25 °C (i.e., include density changes in your calculations). Assume that no sizing of the duct occurs as it leaves the die (by sizing it is meant that no pressure differential is applied to the duct to expand it on leaving the die).

7A.6 *Profile Extrusion: Tubing with an Internal Wall.* Tubing is to be extruded from a profile die, die No. 6 in Figure 7.46, using HDPE No. 27 (see Fig. 7.17). The dimensions of the die are $R_i = 10.0$ cm, $R_o = 10.5$ cm, and $H = 0.5$ cm. The rheological properties of the resin are given in Table 2.3. The resin is to be extruded at 170 °C at the rate of 200 kg/h. Die swell data are given in Figure 7.19. Estimate the dimensions of the tubing including density changes and assuming no sizing takes place as the extrudate

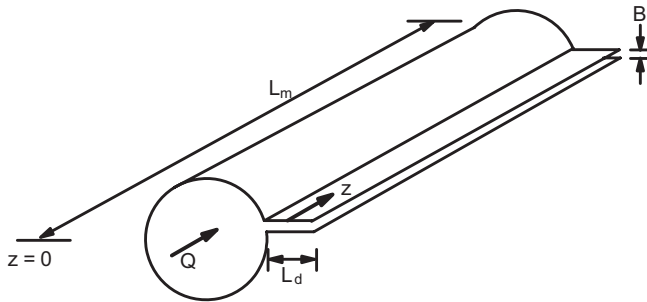


FIGURE 7.58 End-fed film die. Melt enters from the side and is distributed over the width of the die.

leaves the die; that is, no pressure differential is generated to expand the tubing to its final dimensions.

B. Principles

7B.1 *Flow Distribution in an End-Fed Film Die: Newtonian Case.* In some instances end-fed film dies as shown in Figure 7.58 are used to produce sheet and film. Obtain an expression that can be used to determine the uniformity of flow over the width of the die, where uniformity is determined by the ratio of the maximum to minimum flow rates across the width of the die, by carrying out the following steps:

- (a) Show by carrying out a mass balance on a differential element of thickness Δz that the pressure variation along the manifold is given by the following differential equation:

$$\frac{dp}{dz^2} - \beta^2 P = 0 \quad (7.68)$$

where $\beta^2 = 2B^3L/3\pi R^4L_d$ (R is the radius of the manifold) and $z' = z/L_m$.

- (b) Solve this equation using the boundary conditions that $P = P_0$ at $z' = 0$ and $dP/dz' = 0$ at $z' = 1$ and show that

$$\frac{P}{P_0} = e^{-\beta z'} + e^{-\beta} \frac{\sin h\beta z'}{\cos h\beta} \quad (7.69)$$

- (c) If the uniformity of flow (E) is $q_x(0)/q_x(L_m)$, that is, the ratio of the maximum to minimum flow rates per unit width, then show that

$$E = \frac{P(L_m)}{P(0)} = \frac{1}{\cos h\beta} \quad (7.70)$$

- (d) Based on the above equation what design strategy should one follow to keep E near unity?

7B.2 *Analysis of Flow in a T-Die.* For a straight T-die as shown in Figure 7.30 derive an expression which allows one to evaluate the uniformity of flow across the die similar to that given in Problem 7B.1 for the end-fed die. Do this (a) first for the Newtonian case and (b) then for a power-law fluid. Take the radius of the manifold as R , the volumetric flow rate as $2Q_0$, the die width as W , the die Height as B , and the die length as L_d .

7B.3 *Pressure Drop Along a Flow Path in a Coathanger Die.* Show that the pressure drop along any flow path in the coathanger die (see Fig. 7.32) is given by the following expression for a Newtonian fluid:

$$\Delta P = \frac{8Q_0}{\pi L} \int_L^l \frac{l'\mu}{R^4(l')} dl' + \frac{12Q_0\mu}{LH^3} y(l) \quad (7.71)$$

Obtain a similar expression for a power-law fluid.

7B.4 *Residence Time of a Fluid Particle Along a Flow Path.* Show that the residence time in a coathanger die of a particle along any flow path is (note that the residence time consists of the residence time in the manifold plus that in the land region)

$$t(l) = \frac{\pi L}{Q_0} \int_l^L \frac{R^2(l')}{l'} dl' = \frac{LHy(l)}{Q_0} \quad (7.72)$$

7B.5 *Dimensioning of the Distribution System for a Side-Fed Mandrel.* In Figure 7.36 is shown the distribution system for a cylindrically shaped mandrel. Considering the fluid to be Newtonian carry out the following:

- (a) Show that the shear rate at the wall of the manifold tube is

$$\dot{\gamma}_R = \frac{4Q_0\zeta}{\pi R^3(\zeta)} \quad (7.73)$$

- (b) Show that the wall shear rate in the slit is

$$\dot{\gamma}_s = \frac{6Q_0}{\pi r H^2} \quad (7.74)$$

- (c) Show that the radius is given as a function of ζ by

$$R(\zeta) = R_0(\zeta/\pi)^{1/3} \quad (7.75)$$

- (d) Show that y is related to ζ by

$$\frac{y(\zeta)}{y_0} = \left(\frac{\zeta}{\pi}\right)^{2/3} \quad (7.76)$$

- (e) Show that if the shear rate is to be the same in both the manifold and the slit (this is the design criterion) the maximum land length is

$$y_0 = \frac{\pi r^2 H^3}{R_0^4} \quad (7.77)$$

- (f) Show that the maximum radius of the manifold is

$$R_0 = (r H^2)^{1/3} \quad (7.78)$$

- (g) Show that the total pressure drop is

$$\Delta P = \frac{12 Q_0 \mu y_0}{\pi r H^3} \quad (7.79)$$

- (h) Derive similar expressions as in parts (a) to (g) above for a power-law fluid.

7B.6 Dies with a Triangular Cross Section. The velocity field for the flow of a Newtonian fluid through a die of triangular cross section is approximately given by the following expression for the equilateral case (Kakovris and Freakley, 1988):

$$v_z = \left[\frac{3(dp/dz)}{4a\mu} \right] \left(y^2 - \frac{x^2}{3} \right) (x - a) \quad (7.80)$$

where the coordinate system and a are defined in Figure 7.59.

- (a) Obtain an expression for the volumetric flow rate, Q .

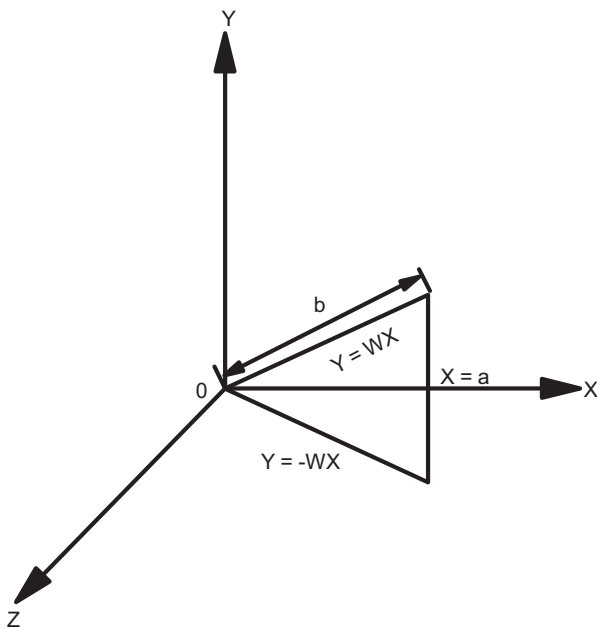


FIGURE 7.59 Cross section of a triangularly shaped die.

- (b) Determine expressions for the components of the rate of deformation tensor.
 (c) Determine where $\dot{\gamma}$ is a maximum.

7B.7 Equivalent Newtonian Viscosity. It has been suggested by Broyer and co-workers (1975) that the solutions to non-Newtonian flow problems can be obtained by using the Newtonian solution with μ replaced by an equivalent Newtonian viscosity, $\bar{\mu}$. For isothermal flow between parallel plates carry out the following:

- (a) Show that the flow rate per unit width is given by

$$q = -\frac{2b^2}{\tau_w^2} \int_0^{\tau_w} \tau \dot{\gamma} d\tau \quad (7.81)$$

where b is one-half the die height.

- (b) Show that for a Newtonian fluid the flow rate per unit width can be written as

$$q = \frac{b^2 \tau_w}{3\mu} \quad (7.82)$$

- (c) Show that by defining an equivalent Newtonian viscosity,

$$\bar{\mu} = \frac{\tau_w^3}{3 \int_0^{\tau_w} \tau \dot{\gamma} d\tau} \quad (7.83)$$

the flow rate of a non-Newtonian fluid can be calculated with the Newtonian equation in part (b) with μ replaced by $\bar{\mu}$.

- (d) For a power-law fluid find an expression for $\bar{\mu}$ in terms of $\dot{\gamma}_w$, m , n , and any geometric factors.

7B.8 Multiple Layer Flow Through an Annulus. Obtain expressions for $Q^{(1)}$ and $Q^{(2)}$ and for finding α similar to those determined for slit flow in Eqs. 7.55, 7.57, and 7.58, respectively, for flow of two fluids through an annulus. Obtain expressions first for Newtonian fluids and then for power-law fluids.

7B.9 Multiple Layer Flow Through a Slit Die. Obtain expressions for the flow of three fluids through a slit die using the notation in Figure 7.51. In particular, find the velocity field and the volumetric flow rate for each layer. Confirm your solution by comparing with the expressions in Eqs. 7.60 and 7.61.

7B.10 Bicomponent Flow in a Wire Coating Die. Derive expressions for the volumetric flow rate in each layer and for determining the position where $\tau_{rz} = 0$ (i.e., α) for the flow of two fluids through the annular region in a wire coating die (see Figs. 2.10 and 2.11) for each of the following cases:

- (a) Newtonian fluids with no imposed pressure gradient.

- (b) Power-law fluids with no imposed pressure gradient.
- (c) Power-law fluids with an imposed pressure gradient.

Take the point where $\tau_{rz} = 0$ as αR and the location of the interface between the two layers as βR .

7B.11 *Flow Distribution in an End-Fed Film Die: Non-Newtonian Case.* Referring to Figure 7.58 and Problem 7B.1 derive a similar expression for determining the flow uniformity in an end-fed die for a power-law fluid. In particular, show that the pressure distribution along the manifold is given by the following differential equation:

$$\frac{d^2 p}{dz^2} - \frac{\beta^2 p^{1/n}}{\left(\frac{-dP}{dz}\right)^{1/n-1}} = 0 \quad (7.84)$$

where

$$\beta^2 = \frac{n(1 + 3n)B^2 L_m^{s+1}}{2\pi(1 + 2n)R^{3+s}} \left(\frac{B}{L_d}\right)^s \quad (7.85)$$

C. Numerical Problems

7C.1 *Multiple Layer Sheet Extrusion.* Three layers of polymer are to be extruded through a sheet die having a height 0.15 cm, a width of 20 cm, and a length of 4.5 cm. Following the notation in Figure 7.51, layers 1 and 2 are to be 0.3 cm thick while layer 3 is to be 0.9 cm thick. The overall flow rate is to be 100 kg/h. The power-law parameters for the three fluids are: layer 1, $m = 2.62 \times 10^3 \text{ Pa} \cdot \text{s}^n$ and $n = 0.63$; layer 2, $m = 1.55 \times 10^3 \text{ Pa} \cdot \text{s}^n$ and $n = 1.0$; layer 3,

$m = 3.73 \times 10^3 \text{ Pa} \cdot \text{s}^n$ and $n = 0.61$. Determine the pressure gradient required to produce this flow and whether the flow will be stable. Assume the densities of all the fluids are 1000 kg/m^3 .

7C.2 *Pressure Distribution in an End-Fed Die.* Solve Eq. 7.84 in Problem 7B.11 numerically using the appropriate ISML subroutine (BVPFD) or MATLAB (bvp4c) for various values of P_0 (in particular, take values of 500, 1000, and 2000 psi) for a fluid with a power-law index of 0.5. With $B = 0.05 \text{ cm}$, $L_m = 40 \text{ cm}$, $R = 5 \text{ cm}$, and $L_d = 1 \text{ cm}$ determine the flow uniformity and the volumetric flow rate for these initial pressures.

D. Design Problems

7D.1 *Profile Extrusion Coating: Processing Conditions.* Profile extrusion coating is a process which is a combination of wire coating and profile extrusion. This technique is used to generate automotive protection molding as shown in Figure 7.60a. PVC is pumped through the cross-head die while a metal core is fed into the die at a constant velocity. The flow is basically combined pressure and drag flow. The shape and dimensions of the flow channel are shown in Figure 7.60b. The melt and the die temperatures are both $150 \text{ }^\circ\text{C}$. The rheological properties of PVC are described by the power-law model with $m = 5.45 \times 10^4 \text{ Pa} \cdot \text{s}^n$ and $n = 0.27$. If the linear speed of the metal core, which is 25 mm in width, is 7 cm/s and the PVC is to be 2.2 mm thick, estimate the pressure at the inlet to the die and the volumetric flow rate required to produced the coating. (This problem is taken from Matsuoka and Takahashi, 1991.)

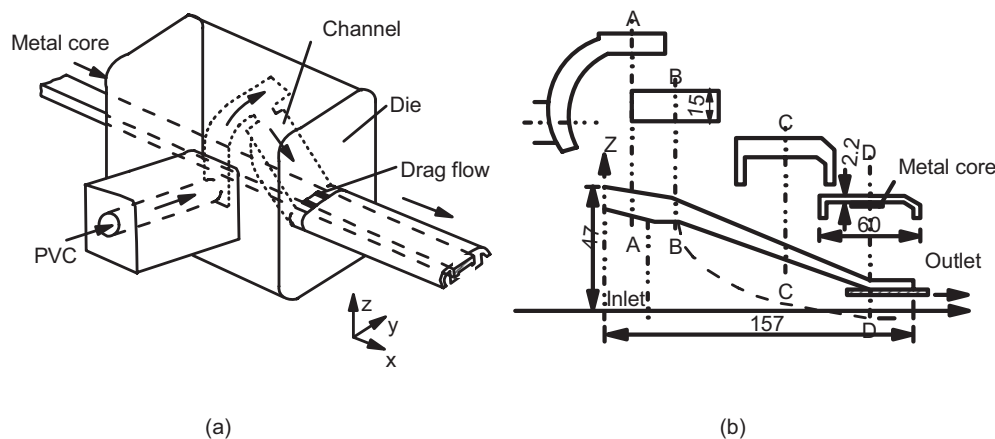


FIGURE 7.60 Profile extrusion coating process: (a) schematic of the process and (b) cross-sectional shape and dimensions of the flow channel. All dimensions are in mm. The distances are: D-Exit = 22 mm, B-D along flow channel = 100 mm, A-B = 15 mm. Curved inlet channel: average arc length is 100 mm and the channel width is 60 mm and the height is 6 mm.

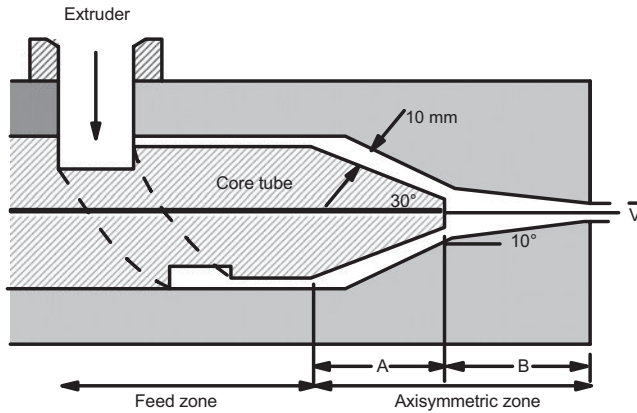


FIGURE 7.61 Wire coating die design with possible variations in the dimensions.

7D.2 Selection of a Wire Coating Die Design. Two dies of design similar to that shown in Figure 7.61 but having the following dimensions:

	Die No. 1	Die No. 2
A	1 cm	1 cm
B	1.5 cm	3 cm
D_0	0.85 mm	1.19 mm

are used to coat a 0.5 mm diameter copper wire with HDPE. (Note: D_0 is the diameter of the die exit.) The wire speed is 200 m/min and the final diameter of the coated wire is to be 0.85 mm. The melt and the die temperatures are set at 200 °C. By analyzing the flow in the region starting with the tapered annular section, determine which die design would be best. Make your decision based on the minimum temperature rise due to viscous dissipation, the minimum amount of mechanical degradation due to shear stresses, the minimum pressure drop required across the section, and the smoothest surface. The rheological properties for HDPE are given in Table 2.3.

REFERENCES

Broyer, E., C. Gutfinger, and Z. Tadmor. 1975. "Evaluating Flows of Non-Newtonian Fluids by the Method of Equivalent Newtonian Viscosity." *AICHE J.*, **21**, 198.

Carley, J. F. 1963. "Problems of Flow in Extrusion Dies." *SPE J.*, **12**, 1263.

Cogswell, F. N. and R. Lamb. 1970. "Polymer Properties Relevant in Melt Processing." *Plast. Polym.*, **38**, 39.

Everage, A. E. 1975. *J. Rheol.*, **19**(4), 509–522.

Garcia-Rejon, A., J. M. Dealy, and M. R. Kamal. 1981. *Can. J. Chem. Eng.*, **59**, 59.

Garcia-Rejon, A., J. M. Dealy, and M. R. Kamal. 1982. "Swell of Extrudate from an Annular Die." *Polym. Eng. Sci.*, **22**(3), 158.

Graessley, W. W., S. D. Glasscock, and R. L. Crawley. 1970. "Die Swell in Molten Polymer." *J. Rheol.*, **14**, 519.

Kakovris, A. P. and P. K. Freakley. 1988. "Flow of a Generalized Power-Law Fluid in Triangular Dies for Rubber Extrusion." *Int. Polym. Proc.*, **III**(3), 156–164.

Laun, H. M. 1989. "Transient Elongational Viscosities and Drawability of Polymer Melts." *J. Rheol.*, **33**(1), 119.

Matsuoka, T. and H. Takahashi. 1991. "Finite Element Analysis of Polymer Melt Flow in a Profile Extrusion Coating Die." *Intern. Polym. Proc.*, **VI**(3), 183–187.

Michaeli, W. 1984. *Extrusion Dies* (Hanser, Munich).

Middleman, S. 1977. *Fundamentals of Polymer Processing* (McGraw Hill, New York).

Mori, Y. and K. Funatsu. 1973. "On Die Swell in Molten Polymers." *J. Appl. Polym. Sci.*, **20**, 209.

Moynihan, R. H. 1990. *The Flow at Polymer and Metal Interfaces* (Ph.D. dissertation, Department of Chemical Engineering, Virginia Tech, Blacksburg, VA).

Pissipati, R. 1983. *A Rheological Characterization of Particulate and Fiber Filled Nylon 6 Melts and Its Application to Formation in Molded Parts* (Ph.D. dissertation, Department of Chemical Engineering, Virginia Polytechnic Institute and State University, Blacksburg, VA).

Röthemeyer, F. 1970. *Elastic Effects in the Extrusion of Plastic Melts* (Ph.D. dissertation, University of Stuttgart).

Schrenk, W. J. and T. Alfrey, J. 1976. "Coextruded Multilayer Polymer Films and Sheets." In J. A. Mason and L. H. Sperling, Eds., *Polymer Blends and Composites* (Plenum, New York).

Schrenk, W. J., N. L. Bradley, and T. Alfrey. 1978. "Interfacial Flow Instability in Multilayer Coextrusion." *Polym. Eng. Sci.*, **18**(8), 620–623.

Tadmor, Z. and U. G. Gagos. 1979. *Principles of Polymer Processing* (Wiley, Hoboken, NJ).

White, J. L. 1973. *Appl. Polym. Symp.*, **20**, 155.

White, J. L. and J. F. Roman. 1976. "Extrudate Die Swell During the Melt Spinning of Fibers—Influence of Rheological Properties and Take-up Forces." *J. Appl. Polym. Sci.*, **20**, 1005.

White, S. A., A. D. Gotsis, and D. G. Baird. 1987. "Review of the Entry Flow Problem: Experimental and Numerical." *J. Non-Newtonian. Fluid Mech.*, **24**, 121–160.

White, S. A. 1987. *Correlation of Entry Flow Behavior with Extensional Viscosity of Polymer Melts* (Ph.D. dissertation, Department of Chemical Engineering, Virginia Polytechnic Institute and State University, Blacksburg, VA).

8

EXTRUDERS

DESIGN PROBLEM VII DESIGN OF A DEVOLATILIZATION SECTION FOR A SINGLE-SCREW EXTRUDER

A self-wiping corotating twin-screw extruder of dimensions shown in Figures 8.1 and 8.2 has been used successfully to remove residual methyl methacrylate (MMA) from poly(methyl methacrylate) (PMMA). It is desired to use a single-screw extruder to reduce the level of MMA, which is initially 0.65% by weight (6500 ppm), to the same level as possible in the twin-screw extruder. Design a devolatilization section for the screw shown in Figure 8.3. In particular, given that the barrel diameter, D_b , is 30 mm and the channel depth in the devolatilization (DV) section is 5.595 mm, determine the length of the DV section, L_e , the number of flights, and the screw rpm to reduce the level of MMA to 0.10% by weight. The vacuum pump is capable of providing a mean pressure of 10 torr (133.3 Pa). Use two approaches to obtain your design: use dimensional analysis and the data given in Table 8.1 first, and then use the diffusion theory presented in Section 8.5.2. Compare the results of the two approaches and specify which solution is most accurate.

Thermodynamic data for MMA, PMMA, and the solution are given in Table 8.2 (Biesenberger et al., 1990).

Extruders are the heart of the polymer processing industry. They are used at some stage in nearly all polymer processing operations. This chapter is concerned with the basic elements

of extruder design. In Section 8.1 we describe some of the technological features of extruders. Section 8.2 is concerned with the design of hoppers, which are often used to feed polymer pellets to the extruder. In Section 8.3 we address the principal features of the design of single-screw extruders. In Section 8.4 we look at some of the most important aspects of the design of twin-screw extruders. Extruders have other functions than to melt and pump polymers. In Section 8.5 we present basic elements concerned with mixing, the removal of gases (devolatilization), and reactions in extruders. Finally, in Section 8.6 the solution to Design Problem VII is presented.

8.1 DESCRIPTION OF EXTRUDERS

There are basically three classifications of extruders: screw extruders, disk extruders, and ram extruders. The most common ones are the screw extruders, and for this reason they are emphasized in this book.

The technology of extruders is extremely vast and with many variations. It is nearly impossible to describe all the technology associated with extruders within the limits of this book. There is no one reference where all this information can be found, but extruder manufacturers usually can provide many details. The book by Rauwendaal (1986) does contain, in addition to a theoretical description of various aspects of extruders, a significant amount of technological information. Here we describe the most salient features of single- and twin-screw extruders.

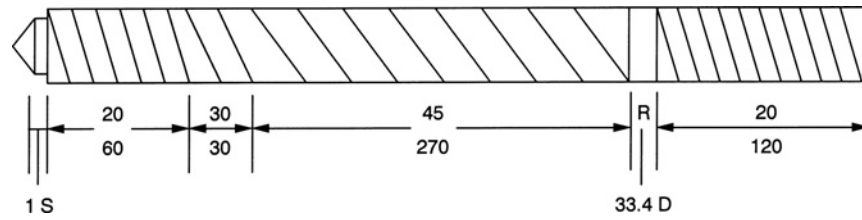


FIGURE 8.1 A 34 mm diameter screw used in a corotating twin-screw extruder. The lead angle and length (in mm) are given for each section. (Data from Biesenberger et al., 1990.)

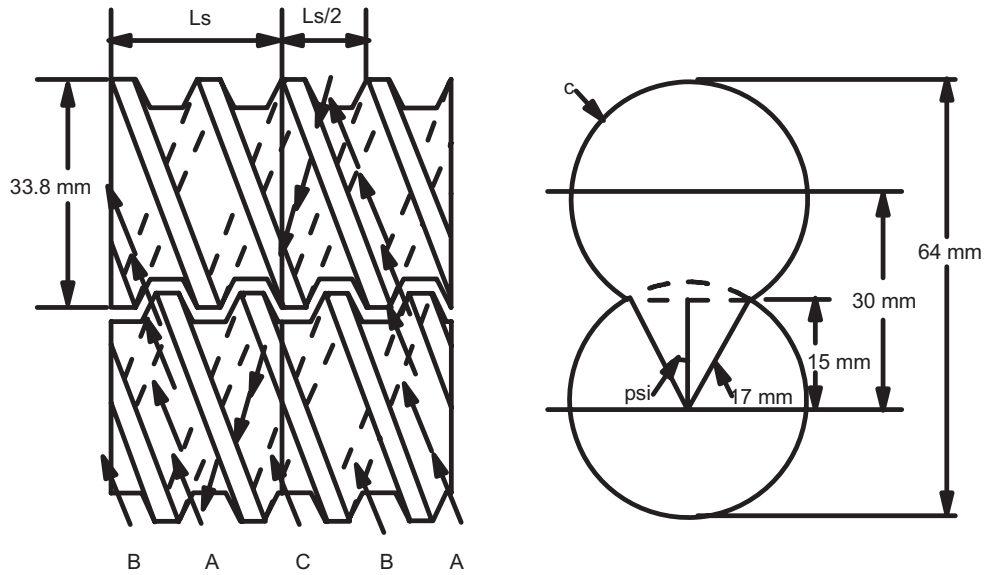


FIGURE 8.2 Self-wiping closely intermeshing corotating twin-screw extruder. Flow of material in double-flighted screw elements (left). Cross section of the barrel showing the pertinent dimensions (right).

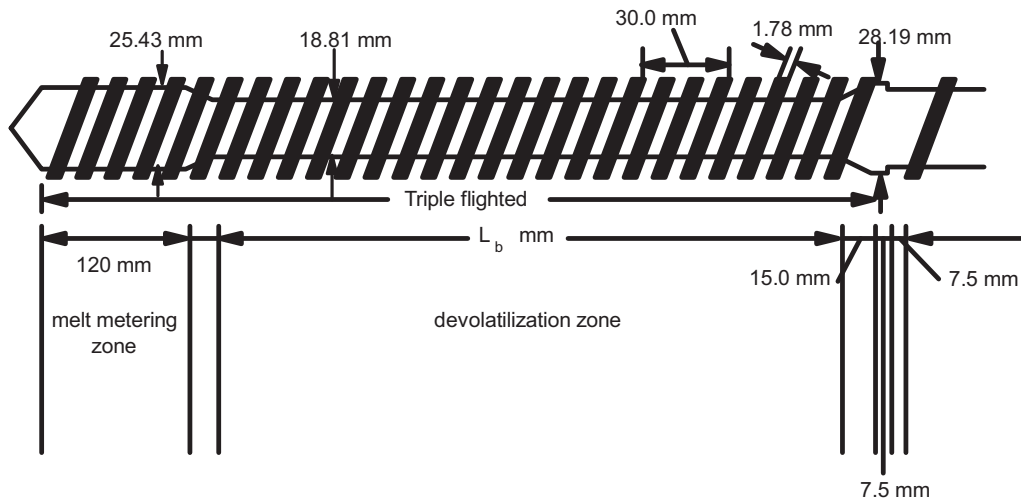


FIGURE 8.3 A 30 mm diameter screw used in a single-screw extruder. (Data from Biesenberger et al., 1990.)

TABLE 8.1 Extrusion Data for the Twin-Screw System

Temperature (°C)	N (rpm)	ρQ (kg/h)	F_s^a	f^b	t (s)	t_p (s)	t/t_p
200	90	3.44	0.91	0.103	13.3	0.099	134.3
	30	2.82	0.78	0.172	36.0	0.297	122.0
	60	4.14	0.82	0.126	18.0	0.127	142.0
230	90	4.92	0.83	0.100	12.0	0.076	158.0
	30	2.18	0.82	0.137	36.0	0.265	135.9
	60	3.83	0.86	0.120	18.0	0.124	145.2
250	90	5.80	0.84	0.120	12.0	0.084	142.9
	30	2.84	0.83	0.180	36.0	0.306	117.6
	60	4.15	0.88	0.133	18.0	0.127	141.7
	90	5.02	0.85	0.107	12.0	0.079	152.9

^a F_s , fractional separation.

^b f , degree of fill of channel.

TABLE 8.2 Thermodynamic Data for Monomer, Polymer, and Solution

Temperature (°C)	ρ_m (g/cm ³)	ρ_p (g/cm ³)	P_s^a (atm)	S^b (atm)
200	0.699	1.118	8.99	64.5
230	0.641	1.083	14.85	113
250	0.592	1.061	20.30	164

^a P_s^o is a coefficient in the Flory–Huggins theory for calculating S .

^b $S' = 1/S$, where S is the Henry's law constant.

8.1.1 Single-Screw Extruders

The single-screw extruder consists of a metallic barrel and a rotating screw as shown in Figure 8.4. The screw is a metallic shaft in which a helical channel has been machined. Sometimes parallel channels are machined in the shaft at the same time leading to what are called multiflighted screws. Typical barrel diameters used in the United States are 0.75,

1.0, 1.5, 2.0, 2.5, 3.5, 4.5, 6.0, 8.0, 10.0, 12.0, 14.0, 16.0, 18.0, 20.0, and 24.0 inches. The length to diameter ratios (L/D) range from 20 to 30, but the most common ratio is 24.

The main geometrical features of a screw are shown in Figure 8.5. The diameter of the screw at the tip of the flight (the flight is the metal that remains after machining the channel), D_s , is less than the diameter of the barrel, D_b , by an amount $2\delta_f$ (i.e., $D_s = D_b - 2\delta_f$). δ_f is on the order of 0.2 to 0.5 mm. Of course, as the screw and barrel wear, δ_f increases and the leakage flow over the flights increases to the point where the screw loses its pumping efficiency. The lead of the screw, L_s , is the axial distance covered in completing one full turn along the flight of the screw. The helix angle, ϕ , is the angle formed between the flight and the plane normal to the screw axis. The helix angle at the flight tip can be related to the lead and diameter as follows:

$$\tan \phi_s = L_s/\pi D_s \quad (8.1)$$

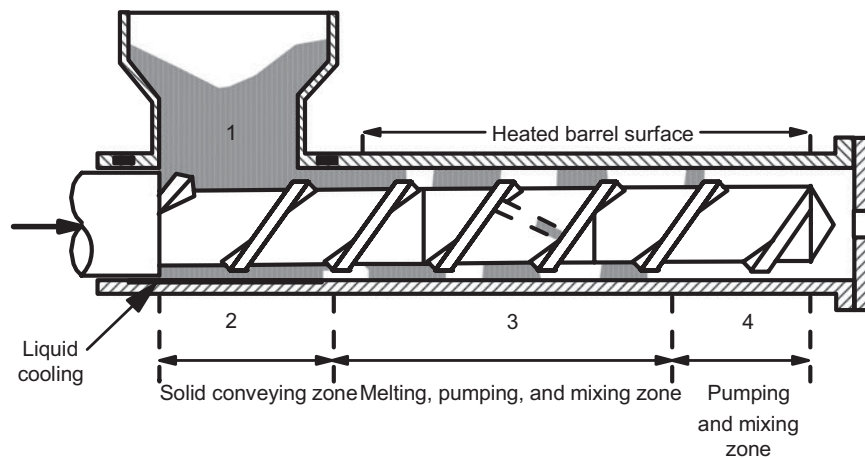


FIGURE 8.4 Single-screw plasticating extruder. Four zones are illustrated: hopper, solids feed, melting, and pumping.

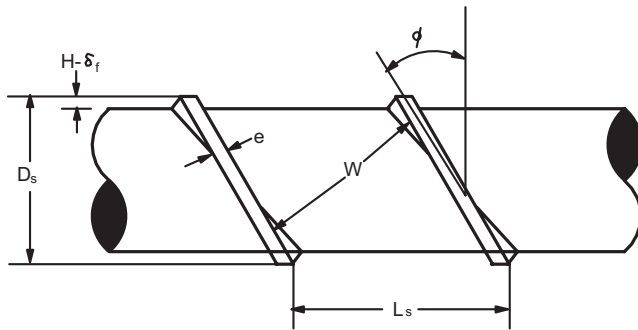


FIGURE 8.5 Geometry of a screw.

The helix angle is a function of the diameter and hence is different at the base of the flight than at the flight tip. The radial distance between the barrel surface and the root of the screw is the channel depth. The main design variable of screws is the channel depth profile along the helical direction (this is taken as the z direction as discussed later). The width of the channel, W , is the perpendicular distance between the flights and is given by

$$W = L_s \cos \phi - e \quad (8.2)$$

where e is the flight width. We note here that W varies with radial position, because ϕ does. Finally, the helical distance along the channel, z , is related to the axial distance, l , by

$$z = \frac{l}{\sin \phi} \quad (8.3)$$

and it is also a function of the distance from the root of the screw.

The most frequently used extruder is a plasticating extruder. Referring back to Figure 8.4, polymer pellets are fed to the extruder by means of a hopper (sometimes the pellets are metered in). The gravitational flow of solids in the hopper is rather complex and will not be covered here. The pellets are compressed in the channel of the screw and then dragged

forward by friction between the pellets and the barrel. Heat generated by sliding friction at the barrel surface and transferred from the heated barrel causes the pellets to melt. The melt film is scraped away and collects at one end of the channel. The solid bed width decreases as the solid plug advances along the screw channel until the solid is completely melted. The melt is pressurized by means of a drag flow mechanism. The pressure generated in the extruder and the performance of the extruder are significantly affected by the die geometry.

Although the main function of the single-screw extruder is to melt and pump polymer, there are a number of other applications. Extruders can be used to remove volatiles such as water or trace amounts of monomers. They can be used to generate foamed polymers as the temperature and pressure history can be controlled. They also serve as continuous mixing and compounding devices. Hence, extruders have a wider range of applications than other pumping devices.

8.1.2 Twin-Screw Extruders

Twin-screw extruders consist of two screws mounted in a barrel having a "figure eight" cross section. The figure eight cross section comes from the machining of two cylindrical bores whose centers are less than two radii apart. Twin-screw extruders are classified by the degree to which the screws intermesh and the direction of rotation of the screws. In Figure 8.6 are shown three types of screw arrangements. In part (a) is shown an intermeshing counterrotating type; in part (b) is shown a corotating intermeshing type; and in part (c) is shown a nonintermeshing counterrotating type. In Figure 8.7a is shown an intermeshing, self-wiping, corotating twin-screw extruder. Not all the elements of a twin-screw extruder are screw elements as shown in Figure 8.7b, and kneading elements may also be used. Probably the most frequently used twin-screw extruders are the corotating intermeshing and the counterrotating types.

There are two main areas where twin-screw extruders are used. One is in the processing of polymers that are difficult to process, because they don't flow easily, and they degrade

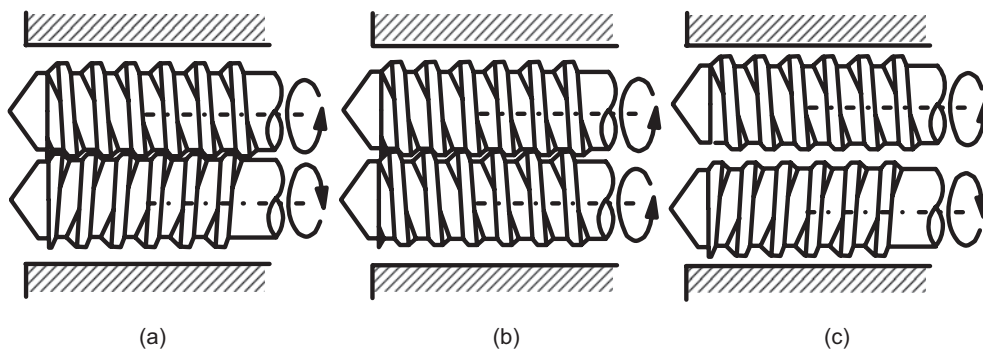


FIGURE 8.6 Various types of twin-screw extruders: (a) counterrotating intermeshing elements, (b) corotating intermeshing elements, and (c) counterrotating nonintermeshing elements.

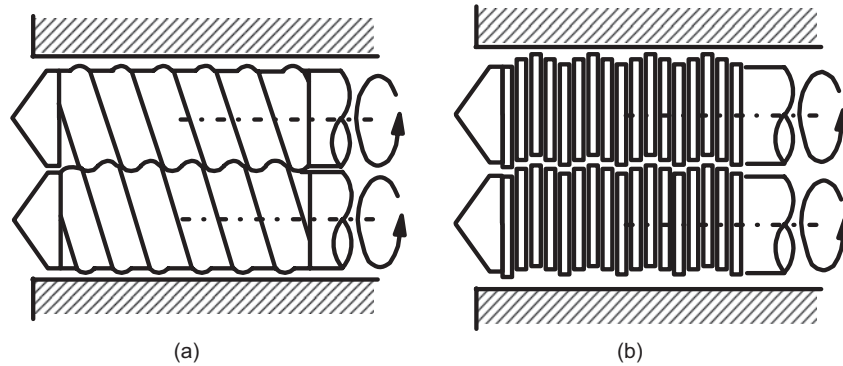


FIGURE 8.7 Corotating screw extruder. (a) self-wiping intermeshing screw elements. (b) self-wiping intermeshing kneading block elements.

readily. For example, they are used in the profile extrusion of PVC compounds, which are thermally sensitive and don't flow well. The other is for specialty processing operations such as compounding, devolatilization, and chemical reactions. In the case of profile extrusion, counterrotating closely intermeshing extruders are used, because their positive conveying characteristics allow the machine to process hard-to-feed materials (powders, rubber particles, etc.) and yield short residence times and a narrow residence time distribution. In the case of specialty operations, high speed intermeshing corotating extruders are often used, but a wide variety of other designs are also used.

Although the differences between single- and twin-screw extruders will be more apparent by the end of the chapter, a few comments will be made now. One of the major differences is the type of transport that takes place in the extruder. Material transport in a single-screw extruder is by drag-induced transport of the solid particles and the molten material. In particular, friction between the barrel walls and the solid pellets advances the polymer in the solids-conveying zone, while viscous drag advances the molten polymer. On the other hand, the transport in an intermeshing twin-screw extruder is to some degree positive displacement. The degree of positive displacement depends on how well the flight of one screw closes the opposing channel of the other screw. Closely intermeshing counterrotating twin-screw extruders provide the most positive displacement. However, some leakage will occur, which reduces the degree of positive conveying that can be achieved.

The flow of material in twin-screw extruders is very complex, and the flow patterns are difficult to predict mathematically. For this reason the simulation of processes in twin-screw extruders is not as well developed as it is for single-screw extruders. It is therefore difficult to predict the performance of a twin-screw extruder based on geometrical features, polymer properties, and processing conditions. Hence, it is difficult to carry out accurate design calculations. For this reason twin-screw extruders are constructed

in modules in which the screw and barrel elements can be changed. The screw design can be changed by changing the sequence of the screw elements. Hence, much of the design of twin-screw extruders is done on an empirical basis. Some of the various types of elements that can be used are shown in Figure 8.8. One can use a combination of screw elements and kneading blocks to accomplish a given operation.

The sizes of twin-screw extruders range from 25 to 244 mm (this is the diameter of one of the barrels). The barrel-length-to-diameter ratio, L/D , ranges from 39 to 48. The length can be altered as required for most twin-screw extruders because of the modular construction.

8.2 HOPPER DESIGN

Most extruders are of the plasticating type in which solid pellets are fed to the extruder where they are converted to melt and pressurized. The extruder is fed by solids that enter the extruder from a hopper (which is a metallic cylinder with a converging section as shown in Fig. 8.9) or are metered in. The flow patterns in the hopper are complex and are still the subject of research. Our intentions here are to estimate the pressure at the base of the hopper as this value is needed to calculate the pressure rise in the extruder.

To understand how to calculate the pressure at the base of the hopper, we consider the pressure exerted by solids on the base of a cylindrical container as shown in Figure 8.10. For a cylinder filled with fluid it is known that the static pressure variation is $P = \rho g(H - h)$ and is the same through the cross section at any position h . For granular solids the pressure distribution is not isotropic, because of the ability of the solids to sustain shear stresses. We now perform a force balance on the differential element of thickness, dh :

$$A\rho_b g dh + (P + dP)A - PA + (C_w + f_w KP)C dh = 0 \quad (8.4)$$

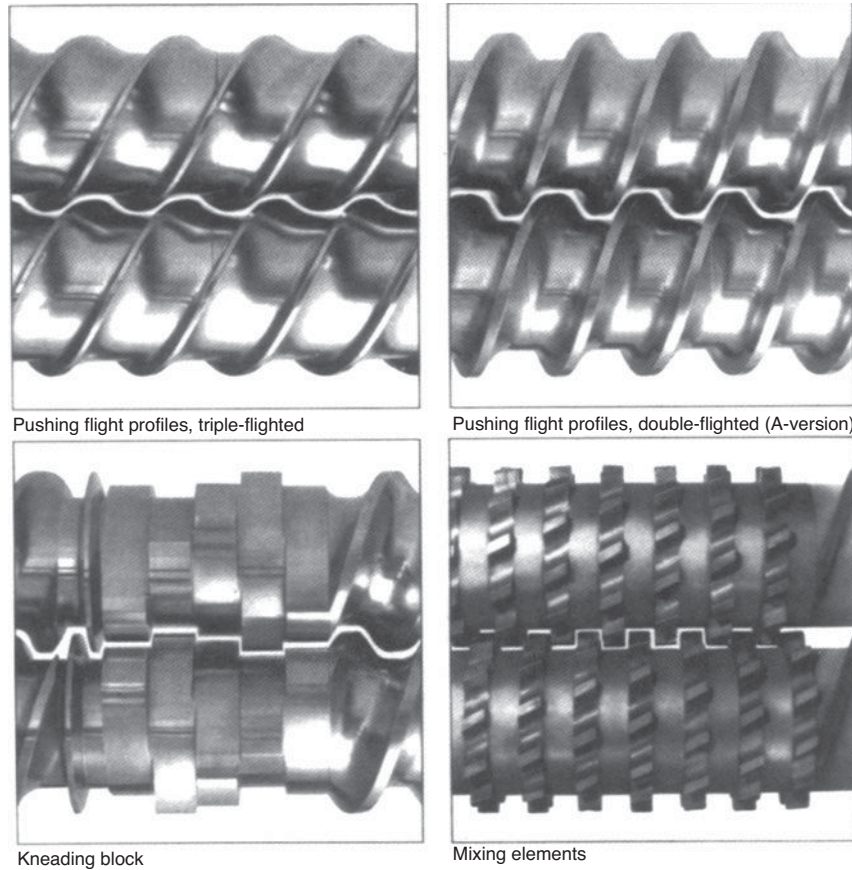


FIGURE 8.8 Photograph of various types of screw elements commonly used in corotating twin-screw elements. (Courtesy of Berstorff Corp., Charlotte, NC.)

where ρ_b is the bulk density, A is the cross-sectional area, C is the wetted circumference, and K is the ratio of compressive stress in the horizontal direction to compressive stress in the vertical direction (note that for a fluid $K = 0$, but because a solid can sustain shear stresses, the pressures are different), C_w is the measure of adhesion of the solids to the wall, and f is the coefficient of friction between the pellets and the wall. The following differential equation is obtained from Eq. 8.4:

$$\frac{dP}{dh} = C(C_w + f_w KPC)/A + A\rho_b g \quad (8.5)$$

which can be integrated to give

$$P = P_H \exp\left[\frac{f_w CK(h - H)}{A}\right] + \frac{(A\rho_b g/C) - C_w}{f_w K} \left\{1 - \exp\left[\frac{f_w CK(h - H)}{A}\right]\right\} \quad (8.6)$$

where P_H is the pressure at H (in this case p_a). With $C_w = 0$ and taking the pressures relative to p_a (this is called the gauge pressure) the pressure at the base of the cylinder is

$$P_0 = \frac{\rho_b g D}{4f_w K} \left\{1 - \exp\left[\frac{4f_w K(-H)}{D}\right]\right\} \quad (8.7)$$

where D is the diameter of the cylinder. In the limit as H goes to infinity we obtain

$$P_{0,max} = \frac{\rho_b g D}{4f_w K} \quad (8.8)$$

Hence, most of the weight is supported by friction between the pellets and the metal walls. The maximum pressure is proportional to the bin diameter and inversely proportional to the coefficient of friction at the wall. Whereas the pressure at the base of a cylindrical bin will continue to increase as H increases for a fluid, for solids it will reach a limiting value.

A few comments need to be made about measuring K , C_w , and f . The device used to obtain these parameters is similar to a parallel disk rheometer used to obtain fluid properties except that a large compressive stress can be applied to the

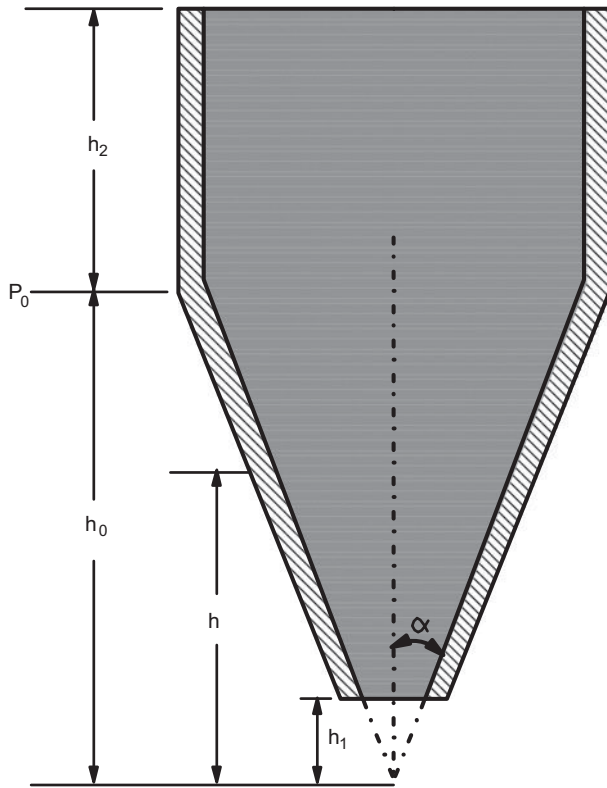


FIGURE 8.9 Typical hopper design consisting of cylindrical and conical sections.

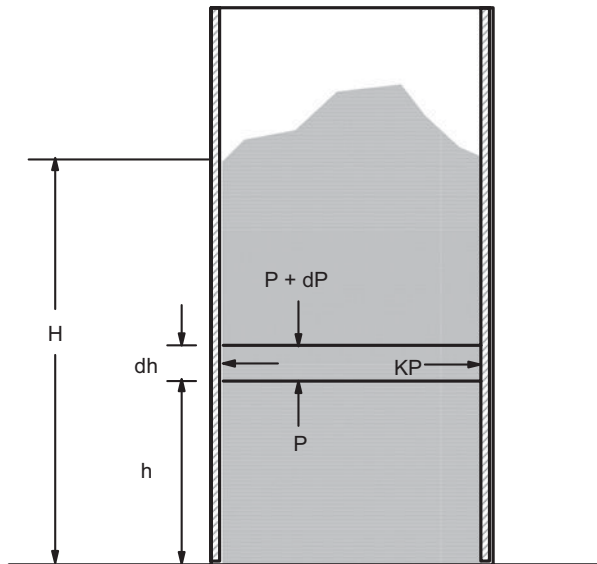


FIGURE 8.10 Cylindrically shaped hopper partially filled with granular solids. The nonisotropic pressure distribution is described by the parameter K .

solid material. The torque required to turn the upper plate is proportional to f . Likewise taking measurements as a function of applied pressure to the upper plate provides K and C_w . K is obtained from the effective angle of friction, δ , using the following equation:

$$K = \frac{1 - \sin \delta}{1 + \sin \delta} \quad (8.9)$$

Most hoppers consist of cylindrical and conical sections as shown in Figure 8.9. Under mass flow conditions the pressure distribution is given as (Walker, 1966)

$$P = (h/h_0)^a P_0 + \frac{\rho_b g h}{a - 1} [1 - (h/h_0)^{a-1}] \quad (8.10)$$

where P_0 is the pressure at h_0 , which is the pressure at the base of the vertical section of the hopper, and a is given for conical and wedge shaped hoppers, respectively, as

$$a = \frac{2B'D^*}{\tan \alpha} \quad (8.11)$$

and

$$a = \frac{B'D^*}{\tan \alpha} \quad (8.12)$$

α in Eqs. 8.11 and 8.12 is one-half the hopper angle and D^* is the distribution function taken as 1.0. B' is given by

$$B' = \frac{\sin \delta \sin(2\alpha + \kappa_0)}{1 - \sin \delta \cos(2\alpha + \kappa_0)} \quad (8.13)$$

where κ_0 is

$$\kappa_0 = \beta_w + \arcsin \left(\frac{\sin \beta_w}{\sin \delta} \right) \arcsin > \frac{\pi}{2} \quad (8.14)$$

where β_w is the wall angle of friction (i.e., $\beta_w = \tan^{-1} f$).

The coverage of this topic was brief, to say the least, but it is not within our goals to give a lengthy derivation. Further details can be found in the book by Tadmor and Gogos (1979, 2007) and in the original paper by Walker (1966). We use the following example to illustrate the calculation of the pressure at the base of a hopper, which is required to determine the pressure at the inlet of an extruder.

Example 8.1. Pressure at the Base of a Hopper

For a hopper of the design shown in Figure 8.9 with $h_0 = 0.190$ m, $h_1 = 0.0635$ m, $\alpha = 45^\circ$, and a cylinder diameter of 0.381 m, calculate the pressure at the base of the hopper for LDPE pellets. The bulk density, ρ_b , is 595 kg/m^3 , $f = 0.3$, and $\delta = 33.7^\circ$.

Solution. P_0 is calculated using Eq. 8.8. To use Eq. 8.8 we must assume that sufficient height of solids are available to give us 99% of the maximum pressure. We first calculate K using Eq. 8.9 and δ :

$$K = \frac{1 - \sin(33.7^\circ)}{1 + \sin(33.7^\circ)} = 0.286$$

Using this value and those given in the problem we find P_0 to be

$$P_0 = (0.99)(595)(9.806)(0.381)/(4)(0.3)(0.286) = 6.41 \times 10^3 \text{ N/m}^2$$

Before using Eq. 8.10 to calculate P we must determine a using Eq. 8.11, which contains the parameters κ_0 and B' :

$$\begin{aligned} \kappa_0 &= 16.7 + \arcsin(\sin 16.7 / \sin 33.7) = 47.9 \\ B' &= \frac{\sin(33.7) \sin((2)(45) + (47.9))}{1 - \sin(33.7) \cos((2)(45) + (47.9))} = 0.2635 \\ a &= \frac{(2)(0.2635)}{\tan(45^\circ)} = 0.527 \end{aligned}$$

We now calculate the pressure at the base of the hopper, P_1 :

$$\begin{aligned} P_1 &= (0.0635/0.190)^{0.527} (6.412 \times 10^3) \\ &\quad + [(595)(9.806)(0.0635)/(0.527 - 1)] \\ &\quad \times (1 - (0.0635/0.190))^{-0.473} \\ &= 3.599 \times 10^3 + 532 = 4.131 \times 10^3 \text{ N/m}^2 \end{aligned}$$

■

8.3 PLASTICATING SINGLE-SCREW EXTRUDERS

Polymer solids (pellets or powder) enter the throat of the extruder either through the hopper or are metered in by gravimetric or auger type feeders. From this point they are transported through the extruder first by frictional drag and then by viscous drag. We first describe solids transport, then melting of the compacted solids, and finally the pumping of the melt.

8.3.1 Solids Transport

To facilitate an understanding of how particulate solids are transported through a single-screw extruder we start with a model for drag-induced flow in straight channels. We then summarize the equations for flow of particulate solids in the single-screw extruder. We next add heat transfer to the transport of the particulate solids.

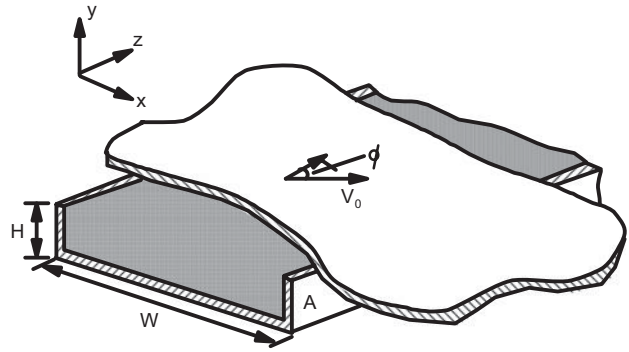


FIGURE 8.11 Rectangular channel filled with granular solids with a plate moving at angle ϕ relative to the down channel direction.

We consider the transport of particulate solids in a rectangular channel as shown in Figure 8.11. Our goal is to determine the mass flow rate and pressure rise as a function of the plate velocity and friction coefficient between the plate and pellets, f_{w1} . Although it would be desirable to somehow treat this situation in a manner similar to that for fluids in which we solve the equation of motion along with an appropriate constitutive equation, it is uncertain as to what constitutive equation best describes the flow of granular solids. For this reason we consider the particulate solids to be a plug of density ρ_b dragged along by the moving upper plate through Coulomb friction. The upper plate moves with a velocity V_0 making an angle ϕ with the down channel direction (i.e., the z direction). The tangential force exerted on the solid plug is in a direction that the plate makes relative to the moving plug as shown in Figure 8.12. The velocity of the plate relative to the solid bed, \mathbf{v}_r , is

$$\mathbf{v}_r = V_0 \sin \phi \delta_x - V_0 \cos \phi \delta_z - u \delta_z \quad (8.15)$$

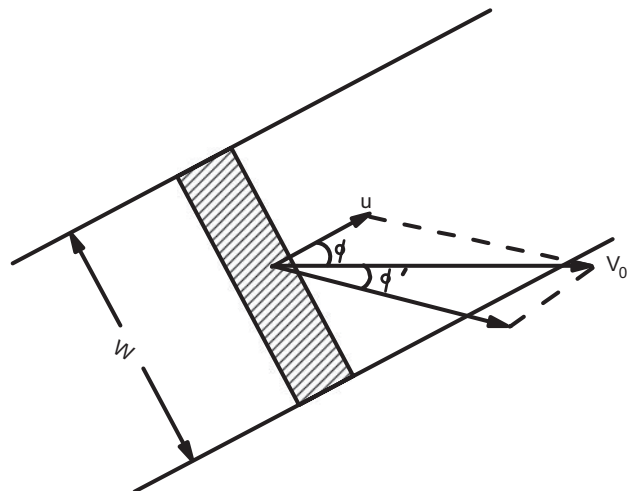


FIGURE 8.12 Motion of the plate relative to the motion of the solid bed. The plate moves at an angle ϕ' relative to the solid bed.

From Eq. 8.15 we find that

$$\tan(\phi + \phi') = \frac{V_0 \sin \phi}{V_0 \cos \phi - u} \quad (8.16)$$

Using a trigonometric identity for $\tan(\phi + \phi')$ we obtain the following expression:

$$\tan \phi' = \frac{u \sin \phi}{V_0 - u \cos \phi} \quad (8.17)$$

Equation 8.17 contains two unknowns, u and ϕ' , and hence an additional equation must be derived.

The additional equation is obtained by performing a steady-state force balance in the z direction on a differential element of thickness Δz (see Fig. 8.12). The contributions to the force balance include the forces due to pressure and the frictional forces at the upper and lower plates. The force balance is

$$P|_z WH - P|_{z+\Delta z} WH + KPWHf_{w1} \cos(\phi + \phi') \Delta z - KPWHf_{w2} \Delta z = 0 \quad (8.18)$$

In this equation f_{w1} and f_{w2} are the friction coefficients between the upper plate and lower plates, respectively, and the solid bed and K is the anisotropy in the stress distribution (see Eq. 8.9). The contribution to the force balance from the side walls has been neglected in this case. On dividing through by the volume of the element and taking the limit as Δz goes to zero, the following differential equation is obtained:

$$-\frac{dP}{dz} + PK(f_{w,1} \cos(\phi + \phi') - f_{w,z})/H = 0 \quad (8.19)$$

This equation is integrated using the initial condition that at $z = 0, P = P_0$, to give

$$P = P_0 \exp \left\{ \left[Kf_{w,1} \cos(\phi + \phi') - Kf_{w,z} \right] z/H \right\} \quad (8.20)$$

Equations 8.17 and 8.20 can be solved for the pressure increase and the mass flow rate (i.e., $uWH\rho_b$). Hence, we see that the lower the flow rate the higher the pressure rise, and it will rise exponentially with distance.

We have neglected the resistance to flow offered by the side walls. A force balance in the x direction allows us to determine the normal force exerted by the wall on the solid plug. Hence, there will be an increased frictional force produced by the side wall, which will reduce the conveying capacity for a given pressure rise.

We next consider the solids conveying capacity of a single-screw extruder. The rectangular channel model cannot be used to describe the solids conveying in a single-screw extruder, because of the presence of deep channels, which

make curvature effects significant. As we don't intend to re-derive the equations for the single-screw extruder, the development for the rectangular channel should serve to facilitate the following discussion.

The model of the feed section of a single-screw extruder is due to Darnell and Mol (1956) and is for the most part similar to the development given for the rectangular channel. The assumptions are as follows:

1. The particulate solid bed is treated as a continuum.
2. The channel depth is constant.
3. The flight clearance is neglected.
4. Plug flow exists.
5. The channel is full so that all surfaces are in contact with the solid. (When the channel is not full, this is referred to as starve feeding.)
6. The stress distribution in the bed is isotropic.
7. The density is constant.
8. Gravitational forces are neglected.
9. Isothermal conditions hold. (This will be relaxed later.)

We first relate the mass flow rate to the angle ϕ' , which is the angle the relative velocity vector makes with the barrel velocity. A cylindrical plug (or a doughnut with a bite taken out of it) is shown in Figure 8.13. The mass flow rate, G , is the product of the plug velocity in the axial direction, v_{pl} , ρ_b , and the cross-sectional area of the plug and is given by

$$G = V_{pl} \rho_b \left[\frac{\pi}{4} (D_b^2 - D_s^2) - \frac{eH}{\sin \phi} \right] \quad (8.21)$$

where the second term on the right-hand side of the equation is where the flight cuts across the doughnut shaped plug. \sin is the sine of the average helix angle. D_b is the diameter of the barrel opening and $D_s = D_b - 2H$. In Figure 8.13 the screw is shown to be rotating in a clockwise direction. It is customary

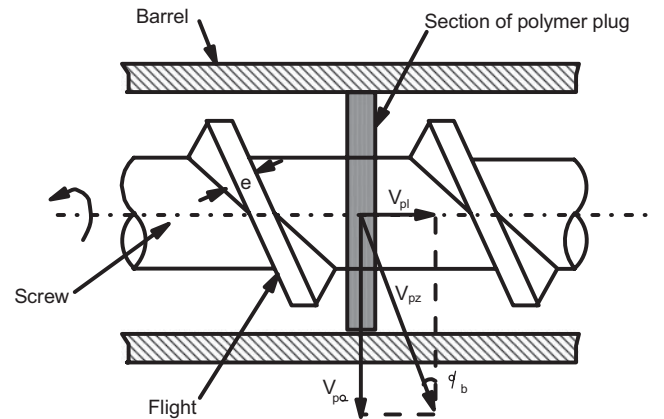


FIGURE 8.13 Cylindrically shaped solid plug.

to attach the coordinates to the rotating screw so the velocity vectors are shown relative to the rotating screw. The plug then has velocity components in the tangential direction, $V_{p\theta}$, and in the down channel direction, V_{pz} . Following arguments similar to those used in the previous section we can relate V_{pl} , V_b , and the angle ϕ' , which is the angle the relative velocity vector makes with the apparently rotating barrel (remember we have attached the axis to the rotating screw so if you are riding around with the screw, it looks like the barrel is rotating relative to you), as follows:

$$V_{pl} = V_b \frac{\tan \phi' \tan \phi_b}{\tan \phi' + \tan \phi_b} \quad (8.22)$$

where $V_b = \pi N D_b$ and N is the angular velocity of the screw in revolutions per second. We next substitute Eq. 8.22 into Eq. 8.21 to obtain

$$G = \pi^2 N H D_b (D_b - H) \rho_b \frac{\tan \phi' \tan \phi_b}{\tan \phi' + \tan \phi_b} \times \left[1 - \frac{e}{\pi (D_b - H) \sin \bar{\phi}} \right] \quad (8.23)$$

This equation contains two unknowns, ϕ' and G , and hence we need an additional equation.

The additional equation is obtained by carrying out force and torque balances on an element of the solid bed as shown in Figure 8.14. For an isotropic stress distribution these forces are as follows:

Barrel frictional force	$F_1 = f_b P W_b dz_b$
Force due to pressure difference	$F_6 - F_2 = H W dP$
Normal force at trailing flight	$F_8 = P H dz$
Normal force at leading flight	$F_7 = P H dz + F^*$
Frictional force at lead flight	$F_3 = f_s F_7$
Frictional force at trailing flight	$F_4 = f_s F_8$
Frictional force at screw	$F_5 = f_s P W_s dz_s$

(8.24)

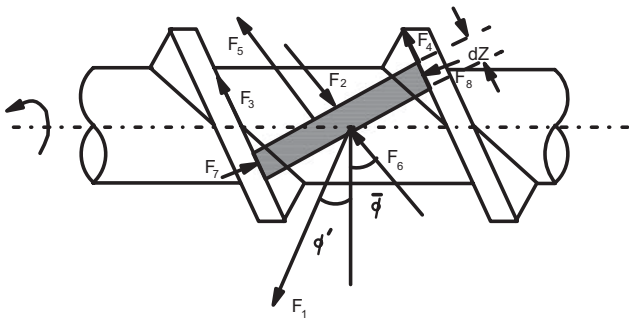


FIGURE 8.14 Element of the solid bed showing various forces acting on it.

where f_s and f_b are the friction coefficients between the polymer and the screw and barrel, respectively. Force and torque balances are then carried out to obtain the following expressions:

$$\cos \phi' = K_s \sin \phi' + M \quad (8.25)$$

where

$$K_s = \frac{\bar{D}}{D_b} \left[\frac{\sin \bar{\phi} + f_s \cos \bar{\phi}}{\cos \bar{\phi} - f_s \sin \bar{\phi}} \right] \quad (8.26)$$

and

$$M = \frac{2H}{W_b} \frac{f_s}{f_b} \sin \phi_b \left(K_s + \frac{\bar{D}}{D_b} \cot \bar{\phi} \right) + \frac{W_s}{W_b} \frac{f_s}{f_b} \sin \phi_b \left(K_s + \frac{D_s}{D_b} \cot \phi_s \right) + \frac{\bar{W}}{W_b} \frac{H}{z_b} \frac{1}{f_b} \sin \bar{\phi} \left(K_s + \frac{\bar{D}}{D_b} \cot \bar{\phi} \right) \ln \left(\frac{P_2}{P_1} \right) \quad (8.27)$$

where $\bar{D} = \frac{1}{2} (D_b + D_s)$ and P_1 is the initial pressure at $z = 0$ and P_2 is the pressure at any down channel distance, Z_b . For a given flow rate ϕ' is obtained from Eq. 8.23, M is calculated from Eq. 8.25, and the pressure rise is then determined from Eq. 8.27.

We next calculate the power consumed in the solids conveying section. The power input through the barrel is obtained from

$$P_w = \int \mathbf{F}_b \cdot \mathbf{V}_b dA = \int F_1 V_b \cos \phi' W_b dz_b \quad (8.28)$$

Substituting into Eq. 8.28 for F_1 using Eq. 8.24 and P using Eq. 8.27, one obtains (Tadmor and Broyer, 1972)

$$P_w = \pi N D_b W_b Z_b f_b \cos \phi' \frac{P_2 - P_1}{\ln(P_2/P_1)} \quad (8.29)$$

Certainly there are questionable assumptions in the theory of solids conveying. The assumption of an isotropic stress distribution was addressed, but it is not clear that the overall predictions of the model were drastically improved by including an anisotropic stress distribution. In fact, when one realizes how sensitive the predictions of the model are to the value of the friction coefficients and how difficult it is to accurately measure these quantities, then one will understand that improvements of this nature may be of little value.

On the contrary, the assumption of constant temperature must be modified, because the solid plug must increase in temperature as it advances along the screw. Eventually the surface of the solid bed must reach the melting temperature of the polymer. The heat is supplied through the heated barrel and frictional heating at the solid and barrel interface. The

nonisothermal analysis of the solids conveying section is due to Tadmor and Broyer (1972). The total power introduced through the shaft is partly dissipated into heat at the barrel, flights, and the root of the screw surfaces and is partly used to generate pressure. Most of the power, however, is dissipated into heat at the barrel surface. The heat generated per unit of barrel surface is given by

$$q_b = f_b \pi N D_b \frac{\sin \phi_b}{\sin(\phi_b + \phi')} \frac{P_2 - P_1}{\ln(P_2/P_1)} \quad (8.30)$$

The heat is conducted into the solid plug and the barrel walls, if the barrel walls are not heated. Tadmor and Broyer (1972) neglected curvature in the system and treated the conveying of the solids as in a rectangular channel as shown in Figure 8.11. Assuming conduction occurs only in the y direction and with bulk flow in the z direction, the equation of energy leads to the following differential equation for the temperature distribution:

$$\rho_b \bar{C}_{p,p} V_{pz} \frac{\partial T_p}{\partial z} = k_p \frac{\partial^2 T_p}{\partial y^2} \quad (8.31)$$

where T_p is the temperature in the plug and $C_{p,p}$ and k_p are the heat capacity and the thermal conductivity, respectively, of the plug. Equation 8.31 can be converted to the one-dimensional transient heat conduction equation just as done in Chapter 5 by replacing dz/V_{pz} by dt :

$$\frac{\partial T_p}{\partial t} = \alpha_p \frac{\partial^2 T_p}{\partial y^2} \quad (8.32)$$

where α_p is the thermal diffusivity of the solid bed. V_{pz} is the velocity of the plug in the down channel direction and is obtained from the equations derived for the isothermal case. The approach here is similar to that used in the forced convection approximation where the velocity field is assumed to be unaffected by changes in temperature. Since heat is assumed to be conducted away through the barrel, the temperature distribution in the barrel, $T_b(y, t)$, is also required. However, since the thermal conductivity of the barrel is at least 100 times higher than the polymer, the temperature distribution is assumed to be linear. The following initial and boundary conditions are used:

$$\text{I.C.:} \quad \text{at } t = 0, \quad T_p(y, t) = T_0 \quad (8.33)$$

$$\text{B.C.1:} \quad \text{at } y = H, \quad T_p = T_b \quad (8.34)$$

The additional boundary condition required to solve Eq. 8.3-18 comes from an energy balance at the interface between the barrel and the solid bed where it is assumed that the frictional heat is conducted away into the barrel and the solid plug:

$$\text{B.C.2:} \quad \text{at } y = H, \quad q_b = -K_p \frac{\partial T_p}{\partial y} + K_b \frac{\partial T_b}{\partial y} \quad (8.35)$$

Tadmor and Broyer (1972) developed a numerical scheme to solve for the temperature profile in the solid bed.

In Problem 8C.2 the IMSL subroutine IVPAG or the MATLAB function *pdede* is used to determine the temperature profile in the solid bed. Two approaches are used in this problem. The first is to assume that the barrel is heated and the solid bed is heated by conduction of heat from the barrel. In the other approach the heat generated by friction is assumed to be conducted into the solid bed only, which may be the case when the barrel is heated to a temperature in the range of the melting point of the polymer.

Properties for a few polymers required in the solids conveying model are presented in Appendix B. Here it is observed that the friction coefficient between the polymer and steel is relatively independent of temperature. As the temperature approaches the melting point the friction coefficients tend to increase, but over a wide range of temperatures f_b is nearly constant. Hence, it seems justifiable to use the mass flow rate and pressure rise calculated by means of the isothermal model in the nonisothermal model.

Example 8.2. Solids Conveying of LDPE (Tadmor and Gogos, 1979)

LDPE is extruded in a single-screw extruder having a diameter of 6.35×10^{-2} m. The square pitched screw (i.e., $L_s = D_b$) is 26.5 turns long with a feed section of 12.5 turns and channel depth of 9.398×10^{-3} m, a transition section of 9.5 turns, and a metering section 3.22×10^{-3} m deep. The flight width is 6.35×10^{-3} m, and the flight clearance is negligible. The screw speed is 60 rpm and the mass flow rate is 67.1 kg/h. The pellets enter the extruder at 25 °C from the hopper described in Example 8.1. The hopper discharge opening is 0.127 m and occupies the first two turns of the screw. The barrel is maintained at 149 °C and melting starts 3 turns from the beginning of the flights. The friction coefficients between the polymer and the barrel and the screw are 0.45 and 0.25, respectively. Calculate (a) the pressure at the end of the solids conveying zone (i.e., over 1 turn), (b) the power consumption in the solids conveying zone, and (c) the energy per unit surface area dissipated into heat.

Solution. We first compute some geometrical values required in the solids conveying model:

ϕ_b , helix angle at barrel surface	17.65°
$\bar{\phi}$, mean helix angle	20.48°
ϕ_s , helix angle at root of screw	24.33°
\bar{W} , mean channel width	5.314×10^{-2} m
W_b , channel width at barrel surface	5.416×10^{-2} m
W_s , channel width at root of screw	5.151×10^{-2} m
l , axial length	10.5 turns, 0.666 m
\bar{Z} , mean helical length	2.270 m

We next calculate the pressure rise from Eq. 8.27. To calculate P_2/P_1 we determine ϕ' from Eq. 8.22, which in

turn is used to calculate M and K_s . The axial velocity of the solid plug is

$$V_{pl} = \frac{61.7/3600}{(595) \left(\frac{(\pi/4)[(0.065)^2 - (0.0447)^2]}{- (0.00635)(0.009398)/\sin(20.48^\circ)} \right)}$$

$$= 0.02195 \text{ m/s}$$

The velocity of the barrel surface $V_b = \pi ND_b = 0.19995 \text{ m/s}$, and hence from Eq. 8.22 we find

$$\tan \phi' = \frac{\tan \phi_b}{(V_b/V_{pl}) \tan \phi_b - 1} = 0.1261$$

and ϕ' is 7.57° . From Eq. 8.26 we find K_s :

$$K_s = \frac{(0.0541) \sin(20.48) + (0.25) \cos(20.48)}{0.0635 \cos(20.48) - (0.25) \sin(20.48)} = 0.5859$$

and from Eq. 8.25

$$M = \cos(7.57) - 0.5859 \sin(7.57) = 0.9141$$

The pressure rise, P_2/P_1 , over one turn of the solids conveying section ($Z_b = 0.0635/\sin 17.6^\circ = 0.209 \text{ m}$), which starts just after the two flights occupied by the hopper throat and ends with the heating of the barrel, is obtained from

$$0.9141 = (2) \frac{(0.009398) (0.25)}{(0.05416) (0.45)} \sin(17.65)$$

$$\times \left[(0.5859) + \frac{(0.0541)}{(0.0635)} \cotan(20.48) \right]$$

$$+ \frac{(0.05151) (0.25)}{(0.05416) (0.45)} \sin(17.65)$$

$$\times \left[(0.5859) + \frac{(0.0447)}{(0.0635)} \cotan(24.33) \right]$$

$$+ \frac{(0.05314)(0.009398) \sin(20.48)}{(0.05416)(0.209)(0.45)}$$

$$\times \left[(0.5859) + \frac{(0.0541)}{(0.0635)} \cotan(20.48) \right] \ln \frac{P_2}{P_1}$$

$$= 0.1676 + 0.34328 + 0.09813 \ln \frac{P_2}{P_1}$$

and this leads to

$$P_2/P_1 = 60.9$$

P_1 is the pressure at the base of the hopper, which was calculated in Example 8.1. Thus, P_2 is $2.52 \times 10^5 \text{ Pa}$ (36.5 psi). The solids conveying zone could in fact extend another turn or two until the surface reaches the melting point, T_m , of

LDPE (135°C). The results indicate that the solids conveying zone is operating properly and that higher outputs could be obtained before the solid bed no longer fills the channel. The condition in which the channel is only partially full is referred to as "starve feeding" and is dealt with in Problem 8B.4. The power input through the barrel is obtained from Eq. 8.29 and is

$$P_w = (\pi)(1)(0.0635)(0.05416)(0.209)(0.45) \cos(7.570)$$

$$((2.52 \times 10^5) - (4.131 \times 10^3))/\ln(60.9) = 60.8 \text{ W}$$

The power dissipated into heat per unit of surface area is obtained from Eq. 8.30 and is

$$q_b = P_w(0.1995)(0.45)(\sin(17.650))/\sin(17.65 + 7.57)$$

$$= 0.0639 P_w$$

■

8.3.2 Delay and Melting Zones

The basic model for the conversion of the solid bed to melt is due to Tadmor (Tadmor and Klein 1970) and is based on his observations of the state of material along the screw channel. According to Tadmor's observations for most polymer systems a melt film first appears at the barrel surface as the result of heat generation due to friction and heat conducted from the heated barrel. Once the melt film forms the conveying mechanism changes at the barrel surface, where viscous drag is now dominant, but frictional drag is still important at the root of the screw and the flights. The thickness of the melt film continues to increase as the plug proceeds down the channel until it attains a value of several times the flight clearance. At this point, the melt film thickness stays nearly constant and the melt is scraped off and accumulated at the pushing flight. The axial distance from where the melt film first appears until melt begins to accumulate at the pushing flight is referred to as the *delay zone*.

There appears to be no reliable mathematical model for predicting the length of the delay zone. Tadmor and Klein (1970), based on limited experimental data, found an empirical correlation between the number of turns (i.e., length of the delay zone) and a dimensionless parameter Ψ , where Ψ is defined later in Eq. 8.64 and represents the ratio of the rate melting to the mass flux of the solid bed in the channel. This relation is

$$N' = 0.008 \left(\frac{1}{\Psi} \right) \quad (8.36)$$

where N' is the number of turns. Although this relation was obtained from data for a limited number of polymers, it is all that is available for estimating the length of this zone at the present time.

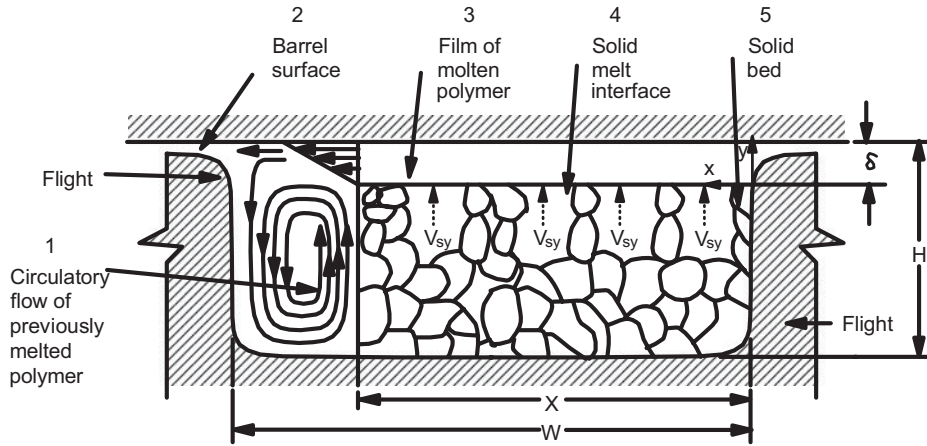


FIGURE 8.15 Tadmor melting model.

Based on visual observations, Tadmor and Klein (1970) proposed a melting mechanism as described in Figure 8.15. The melt film is scraped off and accumulates at the pushing flight. The width of the solid bed, X , decreases as one proceeds down the channel. The solid is pushed inward, and at the melt and solid interface the bed appears to move upward with a velocity, V_{sy} . The melt film thickness, δ , was observed to change along the width of the channel but only slightly, and it did not appear to change significantly along the down channel direction.

The goal of a model of the melting section is to determine the solid bed width, X , as a function of the down channel distance, z . For the situation just described and as shown in Figure 8.15, the basic idea is to determine the temperature distribution in the melt film and solid bed. Then an energy balance is performed at what is assumed to be a distinct melt–solid interface. The heat flowing into the interface is conducted into the solid bed and used to change the solid bed to melt (enthalpy associated with a phase change). The difference between melting in a single-screw extruder and the situation described in Section 5.3.5 is that the melt film is continually dragged away. Hence, not only does the melt film remain at nearly the same thickness, but the temperature does not change along the channel direction. Furthermore, there is also the possibility of a significant contribution to melting from viscous dissipation.

Based on observations, Tadmor and Klein made the following assumptions:

1. Steady-state conditions are reached in the extruder.
2. Melting takes place only at the barrel surface. (In some cases melting has been observed at the root and flights of the screw (Rauwendaal, 1986, p. 271).)
3. The solid bed is homogeneous, continuous, and deformable.
4. Physical and thermophysical properties are assumed constant.

5. The solid bed–melt film interface is assumed to be a distinct interface existing at the melting point, T_m , of the polymer.

The first step in determining the solid bed profile is to determine the temperature distribution in the melt. Referring back to Figure 8.15 we now develop the model. First, we locate a set of axes at the melt–solid interface at the trailing flight (right side of Fig. 8.15). Next, we make the following postulates for the velocity and temperature fields in the melt film:

$$v_x = v_x(y), \quad v_z = v_z(y), \quad v_y = 0, \quad \text{and} \quad T = T(x, y) \tag{8.37}$$

and the solid bed:

$$T_s = T_s(y) \tag{8.38}$$

The solid bed is assumed to move as a plug with down channel velocity of V_{sz} , where

$$V_{sz} = G/(\rho_s HW) \tag{8.39}$$

and is the same as solid bed velocity at the beginning of the melting zone, V_{pz} (the thickness of the melt film has been neglected). For the melt film, the equations of motion and energy are

$$\frac{\partial \tau_{yx}}{\partial y} = 0 \tag{8.40}$$

$$\frac{\partial \tau_{yz}}{\partial y} = 0 \tag{8.41}$$

$$\rho \bar{C}_p v_x \frac{\partial T}{\partial X} = +k \frac{\partial^2 T}{\partial y^2} + k \frac{\partial^2 T}{\partial x^2} - \tau_{yx} \frac{\partial v_x}{\partial y} - \tau_{yz} \frac{\partial v_z}{\partial y} \tag{8.42}$$

To solve this set of equations a constitutive relation is needed, and the power-law empiricism for viscosity is used here for convenience. The equations are coupled because of the dependence of viscosity on temperature. However, the velocity field can be obtained independent of the energy equation. It is the energy equation that is coupled to the equations of motion because of the viscous dissipation terms. The velocity field is obtained by integrating Eqs. 8.40 and 8.41 after substituting in the GNF model and using the following boundary conditions:

$$\begin{aligned} \text{B.C.1:} \quad & \text{at } y = 0, \quad v_x = 0 \\ \text{B.C.2:} \quad & \text{at } y = 0, \quad v_z = V_{sz} \\ \text{B.C.3:} \quad & \text{at } y = d, \quad v_x = V_{bx} \\ \text{B.C.4:} \quad & \text{at } y = d, \quad v_z = V_{bz} \end{aligned} \quad (8.43)$$

Because of the homogeneous nature of Eqs. 8.40 and 8.41 the viscosity function drops out, and the velocity field becomes

$$v_x = \left(\frac{V_{bx}}{\delta} \right) y \quad (8.44)$$

$$v_z = \left(\frac{V_{bz} - V_{sz}}{\delta} \right) y + V_{sz} \quad (8.45)$$

The difficulty comes in solving the energy equation, since η is a function of temperature and because of the term on the left-hand side of this equation. One should remember this term is associated with the transport of heat by convection and if viscous dissipation is large, this term will be important. Tadmor and Klein (1970) assumed a parabolic temperature distribution and initially neglected the conduction and convection terms in the x direction. Rather than assume a temperature distribution (see Problem 8B.3), we use the forced convection assumption. Hence, Eq. 8.42 can be integrated directly (provided we drop the convection term) to obtain the following temperature distribution in the melt:

$$T = \frac{\Phi}{2k_m}(y^2 - y\delta) + y \left(\frac{T_b - T_m}{\delta} \right) + T_m \quad (8.46)$$

where Φ is the viscous dissipation term given by

$$\Phi_v = m \left[\left(\frac{V_{bx}}{\delta} \right)^2 + \left(\frac{V_{bz} - V_{sz}}{\delta} \right)^2 \right]^{(n+1)/2} \quad (8.47)$$

This temperature profile was obtained using the following boundary conditions:

$$\begin{aligned} \text{B.C.1:} \quad & \text{at } y = 0, \quad T = T_m \\ \text{B.C.2:} \quad & \text{at } y = \delta, \quad T = T_b \end{aligned} \quad (8.48)$$

where T_b is the barrel temperature.

The temperature distribution in the solid bed is determined next. Assuming that $T_s = T_s(y)$, then the energy equation becomes

$$\rho_s \bar{C}_{ps} V_{sy} \frac{\partial T_s}{\partial y} = k \frac{\partial^2 T_s}{\partial y^2} \quad (8.49)$$

The boundary conditions used in solving this equation are

$$\begin{aligned} \text{B.C.1:} \quad & \text{at } y = 0, \quad T_s = T_m \\ \text{B.C.2:} \quad & \text{at } y = -\infty, \quad T_s = T_0 \end{aligned} \quad (8.50)$$

where T_0 is the temperature of the bed entering the melting zone. B.C.2 actually presents a problem as there is a temperature gradient in the solid bed and the bed temperature may change as it moves down the channel. Conditions under which one should consider changes in the bed temperature along the channel are discussed by Rauwendaal (1986). Using the boundary conditions given in Eq. 8.50, the temperature profile becomes

$$T_s = (T_m - T_0) \exp\left(\frac{yV_{sy}}{\alpha_s}\right) + T_0 \quad (8.51)$$

The final step in the determination of the melting rate is the energy balance at the melt–solid interface. The energy balance is given by

$$q_y|_{y=0} - q_{sy}|_{y=0} - V_{sy} \Delta \bar{H}_f = 0 \quad (8.52)$$

One now substitutes the temperature distributions given in Eqs. 8.46 and 8.51 into Eq. 8.52 to obtain

$$\frac{\Phi_v \delta}{2} + k_m \frac{(T_b - T_m)}{\delta} = [\bar{C}_{ps}(T_m - T_0) + \Delta \bar{H}_f] \rho_s V_{sy} \quad (8.53)$$

Equation 8.53 contains two unknowns, δ and v_{sy} , and hence an additional equation is required. Using the fact that the rate at which the solid is converted to melt at the interface must equal the rate at which it accumulates at the leading flight, one obtains the following equation:

$$w_L(z) = \rho_s V_{sy} X = \int_0^\delta \frac{V_{bx}}{\delta} y dy = \frac{V_{bx} \delta}{2} \quad (8.54)$$

where X is the bed width at any z distance down the channel and $w_L(z)$ is the rate of melting. For the Newtonian case Φ_v becomes

$$\Phi_v = \frac{\mu}{\delta^2} [V_{bx}^2 + (V_{bz} - V_{sz})^2] \quad (8.55)$$

and hence one finds the following expressions for δ ,

$$\delta = \left[\frac{2k_m(T_b - T_m) + \mu(V_{bx}^2 + (V_{bz} - V_{sz})^2)X}{(\bar{C}_{ps}(T_m - T_0) + \Delta\bar{H}_f)(\rho_m V_{bx})} \right]^{1/2} \quad (8.56)$$

and for $w_L(z)$,

$$w_L(z) = \left\{ \frac{V_{bx}\rho_m [k_m(T_b - T_m) + (\mu/2)V_j^2]X}{\Delta\bar{H}_f + \bar{C}_{ps}(T_m - T_0)} \right\}^{1/2} \quad (8.57)$$

where

$$V_j^2 = V_{bx}^2 + (V_{bz} - V_{sz})^2 \quad (8.58)$$

For a GNF with a viscosity function given by the power-law model, Eq. 8.56 represents a nonlinear algebraic equation that must be solved for δ .

Finally, we determine the solid bed profile as a function of distance down the channel. The change in solid bed width is obtained by taking a mass balance on an element of thickness Δz :

$$\rho_s V_{sz}(H - \delta)X|_z - \rho_s V_{sz}(H - \delta)X|_{z+\Delta z} = w_L(z)\Delta z \quad (8.59)$$

which on taking the limit as $\Delta z \rightarrow 0$ and neglecting the film thickness in the down channel direction reduces to

$$\frac{-d(HX)}{dz} = \frac{w_L(z)}{\rho_s V_{sz}} \quad (8.60)$$

By substituting Eq. 8.57 into Eq. 8.60, we arrive at the following expression:

$$\frac{-d(HX)}{dz} = \frac{\Phi\sqrt{X}}{\rho_s V_{sz}} \quad (8.61)$$

where

$$\Phi = \left\{ \frac{V_{bx}\rho_m [k_m(T_b - T_m) + (\mu/2)V_j^2]}{2(\bar{C}_{ps}(T_m - T_0) + \Delta\bar{H}_f)} \right\}^{1/2} \quad (8.62)$$

For a constant channel depth, Eq. 8.61 can be integrated to give

$$\frac{X_2}{W} = \frac{X_1}{W} \left[1 - \frac{\psi(z_2 - z_1)}{2H} \right]^2 \quad (8.63)$$

where X_1 and X_2 are the widths of the solid bed at locations z_1 and z_2 , respectively, and the dimensionless group is defined as

$$\psi = \frac{\Phi}{V_{sz}\rho_s\sqrt{X_1}} \quad (8.64)$$

Hence, for a constant channel depth we can determine the length of the channel required to melt the solid bed from Eq. 8.63.

For a tapered channel of constant taper, which is usually the case, we write Eq. 8.61 as

$$\frac{d(HX)}{dH} = \frac{\Phi\sqrt{X}}{A\rho_s V_{sz}} \quad (8.65)$$

where

$$A = -\frac{dH}{dz} \quad (8.66)$$

Equation 8.65 can be integrated to give

$$\frac{X_2}{W} = \frac{X_1}{W} \left[\frac{\psi}{A} - \left(\frac{\psi}{A} - 1 \right) \sqrt{\frac{H_1}{H_2}} \right]^2 \quad (8.67)$$

where X_2 and X_1 are the widths of the solid bed at down channel locations corresponding to H_2 and H_1 , respectively.

Equations 8.63 and 8.67 represent the basic equations for the melting model. The total length of melting for a channel of constant depth is

$$z_T = \frac{2H}{\psi} \quad (8.68)$$

while for a tapered channel is

$$z_T = \frac{H}{\psi} \left(2 - \frac{A}{\psi} \right) \quad (8.69)$$

For a channel of constant depth, the length of channel required to melt the solid bed is a function of the channel depth and a dimensionless group ψ , where ψ expresses the ratio of the local rate of melting per unit solid–melt interface to the local solid mass flux. Thus, the length of melting is proportional to the mass flow rate and inversely proportional to the rate of melting. In the case of tapered channels, the higher the taper, the shorter the melting length, z_T . However, if the taper becomes too great, the solid bed can increase in width instead of decrease, which may lead to plugging of the channel and surging conditions.

8.3.3 Metering Section

The fully melted polymer now enters the third zone of the extruder where it is pressurized. The buildup of pressure is required in order to pump the melt through the die at the end of the extruder. The pressurization of the melt is based on a viscous drag mechanism. We first illustrate how viscous drag can lead to a pressurization of the melt. This is followed by the development of a nonisothermal non-Newtonian model of the metering section. Because numerical methods are required to solve the equations generated in this model, we end the section by presenting the isothermal Newtonian case where an analytical solution is possible.

The basic principle of operation of the metering section of the single-screw extruder is illustrated by the simple plate model shown in Figure 8.16. The fluid between the two plates is considered to be Newtonian and under isothermal and steady flow conditions. Because of a restriction at the end of the channel (which is not shown) the pressure increases along the z direction. v_z is assumed to depend only on y , since the aspect ratio of the plates is large (i.e., $W/H > 10$). The equation of motion becomes, after substituting in the expression for the shear stress for a Newtonian fluid,

$$\mu \frac{d^2 v_z}{dy^2} - \frac{dp}{dz} = 0 \quad (8.70)$$

This equation is solved using the following boundary conditions:

$$\begin{aligned} \text{B.C.1: } & \text{at } y = 0, \quad v_z = 0 \\ \text{B.C.2: } & \text{at } y = H, \quad v_z = V_0 \end{aligned} \quad (8.71)$$

After integrating Eq. 8.70 and using the boundary conditions given above, the velocity field is determined to be

$$v_z = \frac{H^2}{2\mu} \left(\frac{dp}{dz} \right) \left[\left(\frac{y}{H} \right)^2 - \frac{y}{H} \right] + \frac{V_0 y}{H} \quad (8.72)$$

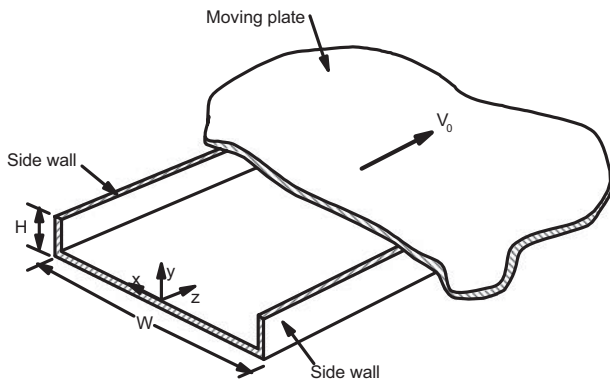


FIGURE 8.16 Drag-induced pressurization of a fluid in a rectangular channel having an aspect ratio, $W/H > 10$.

Equation 8.72 is now integrated over the cross-sectional area to obtain the volumetric flow rate:

$$Q = \frac{V_0 W H}{2} - \frac{dp}{dz} \left(\frac{W H^3}{12 \mu} \right) \quad (8.73)$$

Q is seen to consist of two terms: the first is called the drag flow, Q_d , while the second is referred to as the pressure flow, Q_p . When there is no pressure buildup, the transport is due entirely to the drag flow term. However, if there is a significant pressure increase, then Q is decreased. In this case the pressure term can dominate to the point where flow can be in the opposite direction. (As we will see later this cannot happen in the extruder.) The main point is that as a result of viscous drag the fluid can be advanced against resistance due to pressure buildup. This is in essence the principle of operation of the metering section of the single-screw extruder.

As a pump, however, the parallel plate device is not practical in itself. A way is needed to increase the length of the channel and to return the upper plate to the channel after it has transversed the length of the channel. As shown in Figure 8.17 one way to do this is to machine the channel in a shaft and then give the channel a helical pitch so that the length can be increased. The inner cylinder or outer cylinder could be rotated. In the figure the outer cylinder is rotated. When the channel depth is shallow relative to the radius of the cylinder, then curvature can be neglected, and the flow can be considered as that in flat plates.

We are now in position to develop a model for the metering section of a single-screw extruder. In practice, the screw is rotated inside the barrel and helical or cylindrical coordinates are needed to describe the geometry. However, because the channel depth is usually small relative to the radius of the barrel, we can treat the flow using rectangular Cartesian coordinates as shown in Figure 8.18. It is customary to attach the axes to the rotating screw, which makes it appear

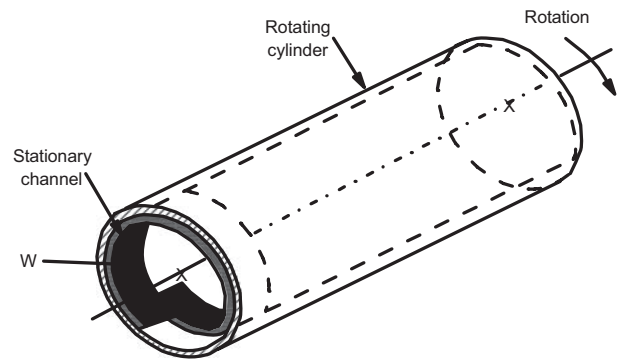


FIGURE 8.17 Principle of operation of the metering section of a single-screw extruder. A helical channel is machined in the inner cylinder. The fluid in the channel is dragged forward in the channel by the rotating cylinder.

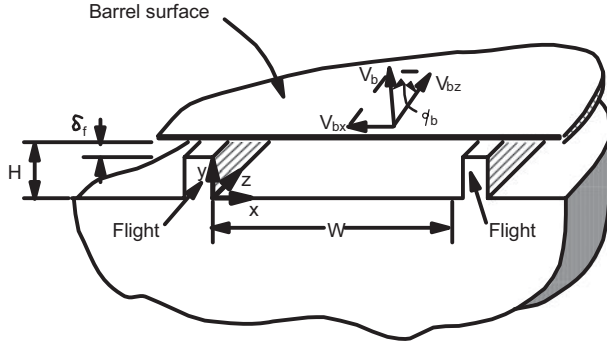


FIGURE 8.18 Parallel plate model of flow in the metering section of a single-screw extruder. The axes are attached to the rotating screw, which makes the barrel appear to move relative to the screw.

to the observer that the plate is moving over the channel at an angle ϕ_b to the down channel direction. In principle, a three-dimensional model is required to describe the velocity and temperature profiles in the extruder channel. However, this type of detail is usually not necessary in the design of screws, nor is it computationally practical. With the assumptions of constant fluid density and steady-state conditions, the following postulates pertaining to the velocity and temperature fields can be made:

$$v_z = v_z(x, y) \quad v_x = v_x(x, y) \quad (8.74)$$

$$T = T(y, z) \quad (8.75)$$

If $W/H > 10$, then we can simplify matters by making the following postulates for the velocity field:

$$v_z = v_z(y) \quad v_x = v_x(y) \quad (8.76)$$

In essence we are neglecting the effect of the side walls of the channel, which is probably valid for most single-flighted screw designs. Using these postulates the equations of motion and energy become, respectively,

$$0 = -\frac{\partial p}{\partial x} - \frac{\partial \tau_{yx}}{\partial y} \quad (8.77)$$

$$0 = -\frac{\partial p}{\partial z} - \frac{\partial \tau_{yz}}{\partial y} \quad (8.78)$$

$$\rho \bar{C}_p v_z \frac{\partial T}{\partial z} = k \frac{\partial^2 T}{\partial y^2} - \tau_{xy} \frac{\partial v_x}{\partial y} - \tau_{yz} \frac{\partial v_z}{\partial y} \quad (8.79)$$

Using the GNF model the shear stress components are given by

$$\tau_{yx} = -\eta(\dot{\gamma}, T) \frac{\partial v_x}{\partial y} \quad (8.80)$$

$$\tau_{yz} = -\eta(\dot{\gamma}, T) \frac{\partial v_z}{\partial y} \quad (8.81)$$

where $\dot{\gamma}$ is given by

$$\dot{\gamma} = \sqrt{\left(\frac{\partial v_x}{\partial y}\right)^2 + \left(\frac{\partial v_z}{\partial y}\right)^2} \quad (8.82)$$

This system of differential equations is nonlinear, and they are coupled through the temperature dependence of viscosity. Numerical techniques are required to solve the above set of equations.

We can obtain reasonable solutions to these equations if we assume the forced convection assumption holds and that the helix angle, ϕ_b , is less than 20° . In fact, most screws are designed with a square pitch (i.e., $L_s = D_b$, which means $\phi_b = 17.7^\circ$). The forced convection assumption allows us to decouple the equations of motion from the equation of energy. Values of $\phi_b < 20^\circ$ allow us to decouple the equations of motion, since $dv_x/dy \ll dv_z/dy$ (to see this we approximate dv_x/dy as $V_b \sin \phi_b/H$ and dv_z/dy as $V_b \cos \phi_b/H$ and $\dot{\gamma}$ is approximately dv_z/dy). The equations of motion become

$$\frac{d}{dy} \left(m \left| \frac{dv_z}{dy} \right|^{n-1} \frac{dv_z}{dy} \right) = \frac{\partial p}{\partial z} \quad (8.83)$$

$$\frac{d}{dy} \left(m \left| \frac{dv_x}{dy} \right|^{n-1} \frac{dv_x}{dy} \right) = \frac{\partial p}{\partial x} \quad (8.84)$$

Equation 8.83 can be integrated subject to the following boundary conditions:

$$\text{B.C.1: at } y = 0, \quad v_z = 0 \quad (8.85)$$

$$\text{B.C.2: at } y = H, \quad v_z = V_{bz} = V_b \cos \phi_b \quad (8.86)$$

We also find it convenient to introduce the following dimensionless variables:

$$u_z = v_z/V_{bz} \quad \xi = y/H$$

Because u_z passes through a maximum at some point β , the solution is obtained over two regions:

For $0 < \xi < \beta$:

$$u_z^< = \left(\frac{GH^{n+1}}{mV_{bz}^n} \right)^s \left(\frac{1}{s+1} \right) [(\beta - \xi)^{s+1} - \beta^{s+1}] \quad (8.87)$$

For $\beta < \xi < 1$:

$$u_z^> = \left(\frac{GH^{n+1}}{mV_{bz}^n} \right)^s \left(\frac{1}{s+1} \right) [(\xi - \beta)^{s+1} - (1 - \beta)^{s+1}] \quad (8.88)$$

where $G = \partial p / \partial z$ and $s = 1/n$. The value for β is obtained by equating the two velocity fields at $\xi = \beta$ to give

$$\beta^{s+1} - (1 - \beta)^{s+1} + \frac{m^s V_{bz}(1 + s)}{G^s H^{1+s}} = 0 \quad (8.89)$$

The volumetric flow rate is obtained by integrating the velocity field over the cross-sectional area and is

$$\frac{Q}{WHV_{bz}} = \left(\frac{GH^{n+1}}{mV_{bz}^n} \right) \left[-\frac{\beta^{s+2}}{s+2} - \frac{(1-\beta)^{s+2}}{s+2} \right] + (1-\beta) \quad (8.90)$$

The expression in Eq. 8.90 is referred to as the screw characteristic and consists of drag flow and pressure flow terms. Finally, the cross-flow term, v_x , is obtained by integrating Eq. 8.44 using the velocity field in Eqs. 8.87 and 8.88 and the following boundary conditions:

$$\begin{aligned} \text{B.C.1:} \quad & \text{at } y = 0, \quad v_x = 0 \\ \text{B.C.2:} \quad & \text{at } y = H, \quad v_x = -V_{bx} = -V_b \sin \phi_b \end{aligned} \quad (8.91)$$

The importance of the cross-flow term to mixing will be discussed in Section 8.5.

Using the forced convection assumption and restricting ourselves to small helix angles, Eq. 8.79 becomes

$$\rho \bar{C}_p v_z(y) \frac{\partial T}{\partial z} = k \frac{\partial^2 T}{\partial y^2} + m \left| \frac{dv_z}{dy} \right|^{n+1} \quad (8.92)$$

We cast the energy equation into dimensionless form by introducing the following variables:

$$z/L = \zeta \quad v_z/V_{bz} = u \quad T^* = (T - T_i)/(T_b - T_i) \quad (8.93)$$

where T_i is the initial temperature of the melt entering the metering zone and T_b is the barrel temperature. Equation 8.92 in dimensionless form is

$$\text{Pe} u_\zeta(\xi) \frac{\partial T^*}{\partial \zeta} = \frac{\partial^2 T^*}{\partial \xi^2} + \text{Br} \left| \frac{du}{d\xi} \right|^{n+1} \quad (8.94)$$

where $\text{Pe} = H^2 \rho C_p V_{bz} / kL$ and $\text{Br} = m V_{bz}^{n+1} / H^{n-1} k (T_b - T_i)$. Even with the assumptions made here, numerical methods are needed to solve Eq. 8.94.

The flow patterns in the extruder channel are difficult to visualize for the power-law fluid, and hence, we consider the flow for the Newtonian case. The brief development here is mostly for pedagogical purposes but does have some applicability to fluids that are nearly Newtonian under extrusion conditions and for isothermal conditions. For a Newtonian

fluid Eqs. 8.83 and 8.84 give the following expressions for u_x and u_z , respectively:

$$u_x = -\xi + \xi(\xi - 1)(GH^2/2\mu V_{bx}) \quad (8.95)$$

$$u_z = \xi - 3\xi(1 - \xi)(H^2G/6\mu V_{bz}) \quad (8.96)$$

Using the fact that there is no net flow in the x direction we can integrate u_x over ξ to find

$$\frac{\partial p}{\partial x} = -\frac{6\mu V_{bx}}{H^2} \quad (8.97)$$

Substituting the expression for $\partial p / \partial x$ back into Eq. 8.95, we obtain the cross-channel velocity profile:

$$u_x = -\xi(2 - 3\xi) \quad (8.98)$$

Equation 8.98 tells us that away from the flights the fluid circulates around a stagnant layer at $y = 2H/3$. Of course, for a pseudoplastic material this position will change. The volumetric flow rate is obtained by integrating Eq. 8.96 over the cross-sectional area of the channel and is

$$Q = \frac{V_{bz}WH}{2} - \left(\frac{\partial p}{\partial z} \right) \frac{WH^3}{12\mu} \quad (8.99)$$

This is the screw characteristic for the Newtonian case, and as shown in the simple one-dimensional flat plate model described at the start of this section, it consists of drag and pressure flow terms. The ratio of pressure to drag flow rates (this is sometimes called the *throttle ratio*) is

$$\frac{Q_p}{Q_d} = - \left(\frac{\partial p}{\partial z} \right) \frac{H^2}{6\mu V_{bz}} \quad (8.100)$$

One may be under the impression that it is possible to cause the fluid to flow backward toward the hopper. Under no condition is this possible as shown below. The axial velocity, v_l , is obtained by taking the vectorial contributions of v_x and v_z along the axial direction, l :

$$v_l = v_x \cos \phi + v_z \sin \phi \quad (8.101)$$

Substituting the expressions from Eqs. 8.95, 8.96, and 8.100 into Eq. 8.101 and defining $u_l = v_l/V_b$, we get

$$u_l = 3\xi(1 - \xi) \left(1 + \frac{Q_p}{Q_d} \right) \sin \phi \cos \phi \quad (8.102)$$

For the Newtonian case (see Fig. 8.19) it is observed that the cross-flow component is independent of the Q_p/Q_d ratio. On the other hand, u_z and u_l are highly dependent on the Q_p/Q_d ratio, and as the ratio becomes more negative, the flow in the axial direction decreases. When $Q_p/Q_d = -1$, there is no

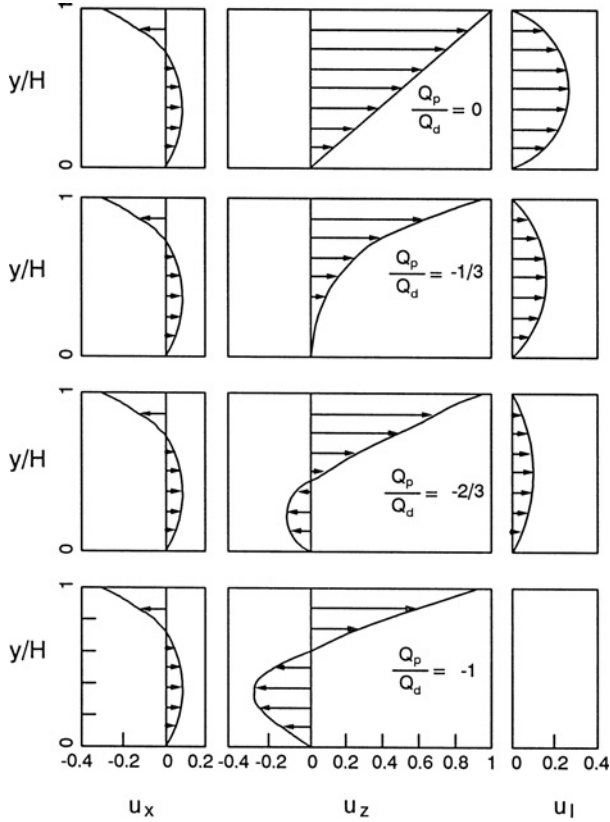


FIGURE 8.19 Velocity profiles for a Newtonian fluid in the screw channel for various operating conditions as determined by the ratio of pressure to drag flow. The cross-channel component is unaffected by the ratio Q_p/Q_d while the down channel and axial velocity components change significantly.

flow out of the extruder (this is known as closed discharge). It is u_x that keeps $v_l > 0$. It should be noted that under closed discharge conditions the residence time of the fluid is infinite and as one approaches open discharge conditions, the residence time is shortest.

The pressure buildup along the axial direction of the extruder is due to the resistance offered by the die and other elements such as connectors and filtration systems. Hence, the operation of the extruder is directly affected by the design of the die and connecting elements. To illustrate this we again consider the fluid to be Newtonian, and we consider only the metering section of the extruder. Furthermore, we assume that the die is a simple capillary, and we neglect any pressure losses due to contractions or expansions in the system. Using Eq. 8.99 we write the screw characteristic as

$$Q_s = \frac{1}{2}\pi D_b N \cos \bar{\phi} WH - \left(\frac{\Delta P_s}{L_b} \right) \frac{WH^3 \sin \bar{\phi}}{12\mu} \quad (8.103)$$

where Q_s is the volumetric flow rate in the extruder, ΔP_s is the pressure rise in the extruder, L is the extruder length,

and is the average helix angle. Referring to Table 2.6 we can write an expression for the circular die in the following form:

$$Q_D = \left(\frac{\pi R^4}{8L_D} \right) \frac{\Delta P_D}{\mu} = \frac{K_D \Delta P_D}{\mu} \quad (8.104)$$

where K_D is referred to as the die characteristic and Q_D and ΔP_D are the volumetric flow rate and pressure drop across the die, respectively. Because $Q_D = Q_s (=Q)$ and $|\Delta P_s| = |\Delta P_D| (= \Delta P)$, Eqs. 8.103 and 8.104 represent two equations with two unknowns. In this case they can be solved for ΔP and Q to give

$$Q = \frac{\frac{1}{2}\pi D_b N \cos \phi_b WH}{1 + (WH^3 \sin \bar{\phi}) / (12\mu L_b K_D)} \quad (8.105)$$

$$\Delta P = \frac{\frac{1}{2}\mu \pi D_b N \cos \phi_b WH}{K_D + (WH^3 \sin \bar{\phi}) / (12L)} \quad (8.106)$$

We remind you that Eqs. 8.105 and 8.106 are most likely of little quantitative use, and they serve only to illustrate the effect of the die on the operating conditions of the extruder. In practice, one would have to generate values of ΔP and Q numerically for both the extruder and the die, and then determine under what operating conditions the values are identical.

8.4 TWIN-SCREW EXTRUDERS

In this section we consider the essential features of two of the most common types of twin-screw extruders: self-wiping corotating (SWCOR) twin-screw extruders and closely intermeshing counterrotating (CICTR) twin-screw extruders. As discussed in Section 8.1.2, there are a vast number of types of twin-screw extruders, and it is not possible to discuss all of these here. Further discussion of the technology and theory for twin-screw extruders is given elsewhere (Rauwendaal, 1986; White, 1990).

8.4.1 Self-wiping Corotating Twin-Screw Extruders

We consider only the melt conveying section of the SWCOR type, because there are no theories available at present for describing the solids transport and melting zones. We first describe some general features of the flow regions in SWCOR types and then geometrical features that are required to understand the more quantitative aspects associated with flow.

SWCOR types have a closely matching flight profile as shown in Figure 8.20a. A cross section taken perpendicular to the screw axes (section A-A) as shown in Figure 8.20b illustrates how the flights of one screw wipe the surface of the other screw. The cross section shown in this figure is for a double-flighted screw. Because both screws are rotating in

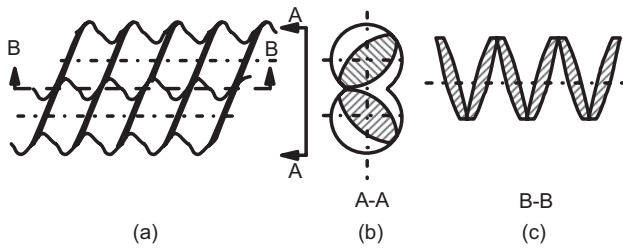


FIGURE 8.20 Self-wiping corotating twin-screw extruder. (a) Closely intermeshing double-flighted screw elements. (b) Section A–A showing the barrel and screw cross sections. (c) Section B–B showing the open region between the screw flights.

the same direction (e.g., counterclockwise in this case) the flight is seen to scrape the surface of the other screw pushing material over to the other screw. Hence, material travels in a figure-eight pattern in the extruder. By cutting a section B–B, which passes through the intermeshing region as shown in Figure 8.20c, we see that there is considerable open space between the adjacent channels. Hence, there is little pressure buildup in the intermeshing region. For this reason SWCOR types have nonpositive conveying characteristics and their operation is pressure sensitive in a manner somewhat similar to single-screw extruders.

To understand the melt conveying characteristics of SWCOR types we must first describe the geometry of SWCOR extruders. We consider the cross section perpendicular to the screw axis as shown in Figure 8.21 for double-flighted screws. The flight and channel geometry are determined by the screw diameter, D_b (note that this is actually $D_b - 2\delta_s$, but we will neglect flight clearance), the centerline distance, C_L , and the number of parallel flights, p . From Figure 8.21 it is easy to see that

$$C_L = D_b \cos \alpha_i \quad (8.107)$$

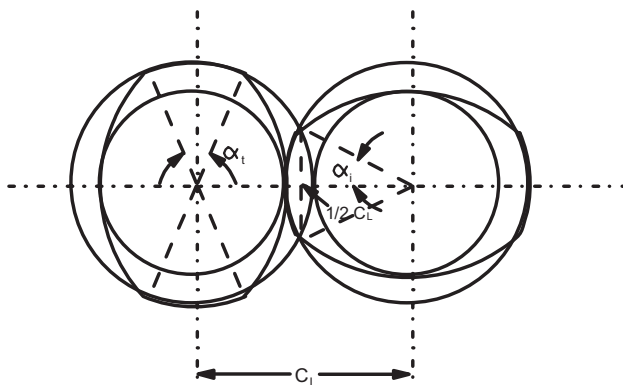


FIGURE 8.21 Cross section of a closely intermeshing twin-screw extruder with double-flighted screw elements (or paddle elements). The tip angle, α_t , the angle of intermesh, α_i , and the centerline distance are shown.

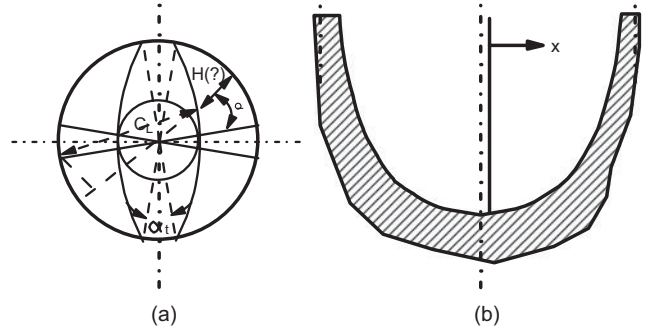


FIGURE 8.22 Channel depth for a double-flighted corotating self-wiping twin-screw extruder. (a) Channel depth as a function of circumferential angle. (b) Channel depth as a function of distance x across channel.

where α_i is one-half the angle of intermesh (i.e., the degree of overlap of the two barrels). α_i is found to be related to the tip angle, α_t , by the following relation:

$$\alpha_i = \pi/2p - \alpha_t/2 \quad (8.108)$$

This relation is not easy to determine from Figure 8.21, but one must consult the work of Booy (1978). We can now determine the channel depth as a function of the circumferential angle, θ . Referring to Figure 8.22 we find $H(\theta)$ to be

$$H(\theta) = \frac{D_b}{2}(1 + \cos \theta) - (C_L^2 - \frac{1}{4}D_b^2 \sin^2 \theta)^{1/2} \quad (8.109)$$

We can now find the cross-channel depth profile along the x direction (note that this is the same as for the single-screw extruder where z is taken along the helical path or down channel direction and x is taken along the channel width) by substituting in the following coordinate transformation:

$$x = \left(\frac{D_b}{2}\right)\theta \sin \phi \quad (8.110)$$

to give

$$H(x) = \frac{D_b}{2} \left[1 + \cos \left(\frac{2x}{D_b \sin \phi} \right) \right] - \left[C_L^2 - \frac{D_b^2}{4} \sin^2 \left(\frac{2x}{D_b \sin \phi} \right) \right] \quad (8.111)$$

The cross-channel depth profile is shown in Figure 8.22b, and it is seen that the channel is no longer rectangular as is the case for the single-screw extruder.

We next determine the open cross-sectional area between the barrel and the screw. This is done by finding the cross-sectional area of the barrel and subtracting the cross-sectional

area of the two screws. The cross-sectional area of the barrel is (Booy, 1978)

$$A_b = \frac{1}{2}(\pi - \alpha_i)D_b^2 + \frac{1}{2}C_L D_b \sin \alpha_i \quad (8.112)$$

For the double-flighted screw shown in Figure 8.21 this area is easily derivable. The cross-sectional area of one screw is (note that this is not easily derived nor seen by referring to Fig. 8.21, but one must consult the paper by Booy, 1978)

$$A_s = p\alpha_i C_L^2 - \frac{1}{2}pC_L D_b \sin \alpha_i + \frac{1}{2}p\alpha_i (C_L^2 + \frac{1}{2}D_b^2 - C_L D_b) \quad (8.113)$$

The open cross-sectional area between the barrel and screw is just the difference of the two expressions above (note that $2A_s$ must be used), which can be written as

$$A_0 = D_b^2 \left[\left(p - \frac{1}{2}\right)\alpha_i + \left(p + \frac{1}{2}\right)\sin \alpha_i \cos \alpha_i - \pi \cos^2 \alpha_i + (\pi - 2p\alpha_i)\cos \alpha_i \right] \quad (8.114)$$

This equation tells us that for a fixed barrel diameter the open area depends on the number of parallel flights and the angle of intermesh, α_i .

We are now in position to consider flow in screw elements. Because of the complicated channel geometry we only consider the isothermal flow of Newtonian fluids. The development here is for pedagogical purposes only and not for quantitative design work. To analyze the flow in SWCORs the flat plate model used for single-screw extruders is again used. The axes are attached to the screws again and because the channel depth is considered to be small relative to the curvature of the barrel, we use the flat model shown in Figure 8.23. (*Note:* Here we show the situation for a double-flighted screw.) However, the channel length is not the fully unwound channel length but merely the length of one turn. If the flight tip angle is small, then we can consider the flow between channels to be relatively unimpeded and hence neglect the excess

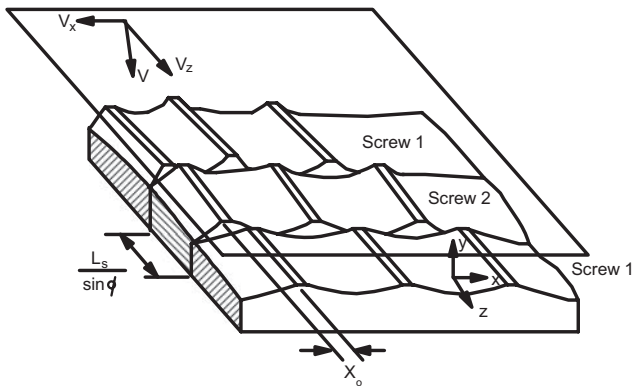


FIGURE 8.23 Flat plate model for the closely intermeshing self-wiping twin-screw extruder.

pressure drop in the intermeshing region. (Booy (1980) and Szydowski et al. (1987) show how to include the intermeshing region.) Assuming isothermal steady flow of a Newtonian fluid and considering the velocity components, v_z and v_x , to depend on y only, the equations of motion are

$$0 = -\frac{\partial p}{\partial z} + \mu \frac{\partial^2 v_z}{\partial y^2} \quad (8.115)$$

$$0 = -\frac{\partial p}{\partial x} + \mu \frac{\partial^2 v_x}{\partial y^2} \quad (8.116)$$

with boundary conditions

$$\begin{aligned} v_z(0) = 0, \quad v_z(H) = V_b \cos \phi \\ v_x(0) = 0, \quad v_x(H) = -V_b \sin \phi \end{aligned} \quad (8.117)$$

Equation 8.115 can be integrated to give the flow rate in one channel:

$$Q = \frac{1}{2}WHV_b \cos \phi - \frac{WH^3}{12\mu} \frac{\partial p}{\partial z} \quad (8.118)$$

According to Booy (1980), there are $(2p - 1)$ independent channels and hence Eq. 8.118 must be multiplied by $(2p - 1)$ to obtain the flow rate in the screw elements. In principle, the screw characteristic of fully filled screw channels of the SWCOR type resembles that of the single-screw extruder. The main differences are in the shape of the channel and when the tip angle becomes large leading to a large degree of intermeshing.

In most cases the SWCOR extruder is starve-fed, and hence the channel is only partially full. The output from the extruder is determined by means of the device feeding the extruder and not the extruder itself. Actually the degree of fill changes over the length of the extruder as the final length of the channel must be full if pressure is to be built up to pump the melt through a die. Over most of the section with regular screw elements there will be no pressure buildup. Sometimes reverse elements or kneading blocks are used as restrictive elements along the extruder.

The fairly simple development which follows is for pedagogical reasons and is due to Werner (1976). A partially filled screw channel is shown in Figure 8.24. The degree of fill is given by the ratio of the filled channel cross-sectional area, A_f , to the total cross-sectional area, A :

$$f = A_f / A \quad (8.119)$$

A is found by integrating Eq. 8.111 over the width of the channel and is

$$\begin{aligned} A = D_b^2 \left[\frac{1}{2}\alpha_i - \left(\alpha_i + \frac{1}{2}\alpha_i\right)\cos^2 \alpha_i \right. \\ \left. + \left(\frac{1}{2}\sin \alpha_i + \frac{1}{2}\alpha_i\right)\cos \alpha_i \right] \sin \phi \quad (8.120) \end{aligned}$$

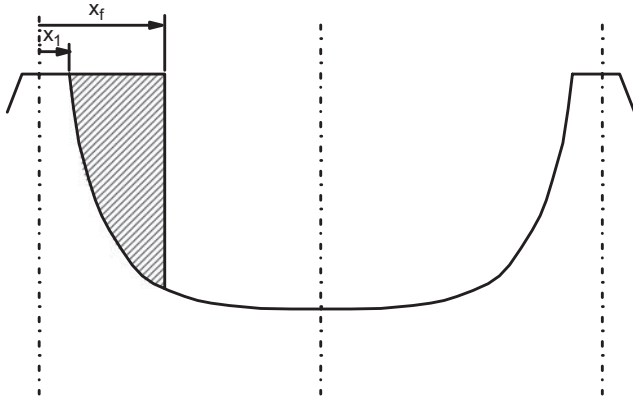


FIGURE 8.24 Partially filled screw channel. The fluid fills the channel up to a distance x_f .

A_f is found by integrating Eq. 8.111 from x_1 to the filled cross-channel distance, x_f :

$$A_f = \int_{x_1}^{x_f} H(x) dx \quad (8.121)$$

where $x_1 = 0.25 \alpha_t D_b \sin \phi$. For isothermal steady-state flow of a Newtonian fluid the equation of motion in the down channel direction is written as

$$\frac{\partial^2 v_z}{\partial x^2} + \frac{\partial^2 v_z}{\partial y^2} = 0 \quad (8.122)$$

By assuming that

$$\frac{\partial^2 v_z}{\partial x^2} \ll \frac{\partial^2 v_z}{\partial y^2} \quad (8.123)$$

then v_z becomes simply

$$v_z = y V_{bz} / H \quad (8.124)$$

The volumetric flow rate is obtained by integrating Eq. 8.124 over the cross section that is filled with fluid, and this is approximately

$$Q = \frac{1}{2}(2p - 1)A_f V_{bz} \quad (8.125)$$

Equation 8.125 can be written as follows using Eq. 8.119:

$$Q = \frac{1}{2}(2p - 1)f\pi D_b N \cos \phi \quad (8.126)$$

Thus, Q is directly proportional to the degree of fill and the screw speed, N . The cross-channel velocity profile, v_x , is

found in much the same way as it was done for the single-screw extruder and is

$$v_x = \frac{3V_{bx}y^2}{H^2} + \frac{4V_{bx}y}{H} + V_{bx} \quad (8.127)$$

Finally, we consider the flow in kneading blocks (see Fig. 8.8) as these are commonly used along with the screw elements. The kneading blocks or paddle elements are the heart of the SWCOR as melting and dispersing of additives occur here. The cross section of a two-lobed paddle element looks the same as that of a double-flighted screw element (see Fig. 8.21). White (1990) has attempted to model flow in paddle elements.

8.4.2 Intermeshing Counterrotating Extruders

The other frequently used twin-screw extruder is the closely intermeshing counterrotating (CICTR) type, which is shown in Figure 8.25. Looking along the axis of the screws from the right side of the figure, we see that the left screw is rotating in a counterclockwise direction and has a right-hand thread while the right screw rotates in a clockwise direction and has a left-hand thread. A cross section taken through the intermeshing region, which is shown in Figure 8.25b, reveals that there is very little opening between the channels of the two screws. Hence, these devices can achieve nearly positive conveying characteristics.

In theory CICTR extruders are positive conveying devices where the maximum possible flow rate is given by

$$Q_{\max} = 2pNV \quad (8.128)$$

where p is the number of parallel flights, N is the screw speed, and V is the volume of the closed C-shaped chamber as shown in Figure 8.26. The volume of the C-shaped chamber is approximately

$$V = \frac{\pi D_b H \bar{W}}{\cos \bar{\phi}} - \frac{\bar{w} D_b^2 (2\alpha_i - \sin 2\alpha_i)}{4 \cos \bar{\phi}} \quad (8.129)$$

where \bar{w} is the mean flight width given by

$$\bar{w} = w + H \tan \psi \quad (8.130)$$

and \bar{W} is the mean channel width given by

$$\bar{W} = \frac{\pi (D_b - \frac{1}{2}H) \sin \bar{\phi}}{p} - \bar{W} \quad (8.131)$$

ψ in Eq. 8.130 is the flight flank angle (i.e., the angle the sides of the flight makes with the line perpendicular to the channel surface).

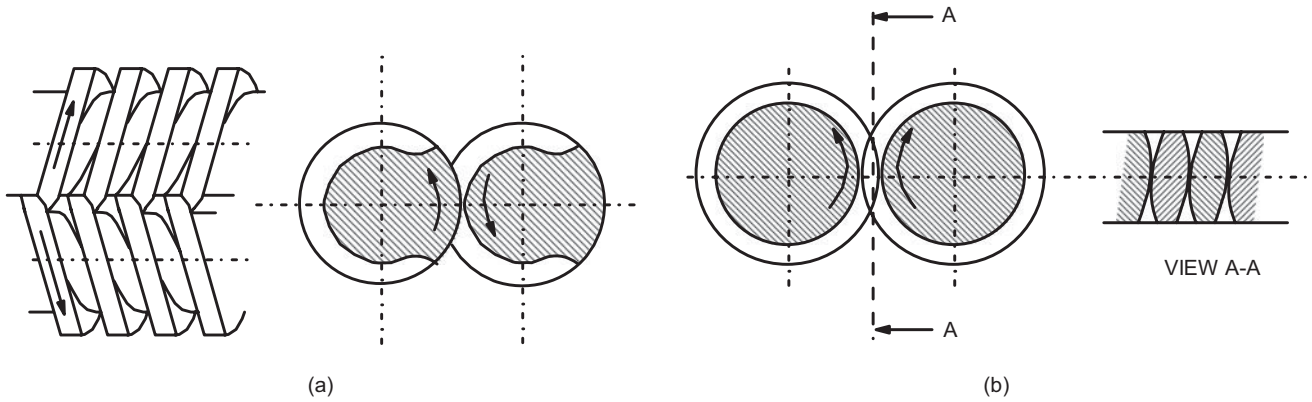


FIGURE 8.25 Closely intermeshing counterrotating twin-screw extruder. (a) Cross-sectional view (end view). (b) Cross-sectional view through flights showing open region.

In practice, the CICTR extruder is not a positive conveying device, and there are a number of places where leakage can occur. Janssen (1978) has identified four places where leakage occurs as shown in Figure 8.27:

1. Leakage through the gap between the flight and the barrel wall, which is called flight leakage, Q_f .
2. Leakage between the bottom of the channel of one screw and the flight of the other screw, which is called calender leakage, Q_c .
3. Leakage through the gap that goes from one screw to the other between the flanks of the flights of the two screws, which is referred to as leakage through the tetrahedron gap, Q_t .

4. Leakage through the gap between the flanks of the screws perpendicular to the plane through the screw axis, Q_s .

Quantitative estimates of each type of leakage are given by Janssen (1978) for Newtonian fluids. Since these derivations are rather lengthy and may be of marginal value for quantitative design work involving non-Newtonian fluids, they are not discussed here. The total output from the extruder is given by

$$Q = 2pNV - 2pQ_s - 2Q_f - Q_t \quad (8.132)$$

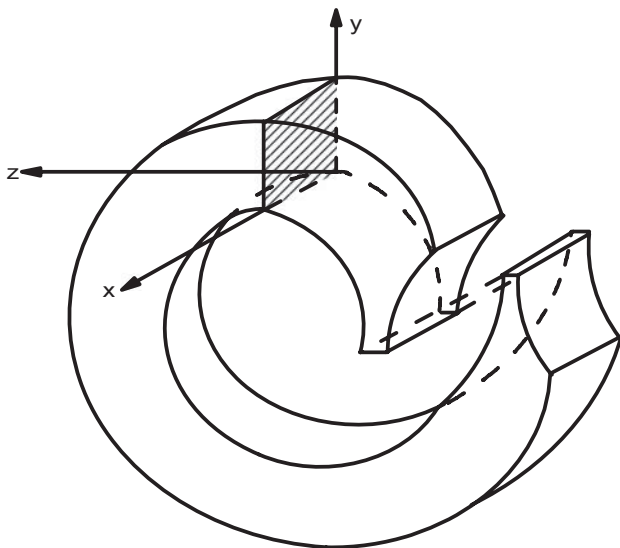


FIGURE 8.26 C-shaped chamber in a counterrotating closely intermeshing twin-screw extruder.

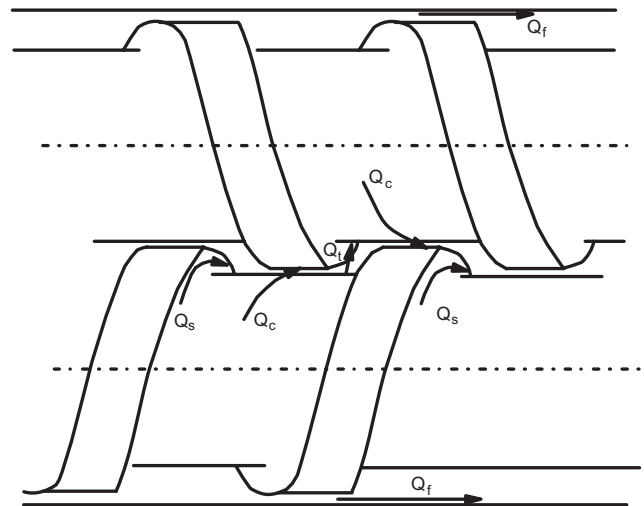


FIGURE 8.27 Leakage flows in a counterrotating closely intermeshing twin-screw extruder: Q_c , calendaring flow between screw flight and opposite screw root; Q_f , leakage flow between screw flight and barrel; Q_s , leakage flow between screw flight walls; Q_t , leakage flow in tetrahedron region between flights.

8.5 MIXING, DEVOLATILIZATION, AND REACTIONS IN EXTRUDERS

Extruders have other functions than the melting and pumping of polymers. In particular, they are used in mixing operations, in the removal of volatiles, and in the processing of reacting systems. Mixing operations involve primarily the blending of polymers and the dispersion of additives and fillers. Examples of devolatilization include the removal of monomers in the production of polymers, the removal of reaction products during condensation polymerization, and the removal of water from hygroscopic polymers. Applications of extruders as reactors are numerous and include condensation reactions (e.g., the generation of high molecular weight PETP), the peroxide degradation of polypropylene, and compatibilization of two polymers through the formation of graft copolymers. The basic elements of these processes are discussed here, and because of the complex nature of these processes we can only present the most elementary analyses.

8.5.1 Mixing

As discussed in Chapter 6, the quality of mixing is related to the increase in interfacial area, which is proportional to strain. The calculation of the average strain, $\bar{\gamma}$, requires the residence time distribution function, $f(t)$. We present the analysis for isothermal Newtonian flow in a single-screw extruder only, which is due to Pinto and Tadmor (1970). We give only a descriptive analysis for twin-screw extruders.

The analysis begins with the assumption that curvature is not important, and hence, one can use the parallel plate model to describe flow in the screw channel. The axial velocity profile was given in Eq. 8.102 and is reproduced here in the following form:

$$u_l = 3\xi(1 - \xi)[1 + \Phi'] \sin \phi \cos \phi \quad (8.133)$$

where $\Phi' = Q_p/Q_d$. The actual path of a fluid particle is quite complex as shown in Figure 8.28. The cross-channel velocity component, v_x , gives rise to a circulation pattern and because there is also a v_z component, the actual path of a particle in the channel is spiral in nature. The goal at this point is to determine how long a particle spends in the channel—that is, its residence time. Because of the circulatory nature of the cross flow being centered at $\xi = 2/3$, a fluid particle located here moves straight down the channel. All other particles move in a helical path. Particles located at $\xi > 2/3$ will turn over on reaching the flight and move in the opposite direction. However, the time spent moving across the channel for the particle located at a position $\xi > 2/3$ is less than the time it takes for the particle to move across the lower portion of the channel. Hence, it is necessary to use an average axial velocity, v_l , to calculate the residence time of a particle.

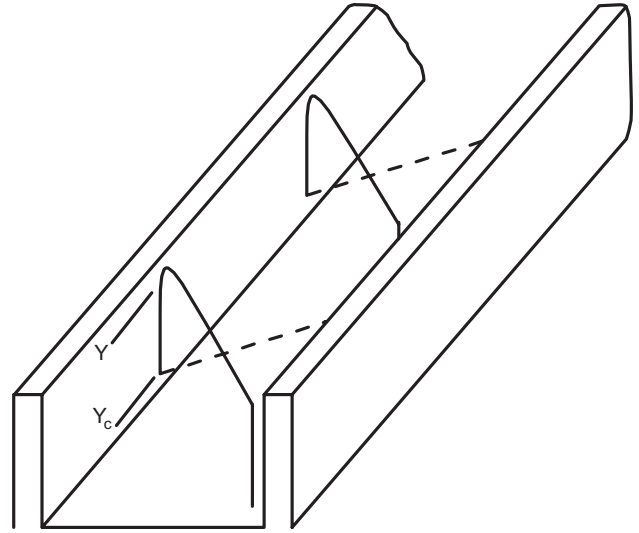


FIGURE 8.28 Spiral path of a fluid element in the channel of a single-screw extruder.

First, it is necessary to locate the position of the particle in the lower part of the channel, ξ_c , which had a position ξ in the upper portion of the channel (i.e., $\xi > 2/3$). Because the flow is circulatory in the x direction, the amount of fluid flowing between ξ and 1.0 (the wall) per unit width in the upper part of the channel must be equal to the amount of fluid flowing per unit width in the opposite direction between 0 and ξ_c in the lower portion of the channel. Mathematically this is given by

$$\int_0^{\xi_c} u_x d\xi + \int_{\xi}^1 u_x d\xi = 0 \quad (8.134)$$

which provides the relation between ξ and ξ_c . Substituting Eq. 8.98 into Eq. 8.134 gives the following expression:

$$\begin{aligned} \xi^2 - \xi^3 &= \xi_c^2 - \xi_c^3 \\ 0 \leq \xi_c \leq \frac{2}{3} \quad \frac{2}{3} \leq \xi \leq 1 \end{aligned} \quad (8.135)$$

A more convenient form for finding ξ_c in terms of ξ is

$$\xi_c = \frac{1 - \xi + \sqrt{1 + 2\xi - 3\xi^2}}{2} \quad (8.136)$$

The average axial velocity, \bar{v}_l , of a fluid particle which alternates its position between ξ and ξ_c , is given by the following equation:

$$\bar{v}_l = v_l(\xi) t_f + v_l(\xi_c)(1 - t_f) \quad (8.137)$$

where t_f is the fraction of time spent by a fluid particle in the upper portion of the channel, which is given by

$$t_f = \frac{1}{1 + u_x(\xi)/u_x(\xi_c)} \quad (8.138)$$

The residence time of a particle is equal to the length of the extruder (or metering section), L , divided by the \bar{v}_l . Substituting u_x from Eq. 8.98 and u_l from Eq. 8.133 into Eqs. 8.137 and 8.138, the residence time, t , becomes

$$t = \left[\frac{L}{3V_b \sin \phi \cos \phi (1 + \Phi')} \right] \times \left(\frac{3\xi - 1 + 3\sqrt{1 + 2\xi - 3\xi^2}}{\xi[1 - \xi + \sqrt{1 + 2\xi - 3\xi^2}]} \right) \quad (8.139)$$

Equation 8.139 represents the distribution of residence times of fluid particles as a function of their initial location in the channel. The minimum residence time occurs for particles located at $\xi = 2/3$ and t decreases as one moves toward the barrel or screw surfaces.

We next would like to know what fraction of the fluid leaving the extruder has a certain residence time. This is given by the residence time distribution function, $f(t)$, which was defined in Chapter 6. By definition $f(t)dt$ is the fraction of material leaving the extruder with a residence time between t and $t + dt$, which is

$$f(t)dt = \frac{dQ + dQ_c}{Q} \quad (8.140)$$

where dQ is the fraction of flow between ξ and $\xi + d\xi$ and dQ_c is the fraction of flow between ξ_c and $\xi_c + d\xi_c$ associated with the residence time t . dQ and dQ_c are given, respectively, by

$$dQ = WHV_{bz} \xi (1 + 3\Phi' - 3\xi\Phi') d\xi \quad (8.141)$$

$$dQ_c = WHV_{bz} \xi_c (1 + 3\Phi' - 3\xi_c\Phi') |d\xi_c| \quad (8.142)$$

where the absolute value sign in Eq. 8.142 was introduced to account for the change of direction of $d\xi$ with respect to $d\xi_c$. From Eq. 8.136 we find a relation between $d\xi_c$ and $d\xi$:

$$d\xi_c = \frac{1 - 3\xi - \sqrt{1 + 2\xi - 3\xi^2}}{2\sqrt{1 + 2\xi - 3\xi^2}} d\xi \quad (8.143)$$

Substituting Eqs. 8.136 and 8.143 into Eq. 8.140 and taking $d\xi_c = -d\xi$ leads to the following expression for $f(t)dt$:

$$f(t)dt = \frac{3\xi}{\sqrt{1 + 2\xi - 3\xi^2}} \left(1 - \xi + \sqrt{1 + 2\xi - 3\xi^2} \right) d\xi \quad (8.144)$$

Using Eq. 8.139, Eq. 8.144 can be written in the following form:

$$f(t)dt = \frac{9}{2} \frac{V_b \sin \phi \cos \phi (1 + \Phi')}{L} \times \left[\frac{\xi^3 (\xi - 1 - \sqrt{1 + 2\xi - 3\xi^2})}{(6\xi^2 - 4\xi - 1)\sqrt{1 + 2\xi - 3\xi^2} + 3\xi - 1} \right] dt \quad (8.145)$$

For simple geometries such as pipe flow discussed in Section 6.4 it was possible to solve for ξ in terms of t , which is not possible in this case using Eq. 8.139. Equations 8.145 and 8.139 must be solved together to calculate $f(t)$. What these two equations do indicate, however, is that $f(t)$ depends only on the group $V_b(1 + \Phi') \sin \phi \cos \phi / L$.

There are two residence time values of specific interest, and these are the mean residence time, \bar{t} , and the shortest residence time, t_0 . The mean residence time was defined in Eq. 6.117 and for the single-screw extruder (i.e., metering section or melt pump) is

$$\bar{t} = 2L / V_b \sin \phi \cos \phi (1 + \Phi') \quad (8.146)$$

\bar{t} is also given by the volume of the channel ($WHL/\sin \phi$) divided by the volumetric flow rate. The minimum residence time, t_0 , is obtained from Eq. 8.139 with $\xi = 2/3$ and is equal to $3\bar{t}/4$.

The cumulative residence time distribution, RTD, function, $F(t)$, is found by integrating Eq. 8.144 from $\xi = 2/3$ (this is t_0) to ξ (this is t):

$$F(t) = F(\xi) = \frac{1}{2} \left[3\xi^2 - 1 + (\xi - 1)\sqrt{1 + 2\xi - 3\xi^2} \right] \quad (8.147)$$

$F(t)$ is plotted versus reduced time, t/\bar{t} , in Figure 8.29, where we also compare $F(t)$ against values for plug flow, laminar flow in a pipe, and a continuous stirred tank reactor. $F(t)$ is seen to lie between plug and laminar flow in pipes. $F(t)$ for the extruder is rather narrow with no long tails.

We next obtain the strain distribution in the metering section of the extruder following the work of Pinto and Tadmor (1970). The shear rate in the upper portion of the channel is

$$\dot{\gamma} = [\dot{\gamma}_{yx}(\xi) + \dot{\gamma}_{yz}(\xi)]^{1/2} \quad (8.148)$$

Using Eqs. 8.95 and 8.96 we find $\dot{\gamma}_{yx}$ and $\dot{\gamma}_{yz}$ to be

$$\dot{\gamma}_{yx} = 2V_{bx}(1 - 3\xi)/H \quad (8.149)$$

$$\dot{\gamma}_{yz} = V_{bz}[1 + 3\Phi'(1 - 2\xi)]/H \quad (8.150)$$

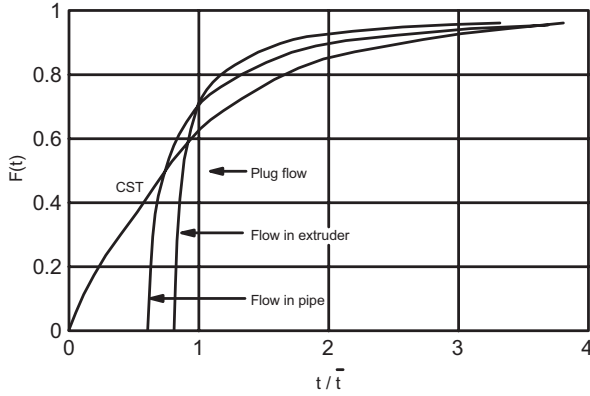


FIGURE 8.29 Cumulative residence time distribution function versus reduced time for flow in an extruder, plug flow, flow of a Newtonian fluid in a pipe, and a continuously stirred tank (CST) vessel.

In the upper portion of the channel we find

$$\dot{\gamma} = V_b R(\xi) / H \quad (8.151)$$

where

$$R(\xi) = [4(1 - 3\xi)^2 \sin^2 \phi + (1 + 3\Phi' - 6\xi\Phi')^2 \cos^2 \phi]^{1/2} \quad (8.152)$$

and in the lower portion of the channel it will be

$$\dot{\gamma}_c = V_b R(\xi_c) / H \quad (8.153)$$

where

$$R(\xi_c) = [4(1 - 3\xi_c)^2 \sin^2 \phi - (1 + 3\Phi' - 6\xi_c\Phi')^2 \cos^2 \phi]^{1/2} \quad (8.154)$$

The average total strain of a fluid particle alternating between the two portions of the channel is

$$\bar{\gamma} = \dot{\gamma} t_f t + \dot{\gamma}_c (1 - t_f) t \quad (8.155)$$

Combining Eqs. 8.139, 8.151, 8.153, and 8.155 leads to

$$\bar{\gamma} = \frac{1}{3} \left(\frac{L}{H} \right) \left(\frac{1}{1 + \Phi'} \right) \left[\frac{2F(\xi, \Phi')}{\cos \phi} + \frac{G(\xi_c, \Phi')}{\sin \phi} \right] \quad (8.156)$$

where

$$F(\xi, \Phi') = \frac{t_f \left[(1 - 3\xi)^2 + \frac{\cotan^2 \phi}{4} (1 + 3\Phi' - 6\xi\Phi')^2 \right]^{1/2}}{\xi_c (1 - \xi_c) + t_f (\xi - \xi_c) (1 - \xi - \xi_c)} \quad (8.157)$$

and

$$G(\xi, \Phi') = \frac{(1 - t_f) [4(1 - 3\xi_c)^2 \tan^2 \phi + (1 + 3\Phi' - 6\xi\Phi')^2]^{1/2}}{\xi_c (1 - \xi_c) + t_f (\xi - \xi_c) (1 - \xi - \xi_c)} \quad (8.158)$$

We are now in position to discuss mixing in the single-screw extruder. The weighted average total strain (WATS) has been proposed by Pinto and Tadmor (1970) to be a measure of mixing in the extruder. WATS was defined in Eq. 6.141, and its calculation requires both $f(t)$ and the strain distribution (Eq. 8.158). WATS is a measure of the total deformation experienced by the material leaving the extruder. It is a single number for a given extruder set at specific operating conditions, and it gives a quantitative measure of the quality of mixing.

It is apparent that WATS depends on three parameters: L/H , the helix angle, ϕ , and the pressure to drag flow ratio, Φ' . Calculations by Pinto and Tadmor (1970) showed that over practical ranges of values for ϕ and Φ' , WATS was not very sensitive to these parameters. Hence, in the metering section of an extruder the most important parameter affecting mixing is the L/H ratio.

Bigg and Middleman (1974) carried out a similar analysis for non-Newtonian fluids using the power-law model. As there are no analytical results available, we only summarize a few of the most pertinent findings. In Figure 8.30 is presented the cumulative distribution function, $F(t)$, versus the reduced time for various values of the power-law index, n , and for a fixed value of $\Phi' = -0.88$. Here it is seen that for values of $n \geq 0.4$ the shape of $F(t)$ is similar (i.e., the $F(t)$ curves for a Newtonian fluid and a power-law fluid with a

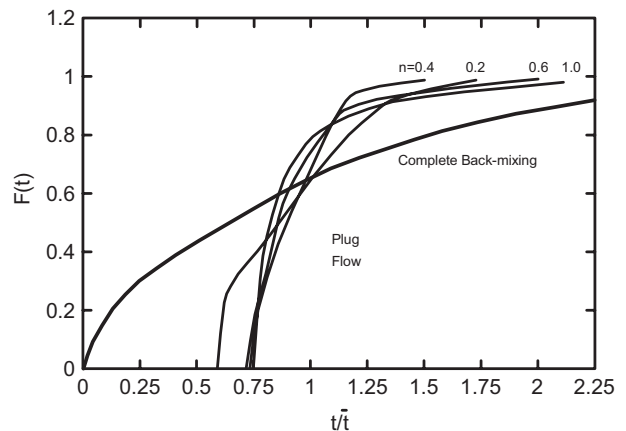


FIGURE 8.30 Cumulative residence time distribution function versus reduced time in an extruder for fluids with various values of the power-law index and compared to values for plug flow and complete back-mixing continuous stirred tank reactor (Bigg and Middleman, 1974).

value of $n \geq 0.4$ are similar for $\Phi' = -0.88$). For a highly shear-thinning fluid, $F(t)$ becomes broader, approaching that of the curve for the well mixed state. The shape of the $F(t)$ curve was found to be sensitive to the value of Φ' .

The analyses carried out by Pinto and Tadmor (1970) for Newtonian fluids and by Bigg and Middleman (1974) for power-law fluids were for the metering section of a single-screw extruder or for the single-screw melt pump only. More frequently, plasticating extruders are used, and mixing probably starts in the melting zone. There are apparently no models available at the time of writing which deal with mixing in the melting zone.

Mixing in twin-screw extruders is much more difficult to estimate because of the complex flow patterns. For intermeshing corotating twin-screw extruders, Montes and White (1991) have developed a model to describe mixing. The model of mixing in the screw elements follows the work of Pinto and Tadmor (1970) for a single-screw extruder. The strains generated in each screw element are added together to get the total strain. The major part of the mixing occurs in the kneading blocks. To analyze mixing here the velocity profiles are needed, and these can only be calculated numerically for power-law fluids. There is no experimental evidence to support the calculations of Montes and White (1991), and hence, it is not known whether their approach is adequate to describe mixing in intermeshing corotating twin-screw extruders. There is apparently no adequate model to describe mixing in intermeshing counterrotating extruders either. Potente and Schultheis (1989) described $F(t)$ in this type of extruder by a distribution function (a double Weibull distribution), which required fitting to experimental data to obtain the constants in the model. The function was based on knowing the minimum and mean residence times. t_{oi} per chamber is given by

$$t_{oi} = \frac{L_i}{V_i} = \frac{L_i}{N\pi D_b \tan \phi_i} \quad (8.159)$$

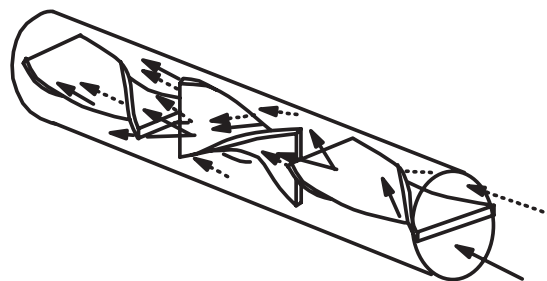


FIGURE 8.31 Flow in a Kenics static mixer. The mixer consists of a pipe with helical elements of alternating reverse pitches.

where L_i is the length of the C-shaped chamber and V_i is the axial velocity. t_o results from adding the values of t_{oi} in each chamber. The mean residence time, \bar{t} , is just the ratio V/Q , where V is the volume of the screw channels. The only certain conclusion is that in general $F(t)$ for twin-screw extruders is narrower than that for single-screw extruders.

Before leaving this section a few comments about static mixers will be made. In order to improve distributive mixing and to provide melt streams with more uniform temperature distribution, especially for single-screw extruders, static mixers are placed between the end of the extruder and the die. Static mixers consist of a pipe with nonmoving elements, which lead to a rearrangement and distribution of fluid elements. For example, a Kenics static mixer is shown in Figure 8.31. It consists of helical elements that are turned 90° relative to each other with each element having alternating pitch. Fluid entering the element near the center is distributed to the wall and fluid entering near the wall is distributed toward the center. A stream entering the first element is split into two streams. The two streams are split into four streams and so on. This is illustrated in Figure 8.32 where two streams enter the first element, and then they are split into four streams in the second element. In general, the

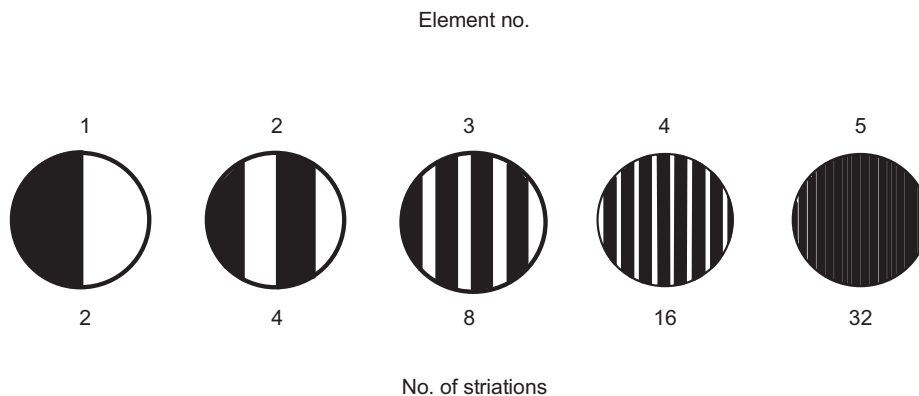


FIGURE 8.32 Illustration of how fluid streams are split and separated in a Kenics static mixer. After passing through five elements there are 32 layers of fluid.

number of striations, N_δ , at the exit of a pipe containing N elements is

$$N_\delta = 2^N \quad (8.160)$$

There are quite a few different types of static mixers (see Rauwendaal, 1986), but they all serve the same function.

The flow patterns in static mixers are very complex and only finite element methods can be used to analyze the details of these flows. The shear rates generated in these devices are rather low (on the order of 10 s^{-1}), and hence, the pressure drop across the static mixer can be estimated from the expression for flow of a Newtonian fluid through a tube with a correction factor for the given geometry as

$$\Delta P = (4/\pi)N_s \mu Q L/D \quad (8.161)$$

where $N_s = 220$ for the Kenics static mixer (see Rauwendaal, 1986, for this and other values) and L and D are the total length and diameter of the pipe containing the mixing elements.

8.5.2 Devolatilization in Extruders

The removal of volatiles such as water or residual monomer can be carried out in both single- and twin-screw extruders. In the case of single-screw extruders, specialized screw designs are required whereas for twin-screw extruders the flexible nature of their design allows the appropriate elements to be added. In the case of the single-screw extruder either an extra long extruder is required having a design as shown in Figure 8.33, or two extruders in a cascade arrangement are used. The general screw design shown in Figure 8.33 consists of a standard plasticating screw design followed by a section possessing a deep channel and a vacuum port and then a metering section. Because the pumping capacity of the section with the deep channel is less than that of the last metering section (section 3 in Fig. 8.33), the channel will not be full. For a single-flighted screw as shown in Figure 8.33 there are a rotating melt pool and a polymer melt film from which volatiles can be removed. The driving force for the diffusion of volatiles from the pool and film is a concentration gradient set up by reducing the surface concentration of the volatile to that of the equilibrium concentration, C_e , which is determined by Henry's law. There is also the possibility that additional mass transfer occurs by the generation of bubbles in the rotating melt pool. In the case of twin screws starve-feeding of the screw elements is accomplished by the addition of paddle elements or reverse screw elements. Because of certain geometric limits only double-flighted screw elements can be used in twin-screw systems. When this is done, there are three melt pools generated as shown in Figure 8.34. To generate a similar number of melt pools in a single-screw extruder, a triple-flighted screw is required as shown in

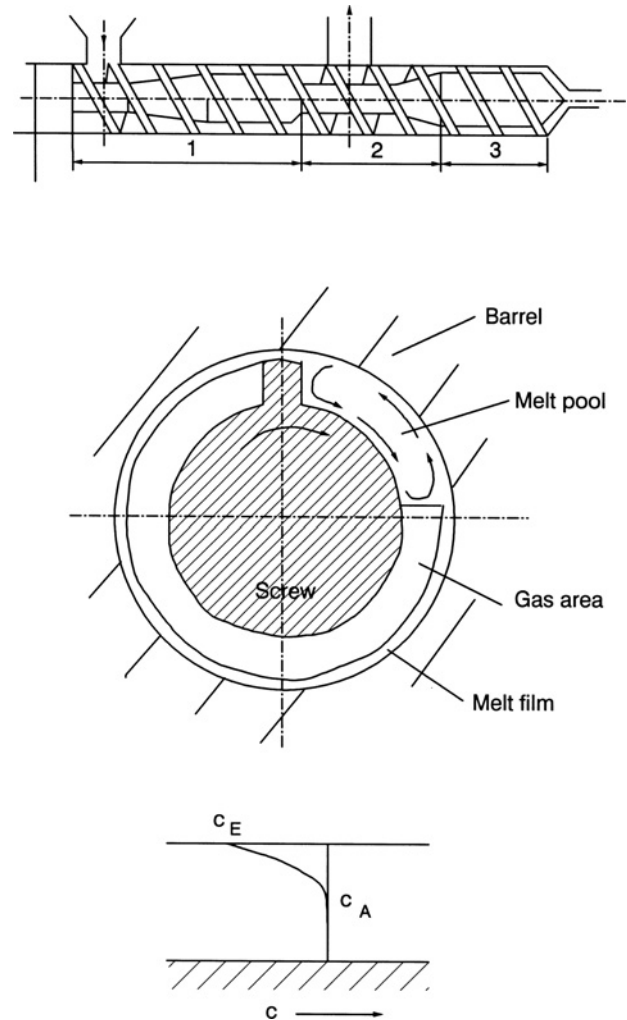


FIGURE 8.33 Degassing in a single-screw extruder. Zone 1 consists of a typical plasticating screw section; zone 2 is a deep channel section with a vacuum port; zone 3 is a metering section. The channels in zone 2 are partially full to facilitate degassing.

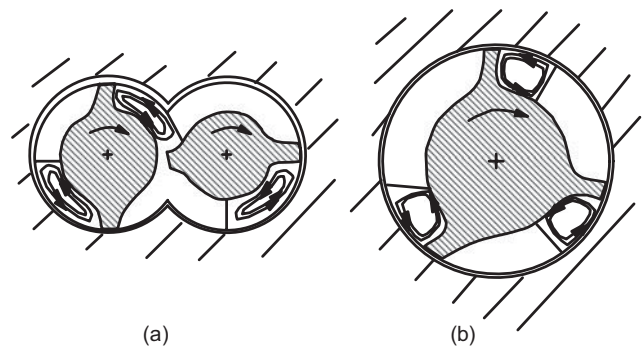


FIGURE 8.34 Cross-sectional views of (a) a double-flighted twin-screw extruder and (b) a triple-flighted single-screw extruder. Each system exhibits three melt pools which are available for degassing.

Figure 8.34b. In principle, the process of removing volatiles is similar in both single- and twin-screw extruders.

The few models available concerned with devolatilization (DV) in single-screw extruders are based on diffusion theory (Biesenberger and Sebastian, 1983). Experimental data available suggest that the process is more rapid than can be accounted for by diffusion alone. However, a summary of the model is useful, because at least the most important variables are brought out.

It is postulated that DV in single-screw extruders occurs by two mechanisms (Roberts, 1970). One is evaporation from the bulk polymer melt flowing in the partially filled screw channel, and the other is evaporation from the film that is generated by the clearance between the flight and barrel as the flight wipes over the barrel surface. The melt in the channel is viewed as an evaporating melt pool that rotates as it flows owing to the angle of drag, ϕ . These mechanisms are shown in Figure 8.35.

The goal of a model for DV is to calculate the concentration of the volatile, C_A , as a function of distance down the channel. Referring to Figure 8.35 a mass balance is performed on the element of thickness Δz . The contributions of mass to this element are from the transport of A by bulk flow, the loss of A by evaporation at the film surface, $E_f(z)$, and by evaporation at the surface of the pool, $\dot{E}_p(z)$, where the dot denotes the rate of evaporation. Mathematically this mass balance is

$$0 = fWH[N_A|_z - N_A|_{z+\Delta z}] - \dot{E}_p(z) - \dot{E}_f(z) \quad (8.162)$$

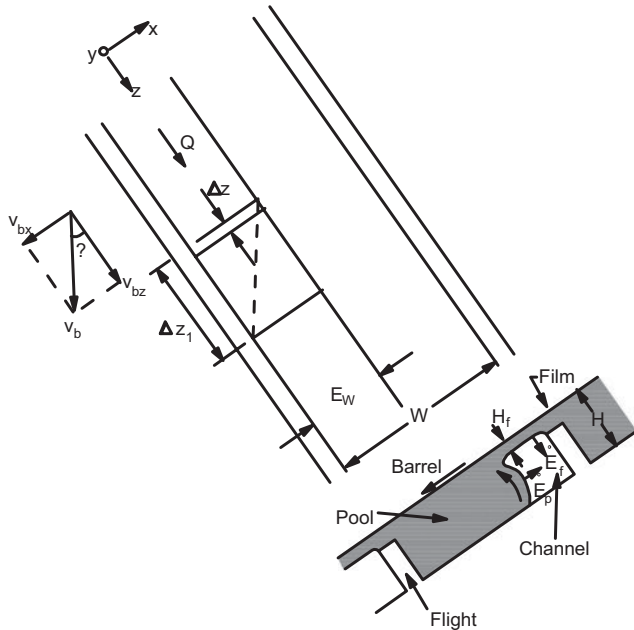


FIGURE 8.35 Model for devolatilization in extruders. Gas removal occurs from the melt film on the barrel wall and from the rotating melt pool.

$\dot{E}_p(z)$ is obtained by methods described in Chapter 4 (in particular, the derivation is similar to that in Example 4.5 but with gas diffusing out of the film) and Eq. 8.162 becomes

$$0 = fWH[N_A|_z - N_A|_{z+\Delta z}] - V_{bx} H_f \Delta z [C_A - C'_A] - \left(\frac{4D_A}{\pi t_p} \right)^{1/2} [C_A - C_{Ae}] \quad (8.163)$$

where C_{Ae} is the equilibrium concentration at the vapor–melt interface, H_f is the film thickness, and t_p is the exposure time of the melt pool surface, which is limited by the circular motion of the pool. Roberts (1970) estimated this exposure time as

$$t_p = H/V_{bx} \quad (8.164)$$

The evaporation rate of A from the film is obtained from a mass balance on the film, which is

$$\dot{E}_f(z) = V_{bx} H_f \Delta z [C_A(z) - C'_A(z)] \quad (8.165)$$

where C'_A is the concentration of A in the melt reentering the melt pool having left the melt pool at a distance of Δz_1 downstream (see Fig. 8.35). Dividing Eq. 8.163 by Δz and taking the limit as $\Delta z \rightarrow 0$, we obtain

$$fWH \frac{dN_{Az}}{dz} = V_{bx} H_f [C_A(z) - C'_A(z)] + \left(\frac{4D_A}{\pi t_p} \right)^{1/2} H [C_A(z) - C_{Ae}] \quad (8.166)$$

We next must relate C'_A to the concentration at $z + \Delta z_1$, $C_A(z + \Delta z_1)$, where this is the concentration of A in the melt leaving the melt pool at a distance $z + \Delta z_1$ downstream minus the amount of the volatile lost through evaporation during the exposure time $t_f = (1 - f)/N$, where N is the screw speed. This relation is obtained through the staged efficiency of the diffusing film, X_f :

$$X_f = \frac{C_A(z + \Delta z_1) - C'_A(z)}{C_A(z + \Delta z_1) - C_{Ae}} \quad (8.167)$$

Following Roberts (1970), $C_A(z + \Delta z_1)$ can be related to $C_A(z)$ by means of a Taylor series in which only terms through second order are kept:

$$C_A(z + \Delta z_1) = C_A(z) + \frac{dC_A(z)}{dz} \Delta z_1 + \frac{d^2 C_A(z)}{dz^2} \frac{\Delta z_1^2}{2} + \dots \quad (8.168)$$

After eliminating $C_A(z + \Delta z_1)$ from Eqs. 8.167 and 8.168 and substituting the result for C'_A into the mass balance

(Eq. 8.166) and replacing N_{Az} by $C_A v_z$, we obtain

$$V_{bx} H_f (1 - X_f) \frac{\Delta z_1^2}{2} \frac{d^2 C_A}{dz^2} + [V_{bx} H_f (1 - X_f) \Delta z_1 - Q] \frac{dC_A}{dz} - [X_f V_{bx} H_f + k_p H] (C_A - C_{Ae}) = 0 \quad (8.169)$$

Equation 8.169 can be written in dimensionless form as

$$\frac{1}{Pe} \frac{d^2 C_A^*}{d\xi^2} - \frac{dC_A^*}{d\xi} - E_x C_A^* = 0 \quad (8.170)$$

where

$$\xi = z/L_e \quad \Delta z_1^* = \Delta z_1/L_e \quad (8.171)$$

and

$$Pe = \left(\frac{2}{\Delta z_1^*} \right) \left[\frac{1}{n_f (1 - X_f) \Delta z_1^*} - 1 \right] \quad (8.172)$$

and

$$E_x = \frac{n_f X_f + k_p H L_e / Q}{1 - n_f (1 - X_f) \Delta z_1^*} \quad (8.173)$$

and

$$n_f = \frac{V_{bx} H_f L_e}{Q} \quad C_A^* = \frac{C_A - C_{Ae}}{C_{A0} - C_{Ae}} \quad (8.174)$$

L_e is the unwound channel length of the devolatilization section.

The Peclet number, Pe , represents the effect of backmixing generated by the film which reenters the melt pool. When $Pe \gg 1$, the effects of backmixing can be neglected. The effect of backmixing is determined directly by the magnitude of Δz_1 . As can be seen in Figure 8.35, Δz_1 is related directly to the degree of fill, f , the channel width, W , and the helix angle, ϕ :

$$\Delta z_1 = \frac{fW}{\tan \phi} = f\pi D_b \cos \phi \quad (8.175)$$

The second equality in the above equation is correct for single-flighted screws and negligible flight widths. Hence, backmixing increases with the degree of fill and decreasing values of ϕ . E_x is the extraction number, and it is a measure of the overall devolatilization efficiency.

If the backmixing effect can be neglected, then Eq. 8.169 becomes

$$\frac{dC_A^*}{d\xi} = E_x C_A^* \quad (8.176)$$

With $C_A^*(0) = 1$, the concentration profile becomes

$$C_A^* = \exp[-E_x \xi] \quad (8.177)$$

where E_x reduces to $n_f X_f + k_p H L_e / Q$. Hence, the concentration of the volatile is an exponential function of distance.

Finally, the devolatilization efficiency of the machine, X_T , is a function of the individual stage efficiency, X , and the extent of surface renewal. In the extruder, the extent of surface renewal is described by n_f in Eq. 8.174. The film stage efficiency, X_f , is a function of the surface-to-volume ratio and the exposure time, t_f . In general X_f is a function of n_f and the ratio t_f/t_D , where t_D is the residence time in the devolatilization section of the extruder.

The model developed here is based on diffusion. However, in many cases the length required to reduce the concentration of a volatile below some specified value is overpredicted. Hence, it is believed that the formation of bubbles or foam accelerates the devolatilization process. There is no model available at the time of writing this book which deals with foam DV.

The process of DV in corotating twin-screw extruders is similar to that in the single-screw extruder. However, no detailed mathematical model for DV in these devices is available.

8.5.3 Reactive Extrusion

There are numerous examples of the use of extruders to carry out chemical reactions in polymeric systems (Xanthos, 1992). In general, two types of reactions are carried out in extruders: polymerization or depolymerization and polymer modification. In this section we illustrate the approach to modeling reactive extrusion by considering the stepwise polycondensation reaction of two species A and B in a single-screw extruder.

The starting point for the analysis is the flat plate model of the extruder shown in Figure 8.18. It is assumed that steady-state conditions exist and that the material properties such as viscosity, thermal conductivity, and heat capacity do not depend significantly on temperature. It is postulated that

$$v_z = v_z(y) \quad v_x = v_x(y) \quad T = T(y, z) \quad C_A = C_A(z) \quad (8.178)$$

The equation of motion becomes

$$\frac{\partial p}{\partial x} = -\frac{\partial}{\partial y} \left(\eta \frac{\partial v_x}{\partial y} \right) \quad \frac{\partial p}{\partial z} = -\frac{\partial}{\partial y} \left(\eta \frac{\partial v_z}{\partial y} \right) \quad (8.179)$$

The energy equation takes on the following form:

$$\rho \bar{C}_p v_z \frac{\partial T}{\partial z} = k \frac{\partial^2 T}{\partial y^2} + \eta \left[\left(\frac{\partial v_x}{\partial y} \right)^2 + \left(\frac{\partial v_z}{\partial y} \right)^2 \right] + \dot{S}_r \quad (8.180)$$

where \dot{S}_r is the energy generated per unit volume per unit time by the reacting system. The conservation of mass equation for species A is

$$v_z \frac{dC_A}{dz} = R_A \quad (8.181)$$

where R_A is the rate at which species A disappears as the result of the reaction of A and B.

The rate of reaction, R_A , is given by the rate at which species A disappears and is assumed to follow n th-order reaction kinetics given by

$$R_A = -k_0 \exp(-E/RT) C_A^n \quad (8.182)$$

where k_0 and E are the reaction rate at the reference temperature and the activation energy, respectively. The heat generated by the reaction is given by

$$\dot{S}_r = (-\Delta \bar{H}_A) R_A \quad (8.183)$$

where $\Delta \bar{H}_A$ is the heat of reaction.

As the two species react the molecular weight of the product increases, leading to an increase in the viscosity of the bulk material. For the polycondensation reaction of species A and B, the weight average molecular weight as a function of the degree of conversion, p , is (Macosko and Miller, 1976)

$$\bar{M}_w = \frac{[r(1+rC^2)M_{A0}^2 + (1+rC^2)M_{B0}^2 + 4rC M_{A0}M_{B0}]}{(rM_{A0} + M_{B0})(1-rC^2)} \quad (8.184)$$

where $C = (C_{A0} - C_A)/C_{A0}$, r is the stoichiometric ratio of species A and B, and M_{A0} and M_{B0} are the initial molecular weights of species A and B, respectively. As a result of the increase in \bar{M}_w the viscosity of the melt is changing as it progresses down the channel. The zero shear viscosity increases with increasing \bar{M}_w in the following manner as described in Chapter 3:

$$\eta_0 = \eta_{CR} \bar{M}_w / M_{CR}, \quad \bar{M}_w \leq M_{CR} \quad (8.185)$$

$$\eta_0 = \eta_{CR} (\bar{M}_w / M_{CR})^{3.4}, \quad \bar{M}_w > M_{CR} \quad (8.186)$$

where M_{CR} is the critical entanglement molecular weight for the given polymer and η_{CR} is the zero shear viscosity at M_{CR} .

The initial and boundary conditions required to solve Eqs. 8.179, 8.180, and 8.181 are similar to those used in Section 8.3 with the exception that the concentration of species A at $z = 0$ is C_{A0} . The solution of this set of equations requires numerical methods, but a direct finite difference solution is not possible because of the velocity field changing signs near the surface of the screw. To overcome this problem the space-fixed coordinate system is replaced by one that travels along the streamlines. Neglecting the viscous dissipation terms, Eqs. 8.180 and 1.181 become, respectively,

$$\rho \bar{C}_p \frac{\partial T}{\partial t^*} = k \frac{\partial^2 T}{\partial y^2} + \dot{S}_r \quad (8.187)$$

$$\frac{\partial C_A}{\partial t^*} = R_A \quad (8.188)$$

where t^* is the residence time of a fluid element along a streamline. The numerical algorithm required to solve these equations is describe in the paper by Tzoganakis and co-workers (1988).

8.6 SOLUTION TO DESIGN PROBLEM VII

The solution is carried out by two methods. Because of the modular nature of twin-screw extruders, experiments were carried out in advance to determine what length of devolatilization section was required to reduce the level of MMA to 0.1%, which corresponds to a fractional separation, F_s , of about 0.85. Because the single-screw extruder is cheaper to build, it is desirable to determine the length of the DV section and the processing conditions (i.e., ρQ , N , and f) required to accomplish the same reduction of MMA in PMMA as done in the SWCOR extruder. The first approach is based on dimensional analysis. In the second approach we use the penetration or diffusion theory summarized in Section 8.5.2.

8.6.1 Dimensional Analysis

The starting point is to make sure that sufficient vacuum is available such that the equilibrium weight fraction, w_e , is less than the desired final weight fraction. From Henry's law and the data given in Table 8.2, we calculate w_e at 250 °C to be

$$w_e = \frac{P}{S'} = \frac{133.3 \text{ Pa}}{164 \times 10^5 \text{ Pa}} = 81 \times 10^{-6} = 8.0 \text{ ppm}$$

while at 200 °C $w_e = 20.4$ ppm. Hence, sufficient vacuum is available to reduce the level of MMA below 1000 ppm.

Dimensional analysis requires that both extruders be geometrically and dynamically similar. To ensure geometric

similarity it is necessary that the length to diameter of the devolatilization (DV) sections be the same:

$$L_{b1}/D_{b1} = L_{b2}/D_{b2} \quad (8.189)$$

where the subscripts 1 and 2 refer to the single- and twin-screw systems, respectively. Furthermore, because double-flighted screw elements are used in the twin-screw extruder, there are three independent flow channels partially filled each with melt pools. Hence, the single screw must be made triple flighted to produce the same number of melt pools. Dynamic similarity is much more difficult to determine, because it is not clear what mechanisms are important in devolatilization. Based on experimental studies, Biesenberger and co-workers (1990) found that mass transfer in the DV process in extruders occurs primarily by flash evaporation in which foam formation and rupture are enhanced by rotational motion of the melt in the partially filled channel. Based on their observations, they proposed that the pool size and rotational speed are the factors on which dynamic similarity should be based. With this they proposed that the main dimensionless group should be the ratio

$$\bar{t}/t_p \quad (8.190)$$

where \bar{t} is the mean residence time and t_p is the time of rotation of the pool. Hence, the fractional separation, F_s , should be expressed as

$$F_s = F_s(L_b/D_b, \bar{t}/t_p) \quad (8.191)$$

The ratio \bar{t}/t_p represents the number of devolatilization stages (N_s) available during the extrusion process.

We first use the condition of geometric similarity to find the length of the DV section:

$$L_{b1} = D_{b1}(L_{b2}/D_{b2}) = 30(300/34) = 265.0 \text{ mm}$$

The calculation of \bar{t}_1/t_{p1} and \bar{t}_2/t_{p2} requires some additional manipulations for the single-screw extruder. The mean residence time in the DV section of the single-screw extruder is

$$\bar{t}_1 = L_{e1}/\langle v_{z1} \rangle \quad (8.192)$$

where L_{e1} is the length of the unwound screw channel and is given by

$$L_{e1} = L_{b1}/\sin \phi_1 \quad (8.193)$$

$\langle v_{z1} \rangle$ is the average velocity in the down channel direction and is approximately

$$\langle v_{z1} \rangle \approx (\pi D_b N/2) \cos \phi \quad (8.194)$$

because the velocity profile in the down channel direction is not known exactly in the partially filled channel. t_p is approximated by

$$t_{p1} = \frac{(f_1 A_1)^{1/2}}{\langle v_{x1} \rangle} = \frac{(f_1 A_1)^{1/2}}{(\pi D_{b1} N_1/2) \sin \phi_1} \quad (8.195)$$

where A_1 is the cross-sectional area of the screw channel and f is the degree of fill. Hence, for the single-screw extruder:

$$N_{s1} = \frac{\bar{t}_1}{t_{p1}} = \frac{L_{b1}}{(f_1 A_1)^{1/2} \cos \phi_1}$$

For the twin-screw extruder the calculations of N_{s2} are more complicated because of the complex geometry. The flow path for PMMA is shown in Figure 8.2. For the single-screw extruder in covering a circumferential distance of πD_{b1} one must travel a distance of $L_{s1}/\tan \phi_1$ along the helical path (i.e., $\tan \phi_1 \approx L_{s1}/\pi D_{b1}$). For the double-flighted twin screw in a plane orthogonal to the screw axis one must travel a circumferential distance, C , given by

$$C = 2(2\pi - 2\alpha_i)(D_{b2}/2)$$

where α_i is the angle of intermesh defined in Section 8.4.1. An apparent helix angle, ϕ'_2 , can be defined as

$$\tan \phi'_2 = \left(\frac{3}{2}\right) \frac{L_{s2}}{C}$$

and the unwound channel length, L_{e2} , would be

$$L_{e2} = L_{b2}/\sin \phi'_2$$

α_i is related to D_{b2} and C_L by means of Eq. 8.107 and is 28.1° (see Fig. 8.21). The mean residence time in the twin-screw extruder, \bar{t}_2 , is

$$\bar{t}_2 = \frac{L_{e2}}{\langle v_{z2} \rangle} \approx \frac{L_e}{(\pi D_{b2} N/2) \cos \phi'} \quad (8.196)$$

where $\langle v_{z2} \rangle$ has been approximated by $(\pi D_{b2} N/2) \cos \phi'$ in the absence of an accurate model for flow in the partially filled screw channels. The time of rotation of the melt pool, t_{p2} , is

$$t_{p2} = \frac{[(f_2 A_o/p_2) \sin \phi'_2]^{1/2}}{\langle v_{x2} \rangle} = \frac{[(f_2 A_o/p_2) \sin \phi'_2]^{1/2}}{(\pi D_b N/2) \sin \phi'_2} \quad (8.197)$$

where A_o is defined in Eq. 8.114. Finally the degree of fill, f , is given by

$$f = Q/Q_D \quad (8.198)$$

We are now in position to calculate the remaining unknowns for the single-screw extruder, which are N and ρQ . Using the data for the twin-screw system given in Table 8.1 we can calculate N_{s2} ($= \bar{t}_2/t_{p2}$). The unwound channel lengths are

$$L_{e1} = \frac{265}{\sin 17.65^\circ} = 874 \text{ mm}$$

$$L_{e2} = (270 \text{ mm} / \sin 20.52^\circ) + (30 / \sin 14.01^\circ) = 894 \text{ mm}$$

At $N = 90$ rpm for the twin-screw extruder,

$$\begin{aligned} \bar{t}_2 &= \frac{770}{(\pi \cdot 34 \cdot 90/60/2)(\cos 20.52^\circ)} + \frac{124}{(80.1) \cos 14.01^\circ} \\ &= 11.9 \text{ s} \end{aligned}$$

Using Eqs. 8.197 and 8.114 and the data given in Table 8.1, t_{p2} is found to be 0.079 s. Now using dynamic similarity (i.e., $N_{s1} = N_{s2}$) we find that

$$\frac{L_{e1} \tan \phi_1}{(f_1 A_1)^{1/2}} = \frac{11.9}{0.079} = 150.6$$

With $A_1 = WH = 58.71$ mm, we find $f_1 = 0.058$. We now use Eq. 8.198 to calculate Q_1 assuming $N_1 = 90$ rpm:

$$\begin{aligned} Q_1 &= f_1 Q_{D1} = (0.058) P_1 < v_{z1} > A_1 \\ &= 0.058(3) (58.71) (67.4) \\ &= 688.1 \text{ mm}^3/\text{s} = 2.62 \text{ kg/h} \end{aligned}$$

Hence, in order to obtain a fractional separation of 0.85 using a single-screw extruder, we must use a triple-flighted screw with a length, L_{b1} , of 265 mm. The processing conditions must be:

Degree of fill	$f = 0.058$
Screw rpm	$N = 90$ rpm
Mass flow rate	$\rho Q = 2.62$ kg/h

It should be added that Biesenberger and co-workers (1990) reported the following experimental results for obtaining $F_s = 0.86$ on a similar single-screw extruder with a triple-flighted screw of $D_b = 30$ mm:

Temperature	$T = 230$ °C (rather than 250 °C)
Degree of fill	$f = 0.092$
Screw rpm	$N = 90$
Mass flow rate	$\rho Q = 3.15$ kg/h
Screw length	$L_b = 270$ mm

The dimensional analysis approach with the choice of \bar{t}/t_p as the dimensionless group for determining dynamic similarity seems to be reasonable.

8.6.2 Diffusion Theory

Because we may not always have data available for carrying out dimensional analysis, it is worthwhile to see whether the penetration theory (diffusion model) described in Section 8.5.2 provides a reasonable design. In Eq. 8.170, we assume that $Pe > 1$, and hence, we can use the expression given in Eq. 8.177, which is

$$C_A^* = \exp[-E_x z/L_e] \quad (8.199)$$

We also assume that the staged efficiency of the film diffusion process is 1 (i.e., $X_p = 1.0$) as there is no way to obtain this quantity directly (with $X_f = 1.0$, $Pe \gg 1$). E_x (the extraction number) is now

$$E_x = n_f + (k_p H L_e)/Q \quad (8.200)$$

where

$$n_f = \frac{V_{bx} H_f L_e}{Q} \quad k_p = \left(\frac{4 D_A}{\pi t_p} \right)^{1/2} \quad (8.201)$$

To calculate n_f we must make assumptions about H_f and f . We take H_f to be similar to the magnitude of the flight clearance or 2.54×10^{-2} mm. The screws are typically run with a degree of fill (f) in the range of 0.1 to 0.3. We take $f = 0.1$. D_A for MMA in PMMA is about 1×10^{-10} mm²/s (see references in Chapter 4). We now find n_f , k_p , and E_x :

$$\begin{aligned} n_f &= \frac{\tan \phi H_f L_e}{p_f WH} = \frac{(0.318)(2.54 \times 10^{-2})}{(3)(0.1)(58.7)} L_e \\ &= 4.59 \times 10^{-4} L_e \\ k_p &= (4 \times 10^{-10} V_{bx}/\pi H)^{1/2} = 2.21 \times 10^{-5} \\ E_x &= 4.59 \times 10^{-4} L_e + \frac{(2.21 \times 10^{-5})(5.595)}{1186} L_e \\ &= 4.59 \times 10^{-4} L_e + 1.04 \times 10^{-7} L_e \approx 4.59 \times 10^{-4} L_e \end{aligned}$$

Substituting the above value back into Eq. 8.199, we can now solve for the unwound channel length required to reduce the amount of MMA to 0.1%:

$$\begin{aligned} \ln(0.143) &= -E_x z/L_e \\ z &= \frac{-\ln(0.143) L_e}{E_x} = \frac{1.944 L_e}{4.59 \times 10^{-4} L_e} \\ &= 4235 \text{ mm} \end{aligned}$$

The barrel length, L_b , is

$$L_b = L_e \sin \phi = (4235)(0.303) = 1283.2 \text{ mm}$$

This value is about 4.6 times the value estimated by means of dimensional analysis and reported by Biesenberger and co-workers (1990). Hence, the theory based on diffusion overestimates the length required to reduce the level of MMA to 0.1%. This is true in spite of the fact that in this case most of the volatiles are predicted to be removed from the melt film and not the pool.

PROBLEMS

A. Applications

- 8A.1** *Solids Conveying of Nylon in a Single-Screw Extruder.* The solids conveying section of a single-screw extruder with a 5.08 cm barrel diameter consists of a screw with a 5.08 cm lead, a screw diameter of 5.06 cm, a 3.49 cm root diameter, and a flight width of 0.508 cm. The bulk density of the nylon pellets is 475 kg/m^3 , and the friction coefficient between nylon and steel is 0.25 (assume this value for both the barrel and screw). Assuming at first no pressure rise, calculate the solids conveying rate (kg/rev) for the following conditions: (a) no friction between the screw and the solids, (b) no friction between the solids and screw flights, (c) no friction between the solids and the trailing flight, and (d) friction on all contacting surfaces. (e) Compare your results with the experimental value of 0.0149 kg/rev reported by Darnell and Mol (1956).
- 8A.2** *Solids Conveying with a Pressure Rise.* Calculate the pressure at the end of the solids conveying zone and the power consumption in Problem 8A.1 when the pressure at the base of the hopper is calculated to be $3.0 \times 10^3 \text{ Pa}$ and the solid conveying zone is one turn of the screw. Assume that $f_s = 0.8f_b$ and that only the friction between the solids and the screw surface and the barrel is important. The mass flow rate is 0.0149 kg/rev.
- 8A.3** *Scaleup of Solids Conveying Section.* The optimum channel depth for the solids conveying zone of a single-screw extruder having a barrel diameter of 5.0 cm was found to be 0.6 cm. At 100 rpm the mass flow rate of nylon was found to be 10.45 g/s and $P_2/P_1 = 100$. $f_s = 0.3$ and $f_b = 0.5$. Determine the screw rpm (N), the channel depth (H), and the mass flow rate (G) in scaling up to a single-screw extruder with $D_b = 11.4 \text{ cm}$.
- 8A.4** *Pressure at the Base of a Silo.* A silo 7.0 ft in diameter and 40 ft high contains LDPE pellets having a bulk density of 40 lb/ft^3 . Assuming the silo is full (i.e., it contains 61,575 lb of pellets), determine the lateral and vertical pressures at the base of the silo

if the coefficient of friction, f'_w , is 0.2 and the angle of repose, δ , is 45° .

- 8A.5** *Delay Zone Length for LDPE.* Using Eq. 8.36 and the data in Example 8.2, estimate the number of turns in the delay zone for LDPE. Use the rheological data given in Appendix A for NPE 953 (Table A.1).
- 8A.6** *Solid Bed Profile in a Single-Screw Plasticating Extruder.* Determine the solid bed profile and the length of screw channel required for melting of LDPE in a 2.5 in. diameter screw extruder with a single-flighted square-pitched screw having the following screw geometry:

Feed section: 3.2 turns and 0.5 in. channel depth
 Compression section: 12 turns with a linear taper
 Metering section: 12 turns and 0.125 in. channel depth
 Flight width: 0.25 in. and a negligible flight clearance

and the following operating conditions:

Screw rpm: 82
 Barrel temperature: 150°C
 $G = 120 \text{ lb/h}$.

Assume that melting starts one turn before the end of the feed section. The physical property data can be found in Chapter 5, and the following relation for the viscosity is to be used:

$$\eta = 5.6 \times 10^4 \exp[-0.01(T - 110)]\dot{\gamma}^{-0.655} \quad (8.202)$$

where η is given in units of $\text{Pa} \cdot \text{s}$ and T in $^\circ\text{C}$.

- 8A.7** *Shear Rate in the Melting Zone.* Using the conditions given in Problem 8A.6, calculate the shear rate in the melt film and compare this with the nominal shear rate in the metering section.
- 8A.8** *Operating Conditions for a Single-Screw Extruder.* The single-screw extruder described in Problem 8A.6 is used to pump LDPE at 150°C through a pelletizing die consisting of ten capillaries each having a diameter of 0.3175 cm and L/D ratio of 20. Considering only the pressure drop across the capillaries (i.e., neglect the pressure drop across the manifold or distribution section and any filtration sections), determine the pressure rise in the metering section and the screw speed in rpm required to extrude

120 lb/h of polymer (i.e., is 82 rpm sufficient?). Assume isothermal conditions and that there is negligible pressure rise in the melting section.

- 8A.9** *Equilibrium Composition by Henry's Law.* Molten polystyrene (PS) produced in a bulk polymerization process is flashed to a styrene content of 1.0% but still requires further devolatilization in an extruder at 260 °C to a final content of 100 ppm. The Henry's law constant, K_w , for styrene in PS at 260 °C is 50 atm (note that $P = K_w w_i$). Vacuum at 10 Torr (1 Torr = 1333.22 microbar) is available. Is this sufficient vacuum and, if not, what final composition can be attained theoretically?
- 8A.10** *Geometry of Self-wiping Corotating Screw Elements.* Screw elements in a corotating self-wiping twin-screw extruder have the following geometric characteristics: $D = 43$ mm, $L_s = 43$ mm, $C_L = 39$ mm. Determine the angle of intermesh, the flight tip angle, the flight width (note that $e = \alpha_t L_s / 2\pi$), and the open cross-sectional area, A_o , for both double- and triple-flighted screw elements. Compare the calculated values for the two cases.
- 8A.11** *Sizing of Reactive Zones in Extruders.* Determine the relative lengths of the reaction zones for a single-screw and corotating and counterrotating twin-screw extruders. The extrusion rate of the melt is to be 1000 kg/h and 3 minutes of residence time is required for the reaction to occur. The following data are given for all three types of extruders: screw lead, $L_s = 0.3 D_b$; fractional degree of fill, $f = 0.5$; $H = 0.175 D_b$; $\rho = 900$ kg/m³. The single screw is to be triple-flighted while the twin-screw devices have double-flighted screw elements. Assume that the L_b/D_b of the reactive section is in the range of 10 to 30.

B. Principles

- 8B.1** *Heat Generation at the Barrel-Solid Interface.* Derive Eq. 8.30, which is the heat generated per unit of barrel surface due to friction between the solid bed and the barrel.
- 8B.2** *Optimum Channel Depth in the Solids Conveying Zone.* Starting with the expression for the mass flow rate given in Eq. 8.23, find an expression for the optimum channel depth (i.e., maximize G with respect to H). Although the value of H must be determined numerically from the expression, specify what parameters H depends on.
- 8B.3** *Optimum Helix Angle in the Solids Conveying Zone.* Find an expression from which the optimum helix

angle for which the mass flow rate in the solids conveying section is a maximum can be determined.

- 8B.4** *Solids Conveying in a Starve-Fed Single-Screw Extruder.* Starve-feeding of a single-screw extruder is a process option whereby solid polymer is metered into the feed throat using a gravimetric or auger type feeder at a rate less than the solids conveying capacity of the screw. The resin compacts further downstream in the screw channel as a result of lower pressures and temperatures are generated that are advantageous for processing thermally sensitive polymers. The degree of fill is given by

$$f = G_s / G_o \quad (8.203)$$

where G_s and G_o are the mass flow rates for the starve-fed and flood-fed cases, respectively, at the same screw rotational speed. The average bed width in the starve-fed case is given in terms of the channel width, W , as $\bar{W}_s = \bar{W} f$.

- (a) If in the case of starve-feeding it is assumed that the forces acting on the trailing flight (i.e., F_4 and F_8 in Fig. 8.14) are zero, obtain an expression similar to that in Eq. 8.27 for the pressure rise.
- (b) Calculate the pressure rise for the conditions given in Problem 8A.2 when the mass flow rate is only 0.5 of that of the fully flooded screw.

- 8B.5** *Maximum Shear Rate in the Metering Section.* Obtain an expression for determining the maximum shear rate in the metering section of a single-screw extruder for the Newtonian fluid case.
- 8B.6** *Pressure Profile in a Single-Screw Extruder.* Show that the pressure profile along the barrel wall of a single-screw extruder for a Newtonian fluid is given by the following expression:

$$P - P_0 = \frac{6 \mu \pi D_b N l}{H^2} \left[1 - \frac{Q_p}{Q_d} \right] \cos \phi_b \sin \phi_b \quad (8.204)$$

where l is the axial distance along the extruder barrel.

- 8B.7** *Power Input to a Single-Screw Extruder.* For the isothermal Newtonian model show that the power input through the screw is given by the following expression:

$$P_w = \frac{\mu \pi^2 N^2 D_b^2 W}{\sin \bar{\phi} H} \left[4 - 3 \cos^2 \phi_b \left(\frac{Q}{Q_d} \right) \right] \quad (8.205)$$

Using the above expression find the helix angle ϕ_b , which minimizes the power input (take $\bar{\phi} = \phi_b$).

- 8B.8** *Optimizing the Design of a Screw.* Using the screw characteristic given in Eq. 8.103 (isothermal Newtonian model) find the following: (a) optimum channel depth for maximum pressure rise for a given flow rate; (b) optimum channel depth and helix angle for maximum flow rate at constant screw speed (assume the flow rate through the die is given by $K \Delta P_D / \mu$); (c) channel depth for lowest screw speed for a given flow rate; and (d) determine the Q/Q_d ratio in part (a).

- 8B.9** *Scaleup of a Single-Screw Extruder: Shear Rate Method.* The shear rate at the barrel wall in the metering section of a single-screw extruder is given approximately by

$$\dot{\gamma}_b = \frac{\pi D_b N}{H} \quad (8.206)$$

If in scaling up from a small extruder (D_1, L_1, N_1 , etc.) to a large extruder (D_2, L_2, N_2 , etc.) dynamic similarity is maintained by keeping the shear rate constant (Chung, 1984) and geometric similarity is maintained by keeping the L/D ratio constant, determine the channel width, channel depth, screw speed, flow rate, and power input through the screw for the large extruder in terms of the corresponding quantities of the small extruder and the ratio D_2/D_1 (e.g., show that $H_2 = H_1 (D_2/D_1)$, $Q_2 = Q_1 (D_2/D_1)^2$, etc.). The helix angle is taken to be the same for both extruders.

- 8B.10** *Scaleup of a Single-Screw Extruder: Mixing Method.* As discussed in Sections 6.4 and 8.5.1, mixing is taken to be a function of strain, which in the metering section of a single-screw extruder is L/H . (This follows from $\gamma = \dot{\gamma}t = (\pi D_b N / H)(L / \pi D_b N)$.)

- (a) Using constant strain as the scaleup criterion, determine W_2, H_2, N_2, Q_2 , and P_{w2} in terms of the corresponding values for the smaller extruder and the ratio of D_2/D_1 (e.g., show that $W_2 = W_1 (D_2/D_1)$, $Q_2 = Q_1 (D_2/D_1)^3$, $P_{w2} = P_{w1} (D_2/D_1)^2$, etc.).
- (b) If the output of a 5.0 cm diameter extruder is 100 kg/h, determine the mass flow rate in a 15 cm diameter extruder where scaleup is based on a constant strain. Compare this value to that obtained when scaleup is based on a constant shear rate.

- 8B.11** *Velocity Profiles in the Curved Channel Model* (Pinto and Tadmor, 1970). Show that the velocity profiles, $v_z(r)$ and $v_\theta(r)$, for flow of a Newtonian fluid in the

channel of an extruder where curvature is included are

$$v_z = \frac{A}{2} \frac{r}{1 - \beta^2} \left[\ln \frac{r}{R_b} - \beta^2 \ln \frac{r}{R_s} - \left(\frac{R_s}{r} \right)^2 \ln \beta \right] + \frac{2\pi N}{1 - \beta^2} \frac{r^2 - R_s^2}{r} \quad (8.207)$$

$$v_\theta = \frac{BR_b}{4} \left[\left(\frac{r}{R_b} \right)^2 + (1 - \beta^2) \frac{\ln(r/R_b)}{\ln \beta} - 1 \right] \quad (8.208)$$

where $\beta = R_s/R_b$ is the ratio between the inner and outer radii and A and B are given as

$$A = 8\pi N \frac{K(\beta)}{G(\beta)} - \frac{4Q}{\pi R_b^3 G(\beta) \tan \phi_b} \quad (8.209)$$

$$B = \frac{8Q}{\pi R_b^3 F(\beta)} \quad (8.210)$$

$K(\beta)$, $G(\beta)$, and $F(\beta)$ are given as

$$K(\beta) = 1 + \frac{2\beta^2 \ln \beta}{1 - \beta} \quad (8.211)$$

$$G(\beta) = (1 - \beta^2) \left[1 - \left(\frac{2\beta \ln \beta}{1 - \beta^2} \right)^2 \right] \quad (8.212)$$

$$F(\beta) = (\beta^2 - 1) \left[1 + \beta^2 + \frac{1 - \beta^2}{\ln \beta} \right] \quad (8.213)$$

Cylindrical coordinates are used where z is in the axial direction of the extruder.

- 8B.12** *Residence Time Distribution: Curved Channel Model* (Pinto and Tadmor, 1970). The residence time distribution (RTD) function for flow of a Newtonian fluid in a rectangular channel was developed in Section 8.5.1. Derive the RTD for the case in which curvature is included. A fluid particle located at position r in the extruder channel will turn over when it hits the screw flight and start moving in the opposite direction at a position r_c .

- (a) Show that the analogous equation in cylindrical coordinates to Eq. 8.134 for finding ξ and ξ_c is

$$\int_{R_s}^{r_c} v_z r dr d\theta + \int_r^{R_b} v_z r dr d\theta = \int_{R_s}^{r_c} v_\theta dr dz + \int_r^{R_b} v_\theta dr dz \quad (8.214)$$

- (b) Show that the above equation can be rewritten after changing the integration limits as

$$\begin{aligned} & \int_r^{r_c} v_z r dr d\theta - \int_r^{r_c} v_\theta dr dz \\ &= - \int_{R_s}^{R_b} v_z r dr d\theta + \int_{R_s}^{R_b} v_\theta dr dz \quad (8.215) \end{aligned}$$

- (c) Substitute in the velocity profiles for the Newtonian case and use the relation $dz = R_b \tan \phi_b d\theta$ to obtain

$$\begin{aligned} & C_1(\rho_c^4 - \rho^4) + C_3(\rho_c^2 \ln \rho_c - \rho^2 \ln \rho) \\ &+ C_4(\rho_c^2 - \rho^2) + C_5(\ln \rho_c - \ln \rho) = 0 \quad (8.216) \end{aligned}$$

where A and B are given in Problem 8B.11 and

$$\begin{aligned} \rho &= r/R_b & \rho_c &= r_c/R_b & \beta &= R_s/R_b \\ C_1 &= \frac{(1 - \beta^2)\beta}{2A \tan \phi_b} \\ C_2 &= \frac{4\pi N}{A} \\ C_3 &= 2 \left[\frac{C_1(1 - \beta^2)}{\ln \beta} - 1 + \beta^2 \right] \\ C_4 &= 1 - 2C_1 - C_1 \frac{1 - \beta^2}{\ln \beta} - \beta^2 - 2C_2 \\ &\quad - 2\beta^2 \ln \beta \\ C_5 &= 4\beta^2(\ln \beta + C_2) \end{aligned}$$

C. Numerical Problems

- 8C.1** *Calculation of the Optimum Channel Depth for Solids Conveying.* In Problem 8B.2 an expression for the optimum channel depth was obtained. For a 11.4 cm diameter extruder running at 60 rpm with values of $f_b = 0.5$ and $f_s = 0.3$ and $P_2/P_1 = 200$, determine the optimum value of H (i.e., find the value of H that makes G/ρ a maximum). It should be noted that in practice it is difficult to obtain accurate values of the friction coefficients, and hence, one must use results of the nature asked for here only as a guideline.
- 8C.2** *Nonisothermal Solids Conveying Model* (Tadmor and Broyer, 1972). As a result of frictional heating at the barrel and plug interface the solid plug

can prematurely melt, inhibiting adequate pressure buildup in the solids conveying zone. The heat generation per unit area of barrel surface is given in Eq. 8.30. Develop a model for predicting the temperature in the solid bed and at the barrel surface, and then use the model to calculate the surface temperature for LDPE under the given conditions. Follow these steps:

- (a) Perform an energy balance on the solid plug to obtain the following differential equation:

$$\rho_b \bar{C}_p b v_{pz} \frac{\partial T_p}{\partial z} = k_p \frac{\partial^2 T_p}{\partial y^2} \quad (8.217)$$

- (b) Assuming that V_{pz} can be obtained from the isothermal theory for solids conveying, Eq. 8.21, show that Eq. 8.217 becomes

$$\frac{\partial T_p}{\partial t} = \alpha_p \frac{\partial^2 T_p}{\partial y^2} \quad (8.218)$$

where $dt = dz/V_{pz}$.

- (c) Carry out an energy balance at the plug and barrel interface, which shows that the heat generated by friction per unit surface area is conducted to the plug and metallic barrel to obtain the following equation:

$$q_b = -k_p \frac{\partial T_p}{\partial y} \Big|_{y=0} + k_b \frac{\partial T_b}{\partial y} \Big|_{y=0} \quad (8.219)$$

where q_b is the heat generated per unit of barrel surface area and the subscript b refers to the barrel.

- (d) As $k_b \gg k_p$, the temperature distribution in the barrel is assumed to be linear. Use this information to specify the boundary condition at the interface where $y = 0$. Specify the remaining boundary condition for solving Eq. 8.217.
- (e) Use the numerical approach described in Example 5.5 to obtain the temperature at the surface of a LDPE plug as a function of position along the channel for the following conditions:

Extruder geometry: $D_b = 2.5$ in.; square-pitched screw, $e = 0.25$ in.; $H = 0.375$ in.

Processing conditions: $G = 150$ lb/h; P_1 (under hopper) = 0.4 psi

T_b (barrel temperature) = 80 °F; bed temperature is initially 80 °F; $N = 80$ rpm
 Material properties: LDPE properties are given in Appendix B

- 8C.3** *Maximum Conveying Rate in a SWCOR Extruder.* Calculate the maximum conveying rate for LDPE at 150 °C in a self-wiping corotating (SWCOR) twin-screw extruder for the geometry described in Problem 8A.10 for $p = 2$, except take $L_s/D_s = 0.71$ and $e = 1.78$ mm. It will be necessary to use the numerical integration such as in the IMSL subroutine QDAGS or the MATLAB function *quad* to find the cross-sectional area. Compare your calculated value to the measured value of 94.3 kg/h at a screw speed of 43 rpm.
- 8C.4** *Effect of Curvature on Fluid Particle Position.* An expression for finding the complementary position of a particle as a function of curvature is given in Eq. 8.216 (Problem 8B.12). Solve this equation for values of $a = 0.95, 0.9, 0.85,$ and 0.82 for $\beta = 0.8$ and $Q = Q_d$, where $a = (\rho - \beta)/(1 - \beta)$ and $a_c = (\rho_c - \beta)/(1 - \beta)$.

D. Design Problems

- 8D.1** *Design of a Tubing Extrusion Process.* A 1 inch diameter garden hose is to be produced at the rate of 500 lb/h using LDPE. The wall thickness of the hose is to be 0.075 in. Design an extruder and die to accomplish this. Use data given for NPE 953 in various places in the book (e.g., Appendix A, Table A.1, and Chapter 3). In addition to specifying the size of extruder, screw geometry, and die dimensions, list all the assumptions you made in arriving at your design.
- 8D.2** *Design of a Coextrusion System.* Two resins, acrylonitrile–butadiene–styrene (ABS) and acrylonitrile–EPDM–styrene (AES), are to be coextruded to form a sheet that is 2.8 mm thick with AES representing 10% of the total thickness of the sheet (i.e., 0.28 mm). The sheet is to be 1.42 m wide, and the overall extrusion rate is to be 455 kg/h. The density of each polymer is similar (i.e., $\rho = 1100$ kg/m³). ABS and AES have similar viscosity functions at 200 °C with values for the power-law model given below:

$$\text{For ABS: } m = 45,455 \text{ Pa} \cdot \text{s}^n, \quad n = 0.342$$

$$\text{For AES: } m = 45,000 \text{ Pa} \cdot \text{s}^n, \quad n = 0.342$$

Size and design extruders for providing the desired output with the only requirement being that the L/D ratio of the extruders be 30. Design a feedblock system for joining the fluids and a sheet die for producing the desired sheet dimensions. Because of the close match in viscosity, the two fluids can be joined in the feedblock before entering the sheet die. Use the thermal and frictional properties given for polystyrene, if necessary, in your design calculations.

REFERENCES

- Biesenberger, J. A. and D. H. Sabastian. 1983. *Principles of Polymerization Engineering* (Wiley, Hoboken, NJ).
- Biesenberger, J. A., S. K. Dey, and J. Brizzolara. 1990. "Devolatilization of Polymer Melts: Machine Geometry and Scale Factors." *J. Polym. Eng. Sci.*, **30**(23), 1493–1499.
- Bigg, D. and S. Middleman. 1974. "Mixing in a Screw Extruder. A Model for Residence Time Distribution and Strain." *Ind. Eng. Chem. Fundam.*, **13**(1), 66.
- Booy, M. L. 1978. "Geometry of Fully Wiped Twin-Screw Equipment." *Polym. Eng. Sci.*, **18**, 973–984.
- Booy, M. L. 1980. "Isothermal Flow of Viscous Liquids in Corotating Twin Screw Devices." *Polym. Eng. Sci.*, **20**(18), 1220.
- Chung, C. I. 1984. "On the Scale-up of Plasticating Extruder Screws." *Polym. Eng. Sci.*, **24**, 626–633.
- Darnell, W. H. and E. A. J. Mol. 1956. "Solids Conveying in Extruders." *Soc. Plast. Eng. J.*, **12**, 20–28.
- Janssen, L. P. B. M. 1978. *Twin Screw Extrusion* (Elsevier, Amsterdam).
- Macosko, C. W. and D. R. Miller. 1976. "A New Derivation, Average Molecular Weights for Newtonian Polymers." *Macromolecules*, **9**, 201.
- Montes, S. and J. L. White. 1991. "Fluid Mechanics of Distributive Mixing in a Modular Intermeshing Corotating Twin Screw Extruder." *Int. Polym. Proc.*, **6**(3), 156.
- Pinto, G. and Z. Tadmor. 1970. "Mixing and Residence Time Distribution in Melt Screw Extruders." *Polym. Eng. Sci.*, **10**(5), 279–288.
- Potente, H. and S. M. Schultheis. 1989. "Investigations of the Residence Time and the Longitudinal Mixing Behavior in Counter-rotating Twin Screw Extruders." *Int. Polym. Proc.*, **4**(4), 255.
- Rauwendaal, C. 1986. *Polymer Extrusion* (Hanser, Munich).
- Roberts, G. W. 1970. "A Surface Renewal Model for the Drying of Polymers During Screw Extrusion." *AIChE J.*, **16**, 878.
- Szydlowski, R., R. Brzoskowski, and J. L. White. 1987. "Modeling Flow in an Intermeshing Co-rotating Twin-Screw Extruder: Flow in Kneading Disks." *Int. Polym. Proc.*, **1**(4), 207–214.

- Tadmor, Z. and E. Broyer. 1972. "Solids Conveying in Screw Extruders. Part II. Non-isothermal Model." *Polym. Eng. Sci.*, **17**, 378–386.
- Tadmor, Z. and G. G. Gogos. 1979. *Principles of Polymer Processing* (Wiley, Hoboken, NJ).
- Tadmor, Z. and C. G. Gogos. 2007. *Principles of Polymer Processing*, 2nd edition (Wiley, Hoboken, NJ).
- Tadmor, Z. and I. Klein. 1970. *Engineering Principles of Plasticating Extrusion* (Van Nostrand Reinhold, New York).
- Tzoganakis, C., J. Vlachopoulos, and A. E. Hamielec. 1988. "Modeling of the Peroxide Degradation of Polypropylene." *Int. Polym. Proc.*, **3**, 141.
- Walker, D. M. 1966. "An Approximate Theory for Pressures and Arching in Hoppers." *Chem. Eng. Sci.*, **21**, 975–999.
- Werner, H. 1976. Ph.D. dissertation, University of Munich.
- White, J. L. 1990. *Twin Screw Extrusion* (Hanser, Munich).
- Xanthos, M., Ed. 1992. *Reactive Extrusion* (Hanser, Munich).

9

POSTDIE PROCESSING

DESIGN PROBLEM VIII DESIGN OF A FILM BLOWING PROCESS FOR GARBAGE BAGS

Garbage bags are made from low-density polyethylene (LDPE; NPE 953) by the process of film blowing, in which the film leaves the nip rolls as a “lay-flat” film, before being cut and sealed to form garbage bags. A typical bag holding 13 gallons of garbage is 25.41 μm (= 1 mil) thick, 61 cm (= 2 ft) wide, and 69.6 cm (= 2 ft 3 $\frac{3}{8}$ in.) long. The production line consists of an extruder with annular die and film blowing instrumentation (air supply for blowing, air ring, guide rolls, nip rolls, etc.), and it can accommodate 1500 bags per hour. This design problem consists of two parts: (a) calculation of the dimensions of the annular die from which LDPE is extruded at 170 °C without any melt fracture present, and (b) calculation of the blowing air pressure and the drawing force at the nip rolls to obtain the desired strength bags.

The LDPE exiting the die is assumed to exhibit die swell (see Fig. 3.1 in Chapter 3), which can be calculated from Eq. 3.89 (i.e., assume that capillary die swell is equal to diameter and thickness swell from an annular die). Melt fracture (Section 7.2.2) for LDPE appears when the maximum wall shear stress exceeds 1.13×10^5 Pa. To secure uninterrupted production a safety factor of 3 is applied with regard to the maximum wall shear stress. The power-law relationship for LDPE at 170 °C and for $\dot{\gamma} \geq 0.1 \text{ s}^{-1}$ is

$$\eta = 5.17 \times 10^3 \dot{\gamma}^{-0.413}$$

where η is in Pa·s. The density of the polymer is 0.77 g/cm^3 at the extrusion temperature and 0.92 g/cm^3 at room temperature, and the following relationship correlates the primary normal stress difference, N_1 , to the shear stress, τ_{xy} :

$$N_1 = 0.119 \tau_{xy}^{1.304}$$

for N_1 and τ_{xy} in Pa. Table 1.1 (p. 6) can be used to provide the film thickness at the maximum die swell level as a function of the final thickness.

We then consider the analysis of the film blowing process, which should be based on the maximum die swell dimensions as the initial dimensions and isothermal conditions are assumed. Calculate the pressure of the blowing air, the drawing force, and the velocity at the nip rolls if the dimensionless frost line height is confined to 5 and the distance of the nip-roll system from the position where the maximum die swell level occurs is 1.5 m.

In spite of the geometry of the final product the processes of fiber spinning, film casting, and film blowing bear an important similarity. There are no constraining surfaces to determine the final dimensions of the product. The surfaces are free, and hence the final dimensions are determined by the rheological properties of the melt as well as processing conditions such as take-up speed, cooling rate, extrusion rate, and die dimensions. Modeling of these processes is complicated by not only the complex rheology of the melt (or solution) but by the crystallization process. In Section 9.1 we discuss

the process of fiber spinning in detail. For the sake of simplicity the analysis starts by considering a single isothermal filament in which the rheological properties are considered to be Newtonian. These results are then extended to the non-isothermal case in which the processes of crystallization and structure formation are considered. The heat transfer process is analyzed in the context of nonisothermal fiber spinning. The approach required for viscoelastic fluids is discussed next. The solution of these equations is the primary goal, but a knowledge of the assumptions in the equations is necessary. Finally, an analysis of the various instabilities that occur in fiber spinning is presented.

In Section 9.2 the process of film casting is considered along with its associated stability. Both fiber spinning and film casting impart uniaxial stretching. One way to impart biaxial stretching is by film stretching, which is discussed next. The other way of producing biaxially oriented films with high mechanical and physical properties is by film blowing, which is discussed in Section 9.3, along with the associated problems of stability and scaleup. In these last two processes we only present the final equations as the emphasis is on solving the equations.

9.1 FIBER SPINNING

A *fiber* is the fundamental unit of textiles, and it is defined as a material unit of axial length scale about 100 times the length scale in the cross direction (width or radius). There are two types of fibers: *natural* and *synthetic* (or *man-made*). The term *spinning* has different meaning for natural and synthetic fibers. Spinning of natural fibers refers to the *twisting of short fibers* into continuous lengths (also called *filaments*). On the other hand, spinning of synthetic fibers refers to production of continuous lengths *by any means*. Finally, the *yarn* is made by twisting many filaments together.

The production of man-made fibers usually includes the following processes (Ziabicki, 1976):

1. Preparation of polymer (polymerization, chemical modification, etc.).
2. Preparation of the spinning fluid (polymer melt or solution).
3. Spinning (extrusion, solidification, and deformation of the spinning line or filament).
4. Drawing (due to higher linear speed at the take-up roll than that at the die; drawing is used to increase the degree of molecular orientation and improve the tensile strength, modulus of elasticity, and elongation of the fibers).
5. Heat treatment.
6. Textile processing (twisting, oiling, dyeing, etc.).

Process 3 can be achieved mainly by three procedures: *melt spinning*, *solution dry spinning*, and *solution wet*

spinning. Of these three procedures, melt spinning is the simplest and the most economical one. Its simplicity stems from the fact that it involves only heat transfer and extensional deformation, whereas the other methods in addition to the above processes involve also mass transfer and diffusion. Melt spinning procedure can be applied to polymers that are thermally stable at the extrusion temperature and that exhibit relatively high fluidity at that temperature. Typical examples of melt-spun polymers are polyamides, polyesters, polystyrene, polyolefins, and inorganic glasses.

In the solution dry-spinning procedure the polymer is dissolved in a volatile solvent and the solution is extruded. Then the spinning line meets a stream of hot air and the solvent is evaporated. The recovery of the solvent increases the cost of the whole process. Typical examples of dry-spun polymers are cellulose acetate, acrylonitrile, vinyl chloride, and acetate. In the 1980s, extended-chain PE fibers (ECPE, Spectra fibers) have been made by solution spinning in a typical melt-spinning apparatus. The solution wet-spinning procedure is applied to polymers that meet neither criteria of the previous two methods (i.e., thermal stability and solubility in a volatile solvent). It involves the extrusion of a polymer solution into a liquid bath of coagulating agents, which drive the solvent out of the filament. The basic principles of wet and dry spinning were discussed in Chapter 4, because mass transfer and diffusion are the controlling mechanisms of those types of spinning. There are four other spinning procedures (*phase separation spinning*, *emulsion spinning*, *gel spinning*, and *reaction spinning*), which will not be addressed in this textbook.

A schematic (not to scale) of the typical melt-spinning procedure is shown in Figure 9.1 (see also Fig. 1.5). Polymer is pumped by means of an extruder through a screen pack, in

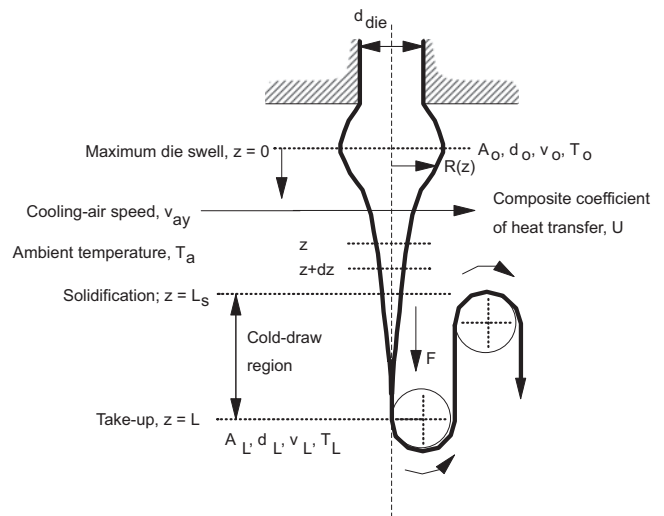


FIGURE 9.1 Melt-spinning process and its geometric characteristics. The origin of the coordinate system is located at the point of maximum die swell.

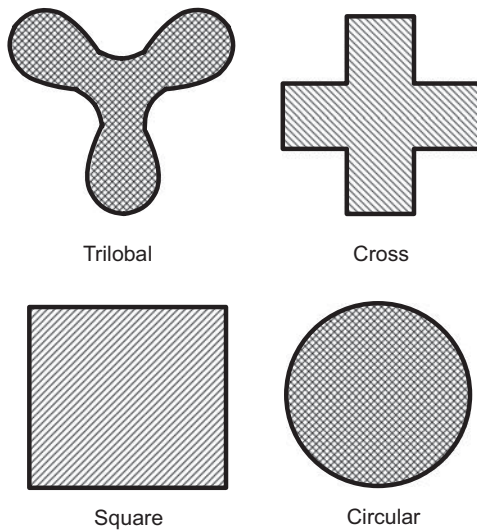


FIGURE 9.2 Examples of various shapes of spinneret holes.

which the polymer is filtered through layers of screens and sand. Then it is divided into many small streams by means of a plate containing many small holes, the *spinneret*. Some spinnerets can have as many as 10,000 holes (rayon spinning from a 15 cm platinum disk spinneret). The extrusion through the spinneret (or die), the subsequent *die swell* (due to the relaxation of the elastic stresses of the polymer; Section 7.2.3), the cooling of the filament by cooling air (or water vapor) flowing perpendicularly to the filament axis, the solidification of the polymer, and its cold drawing in the region from the solidification point to the take-up roll are shown in Figure 9.1. Part of the time the holes in the spinneret are circular in shape, but mostly they are of other regular shapes. Other typical shapes include *trilobal*, square, and cross, and they are shown in Figure 9.2. Note that dry and wet spinning from circular spinneret holes usually result in irregularly shaped fibers.

The key aspects of the modeling of the fiber spinning process are:

1. Extrusion through a short die (usually of nonround cross section) in which the fluid velocity field must undergo rapid rearrangement.
2. Swell of the liquid leaving the hole.
3. Rapid axisymmetric extension to large strains.
4. Rapid temperature changes and hence large changes in the rheological behavior.
5. Crystallization under conditions of high stress and rapid cooling.

The origin of the coordinate axes is considered to be at the point of maximum cross-sectional area, which occurs at a small distance from the face of the spinneret as a result of

die swell. The distance between the spinneret and the point of maximum die swell is only a few die diameters long, and thus it is small compared to the distance between the face of the spinneret and the take-up roll. Therefore, by neglecting it we cause no severe problems in the following analysis.

In terms of the number of the filaments per spinneret plate, as well as the spinning speed, melt spinning is divided into various groups. *Monofilaments* are produced by one-hole spinneret plates, even though most of the time there are numerous filaments extruded through the spinneret (multifilament yarns). *Very-low-speed spinning*, with speeds ranging from 30 to 100 m/min, usually occurs for thick monofilaments spun through liquid baths. *Low-speed spinning* is usually carried out at speeds in the range of 100 to 750 m/min, where the filament tension is constant along the entire length. In order to enhance the degree of orientation and crystallinity and hence physical properties, the yarns are subsequently drawn and annealed, and therefore the melt-spinning process is considered to be a *two-step process* (TSP; first step: spinning; and second step: drawing). At *intermediate speeds* of 750 to 3500 m/min, the filament tension is increased due to inertia and air drag. Finally, at *high spinning speeds* of 3500 m/min and above polymers such as poly(ethylene terephthalate) (PET) undergo stress-induced crystallization. At high spinning speeds (Section 9.1.4) the structure, morphology, and resulting physical properties are somewhat different from those obtained in conventional low-speed spinning processes.

Typical physical and mechanical properties of melt-spun fibers include the following: density, boil-off shrinkage, birefringence, tensile strength, percent elongation, modulus of elasticity, shrinkage tension, and dyeability. Some of these properties are shown in Table 9.1 for PET spun under conventional conditions of a two-step process and in a one-step process at high take-up speed in the range of 6000 m/min. In the same table, we also provide data for the highest performance industrial fibers, Spectra (ECPE) and Kevlar (Aramid). In practice, some of the above properties might be found under different names. *Denier per filament* (dpf; unit: denier, d) is usually substituted for density, and *tenacity* (unit: g-force/d or gf/d) is used in place of tensile strength. More about the definitions of these specific terms and units can be found in Section 9.1.2.

In the following analysis we first present the Newtonian isothermal model, which leads to an analytical solution. Then we discuss the Newtonian nonisothermal model, which gives insight into the complexities of the coupled heat and momentum transfer equations. PET, Nylon, and polysiloxanes are three typical polymers which are almost Newtonian at spinning conditions. Finally, we introduce the non-Newtonian isothermal model together with its associated difficulties. High-density polyethylene (HDPE), LDPE, polypropylene (PP), and polystyrene (PS) are all pseudoplastic and viscoelastic and fall into the latter category.

TABLE 9.1 Typical Properties of Fibers

Property	PET			
	OSP (at 6000 m/min)	TSP (conventional)	ECPE Spectra 1000	Aramid Kevlar 149
Density (g/cm ³)	1.38	1.375	0.97	1.47
Boil-off shrinkage (%)	3–4	8.0		
Birefringence (10 ⁻³)	105–115	150		
Tensile strength (MPa) or tenacity (gf/d)	460–550 3.8–4.5	610 5.0	3000	3450
Elongation at break (%)	45–50	35	2.7	1.5
Modulus of elasticity (GPa)	13–14	18	172	172
Modulus of elasticity (gf/d)	75–80	120		

Source: Kawagushi, 1985; and Cordova and Donnelly, 1990.

9.1.1 Isothermal Newtonian Model

The basic ideas of modeling the fiber-spinning process are best understood by considering the steady-state isothermal Newtonian analysis first. This analysis can be considered to be valid in the case that (1) the drawing takes place in a short distance in air, and then (2) the fiber is quenched into a water bath. In later steps all the other factors will be added. In the isothermal Newtonian analysis we neglect any interaction between the filament and the surrounding medium; that is, no heat transfer is taking place and the surface tension and air drag forces are negligible. Schematically, Figure 9.1 presents the overall melt-spinning picture and Figure 9.3 presents a section of the filament and all the stress, velocity, and direction vectors associated with the problem.

At a point in the filament boundary the unit outward normal vector is **n** and the tangential vector is **t**. The appropriate coordinate system for the problem is cylindrical with the axis of symmetry coinciding with the *z* axis (Fig. 9.3). The velocity vector is **v** and the total stress tensor is **π**. The components

of the total stress tensor are related to the components of the extra stress tensor **τ** by the following relationship (Eq. 3.7):

$$\pi_{ii} = p + \tau_{ii}; \quad \pi_{ij} = \tau_{ij} \quad \text{when } i \neq j \quad (9.1)$$

where *p* is the isotropic pressure.

To start our analysis we postulate the following:

$$v_z = v_z(r, z); \quad v_r = v_r(r, z); \quad p = p(r, z) \quad (9.2)$$

Because of symmetry and no-rotation of the filament, the θ component of the velocity field is zero and there is no θ dependence of the velocity and pressure fields. The equation of continuity yields

$$\dot{m} = \rho A \bar{v}_z = \rho \pi R^2 \bar{v}_z = \text{constant} \quad (9.3)$$

where \dot{m} is the polymer mass flow rate, *A* is the cross-sectional area of the filament, *R*(*z*) is the radius of the filament at the axial position *z*, and \bar{v}_z is the average axial velocity across the filament cross section. The *z* component of the equation of motion is (Table 2.7, Eq. F)

$$\rho \left(v_r \frac{\partial v_z}{\partial r} + v_z \frac{\partial v_z}{\partial z} \right) = -\frac{1}{r} \frac{\partial}{\partial r} (r \pi_{rz}) - \frac{\partial \pi_{zz}}{\partial z} \quad (9.4)$$

where the gravitational force, ρg_z , has been considered to be negligible. Similarly, the *r* component of the equation of motion is (Table 2.7, Eq. D)

$$\rho \left(v_r \frac{\partial v_r}{\partial r} \right) = -\frac{1}{r} \frac{\partial}{\partial r} (r \pi_{rr}) - \frac{\partial \pi_{rz}}{\partial r} + \frac{\pi_{\theta\theta}}{r} \quad (9.5)$$

The Newtonian constitutive equation is used, and thus,

$$\pi_{zz} = p + \tau_{zz} = p - 2\mu \frac{\partial v_z}{\partial z} \quad (9.6)$$

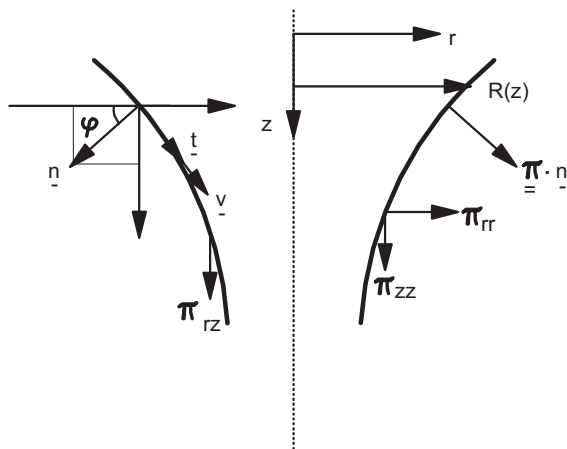


FIGURE 9.3 Velocity, stress vectors, and geometry at a point during melt spinning.

The boundary conditions for the problem are based on the facts that no fluid crosses the interface between the filament and the surrounding medium and that no stresses are imposed on the free boundary because air drag and surface tension forces are neglected in this analysis. These boundary conditions are stated as follows:

$$\text{B.C.1 : } \mathbf{v} \cdot \mathbf{n} = 0; \text{ no flow across the interface} \quad (9.7)$$

$$\text{B.C.2 : } \boldsymbol{\pi} \cdot \mathbf{n} = 0; \text{ no air drag and surface tension} \quad (9.8)$$

From analytical geometry we get

$$\mathbf{n} = n_z \boldsymbol{\delta}_z + n_r \boldsymbol{\delta}_r \quad (9.9)$$

where $\boldsymbol{\delta}_i$ represents the unit vector in the i direction. The z and r components of the unit normal vector are related to the angle ϕ between the unit normal vector and the z axis and the change of the radius of the filament with respect to z by the following relationships:

$$n_z = \sin \phi = -\frac{dR/dz}{\sqrt{1 + (dR/dz)^2}} = -\frac{R'}{\sqrt{1 + (R')^2}} \quad (9.10)$$

$$n_r = \cos \phi = \frac{dR/dz}{\sqrt{1 + (dR/dz)^2}} = \frac{R'}{\sqrt{1 + (R')^2}} \quad (9.11)$$

At the free surface (i.e., at $r = R(z)$), Eq. 9.7 becomes

$$\mathbf{v} \cdot \mathbf{n} = 0 = v_r n_r + v_z n_z \quad (9.12)$$

Combining Eqs. 9.10, 9.11, and 9.12, we get $v_r = (dR/dz)v_z = R'v_z$ at $r = R(z)$. Note that if $R' \ll 1$, that is, if the filament radius is slowly changing with z , then $v_r \cong 0$, which is true over most of the distance between the spinneret and the take-up roll. Also note that the relationship $v_r = R'v_z$ indicates that $R(z)$ is a streamline of fluid flow in the filament.

The z and r components of the total stress vector at the free surface are

$$(\boldsymbol{\pi} \cdot \mathbf{n})_z = \pi_{rz} n_r + \pi_{zz} n_z \quad (9.13)$$

$$(\boldsymbol{\pi} \cdot \mathbf{n})_r = \pi_{rr} n_r + \pi_{rz} n_z \quad (9.14)$$

and using Eq. 9.8 we get

$$\pi_{rz}(R) = -\frac{n_z}{n_r} \pi_{zz}(R) = R' \pi_{zz}(R) \quad (9.15)$$

In this relationship π_{zz} is the tensile stress due to the drawing, and π_{rz} is due to the fact that we do not have a cylindrical geometry (i.e., R is a function of z). Thus, we expect that π_{rz} is approximately zero for R changing very slowly with z and neglecting air drag on the filament surface. Mathematically the previous argument follows from Eq. 9.15 for $R' \ll 1$.

If we further assume that $v_z = v_z(z) = \bar{v}_z$, then the average of the z component of the equation of motion obtained by multiplication of each term by $2\pi r dr$ and integration from 0 to $R(z)$ leads to (Middleman, 1977)

$$\int_0^R \rho v_r \frac{\partial v_z}{\partial r} r dr = 0, \text{ since } v_z \neq v_z(r) \quad (9.16)$$

$$\int_0^R \rho v_z \frac{\partial v_z}{\partial z} r dr = \frac{1}{2} \rho v_z v_z' R^2 \quad (9.17)$$

$$\int_0^R \frac{1}{r} \left[\frac{\partial}{\partial r} (r \pi_{rz}) \right] r dr = R \pi_{rz}(R) = R R' \pi_{zz}(R) \quad (9.18)$$

$$\int_0^R \frac{\partial \pi_{zz}}{\partial z} r dr = \frac{d}{dz} \int_0^R \pi_{zz} r dr - \pi_{zz} R R'(R) = \frac{1}{2} \pi_{zz}' R^2 \quad (9.19)$$

where v_z' is the derivative of v_z with respect to z . Note that the right equality in Eq. 9.19 is based on Leibnitz's rule of differentiation of an integral. Substitution of Eqs. 9.16 to 9.19 into Eq. 9.4 yields

$$\rho v_z v_z' = -2 \frac{R'}{R} \pi_{zz} - \pi_{zz}' = -\frac{1}{R^2} \frac{d}{dz} (R^2 \pi_{zz}) \quad (9.20)$$

which is the general equation of the isothermal fiber-spinning problem. Note that we have not yet introduced the constitutive equation, which is given in Eq. 9.6.

Equation 9.20 can be transformed into a differential equation containing only v_z and its derivatives by substituting expressions for π_{zz} and π_{zz}' obtained from Eq. 9.6. These relations are found from Eq. 9.6 by eliminating the pressure term as follows. The isotropic pressure is one-third of the trace of the total stress tensor, that is,

$$p = \frac{1}{3} (\pi_{rr} + \pi_{zz} + \pi_{\theta\theta}) \quad (9.21)$$

Because only the z component of the velocity field exists (see also Eq. 9.14 for π_{rr}) $\pi_{rr} = \pi_{\theta\theta} = 0$, and thus Eq. 9.21 yields

$$\pi_{zz} = 3p = -3\mu \frac{dv_z}{dz} = -\bar{\eta}_1 \frac{dv_z}{dz} \quad (9.22)$$

where $\bar{\eta}_1$ is the uniaxial elongational viscosity (Eq. 3.36). For Newtonian fluids, this viscosity is equal to three times the viscosity (Trouton's rule; $\bar{\eta}_1 = 3\mu$).

Substitution of Eq. 9.22 and its derivative into the equation of motion, Eq. 9.20, yields

$$\frac{d}{dz} (v_z)^2 = 12 \frac{\mu}{\rho} \frac{R'}{R} \frac{dv_z}{dz} + 6 \frac{\mu}{\rho} \frac{d^2 v_z}{dz^2} \quad (9.23)$$

Neglecting the inertial term we obtain, as a solution to Eq. 9.3 (i.e., $R'/R = -v'_z/2v_z$), $(v'_z/v_z)' = 0$, which is solved as

$$v_z = C_1 e^{C_2 z} \quad (9.24)$$

The melt-spinning problem has the following boundary conditions:

$$\text{B.C.1: } v_z = v_0, \text{ at } z = 0 \quad (9.25)$$

$$\text{B.C.2: } v_z = v_L, \text{ at } z = L$$

With the help of the above boundary conditions Eq. 9.24 becomes

$$v_z = v_0 \exp\left[\frac{z \ln D_R}{L}\right] = v_0 (D_R)^{z/L} \quad (9.26)$$

where D_R is the *draw* (or *draw-down*) *ratio*, and it is equal to

$$D_R = \frac{v_L}{v_0} \quad (9.27)$$

Finally, the radius of the filament, R , as a function of the axial distance z is found from the continuity equation as

$$R(z) = R_0 \exp\left[-\frac{1}{2}z \frac{\ln D_R}{L}\right] \quad (9.28)$$

In summary, the steady-state Newtonian isothermal model is able to provide the axial velocity profile as well as the filament radius profile, and it is based on the following additional assumptions: (1) slowly changing radial profile with axial distance, (2) negligible inertial and gravitational forces, (3) nonexistent radial velocity profile, (4) circular filament, (5) axial velocity profile not dependent on the radial coordinate, and (6) negligible surface tension and air drag forces. (See also Problem 9A.1 for the validity of some of the above assumptions and Schultz (1987) for a challenge of these assumptions.)

Example 9.1. Newtonian and Isothermal Model for Melt-Spun Nylon 6,6

Nylon 6,6 is extruded at 285 °C under isothermal conditions (in a temperature-controlled chamber), and it is drawn in such a way that $L = 400$ cm and the draw ratio is equal to 100. If the take-up speed is 1000 m/min, the polymer volumetric flow rate is 0.1 cm³/s, and the die swell diameter is three times the die diameter, carry out the following:

- Calculate the maximum stretching rate of the melt.
- Compare this stretching with the shear rate inside the die, if the die diameter is 0.16 cm.

- Assess the validity of the approximate relation $v_r \cong 0$.
- Determine the maximum tensile stress in the melt and the force required to draw the melt.

Assume that Nylon 6,6 is Newtonian at the spinning temperature.

Solution. The stretching rate is calculated by differentiating Eq. 9.26 as follows:

$$\dot{\epsilon} = v'_z = \frac{dv_z}{dz} = v_0 \exp\left[\frac{z \ln D_R}{L}\right] \frac{\ln D_R}{L} \quad (9.29)$$

The maximum in $\dot{\epsilon}$ occurs at $z = L$:

$$\dot{\epsilon}_{\max} = (v'_z)_{\max} = v_L \frac{\ln D_R}{L} \quad (9.30)$$

and it is equal to 19 s⁻¹.

The maximum shear rate (at the walls) inside the die is given by the relation (Table 2.4)

$$\dot{\gamma}_{\max} = \frac{4Q}{\pi R_{\text{die}}^3} \quad (9.31)$$

where Q is the polymer volumetric flow rate. Thus, $\dot{\gamma}_{\max}$ is equal to about 250 s⁻¹, which is one order of magnitude higher than the maximum stretching rate of 19 s⁻¹.

The validity of the relation $v_r \cong 0$ depends on the value of the slope of the filament radius, which follows from Eq. 9.28:

$$|R'| = \left|\frac{dR}{dz}\right| = \frac{R_0 \ln D_R}{2L} \exp\left[-\frac{1}{2}z \frac{\ln D_R}{L}\right] \quad (9.32)$$

The maximum of the slope occurs at $z = 0$ (i.e., at the die swell level), and it is equal to

$$|R'|_{\max} = \frac{R_0 \ln D_R}{2L} \quad (9.33)$$

Numerically the maximum slope is calculated to be 1.4×10^{-3} , which is much smaller than 1, and so the radial velocity is about equal to zero.

The maximum tensile stress in the melt occurs at the location where the maximum stretching takes place, that is, at the take-up roll. It is calculated from Eq. 9.22 as

$$(\pi_{zz})_{\max} = -3\mu(v'_z)_{\max} \quad (9.34)$$

The viscosity of Nylon 6,6 at 285 °C is taken from Table A.11 in Appendix A as 250 Pa·s, and so the maximum tensile

stress is calculated to be equal to -14.3 kPa. Finally, the force required to draw the melt is

$$F = -\pi R_L^2 (\pi_{zz})_{\max} = 9\pi \frac{R_{\text{die}}^2}{D_R} (\pi_{zz})_{\max} \quad (9.35)$$

which is calculated to be -2.6 mN (i.e., 2.6 mN in tension). ■

9.1.2 Nonisothermal Newtonian Model

The dynamics of the nonisothermal melt-spinning process has been analyzed since the early 1960s. The analysis that follows is drawn from the work of Kase and Matsuo (1965, 1967) and Kase (1985). These authors presented a model called *thin-filament theory*, and it is based on purely extensional flow field in the filament. The model in its unsteady-state form consists of four partial differential equations based on the continuity, momentum, constitutive, and energy equations. Compared to the previous Newtonian isothermal model, the present model includes the additional complication of nonconstant temperature along the axial distance z . The independent variables are time, t , and distance, z , from the spinneret, and the dependent variables are cross-sectional area of the filament, $A(z, t)$, temperature, $T(z, t)$, axial velocity, $v_z(z, t)$, and rheological tensile force, $F(z, t)$. Obviously, the steady-state solution of the four equations gives the dependent variables as a function of the axial distance z only. Figure 9.1 shows a typical melt-spinning process valid in this section.

Assumptions. The simplifying assumptions of the thin-filament theory are as follows:

1. Circular cross section of the filament; $A = \pi R^2$.
2. Constant polymer density; $\rho = \text{constant}$.
3. Constant specific heat of the polymer; $\bar{C}_p = \text{constant}$.
4. No die swell effect.
5. Newtonian viscosity with Arrhenius-type dependence on temperature.
6. No resistance to radial heat conduction within the filament; that is, $\partial T / \partial r = 0$.
7. No heat conduction within the filament in the axial direction.
8. Vertical filament.
9. Heat transfer at the surface (with composite coefficient U) consists of two parts: convective (with coefficient h) and radiant heat transfer with governing equation $\sigma \varepsilon (T^4 - T_a^4)$ with $U = h + \sigma \varepsilon (T^4 - T_a^4) / (T - T_a)$, where T_a is the ambient air temperature, σ is the Stefan–Boltzmann constant, and ε is the emissivity.
10. Empirical dependence of the heat transfer coefficient U on the filament velocity, v_z , and the cooling air cross-flow velocity, v_{ay} .

11. No interactions, either hydrodynamic or thermal, between adjacent filaments.
12. Purely extensional flow field in the filament, that is, $\partial v_z / \partial r = 0$.

Most of the assumptions are valid for industrial melt-spinning conditions. However, assumptions 4 and 5 may not be absolutely valid, because die swell exists and polymers exhibit viscoelastic behavior. To accommodate assumption 4, we consider the origin of the coordinate axis to be at the point of maximum die swell. Furthermore, other developments in numerical schemes (Fisher et al., 1980; and Keunings et al., 1983) have verified that the thin-filament theory and finite element calculations give comparable results in a region only a few die diameters downstream from the die swell region. Consequently, for all practical purposes, the thin-filament theory is satisfactorily accurate for most fiber-spinning processes. Finally, industrial and laboratory experience suggests that the neglect of viscoelasticity might not be a serious problem (Ziabicki and Kawai, 1985), except when dealing with instability issues.

Equations. The continuity equation is the same as Eq. 9.3. It can easily be shown to be of the following form:

$$\frac{\partial A}{\partial t} + v_z \frac{\partial A}{\partial z} + A \frac{\partial v_z}{\partial z} = \frac{\partial A}{\partial t} + \frac{\partial (Av_z)}{\partial z} = 0 \quad (9.36)$$

The unsteady-state equation of motion (Table 2.7, Eq. F), taking also assumptions 8 and 12 into consideration, becomes

$$\rho \left(\frac{\partial v_z}{\partial t} + v_z \frac{\partial v_z}{\partial z} \right) = \rho g - \frac{1}{r} \frac{\partial}{\partial r} (r \pi_{rz}) - \frac{\partial \pi_{zz}}{\partial z} \quad (9.37)$$

The equation of energy (Table 5.1, Eq. B) using also assumption 2 becomes

$$\rho \bar{C}_p \left(\frac{\partial T}{\partial t} + v_z \frac{\partial T}{\partial z} \right) = -\frac{1}{r} \frac{\partial}{\partial r} (r q_r) - \frac{\partial q_z}{\partial z} + \dot{S} \quad (9.38)$$

where \dot{S} is the rate of energy production (examples: phase change and chemical reaction). Because there is no significant heat production and no heat conduction in the axial direction (assumption 7), Eq. 9.38 simplifies to

$$\rho \bar{C}_p \left(\frac{\partial T}{\partial t} + v_z \frac{\partial T}{\partial z} \right) = -\frac{1}{r} \frac{\partial}{\partial r} (r q_r) \quad (9.39)$$

The heat transfer in the radial direction is given by the following relation (assumption 9):

$$q_r = U (T - T_a) = h (T - T_a) + \sigma \varepsilon (T^4 - T_a^4) \quad (9.40)$$

By averaging the equation of motion over the cross section (i.e., multiplying each term by $2\pi r dr$ and integrating them from 0 to $R(z)$), we get

$$\rho A \left(\frac{\partial v_z}{\partial t} + v_z \frac{\partial v_z}{\partial z} \right) = \rho g A - 2\pi (r \pi_{rz} |_{R(z)}) - 2\pi \int_0^{R(z)} \frac{d\pi_{zz}}{dz} r dr \quad (9.41)$$

The left-hand-side term in Eq. 9.41 represents the inertia of the filament and the first term on the right-hand side represents the force due to gravity acting on the filament. The second term on the right-hand side represents the drag force due to air, and the last term represents the tensile stress in the polymer and the surface tension forces. Thus, Eq. 9.41 presents the balance of the acting forces:

$$\begin{aligned} (\text{inertia}) &= (\text{gravity}) - (\text{air drag}) - (\text{surface tension}) \\ &+ (\text{rheological forces}) \end{aligned}$$

The air drag force acts along the tangential direction, \mathbf{t} , as shown in Figure 9.3 and thus can be decomposed into two components: one in the r direction and one in the z direction. The summation of the r components of the traction vector over the circumference of the filament at a specific z plane is zero, because they cancel out, and the summation of the z components results in the shear stress π_{rz} evaluated at the surface of the filament. When $R' \ll 1$, we are allowed to consider the z component of the air drag to be the same as the air drag itself, for all practical purposes. Thus, the summation of the z components gives: $r \pi_{rz} |_{R(z)} = R \pi_{rz,s} = R(1/2)C_D \rho_a v_z^2 = RD$, where C_D is the hydrodynamic drag (or friction) coefficient, ρ_a is the density of the surrounding medium, that is, the density of air, and the subscript s denotes the surface of the filament.

Using the Leibnitz rule for the last term in Eq. 9.41, we get

$$\frac{d}{dt} \int_0^{R(z)} \pi_{zz} r dr = \pi_{zz} |_{R(z)} R(z) \frac{dR}{dz} + \int_0^{R(z)} \frac{d}{dz} (\pi_{zz}) r dr \quad (9.42)$$

Based on Eq. 9.42, the equation of motion becomes

$$\begin{aligned} \rho A \left(\frac{\partial v_z}{\partial t} + v_z \frac{\partial v_z}{\partial z} \right) &= \rho g A - 2D\pi R + 2\pi \pi_{zz} |_R R \frac{dR}{dz} - 2\pi \frac{d}{dz} \int_0^{R(z)} \pi_{zz} r dr \\ & \quad (9.43) \end{aligned}$$

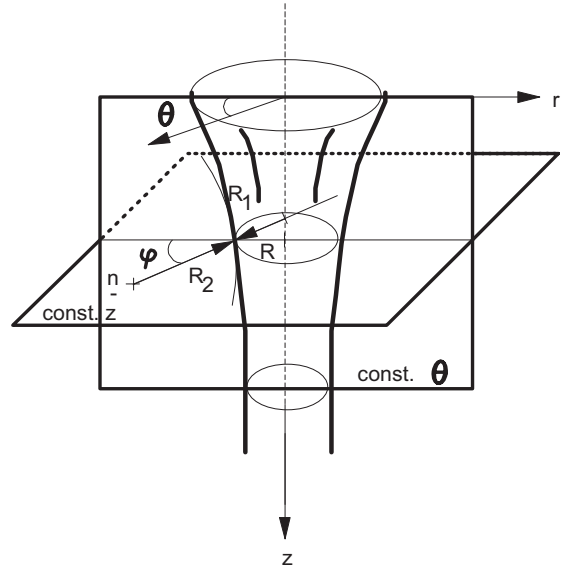


FIGURE 9.4 Definition of the principal radii R_1 and R_2 associated with the surface tension force during melt spinning.

A curved surface always creates a surface tension term that relates the pressure differential across the interface between the melt and air. The term $\pi_{zz}|_R = \pi_{zz,s}$ is related to the surface tension force via the relationship

$$\pi_{zz,s} = 3\Delta p = 3(p - p_a) = 3\gamma \left(\frac{1}{R_1} + \frac{1}{R_2} \right) \quad (9.44)$$

where Eq. 9.22 was used, R_1 and R_2 are the principal radii of curvature of the fiber surface at position z (Fig. 9.4), γ is the surface tension, and p_a is the ambient pressure. The last equality in Eq. 9.44 is the Young–Laplace equation. Note that the principal radii of curvature have opposite signs, as they are on opposite sides of the filament surface. For a slowly changing filament radius (i.e., for $R' \ll 1$) $R_1 \cong R$ and $R_2 \gg R$ so that

$$\pi_{zz,s} \cong 3\gamma/R \quad (9.45)$$

is a good approximation. Based on this, the unsteady-state equation of motion attains the following form:

$$\begin{aligned} \rho A \left(\frac{\partial v_z}{\partial t} + v_z \frac{\partial v_z}{\partial z} \right) &= \rho g A - 2D\sqrt{\pi A} \\ & \quad + \frac{d}{dz} (H\sqrt{\pi A}) - \frac{dF}{dz} \quad (9.46) \end{aligned}$$

where $H = 6\gamma$ and F is the tensile force (also called tension), which is equal to $2\pi \int_0^{R(z)} \pi_{zz} r dr$.

Similarly, the energy equation is integrated over the cross section to give

$$2\pi\rho\bar{C}_p\frac{R^2}{2}\left(\frac{\partial T}{\partial t}+v_z\frac{\partial T}{\partial z}\right)=-2\pi RU(T-T_a) \quad (9.47)$$

which finally can be brought into the following format:

$$\frac{\partial T}{\partial t}+v_z\frac{\partial T}{\partial z}=-\frac{2\sqrt{\pi U}}{\rho\bar{C}_p\sqrt{A}}(T-T_a) \quad (9.48)$$

Finally, the Newtonian constitutive equation, Eq. 9.6, can be used where the viscosity, μ , follows an Arrhenius type equation:

$$\mu=\mu_0\exp\left[-\frac{E}{R_g}\left(\frac{1}{T_0}-\frac{1}{T}\right)\right] \quad (9.49)$$

where R_g is the universal gas constant ($=8.314$ J/mol·K), E is the activation energy, and μ_0 is the viscosity at some reference temperature T_0 . Note that a WLF relationship (see Section 5.1) or an empirical relationship can also be used to express the effect of temperature on viscosity. In conclusion, Eqs. 9.36, 9.46, 9.48, and 9.49 are the four transient equations that describe the Newtonian nonisothermal unsteady-state melt-spinning problem.

Experimental Correlations. In order to solve the previous set of equations, we need correlations for the heat transfer coefficient, U , and for the hydrodynamic drag coefficient, C_D . For typical melt-spinning conditions, typical values of the cooling air parameters are: thermal conductivity, $k_a=0.808\times 10^{-4}$ cal/cm·s·°C; kinematic viscosity, $\nu_a=0.290$ cm²/s; and density, $\rho_a=0.815\times 10^{-3}$ g/cm³.

The literature (Kase and Matsuo, 1967) presents the experimental correlations of the various parameters used in the equations of motion and energy:

$$U=0.473\times 10^{-4}\left(\frac{\nu_z}{A}\right)^{1/3}\left[1+\left(8\frac{\nu_{ay}}{\nu_z}\right)^2\right]^{1/6} \quad (9.50)$$

where ν_{ay} is the velocity of cross air flow, ν_z is in cm/s, A is in cm², and U is in cal/cm²·s·°C. Equation 9.50, which is valid for any polymer, is based on the following formula:

$$\text{Nu}=\frac{(2R)U}{k_a}=\frac{2U\sqrt{A}}{k_a\sqrt{\pi}}=0.42(\text{Re}^*)^{1/3}\left[1+\left(8\frac{\nu_{ay}}{\nu_z}\right)^2\right]^{1/6} \quad (9.51)$$

where Re^* is the air-side Reynolds number:

$$\text{Re}^*=\frac{(2R)\nu_z}{\nu_a}=\frac{2\nu_z\sqrt{A}}{\nu_a\sqrt{\pi}} \quad (9.52)$$

Also, note that the term $\left[1+\left(8\nu_{ay}/\nu_z\right)^2\right]^{1/6}$ expresses the effect of the direction angle of the air flow measured from the filament axis. Equation 9.50 was developed from data for air moving past a stationary cylinder, and thus it does not take into account the effect of the moving cylinder. George (1982) provides a more accurate relation for moving cylinders, which is similar to Eq. 9.50, but with the two first terms replaced by $1.37\times 10^{-4}(\nu_z/A)^{0.259}$.

In terms of the hydrodynamic drag (or friction) coefficient, the following equation is used:

$$C_D=0.65(\text{Re}^*)^{-0.81} \quad (9.53)$$

and thus

$$2D\sqrt{\pi A}=3.12\times 10^{-4}\nu_z^{1.19}A^{0.095} \quad (9.54)$$

Note that other researchers (e.g., George, 1982) have used expressions such as $0.44(\text{Re}^*)^{-0.61}$ or $0.37(\text{Re}^*)^{-0.61}$ in Eq. 9.53. Also

$$F=-3\mu\frac{d\nu_z}{dz}A \quad (9.55)$$

with the following relationship for the viscosity function, which is typical for PET:

$$\mu=\mu_\infty\exp\left(\frac{E'}{T+273}\right), \text{ when } T\geq 60^\circ\text{C} \quad (9.56)$$

$$\mu=\infty, \text{ when } T<60^\circ\text{C}$$

where E' ($=E/R_g$) and μ_∞ are material properties of PET. The above form of the viscosity function indicates that crystallization (or solidification) takes place at 60 °C. Figure 9.1 shows the solidification point at $z=L_s$, beyond which the polymer is being cold-drawn.

The final form of the equations of continuity, Eq. 9.36, motion, Eq. 9.46, energy, Eq. 9.48, and constitutive, Eq. 9.55, for the steady state are (Kase, 1985)

$$\frac{d(A\nu_z)}{dz}=0 \quad (9.57)$$

$$\frac{dF}{dz}=\frac{d}{dz}\left(H\sqrt{\pi A}\right)+\rho gA-\rho A\nu_z\frac{d\nu_z}{dz}-3.12\times 10^{-4}A^{0.095}\nu_z^{1.19} \quad (9.58)$$

$$v_z \frac{dT}{dz} = \frac{1.67 \times 10^{-4} v_z^{1/3}}{\rho \bar{C}_p A^{5/6}} \left[1 + \left(8 \frac{v_{ay}}{v_z} \right)^2 \right]^{1/6} (T_a - T) \quad (9.59)$$

$$-\frac{dv_z}{dz} = \begin{cases} F / [3A\mu_\infty \exp(E'/(T + 273))], & \text{for } T \geq 60^\circ\text{C} \\ 0, & \text{for } T < 60^\circ\text{C} \end{cases} \quad (9.60)$$

In this set of four equations with four unknowns (v_z , A , T , and F) the following boundary conditions apply:

$$\text{B.C.1: at } z = 0, A = A_0 = \pi R_0^2; v_z = v_0; T = T_0; F = F_0 \quad (9.61)$$

$$\text{B.C.2: at } z = L \text{ or at } z \text{ such that } T(z) = 60^\circ\text{C}, v_z = v_L \quad (9.62)$$

Equation 9.62 is considered to apply to a constant-take-up-speed filament and the last part of Eq. 9.61 to a constant-tension filament.

Dimensionless Forms of the Equations. It is useful to make the governing equations nondimensional, so that the relative importance of the various terms becomes easily identifiable. To this end we define the following dimensionless variables:

$$\zeta = \frac{z}{L}, \quad \xi = \frac{A}{A_0}, \quad \psi = \frac{v_z}{v_0}, \quad \tau = \frac{v_0 t}{L}, \quad \theta = \frac{T}{T_0} \quad (9.63)$$

$$\lambda = \frac{(-F)L}{3A_0 v_0 \mu_\infty \exp[E'/(T_0 + 273)]} = \frac{(-F)L}{3A_0 v_0 \mu_\infty}$$

and the following dimensionless parameters:

$$\psi_{ay} = \frac{v_{ay}}{v_0}, \quad \theta_a = \frac{T_a}{T_0}, \quad \psi_L = \frac{v_L}{v_0}, \quad \lambda_0 = \frac{(-F_0)L}{3A_0 v_0 \mu_\infty} \quad (9.64)$$

Substituting these dimensionless variables and parameters into the equations of continuity, motion, and energy and into the constitutive equation yields

$$\xi \psi = 1 \quad (9.65)$$

$$\frac{d\lambda}{d\zeta} = \frac{d}{d\zeta} \left(\frac{C_1}{\xi} - C_4 \sqrt{\xi} \right) - C_3 \xi + \frac{C_2}{\xi^{1.095}} \quad (9.66)$$

$$\frac{d\theta}{d\zeta} = (\text{St}) \frac{\left[1 + (8\xi \psi_{ay})^2 \right]^{1/6}}{\xi^{1/6}} (\theta_a - \theta) \quad (9.67)$$

$$\frac{d\xi}{d\zeta} = \begin{cases} \lambda \xi \frac{\exp(E'/(T_0 + 273))}{\exp(E'/(T_0 + 273))}, & \text{for } \theta T_0 \geq 60^\circ\text{C} \\ 0, & \text{for } \theta T_0 < 60^\circ\text{C} \end{cases} \quad (9.68)$$

where the definitions of the various constants are

$$C_1 = \frac{\rho L v_0}{\mu_\infty} = \text{Re} \quad C_2 = \frac{3.12 \times 10^{-4} v_0^{0.19} L^2}{A_0^{0.905} \mu_\infty}$$

$$C_3 = \frac{\rho g L^2}{v_0 \mu_\infty} = \frac{\text{Re}}{\text{Fr}} = \left(\frac{\rho L v_0}{\mu_\infty} \right) \left(\frac{g L}{v_0^2} \right)$$

$$C_4 = \frac{L H \sqrt{\pi}}{v_0 \mu_\infty \sqrt{A_0}} = \frac{\text{Re}}{\text{Ca}} = \left(\frac{\rho L v_0}{\mu_\infty} \right) \left(\frac{H \sqrt{\pi}}{\rho v_0^2 \sqrt{A_0}} \right)$$

$$\text{St} = \frac{1.67 \times 10^{-4} L}{\rho \bar{C}_p A_0^{5/6} v_0^{2/3}} \quad (9.69)$$

and where Re, Fr, Ca, and St are the Reynolds, Froude, capillary (or Weber), and Stanton numbers, respectively. Also, note that in Eqs. 9.66, 9.67, and 9.68 the continuity equation, Eq. 9.65, was used. The boundary conditions, Eqs. 9.61 and 9.62, become

$$\text{B.C.1: at } \zeta = 0, \xi = \psi = \theta = 1; \lambda = \lambda_0 \quad (9.70)$$

$$\text{B.C.2: at } \zeta = 1 \text{ or at } \zeta \text{ such that } \theta = 60/T_0, \psi = \psi_L \quad (9.71)$$

The solution for the Newtonian and isothermal case developed in Section 9.1.1 can be found by solving Eqs. 9.66 to 9.68 (see Problem 9A.3) using the appropriate simplifications. Furthermore, the Newtonian and isothermal case can be extended to include all the additional forces, that is, to include the forces of air drag, surface tension, gravity, and inertia. The numerical solution of Eqs. 9.66 to 9.68 and its comparison with experimental data were shown by Kase and Matsuo (1967) for low-speed melt-spun polypropylene, with the following parameters: $C_1 = C_2 = C_3 = C_4 = 0$, $v_L = 500$ m/min, $v_{ay} = 20$ cm/s, $T_a = 20^\circ\text{C}$, $\rho = 0.83$ g/cm³, $\bar{C}_p = 0.7$ cal/g $^\circ\text{C}$, $E' = 3500$ K (i.e., $E \approx 7000$ cal/mol), and take-up denier (dpf) = 8 (see Problem 9C.1). The denier per filament (dpf) is the weight in grams of a 9000 m long filament. Thus, for \dot{m} in g/s, v_L in m/s, ρ in g/cm³, and R_L in cm, the definition becomes

$$\text{dpf} = 9000 \frac{\dot{m}}{v_L} = 2.83 \times 10^6 \rho R_L^2 \quad (9.72)$$

The tenacity of a fiber is the ultimate stress expressed as grams-force per denier (gf/d): (tenacity) = (strength)/($9 \times 10^5 \rho$), where the strength is expressed in grams-force/cm². Figure 9.5 shows the data from Kase and Matsuo (1967). The agreement between the theory and experiments is good. Note that similar analyses have been carried out by other groups for polymers such as HDPE, LDPE, PET, and so on (Ziabicki and Kawai, 1985).

The simulation of nonisothermal fiber spinning of PET at intermediate spinning speeds by George (1982) is worth mentioning at this point. His model works well for spinning speeds from 1000 to 3000 m/min. For PET with an intrinsic viscosity (IV) equal to 0.675 dL/g (1 dL = 100 cm³), which is a measure of molecular weight, extrusion temperatures

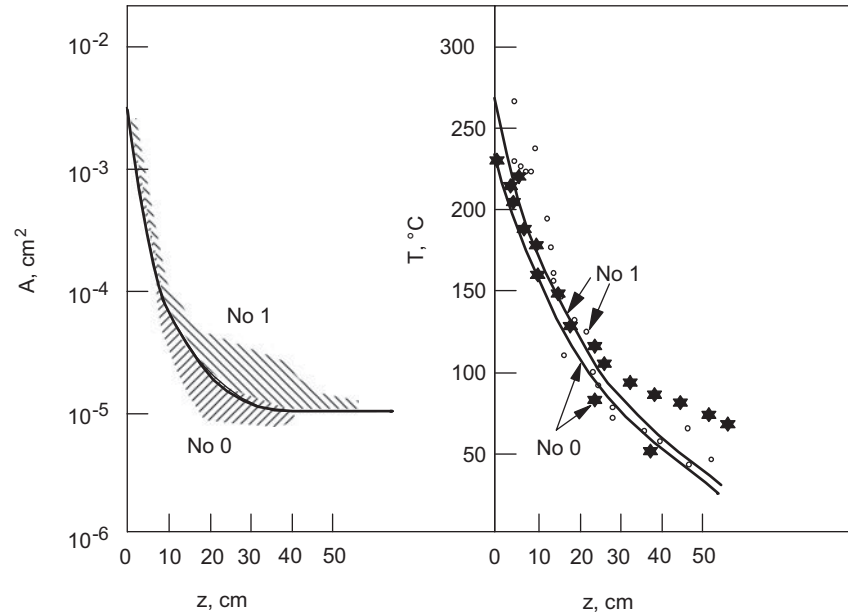


FIGURE 9.5 Filament cross-sectional area, A , and temperature, T , at different spinneret temperatures. Data points represent experiments of polypropylene filaments with the following parameters: take-up speed, 500 m/min; cooling cross air flow, 20 cm/s; temperature of cooling air, 20 °C; filament denier, 8; and diameter of the spinneret nozzle, 0.6 mm; (No 0), spinneret temperature is 240 °C; and (No 1), spinneret temperature is 270 °C. Solid lines represent the theoretical calculations. (Reprinted by permission of the publisher from Kase and Matsuo, 1967.)

of 290–315 °C, and shear rates of 2500–32000 s⁻¹, the die swell, B , is calculated as

$$B \cong 0.627 \exp \left[-3650 \left(\frac{1}{548} - \frac{1}{T + 273} \right) \right] \dot{\gamma}^{0.134} \quad (9.73)$$

where $\dot{\gamma}$ is the shear rate at the die wall. The elongational viscosity, $\bar{\eta}_1$, is given by

$$\bar{\eta}_1 = 3.82 \times 10^{-5} \exp \left[\frac{6802}{T + 273} \right] \quad (9.74)$$

and the momentum equation contains only inertia, air drag, gravitational, and tension forces. (Note that surface tension forces are not included.) The air drag force and the heat transfer coefficient are calculated as described in the subsection “Experimental Correlations” (George, 1982). Some results from the numerical solution of the four equations, continuity, momentum, heat transfer, and constitutive, and experimental data are shown in Figure 9.6.

Finally, the relative importance of the various forces in Eq. 9.58 is shown in Figure 9.7 (from Ziabicki and Kawai, 1985) as a function of the take-up speed. The melt-spun polymer is a polyester, the spinneret radius is 125 μm, the filament radius at take-up is 9.25 μm, the viscosity is 300 Pa·s, the cooling air is stationary, and the mass flow rate is proportional to the spinning speed. It is clear from this figure that for low take-up speeds the rheological and

inertial forces are significant. As the take-up speed increases the air drag force increases dramatically, while the inertial force increases to a lesser extent and the rheological force remains constant. Gravity and surface tension forces are negligible at all take-up speeds.

9.1.3 Isothermal Viscoelastic Model

Analyses of the Newtonian isothermal and nonisothermal models can be even further complicated by the introduction of the viscoelastic nature of the polymers in the melt state. The viscoelasticity of the polymer is important in cases where the relaxation time, λ , is of the same order of magnitude or slower than the characteristic time constant of the process, which might be taken to be equal to v_0/L . The ratio of these two time constants is called the Deborah number (Eq. 3.90), and it is equal to

$$De = \frac{v_0 \lambda}{L} \quad (9.75)$$

where λ is the relaxation time of the polymer in extensional flows.

The complete analysis should include both the nonisothermal nature of the melt-spinning process and the viscoelastic nature of the polymer. Analytical solutions for this situation do not exist. We outline, for pedagogical reasons, the solution to the isothermal case but without going into significant

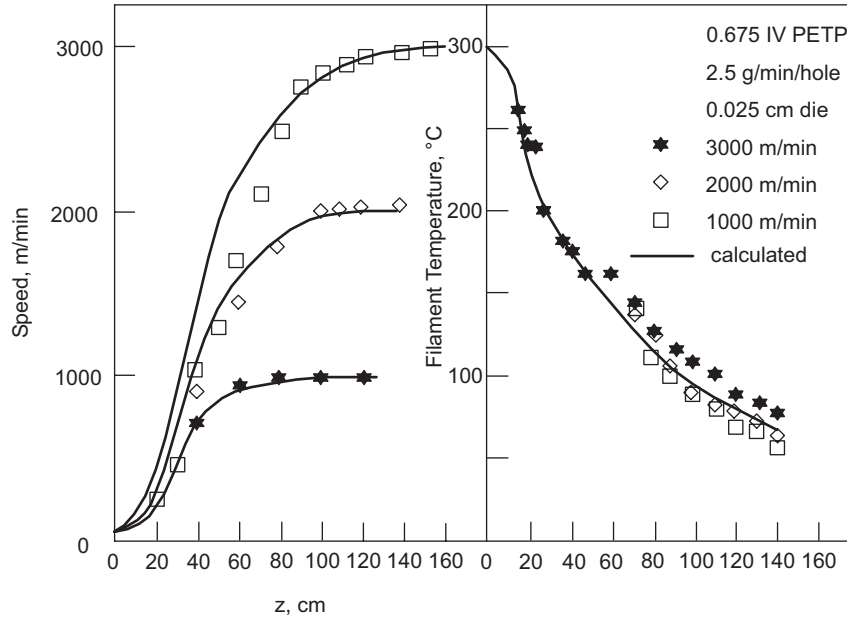


FIGURE 9.6 Comparison of calculated and experimental speed and temperature profiles for PET. (Reprinted by permission of the publisher from George, 1982.)

details. Denn et al. (1975) and Fisher and Denn (1976) evaluated the effect of the viscoelastic nature of the fluid on melt spinning.

The momentum equation for the Newtonian case, Eq. 9.20, can also be used in the viscoelastic case and can be written for the case of negligible inertia as

$$2\frac{R'}{R}\pi_{zz} + \pi'_{zz} = \frac{1}{R^2} \frac{d}{dz} (R^2 \pi_{zz}) = 0 \quad (9.76)$$

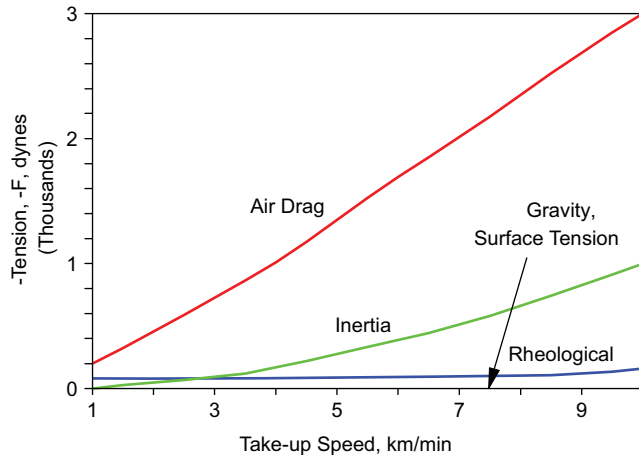


FIGURE 9.7 Calculated relative importance of the various forces in the melt-spinning process as a function of the take-up speed. The spinning conditions are: spinneret radius, 125 μm ; filament radius at take-up, 9.25 μm ; extrusion viscosity, 300 Pa-s; and stationary cooling air. (Reprinted by permission of the publisher from Ziabicki and Kawai, 1985.)

The force at the take-up point, F , is given by

$$F = \pi R_L^2 \pi_{zz}|_L \quad (9.77)$$

Combining Eqs. 9.76 and 9.77, together with Eq. 9.3, we get

$$\pi_{zz} = \frac{\rho F v_z}{\dot{m}} \quad (9.78)$$

A more convenient way of expressing Eq. 9.78 is by considering that $\pi_{rr} \cong 0$ (Eqs. 9.14 and 9.15). Thus,

$$\pi_{zz} - \pi_{rr} = \tau_{zz} - \tau_{rr} = \frac{\rho F v_z}{\dot{m}} \quad (9.79)$$

The constitutive equation used by Denn and co-workers (Denn et al., 1975; Fisher and Denn, 1976) was the White-Metzner model (see also Section 3.2.1; Eq. 3.42), which was thought to be applicable to high Deborah number processes such as melt spinning. The zz and rr components of the constitutive equation in cylindrical coordinates are

$$\begin{aligned} \tau_{zz} + \lambda \left(v_z \frac{d\tau_{zz}}{dz} - 2\tau_{zz} \frac{dv_z}{dz} \right) &= -\eta \dot{\gamma}_{zz} = -2\eta \frac{dv_z}{dz} \\ \tau_{rr} + \lambda \left(v_z \frac{d\tau_{rr}}{dz} + \tau_{rr} \frac{dv_z}{dz} \right) &= -\eta \dot{\gamma}_{rr} = \eta \frac{dv_z}{dz} \end{aligned} \quad (9.80)$$

where the relaxation time, λ , is related to viscosity, η , by the relationship

$$\lambda = \frac{\eta}{G} \quad (9.81)$$

and G is the shear modulus of the polymer. Finally, the viscosity function, η , was considered to obey the power law, so that the model includes both the shear-thinning and the elastic character of the polymer. Equations 9.79 and 9.80 can be combined to eliminate the stress components and yield the following equation (Fisher and Denn, 1976):

$$\psi + (\alpha\psi - 3\varepsilon)(\psi')^n - 2\alpha^2\psi(\psi')^{2n} - n\alpha\psi^2(\psi')^{n-2} = 0 \quad (9.82)$$

where ψ is the dimensionless velocity, v_z/v_0 , ψ' means differentiation of ψ with respect to ζ ($= z/L$), α and ε are dimensionless parameters given by

$$\alpha = \frac{m(3)^{(n-1)/2}}{G} \left(\frac{v_0}{L}\right)^n \quad \varepsilon = \frac{m\dot{m}(3)^{(n-1)/2}}{\rho|F|L} \left(\frac{v_0}{L}\right)^{n-1} \quad (9.83)$$

and m is the consistency of the polymer melt. Note that the ratio of the two dimensionless parameters is $\varepsilon/\alpha = GA_0/|F|$ and that α is a purely rheological parameter whereas $1/\varepsilon$ is a dimensionless force.

The boundary conditions of the problem are the same as for the Newtonian isothermal case (Eq. 9.25) but with the addition of one more boundary condition:

$$\text{B.C.3: at } z = 0, \quad \tau_{zz} = \tau_0 \quad (9.84)$$

It is difficult to make a good estimate of the value of τ_0 , but Fisher and Denn (1976) showed that this posed no major problem. The numerical solution of Eq. 9.82 with boundary conditions, Eqs. 9.25 and 9.84, is shown in Figure 9.8 (from Fisher and Denn, 1976), where also experimental data of melt-spun polystyrene (Zeichner, 1973) are shown. The agreement between theory and experiments is not good, because the parameter α for polystyrene has an experimental value of about 0.2 to 0.3 while the theory fits the data with α about 0.4 to 0.5. Nevertheless, the viscoelastic theory described above provides the general effect of viscoelasticity on the melt-spinning process.

Better agreement with experiments was achieved by Phan-Thien (1978), who solved the fiber-spinning problem using the PTT viscoelastic model (see Eq. 3.45). In this case the constitutive equation was fitted to data for LDPE and PS and the solutions to the fiber-spinning problem were compared to experimental data.

Example 9.2. Dimensionless Tension, $1/\varepsilon$, for Newtonian and Power-Law Fluids

Calculate the dimensionless tension, $1/\varepsilon$ (Eq. 9.83), for a power-law fluid. Then find $1/\varepsilon$ in the limit as $n \rightarrow 1$ (i.e., for a Newtonian fluid). Use $n = 0.4$ and $D_R = 15$ in both cases.

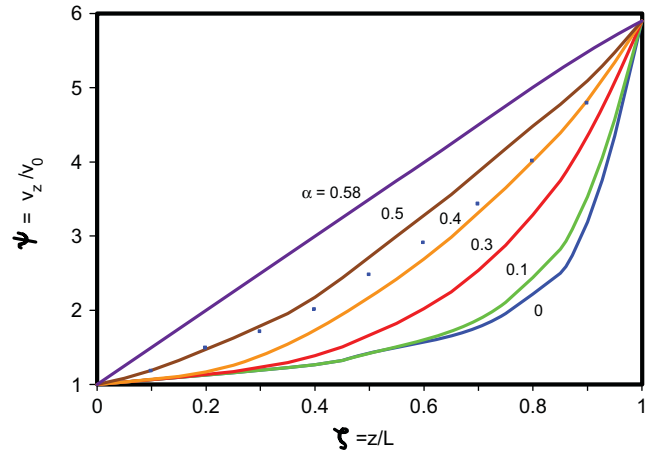


FIGURE 9.8 Theoretical dimensionless velocity profiles, ψ , as a function of the dimensionless axial distance, ζ , for the following values of the parameters: $n = 1/3$, $D_R = 5.85$, and $\tau_0\dot{m}/\rho v_0 F = 1$. Data shown are for the isothermal spinning of polystyrene at 170 °C. (Reprinted by permission of the publisher from Fisher and Denn, 1976.)

Solution. To calculate $1/\varepsilon$ we need to provide expressions for the tension, F , and the mass flow rate, \dot{m} . The mass flow rate is calculated as

$$\dot{m} = \rho\pi R_L^2 v_L = \rho\pi R_L^2 v_0 D_R \quad (9.85)$$

and the force as

$$F = \pi R_L^2 \pi_{zz}|_L = -\pi R_L^2 m (3)^{(n+1)/2} (v'_z)^n |_L \quad (9.86)$$

Substitution of Eqs. 9.85 and 9.86 along with the velocity profile obtained in Problem 9B.1 into Eq. 9.83 yields

$$\frac{1}{\varepsilon} = 3 \left\{ \frac{n}{1-n} \left[1 - (D_R)^{n-(1/n)} \right] \right\}^n \quad (9.87)$$

The limit of Eq. 9.87 for $n \rightarrow 1$ is easily calculated to be

$$\frac{1}{\varepsilon} = 3 \ln D_R \quad (9.88)$$

Finally, we obtain

$$\left(\frac{1}{\varepsilon}\right)_{n=0.4} = 2.53; \quad \left(\frac{1}{\varepsilon}\right)_{n=1} = 8.12 \quad (9.89)$$

9.1.4 High-Speed Spinning and Structure Formation

The discussion of fiber spinning in the preceding sections referred to low and moderate spinning speeds in which very little degree of crystallinity can be generated in the spun fibers especially for slowly crystallizing polymers (e.g., PET,

Table 5.17). For example, PET needs to be spun at speeds of 5000 m/min and above in order to exhibit significant crystallinity (see Fig. 5.23). As mentioned at the beginning of this chapter, the lack of crystallinity during the conventional low-speed spinning process forced the industry to use an additional step (drawing) immediately after the spinning process (two-step process, TSP). In this way, the PET fibers exhibit a high degree of orientation, and they are *fully oriented yarns* (FOY).

Nevertheless, the objective of the synthetic fiber industry is to make fibers in a simple one-step process, in which melt-spun fibers will have a high degree of orientation and crystallinity (structure formation). For slowly crystallizing polymers that simple process is high-speed (3500–5000 m/min) or very-high-speed (>5000 m/min) spinning, which is a one-step process (OSP) in which a high degree of orientation and crystallinity occur during the spinning process. In this way, relatively lower cost equipment and energy costs are required as compared to conventional TSP spinning. Furthermore, increased productivity can be achieved.

High-speed spinning is an attractive process. The mechanical properties of high-speed-spun PET fibers are no better than those produced by a TSP (see Table 9.1). The density of the OSP fibers is higher than that of the TSP fibers, which means that the crystallinity is higher, but the birefringence is lower, which means that the orientation is lower. However, the boil-off shrinkage and the elongation at break are better for fibers generated by a OSP than by a TSP.

Next, we discuss the *formation of structure*, that is, crystallization, crystalline morphology, and orientation, during the spinning process. We use PET as a model polymer, because data for this polymer are abundant in the literature. PET is a slowly crystallizing polymer ($t_{1/2} \cong 50$ s, Section 5.5.1), but under high stress conditions stress-induced crystallization takes place. Thus, high-speed spinning is necessary for PET crystallization. However, rapidly crystallizing polymers, like Nylon 6,6 ($t_{1/2} \cong 0.42$ s) and PE (see also Section 5.5.1), can crystallize even in low- or intermediate-speed spinning processes. Finally, crystallization does not take place in non-crystallizable polymers (e.g., atactic PS), and thus orientation is the only structure formation achieved during the spinning process of these polymers.

Crystallinity is important in fibers, because its degree affects the mechanical, diffusional, and solubility properties, as well the shrinkage of the fibers. In general, crystallization takes place under either quiescent or stress conditions. The effects of both these states on crystallinity were discussed in Section 5.5. When crystallization takes place during the spinning process the energy equation, Eq. 9.38, should be rewritten as

$$\rho \bar{C}_p \left(\frac{\partial T}{\partial t} + v_z \frac{\partial T}{\partial z} \right) = -\frac{1}{r} \frac{\partial}{\partial r} (r q_r) - \frac{\partial q_z}{\partial z} + \rho_c \Delta \bar{H}_c \frac{d\phi_c}{dt} \quad (9.90)$$

TABLE 9.2 Kinetic Crystallization Characteristics of Various Polymers

Polymer	K_{\max} (s ⁻¹)	D (°C)	J (°C/s)
PP (isotactic)	0.55	60	35.0
PET	0.016	64	1.1
Nylon 6	0.14	46	6.8
Nylon 6,6	1.64	80	139
PS (isotactic)	0.0037	40	0.16

Source: Ziabicki, 1976.

where $\Delta \bar{H}_c$ is the latent heat of crystallization per unit mass (see Appendix C for tabulated values), ρ_c is the density of the crystalline phase, and ϕ_c is the volume fraction of the crystalline phase (Eq. 5.160). Consequently, the steady-state form of Eq. 9.48 becomes (Lin et al., 1992)

$$\frac{dT}{dz} = -\frac{2\pi R U (T - T_a)}{\dot{m} \bar{C}_p} + \frac{\rho_c \Delta \bar{H}_c}{\rho \bar{C}_p} \frac{d\phi_c}{dz} \quad (9.91)$$

This equation adds one more unknown, the degree of crystallinity, ϕ_c , to the system of equations: continuity, constitutive, momentum, and energy. Thus, one additional equation is needed, which relates the crystallization rate to the spinning and physical characteristics of the system. This additional equation comes from a simplified approach to nonisothermal crystallization under conditions of molecular orientation, which is discussed next.

Nucleation and growth rates, and thus crystallization rates, are very sensitive to temperature. This sensitivity comes from the effect of the temperature on the energy terms in the respective equations of nucleation and growth rate. The experimentally observed crystallization half-time, $t_{1/2}$ (time for $\phi_c/\phi_\infty = 1/2$), or its reciprocal rate constant, $K(T)$ ($t_{1/2} = (\ln 2/K(T))^{1/n}$; see also Eq. 5.159), was shown to obey an empirical relationship of the following form (Ziabicki, 1976):

$$K(T) = K_{\max} \exp(-4 \ln 2 (T - T_{\max})^2 / D^2) \quad (9.92)$$

where D is the half-width of the $K(T)$ curve (similar to Fig. 5.20), K_{\max} is the maximum in the rate-temperature curve, and T_{\max} is the temperature at which $K = K_{\max}$. Table 9.2 shows some typical values of K_{\max} and D for various polymers. Note that Eq. 5.163 is another form of an empirical equation used to fit crystallization rate-versus-time data.

The area under the rate curve can be shown to be

$$\int_{T_g}^{T_m} K(T) dT \cong 1.064 K_{\max} D = J \quad (9.93)$$

where J is called *kinetic crystallizability*, and it characterizes the degree of crystallinity achieved when the material is cooled from the melting temperature, T_m , to the glass transition temperature, T_g , at unit cooling rate. Typical values of the kinetic crystallizability are shown in Table 9.2. Thus, for the same cooling rate and for $\phi_c \ll \phi_\infty$, the degree of crystallinity of Nylon 6,6 will be 125 times higher than that for PET.

Polymer crystallization is also very sensitive to molecular orientation in the amorphous regions. Orientation affects the entropy and enthalpy of fusion, the nucleation rate, and so on, but the mathematics of the problem goes beyond the scope of the present textbook. Instead, we use Ziabicki's (1976) idea that any function of molecular orientation, $X(f_{am})$, that is, melting temperature T_m , crystallization rate K , free energy ΔF , and so on, can be expanded as a series:

$$X(f_{am}) = X(0) + \alpha_2 f_{am}^2 + \dots \quad (9.94)$$

where f_{am} is the orientation of the amorphous region of the polymer before crystallization. Note that for symmetry reasons, Eq. 9.94 does not include a linear term. For low degrees of orientation we can obtain

$$\ln [K(f_{am})/K(0)] \cong A(T) f_{am}^2 \quad (9.95)$$

or, after combination with Eq. 9.92,

$$\begin{aligned} K(T, f_{am}) &= K(T, 0) \exp[A(T) f_{am}^2] \\ &= K_{max}^0 \exp\left[-4 \ln 2 (T - T_{max}^0)^2 / (D^0)^2\right. \\ &\quad \left.+ A(T) f_{am}^2\right] \end{aligned} \quad (9.96)$$

where the parameters with superscript 0 refer to the unoriented state. Equation 9.96 shows that the rate of crystallization increases with orientation, f_{am} , as $A(T)$ is always positive. Note that Eq. 9.96 is similar to Eq. 5.163. For PET the function $A(T)$ is shown to be equal to

$$A(T) = \frac{3.09 \times 10^{10} - 1.55 \times 10^8 (284 - T)}{(284 - T)^3} \quad (9.97)$$

The rate of crystallization can now be assessed using the modified Avrami equation (Eq. 5.162) as

$$\begin{aligned} \frac{d\phi_c}{dz} &= \frac{n\phi_\infty K(T, f_{am})}{v_z} \left(\int_0^z \frac{K(T, f_{am})}{v_z} dz' \right)^{n-1} \\ &\quad \times \exp\left(-\left(\int_0^z \frac{K(T, f_{am})}{v_z} dz'\right)^n\right) \end{aligned} \quad (9.98)$$

where K is given by Eq. 9.96. The boundary condition for the above equation is

$$\phi_c = 0 \quad \text{at } z = 0 \quad (9.99)$$

The relation between the orientation of the amorphous region and the state of stress in the filament is shown next. From Eq. 5.180 we know that the orientation of the amorphous region of a polymer melt is related directly to the stress applied to the polymer. But during the spinning process, temperature, polymer relaxation, and extensional rate might have an effect on the orientation. The equations that relate birefringence to stress in the filament are usually empirical. For polyesters the relevant equation can be either (Katayama and Yoon, in Ziabicki and Kawai, 1985)

$$\Delta N = 0.2 \left[1 - \exp\left\{-\frac{1.65 \times 10^{-6} (F/A)}{T + 273}\right\} \right] \quad (9.100)$$

or (Shimizu et al., in Ziabicki and Kawai, 1985)

$$\frac{d(\Delta N)}{dz} = \frac{C_{opt}}{v_z} \frac{dv_z}{dz} - \frac{G}{\eta} \frac{\Delta N}{v_z} \quad (9.101)$$

where C_{opt} is equal to 0.53. For LDPE the relevant equation is (Ziabicki, 1976)

$$\frac{\Delta N}{dv_z/dz} = C_{opt} \left[\frac{F/A}{dv_z/dz} - \eta_1 \right] \quad (9.102)$$

where η_1 is equal to 6000 Pa·s, and C_{opt} is equal to 1.5×10^{-11} Pa.

In conclusion, when crystallization takes place due to either the nature of the polymer or high-speed spinning (like in PET), the system of steady-state equations which describes the spinning process consists of the following equations: continuity, Eq. 9.57; momentum, Eq. 9.58; energy, Eq. 9.91; constitutive, Eq. 9.60; crystallization, Eq. 9.98; and orientation, Eq. 9.100 or 9.101 or 9.102. The relevant boundary conditions are Eqs. 9.61, 9.62, and 9.99. Various numerical solutions of the system of equations relevant to specific polymers are presented in Ziabicki and Kawai (1985) and they go beyond the scope of this textbook.

Finally, the manner in which individual molecules crystallize depends on the nature of the polymer molecule and the conditions under which crystallization takes place (see Fig. 5.18). It is worth noting at this point the work of Dees and Spruiell (1974) concerned with the structure development during melt spinning of HDPE fibers. Figure 9.9 presents their morphological model based on crystallite orientation factors and some other information. At low take-up speeds

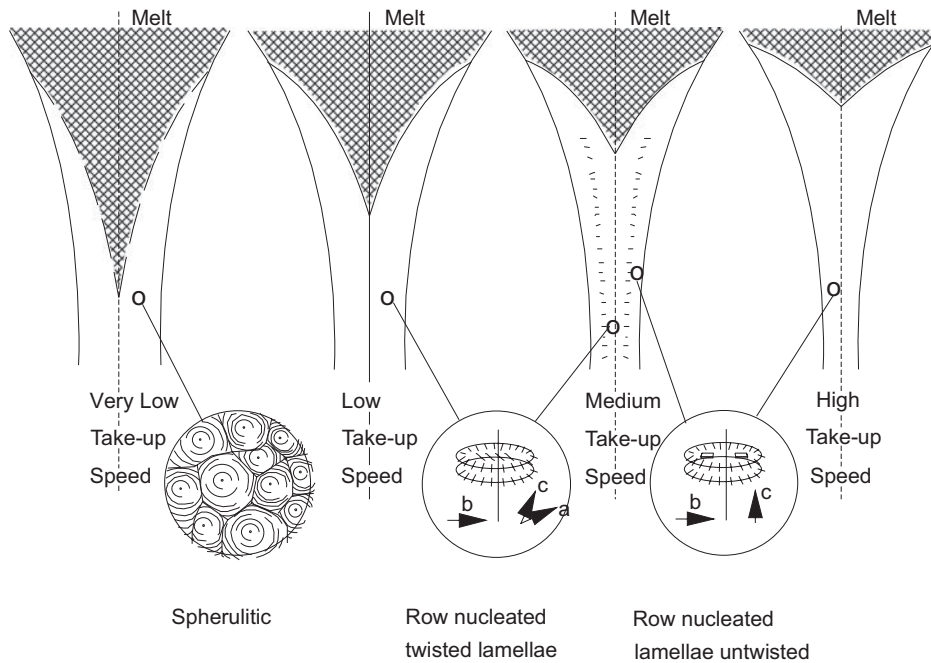


FIGURE 9.9 Morphological model of structures developed in as-spun HDPE at various take-up speeds. (Reprinted by permission of the publisher from Dees and Spruiell, 1974.)

they assumed spherulitic growth. At higher speeds the morphological model is that of row nucleated, twisted, ribbon-like lamella and at even higher speeds that of row nucleated untwisted lamellae.

9.1.5 Instabilities in Fiber Spinning

In general, the rate of production in many polymer processing operations is limited by the onset of instabilities. In melt spinning there are two major types of instabilities (Petrie and Denn, 1976). The first type is called *spinnability* and refers to the ability of a polymer melt to be transformed into long fibers (i.e., to be drawn to large elongations) without breaking because of either *capillary waves* and *necking (ductile)* or *cohesive (brittle) fracture*. The spinnability is due to the free boundary flow between the spinneret and the take-up roll. The second type is called *draw resonance*, and it appears as a periodic fluctuation in the take-up cross-sectional area. Besides these two types of instability specific to melt spinning, typical instabilities associated with flow through dies usually referred to as *melt fracture* (Section 7.2.2) are also present. We first discuss spinnability followed by draw resonance.

Brittle fracture refers to the situation of the tensile stress, τ_{zz} , of a polymer jet exceeding some critical tensile strength, τ^* . This type of fracture is possible in viscoelastic materials because these materials store some of the deformational energy, whereas purely viscous materials dissipate all the deformational energy. Figure 9.10 shows a schematic of a

polymer filament failing by means of cohesive fracture. As the polymer fiber is being drawn, its tensile stress, $\tau_{zz}(z)$, and strength, $\tau^*(z)$, increase with the axial distance z . At a certain axial distance, z_{coh}^* , both the tensile stress and strength are equal. Beyond that point, the tensile stress exceeds the strength and the material fails cohesively. For isothermal spinning of Newtonian fluids the maximum length of a polymer fiber is calculated as (Ziabicki, 1976)

$$z_{coh}^* = \frac{1}{\beta} \ln \left(\frac{(2e_{coh}E)^{1/2}}{3\eta v_0 \beta} \right) \tag{9.103}$$

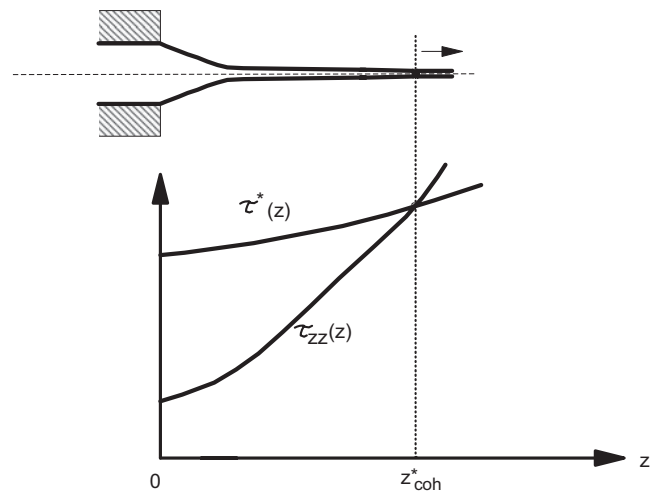


FIGURE 9.10 Cohesive (brittle) fracture of a molten thread.

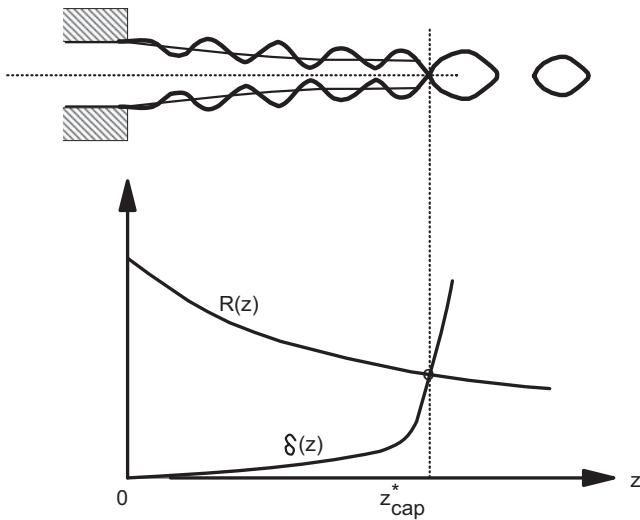


FIGURE 9.11 Breakup of a molten thread due to capillary wave instability.

where e_{coh} is the cohesive energy density (CED) of the material, β is the deformation gradient defined as $d \ln v / dz$, and E is the modulus of elasticity of the polymer.

The other mechanism responsible for instabilities during melt spinning is referred to as capillary waves or Rayleigh instabilities. Depending on the velocity of the polymer melt in the spinneret hole, three broad regimes can be distinguished: (1) formation of droplets, (2) formation of a liquid jet sustaining waves at its interface, which finally disintegrates into droplets, Figure 9.11, and (3) complete atomization. For polymer melts, the disintegration step can be described by the following equation:

$$z_{\text{cap}}^* = 12d \left(\text{Ca}^{1/3} + 3 \frac{\text{Ca}}{\text{Re}} \right) \quad (9.104)$$

where z_{cap}^* is the maximum uninterrupted jet length, d is the diameter of the jet, Ca ($= v^2 d \rho / \gamma$) is the capillary number of the jet, and Re ($= v d \rho / \eta$) is the jet Reynolds number. Note that the analysis of the stability of a molten jet is similar to the stability analysis of an extended droplet (mentioned in more detail in Section 6.5.2). Finally, note that polymers, due to their higher viscosity and lower surface tension, compared to metals and glass, can be drawn safely to larger lengths as Eq. 9.104 indicates (for the same extrusion velocity).

Diagrammatically, Figure 9.12 shows the space of all possible conditions of material properties and spinning characteristics. This space is further divided into the various regions of spinnability S , hydrodynamic stability H , cohesive fracture F , capillary breakup C , and hydrodynamic instability $x-H$. A system is called hydrodynamically stable, if an imposed small perturbation decays with time to either zero or some small steady value (see about the growth factor q in Eqs. 6.194

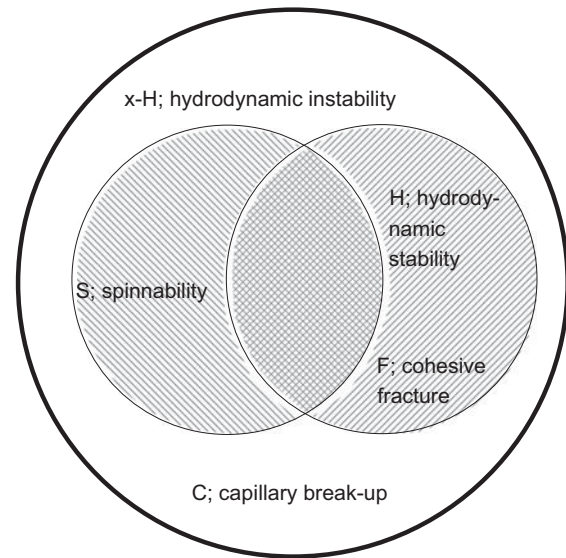


FIGURE 9.12 Space of all possible melt-spinning conditions, including regions of: hydrodynamic stability H , cohesive fracture F , capillary breakup C , spinnability S , and hydrodynamic instability $x-H$. (Reprinted by permission of the publisher from Ziabicki, 1976.)

and 6.195). The cohesive fracture region F is included into the hydrodynamic stability region. Finally, the spinnability region S consists of the part of region H where no cohesive fracture takes place, and the part of the $x-H$ region where the growth is too slow to cause breakage.

The various melt-spun materials can be divided into three groups (Ziabicki, 1976): (1) metals and glasses, (2) linear polycondensates (polyesters and polyamides) with relatively low molecular weights (from 10,000 to 30,000), and (3) linear polyolefins and vinyl polymers (PE, PP, PVC, etc.), with relatively high molecular weights (from 50,000 to 1,000,000). The basic differences between these groups are the following:

1. Metals and glasses are primarily Newtonian fluids with high surface tension (from 100 to 500 mN/m) and thus a high probability of capillary breakup.
2. Linear polycondensates are also primarily Newtonian (or slightly viscoelastic with short relaxation times) with low shear viscosity (about 100 Pa·s) and high spinnability. The die swell is obviously low (about 1.0 to 1.5) and cohesive fracture is not usually a problem. For example, the critical shear rate for the onset of melt fracture in Nylon 6,6 is about 10^5 s^{-1} at 275 °C, and the maximum spinneret shear rate is usually not higher than 10^4 s^{-1} . Usually, take-up velocities of 4000 to 5000 m/min cause no brittle fracture of these materials.
3. Linear polyolefins and vinyl polymers include melts with high shear viscosity (higher than 1000 Pa·s), with strong viscoelastic behavior, and long relaxation times. Usually, the spinning velocities of polyolefins

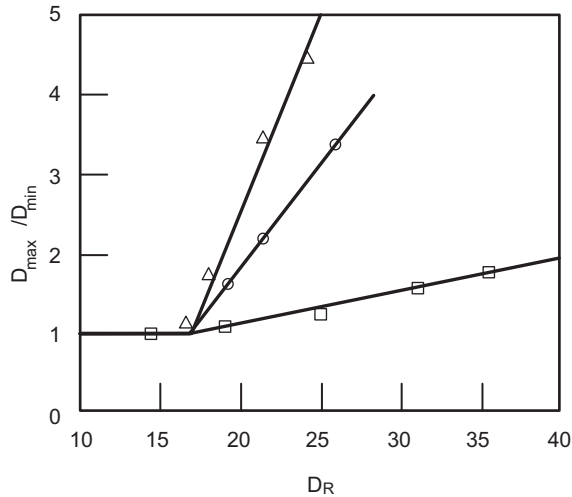


FIGURE 9.13 Diameter ratio of a drawn silicone oil filament as a function of draw ratio. Polymer volumetric flow rate in mm^3/s and spinning length in mm are: Δ —64.1, 20; \circ —44.4, 20; \square —30.8, 40. (Reprinted by permission of the publisher from Donnelly and Weinberger, 1975.)

are lower than those of polycondensates due to cohesive fracture. Also, die swell is extremely pronounced in these melts.

Draw resonance appears as a sustained periodic fluctuation with a well-defined and steady period and amplitude of the cross section at the take-up roll, and it occurs even when the flow rate and the take-up speed are constant. This instability should not be confused with the spinnability, as it has nothing to do with breakup of the filament. It appears in both purely viscous and elastic fluids, and there are two factors that reduce its effect: elasticity and nonisothermal conditions of spinning.

The steady-state solution for fiber spinning (Newtonian and isothermal case) was presented in Section 9.1.1, and it consists of Eqs. 9.26 and 9.28. Linearized (small disturbances) stability analysis involves (Fisher and Denn, 1976) the study of finite amplitude disturbances, and we do not present it. Rather, we present the results of such an analysis. The value of $D_R = 20.21$ is considered to be the critical draw ratio beyond which the flow becomes unstable. Figure 9.13 (Donnelly and Weinberger, 1975) shows experimental data that confirm the theory. More specifically, silicone oil (of viscosity equal to $100 \text{ Pa}\cdot\text{s}$), which seems to be Newtonian, was extruded and the ratio of maximum to minimum filament diameters was plotted against the draw ratio. An instability appears at a draw ratio of about 17, or about 22 if we take into consideration about 14% die swell. The value of the critical draw ratio of 22 compares well with the theoretical value of 20.21. Pearson and Shah (1974) extended the analysis to a power-law fluid and included surface tension, gravitational,

and inertial forces in the momentum balance and found that the critical draw ratio is lower than 20.21 for shear-thinning fluids and larger than 20.21 for shear-thickening fluids. For example, the critical draw ratio range is from 3 to 5 for a power-law index of 0.4 to 0.5.

The energy equation, Eq. 9.39, should be incorporated into the model to account for temperature variation along the filament axial length. Pearson and Shah (1974) solved the system of equations subjected to a linearized analysis and found that the critical draw ratio depends, besides on the power-law index, on the dimensionless number, S :

$$S = k(T_0 - T_a)(St)e^{-St} \quad (9.105)$$

where k is the viscosity temperature coefficient ($\eta_0 \propto \exp[-k(T - T_a)]$), and St is the Stanton number defined as

$$St = 2\sqrt{\frac{\pi v_0^{1/3} \zeta L}{\rho \dot{m} C_p}} \quad (9.106)$$

where ζ (units: $\text{cal}/\text{cm}^{8/3}\cdot\text{s}^{1/3}\cdot^\circ\text{C}$) is the ratio $U/v_z^{2/3}$. Note that the theoretical analysis of Pearson and Shah is based on the assumption that $U \propto v_z^{2/3}$ (valid if Eq. 9.50 is used). For shear-thinning fluids the critical draw ratio increases very slowly with S , whereas for Newtonian and shear-thickening fluids the increase is dramatic for $S > 0.1$.

Fisher and Denn (1976) presented the linearized stability analysis for the isothermal viscoelastic case as an extension of the steady-state case presented in Section 9.1.3. The analysis showed (Fig. 9.14) that the critical draw ratio depends on the power-law index, n , and on the viscoelastic parameter $\alpha^{1/n}$, where α is defined in Eq. 9.83. Three regions are shown in Figure 9.14: stable, unstable, and unattainable. The lower boundary of the unattainable region is described by the relationship $D_R = 1 + \alpha^{-1/n}$. At low values of the parameter α , the constant viscosity fluids exhibit higher critical draw ratio, and the power-law fluids exhibit a critical draw ratio value as low as 3 to 5 for n from 0.33 to 0.5. Finally, as the viscoelastic parameter α increases the critical draw ratio can increase dramatically, and it can be extended up to the unattainable region.

Experimentally, the critical draw ratio for various polymers is measured as the draw ratio at which the ratio of maximum to minimum filament diameters increases above 1. Figure 9.15 shows experimental data for PP, HDPE, and PS. The corresponding critical draw ratios are 2.7, 3.8, and 4.6. The power-law index of PP and PS is about 0.5, and thus the agreement between experimental data and theory is generally good.

Finally, finite (large) amplitude stability analysis, which can give information about the large disturbances and macroscopic diameter variations, supports the findings of the linearized stability analysis. Thus, for draw ratios less than

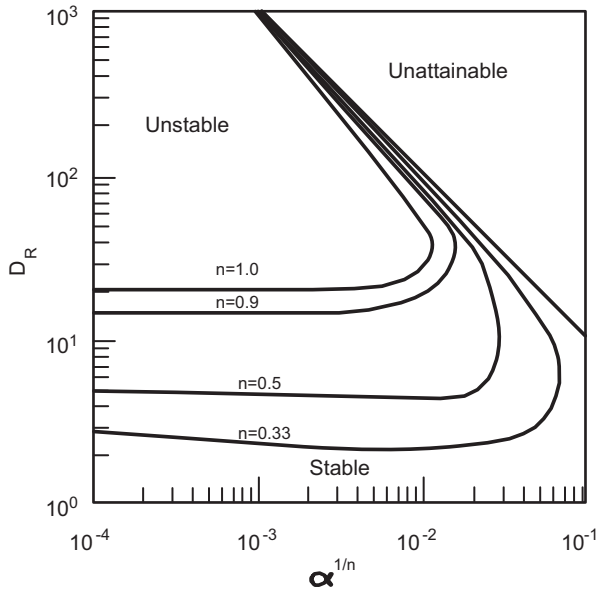


FIGURE 9.14 Critical draw ratio, D_R , as a function of the viscoelastic parameter α and the power-law index, n , for the fiber-spinning process. (Reprinted by permission of the publisher from Fisher and Denn, 1976.)

20.21 a Newtonian system is stable to finite amplitude disturbances, and for draw ratios larger than 20.21 disturbances grow and reach a sustained oscillation (draw resonance).

Example 9.3. Critical Draw Ratio and Spinning Length

A viscoelastic material is being melt spun at $D_R = 10$. Estimate the possibility of draw resonance if the spinning length

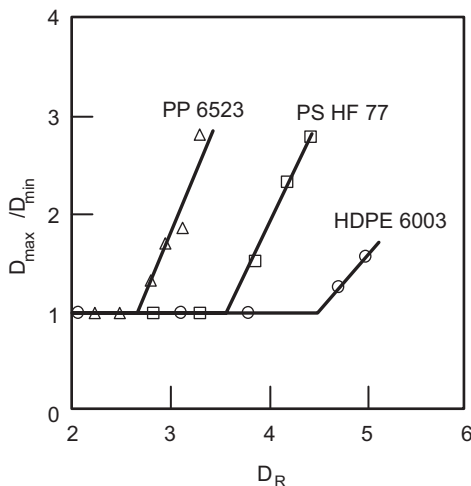


FIGURE 9.15 Diameter ratio of drawn polymers as a function of draw ratio for isothermal spinning at 218 °C. Other conditions are $v_0 = 5$ cm/s; $L = 16.5$ cm; and $R_0 = 0.08$ cm. (Reprinted by permission of the publisher from Weinberger et al., 1976.)

is 3 m. The various properties of the material are $n = 1/3$, $m = 3000$ Pa·s^{1/3}, $G = 2000$ Pa, $R_0 = 200$ μm, $\rho = 1$ g/cm³, and $\dot{m} = 0.02$ g/s. Apply the analysis of Fisher and Denn (1976). Also indicate the maximum spinning length for stable operation at the same draw ratio.

Solution. At a draw ratio of 10 and power-law index of 1/3, Figure 9.14 shows that the minimum and the maximum attainable values of the viscoelastic parameter $\alpha^{1/n}$ are 0.043 and 0.1, respectively. The velocity at zero axial distance is given as 7.09 cm/s. Thus, the parameter $\alpha^{1/n}$ is calculated as 0.027, which is outside the limits of 0.043 and 0.1. Melt spinning with these conditions is expected to result in draw resonance. To get rid of this problem we need to decrease the spinning length to about 180 cm. ■

9.2 FILM CASTING AND STRETCHING

A large activity of the polymer processing industry is the production of films and sheets of thermoplastic polymers. By definition, the term *film* is used for thicknesses less than 250 μm (equal to about 0.010 in.), and the term *sheet* is used for thicker films. Note that in this section we use the term film generically, and we occasionally mention the term sheet when confusion might occur. These products are used primarily in the packaging industry for either foodstuffs (groceries, dairy produce, etc.) or other consumer products. Quite frequently, the properties of various polymers need to be combined by coating, lamination, or coextrusion. The major properties of the films and sheets are transparency, toughness, flexibility, and a very large aspect ratio (width or length to thickness) of about 10³. Typical values of the thickness range from about 10 to 2500 μm, whereas the other two dimensions can vary from 40 to 320 cm.

Flat-film production consists mainly of the following three processes: *extrusion*, *casting*, and *stabilization*. Depending on the film thickness there are three major groups: fine film, with thickness of 10 to 50 μm; thicker cast film and sheet, with thickness of 100 to 400 μm; and thermoformable sheet, with thickness of 200 to 2500 μm. The first two groups are produced on chrome-plated chill-roll or water bath lines (see Fig. 9.16), whereas the third one is produced with a special roll. All film types, after the chill-roll or water bath, are trimmed at the edges (some curling might occur there) and either wound or undergo stretching (uniaxial or biaxial) or thermoforming. Polypropylene, polyethylene, polyester and polyamide are the four most frequently used polymers on chill-roll lines.

9.2.1 Film Casting

Figure 9.16 shows two typical configurations for film casting: the film freezes upon contact with a chill-roll or upon

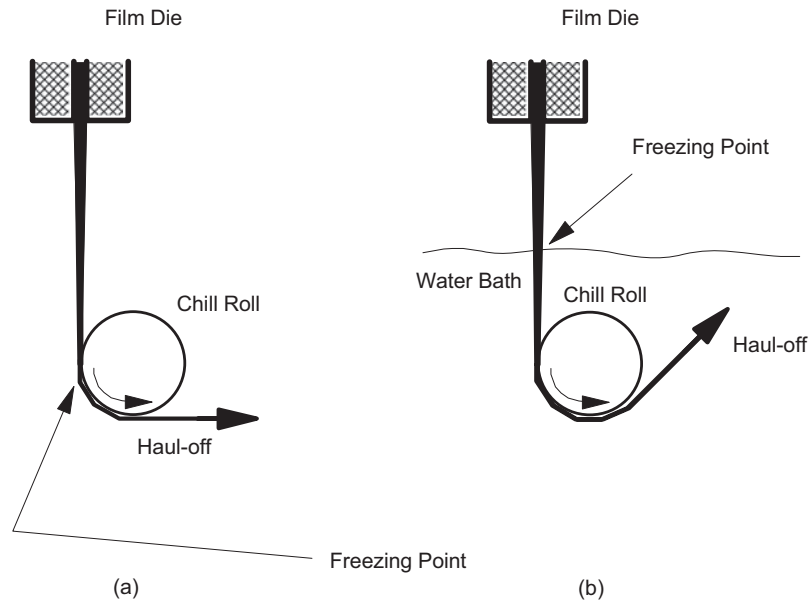


FIGURE 9.16 (a) Sectional view of chill-roll casting. (b) Sectional view of water bath casting.

submersion in a water bath. In both cases freezing occurs at a fixed point, which moves at a known velocity. Figure 9.17 shows two views of the film between the extrusion die and the chill-roll. In the following sections we describe first the general form of equations for very thin films ($|\nabla h| \ll 1$), and then we present the isothermal Newtonian case for thicker films.

Consider the origin of the Cartesian coordinate system, xyz , at the intersection of the line of symmetry and the die lips (Fig. 9.17). The original width of the polymer film (in the x direction and at the die lips) is w_0 and the extension length is L . The width of the film decreases along the z direction, because the film is being drawn in that direction by the chill-roll. Its width at the roll is w_L . Similar drawing takes place in

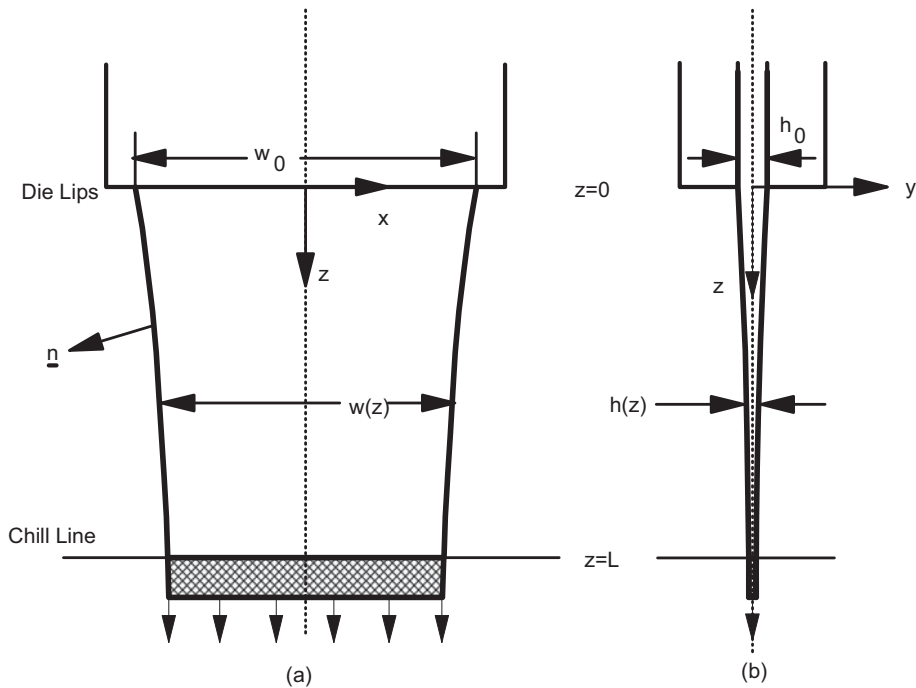


FIGURE 9.17 (a) Geometry of the front view of the film-casting process. The polymer film between the die and the roll is called the web. (b) Side view of the film-casting process.

the y direction as well, where the thickness changes from h_0 at the die lips to h_L at the chill-roll. The deformation in the y and x directions distinguishes the film-casting flow from a typical plane flow.

The die swell effect is neglected here as was done in the fiber-spinning analysis. In film casting no significant cooling is obtained between the face of the die and the chill-roll (see Section 5.2), whereas in the melt spinning of fibers cooling was very important. If the z component of the film velocity at the die lips is v_{z0} and at the freeze line is v_{zL} , then the draw ratio, D_R , is defined as (see Eq. 9.27)

$$D_R = \frac{v_{zL}}{v_{z0}} \quad (9.107)$$

Typical values of the draw ratio range from 2 to 20.

The objective of the analysis is to calculate the thickness and temperature at the chill-roll as a function of the take-up speed, rheology, distance L , and conditions at the die lips. In the case of $w_0 > L \gg h_0$, changes in the y direction can be considered insignificant for the rest of the analysis. Then, we postulate the following surface velocity field for the steady-state film-casting problem:

$$v_x = v_x(x, z); \quad v_z = v_z(x, z) \quad (9.108)$$

with the associated thickness, h , being $h(x, z)$. The continuity equation at steady state can be written as

$$\frac{\partial}{\partial x}(\rho h v_x) + \frac{\partial}{\partial z}(\rho h v_z) = 0 \quad (9.109)$$

The x and z components of the equation of motion are (Table 2.7)

$$\frac{\partial}{\partial x}(\rho h v_x^2) + \frac{\partial}{\partial z}(\rho h v_x v_z) = -\frac{\partial(h\pi_{xx})}{\partial x} - \frac{\partial(h\pi_{xz})}{\partial z} \quad (9.110)$$

$$\frac{\partial}{\partial x}(\rho h v_x v_z) + \frac{\partial}{\partial z}(\rho h v_z^2) = -\frac{\partial(h\pi_{xz})}{\partial x} - \frac{\partial(h\pi_{zz})}{\partial z} + \rho g h \quad (9.111)$$

where the surface tension and air drag forces are neglected because they are really unimportant. Also, note that we assume that the z coordinate is vertical. If the film is drawn away from the vertical, the above equations need modifications. Finally, the energy equation can be written as follows. Since the thickness of the film is considered small, the average temperature (Pearson, 1985) over the film thickness is

$$\bar{T} = \bar{T}(x, z) = \int_{-h/2}^{+h/2} T(x, y, z) \frac{dy}{h} \quad (9.112)$$

The energy equation can now be based on the average temperature as

$$\frac{\partial}{\partial x}(\rho h \bar{C}_p \bar{T} v_x) + \frac{\partial}{\partial z}(\rho h \bar{C}_p \bar{T} v_z) = -2h_a(\bar{T} - T_a) \quad (9.113)$$

where T_a is the temperature of the surrounding medium (air), and h_a is the air-side heat transfer coefficient. The heat generation by viscous dissipation has been neglected in Eq. 9.113.

The boundary conditions are:

$$\begin{aligned} \text{B.C.1: at } z = 0, \quad & v_x = 0; \quad v_z = v_{z0}; \quad h = h_0; \quad \bar{T} = \bar{T}_0 \\ \text{B.C.2: at } z = L, \quad & v_x = 0; \quad v_z = v_{zL} \\ \text{B.C.3: at } x = \pm 1/2 w(z), \quad & \boldsymbol{\pi} \cdot \mathbf{n} = 0 \end{aligned} \quad (9.114)$$

Note that B.C.3 is valid in cases where symmetry along the z axis is preserved, and surface tension is insignificant (see also Eq. 9.8). There is one additional condition, which specifies the edge:

$$\frac{\partial w}{\partial z} = \frac{v_x}{v_z} \quad (9.115)$$

Finally, the set of equations is complete with the incorporation of the rheological constitutive equation. The complicated set of equations, Eqs. 9.109, 9.110, 9.111, and 9.113, along with the constitutive equation can be simplified in the following special cases for Newtonian and isothermal conditions: (1) $L \gg w_0$, and (2) $L \ll w_0$ (see Problem 9B.5).

In the case of thicker films the flow of the polymer is considered as two-dimensional along the z (machine) and y (transverse) axes instead of the z and x axes as in the previous section (Fig. 9.17b). Thus, the width of the film will be considered constant:

$$w(z) = w_0 \quad (9.116)$$

The steady-state continuity equation now becomes

$$\frac{\partial v_z}{\partial z} + \frac{\partial v_y}{\partial y} = 0 \quad (9.117)$$

and because $v_z = v_z(z)$ Eq. 9.117 yields

$$v_y = -\frac{dv_z}{dz} y \quad (9.118)$$

The mass flow rate is calculated as

$$\dot{m} = w_0 \int_{-h/2}^{+h/2} \rho v_z dy = \rho v_z h w_0 \quad (9.119)$$

and because it is constant over time, it follows that

$$\frac{1}{h} \frac{dh}{dz} = -\frac{1}{v_z} \frac{dv_z}{dz} \tag{9.120}$$

for constant density.

The steady-state momentum equation in the z direction (for vertical casting) after neglecting inertia and gravity becomes

$$\frac{\partial \tau_{yz}}{\partial y} + \frac{\partial \pi_{zz}}{\partial z} = 0 \tag{9.121}$$

Note that the shear stress in Eq. 9.121 comes from the geometry of the system (as in the fiber-spinning case). Integration of Eq. 9.121 from $-h/2$ to $+h/2$ yields

$$w_0 h \pi_{zz} = F \tag{9.122}$$

where F is the force necessary to draw the film. π_{zz} is now correlated to the velocity gradient through an equation similar to Eq. 9.22 in the fiber-spinning case as

$$\pi_{zz} = -4\mu \frac{dv_z}{dz} = -\bar{\eta}_p \frac{dv_z}{dz} \tag{9.123}$$

where $\bar{\eta}_p$ is the planar elongational viscosity (equal to 4μ).

Upon combining Eqs. 9.119, 9.120, 9.122, and 9.123, we get the following differential equation:

$$\frac{1}{h} \frac{dh}{dz} = \frac{\rho F}{\bar{\eta}_p \dot{m}} \tag{9.124}$$

which is solved as

$$\frac{h}{h_0} = \exp \left[-z \frac{\rho |F|}{\bar{\eta}_p \dot{m}} \right] = \exp \left[z \frac{\rho F}{\bar{\eta}_p \dot{m}} \right] = (D_R)^{-z/L} \tag{9.125}$$

and consequently,

$$v_z = v_{z0} \exp \left[z \frac{\rho |F|}{\bar{\eta}_p \dot{m}} \right] = v_{z0} \exp \left[-z \frac{\rho F}{\bar{\eta}_p \dot{m}} \right] = v_{z0} (D_R)^{z/L} \tag{9.126}$$

Note that the draw ratio, D_R , in this case can be written as

$$D_R = \exp \left[-L \frac{\rho F}{\bar{\eta}_p \dot{m}} \right] = \exp \left[L \frac{\rho |F|}{\bar{\eta}_p \dot{m}} \right] \tag{9.127}$$

Equation 9.126 is similar to Eq. 9.26 of the fiber-spinning case, and in general the film-casting process can be considered the two-dimensional counterpart of the fiber-spinning process (see also Problem 9A.4).

9.2.2 Stability of Film Casting

Theoretical analysis of the stability problem for film casting shows the similarities between fiber spinning and film casting. Yeow (1974) showed that the critical draw ratio for draw resonance of Newtonian fluids is 20.21, which is exactly the same as that in the fiber-spinning case (Section 9.1.5). For non-Newtonian fluids the similarity is not necessarily preserved, but the qualitative effects of the non-Newtonian viscosity, viscoelasticity, and cooling are expected to be the same. For power-law fluids the theory suggests that the critical draw ratio increases with increasing power-law index n , being 40 and 91 for $n = 1.2$ and 1.5 , respectively. Kase (1974a) and Bergonzoni and DiCresce (1966) studied the problem experimentally and showed that the ratio of maximum to minimum film thickness ranges from 1.8 to about 4.5. Furthermore, data for PS and PP exhibited a critical draw ratio of about 20, which is in agreement with the theory.

Anturkar and Co (1988) studied the effects of viscoelasticity on the stability of the film-casting process in a similar fashion to that of Fisher and Denn (1976). The constitutive equation used in their theoretical analysis is the UCM (Eqs. 3.40 and 3.41) with the Carreau viscosity function (Eq. 2.8; with $\eta_\infty = 0$) $\eta(\dot{\gamma}) = \eta_0 (1 + \lambda_u^2 \dot{\gamma}^2)^{(n-1)/2}$, which is the White–Metzner model, and a similar function for the characteristic fluid time, $\lambda(\dot{\gamma}) = \lambda_0 (1 + \lambda_u^2 \dot{\gamma}^2)^{(n'-1)/2}$. The critical draw ratio, D_R , as a function of the viscoelastic parameter defined below,

$$\Lambda_0 (2\Lambda_t)^{n'-1} = \lambda_0 (2\lambda_u)^{n'-1} / (L/v_{z0}) \tag{9.128}$$

is shown in Figure 9.18. Note the similarity between Figures 9.14 and 9.18 for the fiber-spinning and film-casting processes.

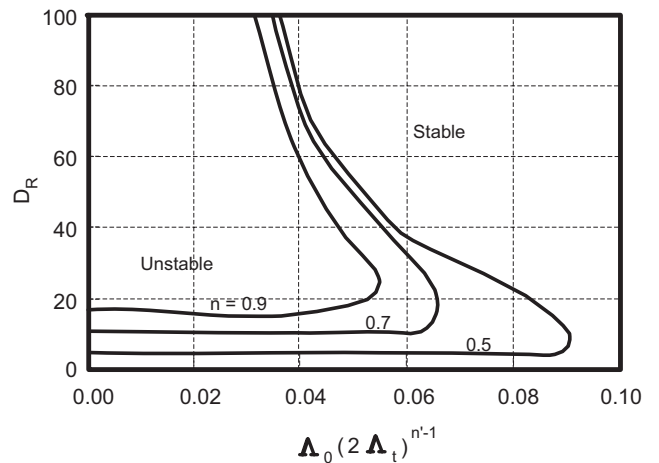


FIGURE 9.18 Critical draw ratio, D_R , as a function of the viscoelastic parameter $\Lambda_0(2\Lambda_t)^{n'-1}$ and the power-law index n , for the film-casting process. (Reprinted by permission of the publisher from Anturkar and Co, 1988.)

Finally, one problem associated with film casting is the presence of edge beads (Dobroth and Erwin, 1985; d'Halewyn et al., 1990). These edge beads in the form of thick edges appear in the web, and they cause problems in other downstream processes such as winding. The most common way to get rid of the edge beads is to cut them and either recycle or scrap them, and the associated cost is about 12% of the production cost. The main cause of this instability is the difference in stress that the center and the edges of the web experience (plain strain at the center, Section 6.3.1, "Planar Elongation (or Pure Shear)"; and uniaxial elongational stress at the edges, Section 6.3.1, "Uniaxial (or Pure) Elongation"). The experimentally observed ratio of the thicknesses of the edge to the centerline, also called *bead ratio*, is about 2 to 4. The theory based on the plain strain at the centerline and plane stress at the edges predicts a bead ratio equal to the square root of the draw ratio, and experiments confirm such a relationship.

9.2.3 Film Stretching and Properties

The term *film stretching* can also be encountered in the literature as *cold drawing* of the film. The objective of this process is to impart biaxial orientation in the film and to increase its modulus. These improvements are achieved by stretching the film in two directions (x and z ; transverse (TD) and machine (MD) directions, respectively) simultaneously. The operation temperature should be below the temperature of maximum crystallization rate and above the glass transition temperature. PP and PET have been used successfully in this process. Industrially, the process is carried out in the *stender* (or *tender*; from the textile industry). This device grips the edges of the film and extends them to larger widths as the film moves from the inlet to the exit roller. As soon as the film reaches the exit roller, the stender clamps release the grips of the film. During this stretching the polymer experiences an extensional flow.

The biaxially stretched films are characterized by the amounts of crystallinity and orientation, and their mechanical properties are correlated to the extension rates in both the machine and transverse directions. As an example we present the results for poly(phenylene sulfide) (PPS) (Maemura et al., 1989), which is an important engineering thermoplastic because of its high dimensional stability, solvent resistance, and temperature stability. PPS film 300 μm in thickness was biaxially stretched at temperatures in the range of 90–115 $^{\circ}\text{C}$ and at 600–15,000 %/min stretching rates. PPS crystallizes under stress, and the increase of stretching rate increases birefringence and crystalline orientation. As far as the tensile properties of the stretched film are concerned, the modulus of elasticity and tensile strength increase, and the elongation at break decreases with stretching. Figure 9.19 shows the effect of the stretching and the testing angle on the modulus of elasticity. The testing angle refers to the angle

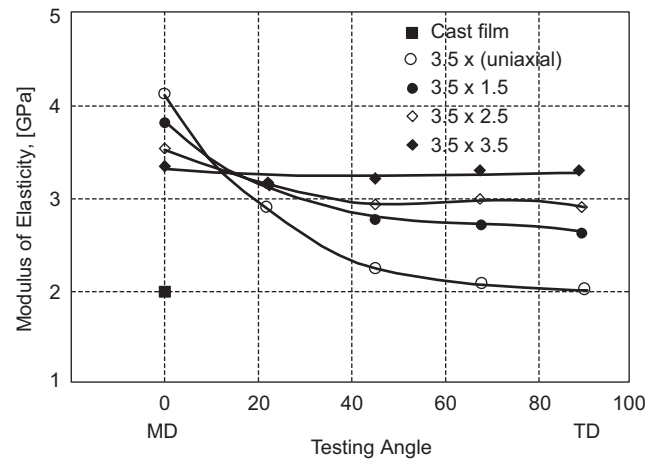


FIGURE 9.19 Modulus of elasticity of stretched and unannealed PPS films as a function of testing angles, for various stretch ratios. (Reprinted by permission of the publisher from Maemura et al., 1989.)

between the machine direction and the direction of the sample cut for testing. The most anisotropic material is that which is uniaxially drawn, while the most isotropic is that which is equally biaxially drawn. All of the samples have modulus of elasticity greater than that of the cast film, which is 2.0 GPa.

9.3 FILM BLOWING

One method to produce film with a good balance of mechanical properties is by extruding a polymer through a film die and then subsequently stretching the film in two directions as described in the previous section. The other technique involves extrusion through an annular die. Then, the moving tubular film is stretched and inflated by an air stream flowing from inside the annular die (the pressure is slightly higher than atmospheric pressure, Fig. 9.20) creating a "bubble" (see also Section 1.2). This bubble is cooled by an air jet flowing from an air ring toward its outside surface. The cooling results in crystallization and solidification, which start at the freeze line. Beyond this line the bubble boundaries become parallel to the centerline, and the polymer melt is transformed into a two-phase mixture consisting of molten and solidified polymer. Finally, the frost line (Campbell and Cao, 1987) is the other boundary of the region which starts with the freeze line. Beyond the frost line the deformation of the bubble is practically zero, and the bubble consists of one-phase material only, the solidified polymer.

This cylinder is then flattened by a set of guide rolls and taken up by a set of rubber nip rolls, which form an airtight seal at the upper end of the bubble. The takeoff at the nip rolls may be of either constant speed or constant torque. Finally, the film is wound onto cylinders and sold as "lay-flat" tubing or trimmed at the edges and wound into two rolls of flat film. Figure 9.20 (or Fig. 1.6) shows a schematic of the film

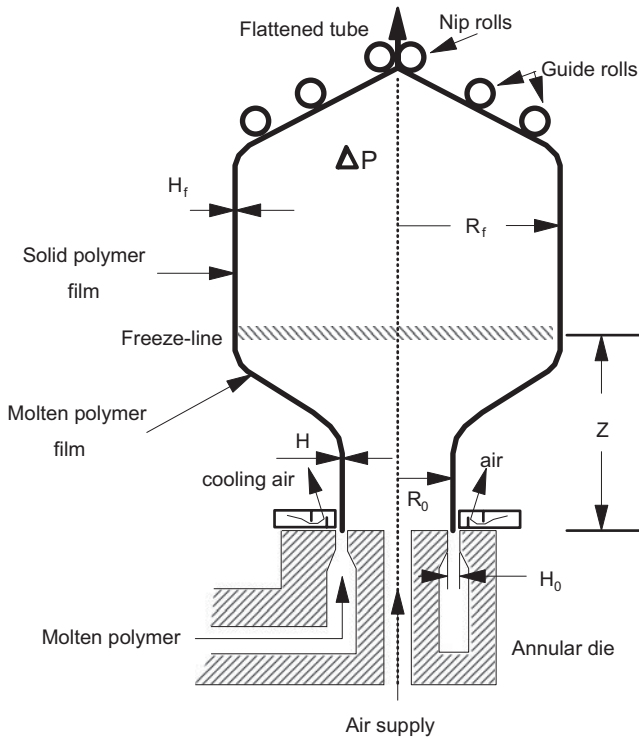


FIGURE 9.20 Film blowing process.

blowing process, which is called *tubular film blowing* (or simply film blowing). In terms of direction, most frequently this process takes place vertically upward and less frequently vertically downward and horizontally. The major advantages of this method over the first method are the economics and the speed of production.

Film blowing and fiber spinning have general similarities. Both processes have free boundaries, and the flows are predominantly elongational. They differ with respect to the orientation generated. The fiber-spinning process imparts orientation in the axial direction only, whereas the film blowing process imparts unequal (in general) biaxial orientation. The two axes of orientation are the axial (*machine*; MD) direction due to the drawing of the tube and the circumferential (*non-machine*, or *transverse*; TD) direction due to the blowup of the tube. The mechanical properties of blown film are nearly uniform in both directions as a result of biaxial orientation, and this is the reason for producing flat film by the film blowing process.

The two main parameters of this process are the *blow ratio* (or *blowup ratio*), B_R (or BUR), and the *machine-direction draw* (or *draw-down*) ratio, D_R . The blow ratio is defined as the ratio of the final tube radius, R_f , to the initial tube outside radius just downstream of the annular die, R_0 (see also Figs. 9.20 and 9.21, and Section 1.2):

$$B_R = \frac{R_f}{R_0} \quad (9.129)$$

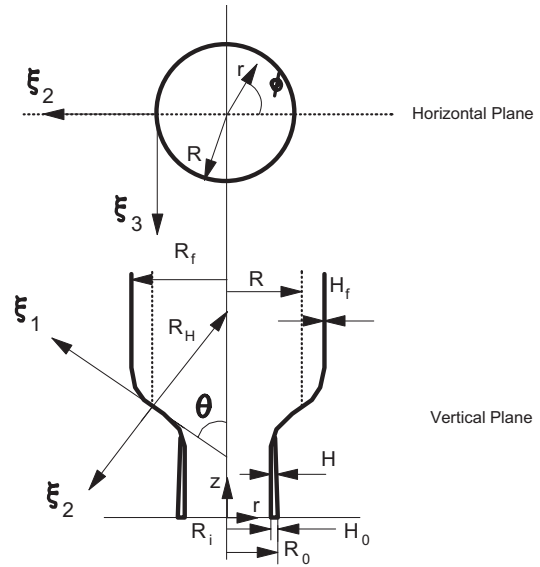


FIGURE 9.21 Moving Cartesian coordinate system and cylindrical polar coordinate system, for the film blowing process.

Similarly, the draw ratio is defined as

$$D_R = \frac{V}{v_0} \quad (9.130)$$

where V is the take-up speed, and v_0 is the die extrusion speed. The final film thickness, H_f , can be calculated from the blow and draw ratios and the mass conservation equation as follows:

$$H_f = \frac{H_0}{B_R D_R} \quad (9.131)$$

where H_0 is the initial film thickness, or equivalently the die gap thickness. Typical parameters in the film blowing process are $H_0 = 1\text{--}2$ mm; $R_0 = 2.5\text{--}25$ cm; $v_0 = 1\text{--}5$ cm/s; $B_R = 1.5\text{--}5$; $D_R = 5\text{--}25$; $\Delta P = 50$ Pa, that is, the internal pressure is about 0.05% of the atmospheric pressure; and freeze-line height $Z = 0.25\text{--}5$ m. An average value of the blow and draw ratios and of the initial film thickness yields a final film thickness on the order of $50\ \mu\text{m}$ (i.e., about 2 mils in English units). In terms of nomenclature, the final film is considered to be thick gauge blown film whenever its thickness exceeds $75\ \mu\text{m}$ or equivalently 3 mils. In terms of applications, thick gauge blown film is used in the production of dunnage bags, heavy duty shrink film, greenhouse film, lawn and garden bags, and resin and chemical packaging.

As far as the mechanical properties are concerned, the tear (test name: Elmendorf tear), impact (test name: dart drop), and tensile strengths give an indication of the mechanical strength of the tubular film. Some of these properties and the effect the processing parameters have on them were discussed in Section 1.2. The amorphous as well as the crystalline orientation developments during the blowing process depend on

the stretching imparted in the machine and transverse directions. Finally, besides orientation, the amount of crystallinity as well as the size of the crystallites may play a significant role in the mechanical and physical properties of the blown film.

This process is not as fast as fiber spinning, which results in a more uniform temperature distribution in the film relative to that in the fiber. Usually, cooling is achieved by blowing an air stream from an axisymmetric air ring toward the external film surface (see Fig. 9.20). In some cases, in addition to the external air ring, an internal air cooling system is provided. Finally, in some other cases, especially in thick tube and large bag production, cooling is achieved by a water spray or ring. Note that in the latter cases the film must be dried before winding up, which leads to an additional step.

Commercially, the film blowing process is extensively used for the production of polyolefin (LDPE, HDPE, and PP) wrapping film. Mechanical strength, optical clarity, which depends on the degree and type of crystallinity for crystallizable polymers, and the uniformity of thickness (variations of about 5% for films with a length scale of 10 mm to 10 m is acceptable) are the three most important and general properties of the film.

Before we start analyzing the equations describing the film blowing process in detail, it is worth mentioning a variation of the main technique referred to as that of the double bubble tubular film extrusion process. It has been applied by White and co-workers (Kang et al., 1990; Kang and White, 1990) to PPS and PET. It consists of producing two bubbles. The first one is generated under conditions of moderate blow and draw ratios, while the second is produced by reheating and blowing the first bubble. The process is usually employed for polymers with low melt strength and slow crystallization rates. By quenching the bubble in the first step very little crystallization occurs. The material is then heated above T_g and blown again.

As in the fiber-spinning section, we first gain extensive understanding of the film blowing process by analyzing the simplest case, that of the isothermal Newtonian film blowing case. Then, we discuss some points about the nonisothermal film blowing for Newtonian and viscoelastic materials. The stability analysis of this process is introduced, and some overall remarks are presented at the end of this section.

9.3.1 Isothermal Newtonian Model

Figure 9.21 shows a schematic of the geometry of the film blowing process. The analysis that follows comes from the work of Pearson and Petrie (1970a,b,c). Besides the assumptions of isothermal conditions and Newtonian (homogeneous and incompressible) behavior of the polymer, the following assumptions are also incorporated:

1. Inertial, gravitational, air drag, and surface tension forces are neglected.

2. The film thickness is small with respect to other characteristic dimensions (i.e., $H \ll R$ which is the *thin-sheet approximation*).
3. Die swell is neglected or the origin of the fixed coordinate system is assumed to be just beyond the maximum die swell.
4. Steady-state conditions exist.
5. The fluid bubble is axisymmetric.
6. The region between the freeze and frost lines is collapsed into a single line demarking a sharp transition between liquid and solid phases.

The significance of the second assumption is that the deformation field in the film is essentially elongational. Shear stresses are not present, if the film thickness is very small. The first assumption makes the final equations simpler without losing any significant information. Finally, overall these assumptions resemble those used in Section 9.1.2 in the thin-film theory for the fiber-spinning process.

Cylindrical polar coordinates (r, ϕ, z) are taken with z in the direction of flow (or axial direction). Also, symmetry around the z axis is assumed. Although the cylindrical system is space-fixed, for the calculation of stresses, a moving Cartesian coordinate system, ξ_1, ξ_2, ξ_3 , embedded in the inner surface of the bubble is used, as shown in Figure 9.21 (where both coordinate systems are shown). The ξ_2 direction is normal to the film (i.e., thickness direction); the ξ_1 direction is in the direction of flow (i.e., machine direction); and the ξ_3 direction is perpendicular to ξ_2 and ξ_1 and tangent to the circumferential directions.

We first calculate the strain field, then the stress field in the bubble, and finally the force balance at the frost line is written in terms of the radius and thickness of the bubble. The principal rates of strain are

$$\dot{\gamma}_{ii} = 2 \frac{\partial v_i}{\partial \xi_i} \quad (9.132)$$

where $i = 1, 2, 3$, and v_i is the i th component of the velocity vector in the moving coordinate system. Note that the $\dot{\gamma}_{ii}$ terms are equal to zero for $i \neq j$. Also note that for an incompressible fluid

$$\sum_{i=1}^3 \dot{\gamma}_{ii} = 0 \quad (9.133)$$

The goal for the subsequent analysis is to relate the various strain rates to the geometry of the film.

The v_2 velocity component is zero at the inner surface of the bubble ($\xi_2 = 0$), and it is equal to dH/dt at the outer surface of the bubble ($\xi_2 = H$). Then the velocity gradient across the

thickness of the bubble for very thin-walled bubbles is

$$\begin{aligned}\dot{\gamma}_{22} &\cong 2 \frac{v_2}{H} = \frac{2}{H} \frac{dh}{dt} = \frac{2}{H} \frac{dh}{d\xi_1} \frac{d\xi_1}{dt} = \frac{2v_1}{H} \frac{dh}{d\xi_1} \\ &= \frac{2v_1 \cos \theta}{H} \frac{dh}{dz}\end{aligned}\quad (9.134)$$

where use of the following correspondence between the space-fixed cylindrical and the moving Cartesian systems was made:

$$d\xi_1 = \frac{1}{\cos \theta} dz \quad (9.135)$$

Similarly, the extension rate in the ξ_3 direction is calculated using the circumferential velocity, v_3 , which in turn is related to the rate of bubble expansion. Thus,

$$\dot{\gamma}_{33} = \frac{2v_1 \cos \theta}{R} \frac{dR}{dz} \quad (9.136)$$

and from Eq. 9.133 we get the following expression for the last extension rate:

$$\dot{\gamma}_{11} = -2v_1 \cos \theta \left(\frac{1}{H} \frac{dh}{dz} + \frac{1}{R} \frac{dR}{dz} \right) \quad (9.137)$$

The continuity equation relates the mass polymer flow rate, \dot{m} , to v_1 as follows:

$$\dot{m} = 2\rho\pi RHv_1 \quad (9.138)$$

Equation 9.138 can be incorporated into Eqs. 9.134, 9.136, and 9.137 to yield the following rate of deformation tensor:

$$\dot{\boldsymbol{\gamma}} = \frac{\dot{m} \cos \theta}{\rho\pi RH} \begin{bmatrix} -\frac{1}{H} \frac{dH}{dz} - \frac{1}{R} \frac{dR}{dz} & 0 & 0 \\ 0 & \frac{1}{H} \frac{dH}{dz} & 0 \\ 0 & 0 & \frac{1}{R} \frac{dR}{dz} \end{bmatrix} \quad (9.139)$$

Now, we can calculate the stress field in the bubble. For a Newtonian fluid,

$$\pi_{ij} = p\delta_{ij} - \mu\dot{\gamma}_{ij} \quad (9.140)$$

where the components of $\boldsymbol{\pi}$ refer to the ξ coordinate system. Because no external forces act on the bubble, $\pi_{22} = 0$ (for $\Delta P \ll p$), and thus the isotropic pressure in the fluid is

$$p = \mu\dot{\gamma}_{22} = \frac{\mu\dot{m} \cos \theta}{\rho\pi RH} \frac{1}{H} \frac{dH}{dz} \quad (9.141)$$

Thus, the rest of the nonzero total stress components are equal to

$$\pi_{11} = \frac{\mu\dot{m} \cos \theta}{\rho\pi RH} \left(\frac{2}{H} \frac{dH}{dz} + \frac{1}{R} \frac{dR}{dz} \right) \quad (9.142)$$

$$\pi_{33} = \frac{\mu\dot{m} \cos \theta}{\rho\pi RH} \left(\frac{1}{H} \frac{dH}{dz} + \frac{1}{R} \frac{dR}{dz} \right) \quad (9.143)$$

In order to be able to determine the thickness and the radius of the bubble, we must apply force balances on the bubble. Taking a fluid element with dimensions $2\pi R$, H , and $d\xi_1$, the viscous forces in the axial (L) and transverse (H) directions are, respectively,

$$\begin{aligned}F_L &= 2\pi RH\pi_{11} \\ dF_H &= Hd\xi_1\pi_{33}\end{aligned}\quad (9.144)$$

The above equations can also be written in terms of viscous forces per unit length as

$$\begin{aligned}P_L = H\pi_{11} &= \frac{F_L}{2\pi R} = \frac{\mu\dot{m} \cos \theta}{\rho\pi R} \left(\frac{2}{H} \frac{dH}{dz} + \frac{1}{R} \frac{dR}{dz} \right) \\ P_H = H\pi_{33} &= \frac{dF_H}{d\xi_1} = \frac{\mu\dot{m} \cos \theta}{\rho\pi R} \left(\frac{1}{H} \frac{dH}{dz} + \frac{1}{R} \frac{dR}{dz} \right)\end{aligned}\quad (9.145)$$

For thin shells the pressure difference between the inside and outside of the film, ΔP (also called internal overpressure), is related to the forces per unit length in the film as follows:

$$\Delta P = \frac{(-P_L)}{R_L} + \frac{(-P_H)}{R_H} \quad (9.146)$$

which is similar to the Young and Laplace equation (Eq. 9.44) for the pressure inside a bubble. In the above equation, R_L and R_H are the principal radii of curvature of the bubble surface at the point of interest (Fig. 9.21). These radii are calculated by geometrical arguments as

$$R_H = R \sec \theta = R \left(1 + \left(\frac{dR}{dz} \right)^2 \right)^{1/2} \quad (9.147)$$

$$R_L = -\frac{\sec^3 \theta}{d^2 R / dz^2} = -\frac{(1 + (dR/dz)^2)^{3/2}}{d^2 R / dz^2} \quad (9.148)$$

Finally, the draw (or draw-down) force at the frost line, F_Z , is related to the pressure difference and the viscous force in the axial direction as

$$2\pi R P_L \cos \theta - \pi (R_f^2 - R^2) \Delta P = F_Z = -|F_Z| \quad (9.149)$$

where R_f is the constant bubble radius beyond the frost line, and F_Z is considered to be constant beyond the frost line.

Equations 9.145–9.149 can be combined together to yield the following two differential equations:

$$2r^2(\hat{T} + r^2B)r'' = 6r' + r \sec^2 \theta(\hat{T} - 3r^2B) \quad (9.150)$$

and

$$\frac{w'}{w} = -\frac{r'}{2r} - \sec^2 \theta \frac{\hat{T} + r^2B}{4} \quad (9.151)$$

where the various dimensionless variables and parameters are defined as follows:

$$r = \frac{R}{R_0}; \quad w = \frac{H}{R_0}; \quad x = \frac{z}{R_0}; \quad \sec^2 \theta = 1 + (r')^2 \quad (9.152)$$

$$B = \frac{\rho\pi R_0^3 \Delta P}{\mu \dot{m}}; \quad T_Z = \frac{\rho R_0 |F_Z|}{\mu \dot{m}}; \quad \hat{T} = T_Z - B_R^2 B \quad (9.153)$$

and (') means differentiation with respect to x (i.e., $\equiv d/dx$). Thus, B is the dimensionless internal overpressure, and \hat{T} is the dimensionless stress. Typical values of these parameters are $0.075 \leq B \leq 0.4$ and $0.5 \leq T_Z \leq 2.5$. Equation 9.150 is a second-order differential equation for the bubble radius, and Eq. 9.151 is a first-order differential equation for the bubble wall thickness. The boundary conditions for these equations are

$$\text{B.C.1: at } x = 0, \quad r = 1 \quad (9.154)$$

$$\text{B.C.2: at } x = X = \frac{Z}{R_0}, \quad r' = 0 \quad (9.155)$$

$$\text{B.C.3: at } x = 0, \quad w = w_0 = \frac{H_0}{R_0} \quad (9.156)$$

Typical values of X range from 5 to 20. Equation 9.150 with boundary condition Eqs. 9.154 and 9.155, and Eq. 9.151 with boundary condition Eq. 9.156 constitute the set of differential equations and boundary conditions that describe the isothermal Newtonian model. Note that to solve this model we need to specify Z and H_0 , which in general are not known a priori. Pearson and Petrie (1970c) solved this model numerically with three parameters: B , T_Z , and X (see also Problem 9C.2). Their results are shown in parametric graphs such as Figure 9.22. Similarly, Figure 9.23 shows the blow ratio as a function of the thickness reduction for $X = 5$. Furthermore, if one specifies one of these parameters, the other two must be adjusted to give the desired product dimensions (see Table 9.3). Finally, note that in the following relationship the thickness ratio is calculated as a function of the draw and blow ratios (see also Eq. 9.131):

$$\frac{H_0}{H_f} = B_R D_R \quad (9.157)$$

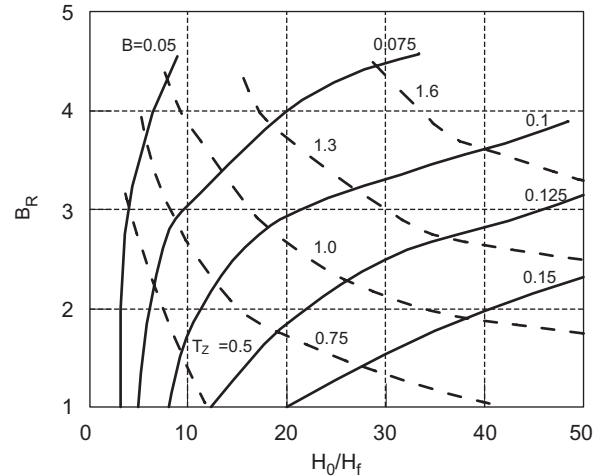


FIGURE 9.22 Calculated isoparametric curves of blowup versus thickness ratio, for the Newtonian isothermal model and $X = 20$. (Reprinted by permission of the publisher from Pearson and Petrie, 1970c.)

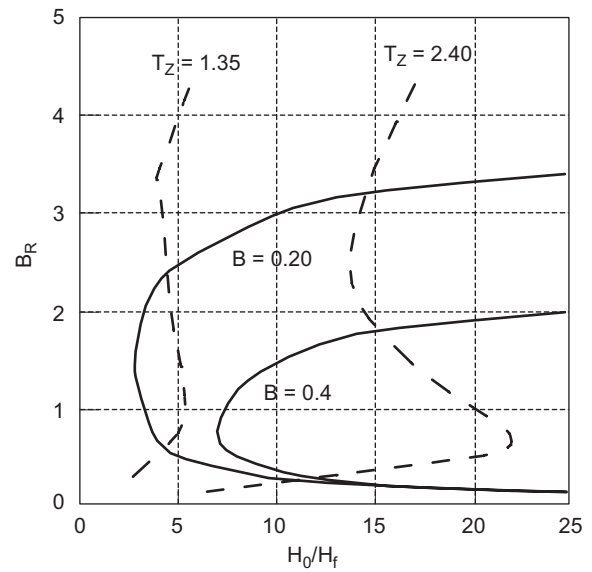


FIGURE 9.23 Calculated isoparametric curves of blowup versus thickness ratio, for the Newtonian isothermal model and $X = 5$. (Reprinted by permission of the publisher from Cain and Denn, 1988.)

TABLE 9.3 X , B , and T_Z Required to Give $B_R = 3$ and $D_R = 20/3$

X	8	9	10	20	23
B	0.2	0.175	0.165	0.1	0.09
T_Z	2.3	2.0	1.85	1.15	1.0

Source: Pearson and Petrie, 1970c.

Example 9.4. Blown LLDPE Film

Tubular linear low-density polyethylene (LLDPE) film of thickness equal to 34.1 μm is produced (Kanai and White, 1984) by a blown film operation with draw ratio equal to 4. The annular die has an inner diameter 1.387 cm and outer diameter 1.496 cm. Calculate the pressure of the air to blow a bubble (i.e., the internal overpressure) of the given specifications and the axial tension to draw such a bubble. Consider that LLDPE is Newtonian with viscosity 720 Pa·s, the process is isothermal at 180 °C, and LLDPE freezes at an axial distance of 15 cm. The mass flow rate of the polymer is 0.21 g/s, and its density is 0.919 g/cm³.

Solution. We have $Z = 15$ cm and $R_0 = 1.496/2$ cm = 0.748 cm. Thus,

$$X = \frac{Z}{R_0} = \frac{15}{0.748} = 20 \quad (9.158)$$

Consequently, Figure 9.22 applies to this blown film case. The thickness ratio is easily calculated to be

$$\frac{H_0}{H_f} = \frac{\left(\frac{1.496 - 1.387}{2}\right)}{34.1 \times 10^{-4}} \cong 16 \quad (9.159)$$

and the blow ratio is then

$$B_R = 16/4 = 4 \quad (9.160)$$

From Figure 9.22 and for a blow ratio of 4 and thickness ratio of 16 the corresponding approximate values of the parameters B and T_Z are 0.0675 and 1.15, respectively. Finally, Eq. 9.153 yields the following values for the pressure and tension:

$$\Delta P = 8.45 \text{ Pa} \quad F_Z = -25 \text{ mN} \quad (9.161)$$

9.3.2 Nonisothermal Newtonian Model

The isothermal Newtonian model is a useful model, because it reveals most of the characteristics of the tubular film blowing process. Nevertheless, it suffers from two disadvantages: the actual film blowing process is basically a nonisothermal process, and the polymer melt is non-Newtonian in character. In this section we address the nonisothermal case, and in the next section the matter of the non-Newtonian character of the polymer melt.

In industrial practice, cooling of the blown film is enhanced from the outside by an annular air jet, which flows from an air ring (see Fig. 9.20) attached very close to the die and/or the inside by a process called *internal bubble cooling* (IBC). Note that the air jet usually “hits” the film

bubble at a point slightly above the die, so that the heat transfer that occurs in the region between the die and that point is rather low. There are two ways to approach the nonisothermal nature of the film blowing process. The first one includes the temperature dependence of viscosity and density only, but does not employ the energy equation, whereas the second approach includes the use of the energy equation.

Petrie (1975) incorporated the effect of temperature on Newtonian viscosity and density through exponential and linear relationships, respectively (for the viscosity function see also Eq. 9.105),

$$\mu = \mu_0 \exp[-k(T - T_0)] \quad (9.162)$$

$$\rho = \frac{\rho_0}{1 + c(T - T_0)} \quad (9.163)$$

where the various constants have the following values for LDPE: $k = 0.03$ °C⁻¹; $c = 0.00069$ °C⁻¹; $\rho_0 = 0.801$ g/cm³; and $T_0 = 115$ °C. Note that the actual value of μ_0 is not needed until the pressure difference across the film is calculated. In this model, $\dot{\gamma}_{11}$ differs from that of Eq. 9.137, and it is equal to

$$\dot{\gamma}_{11} = -2v_1 \cos \theta \left(\frac{1}{H} \frac{dH}{dz} + \frac{1}{R} \frac{dR}{dz} + \frac{1}{\rho} \frac{d\rho}{dT} \frac{dT}{dz} \right) \quad (9.164)$$

The temperature profile was taken from experimental data. This theory underestimates the actual bubble size obtained from experimental data.

The next approach incorporates the energy equation (Wagner, 1976). By assuming no heat transfer at the inner surface the steady-state energy equation (Eq. 9.38) takes the following form (see also Eq. 9.47):

$$\bar{C}_p \frac{\dot{m} \cos \theta}{2\pi R} \frac{dT}{dz} = h_a(T_a - T) + \sigma \varepsilon (T_a^4 - T^4) \quad (9.165)$$

where all the variables are defined as in Eq. 9.40. The boundary condition required to solve Eq. 9.165 is

$$\text{B.C.1: at } z = 0, \quad T = T_0 \quad (9.166)$$

Moreover, the temperature at the frost line X is equal to the solidification temperature of the polymer, which is the crystallization temperature for semicrystalline polymers (about 116 °C for LDPE) and the glass transition temperature for amorphous polymers. Wagner (1976) assumed a constant heat transfer coefficient, h , equal to 8.33×10^{-4} cal/cm²·s·°C, relative emissivity, ε , equal to 0.3, exit temperature, T_0 , equal to 160 °C, $k = 0.033$ °C⁻¹, $c = 0.00073$ °C⁻¹, $\rho_0 = 0.782$ g/cm³, and

$$\bar{C}_p = 0.478 + 8.46 \times 10^{-4} T \quad (9.167)$$

in cal/g·°C (see also Table 5.6 for equivalent relationships). These values of the parameters are for LDPE. Note that general relations for the heat transfer coefficient can be found in Kanai and White (1984). The prediction of the model agreed well with experimental data, only when an average Newtonian viscosity was assumed for the process, which also depended on the draw ratio.

Kanai and White (1985) combined the dynamics of the process, which is expressed in Eqs. 9.138, 9.150, 9.151, and the following equations for the energy balance and the Newtonian viscosity:

$$\bar{C}_p \frac{\dot{m} \cos \theta}{2\pi R} \frac{dT}{dz} = h_a(T_a - T) + \sigma \varepsilon (T_a^4 - T^4) + \frac{\rho_c \dot{m} \cos \theta}{\rho} \frac{\Delta \bar{H}_c}{2\pi R} \frac{d\phi_c}{dz} \quad (9.168)$$

$$\mu = \mu_0 \exp \left[\frac{E}{R_g} \left(\frac{1}{T} - \frac{1}{T_0} \right) \right] \exp[C\phi_c] \quad (9.169)$$

where C is a constant obtainable from experimental results of viscosity versus percent crystallinity. The resulting set of four differential equations was solved numerically, and it was shown that the predicted and experimental data agree well at least qualitatively.

9.3.3 Nonisothermal Non-Newtonian Model

A purely viscous non-Newtonian approach was followed by Han and Park (1975b). They used the power-law model and the energy equation, assuming that the effects of crystallization were insignificant. The agreement of this model with experimental data in terms of the bubble radius and thickness as a function of the axial distance for LDPE and HDPE was reported to be reasonable. In terms of viscoelastic models, Luo and Tanner (1985) considered the Leonov model, and Cain and Denn (1988) considered the upper convected Maxwell and Marrucci models in nonisothermal cases of film blowing. In some of the cases analyzed, multiple steady-state solutions were present (see also Problem 9C.2).

Campbell and Cao (1987) presented a different model that incorporates the interaction of crystallinity, viscoelasticity, and the two phases, liquid and solid, on the bubble shape. Equations 9.139 and 9.146–9.149 remain the same, whereas Eq. 9.145 is now given by

$$\begin{aligned} P_L &= H^l \pi_{11}^l + H^s \pi_{11}^s \\ P_H &= H^l \pi_{33}^l + H^s \pi_{33}^s \end{aligned} \quad (9.170)$$

where the superscripts l and s denote liquid and solid phase, respectively. The mass conservation equation is

$$\dot{m} = 2\rho\pi R(H^l \rho^l + H^s \rho^s)v_1 \quad (9.171)$$

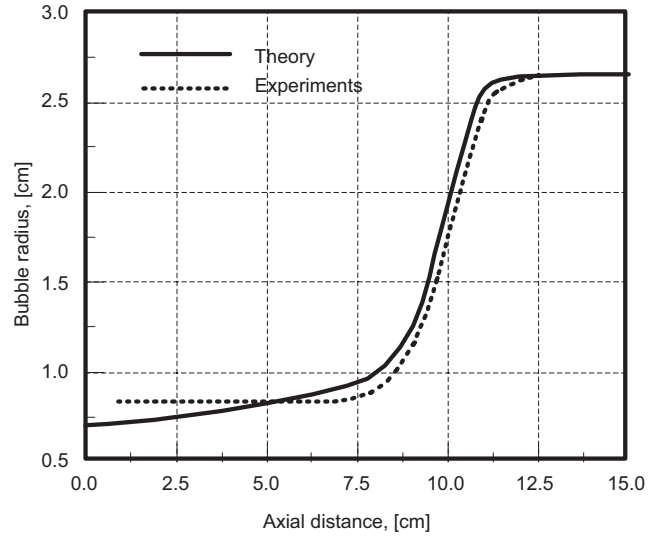


FIGURE 9.24 Comparison of model and experimental bubble shape. (Reprinted by permission of the publisher from Campbell and Cao, 1987.)

The rheological modeling of the solid phase was based on a mechanical model of a dashpot connected in parallel with a spring and a slide. For small stresses, the model is equivalent to a dashpot and a spring (Kelvin–Voigt two-element model). For large stresses, the model is equivalent to the Bingham model. The rheology of the liquid phase was described by a truncated power-law model. The overall model is essentially a UCM model with altered parameters. By combining all these equations, as well as the energy equation (similar to Eq. 9.91), Campbell and co-workers solved the tubular film blowing problem numerically, and their results are shown in Figures 9.24 and 9.25. Figure 9.24 shows the bubble radius as a function of the axial distance. The agreement between

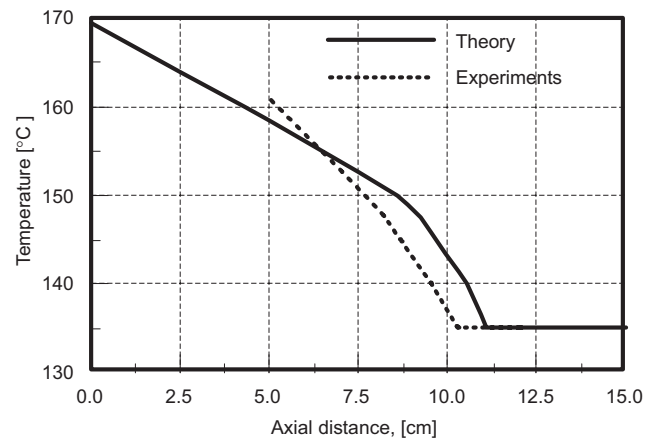


FIGURE 9.25 Comparison of model and experimental temperature profiles. (Reprinted by permission of the publisher from Campbell and Cao, 1987.)

theory and experiments (HDPE, from Kanai and White, 1984) is quite good, especially near the freeze and frost lines. The agreement is better near the freeze and frost lines for the temperature as a function of the axial distance (Fig. 9.25). Cao and Campbell (1990) also found similar agreement between experimental data for PS and theoretical results.

It is clear from all this that the film blowing process still remains difficult to analyze theoretically. In practice, the operator of the film blowing tower adjusts the various parameters by trial and error. Consequently, one major consideration is the scaleup (Section 9.3.6) of a small experimental setup to an industrial scale film blowing tower, especially for polymers tested for the first time in the experimental setup.

9.3.4 Biaxial Stretching and Mechanical Properties

Biaxial stretching is part of the tubular blown film process. This type of stretching was also encountered in the second step of a film casting process (see Section 9.2.3). Biaxially stretched PPS from a film casting process was analyzed in Section 9.2.3, where it was shown that the modulus of elasticity in the MD decreases with increasing TD stretching. On the other hand, the TD modulus of elasticity increases with increasing stretching in the same direction. The same trend was shown to be followed by PET in tubular film blowing experiments (Ma and Han, 1988). As far as the effect of MD stretching (which in the film blowing nomenclature is called draw ratio) on the modulus of elasticity is concerned, Ma and Han (1988) showed experimentally that the MD modulus increases and the TD modulus decreases with increasing draw ratio.

9.3.5 Stability of Film Blowing

Unstable flow in film blowing, fiber spinning, and film casting is unacceptable for two reasons: (1) it limits the production rate of the facility, and (2) it lowers the quality of the product. As was mentioned in Section 9.1.5 for melt spinning, besides melt fracture, which is associated with die flow, *draw resonance* is present as a periodic diameter fluctuation, when the draw ratio exceeds a critical value. Draw resonance as it applies to the uniaxial extension cases of fiber spinning and film casting was analyzed in Section 9.1.5. On the other hand, film blowing in the general sense imparts biaxial orientation in the film, and the equivalence of draw resonance appears now as a sequence of surface waves (Han and Park, 1975c; Fig. 9.26). Furthermore, if the blow and draw ratios are such that uniaxial extension (see Problem 9B.7) is dominant in the film blowing process, then draw resonance appears as in the fiber-spinning case.

Han and Park (1975c) experimentally studied flow instabilities in film blowing by introducing disturbances in the air overpressure or the take-up speed. They found that HDPE and LDPE are more sensitive to take-up speed disturbances

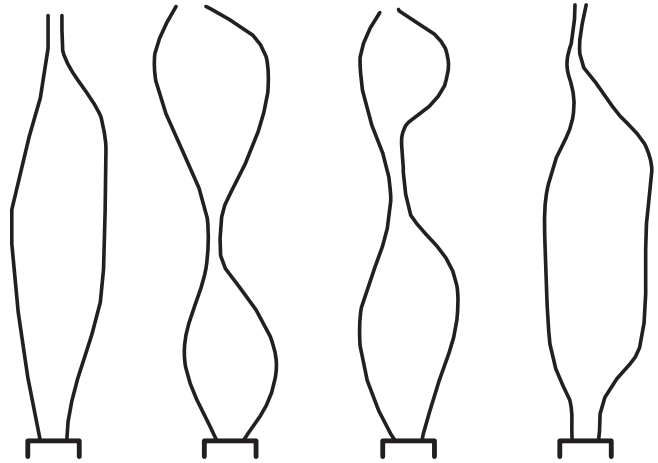


FIGURE 9.26 Typical bubble instability shapes. (Reprinted by permission of the publisher from Kanai and White, 1984.)

than to air overpressure disturbances and that a decrease in melt temperature tends to stabilize the bubble after it has been disturbed. Finally, the disturbed bubble stabilized itself when the size of the disturbance is below a critical value.

Yeow (1976) theoretically analyzed the instabilities due to axisymmetric disturbances in an isothermal Newtonian fluid and presented neutral stability curves in the space w_f ($= H_f/R_0$) and B_R and for various values of the parameter X ($X = Z/R_0$, which is the dimensionless freeze line). Kanai and White (1984) experimentally studied the stability of nonisothermal film blowing of viscoelastic melts, such as LLDPE, LDPE, and HDPE, and their results are shown in Figures 9.27 and 9.28. LDPE is more stable than LLDPE and HDPE, which is in accord with LDPE's strain hardening

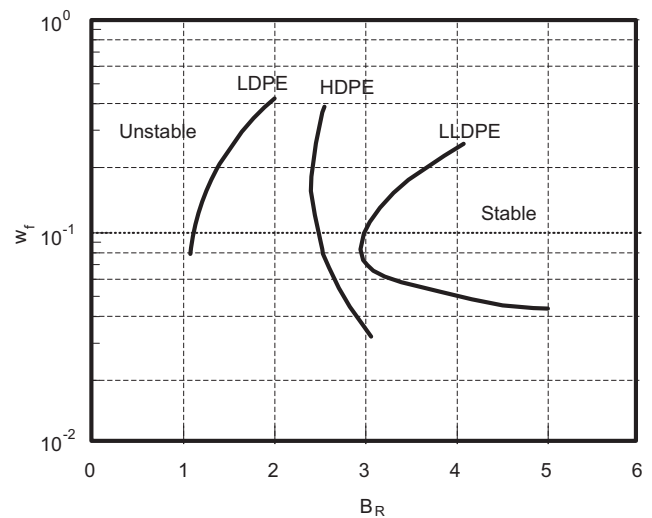


FIGURE 9.27 Stability and instability regions in the space: w_f and B_R , for $X = 16$. (Reprinted by permission of the publisher from Kanai and White, 1984.)

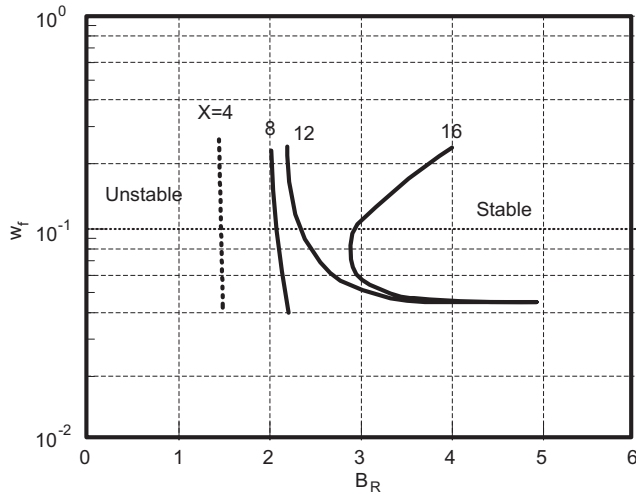


FIGURE 9.28 Stability and instability regions in the space: w_f and B_R , for various X , and for LLDPE. (Reprinted by permission of the publisher from Kanai and White, 1984.)

extensional behavior. In addition, for LLDPE as the frost-line height increases, the bubble becomes more unstable.

9.3.6 Scaleup

Scaleup is a process that is best investigated through the use of dimensionless numbers and scaleup criteria. The latter determine the variables that are expected to be the same in the laboratory and industrial scale, and the equality of the various dimensionless numbers and groups ensure that the solution of the governing equations remains the same in both scales. For example, if the ratios of various geometrical lengths in both cases are the same, then *geometrical similarity* is observed. Similarly, both scales are considered to be *dynamically similar* if the Reynolds number is the same. Weissenberg, Deborah, Reynolds, Froude, and Weber numbers are some of the most frequently encountered dimensionless numbers in the scaleup process. The best approach for scaleup is discussed in Problem 9D.3. See also Pearson (1985) for a detailed discussion of film blowing scaleup and the relevant dimensionless groups for a viscoelastic polymer melt.

9.4 SOLUTION TO DESIGN PROBLEM VIII

In this design problem we need to analyze the process in two sections: (a) from the die to the die swell level, and (b) from the die swell level to the nip rolls. In the first section, the critical wall shear rate for melt fracture, taking into consideration the safety factor, will dictate the dimensions of the die. The volume of material in each bag is calculated as $2 \times (61 \times 69.6 \times 0.002541) = 21.6 \text{ cm}^3$. The mass flow

rate is then calculated from the requirement of production of 1500 bags/h as

$$\dot{m} = 1500 \frac{\text{bags}}{3600 \text{ s}} \times 0.92 \frac{\text{g}}{\text{cm}^3} \times 21.6 \frac{\text{cm}^3}{\text{bag}} = 8.3 \text{ g/s} \quad (9.172)$$

From the statement of the problem we know that

$$R_f = \frac{2 \times 61}{2\pi} \text{ cm} = 19.4 \text{ cm}; \quad H_f = 0.002541 \text{ cm} \quad (9.173)$$

Assume that R_0 is the die outer radius, and that κR_0 is the die inner radius. As the final thickness of the film is $25.41 \text{ }\mu\text{m}$, it is reasonable to expect that the die gap is small, and consequently that the annular die can be approximated by a slit of thickness, H_0 , and width, W_0 , where

$$H_0 = R_0(1 - \kappa) \quad (9.174)$$

$$W_0 = \pi R_0(1 + \kappa) \quad (9.175)$$

Die swell is present in this problem, and the radius and thickness at the maximum die swell level will be noted as R_p and H_p , respectively (see Fig. 3.1). Note that the dimensions at this die swell level will be considered as the initial dimensions for the film blowing process. From Table 1.1 we get that $H_p = 0.018 \text{ in.} = 0.0457 \text{ cm}$ for a die land length of 3.81 cm . Thus, the reduction in film thickness becomes

$$\frac{H_p}{H_f} = B_R D_R = 18 \quad (9.176)$$

The dimensions of the die are determined by means of a mass balance and the thickness increase in the film due to die swell as follows. Equation 3.89 is used as

$$B = \frac{R_p}{R_0} = \frac{H_p}{H_0} = 0.1 + \left[1.0 + \frac{1}{2} \left(\frac{N_{1,w}}{2\tau_{xy,w}} \right)^2 \right]^{1/6} \quad (9.177)$$

The wall shear stress inside the die is one-third of the maximum wall shear associated with the onset of melt fracture; that is, it is equal to $([1.13 \times 10^5]/3) \text{ Pa} = 37,667 \text{ Pa}$. Thus, the allowed ratio in parentheses in Eq. 9.177 (primary normal stress difference over wall shear stress) is equal to

$$\frac{N_{1,w}}{2\tau_{xy,w}} = \frac{0.119}{2} \tau_{xy,w}^{0.304} = 1464 \quad (9.178)$$

Consequently, the die swell ratio (Eq. 9.177) becomes

$$\frac{R_p}{R_0} = \frac{H_p}{H_0} = 1.23 \quad (9.179)$$

Substituting the known die swell film thickness into Eq. 9.179, we get the first equation for the unknowns R_0 and κ :

$$R_0(1 - \kappa) = \frac{0.0457}{1.23} \text{ cm} = 0.03721 \text{ cm} \quad (9.180)$$

The second equation comes from the mass balance and is

$$\dot{m} = \frac{\rho\pi R_0^3(1 - \kappa^2)}{2(s + 2)} \left(\frac{\tau_{xy,w}}{m} \right)^s \quad (9.181)$$

where the use of Table 2.5 for flow in a slit die was made. Thus, Eq. 9.181 yields

$$R_0^3(1 - \kappa^2) = 0.8641 \text{ cm}^3 \quad (9.182)$$

Equations 9.180 and 9.182 can be recast into a single quadratic equation with the following solution:

$$R_0 = 3.41 \text{ cm} \quad \kappa = 0.99 \quad (9.183)$$

The value of κ , which is very close to 1, justifies the approximation of the annular die with a slit die made at the beginning of this section. The die gap is thus calculated to be 0.03721 cm = 372.1 μm or 14.65 mils. Equations 9.179 and 9.183 can be combined to yield $R_p = 4.1 \text{ cm}$ or 1.65 in.

The blow and draw ratios of the film blowing process can be calculated from the known values of the radii of the die and final bubble, and from Eq. 9.176 as

$$B_R = \frac{R_f}{R_p} = \frac{19.4}{4.2} = 4.62 \quad (9.184)$$

$$D_R = \frac{V}{v_p} = \frac{18}{B_R} = 3.89 \quad (9.185)$$

To calculate the drawing velocity we need to calculate first the velocity at the die and the die swell level. This is done through mass balances as follows:

$$v_0 = \frac{\dot{m}}{\rho\pi R_0^2(1 - \kappa^2)} = 13.6 \text{ cm/s} \quad (9.186)$$

and

$$v_p = v_0 \frac{R_0^2 - (R_0 - H_0)^2}{R_p^2 - (R_p - H_p)^2} = 9.0 \text{ cm/s} \quad (9.187)$$

Thus, the drawing velocity is calculated as

$$V = D_R v_p = 35.0 \text{ cm/s} \quad (9.188)$$

which is equivalent to 68.8 fpm (feet per min).

The film blowing process in this case is assumed to be isothermal, and we consider the viscosity to be Newtonian as well. For $X = 5$, $B_R = 4.62$, and $D_R = 3.89$, solution of Eqs. 9.150 and 9.151 with boundary conditions given in Eqs. 9.154 through 9.156 (see also Problem 9C.2 or Figure 9.23) yields

$$B = 0.1 \Rightarrow \Delta P = 22.9 \text{ Pa} \quad (9.189)$$

and

$$T_Z = 2.23 \Rightarrow |F_Z| = 2.6 \text{ N} \quad (9.190)$$

The viscosity required to get the above values is calculated as follows. The total strain in the ξ_1 direction is calculated from Eq. 9.132 as

$$\dot{\gamma}_{11}(t_Z - t_p) = \ln \frac{v_Z}{v_p} \quad (9.191)$$

where v_Z is the velocity at the frost line, and $t_Z - t_p$ represents the travel time from the die swell level to the frost-line level. Based on the mass balance, v_Z is calculated to be equal to 29.1 cm/s, and thus the total strain is equal to 1.2 units. Similarly, the total strain in the transverse direction ξ_3 is equal to 1.5 units. The average strain rates in those directions are about 1.2 and 1.5 s^{-1} , respectively, as the travel time is approximated to be 1 s. Then, the viscosity is calculated to be equal to 4500 Pa·s.

Finally, the force at the nip rolls is calculated by applying a force balance on the film from the frost line to the nip rolls to give

$$F_L = F_Z - \rho g(L - Z)2\pi R_f H_f \quad (9.192)$$

Based on Eq. 9.192, the force at the nip rolls is calculated as $F_L = -3.0 \text{ N}$ (i.e., 3.0 N in tension).

PROBLEMS

A. Applications

9A.1 *Significance of Inertia in Newtonian Isothermal Fiber Spinning.* Calculate the relative importance of the inertial terms to viscous terms in the Newtonian and isothermal fiber-spinning process. Use the data of Example 9.1 to assess this importance in the isothermal fiber spinning of Nylon 6,6 at 285 °C. Furthermore, estimate the relative importance of (1) gravitational forces and (2) shear rate.

9A.2 Heat Transfer Coefficient and the Melt-Spinning Process

- (a) Prove that the heat transfer coefficient for cross flow is twice that for parallel flow.
- (b) Show that in the upper part of the spinning chamber (i.e., close to the spinneret) the heat transfer coefficient depends on the cooling air velocity only, while in the lower part it depends on the filament speed only.

9A.3 The Newtonian and Isothermal Model as a Special Case of the Newtonian and Nonisothermal Model. Prove that the solution of the Newtonian isothermal model, Eq. 9.26, can be deduced from Eqs. 9.66 to 9.68 with the appropriate simplifications.

9A.4 Draw Ratios in Fiber Spinning and Film Casting. Prove that the following relationship holds for isothermal and Newtonian fiber spinning and film casting:

$$\frac{[\ln D_R]_{\text{spin}}}{[\ln D_R]_{\text{cast}}} = \frac{4}{3}$$

9A.5 Principal Radii of Curvature. Prove Eqs. 9.147 and 9.148.

B. Principles
9B.1 Isothermal Spinning of a Power-Law Fluid. Show that the axial velocity profile of a power-law fluid in the fiber-spinning process is given by the following equation:

$$v_z = v_0 \left[1 + \left((D_R)^{1-(1/n)} - 1 \right) \frac{z}{L} \right]^{n/(n-1)}$$

where n is the power-law index. To show that, use all the assumptions of the Newtonian case. Also, show diagrammatically the effect of the power-law index on the axial velocity profile.

9B.2 Centerline Temperature in Intermediate Speed PET Spinning. Melt-spun PET is cooled by an air cross flow of 20 cm/s. The extrusion temperature is 300 °C, the take-up velocity is 2000 m/min, the polymer mass flow rate is 2.5 g/min, and the filament surface temperature and speed are shown in Figure 9.6. Estimate the centerline filament temperature at a distance of 60 cm below the spinneret plate. The physical parameters of PET are $\rho = 1.37 \text{ g/cm}^3$, $k = 6.9 \times 10^{-4} \text{ cal/cm}\cdot\text{s}\cdot\text{°C}$, and $\bar{C}_p = 0.3 \text{ cal/g}\cdot\text{°C}$. The cooling air temperature is 25 °C. Also, comment on the validity of assumption 6 in Section 9.1.2 (p. 281), that is, there is no radial heat conduction within the filament.

9B.3 Draw Resonance of a Power-Law Nonisothermal Melt Spinning. Estimate the critical draw ratio for draw

resonance for a melt-spun polymer. The properties of the polymer are $\bar{C}_p = 0.7 \text{ cal/g}\cdot\text{°C}$, $k = 0.02 \text{ °C}^{-1}$ (see Eq. 9.105), $\rho = 0.83 \text{ g/cm}^3$, and $T_0 = 270 \text{ °C}$, and the characteristics of the spinning system are $L = 50 \text{ cm}$, dpf (at take-up) = 8, $v_L = 500 \text{ m/min}$, $T_a = 20 \text{ °C}$, $v_{\text{ay}} = 20 \text{ cm/s}$, and $R_0 = 0.3 \text{ cm}$. The power-law index of the polymer is about 0.4. Base your calculations on Section 9.1.5.

9B.4 Spinning Length for Stable Melt Spinning. Using the data of Example 9.3 sketch the spinning length as a function of the draw ratio for stable and attainable operation. Apply the results of the theoretical analysis by Fisher and Denn (1976). Propose changes that will decrease the spinning length.

9B.5 Special Cases of Very Thin Film Casting. Prove that the following relationship holds for two special cases of very thin film casting:

$$[h/h_0]_{L \ll w_0} = ([h/h_0]_{L \gg w_0})^2$$

Assume Newtonian and isothermal flow in the case of $L \ll w_0$, and the same draw ratio in both cases.

9B.6 Straight Tubular Film Extrusion. Prove that in the case where there is no blowing of the polymer film that is extruded from an annular die the film thickness is given by the following relationship:

$$H = H_0 \exp \left[-B \frac{z}{R_0} \right]$$

where B is given by Eq. 9.153. Compare this case to the isothermal fiber spinning of a Newtonian fluid.

9B.7 Various Forms of Extension in Film Blowing. Prove that the following relationships hold for the film blowing operation:

- (1) For uniaxial extension: $D_R B_R^2 = 1$
- (2) For equibiaxial extension: $D_R = B_R$
- (3) For planar extension: $B_R = 1$

Then, for $D_R = 3$ calculate the relative values of the air pressure and the axial tension at the nip rolls in each extensional case.

9B.8 Production of Straight Tube. Calculate the air pressure and the nip rolls tension for the production of a straight tube of LLDPE from the extruder of Example 9.4.

9B.9 Draw Resonance in Coextrusion Fiber Spinning. Coextrusion fiber spinning is an industrial process used for the production of plastic optical fibers. Based

on the rheological differences between LDPE and LLDPE (i.e., LDPE has a longer relaxation time than LLDPE, and it exhibits strain hardening), provide qualitative arguments about the expectation of draw resonance for a bicomponent fiber-spun with LLDPE as the core material. (*Hint*: Read the paper by Lee and Park, 1992.)

C. Numerical Problems

- 9C.1** *Newtonian and Nonisothermal Fiber Spinning.* Calculate the diameter of the filament at the take-up roll for the Newtonian and nonisothermal model using Eqs. 9.66 to 9.68. Use the same parameters as Kase and Matsuo (1967), which are given in the figure caption under Figure 9.5. **(a)** Neglect air drag, surface tension, inertial, and gravitational forces. **(b)** Include only the air drag forces ($\mu_{\infty 0} = 200 \text{ Pa}\cdot\text{s}$).
- 9C.2** *Isothermal Newtonian Film Blowing.* Consider the isothermal Newtonian film blowing process described by Eqs. 9.150 and 9.151 and boundary conditions and Eqs. 9.154, 9.155, and 9.156. Show that the following two sets of conditions constitute steady-state solutions of the model: (1) $B = 0.2$, $X = 5$, $T_Z = 1.35$, $B_R = 2.4$, $H_0/H_f = 4.4$, and (2) $B = 0.2$, $X = 5$, $T_Z = 1.35$, $B_R = 0.5$, $H_0/H_f = 4.2$; and thus, multiple solutions might exist for a certain set of conditions (Cain and Denn, 1988). More specifically, plot the dimensionless bubble radius, r , and the dimensionless film thickness, w , versus the dimensionless axial distance, x .

D. Design Problems

- 9D.1** *Elongational Viscosity Measurements and the Fiber-Spinning and Film Blowing Processes.* Design a set of experiments, based on the fiber-spinning and film blowing processes, which allow one to calculate extensional viscosity (uniaxial, biaxial, and planar) as a function of extension rate. (*Hint*: Read the paper by Han and Park, 1975a.)
- 9D.2** *Spinning of Hollow Fibers.* Consider the fiber-spinning process of a hollow fiber (Freeman et al., 1986). Formulate the continuity, momentum, energy, and rheological equations for this process along the same principles as in Sections 9.1.1 and 9.1.2. For the special case of isothermal Newtonian low-speed (no inertia, air drag, and gravity) spinning and using the thin-filament theory, prove that the average velocity profile is given by the relation

$$v_z = v_0 \exp \left[\frac{z}{R_{00} - R_{i0}} \left(\frac{|F| - \pi R_{i0}^2 p_i}{3\pi\mu v_0 (R_{00} + R_{i0})} \right) \right]$$

where R_0 and R_i are the initial outside and inside radii, respectively, at $z = 0$, p_i is the internal pressure, and F is the axial tension needed to draw the hollow fiber.

- 9D.3** *Scaleup of the Film Blowing Process.* It is very useful to be able to predict industrial scale film processability and resulting physical and mechanical properties from laboratory scale film blowing experiments. Based on the nonisothermal model analyzed in Section 9.3.2, discuss the scaleup principles and dimensionless numbers for the film blowing process. Then assume that the scaleup criterion requires equal stresses at the freeze line for machine and transverse directions. Propose a scaleup model for the radii of the annular die (multiplication factor is α) and the final (beyond freezing) bubble radius (multiplication factor is κ). Show that the scaleup criterion is satisfied as long as the reciprocal of the internal pressure and the freeze-line tension, both at the industrial scale, are κ times the corresponding variables in the laboratory scale, for the same temperature profiles and final film thickness in both scales.

REFERENCES

- Alaie, S. M. and T. C. Papanastasiou. 1993. "Modeling of Non-isothermal Film Blowing with Integral Constitutive Equations." *Intern. Polym. Proc.*, **8**(1), 51–65.
- Anturkar, N. R. and A. Co. 1988. "Draw Resonance in Film Casting of Viscoelastic Fluids: A Linear Stability Analysis." *J. Non-Newtonian Fluid Mech.*, **28**, 287–307.
- Bergonzoni, A. and A. J. DiCresce. 1966. "The Phenomenon of Draw Resonance in Polymeric Melts." *Polym. Eng. Sci.*, **6**, 45–59.
- Cain, J. J. and M. M. Denn. 1988. "Multiplicities and Instabilities in Film Blowing." *Polym. Eng. Sci.*, **28**(23), 1527–1541.
- Campbell, G. A. and B. Cao. 1987. "The Interaction of Crystallinity, Elasticoplasticity, and a Two-Phase Model on Blown Film Bubble Shape." *J. Plast. Film Sheet.*, **3**, 158–170.
- Cao, B. and G. A. Gampbell. 1990. "Viscoplastic-Elastic Modeling of Tubular Blown Film Processing." *AICHE J.*, **36**(3), 420–430.
- Cordova, D. S. and Donnelly D. S. 1990. "Reinforced Plastics, Extended-Chain Polyethylene Fibers." In I. I. Rubin, Ed. *Handbook of Plastic Materials and Technology* (Wiley, Hoboken, NJ).
- Dees, J. R. and J. E. Spruiell. 1974. "Structure Development During Melt Spinning of Linear Polyethylene Fibers." *J. Appl. Polym. Sci.*, **18**, 1053–1078.
- Denn, M. M., C. J. S. Petrie, and P. Avenas. 1975. "Mechanics of Steady Spinning of a Viscoelastic Liquid." *AICHE J.*, **21**(4), 791–799.
- Dobroth, T. and L. Erwin. 1985. "Causes of Edge Beads in Cast Films." 43rd SPE Annual Technical Conference, Washington DC, **31**, 89–92.
- Donnelly, G. J. and C. B. Weinberger. 1975. "Stability of Isothermal Spinning of a Newtonian Fluid." *Ind. Eng. Chem. Fundam.*, **14**, 334–337.

- Fisher, R. J. and M. M. Denn. 1976. "A Theory of Isothermal Melt Spinning and Draw Resonance." *AIChE J.*, **22**(2), 236–246.
- Fisher, R. J., M. M. Denn, and R. I. Tanner. 1980. "Initial Profile Development in Melt Spinning." *Ind. Eng. Chem. Fundam.*, **19**, 195–197.
- Freeman, B. D., M. M. Denn, R. Keunings, G. E. Molau, and J. Ramos. 1986. "Profile Development in Drawn Hollow Tubes." *J. Polym. Eng.*, **6**(1–4), 171–186.
- George, H. H. 1982. "Model of Steady-State Melt Spinning at Intermediate Take-up Speeds." *Polym. Eng. Sci.*, **22**(5), 292–299.
- d'Halewyn, S., J. F. Agassant, and Y. Denouy. 1990. "Numerical Simulation of the Cast Film Process." *Polym. Eng. Sci.*, **30**(6), 335–340.
- Han, C. D. and J. Y. Park. 1975a. "Studies on Blown Film Extrusion. I. Experimental Determination of Elongational Viscosity." *J. Appl. Polym. Sci.*, **19**, 3257–3276.
- Han, C. D. and J. Y. Park. 1975b. "Studies on Blown Film Extrusion. II. Analysis of the Deformation and Heat Transfer Processes." *J. Appl. Polym. Sci.*, **19**, 3277–3290.
- Han, C. D. and J. Y. Park. 1975c. "Studies on Blown Film Extrusion. III. Bubble Instability." *J. Appl. Polym. Sci.*, **19**, 3291–3297.
- Kanai, T. and J. L. White. 1984. "Kinematics, Dynamics and Stability of the Tubular Film Extrusion of Various Polyethylenes." *Polym. Eng. Sci.*, **24**(15), 1185–1201.
- Kanai, T. and J. L. White. 1985. "Dynamics, Heat Transfer and Structure Development in Tubular Film Extrusion of Polymer Melts: A Mathematical Model and Predictions." *J. Polym. Eng.*, **5**(2), 135–157.
- Kang, H. J. and J. L. White. 1990. "A Double Bubble Tubular Film Extrusion Process of Poly *p*-phenylene Sulfide (PPS)." 48th SPE Annual Technical Conference, Dallas, TX, **36**, 104–109.
- Kang, H. J., J. L. White, and M. Cakmak. 1990. "Single and Double Bubble Tubular Film Extrusion of Polyethylene terephthalate." *Intern. Polym. Proc.*, **5**(1), 62–73.
- Kase, S. 1974a. "Studies on Melt Spinning. IV. On the Stability of Melt Spinning." *J. Appl. Polym. Sci.*, **18**, 3279–3304.
- Kase, S. 1974b. "Studies on Melt Spinning. III. Velocity Field Within the Thread." *J. Appl. Polym. Sci.*, **18**, 3267–3278.
- Kase, S. 1985. "Mathematical Simulation of Melt Spinning Dynamics." In A. Ziabicki and H. Kawai, Eds. *High-Speed Fiber Spinning* (Wiley, Hoboken, NJ).
- Kase, S. and T. Matsuo. 1965. "Studies on Melt Spinning. I. Fundamental Equations on the Dynamics of Melt Spinning." *J. Polym. Sci. A*, **3**, 2541–2554.
- Kase, S. and T. Matsuo. 1967. "Studies on Melt Spinning. II. Steady-State and Transient Solutions of Fundamental Equations Compared with Experimental Results." *J. Appl. Polym. Sci.*, **11**, 251–287.
- Kawagushi, T. 1985. "Industrial Aspects of High Speed Spinning." In A. Ziabicki and H. Kawai, Eds. *High-Speed Fiber Spinning* (Wiley, Hoboken, NJ).
- Keunings, R., M. J. Crochet, and M. M. Denn. 1983. "Profile Development in Continuous Drawing of Viscoelastic Liquids." *Ind. Eng. Chem. Fundam.*, **22**, 347–355.
- Lee, W. S. and C.-W. Park. 1992. "Draw Resonance Instability in Coextrusion Fiber Spinning." 50th SPE Annual Technical Conference, Detroit, MI, **38**, 2181–2183.
- Lin, C.-Y., P. A. Tucker, and J. A. Cuculo. 1992. "Poly(ethylene terephthalate) Melt Spinning Via Controlled Threadline Dynamics." *J. Appl. Polym. Sci.*, **46**, 531–552.
- Luo, X.-L. and R. I. Tanner. 1985. "A Computer Study of Film Blowing." *Polym. Eng. Sci.*, **25**, 602–609.
- Ma, T. C. and C. D. Han. 1988. "Processing–Structure–Property Relationships in Poly(ethylene terephthalate) Blown Film." *J. Appl. Polym. Sci.*, **35**, 1725–1757.
- Maemura, E., M. Cakmak, and J. L. White. 1989. "Characterization of Crystallinity, Orientation, and Mechanical Properties in Biaxially Stretched Poly(*p*-phenylene sulfide) Films." *Polym. Eng. Sci.*, **29**(2), 140–150.
- Middleman, S. 1977. *Fundamentals of Polymer Processing*, Chapter 9 (McGraw Hill, New York).
- Pearson, J. R. A. 1985. *Mechanics of Polymer Processing* (Elsevier, New York).
- Pearson, J. R. A. and C. J. S. Petrie. 1970a. "A Fluid-Mechanical Analysis of the Film Blowing Process." *Plastics & Polymers*, **38**, 85–94.
- Pearson, J. R. A. and C. J. S. Petrie. 1970b. "The Flow of Tubular Film. Part 1. Formal Mathematical Representation." *J. Fluid Mech.*, **40**(1), 1–19.
- Pearson, J. R. A. and C. J. S. Petrie. 1970c. "The Flow of Tubular Film. Part 2. Interpretation of the Model and Discussion of Solutions." *J. Fluid Mech.*, **42**(3), 609–625.
- Pearson, J. R. A. and Y. T. Shah. 1974. "On the Stability of Isothermal and Nonisothermal Fiber Spinning of Power-Law Fluids." *Ind. Eng. Chem. Fundam.*, **13**(2), 134–138.
- Petrie, C. J. S. 1975. "A Comparison of Theoretical Predictions with Published Experimental Measurements on the Blown Film Process." *AIChE J.*, **21**(2), 275–282.
- Petrie, C. J. S. and M. M. Denn. 1976. "Instabilities in Polymer Processing." *AIChE J.*, **22**(2), 209–236.
- Phan-Thien, N. 1978. "A Nonlinear Network Viscoelastic Model." *J. Rheol.*, **22**(3), 259–283.
- Schultz, W. W. 1987. "Slender Viscoelastic Fiber Flow." *J. Rheol.*, **31**(8), 733–750.
- Wagner, M. H. 1976. "Das Folienblasverfahren als rheologisch-thermodynamischer Prozeß." *Rheol. Acta*, **15**, 40–51.
- Weinberger, C. B., G. F. Cruz-Saenz, and G. J. Donnelly. 1976. "Onset of Draw Resonance During Isothermal Melt Spinning: A Comparison Between Measurements and Predictions." *AIChE J.*, **22**(3), 441–448.
- Yeow, Y. L. 1974. "On the Stability of Extending Films: A Model for the Film Casting Process." *J. Fluid Mech.*, **66**(3), 613–622.
- Yeow, Y. L. 1976. "Stability of Tubular Film Flow: A Model of the Film-Blowing Process." *J. Fluid Mech.*, **75**(3), 577–591.
- Zeichner, G. R. 1973. "Spinnability of Viscoelastic Fluids" (M.Ch.E. thesis, University of Delaware, Newark).
- Ziabicki, A. 1976. *Fundamentals of Fiber Formation* (Wiley, London).
- Ziabicki, A. and H. Kawai, Eds. 1985. *High-Speed Fiber Spinning* (Wiley, Hoboken, NJ).

10

MOLDING AND FORMING

DESIGN PROBLEM IX DESIGN OF A COMPRESSION MOLDING PROCESS

Polypropylene (PP) containing 30 wt% glass fiber mat is to be compression molded to form a panel with curved ends as shown in Figure 10.1. The PP/glass composite, an example of which is Azdel PM 10300 (Giles and Reinhard, 1991), comes in the form of sheets that are 3.6 mm thick by 19.1 cm by 21.6 cm. The final part is to be 3.2 mm thick, have a breadth of 64.8 cm, and the remaining dimensions as shown in Figure 10.1. The sheets, also referred to as blanks, are to be heated to the processing temperature by means of an infrared oven through which the blanks are able to pass on a continuous basis. The infrared heaters are located on both sides of the conveyor system and are considered to be parallel plate sources with a maximum surface temperature of 427 °C. Based on dynamic mechanical thermal analysis, in which a strip of the composite is tested in the dynamic oscillatory mode as a function of temperature (see Fig. 10.21), the material begins to flow at about 160 °C, which is about the melting point of PP. Because of the complex nature of these composite materials, the only rheological data available are the complex viscosity versus frequency at three temperatures as shown in Figure 10.22. The upper processing temperature limit for PP is known to be 230 °C. Typical presses can be operated in a speed range of 4.23 to 33.9 mm/s. Determine the arrangement of the blanks in the mold and the number of blanks required, the minimum time required to heat the blanks to a temperature where the material will flow into the remainder of the mold, the rate of closing of the press and the required operating

force, and the temperature of the mold plattens which will minimize the time required for the part to remain in the mold.

This chapter is concerned with processes in which a discrete mass of polymer, which is either above its melting temperature in the case of semicrystalline polymers or above its glass transition temperature in the case of amorphous polymers, is forced to take the shape of a cavity by means of applied pressure. The processes vary somewhat in the details but in general involve heating the polymer mass, pressurizing it, and then cooling the formed sample. Processes of this nature include injection molding, compression molding, thermoforming, and blow molding. In this chapter we discuss these various processes in the order just mentioned. Our intentions are to describe the most important features as well as point out where design and analysis can be carried out.

10.1 INJECTION MOLDING

Injection molding is probably the most widely used cyclic process for manufacturing parts from thermoplastics. In this section we discuss some of the general aspects of the process, the fluid mechanics of mold filling, the method by which structuring occurs, and the basis for computer-aided design.

10.1.1 General Aspects of Injection Molding

A general description of injection molding was given in Chapter 1. In essence, polymer pellets are plasticated in a

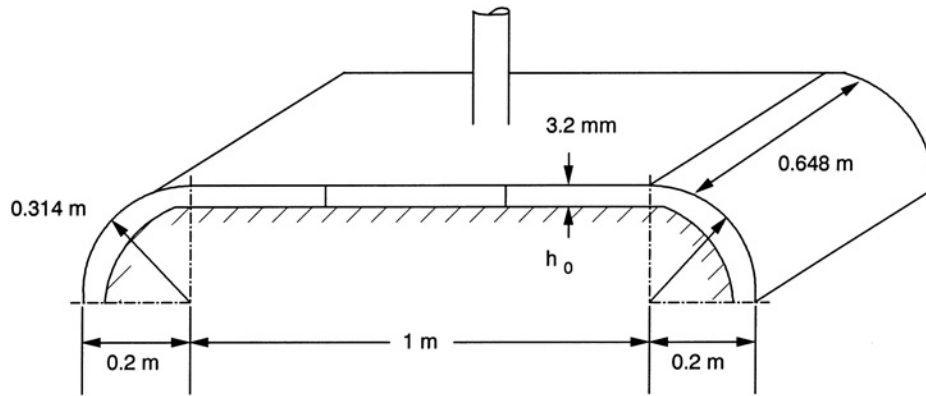


FIGURE 10.1 Compression molding process for producing a panel from polypropylene and glass fiber mat composite sheets.

single-screw extruder, and the molten polymer accumulates at the tip of the screw in a reservoir. As this part of the process has been described in Chapter 8, we concentrate on what happens to the melt from this point on. In Figure 10.2 is shown the end of the extruder and its connection to the mold. The melt, which has accumulated in the reservoir, is pushed forward by the screw whose displacement is controlled by hydraulic pressure. The melt flows through the nozzle, which connects the extruder to the mold, passes through the sprue, along the runner, through the gate, and into the mold cavity. The sprue

is designed to offer the least resistance to flow as possible while minimizing the amount of polymer that is wasted. The runner is designed to carry melt to the mold cavity, and when multiple cavities are involved, it must be designed to ensure that each cavity fills at the same time. The gate represents the entrance to the mold. Its location is of utmost importance to the appearance of the part. Furthermore, it is desirable to make the gate as small as possible, for not only cosmetic reasons but to facilitate the separation of the part from the rest of the material solidified in the runner. The melt enters the mold cavity where it begins to solidify as it touches the mold wall. As semicrystalline polymers solidify, they shrink as a result of increases in density. Pressure is maintained during the cooling process to ensure that melt continues to flow into the mold. Once solidification is complete, the mold plates open and the part is ejected. While the screw is being pulled back, it rotates, plasticating more polymer.

The flow rate and pressure in the reservoir are shown schematically in Figure 10.3. The injection pressure, which is the hydraulic pressure applied to the screw, is one of the variables that can be selected. Because of little resistance to flow in the beginning, the flow rate through the nozzle is constant. However, as the melt advances through the sprue and runner, the resistance to flow increases, and the pressure increases. As the cavity fills, the set pressure reaches a constant pressure (this is the injection pressure and is a machine setting), but the resistance to flow continues to increase. The flow rate through the nozzle as well as the flow rate into the cavity must decrease. If the resistance to flow is too great either as a result of the polymer solidifying or the melt viscosity being too high, the polymer will fail to fill the mold, leading to what is known as a “short-shot.” Once the mold fills, the hydraulic pressure applied to the screw is reduced (this is called the holding pressure) to a value which maintains enough flow of material into the mold to compensate for the volume changes due to shrinkage. Some pressure is maintained during the complete cooling cycle.

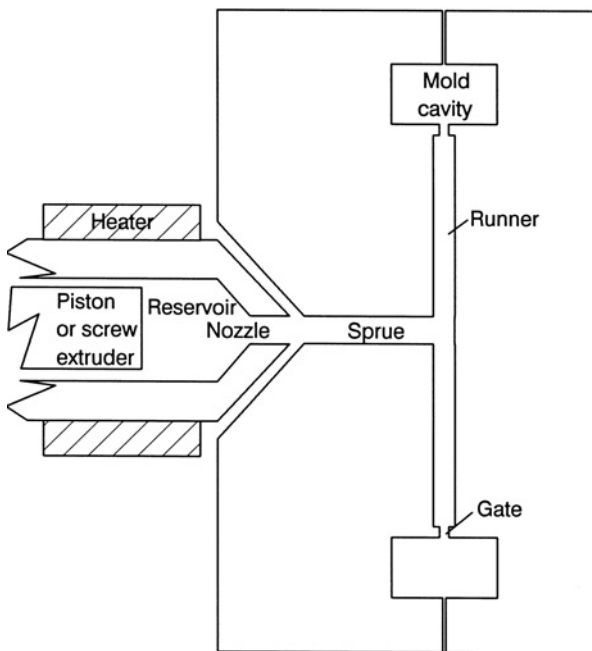


FIGURE 10.2 Injection molding tooling showing the tip of the injection system and its connection to the mold. Melt passes from the reservoir through the nozzle, the sprue, and runner system entering the mold cavities through the gate.

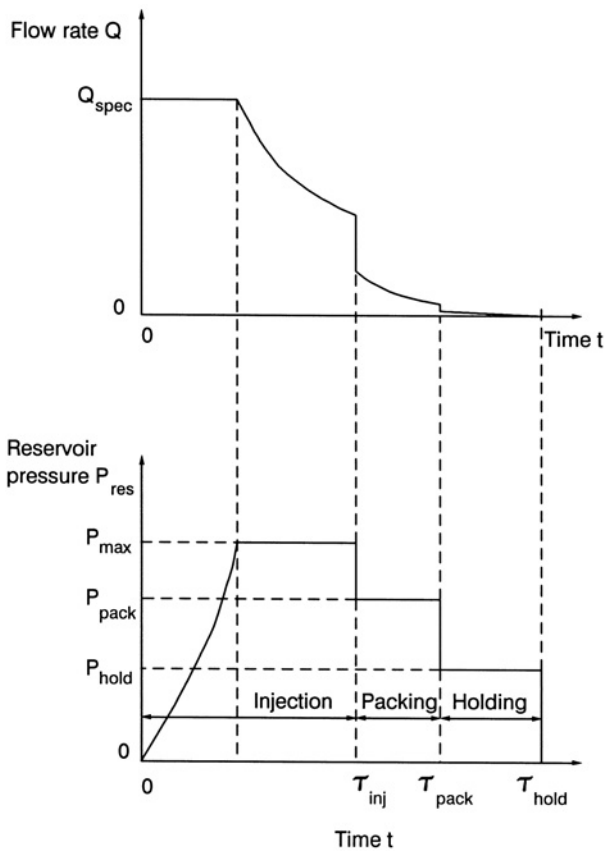


FIGURE 10.3 Flow rate and pressure in the reservoir of an injection molding unit as a function of time.

Mold filling involves both high deformation and cooling rates. For this reason a considerable amount of orientation and structure or morphology can be developed in an injection molded part. The shrinkage distribution in an injection molded sample of polystyrene, an amorphous polymer, is shown in Figure 10.4. Shrinkage is used here as a measure of molecular orientation with the highest amount of shrinkage representing material with the highest degree of orientation. In part (a) of this figure the shrinkage distribution is shown as a function of thickness for two different fill rates. For the highest fill rate the highest shrinkage is at the mold wall, while there is a local maximum at a distance of about 0.22 mm from the mold wall. The shrinkage then decreases as one approaches the centerline of the mold. For the lowest fill rate the shrinkage is still highest at the mold wall, but it is lower in value than that for the higher fill rate. There is also a local maximum, but it is now at a distance of about 0.44 mm from the wall. In Figure 10.4b the shrinkage distributions along and transverse to the flow direction are compared. The shrinkage along the transverse direction is negligible over most of the part thickness except near the wall. It is always lower along the transverse direction than along the flow direction, which suggests a significant amount of anisotropy will exist in the properties.

To account for this distribution of shrinkage (orientation) Tadmor (1974) proposed the fountain flow mechanism, which occurs in the advancing front. In Figure 10.5 the flow patterns in normal mold filling are shown schematically. As the melt leaves the gate, the front is found to occupy various positions in the mold at different times. The velocity profiles in the fully developed flow behind the front are shown in Figure 10.5b. The flow well behind the front is primarily

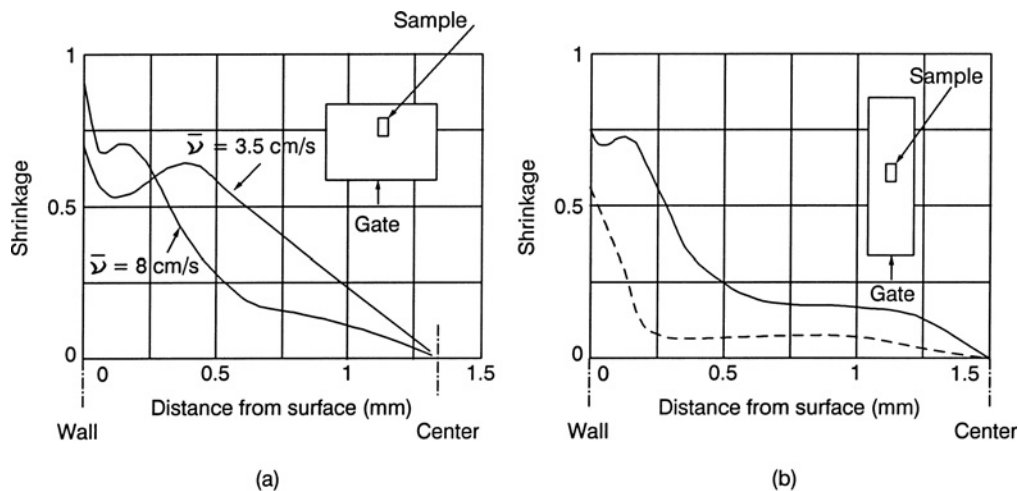


FIGURE 10.4 Shrinkage distribution as a function of distance from the surface of an injection molded part consisting of amorphous polystyrene. (a) Shrinkage along the flow direction for two different fill rates. (b) Comparison of the shrinkage distribution along the flow direction (solid line) and transverse to the flow direction (broken line). (Reprinted by permission of the publisher from Menges and Wübken, 1973.)

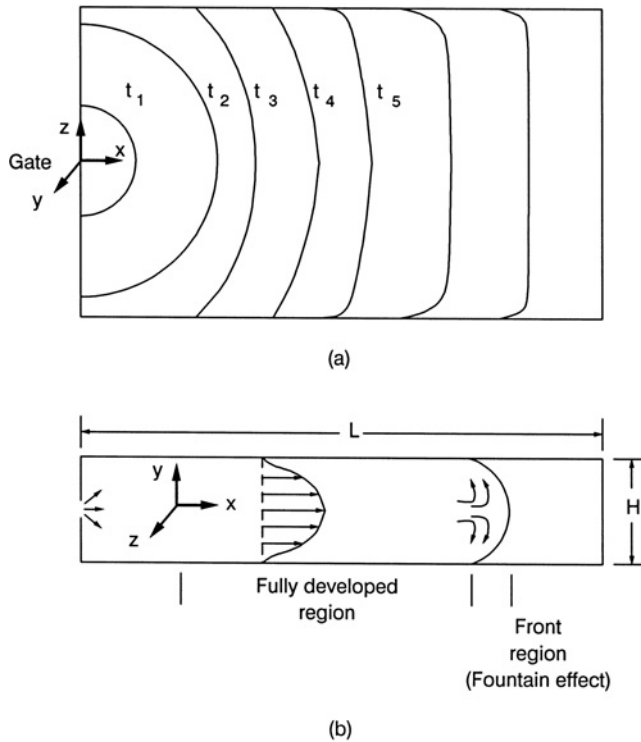


FIGURE 10.5 Flow patterns in an end-gated mold. (a) Top view of fronts as a function of time. (b) Side view of velocity profiles in the fully developed region and frontal region. (Reprinted by permission of the publisher from Tadmor and Gogos, 1979.)

shear flow, while that at the front involves stagnation flow. In essence, fluid passes through the center of the cavity to the front where it turns and then is laid up on the wall of the mold where it solidifies. In Figure 10.6 the velocity profile in the fully developed region as seen by an observer moving with the average velocity of the flow is shown. The velocity gradient, and hence stress, is seen to pass through a maximum at an interior point in the flow. Because orientation is directly related to stress (see Section 5.5), one can see why there would be at least a local maximum in shrinkage at this point. A fluid element near the centerline will decelerate as it approaches the front and become compressed along the x direction and stretched along the y direction. The element is then stretched further at the front and laid up on the wall where it is rapidly solidified in a highly oriented state. Hence, the extensional flow at the front stretches the fluid element and leads to a higher degree of orientation in the material at the mold wall than at the interior of the material.

The fountain flow associated with the advancing front is extremely important to the properties of materials generated by means of injection molding. In the case of homogeneous polymer systems we have already seen how the molecular orientation is affected. For fiber-filled systems, the flow at the front can lead to highly oriented fibers at the surface of

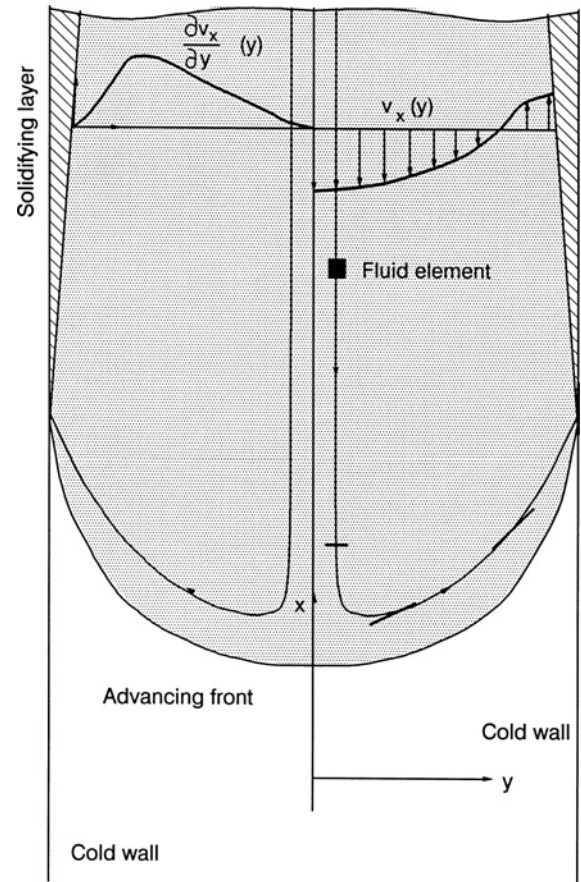


FIGURE 10.6 Flow pattern in the advancing front for flow between two parallel plates as observed relative to the average velocity. A fluid element approaching the front is compressed along the flow direction and stretched along the y direction before being laid up on the cold wall. (Reprinted by permission of the publisher from Tadmor, 1974.)

an injection molded part, which certainly will affect the flexural properties of the part. In the case of blends, extensional flow at the front leads to a morphology in which the minor component exists as fibrils. Hence, in simulating the injection molding process it is important that frontal flow eventually be included.

On occasion the opening at the gate is smaller than the cavity thickness, and the melt no longer fills the mold by an advancing front mechanism. Rather, it “snakes” its way into the mold, leading to a material with a poor surface appearance and reduced physical properties. Snaking does not seem to be a common method found in the filling of molds, but it can occur.

One of the major problems in injection molding of parts is the formation of *weld lines* that lead to surface imperfections and weak spots in the part. Weld lines arise from the presence of obstructions in the flow and from the impingement of advancing fronts from different gates. The former type

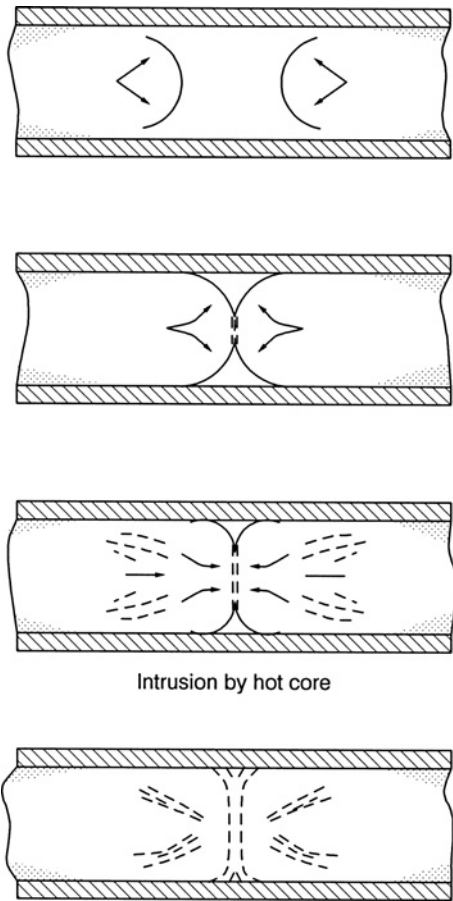


FIGURE 10.7 Impingement of two fronts during injection molding to form a weld line. (Reprinted by permission of the publisher from Hobbs, 1974.)

of weld line is referred to as a *hot weld*, while the latter is referred to as a *cold weld*. In the case of the hot weld the melt, as it flows into the cavity, is split by an obstruction such as a pin, for example, and then the streams are brought back together. Usually the temperature at the interface does not change much, and hence the streams are brought back together at the processing temperature. On the other hand, when two fronts impinge on each other as shown in Figure 10.7, the temperature of the free surfaces has dropped somewhat, leading to the formation of what are called cold welds. Healing of these weld lines is controlled by self-diffusion, which was discussed in Section 4.2.5. According to theory of self-diffusion one must either use higher melt temperatures and longer hold times in the mold or use lower-molecular-weight polymers to accelerate the healing process.

10.1.2 Simulation of Injection Molding

The design of injection molding tooling is a complex process. In a commercial process the tooling usually contains multiple

cavities and the cavities are fed by several gates. The simulation of the injection molding process must at least contain the capability to predict cavity layout and runner design, the fill rate as a function of injection pressure, gate location, weld line positions, and cooling time. In addition, it would be desirable to predict molecular orientation, morphology, residual stresses, warpage, and shrinkage. In this section we discuss the approach presently taken in simulating injection molding and its role in computer-aided design. Because quite large computer programs are required to simulate injection molding, our goal is to explain the approach and its capabilities. Those aspects of design that can be handled at this level, such as heat transfer and the cooling of parts, will be discussed.

The flow geometries frequently encountered in injection molding can be reduced to the three geometrically simple units shown in Figure 10.8 (Pearson and Richardson, 1983). Flow through runners and the sprue can be handled by the

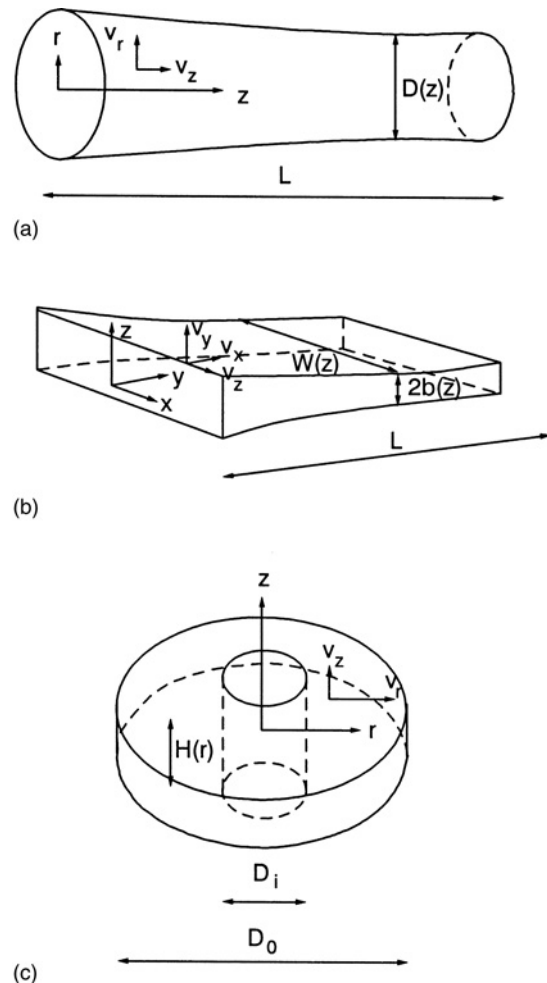


FIGURE 10.8 Basic geometric elements to which runners and mold cavities can be reduced: (a) tubular element, (b) planar element, and (c) center-gated disk.

first geometric unit as shown in Figure 10.8a, although many times the runners are semicircular in cross-sectional shape. The cavities can be considered to be a combination of thin planar geometries as shown in Figure 10.8b or as center-gated disk geometries as shown in Figure 10.8c.

We consider the flow of polymer melt into thin rectangular cavities as a means of illustrating the approach taken. Hieber and Shen (1980) model the flow of polymer melt in a thin cavity using classical Hele–Shaw flow. In this approach the velocity field is considered to consist of two components, v_x and v_y , which depend primarily on z but not on x or y (i.e., $\partial v_x/\partial x \ll \partial v_x/\partial z$). The components of the equation of motion are then taken as

$$0 = \frac{\partial}{\partial z} \left(\eta \frac{\partial v_x}{\partial z} \right) - \frac{\partial p}{\partial x} \quad (10.1)$$

$$0 = \frac{\partial}{\partial z} \left(\eta \frac{\partial v_y}{\partial z} \right) - \frac{\partial p}{\partial y} \quad (10.2)$$

where η is the viscosity taken to be of the form

$$\eta = \eta(\dot{\gamma}, T) \quad (10.3)$$

and is

$$\dot{\gamma} = \sqrt{\left(\frac{\partial v_x}{\partial z} \right)^2 + \left(\frac{\partial v_y}{\partial z} \right)^2} \quad (10.4)$$

The continuity equation is of the following form for this flow:

$$0 = \frac{\partial}{\partial x} (b \bar{v}_x) + \frac{\partial}{\partial y} (b \bar{v}_y) \quad (10.5)$$

where b is the half gap width, which may depend on x and y and the bar denotes an average over the gapwise coordinate, z . The energy equation takes the following form:

$$\rho \bar{C}_p \left(\frac{\partial T}{\partial t} + v_x \frac{\partial T}{\partial x} + v_y \frac{\partial T}{\partial y} \right) = k \frac{\partial^2 T}{\partial z^2} + \eta \dot{\gamma}^2 \quad (10.6)$$

In the development of these equations the viscoelastic nature of the fluid and the fountain flow at the advancing front have been neglected. The above set of equations are solved using the following boundary conditions:

$$\text{at } z = b, \quad v_x = v_y = 0, \quad T = T_w \quad (10.7)$$

$$\text{at } z = 0, \quad \frac{\partial v_x}{\partial z} = \frac{\partial v_y}{\partial z} = 0 = \frac{\partial T}{\partial z} \quad (10.8)$$

The solution of this set of equations is facilitated by the following procedure. Because p is independent of z , Eqs. 10.1

and 10.2 can be integrated to give

$$\eta \left(\frac{\partial v_x}{\partial z} \right) = \left(\frac{\partial p}{\partial x} \right) z \quad (10.9)$$

$$\eta \left(\frac{\partial v_y}{\partial z} \right) = \left(\frac{\partial p}{\partial y} \right) z \quad (10.10)$$

where Eq. 10.8 has been used. These equations can be integrated again using Eq. 10.7 to give

$$v_x = \left(-\frac{\partial p}{\partial x} \right) \int_z^b \frac{z' dz'}{\eta} \quad (10.11)$$

$$v_y = \left(-\frac{\partial p}{\partial y} \right) \int_z^b \frac{z' dz'}{\eta} \quad (10.12)$$

The gapwise-averaged velocities are obtained by integration of Eqs. 10.11 and 10.12:

$$\bar{v}_x = \left(-\frac{\partial p}{\partial x} \right) \frac{S}{b} \quad \bar{v}_y = \left(-\frac{\partial p}{\partial y} \right) \frac{S}{b} \quad (10.13)$$

where

$$S = \int_0^b \frac{z^2 dz}{\eta} \quad (10.14)$$

Substituting Eq. 10.13 into Eq. 10.5 gives

$$\frac{\partial}{\partial x} \left(S \frac{\partial p}{\partial x} \right) + \frac{\partial}{\partial y} \left(S \frac{\partial p}{\partial y} \right) = 0 \quad (10.15)$$

Equation 10.15 is solved subject to the following boundary conditions:

$$\text{Along the advancing front: } p = 0 \quad (10.16)$$

$$\text{At the entry to the mold: } p = p_e(x, y, t) \quad (10.17)$$

$$\text{At the mold wall: } \partial p / \partial n = 0 \quad (10.18)$$

Finally, when two melt fronts coalesce, forming a weld line, the boundary conditions are that the pressure and normal velocity be continuous; that is,

$$p^+ = p^- \quad (10.19)$$

and

$$(S \partial p / \partial n)^+ = -(S \partial p / \partial n)^- \quad (10.20)$$

where the $+$ and $-$ signs denote values on either side of the weld line.

In summary, the primary governing equations are given by Eqs. 10.15 and 10.6 for p and T , respectively, while S , v_x , v_y , $\dot{\gamma}$, and η are calculated by means of Eqs. 10.14, 10.11,

10.12, 10.4, and 10.3, respectively. To complete the solution of these equations an empiricism for viscosity must be used. The power-law and the Carreau models are often used. The solution of these equations requires numerical methods as discussed by Hieber and Shen (1980) and Wang and co-workers (1986).

In Example 10.1 the solution to Eq. 10.15 is illustrated for the isothermal Newtonian case.

Example 10.1. Isothermal Newtonian Flow in a Rectangular Cavity

Consider the isothermal flow of a Newtonian fluid in a rectangular mold as shown in Figure 10.8b but with W and $2b$ constant and $W/2b > 10$. The gate at the entrance to the mold is a fan gate so that the flow is considered to occur only in the y direction: that is, $v_y = v_y(z)$ and $p = p(y)$. The location of the front at any instant is $L(t)$. The pressure at the gate is constant and is P_0 . Determine $Q(t)$ and the time to fill a cavity of length L using the approach of Hieber and Shen (1980).

Solution. The pertinent equations are

$$\mu \frac{\partial^2 v_y}{\partial z^2} - \frac{\partial p}{\partial y} = 0 \quad (10.21)$$

$$\frac{\partial}{\partial y} \left(S \frac{\partial p}{\partial y} \right) = 0 \quad S = \frac{b^3}{3\mu} \quad (10.22)$$

Equation 10.22 can be integrated to find the pressure distribution, which is

$$P = \frac{-P_0}{L(t)} y + P_0 \quad (10.23)$$

where P_0 is the pressure at $y = 0$ and $P = 0$ at $y = L(t)$, which is the position of the front. v_y is obtained from Eq. 10.12:

$$v_y = \frac{b^2 P_0}{2L(t)\mu} \left[1 - \left(\frac{z}{b} \right)^2 \right] \quad (10.24)$$

The position of the front is found from a mass balance:

$$Q = \frac{b^3 P_0}{3L(t)\mu} = 2bW \frac{dL}{dt} \quad (10.25)$$

where Q is obtained by integrating Eq. 10.24 over the cross-sectional area. Equation 10.25 can be solved to find the position of the front as a function of time:

$$L(t) = \sqrt{\frac{b^2 P_0 t}{3\mu W}} \quad (10.26)$$

The time for filling the mold is determined by setting $L(t) = L$. One can also see by substituting Eq. 10.26 back into Eq. 10.25 that Q decreases with increasing time as follows:

$$Q = b^2 \sqrt{\frac{P_0 W}{3\mu t}} \quad (10.27)$$

Once the cavity is filled, additional material is forced into the cavity to compensate for an increasing polymer density arising from crystallization and compressibility of the melt. Wang and co-workers (1986) have included compressibility throughout the entire filling, packing, and cooling phases for amorphous polymers. However, for semicrystalline polymers their approach may not be satisfactory.

If one is to predict the orientation distribution in a part, then it is necessary to include fountain flow at the advancing front. Mavridis and co-workers (1988) have presented an approach for modeling fountain flow under isothermal conditions.

Referring to Figure 10.6, axes are attached to the moving front that move with the average velocity of the flow, $\langle v_x \rangle$. At the upstream boundary the flow is modeled as a one-dimensional shear flow. The equation of motion and the boundary conditions for this flow are

$$\frac{dp}{dx} = \frac{d}{dy} \left(\eta \frac{dv_x}{dy} \right) \quad (10.28)$$

$$\text{B.C.1: at } y = 0, \quad \frac{dv_x}{dy} = 0 \quad (10.29)$$

$$\text{B.C.2: at } y = 1, \quad v_x = B \left(\eta \frac{dv_x}{dy} \right) \quad (10.30)$$

where B is the slip coefficient. The flow in the rest of the region is such that the following postulates are made:

$$v_x = v_x(x, y); \quad v_y = v_y(x, y); \quad p = p(x, y) \quad (10.31)$$

The boundary conditions are as follows:

$$\text{at } x = 0, \quad v_x = v_x(y) \quad (10.32)$$

$$\text{at } y = b, \quad v_y = 0, \quad v_x = B\tau_{yx} \quad (10.33)$$

$$\text{At the front, } v \cdot n = 0, \quad \pi \cdot n = 0 \quad (10.34)$$

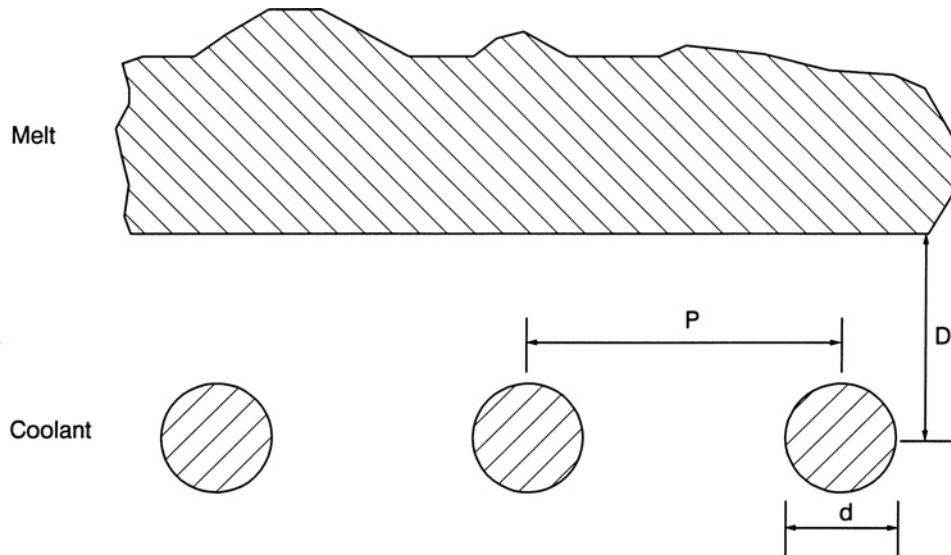
where $v \cdot n$ means there is no flow across the front and $\pi \cdot n$ means there are no forces acting on the front. The parameter B is a measure of slip, and when $B \rightarrow 0$ there is no slip and when $B \rightarrow \infty$ there is perfect slip. The postulates in Eq. 10.31 along with the equation of motion and a constitutive equation lead to a set of nonlinear differential equations which must be solved by means of numerical methods, preferably finite element methods. At present, most simulations of injection molding do not include fountain flow.

The cooling of the melt can be considered as a transient one-dimensional heat transfer problem. The approach used in Chapter 5 can be employed to calculate temperature distributions and cooling times as well as estimate the degree of crystallinity and the morphology. The main difficulty is establishing the appropriate boundary conditions at the mold walls. In a commercial process where a large number of parts are made per hour, it may take several hours before the mold surfaces reach an equilibrium temperature. This temperature can be somewhat higher than what is expected based on the temperature settings of cartridge heaters inserted in the mold base or fluids circulated through channels machined in the mold base. The most accurate way to determine the temperature distribution in the melt is to use a heat transfer coefficient. The overall heat transfer coefficient per unit length of coolant line, U , is given by

$$\frac{1}{U} = \frac{1}{Sk_m} + \frac{1}{\pi Dh} \tag{10.35}$$

where k_m is the thermal conductivity of the mold material (e.g., 43.3 W/m · K for steel), h is the convective heat transfer coefficient for flow through tubes (see Chapter 5 for determining this value), D is the diameter of the coolant line, and S is the shape factor, which is defined in Figure 10.9 and given as (Throne 1979)

$$S = \frac{2\pi}{\ln[(2P/\pi d) \sinh(2\pi D/P)]} \tag{10.36}$$



$$S = \frac{2\pi}{\ln[(2P/\pi d) \sinh(2\pi D/P)]}$$

FIGURE 10.9 Shape factor geometry for coolant lines in a mold block.

10.1.3 Microinjection Molding

The microinjection molding (μ IM) process is not just a scaling down of the conventional injection process, but it requires a rethinking of each part of the process. The molding machine, tooling, material, and process, as well as component handling and inspection need to be specially addressed (Giboz et al., 2007). In order to fill the mold, the mold temperature is typically held just under the melting point for semicrystalline polymers while for glassy polymers it is held around T_g . For example, for PP ($T_m \sim 168^\circ\text{C}$) the mold temperature is held at 163°C in μ IM while for conventional injection molding the mold is held between 30 and 60°C . For PC, a glassy polymer with a T_g of 150°C , the mold is held at 140°C for μ IM while for conventional molding it is held at temperatures between 90 and 110°C . In Table 10.1 we have summarized the molding conditions and some applications of a range of polymeric materials. In this table, the minimum part thickness that can be produced along with the largest aspect ratio, that is, the largest lateral dimension to the part thickness ratio, are indicated. Shear rates are estimated to be between 10^5 and $5 \times 10^6 \text{ s}^{-1}$ for μ IM (gate region) while for conventional injection molding they are estimated to be in the range of 10^4 s^{-1} . The high shear rates can have two detrimental effects: mechanical degradation due to high stresses and thermal degradation due to viscous heating. The control of the classical IM process is generally ensured by measuring the injection pressure. The injection pressures used in the μ IM process can reach 200 MPa and more, whereas conventional injection pressures are generally ten times lower. The mold

TABLE 10.1 Polymer Materials Often Used in Microinjection Molding, Mold Temperature (Micromolding/Conventional Molding), Maximum Aspect Ratios (ARs), Minimum Structural Thickness (S_{\min}), and Typical Applications

Polymer	Mold Temperature Micro/Conventional Mold ($^{\circ}\text{C}$)	Aspect Ratio (AR)	Minimum Thickness, S_{\min} (μm)	Application
PMMA		20	20	Optical fiber connector
PC	60–140/90–110			Cell container
PA		10	50	Microgear wheels
HDPE	125–150/30–60	230	20	Components for microactuators
PEEK		5	270	Housings for micropumps
PP	163/30–60	230	20	Components for microactuators

Source: Data from Giboz et al., 2007, and Piotter et al., 2002.

temperature and the injection pressure have to be higher than that of conventional IM. The high mold temperatures lead to a significant increase of the cycle times.

The tools used in the simulation of μIM are similar to those used in the simulation and design of conventional injection molding processes. However, there are a number of considerations that are significantly different, such as high shear rates and rapid cooling due to the small dimensions (Giboz et al., 2007). Furthermore, because the aspect ratio of the parts produced by means of μIM are typically small, the use of the Hele–Shaw approximation for simulating mold filling may be adequate and the inclusion of the advancing front may not be necessary. Furthermore, because the mold temperatures are held near the T_m for semicrystalline polymers or T_g for glassy polymers, there may be considerable relaxation of chain orientation. Furthermore, crystallization may occur under nearly quiescent conditions leading to a difference in morphology versus that in conventional injection molding.

Before leaving this section, we should make a few comments on the size and features of μIM machines (see Giboz et al., 2007). Typically the screw ranges from 5 to 16 mm in diameter. Some systems use a screw to plasticate the polymer and a plunger to push the melt into the mold. The clamping force runs from 49 to 147 kN, the injection capacity is from 0.082 to 10 cm^3 , the injection pressure is from 1700 to 3500×10^5 Pa, and the injection speed is from 180 to 1200 mm/s.

10.2 COMPRESSION MOLDING

Compression molding is used primarily to process thermosetting systems and difficult-to-process thermoplastics, such as fiber-filled systems or thermoplastic elastomers. We first describe some of the basic features of the process and the areas where design is needed. This is followed by discussion of the elementary ideas in the modeling of compression molding.

10.2.1 General Aspects of Compression Molding

The essential features of the compression molding process are illustrated in Figure 10.10. In the case of thermoplastics a preheated mass of polymer, which may be either a sheet or

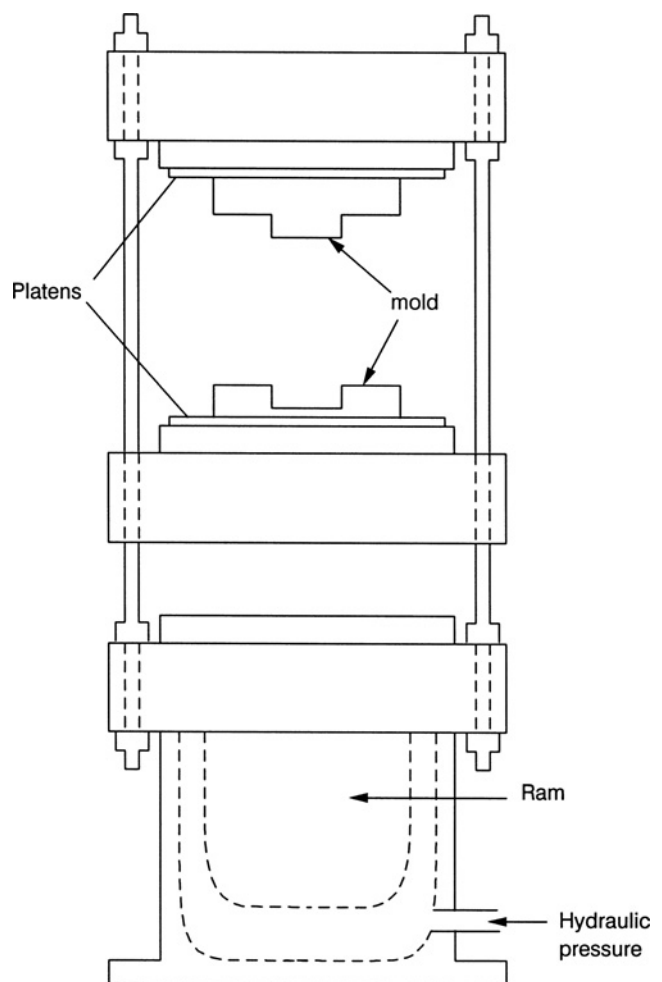


FIGURE 10.10 Compression molding process showing the hydraulic system and mold.

a pile of pellets or powder, is placed in the mold. The temperature of the mold is set low enough to cause the polymer to solidify but not so rapidly that it will not flow. Hydraulic pressure is applied to the top or bottom plate pushing the plattens together. The molds are designed to prevent the top part of the mold from touching the bottom part, which would squeeze the resin from the mold.

The design of a compression molding process consists of four aspects. The first is the selection of the proper amount of material to fill the cavity when the mold halves are closed. The second is determining the minimum time required to heat the blank to the desired processing temperature and the selection of the appropriate heating technique (radiation heating, forced convection, etc.). It is necessary to make sure that the center reaches the desired processing temperature without the surface being held at too high a temperature for too long of time. The third is the prediction of the force required to fill out the mold. Finally, the temperature of the mold must be determined, keeping in mind that one wants to cool the part down as rapidly as possible, but that too rapid of a cooling rate will prevent the polymer from filling the mold.

Compression molding is used for processing thermoplastics, which do not flow readily, such as highly filled systems and granular materials that don't really melt but only fuse under pressure. In the case of thermoplastic composite systems reinforced with long fibers, the process is referred to as stamping. It is a process that is being used more frequently for processing thermoplastic composites used in the manufacture of panels such as would be found in car trunks and hoods. Typically, the process involves much less flow than found in injection molding or other forming processes discussed in the remainder of the chapter.

10.2.2 Simulation of Compression Molding

Compression molding of thermoplastics typically involves very little flow. A discrete mass of material is placed in the mold whose volume is adequate to fill the mold when the plates are pushed together. The preliminary material may be in the form of a sheet, referred to as a *blank*, or stacked sheets reinforced with long continuous fibers, called *pregreg*. Initially, the surface area of the plates may be completely covered or only partially covered with material. When the plates of the mold are brought together, the material is forced to cover the rest of the mold surface. For example, blanks may cover initially from 20% to 80% of the mold surface. Thermoplastic preregs are placed over the entire mold surface, and hence the application of pressure leads only to shaping, compaction, and bonding of the stacked sheets.

Compression molding is a highly nonisothermal process. In the processing of blanks consisting of a thermoplastic reinforced with long fibers, the blanks are preheated and then placed in the mold, which is at a temperature lower than that of the blanks. In the case of thermoplastic preregs, the

stacked sheets are heated and cooled in the same mold. In either case there is a temperature distribution in the sample before being molded, and it is enhanced during molding. The accurate simulation of the compression molding process requires a solution of the coupled momentum and energy equations.

When there is significant flow, the deformation of the blank can be complex. For example, the blank initially may be square but during compression may be required to deform more in one direction than the other. In any event, the modeling of the deformation may not be handled easily without the use of numerical techniques such as the finite element method.

To illustrate the modeling of the compression molding process we consider the compression molding of a blank as shown in Figure 10.11. The blank is constrained on the sides so that it can only flow on squeezing along the x direction. In principle, one would like to develop the nonisothermal viscoelastic model of the process, but this disguises some of the essential features of the modeling process. For this reason we first develop the isothermal Newtonian model of the process and then look at the difficulties involved with the development of a complete nonisothermal viscoelastic model.

In the process shown in Figure 10.11 a blank of polymeric material is compressed in a mold, which allows the material to deform in the x direction only. The mold is of width W and the blank is of width W , initial thickness h_0 , and initial length $2X_0$. The blank is assumed to cover 50% of the surface area of the plates, and hence only low deformation of the blank occurs. We assume that the blank rheology is Newtonian and that the flow is isothermal and quasisteady. With these assumptions we postulate the following for the velocity and pressure fields:

$$v_x = v_x(x, z); \quad v_z = v_z(z); \quad p = p(x, z) \quad (10.37)$$

The continuity equation for this situation is

$$\frac{\partial v_x}{\partial x} + \frac{\partial v_z}{\partial z} = 0 \quad (10.38)$$

The equations of motion are

$$-\frac{\partial p}{\partial x} - \frac{\partial \tau_{zx}}{\partial z} - \frac{\partial \tau_{xx}}{\partial x} = 0 \quad (10.39)$$

$$-\frac{\partial p}{\partial z} - \frac{\partial \tau_{zz}}{\partial z} = 0 \quad (10.40)$$

For the Newtonian fluid the stress components are

$$\tau_{xx} = -2\mu \frac{\partial v_x}{\partial x}; \quad \tau_{zz} = -2\mu \frac{\partial v_z}{\partial z}; \quad \tau_{zx} = -\mu \frac{\partial v_x}{\partial z} \quad (10.41)$$

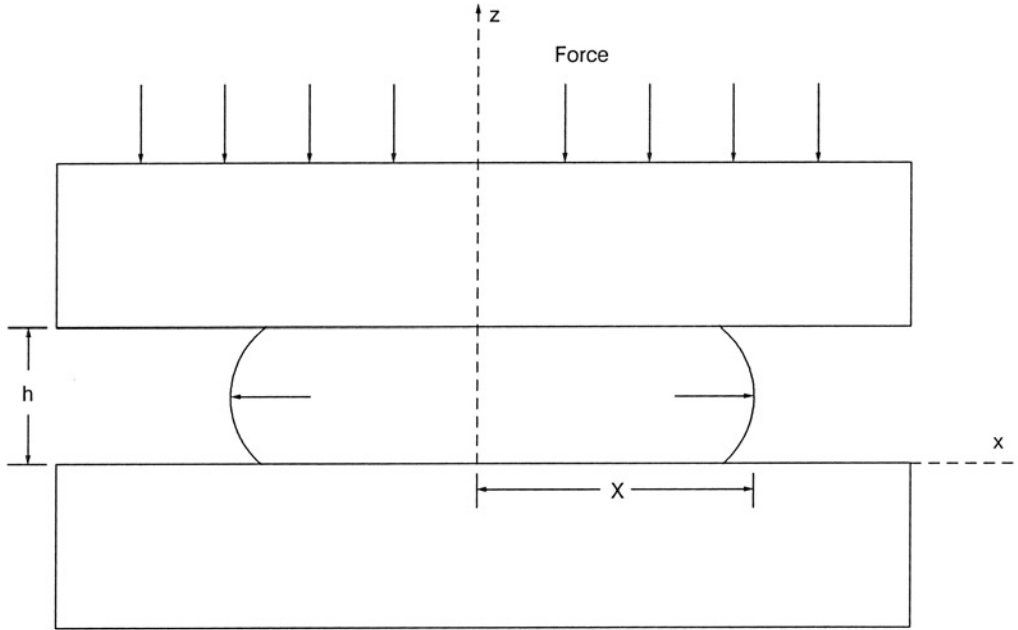


FIGURE 10.11 Two-dimensional flow in compression molding between two parallel platens. Flow occurs in the z and x directions only.

From the conditions given in the problem it is possible to show

$$\frac{\partial v_x}{\partial z} \gg \frac{\partial v_x}{\partial x} \text{ and } \frac{\partial v_z}{\partial z} \quad (10.42)$$

and hence the dominant stress component is τ_{zx} . The equations of motion become, on introducing the expression for τ_{zx} in Eq. 10.41 and conditions in Eq. 10.42,

$$\mu \frac{d^2 v_x}{dz^2} = \frac{dp}{dx} \quad (10.43)$$

Equation 10.43 is integrated using the following boundary conditions:

$$\begin{aligned} \text{at } z = 0, \quad v_x &= 0 \\ \text{at } z = h, \quad v_x &= 0 \end{aligned} \quad (10.44)$$

to give

$$v_x = \frac{Gh^2}{2\mu} \left[\left(\frac{z}{h} \right)^2 - \frac{z}{h} \right] \quad (10.45)$$

where $G = dp/dx$.

The goal is to determine a relation between the rate of plate closing (dh/dt), which is usually constant in most commercial presses, the force required to maintain this rate, the plate geometry, and the viscosity of the fluid. It is also desired to know how long it takes to completely fill out the mold. The first step is to relate the rate of flow out through a plane

perpendicular to the x direction to the rate of closing of the plate, which is given by

$$\left(\frac{dh}{dt} \right) WX = W \int_0^h v_x dz \quad (10.46)$$

or on substituting Eq. 10.45 into Eq. 10.46 for v_x we obtain

$$\left(\frac{dh}{dt} \right) WX = \frac{Gh^3 W}{\mu} \int_0^1 (\xi^2 - \xi) d\xi = \frac{-Gh^3 W}{6\mu} \quad (10.47)$$

where $G = dp/dx$, X is the half-width of the sheet, and $\xi = z/h$. From Eq. 10.47 we obtain the pressure distribution in the sample:

$$p - p_a = \left(\frac{dh}{dt} \right) \left(\frac{6\mu}{h^3} \right) X(X - x) \quad (10.48)$$

Finally, we carry out a force balance on the upper plate:

$$-F + p_a W 2X + 2W \int_0^X p(x) dx = 0 \quad (10.49)$$

to obtain the following relation (note that Eq. 10.48 is substituted into Eq. 10.49 and the integration is carried out):

$$F = \frac{6W\mu\dot{h} X^3}{h^3} \quad (10.50)$$

Equation 10.50 can be used to determine the force as a function of plate position if $dh/dt = \dot{h}$ is constant, or if F is constant, a nonlinear ordinary differential equation arises

which can be solved for $h(t)$. In the following example we use the equations just presented to estimate conditions in a compression molding process.

Example 10.2. Compression Molding of a Newtonian Fluid

Consider the compression molding of a blank of polypropylene reinforced with glass fiber as shown in Figure 10.11. For the time being, consider the material to be Newtonian with a viscosity of $5 \times 10^2 \text{ Pa} \cdot \text{s}$. The thickness of the blank is 3.6 mm, and it is to be molded to fill the mold which has a length of 1 m, a width of 0.25 m, and a thickness of 3.2 mm. Determine the initial dimensions of the sheet required to fill out the mold (take the width as 0.25 m), the time for filling the mold, and the force required to complete the filling of the mold. The press can exert a maximum force of 20 MN and operate at rates between 4.23 and 33.9 mm/s.

Solution. Starting with the lowest closing rate of 4.23 mm/s we obtain

$$h(t) = -4.23 \times 10^{-3}t + 3.6 \times 10^{-3}$$

The time for the gap to reach 3.2 mm is then 0.0946 s. Using Eq. 10.50 the force required to fill out the mold is

$$F = \frac{6(0.25)(5.0 \times 10^2) (4.23 \times 10^{-3}) (0.5)^3}{(3.2 \times 10^{-3})^3} = 12.1 \text{ MN}$$

Hence, one could operate at a slightly higher closing rate if necessary, because the force required at the lowest rate is less than the maximum force available. ■

Although we have considered a highly idealized case of isothermal Newtonian flow, the model and calculations give an idea of the approach one must take in modeling and designing an actual process. In practice the time for heating the blank up to the processing temperature and the time for cooling the sample in the mold are by far the longest times. The time for filling out the mold may be on the order of seconds. Hence, although there will be an initial temperature distribution in the sample, very little change in temperature will occur during the deformation process. As a first approximation, provided we can handle the initial temperature variation in the sample, we can decouple the equation of motion from the energy equation. Once the mold is filled out, the time for cooling the part can be determined by treating the situation as a one-dimensional transient heat conduction.

There are still several parts of the problem that cannot be dealt with at this level. First, the viscoelastic nature of the flow must be considered as the deformation occurs over short times and may involve a significant extensional component. Second, the rheological properties of materials that are usually processed by means of compression molding are difficult

to obtain. Materials such as PP filled with long glass fibers are extremely difficult to characterize rheologically (see Ortman et al., 2011, for discussion of a method). In fact, the best approach may be to use lubricated squeezing flow, which was discussed in Chapter 3. Finally, the shape changes that the blank may undergo may require the use of finite element methods.

10.3 THERMOFORMING

Thermoforming is used primarily for the manufacturing of packaging and disposable containers. However, it is also becoming a useful technique in the processing of engineering thermoplastics to produce parts used in the transportation industry. Polymers that are processed by this technique must have sufficient melt strength so that on heating they do not sag significantly under their own weight, yet they can be deformed under pressure to take the shape of a mold. Hence, highly crystalline polymers with high melting temperatures and low molecular weight cannot readily be thermoformed. For example, nylon 66 ($T_m = 265 \text{ }^\circ\text{C}$ and $M_w = 30,000$) is not usually processed by means of thermoforming, while LDPE ($T_m = 110 \text{ }^\circ\text{C}$ and $M_w = 200,000$) is. In this section we first describe the general aspects of thermoforming and then some basic features of modeling this process as required in design.

10.3.1 General Aspects of Thermoforming

The essential features of the thermoforming process are shown in Figure 10.12. Thermoplastic sheet is heated usually by means of radiation but sometimes in conjunction with convection cooling to temperatures either just above T_g in the case of amorphous polymers or T_m in the case of semicrystalline polymers. The exact temperature depends on the degree of sag exhibited by the material under its own weight, which is determined by its rheological properties. The sample is then removed from the heating system and brought into position over the mold. The sample is forced to take the shape of the mold by applying pressure to the top of the sheet or by generating a vacuum on the underside of the sheet as shown in Figure 10.12. The forming step occurs in the matter of a second. The sample is maintained in the mold until it is rigid enough to be removed from the mold without altering its shape.

There are a number of variations on the basic process, which are described in more detail by Throne (1986). For example, in plug-assisted vacuum forming the heated sheet is forced by a plug into the mold with the remainder of the shape being produced by the application of vacuum to the underside of the sheet. This method is used to help maintain a more uniform wall thickness throughout the part. Another example is matched die molding, which is shown in Figure 10.13.

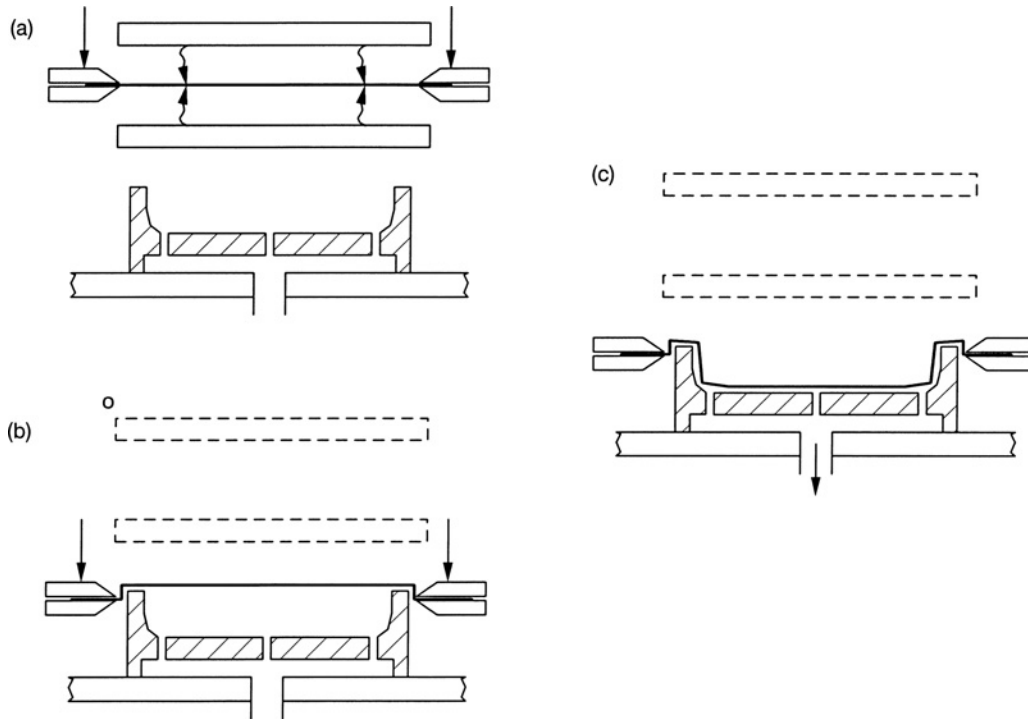


FIGURE 10.12 Typical pressure thermoforming process. (a) The clamped sheet is heated to the processing temperature by means of infrared heaters. (b) The heated sheet is removed from the radiation heating source and placed into position for forming. (c) Vacuum is applied to the underside of the sheet or air pressure is applied to the top side of the sheet, forcing the heated sheet into the mold.

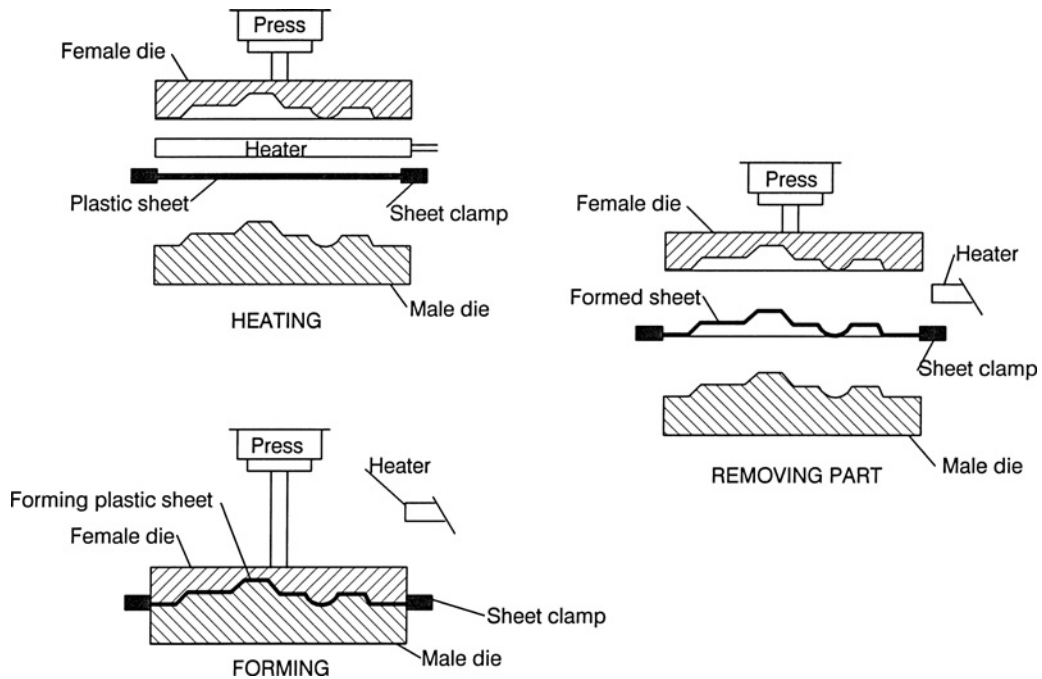


FIGURE 10.13 Forming in a matched metal die system. After heating, the sheet is formed by the application of mechanical pressure to the upper part of the mold.

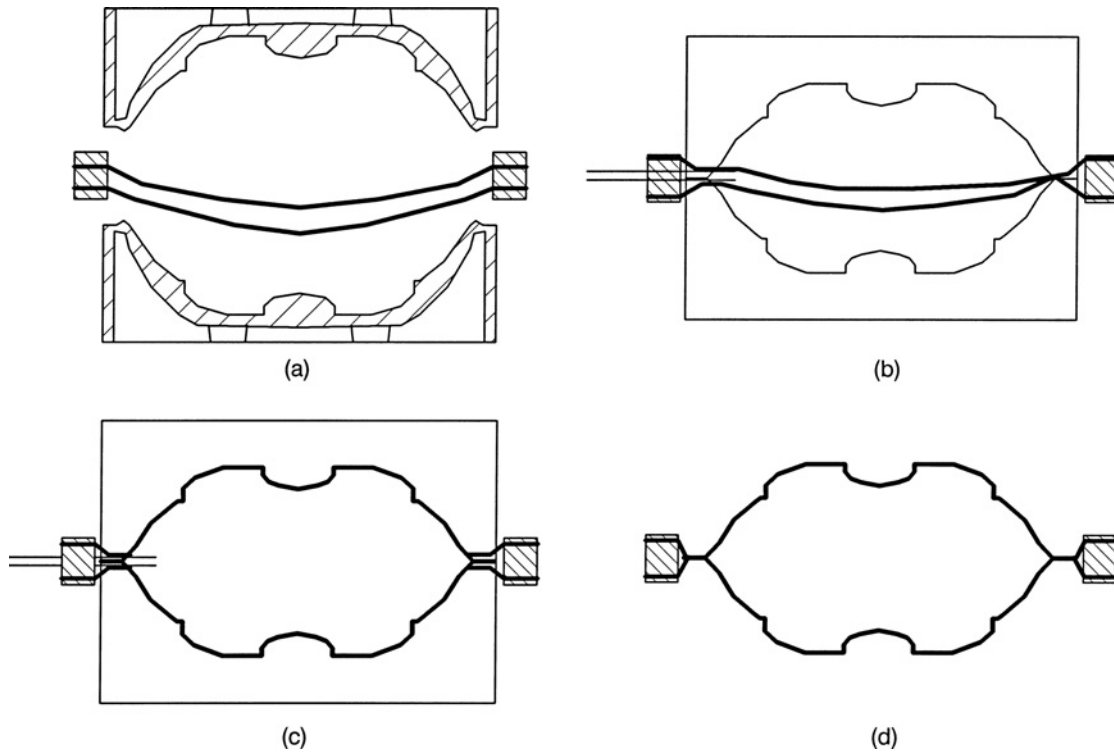


FIGURE 10.14 Twin sheet thermoforming process. (a) Heated sheets are placed between the mold halves. (b) The mold is closed, sealing the two sheets at the edges and around an inflation tube. (c) Air pressure is supplied through the tube, causing the sheets to inflate against the mold walls. (d) The mold is opened once the sheets are cooled and the part is removed.

The heated sheet is forced to take the shape of the female portion of the mold by the male part. This process is characterized by the formation of parts with more intricate shapes and uniform wall thickness. Finally, one last technique is that of twin sheet thermoforming as shown in Figure 10.14. Here two sheets are heated and then forced to take the shape of the mold by applying air pressure on the inside of the sheets and possibly vacuum on the outside. This process resembles somewhat that of blow molding, which is discussed in Section 10.4. However, the sheets can be forced to take on different shapes as each half of the mold can have a different shape. Furthermore, different polymers can be used for each half. The sheets must be held in the mold long enough for bonding to occur.

Thermoforming can be divided into four sections: (1) sheet heating without deformation, (2) sheet stretching without significant heat transfer, (3) part cooling in the mold and (4) postmolding operations such as trimming. The time to make a part is primarily determined by steps 1 and 3 as these are the order of minutes. However, the successful functioning of the part is determined by step 2 as the distribution of wall thickness is determined in this step. In the next section we consider the modeling of each of these steps.

10.3.2 Modeling of Thermoforming

Of the four subdivisions we discussed the first three—heating, forming, and cooling—lend themselves to simulation and modeling, which in turn lead to the possibility of carrying out effective design considerations. We first discuss the heating and cooling aspects followed by ideas on the forming step.

The success of a thermoforming process depends primarily on the rate at which a part can be produced. This is controlled by the time required to heat the sheet to the processing temperature and the time to cool the part down once it has been formed. The time required to heat a sheet to the processing temperature depends on the heat transfer conditions and, of course, the temperature at which the sheet becomes sufficiently formable but not so low in melt strength that significant sagging occurs. In the case of amorphous polymers this is usually 30 to 60 °C above T_g , while for semicrystalline polymers it is usually just above the temperature where melting is just completed. In the case of semicrystalline polymers the molecular weight must be sufficiently high to impart a viscosity that is high enough to resist sagging.

At present there seems to have been no quantitative attempts to estimate the temperature at which a polymer is

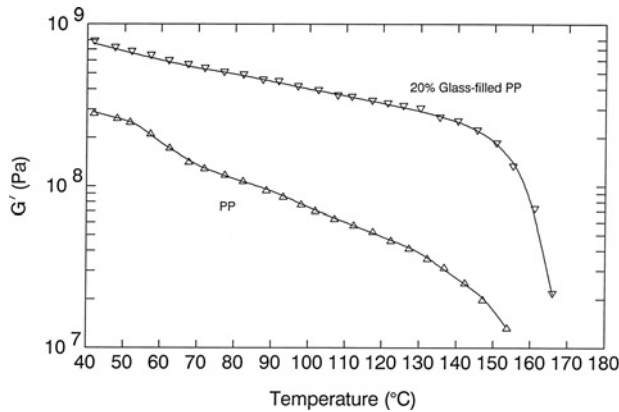


FIGURE 10.15 Dynamic mechanical thermal analysis (G' versus temperature at an angular frequency of 1.0 rad/s) of polypropylene (PP) and PP filled with 20 wt% glass fiber determined using the torsional mode of a rheometer.

suitably formable. There are some empirical guidelines based on experience with given polymers. For example, Gruenwald (1987) gives the thermoforming temperature for polypropylene to be between 150 and 199 °C and for polystyrene to be between 143 and 177 °C. (Note: T_g for PS is about 100 °C.) Dynamic mechanical properties obtained as a function of temperature may provide a way to estimate the processing temperatures. For example, the storage modulus (G') versus temperature at an angular frequency of 10 rad/s is shown in Figure 10.15 for PP and glass-filled PP. Based on experience when G' reaches about 1×10^7 Pa the material is formable. This appears to occur at a temperature above 150 °C for PP. For glass-filled PP this temperature appears to be above 170 °C. Experience coupled with dynamic mechanical properties may provide the best approach for estimating the processing temperature.

Once the processing temperature has been determined, the time required to heat the sheet to this temperature can be calculated by methods given in Chapter 5. Basically the problem becomes one of one-dimensional transient heat conduction. Heating is usually accomplished by radiation combined with convection. The radiation heat transfer coefficient is given in Eq. 5.138, while the view factor for two parallel planes (Eq. 5.134) is most frequently used. The emissivities of the heating source fall in the range of 0.9 to 0.95, while that of the polymer sheet is about 0.9. The rating of the heating source is available from the manufacturer of the radiant heating source. For example, resistance heated strip elements usually found in commercial thermoforming machines have a surface temperature of 427 °C at the highest power input. If the distance of the heaters from the sheet is greater than about 30 cm, then free convection cooling of the sheet surface can occur. Throne (1986) has estimated the free convection heat transfer coefficient to be on the order of $11.3 \text{ W/m}^2 \cdot \text{K}$, but this can be calculated via methods given in Chapter 5.

Sometimes forced convection is used cyclically to cool the sheet surface and again the methods described in Chapter 5 can be used to estimate the heat transfer coefficient. The numerical procedure associated with Example 5.5 (p. 127) can be used for determining the heating time and temperature distribution in the sheet.

Although the time for producing a part is determined by the heating and cooling times, the utility of the part is determined by the wall thickness distribution. If during the forming process the wall becomes too thin in certain regions, then the part may fail under loading or have reduced barrier properties. The ability to estimate the wall thickness distribution is crucial to the design of a thermoforming process.

Estimating the wall thickness distribution is extremely difficult especially for irregularly shaped parts. Numerical methods, such as the finite element method, are required. Furthermore, an appropriate nonlinear constitutive equation for the polymer is required, and this may be difficult to obtain for materials that exist in the near rubbery state at the forming temperature. Obtaining rheological data at the forming temperature is very difficult. Finally, the solution of the coupled equations of motion and the nonlinear constitutive equation requires sophisticated numerical codes, which are not readily available at this time.

In principle, it is desirable to be able to predict wall thickness distribution for a given polymer being formed into a given shape. Then given the various processing variables, including temperature, differential pressure, and sheet rheological properties, determine how to move the material around in order to meet the necessary part design criteria while using the minimum initial sheet thickness. We are not in position at this point to be able to accurately do this. However, there are at least two things we can do. First, we can estimate whether sufficient material is available to maintain a desired average wall thickness; and second, we can see how for simple geometries the wall thickness distribution is obtained using geometric arguments and a mass balance.

As a first estimate we must be able to determine on the average whether sufficient material is available in the sheet for producing a certain part. This is in essence done by carrying out a mass balance on the sheet. For example, consider Figure 10.16 in which a sheet of arbitrary dimensions is to be formed into a female mold. Since the original volume of material available for forming in this configuration is CDt_i (note that $AB - CD$ is the area that contacts the mold surface first and this will deform very little, leaving only the area CD) where t_i is the initial thickness of the sheet. After forming the volume of the material is

$$V_f = (2DE + 2CE + CD)t_f \quad (10.51)$$

and hence using the dimensions given in arbitrary units $t_f = t_i/4$. Obviously, if the average thickness doesn't meet the design requirements, then sufficient material is not available.

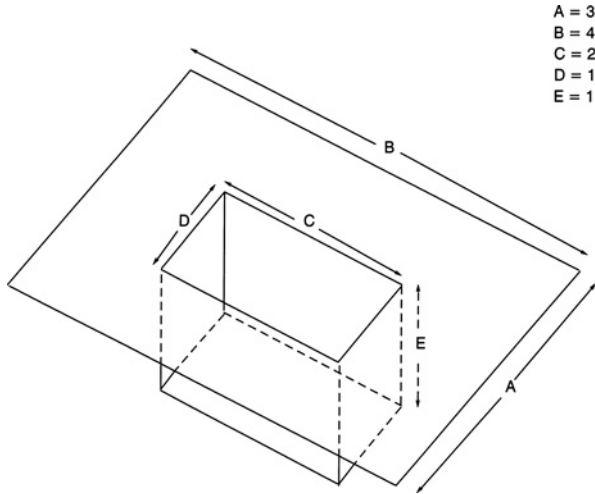


FIGURE 10.16 Relative dimensions of a container generated from a thermoformed sheet using a female mold. Before forming, the area of the section to be formed is 2 units. After forming, the surface area of the box is 8 units.

However, because there will be a distribution of wall thickness, there may be regions that don't satisfy the design requirements. This is in spite of sufficient material being available to provide the wall thickness on the average. It is desirable, therefore, to be able to predict the wall thickness distribution as a function of processing conditions and rheological properties of the polymer. This has been done for several simple geometries (Rosenzweig et al., 1979) and we illustrate the approach in the following example.

Example 10.3. Wall Thickness Distribution in a Conical Mold

Consider the thermoforming of a sheet in which the mold is conical in shape as shown in Figure 10.17. The sheet is forced into the mold by means of an applied pressure differential (e.g., air pressure is applied to the surface). The sheet is initially of uniform thickness, h_0 , and the process is isothermal. Obtain an expression for the thickness distribution as a function of the initial sheet thickness and mold geometry.

Solution. The following assumptions are made:

1. The polymer is incompressible.
2. Polymer deformation occurs only in the bubble.
3. The free surface is uniform in thickness and has a spherical shape.
4. The sheet solidifies on touching the mold walls, but the spherical surface remains isothermal.
5. The polymer does not slip on the walls.
6. The spherical surface, or bubble, thickness is small compared to its radius.

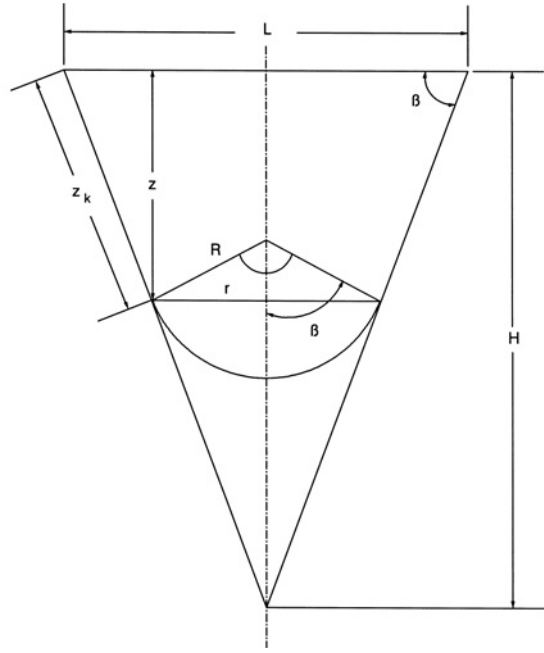


FIGURE 10.17 Geometry of a conical mold used in the thermoforming of a sheet. The sheet is assumed to expand as a spherically shaped bubble freezing as it contacts the walls.

Referring to Figure 10.17 a differential mass balance is made to obtain the thickness distribution:

$$2\pi R^2(1 - \cos \beta)h \Big|_{z_k} - 2\pi R^2(1 - \cos \beta)h \Big|_{z_k + \Delta z_k} = 2\pi r h \Delta z_k \tag{10.52}$$

where the first term is the volume of the spherical bubble at position z_k along the wall and the second term is the volume of the bubble at a position $z_k + \Delta z_k$. The volume of material deposited on the wall as the bubble moves from z_k to $z_k + \Delta z_k$ is represented on the right side of Eq. 10.52. Dividing through by Δz_k and taking the limit as Δz_k goes to zero gives the following differential equation:

$$-\frac{d}{dz_k}(R^2 h) = \frac{r h}{(1 - \cos \beta)} \tag{10.53}$$

From geometrical considerations we can replace r by $R \sin \beta$ and R by

$$R = \frac{H - z_k \sin \beta}{\sin \beta \tan \beta} \tag{10.54}$$

to give the following differential equation for h :

$$\frac{dh}{h} = \left(2 - \frac{\tan \beta \sin \beta}{1 - \cos \beta} \right) \sin \beta \frac{dz_k}{H - z_k \sin \beta} \tag{10.55}$$

Equation 10.55 can be integrated using the initial condition that $h(0) = h_1$, where h_1 is the initial thickness of the bubble tangent to the cone at $z_k = 0$, to give

$$\frac{h}{h_1} = \left(1 - \frac{z_k}{H} \sin \beta\right)^{\sec \beta - 1} \quad (10.56)$$

Finally, it is possible to relate the initial thickness, h_1 , to the original sheet thickness, h_0 , by the following relation:

$$\frac{\pi L^2 h_0}{4} = \frac{\pi L^2 (1 - \cos \beta) h_1}{2 \sin^2 \beta} \quad (10.57)$$

where the left side of this equation is just the volume of the circular piece of sheet above the mold opening before forming and the right side is the spherical surface when $z_k = 0$. On replacing h_1 in Eq. 10.56 with the value for h_1 in terms of h_0 in Eq. 10.57, the thickness distribution is thus given by

$$\frac{h}{h_0} = \frac{1 + \cos \beta}{2} \left(1 - \frac{z_k}{H} \sin \beta\right)^{\sec \beta - 1} \quad (10.58)$$

The approach described in Example 10.3 is based totally on conservation of mass with no mention of the role played by the rheological properties of the polymer. In spite of this, the approach used in Example 10.3 seems to work reasonably well for shallow geometries, which lend themselves to geometric analysis. When then is the constitutive equation required in the analysis of thermoforming? In principle, the shape of the bubble is not known but is related to both processing conditions and the rheology of the polymer. Furthermore, the pressure required to deform the sheet and the time to fill the mold are determined by the rheology of the polymer. In the following example we illustrate how the constitutive equation is used in simulating thermoforming.

Example 10.4. Inflation Pressure of the Bubble

Establish the equations required to determine the pressure and time to form a sheet in the conical mold shown in Figure 10.17 for two cases: (1) a Newtonian fluid and (2) a viscoelastic fluid.

Solution. In addition to the assumptions used in Example 10.3, we assume that the deformation of the spherical film is occurring under quasisteady-state conditions, and hence we use an unsteady-state mass balance but the steady-state equation of motion. The bubble thickness is also assumed to be small relative to the radius. Using spherical coordinates the following postulates are made:

$$v_r = v_r(r) \quad p = p(r) \quad (10.59)$$

where r is the spherical coordinate taken along R in Figure 10.17 and not the radius of the conical cross section as indicated in this figure. The continuity equation becomes

$$\frac{\partial}{\partial r} (r^2 v_r) = 0 \quad (10.60)$$

which can be integrated to give

$$v_r = A(t)/r^2 \quad (10.61)$$

where $A(t)$ is an arbitrary function of time. At the inside surface of the bubble, which is located at R , the velocity of the fluid just equals the velocity of the surface which is dR/dt (we denote this as \dot{R}): that is,

$$v_r(R) = \dot{R} \quad (10.62)$$

From Eqs. 10.61 and 10.62 we find that $A(t) = \dot{R}R^2$, and v_r becomes

$$v_r = \frac{\dot{R}R^2}{r^2} \quad (10.63)$$

Hence, an expression for the velocity field has been obtained directly from the continuity equation without using the equation of motion.

In order to relate the rate at which the mold is filled to the applied pressure it is necessary to use the equation of motion. Independent of the choice of constitutive equation the equation of motion becomes

$$0 = -\frac{\partial p}{\partial r} - \frac{1}{r^2} \frac{\partial}{\partial r} (r^2 \tau_{rr}) + \frac{\tau_{\theta\theta} + \tau_{\phi\phi}}{r} \quad (10.64)$$

Equation 10.64 can be rewritten in the following form:

$$\frac{\partial \pi_{rr}}{\partial r} = \frac{\tau_{\theta\theta} + \tau_{\phi\phi} - 2\tau_{rr}}{r} \quad (10.65)$$

where π_{rr} is the total stress (see Chapter 3). At the inside surface (i.e., at R) it can be shown that $\pi_{rr}(R) = -P(R)$ while at the outside surface $\pi_{rr}(R + h) = -P(R + h)$. Therefore, the pressure differential across the film is given by

$$P(R) - P(R + h) = \Delta P = \int \frac{\tau_{\theta\theta} + \tau_{\phi\phi} - 2\tau_{rr}}{r} dr \quad (10.66)$$

In our case it is assumed that the film is thin, and hence the stresses don't vary significantly over the film thickness, and hence Eq. 10.66 becomes

$$\Delta P = \frac{h (\tau_{\theta\theta} + \tau_{\phi\phi} - 2\tau_{rr})|_{R+h}}{R} \quad (10.67)$$

To complete our goal we now must assume a constitutive equation for the polymer. We first assume the Newtonian model, as this allows one to obtain an analytical solution. This is also an advisable procedure to follow before embarking on a solution using a viscoelastic model, which will more than likely require numerical methods to obtain an answer. For the Newtonian model (see Chapter 2) the stress components are

$$\begin{aligned}\tau_{\theta\theta} &= -2\mu \frac{v_r}{r} = \frac{-2\mu \dot{R}R^2}{r^3} \\ \tau_{\phi\phi} &= -2\mu \frac{v_r}{r} = \frac{-2\mu \dot{R}R^2}{r^3} \\ \tau_{rr} &= -2\mu \frac{\partial v_r}{\partial r} = \frac{4\mu \dot{R}R^2}{r^3}\end{aligned}\quad (10.68)$$

These quantities are now substituted back into Eq. 10.67 to obtain an expression for the pressure difference:

$$\Delta P = \frac{-8\mu \dot{R}h}{R^2} \quad (10.69)$$

By using Eqs. 10.58 and 10.54 we can express Eq. 10.69 as

$$\Delta P = \frac{-8\mu \dot{R}h_0}{R^2} \left[\frac{R \sin \beta \tan \beta}{H} \right]^{\sec \beta - 1} \quad (10.70)$$

Equation 10.70 represents a nonlinear ordinary differential equation for finding $R(t)$ for a given pressure differential across the film or bubble. The solution of this equation is obtained numerically in Problem 10C.3 using either the IMSL subroutine IVPAG or an ordinary differential equation solver in MATLAB.

We next consider the formulation of the problem for the viscoelastic case. We select the PTT model again (see Eq. 3.45), which in spherical coordinates (Bird et al., 1987) leads to the following equations for the stress components:

$$\exp\left(-\frac{\varepsilon \lambda t r \tau}{\mu}\right) \tau_{rr} + \lambda \frac{\partial}{\partial t} \tau_{rr} + \frac{4\lambda \dot{R}}{R} (1 - \xi) \tau_{rr} = \frac{4\mu \dot{R}}{R} \quad (10.71)$$

$$\exp\left(-\frac{\varepsilon \lambda t r \tau}{\mu}\right) \tau_{\theta\theta} + \lambda \frac{\partial \tau_{\theta\theta}}{\partial t} - \frac{2\lambda \dot{R}}{R} (1 - \xi) \tau_{\theta\theta} = \frac{-2\mu \dot{R}}{R} \quad (10.72)$$

$$\exp\left(-\frac{\varepsilon \lambda t r \tau}{\mu}\right) \tau_{\phi\phi} + \lambda \frac{\partial \tau_{\phi\phi}}{\partial t} - \frac{2\lambda \dot{R}}{R} (1 - \xi) \tau_{\phi\phi} = \frac{-2\mu \dot{R}}{R} \quad (10.73)$$

The above set of equations represents three coupled nonlinear ordinary differential equations for finding τ_{rr} , $\tau_{\theta\theta}$, and $\tau_{\phi\phi}$.

Since they can't be solved explicitly for the stresses as was the case for the Newtonian fluid, it is not possible to obtain a differential equation such as Eq. 10.70, which can be solved to find \dot{R}/R directly. To solve these equations one must guess at values of \dot{R}/R first, solve the set of coupled differential equations numerically, and then determine whether the stress values satisfy Eq. 10.67. One must repeat this process until Eq. 10.67 is satisfied for a given pressure differential. (This approach is used in Problem 10C.3.) Because the solution is obtained numerically, the guess for \dot{R}/R is made for a small time step over which it is assumed that \dot{R}/R is constant, and hence $R(t) = R_0 \exp(Ct)$. The thickness distribution is then determined using the calculated value of $R(t)$ and Eqs. 10.58 and 10.54. ■

Before leaving this section we make a few comments about solving problems using nonlinear rheological equations of state. The solution of the nonlinear equations is facilitated by obtaining the Newtonian solution first. In the example just presented the solution of the Newtonian case serves to provide an estimate of the time required to fill the mold, the magnitude of the pressure difference, and \dot{R}/R . Because the solution must be obtained numerically using an iterative procedure in the viscoelastic case, the rate of convergence of the solution is greatly enhanced by the initial guesses for \dot{R}/R and the time for filling the mold provided by the solution for the Newtonian case. Hence, it is advisable to obtain a solution to the Newtonian case before embarking on the solution to the viscoelastic case.

10.4 BLOW MOLDING

Blow molding is a process for generating hollow plastic articles such as bottles and containers. It is a process that was used initially by the packaging industry but more recently has been used by the automotive industry to produce parts such as fuel tanks, bumpers, dashboards, and seatbacks. In other words, plastic parts are being manufactured for applications where some structural integrity is required.

In this section we first review some of the more salient technological features of blow molding. We then consider the parts of the process which can be subjected to quantitative analysis and design.

10.4.1 Technological Aspects of Blow Molding

Although there are a number of variations in the way in which blow molding is carried out, there are a number of common steps. First, conventional melt processes are used to make a cylindrical tube. (*Note:* The preformed sample may be of other shapes.) When extrusion is used, this tube is referred to as a parison, and when injection molding is used, it is referred to as a preform. The softened preformed tube is transferred

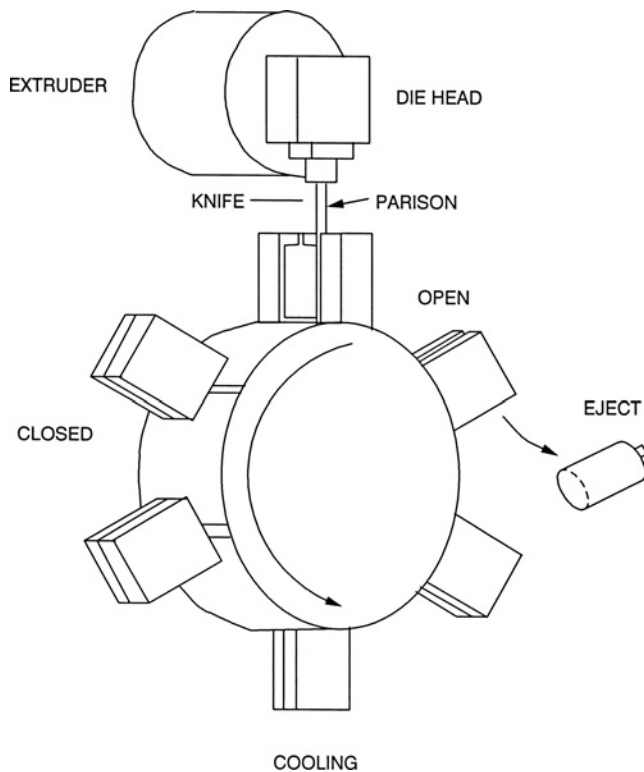


FIGURE 10.18 Commercial extrusion blow molding process. The tubular parison is extruded into position between the walls of the open mold. The mold walls close, pinching the ends of the parison, and simultaneously the parison is cut from the continuously extruded tube. The parison is inflated against the mold walls, where the part cools and is removed when the mold is opened.

to a mold consisting of two halves, where it is sealed and inflated to assume the internal contours of the mold. The part is cooled in the mold, until it reaches a temperature where it will maintain the shape of the mold when the mold is opened.

Extrusion blow molding is used frequently for polymers that exhibit high melt strength such as polyolefins. The process is shown schematically in Figure 10.18. In this figure the tubular parison is continuously extruded from a die into position between the two mold halves and then separated from the main stream by means of a knife. The mold closes sealing the end of the parison, and air pressure is applied inflating the parison against the walls of the mold. The time for inflation is very short, usually in the range of a second depending on the size of the part. The longest step in the process is the cooling of the part. The time for cooling depends on the temperature to which the part must be lowered in order for it to maintain the shape of the mold and the rate of heat transfer between the mold wall and the part. The mold opens finally and the part is ejected.

In some cases injection molding is used to generate preforms rather than extrusion, but otherwise the process is nearly the same. Injection molding is used primarily when the

screw-thread dimensions must be precise and to avoid flash, weld lines, and material waste at the base of the container. Just as in the case of extrusion blow molding, it is possible to generate preforms with multiple layers for situations where barrier properties are required.

In continuous processes the parison or preform must have sufficient melt strength so that it does not sag under its own weight. Sagging leads to unacceptable variations in the wall thickness of the part. For polymers such as PETP it is usually not possible to use extrusion blow molding because of severe sagging problems. To overcome sagging problems preforms are injection molded in a separate step where they can rapidly be quenched to inhibit crystallization and hence remain clear. The preforms are then heated by means of radiation to a temperature about $30\text{ }^{\circ}\text{C}$ above T_g , where crystallization kinetics are slow, but the material is deformable. The heated preforms are then transferred to the mold, where they are inflated by means of air pressure. This type of two-step process can be used for resins such as PPS, which also has slow crystallization kinetics and low melt strength.

Resistance to sagging is due to the rheological properties of the melt. It is preferable to modify the polymer such that the extensional behavior of the melt is altered rather than raise η_0 by means of increasing the molecular weight. In Figure 10.19 the length of a parison as function of time is presented for PETP and a modified form of PETP which presumably contains branching (Birley et al., 1991). The broken lines in Figure 10.19 represent the length of the parison in the absence of any swell or sagging (i.e., $\langle v_z \rangle > t$). One can see for short times that the parison length is below that given by the broken line (this is for extrusion times up to about 5 s, which

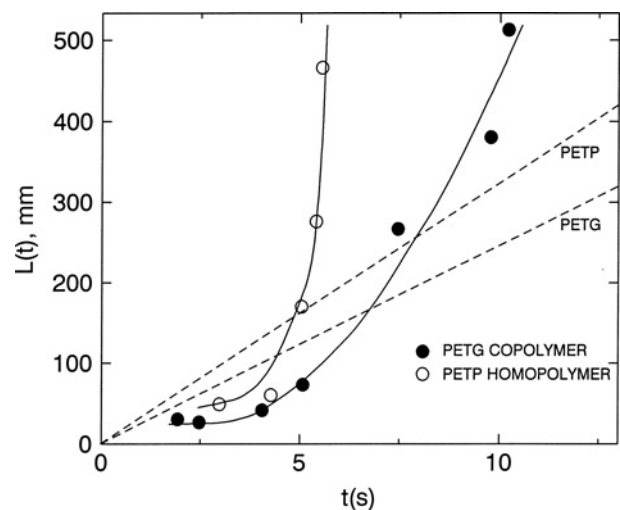


FIGURE 10.19 Length of an extruded parison of PETP and PETG (modified PETP) versus time. The lines represent the length of the parison as a function of time under conditions of no extrudate swell or sagging. (Reprinted by permission of the publisher from Birley et al., 1991.)

corresponds to a parison length of about 12 cm), while after about 5 s there is considerable parison sagging. For the modified PETP, referred to as PETG, parisons of length of about 20 cm can be extruded before sagging starts, but even then there is less sagging than for PETP. Although no rheological data were given, it is assumed that PETG contains branching, and the material exhibits extensional strain hardening.

The process of inflating the parison is primarily one of planar extensional flow especially away from the ends of the parison. Since the ends of the parison are constrained as the parison expands, the thickness of the wall decreases as the diameter expands, leading to primarily planar extensional deformation. For this reason the blow molded part contains primarily orientation along the circumferential or hoop direction and hence exhibits mechanical anisotropy.

In order to generate a better balance of mechanical properties it is necessary to create biaxial orientation in the part. Stretch blow molding is used to accomplish this. In essence the parison is stretched along the axial direction before being inflated. Biaxial orientation is specifically required in large containers for fluids. For example, bottles for carbonated beverages are typically processed by means of stretch blow molding.

This coverage of blow molding is by no means thorough, as it only serves to provide enough background for the following section, which is concerned with more quantitative aspects of blow molding as required in design and analysis. More details about the technology of blow molding can be found elsewhere (Lee, 1990). We now turn our attention to the aspects of blow molding which can be handled in a quantitative fashion.

10.4.2 Simulation of Blow Molding

In order to emphasize the basic parts of blow molding, the process is shown schematically in Figure 10.20. There are basically four steps that must be considered in the analysis of a blow molding process (these are in addition to the extrusion or injection molding steps which have already been considered): (1) the cooling of the hanging parison or preform by free convection before the mold closes or the heating of the preform in a two-step process; (2) the sagging of the parison in the case of extrusion processes; (3) the expansion of the parison or preform against the mold walls; and (4) the cooling of the part by means of forced convection. Although we make a few comments about the heat transfer parts of the process, most of this analysis falls under the area of transient heat transfer, which was discussed in Chapter 5. We emphasize topics such as parison sagging and expansion.

During the hanging of the parison in the case of extrusion blow molding, there is some cooling of the parison as the hang times may be on the order of 10 to 20 s for large parts. There is probably little heat transfer at the inner surface, and hence, this can be considered as an insulated surface. At the exterior

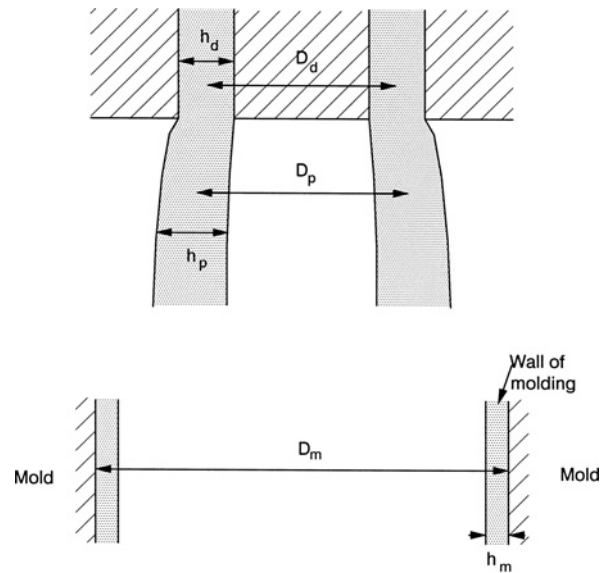


FIGURE 10.20 Blow molding process showing an extruded parison of cylindrical shape leaving an annular die and the walls of the mold.

surface heat transfer occurs by means of free convection. The heat transfer coefficient can be estimated using the material given in Section 5.3. The problem can be considered as that of one-dimensional transient heat conduction with the axes attached to the moving parison. There will be some thickness variation along the length of the hanging parison which may present some problem in the analysis. Certainly if there is a significant drop in temperature, then the temperature of the melt leaving the die will have to be adjusted accordingly.

In two-step processes, such as used for blow molding PETP, the preform must be heated up to a temperature suitable for inflation. This is usually accomplished by means of radiation heating as discussed in Section 5.4. As this topic was discussed in some detail in Section 5.4, we do not discuss it further here.

Once the parison has been inflated, it is cooled primarily by means of heat transfer at the mold surface. Channels through which water can be circulated are machined in the mold walls similar to what is done in injection molding. Approximately 50–95% of the total processing time is involved in cooling the part. At the inner surface very little heat transfer occurs with the heat transfer coefficient due to free convection being estimated to be in the range of $5.7\text{--}57 \text{ W/m}^2 \cdot \text{K}$. Hence, the cooling time of the part can be shortened by increasing the heat transfer at the inner surface. Using chilled air in the blowing process certainly helps, but other methods such as injecting liquid nitrogen (Gibbs, 1989) or a high-pressure mixture of air and water in which the water freezes as the air expands to form fine ice crystals (Hunkar, 1973) may provide more rapid cooling. Again the cooling of

the side walls is described by the one dimensional transient heat conduction equation.

Sagging of the parison as discussed above leads to a nonuniform distribution of the wall thickness. If the wall becomes too thin, it will fail during the inflation process. In the next example we consider how to approach the modeling of sagging.

Example 10.5. Sagging of a Cylindrical Parison

Determine the equations required to calculate the length of the parison shown in Figure 10.20 as a function of time and the thickness of the parison as a function of position. Assume that the melt is Newtonian and that the thickness of the parison is small relative to the diameter so that curvature can be neglected. Take the initial thickness as the maximum thickness due to extrudate swell.

Solution. For most cases it can be assumed that the thickness of the parison is small relative to the diameter, and hence we can treat the parison as a flat sheet. Furthermore, we assume that the deformation occurs along the axis of the parison and in the thickness direction but that the diameter does not change significantly. With these assumptions we can follow the development for thick films given in Section 9.1 and refer to Figure 9.17b. We assume quasisteady-state conditions in which the mass balance is unsteady, but the steady-state equation of motion holds. With these assumptions we postulate that

$$v_z = v_z(z) \quad v_y = v_y(y) \quad (10.74)$$

Following the development given in Eqs. 9.116 through 9.119, we can determine a relation between v_z and h , which is given below (Eq. 9.120):

$$\frac{1}{h} \frac{dh}{dz} = -\frac{1}{v_z} \frac{dv_z}{dz} \quad (10.75)$$

The equation of motion in the z direction including the gravitational term is

$$\frac{\partial \tau_{yz}}{\partial y} + \frac{\partial \pi_{zz}}{\partial z} - \rho g = 0 \quad (10.76)$$

Neglecting the effect of surface tension and air drag, which means the surface is stress free, we can relate τ_{yz} to π_{zz} by the following relation:

$$\tau_{yz} = \frac{1}{2} \frac{dh}{dz} \pi_{zz} \quad (10.77)$$

where h is the wall thickness at any z position. Since v_z is assumed to be nearly constant over the cross section of the parison, we can integrate Eq. 10.76 across the thickness to obtain the following form of the equation of motion:

$$\frac{h'}{h} \pi_{zz} + \frac{d\pi_{zz}}{dz} = \rho g \quad (10.78)$$

where $h' = dh/dz$. At this point we assume that the fluid can be described as Newtonian, but a viscoelastic constitutive equation could be used as well. Using Eq. 9.123, Eq. 10.78 becomes

$$-4\mu \frac{d^2 v_z}{dz^2} + \frac{4\mu}{v_z} \left(\frac{dv_z}{dz} \right)^2 - \rho g = 0 \quad (10.79)$$

Equation 10.79 can be solved numerically using the following boundary conditions:

$$\begin{aligned} \text{at } z = 0, \quad v_z &= \langle v_z \rangle \\ \text{at } z = L, \quad \frac{dv_z}{dz} &= 0 \end{aligned} \quad (10.80)$$

The solution to Eq. 10.79 must be obtained numerically as it is a nonlinear ordinary differential equation. (See Problem 10C.6 for a solution.) The solution is obtained for arbitrary values of L . The thickness profile can be obtained by means of Eq. 10.75 using the initial thickness estimated from die swell data. One must assume that die swell is unaffected by the weight of the hanging parison. The complete solution of the problem can only be obtained using numerical techniques. ■

Finally, we consider one more example and this is the pressure required to inflate a cylindrical parison. In the following example we consider the inflation process up to the point where the cylinder just touches the walls of the mold. In the central region of the parison the deformation is primarily that of planar extensional flow. The complete filling of the mold requires the use of finite element methods, as once the parison touches the wall the deformation of the remaining parison is very complex.

Example 10.6. Inflation of a Cylindrical Parison

Referring to Figure 10.20, determine the time required at a given inflation pressure for a cylindrically shaped parison of length L to contact the mold wall. Assume that because the ends of the parison are clamped, the process is primarily one of planar extensional flow. Furthermore, assume that surface tension is negligible, ρ is constant, inertial effects are negligible, $h \ll R$, and the process is isothermal. Obtain solutions for first the Newtonian case and then the viscoelastic case.

Solution. The solution follows closely that used in Example 10.3 for the inflation of a spherical bubble, and hence, some steps are carried out without detailed justification. With the postulate that $v_r = v_r(r, t)$ the continuity equation plus the boundary condition that $v_r(R, t) = dR/dt$ leads to the following velocity field:

$$v_r = \dot{R}R/r \quad (10.81)$$

where $\dot{R} = dR/dt$. Assuming that the fluid can be described as Newtonian, the stresses are

$$\begin{aligned} \tau_{rr} &= -2\mu \frac{\partial v_r}{\partial r} = \frac{2\mu \dot{R}R}{r^2} \\ \tau_{\theta\theta} &= -2\mu \frac{v_r}{r} = -\frac{2\mu \dot{R}R}{r^2} \end{aligned} \quad (10.82)$$

The equation of motion for this type of flow is

$$0 = -\frac{\partial p}{\partial r} - \frac{1}{r} \frac{\partial}{\partial r} (r\tau_{rr}) + \frac{\tau_{\theta\theta}}{r} \quad (10.83)$$

Using the definition for the total stress Eq. 10.83 can be rewritten as

$$-\frac{\partial \pi_{rr}}{\partial r} = \frac{\tau_{rr} - \tau_{\theta\theta}}{r} \quad (10.84)$$

With the assumptions that $h \ll R$ and that the stresses are constant over the thickness of the parison, Eq. 10.84 is integrated to give

$$P - p_a = (\tau_{rr} - \tau_{\theta\theta})(h/R) \quad (10.85)$$

where P is the applied pressure and p_a is the pressure on the outside of the parison. For the Newtonian case the expressions for the stresses given in Eq. 10.82 are substituted into Eq. 10.85 to give

$$P - p_a = 4\mu \dot{R}h/R^2 \quad (10.86)$$

In order to solve Eq. 10.86 another expression that relates h and R must be obtained from the conservation of mass. Because ρ is constant and the length of the parison is constant, one finds that $\dot{h}/h = -\dot{R}/R$. (Note: This is obtained by differentiating $V = 2\pi R h L$ with respect to time.) Equation 10.86 plus this last equation must be solved simultaneously to find $R(t)$ and $h(t)$ using the initial conditions that at $t = 0$, $R = R_p$ and $h = h_p$. The solution of these equations is obtained numerically in Problem 10C.4.

We next obtain the equations required to find $R(t)$ and $h(t)$ for the case of a viscoelastic fluid. Using the PTT model and the velocity field given in Eq. 10.81, the equations for determining the stress components are

$$\begin{aligned} \lambda \frac{\partial \tau_{rr}}{\partial t} + \exp[-(\varepsilon\lambda/\mu)(\tau_{rr} + \tau_{\theta\theta})] \tau_{rr} \\ + (2\lambda \dot{R}/R)(1 - \xi)\tau_{rr} = 2\mu \dot{R}/R \end{aligned} \quad (10.87)$$

$$\begin{aligned} \lambda \frac{\partial \tau_{\theta\theta}}{\partial t} + \exp[-(\varepsilon\lambda/\mu)(\tau_{rr} + \tau_{\theta\theta})] \tau_{\theta\theta} \\ - (2\lambda \dot{R}/R)(1 - \xi)\tau_{\theta\theta} = -2\mu \dot{R}/R \end{aligned} \quad (10.88)$$

The details of determining Eqs. 10.87 and 10.88 are considered in Problem 10B.6. As in the situation in Example 10.4, Eqs. 10.87 and 10.88 represent two nonlinear ordinary differential equations that must be solved numerically using guesses for \dot{R}/R based on the Newtonian solution. The stresses must satisfy Eq. 10.85 as well as the expression relating h and R obtained from the mass balance. The solution requires an iterative approach, as is discussed in Problem 10C.5. ■

The discussed approach for dealing with the inflation of a parison certainly represents a way to estimate the required inflation pressure and inflation time. However, the complete filling of the mold cavity is more complicated than that represented by planar extensional flow, and hence, finite element methods are required to more accurately handle the simulation of the inflation of the parison. The capability of accurately predicting the wall thickness distribution in the part is crucial in the successful design of a blow molding process. Furthermore, it would be desirable to be able to predict molecular orientation and associated physical properties as a function of processing conditions. The ultimate goal would be to model the complete extrusion blow molding process including extrudate swell, parison sag, and the blowing process.

10.5 SOLUTION TO DESIGN PROBLEM IX

The solution to Design Problem IX is presented in this section. The solution basically consists of four parts: (1) determining the number of sheets required to fill the mold when the mold is closed; (2) determining the temperature setting of the infrared heaters in order to heat the blanks to the processing temperature as fast as possible without exceeding the upper processing temperature of PP at the surfaces; (3) determining the rate of closing of the press and the maximum operating force required to fill out the mold; and (4) specifying the cooling conditions at the mold wall to minimize the time required for the part to remain in the mold.

We first determine the arrangement of the sheets in the mold and the number of sheets required. The total length of the mold including the curved sections is 1.628 m. The breadth of the mold as given is 64.8 cm, and the final thickness is given as 3.2 mm. Hence, the total volume of the final part will be $3.3758 \times 10^{-3} \text{ m}^3$. Because the mold is 64.8 cm in breadth, we can place three sheets across this dimension. If we fill the flat section of the mold with 5.23 sheets that are 19.1 cm in width, they will not fill the curved section of the

mold when it is closed. Therefore, we must stack the sheets. If we stack the sheets 2 deep, then covering 72.39 cm of the flat section of the mold will provide enough material to fill the mold when it is closed. Hence, we need two layers of sheet in which three are needed to cover the breadth of the mold, and 3.79 are needed along the width of the mold. A total of 12 sheets are needed in which three of the sheets must be cut to a width of 15.1 cm.

We next consider at what temperature the infrared heaters should be set in order to heat the sheets to an acceptable processing temperature in the shortest time possible. The sheets are heated in the oven from both sides and the maximum temperature of the surface of the infrared heaters is given as 427 °C. The problem is that if the infrared heaters are used at the highest temperature, then the surface will come up to temperature in a time much shorter than required to heat the centerline to temperature. Hence, the PP will degrade at the surface, leading to a reduction in properties. The other problem is determining the temperature to which the sheets must be heated in order for them to flow under a reasonable force level. It is suggested by the dynamic mechanical properties of the composite sheet presented in Figure 10.21 that at a temperature between 160 °C and 168 °C a sheet begins to soften. (*Note:* The melting point of polypropylene is about 165 °C.) The storage modulus decreases rapidly with increasing temperature at this point. Above 184 °C the method of testing changes, and the parallel plate fixtures must be used. Dynamic mechanical properties (η^* and G') at three temperatures are presented in Figure 10.22 for this material. Based on past experience it is known that the complex viscosity at low values of ω (1.0 rad/s) should be no more than about 2×10^5 Pa · s in order for the material to flow with the

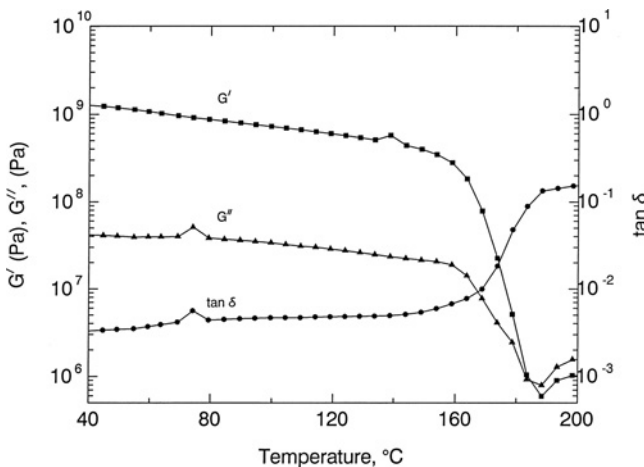


FIGURE 10.21 Dynamic mechanical thermal analysis of polypropylene reinforced with 30 wt% glass fiber mat (Azdel PM 10300). Measurements were made at an angular frequency of 1.0 rad/s on rectangular strips in a rheometer operated in the torsional mode.

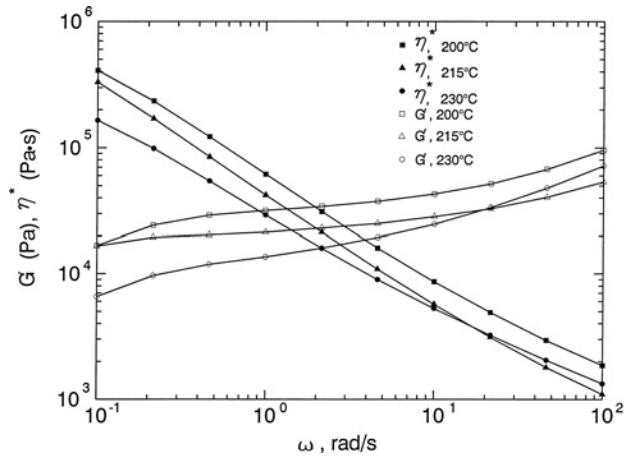


FIGURE 10.22 Dynamic oscillatory shear properties (i.e., η^* and G') of Azdel PM 10300 obtained at three temperatures.

application of reasonable pressure levels. Hence, it is desirable to keep the sheet or blank between about 230 °C and 215 °C during compression molding.

We next formulate the solution to the heat transfer problem. Although the blanks will be stacked two deep in the compression mold, they will pass through the oven as single blanks. The problem to be solved is that of one-dimensional transient heat conduction in which the top and bottom surfaces are subjected to radiation heating. Following the development in Sections 5.3 and 5.4, the differential equation for the heat transfer process becomes

$$\frac{\partial \theta}{\partial t} = \left(\frac{k}{\rho C_p b^2} \right) \frac{\partial^2 \theta}{\partial \xi^2} \quad (10.89)$$

where the dimensionless variables θ and ξ are defined, respectively, as

$$\theta = \frac{T - T_i}{T_R - T_i} \quad \text{and} \quad \xi = \frac{x}{b} \quad (10.90)$$

where T_R is the surface temperature of the infrared heater, T_i is the initial temperature of the blank, and b is the half-thickness of the blank (1.8×10^{-3} m). The initial and boundary conditions in dimensionless form are

$$\text{I.C.: at } t = 0, \quad \theta(0, \xi) = 0$$

$$\text{B.C.1: at } \xi = 0, \quad \frac{\partial \theta}{\partial \xi}(t, 0) = 0$$

$$\text{B.C.2: at } \xi = 1, \quad \frac{\partial \theta}{\partial \xi}(t, 1) \quad (10.91)$$

$$= - \left(\frac{bh_r}{k} \right) \left[\frac{\theta(t, 1)(T_R - T_i) + T_i}{T_R - T_i} \right]$$

where h_r is the radiation heat transfer coefficient defined in Eq. 5.137 and in terms of θ is given as

$$h_r = \frac{\sigma F [(\theta(t, 1)(T_R - T_i) + T_i)^4 - T_R^4]}{(T_i - T_R)(1 - \theta(t, 1))} \quad (10.92)$$

For parallel flat plates F is given in Eq. 5.134 and taking values of e_1 and e_2 to be about 0.9, F becomes 0.82.

Before solving Eq. 10.89 a few comments regarding the material properties and energy absorbed on melting of PP must be made. In order to solve Eq. 10.89 values of ρ , \bar{C}_p , and k for both the glass and PP are required. For PP the values at 180 °C are given in Table 5.5 (p. 121). For glass, values are given only at 22 °C (Harper, 1992), and these are 2500 kg/m³, 2584.3 J/kg·°C, and 1.021 W/m·°C for ρ , \bar{C}_p , and k , respectively. Blending rules for calculating k and \bar{C}_p were given in Section 5.3, where Eq. 5.73 was used for k and Eq. 5.74 for \bar{C}_p . The values for the composite sample are

$$\rho_b = 1084 \text{ kg/m}^3, \quad \bar{C}_{pb} = 2207 \text{ J/kg}\cdot\text{K}, \\ k_b = 0.162 \text{ W/m}\cdot\text{K}$$

The melting point of PP is around 165 °C, and as the polymer reaches this temperature during the heat-up cycle, additional energy is absorbed, delaying the time for the blank to reach the desired processing temperature. Although as a first approximation we neglect the latent heat of fusion, this should be included as a source term in the energy equation. (See Example 5.11.)

To solve Eq. 10.89 we use the numerical approach discussed in Section 5.4. We can adopt the numerical solutions used to solve Example 5.5 (see the solutions for problems in Chapter 5). The main differences are in the form of the heat transfer coefficient, h_r , which is given in Eq. 10.92, the expression for the surface node temperature changes to

$$\theta_{\text{NEQ}+1} = \frac{4\theta_{\text{NEQ}} - \theta_{\text{NEQ}-1} + \left(\frac{2hb \Delta \xi}{k}\right)(T_R - T_i)}{3 + (2hb \Delta \xi(T_R - T_i)/k)} \quad (10.93)$$

and the ordinary differential equation for the nodal temperature next to the last node at the surface changes to

$$\frac{\partial \theta_{\text{NEQ}}}{\partial t} = \left(\frac{k}{\rho \bar{C}_p b^2 (\Delta \xi)^2}\right) * (\theta_{\text{NEQ}+1} - 2.0\theta_{\text{NEQ}} + \theta_{\text{NEQ}-1}) \quad (10.94)$$

The computer code for solving Eq. 10.89 with a heat flux due to radiation at the slab surface is given in “Numerical Solutions, Chapter 10” on the accompanying website. Some experimentation with the numerical technique was needed before a stable numerical solution was obtained. Because the size of the time steps was relatively large (1×10^{-4} s), it was necessary to refine the spacing of the nodal points until a

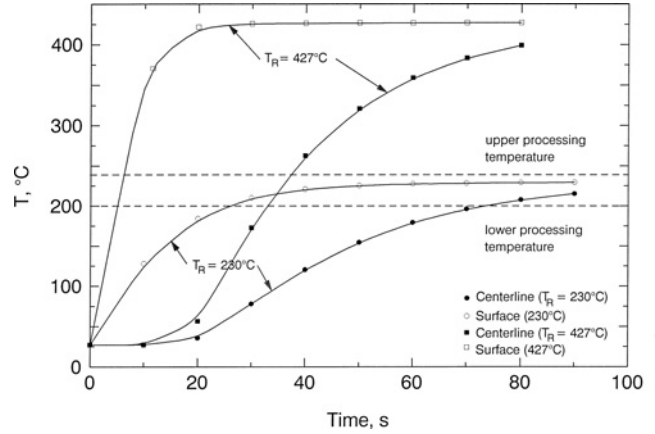


FIGURE 10.23 Calculated surface and centerline temperatures as a function of time for Azdel sheets 3.6 mm thick subjected to two different infrared heater surface temperatures.

stable solution was obtained. Division of the half-thickness of the slab into 10 segments was not sufficient to obtain a stable solution. However, 20 segments or 21 nodal points gave a stable solution that improved only slightly with further refinement of the nodal spacings.

Results for two different heater settings are plotted in Figure 10.23. Using the highest temperature of the heating elements of 427 °C resulted in the surface of a blank reaching the upper processing temperature (UPT) of 230 °C in less than 10 s. Meanwhile, it took about 30 s for the centerline to reach the suggested lowest processing temperature (LPT) limit. Severe degradation of the blank will occur under these conditions. Taking the heater temperature at 230 °C, which is the UPT limit, it is observed that it takes about 70 s before the centerline reaches the LPT limit and 90 s before it reaches 215 °C. However, the surface of the blank remains below the UPT limit. Certainly one could optimize the time for heating the centerline to the processing temperature by trying different values of the heating element surface temperature. The actual time for heating the blank to the processing temperature will be longer than this as there will be some cooling of the blank by convection and energy will be absorbed at the melting temperature. Furthermore, it has been observed that when the temperature of the blank reaches the melting point of PP, then there is a swelling of the blank to almost twice its original thickness due to the recovery of elastic stresses imparted to the material during the fabrication of the composite sheet. These calculations at least give an estimate of the time required to heat the blank to the processing temperature and more importantly an approach for more accurately calculating this temperature.

We next estimate the pressure required to fill out the mold. A relation relating the force required to close the mold platens to the viscosity, geometric factors, and the rate of closing the platens was given in Eq. 10.50. In the derivation of Eq. 10.50

it was assumed that the fluid was Newtonian and isothermal conditions prevailed. Some cooling of the blanks will occur during the time of transfer from the oven to the mold. Giles and Reinhard (1991) have reported this time to be in the range of 15 s to a minute. There will be some drop in surface temperature due to free convection cooling. It can be estimated using the numerical approach presented in Section 5.4 that the average temperature of the blanks will be about 215 °C when the compression process starts for transfer times less than 30 s. At the lowest closing rate available of $\dot{h} = 4.23 \text{ mm/s}$ it takes only about 0.76 s to close the mold. Hence, there should be little drop in the temperature of the blanks during the compression process, and the assumption of isothermal conditions should be valid. The maximum force required is that which occurs just as the mold is filled with the composite blank. In calculating this quantity by means of Eq. 10.50 the viscosity is required. The only data available is the complex viscosity as a function of angular frequency as shown in Figure 10.22. The rheology of the composite blanks consisting of PP and random long glass fiber mat is unknown at this point and difficult to obtain. (Lubricated squeezing flow discussed in Section 3.5 may be a way to obtain this data.) We must therefore estimate the viscosity of the blank. At the point of closing the mold the average rate of deformation (based on planar extensional deformation only) is $\dot{h}/h = 1.32 \text{ s}^{-1}$. From the data in Figure 10.22, $|\eta^*| = 500 \text{ Pa} \cdot \text{s}$. Using this value for the viscosity, the force is given by

$$F = \frac{8(0.648)(500)(2.23 \times 10^{-3})(0.814)^3}{(3.2 \times 10^{-3})^3} = 5.16 \times 10^7 \text{ N}$$

$$= 1.16 \times 10^7 \text{ lb}_f = 5.80 \times 10^3 \text{ tons} \quad (10.95)$$

Hence, to manufacture a part of this size a high force hydraulic press is required.

Finally, we make a few comments about the cooling of the part in the mold. If the mold wall temperature is set too low, then the blanks will cool too rapidly and not flow well enough to fill out the mold. On the other hand, if the mold temperature is set too high, then the part will take too long to cool. The maximum rate of crystallization for PP occurs at about 90 °C. By setting the mold temperature at this value it may be possible to keep the material at a high enough temperature so that it will flow without the application of excessively high pressures and yet crystallize rapidly enough so that the part can be removed from the mold in the shortest time possible. At this point one can use the numerical approach described in Section 5.4 to calculate the time for cooling. One may find that variations of the mold temperature around 90 °C will lead to the optimum time for cooling. However, because these calculations are straightforward as already described, there is little to be gained in repeating them. The main point is to provide some insight for selecting an initial guess for the mold temperature.

PROBLEMS

A. Applications

10A.1 *Heat Removal from an Injection Mold Using Coolant Lines.* The overall heat transfer coefficient per unit length of coolant line is given in Eq. 10.35. Using this equation answer the following questions if k_m and h are held fixed:

- (a) If the coolant line diameter is doubled from initial values of $P/d = 2$ and $D/d = 2$, how does U change?
- (b) If a second row of coolant lines are added decreasing P/d from 4 to 2, how is U changed? (Remember h is held constant.)
- (c) If D/P is decreased from 1 to 0.5 by decreasing D , how is U changed?

10A.2 *Equilibration Temperature of a Mold Base.* Polypropylene containing 30 wt% glass is injection molded into a rectangular cavity 8.9 cm \times 8.9 cm by 0.15 cm thick. The mold base consists of two rectangular stainless steel plates 15 cm \times 30 cm by 2.5 cm thick. One-half the cavity thickness is machined in each of the bottom and top plates of the mold. The polymer enters the cavity at 230 °C with a fill time of 1.0 s. The mold temperature is originally 25 °C. The mold is held closed for 25 s while the polymer cools and is in the open position for 5 s. During the time that the mold is opened it is subjected to free convection cooling by air at 25 °C. The following properties are given for stainless steel:

$$\rho = 7750 \text{ kg/m}^3, \quad k_m = 2.30 \text{ W/m}\cdot\text{K},$$

$$\bar{C}_{pm} = 460.2 \text{ J/kg}\cdot\text{°C}$$

Show the procedure for determining the time required for the mold base to come to an equilibrium temperature, listing all your assumptions, and carry the calculations out for two cycles of the process.

10A.3 *Flow Rate of Coolant Through a Mold Base.* Coolant lines of 1.27 cm in diameter are machined in the base of a mold with a spacing of 3.81 cm (this is the centerline distance) and a distance of 2.54 cm from the mold surface. The total length of the line is 1.83 m. Tap water is used as the coolant and enters the line at 12 °C with a line pressure of $1 \times 10^8 \text{ Pa}$. The coolant must remove heat at the rate 1758.3 J/s. The mold base is made of stainless steel with the thermal properties given in Problem 10A.2. Determine the convection heat transfer coefficient in the coolant lines, the increase in temperature of the water (i.e., the temperature of water at the exit of the

coolant line), and the flow rate of water required to produce the heat transfer coefficient.

10A.4 *Time for Healing a Weld Line.* LDPE (NPE 953) is injection molded into a cavity from two gates. The fronts meet at the center of a mold cavity, which is 0.3175 cm thick, with a melt temperature of 180 °C. Determine the mold temperature and the length of time required for the melt to remain in the mold in order to obtain a part with adequate weld line strength. Treat the geometry as that of a slab and use the conditions given in Section 4.2.5 for determining weld line strength.

10A.5 *Effect of CaCO₃ on the Thermal Properties of Polypropylene.* CaCO₃ is added to polymers as a filler with the intent of lowering material costs. Calculate the thermal conductivity, the heat capacity, and the density of a polypropylene composite containing 40 wt% CaCO₃. Take the following properties for PP:

$$\rho = 900 \text{ kg/m}^3, \quad k = 0.20 \text{ W/m}\cdot\text{°C}, \\ \bar{C}_p = 1.8 \text{ kJ/kg}\cdot\text{°C}$$

while the following properties are reported for CaCO₃:

$$\rho = 3000 \text{ kg/m}^3, \quad k = 2.7 \text{ W/m}\cdot\text{°C}, \\ \bar{C}_p = 0.86 \text{ kJ/kg}\cdot\text{°C}$$

Compare your calculated values to the experimental values, which are given as

$$\rho = 1250 \text{ kg/m}^3, \quad k = 0.56 \text{ W/m}\cdot\text{°C}, \\ \bar{C}_p = 1.34 \text{ kJ/kg}\cdot\text{°C}$$

Under similar conditions of heating, which material will come to temperature sooner: PP or PP/CaCO₃?

10A.6 *Average Wall Thickness in a Thermoformed Sheet.* Consider the sheet of arbitrary dimensions shown in Figure 10.24, which is formed by draping over a positive or male mold. Calculate the average reduction in wall thickness assuming that the hot sheet first contacts area CD, which retains its original thickness.

B. Principles

10B.1 *Extension Rate at the Advancing Front.* Tadmor (1974) estimated the extension rate at the advancing front in the filling of a rectangular cavity to be

$$\dot{\epsilon} = \frac{dv_y}{dy} = -\frac{dv_x}{dx} = \frac{\langle v_x \rangle - v_{\max}}{2b} \quad (10.96)$$

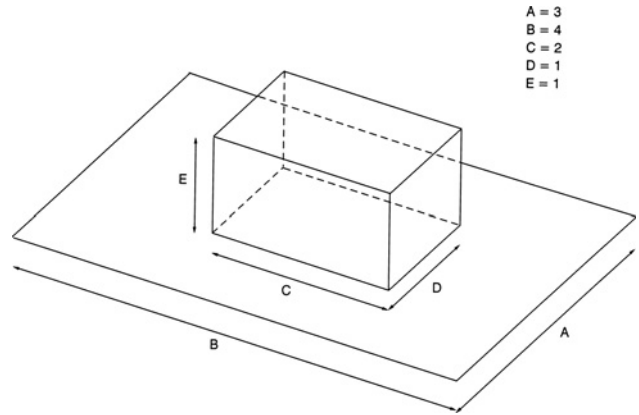


FIGURE 10.24 Drape forming over a positive or male mold.

where $2b$ is the thickness of the mold, $\langle v_x \rangle$ is the average velocity in the x direction, and v_{\max} is the maximum velocity. For a power-law fluid show that Eq. 10.96 becomes

$$-\dot{\epsilon} = \left(\frac{n}{n+1} \right) \frac{\langle v_x \rangle}{2b} \quad (10.97)$$

For LDPE (NPE 953) at 170 °C calculate $\dot{\epsilon}$ for the filling of a square cavity, 8.89 cm \times 8.89 cm and 0.16 cm thick, in the times of 0.5 and 1.0 s.

10B.2 *Lubricated Compression Molding.* For the compression molding process shown in Figure 10.11 the plates are lubricated either with mold-release agent or by using Teflon sheets. Calculate an expression for the force required to close the plates similar to Eq. 10.50 when the polymer is assumed to exhibit complete slip. Do this first for a Newtonian fluid and then a polymer melt with rheological properties described by the PTT model.

10B.3 *Compression Molding in a Cup-Shaped Cavity.* Consider the compression molding of a polymeric material in the cup-shaped mold shown in Figure 10.25. For isothermal flow of a power-law fluid carry out the following steps to obtain an expression for the compression force.

(a) Show that the velocity field for the radial flow portion of the flow (i.e., the flow between the two parallel disks up to R_i) is

$$v_r(z, r, t) = \frac{h^{1+s}}{1+s} \left(-\frac{1}{m} \frac{\partial p}{\partial r} \right)^s \\ \times \left[1 - \left(\frac{z}{h} \right)^{1+s} \right] \quad (10.98)$$

What assumptions are made in obtaining Eq. 10.98?

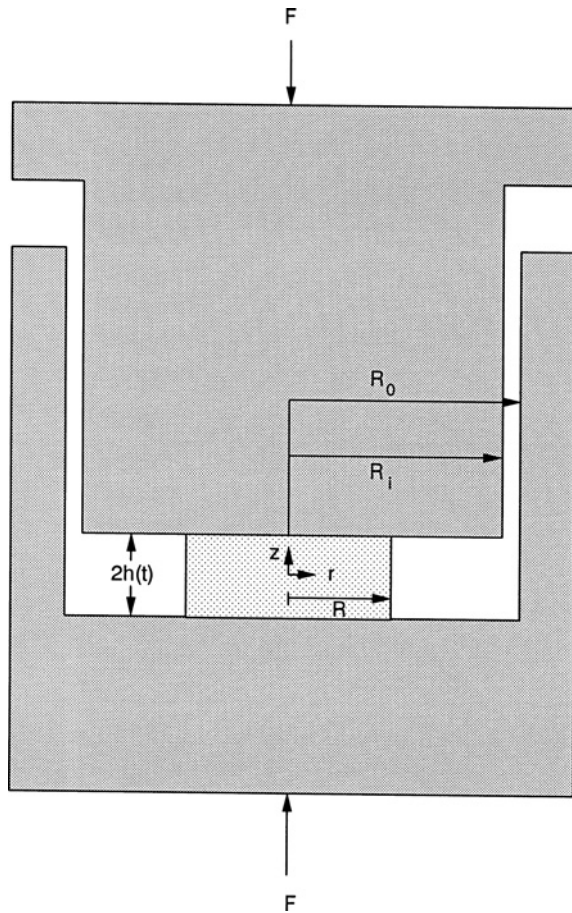


FIGURE 10.25 Cup-shaped cavity used in compression molding of a thermoplastic.

- (b) Show that the pressure required to compress the polymer sample is

$$P - p_a = \frac{m(2 + s)^n (-\dot{h}) R^{n+1}}{2^n (n + 1) h^{2n+1}} \times \left[1 - \left(\frac{r}{R} \right)^{n+1} \right] \quad (10.99)$$

- (c) Show that the applied force is

$$F = \frac{m\pi(2 + s)^n (-\dot{h})^n R^{n+1}}{2^n (n + 3) h^{2n+1}} \quad (10.100)$$

- (d) When the flowing material reaches the outer wall at $r = R_o$, it is forced to flow in the annular space. Show that for a constant squeeze rate the rate of increase of material along the axial distance in the annulus is

$$-\pi R_i^2 \dot{h}(t) = \pi (R_o^2 - R_i^2) \dot{l} \quad (10.101)$$

where l is the axial coordinate.

- (e) For a thin annulus (i.e., $\Delta R = (R_o - R_i) \ll R_o$) show that the volumetric rate of flow, Q , is

$$Q = \pi \bar{R}^2 \dot{h} \quad (10.102)$$

where $\bar{R} = 0.5 (R_i + R_o)$.

- (f) Because $\dot{h} \ll \dot{l}$ for a thin annulus (i.e., the plunger travel rate, \dot{h} , is small compared to the rate of advancement of the fluid in the annulus, \dot{l}), the flow can be considered to be one of pressure flow only and not combined drag and pressure flow. Show that the pressure drop across the annular flow region for the case of a small gap is

$$P(R_i) - p_a = \left(\frac{2ml}{R_o^{3n+1}} \right) \frac{[2(s + z)\bar{R} \Delta R \dot{l}]^n}{(1 - \kappa)^{1+2n}} \quad (10.103)$$

- (g) Obtain a final expression for the plunger force when flow exists in the annular space.

- 10B.4** *Wall Thickness Distribution in a Deep Truncated Conical Mold.* The problem of determining the wall thickness distribution in a deep truncated conical mold as shown in Figure 10.26, along with several other geometries, was analyzed by Rosenzweig (1983). Until the spherical bubble touches the bottom of the mold, the thickness distribution was assumed to be that given in Eq. 10.58. Carry out the following steps to show how Rosenzweig arrived at an expression for the thickness distribution once the bubble touched the bottom of the mold.

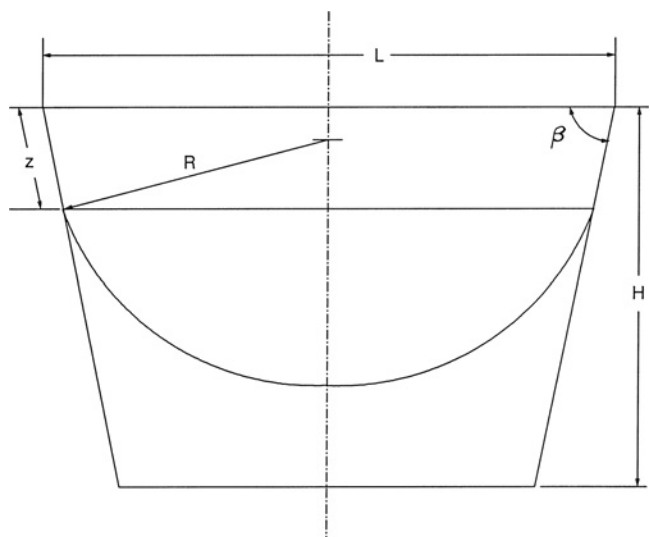


FIGURE 10.26 Truncated conical mold.

- (a) When the spherical bubble just touches the bottom of the mold, show that the position of detachment along the wall, z_T , is

$$z_T = \frac{H(1 + \cos \beta)}{\sin \beta} - \frac{L}{2} \quad (10.104)$$

- (b) Show that the initial area of the free bubble just as it makes contact with the bottom of the mold is

$$S_1 = 2\pi(1 + \cos \beta)(H/\sin \beta - z_T)^2 \quad (10.105)$$

- (c) Show that the area of the free bubble at any instant is

$$S = (2\pi/(1 - \cos \beta))(H - z \sin \beta) \times [(z - z_r)\beta + (H - z \sin \beta)] \quad (10.106)$$

- (d) Finally, show that the thickness distribution in this part of the forming process is

$$h/h_1 = S_1/SF \quad (10.107)$$

where h_1 is the initial thickness calculated by substituting z_T into Eq. 10.68 and F is given by

$$F = \left| \frac{az^2 + bz + c}{az_T^2 + bz_T + c} \right|^{f \sin \beta/2a(2-f)} + \left| \frac{(2az + b - g)(2az_T + b + g)}{(2az_T + b - g)(2az + b + g)} \right|^{\sin \beta(d-fb/2a)/g(2-f)} \quad (10.108)$$

where

$$\begin{aligned} a &= \sin \beta - \beta \\ b &= \beta(H/\sin \beta + z_T) - 2H \\ c &= (H - z_T\beta)H/\sin \beta \\ d &= \frac{W}{2} - z_T - H \left(\frac{1}{\tan \beta} - \cos \beta \right) \\ f &= 1 - \cos \beta \\ g &= \sqrt{b^2 - 4ac} = \beta \left(\frac{H}{\tan \beta} - \frac{W}{2} \right) \end{aligned} \quad (10.109)$$

10B.5 *Wall Thickness Distribution in a Long Triangular Prism Mold* (Rosenzweig, 1983). Following the development used in Example 10.3, obtain an expression for the wall thickness distribution in a long triangular prism mold, which is shown in Figure 10.27, by carrying out the following steps.

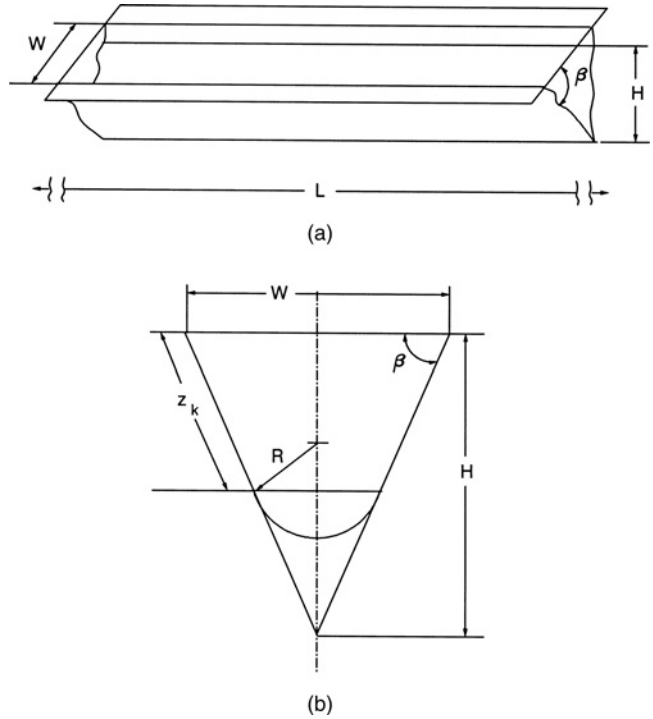


FIGURE 10.27 Triangular prism mold: (a) end view and (b) top view.

- (a) Neglecting the deformation at the ends of the mold perform a mass or volume balance to obtain the following differential equation for the thickness, h :

$$\frac{-dh}{h} = \frac{dR}{R} + \frac{dz_k}{\beta R} \quad (10.110)$$

- (b) Show that the radius of the bubble as a function of contact position along the wall, z_k , is

$$R = \frac{H - z_k \sin \beta}{\sin \beta \tan \beta} \quad (10.111)$$

- (c) On integrating, Eq. 10.110 becomes

$$\frac{h}{h_1} = \left[\frac{H - z_k \sin \beta}{H} \right]^{(1/\beta)(\tan \beta - 1)} \quad (10.112)$$

where h_1 is related to the initial sheet thickness by $h_1 = [(\sin \beta)/\beta]h_0$. The thickness distribution is obtained by substituting the expression for h_1 into Eq. 10.112.

10B.6 *Inflation of a Viscoelastic Cylindrical Parison*. In determining $R(t)$ for the expansion of a cylindrically shaped parison, the components of stress for the PTT model were given in Eqs. 10.87 and 10.88. Show

how to obtain these two equations. (See Bird et al., 1987, for convected time derivatives in cylindrical and spherical coordinates.)

- 10B.7** *Inflation of a Bicomponent Parison.* A cylindrically shaped parison consists of two layers of polymer: an inner layer of initial thickness h_{01} and viscosity μ_1 and an outer layer of initial thickness h_{02} and viscosity μ_2 . Assuming the fluids are Newtonian, derive expressions for determining $R_i(t)$ and $h_i(t)$ where the subscript i is 1 or 2.

C. Numerical Problems

- 10C.1** *Effect of Filler on the Thermoforming Time of Polypropylene.* In the thermoforming of pen barrels CaCO_3 is added to PP to reduce material costs. The pen barrel is formed from a cylindrical tube having an O.D. of 5.28 mm and an I.D. of 2.82 mm. The tube is heated by conduction heating in which the tube is in contact with a metal ring having a temperature of 143 °C. The inside of the tube is not heated, and no heat transfer is considered to occur there. Determine the time required for the inner wall of the tube to reach a temperature of 143 °C for both pure PP and PP/40% CaCO_3 . The thermal properties are given in Problem 10A.5. How much does the presence of CaCO_3 reduce the heating time?
- 10C.2** *Infrared Heating of a Transparent Sample of Polyurethane.* A clear disk of polyurethane, 25.4 cm in diameter and 3.5 mm thick, is to be heated by means of an infrared heater with a surface temperature rating of 2400 K. Menezes and Watt (1992) obtained by means of a bolometric detector the following expression for the transmitted intensity:

$$I = 6.432 \times 10^6 e^{-536x} \quad (10.113)$$

Calculate the time to heat the sheet from an initial temperature of 27 °C to 180 °C for the following two cases: (a) the convective heat transfer coefficient at both surfaces is $100 \text{ W/m}^2 \cdot \text{K}$; (b) the convective heat transfer coefficient at the top surface is $12 \text{ W/m}^2 \cdot \text{K}$ and $5 \text{ W/m}^2 \cdot \text{K}$ at the bottom surface. The thermal properties of polyurethane are $\rho = 1250 \text{ kg/m}^3$, $k = 0.31 \text{ J/ms} \cdot \text{K}$, $\bar{C}_p = 1.88 \times 10^3 \text{ J/kg} \cdot \text{K}$. Consider the problem to be that of one-dimensional transient heat conduction.

- 10C.3** *Pressure Forming of a Polymeric Sheet in a Conical Mold.* A sheet of LDPE (NPE 953) of thickness 0.3175 cm is thermoformed in the conical cavity shown in Figure 10.17 at a temperature of 170 °C.

The dimensions of the mold are $H = 30.48 \text{ cm}$ and $L = 20.0 \text{ cm}$. The applied pressure differential is $6.9 \times 10^5 \text{ Pa}$. Calculate the wall thickness distribution and the time to fill the mold using first the Newtonian constitutive equation and then the PTT model. Compare the predictions of the two models.

- 10C.4** *Expansion of a Cylindrical Parison: Newtonian Case.* A cylindrical parison consisting of LDPE (NPE 953) at 170 °C is inflated with a pressure differential of $3.5 \times 10^5 \text{ Pa}$. Initially, the diameter of the parison is 2.60 cm and the wall thickness is 0.13 cm. Determine the time for the parison to contact the mold walls and the thickness of the inflated parison at this point, if the diameter of the mold is 13 cm (see Fig. 10.20). Assume the melt can be considered as a Newtonian fluid and use the rheological properties given for LDPE (NPE 953) in Appendix A, Table A.1. The equations to be solved are Eq. 10.86 and the expression based on conservation of mass (i.e., $\dot{h}/h = -\dot{R}/R$).
- 10C.5** *Expansion of a Cylindrical Parison: Viscoelastic Case.* Do Problem 10C.4 again, but use the PTT model. The solution requires the solving of Eqs. 10.85, 10.87, and 10.88. Compare the solution against that obtained for the Newtonian case.
- 10C.6** *Sagging of a Cylindrical Parison.* Solve Eqs. 10.79 and 10.80 to find the thickness distribution and velocity as a function of position for a thin-walled parison. Also determine the length of the parison as a function of time and compare the results against the ideal case (i.e., $L = \langle v_z \rangle t$). The viscosity of the melt is $500 \text{ Pa} \cdot \text{s}$, and its density is 900 kg/m^3 . The wall shear rate in the die is 200 s^{-1} . The outer diameter of the parison is 2.54 cm, and its thickness is 0.127 cm. The parison thickness and diameter swell are 1.5.

D. Design Problems

- 10D.1** *Design of a Cooling Line System for Injection Molding.* Nylon 66 containing 30 wt% glass is injection molded to form a manifold cover for an engine block. The manifold is basically a box 0.76 m long by 0.20 m wide by 0.10 m high with a wall thickness of 0.635 cm. Design a cooling line system that uses tap water at 10 °C, which will minimize the time the part must remain in the mold. The melt enters the mold at 285 °C. The mold base consists of stainless steel. The coolant lines are to be continuous with a single inlet and outlet. In your design specify the dimensions of the coolant lines, their spacing, and their location relative to the melt

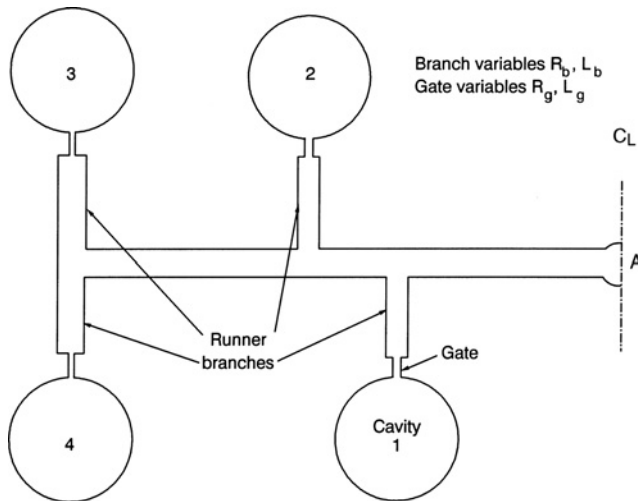


FIGURE 10.28 Schematic of a multicavity mold. Only half of the symmetric arrangement of the cavities is shown.

(i.e., D in Fig. 10.9). Furthermore, specify the velocity of the water, the pressure drop, and the temperature of the water on leaving the mold. The only restriction is that the coolant lines should not exceed a diameter of 1.27 cm. Also assume that the cavity is machined in one side of the mold base.

10D.2 *Design of a Multiple Cavity Runner System* (Tadmor and Gogos, 2007). In many commercial situations molds are designed with multiple cavities. In order that each part have identical physical properties it is necessary that the cavities fill simultaneously. For the runner–cavity system shown in Figure 10.28 (here only one-half of the cavity and runner system are shown) it is desired to have the cavities fill at the same time. First assuming that the fluid is Newtonian and then non-Newtonian with the viscosity described by the power-law model, carry out the following for isothermal conditions:

- (a) Design the runner branches for each of the four cavities with the gates taken identical in order to get simultaneous filling.
- (b) Design the gates so that there is simultaneous filling in each of the cavities with the runner branches taken to be identical. The runners and gates are taken to be cylindrical. Neglect pressure losses across the contractions and the expansions.

10D.3 *Cooling Conditions for a Two-Layer Blow-Molded Tank.* A gasoline tank consisting of an inner layer of nylon 6 and an outer layer of HDPE is to be produced by blow molding. Design a cooling process that will provide the minimum amount of cooling

time. Consider both the cooling of the interior and exterior walls of the blown parison. Tap water at 12 °C is available for cooling the mold and air as cool as 12 °C or as hot as 100 °C can be used on the interior. The temperature of the parison as it contacts the mold wall is 220 °C. The thickness of the parison as it contacts the mold is 0.635 cm with one-fifth of the thickness being nylon 6. In order for the nylon to act as an effective barrier to gasoline it must reach 75% of its maximum degree of crystallinity, and the HDPE should reach 100% of its maximum degree of crystallinity to have adequate impact properties.

REFERENCES

- Bird, R. B., R. C. Armstrong, and O. Hassager. 1987. *Dynamics of Polymeric Liquids: Volume I, Fluid Mechanics* (Wiley, Hoboken, NJ).
- Birley, A. W., B. Haworth, and J. Batchelor. 1991. *Physics of Plastics* (Hanser Publishers, Munich).
- Gibbs, M. L. 1989. “Liquid Nitrogen Cooling for Blow Molded Parts: Effect on Cycle Time and Bottle Performance.” *Society of Plastics Engineers Technical Papers*, **35**, 918.
- Giles, H. F. and D. L. Reinhard. 1991. “Compression Molding of Polypropylene Glass Composites.” *SAMPE*, **36**, 556.
- Giboz, J., T. Copponnex, and P. Mélé. 2007. “Microinjection Molding of Thermoplastic Polymers: A Review.” *J. Micromech. Microeng.*, **17**, R96–R109.
- Gruenwald, G. 1987. *Thermoforming* (Technomatic, Lancaster).
- Harper, C. A., Ed. 1992. *Handbook of Plastics, Elastomers, and Composites*, 2nd edition (McGraw Hill, New York).
- Hieber, C. A. and S. F. Shen. 1980. “A Finite Element/Finite Difference Simulation of the Injection Molding Filling Process.” *J. Non-Newtonian Fluid Mechanics*, **7**, 1–32.
- Hobbs, S. W. 1974. *Polym. Eng. Sci.*, **14**, 621.
- Hunkar, D. B. 1973. “Internal Surface Cooling of Blow Molded Articles.” *Society of Plastics Engineers Technical Papers*, **19**, 448.
- Lee, N., Ed. 1990. *Plastic Blow Molding Handbook* (Van Nostrand Reinhold, New York).
- Mavridis, H., A. N. Hrymak, and J. Vlachopoulos. 1988. “The Effect of Fountain Flow in Molecular Orientation in Injection Molding.” *J. Rheol.*, **32**(6), 639.
- Menezes, M. and D. F. Watt. 1992. “Modeling of Infrared Heating of Transparent Polyurethane.” *Society of Plastics Engineers Technical Papers*, **38**, 109–113.
- Menges, G. and W. Wübken. 1973. “Influence of Processing Conditions on Molecular Orientation in Injection Molds.” *Society of Plastics Engineers Technical Papers*, **31**, 519.
- Ortman, K. C., N. Agarwal, D. G. Baird, P. Wapperom, and A. J. Giacomini. 2011. “Transient Shear Flow Behavior of Concentrated Long Glass Fiber Suspensions in a Sliding Plate Rheometer.” *J. Non-Newtonian Fluid Mech.*, **166** (11), 533–547.

- Pearson, J. R. A. and S. M. Richardson. 1983. *Computational Analysis of Polymer Processing* (Applied Science Publishers, London).
- Piotter, V., K. Mueller, K. Plewa, R. Ruprecht, and J. Hausselt. 2002. "Performance and Simulation of Thermoplastic Micro-injection Molding." *Microsystem Technol.*, **8**, 387–390.
- Rosenzweig, N. 1983. "Wall Thickness Distribution in Thermoforming." *Society of Plastics Engineers Technical Papers*, **29**, 478–482.
- Rosenzweig, N., M. Narkis, and Z. Tadmor. 1979. "Wall Thickness Distribution in Thermoforming." *Polym. Eng. Sci.*, **19**, 946.
- Tadmor, Z. 1974. "Molecular Orientation in Injection Molding." *J. Appl. Polym. Sci.*, **18**, 1753.
- Tadmor, Z. and C. G. Gogos. 1979. *Principles of Polymer Processing* (Wiley, Hoboken, NJ).
- Tadmor, Z. and C. C. Gogos. 2007. *Principles of Polymer Processing*, 2nd edition (Wiley, Hoboken, NJ).
- Throne, J. L. 1979. *Plastics Process Engineering* (Marcel Dekker, New York).
- Throne, J. L. 1986. *Thermoforming* (Hanser Verlag, Munich).
- Wang, V. W., C. A. Hieber, and K. K. Wang. 1986. "Dynamic Simulation and Graphics for the Injection Molding of Three-Dimensional Thin Parts." *J. Polym. Eng.*, **7**, 21.

11

PROCESS ENGINEERING FOR RECYCLED AND RENEWABLE POLYMERS

This chapter is concerned with the recycling of thermoplastics and the processing of renewable polymers. However, the decision to recycle a polymer cannot be made without the appropriate analysis guided by the purpose to recycle, as inappropriate recycling can not only be economically unsound but can lead to more pollution than merely discarding the polymer to landfills. For this reason we introduce the concept of *life-cycle assessment* (LCA) in Section 11.1, which provides a systematic method for determining whether recycling and which form of recycling is the proper environmental choice. Furthermore, in this section we consider material and energy flows associated with various types of recycling streams as it is important that more energy not be used in recycling plastics than is required in the conversion of raw materials to virgin resin. Also, this section includes an example of using LCA as a decision support tool, that is, to identify the best plastic to use in specific applications, a description of the 12 principles of green chemistry and engineering that could guide the development of new materials and polymer processes, and an example of combining LCA and the 12 principles to identify the best plastic to use in various applications. The next three sections are concerned with technical aspects of recycling. In Section 11.2 reprocessing at the equipment site, referred to as primary recycling, is addressed in which scrap polymer is reground and blended back in with the fresh polymer. In Section 11.3 the topic of mechanical or secondary recycling is presented, which is concerned with the reprocessing of polymeric materials after they have been used. In this case separation of polymer streams is required. In Section 11.3 we limit our coverage to topics concerned with the rheology and flow of mixed polymers and filtration.

In instances where mechanical recycling is not possible, the polymer may be reduced to chemical feedstock suitable for polymerization. This topic, also referred to as tertiary recycling, is discussed in Section 11.4, but we limit the coverage to processing in extruders. In Section 11.5 we discuss the processing of new-to-world renewable polymers (i.e., polymers that come from renewable resources (e.g., carbohydrates) and are not identical to today's petroleum-derived polymers). Examples of these polymers are poly(lactic acid) (PLA), thermoplastic starch (TPS), and polyhydroxyalkanoate (PHA). The other category of renewable polymers is that of identical renewable polymers (also called bioidentical polymers). These renewable polymers have identical structure, performance, and processing to petroleum-derived polymers, with examples being bio-HDPE, bio-PP, and biopoly(butylene succinate) (bio-PBS). The reader is directed to the previous chapters in this book for processing information on the bioidentical polymers.

11.1 LIFE-CYCLE ASSESSMENT

The decision to recycle polymers is by no means straightforward. In some instances recycling polymers can lead to more energy usage and more pollution than merely disposing of them in landfills. The decision to recycle polymers depends on the ultimate goal. Is it to reduce consumption of raw materials (i.e., feedstock)? Is it to reduce the consumption of fuel? Is it to reduce the generation of solid waste? To determine whether recycling is the appropriate option and what type of recycling option should be selected, one

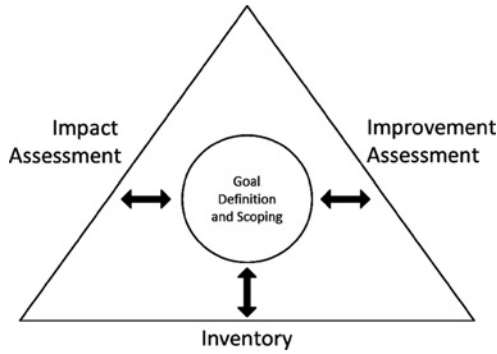


FIGURE 11.1 Life-cycle assessment conceptual model. (Data from Curran, 1996.)

turns to a systems analysis which accounts for all energy and raw materials used to produce a product or process and all wastes produced. This type of analysis is referred to here as *life-cycle assessment* (LCA), but other names are often used, such as *ecobalance*, *cradle-to-grave analysis*, and *life-cycle analysis*. LCA is used defensively to justify recycling and offensively to improve products and processes and help select the appropriate polymers and processes for various applications. Although considerable discussion of the technique and its application is given in the books by Curran (1996) and Horne et al. (2009), we present an overview of the topic with enough detail to hopefully make the concept useful to the process engineer.

The LCA conceptual model is shown in Figure 11.1. At the center of LCA is *initiation* or *scoping* in which the

goals of the study and the system boundaries are defined. All operations that contribute to the life cycle of the product or process fall within the system boundaries as shown in Figure 11.2. The environment is the surroundings for the system. Inputs to the system are the natural resources, including energy resources. Outputs of the system are the collection of releases to the environment (i.e., land, water, or air) as well as discarded product. The quantification of energy and raw material requirements, air emissions, waterborne effluents, solid waste, and other environmental releases throughout the life cycle of a product is referred to as *life-cycle inventory* (LCI). *Impact analysis* is an attempt to quantify the effects of the environmental loadings identified in the inventory phase. It mainly refers to the pollution of the ecosystems and the effects on human health. *Improvement assessment* is a systematic evaluation of the opportunities to reduce the environmental burden associated with energy and raw materials use and environmental releases throughout the whole life cycle of the product or process. This assessment may include both quantitative and qualitative measures of improvement, such as changes in the product or process design, use of raw materials, consumer use, and waste management. The emphasis in this book is on the technical and scientific aspects of recycling, which are key elements in life-cycle inventory. Although the whole purpose for LCA is to judge the effect of recycling on the environment and human health, it is beyond the scope of the material coverage in this chapter and the reader is referred to the books by Curran (1996) and Horne et al. (2009).

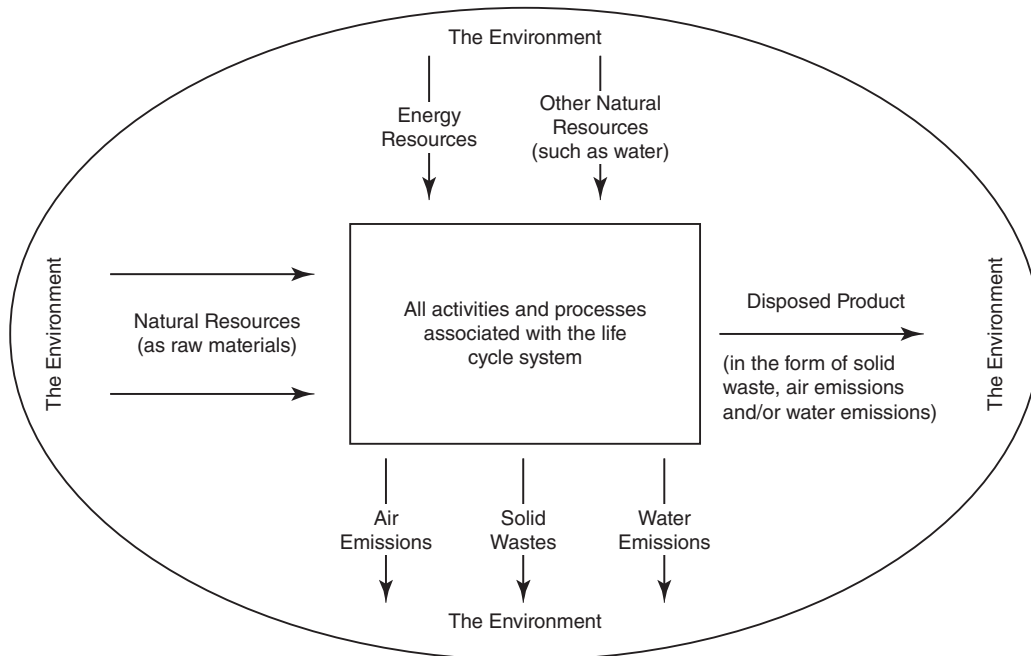


FIGURE 11.2 Life-cycle system concept showing the boundaries on which the life-cycle assessment must be performed. (Reprinted by permission of the publisher from Curran, 1996.)

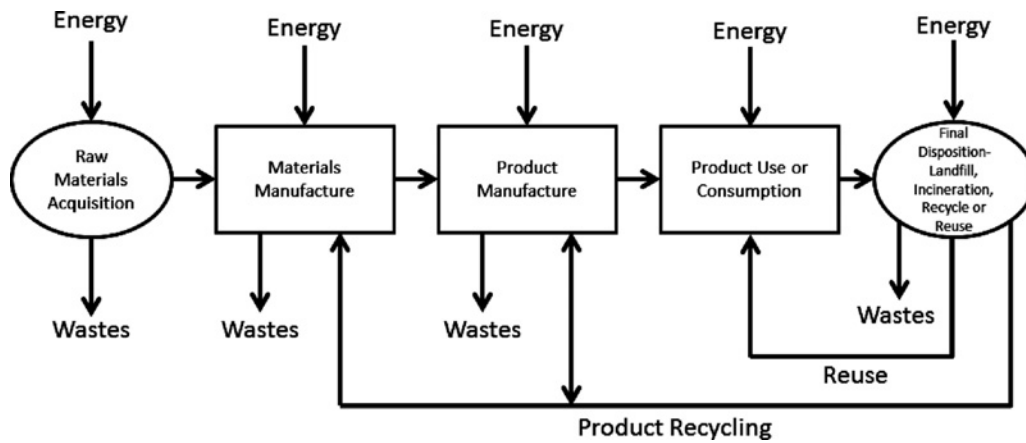


FIGURE 11.3 The flow diagram, sometimes referred to as a *cradle-to-grave* materials flow diagram, of a recycling scheme showing both materials and energy flow in and out of the system for a product life cycle. (Reprinted with permission of the publisher from Curran, 1996.)

The life-cycle system concept for a product life cycle is illustrated in Figure 11.3. This diagram is often referred to as a cradle-to-grave materials flow diagram. The boundaries for the LCI encompass the acquisition of raw materials, manufacture of intermediate materials, manufacture of the product being studied, use of the product, and the final disposition. Recycling or reuse of the product is part of the LCI analysis. Reuse here means the direct reuse of the product for its initial intended use, such as a beverage bottle being placed back into service. The product could be separated from a mixed stream, ground, and returned to the product manufacturing step. In the figure is also shown the return of the product all the way back to the materials manufacturing step, which is referred to as feedstock recycling. Furthermore, the product can be incinerated to recover the inherent energy associated with the polymer. In this diagram various types of recycling options are illustrated. The use of energy, as shown for each step in Figure 11.3, carries with it the input of energy resources as well as the inputs and outputs for processing these energy

resources into usable fuels. The inputs and outputs for transportation of materials between process steps are implied by the arrows showing the flow of materials between steps.

Before any recycling scheme is introduced, it is essential that the ultimate goal be specified. If the goal is not specified, then it is impossible to judge whether the recycling scheme has achieved its purpose. If the goals are to reduce the consumption of raw materials or the generation of solid waste, then it is clear that recycling should be practiced. If the goal is to reduce energy consumption, then the process must be examined very closely. The basis for making the decision is centered on the use of material and energy balances.

Several types of recycling schemes exist: (1) closed-loop recycling with no losses in the recycling loop; (2) closed-loop recycling when losses occur in the recycling loop; and (3) open-loop recycling. To illustrate how mass and energy balances are employed in the analysis of recycling schemes we consider closed-loop recycling with losses as shown schematically in Figure 11.4. Unit operation 1 or stage 1 in

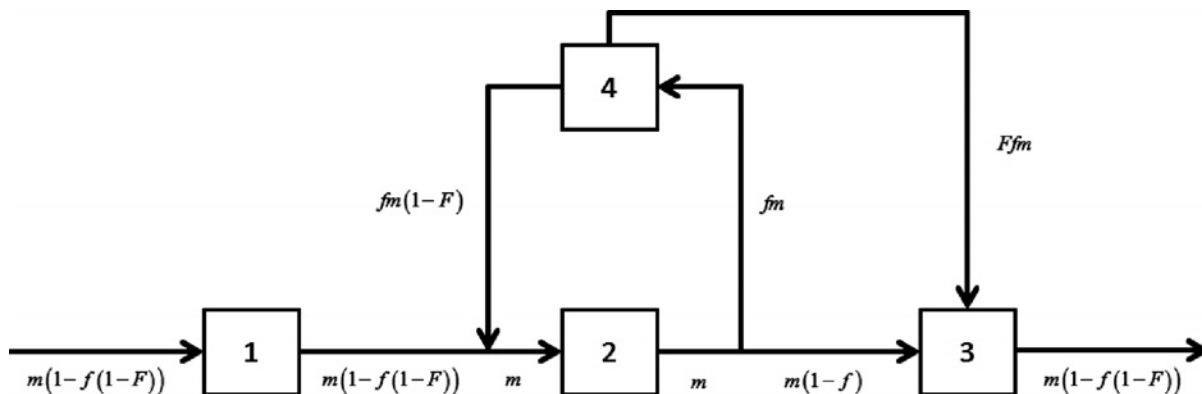


FIGURE 11.4 Simple closed-loop recycling when the reprocessing stage produces waste materials. (Reprinted with permission of the publisher from Brandrup et al., 1996.)

this figure represents the conversion of raw material to product (e.g., polyethylene milk bottles). Stages 2 and 3 represent the consumer and the disposal phase, respectively. Stage 4 is the reprocessing operation for converting the waste back into useful product. Consider that a single mass, m , of 1 kg of product is passed initially to the consumer. Our goal is to determine with an infinite number of recycles how much material is passed by the consumer. A fraction f of the material leaving the consumer is now fed into the recycling loop, and the recycling loop is responsible for a loss of a fraction F of the material passing through the reprocessing stage 4. The amount of material returned to the main production sequence will be of mass $mf(1 - F)$. The amount of material sent to the disposal stage after the first pass consists of the sum of the material disposed of directly after consumer use, $m(1 - f)$, plus the amount lost from the reprocessing step, mFf (total = $m((1 - f) + fF)$ or $= m(1 - f(1 - F))$). The amount of mass that passes the consumer after the first recycle is reduced to

$$m_{p1} = mf(1 - F) \quad (11.1)$$

After a second recycle the mass of original product, m_{p2} , passing the consumer will be reduced to

$$m_{p2} = mf^2(1 - F)^2 \quad (11.2)$$

and so on. If the material is continually recycled under the same conditions, then after a large number of cycles the total mass of the original product that will have passed the consumer, M_p , is

$$M_p = m + mf(1 - F) + mf^2(1 - F)^2 + mf^3(1 - F)^3 + \dots \quad (11.3)$$

Summing Eq. 11.3, assuming there is an infinite number of terms, gives

$$M_p = \frac{m}{1 - f(1 - F)} \quad (11.4)$$

For example, if there is a loss of 20% of the recycled materials (i.e., $F = 0.2$) and the recycle rate f is 50%, then the product flow past the consumer will be 1.67 kg. From this equation it is obvious that F should be as small as possible if we are to minimize the amount of raw material used. This is further illustrated by referring to Figure 11.4. The amount of raw material required from operation 1 to provide a mass m to the customer increases as F increases.

Example 11.1. Amount of Virgin PE Passing by a Consumer

Suppose 50 kg of milk bottles consisting of PE pass by a consumer each year and the recycle ratio is 50% while the loss during recycle is 20%. How many kilograms of virgin

resin pass by the consumer per year assuming the number of recycles is very large?

Solution. Using Eq. 11.4 with $M_p = 50$ kg/yr, $f = 0.5$, and $F = 0.2$, we find that $m = 30$ kg/yr. ■

We are primarily interested in the amount of energy that is required to execute a particular recycling scheme. Following Figure 11.4 the energies per unit mass associated with each operation are, respectively, E_1 , E_2 , E_3 , and E_4 . The total energy requirement for the overall system, E_s , is the sum of the energies for each operation:

$$E_s = E_1m(1 - f(1 - F)) + E_2m + E_3m(1 - f(1 - F)) + E_4mf(1 - F) \quad (11.5)$$

Equation 11.5 can be rearranged to emphasize various contributions to the energy requirements:

$$E_s = m(E_1 + E_2 + E_3) + mf(E_4 - E_1 - E_3) - mfF(E_4 - E_1 + E_3) \quad (11.6)$$

It is now easier to see the significance of the energy balance as the first term on the right side of Eq. 11.6 represents the energy requirements when no recycling is employed. The second term represents the energy associated with the recycling loop if no losses occur. It is obvious if the amount of energy associated with the reprocessing of the polymer is less than the energy required to process the virgin resin, then the amount of energy consumed would be less than with no recycling. The third term represents the energy requirements associated with losses in the recycling loop. Hence, energy savings in the recycling step will be reduced as a result of the loss of material.

We are now at a point to answer the question: When does one implement recycling? In general, recycling will always result in a reduction in raw-materials consumption and solid-waste generation per unit product used by the consumer. For energy, however, there is no guarantee that savings will occur when recycling is implemented as this factor is governed by a number of different parameters. Furthermore, because the other parameters, such as air and water emissions, usually follow the same general pattern as energy, we will concentrate on energy savings as a criterion for determining whether to recycle (Brandrup et al., 1996). The saving of energy depends on whether the sum of the energies required for recovery (E_{RC}) and reprocessing (E_{RP}) of a polymer are less than the sum of the energies required for processing the virgin resin (E_V) and disposal (E_D), that is:

$$E_V + E_D > E_{RC} + E_{RP} \quad (11.7)$$

In terms of the notation in Figure 11.4:

$$E_1 = E_V \quad E_4 = E_{RC} + E_{RP} \quad E_3 = E_D \quad (11.8)$$

If we are to implement a recycle program, then the energy required for reprocessing and recovery of the waste cannot exceed the energy used in making the virgin resin and disposing of the product.

The next question one must answer is what type of recycling should be implemented: that is, which type of recycling will provide the greatest energy savings. There are basically three choices. We can separate polymer streams, grind the product, and reprocess the resin to form new product. This is referred to as *mechanical recycling*. The separated polymer can be treated chemically and subjected to high temperatures to reduce the molecular weight back to the level of monomer. The recycling of the polymer back to feedstock is referred to as *tertiary recycling*. Finally, we can recover plastics and incinerate them to recover their calorific value (e.g., for PE the calorific value is about 45 MJ/kg, which is similar to that of crude oil). (Note that wood's calorific value is about 15 MJ/kg.) Hence, we can recycle plastics for the purpose of energy recovery.

In order to illustrate how the choice is made to select a method of recycle we consider the following example. We have simplified the selection of data to illustrate our points, but one must be aware of the immense uncertainty involved in obtaining this data.

Example 11.2. Energy Gained in the Mechanical Recycling of Polyethylene Milk Bottles (Brandrup et al., 1996)

Determine how much energy can be gained by mechanical recycling of PE milk bottles given the following data:

1. Average production energy of virgin PE (E_1) = 40 MJ/kg. (Note: This does not include the small amount of energy for converting PE to bottles.)
2. Disposal energy (E_3) = 1 MJ/kg.
3. Twenty percent loss of material during recycling.
4. Recovery: E_{RC} = 3 MJ/kg (includes energy for collection, transport to reprocessing site, and energy for transporting to converter).
5. The energy for converting the virgin resin and ground recycled bottles is similar and is on the order of 0.5 MJ/kg.
6. The bottles are completely recycled at the consumer step (i.e., $f = 1$).

Solution. Using Eq. 11.5 we first calculate the total energy requirements with no recycling, $E_s(\text{NR})$:

$$\begin{aligned} E_s(\text{NR})/m &= (E_1 + E_2 + E_3) = (40 + E_2 + 1) \\ &= (41 + E_2) \text{ MJ/kg} \end{aligned}$$

where we have taken $m = 1$ kg/yr. Using Eq. 11.5 again for the case that the bottles are completely recycled and 20% of the bottles are lost during the recycle step we calculate the total energy usage, $E_s(\text{R})$:

$$\begin{aligned} E_s(\text{R})/m &= (FE_1 + E_2 + E_3F + (1 - F)E_4) \\ &= (8 + E_2 + 0.2 + 2.4) = (10.6 + E_2) \text{ MJ/kg} \end{aligned}$$

Therefore, the amount of energy available for reprocessing is

$$E_{RP}/m = (E_s(\text{NR}) - E_s(\text{R}))/m = 30.4 \text{ MJ/kg}$$

Hence, it appears that considerable energy can be saved in the case of PE by mechanical recycling. However, it should be recognized that if all the energy consumed in the equipment used for reprocessing is electricity and the plants for producing electricity are only 50% efficient, then we really only have about 15 MJ/kg. Without going into details, the value of energy available for heating from PE is about 14.5 MJ/kg (Brandrup et al., 1996). Hence, one wonders whether recycling is economically and energetically favorable. ■

As mentioned at the beginning of this section, LCA is also used as a toll to help make decisions on which plastics to use in specific applications, which processes to use in the production of various plastic articles, and how to improve the environmental profile of plastic processes. An example of such use of LCA is reported in the Athena Institute Report (2006). In this report, the Institute presents the life-cycle inventory (LCI), consistent with the methodology described in the ISO 14040 and 14044 Standards, of five products: 16 ounce cups, two-piece 16 ounce deli containers, envelope window film, foam meat trays, and 12 ounce water bottles, produced from corn-based polylactic acid, PLA, high impact polystyrene (HIPS), polyethylene terephthalate (PET), polypropylene (PP), and general purpose PS (GPPS). The report also includes calculations for the global warming potential (GWP) effects for the various products using the 2001 work by the International Panel of Climate Change (IPCC). Without going into great detail, the LCI results include energy consumption, solid waste generation, environmental emissions to air and water, and GWP. Some of the results are shown in Table 11.1. It is clear from the table that in some cases the specific renewable polymer, polylactic acid, PLA, examined in the report has lower environmental metrics (e.g., total energy and greenhouse gases in the water bottle case) than PET, and in some other cases it has higher metrics (e.g., postconsumer solid waste in the cold drink cup) than PP. Thus, each application of plastic materials needs to be examined separately to reach a conclusion about which material has the best environmental profile.

However, before one uses LCA for the reasons mentioned above, one should employ one or more of the 12 principles of green engineering (Anastas and Zimmerman, 2003) and

TABLE 11.1 Life-Cycle Inventory for Some Standard Consumer Products

Product	Total Energy (GJ)	Postconsumer Solid Waste (kg)	Greenhouse Gases (kg of CO ₂ equivalents)
16 ounce cold drink cup (basis: 10,000 cups)			
PLA	14.5	118	510
HIPS	13.3	98.4	576
PP	9.8	84	345
PET	16.1	126	719
Envelope window film (basis: 1,000,000 in. ²)			
PLA	2.03	18.8	62.6
GPPS	1.87	15.8	76.1
Foam meat tray (basis: 10,000 trays)			
PLA	5.59	43.8	192
GPPS	5.77	41.8	231
12 ounce water bottle (basis: 10,000 bottles)			
PLA	19.8	168	744
PET	21.4	162	961

Source: Athena Institute Report, 2006.

green chemistry (Anastas and Warner, 2000) shown in Table 11.2 in the processes to make plastic articles. These principles should be viewed as capable of providing a framework for chemists and engineers to employ when designing new plastics and processes. Combining the LCA metrics and the 12 principles summarized in Table 11.2 could lead to a composite assessment of a particular set of polymers. Tabone et al. (2010) did exactly that in their study of 12 polymers, 7 of which were derived from petroleum (i.e., PET, HDPE, LDPE, PP, PC, PVC, and GPPS), 4 from renewable sources (i.e., PLA-G (via a general process), PLA-NW (via a Nature-Works LLC process), PHA-G (from corn grain), and PHA-S (from corn stover)), and 1 from both (i.e., bio-PET made with bioethylene glycol and terephthalic acid). We note that the structures for the 4 polymers from renewable sources are given in Table 11.9. The authors used a functional unit of comparison of 1 liter of polymer pellets, and a decision matrix to generate a single metric for each polymer to measure its LCA “cradle-to-gate” environmental impact and another single metric to measure its adherence to the 12 principles.

11.2 PRIMARY RECYCLING

The first opportunity to practice recycling is at the processing facility. As no separation of material is required, this can be considered a form of mechanical recycling. In all major forming operations, such as extrusion, injection molding, calendaring, and thermoforming, a certain amount of scrap is produced. For example, scrap can originate from rejected parts, sprues and runners generated during injection molding, and trim from thermoformed parts. In some cases, such as in thermoforming, the scrap can represent 50 wt% of the material processed. This scrap (also called regrind) can be

ground and combined with virgin resin to not only improve the economics of the process but to prevent disposing of the material in landfills. However, one cannot repeatedly process the polymer without consequences. In particular, repeated processing leads to degradation of the polymer resulting in the loss of mechanical properties, surface appearance, and processability. The major changes that occur in a polymer are a loss of molecular weight, increase in molecular weight due to crosslinking, and cyclization. In the case of glass filled polymer, the aspect ratio of the reinforcing fibers is reduced with each pass through an injection molding machine resulting in a loss in mechanical properties.

The major question to be answered is: How much regrind can we use relative to the virgin resin and still maintain mechanical properties that are similar to those of the virgin resin? Of course, one way to answer this question is to carry out a set of experiments in which the level of regrind and the number of recycling steps is changed systematically. However, it would be expeditious to estimate the amount of regrind and the resulting properties after n recycle steps. Information needed to make decisions of this nature include the amount of original material left in a sample after n recycle steps, the decrease in mechanical properties with each pass through the process, or the decrease in MW with each pass and the relation between properties and MW, and a mixing rule for weighting the contributions from each fraction to the final mechanical properties.

To illustrate how one would go about determining the level of original polymer remaining in a product after n recycle steps, we consider the following example. Polymer scrap is collected, ground, and combined with virgin resin at a constant ratio. The combination of virgin resin and regrind is then always processed with the ratio of regrind to virgin resin held fixed. The flow chart for this process is shown in

TABLE 11.2 Twelve Principles of Green Engineering and Green Chemistry

Principle	Green Engineering	Green Chemistry
Principle 1	Designers need to strive to ensure that all material and energy inputs and outputs are as inherently nonhazardous as possible.	It is better to prevent waste than to treat or clean up waste after it is formed.
Principle 2	It is better to prevent waste than to treat or clean up waste after it is formed.	Synthetic methods should be designed to maximize the incorporation of all materials used in the process into the final product.
Principle 3	Separation and purification operations should be designed to minimize energy consumption and materials use.	Wherever practicable, synthetic methodologies should be designed to use and generate substances that possess little or no toxicity to human health and the environment.
Principle 4	Products, processes, and systems should be designed to maximize mass, energy, space, and time efficiency.	Chemical products should be designed to preserve efficacy of function while reducing toxicity.
Principle 5	Products, processes, and systems should be “output pulled” rather than “input pushed” through the use of energy and materials.	The use of auxiliary substances (solvents, separation agents, etc.) should be made unnecessary wherever possible and innocuous when used.
Principle 6	Embedded entropy and complexity must be viewed as an investment when making design choices on recycle, reuse, or beneficial disposition.	Energy requirements should be recognized for their environmental and economic impacts and should be minimized. Synthetic methods should be conducted at ambient temperature and pressure.
Principle 7	Targeted durability, not immortality, should be a design goal.	A raw material of feedstock should be renewable rather than depleting wherever technically and economically practicable.
Principle 8	Design for unnecessary capacity or capability (e.g., “one size fits all”) solutions should be considered a design flaw.	Unnecessary derivatization (blocking group, protection/deprotection, temporary modification of physical/chemical processes) should be avoided wherever possible.
Principle 9	Material diversity in multicomponent products should be minimized to promote disassembly and value retention.	Catalytic reagents (as selective as possible) are superior to stoichiometric reagents.
Principle 10	Design of products, processes, and systems must include integration and interconnectivity with available energy and material flows.	Chemical products should be designed so that at the end of their function they do not persist in the environment and break down into innocuous degradation products.
Principle 11	Products, processes, and systems should be designed for performance in a commercial “afterlife.”	Analytical methodologies need to be developed further to allow for real-time in-process monitoring and control prior to the formation of hazardous substances.
Principle 12	Material and energy inputs should be renewable rather than depleting.	Substances and the form of a substance used in a chemical process should be chosen so as to minimize the potential for chemical accidents, including releases, explosions, and fires.

Source: Data from Anastas and Zimmerman, 2003, and Anastas and Warner, 2000.

Figure 11.5. The process could be any one used for thermoplastics, such as injection molding or thermoforming. All scrap is sent for regrinding, but some may be lost as waste, stream F_6 . In Figure 11.5 the flow rates (units of kg/h) of the various streams are labeled as F_i and defined in Table 11.3. The basis for the process is taken as the feed to the process, F_2 , which consists of virgin plus recycle resin. The ratio of recycle resin (F_7) to the total feed to the process (F_2) is taken as r ($r = F_7/F_2$). Following the notation of Figure 11.4 with f being the fraction that is recycled and F being the fraction of regrind which is loss in the grinding process, we can also express the recycle ratio as $r = f/(1 - F)$.

The goal now is to determine the composition of the product as a function of the number of recycles (i.e., determine

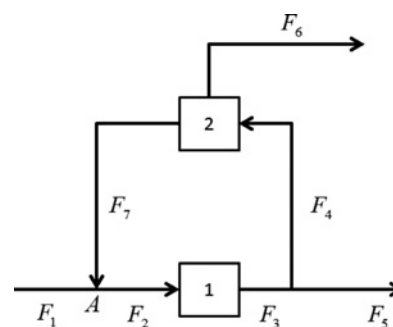


FIGURE 11.5 Flow chart for a recycling scheme in which the ratio of regrind to virgin resin is held fixed. The flow streams are defined in Table 11.3.

TABLE 11.3 Definitions of Streams in the Recycling Scheme Shown in Figure 11.5

Stream Flow (kg/h)	Description
F_1	Virgin resin feed
F_2	Feed of virgin plus recycle resin to the process
F_3	Flow of resin leaving process
F_4	Scrap resin sent to be recycled
F_5	Product
F_6	Waste
F_7	Scrap resin combined with virgin resin

the age distribution of material in the product as a function of number of recycles). From an overall mass balance on the system it can be shown that the amount of product leaving the process, F_5 , is equal to $F_1 - F_6$. Next, we can calculate the amount of material associated with each pass through the process, P_i . After one pass the fraction of material with two passes through the equipment is r^2 while the fraction of material with one pass through the equipment is $1 - r$. The regrind now contains material with both 1 pass ($r(1 - r)$) and two passes (r^2). When this passes through the equipment during a second recycle, the product contains material with one pass ($1 - r$), two passes ($r(1 - r)$), and three passes (r^2). In Table 11.4 we summarize the age distribution of material within the product through n recycles.

Example 11.3. Determination of the Age Distribution of Polymer in a Product Stream

For the recycle scheme shown in Figure 11.5 determine the age distribution of polymer (i.e., the fraction of material with one pass, two passes, and so on through the processing equipment) in the product stream for the following conditions:

- (a) $F_2 = 100$ kg/h (basis), $F_6 = 0$, $F_7 = 5$ kg/h, $n = 4$.
- (b) $F_2 = 100$ kg/h, $F_6 = 5$ kg/h, $F_7 = 5$ kg/h, $n = 4$.
- (c) Derive a general equation for the conditions in part (b) for n recycles.

TABLE 11.4 Fraction of Polymer in the Product Stream with Various Numbers of Passes Through the Processing Equipment

Recycle Number	P_1	P_2	P_3	P_4	P_{n-1}	P_n
1	$1 - r$	r				
2	$1 - r$	$r(1 - r)$	r^2			
3	$1 - r$	$r(1 - r)$	$r^2(1 - r)$	r^3		
n	$1 - r$	$r(1 - r)$	$r^2(1 - r)$	$r^3(1 - r)$	$r^{n-1}(1 - r)$	r^n

Solution. We have $r = F_7/F_2 = 5/100 = 0.05$. From a mass balance on point A, $F_1 + F_7 = F_2$, and on the system, $F_1 = F_5 + F_6$, we find that $F_5 = 95$ kg/h. From Table 11.4 the composition of the product stream is

$$F_5 = 95(0.95) + 95(0.0475) + 95(0.002375) + 95(0.00011875) = 90.25 + 4.51 + 0.23 + 0.011 \text{ kg/h}$$

Hence, after four passes through the processing equipment only 1.1% of the original material remains in the product stream. That means 95% of the material is essentially virgin material, only having passed through the processing equipment once.

For part (b) in which there is loss of material from the system, we can combine the two mass balances above to show that $F_5 = F_2 - F_7 - F_6 = 90$ kg/h. Hence, after four recycles the composition of the product stream is

$$F_5 = 90(0.95) + 90(0.0475) + 90(0.002375) + 90(0.00011875) \text{ kg/h}$$

Hence, although there is loss in the system, the age distribution of material (i.e., the fraction of material remaining in the product with n passes through the system) remains unchanged.

We can generalize the expression for determining the composition of the product stream by again referring to Table 11.4:

$$F_5 = (F_2 - F_7 - F_6) \left(\sum_{j=0}^{n-1} r^j(1 - r) + r^n \right) \quad (11.9)$$

■

Now that we know how to determine the age distribution of the polymer in the product, the next question is: How do we use this information to determine the properties of the product? In particular, it is desirable to predict the tensile strength and modulus of the polymer product as a function of the number of recycles, the recycle ratio. Furthermore, it would be useful to know how the rheology and, hence, processability of the polymer have changed. One way to use the results might be to determine how the molecular weight of the product changes and then use correlations between molecular weight and physical properties. Another way would be to develop correlations between the physical properties and the number of recycles of the polymer (Abbas et al., 1978). However, to use either of these approaches, mixing rules are needed. In Section 5.3.2 we discussed how properties were

combined using either parallel or series combination of properties. Another mixing rule involves taking the logarithmic combination of properties as shown in Eq. (11.10) below:

$$\ln P_p = \sum_{i=1}^n w_i \ln P_i \quad (11.10)$$

In the approach taken by Abbas and co-workers (1978) they assumed the parallel arrangement of properties, and, hence, the properties of the product are given by

$$P_p = \sum_{i=1}^n w_i P_i \quad (11.11)$$

where P_p is the property of the product, w_i is the weight fraction of material with age distribution i (or the weight fraction of material that has passed through the process i times), and P_i is the property of the material after i processing cycles. It should be noted that the method of combining properties is crucial to the success of the approach, and the approach described by Eq. 11.11 may not always be the best. Abbas and co-workers (1978) then obtained properties of a polymer as a function of the number of processing cycles. Results of this nature can be obtained, for example, by injection molding a polymer, measuring the properties, grinding the samples, processing them again, and so on. For example, a linear decrease in properties was observed for the notched impact strength of polycarbonate and the impact strength of glass-reinforced Nylon 6,6. In polymers containing thermal stabilizers or antioxidants, there is typically an induction period followed by a nonlinear decrease in properties. When degradation involves formation of compounds promoting main chain scission, the degradation rate increases with an increase in the number of recycles. For a linear decrease in properties, P_i after i cycles of processing is given by

$$P_i = P_0 + i \Delta P \quad (11.12)$$

where P is the change in property from one cycle to another. P_0 represents the initial properties of the polymer (one pass through the equipment). In the case of decreasing properties, this value will be negative. Another choice for change in properties with the number of cycles of processing is a power-type dependence:

$$P_i = P_0(1 + i \Delta P)^a \quad (11.13)$$

where a is an exponent similar to that for the power-law model discussed in Section 2.1. To illustrate how we use a relationship, such as in Eq. 11.13, and the age distribution of material after n recycle steps we consider the following example.

Example 11.4. Determination of the Percent of Original Properties for a Linear Decay in Properties

The decay in tensile strength of an injection molded sample is given by the following equation:

$$\frac{P_i}{P_{0i}} = 1.0 - \frac{P_0 - P_f}{20P_0} i \quad (11.14)$$

where $P_f = (1/5)P_0$ is the strength after 20 cycles of reprocessing the polymer, and after 20 cycles there is negligible change in the tensile strength. After 5 recycles of the polymer determine the percent of original properties for regrind ratios of 20% and 50% for the situation described in Table 11.4.

Solution. Assuming Eq. 11.11 is valid for determining the tensile strength and using Table 11.4 for determining the weight fraction with given age or process history, we can write a general expression for the percent reduction in properties as

$$P_p = (1-r)(1) + r(1-r)(0.96) + r^2(1-r)(0.92) + r^3(1-r)(0.88) + r^4(1-r)(0.84) + r^5(0.8) \quad (11.15)$$

The numbers in parentheses result from evaluating Eq. 11.14. Now, for a recycle ratio of 0.2, the reduction in properties is only 1.2% or the polymer retains 98.8% of the original properties. For a recycle ratio of 0.5, 91% of the original properties are retained. Actually, after about 3 recycle steps, there is very little change in the properties. ■

11.3 MECHANICAL OR SECONDARY RECYCLING

Secondary recycling refers to the use of plastics unsuitable for primary recycling using standard plastics processing equipment. Sources of plastic wastes potentially suitable for secondary recycling processes include (1) *post-consumer waste recovered from municipal refuse*, (2) *post-consumer waste obtained from returnable packages*, (3) *mixed industrial plastic waste*, and (4) *industrial plastic waste consisting of a single type of plastic* (Leidner, 1981). Sometimes secondary recycling is also referred to as mechanical recycling, which means reusing the recovered product as material for either the original purpose or for different ones. Once the plastic article is put into use, recovery and recycling become much more complicated. The complications arise as a result of the mixing of polymer types and the presence of impurities (metal, sand, glass, paper, etc.). The problem with mixed polymer types is that polymers are highly incompatible, and their properties are significantly lower than those of the pure

TABLE 11.5 Plastic in Municipal Solid Waste of Hamilton, Ohio

Plastic Type (SPI #) ^a	Percent by Weight in MSW	Percent by Weight of Plastics
PS (6) foam	0.5	8.0
PET (1) soda bottles	1.0	16.0
HDPE (2) milk/water bottles	0.7	11.0
Bags (4) LDPE film	1.8	29.0
Other (LDPE (4), PVC (3) bottles, PS (6) caps, and other (7) plastics)	2.2	36.0
Total	6.2	100.0

^aSPI is the Society of the Plastics Industry. The SPI resin identification coding system was introduced in 1988 and is used internationally.

Source: Hegberg et al., 1992.

components. In some cases, such as in the generation of parts with thick walls (e.g., plastic lumber), mixed polymers can be tolerated.

The breakdown in plastics composition of a typical municipal solid waste (MSW) stream is shown in Table 11.5. Here we see that not only are a wide variety of plastics present but a wide variety of other materials are present as plastics make up only 6.2% of MSW. Because of the incompatibility of polymers and because of differences in their melting points and processing temperatures, it is difficult to directly reprocess a mixture of polymeric materials. Hence, it is preferred to separate the polymers before recycling. Separation can be as simple as sorting by hand but is usually based on density, wettability, magnetizability, electrical properties, chemical properties, optical properties, and solubility (Brandrup et al., 1996). The discussion of the various techniques is given in the book by Brandrup et al. (1996). Another issue arises in that even when a polymer is completely separated from a mixture of polymers, the initial molecular weights of the starting material can be variable. For example, as shown in Table 11.6, PPs with a wide range of MW (as indicated by the melt index) can be found in the waste stream. Hence, the quality of the recycled material can be variable.

Technical approaches to secondary or mechanical recycling include direct reprocessing, reprocessing using specialized equipment, chemical modification of mixed plastic waste (compatibilizers), using recyclate in the core, using waste as a filler, and using waste as a binder for a low-cost filler. As the technology of separation is discussed more fully in Brandrup et al. (1996), we concentrate on those aspects that lend themselves to engineering analysis. In particular, we cover the topics of blend rheology, filtration, and compatibilization.

11.3.1 Rheology of Mixed Systems

During the processing of a mixture of polymers, such as in the manufacture of plastic lumber or in the presence of a

TABLE 11.6 Melt Indices of Polypropylene for Various Processing Applications

Processing Operation	Melt Index (230 °C/2.16 kg)
Compression molded sheet	0.1
Extruded tube and sheet	0.1–0.6
Blow molding	0.3–2.0
Thermoforming	1–5
Cast film	8–15
Biaxially oriented film	1–4
Blown film	2–10
Thin-walled injection molding	30–100
Injection molding	2–50
Fibers	8–35
Monofilaments	5–10
Tapes	2–4

Source: Brandrup et al., 1996.

compatibilizer, it is necessary to estimate at least the viscosity of the mixture as a function of shear rate. Various mixing rules exist as discussed for estimating the viscosity of a mixture of the same polymer of different MWs. Grizzuti et al. (2000) found that for shear rates $> 1.0 \text{ s}^{-1}$, the reciprocal and linear–ln mixing rules given below represented the experimental data for a blend of two incompatible polymers very well (ϕ_i is the volume fraction of the i th component):

$$\frac{1}{\eta} = \sum_{i=1}^n \frac{\phi_i}{\eta_i} \quad (11.16)$$

$$\ln \eta = \sum_{i=1}^n \phi_i \ln \eta_i \quad (11.17)$$

Below shear rates of 1 s^{-1} , these empirical mixing rules underpredicted the viscosity of the blend, which tended to continue to increase at low shear rates. This was attributed to the continuous change in morphology that occurred during shearing as the drops continued to break down finally reaching an equilibrium size. Grizzuti et al. (2000) applied these empirical rules using viscosity data at each shear rate from the given polymers. Equation 11.16 seemed to work the best. These same mixing rules can be applied to a mixture of plastics of the same type but of different MW. Hence, given PP consisting of a mixture of different MIs, one can estimate the viscosity of the mixture.

11.3.2 Filtration

The processing of recyclates puts a high demand on the polymer purity. Numerous types of contaminants exist including solid particles of foreign matter (e.g., glass, paper, metal, paint, sand) and polymer particles. Separation of foreign particles is typically carried out by placing filters (also called

filtration media) between the end of the extruder and the die. The filtration media typically consist of woven and nonwoven screens or porous plates with sintered powdered metal particles supported by a breaker plate. The geometry of the filtration system may be as simple as that of a screen supported by a breaker plate (plate with small holes), which is placed between the end of the extruder and the die. More complicated geometries, such as cartridge filters, drum filters, and disk filters, are also used (Brandrup et al., 1996). The screen medium can be removed discontinuously or continuously out of the melt stream for the purpose of cleaning. Brandrup et al. (1996) list some of the common impurities, the appropriate screen system, the required mesh size given in microns, pore size, porosity, the required screen surface area, the resultant load on the screen, and the final product with which they are usually associated. For example, for removing fiber and paper it is recommended to use a cartridge filter with a mesh size of 100 to 200 μm with mass flow rates of 700 to 1000 kg/h/m^2 .

The main issue in using filtration is the increase in pressure drop through the screens and filters and the buildup of pressure during the accumulation of contaminants. Hence, in this section we provide the background for estimating pressure drop through various types of porous media. Before proceeding onto estimating the pressure drop across screens and filters, a few comments about relating mesh size to the size of the openings in the screen and the fraction of material with voids are necessary. In Table 11.7 a few values of mesh size to the size of the openings and the volume fraction of voids is presented. Mesh refers to the number of openings per linear inch of screen. Hence, 40 mesh means that there are 40 openings per linear inch of screen, or equivalently, that each opening size and wire diameter is equal to 1/40 in., that is, 0.025 in. (or 0.635 mm or 635 μm). Another characteristic of the screen is its open area fraction (also called percent open area) or void fraction. The open area fraction is calculated as: opening size/(opening size + wire diameter), assuming square openings. In the example of the U.S. 40 mesh screen, the opening size is 0.0165 in. (see Table 11.7), and therefore, the open area fraction is calculated as: $0.0165/0.025 = 0.66$,

TABLE 11.7 Values of the Size of the Openings as a Function of Mesh Size

U.S. Mesh	Opening (in.)	Opening (μm)	Opening (mm)	Void Fraction or Open Area Fraction
4	0.1875	4760	4.760	0.75
40	0.0165	420	0.420	0.66
100	0.0059	149	0.149	0.59
400	0.0015	37	0.037	0.60

Source: This data was taken from a table found at: [http://en.wikipedia.org/wiki/Mesh_\(scale\)](http://en.wikipedia.org/wiki/Mesh_(scale)).

which means that the openings account for 66% of the screen area.

The most effective way for calculating the pressure drop through a packed column is based on considering the flow to be that of flow through a bundle of tangled tubes of irregular cross section (Bird et al., 2007). The starting point is to consider the flow through a tube and then replace the diameter by 4 times the mean hydraulic radius, R_H . Of course, one of the key issues here is to replace R_H by the characteristics of the packed bed, which are usually related to the porosity or permeability. The derivation that follows here is similar to that presented by Bird et al. (2007) for a Newtonian fluid. For a power-law fluid the average velocity for flow through a tube is (Table 2.4)

$$\langle v_z \rangle = \frac{R^{s+1}}{s+3} \left(\frac{\Delta P}{2mL} \right)^s \quad (11.18)$$

The mean hydraulic radius, R_H , is the ratio of the cross-sectional area available for flow to that of the wetted perimeter. If we multiply these values by the length of the column of porous media and divide both by the volume of the bed, we can find R_H in terms of ε , and the parameter a , given as the ratio of the total particle surface to the volume of the particles:

$$R_H = \frac{\frac{\text{volume of voids}}{\text{volume of bed}}}{\frac{\text{wetted surface}}{\text{volume of bed}}} = \frac{\varepsilon}{a} \quad (11.19)$$

The quantity a is related to the specific surface, a_v (the total particle surface/the volume of the particles making up the bed) by

$$a = a_v(1 - \varepsilon) \quad (11.20)$$

The average particle diameter for any geometry of particle is given as

$$\bar{D}_p = \frac{6}{a_v} \quad (11.21)$$

where \bar{D}_p is defined so that for spherical particles, $a_v = (4\pi R_p^2/4\pi R_p^3/3) = 6/D_p$. Hence, R_H is now in terms of variables that can be measured as shown in Eq. 11.22 below:

$$R_H = \frac{\bar{D}_p \varepsilon}{6(1 - \varepsilon)} \quad (11.22)$$

Rather than using the average velocity in the twisted tubes, it is customary to use the superficial velocity, v_o , which is defined so that when v_o is multiplied by the cross-sectional area of the bed, one obtains the volumetric flow rate. With

$v_o = \varepsilon \langle v_z \rangle$ and D (or $2R$) replaced by $4R_H$, Eq. 11.18 becomes

$$v_o = \frac{n\varepsilon}{3n+1} \left[\frac{\bar{D}_p \varepsilon}{3(1-\varepsilon)} \right]^{1+s} \left[\frac{6\Delta P}{25 mL} \right]^s \quad (11.23)$$

In Eq. 11.23 the length of the column has been replaced by $(25/12)L$ to account for the additional length of the twisted tubes as explained by Bird et al. (2007). Similar expressions for the Newtonian fluid (see Problem 11B.8) and generalized Newtonian fluid with an Ellis empiricism for viscosity (see Problem 11B.9) can be obtained. In many instances it is impossible to estimate \bar{D}_p , so we rewrite Eq. 11.23 in terms of the permeability, κ , which is defined from the Newtonian solution (see Problem 11B.8) as follows:

$$\kappa = \frac{\bar{D}_p^2 \varepsilon^3}{9(1-\varepsilon^2)} \quad (11.24)$$

Rearranging Eq. 11.23 using Eq. 11.24 we find

$$v_o = \frac{n\varepsilon}{3n+1} \left(\frac{50\kappa}{3\varepsilon} \right)^{(1+s)/2} \left(\frac{6}{25m} \right)^s \left(\frac{\Delta P}{L} \right)^s \quad (11.25)$$

Example 11.5. Estimate the Initial Pressure Drop Across a 40 Mesh Filter Screen

A 40 mesh (meaning 40 openings per linear inch) screen of thickness 1.04 mm and diameter 18.75 mm is supported on a breaker plate and is used to filter sand and dirt from polypropylene (PP). The mass flow rate produced by the extruder is 12.5 kg/h. Estimate the initial (i.e., before accumulation of any sand) pressure drop across the screen for a PP in which the viscosity is described by the power-law model having parameters of $m = 3.21 \times 10^4 \text{ Pa} \cdot \text{s}^n$ and $n = 0.25$, and $\rho = 867 \text{ kg/m}^3$.

Solution. Starting with Table 11.7 we can calculate the number of holes or openings in the screen of diameter 0.75 in. and the size of the holes, which are assumed to be square. The number of holes is found by dividing the open area of the screen by the area of hole:

$$\begin{aligned} & (\text{Screen area} \times \text{void fraction}) / \text{hole area} \\ & = (0.375 \text{ in.})^2 \pi 0.66 / (0.0165 \text{ in.})^2 = 1071 \text{ holes} \end{aligned}$$

We can then calculate the volumetric flow rate per hole:

$$\begin{aligned} & (12.5 \text{ kg/h}) / (1071 * (867 \text{ kg/m}^3) * (3600 \text{ s/h})) \\ & = 4 \times 10^{-9} \text{ m}^3/\text{s} \end{aligned}$$

The mean hydraulic radius, R_H , of the hole is

$$\begin{aligned} R_H & = (0.0165)^2 / (4 \times 0.0165) = 4.125 \times 10^{-3} \text{ in.} \\ & = 1.0478 \times 10^{-4} \text{ m} \end{aligned}$$

We now use Eq. 11.18 to solve for ΔP :

$$\begin{aligned} \Delta P & = \langle v_z \rangle^n (S+3)^n \text{ mL} / (2R_H)^{(1+n)} \\ & = (4 \times 10^{-9} / 1.6 \times 10^{-7})^{0.25} 1.626 \\ & \quad \times 2(3.21 \times 10^4) 1.0414 \times 10^{-3} / (2 \times 10^{-4})^{1.25} \\ & = 1.786 \times 10^6 \text{ Pa} = 259 \text{ psi} \end{aligned}$$

11.4 TERTIARY OR FEEDSTOCK RECYCLING

Mechanical recycling is primarily limited to single-polymer waste because of the desire for the recycled products to match the original products as closely as possible in quality. When efficient and economical separation of the plastic stream is not feasible, then in some cases the plastic waste can be used as raw material for petrochemical processes, such as hydrogenation, gasification, cracking, and coking. This type of recycling is referred to as *tertiary* or *feedstock*, and there are also restrictions on the quality of the feedstock, especially in regards to traces of halogens, heavy metals, and fillers. One way of preparing plastic scrap for chemical materials recycling is to subject it to degradative extrusion, which allows highly diverse mixed-plastic stockpiles to be homogenized, sterilized, compacted, chemically modified, and converted into a form fit for transport. In this section we focus on the degradative extrusion of plastics scrap.

Degradative extrusion used to prepare plastic scrap for feedstock recycling is a special type of extrusion process that is characterized by the following features (Brandrup et al., 1996):

1. Reduction in molecular weight of the thermoplastic scrap to low-molecular weight and consequently low-viscosity polymer melts.
2. Degradation occurs by means of exposure of the sample to high temperatures and viscous dissipation coupled with the catalytic effect of chemical agents and reactive gases.
3. Suitable compounds for generating the catalytic effect are air or oxygen, steam, hydrogen, metal oxides, and other catalysts.
4. Decomposition products (e.g., HCl gas) that interfere with downstream processing are eliminated as much as possible by means of devolatilization (see Chapter 7) or bonded to compounds, such as CaCO_3 , and then filtered.

5. The product at the extruder exit is either a homogeneous liquid or solid strands, which are granulated at the exit.
6. The product at the exit can be heated to temperatures $>520\text{ }^{\circ}\text{C}$, which leads to volatilization.

The process may consist of cascaded extruders (two extruders connected together) or single extruders with a venting zone (see Fig. 8.33, p. 262). The first step is the elimination of HCl by means of thermal decomposition. In the venting zone the HCl gas is extracted along with other volatile fractions, which are primarily water and low-boiling substances. The HCl gas forms in large amounts at temperatures above $250\text{ }^{\circ}\text{C}$. After the removal of HCl the melt can then be degraded further with additives that promote degradation. Both twin-screw and single-screw devices are used.

As representative of other polymers, we begin our discussions on polymer degradation with HDPE. Various authors have proposed that the polyethylene (PE) thermal degradation proceeds mainly by a random chain scission mechanism to form intermediate species (heavy waxes and tars), which are further cracked to produce the final products (gases, aromatics, long-chain paraffins and olefins, coke, etc.) (Aguado and Serrano, 1999). In other cases, it is assumed that end-chain cleavage takes place simultaneously to yield some of the observed gaseous products. Most of the kinetic studies on PE thermal degradation have been based on thermogravimetric analysis (TGA) measurements, mainly using a power-law model to describe the rate of weight loss. In a paper by Westerhout et al. (1997) these studies have been reviewed and a new model referred to as the random chain dissociation (RCD) model was developed to describe the low-temperature thermal cracking of polyolefins. The RCD model takes into account the influence of factors, such as molecular weight, extent of branching (i.e., frequency of side groups) and β -scission, and evaporation of species from the reaction medium. PE volatilization was observed to begin at temperatures close to $400\text{ }^{\circ}\text{C}$, although the degradation of the polyolefin chains started at lower temperatures. Results are also reported that illustrate the changes in the average molecular weight of LDPE, determined by gel permeation chromatography (GPC), and the amount of volatile products formed when this polymer is treated at different temperatures in a stirred tank reactor under a nitrogen atmosphere. Although the production of gases is negligible up to $400\text{ }^{\circ}\text{C}$, from 350 to $400\text{ }^{\circ}\text{C}$ the polymer undergoes significant degradation, leading to a large decrease in the average molecular weight.

While for polypropylene (PP) similar mechanisms and, therefore, similar models apply to describe the pyrolysis kinetics as used for PE, the pyrolysis of polystyrene (PS) differs from that of PE and PP. In particular, the pyrolysis of PS yields a large amount of its monomer, styrene, while the

products of PE and PP are more or less random. However, as in the case of PP, half of the carbons in the polystyrene chain are tertiary due to the presence of side benzyl groups. Therefore, thermal degradation of PS also occurs at relatively low temperatures. TGA of PS in a nitrogen flow shows that the thermal cracking of this polymer with formation of volatiles starts at temperatures around $350\text{ }^{\circ}\text{C}$. PS thermal degradation also proceeds through a free-radical mechanism initiated by random chain scission. Primary, secondary, and tertiary radicals are involved in a series of transformations, mainly hydrogen transfer reactions and β -scissions, to yield the final degradation products. Detailed descriptions of the PS thermal degradation mechanism can be found in the paper by Westerhout et al. (1997). A number of studies have been performed on the kinetics of PS thermal decomposition mainly based on TGA measurements, which were recently summarized by Westerhout et al. (1997). Likewise, a model has recently been developed to describe the MWD evolution during PS thermal degradation.

The first model used to interpret the TGA experimental data was a simple first-order power-law model, but this model was only applicable in a small conversion range, because the actual reaction order varies with the conversion (Westerhout et al., 1997). In their study the use of the first-order power-law model was restricted to the 70–90% conversion range, because most studies have revealed that this description is valid only in this conversion range. Hence, the power-law model has limited utility in carrying out design calculations and will not be considered further.

A second model was developed to describe the pyrolysis kinetics on a more fundamental basis (Westerhout et al., 1997). The model accounts for the fact that both physical and chemical processes play an important role during the pyrolysis of polymers. When an apparatus, such as a TGA, is used for a kinetic study of a pyrolysis process, the rate of evaporation of pyrolysis products is measured, but not the intrinsic chemical reaction (the breaking of bonds) rate. Not every broken bond in the polymer chain leads to the evaporation of product. Only polymer chain fragments small enough to evaporate at the given reaction temperature will actually leave the polymer sample. This implies that both physical and chemical processes influence the measured rate of change of the polymer mass and hence the observed pyrolysis kinetics.

To account for the physical and chemical processes in the model proposed by Westerhout et al. (1997), termed the random chain dissociation (RCD) model, a polymer chain is represented as a chain of carbon atoms with side groups. A certain rate constant, k_i , can be associated with each bond type i between the carbon atoms. The number of bonds of type i is represented by N_i , and the rate of change of the number of each bond type is described by a simple first-order model:

$$\frac{\partial N_i}{\partial t} = -k_{0i} e^{(-E_{\text{act},i}/RT)} N_i = -k_i N_i \quad (11.26)$$

Different types of bonds possess different breakage rates and associated rate constants, such as β -bonds and bonds between carbon atoms to which a side chain is attached have higher breakage rates, due to the formation of relatively stable radicals during the reaction. This is accounted for in the model by distinguishing between different types of bonds and the specification of different kinetic parameters (i.e., k_{0i} and $E_{act,i}$) for each type of bond. The conversion is calculated by determining the number and weight of the fragments in the polymer chain with a length (including side chains) less than a certain length L_c , which just can evaporate. This parameter L_c is a function of temperature and pressure, and its value can be estimated from the boiling points of normal alkanes and alkenes. Other input parameters required by the model are the length and the extent of branching (or the frequency of the side groups, such as CH_3 in the case of PP) of the main chain. These parameters can be determined from the initial molecular weight and the structure of the polymer. The side groups (which can be branches in the case of LDPE) on the main chain can be either methyl, ethyl, propyl, or even benzyl groups. These groups are assumed to be distributed evenly over the main chain.

The most important difference between the first-order model and the RCD model is that the latter model accounts for the influence of physical processes (not every broken bond leads to the evaporation of a fragment of the polymer chain). However, at high conversions the polymer chain is degraded to relatively small fragments, which will immediately evaporate if another bond in the fragment is broken. Therefore, every broken bond leads to the evaporation of a chain fragment at high conversions and, because of the direct coupling of the breakage rate and the evaporation rate at high conversions, the evaporation rate exhibits first-order behavior as does the breakage rate. The RCD model combines the most relevant features of the different models proposed in the literature without introducing a large number of fit parameters: the difference between evaporation rate and breakage rate is accounted for, and the model also accounts for the presence of weaker bonds in the polymer chain (weak bond model) by accounting for side groups and different types of bonds. With the RCD model the conversion-versus-time curve can be calculated and from this information the conversion rate-versus-time or conversion can be determined. The RCD model can also be used to predict the product spectrum of the primary pyrolysis reaction. Representative data for commonly used polymers are shown in Table 11.8. The values shown in this table were obtained at temperatures in the range of 400–450 °C for the PEs and PPs while for PS in the range of 365–400 °C. Although LDPE has about 50 branches per 1000 carbon atoms and PP has CH_3 groups on every other carbon atom (likewise PS has a benzyl group on every other carbon atom), we only observe single values for k_0 and E_{act} . This is because in the case of LDPE only a few carbon atoms have side chains or branches and in the case of,

TABLE 11.8 Fitted Kinetic Parameters for the RCD Model for the Pyrolysis of Different Polymers

Polymer	k_0 (s^{-1})	E_{act} (kJ/mol)	k at 703 K (10^{-4} s^{-1})
HDPE ($\bar{M}_w = 125,000$)	1.3×10^{11}	207	0.5
LDPE1 ($\bar{M}_w = 350,000$)	9.2×10^{13}	244	0.7
PP ($\bar{M}_w = 250,000$)	9.4×10^{13}	237	2.1
PS ($\bar{M}_w = 280,000$)	1.3×10^{14}	219	69.4

Source: Westerhout et al., 1997.

for example, PP every carbon–carbon bond is influenced by the presence of the CH_3 group. We should also add that the molecular weight and its distribution have an insignificant effect on the rate of degradation.

In practice, mixtures of polymers will be present in household waste. It is therefore important to know whether the pyrolysis kinetics of a polymer is influenced by the presence of a second polymer, which would be the case if intermolecular reactions play a dominant role during the pyrolysis process. To examine whether this effect exists, mixtures of LDPE1 and PP2 were prepared in an extruder and subsequently pyrolyzed (Westerhout et al., 1997). Three mixtures (25, 50, and 75 wt% PE) were examined at a temperature of 425 °C. In the pyrolysis experiments with pure and mixed polymers, no significant difference in pyrolysis kinetics could be observed, which might be due to the fact that the kinetic constants for PE and PP pyrolysis only differ by a factor of 2 in the temperature range from 400 to 450 °C. It can be concluded, however, that there is no large mixing effect on the conversion rate. It is therefore possible to apply a linear mixing rule for the kinetic constants to calculate the kinetic constant of the mixture.

Example 11.6. Time to Degrade HDPE and PS

Determine the time to degrade the HDPE and PS materials, whose properties are given in Table 11.8, to \bar{M}_w 's of 420 and 3120 g/gmol (~ 30 C-C bonds), respectively. In the case of HDPE use a temperature of 450 °C, while for PS use a temperature of 400 °C.

Solution. For HDPE at 450 °C we calculate the rate constant, k , as

$$k = k_0 e^{(-E_{act}/RT)} = 1.3 \times 10^{11} \exp(-207 \times 10^3 / (8.3145 * 723)) \\ = 1.443 \times 10^{-4} \text{ s}^{-1}$$

We next solve Eq. 11.26 to find the time required to degrade the HDPE sample:

$$-\ln(N/N_0) = kt$$

We now substitute in the values from Table 11.8 to find the time:

$$\begin{aligned} -\ln(420/125,000)/1.443 \times 10^{-4} &= 39,472 \text{ s} \\ &= 10.96 \text{ hours} \end{aligned}$$

A similar procedure is used for PS as we first calculate k :

$$\begin{aligned} k &= k_0 e^{(-E_{\text{act}}/RT)} = 1.3 \times 10^{14} \exp(-219 \times 10^3 / (8.3145 \times 673)) \\ &= 1.3084 \times 10^{-3} \text{ s}^{-1} \end{aligned}$$

and then time:

$$-\ln(3120/280,000)/1.3084 \times 10^{-3} = 3437 \text{ s} = 0.95 \text{ hour}$$

11.5 RENEWABLE POLYMERS AND THEIR PROCESSABILITY

For the purposes of this book, the term “petroleum-derived polymers” refers to polymers produced from nonrenewable crude oil or natural gas. Also, the term “renewable polymers” refers to polymers produced from renewable resources, that is, natural resources that can be replenished within a 100 year time frame. The resources may be replenished naturally or via agricultural techniques. Examples of natural resources are carbohydrates from lignocellulosic biomass, plant oils, and animal fats. Note that the term “renewable” is used interchangeably with the term “sustainable” for the purposes of this book.

There are typically two types of renewable polymers: identical and new-to-world. The identical renewable polymers (sometimes called bioidentical polymers or drop-in renewable polymers) are polymers that have an identical chemical structure to today’s petroleum-derived polymers. Examples of these polymers are bio-PE, bio-PP, and bio-PET. The various properties and processing characteristics of these polymers are identical to those from their petroleum-derived polymer equivalents, and as such the reader is directed to use the information in this book interchangeably between the bioidentical and the petroleum-derived polymers. Braskem, which is presently the largest manufacturer of thermoplastic resins in the Americas, started producing biopolyethylene (Green PE; HDPE and LLDPE) in commercial quantities in September 2010 from sugarcane. The biopolyethylene produced is identical to petroleum-derived polyethylene with the only difference being that it is made from sugar. The technology is based on fermenting sugarcane sugar into ethanol, dehydrating ethanol to ethylene, purifying ethylene to polymer-grade ethylene, and polymerizing the polymer-grade ethylene to polyethylene using conventional technolo-

gies. As such, the biopolyethylene does not require any change in equipment or processes compared to petroleum-derived polyethylene as it gets converted to bottles, films, fibers, and so on. Based on the Braskem literature and LCA, their Green PE captures and sequesters up to 2.5 metric tons of CO₂ from the atmosphere for each ton produced. Note that the respective number for each ton of petroleum-derived polyethylene produced is about 2.5 metric tons of CO₂ emitted. Also, Braskem recently announced that it will introduce to the market Green PP by the end of 2013. Similarly to the Green PE, the Green PP is expected to capture and sequester about 2.3 metric tons CO₂ from the atmosphere for each ton produced, whereas the respective number for each ton of petropolypropylene produced is about 2.5 metric tons of CO₂ emitted.

On the other hand, the new-to-world renewable polymers are polymers that do not have an identical chemical structure to any of today’s petroleum-derived polymers. Examples of these polymers are PLA, PHA and its copolymers, PBS, thermoplastic starch (TPS), poly(ethylene furanoate) (PEF), poly(propylene carbonate) (PPC), and poly(ethylene carbonate) (PEC). The structures of these polymers and their thermal transitions are given in Table 11.9. As we move toward the new “green” economy and away from the petroleum-based economy, it is expected that the new-to-world renewable polymers will dominate the market applications.

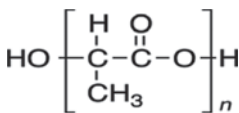
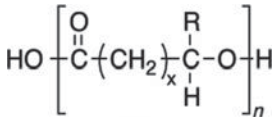
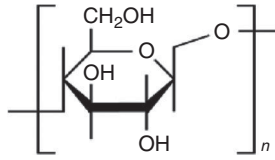
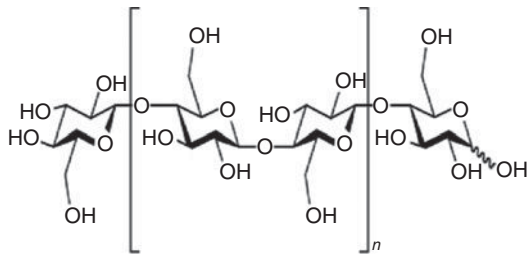
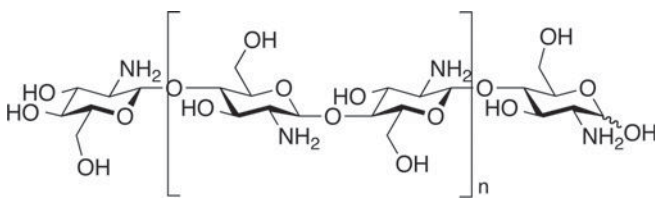
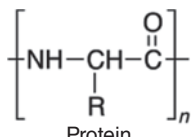
With the desire to reduce the amount of waste remaining in landfills, there is a need to use biodegradable (sometimes also referred to as compostable) polymers in parts of the world where the infrastructure to capture the gases formed exists. Biodegradable polymers come from either renewable resources or petroleum sources. The primary biodegradable polymers from renewable resources are PLA, PHA, TPS, cellulose, chitin, and proteins. The basic structures of these polymers along with some key thermal characteristics are shown in Table 11.9 and will be discussed in more detail in the following section.

There are three principal ways to produce the new-to-world renewable polymers:

1. Make use of natural polymers, which may be modified but remain intact to a large extent (e.g., starch polymers).
2. Produce bio-based monomers by fermentation, which are then polymerized (e.g., polylactic acid).
3. Produce bio-based polymers directly in microorganisms or in genetically modified crops (e.g., PHA).

These synthesis mechanisms are significantly different from those for synthetic polymers and are discussed in more detail in the book by Rudnik (2008).

TABLE 11.9 Renewable Polymers and Their Thermal Transitions

Chemical Structure	T_g (°C)	T_m (°C)	T_c (°C)
 <p>PLA</p>	45–60	150–162	190
 <p>PHA</p>	5–15	168–182	160
 <p>Starch</p>	240–250		300
 <p>Cellulose</p>	—		—
 <p>Chitosan Acetate</p>	—		—
 <p>Protein</p>			180

Biodegradable polymers can also be produced from petroleum sources and are comprised of aliphatic polyesters and copolyesters (e.g., PBS, and poly(butylene succinate adipate)—PBSA), aromatic copolyesters (e.g., poly(butylene adipate terephthalate)—PBAT), poly(ϵ -caprolactone) PCL, polyesteramides (PEA), and poly(vinyl alcohol) (PVA). Further details concerning the synthesis of these polymers can be found in the book by Rudnik (2008). In this section we summarize some of the key properties of these materials

and emphasize some of the issues associated with processing these polymers.

11.5.1 Thermal Stability and Processing of Renewable Polymers

In this section we summarize some of the key temperatures, such as T_m , T_g , and that for the onset of thermal degradation (T_c) for renewable polymers. In general, most of these

TABLE 11.10 Summary of Thermal Properties of Renewable Polymers Based on PLA and PHB

Property	PLA	L-PLA	DL-PLA	PHB
Density, g/cm ³	1.21–1.25	1.24–1.30	1.25–1.27	1.18–1.26
Glass transition, °C	45–60	55–65	50–60	5–15
Melting temperature, °C	150–162	170–200	Amorphous	168–182

materials have temperature limits above which rapid degradation sets in. We refer to this temperature as the critical processing temperature, T_c , above which significant thermal degradation occurs, reducing the polymer molecular weight. Properties such as \bar{C}_p and k do not seem to be readily available.

We start with a brief discussion of PLA because of the wide range of structures and associated properties (Rudnik, 2008). The basic chemical structure of PLA is shown in Table 11.9. PLA is a compostable/biodegradable plastic derived from the polymerization of lactic acid, which is predominantly produced via fermentation of sugar or starch and, to a lesser extent, via chemical catalysis. Lactic acid exists in optically active D- or L-enantiomers, and their polymer versions are noted as PDLA and PLLA, respectively. The copolymer of the two enantiomers is also called PDLLA. The proportion of the enantiomers in PLA determines its properties and the process used to form the PLA articles (e.g., blow molding, injection molding, thermoforming).

The thermal characteristics of PLA, as shown in Table 11.10, are highly dependent on the copolymer ratio of the two enantiomers and, as such, this polymer deserves separate attention as the properties vary widely. Generally, commercial PLA grades are copolymers of poly(L-lactic acid), PLLA, and poly(D,L-lactic acid), PDLLA, which are produced from

L-lactides and D,L-lactides, respectively. The ratio of L- to D,L-enantiomers is known to affect the properties of PLA, such as T_m and the degree of crystallinity. Pure PLA is a semicrystalline polymer with a T_g of about 55 °C (it reaches 60 °C at infinite molecular weight for 100% L-isomer), T_m of about 180 °C, and β transition of about –45 °C. Introduction of stereochemical defects into PLA reduces the melting point, rate of crystallization, and the extent of crystallization of the resulting polymer but has little effect on T_g . After roughly 15% incorporation of mesolactide, the polymer is no longer crystallizable. For example, introduction of mesolactide depresses T_m to 130 °C. The comparison of the glass transition, T_g , and melting, T_m , temperatures of PLA with other thermoplastics is shown in Fig 11.6.

Melt viscosities of high-molecular-weight PLA (about 100,000 g/mol to about 300,000 g/mol) are typically between 500 and 1000 Pa·s at shear rates between 10 and 50 s⁻¹. PLA exhibits a typical pseudoplastic non-Newtonian fluid behavior. The zero-shear viscosity, η_0 , is shown in Figure 11.7 as a function of the weight-average molecular weight, M_w , of poly(L-lactic acid), PLLA, and copolymers of L- and D-lactic acid, PDLLA. In terms of extensional behavior, studies have shown that PLA strain hardens, which is an important characteristic for processing operations (e.g., fiber spinning, blow molding, and film casting). Similarly to the thermal

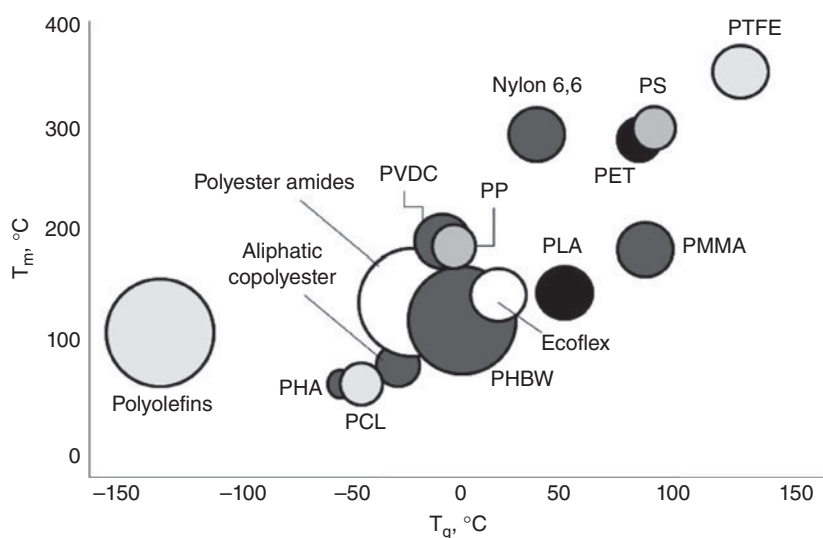


FIGURE 11.6 Comparison of melting and glass transition temperatures of various thermoplastics. (Reprinted with permission of the publisher from Lim et al., 2008.)

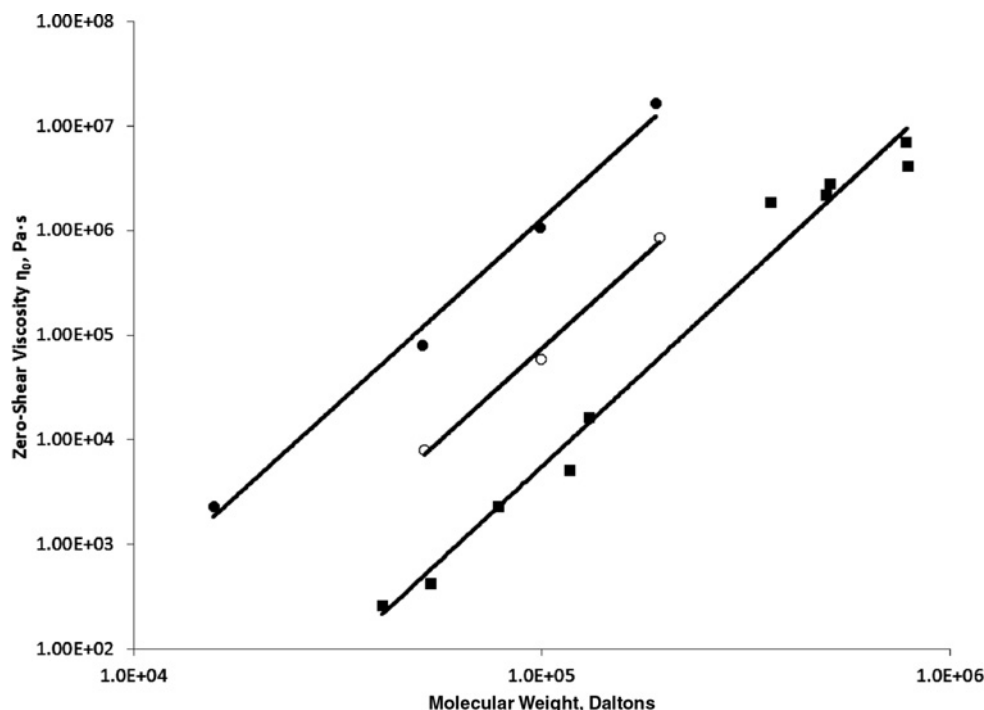


FIGURE 11.7 Comparison of zero-shear viscosity and molecular weight for various PLA materials. squares: PLLA at 180 °C; open circles: Poly(85%L-co-15% D-lactide) at 100 °C; filled circles Poly(85%L-co-15% D-lactide) at 85 °C. (Reprinted with permission of the publisher from Lim et al., 2008.)

behavior described above, the strain hardening is enhanced significantly by the addition of even low amounts of PDLA in PLLA.

Processing of PLA requires attention to its thermal degradation, which relates to the process temperature and residence time. PLA is found to be highly sensitive to heat, especially at temperatures higher than 190 °C (Rudnik, 2008). There may be several reasons for its poor thermal stability: (1) hydrolysis by trace amounts of water catalyzed by hydrolyzed monomer (lactic acid); (2) zipper-like depolymerization, catalyzed by residual polymerization catalyst; (3) oxidative, random main-chain scission; (4) intermolecular transesterification to monomer and oligomeric esters; and (5) intermolecular transesterification resulting in formation of the monomer and oligomeric lactides of low molecular weight. However, with controlled residence time in the processing equipment, higher temperatures can be reached with one commercial PLA system in which processing in the range of 190 to 240 °C is recommended.

Prior to melt processing, PLA requires sufficient drying to prevent hydrolysis, which can reduce the mechanical properties of the PLA article due to reduced molecular weight. NatureWorks LLC, one of the main suppliers of PLA, recommends drying PLA to a maximum of 250 ppm moisture before extrusion. In terms of extrusion equipment, PLA resins can be processed using a conventional extruder with a general purpose screw of 24 to 30 L/D or typical PET extruder with

low-shear screw to minimize resin degradation. Furthermore, the recommended screw compression ratio is 2 to 3, and the extrusion temperature is 200 to 210 °C.

PLA resins can be tailor-made for different fabrication processes, including injection molding, sheet extrusion, blow molding, thermoforming, film forming, and fiber spinning. The key is controlling certain molecular parameters in the process, such as branching, D-isomer content, and molecular weight distribution. Injection molding of heat-resistant PLA materials requires rapid crystallization rates, which can be achieved by PLA that contains less than 1% D-isomer and often with the addition of nucleating agents. Extrusion-thermoforming is optimized at a D-isomer content that does not allow crystallization to occur during the melt processing steps, with 4–8% D-isomer content being the effective range.

PLA bottles are used today with beverages that are not sensitive to oxygen (e.g., water or pasteurized milk). The production of PLA bottles is based on injection stretch blow molding (ISBM). PLA films and sheets, containing between 92% and 98% L-lactide, have been extruded successfully using typical film casting and extrusion equipment. However, because PLA has low elongation, tear, and burst strengths, it is often coextruded to form multilayer structures and enhance its properties. Finally, the high surface energy of PLA allows for better printing than polyolefin films. PLA fibers can be made with either the dry- or melt-spinning process. Commercially, PLA fibers are produced by the melt-spinning process

at 185 to 240 °C and using spinnerets with L/D ratios ranging from 2 to 10.

Poly(hydroxy butyrate) (PHB) has a density in the range of 1.18 g/cm³ (amorphous) to 1.26 g/cm³ (crystalline), as summarized in Table 11.10. PHB is water insoluble and relatively resistant to hydrolytic degradation. This differentiates it from most other currently available renewable plastics, which are water soluble. Mechanical properties of PHB, such as Young's modulus and tensile strength, are similar to those of polypropylene although its elongation to break is markedly lower than that of PP. Due to its high stereoregularity, it is highly crystalline, which makes it stiff and brittle. PHB has a melting point of 180 °C and forms highly crystalline solids, which crystallize slowly and form large spherulitic structures that impart poor mechanical properties in molded plastics and films. Because of its high melting point, PHB is also susceptible to thermal degradation during melt processing by ester pyrolysis of the aliphatic secondary esters of the repeating units. It is thermally unstable during processing and readily degrades at 180 °C and is unstable at temperatures as low as 160 °C. In spite of the degradation issues, with careful control of the thermal conditions PHB can be processed by means of many of the conventional thermoplastic processes, such as extrusion, injection molding, film casting, thermoforming, and fiber spinning (Rudnik, 2008). The rheological properties of four commercial PHA resins are reported in Corre et al. (2012).

The T_g of dry amorphous starch (see Table 11.9 for the structure) is estimated to be in the range of 240–250 °C, but is inaccessible owing to thermal degradation, which leads to the use of plasticizers to allow melt processing (Rudnik, 2008). Native starch is a nonplasticized material because of the intra- and intermolecular hydrogen bonds between hydroxyl groups of the starch molecules. In the presence of a plasticizer the semicrystalline granules of starch are transformed into homogeneous material with hydrogen-bond cleavage between starch molecules leading to the loss of crystallinity. Various industrial processing techniques have been used to prepare starch plastics, including kneading, extrusion, compression molding, and injection molding. Processing temperatures are in the range of 100–200 °C, although care has to be taken at temperatures above 175 °C because of starch's molecular breakdown. Most research has focused on water and glycerol as the most important additives. Several native starches have been processed, such as wheat, rice, corn, waxy maize starch, high amylose corn starch, and potato starch. The dimensions of molded objects from hydrophilic polymers, such as starch, depend on their water content. If precise dimensions are required, processing should be carried out so that products are formed at approximately the equilibrium in-used water content. For potato starch, for example, this means water contents of around 14 wt% for use under ambient conditions. If higher water contents are used in processing, distortion and shrinkage will occur as

the equilibrium water content is naturally achieved after processing. In addition, higher water content can induce more hydrolytic degradation of the starch chains during processing and also gelatinization rather than melt formation. If lower water contents are used, thermal degradation can occur during processing. Rheological measurements in the time sweep mode for thermoplastic wheat starch with 40% glycerol content demonstrate that TPS has excellent thermal stability at 150 °C, but becomes unstable at temperatures above 380 °C. However, it was found that TPS stability is maintained for short time periods at temperatures up to 300 °C.

Cellulose (see Table 11.9 for its structure) cannot be processed by means of techniques used for thermoplastics, but esterification can yield materials suited for thermoplastic processing. A variety of raw materials, such as cotton, recycled paper, wood cellulose, and sugarcane, are used in making cellulose ester biopolymers in powder form. Cellulose esters are easy to extrude and injection mold. Through plasticization of cellulose acetate with environmentally friendly triethyl citrate, they are processable at 170–180 °C, which is below their melting point of 233 °C.

Chitosan (see Table 11.9 for its chitosan acetate structure) possesses an excellent ability to form porous structures. It can be molded into various forms as porous membranes, blocks, tubes, and beads. It also readily forms films and produces materials with very high gas barrier. Chitosan films are prepared by dissolving it in dilute acid and spreading on a flat surface and air-drying to room temperature. It has potential applications in many fields, such as biomedical, wastewater treatment, functional membranes, and flocculation. It has been used in the purification of drinking water and in cosmetics and personal care products. Due to its excellent biological properties, such as biodegradation in the human body, biocompatibility, and immunological, antibacterial, and wound-healing, it also has a variety of medical uses. It has found a potential application as a support material for gene delivery, cell culture, and tissue engineering. Chitosan, like other polysaccharides, is susceptible to a variety of degradation mechanisms, including oxidative/reductive free radical depolymerization and acid-, alkaline- and enzyme-catalyzed hydrolysis. Degradation of polysaccharides occurs via cleavage of the glycosidic bonds. Depolymerization of chitosan is useful in order to control properties, such as viscosity, solubility, and biological activity. Potential mechanisms for temperature-induced degradation are oxidative/reductive degradation and acid-catalyzed degradation. The thermal degradation of chitosan has been studied in nitrogen atmosphere and found to follow a random scission pathway.

Most proteins (see Table 11.9 for their structure) have been used in food sciences, but recently a number of proteins of plant origin have received attention for the production of biodegradable polymers. These proteins include corn zein, wheat gluten, soy protein, and sunflower protein. The major drawback of protein-based plastics, apart from keratin, is

TABLE 11.11 Summary of Characteristics Useful in Processing Compostable Polymer Materials Derived from Petrochemical Resources

Property	Poly(caprolactone) (PCL)	Poly(ester amide) (PEA)	Poly(butylene succinate/adipate) (PBSA)	Poly(butylene adipate-co-terephthalate) (PBSA)	Poly(vinyl alcohol) (PVA)
Density, g/cm ³	1.11	1.05	1.23	1.21	1.19–1.31
Glass transition temperature, °C	–60	–30	–45	–30	85
Melting temperature, °C	60–62	125	92–94	110–115	230

their sensitivity to relative humidity. Soy protein plastics in nitrogen gas were stable up to 300 °C, but in the presence of oxygen the plastic decomposed at 180 °C. Native soy protein was converted into a thermoplastic material in a corotating twin-screw extruder in the presence of 35% water and 10% glycerol (Rudnik, 2008). The extrusion was carried out at temperatures ranging from 70 to 80 °C. Glycerol plasticized wheat gluten sheet was produced by extrusion at the barrel and die set temperature of 130 °C.

The five main types of renewable polymers that can be produced from either petroleum or renewable sources are, in general, melt processable with less stability issues than those obtained from natural resources. We summarize the properties of the main types of polymers in Table 11.11 and present values of T_g and T_m which are important to their processing. The only polymer with melt processing stability issues is PVA, which begins to degrade around 150 °C, which is similar to its melting point. A discussion of the uses, properties, and methods of processing of these polymers is summarized in the book by Rudnik (2008). All of the materials listed in Table 11.11 can be processed by means of conventional processes.

PROBLEMS

A. Applications

11A.1 *Estimation of Energy Gained in Mechanical Recycling with No Loss at the Consumer.* Considering a closed-loop process in which plastic bags are recycled with a loss of 15% at the recycling site (i.e., $F = 0.15$), calculate the energy available per kilogram for reprocessing.

- Assume that the production energy of virgin PE is 40 MJ/kg, $f = 100\%$, and the energy to collect and transport to the reprocessing site and then to the converter is 3 MJ/kg. Disposal of PE bags requires about 1 MJ/kg. From the estimated value of energy available for reprocessing, is recycling energy efficient?
- Redo the calculations but use updated values of energy required for the various sources such as

collection and transport obtained from various websites.

11A.2 *Use of the Logarithmic Mixing Rule.* Redo Example 11.4 using a logarithmic decay in mechanical properties.

11A.3 *Dependence of Mechanical Properties on Molecular Weight.* The mechanical properties of a polymer have been proposed to depend on molecular weight according to the following empirical equation:

$$P = A + B/M_w$$

where A and B are constants. For the tensile strength (MPa) of a polypropylene the coefficients are $A = 38.5$ and $B = -3.58 \times 10^5$. Determine the tensile strength for a PP of $M_w = 160,000$ g/mol.

11A.4 *Estimate the Flow Curve for a Blend of PP and LDPE.* Estimate the flow curve for a blend of PP and LDPE at 190 °C over a shear rate range of 0.1 to 1000 s⁻¹ using Eqs. 11.16 and 11.17. Use the viscosity data for LDPE in Appendix A.1 and the following viscosity for a PP at 190 °C:

$$(\eta \text{ (Pa} \cdot \text{s)})/\dot{\gamma} \text{ (s}^{-1}\text{)} = 9821/0.01; 9500/0.1; \\ 6178/1.0; 2690/10.0; 1181/50; 780/100)$$

11A.5 *Estimation of Energy Gained in Mechanical Recycling with Loss at the Consumer.* Redo Problem 11A.1 with a recycle ratio $f = 0.75$, that is, loss of material at the consumer step.

B. Principles

11B.1 *Amount of Material to Pass by the Consumer.* Obtain the series in Eq. 11.3 which gives the total amount of product to pass by the consumer after a number of recycles.

11B.2 *Series Summation.* Obtain the sum (i.e., Eq. 11.4) for the geometric series given in Eq. 11.3.

11B.3 *Effect of No Losses on Amount of Product Seen by the Consumer.* Following Figure 11.4, obtain the total mass M_p of product passing through the consumer for closed-loop recycling with no losses. With an input of 1 kg of product, determine how much product the consumer sees with a large number of recycles.

11B.4 *Open-Loop Recycling of PET.* Used PET bottles are recycled to provide polymer for textiles fiber production. In this case PET bottles are of higher MW and when recycled are used in an application requiring lower MW PET. Let m be the mass flow rate of PET bottles past the consumer and let M be the mass flow rate of fiber past the consumer. Following the notation in Figure 11.4, let box “1” be the unit operation involved with the production of bottles, box “2” be the consumer of the bottles, and box “3” the unit operation involved with the disposal of the PET bottles. Unit operations “4,” “5,” and “6” are similar operations for the fiber. The recycling unit operation “7” links the two production sequences. In the case of the bottles m kg/yr pass by the consumer while M kg/yr of fiber pass by the consumer. The fraction of bottles being reprocessed is f while the fraction of the bottles listed as solid waste from the reprocessing step is F .

- Construct a flow chart for this process.
- Show that the demand for input material is now reduced by $fm(1 - F)$ relative to the case when no recycling is implemented.
- Show that mass of solid waste generated when recycling is practiced is reduced by $mf(1 - F)$.
- Carry out an energy balance and show that the total energy involved with open-loop recycling is

$$E_s = [m(E_1 + E_2 + E_3) + M(E_4 + E_5 + E_6)] \\ - [fm(E_3 + E_4 - E_7)] \\ + [Ffm(E_3 + E_4 + E_7)]$$

11B.5 *Recycling of Polymer Scrap at the Processing Stage.* Consider the flow sheet in Figure 11.5, which is associated with recycling at the processing step. Let the basis $F_2 = m$, f be the fraction of scrap that is recycled (i.e., $F_4 = fm$), and the fraction of material lost at the regrinding step (i.e., stage “2”) be F (i.e., $F_6 = Ffm$). Find F_1 , F_5 , and F_7 . The recycle ratio is $r = F_7/F_2$. Also find r in terms of f and F .

11B.6 *Age Distribution of Polymer in the Product Steam.* Consider the recycle scheme shown in Figure 11.5

for recycling at the processing stage. Calculate the mass fraction of material with variable number of passes through the process for 2 and 3 recycles (i.e., show how to get entries 2 and 3 in Table 11.2).

11B.7 *Composition of the Product Stream.* Derive Eq. 11.9 for the general case of a variable number of recycling steps when recycling occurs at the processing step.

11B.8 *Pressure Drop Across a Packed Column for a Newtonian Model.* Derive Eq. 11.25 for a Newtonian fluid.

11B.9 *Pressure Drop Across a Packed Column for an Ellis Model.* Derive Eq. 11.25 for an Ellis model.

11B.10 *Radial Flow Through a Porous Disk.* Consider radial flow (see Example 2.4) through a porous disk. Derive an expression similar to that for Eq. 11.25 for a Newtonian fluid and then a power-law fluid.

REFERENCES

- Abbas, K. B., A. B. Knutsson, and S. H. Berglund. 1978. “New Thermoplastics from Old.” *Chemtech*, August, 502–508.
- Aguado, J. and D. P. Serrano. 1999. *Feedstock Recycling of Plastic Wastes* (Royal Society of Chemistry, Cambridge, UK).
- Anastas, P. T. and J. C. Warner. 2000. *Green Chemistry: Theory and Practice* (Oxford University Press, Oxford, UK).
- Anastas, P. T. and J. B. Zimmerman. 2003. “Design Through the 12 Principles of Green Engineering.” *Environ. Sci. Technol.*, **37**(5), 94A–101A.
- Athena Institute. 2006. Life Cycle Inventory of Five Products Produced from Polylactide (PLA) and Petroleum-Based Resins (www.athenasmi.org/projects/docs/Plastic_Products_LAC_Technical_Rpt.pdf).
- Bird, R. B., W. E. Stewart, and E. N. Lightfoot. 2007. *Transport Phenomena* (Wiley, Hoboken).
- Brandrup, J., M. Bittner, W. Michaeli, and G. Menges. 1996. *Recycling and Recovery of Plastics* (Hanser/Gardner, Cincinnati, OH).
- Corre, Y.-M., S. Bruzard, J.-L. Audic, and Y. Grohens. 2012. “Morphology and Functional Properties of Commercial Polyhydroxyalkanoates: A Comprehensive and Comparative Study.” *Polymer Testing*, **31**, 226–235.
- Curran, M. A., Ed. 1996. *Environmental Life-Cycle Assessment* (McGraw Hill, New York).
- EPA. 2010. Municipal Solid Waste Generation, Recycling, and Disposal in the United States: Facts and Figures for 2010. (<http://www.epa.gov/osw/nonhaz/municipal/msw99.htm>).
- Grizzuti, N., G. Buonocore, and G. Lorio. 2000. “Viscous Behavior and Mixing Rules for an Immiscible Model Polymer Blend.” *J. Rheol.*, **44**(1), 149–164.

- Hegberg, B., G. Brenniman, and W. Hallenbeck. 1992. *Mixed Plastics Recycling Technology* (Noyes Data Corporation, Park Ridge, NJ).
- Horne, R., T. Grant, and K. Verghese. 2009. *Life Cycle Assessment: Principles, Practice and Prospects* (CSIRO Publishing, Collingwood, Australia).
- Leidner, J. 1981. *Plastics Waste: Recovery of Economic Value* (Marcel Dekker, New York).
- Lim, L.-T., R. Auras, and M. Rubino. 2008. "Processing Technologies for Poly(lactic acid)." *Prog. Polym. Sci.*, **33**, 820–852.
- Rudnik, E. 2008. *Compostable Polymer Materials* (Elsevier, Oxford, UK).
- Schott, N. R., L. Lak, and G. Smoluk. 1977. "Recycle Calculations in Plasticating Extrusion." *Society of Plastics Engineers Technical Papers*, **32**, 43–46.
- Tabone, M. D., J. J. Cregg, E. J. Beckman, and A. E. Landis. 2010. "Sustainability Metrics: Life Cycle Assessment and Green Design in Polymers." *Environ. Sci. Technol.*, **44**(21), 8264–8269.
- Westerhout, R. W. J., J. Waanders, J. A. M. Kuipers, and W. P. M. van Swajj. 1997. "Kinetics of the Low-Temperature Pyrolysis of Polyethene, Polypropylene, and Polystyrene Modeling, Experimental Determination, and Comparison with Literature Models and Data." *Ind. Eng. Chem. Res.*, **36**, 1955–1964.

NOMENCLATURE

A	Area of the plates	Eq. 2.1	B'	Length	Eq. 6.104
A	Hamaker constant	Eq. 6.173	B_1	Diameter swell	Eq. 7.6
A	Radius of a set of unit cells	Eq. 6.24	B_2	Thickness swell	Eq. 7.7
A	Interface	Eq. 6.36	Bi_r	Radiative Biot number	
A	Cross-sectional area	Eq. 8.4	Bi^{-1}	Reciprocal of Biot number, k/hb	
A_L	Cross-sectional area of land	Eq. 7.27	b	Shear-free flow constant	Eq. 3.2
A_e	Cross-sectional area of entry	Eq. 7.27	b	Crystallographic axis	Eq. 5.172b
A_f	Filled channel cross-sectional area	Eq. 8.119	b	Number of black particles	Eq. 6.1
A_1	Area of polymer	Eq. 5.135	\mathbf{b}	Vector that forms interface A_0	Eq. 6.33
A_2	Area of source	Eq. 5.135	\mathbf{b}'	Vector that forms interface A	Eq. 6.36
A_s	Area across which mass transfer takes place	Eq. 4.99	b	Crystal dimension	Eq. 5.21
A_v	Interfacial area per unit volume	Eq. 6.31	C	Characteristic constant for every polymer; for a number of polymers, $C = 265$ K	Eq. 5.155
A_0	Interfacial area	Eq. 6.35	C	Stress optic coefficient	Eq. 5.177
\mathbf{a}	Acceleration	Eq. 2.68	C	Wetted circumference	Eq. 8.4
a	Coefficient	Eq. 5.165	\mathbf{C}	Cauchy–Green strain tensor	Eq. 6.85
a	Crystallographic axis	Eq. 5.172a	C_A	Concentration of the volatile	Eq. 8.163
a	Radius of a particle	Eq. 6.24	C_e	Equilibrium concentration	Eq. 8.163
a_T	Shifting factor	Eq. 5.3	C_D	Constant	Eq. 5.154
\mathbf{a}	Vector that forms interface A_0	Eq. 6.32	C_D	Hydrodynamic drag coefficient	Eq. 9.53
\mathbf{a}'	Vector which forms interface A	Eq. 6.62	C_i	Molar concentration of i th species	Eq. 4.1
a	Average diameter of crystallites	Eq. 5.148	C_L	Centerline distance	Eq. 8.107
B	Scaling constant relating the fraction of $E(\lambda)$ that reaches the preform	Eq. 5.139	C_w	Measure of adhesion of solids to wall	Eq. 8.4
B	Holdback	Eq. 6.138	\overline{C}_A	Concentration of A in melt reentering melt pool	Eq. 8.165
B	Short axis	Eq. 6.184	\overline{C}_p	Constant pressure heat capacity per unit mass	Eq. 5.16
B	Capillary die swell	Eq. 7.5	$\overline{C}_{p,p}$	Heat capacity of plug	Eq. 8.31
B	Dimensionless internal overpressure	Eq. 9.150	\overline{C}_v	Constant volume heat capacity per unit mass	
B	Slip coefficient	Eq. 10.30			
Br	Dimensionless number	Eq. 8.94			
B_R	Blow (blowup) ratio	Eq. 9.129			

C_1	Constant	Eq. 9.69	F	Combined configuration emissivity factor	Eq. 5.133
C_2	Constant	Eq. 9.69	F	Distribution	Eq. 6.13
C_3	Constant	Eq. 9.69	F	Force at take-up point	Eq. 9.77
C_4	Constant	Eq. 9.69	F	Cohesive fracture	
Ca	Capillary (or Weber) number	Eq. 6.183	F	Drawing force acting on film	Eq. 9.16
c	Coefficient	Eq. 5.165	Fr	Froude number	Eq. 9.69
c	Crystallographic axis	Eq. 5.173	F'	Related to surface geometry and called view factor	Eq. 5.133
\mathbf{c}	Vector perpendicular to A_0	Eq. 6.34	F_Z	Force at frost line	Eq. 9.149
\mathbf{c}'	Vector perpendicular to A	Eq. 6.36	ΔF_n^*	Free energy of the nucleus with n -dimensional growth	Eq. 5.152
D_p	Diameter of extrudate	Eq. 3.89	$\Delta F_n^*/k_B T$	Nucleation factor	Eq. 5.155
D	Characteristic length	Eq. 6.184	F^T	Transpose of deformation gradient tensor	Eq. 6.84
D	Deformation	Eq. 5.127	$F(t)$	Cumulative RTD function, or F function	Eq. 6.115
D	Tube diameter	Eq. 5.127	f	Packing factor	Eq. 5.148
D	Film thickness	Eq. 9.92	f	Degree of fill	Eq. 8.119
D	Half-width of $K(T)$ curve	Eq. 9.92	f_{am}	Amorphous orientation function	Eq. 5.179
D/DT	Material time derivative or time derivative following the fluid motion	Eq. 5.58	f'_w	Coefficient of friction between pellets and wall	Eq. 8.4
D_b	Barrel diameter	Eq. 8.21	$f(t)$	External RTD function	Eq. 6.116
De	Deborah number	Eq. 3.90	G	Shear modulus	Eq. 3.51
D_R	Draw (or draw-down) ratio	Eq. 9.26	G	Pressure gradient	Eq. 7.17
D_s	Screw diameter	Eq. 8.1	G	Linear rate of growth	Eq. 5.152
D^*	Distribution function	Eq. 8.11	G	Shear modulus	Eq. 9.81
\bar{D}	$\frac{1}{2}(D_b + D_s)$	Eq. 8.26	$G(t)$	Mass flow rate	Eq. 5.127
D_{Air}	Diffusivity of solvent in the air stream		Gr	Cumulative RTD function	Eq. 6.133
D_{AB}	Mutual diffusion coefficient	Eq. 4.12	G_{or}	Grashof number	Eq. 4.103
D_w	Diffusivity of moisture	Eq. 4.83	G_{un}	Oriented linear growth rate	Eq. 5.167
D_0	Pre-exponential factor	Eq. 4.53	G_{rf}	Unoriented linear growth rate	Eq. 5.167
D_s	Self-diffusion coefficient	Eq. 4.87	ΔG_{un}	Grashof number evaluated at the film temperature	Eq. 5.130
d	Distance between spheres		ΔG_{mix}	Free energy difference between amorphous and crystalline states under random orientation	Eq. 5.167
d	Diameter of jet	Eq. 9.104	G_0	Change of Gibbs free energy of mixing	Eq. 6.202
dpf	Take-up denier (denier per filament)	Eq. 9.72	G^*	Molecular jump frequency	Eq. 5.152
E	Young's modulus of elasticity		G'	Complex shear modulus	Eq. 3.24
E	Exit geometry	Eq. 7.5	G''	Storage modulus	Eq. 3.24
E	Activation energy	Eq. 9.49	g_c	Loss modulus	Eq. 3.24
EG	Entrance geometry	Eq. 7.5	$g(t)$	Mass of crystalline material	
E_D	Activation energy of diffusion	Eq. 4.53	H	Internal RTD function	Eq. 6.134
$-E_D/RT$	Diffusive transport of molecules in melt	Eq. 5.152	H	Separation distance	Eq. 2.1
E_f	Evaporation at film surface	Eq. 8.162	H	Distance of the capillary to the wheel	Eq. 3.105
E_p	Evaporation at surface of pool	Eq. 8.162	H	Slit height	Eq. 7.30
E_v	Friction loss	Eq. 2.69	H	Hydrodynamic stability	
E_x	Extraction number	Eq. 8.173	$H(t)$	Unit step function	Eq. 3.25
e	Emissivity		H_f	Final film thickness	Eq. 9.131
e	Flight width	Eq. 8.2	H_0	Initial film thickness	Eq. 9.131
erf	Error function	Eq. 4.51	H^l	Film thickness in liquid phase	Eq. 9.170
erfc	Complementary error function	Eq. 4.92			
e_L	Efficiency of mixing	Eq. 6.89			
e_{coh}	Cohesive energy density	Eq. 9.103			
e_1	Emissivity of sheet	Eq. 5.134			
e_2	Emissivity of source	Eq. 5.134			
F	Force	Eq. 2.1			
F	Tensile force	Eq. 3.106			

H^s	Film thickness in the solid phase	Eq. 9.170	k_B	Boltzmann constant	Eq. 5.152
$\Delta \bar{H}_A$	Heat of reaction	Eq. 8.183	k_c	Convective mass transfer coefficient	Eq. 4.98
$\Delta \bar{H}_c$	Heat of crystallization		k_m	Thermal conductivity	Eq. 10.35
$\Delta \bar{H}_f$	Heat of fusion		k_x	Convective mass transfer coefficient	Eq. 4.98
$\Delta \bar{H}_m$	Enthalpy change of melting process	Eq. 5.164	k_c^i	Convective local mass transfer coefficient	Eq. 4.96
$\Delta \bar{H}_c$	Latent heat of crystallization per unit mass	Eq. 9.90	k_x^i	Convective local mass transfer coefficient	p. 98
$\Delta \bar{H}_s$	Molar heat of sorption	Eq. 4.62	k_0	Reaction rate	Eq. 8.182
ΔH_{mix}	Change in enthalpy of mixing	Eq. 6.202	\bar{k}_c	Average mass transfer coefficient	Eq. 4.99
h	Heat transfer coefficient	Eq. 5.122	\bar{k}_x	Average local mass transfer coefficient	Eq. 4.100
h	Wall thickness	Eq. 10.75	L	Length	Eq. 2.15
h_a	Air-sided heat transfer coefficient	Eq. 9.113	L	Long axis of an ellipse	Eq. 6.184
h_L	Thickness of film at chill roll		L_e	Unwound length of devolatilization section	Eq. 8.174
h_m	Total surface of submerged object		L_n	Horizontal length	
h_P	Planck constant		L_s	Lead of screw	Eq. 8.1
h_r	Radiation heat transfer coefficient	Eq. 5.138	L_v	Thickness of plate	
\bar{h}	Average heat transfer coefficient	Eq. 5.124	l_N	Total spiral length	Eq. 6.111
I	Intensity of segregation	Eq. 6.19	M	Degree of mixing	Eq. 6.15
	Intensity diffracted from (hkl) planes which are normal to the i crystallographic axis	Eq. 5.174	M_i	Molecular weight of component i	Eq. 4.4
$I_{hkl}(\phi_{i,z})$			M_t	Amount absorbed or desorbed at time t	Eq. 4.91
$I_s(\lambda)$	Intensity of radiation at surface for a given λ	Eq. 5.140	\bar{M}_w	Weight average molecular weight	Eq. 3.142
I_1	First invariant of the rate of deformation tensor	Eq. 2.60	M_∞	Total amount absorbed or desorbed	Eq. 4.91
I_2	Second invariant of the rate of deformation tensor	Eq. 2.61	M_{A0}, M_{B0}	Initial molecular weight	Eq. 8.184
I_3	Third invariant of the rate of deformation tensor	Eq. 2.62	m	Mass	Eq. 2.68
J	Kinetic crystallizability	Eq. 9.93	\mathbf{m}	Orientation vector	Eq. 6.88
\mathbf{J}_i^*	Molar flux of species i	Eq. 4.11	m	Consistency, power-law parameter	Eq. 2.6
j_D	Mass transfer Chilton–Colburn j -factor	Eq. 4.106	m°	Value of parameter at reference temperature	Eq. 5.12
\mathbf{j}_A	Mass flux of species A	Table 4.3	\dot{m}	Polymer mass flow rate	Eq. 9.3
\mathbf{j}_i^*	Mass flux of species i	Eq. 4.11	m'	Power-law parameter in the Hershel–Bulkley model	Eq. 2.11
K	Related to half-time for crystallization; volume rate of crystallization	Eq. 5.161	\dot{m}_P	Dope output	Eq. 4.124
K	Partition coefficient	Problem 4C.1	N	Number of crystalline units	Eq. 5.148
K	Ratio of compressive stress in horizontal direction to compressive stress in vertical direction	Eq. 8.4	N	Number of samples tested	Eq. 6.3
$k(\lambda)$	Absorption coefficient	Eq. 5.140	N	Number of steps	Eq. 6.71
K_{max}	Maximum of rate–temperature curve	Eq. 9.92	N	Number of revolutions	Eq. 6.111
k_p	Thermal conductivity of plug	Eq. 8.31	N	Angular velocity of screw, rad/s	Eq. 8.23
K_{tot}	Total kinetic energy	Eq. 2.69	N'	Number of turns	Eq. 8.36
k	Rate constant for mixing	Eq. 6.18	N_{min}	Minimal rotational frequency	Eq. 6.220
k	Viscosity temperature coefficient	Eq. 9.105	$N d\theta$	Displacement after N revolutions	Eq. 6.111
			Nu	Nusselt number	Eq. 5.23
			N_δ	Number of striations	Eq. 8.160
			N_A	Molar rate over entire interface	Eq. 4.99
			N_B	Molar rate over entire interface	Eq. 4.99
			ΔN	Birefringence	Eq. 5.177
			ΔN^0	Intrinsic birefringence	p. 144
			ΔN_{cr}^0	Birefringence value of perfectly oriented crystalline region	Eq. 5.189

ΔN_{am}^0	Birefringence value of perfectly oriented amorphous region	Eq. 5.179	p	Isotropic pressure	Eq. 2.71
N_i	Molar flux of species i	Eq. 4.9	p	Number of parallel flights	Eq. 8.128
N_1	Primary normal stress difference	Eq. 3.11	p	Degree of conversion	
Nu_m	Nusselt number for entire surface	Eq. 5.129	p_a	Atmospheric pressure	Eq. 3.102
n	Power-law index	Eq. 2.6	p_0	Dynamic pressure at the die entry	Eq. 2.16
n	Dimensionality of nucleation process which is usually taken as 2.0	Eq. 5.155	p_L	Dynamic pressure at the end of the die	Eq. 2.16
n	Number of species in the system	Eq. 4.2	Q	Volumetric flow	Eq. 2.31
n	Total number of individual groups per structural unit of the macromolecule	Eq. 4.79	Q_c	Calender leakage	
n	Number of particles	Eq. 6.1	Q_d	Drag flow	Eq. 8.100
n^0	Value of power-law index at reference temperature	Eq. 5.13	Q_f	Flight leakage	Eq. 8.132
n'	Power-law parameter in the Hershel–Bulkley model	Eq. 2.11	Q_p	Pressure flow	Eq. 8.100
P	Partial pressure	Eq. 4.61	Q_s	Volumetric flow rate in the extruder	Eq. 8.103
P	Probability	Eq. 6.1	Q_t	Volumetric flow rate through tetrahedron gap	Eq. 8.132
p	Ratio of viscosity of dispersed to continuous phase μ_c/μ_d	Eq. 6.185	q	Flow rate per unit width	Eq. 7.21
P	Perimeter	Eq. 6.206	$q_{\text{nl}s}$	Heat flux in the direction normal to the surface and evaluated at the surface	Eq. 5.122
$P(n)$	Spectral description or power spectrum	Eq. 6.30	q_r	Heat flux due to conduction in the r direction	Eq. 5.43
P_H	Pressure at H	Eq. 8.6	q_z	Heat flux due to conduction in the z direction	Eq. 5.43
P_w	Power input through barrel	Eq. 8.28	R	Radius of capillary	Eq. 3.120
P_0	Pressure at h_0	Eq. 8.10	R	Function	Eq. 9.15
P_1	Initial pressure at $z = 0$	Eq. 8.27	R	Radius of outer cylinder	Eq. 2.19
P_2	Pressure at any down channel distance	Eq. 8.27	κR	Radius of inside cylinder	Eq. 2.19
P_v	Power consumption per unit volume (specific power)	Eq. 6.74	R	Radius of roll	
P_0	Pure solvent vapor pressure	Eq. 4.86	$R(\mathbf{r})$	Correlation function	Eq. 6.20
\bar{P}	Permeability	Eq. 4.71	$R(z)$	Radius of spinning line at every z distance	Eq. 4.117
\bar{P}_0	Pre-exponential factor	Eq. 4.75	Re	Reynolds number	
P_{sc}	Permeability in semicrystalline materials	Eq. 4.81	\dot{R}_A	Net rate of molar production of species A	Eq. 4.21
\bar{P}^*	Pre-exponential permeability factor	Eq. 4.78	R_A	Rate of reaction of species A	Eq. 8.181
Pe_D	Peclet number for diffusion	Eq. 4.105	Re_x	Local Reynold's number	Eq. 5.123
Pr	Prandtl number	Eq. 5.123	R_f	Initial tube outside radius	Eq. 9.129
Pr_f	Prandtl number evaluated at the film temperature	Eq. 5.130	R_f	Constant bubble radius beyond frost line	Eq. 9.149
P_{end}	End pressure	Eq. 3.121	R_g	Universal gas constant	Eq. 4.53
P_{ent}	Entrance pressure	Eq. 3.121	R_H	Mean hydraulic radius	Eq. 7.27
P_{ex}	Exit pressure	Eq. 3.121	R_H	Principal radius of curvature of bubble surface at point of interest	Eq. 9.146
P_H	Hole pressure	Eq. 3.129	R_L	Radius of die at exit	Eq. 2.111
P'_0	Combined pressure at the die entry	Eq. 2.17	R_L	Principal radius of curvature of bubble surface at point of interest	Eq. 9.146
P'_L	Combined pressure at die exit	Eq. 2.17	R_1, R_2	Principal radii of curvature of fiber	Eq. 9.44
P_{tot}	Total pressure	Eq. 3.122	R_s	Radius of outer surface	Eq. 5.144
ΔP	Internal overpressure	Eq. 9.146	R_T	Droplet radius according to Taylor's theory	Eq. 6.198
p	Pressure	Eq. 2.71	R_0	Die radius at entrance	Eq. 2.11
p	Fraction of black particles in entire mixture	Eq. 6.1	R_w	Wheel radius	Eq. 3.135
			Re^*	Air-side Reynold's number	Eq. 9.51

R_{cl}	Cluster radius	Eq. 6.181	T_r	Temperature of radiation source	Eq. 5.133
r	Thickness of a thin cylindrical shell	Eq. 2.16	T_x	Crystallization temperature	Eq. 5.155
r	Distance between molecules	Eq. 4.52	ΔT	$T_0 - T_\infty$	
r	Stoichiometric ratio	Eq. 8.184	ΔT	$T'_m - T_x$ (undercooling)	Eq. 5.155
r	Spherical coordinate	Eq. 10.59	T_b	Barrel temperature	Eq. 8.46
\mathbf{r}	Separation vector	Eq. 6.20	T_p	Temperature in plug	Eq. 8.31
\dot{r}_A	Net rate of mass production of species A	Eq. 4.18	T_0	Temperature of bed entering melting zone	Eq. 8.50
S	Solubility	Eq. 4.61	t	Time after a fluid element leaves the die	Eq. 7.5
S	Segregation		t	Residence time	Eq. 8.139
S	Spinnability		t	Confidence coefficient	Eq. 6.10
S	Shape factor	Eq. 10.36	t_{av}	Process time	Eq. 3.90
Sc	Schmidt number	Eq. 4.102	t_b	Burst time	Eq. 6.194
Sh	Sherwood number	Eq. 4.101	t_f	Fraction of time spent in upper portion of channel	Eq. 8.138
St	Stanton number	Eq. 9.69	t_f	Exposure time	
St_D	Stanton number for diffusion	Eq. 4.104	t_H	Hang time	Eq. 2.127
S_L	Linear scale of segregation	Eq. 6.28	t_{lag}	Time lag	Eq. 4.90
S_V	Volumetric scale of segregation	Eq. 6.29	t_p	Time required for melt to pass through the land	Eq. 7.5
S_w	Weight swell	Eq. 7.9	t_p	Exposure time of melt pool surface	
S_∞	Unconstrained elastic recovery	Eq. 7.3	t_p	Time of rotation of pool	Eq. 8.190
\dot{S}	Source term	Eq. 5.43	t_0	Shortest residence time	Eq. 6.121
\dot{S}	Rate of energy production	Eq. 9.38	\mathbf{t}	Tangential vector	Fig. 9.3
ΔS_{un}	Entropy difference between amorphous and crystalline states under random orientation	Eq. 5.168	t^*	Dimensionless time	Eq. 5.107
ΔS_{mix}	Change in entropy of mixing	Eq. 6.202	t^*	Residence time of fluid element along streamline	
\dot{S}_r	Energy generated per unit volume per unit time by a reacting system	Eq. 8.180	t_b^*	Dimensionless burst time	Eq. 6.196
S_0	Pre-exponential factor	Eq. 4.62	\bar{t}	Mean residence time	Eq. 6.117
S_a	Solubility in amorphous regions	Eq. 4.67	$t_{1/2}$	Half-time	Eq. 4.94
S_{sc}	Solubility in semicrystalline polymers	Eq. 4.67	U	Combined heat transfer coefficient	Eq. 9.40
S	Cross-sectional contact area of rupture plate	Eq. 6.176	u_z	Dimensionless velocity	Eq. 8.87
s	Constant	Eq. 2.42	V	Velocity	Eq. 2.1
s	Scaling factor	Eq. 4.78	V	Air speed	
s	Standard deviation	Eq. 6.8	V	Length of a needle	
s_N^2	Variance of the binomial distribution	Eq. 6.3	V	Take-up speed	Eq. 9.130
\hat{T}	Dimensionless stress	Eq. 9.150	V	Volume of closed C-shaped chamber	Eq. 8.128
T_a	Temperature of the cooling fluid	Eq. 5.81	\bar{V}	Velocity of filament	Eq. 4.123
T_a	Ambient air temperature		V_A	Volume of gas at STP dissolved into polymer per unit volume of solution	Eq. 4.61
T_{abs}	Absolute temperature	Eq. 7.1	V_b	Velocity of barrel surface	
T_f	Film temperature		V_{cell}	Volume of a cell	Eq. 6.24
T_g	Glass transition temperature	Eq. 4.54	V_p	Volume of polymer per unit volume of solution	Eq. 4.61
T^K	Absolute temperature		V_I	Volume of region I	Eq. 6.24
T_m	Melting temperature		V_0	Velocity of plate	Eq. 8.15
T_{max}	Temperature at K_{max}	Eq. 9.92	\bar{V}_i	Molar volume of i	Eq. 4.4
$T_m^{(K)}$	Melting point in Kelvin		$\Delta \bar{V}_m$	Volume change of melting process	Eq. 5.164
T'_m	Thermodynamic equilibrium melting point	Eq. 5.155	v_{ay}	Cooling air cross-flow velocity	Eq. 9.64
T_m^0	Melting point at atmospheric conditions	Eq. 5.164	v_x	Velocity component	Eq. 6.75
T_R	Reference temperature	Eq. 5.16	v_y	Velocity component	Eq. 6.75

ε	Extensional strain	Eq. 6.54	ξ	Dimensionless variable	Eq. 8.87
ε	Void volume fraction or porosity of cluster	Eq. 6.175	ξ_c	Particle position in lower part of channel	Eq. 8.134
ε	Dimensionless parameter	Eq. 9.83	ξ'	Dummy variable of integration	Eq. 2.25
$\dot{\varepsilon}$	Extension rate	Eq. 3.2	π	Permachor	Eq. 4.78
$1/\varepsilon$	Dimensionless force		π_a	Permachor for amorphous materials	Eq. 4.80
ε/k	Lennard-Jones temperature	Table 4.8	π_{ii}	Normal component of total stress tensor	Eq. 9.1
ζ	Dimensionless coordinate	Eq. 5.21	π_{ij}	ij th Component of the total stress tensor	Eq. 3.7
ζ	Dimensionless variable	Eq. 9.63	π_{rr}	r Component of the total stress tensor	Eq. 10.65
η	Shear viscosity	Eq. 2.5	π_{sc}	Permachor for semicrystalline materials	Eq. 4.80
η	$x/\sqrt{4D_{AP}t}$	Eq. 4.51	ρ	Density	Eq. 2.15
$\bar{\eta}_p$	Planar elongational viscosity	Eq. 9.123	ρ	Total mass concentration	Eq. 4.1
η_r	Reduced viscosity	Eq. 5.1	ρ	Density of surrounding medium	
η_0	Zero shear viscosity	Eq. 2.7	ρ_a	Density of amorphous phase	Eq. 5.160
$\eta_0(T)$	Zero shear viscosity at temperature T	Eq. 5.3	ρ_b	Bulk density	Eq. 8.4
$\eta_0(T_0)$	Zero shear viscosity at temperature T_0	Eq. 5.3	ρ_c	Density of spherulitic phase	Eq. 5.160
η_∞	Viscosity as shear rate $\rightarrow \infty$	Eq. 2.8	ρ_c	Density of crystalline plane	Eq. 5.156
η^*	Complex viscosity	Eq. 3.21	ρ_i	Mass concentration	Eq. 4.1
η'	Viscous contribution to dynamic viscosity	Eq. 3.21	$\rho(\mathbf{r})$	Correlation coefficient	Eq. 6.22
η''	Elastic contribution to dynamic viscosity	Eq. 3.21	σ	Stefan–Boltzmann radiation constant	Eq. 5.133
$\bar{\eta}$	Uniaxial elongational viscosity	Eq. 3.36	σ	Liapunov exponent	Eq. 6.205
θ	Dimensionless variable	Eq. 9.63	σ	Potential length, or collision diameter	Eq. 4.52
θ	Dimensionless temperature	Eq. 5.112	$\Delta\sigma$	Difference between the principal stresses	Eq. 5.177
θ	Spherical coordinate angle	Eq. 6.51	σ_e	End surface energy associated with lamellar growth	Eq. 5.156
θ	Circumferential angle	Eq. 8.109	σ_s	Side surface energy	Eq. 5.156
$\bar{\theta}$	Mean temperature	Eq. 5.25	σ_n^2	Variance of the distribution	Eq. 6.2
θ_a	Dimensionless parameter	Eq. 9.64	σ_x	Collision diameter of molecule x	Eq. 4.54
κ	Limit of integration	Eq. 2.25	τ	Dimensionless variable	Eq. 9.63
κR_0	Die inner radius	Eq. 9.180	$\boldsymbol{\tau}$	Stress tensor	Eq. 2.59
λ	Dimensionless variable	Eq. 9.63	τ	Time scale of burst process	Fig. 6.21
λ	$\sim 1/\dot{\gamma}$ for the onset of shear thinning	Eq. 2.8	τ_{cr}	Critical wall shear stress	Eq. 7.1
λ	Wavelength	Eq. 5.139	τ_{ii}	Normal component of extra stress tensor	Eq. 9.1
λ	Relaxation time	Eq. 3.39	τ_{ij}	ij th component of the extra stress tensor	Eq. 3.7
λ_x	Principal elongational ratio	Eq. 6.37	τ_R	Wall shear stress for a capillary	Eq. 7.5
λ_y	Principal elongational ratio	Eq. 6.37	τ_0	Yield stress	Eq. 2.9
λ_z	Principal elongational ratio	Eq. 6.37	τ_0	Tortuosity	Eq. 4.81
λ_0	Dimensionless parameter	Eq. 9.64	τ_w	Wall shear stress for slit flow	Eq. 3.127
λ_0	Elongation ratio	Eq. 6.47	$\tau_{1/2}$	τ_{yx} when $\eta = \frac{1}{2} \eta_0$	Eq. 2.7
λ_0	Characteristic time	Eq. 9.128	τ_{xy}^*	Shear stress (mechanics convention)	Eq. 2.4
μ	Newtonian viscosity	Eq. 2.1	τ_{xx}	Extra normal stress component	Eq. 3.6
μ	Mean value	Eq. 6.9	τ_{yx}	Shear stress, viscous flux of x momentum in the y direction	Eq. 2.3
μ_c	Viscosity of major (continuous) phase		τ_{yy}	Extra normal stress component	Eq. 3.6
μ_d	Viscosity of minor (dispersed) phase				
μ_k	Roots of Bessel function $J_0(\mu_k) = 0$	Eq. 4.121			
μ_0	Bingham model parameter	Eq. 2.9			
ξ	Limit of integration	Eq. 2.25			
ξ	T'_m/T_x	Eq. 5.157			

v	Angular velocity	Eq. 3.134	$\phi(r)$	Intermolecular energy of two molecules r distance apart	Eq. 4.52
ν	Kinematic viscosity		ϕ_s	Helix angle screw surface	Eq. 8.1
v_0	Die extrusion speed	Eq. 9.130	ϕ_{tot}	Total potential energy	Eq. 2.69
Φ	Viscous dissipation term	Eq. 8.47	ϕ_1	Volume fraction of mixture	Eq. 6.203
Φ	Phase shift angle	Eq. 3.19	ϕ_2	Volume fraction of mixture	Eq. 6.203
ϕ_c	Volume fraction of crystallinity	Eq. 5.159	$\hat{\phi}$	Potential energy per unit mass	Eq. 2.69
$\phi_{i,z}$	Angle each orthographic axis makes with the z axis	Eq. 5.174	χ	Interaction parameter of solvent-polymer system	Eq. 4.86
ϕ_c	Equilibrium volume fraction of crystallinity	Eq. 5.159	χ	Confidence coefficient	Eq. 6.11
ϕ_1	Volume fraction matrix	Eq. 5.73	χ_{opt}	Principal optical direction	Eq. 5.185
ϕ_2	Volume fraction second component	Eq. 5.73	χ_{stress}	Principal stress direction	Eq. 5.185
ϕ_∞	Equilibrium volume fraction of crystallinity	Eq. 5.159	Ψ_1	Primary normal stress difference coefficient	Eq. 3.16
ϕ	Spherical coordinate angle	Eq. 6.51	Ψ_2	coefficient	Eq. 3.17
ϕ	Angle between unit normal vector and z -axis	Eq. 9.10	ψ	Stream function	Eq. 6.204
ϕ	Helix angle	Eq. 8.16	ψ	Dimensionless variable	Eq. 8.64
ϕ	Angle of drag		ψ	Flight flank angle	Eq. 8.130
ϕ	Angle of deformed droplet	Eq. 6.188	ψ_{ay}	Dimensionless parameter	Eq. 9.64
ϕ_A	Solvent volume fraction	Eq. 4.86	ψ_L	Dimensionless parameter	Eq. 9.64
ϕ_b	Helix angle at barrel surface		ω	Angular frequency	Eq. 3.18
ϕ_c	Crystallinity of material	Eq. 4.58	ω_i	Mass fraction of i th species	Eq. 4.1
			ω_r	Reduced angular frequency	

APPENDIX A

RHEOLOGICAL DATA FOR SEVERAL POLYMER MELTS

This appendix contains rheological data for a few polymer melts (LDPE, LLDPE, HDPE, mineral filled Nylon 6,6, and PPS).

A.1 LDPE DATA

TABLE A.1 Steady Shear Viscosity and Primary Normal Stress Difference Data for LDPE (NPE 953, Quantum Chemicals)

$\dot{\gamma}$ (s ⁻¹)	η (Pa · s)	η (Pa · s)	η (Pa · s)
	170 °C	180 °C	190 °C
0.010	2.310E + 04	1.530E + 04	1.112E + 04
0.0215	2.215E + 04	1.526E + 04	1.147E + 04
0.0464	2.013E + 04	1.446E + 04	1.129E + 04
0.100	1.693E + 04	1.309E + 04	1.088E + 04
0.215	1.437E + 04	1.124E + 04	9.237E + 03
0.464	1.122E + 04	9.224E + 03	7.538E + 03
1.00	8.192E + 03	7.023E + 03	5.845E + 03

$\dot{\gamma}$ (s ⁻¹)	N_1 (Pa)	N_1 (Pa)	N_1 (Pa)
	170 °C	180 °C	190 °C
0.0100			
0.0215			
0.0464	6.474E + 02	2.486E + 02	1.498E + 02
0.100	1.216E + 03	6.852E + 02	5.568E + 02
0.215	3.717E + 03	2.184E + 03	1.765E + 03
0.464	1.071E + 04	5.051E + 03	5.104E + 03
1.00	2.652E + 04	1.328E + 04	1.306E + 04

TABLE A.2 Dynamic Oscillatory Shear Data for LDPE (NPE 953, Quantum Chemicals) at 170 °C and 190 °C

170 °C			
Frequency (rad/s)	G' (Pa)	G'' (Pa)	η^* (Pa · s)
1.000E-01	5.851E + 02	1.339E + 03	1.461E + 04
2.154E-01	1.189E + 03	2.127E + 03	1.131E + 04
4.642E-01	2.204E + 03	3.326E + 03	8.597E + 03
1.000E + 00	3.895E + 03	5.013E + 03	6.349E + 03
2.154E + 00	6.477E + 03	7.336E + 03	4.542E + 03
4.641E + 00	1.023E + 04	1.027E + 04	3.123E + 03
1.000E + 01	1.556E + 04	1.422E + 04	2.108E + 03
2.154E + 01	2.297E + 04	1.935E + 04	1.394E + 03
4.641E + 01	3.285E + 04	2.585E + 04	9.008E + 02
1.000E + 02	4.539E + 04	3.366E + 04	5.651E + 02

190 °C			
Frequency (rad/s)	G' (Pa)	G'' (Pa)	η^* (Pa · s)
1.000E-01	3.291E + 02	9.073E + 02	9.651E + 03
2.154E-01	7.283E + 02	1.535E + 03	7.888E + 03
4.642E-01	1.456E + 03	2.525E + 03	6.280E + 03
1.000E + 00	2.644E + 03	3.877E + 03	4.693E + 03
2.154E + 00	4.589E + 03	5.785E + 03	3.428E + 03
4.641E + 00	7.565E + 03	8.476E + 03	2.448E + 03
1.000E + 01	1.190E + 04	1.193E + 04	1.685E + 03
2.154E + 01	1.807E + 04	1.665E + 04	1.141E + 03
4.641E + 01	2.661E + 04	2.260E + 04	7.523E + 02
1.000E + 02	3.765E + 04	2.984E + 04	4.804E + 02

TABLE A.3 Capillary Rheometer Data for LDPE (NPE-953, Quantum Chemicals) at 170 °C

$L/D = 12.5$			
$\dot{\gamma}_a$ (s ⁻¹)	τ_a (Pa)	$\dot{\gamma}_c$ (s ⁻¹)	τ_c (Pa)
0.37504E+02	0.66010E+05	0.56246E+02	0.64136E+05
0.75007E+02	0.88013E+05	0.11249E+03	0.65933E+05
0.11251E+03	0.10617E+06	0.16874E+03	0.74074E+05
0.22502E+03	0.14082E+06	0.33747E+03	0.96463E+05
0.37504E+03	0.17603E+06	0.56246E+03	0.13049E+06
0.75007E+03	0.24204E+06	0.11249E+04	0.14130E+06
0.11251E+04	0.26844E+06	0.16874E+04	0.17624E+06
0.22502E+04	0.39166E+06	0.33747E+04	0.23477E+06
0.37504E+04	0.44006E+06	0.56246E+04	0.25862E+06
$L/D = 37.1$			
$\dot{\gamma}_a$ (s ⁻¹)	τ_a (Pa)	$\dot{\gamma}_c$ (s ⁻¹)	τ_c (Pa)
0.37504E+02	0.48188E+05	0.54467E+02	0.47556E+05
0.75007E+02	0.63756E+05	0.10893E+03	0.56317E+05
0.11251E+03	0.74135E+05	0.16340E+03	0.63322E+05
0.22502E+03	0.96375E+05	0.32680E+03	0.81430E+05
0.37504E+03	0.11584E+06	0.54467E+03	0.10049E+06
0.75007E+03	0.17422E+06	0.10893E+04	0.14028E+06
0.11251E+04	0.17978E+06	0.16340E+04	0.14871E+06
0.22502E+04	0.24464E+06	0.32680E+04	0.19179E+06
0.37504E+04	0.29191E+06	0.54467E+04	0.23077E+06
$L/D = 75.1$			
$\dot{\gamma}_a$ (s ⁻¹)	τ_a (Pa)	$\dot{\gamma}_c$ (s ⁻¹)	τ_c (Pa)
0.37504E+02	0.54935E+05	0.55277E+02	0.54623E+05
0.75007E+02	0.64091E+05	0.11055E+03	0.60416E+05
0.11251E+03	0.73246E+05	0.16583E+03	0.67905E+05
0.22502E+03	0.95220E+05	0.33166E+03	0.87837E+05
0.37504E+03	0.12086E+06	0.55277E+03	0.11328E+06
0.75007E+03	0.15748E+06	0.11055E+04	0.14071E+06
0.11251E+04	0.17579E+06	0.16583E+04	0.16045E+06
0.22502E+04	0.23622E+06	0.33166E+04	0.21011E+06
0.37504E+04	0.27284E+06	0.55277E+04	0.24264E+06

Source: Data from R. H. Moynihan. 1990. *Flow Stability of Linear Low Density Polyethylene at Polymer and Metal Interfaces* (Ph.D. Thesis, Virginia Tech, Blacksburg, VA).

TABLE A.4 Extensional Data for LDPE (NPE 953, Quantum Chemicals) at 170 °C

$\dot{\epsilon} = 0.020$ s ⁻¹			
Time (S)	Strain	$\bar{\eta}$ (Pa · s)	σ (Pa)
0.00000E+00	0.00000E+00	0.00000E+00	0.00000E+00
0.50000E+01	0.10000E+00	0.39900E+05	0.79800E+03
0.12500E+02	0.25000E+00	0.53850E+05	0.10770E+04
0.20000E+02	0.40000E+00	0.61050E+05	0.12210E+04
0.27500E+02	0.55000E+00	0.65200E+05	0.13040E+04
0.35500E+02	0.71000E+00	0.72450E+05	0.14490E+04
0.43000E+02	0.86000E+00	0.76500E+05	0.15300E+04
0.50500E+02	0.10100E+01	0.78200E+05	0.15640E+04
0.58000E+02	0.11600E+01	0.81550E+05	0.16310E+04
0.65500E+02	0.13100E+01	0.83600E+05	0.16720E+04
0.73000E+02	0.14600E+01	0.85350E+05	0.17070E+04
0.80500E+02	0.16100E+01	0.93650E+05	0.18730E+04
0.88500E+02	0.17700E+01	0.98050E+05	0.19610E+04
0.96000E+02	0.19200E+01	0.94550E+05	0.18910E+04
$\dot{\epsilon} = 0.053$ s ⁻¹			
Time (s)	Strain	$\bar{\eta}$ (Pa · s)	σ (Pa)
0.00000E+00	0.00000E+00	0.00000E+00	0.00000E+00
0.28302E+01	0.15000E+00	0.37679E+05	0.19970E+04
0.58491E+01	0.31000E+00	0.50811E+05	0.26930E+04
0.88679E+01	0.47000E+00	0.57604E+05	0.30530E+04
0.11887E+02	0.63000E+00	0.65792E+05	0.34870E+04
0.14906E+02	0.79000E+00	0.72755E+05	0.38560E+04
0.17925E+02	0.95000E+00	0.76774E+05	0.40690E+04
0.20943E+02	0.11100E+01	0.83415E+05	0.44210E+04
0.23962E+02	0.12700E+01	0.91453E+05	0.48470E+04
0.26981E+02	0.14300E+01	0.96755E+05	0.51280E+04
0.30000E+02	0.15900E+01	0.10666E+06	0.56530E+04
0.33019E+02	0.17500E+01	0.11323E+06	0.60010E+04
0.36038E+02	0.19100E+01	0.12523E+06	0.66370E+04
0.39057E+02	0.20700E+01	0.14026E+06	0.74340E+04
0.42075E+02	0.22300E+01	0.15343E+06	0.81320E+04
$\dot{\epsilon} = 0.200$ s ⁻¹			
Time (s)	Strain	$\bar{\eta}$ (Pa · s)	σ (Pa)
0.00000E+00	0.00000E+00	0.00000E+00	0.00000E+00
0.70000E+00	0.14000E+00	0.20565E+05	0.41130E+04
0.14500E+01	0.29000E+00	0.30115E+05	0.60230E+04
0.22000E+01	0.44000E+00	0.37800E+05	0.75600E+04
0.29500E+01	0.59000E+00	0.44105E+05	0.88210E+04
0.37000E+01	0.74000E+00	0.52050E+05	0.10410E+05
0.44500E+01	0.89000E+00	0.59800E+05	0.11960E+05
0.52000E+01	0.10400E+01	0.68650E+05	0.13730E+05
0.59500E+01	0.11900E+01	0.79300E+05	0.15860E+05
0.67000E+01	0.13400E+01	0.89700E+05	0.17940E+05
0.74500E+01	0.14900E+01	0.10190E+06	0.20380E+05
0.82000E+01	0.16400E+01	0.11495E+06	0.22990E+05
0.89500E+01	0.17900E+01	0.12975E+06	0.25950E+05
0.97500E+01	0.19500E+01	0.14495E+06	0.28990E+05

Source: Data from S. A. White. 1987. *The Planar Entry Flow Behavior of Polymer Melts: An Experimental and Numerical Analysis* (Ph.D. Thesis, Department of Chemical Engineering, Virginia Tech, Blacksburg, VA).

A.2 HDPE DATA

TABLE A.5 Steady Shear Data for HDPE (EMN 885, Phillips Petroleum Co.)

$\dot{\gamma}$ (s ⁻¹)	η (Pa · s)	η (Pa · s)	η (Pa · s)
	170 °C	180 °C	190 °C
0.100	7.801E+02	6.649E+02	5.575E+02
0.2154	7.608E+02	6.657E+02	5.390E+02
0.4641	7.049E+02	6.111E+02	4.846E+02
1.00	6.396E+02	5.689E+02	4.561E+02
2.154	5.908E+02	5.138E+02	4.139E+02
4.641	5.207E+02	4.535E+02	4.267E+02
10.0	4.336E+02	3.922E+02	3.705E+02

$\dot{\gamma}$ (s ⁻¹)	N_1 (Pa)	N_1 (Pa)	N_1 (Pa)
	170 °C	180 °C	190 °C
0.464	1.161E+02	9.379E+01	8.240E+01
1.00	2.917E+02	2.165E+02	2.075E+02
2.15	7.430E+02	5.089E+02	4.743E+02
4.64	1.608E+03	1.423E+03	1.098E+03
10.0	3.658E+03	3.052E+03	2.640E+03

TABLE A.6 Dynamic Oscillatory Shear Data for HDPE (EMN 885, Phillips Petroleum Co.)

170 °C			
ω (rad/s)	G' (Pa)	G'' (Pa)	η^* (Pa · s)
1.000E-01	1.171E+01	1.044E+02	1.050E+03
2.154E-01	4.193E+01	1.523E+02	7.330E+02
4.642E-01	5.541E+01	3.120E+02	6.826E+02
1.000E+00	1.267E+02	6.364E+02	6.489E+02
2.154E+00	2.819E+02	1.165E+03	5.566E+02
4.641E+00	5.850E+02	2.238E+03	4.984E+02
1.000E+01	1.290E+03	4.173E+03	4.368E+02
2.154E+01	2.746E+03	7.680E+03	3.786E+02
4.641E+01	5.586E+03	1.370E+04	3.189E+02
1.000E+02	1.095+04	2.348E+04	2.591E+02

180 °C			
ω (rad/s)	G' (Pa)	G'' (Pa)	η^* (Pa · s)
1.000E-01	1.359E+01	6.945E+01	7.077E+02
2.154E-01	2.167E+01	1.366E+02	6.420E+02
4.642E-01	2.567E+01	2.642E+02	5.718E+02
1.000E+00	1.146E+02	5.296E+02	5.418E+02
2.154E+00	2.196E+02	1.044E+03	4.951E+02
4.641E+00	5.022E+02	1.986E+03	4.413E+02
1.000E+01	1.122E+03	3.696E+03	3.862E+02
2.154E+01	2.367E+03	6.841E+03	3.360E+02
4.641E+01	4.859E+03	1.227E+04	2.843E+02
1.000E+02	9.585E+03	2.107E+04	2.314E+02

(continued)

TABLE A.6 (Continued)

190 °C			
ω (rad/s)	G' (Pa)	G'' (Pa)	η^* (Pa · s)
1.000E-01	8.319E+00	4.105E+01	4.189E+02
2.154E-01	1.635E+01	1.141E+02	5.351E+02
4.642E-01	3.233E+01	2.151E+02	4.687E+02
1.000E+00	7.965E+01	4.210E+02	4.284E+02
2.154E+00	1.711E+02	8.179E+02	3.879E+02
4.641E+00	3.893E+02	1.581E+03	3.508E+02
1.000E+01	8.810E+02	3.017E+03	3.143E+02
2.154E+01	1.872E+03	5.602E+03	2.742E+02
4.641E+01	3.854E+03	1.013E+04	2.335E+02
1.000E+02	7.679E+03	1.759E+04	1.920E+02

A.3 LLDPE DATA

TABLE A.7 Steady Shear Data for LLDPE (NTA 101, Mobil) at 170 °C

$\dot{\gamma}$ (s ⁻¹)	η (Pa · s)	N_1 (Pa)
0.1000E-01	0.1334E+05	0.7010E+00
0.2154E-01	0.1321E+05	0.4717E+01
0.4641E+01	0.1296E+05	0.9272E+02
0.1000E+00	0.1250E+05	0.4520E+03
0.2154E+00	0.1168E+05	0.1444E+04
0.4641E+00	0.1061E+05	0.3925E+04
0.1000E+01	0.8871E+04	0.9759E+04
0.2154E+01	0.6962E+04	0.2043E+05

Source: Data from R. H. Moynihan. 1990. *Flow Stability of Linear Low Density Polyethylene at Polymer and Metal Interfaces* (Ph.D. Thesis, Virginia Tech, Blacksburg, VA).

TABLE A.8 Dynamic Shear Data for LLDPE (NTA 101, Mobil) at 170 °C

ω (rad/s)	η^* (Pa · s)	G' (Pa)
0.1000E+00	0.1213E+05	0.1709E+03
0.1585E+00	0.1155E+05	0.3031E+03
0.2512E+00	0.1102E+05	0.5204E+03
0.3981E+00	0.1042E+05	0.8915E+03
0.6310E+00	0.9781E+04	0.1500E+04
0.1000E+01	0.9109E+04	0.2514E+04
0.1585E+01	0.8374E+04	0.4137E+04
0.2512E+01	0.7613E+04	0.6707E+04
0.3981E+01	0.6833E+04	0.1069E+05
0.6310E+01	0.6046E+04	0.1666E+05
0.1000E+02	0.5265E+04	0.2535E+05
0.1585E+02	0.4508E+04	0.3760E+05
0.2512E+02	0.3794E+04	0.5433E+05
0.3981E+02	0.3140E+04	0.7653E+05
0.6310E+02	0.2551E+04	0.1049E+06
0.1000E+03	0.2026E+04	0.1394E+06

Source: Data from R. H. Moynihan. 1990. *Flow Stability of Linear Low Density Polyethylene at Polymer and Metal Interfaces* (Ph.D. Thesis, Virginia Tech, Blacksburg, VA).

TABLE A.9 Capillary Data for LLDPE (NTA 101, Mobil) at 170 °C

<i>L/D = 12.5</i>			
$\dot{\gamma}_a$ (s ⁻¹)	τ_a (Pa)	$\dot{\gamma}_c$ (s ⁻¹)	τ_c (Pa)
0.37504E+02	0.14082E+06	0.77567E+02	0.15929E+06
0.75007E+02	0.19803E+06	0.15513E+03	0.23295E+06
0.11251E+03	0.23983E+06	0.23270E+03	0.28144E+06
0.22502E+03	0.31685E+06	0.46540E+03	0.28939E+06
0.37504E+03	0.37846E+06	0.77567E+03	0.29303E+06
0.75007E+03	0.45327E+06	0.15513E+04	0.29107E+06
0.11251E+04	0.48847E+06	0.23270E+04	0.39236E+06
0.22502E+04	0.55888E+06	0.46540E+04	0.40904E+06
0.37504E+04	0.73491E+06	0.77567E+04	0.45584E+06
<i>L/D = 37.1</i>			
$\dot{\gamma}_a$ (s ⁻¹)	τ_s (Pa)	$\dot{\gamma}_c$ (s ⁻¹)	τ_c (Pa)
0.37504E+02	0.12974E+06	0.65226E+02	0.13596E+06
0.75007E+02	0.16680E+06	0.13045E+03	0.17857E+06
0.11251E+03	0.20387E+06	0.19568E+03	0.21789E+06
0.22502E+03	0.26503E+06	0.39136E+03	0.25578E+06
0.37504E+03	0.32249E+06	0.65226E+03	0.29370E+06
0.75007E+03	0.38179E+06	0.13045E+04	0.32714E+06
0.11251E+04	0.41515E+06	0.19568E+04	0.38277E+06
0.22502E+04	0.48188E+06	0.39136E+04	0.43139E+06
0.37504E+04	0.53933E+06	0.65226E+04	0.44530E+06
<i>L/D = 75.1</i>			
$\dot{\gamma}_a$ (s ⁻¹)	τ_a (Pa)	$\dot{\gamma}_c$ (s ⁻¹)	τ_c (Pa)
0.37504E+02	0.14283E+06	0.69768E+02	0.14591E+06
0.75007E+02	0.19593E+06	0.13954E+03	0.20175E+06
0.11251E+03	0.23805E+06	0.20930E+03	0.24498E+06
0.22502E+03	0.27467E+06	0.41861E+03	0.27010E+06
0.37504E+03	0.30763E+06	0.69768E+03	0.29342E+06
0.75007E+03	0.33876E+06	0.13954E+04	0.31177E+06
0.11251E+04	0.40285E+06	0.20930E+04	0.38686E+06
0.22502E+04	0.44680E+06	0.41861E+04	0.42186E+06
0.37504E+04	0.49624E+06	0.69768E+04	0.44979E+06

TABLE A.10 Extensional Data for LLDPE (NTA 101, Mobil) at 170 °C

$\dot{\epsilon} = 0.200$ s ⁻¹			
Time (s)	Strain	$\bar{\eta}$ (Pa · s)	σ (Pa)
0.00000E+00	0.00000E+00	0.00000E+00	0.00000E+00
0.80000E+00	0.16000E+00	0.33755E+05	0.67510E+04
0.15500E+01	0.31000E+00	0.36615E+05	0.73230E+04
0.24000E+01	0.48000E+00	0.38480E+05	0.76960E+04
0.31500E+01	0.63000E+00	0.39485E+05	0.78970E+04
0.39000E+01	0.78000E+00	0.38780E+05	0.77560E+04
0.47000E+01	0.94000E+00	0.40495E+05	0.80990E+04
0.54500E+01	0.10900E+01	0.39770E+05	0.79540E+04
0.62500E+01	0.12500E+01	0.40085E+05	0.80170E+04
0.70000E+01	0.14000E+01	0.40045E+05	0.80090E+04
0.77500E+01	0.15500E+01	0.40805E+05	0.81610E+04
0.85500E+01	0.17100E+01	0.40295E+05	0.80590E+04
0.93000E+01	0.18600E+01	0.39560E+05	0.79120E+04
0.10050E+02	0.20100E+01	0.39670E+05	0.79340E+04

(continued)

TABLE A.10 (Continued)

$\dot{\epsilon} = 0.053$ s ⁻¹			
Time (s)	Strain	$\bar{\eta}$ (Pa · s)	σ (Pa)
0.00000E+00	0.00000E+00	0.00000E+00	0.00000E+00
0.30189E+01	0.16000E+00	0.37962E+05	0.20120E+04
0.60377E+01	0.32000E+00	0.33245E+05	0.17620E+04
0.90566E+01	0.48000E+00	0.38943E+05	0.20640E+04
0.12075E+02	0.64000E+00	0.39321E+05	0.20840E+04
0.15094E+02	0.80000E+00	0.39000E+05	0.20670E+04
0.18113E+02	0.96000E+00	0.38019E+05	0.20150E+04
0.21132E+02	0.11200E+01	0.37925E+05	0.20100E+04
0.24151E+02	0.12800E+01	0.39642E+05	0.21010E+04
0.27170E+02	0.14400E+01	0.37189E+05	0.19710E+04
0.30189E+02	0.16000E+01	0.35925E+05	0.19040E+04
0.33208E+02	0.17600E+01	0.35226E+05	0.18670E+04
0.36226E+02	0.19200E+01	0.34358E+05	0.18210E+04
$\dot{\epsilon} = 0.020$ s ⁻¹			
Time (s)	Strain	$\bar{\eta}$ (Pa · s)	σ (Pa)
0.00000E+00	0.00000E+00	0.00000E+00	0.00000E+00
0.75000E+01	0.15000E+00	0.31550E+05	0.63100E+03
0.15000E+02	0.30000E+00	0.32750E+05	0.65500E+03
0.22500E+02	0.45000E+00	0.33900E+05	0.67800E+03
0.30000E+02	0.60000E+00	0.38600E+05	0.77200E+03
0.38000E+02	0.76000E+00	0.40300E+05	0.80600E+03
0.45500E+02	0.91000E+00	0.39550E+05	0.79100E+03
0.53000E+02	0.10600E+01	0.39400E+05	0.78800E+03
0.60500E+02	0.12100E+01	0.36950E+05	0.73900E+03
0.68000E+02	0.13600E+01	0.42550E+05	0.85100E+03
0.75500E+02	0.15100E+01	0.42450E+05	0.84900E+03
0.83000E+02	0.16600E+01	0.38500E+05	0.77000E+03
0.90500E+02	0.18100E+01	0.39500E+05	0.79000E+03
0.98500E+02	0.19700E+01	0.37900E+05	0.75800E+03

A.4 NYLON 6,6 DATA

TABLE A.11 Steady Shear Cone-and-Plate Data for Mineral-Filled Nylon 6,6 at 285 °C

$\dot{\gamma}$ (s ⁻¹)	η (Pa · s)	N_1 (Pa)
3.981E-02	2.978E+03	
6.310E-02	2.642E+03	
1.000E-01	2.046E+03	
1.585E-01	1.680E+03	
2.512E-01	1.350E+03	
3.981E-01	1.014E+03	
6.310E-01	8.116E+02	9.482E+01
1.000E+00	6.369E+02	9.311E+01
1.585E+00	5.232E+02	8.648E+01
2.512E+00	4.359E+02	7.696E+01
3.981E+00	3.861E+02	7.101E+01
6.310E+00	3.444E+03	8.464E+01
1.000E+01	3.105E+02	1.257E+02
1.585E+01	2.703E+03	3.937E+02
2.512E+01	2.067E+02	5.958E+02
3.982E+01	1.505E+02	1.437E+03
6.310E+01	1.557E+02	3.284E+03

Source: Data from R. Pisipati. 1983. *A Rheological Characterization of Particulate and Fiber Filled Nylon 6,6 Melts and Its Application to Weldline Formation in Molded Parts* (Ph.D. Thesis, Department of Chemical Engineering, Virginia Tech, Blacksburg, VA).

A.5 PPS DATA

TABLE A.12 Dynamic Oscillatory Shear Data for PPS (Ryton, Phillips Petroleum Co.)

Temperature = 293 °C			
ω (rad/s)	G' (Pa)	G'' (Pa)	η^* (Pa · s)
0.1	45	170	1759
0.32	89	481	1529
1.00	248	1406	1428
3.16	1008	3508	1155
10.00	2277	8373	868
31.62	10100	18250	660
100.00	24660	35740	434
Temperature = 330 °C			
ω (rad/s)	G' (Pa)	G'' (Pa)	η^* (Pa · s)
0.1	13	89	899
0.32	39	238	754
0.46	50	360	790
1.00	89	790	795
2.15	230	1654	777
3.16	394	1974	637
6.81	1105	4366	661
10.00	1500	5150	536
21.54	4055	10680	530
31.62	5267	12330	424
68.13	12060	23310	385
100.00	14690	25930	298

TABLE A.13 Shift Factors for PPS for a Reference Temperature of 330 °C

Temperature (°C)	Shift Factor
330	1.000
312	1.307
293	1.708
273	2.918
253	4.546

APPENDIX B

PHYSICAL PROPERTIES AND FRICTION COEFFICIENTS FOR SOME COMMON POLYMERS IN THE BULK STATE

TABLE B.1

Polymer	ρ_b (kg/m ³)	k_b (W/m·K)	α_b (m ² /s)	Friction Coefficient on Steel Temperature (°C)		
				20	60	100
LDPE	500	0.346	9.29×10^{-8}	0.34	0.40	0.32
PVC	620	0.156	9.55×10^{-8}	0.43	0.46	0.76
Nylon 66				0.25		
Teflon	1000	0.208	9.55×10^{-8}	0.04	0.04	0.04
PS				0.45		

APPENDIX C

THERMAL PROPERTIES OF MATERIALS

TABLE C.1 Thermal–Physical Properties of Polyethyleneterephthalate

Parameter	Value	Units
T	540	K
T_g	353	K
ΔH_c	30	cal/gm
ρ_m	1.335	g/cm ³
ρ_c	1.455	g/cm ³
b_0	4.04×10^{-8}	cm
a_0	5.76×10^{-8}	cm
σ	5	ergs/cm ²
σ_e	40	ergs/cm ²
$\sigma\sigma_e$	200	ergs ² /cm ⁴
ϕ_∞	0.34	

Source: Data from D. G. Bright. 1975. *Quantitative Studies of Polymer Crystallization Under Non-Isothermal Conditions* (Ph.D. Thesis, Georgia Institute of Technology, 1975).

TABLE C.2 Thermal–Physical Properties of High Density Polyethylene

Parameter	Value	Units
T	415	K
T_g	231	K
ΔH_c	68.4	cal/gm
ρ_m	0.8838	g/cm ³
ρ_c	1.0075	g/cm ³
b_0	4.13×10^{-8}	cm
a_0	4.46×10^{-8}	cm
σ	10.25	ergs/cm ²
σ_e	57.0	ergs/cm ²
$\sigma\sigma_e$	584.0	ergs ² /cm ⁴
ϕ_∞	0.72	

Source: Data from D. G. Bright. 1975. *Quantitative Studies of Polymer Crystallization Under Non-Isothermal Conditions* (Ph.D. Thesis, Georgia Institute of Technology, 1975).

TABLE C.3 Thermal–Physical Properties of Polycaprolactam, Nylon 6

Parameter	Value	Units
T	505	K
T_g	323	K
ΔH_c	45.3	cal/gm
ρ_m	1.0840	g/cm ³
ρ_c	1.2255	g/cm ³
b_0	8.62×10^{-8}	cm
a_0	8.83×10^{-8}	cm
σ	8	ergs/cm ²
σ_e	60	ergs/cm ²
$\sigma\sigma_e$	480	ergs ² /cm ⁴
ϕ_∞	0.31	

Source: Data from D. G. Bright. 1975. *Quantitative Studies of Polymer Crystallization Under Non-Isothermal Conditions* (Ph.D. Thesis, Georgia Institute of Technology, 1975).

TABLE C.4 Thermal–Physical Properties of Poly(hexamethylene adipamide), Nylon 6,6

Parameter	Value	Units
T	545	K
T_g	330	K
ΔH_c	46.6	cal/gm
ρ_a	1.07	g/cm ³
ρ_c	1.266	g/cm ³
b_0	4.77×10^{-8}	cm
a_0	4.04×10^{-8}	cm
σ	8.5	ergs/cm ²
σ_e	42.35	ergs/gm ²
$\sigma\sigma_e$	360	ergs ² /cm ⁴
ϕ_∞	0.32	

Source: Data from D. G. Bright. 1975. *Quantitative Studies of Polymer Crystallization Under Non-Isothermal Conditions* (Ph.D. Thesis, Georgia Institute of Technology, 1975).

TABLE C.5 Crystallization Parameters for Polyetheretherketone (PEEK)

Crystal dimension	$b_0 = 4.7 \text{ \AA}$
Side surface energy	$\sigma_s = 38 \text{ ergs/cm}^2$
End surface energy	$\sigma_e = 49 \text{ ergs/cm}^2$
Heat of fusion	$\Delta \bar{H}_f = 130 \text{ J/g}$
Thermodynamic melting point	$T'_m = 395 \text{ }^\circ\text{C}$
Glass transition temperature	$T_g = 144 \text{ }^\circ\text{C}$
Activation energy	$E_D = 2000 \text{ cal/mol}$
Crystal density	$\rho_c = 1.40 \text{ g/cm}^3$
Amorphous density	$\rho_a = 1.263 \text{ g/cm}^3$
ϕ_∞	0.33

Source: Data from D. J. Blundell and B. N. Osborn. 1983. "The Morphology of Poly(aryl-ether-ether-ketone)." *Polymer*, **24**, 753.

TABLE C.6 Properties of Water (Saturated Liquid)

T (°C)	C_p (kJ/kg · °C)	ρ (kg/m ³)	μ (kg/m · s)	k (W/m · °C)	Pr	$\frac{g\beta \rho^2 c_p}{\mu k}$ (1/m ³ · °C)
0.0	4.225	999.8	1.79×10^{-3}	0.566	13.25	1.91×10^9
4.44	4.208	999.8	1.55	0.575	11.35	6.34×10^9
10.0	4.195	999.2	1.31	0.585	9.40	1.08×10^{10}
15.56	4.186	998.6	1.12	0.595	7.88	1.46×10^{10}
21.11	4.179	997.4	9.8×10^{-4}	0.604	6.78	1.91×10^{10}
26.67	4.179	995.8	8.60	0.614	5.85	2.48×10^{10}
32.22	4.174	994.9	7.65	0.623	5.12	3.3×10^{10}
37.78	4.174	993.0	6.82	0.630	4.53	4.19×10^{10}
43.33	4.174	990.6	6.16	0.637	4.04	4.89×10^{10}
48.89	4.174	988.8	5.62	0.644	3.64	5.66×10^{10}
54.44	4.179	985.7	5.13	0.649	3.30	6.48×10^{10}
60.0	4.179	983.3	4.71	0.654	3.01	7.62×10^{10}
65.55	4.183	980.3	4.30	0.659	2.73	8.84×10^{10}
71.11	4.186	977.3	4.01	0.665	2.53	9.85×10^{10}
76.67	4.191	973.7	3.72	0.668	2.33	1.09×10^{11}
82.22	4.195	970.2	3.47	0.673	2.16	
87.78	4.199	966.7	3.27	0.675	2.03	
93.33	4.204	963.2	3.06	0.678	1.90	1.23×10^{11}
104.4	4.216	955.1	2.67	0.684	1.66	
115.6	4.229	946.7	2.44	0.685	1.51	
126.7	4.250	937.2	2.19	0.685	1.36	
137.8	4.271	928.1	1.98	0.685	1.24	
148.9	4.296	918.0	1.86	0.684	1.17	2.81×10^{11}
176.7	4.371	890.4	1.57	0.677	1.02	
204.4	4.467	859.4	1.36	0.665	1.00	5.02×10^{11}
232.2	4.585	825.7	1.20	0.646	0.85	
260.0	4.731	785.2	1.07	0.616	0.83	8.59×10^{11}
287.7	5.024	735.5	9.51×10^{-5}			
315.6	5.703	678.7	8.68			

TABLE C.7 Properties of Saturated Liquids

T ($^{\circ}\text{C}$)	ρ (kg/m^3)	C_p ($\text{kJ}/\text{kg} \cdot ^{\circ}\text{C}$)	ν (m^2/s)	k ($\text{W}/\text{m} \cdot ^{\circ}\text{C}$)	α (m^2/s)	Pr	β (K^{-1})
Ethylene glycol, $\text{C}_2\text{H}_4(\text{OH})_2$							
0	1130.75	2.294	57.53×10^{-6}	0.242	0.934×10^{-7}	615	
20	1116.65	2.382	19.18	0.249	0.939	204	0.65×10^{-3}
40	1101.43	2.474	8.69	0.256	0.939	93	
60	1087.66	2.562	4.75	0.260	0.932	51	
80	1077.56	2.650	2.98	0.261	0.921	32.4	
100	1058.50	2.742	2.03	0.263	0.908	22.4	
Engine Oil (Unused)							
0	899.12	1.796	0.00428	0.147	0.911×10^{-7}	47,100	
20	888.23	1.880	0.00090	0.145	0.872	10,400	0.70×10^{-3}
40	876.05	1.964	0.00024	0.144	0.834	2870	
60	864.04	2.047	0.839×10^{-4}	0.140	0.800	1050	
80	852.02	2.131	0.375	0.138	0.769	490	
100	840.01	2.219	0.203	0.137	0.738	276	
120	828.96	2.307	0.124	0.135	0.710	175	
140	816.94	2.395	0.080	0.133	0.686	116	
160	805.89	2.483	0.056	0.132	0.663	84	

TABLE C.8 Properties of Air at Atmospheric Pressure

T (K)	ρ (kg/m^3)	C_p ($\text{kJ}/\text{kg} \cdot ^{\circ}\text{C}$)	μ ($\text{kg}/\text{m} \cdot \text{s} \times 10^5$)	ν ($\text{m}^2/\text{s} \times 10^6$)	k ($\text{W}/\text{m} \cdot ^{\circ}\text{C}$)	α ($\text{m}^2/\text{s} \times 10^4$)	Pr
100	3.6010	1.0266	0.6924	1.923	0.009246	0.02501	0.770
150	2.3675	1.0099	1.0283	4.343	0.013735	0.05745	0.753
200	1.7684	1.0061	1.3289	7.490	0.018090	0.10165	0.739
250	1.4128	1.0053	1.4880	9.49	0.022270	0.13161	0.722
300	1.1774	1.0057	1.9830	16.840	0.026240	0.22160	0.708
350	0.9980	1.0090	2.0750	20.760	0.030030	0.29830	0.697
400	0.8826	1.0140	2.2860	25.900	0.033650	0.37600	0.689
450	0.7833	1.0207	2.4840	31.710	0.037070	0.42220	0.683
500	0.7048	1.0295	2.6710	37.900	0.040380	0.55640	0.680
550	0.6423	1.0392	2.8480	44.340	0.043600	0.65320	0.680
600	0.5879	1.0551	3.0180	51.340	0.046590	0.75120	0.680
650	0.5430	1.0635	3.1770	58.510	0.049530	0.85780	0.682
700	0.5030	1.0752	3.3320	66.250	0.052300	0.96720	0.684
750	0.4709	1.0856	3.4810	73.910	0.055090	1.07740	0.686
800	0.4405	1.0978	3.6250	82.290	0.057790	1.19510	0.689
850	0.4149	1.1095	3.7650	90.750	0.060280	1.30970	0.692
900	0.3925	1.1212	3.8990	99.300	0.062790	1.42710	0.696
950	0.3716	1.1321	4.0230	108.200	0.065250	1.55100	0.699
1000	0.3524	1.1417	4.1520	117.800	0.067520	1.67790	0.702
1100	0.3204	1.1600	4.4400	138.600	0.07320	1.9690	0.704
1200	0.2947	1.1790	4.6900	159.100	0.07820	2.2510	0.707
1300	0.2707	1.1970	4.9300	182.100	0.08370	2.5830	0.705
1400	0.2515	1.2140	5.1700	205.500	0.08910	2.9200	0.705
1500	0.2355	1.2300	5.4000	229.100	0.09460	3.2620	0.705
1600	0.2211	1.2480	5.6300	254.500	0.10000	3.6090	0.705
1700	0.2082	1.2670	5.8500	280.500	0.10500	3.9770	0.705
1800	0.1970	1.2870	6.0700	308.100	0.11100	4.3790	0.704
1900	0.1858	1.3090	6.2900	338.500	0.11700	4.8110	0.704
2000	0.1762	1.3380	6.5000	369.000	0.12400	5.2600	0.702
2100	0.1682	1.3720	6.7200	399.600	0.13100	5.7150	0.700
2200	0.1602	1.4190	6.9300	432.600	0.13900	6.1200	0.707
2300	0.1538	1.4820	7.1400	464.000	0.14900	6.5400	0.710
2400	0.1458	1.5740	7.3500	504.000	0.16100	7.0200	0.718
2500	0.1394	1.6880	7.5700	543.500	0.17500	7.4410	0.730

Source: Data from J. P. Holman. 1981. *Heat Transfer* (McGraw Hill, New York).

TABLE C.9 Experimental Heat Capacities of Polymers

Polymer	\bar{C}_p^s (298 K) (J/kg · K)	\bar{C}_p^m (J/kg · K)
Polyethylene	1550/1760	2260
Polypropylene	1630/1760	2140
Polybutene	1550/1760	2140
Polyvinylchloride (PVC)	960/1090	1220
Nylon 6	1470	2140/2470
Nylon 6,6	1470	
Polystyrene	1220	1720
PET	1130	1550

Source: Data from D. W. Van Krevelen. 1992. *Properties of Polymers* (Elsevier, Amsterdam).

In the event experimental data are not available for $C_p(T)$, the following expressions can be used for estimating the heat

capacity in the solid state, C_p^s , and in the melt state, C_p^m (Van Krevelen, 1990):

$$\bar{C}_p^s(T) = \bar{C}_p^s(298 \text{ K})[0.106 + 3 \times 10^{-3}T] \quad (\text{C.1})$$

$$\bar{C}_p^m(T) = \bar{C}_p^m(298 \text{ K})[0.64 + 1.2 \times 10^{-3}T] \quad (\text{C.2})$$

where T is in kelvin units (K) and C (298 K) and C are given in Table C.9 for a number of common polymers. Equation C.1 is valid for $T_g \leq T \leq T_m$ and Eq. C.2 for $T > T_m$ for semicrystalline polymers. For amorphous polymers, Eq. C.2 is used for $T > T_g$.

APPENDIX D

CONVERSION TABLE

To Convert from	To	Multiply by
Force		
lb _f	kg · m · s ⁻² (newtons)	4.4482
lb _m · ft · s ⁻² (poundals)	newtons	1.3826 × 10 ⁻¹
Pressure		
lb _f · in. ⁻²	kg · m ⁻¹ · s ⁻² (N · m ⁻²)	6.8947 × 10 ³
atmospheres	N · m ⁻²	1.0133 × 10 ⁵
Energy		
Btu	kg · m ² · s ⁻² (joules)	1.0550 × 10 ³
cal	kg · m ² · s ⁻²	4.1840
Viscosity		
lb _f · s · ft ⁻²	kg · m ⁻¹ · s ⁻¹ (Pa · s)	4.7880 × 10 ¹
g · cm ⁻¹ · s ⁻¹ (poise)	kg · m ⁻¹ · s ⁻¹	10 ⁻¹
Thermal conductivity		
Btu · h ⁻¹ · ft ⁻¹ · °F ⁻¹	kg · m · s ⁻³ · K ⁻¹	1.7307
cal · s ⁻¹ · cm ⁻¹ · K ⁻¹	(W · m ⁻¹ · K ⁻¹) W · m ⁻¹ · K ⁻¹	4.184 × 10 ²
Heat transfer coefficients		
Btu · ft ⁻² · h ⁻¹ · °F ⁻¹	kg · s ⁻³ · K ⁻¹ (W · m ⁻² · K ⁻¹)	5.6782
cal · cm ⁻² · s ⁻¹ · K ⁻¹	W · m ⁻² · K ⁻¹	4.1840 × 10 ⁴
Mass transfer coefficients		
lb _m · ft ⁻² · h ⁻¹	kg · m ⁻² · s ⁻¹	1.3562 × 10 ⁻³
lb _f · ft ⁻³ · s	kg · m ⁻² · s ⁻¹	1.5709 × 10 ²

INDEX

- Absorption coefficient, 135
- Activation energy of diffusion, 84–86
- Air, properties at atmospheric pressure, 383
- Amorphous polymers, thermal properties, 120
- Annular dies, 216–219
 - center-fed, 216–217
- Annular swell, 209
- Avrami equation, 140, 143, 289

- Baker's transformation, 190
- Ballman method, 58–59
- Barrier polymers, 87, 102
- Beer's law, 134
- Biaxial stretching, 38, 68, 304
- Binary systems
 - definitions for concentrations, 75
 - definitions for velocities, 75
 - mass and molar fluxes, 77
- Bingham fluid, 11
- Bingham model, 12, 303
- Binomial distribution, 158
- Birefringence, 142–145, 278, 289
- Blending, 156
- Blend morphology, 187
- Blow molding, 3
 - die design, 212–225
 - simulation, 329–331
 - technological aspects, 328
- Blow ratio, 298, 301–302
- Blowup ratio (BUR), 298
- Bradley–Hamaker theory, 181
- Branching, 61–62
- Bulk diffusion, 155

- Burst time, 184, 186–188
- Bursting modes, 184
- Bursting process, 184, 187

- Capillary breakup, 187, 291
- Capillary rheometer, 56–57
- Capillary waves, 186, 290–291
- Carbon dioxide, 84
 - in polycarbonate, 85
 - permeability, 89
- Carreau viscosity model, 65
- Cartesian coordinate system, 294, 298–299
- Cauchy–Green strain tensor, 170, 194
- Circular tube pressure flow, 21
- Clapeyron equation, 142
- Closed-loop recycling, 345
- Closely intermeshing
 - corotating twin screw extruders, 236, 254
 - counter-rotating twin screw extruders, 239, 253, 256
- Coathanger manifolds, 230
- Coextrusion, 153
 - blow-molding die, 201
 - dies, 223, 224
 - film die, 225
- Cohesionless cluster, 181
- Cohesive (brittle) fracture, 290
- Cohesive cluster, 181
- Cohesive energy density (CED), 291
- Cold drawing, 2, 142, 297
- Collision diameter, 84–85
- Complementary error function, 94
- Composite systems, thermal properties of, 123–124
- Compounding, 155

- Compression molding, 4
 general aspects, 319–320
 Newtonian fluid, 322
 process, 311
 simulation, 320–321
 Computer solution, 29–30
 Cone-and-plate rheometer, 56
 Confidence intervals, 158
 Connectivity indices, 90
 Consistency, 11
 Constitutive equation, 51
 nonlinear, 44–54
 nonlinear viscoelastic, 38, 51
 viscoelastic fluids, 38
 Continuity equations, 78
 Continuous filament-reinforced composite extruded profiles, 4
 Convective transport, 155
 Conversion tables, 385
 Cooling
 injection-molded slab, 127
 nondeforming polymeric materials, 124
 of strand in pelletizing bath, 131
 Correlation coefficient, 161–163
 Correlation function, 161
 Correlogram, 162–163
 Couette flow, 171–175
 Cox–Merz rule, 61
 Cradle-to-grave analysis, 344
 Crystalline morphology, 288
 Crystallinity, 85–86, 287–288
 Crystallization, 124, 135–149, 288–289
 factors affecting, 142
 in quiescent state, 136

 Deborah number, 42, 51, 95, 221, 285
 Devolatilization, 235, 262–266
 Die, 1, 201–234. *See also* Under specific types of dies
 design, 9–30
 geometries, 1
 land length, 6
 radius, 18
 recommendations, 6
 swell, 207–212
 Diffusion, 73–109
 activation energy of, 84–86
 case I (or Fickian), 95
 case II (or non-Fickian), 93, 95
 in falling polymer film, 83–84
 Fick's first law, 74, 76–77, 103
 Fick's second law, 80, 106
 in multidimensional objects, 82
 polymer–polymer, 93
 similarity with heat transfer, 80–81
 in slab, 81
 theory, 105, 267
 velocity, 75–76
 Diffusion coefficient, 76, 80, 84
 Diffusion equation, 80, 99–100

 Diffusivity, 84–103
 measurement technique, 94–95
 Dilatant, 11
 Dimensional analysis, 265–268
 Dimensionless tension, 287
 Dimethylformamide (DMF), 73, 100–101
 Dipole throwing, 162
 Dispersion of agglomerates, 180–182
 Draw ratio, 142–143, 292
 Draw resonance, 290, 296, 304
 Dry-spinning system, 73, 100

 Eddy diffusion, 155, 157
 Elliptic point, 189
 Ellis model, 10–14, 226
 Elongational flow, 38, 45, 165
 Energy equation, 113–120
 Energy flux, components of, 118
 Equation of thermal energy, 118, 119
 Error function, 84
 Extra stress tensor, 39, 168, 278
 Extrudate
 nonuniformities, 202
 swell, 207, 212
 Extruders, 234–273. *See also* Single-screw extruders; Twin-screw extruders, and under specific types
 description of, 235–238
 Extrusion, 1
 instabilities, 203
 of polymer melt for film blowing, 26
 Extrusion blow molding, 329
 Extrusion die, *see* Die

 Fast Fourier transform (FFT) method, 163
 Feedstock recycling, 345, 354
 Fiber aspect ratio, 52, 54
 Fiber flexibility, 52
 Fiber spinning, 2, 276–293
 high-speed spinning and structure formation, 287–290
 instabilities, 290–293
 key aspects of, 277
 processes involved, 277–278
 speeds, 277
 steady-state solution, 281
 Fiber suspensions, 52–55
 Fick's first law of diffusion, 74, 76–77, 103
 Fick's second law of diffusion, 80, 106
 Film blowing, 2–3, 297–305
 case study, 5–7
 garbage bags, 275–276
 physical properties of film, 5–6
 stability, 304
 Film casting, 112, 293–297
 stability, 296–297
 Film die, 114, 212–215, 225–226
 Film stretching, 297
 Filtration media, 353
 Flat-film production, 293

- Flory–Huggins swelling behavior, 91
- Flow
- instabilities in multiple layer, 227–228
 - through a tapered tube, 27
 - through an annular die, 14–17
 - in wirecoating die, 17–18
- Fluxes, 76–79
- Folgar–Tucker model, 53–54
- Forming, 2–5
- Fourier’s law, 114, 115, 119–120
- Friction coefficient, 70, 379
- Fully oriented yarn (FOY), 288
- Garbage bag, film-blowing process for, 275
- Gas-polymer system, 85, 87
- Gas, simple, 84, 87–90
- Generalized Newtonian fluid (GNF), 13, 24, 44, 116, 118–120, 119, 220, 354
- Glass transition temperature, 86, 120, 187–188, 359, 362, 382
- Glasses, 276, 291
- Gleissle’s mirror relation, 61
- Growth rate, 138–140, 288
- Hamiltonian structure, 189
- HDPE
- branching, 61
 - coathanger manifolds, 230
 - coextrusion, 225
 - cooling injection-molded slab, 127
 - dynamic oscillatory shear data, 373
 - film blowing, 206
 - flow behavior, 203
 - flow rate, 226
 - flow through pipe die, 116
 - forming, 2
 - fracture, 203
 - molecular weight parameters, 209
 - parameters, 20
 - parison, 9
 - physical properties, 136
 - pipe, 14
 - and shear rate, 206
 - slip-stick, 207
 - steady shear data, 373
 - thermal-physical properties, 381
 - viscosity, 229
 - viscous dissipation, 115
- Heat capacity, 113, 120–121, 384
- Heat conduction, 80–81
- in nondeforming systems, 125–130
- Heat flux, 130, 132
- Heat of fusion, 120, 124
- Heating, nondeforming polymeric materials, 124
- Heat of sorption, 87
- Heat transfer, 124
- and mass transfer, 97
 - similarity with diffusion problems, 80–84
- Heat transfer coefficient, 129, 130–132
- Hele–Shaw flow, 316, 319
- Helix angle, 237
- Henry’s law, 86, 90, 93, 237
- Hershel–Bulkley model, 12
- Heteroclinic point, 189
- High density polyethylene, *see* HDPE
- Hole pressure, 58
- Homoclinic point, 189
- Hopper design, 239–242
- Hydrodynamic force, 181–183
- Hydrodynamic stability/instability, 291
- Hydrophilic polymer, 90
- Hydrophobic polymer, 90
- Hyperbolic point, 189
- Injection molding, 4, 311–319
- general aspects, 319–320
 - simulation, 315–318
 - tooling design, 315
- Intensity of segregation, 161–163
- Interdiffusion coefficient, 76
- Interface growth function, 167–168
- Internal bubble cooling (IBC), 302
- Isothermal flow
- one-dimensional, 13–19
 - purely viscous non-Newtonian fluids, 9–35
- Isothermal systems, equations of change for, 19–25
- Jeffrey’s equation, 53
- Kelvin–Voight two-element model, 303
- Kenics static mixer, 190, 261
- Kinetic crystallizability, 289
- Kneading, 156
- Kronecker delta, 39
- LDPE
- branching, 61
 - capillary rheometer data, 374
 - and die swell, 207
 - dynamic oscillatory shear data, 373
 - extensional data, 374
 - and extrudate swell, 207
 - film blowing, 275, 304
 - flow behavior, 203
 - fracture, 204
 - melt flow characteristics, 63
 - primary normal stress difference data, 373
 - and shear rate, 206, 207
 - solids conveying, 245
 - steady shear viscosity, 373
 - viscosity, 203
- Leibnitz rule, 282
- Lennard–Jones equation, 84
- Lennard–Jones scaling factors, 84
- Lennard–Jones temperature, 84, 86
- Level of significance, 159–160

- Liapunov exponent, 189–190
- Life-cycle analysis, 344
- Life-cycle assessment, 344
- Life-cycle inventory, 344
- Linear low density polyethylene, *see* LLDPE
- Linear polycondensates, 291
- Liquid-liquid dispersion, 182–188
- LLDPE
- branching, 61
 - capillary data, 376
 - dynamic shear data, 375
 - extensional data, 376
 - film, 302
 - film blowing, 304
 - fracture, 205, 207
 - power-law parameters, 13
 - slip-stick, 207
 - steady shear data, 375
- Low density polyethylene, *see* LDPE
- Loss angle, 188
- Lubrication approximation, 26–28, 215–217
- Machine direction (MD), 6
- Mandrel support system, 217
- Mass average bulk velocity, 74
- Mass average velocity, 75–77
- Mass concentration, 74–75
- Mass diffusion, 81
- Mass diffusivity, 76
- Mass flux, 76–79
- Mass fraction, 73–75
- Mass transfer, 73–109
- Chilton–Colburn j -factor, 98
 - fundamentals, 74–84
 - and heat transfer, 97
- Mass transfer coefficient, 73, 96–99
- Masterbatch, 182
- Material functions
- for shear flow, 40–43
 - for shear-free flow, 43
 - useful relations for, 60–62
 - for viscoelastic fluids, 38–44
- Mechanical recycling, 347–348
- Mesh size, 353
- Meissner method, 58–59
- Melt extrusion temperature, 6
- Melt flow characteristics, 63
- Melt fracture, 2, 203, 290
- Melt spinning, 2, 276
- materials, 290
 - physical and mechanical properties of fibers, 278
 - process, 277
- Melt temperature, 123
- Metal, 291, 354
- Methane, 84, 90–92
- Methyl methacrylate (MMA), 235, 265, 267–268
- Microinjection molding, 4, 318–319
- Milling, 156
- Mixing, 153–199, 258–262
- basic types, 155
 - chaotic, 189–191
 - characterization of the state degree of, 157, 160, 191
 - description of, 154–156
 - dispersive, 155–157, 180–188
 - effects of deformation types, 165–167
 - efficiency, 169–171
 - goodness of, 160
 - index of, 160
 - laminar, 164–173
 - measurement techniques, 163–164
 - of mixture, 156–164
 - perfect, 160, 174–177
 - in plane Couette flow, 171
 - rule, 348, 350–352
 - in simple geometries, 171–173
 - statistical description, 157–161
 - thermodynamics of, 188–189
 - time average efficiency, 170, 188
- Modulus of elasticity, 297
- Moisture sorption, 90
- Molar average bulk velocity, 75
- Molar average velocity, 75–76, 80
- Molar concentration, 74–75
- Molar flux, 76–78, 79
- Molar permachor, 89
- Molar water content, 91
- Molecular diffusion, 75, 155
- Molecular orientation, 135, 143–145, 288–289
- Molecular stresses, 39
- Molecular weight, 60, 209
- Mole fraction, 74–77
- Monofilament, 277, 352
- Morphology, crystalline, 135, 288, 291
- Mulling, 156
- Multilayer extrusion, 222–228
- Multilayer flow, flow instabilities in, 227–228
- Multilayered extrusion die, 153
- Multistage die, 220
- Mutual diffusion coefficient, 76
- Natural rubber, 86–87, 89, 124
- Navier–Stokes equations, 20
- Necking, 59, 290
- Needle throwing, 162
- Nematic liquid crystalline phase, 52
- New-to-world renewable polymer, 343, 357
- Newtonian fluid, 10, 11, 15, 20, 24, 39, 175, 180–185, 220, 247, 252, 254, 255, 261, 317, 327
- compression molding, 322
 - radial flow between two parallel disks, 24
- Newtonian isothermal model, 278–281, 299–302
- Newtonian nonisothermal model, 281–285, 302–303
- Newton's law of cooling, 130
- Newton's law of viscosity, 11, 15, 20
- Non-Fickian transport, 95–96
- Non-Newtonian fluid, 11, 16, 26, 260

- Non-Newtonian nonisothermal model, 303–304
 Normal distribution, 159
 Nucleation, 136–139, 288–289
 Nucleation factor, 139
 Nusselt number, 80, 114
 Nylon 6, 89, 227, 228
 thermal-physical properties, 381
 Nylon 6,6, 89, 140, 280–281
 steady shear cone-and-plate data, 376
 thermal-physical properties, 382

 Open-loop recycling, 345
 Orientation function, 143–144
 Orientation tensor, 52–54
 Orifice die, 220
 Ostwald–de Waele power-law, 11

 Parallel plate pressure flow, 20
 Parison, 9, 14, 328–330
 diameter, 27
 inflation, 331
 sagging, 331
 Parison die, design for viscoelastic fluid, 37
 Peclet number, 52, 97, 114, 264
 Permachor, 87–90
 Permanent gas, 84
 Permeability, 87–90
 measurement techniques, 94–95
 Permeability parameter, 88
 PETG, 329–330
 PETP, 86–87, 121, 139, 286, 329–330
 Phan–Thien–Tanner (PTT) model, 45–49, 65
 Pipe die, 216
 nonisothermal flow, 116
 Planar elongational flow, 165, 169, 171, 184–185
 Planar extensional flow, 38–39, 330–332
 Planck's distribution, 134
 Plasticating extruder, 237, 239, 242–253
 Plate-plate (P-P) rheometer, 51
 Plug flow, 101, 164, 174–177, 259–260
 Poiseuille flow, 166, 174–176, 179, 191
 Poisson distribution, 158
 Polyacrylonitrile (PAN), 73, 89, 100–101, 188
 Poly(aryl ether ketone ketone) (PEKK), 123
 Polybutylene (PB1), 5–7
 Polycaprolactam, thermal-physical properties, 381
 Polycarbonate (PC), 85, 87, 89, 92, 120–121, 351
 carbon dioxide in, 92
 Polyetheretherketone (PEEK), 112, 123, 124, 140, 319
 crystallization parameters, 382
 Polyetheretherketone, (PEEK)/carbon fiber composites, 124
 Polyethylene (PE), 5, 61–62, 93, 143, 155, 347, 357. *See also*
 HDPE, LDPE, LLDPE
 Poly(ethylene carbonate), 357
 Poly(ethylene furanone), 357
 Polyethyleneterephthalate (PET), 3, 124, 134, 135, 142, 277–278,
 283, 287–288, 348
 thermal-physical properties, 381

 Poly(hydroxyl butyrate), 361
 Poly(hexamethylene adipamide) thermal-physical properties, 382
 Polyisobutylene (PIB), 61, 89, 206
 Polylactic acid, 347, 357
 Polymer melts
 rheological data for, 373
 viscous behavior of, 10–11
 Polymer membrane-penetrant system, 77
 Polymer-polymer diffusion, 93
 Polymer processability, 62–64
 Polymer process design, 1–8
 basics of, 7–8
 Polymer processes, classification, 1–5
 Polymer processing, Nonisothermal aspects, 111–151
 Poly(methyl acrylate) (PMA) 90
 Polymethylmethacrylate (PMMA), 103, 121, 153, 235, 265, 266,
 319
 Polymethylmethacrylate (PMMA)-methanol system, 96
 Polyolefins, 59, 61, 90, 291, 329
 Polyphenylene sulfide (PPS), 41–43, 112, 123–124, 139, 297
 dynamic oscillatory shear data, 377
 shift factors, 377
 Polypropylene (PP), 81, 89, 138, 140, 145, 211, 284, 297, 311,
 322, 352
 cooling of film, 113
 film-casting, 111
 Polystyrene (PS), 43–46, 93, 153, 205, 287, 313
 Polysulfone, 123
 Poly(vinyl acetate) (PVAc), 86–87
 Poly(vinylchloride) (PVC), 121–122, 220–222, 239
 Poly(vinylidene chloride), 88–89
 Postdie processing, 2, 275–309
 Power law fluid, radial flow of, 25
 Power law parameters, program listing, 12, 13
 Power spectrum, 163
 Pre-exponential factor, 86, 90
 Pre-exponential permeability factor, 88
 Preform, 125, 328–330
 Pressure coating dies, 218
 Primary recycling, 343, 348
 Profile extrusion dies, 220–222
 Pultrusion, 4–5
 Pure shear, 165, 184–185, 297

 Radial flow
 of power-law fluid, 25
 between two parallel disks, 24
 Radiation heat transfer, 132–135
 Random chain dissociation, 355
 Regrind, 348–351
 Renewable polymers, 343, 357–362
 Rate-of-strain tensor, 23
 Rayleigh instabilities, 291
 Reaction injection molding (RIM), 4
 Reactive extrusion, 264–265
 Refractive index, 95, 153
 Reptation theory, 94
 Residence time, 174–180, 187–188, 259–261, 360

- Residence time distribution (RTD), 174–177, 258–260
- Reynolds number, 19, 99, 291
- Rheological data for polymer melts, 373
- Rheological measurements, 62–64
- Rheological properties, temperature and pressure effects, 111–113
- Rheometry, 55–60
- Rheotens, 59
- Rotary diffusivity, 52
- Rotary Peclet number, 52
- Rotary rheometer, 56, 60
- Rotational Couette flow (RCF), 172–173, 179
- Saturated liquids, properties of, 383
- Saturation moisture content, 90
- Scale factor, 194
- Scale of segregation, 161, 163–164
- Scaleup, 305
- Scaling factor, 84, 88
- Scoping, 344
- Screw
 - elements of, 240
 - geometry of, 238
- Secondary recycling, 351
- Self-diffusion coefficient, 93, 94
- Self-wiping corotating twin-screw extruders, 253–256
- Semicrystalline polymer
 - physical properties, 136
 - thermal properties, 121–122
- Shear, flow measurements, 56–58
- Shear flow, 38, 39
 - experiments, 40
 - material functions for, 40–43
- Shear-free flow, 37–40
 - material functions for, 43–44
 - measurements of, 58–60
- Shear strain, 165, 167
- Shear stress, 11
- Shear thinning, 13, 16
- Sheet dies, 212–215
- Sheet forming, 2
- Shell energy balances, 113–117
- Sherwood number, 80, 97, 99
- Side-fed mandrel dies, 216
- Significance test, 159–160
- Silicone oil, 61, 292
- Silicone rubber, 86–92
- Simple shear flow, 166–169
- Single-screw extruders, 1, 235–238, 242–253
 - delay and melting zones, 246–249
 - devolatilization, 262–264
 - metering section, 250–253
 - mixing, 260–261
 - solids transport through, 242–246
- Slip coefficient, 54
- Slit-die rheometers, 53
- Smale horseshoe map, 189–190
- Solid-phase forming, 4
- Solids transport through single-screw extruder, 242–246
- Solubility, 84, 188
 - measurement techniques, 94
- Solution casting, 99
- Spinnability, 290–292
- Spinneret plate, 277
- Spinning, *see* Fiber spinning
- Spiral mandrel dies, 216–218
- Static mixer, 190, 261–262
- Steady shear flow, 40–42, 48, 189
- Steady shear-free flow, 48
- Steady simple shear flow, 11, 38, 47–48
- Stereology science, 163
- Strain, 166–168
- Strain distribution function (SDF), 177–180
- Strain distributions, 174, 177–180
- Stress growth experiment, 42, 44, 48
- Stress-optical coefficient, 145
- Stress relaxation, 40, 48
- Stress tensor component, 39, 49
- Striation thickness, 164–173
 - reduction from geometrical arguments, 164–167
 - reduction from kinematical arguments, 169–171
 - in rotational Couette flow (RCF), 172
- Striation thickness reduction, effects of reorientation, 171–172
 - function, 170, 173, 193
- Student's *t* distribution, 159
- Sulfur dioxide, 84
- Superconcentrates, 182
- Surface temperature, step change in, 125–127
- Tadmor melting model, 247
- Tapered profile dies, 220
- Temperature dependence of physical properties, 122
- Tensile moduli, 136
- Tertiary recycling, 347, 354
- Thermal conductivity, 114, 120–121, 318
- Thermal properties, 381
 - of composite systems, 123–124
 - homogeneous polymer systems, 120
 - semicrystalline polymer, 121–122
- Thermal transport properties, 120–124
- Thermoforming, 3, 133
 - general aspects, 322
 - inflation pressure of bubble, 327
 - modeling, 322–328
 - wall thickness distribution, 325, 326
- Thermoplastics, processing, 1, 4
- Thermoplastic starch, 343, 357
- Thermosetting systems, processing, 4
- Thickness swell, 65
- Thin-filament theory, 281, 308
 - assumptions of, 281
 - equations of, 281–283
 - experimental correlations, 283–285
- Thread breakup, 186–187
- Throttle ratio, 252
- Time lag, 94, 176
- Toluene-polystyrene system, 92

- Tortuosity of crystallites, 89
- Total stress components, 39
- Tracer diffusion coefficient, 93
- Transverse direction (TD), 6
- Transverse heteroclinic point, 189
- Transverse homoclinic point, 189
- Tube-coating dies, 218
- Tubular blownfilm process, 304
- Twin-screw extruders, 1, 237, 238–239, 253–257
 - devolatilization, 262–264
 - mixing, 260

- Uniaxial elongational flow, 166, 169, 185
- Uniaxial extensional flow, 38, 43, 58, 166
- Upper convected Maxwell (UCM) model, 45

- Van der Waals force, 181
- Vinyl polymers, 291
- Viscoelastic fluids, 327
 - material functions for, 38–44

- Viscoelastic isothermal model, 285–287
- Viscoelastic phenomena, 203
- Viscoelastic properties, linear, 61
- Viscoelastic response of polymeric fluids, 37–71
- Viscoelastic functions, 61
- Viscous behavior of polymer melts, 10–13
- Viscous dissipation, 114

- Water, properties of, 382
- Weighted average total strain (WATS), 177, 260
- Weissenberg number, 42
- Weld lines, 217, 314–315
- White–Metzner (WM) model, 45–48, 65, 286, 296
- Wide-angle X-ray diffraction, 144
- Wide-angle X-ray scattering (WAXS), 143–144
- Williams–Landel–Ferry (WLF) equation, 112, 139, 283
- Wire coating die, 2, 17, 217–220
- Wire speed, 18

- Yield stress, 11–12, 140